SCHOLARLY PUBLICATIONS

A CURRENT AWARENESS BULLETIN
OF RESEARCH OUTPUT

@DTU

(99th Edition)

MARCH 2021

BY: CENTRAL LIBRARY

DELHI TECHNOLOGICAL UNIVERSITY
(FORMERLY *DELHI COLLEGE OF ENGINEERING)*
GOVT. OF N.C.T. OF DELHI
SHAHBAD DAULATPUR, MAIN BAWANA ROAD
DELHI 110042

PREFACE

This is the **Ninety Ninth** Issue of Current Awareness Bulletin started by Delhi Technological University, Central Library. The aim of the bulletin is to compile, preserve and disseminate information published by the faculty, students and alumni for mutual benefits. The bulletin also aims to propagate the intellectual contribution of Delhi Technological University (DTU) as a whole to the academia.

The bulletin contains information resources available in the internet in the form of articles, reports, presentations published in international journals, websites, etc. by the faculty and students of DTU. The publications of faculty and student which are not covered in this bulletin may be because of the reason that the full text either was not accessible or could not be searched by the search engine used by the library for this purpose.

The learned faculty and students are requested to provide their uncovered publications to the library either through email or in CD, etc. to make the bulletin more comprehensive.

This issue contains the information published during **March, 2021**. The arrangement of the contents is alphabetical. The full text of the article which is either subscribed by the university or available in the web is provided in this bulletin.

Central Library

CONTENTS

1. A Comparative Analysis of Query-Constrained Video Summarization Techniques, ***3.Anil Singh Parihar***, ***8.Priyansh Verma***, ***8.Prashansa Bhattacharyya*** and ***8.Rohit Goyal***, CSE, DTU

2. A Comparative Study on CNN based Low-light Image Enhancement, ***8.Kanishk Jayant Lal***, ***8.Deepanshu Rana*** and ***3.Anil Singh Parihar***, CSE, DTU

3. A delayed version of prey predator system with modified Holling-Tanner response, Charu Arora and ***3.Vivek Kumar***, Mathematics, DTU

4. A Novel Approach to Computationally Lighter GNSS-Denied UAV Navigation Using Monocular Camera, ***8.Joyraj Bhowmick***, ***8.Anurag Singh***, ***8.Harshit Gupta*** and ***3.Raghava Nallanthighal***, Electrical, DTU

5. A novel biometric crypto system based on cryptographic key binding with user biometrics, ***6.Rajesh Asthana***, Gurjit Singh Walia and ***3.Anjana Gupta***, Mathematics, DTU

6. A Particle Swarm Optimization-Based Cooperation Method for Multiple-Target Search by Swarm UAVs in Unknown Environments, ***8.Aniket Gupta***, ***8.Aman Virmani***, ***8.Parth Mahajan*** and ***3.Raghava Nallanthigal***, DTU

7. A Study on Machine Learning Applied to Software Bug Priority Prediction, ***3.Ruchika Malhotra***, ***8.Ajay Dabas***, ***8.Hariharasudhan A S*** and ***8.Manish Pant***, CSE, DTU

8. Adaptation to climate change induced water stress in major glacierized mountain regions, ***6.Anubha Aggarwal***, Holger Frey, Graham McDowell, Fabian Drenkhan, Marcus Nuesser, Adina Racoviteanu and Martin Hoelzle, Civil, DTU

9. ADAPTIVE MPPT ALGORITHM FOR SPV SYSTEM UNDER PARTIAL SHADING CONDITION, ***6.Pallavi Verma***, ***3.Rachana Garg*** and ***3.Priya Mahajan***, Electrical, DTU

10. AlignPIN: Indirect PIN Selection For Protection Against Repeated Shoulder Surfing, ***8.Shreyans Jain***, ***8.Shristi Dabola***, ***8.Shikhar Binjola*** and ***3.Rajni Jindal***, CSE, DTU

11. An efficient image encryption scheme using elementary cellular automata with novel permutation box, ***6.Ashish Kumar*** and ***3.N. S. Raghava***, IT and Electronics, DTU

12. An Intelligent PI Controller-Based Hybrid Series Active Power Filter for Power Quality Improvement, Arjun Baliyan , Majid Jamil, ***3.M. Rizwan***, Ibrahim Alsaidan and Muhannad Alaraj, Electrical, DTU

13. Analysis of Photovoltaic (PV) Power Technology, ***8.Harsh Kumar Mishra***, ***8.Adarsh*** and ***3.Dr. Janardan Prasad Kesari***, Mechanical, DTU

14. ANALYSIS OF WAVE POWER TECHNOLOGIES, ***3.Dr JP Kesari***, ***8.Siddharth Sharma*** and ***8.Chanda Singh***, Mechanical, DTU

15. Application of Particle Swarm Optimization for Software Defect Prediction Using Object Oriented Metrics, ***3.Dr. Ruchika Malhotra***, ***8.Nishant***, ***8.Spandun Gurha*** and ***8.Vishal Rathi***, CSE, DTU

16. Assessment of elemental Carbon, Nitrogen, Hydrogen and Sulphur in alluvial sediments of River Yamuna in Delhi region, Vivek Chopra and ***3.Jai Gopal Sharma***, Biotechnology, DTU

17. Bag-of-Visual-Words codebook generation using deep features for effective classification of imbalanced multi-class image datasets, ***6.Manisha Saini*** and ***3.Seba Susan***, DTU

18. Car Traffic Sign Recognizer Using Convolutional Neural Network CNN, ***8.Abhay Lodhi***, ***8.Sagar Singhal*** and ***3.Massoud Massoudi***, CSE and Electronics, DTU

19. Comparison of ECC and RSA Algorithm with DNA Encoding for IoT Security, ***3.Malti Bansal***, ***8.Shubham Gupta*** and ***8.Siddhant Mathur***, Electronics, DTU

20. Comparison of Ferroelectric Photovoltaic Performance in BFO/ BTO Multilayer Thin Film Structure Fabricated Using CSD & PLD Techniques, SAVITA SHARMA, ANJALI SHARMA, VINAY GUPTA, ***3.NITIN K. PURI*** and MONIKA TOMAR, Physics, DTU

21. Computational Analysis of Machine Learning Algorithms to Predict Heart Disease, ***7.Kunal Rao***, ***7.Pawan Raj Gopal*** and ***3.Kusum Lata***, USME, DTU

22. Conceptual Design of Localized Vibration Proximity Belt for the Visually Impaired, ***8.Ayan Ahmad***, Applied Physics, DTU

23. Contrast Analysis of TTV-TDV Phase Difference Induced by Possible Exomoons, ***8.Ayan Ahmad***, Binayyak B. Roy, Aayushi Rajgor, Charmi Bhatt, Kedar Kulkarni and Pulkit Ojha, Physics, DTU

24. Control of Two-Stage OFF-Board Electric Vehicle Charger, ***6.Aakash Kumar Seth*** and ***3.Mukhtiar Singh***, Electrical, DTU

25. Controlled release and release kinetics studies of boron through the functional formulation of carboxymethyl tamarind kernel gum-based superabsorbent hydrogel, ***6.Khushbu***, ***3.Sudhir G. Warkar*** and Nandkishore Thombare, Chemistry, DTU

26. ConvNet Based Single Image Deraining Methods: A Comparative Analysis, ***3.Anil Singh Parihar***, ***8.Chirag Jasuja***, ***8.Devanshu Gupta*** and ***8.Harshit Gupta***, CSE, DTU

27. ConvNet frameworks for multi-modal fake news detection, ***7.Chahat Raj*** and ***3.Priyanka Meel***, IT, DTU

28. COVID-19: A Comprehensive Review of Epidemiology and Public Health System Response in Nordic Region, ***6.Mehak Nanda***, ***6.Aashima*** and ***3.Rajesh Sharma***, USME, DTU

29. Critical assessment on application of software for designing hybrid energy systems, ***8.Khemshika Ram***, ***8.Prasanna Kumar Swain***, ***8.Ruchita Vallabhaneni*** and ***3.Anil Kumar***, Mechanical, DTU

30. Cultural Exploitation of Rural Women Subjected to Menstrual Exile: A Review of Nepal and India, ***8.Pearl Khurana*** and Ankita Singh Gujjar, Economics, DTU

31. Current-mode Positive and Negative Rectifier based on DDCC suitable for Higher Frequency operations, ***6.Sweta Kumari*** and ***3.Deva Nand***, Electronics, DTU

32. Decentralized Multi-agent Formation Control via Deep Reinforcement Learning, ***8.Aniket Gutpa*** and ***3.Raghava Nallanthighal***, Electrical and Electronics, DTU

33. Deep Neural Architecture for Veracity Analysis of Multimodal Online Information, ***3.Priyanka Meel*** and ***3.Dinesh Kumar Vishwakarma***, IT, DTU

34. DETAILED ANALYSIS OF WIND ENERGY TECHNOLOGY AND ITS FUTURE IN INDIA, ***3.Dr. J.P Kesari***, ***8.Aditya Vikram Kochar*** and ***8.Anand Kumar Jha***, Mechanical, DTU

35. Development of Web Based Laboratory Prototype for Remote Monitoring and Control of Electrical Appliances, ***3.Mohammad Rizwan***, Ibrahim Alsaidan and Muhannad Alaraj, Electrical, DTU

36. Devising a Knowledge Culture, ***3.Nishant Gaur***[1] and ***6.Dr. Vikas Gupta***[2], [1]USME and [2]DSM, DTU

37. Diagnosing Covid-19 by CRISPR Technology, ***7.Vijay Pratap Singh***, Biotechnology, DTU

38. Effect of layering pattern and fiber hybridization on viscoelastic properties of PALF/COIR hybrid epoxy composites, ***6.Mohit Mittal*** and ***3.Rajiv Chaudhary***, Mechanical, DTU

39. Effects of Nonmonotonic Functional Responses on a Disease Transmission Model: Modeling and Simulation, ***6.Abhishek Kumar*** and ***3.Nilam***, Mathematics, DTU

40. ELECTRICITY GENERATION FROM SOLAR ENERGY, ***3.Dr. J.P Kesari***, ***8.Prashant Meena*** and ***8.Pankaj Garhwal***, Mechanical, DTU

41. Exploring the Effects of Different Embedding Algorithms and Neural Architectures on Early Detection of Alzheimer's Disease, ***3.Minni Jain***, ***8.Rishabh Doshi***, ***8.Vibhu Sehra*** and ***3.Divyashikha Sethia***, CSE, DTU

42. Facial Expression Recognition from 3D Facial Landmarks Reconstructed from Images, ***8.Limysh Kalapala***, ***8.Harshit Yadav***, ***8.Himanshu Kharwar*** and ***3.Seba Susan***, IT, DTU

43. Genetic particle filter improved fuzzy-AEEMD for ECG signal de-noising, ***3.Rajiv Kapoor*** and ***3.Rajesh Birok***, ECE, DTU

44. GPS2Vec: Pre-trained Semantic Embeddings for Worldwide GPS Coordinates, Yifang Yin, Ying Zhang, Zhenguang Liu, Sheng Wang, ***7.1.Rajiv Ratn Shah***, and Roger Zimmermann, CSE, DTU

45. Heat sink analysis in jet impingement with air foil pillars and nanoparticles, ***6.Deepak Kumar***, ***3.Mohammad Zunaid*** and ***3.Samsher Gautam***, Mechanical, DTU

46. High-efficient photoacoustic generation with an ultrathin metallic multilayer broadband absorber, CHUNQI ZHENG, HUANZHENG ZHU, ZIQUAN XU, ***3.RAVINDRA K. SINHA***, QIANG LI AND PINTU GHOSH, Applied Physics, DTU

47. IM-ELPR: Influence maximization in social networks using label propagation based community structure, ***3.Sanjay Kumar***, Lakshay Singhla, Kshitij Jindal, Khyati Grover and B. S. Panda, CSE, DTU

48. In Silico Drug Repositioning Of Hydroxychloroquine (HCQ) For the Treatment of Viral Diseases, ***6.Bhawna Singh*** and ***3.Asmita Das***, Biotechnology, DTU

49. Innovation Framework for Excellence in Higher Education Institutions, ***3.Manoj Kumar Sharma*** and ***3.R. C. Sharma***, USME, DTU

50. Integrated Vendor-Managed Time Efficient Application to Production of Inventory Systems, ***8.Bickey Kumar Shah***, ***8.Vansh Kedia*** and ***8.Rahul Kumar Jha***, CSE, DTU

51. Internet of Things (IoT) based Assistive Devices, ***3.Malti Bansal*** and ***8.Samarth Garg***, Electronics, DTU

52. Leveraging retention sales based innovative incentive structure to turnaround automobile dealership, Fateh Bahadur Singh, Brajesh Mishra and ***8.1.Anjali Singh***, DSM, DTU

53. Levofloxacin Detection Using L-Cysteine Capped MgS Quantum Dots via the Photoinduced Electron Transfer Process, S. Z. H. Hashmi, Tarun Kumar Dhiman, ***6.Navneet Chaudhary***, Avinash Kumar Singh, Rahul Kumar, ***3.Jai Gopal Sharma***, Anil Kumar and Pratima R. Solanki1, Biotechnology, DTU

54. Machine Learning Approach Based on Hybird Features for Detection of Phishing URLs, ***8.Awishkar Ghimire***, ***6.Avinash kumar Jha***, ***8.Surendrabikram Thapa***, ***8.Sushruti Mishra*** and ***8.Aryan Mani Jha***, CSE, Civil and Mechanical, DTU

55. MAGLEV TECHNOLOGY, ***3.Dr. J.P Kesari***, ***8.Aditya Shukla*** and ***8.Kumar Rahul***, Mechanical, DTU

56. Multiclass classification for predicting Remaining Useful life (RUL) of the turbofan engine, ***8.Piyush Soni***, ***8.Mohd Anas Khan***, ***8.Mohammad Zubair*** and ***3.Prof. Suresh Kumar Garg***, Mechanical, DTU

57. Near-surface seismic refraction tomography and MASW for site characterization in Phuentsholing, Bhutan Himalaya, ***3.Raju Sarkar***, Sreevalsa Kolathayar, Dowchu Drukpa, Kinley Choki, Shrijana Rai, Sangay Tenzin Tshering and Kezang Yuden, Civil, DTU

58. Organ Simulation and Healthcare Services: An Application of IoT, ***3.Malti Bansal***, ***8.Tushar Chopra*** and ***8.Souradip Biswas***, Electronics, DTU

59. Phytochemicals and antioxidant activity of Sisymbrium irio L. seeds, ***6.T Hailu***, ***3.R K Gupta*** and ***3.A Rani***, Chemistry, DTU

60. Post-translational modifications: Regulators of neurodegenerative proteinopathies, ***6.Rohan Gupta***, ***7.Mehar Sahu***, ***7.Devesh Srivastava***, ***7.Swati Tiwari***, ***6.Rashmi K. Ambasta*** and ***3.Pravir Kumar***, Biotechnology, DTU

61. Random area-perimeter method for generation of unimodal and multimodal cancelable biometric templates, ***6.Rajesh Asthana***, ***6.Gurjit Singh Walia*** and ***3.Anjana Gupta***, Mathematics, DTU

62. Review of Text Summarization in Indian Regional Languages, ***8.Surendrabikram Thapa***, ***8.Surabhi Adhikari*** and ***8.Sushruti Mishra***, CSE, DTU

63. Robust copy-move forgery detection using modified superpixel based FCM clustering with emperor penguin optimization and block feature matching, ***3.Ritu Agarwal*** and ***3.Om Prakash Verma***, CSE, DTU

64. Security and privacy Aspects for Internet of Things (IoT), ***3.Malti Bansal***, ***8.Marshal Nanda*** and ***8.Md. Nazir Husain***, Electronics, DTU

65. Security in Mobile ADHOC Networks: Survey, ***8.Sharat S Kariyannavar***, ***8.Shreyas Thakur*** and ***6.Aastha Maheshwari***, CSE, DTU

66. SEM-EDAX analysis of the Soil Samples of River Yamuna in Delhi Region, Vivek Chopra and ***3.Jai Gopal Sharma***, Biotechnology, DTU

67. Sensorless Speed Control of PMSM Motor for Wide Speed Range, ***7.Pratyush Kumar Dwivedi***, ***6.Aakash Kumar Seth*** and ***3.Mukhtiar Singh***, Electrical, DTU

68. Smart Traffic Management and Control system Based on IoT, ***7.Dominic Abuga*** and ***3.Nallanthighal Raghava***, Electronics, DTU

69. Software Reliability Prediction Using Various Ensemble Methods, ***8.Rohit Prasad***, ***8.Abhishek Kumar*** and ***8.Perdun Kumar Mandal***, CSE, DTU

70. Spectral library creation and analysis of urban built-up surfaces and materials using field spectrometry, ***6.Dwijendra Pandey*** and ***3.Kailash Chandra Tiwari***, Electronics and Civil, DTU

71. Study of a prey–predator model with preventing crop pest using natural enemies and control, ***6.Sudhakar Yadav*** and ***3.Vivek Kumar***, Mathematics, DTU

72. Support Vector based Oversampling Technique for Handling Class Imbalance in Software Defect Prediction, ***3.Ruchika Malhotra***, ***8.Vaibhav Agarwal***, ***8.Vedansh Pal*** and ***8.Tushar Agarwal***, CSE, DTU

73. TCAD Temperature Analysis of Gate Stack Gate All Around (GS-GAA) FinFET for Improved RF and Wireless Performance, ***6.Bhavya Kumar*** and ***3.Rishu Chaujar***, Physics, DTU

74. TWO-STAGE CUSTOMER SEGMENTATION USING K-MEANS CLUSTERING AND ARTIFICIAL NEURAL NETWORK, ***8.Harshit Muhal*** and ***8.Harsh Jain***, CSE, DTU

1. *Vice Chancellor*
2. *Pro Vice Chancellor*
3. *Faculty*
4. *Teaching-cum-Research Fellow*
5. *Asst. Librarian*
6. *Research Scholar*
7. *PG Scholar*
8. *Undergraduate Student*

1.1. *Ex Vice chancellor*
2.1. *Ex Pro Vice Chancellor*
3.1. *Ex Faculty*
4.1. *Alumni*
5.1 *Others*
6.1. *Ex Research Scholar*
7.1. *Ex PG Scholar*
8.1. *Ex Undergraduate Student*

Proceedings of the Sixth International Conference on Inventive Computation Technologies [ICICT 2021]
IEEE Xplore Part Number: CFP21F70-ART; ISBN: 978-1-7281-8501-9

A Comparative Analysis of Query-Constrained Video Summarization Techniques

Anil Singh Parihar*, Priyansh Verma†, Prashansa Bhattacharyya‡, and Rohit Goyal
Dept. of Computer Science and Engineering
Delhi Technological University
New Delhi, India
Email: *parihar.anil@gmail.com, †propriyanshh@gmail.com, ‡prashansa.bhattacharyya@gmail.com, rohit.goyal069@gmail.com

***Abstract*—This paper is an analysis of the literature available in the field of query-constrained video summarization. For the sake of concision, five of the more recent, prominent research works have been explored. This research work will dive deep into the datasets used by each of the models, concerning their preparation methods, scale, description, and comparison. Next, the methodologies associated with each of these papers covering their models used, metrics employed, and draw parallels between them are described. The ablation analyses among model variants are discussed to gauge the importance of specific features in each paper. Finally, a description of each model's metric results has been provided for a quantitative comparison among the models, built on some standard metrics described by each of these papers.**

Keywords—Query-Constrained, Query-Based, Query-Focused, Query-Controllable, Video Summarization, Adversarial Networks, Self-Attention Mechanism, Vision, and Language.

2021 6th International Conference on Inventive Computation Technologies (ICICT) | 978-1-7281-8501-9/21/$31.00 ©2021 IEEE | DOI: 10.1109/ICICT50816.2021.9358711

I. INTRODUCTION

In today's era of abundant video content creation, video data is undoubtedly a very potent source of information extraction, the only caveat being the fact that such data is largely unstructured and possesses high variability. As a result, recent literary works have witnessed a surge in exploring video summarization. The domain of video summarization can be divided into two sub-domains: generic video summarization and query-constrained video summarization. Generic video summarization seeks to summarize a source video as a whole while retaining essential information to condense it in a pithy manner. On the other hand, query-constrained video summarization takes a text query as an additional input to create a video summary relevant to the user's preferences. Query-constrained video summarization is a relatively recent domain with varying novel ideas and implementations. In this paper, five prominent research works in the field of Query-Constrained Video Summarization have been explored, namely Hierarchical Variational Network for User-Diversified & Query-Focused Video Summarization (HVN) [1], Query-Biased Self-Attentive Network for Query-Focused Video Summarization (QSAN) [2], Query-adaptive Video Summarization via Quality-aware Relevance Estimation (QAR) [3], Query-Conditioned Three-Player Adversarial Network for Video Summarization (TPAN) [4], Query-controllable Video Summarization (QCV) [5].

The paper provides a comparative analysis of these papers in section II. Subsection A discusses in detail their datasets used. Subsection B details the methodologies of each paper. Subsection C deals with the various evaluation metrics defined in each paper, which are used to gauge the performance of the query-constrained summary generated. Finally, subsection D compares the results of each paper. The conclusion and the results of the analysis are presented in section III.

II. COMPARATIVE ANALYSIS OF RELATED WORK

A. Methods of dataset preparation

The domain of query-constrained video summarization is rather recent and still undergoing research. Many new research works contribute a novel dataset and use novel metrics of evaluation. Hence, there is an apparent lack of uniform standards in this domain. To this end, a collated analysis is presented that covers some of the most recent and recognized models in this domain. This section covers the datasets used in all the mentioned research works and discusses their scale & preparation methods.

1) Datasets used in TPAN, HVN and QSAN

The existing UT Egocentric (UTE) dataset [6] and the query-conditioned dataset built on it is used to evaluate most of the approaches. The UTE dataset contains four videos of three to five hours each, captured in a natural setting. These papers make use of a diverse and concise dictionary of forty-eight concepts for user queries supplied (proposed in QC-DPP [7]). TPAN trains the model on two random videos and uses the third one for testing and the fourth for validation. Four experiments are performed to test all four results.

HVN and the QSAN models also use the UTE dataset. In addition, for training, the authors of both the papers employ the ActivityNet dataset [8] since the UTE dataset only has four videos in it. So, in both the approaches, this limitation is handled by training them using a significantly larger video description dataset and then using those parameters into the query-constrained model. ActivityNet dataset has 20,000 videos, each running for an average time of 3 minutes and with descriptions.

After the QSAN and HVN models generate the required query-constrained video summaries, the SumMe [9] and TVSum [10] datasets are used to conduct experiments on generic video summarization. SumMe dataset comprises 25 videos with an average time of 2 minutes 40 seconds and encompasses diverse types of videos from all walks of life, viewed from various perspectives. TVSum dataset comprises an amalgamation of 50 YouTube videos with their duration ranging from 2-10 minutes and divided into various categories. The videos are uniformly divided into each category. These experiments are used to evaluate said models' performance in the scope of a generic video summarization task, where the

Authorized licensed use limited to: DELHI TECHNICAL UNIV. Downloaded on March 03,2021 at 06:07:46 UTC from IEEE Xplore. Restrictions apply.

weightage of query-relevance is nil simply for lack of queries.

2) Datasets used in QAR and QCV

QAR and QCV have created a dataset for their evaluation in a strikingly similar fashion. Using top searched queries from YouTube (2008-2016), about 200 queries are obtained from 22 categories, assisted by the autocomplete feature to factor in larger queries as well. The top video result of two to three minutes is chosen and sampled at one frame per second. Then, using Amazon Mechanical Turk (AMT), a task of annotating these video frames is set up with the assistance of 48 subjects in QAR. Each video is annotated with respect to the relevance of frames with the query by five or more different people to avoid bias from personalization. The relevance annotation classes are also nearly the same in both QAR and QCV - "very good", "good", "not good" and "trash"/ "bad". Label distribution achieved for these four annotation classes is also reasonably similar - "Very Good": 17.55%, "Good": 57.40%, "Not good": 12.31% and "Trash": 12.72% in QAR and "Very Good": 18.65%, "Good": 55.33%, "Not good": 13.03% and "Bad": 12.99% in QCV. The first significant difference between their dataset preparation methods is establishing the ground-truth value of the labels for a particular video frame. QCV uses the majority vote rule, whereas QAR assigns weight 1 to "Very Good", 0.5 to "Good" and 0 to others and computes the average of the five relevance labels. Each frame is labeled negative if the mean is ≤ 0.5, else positive.

Further, QAR also sets up another task of distribution of frames into disjoint clusters on AMT. The number of clusters in each video is left at the discretion of the AMT worker (on average, 13.4 clusters per video have been observed). These cluster annotations are also merged to form a single ground-truth value using the Normalized Mutual Information metric (NMI). Authors of QAR believe that, as of that point in time, the paper was the first attempt to annotate multiple clustering and evaluate the consistency of multiple annotators. QAR has thus contributed a novel dataset, the Relevant and Diversity dataset (RAD) [3].

B. Analysis and comparison of methodologies employed

In this section, each model is described along with its unique methodology to elucidate the working of their components.

1) TPAN

TPAN makes use of a three-player generative adversarial network. The joint representation of the input query and the source video is used for learning by the generator. The discriminator is used to discriminate between the generated and a random summary, with the real summary. The discriminator takes as input three pairs of the generated summaries. The model trains both together and initiates a three-player loss. In this, the generator can learn better and improve its performance simply because of the feedback given by the discriminator and can avoid creating trivial outputs. The first step is to encode query and visual information jointly using an adversarial network that uses three players. The video is input into a query constrained feature representation module, G_r, in the generator, whose function is to integrate text query and video information. In module G_e, a compact video encoding occurs, and after that, module G_p is used to predict shot scores. The regularization of the model is undertaken by the discriminator using the three-player loss. The final results are obtained after G_g outputs the video synopsis. Further, for a more compact summary, two regularizations are introduced, $\mathcal{L}_{summary}$ and $\mathcal{L}_{length}$, one of the losses is used to regularize the length while the other loss is used to align the correct ground truth and the prediction. Three query-constrained representations are the input taken by the discriminator, and that is tasked with distinguishing between the three queries for the real summary, and it is done using an adversarial learning method.

The feature representation module G_r consists of shot level, frame level, and textual representation. These feature vectors are combined to get a query-constrained feature encoding for the video. The video encoding module G_e takes in this feature encoding and learns temporal dependencies among video shots. Further, this is input into a BiLSTM [11] layer, which uses normalization and rectified layer unit (ReLU). From the scoring module G_p, G_g generates the final result by scaling it. For the purpose of training the textual representation, text query is passed through a 300-dimensional semantic space leveraging the word2vec model (trained on GoogleNews and ClickTure dataset) and then an LSTM where the individual word representations are encoded into a singular embedding.

TPAN uses query conditioned summary (q_{sum}), ground truth summary (g_{sum}), and randomly generated query conditioned summary (r_{sum}) are passed into the discriminator module.

The video shots used are a result of the training from the joint embedding of visual and query information. r_{sum} assists the generator create more desirable summaries which are free from insignificant short sentences. This is one of the reasons for the efficient performance of this model.

The regularization techniques used in TPAN, which comprises of the summary regularization, calculated as:

$$\mathcal{L}_{summary} = \frac{1}{T}\sum_{t=1}^{T}(s_t - s_t^g)^2 \quad (1)$$

where s_t^g is the ground truth score and s_t is the predicted shot score. It also comprises of length regularization, which is used to control the length of the summaries and is calculated as:

$$\mathcal{L}_{length} = \left|\frac{1}{T}\sum_{t=1}^{T} k_t - \gamma\right| \quad (2)$$

where γ signifies the ratio of the video's key-shots based on the ground-truth summary in percent, and k_t is the summary result.

$$\mathcal{L} = \mathcal{L}_{summary} + \mathcal{L}_{length} \quad (3)$$

Authorized licensed use limited to: DELHI TECHNICAL UNIV. Downloaded on March 03,2021 at 06:07:46 UTC from IEEE Xplore. Restrictions apply.

2) HVN

The authors propose a model that consists of a Hierarchical Variational Network, which is chiefly divided into two modules: Query-focused Attention Module (QAM), which is used to merge the logical information of the query, and the other one is the Multilevel Self-attention Variational Block (MSVB) to get contextual information and add stochasticity as well as diversity to the process. A scene is defined as a collection of *K* shots. A long video is converted into *M* key shots, and subsequently, the authors use C3D [12] to obtain a sequence of video shot features of size *M* for each of the key-shots. Besides this, words of a query are also converted into a feature vector using word2vec. The model uses two types of LSTM: Shot Layer and Scene Layer LSTM. Each shot is passed through a shot layer BiLSTM [11] to obtain a sequence of length *K,* which is used in further processing. The shot layer LSTM output is passed through the QAM module, which utilizes softmax function and produces 2 query related outputs through softmax convolution with the pre-learned weight matrix and the vectorized query: one is the weight result for each shot, and the other one is the average weight result for the respective shot. The shot layer LSTM output is passed through the MSVB layer, which finds different levels of visual content of video scenes. MSVB also utilizes a diversity regularization factor, found using Hellinger distance. It also adds stochasticity to the process using a Stochastic Latent Variable Module. The outputs of both modules are passed to the scene layer LSTM. After that, a key-shot selector optimizes on a maximization problem to select the key-shots used for summary using the shot scores produced in QAM. Added to the regularization terms used in TPAN, it can be seen that HVN uses the following extra parameters:
The diversity regularization term is calculated as the following:

$$\mathcal{L}_{diversity} = \left\| \left(\sqrt{W_{n,l}} \sqrt{W_{n,l}}^{T} - I \right) \right\|_F^2 \qquad (4)$$

Regularization of HVN is described using:

$$\mathcal{L} = \mathcal{L}_{summary} + \beta_1 \mathcal{L}_{prior} + \beta_2 \mathcal{L}_{reconst} + \beta_2 \mathcal{L}_{div} \qquad (5)$$

where $\mathcal{L}_{\text{summary}}$ is the same as that of TPAN (1), $\mathcal{L}_{\text{prior}}$ and $\mathcal{L}_{\text{reconst}}$ are the Prior and Reconst Regularization factors for the stochastic module, $\mathcal{L}_{\text{div}}$ is the diversity regularization term.

3) QSAN

The authors in QSAN have put forth a novel self-attentive model, which is initially made to train on a comparatively large dataset that provides video annotations to better learn the relationship between the video frames under consideration and their caption-level meaning. A hierarchical self-attentive network (HSAN) learns the relationship among frames of the video at both levels − segment-level & frame-level, by utilizing local and global self-attention modules, which leverage segment-level features and frame-level features, respectively. It uses a pre-trained Convolutional Neural Network and outputs weighted-segment level features. Then, a reinforcement-learning based description/ caption generator is employed to augment the learned relationship between video contents and textual transcripts. It does so by minimizing the difference between generated captions and ground truth descriptions. This caption generator is LSTM-based and is used to render a description of the video in order to highlight relatively important frames/segments in the source video. Finally, a query-aware-scoring-module evaluates a per-segment score value based on its relevance to the query. Consequently, the final video summary involves these segments.

4) QAR

QAR builds on the work done by Liu *et al.* [13] and [14]. The first part of the model poses the task of query-constrained video summarization as a ranking-based frame subset-selection task. Using Bing ClickTure and their proposed RAD dataset, the model is trained in the same embedding space to optimize relevance, defined as the sum of query-similarity (similarity of a frame with the query) and a query-independent term (an overall quality measure of the frame − contrast, composition, etc.). The loss function is modeled to answer, 'is this a good frame for this query', which is an improvement over Liu *et al.* [13], which models it in the opposite fashion. For training, the text query is passed through a 300-dimensional semantic space leveraging the word2vec model (trained on GoogleNews and ClickTure dataset) and then an LSTM, where the individual word representations are encoded into a singular embedding. Similarly, the VGG-19 network is employed to represent a frame, albeit its softmax layer is replaced by a linear 301-dimensional layer, the last dimension of which represents query independent quality score, and others are used in joint-embedding with text query. With this done, a subset of frames optimized for query-relevance and quality scores can be achieved, but the second part of their proposed model builds on further to optimize diversity (to factor in the inclusion of dissimilar frames) and representativeness (to favor the inclusion of medoid-type frames) scores. These four scores are modeled as objective functions, and the framework of submodular optimization is employed to this end. [14] [15]

5) QCV

The proposed model in QCV first forms a dictionary of words from the set of training queries. The model consists of 3 modules: summary controller, summary generator, and summary output module. In the summary controller, the model encodes the incoming text query using the dictionary of words and returns its vector representation to the summary generator module. The summary generator uses a CNN structure trained on the training data and includes ResNet-34, which takes the source video and extracts the video frame features. It also includes a feature fusion submodule which takes the extracted video frame features and text features obtained previously from the first module and fuses them based

Authorized licensed use limited to: DELHI TECHNICAL UNIV. Downloaded on March 03,2021 at 06:07:46 UTC from IEEE Xplore. Restrictions apply.

on one of the three known fusion techniques viz.: Summation, Concatenation, and element-wise Multiplication, and a fully connected layer which takes input as the fused feature vector obtained from the fusion submodule, classifies frames into their label values and generates a frame relevance score vector. Apart from these, the second module also utilizes the Cross-Entropy Loss function and Adam optimizer for training. Finally, the frame relevance score vector obtained from the second module is passed onto the summary output module, which takes several desired frames from the set of frames in a sequential order which have a relevance score value of 2 ("Good") or 3 ("Very Good"), and outputs them.

C. *Comparison of evaluation metrics*

QSAN, HVN and TPAN use the same evaluation metric proposed in QC-DPP. Authors in QC-DPP felt an imminent need to model the evaluation metric of generated summaries in a way that should accurately trace what humans understand from summaries thus generated and that it is vital to evaluate the retention capabilities of these generated summaries with respect to the semantics and not just visual quantities, present in user-provided summaries. To this end, the authors proposed that the aptest methodology to express semantic information is to encapsulate the various 'concepts' prevalent fundamentally in the source video. Thus, the authors sought to tag the UTE dataset's videos using dense per-video-shot annotations of said concepts, called semantic vector representations. Owing to these dense annotations of concepts for each video shot, the generated summaries can then be evaluated against user-provided summaries, using maximum weight matching on a bipartite graph whose edge weights are values of Intersection over Union similarity (IoU) between the concepts covered by the summaries on edge vertices. Consequently, the number of matched pairs helps compute precision, recall and F1 score - all calculated with human-level semantics considered at the core.

QAR also uses precision, recall and F1 score to evaluate its summarization performance, albeit on its own dataset, RAD. Note that, contrary to HVN, QSAN and TPAN, which use IoU similarity on 'concepts' (originally defined in QC-DPP) for obtaining ground truth relevance values of individual frames w.r.t the query, here the weighted average of the numerical value of classes ('very good'-1, 'good'-0.5, 'bad'-0, 'trash'-0) is used.

QCV defines its own evaluation metric, which is defined as the ratio of the number of frames with correct predicted relevance score divided by the total number of frames in the video (which is 199 in the model).

D. *Ablation analyses of individual models*

An ablation study is carried out in TPAN, such that the first model is trained without the $\mathcal{L}_{\text{length}}$ regularization parameter. In this, the performance in the form of F1 score is minorly reduced to 44.08% from the average value of 46.05% of the original model. But, the values of precision and recall grow further apart, indicating the importance of the query length regularization. The second model is trained without the ground truth summary regularization and shows the maximum dip in the F1 score (35.19%). Third model, which does not consider the random summary also shows a dip in the F1 score (44.37%).

Similarly, HVN's performance is tested in three modes: HVN_{bas}, which is HVN with only QAM module, $\text{HVN}_{\text{w-Ldiv}}$, which is complete HVN without the stochastic module, and the final one is HVN, which is the complete HVN described above. Based on the average F1 score, the performance becomes better when the MSVB module (without stochastic module) is added and then again when the stochastic module is added to MSVB. The exceptional performance of HVN over the other modes is evidently due to its MSVB module. As the stochastic module is added, its ability to generate a diverse summary increases, thus augmenting the ability to generate a desirable summary.

The ablation study in QSAN is also conducted in three modes. The first model is obtained after removing the local self-attention module (LSAN). Here, the segment level is computed as the mean of its visual features. The performance of this model is worse than the complete model. The second model is obtained after removing the global self-attention module (GSAN) from the model produced in QSAN. Here only the output obtained from the LSAN is used to create the query-constrained video summary, and this model also performs worse than the complete model.

TABLE I. COMBINED RESULTS FROM THE ABLATION ANALYSES OF TPAN, HVN AND QAR HIGHLIGHTING EACH FEATURE-SPECIFIC SCORE

Method	P	R	F1
$\text{TPAN}_{\text{model}}$	0.430	0.487	0.453
$\text{TPAN}_{\text{without } \mathcal{L}_{\text{length}}}$	0.347	0.618	0.440
$\text{TPAN}_{\text{without } \mathcal{L}_{\text{summary}}}$	0.283	0.475	0.351
$\text{TPAN}_{\text{two player}}$	0.433	0.512	0.443
$\text{HVN}_{\text{model}}$	0.445	0.581	0.488
HVN_{bas}	0.414	0.581	0.460
$\text{HVN}_{\text{w-Ldiv}}$	0.426	0.592	0.472
$\text{QSAN}_{\text{model}}$	0.455	0.529	0.465
$\text{QSAN}_{\text{without LSA}}$	0.421	0.490	0.431
$\text{QSAN}_{\text{without GSA}}$	0.371	0.432	0.379

P, *R* and *F1* denote precision, recall and F1 scores, respectively.

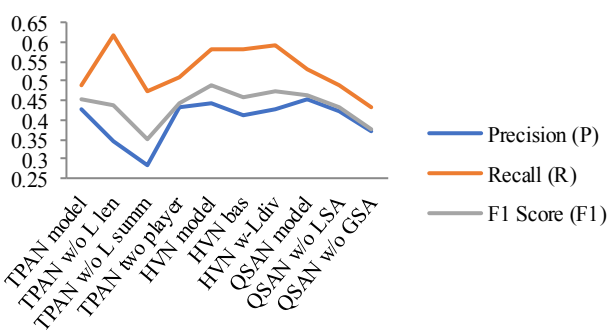

Fig. 1. Comparative plot of ablation analysis of TPAN, HVN and QAR

Authorized licensed use limited to: DELHI TECHNICAL UNIV. Downloaded on March 03,2021 at 06:07:46 UTC from IEEE Xplore. Restrictions apply.

The ablation study in QAR is done by initially taking, at a time, one out of the four objective functions of Query Similarity, Quality, Diversity and Representativeness. Then, a combination of Query Similarity and Quality is also tried out, where it is observed that relevance precision is best achieved here (0.775), whereas the best cluster recall (0.825) and F1-score (0.721) are achieved when using the complete QAR model with all objective functions combined. It is noted that whenever Query Similarity is included, relevance precision is consistently high, hinting that it is the most crucial objective - in line with what is expected.

TABLE II. RESULTS FROM THE ABLATION STUDY OF QAR. UPPER BOUND ACHIEVED USING GROUND TRUTH SUMMARIES.

	P	R	F1
Representativeness	0.654	0.817	0.672
Quality	0.671	0.542	0.522
Diversity	0.575	0.808	0.629
Similarity	0.763	0.550	0.578
Similarity + Quality	0.775	0.563	0.594
Representativeness + Quality + Diversity + Similarity	0.704	0.825	0.721
Upper Bound	0.938	0.925	0.928

P, *R* and *F1* denote precision, recall and F1 scores, respectively.

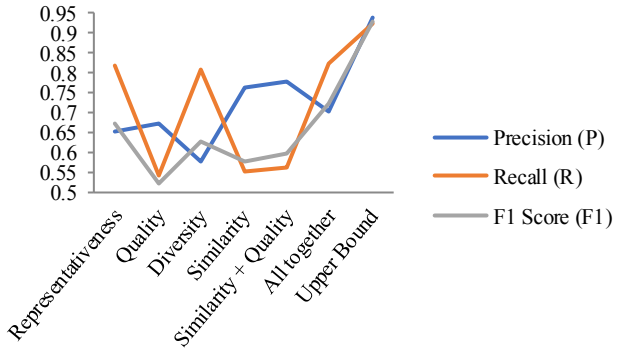

Fig. 2. Plot of evaluation metrics in the ablation analysis of QAR

In QCV, using the accuracy metric of this model for testing all the three fusion methods mentioned in the research work, namely: Summation, Concatenation and Multiplication, the respective attained metric accuracies come out to be 0.5514, 0.5803 and 0.6191, depicting that the Multiplication feature fusion technique performed the best.

TABLE III. RESULTS FROM THE ABLATION STUDY OF QAR. UPPER BOUND ACHIEVED USING GROUND TRUTH SUMMARIES

Model	Accuracy
Summation	0.5514
Concatenation	0.5803
Multiplication	0.6191

E. Cumulative analysis of results across models

TABLE IV. AN OVERALL COMPARISON OF PERFORMANCES ACROSS THE MODELS OF HVN, TPAN, QSAN TESTED ON UTE-DATASET

	HVN			TPAN			QSAN		
	P	R	F1	P	R	F1	P	R	F1
V1	52.55	52.91	51.45	49.66	50.91	48.74	48.41	52.34	48.52
V2	38.66	62.70	47.49	43.02	48.73	45.30	46.51	51.36	46.64
V3	60.28	62.58	61.08	58.73	56.49	56.51	56.78	61.14	56.93
V4	26.79	54.21	35.47	36.70	35.96	33.64	30.54	46.90	34.25
av	44.57	58.10	48.87	47.03	48.02	46.05	45.56	52.94	46.59

V_i denotes i^{th} video, *av* denotes average performance. *P*, *R* and *F1* denote precision, recall and F1 scores, respectively, in percent.

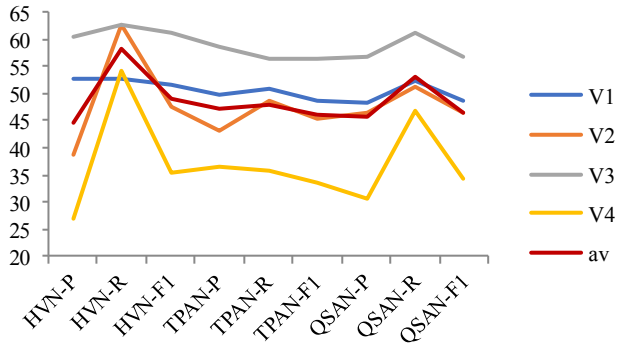

Fig. 3. Plot of performance of HVN, TPAN and QSAN on UTE-Dataset

It is evident that QSAN beats TPAN by 1.2% with respect to the F1 score on average, which was considered state-of-the-art. One of the reasons for this behavior is that it uses a self-attention mechanism that helps it to tie in frame-level detail in segments. Further, QSAN eliminates the bias of preference by first training on the ActivityNet dataset, which is significantly more extensive and adds to the diversity of the semantic data.

The performance of HVN is 2.82% better on average as compared to TPAN. There are majorly two reasons behind this: first is that HVN has an additional diversity regularization factor compared to TPAN and the other one is that HVN utilizes two modules specifically for scoring compared to a single attentive module in TPAN.

The F1 score of HVN was found to be greater than that of QSAN due to a more variational and intricate structure of the module and primarily due to the presence of a stochastic latent variable module in HVN, which allows it to produce different weights in the attention mechanism.

While there is no quantitative comparison between the self-attentive adversarial models (namely QSAN, HVN, TPAN) against those of QAR and QCV, it can be suggested that only HVN is a model that assures diversity, not only based on the difference in shots and frames but in also amalgamating context-related information. HVN specifically incorporates the stochasticity in the generated query-constrained summary by involving the above

Authorized licensed use limited to: DELHI TECHNICAL UNIV. Downloaded on March 03,2021 at 06:07:46 UTC from IEEE Xplore. Restrictions apply.

mentioned stochastic latent variable module to increase the stochastic factor and diversify the summary.

III. CONCLUSION

Query-constrained video summarization is a recent yet promising domain in the field of computer vision. This paper has analyzed five prominent models that have proposed novel methodologies for summarizing videos in a manner that considers user preferences in the form of text queries. Their datasets are compared based on their preparation methods and size. Further, their model architecture and results are explored. Our analysis concludes that among the adversarial models, HVN and QSAN outperform TPAN in terms of average F1 score. Further, this research work also quantitatively compared the models based on various evaluation metrics stated in each paper and have observed that HVN produces the most diverse query-constrained video summary among all models.

REFERENCES

[1] P. Jiang and Y. Han, "Hierarchical Variational Network for User-Diversified & Query-Focused Video Summarization," in *International Conference on Multimedia Retrieval*, 2019.

[2] S. Xiao, Z. Zhao, Z. Zhang, Z. Guan and D. Cai, "Query-Biased Self-Attentive Network for Query-Focused Video Summarization," in *IEEE Transactions on Image Processing*, 2020.

[3] A. B. Vasudevan, M. Gygli, A. Volokitin and L. V. Gool, "Query-adaptive video summarization via quality-aware relevance estimation," in *ACM international conference on Multimedia*, 2017.

[4] Y. Zhang, M. Kampffmeyer, X. Liang, M. Tan and E. P. Xing, "Query-conditioned three-player adversarial network for video summarization," 2018. [Online]. Available: https://arxiv.org/abs/1807.06677.

[5] J.-H. Huang and M. Worring, "Query-controllable Video Summarization," in *International Conference on Multimedia Retrieval*, 2020.

[6] Y. J. Lee, J. Ghosh and K. Grauman, "Discovering important people and objects for egocentric video summarization," in *IEEE conference on computer vision and pattern recognition*, 2012.

[7] A. Sharghi, S. J. Laurel and B. Gong, "Query-focused video summarization: Dataset, evaluation, and a memory network based approach," in *IEEE Conference on Computer Vision and Pattern Recognition*, 2017.

[8] F. C. Heilbron, V. Escorcia, B. Ghanem and J. C. Niebles, "Activitynet: A large-scale video benchmark for human activity understanding," in *Proceedings of the IEEE conference on computer vision and pattern recognition*, 2015.

[9] M. Gygli, H. Grabner, H. Riemenschneider and L. V. Gool, "Creating summaries from user videos," in *European conference on computer vision*, 2014.

[10] Y. Song, J. Vallmitjana, A. Stent and A. Jaimes, "Tvsum: Summarizing web videos using titles," in *IEEE conference on computer vision and pattern recognition*, 2015.

[11] A. Graves and J. Schmidhuber, "Framewise phoneme classification with bidirectional LSTM and other neural network architectures," in *Neural Network*, 2005.

[12] D. Tran, L. Bourdev, R. Fergus, L. Torresani and M. Paluri, "Learning spatiotemporal features with 3d convolutional networks," in *Proceedings of the IEEE international conference on computer vision*, 2015.

[13] W. Liu, T. Mei, Y. Zhang, C. Che and J. Luo, "Multi-task deep visual-semantic embedding for video thumbnail selection," in *IEEE Conference on Computer Vision and Pattern Recognition*, 2015.

[14] M. Gygli, H. Grabner and L. V. Gool, "Video summarization by learning submodular mixtures of objectives," in *IEEE conference on computer vision and pattern recognition*, 2015.

[15] H. Lin and J. A. Bilmes, "Learning mixtures of submodular shells with application to document summarization," 2012. [Online]. Available: https://arxiv.org/abs/1210.4871.

Authorized licensed use limited to: DELHI TECHNICAL UNIV. Downloaded on March 03,2021 at 06:07:46 UTC from IEEE Xplore. Restrictions apply.

2021 11th International Conference on Cloud Computing, Data Science & Engineering (Confluence) | 978-1-6654-1451-7/20/$31.00 ©2021 IEEE | DOI: 10.1109/Confluence51648.2021.9377195

A Comparative Study on CNN based Low-light Image Enhancement

Kanishk Jayant Lal[1], Deepanshu Rana[2], Anil Singh Parihar[3]
Machine Learning Research Laboratory
Department of Computer Science and Engineering
Delhi Technological University
New Delhi, India
[1]kanishklal2012@gmail.com, [2]deepanshurana0@gmail.com, [3]parihar.anil@gmail.com

***Abstract*—Images collected under low-light conditions have an intrinsic property of poor illumination, due to the environment that they're captured in. Improving the quality of images proposes various challenges such as low contrast, low brightness, noise etc. Simply increasing the brightness of the dark regions will inevitably amplify the hidden artifacts. Deep Learning has shown great promise in this task, and it's black-box nature is used heavily for the enhancement of under-exposed images. In this paper we present a comparative analysis of various techniques based on Convolutional Neural Networks (CNN) that aim to enhance under-exposed images and perform extensive experiments on these techniques. The performance of these algorithms are analyzed subjectively and quantitatively using established metrics.**

***Index Terms*—Retinex theory, CNN, Low-light enhancement, Deep learning, SSIM, FSIM.**

I. Introduction

Capturing good quality images under poorly lit conditions is a difficult task. These images usually contain low illumination and brightness, poor contrast and noise [21]. Certain operations such as increasing exposure, high ISO and flash could be used to improve the low light conditions of the environment. But these methods have some drawbacks, for instance, a higher ISO could introduce graininess. Increasing the exposure could make the image blurry and using flash may introduce irregular illumination. All these methods potentially destroy the naturalness of the image.

In the past, many algorithms have been proposed for improving the visual appearance of under-exposed images. One such widely used technique is Histogram Equalization [18]. It is a simple technique that improves the contrast of images by restraining the histogram of the output images to meet some constraints. Many variations of histogram equalization such as Contrast Limited Adaptive Histogram Equalization (CLAHE) [17] are also made to effectively improve the contrast of images. Retinex Theory is a popular model utilized for image enhancement. By decomposing the image into the reflectance and illumination components, and enhancing either or both these components, we may get an improved image with better illumination and visual appeal. Retinex theory is a model that describes how images are perceived by humans. Single Scale Retinex (SSR) [12] changes only the reflectance part of the image and considers it as an enhanced version of the original image. Multi Scale Retinex with Color Restoration (MSRCR) [11] takes the single-scale to the multiscale version and uses multiscale Gaussian Filters and Color Restoration. However, Retinex based methods suffer from the lack of availability of "correct" decompositions to refer to as ground truths. Correctly calculating the illumination and reflectance of the input image under various conditions is a major challenge which needs to be tackled while using retinex theory for low-light image enhancement. Many new variants of retinex theory are also being made, Structure and Texture Aware Retinex Theory (STAR) [25] considers texture and structure part of the image while calculating the illumination and reflectance of images. Dehazing based methods [27] take advantage of the similar structure of images with dense fog and those taken under poorly lit conditions.

Due to innovations in the field of deep learning and data-data driven approaches, architectures based on Convolutional Neural Networks (CNNs) [16] are being utilized popularly by scholars to solve tasks such as Dehazing [2] and super resolution [28]. CNN based architectures are often used for low-light image enhancement. Many pipelines use paired supervised learning by synthesizing low-light images and using their original images as ground truths [26]. GANs following an unsupervised approach are also used popularly for the task of enhancement [4]. Collecting paired data is highly impractical and forms the major limitation for supervised learning and therefore, requires low light images to be synthesized artificially. GANs face an advantage when it comes to data collection, but are computationally expensive compared to CNNs. In this paper, we explore and analyse some recent innovations utilizing CNNs for the enhancement of low-light images.

II. Related Work

This section briefly discusses some recent CNN based approaches for enhancing low-light images.

Many CNN based techniques use paired images for the training of models. Deep Learning models have produced

978-0-7381-3160-3/21/$31.00 ©2021 IEEE

Authorized licensed use limited to: DELHI TECHNICAL UNIV. Downloaded on March 27,2021 at 05:46:41 UTC from IEEE Xplore. Restrictions apply.

superior results from those of traditional enhancement techniques. CNN based techniques have shown better results in image denoising, improving visual quality, image super resolution and image-to-image translation. LLNet [14] uses a deep autoencoder for removing noise from the images. Tao et al. [19] used bright channels prior to estimate the transmission parameter and an effective filter to estimate region wise lighting conditions present in images. Some methods use both deep learning and traditional methods for improving the quality. Xiao et al. [24] trained VGG16 for identifying the illumination of an image based on retinex theory. Then finding the low light regions based on this illumination, it applies histogram equalization only on the low light regions to produce output images.

Ignatov et al. [8] presented a method to transform lower quality images captured from smartphones to DSLR quality images. They used cropping and alignment techniques within limits to create paired data of a camera and the DSLR images and trained an end-to-end CNN to transform the lower quality camera image into DSLR quality image. Their main objective was to improve the visual appearance of images and proposed a loss function to accomplish the same. Gharbi et al. [6] proposed a pipeline that is capable of real time performance on mobile devices. They used a supervised approach and trained their network using low resolution copies of input images to estimate affine transformations. These transformations, upsampled and combined with a guidance map, produced the output enhanced image. Lv and Lu [15] proposed a multi-branch enhancement network that used attention maps to provide information about exposure and noise to guide the enhancement process and used a multi-branch fusion network to generate the corresponding enhanced image.

Unsupervised GAN based methods take advantage of the fact that training does not require paired data. EnlightenGAN [10] is one such method having a generator doing the decomposition, enhancing the illumination and then producing the enhanced image. The discriminator and loss functions are carefully designed for training. WESPE [9] is another GAN based image enhancement method which defines generative mappings paired with inverse generative mappings for training. It also defines two discriminators for distinguishing between the high quality images and enhanced images, one based on color of image and other based on texture. However, GAN based methods require careful selection of unpaired data for training.

III. Methodology

In this section we discuss some recently developed CNN based enhancement approaches and see how each of these techniques work in brief.

A. Multi-Branch Low-Light Enhancement Network

Feifan et al. [5] presented the Multi-Branch Low-Light Enhancement Network (MBLLEN) which works by extracting rich features at different levels and enhancing them through multiple subnets and then producing the final result via multi-branch fusion. Their architecture comprises of three different modules i.e., Feature Extraction Module (FEM), Enhancement Module (EM) and Fusion Module (FM). FEM consists of 10 consecutive convolutional layers, each using unit stride and a 3x3 kernel. All of the layers produce equally sized output maps that serve as inputs for the EM. The main function of FEM is to extract rich features upto different levels. EM consists of multiple subnets whose number is equal to the number of layers in FEM. Each subnet is identical and applies three convolutions and three deconvolutions in a symmetric fashion. All subnets are trained simultaneously. EM is specifically designed for enhancing the multi-level features extracted by FEM. FM takes outputs from EM and concatenates them to form N x H x W x 3 input where N is the number of subnets in the EM and uses 1x1 kernel in a convolution layer to produce output image, which is of the same shape as that of the original input image. The losses for training are calculated as follows:

$$L_{tot} = L_{str} + L_{VGG/i,j} + L_{region} \tag{1}$$

The structure loss incorporates image quality assessment metrics like SSIM [31] and MS-SSIM [5], calculated as:

$$L_{str} = L_{SSIM} + L_{MS-SSIM} \tag{2}$$

Context loss uses intermediate activations from *Convi_j* layer of the VGG19 network, which is pre-trained on ImageNet.

$$L_{VGG/i,j} = \frac{1}{W_{i,j}H_{i,j}C_{i,j}} \sum_{x=1}^{W_{i,j}} \sum_{y=1}^{H_{i,j}} \sum_{z=1}^{C_{i,j}} ||\phi_{i,j}(E)_{x,y,z} - \phi_{i,j}(G)_{x,y,z}|| \tag{3}$$

L_{region} is calculated by taking the weighted sum of error between the enhanced image and ground truth for both, the chosen 40% pixels in the low-light region and the remaining well exposed pixels.

B. GLADNet

Wang et al. [20] presented GLADNet, which stands for Global Illumination-Aware and Detail-preserving Network that attempts to perform enhancement by constructing a global illumination map from a lower resolution image and then using this map for the reconstruction of the enhanced image. The input image was downsized to fixed dimensions of 96 x 96 x 3 using nearest neighbour interpolation. This lower resolution input was fed into an encoder-decoder network with skip connections to generate a global illumination map of the same dimensions. This map was then resized to the dimensions of the original input image using nearest neighbour interpolation and concatenated with the low-light input image. The concatenated input was fed into a convolutional network for details reconstruction, with the output being an enhanced image having the same dimensions as the original image. A key thing to note is that the decoder network used resize and convolutional operations instead of deconvolutional layers to

Authorized licensed use limited to: DELHI TECHNICAL UNIV. Downloaded on March 27,2021 at 05:46:41 UTC from IEEE Xplore. Restrictions apply.

increase dimensions of the image. The loss function used for the purpose of training was L1 loss, which was taken as the weighted average across the R, G and B channels of the image.

$$L_{total} = \frac{1}{N}\sum_{i=1}^{N} ||F(X_i, \theta) - Y_i||_1 \quad (4)$$

Training data was obtained from RAISE and paired data was generated using Adobe Photoshop Lightroom.

C. Kindling the Darkness: A Practical Low-Light Image Enhancer

KinDNet [30] is also based on retinex theory. It consists of three parts, namely Layer Decomposition Net, Reflectance Restoration Net and Illumination Adjustment Net. Layer Decomposition Net tries to correctly find the illumination and reflectance component of the low-light image. It is trained on paired data using a loss with well defined constraints.

$$L^{LD} = L^{LD}_{rec} + 0.01L^{LD}_{rs} + 0.15L^{LD}_{is} + 0.2L^{LD}_{mc}, \quad (5)$$

Reflectance Restoration Net takes low light reflectance and illumination as input and gives the improved reflectance ($\hat{R}$) as output. Ground truth reflectance (R_h) acts as the reference to the network and the loss function is calculated as:

$$L^{RR} = ||\hat{R} - R_h||^2_2 - SSIM(\hat{R}, R_h) + ||\nabla\hat{R} - \nabla R_h||^2_2 \quad (6)$$

Illumination Adjustment Net converts one lighting condition to another, by roughly calculating the ratio of L_t (target lighting condition) and L_s (source lighting conditions). This ratio could be greater than 1 (when $L_t = L_h$) to increase lightning and less than 1 (when $L_t = L_l$) to decrease lighting. $\hat{L}$ represents the output of the network.

$$L^{IA} = ||\hat{L} - L_t||^2_2 + ||\ |\nabla\hat{L}| - |\nabla L_t|\ ||^2_2 \quad (7)$$

KinDNet assumes that to enhance under-exposed images, one needs to correct both, reflectance and illumination. It works towards enhancing these decompositions, and uses the guidance of illumination to improve reflectance. Ultimately, the output image is achieved by element-wise multiplication of these processed components.

D. RetinexNet

Wei et al. [23] presented an approach combining deep learning and retinex theory for low-light image enhancement. RetinexNet consists of two separate networks Decom-Net and Enhance-Net. Decom-Net estimates the decomposition for under-exposed images and its corresponding good quality images under the assumption that they are both composed of equal reflectance. At the time of training, it's not required to provide the ground truths for illumination or reflectance. The information regarding the consistency of reflectance and smoothness of illumination is provided in terms of specially formulated loss functions. The network learns the decomposition of input images into reflectance and illumination. Enhance-Net corrects the illumination of low-light input images and a denoising operation is done on reflectance. The loss function used consists of three parts:

- Reconstruction Loss: RetinexNet assumes that both low light reflectance and normal light reflectance can reconstruct the image with the corresponding illumnination map. Reconstruction loss is defined as:

$$L_{recon} = \sum_{i=low,normal}\ \sum_{j=low,normal} \lambda_{i,j}||R_i \cdot I_j - S_j||_1 \quad (8)$$

- Invariable Reflectance Loss: Constrains the consistency of reflectance.

$$L_{ir} = ||R_{low} - R_{normal}||_1 \quad (9)$$

- Illumination Smoothness Loss: Improves the structural information of the image. The original Total Variation minimization(TV) [3] function is a weighted sum of the gradients of reflectance, which makes the loss aware of image structure. It is calculated as:

$$L_{is} = \sum_{i=low,normal} ||\nabla I_i \cdot exp(-\lambda_g \nabla R_i)|| \quad (10)$$

The total loss is calculated as follows:

$$L_{total} = L_{recon} + \lambda_{ir}L_{ir} + \lambda_{is}L_{is} \quad (11)$$

E. Zero-Reference Deep Curve Estimation for Low-Light Image Enhancement

Guo et al. [7] presented a novel method that poses enhancement as a task of estimation of higher order curves specific to an image where the corresponding output image is generated by pixel-to-pixel mapping. These curves are estimated using a lightweight deep network (DCE-Net) and doesn't require paired/unpaired image data. The curves are proposed to be monotonous to preserve contrast among neighbouring regions, and differentiable, so that it's trainable. These curves are applied iteratively *n* times (taken to be 8 by DCE-Net) using the following equations:

$$LE_1(I(x), A_1(x)) = I(x) + A_1(x)I(x)(1 - I(x)) \quad (12)$$

$$LE_n(x) = LE_{n-1}(x) + A_n(x)LE_{n-1}(x)(1 - LE_{n-1}(x)) \quad (13)$$

where $A_n(x)$ represents the pixel wise mapping and is different for the R, G and B channels, $A_n(x) \in [-1, 1]$, $I(x) \in [0, 1]$, $LE_n(x) \in [0, 1]$.

ZeroDCE uses non-reference losses which are calculated as follows:

- Spatial Consistency Loss: Maintains consistency between neighboring regions of the image, which were empirically set to 4x4.

$$L_{spa} = \frac{1}{K}\sum_{i=1}^{K}\sum_{j\in\omega(i)} (|(Y_i - Y_j)| - |(I_i - I_j)|)^2 \quad (14)$$

Authorized licensed use limited to: DELHI TECHNICAL UNIV. Downloaded on March 27,2021 at 05:46:41 UTC from IEEE Xplore. Restrictions apply.

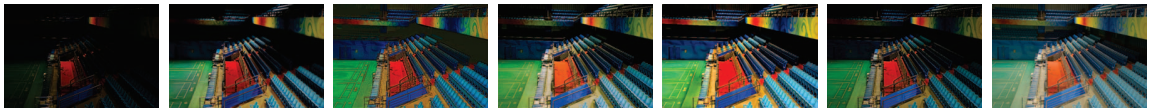

(a) Input | (b) KinD, PSNR: 15.4626, SSIM: 0.4875, FSIM: 0.6086 | (c) RetinexNet, PSNR: 15.5084, SSIM: 0.5305, FSIM: 0.6148 | (d) GLADNet, PSNR: 19.2492, SSIM: 0.6654, FSIM: 0.6896 | (e) MBLLEN, PSNR: 16.6122, SSIM: 0.5883, FSIM: 0.6576 | (f) ZeroDCE, PSNR: 14.1307, SSIM: 0.4693, FSIM: 0.7317 | (g) Ground truth

Fig. 1: Stadium - Comparison with Results and Ground Truth

(a) Input | (b) KinD, PSNR: 18.0901, SSIM: 0.7901, FSIM: 0.7621 | (c) RetinexNet, PSNR: 14.8874, SSIM: 0.6367, FSIM: 0.6646 | (d) GLADNet, PSNR: 21.3825, SSIM: 0.8614, FSIM: 0.7882 | (e) MBLLEN, PSNR: 14.3198, SSIM: 0.5710, FSIM: 0.6743 | (f) ZeroDCE, PSNR: 16.7981, SSIM: 0.7592, FSIM: 0.8357 | (g) Ground truth

Fig. 2: Monarch - Comparison with Results and Ground Truth

- Exposure Control Loss: Controls exposure by keeping the average intensity in local regions close to a defined exposure level, E (set to 0.6)

$$L_{exp} = \frac{1}{M}\sum_{k=1}^{M}|Y_i - E| \tag{15}$$

- Colour Constancy Loss: Calculates colour loss as the sum of squares of average intensities across R, G and B channels.

$$L_{col} = \sum_{\forall(p,q)\in\epsilon}(J^p - J^q)^2, \epsilon = \{(R,G),(G,B),(B,R)\} \tag{16}$$

- Illumination Smoothness Loss: Preserves monotonicity between neighbouring pixels.

$$L_{tv,A} = \frac{1}{N}\sum_{n=1}^{N}\sum_{c\in\{R,G,B\}}(|\nabla_x A_n^c| + |\nabla_y A_n^c|)^2 \tag{17}$$

The total loss is calculated as:

$$L_{total} = L_{spa} + L_{exp} + W_{col}L_{col} + W_{tv,A}L_{tv,A} \tag{18}$$
$$where\ W_{col} = 0.5\ and\ W_{tv,A} = 20$$

IV. Results and Performance Analysis

A. Quantitative Assessment

The human eye perceives images subjectively, but it is possible that quantitative assessment may be able to spot differences that the human eye neglects. Quantitative assessment is difficult but is a very important task for the evaluation of image quality. There isn't a universally accepted metric for measuring image quality but there are many metrics for Image Quality Assessment [22] which are commonly used, such as SSIM [31], FSIM [29], PSNR and MSE [13]. In this section, we present evaluations of the following metrics for the compared algorithms.

Peak Signal-to-Noise Ratio (PSNR) [13] is the ratio of maximum power of signal to maximum power of corrupting noise that affects the fidelity of its representation. It is calculated with respect to peak signal power and is usually expressed in the terms of a logarithmic decibel scale. PSNR is useful in images containing higher dynamic ranges and is an excellent measure of quality for white noise distortion.

$$PSNR = 20\log_{10}\frac{L^2MN}{\sum_{i=0}^{M-1}\sum_{j=0}^{N-1}(f(x,y) - g(x,y))^2} \tag{19}$$

Structural Similarity Index (SSIM) is a perception-based model given by Wang et al. in [31]. SSIM considers degradation of an image as changes done in structural information, while also considering both luminance and contrast masking terms. It is considered by structural information that neighbouring pixels are strongly interdependent on each other. It is different from PSNR and MSE as they consider absolute error only. SSIM is calculated as:

$$SSIM(X,Y) = \frac{(2\mu_X\mu_Y + c_1)(2\sigma_{XY} + c_2)}{(\mu_X^2 + \mu_Y^2 + c_1)(\sigma_X^2 + \sigma_Y^2 + c_2)} \tag{20}$$

Feature Similarity Index (FSIM) [29] presents an Image Quality Index built upon the aspect of Human Visual System (HVS) that apprehends an image mainly because of its low level features, specifically Phase Congruency (PC) which is

Metrics	KinD	RetinexNet	GLADNet	MBLLEN	ZeroDCE
SSIM	0.70268	0.48055	0.87537	0.66894	0.53157
FSIM	0.67713	0.53767	0.78616	0.66494	0.65600
PSNR	17.86704	15.05347	19.91510	16.43938	13.81156

TABLE I: Average Metric Analysis for Custom Dataset

Authorized licensed use limited to: DELHI TECHNICAL UNIV. Downloaded on March 27,2021 at 05:46:41 UTC from IEEE Xplore. Restrictions apply.

a dimensionless measure of the underlying local structure of an image and is thus, a primary aspect of FSIM. Gradient Magnitude (GM) encodes information about contrast of the image. FSIM is developed for grayscale images and a different version, FSIMc is used for evaluation of colored images. A drawback however, is that it is a computationally expensive metric.

The aforementioned metrics have been calculated on a custom dataset and are shown in Table I. The dataset comprisese of images from LOw-Light (LOL) [23] dataset and artificially synthesized low-light images from the DIV2K [1] dataset.

B. Visual Analysis

The measurement of low-light image enhancement in its entirety, is not possible by metrics alone. Often these methods are unable to distinguish between good contrast management, noise and over-enhancement. Therefore, a visual comparison is required to make sure that no over-enhancement and artifacts are introduced by these algorithms during the process of enhancement. The output of these techniques is given in Fig. 3 - 6 for some images captured under poor illumination conditions. The discussed techniques are compared in this section based on the visual appearance of results given by these algorithms.

In fig 3(b) - 3(f), RetinexNet correctly identifies the green colours of the trees but produces an overall noisy image. All the other methods perform equally good, but KinD preserves the details of the image and doesn't over-enhance the low-light regions. MBLLEN introduces artifacts in the bottom-right darker regions of the image. In fig 4(b) - 4(f), ZeroDCE seems to preserve the texture between the sky and the clouds while GLADNet misses the cloud-sky distinction. KinD performs over-smoothening in the darker regions near the rocks causing loss of detail. In fig 5(b) - 5(f), it can be seen that GLADNet has overall best improved the contrast and maintained clarity and colour in the poorly illuminated regions of the image. KinDNet has improved the contrast but also introduces blurriness in the darker regions of the image. MBLLEN shows visible colour distortion in the buildings and has tampered with the natural colour of the sky.In fig 6(b) - 6(f), MBLLEN misses the naturalness of the picture due to over-enhancement. RetinexNet produces a grainy sky with inaccurate colour of the water. GLADNet, KinD and ZeroDCE produce similar results with KinD and ZeroDCE preserving the lightning bolt.

(a) Input (b) KinD (c) RetinexNet (d) GLADNet (e) MBLLEN (f) ZeroDCE

Fig. 3: Lake

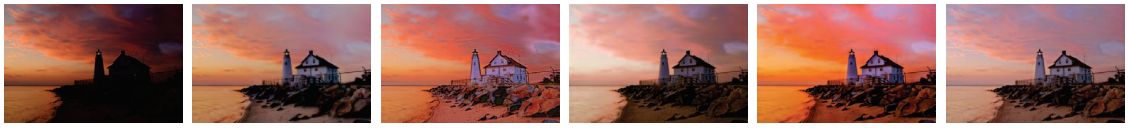

(a) Input (b) KinD (c) RetinexNet (d) GLADNet (e) MBLLEN (f) ZeroDCE

Fig. 4: Lighthouse

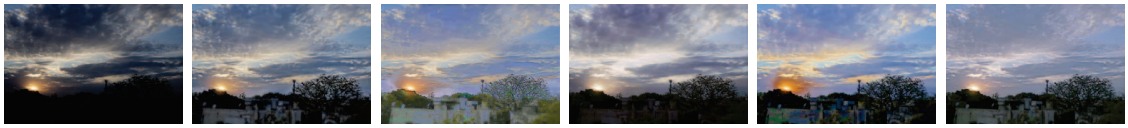

(a) Input (b) KinD (c) RetinexNet (d) GLADNet (e) MBLLEN (f) ZeroDCE

Fig. 5: Sky

(a) Input (b) KinD (c) RetinexNet (d) GLADNet (e) MBLLEN (f) ZeroDCE

Fig. 6: Grand Canal

Authorized licensed use limited to: DELHI TECHNICAL UNIV. Downloaded on March 27,2021 at 05:46:41 UTC from IEEE Xplore. Restrictions apply.

C. Computational Assessment

We calculated the runtime on our custom dataset (mentioned above) consisting of 300 low-light images, where each image was typically around 600x400 in dimensions. The runtime assessments for these images were performed on an Nvidia Titan RTX GPU and Intel Xeon Silver 4114 Processor with 128GB RAM. Upon testing, we noticed that GLADNet and RetinexNet had similar runtimes of 0.0941s and 0.0978s per image. MBLLEN took an average time of 0.1758s with post processing and 0.1501s without post-processing, which is comparable to the average 0.1650s taken by KinD. ZeroDCE outperformed all the models with the best average runtime of 0.0012s taking advantage of it's lightweight model architecture.

V. Conclusion

After performing extensive experiments and analyzing the results of CNN based enhancement techniques, it can be observed that every approach excels in some conditions but also shows limitations in the others. Multibranch fusion based MBLLEN had the largest runtime and suffered from over-enhancement in brighter regions. Based on Retinex theory, KinD performed significantly better than RetinexNet but showed loss of details and smoothening in the darker regions, but retained structure. RetinexNet, maintained accurate color descriptions, but introduced a significant amount of noise as is also evident by it's PSNR metric. GLADNet, despite having a simple architecture, delivered superior metrics and performed well in the underexposed regions and maintained the naturalness of the image. ZeroDCE, the quickest method, although not having shown promising metrics, produced visually appealing images with good feature similarity and colour constancy. It demonstrates the necessity of qualitative assessment instead of relying on metrics alone. It also showed the fastest runtime and introduced a novel method of non-reference training using Deep Learning without using GANs.

References

[1] E. Agustsson and R. Timofte. Ntire 2017 challenge on single image super-resolution: Dataset and study. In *2017 IEEE Conference on Computer Vision and Pattern Recognition Workshops (CVPRW)*, pages 1122–1131, 2017.

[2] B. Cai, X. Xu, K. Jia, C. Qing, and D. Tao. Dehazenet: An end-to-end system for single image haze removal. *IEEE Transactions on Image Processing*, 25(11):5187–5198, 2016.

[3] S. H. Chan, R. Khoshabeh, K. B. Gibson, P. E. Gill, and T. Q. Nguyen. An augmented lagrangian method for total variation video restoration. *IEEE Transactions on Image Processing*, 20(11):3097–3111, 2011.

[4] Yubin Deng, Chen Change Loy, and Xiaoou Tang. Aesthetic-driven image enhancement by adversarial learning, 2018.

[5] Jianhua Wu Feifan Lv, Feng Lu and Chongsoon Lim. Mbllen: Low-light image/video enhancement using cnns. *British Machine Vision Conference*, 2018.

[6] Michaël Gharbi, Jiawen Chen, Jonathan T Barron, Samuel W Hasinoff, and Frédo Durand. Deep bilateral learning for real-time image enhancement. *ACM Transactions on Graphics (TOG)*, 36(4):118, 2017.

[7] Chunle Guo, Chongyi Li, Jichang Guo, Chen Change Loy, Junhui Hou, Sam Kwong, and Runmin Cong. Zero-reference deep curve estimation for low-light image enhancement, 2020.

[8] Andrey Ignatov, Nikolay Kobyshev, Radu Timofte, Kenneth Vanhoey, and Luc Van Gool. Dslr-quality photos on mobile devices with deep convolutional networks, 2017.

[9] Andrey Ignatov, Nikolay Kobyshev, Radu Timofte, Kenneth Vanhoey, and Luc Van Gool. Wespe: Weakly supervised photo enhancer for digital cameras, 2018.

[10] Yifan Jiang, Xinyu Gong, Ding Liu, Yu Cheng, Chen Fang, Xiaohui Shen, Jianchao Yang, Pan Zhou, and Zhangyang Wang. Enlightengan: Deep light enhancement without paired supervision, 2019.

[11] D. J. Jobson, Z. Rahman, and G. A. Woodell. A multiscale retinex for bridging the gap between color images and the human observation of scenes. *IEEE Transactions on Image Processing*, 6(7):965–976, 1997.

[12] D. J. Jobson, Z. Rahman, and G. A. Woodell. Properties and performance of a center/surround retinex. *IEEE Transactions on Image Processing*, 6(3):451–462, 1997.

[13] P. Kaushik and Y. Sharma. Comparison of different image enhancement techniques based upon psnr & mse. 7:2010–2014, 01 2012.

[14] Kin Gwn Lore, Adedotun Akintayo, and Soumik Sarkar. Llnet: A deep autoencoder approach to natural low-light image enhancement, 2016.

[15] Feifan Lv, Yu Li, and Feng Lu. Attention guided low-light image enhancement with a large scale low-light simulation dataset, 2020.

[16] Keiron O'Shea and Ryan Nash. An introduction to convolutional neural networks, 2015.

[17] S. M. Pizer, R. E. Johnston, J. P. Ericksen, B. C. Yankaskas, and K. E. Muller. Contrast-limited adaptive histogram equalization: speed and effectiveness. In *[1990] Proceedings of the First Conference on Visualization in Biomedical Computing*, pages 337–345, 1990.

[18] Stephen M. Pizer, E. Philip Amburn, John D. Austin, Robert Cromartie, Ari Geselowitz, Trey Greer, Bart ter Haar Romeny, John B. Zimmerman, and Karel Zuiderveld. Adaptive histogram equalization and its variations. *Computer Vision, Graphics, and Image Processing*, 39(3):355 – 368, 1987.

[19] L. Tao, C. Zhu, J. Song, T. Lu, H. Jia, and X. Xie. Low-light image enhancement using cnn and bright channel prior. In *2017 IEEE International Conference on Image Processing (ICIP)*, pages 3215–3219, 2017.

[20] W. Wang, C. Wei, W. Yang, and J. Liu. Gladnet: Low-light enhancement network with global awareness. In *2018 13th IEEE International Conference on Automatic Face Gesture Recognition (FG 2018)*, pages 751–755, 2018.

[21] W. Wang, X. Wu, X. Yuan, and Z. Gao. An experiment-based review of low-light image enhancement methods. *IEEE Access*, 8:87884–87917, 2020.

[22] Zhou Wang, Alan Bovik, and Hamid Sheikh. Structural similarity based image quality assessment. *Digital Video Image Quality and Perceptual Coding, Ser. Series in Signal Processing and Communications*, 11 2005.

[23] Chen Wei, Wenjing Wang, Wenhan Yang, and Jiaying Liu. Deep retinex decomposition for low-light enhancement, 2018.

[24] B. Xiao, Y. Xu, H. Tang, X. Bi, and W. Li. Histogram learning in image contrast enhancement. In *2019 IEEE/CVF Conference on Computer Vision and Pattern Recognition Workshops (CVPRW)*, pages 1880–1889, 2019.

[25] J. Xu, Y. Hou, D. Ren, L. Liu, F. Zhu, M. Yu, H. Wang, and L. Shao. Star: A structure and texture aware retinex model. *IEEE Transactions on Image Processing*, 29:5022–5037, 2020.

[26] Ke Xu, Xin Yang, Baocai Yin, and Rynson W.H. Lau. Learning to restore low-light images via decomposition-and-enhancement. In *Proceedings of the IEEE/CVF Conference on Computer Vision and Pattern Recognition (CVPR)*, June 2020.

[27] Xuan Dong, Guan Wang, Yi Pang, Weixin Li, Jiangtao Wen, Wei Meng, and Yao Lu. Fast efficient algorithm for enhancement of low lighting video. In *2011 IEEE International Conference on Multimedia and Expo*, pages 1–6, 2011.

[28] W. Yang, X. Zhang, Y. Tian, W. Wang, J. Xue, and Q. Liao. Deep learning for single image super-resolution: A brief review. *IEEE Transactions on Multimedia*, 21(12):3106–3121, 2019.

[29] L. Zhang, L. Zhang, X. Mou, and D. Zhang. Fsim: A feature similarity index for image quality assessment. *IEEE Transactions on Image Processing*, 20(8):2378–2386, 2011.

[30] Yonghua Zhang, Jiawan Zhang, and Xiaojie Guo. Kindling the darkness: A practical low-light image enhancer. *Proceedings of the 27th ACM International Conference on Multimedia*, 2019.

[31] Zhou Wang, A. C. Bovik, H. R. Sheikh, and E. P. Simoncelli. Image quality assessment: from error visibility to structural similarity. *IEEE Transactions on Image Processing*, 13(4):600–612, 2004.

Authorized licensed use limited to: DELHI TECHNICAL UNIV. Downloaded on March 27,2021 at 05:46:41 UTC from IEEE Xplore. Restrictions apply.

AIP Conference Proceedings

A delayed version of prey predator system with modified Holling-Tanner response

Cite as: AIP Conference Proceedings **2336**, 020005 (2021); https://doi.org/10.1063/5.0046306
Published Online: 26 March 2021

Charu Arora, and Vivek Kumar

View Online Export Citation

ARTICLES YOU MAY BE INTERESTED IN

Study of a prey–predator model with preventing crop pest using natural enemies and control
AIP Conference Proceedings **2336**, 020002 (2021); https://doi.org/10.1063/5.0045745

Enhanced absorption in thin film silicon solar cell using plasmonic nanoparticles: An FDTD study
AIP Conference Proceedings **2336**, 020003 (2021); https://doi.org/10.1063/5.0045725

A hybrid deep learning network for atmospheric carbon monoxide prediction in the Indian region
AIP Conference Proceedings **2336**, 020006 (2021); https://doi.org/10.1063/5.0045784

Challenge us.
What are your needs for periodic signal detection?
Watch

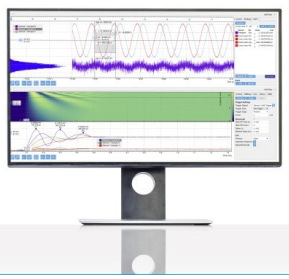

Zurich Instruments

AIP Publishing

© 2021 Author(s).

A Delayed Version of Prey Predator System with Modified Holling-Tanner Response

Charu Arora[1,a)] and Vivek Kumar[2,b)]

[1] *Department of Applied Sciences, Bharati Vidyapeeth's College of Engineering, Paschim Vihar, Delhi-110063, India*

[2]*Department of Applied Mathematics, Delhi Technological University, Shahbad Daulatpur, Main Bawana Road, Delhi-110042, India.*

[a)]*Corresponding author: charuarora099@gmail.com*
[b)]*Electronic mail: vivekkumar.ag@gmail.com*

Abstract. The paper deals with a delayed version of prey predator model with the incorporation of modified Holling-Tanner functional response in predator population. The model highlights the loss in prey population via migration and the natural death rate due to age factor and other reasons such as prenatal death, infection etc. The model also considers the significance of delay in the predator population which is taken as a parameter of bifurcation. Local stability analysis is done in the paper and it is examined that delay is important in attaining system's stability. Hopf bifurcation is discussed in brief along with the stability of bifurcated type of periodic solutions stability by considering normal form and central manifold theories is applied. Numerical simulations asserts the theory and concludes the paper.

Keywords: Bifurcation Analysis, Prey Predator Model, Stability

INTRODUCTION

In Ecology, the study of prey predator systems form a significant part. Various types of models exist in literature which depicts the role of numerous factors for representing an ideal ecological system. Moreover, the delayed form of prey predator models have gained recognition from long time. The system below describes the prey predator model with delay using Holling Type II response [1] and takes the form as;

$$\begin{cases} \frac{dx}{dt} = rx(1-\frac{x}{k}) - \frac{mx}{A+x}y, \\ \frac{dy}{dt} = y[s(1-h\frac{y}{x})], \end{cases} \tag{1}$$

where, x, y represents the density of prey population and predator population respectively. k is the carrying capacity and r is the rate of intrinsic growth. m represents the maximal predator per capita consumption rate. A symbolizes the number of prey density needed to achieve one-half of the maximum rate m. The expression $\frac{hy}{x}$ is known to be as Leslie Gower term [2]. The Holling Type II system (1) is remodelled in [3] using the Beddington DeAngelis response which takes the form as;

$$\begin{cases} \frac{dx}{dt} = rx(1-\frac{x}{k}) - \frac{\alpha xy}{a+bx+cy}y, \\ \frac{dy}{dt} = y[s(1-h\frac{y(t-\tau)}{x(t-\tau)})], \end{cases} \tag{2}$$

where x and y have the usual definitions as above. The model 2 can be made simpler by taking $\widetilde{t} = rt$, $\widetilde{x} = \frac{x(t)}{k}$, $\widetilde{y} = \frac{\alpha y(t)}{rk}$ and the non-dimensional model is (after omitting the tildes);

$$\begin{cases} \frac{dx}{dt} = x(1-x) - \frac{xy}{a_1+bx+c_1y}, \\ \frac{dy}{dt} = y[(\delta - \beta\frac{y(t-\tau)}{x(t-\tau)})], \end{cases} \tag{3}$$

where, $\delta = \frac{s}{r}$, $\beta = \frac{sh}{\alpha}$, $a_1 = \frac{a}{k}$, $c_1 = \frac{cr}{\alpha}$, $\widetilde{\tau} = r\tau$. This system is studied from the view of stability and certain properties of the system.

In the proposed system, we have investigated the effect of migration in the allee type of growth rate. Crowley Martin type response (C-M type functional response) [4] is considered for examining the interaction by feeding on

International Conference on Computational Sciences-Modelling, Computing and Soft Computing (CSMCS 2020)
AIP Conf. Proc. 2336, 020005-1–020005-8; https://doi.org/10.1063/5.0046306
Published by AIP Publishing. 978-0-7354-4080-7/$30.00

prey by the predator population. The model after the incorporation of Allee effect with C-M type functional response in prey population and the modified Holling Tanner response in predator population is follows;

$$\begin{cases} \frac{dx}{dt} = rx(1-\frac{x}{k})(\frac{x}{k'}-1) - \frac{\beta xy}{a'+b'y+cx+d'xy} - m_1'x, \\ \frac{dy}{dt} = y[s(1-\frac{hy(t-\tau)}{x(t-\tau)})] - m_2'y, \end{cases} \tag{4}$$

where, r represents the intrinsic growth rate of prey population. k is the carrying capacity of prey population. k' is the threshold population. β is the rate of capturing the prey by predators. b', c denote the handling time by predators, interference among predators respectively. m_1', m_2' denote the coefficients of migration in prey population and predator population respectively.
Further, the above defined system can be reduced into a much simplified form by taking the assumptions as $\tilde{t} = rt, \tilde{x} = \frac{x}{k}, \tilde{y} = \frac{y}{rk}, \tilde{\tau} = r\tau$, $\frac{s}{r} = \delta, hr = \xi, \frac{m_1'}{r} = m_1, \frac{m_2'}{r} = m_2, \frac{\beta'}{k} = \beta, \frac{a'}{k} = a, b'r = b, d'rk = d, k_0 = \frac{k'}{k} = 1$. After ignoring the tildes in variables and writing the system in usual variables, we get as;

$$\begin{cases} \frac{dx}{dt} = x(1-x)(x-1) - \frac{\beta xy}{a+by+cx+dxy} - m_1x, \\ \frac{dy}{dt} = y[\delta(1-\frac{\xi y(t-\tau)}{x(t-\tau)})] - m_2y. \end{cases} \tag{5}$$

x and y with the usual meaning as described above. In the paper, we have focussed on the existence of interior equilibrium point and its stability conditions in the next section. The Hopf bifurcation process [5] has been explained for the delay system in further section followed by the numerical simulation part in section 4. Finally, the section 5 comprises of the conclusion.

LOCAL STABILITY AND HOPF BIFURCATION

The system 5 possesses the following equilibrium points as;

- $(0,0)$
- (x^*, y^*), where, x^* is the nonzero positive root given by the equation as, $x^4(-dD)+x^3(2dD-bD-c-m_1dD)+x^2(2bD+2c-dD-a-m_1bD-m_1c)+x(2a-bD-c-\beta-m_1a)-a=0$, where, $D=\frac{\delta-m_2}{\delta\xi}$ and $y^*=Dx^*$. x^* is the root of the equation which is obtained by substituting $y=Dx$ in the equation $(1-x)(x-1)-\frac{\beta y}{a+by+cx+dxy}-m_1$.
- The equilibrium points $(x',0)$ and $(0,y')$ do not exist where, x' is a complex root obtained from $x^2-2x+(m_1+1)=0$ and y' is undefined.

The corresponding Jacobian matrix of the system 5 is given as;

$$J = \begin{pmatrix} \alpha_{11} & \alpha_{12} \\ \alpha_{21} & \alpha_{22} \end{pmatrix}, \text{ where,}$$

$$\alpha_{11} = (4x^* - 1 - 3x^{*2}) - \frac{\beta y^* a + \beta b y^{*2}}{(a+by^*+cx^*+dx^*y^*)^2} - m_1,$$

$$\alpha_{12} = \frac{-\beta x^*(a+cx^*)}{(a+by^*+cx^*+dx^*y^*)^2},$$

$$\alpha_{21} = \frac{\delta\xi y^{*2}}{x^{*2}},$$

$$\alpha_{22} = \delta - \frac{\delta\xi 2y^*}{x^*} - m_2.$$

The characteristic equation becomes as;
$\lambda^2 - (Tr.J)\lambda + (Det.J) = 0$ or $\lambda^2 - (\alpha_{11}+\alpha_{22})\lambda + (\alpha_{11}\alpha_{22} - \alpha_{12}\alpha_{21}) = 0$.

On applying the Routh-Hurwitz rule [6] for determining the stability of the model, we get the following result;

$\alpha_{11}\alpha_{22} - \alpha_{12}\alpha_{21} > 0$ and $\alpha_{11} + \alpha_{22} < 0$.

On the basis of the conditions of local stability for the proposed model in the absentia of delay, we state the following theorem.

Theorem 1. *The nonzero equilibrium point $E^*(x^*,y^*)$ for the system 5 is said to be locally asymptotically stable with the below conditions;*

I. $\left(4x^* - 1 - 3x^{*2} - \frac{\beta y^* a + \beta b y^{*2}}{(a+by^*+cx^*+dx^*y^*)^2} - m_1\right)\left(\delta - \frac{\delta\xi 2y^*}{x^*} - m_2\right) - \left(\frac{-\beta x^*(a+cx^*)}{(a+by^*+cx^*+dx^*y^*)^2}\right)\left(\frac{\delta\xi y^{*2}}{x^{*2}}\right) > 0.$

II. $\left(4x^* - 1 - 3x^{*2} - \frac{\beta y^* a + \beta b y^{*2}}{(a+by^*+cx^*+dx^*y^*)^2} - m_1\right) + \left(\delta - \frac{\delta\xi 2y^*}{x^*} - m_2\right) < 0.$

The conditions of the occurrence for the Hopf bifurcation process [5] is discussed below.
The characteristic equation of the system 5 is taken as;

$$\lambda^2 - (\alpha_{11} + \alpha'_{22})\lambda + (-\beta_{11}\alpha_{11} + \beta_{11}\lambda - \alpha_{12}\alpha_{21})e^{-\lambda\tau} + \alpha_{11}\alpha'_{22} = 0, \tag{6}$$

where, $\alpha'_{22} = \frac{-\delta\xi y^*}{x^*} - m_2$.

On substituting, $\lambda = i\omega$ in the above characteristic equation, we get,
$-\omega^2 + (-\beta_{11}\alpha_{11} - \alpha_{12}\alpha_{21})\cos\omega\tau + \beta_{11}\omega\sin\omega\tau + \alpha_{11}\alpha'_{22} +$
$i[\beta_{11}\omega\cos\omega\tau + (\alpha_{11}\beta_{11} + \alpha_{12}\alpha_{21})\sin\omega\tau - (\alpha_{11} + \alpha_{22})\omega] = 0 + 0i.$
On separating both the real as well as the imaginary parts of the above expression, we get,

$$-\omega^2 - (\alpha_{11}\beta_{11} + \alpha_{12}\alpha_{21})\cos\omega\tau + \beta_{11}\omega\sin\omega\tau + \alpha_{11}\alpha_{22} = 0, \tag{7}$$

$$\beta_{11}\omega\cos\omega\tau + (\alpha_{11}\beta_{11} + \alpha_{12}\alpha_{21})\sin\omega\tau - (\alpha_{11} + \alpha_{22})\omega = 0. \tag{8}$$

Squaring and adding the equations 7 and 8, we get,

$$\omega^4 + (\alpha_{11}^2 + \alpha_{22}^2)\omega^2 + (\alpha_{11}^2\alpha_{22}^2 - 2\alpha_{11}\alpha_{21}\alpha_{22}\alpha_{12} + \alpha_{21}^2\alpha_{12}^2 - \beta_{11}^2\alpha_{11}^2) = 0. \tag{9}$$

Let $z = \omega^2$, we get,

$$z^2 + (\alpha_{11}^2 + \alpha_{22}^2)z + (\alpha_{11}^2\alpha_{22}^2 - 2\alpha_{11}\alpha_{21}\alpha_{22}\alpha_{12} + \alpha_{21}^2\alpha_{12}^2 - \beta_{11}^2\alpha_{11}^2) = 0, \tag{10}$$

The roots of the above equation are given by,

$z = \frac{-(\alpha_{11}^2+\alpha_{22}^2) \pm \sqrt{(\alpha_{11}^2+\alpha_{22}^2)^2 - 4(\alpha_{11}^2\alpha_{22}^2 - 2\alpha_{11}\alpha_{21}\alpha_{22}\alpha_{12} + \alpha_{21}^2\alpha_{12}^2 - \beta_{11}^2\alpha_{11}^2)}}{2}$.
Considering the positive root only, we get as,

$z = \frac{-(\alpha_{11}^2+\alpha_{22}^2) + \sqrt{(\alpha_{11}^2-\alpha_{22}^2)^2 - 4(\alpha_{11}^2\alpha_{22}^2 - 2\alpha_{11}\alpha_{21}\alpha_{22}\alpha_{12} + \alpha_{21}^2\alpha_{12}^2 - \beta_{11}^2\alpha_{11}^2)}}{2}$.
So,

$$\omega = \pm\sqrt{\frac{-(\alpha_{11}^2 - \alpha_{22}^2) + \sqrt{(\alpha_{11}^2 - \alpha_{22}^2)^2 - 4(\alpha_{11}^2\alpha_{22}^2 - 2\alpha_{11}\alpha_{21}\alpha_{22}\alpha_{12} + \alpha_{21}^2\alpha_{12}^2 - \beta_{11}^2\alpha_{11}^2)}}{2}}. \tag{11}$$

On the consideration of positive root only and denoting them by $\omega_{pos.}$, we get,

$\omega_{pos} = \sqrt{\frac{-(\alpha_{11}^2-\alpha_{22}^2) + \sqrt{(\alpha_{11}^2-\alpha_{22}^2)^2 - 4(\alpha_{11}^2\alpha_{22}^2 - 2\alpha_{11}\alpha_{21}\alpha_{22}\alpha_{12} + \alpha_{21}^2\alpha_{12}^2 - \beta_{11}^2\alpha_{11}^2)}}{2}}$.
Again, using equations 7 and 8 to obtain τ which are the critical values;
$\tau_j = \frac{1}{\omega_{pos}}\cos^{-1}\frac{\omega_{pos}^2(\alpha_{12}\alpha_{21} - \alpha_{22}\beta_{11}) - \alpha_{11}^2\alpha_{22}\beta_{11} + \alpha_{11}\beta_{11}\alpha_{12}\alpha_{21} + \alpha_{12}^2\alpha_{21}^2}{(\alpha_{11}\beta_{11} + \alpha_{12}\alpha_{21})^2 + \beta_{11}^2\omega_{pos}^2} + \frac{2\pi j}{\omega_{pos}}$, where j=0,1,2....

We take one of τ_j as τ_{cr} to get the following;

$\tau_{cr} = \frac{1}{\omega_{pos}} \cos^{-1} \frac{\omega_{pos}^2(\alpha_{12}\alpha_{21}-\alpha_{22}\beta_{11})-\alpha_{11}^2\alpha_{22}\beta_{11}+\alpha_{11}\beta_{11}\alpha_{12}\alpha_{21}+\alpha_{12}^2\alpha_{21}^2}{(\alpha_{11}\beta_{11}+\alpha_{12}\alpha_{21})^2+\beta_{11}^2\omega_{pos}^2}$.,
Given below is the lemma as in [5];

Lemma 1. *Let the positive nonzero equilibrium point for the system 5 is locally asymptotically stable without the presence of delay. At,*
$\tau_j = \frac{1}{\omega_{pos}} \cos^{-1} \frac{\omega_{pos}^2(\alpha_{12}\alpha_{21}-\alpha_{22}\beta_{11})-\alpha_{11}^2\alpha_{22}\beta_{11}+\alpha_{11}\beta_{11}\alpha_{12}\alpha_{21}+\alpha_{12}^2\alpha_{21}^2}{(\alpha_{11}\beta_{11}+\alpha_{12}\alpha_{21})^2+\beta_{11}^2\omega_{pos}^2} + \frac{2\pi j}{\omega_{pos}}$, *(where $j = 0,1,2...$), system possesses a pair of conjugate pure roots of imaginary nature $\pm i\omega_{pos}$, where,*
$\omega_{pos} = \sqrt{\frac{-(\alpha_{11}^2-\alpha_{22}^2)+\sqrt{(\alpha_{11}^2-\alpha_{22}^2)^2-4(\alpha_{11}^2\alpha_{22}^2-2\alpha_{11}\alpha_{21}\alpha_{22}\alpha_{12}+\alpha_{21}^2\alpha_{12}^2-\beta_{11}^2\alpha_{11}^2)}}{2}}$. *Based on the value of τ obtained, we have the result as;*
(i) If $\tau \in [0,\tau_{cr})$, it implies that roots for 5 have negative real parts.
(ii) If $\tau = \tau_{cr}$, it implies that 5 has a pair of conjugate pure roots with imaginary nature $\pm\omega_{pos}$, and all other roots with real parts as negative.

On taking $\lambda = v(\tau) + i\omega(\tau)$ which is the root of characteristic equation 6 having the defined condition as;
$\tau = \tau_{cr}$,

$$\begin{cases} v(\tau_{cr}) = 0, \\ \omega(\tau_{cr}) = \omega_{pos}. \end{cases}$$

Using 6 and getting the below result to prove the existence of transversality condition is as follows;

$[Re\left(\frac{d\lambda}{d\tau}^{-1}\right)]_{i\omega_{pos}} > 0,$
On this basis, the bifurcation theorem is stated as; (1.6).

Theorem 2. *Lets assume that theorem 1 is true along with the following conditions.*
(i) If $\tau \in [0,\tau_{cr})$, $E^*(x^*,y^*)$ for 5 is asymptotically stable.
(ii) If $\tau > \tau_{cr}$, $E^*(x^*,y^*)$ of system 5 is unstable.
(iii) System 5 shows Hopf bifurcation at $E^*(x^*,y^*)$ if $\tau = \tau_j$, with,
$\tau_j = \frac{1}{\omega_{pos}} \cos^{-1} \frac{\omega_{pos}^2(\alpha_{12}\alpha_{21}-\alpha_{22}\beta_{11})-\alpha_{11}^2\alpha_{22}\beta_{11}+\alpha_{11}\beta_{11}\alpha_{12}\alpha_{21}+\alpha_{12}^2\alpha_{21}^2}{(\alpha_{11}\beta_{11}+\alpha_{12}\alpha_{21})^2+\beta_{11}^2\omega_{pos}^2} + \frac{2\pi j}{\omega_{pos}}$, *(where $j = 0,1,2...$).*

DIRECTION OF HOPF BIFURCATION

By making use of normal form and central manifold theories, the direction of Hopf bifurcation is depicted as in [7, 8, 9]. Result of theorem 2 states that for a specific value of τ say τ_j, system shows Hopf bifurcation. We call one of the specific value as $\overline{\tau}$. The characteristic equation of the system possesses a pair of imaginary roots as $\pm i\omega_{pos}$. A functional differential equation is used to reduce the system 5 and τ is taken as $\tau = \overline{\tau} + \mu$ where $\mu \in \mathbb{R}$. $\mu = 0$ is the Hopf bifurcation value for the system and taking time parameter as $\rightarrow \frac{t}{\tau}$, system becomes;

$$u'(t) = L_\mu u(t) + F(u_t, \mu), \tag{12}$$

in $\mathbb{C}([-1,0],\mathbb{R}^2)$, which is a Banach space where u=$\begin{pmatrix} u_1 \\ u_2 \end{pmatrix} \in \mathbb{C}$ and $L_\mu : \mathbb{C} \rightarrow \mathbb{R}$, $F : \mathbb{R} \times \mathbb{C} \rightarrow \mathbb{R}$ [4]. The following values can be obtained as;
$C_1(0) = \frac{i}{2\omega_{pos}\overline{\tau}}\left(g_{20}g_{11} - 2|\, g_{11}\,|^2 - \frac{|g_{02}|^2}{3}\right) + \frac{g_{21}}{2}$,
$\mu_2 = \frac{Re\{C_1(0)\}}{Re\{\lambda'(\overline{\tau})\}}$ and $\beta_2 = 2Re\{C_1(0)\}$.

The theorem below is stated as;

Theorem 3. *(i) μ_2 provides the Hopf bifurcation direction i.e. the sign of μ_2 governs the type of Hopf bifurcation. Depending upon $\mu_2 > 0 (< 0)$, the Hopf bifurcation becomes supercritical(subcritical);*
(ii) β_2 provides the stability aspect of the bifurcated periodic solutions. Depending upon $\beta_2 > 0 (< 0)$, the bifurcated periodic solutions are stable (unstable).

Proof: Based on the result of Lemma 1, we get the following as;

$$\frac{d(Re\lambda(\tau))}{d\tau} \neq 0 \text{ at } \tau^*.$$

Using the result of Theorem 2, the system undergoes Hopf bifurcation when $\tau = \tau^*$. Therefore, the theorem follows from the results in [8].

NUMERICAL SIMULATIONS

This section deals with the numerical simulations by assuming the hypothetical values for the parameters and the system in the absence of migration becomes as;

$$\begin{cases} \frac{dx}{dt} = x(1-x)(x-1) - \frac{0.9xy}{2+2x+y+xy}, \\ \frac{dy}{dt} = y[3.5(1 - \frac{2y(t-\tau)}{0.9x(t-\tau)})]. \end{cases} \tag{13}$$

The system above defined with no migration factor in prey as well as in predator populations($m_1 = m_2 = 0$). Dynamics is studied in figure 1 and figure 2. System is stable for $\tau \in [0, 0.44)$ and unstable for $\tau > 0.44$. The system with migration is as follows;

$$\begin{cases} \frac{dx}{dt} = x(1-x)(x-1) - \frac{0.9xy}{2+2x+y+xy} - 0.9x, \\ \frac{dy}{dt} = y[3.5(1 - \frac{7y(t-\tau)}{x(t-\tau)})] - 0.9y. \end{cases} \tag{14}$$

The above system with the migration parameter in populations as ($m_1 = m_2 = 0.6$) along with the delay parameter. System possesses a unique positive equilibrium $(0.67, 0.45)$ and using the already stated lemma 1, $\omega_{pos} = 2.909$ and $\tau_{cr} = 0.50$. It is examined that the equilibrium point becomes $(0.67, 0.45)$ for the system and it is locally stable without the delay factor τ which asserts with theorem 1. It is to be seen in figure 1 that system possesses the stable nature when migration factor is completely ignored and $\tau = 0.35$ is considered. But, on changing the value of τ, the same system oscillates as shown in figure 2. Using theorem 2, the system gets asymptotically stable for $\tau \in [0, 0.5)$ and unstable for $\tau > 0.5$ and Hopf bifurcation process occurs at $\tau = 0.5$.(figure 3 and figure 4).
Thereafter, dynamics of the system is studied by taking some different value of τ which depicts that the system with allee effect shows wide variety of changed dynamics(figure 5). Figure 5 portrays the effect of allee in the system in the time plot graph and two dimensional plot between x and y.

DISCUSSION

In this paper, the interaction among the prey predator population has been described by means of Crowley Martin type response. Further, the system has been incorporated with Allee effect in the prey population. Also, migration factor is taken into consideration to depict the loss in population in both prey and predator population. To prove the theoretical aspects of the system, we perform numerical analysis of the paper. The Hopf Bifurcation process has been investigated in the paper, in brief and the role of τ is highlighted in the bifurcation process. It is observed that Hopf bifurcation occurs around the nonzero equilibrium point at some critical value of the parameter say τ_{cr}. The figures illustrate that the prey and predator population converge towards their equilibrium point in a finite interval of time at

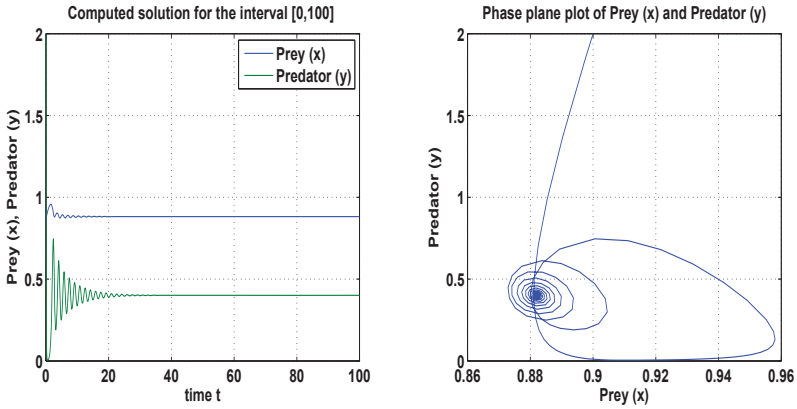

FIGURE 1. Solution of the System 5 without migration $m_1 = m_2 = 0$ and $\tau = 0.35$ computed over the interval [0,100].

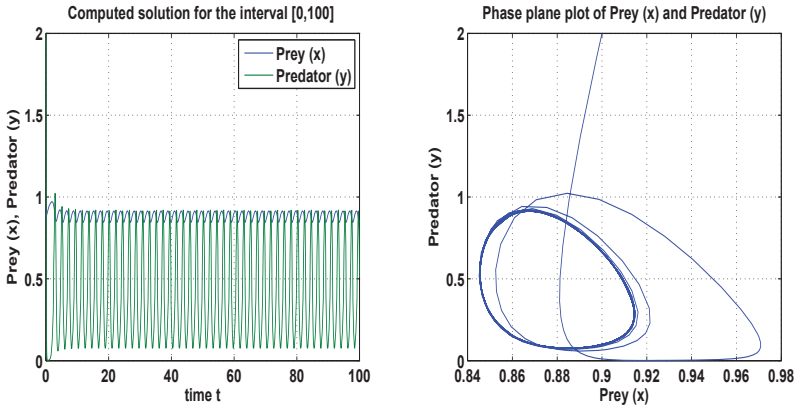

FIGURE 2. Solution of the System 5 without migration $m_1 = m_2 = 0$ and $\tau = 0.50 > \tau_{cr}$ computed over the interval [0,100].

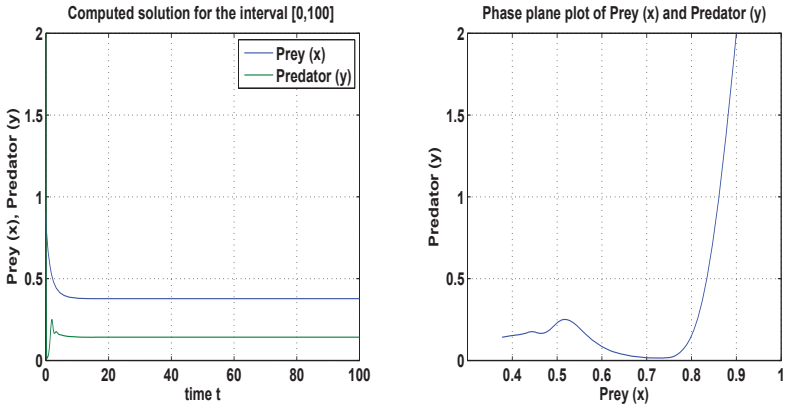

FIGURE 3. Solution of the System 5 with migration $m_1 = m_2 = 0.6$ and $\tau = 0.2$ computed over the interval [0,100].

some interval of time lag(delay). As the time lag increases, prey and predator population shows periodic oscillations during the time. It suggests that prey and predator dynamics depends upon the population at some earlier time also.

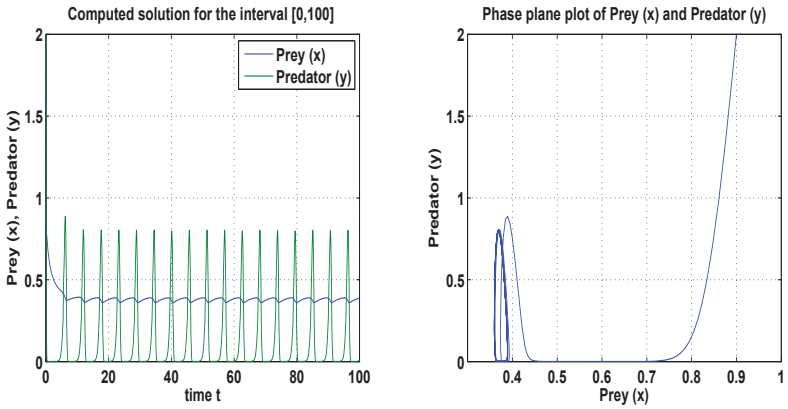

FIGURE 4. Solution of the System 5 with migration $m_1 = m_2 = 0.6$ and $\tau = 0.9 > \tau_{cr}$ computed over the interval [0,100].

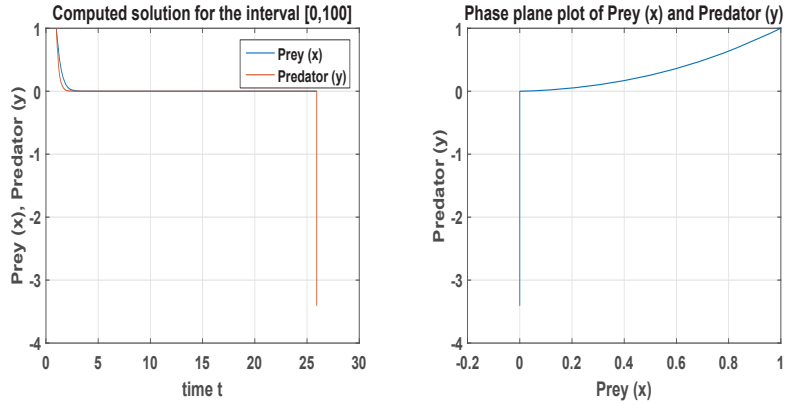

FIGURE 5. Solution of the System 5 with migration $m_1 = m_2 = 0.6$, and $\tau = 5$ computed over the interval [0,100].

The system in the paper has been studied taking into consideration the role of allee effect unlike in [7, 9] where the aspect of refuge is significantly observed.
In future, the same model can further be studied by taking into consideration the refuge factor along with the logistic growth model([10, 11]) and the comparison study can be performed based on certain theoretical and analytical results as in [12, 13, 14].

ACKNOWLEDGEMENT

Authors are thankful to anonymous reviewers for their very useful and valuable suggestions.

REFERENCES

1. G.T Skalski and J.F Gilliam: Functional responses with predator interference: viable alternatives to the Holling type II model, Ecology, 82(11) (2001) 3083-3092.
2. P.H Leslie, J.C Gower: The properties of a stochastic model for the predator-prey type of interaction between two species, Biometrika 47 (1960) 219-234.
3. Z. Lu, X. Liu : Analysis of a predator prey model with modified Holling-Tanner functional response and time delay, Nonlinear Analysis-Real World Appl. 9 (2008) 641-650.

4. Upadhyay, R.K Upadhyay, R.K Naji : Dynamics of a three species food chain model with CrowleyMartin type functional response, Chaos, solitons and fractals 42(3) (2009) 1337-134
5. J.F Zhang: Bifurcation analysis of a modified Holling-Tanner predator-prey model with time delay, Applied Mathematical Modeling 36 (2012) 1219-1231.
6. E.X DeJesus, C. Kaufman : Routh-Hurwitz criterion in the examination of eigenvalues of a system of nonlinear ordinary differential equations. Physical Review A., 35(12) (1987): 5288.
7. C. Arora, V. Kumar: Bifurcation Analysis of a Delayed Modified Holling-Tanner Predator-Prey Model with Refuge, Proceedings of International Conference on Mathematics and Computing, ICMC (2017) 246-254.
8. B.D Hassard, N.D Kazarinoff, Y.H Wan: Theory and Applications of Hopf Bifurcation, Camb. Uni. Press, Cambridge (1981).
9. C. Arora, V. Kumar: Dynamical Behavior of a Stage Structured Prey Predator Model with Two Delays and Monod Haldane Functional Response, International Journal of Applied and Computational Mathematics, 4(1), (2018), 4-46.
10. S. Kant, V. Kumar: Delayed prey-predator system with habitat complexity and refuge, Proceedings of International Conference on Mathematical Sciences, ICMS (2014) 584-591.
11. S. Kant, V. Kumar: Stability analysis of predator-prey system with migrating prey and disease infection in both species Applied Mathematical Modeling, 42(2017) 509-539.
12. S. Kant, V. Kumar: Dynamics of a prey-predator system with infection in prey, Electronic Journal of Differential Equations 209(2017), 1-27.
13. S. Kant, V. Kumar: Dynamical behavior of a stage structured prey-predator model, International Journal of Nonlinear Analysis and Applications 7 (1), (2016) 231-241.
14. M. Mehra, R.K Mallik: Solutions of DifferentialDifference Equations Arising from Mathematical Models of Granulocytopoiesis, Differential Equations and Dynamical Systems 22 (1), (2014) 33-49.

2021 International Conference on Automation, Robotics and Applications

A Novel Approach to Computationally Lighter GNSS-Denied UAV Navigation Using Monocular Camera

Joyraj Bhowmick*
Delhi Technological University
New Delhi, India
joyrajbhowmick_2k17ee100@dtu.ac.in

Anurag Singh*
Delhi Technological University
New Delhi, India
anuragsingh_2k17ec32@dtu.ac.in

Harshit Gupta*
Delhi Technological University
New Delhi, India
harshitgupta_2k19co151@dtu.ac.in

Raghava Nallanthighal**
Delhi Technological University
New Delhi, India
nsraghava@dtu.ac.in

***Abstract*—A good receptivity of GNSS signals during autonomous navigation is of prime importance. Due to this, navigation becomes close to impossible with places having low receptivity or GNSS-denied zones. In this paper, a navigational system is presented for a multi-rotor UAV in a GNSS-denied environment. The global positioning problem is solved by taking a local reference frame and estimating the UAV's position and velocity w.r.t it, using an onboard monocular camera and barometer. The navigational problem is solved by designing a required velocity function and tuning the system's response to this input by a PID controller. The results of both simulations and actual flight tests show the effectiveness and reliability of the presented work, which enables a UAV to perform full automated missions from takeoff, waypoint navigation and landing, in complete absence of any GNSS signals.**

Keywords—GNSS-denied outdoor navigation, Unmanned Aerial Vehicles, Visual Odometry

NOMENCLATURE

UAV	Unmanned Aerial Vehicle
fps	Frames Per Second
GNSS	Global Navigation Satellite System
NED	North East Down
f_w, f_h	Image frame width (in pixels) and height (in pixels)
fov_w, fov_h	Horizontal and vertical field of view of camera (in degrees)
(r_i, c_i)	Row and column of the of the i^{th} detected feature in the image frame
n	Frame number
d_n	Displacement vector of the UAV in pixels
D_n	Displacement vector of the UAV in meter w.r.t the inertial frame
v'	Unfiltered velocity estimates
v	Filtered velocity estimates
k	Low-pass filter constant
v_r	Required velocity to towards destination
K_p, K_i, K_d	Proportional, integral and derivative constants of PID
e_v	Difference between required velocity and current velocity
acc	Acceleration vector required to reduce the velocity difference

*These authors contributed equally.
**Corresponding author (phone: +91 97117 24842).

I. INTRODUCTION

UAVs are actively being developed and used for a wide range of civilian and military applications ranging from aerial photography, precision farming, land surveying, surveillance, reconnaissance, search and rescue operations, etc. [1]. Due to active research in UAVs and availability of reliable platforms, they are often used in HADR (Humanitarian Assistance and Disaster Relief) scenarios. They are required to navigate to a location, assess the situation, search for survivors, send back required data and finally return back to base. To achieve this, almost all UAVs rely on a combination of multiple GNSS systems for accurate positioning and hence navigation.

The loss of GNSS signals during a mission can occur due to multiple reasons: navigation in hilly terrain, presence of jammers, low signal patches, faulty sensors, etc. This can be devastating for the UAV and the mission and often leads to abortion of a critical mission. Various solutions have been proposed to counter this, but they majorly focus on indoor localization and navigation. In [2], a comparative study of different indoor navigation techniques is done. The author used reflective markers and installed multiple cameras in the lab to accurately locate the UAV. Another approach for indoor localization of UAVs is taken up by installing fiducial markers at various locations all over the building [3]. Since, both these methods require preparing the surrounding environment prior to flying, these cannot be used for outdoor navigation.

Various studies for outdoor navigation are also available as well, using a wide variety of approaches and sensors such as, lidars, optical flow sensors, IMUs, monocular vision cameras, stereo vision cameras, UWB radio modules, etc. In [4], the authors propose a method of geolocation by registering the aerial images taken during flight to the Google Satellite images of that location. This method is not readily deployable as the Google Satellite images are a prerequisite to flying at any new place. Moreover, this leads to errors if the Google Satellite images are not updated.

2021 7th International Conference on Automation, Robotics and Applications (ICARA) | 978-1-6654-0469-3/21/$31.00 ©2021 IEEE | DOI: 10.1109/ICARA51699.2021.9376502

Authorized licensed use limited to: DELHI TECHNICAL UNIV. Downloaded on March 27,2021 at 05:22:07 UTC from IEEE Xplore. Restrictions apply.

An approach using a stereo vision camera, an on-board computer running a ROS architecture is proposed for a rover [5]. However, the weight and power constraints for a UAV is much more stringent, hence the same approach cannot be used for a UAV. The solution proposed in [6] uses the PX4Flow optical flow sensor (directly compatible with ArduCopter) along with IMUs and barometer. Although the optical flow sensor used provides a low-cost solution to motion tracking and perception, they are not suitable for low feature rich areas and high-flying altitudes (>50m).

The authors in [7] used a monocular camera and IMUs to present a method of UAV localization through a landmark and developed a navigation solution that works till the landmark is in the FOV of the camera. This was further improved in [8] where a better navigational solution was presented where the UAV does not need any landmark but stores multiple features present on the ground during navigation. A different approach was presented for the same UAV and sensors in [9] where the flight performance was further improved. However, the approaches were computationally intensive, the authors in [8] used two flight computers and the authors in [9] used a flight computer with Intel i7 processor. Moreover, the flying altitude was <50m.

A solution for GNSS denied navigation with transition from outdoor to indoor environments was presented in [10]. The authors used a stereo vision camera and a 2D 360 lidar and achieved navigational speeds up to 18m/s. A similar approach was presented in [11], using a 2D 360 lidar capable of navigation in clustered outdoor environments. However, these solutions are feasible if the vehicle detects features/objects in its lateral plane (such as trees, walls, doors, etc.) while navigating, hence won't be applicable to UAV flying at higher altitudes (>50m).

It is evident that outdoor GNSS denied navigation solutions have been developed but they are not applicable at altitudes >50m. Also, most of these use an additional payload such as a particular optical flow sensor, lidar, stereo vision camera, etc. The aim of this paper to present a novel, computationally lighter approach to outdoor GNSS denied navigation applicable at altitudes >50m using only the most common and standard payload: barometer, flight computer and a monocular camera. The proposed navigational system comprises two major components:

- Position and Velocity Estimator: The image processing algorithm detects and tracks features on ground and processes them to calculate relative position and velocity of the UAV w.r.t ground.
- Navigational Controller: The navigational controller generates the trajectory and optimal control inputs for roll, pitch and thrust to follow the generated trajectory.

The solution outlined in this paper can be used as a backup navigational controller which remains active till the time the UAV flies through a GNSS dead zone, or can be used as a complete navigational controller for a UAV from takeoff to landing in a GNSS denied environment.

The rest of the paper is organized as follows: *Section II* provides some key concepts and notations used throughout the paper. *Section III* derives the position and velocity estimates. *Section IV* presents the navigational controller with required control inputs. *Section V* lists the results of tests conducted in simulations as well as actual flight tests, giving an optimum operating point. *Section VI* provides a brief conclusion and scope of future work.

II. Preliminaries

A. Reference Frames

Two reference frames are used in this paper:

- Inertial Frame: The origin and axes in this frame are fixed at a point in the ground (earth) and do not change w.r.t time. The conventional NED frame is used as inertial frame. The orientation of axes in this frame are:

  x-axis—positive towards north.
  y-axis—positive towards east.
  z-axis—positive downwards (towards gravity).

  The takeoff point of the UAV is taken as the origin for the inertial frame.

- Body Frame: The origin and axes in this frame are fixed at a point on the UAV and thus change w.r.t time. In the body frame the orientation of the axes are:

  x -axis—positive towards the heading of UAV (in UAV plane).
  y-axis—positive towards 90 degree clockwise from the heading (in UAV plane)
  z -axis—positive towards the $\frac{\vec{x}\times\vec{y}}{|\vec{x}\times\vec{y}|}$ direction, perpendicular to UAV plane.

  where, UAV plane is parallel to the plane of the Autopilot.

B. UAV Dynamics

The state of the UAV at any point of time is defined by 6 state variables:

$$[x \quad y \quad z \quad \phi \quad \theta \quad \psi]^T \tag{1}$$

where (x, y, z) represents the position of the UAV w.r.t the inertial frame and (ϕ, θ, ψ) represents the attitude of the UAV.

ϕ: Roll angle (about x-axis in body frame)
θ: Pitch angle (about y-axis in body frame)
ψ: Yaw angle (about z-axis in body frame)

The rotation matrix R_M is used to convert vectors from body frame to inertial frame [12].

$$R_M = \begin{bmatrix} C_\psi C_\theta & C_\psi S_\theta S_\phi - S_\psi C_\phi & C_\psi S_\theta C_\phi + S_\psi S_\phi \\ S_\psi C_\theta & S_\psi S_\theta S_\phi + C_\psi C_\phi & S_\psi S_\theta C_\phi - C_\psi S_\phi \\ -S_\theta & C_\theta S_\phi & C_\theta C_\phi \end{bmatrix} \tag{2}$$

here S_ϕ is $\sin\phi$, C_ϕ is $\cos\phi$, and so on.

For our system, the use of 3-axis gimbal helps the camera plane always lie parallel to the inertial x-y plane. We have also maintained $\psi = 0$, i.e., heading always pointing towards north during the entire flight. This provides a number of advantages:

Authorized licensed use limited to: DELHI TECHNICAL UNIV. Downloaded on March 27,2021 at 05:22:07 UTC from IEEE Xplore. Restrictions apply.

- Any trajectory can still be followed by a multirotor without changing its yaw angle.
- The constant yaw angle during flight excludes a lot of computational complexities.
- The rotation matrix formed is highly simplified and the camera being parallel to the inertial x-y plane allows the displacements calculated through the camera to be directly used as displacements in inertial frame.

Thus, for $\psi = 0$, the rotation matrix is reduced to:

$$R_M = \begin{bmatrix} C_\theta & S_\theta S_\phi & S_\theta C_\phi \\ 0 & C_\phi & -S_\phi \\ -S_\theta & C_\theta S_\phi & C_\theta C_\phi \end{bmatrix} \quad (3)$$

The only force acting in the UAV's frame (body frame) neglecting the drag due to the translational motion, is the upward force due to propulsion. Therefore, the force acting in the body frame is F_B. To convert this force and the roll pitch angles to the inertial frame of reference [13], the following equation is used:

$$\begin{bmatrix} \ddot{x} \\ \ddot{y} \\ \ddot{z} \end{bmatrix} = \frac{1}{m}\left(\begin{bmatrix} 0 \\ 0 \\ mg \end{bmatrix} + R_M \begin{bmatrix} 0 \\ 0 \\ -F_B \end{bmatrix}\right) \quad (4)$$

By simplifying the above equations, the relationship between linear accelerations of the UAV in the inertial frame and the roll angle, pitch angle and thrust is obtained:

$$\begin{bmatrix} \ddot{x} \\ \ddot{y} \\ \ddot{z} \end{bmatrix} = \frac{1}{m}\left(\begin{bmatrix} -F_B S_\theta C_\phi \\ F_B S_\phi \\ -F_B C_\theta C_\phi + mg \end{bmatrix}\right) \quad (5)$$

III. Estimation

A. Feature Detection and Tracking

The monocular camera used has been first calibrated to undistort the captured images. The camera is mounted on a 3-axis gimbal which counters the UAVs attitude and keeps the camera pointing downwards at all times during the flight. The gimbal is attached to the UAV through vibration isolation balls, reducing high-frequency vibrations in images. Images of the ground is continuously captured at a specified frame rate. Features are regions at an image with a large variation in intensity in all directions. Shi-Tomasi [14] and SURF [15] are found to be better feature detection algorithms [16]. To find the most suitable one for our case, these two algorithms were tested on a video of resolution 640×480 having 4857 frames captured by a UAV moving in a straight line at a speed of 5m/s and altitude 100m. The displacement of these features was tracked using the Lucas-Kanade optical flow algorithm as it can be easily applied to a subset of points in the input image combined with features improving efficiency (discussed further in [17]). It directly recovers motion at some required pixels from spatio-temporal image brightness variations in the image. It works under certain implicit assumptions:

- The displacement of the features in two consecutive images must not be significantly large.
- The images must depict texture objects, exhibiting varying brightness levels, changing smoothly.

The graphs of the estimated trajectory generated is plotted against actual trajectory in Fig. 1. The processing time for both the algorithms is shown in Table I.

The Shi-Tomasi corner detection algorithm was selected due to lower processing time and better accuracy which will suite high speed operations.

The UAV's motion is estimated by calculating the displacement vector of the distinct features between every two consecutive frames captured by the camera. Approximately 50-60 features are tracked on each frame. The features near the edges of the frame tend to accumulate at the same position for successive frames due to aperture problem, giving erroneous results. Thus, features within a pixel width of b from the edges of the image frame are discarded in the displacement calculation. The pixel width b is taken to be 20 pixels in our case. This significantly reduces errors without compromising on number of features. If a particular feature goes out of the image frame, it is neglected and estimation is continued with the rest of the features. If the number of features falls below 30, features are recomputed using the feature detection algorithm.

B. Position and Velocity Estimates

The position vector P, is the position of the UAV with respect to the inertial frame.

$$P = [x \quad y \quad z]^T \quad (6)$$

The point of takeoff (P_0) is taken as the home location of the UAV, with

$$P_0 = [0 \quad 0 \quad 0]^T \quad (7)$$

Feature tracking is used to calculate the displacement along the x and y axes. The displacement along the z-axis or altitude is obtained from the readings of the barometer of the autopilot.

TABLE I. Processing Time Comparison

Algorithm	Time (in seconds)
Shi-Tomasi	40.11
SURF	45.47

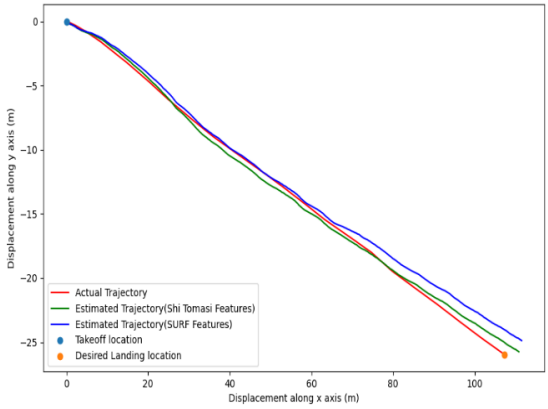

Fig. 1. Plot of actual trajectory (red) and estimated trajectory for Shi-Tomasi (green) and SURF (blue)

Authorized licensed use limited to: DELHI TECHNICAL UNIV. Downloaded on March 27,2021 at 05:22:07 UTC from IEEE Xplore. Restrictions apply.

f_n is the matrix consisting of positions of features (in pixels) detected in the n^{th} frame and m is the total number of features detected in that frame, (r_i, c_i) is the position of the i^{th} feature in that frame. F_n is the average of the positions of features in that frame.

$$f_n = \begin{bmatrix} r_1 & c_1 \\ r_2 & c_2 \\ \vdots & \vdots \\ r_m & c_m \end{bmatrix} \tag{8}$$

$$F_n = \begin{bmatrix} \frac{\sum_{i=1}^{m} r_i}{m} & \frac{\sum_{i=1}^{m} c_i}{m} \end{bmatrix} \tag{9}$$

The average position of features in the n^{th} frame is compared with their average position in the $(n-1)^{th}$ frame, to estimate the displacement along the x and y axes. The average position of features is also affected by change in altitude of the UAV, as with increase in altitude features tend to aggregate and with decrease in altitude features tend to disperse. Hence, the projection of the average position of features in the previous frame is taken on the current altitude using the formula:

$$F'_{n-1} = \frac{z_{n-1}}{z_n} F_{n-1} + \left(\frac{z_{n-1}}{z_n} - 1\right)\begin{bmatrix} \frac{f_h}{2} & \frac{f_w}{2} \end{bmatrix} \tag{10}$$

The difference between the average of current features and projection of the average of previous features is then calculated:

$$d_n = F_n - F'_{n-1} \tag{11}$$

The d_n vector gives displacement along the x and y axes in pixels. To convert it into displacement w.r.t the ground, the following equations are used:

$$D = 2 z_n d_n \begin{bmatrix} \frac{\tan\frac{fov_h}{2}}{f_h} & 0 \\ 0 & \frac{\tan\frac{fov_w}{2}}{f_w} \end{bmatrix} \tag{12}$$

$$D = [D_x \quad D_y] \tag{13}$$

The velocity vector is obtained by dividing the calculated displacement vector D with the time interval Δt.

$$v' = \begin{bmatrix} \frac{D_x}{\Delta t} & \frac{D_y}{\Delta t} & \frac{z_n - z_{n-1}}{\Delta t} \end{bmatrix}^T \tag{14}$$

The displacement vectors are added over time to calculate the total displacement of the UAV, providing its current position P_c w.r.t the takeoff point P_0:

$$P_c = \begin{bmatrix} \sum D_x & \sum D_y & \sum [z_n - z_{n-1}] \end{bmatrix}^T \tag{15}$$

The velocity estimates given by the image processing algorithm is highly oscillatory in nature. It is fed to a low-pass filter which smoothens the velocity output. The constant k of the low-pass filter is tuned manually by examining the smoothness of the output curve and time delay.

$$\alpha = \frac{\Delta t}{k + \Delta t} \tag{16}$$

$$v = \alpha v' + (1 - \alpha) v_{n-1} \tag{17}$$

Fig. 2 and Fig. 3 plots the raw unfiltered velocity estimate and the low-pass filtered velocity in x and y axes respectively.

IV. Navigational Controller

The destination position is given as a setpoint vector (P_s) from the origin of the inertial frame:

$$P_s = [x_s \quad y_s \quad z_s]^T \tag{18}$$

To obtain the desired velocity for the UAV to reach the destination, a positional error term is calculated using:

$$e = P_s - P_c \tag{19}$$

The desired velocity is given by:

$$\overrightarrow{v_r} = \frac{v_m r^2}{a^2 + r^2} \vec{u} \tag{20}$$

$$r = |e| \tag{21}$$

$$\vec{u} = \frac{e}{r} \tag{22}$$

where,

v_m—upper bound to the UAV's velocity
a—constant determining the smoothness of the velocity curve (in meters)
r— Magnitude of positional error
$\vec{u}$—unit vector pointing in the direction of destination

The magnitude of $\overrightarrow{v_{r_x}}$ vs positional error in x-axis is plotted in Fig. 4 with $v_m = 5m/s$ and $a = 5m$. To follow the desired velocity, a velocity error term is calculated and fed

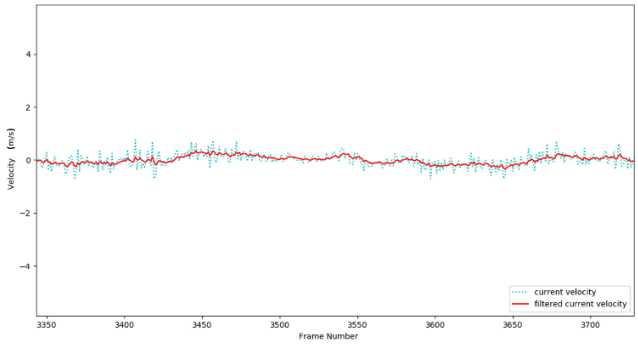

Fig. 2. Plot of raw (blue) and filtered (red) current velocity along x-axis

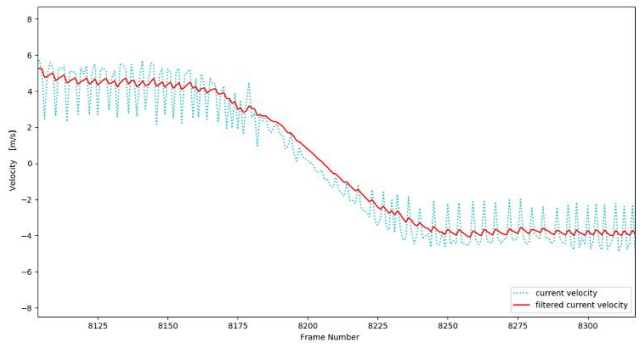

Fig. 3. Plot of raw (blue) and filtered (red) current velocity along y-axis

Authorized licensed use limited to: DELHI TECHNICAL UNIV. Downloaded on March 27,2021 at 05:22:07 UTC from IEEE Xplore. Restrictions apply.

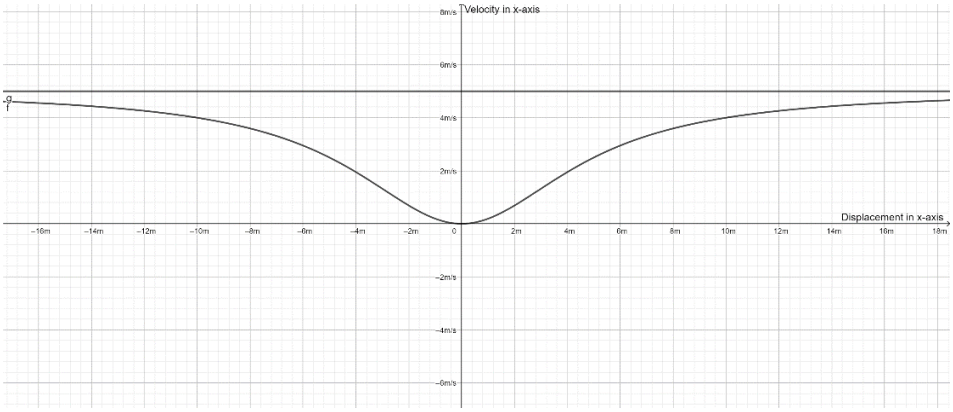

Fig. 4. Plot of magnitude of required velocity along x-axis (v_{r_x}) vs positional error (e) along x-axis

into a PID controller. The velocity error term is given by:

$$e_v = v_r - v \tag{23}$$

The PID controller outputs the optimum control input in the form of linear accelerations w.r.t the inertial frame, in x, y and z directions:

$$acc = K_p e_v + K_d \frac{1}{\Delta t} e_v + K_i \sum e_v \tag{24}$$

$$acc = [a_x \quad a_y \quad a_z] \tag{25}$$

The obtained linear acceleration values are converted to roll angle, pitch angle and thrust using the following equations:

$$\theta = \tan^{-1} \frac{a_x}{a_z - g} \tag{26}$$

$$\phi = \tan^{-1} \left(\frac{a_y}{a_x} \sin \theta \right) \tag{27}$$

$$F_B = \frac{m(g - a_z)}{C_\theta C_\phi} \tag{28}$$

The roll, pitch and thrust values are fed as to the autopilot which follows the given attitude commands.

During takeoff and return to home, the desired position is set as $[0 \quad 0 \quad z]^T$ where z is the hovering altitude after takeoff or before landing. For landing, the altitude is decreased at this position until the altitude readings from the barometer stops changing.

The time required by our algorithm to detect GNSS signal loss is 1 second. To efficiently switch between GNSS and Non-GNSS navigation, the GNSS location and velocity estimates of the last 5 seconds of GNSS aided flight are stored and the displacement from the takeoff point is continuously tracked. This data is used to switch to Non-GNSS navigation when GNSS signals are weak or lost. A switch is made if the number of satellites <6 or if a GNSS glitch occurs.

V. Simulation and Flight Results

A. System Overview

The hardware setup is mentioned in Table II. The gimbal is controlled by the autopilot and is commanded to always point the camera downward facing. The image processing and navigational control algorithms are running on the onboard computer. The onboard computer is interfaced to the camera using a USB cable and to the autopilot using the serial interface. The system architecture is depicted in Fig. 5.

Several experiments were conducted at varying camera resolutions and terrain types. The complete software (position and velocity estimation and navigational controller) runs at ~20fps and ~16fps at resolutions of 640×480 and 1280×720 respectively. The navigational controller gave promising results with update rates of the estimates as low as ~6fps. The proposed system has been tested for navigational speeds up to 5m/s and for altitudes up to 70m above the ground level.

B. Optical Flow Algorithm

Raw videos at a resolution of 640×480 were captured by our system at varying altitudes and varying speeds up to 5m/s. The positional estimation algorithm was first tested on these videos. The estimated co-ordinates of the followed trajectory were compared with the actual GPS co-ordinates. The obtained results were analysed and the error was found to be acceptable at altitudes from 5m to 70m with a frame rate of ~15fps. Higher resolution resulted in lower error on altitudes above

TABLE II. System Hardware Components

Airframe	Tarot 650mm quadcopter
Autopilot Board	Pixhawk 2.1 Cube
Autopilot Firmware	ArduPilot's ArduCopter
Camera	GitUp Git2P (RGB, monocular, diagonal FOV: 90°)
Gimbal	Tarot T4-3D (3-axis)
Onboard Computer	Nvidia Jetson Nano

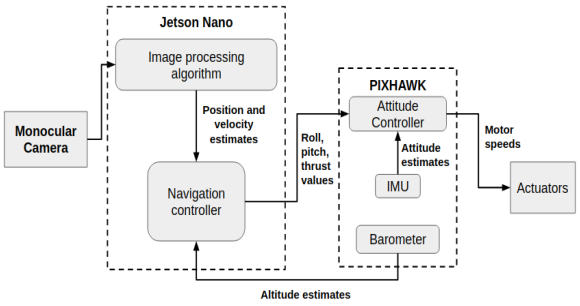

Fig. 5. System architecture

Authorized licensed use limited to: DELHI TECHNICAL UNIV. Downloaded on March 27,2021 at 05:22:07 UTC from IEEE Xplore. Restrictions apply.

Algorithm I: GNSS-Denied Navigation

Get list of waypoints and current location
Initialize: $n = 0$,
Initialize: current location at origin ($P_c = [0 \quad 0 \quad 0]^T$)
while number_of_waypoints > 0 **do**
  if $n = 0$ **then**
    Capture the first frame and features
  else
    Calculate displacement vector (D_n)
    Update current location (P_c)
    if number_of_features < 31 **then**
      Calculate 30 more features
    Calculate current velocity (v')
    Calculate filtered current velocity (v)
    Calculate positional error from first waypoint (e)
    Calculate velocity error (e_v)
    Calculate linear accelerations (acc)
    Calculate roll angle (ϕ), pitch angle (θ) and thrust (F_B)
    Send the attitude commands to the flight controller
    if $[-2 \quad -2 \quad -1]^T < e < [2 \quad 2 \quad 1]^T$ **then**
      Delete the first waypoint
    $n := n + 1$
  end if
end while

70m, however it resulted in a lower frame rate. Lowering the speed also reduced the error. Therefore, a maximum speed of 5m/s and a maximum flying altitude of 70m was chosen for our subsequent testing. Values above these tend to have high errors.

C. Motion Estimation

Due to high frequency vibrations in the raw position and velocity estimates, a low-pass filter was used. The constant k of the low pass filter was then tuned by observing the smoothness and time delay of the velocity plots before and after applying the filter. Increasing the value of k increased the smoothness of the curve but also increased the time delay. The amplitude of vibrations tends to increase on higher altitudes. Thus, instead of having a constant value for k, it was set as a linear function of altitude.

$$k = 0.1 + 0.0036 * z \tag{29}$$

where z is the altitude of the UAV.

D. Navigational Controller

The navigational controller was first tested in the ArduPilot SITL (Software In The Loop) simulator. A setpoint $P_s = (20, 20, 20)$ was given to the UAV and the motion of the UAV was analysed by varying wind direction and wind speed from 0 to 7m/s. The displacement vector D_n was simulated by calculating displacements along two perpendicular directions, the UAV's heading and 90° clockwise to it using GPS locations.

As the navigational controller always directs the UAV to the destination, deviation due to wind causes a deviation from its trajectory but not a deviation from its destination. This was also seen in the simulations where, the UAV was able to reach the destination with very less deviations (3-4m) even when it was subjected to wind gusts. The displacement plots were analysed to tune the PID controller's parameters: K_p, K_d, K_i in consecutive iterations of the code. Fig. 6 shows the desired trajectory and the actual trajectory followed in SITL. The RMS error was 1.16m, max error was 2.25m for a total distance of 28.28m. The percentage RMS error per distance travelled was 4.1%.

After tuning the parameters of the PID controller in SITL, they were tweaked manually during test flights for required velocity vector ($\overrightarrow{v_r}$) set as 0, till the desired response was obtained. Further, the required velocity vector's ($\overrightarrow{v_r}$) curve with varying slopes by changing a was tested in actual flights. Higher values of a resulted in very gradual slope which reduced the speed of the UAV near the destination point. Lower values of a resulted in a steep slope which caused overshooting and oscillations. Therefore, an optimal value was chosen after analysing the response on multiple outdoor flight tests.

Finally, the state estimator and navigational controller were coupled together and actual flights were performed with various trajectories at various altitudes. The obtained parameters were finalised through multiple flight tests. Fig. 7 and Fig. 8 show the response of actual filtered current velocity to the input required velocity along x and y axes respectively. The tuned values of all the parameters of the controller are listed in Table III. Complete outdoor flight missions from take-off, waypoint navigation, landing and return to launch were performed on the UAV.

Such a mission's planned trajectory and actual followed trajectory is plotted in Fig. 9. The RMS error was 15.45m, max error was 50.25m for a total distance of 2093.56m. The flight was done on a desert terrain with patches of plants. The UAV flew in wind gusts of 2-3m/s at an altitude of 70m above ground. The results of some other flight tests are tabulated in Table IV. Shifting from autonomous GNSS aided navigation to the developed GNSS-denied navigation solution was tested multiple times. Switching between these modes and the trajectory followed is plotted in Fig. 10.

As mentioned previously in *Section I*, the aim was to come up with a solution applicable at high altitudes (>50m) using the most trivial payloads on the UAV. A monocular camera is required in any surveillance, reconnaissance or HADR missions. The same can be simultaneously used by our presented solution. Hence, our solution does not need any additional sensor payloads like [6] & [10]. The Nvidia Jetson Nano is chosen due to its high performance and low power, space and weight constraints. It has a Quad-Core ARM Cortex-A57 processor which has been proved to be sufficient for our algorithm. Thus, our solution is computationally lighter as neither it requires multiple flight computers as in [7] & [8] nor it needs a significantly powerful CPU as in [9].

Authorized licensed use limited to: DELHI TECHNICAL UNIV. Downloaded on March 27,2021 at 05:22:07 UTC from IEEE Xplore. Restrictions apply.

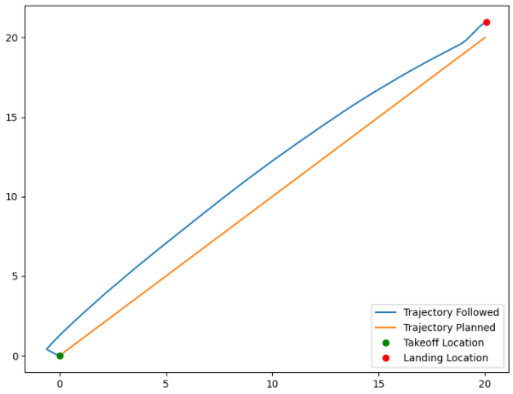

Fig. 6. Plot of desired trajectory (blue) and followed trajectory (orange) in SITL

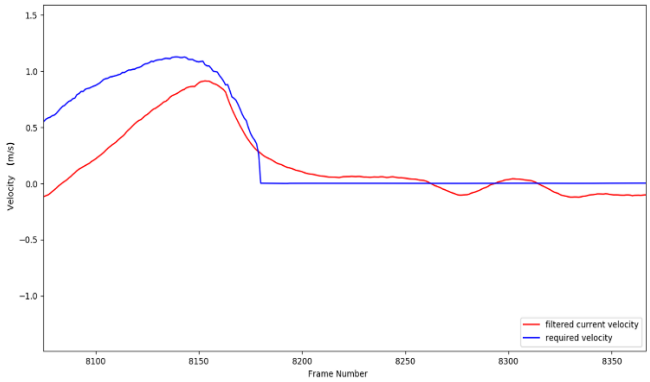

Fig. 7. Plot of required velocity (blue) and current filtered velocity (red) along x-axis

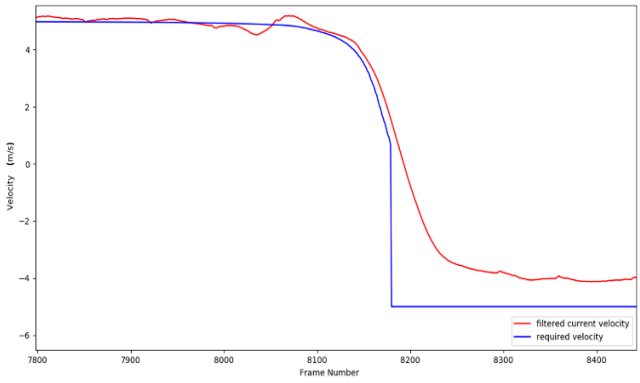

Fig. 8. Plot of required velocity (blue) and current filtered velocity (red) along y-axis

TABLE III. VALUES OF ALL PARAMETERS

Parameter	Value after simulations	Final value after flight tests
k	0.1	0.1 – 0.28
K_p	0.9	0.9
K_d	0.03	0.02
K_i	0.02	0.015
a	4	5

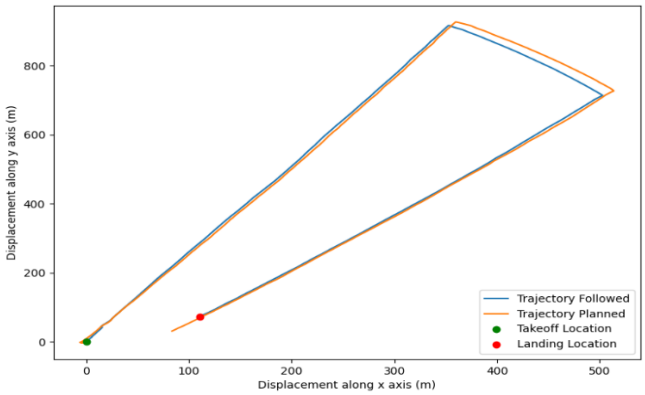

Fig. 9. Plot of planned trajectory (orange) and actual trajectory (blue) in outdoor flight

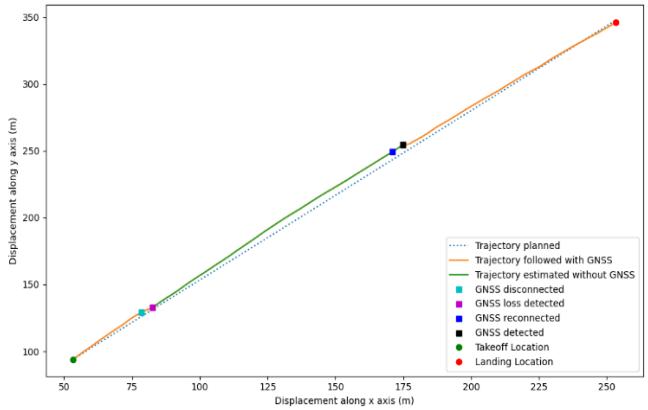

Fig. 10. Switching between GNSS enabled and GNSS disabled flight modes

TABLE IV. FLIGHT TEST RESULTS

Distance Travelled (in m)	Maximum distance from home (in m)	Maximum error (in m)	% error (in %)
100	100	2	2
340	100	4	1.17
400	280	5	1.25
600	200	10	1.67
2000	1000	50	2.5

Moreover, the GPU of the flight computer is left unutilized to run GPU extensive applications such as ML algorithms parallelly. For example, in an HADR mission, our solution navigates the UAV in GNSS denied/loss patches using the monocular camera and the CPU of the flight computer, while its GPU is utilized to run an object classifier (like YOLO) to detect humans using feed from the same monocular camera. The overall system is highly modular as it has no constraints on hardware used, using high resolution cameras with more powerful computers will result in higher accuracy at even higher flight altitudes.

VI. CONCLUSION

With this paper, the problem of GNSS signal loss during outdoor navigation has been addressed by presenting a novel computationally lighter solution of GNSS-denied navigation.

Authorized licensed use limited to: DELHI TECHNICAL UNIV. Downloaded on March 27,2021 at 05:22:07 UTC from IEEE Xplore. Restrictions apply.

The hardware used is low-cost and has low space and power requirements, making our solution implementable on lighter and smaller UAVs. Moreover, due to its computationally lighter nature, it can run in parallel with other applications such as video-downlink, target detection, etc. on the same onboard computer. This makes this solution suitable for practical HADR missions.

Some extensions to this work are planned for future, aimed at increasing the reliability of GNSS-denied navigation:

- Introduction of an EKF based switching between GNSS aided and GNSS denied navigation.
- Using pre fetched satellite images of terrain with GPS locations and matching them with terrain images taken during flight as a corrective measure to significantly reduce error during long distance flights.
- Integrating the present algorithm with IMUs along with rangefinder/altimeter to increase accuracy and relaxing zero-yaw constraint to increase practicality.

REFERENCES

[1] K. P. Valavanis, and G. J. Vachtsevanos, "UAV applications: introduction." Dordrecht: Springer Netherlands, 2015, pp. 2639–2641

[2] Y. Li, M. Scanavino, E. Capello, F. Dabbene, G. Guglieri, and A. Vilardi, "A novel distributed architecture for UAV indoor navigation", Transportation Research Procedia Volume 35, Dec. 2018, pp. 13-22

[3] M. Nahangi, A. Heins, B. McCabe, and A. Schoellig, "Automated localization of UAVs in GPS-denied indoor construction environments using fiducial markers", 35th International Symposium on Automation and Robotics in Construction, July 2018.

[4] M. Shan, F. Wang, F. Lin, Z. Gao, Y. Z. Tang, and B. M. Chen, "Google Map aided visual navigation for UAVs in GPS-denied environment", IEEE Conference on Robotics and Biomimetics, 2015

[5] M. Sharifi, X. Chen, and C. G. Pretty, "Experimental study on using visual odometry for navigation in outdoor GPS-denied environments", 12th IEEE/ASME International Conference on Mechatronic and Embedded Systems and Applications (MESA), 2016

[6] S. Ashraf, P. Aggarwal, P. Damacharla, H. Wang, A. Y. Javaid and V. Devabhaktuni, "A low-cost solution for unmanned aerial vehicle navigation in a global positioning system–denied environment", International Journal of Distributed Sensor Networks, Vol. 14, 2018.

[7] A. D. Wu, E. N. Johnson, M. Kaess, F. Dellaert, and G. Chowdhary, "Autonomous flight in GPS-denied environments using monocular vision and inertial sensors", AIAA J. of Aerospace Information Systems, Vol. 10, No. 4, pp. 172-186, 2013.

[8] G. Chowdhary, E. N. Johnson, D. Magree, and A. Wu, "GPS-denied indoor and outdoor monocular vision aided navigation and control of unmanned aircraft", Journal of Field Robotics, 2013

[9] D. Magree, and E. N. Johnson, "A monocular vision-aided inertial navigation system with improved numerical stability" AIAA Guidance, Navigation, and Control Conference, 2015

[10] K. Mohta, K. Sun, S. Liu, M. Watterson, B. Pfrommer, J. Svacha, Y. Mulgaonkar, C. J. Taylor, and V. Kumar, "Experiments in fast, autonomous, GPS-denied quadrotor flight", IEEE International Conference on Robotics and Automation (ICRA), 2018

[11] Antonio C. B. Chiella,1 Henrique N. Machado,1 Bruno O. S. Teixeira,1 and Guilherme A. S. Pereira2 GNSS/LiDAR-Based Navigation of an Aerial Robot in Sparse Forests

[12] K. Thu, and A. I. Gavrilova, "Designing and modeling of quadcopter control system using L1 adaptive control", 12th International Symposium Intelligent Systems INTELS'16, Oct. 2016

[13] E. G. Hernandez-Martinez, G. Fernandez-Anaya, E. D. Ferreira, J. J. Flores-Godoy, and A. Lopez-Gonzalez, "Trajectory tracking of a quadcopter UAV with optimal translational control", 11th IFAC Symposium on Robot Control (SYROCO), 2015, pp. 226-231

[14] J. Shi, and C. Tomasi, "Good features to track", 9th IEEE Conference on Computer Vision and Pattern Recognition, 1994, Springer pp. 593–600.

[15] H. Bay, A. Ess, T. Tuytelaars, and L. V. Gool, "Speeded up robust features", Computer Vision and Image Understanding, Vol. 10, 200

[16] Y. Zhang, T. Wang, Z. Cai, Y. Wang, and Z. You, "The use of optical flow for UAV motion estimation in indoor environment", IEEE Chinese Guidance, Navigation and Control Conference (CGNCC), Nanjing, 2016, pp. 785-790, doi: 10.1109/CGNCC.2016.7828885.

[17] J. Bouguet, "Pyramidal implementation of the affine Lucas Kanade feature tracker description of the algorithm", Intel Corporation, 2001.

Authorized licensed use limited to: DELHI TECHNICAL UNIV. Downloaded on March 27,2021 at 05:22:07 UTC from IEEE Xplore. Restrictions apply.

Multimedia Systems
https://doi.org/10.1007/s00530-021-00768-8

REGULAR PAPER

A novel biometric crypto system based on cryptographic key binding with user biometrics

Rajesh Asthana[1] · **Gurjit Singh Walia**[2] · **Anjana Gupta**[1]

Received: 22 November 2020 / Accepted: 24 February 2021
© The Author(s), under exclusive licence to Springer-Verlag GmbH Germany, part of Springer Nature 2021

Abstract
Cryptography plays a significant role in ensuring data security and confidentiality. The security provided by a crypto system mainly depends on the secrecy of the cryptographic key. If the secret key gets compromised, then it may lead to compromise of the protected data. Biometric cryptosystem provides a solution for securing the cryptographic key by binding the secret key with user biometric data. In this paper, we have proposed a novel biometric crypto system involving key binding mechanism. New objective functions have been introduced to create helper data by binding the secret key with biometric data of the user. In the retrieval phase, local minima of the objective functions act as anchors to get the secret key. Performance evaluation shows that the proposed method achieves more than 98% success rate even in presence of limited noise in the biometric data. Further, performance metrics viz., FAR, GAR, GWDR and IWDR have been obtained for cryptographic key sizes of 256, 512, 1024 and 2048 bits. Security analysis shows that the proposed method is robust against brute force attack and correlation attack.

Keywords Biometric crypto system · Key-binding · Key-retrieval · Objective function

1 Introduction

Data and information protection is paramount in the present age of digital world. Unauthorized person or agency may exploit or misuse the unprotected data. Cryptography is extensively used for protection of data, and also for authenticating people and devices [1]. Information and communications are secured using a set of rules that allows only those intended—and no one else—to retrieve the information [2]. In cryptography, "plain-text" or message is encrypted or enciphered to get a "cipher text". At the sender side, there is an encryption algorithm which takes plain text and secret key as inputs and generates a cipher text as output. At the receiving end, there is a decryption algorithm which takes cipher text and the secret key (or its transformed form) to retrieve the plain text [3, 4]. Thus, for a particular encryption/decryption algorithm, the security of the information which are being communicated from one end to other lies in the security of the key. If an adversary is able to determine (guess) the key, then he would have access to the very information that are being protected [5, 6]. Hence, to make it resistant against brute force attack, the key size is taken very large [7]. Remembering such a large key is practically difficult and saving the secret key in the system is very risky. To overcome these challenges, a concept was developed for binding secret key with biometrics of the user.

Biometric has the inherent potentiality to differentiate a genuine individual from a fraudulent impostor. For this reason, biometric is integrated with cryptography to enhance the security of traditional cryptography. Biometrics refers to the physiological or behavioural characteristics of the individual. Physiological characteristics, like face, fingerprints, iris etc., and behavioural characteristics like voice, gait, keystroke dynamics etc., are unique to an individual. In addition, biometric traits are invariant with time and hence can be used for user characterization [8]. Biometrics have less chance of getting compromised as they cannot be copied, shared or distributed, so in a way they are attached to a particular user. Another advantage is that unlike passwords, they cannot be forgotten or lost. Thus, an authentication

Communicated by Y. Zhang.

✉ Rajesh Asthana
asthana.rajesh30@gmail.com

[1] Department of Applied Mathematics, Delhi Technological University, Delhi, India

[2] Scientific Analysis Group, DRDO, Delhi, India

system which is based on password or smart token, may be replaced with biometric-based authentication system. Moreover, they can be combined to provide two-factor authentication mechanism [9, 10].

In spite of the aforesaid advantages, there are some challenges to biometric based authentication system. There are various security and privacy concerns which are illustrated as under [11]:

(a) *Biometrics are authentic but not secret* Even though most of the biometrics possess quite a personalized attribute, it can potentially be misused without the user's consent. In contrast, tokens and passwords get compromised when user willingly shares them.
(b) *Biometrics cannot be cancelled or revoked* Knowledge-based authentication entities can be reset if they get compromised. Similarly, token-based items can be replaced if they are stolen. However, biometric characteristics of an individual are of permanent nature and therefore they are non-replaceable or non-revocable if they get compromised.
(c) *Biometrics may be compromised forever* Biometrics provide usability advantages as passwords are no longer needed to be remembered and their management becomes easier. However, compromise of a biometric in one application may lead to compromise of all other applications where the same biometric has been used.
(d) *Individuals can be tracked by cross-matching of biometrics* In case, a particular biometric is used repeatedly in several applications and locations, there is possibility of tracking of individual when the concerned agencies collude and share the enrolled or registered biometric templates.

Additionally, acquired biometric data depends upon dynamic environment which leads to its variation under different deployments. For authentication applications, these variations can be accommodated by threshold-based decision making. However, in cryptography such variation in biometric data plays a crucial role as a little change in the plain input data leads to a large variation (50% in ideal case) in the encrypted output. Therefore, combining cryptography with biometrics is quite a challenging task and needs extensive research for potential applications.

Some abbreviations and notations used in the manuscript are listed below (Table 1) for a convenient reading and understanding:

The rest of the paper is organised in the following manner: motivation of the research work and our contributions have been listed in the Sect. 2. Related works in the field of biometric cryptosystems in recent years have been elaborated in the Sect. 3. In Sect. 4, core design of the proposed key binding based biometric crypto system is introduced.

Table 1 Abbreviations and notations

FAR	False acceptance rate
FRR	False rejection rate
GAR	Genuine acceptance rate
EER	Equal error rate
GWDR	Genuine wrongly decoded bit rate
IWDR	Imposter wrongly decoded bit rate
ECC	Elliptic curve cryptography
ASC	Absolute coefficients sum
PCA	Principal component analysis
BCH	Bose, Chaudhuri, and Hocquenghem
$\{\alpha_1, \alpha_2, \ldots, \alpha_t\}$	Set of bio-components
$\{\beta_1, \beta_2, \ldots, \beta_q\}$	Set of crypto-components
Δ	Neighborhood threshold
$\{[\xi_1, \xi_2, \ldots, \xi_t], [\Phi_1, \Phi_2, \ldots, \Phi_q]\}$	Helper data

Also, pseudo code for the proposed system is detailed. Various Datasets and Performance Evaluation Metrics for measuring the performance of the proposed method have been discussed in the Sect. 5. Experimental results obtained and Performance analysis and security analysis have been discussed in this section. Finally, the concluding remarks and future directions for research have been discussed in the Sect. 6.

2 Motivation and contributions

Key binding based biometric cryptosystem protects the secret key by combining it with user biometric data. Generally, secret key is a random binary string, so it is difficult to remember such a large random key. To address this, mostly keys are stored in storage devices like cd, pen-drive, smart card, hard drive etc. Whenever these keys are required, they are released using authentication mechanism (usually a password or smart token). The security of the encryption/decryption keys solely depends on the security of the password or smart token used for authentication to release the key. There are limitations to both these as it is quite possible that "passwords" and "tokens" could be forgotten, duplicated, stolen, or lost, which would ultimately nullify the security provided by the cryptographic algorithms [12, 13]. To address these issues, biometric crypto system is considered as best alternative among the existing solutions.

Above issues can effectively be resolved using biometrics of the user as it offers a positive human identifier based on an intrinsic aspect of a human being [14]. The advantages of key binding schemes are that

(i) A cryptographic key cannot be retrieved without the knowledge of the biometric data of the user.

(ii) It ensures privacy of the user as his biometric data is unrelated to the secret key which is being protected [15, 16].

The proposed biometric crypto system binds the cryptographic key with the biometric data of the user through minimization of an objective functions. A brief summary of the contributions is as follows:

- A novel biometric cryptosystem has been proposed for securing the cryptographic key wherein a secret key is bound with the user biometric data.
- New objective functions have been defined for creation of helper data by hiding the secret key. This helper data is subsequently used to retrieve the key.
- Performance evaluation of the proposed method have been done using various performance metrics like FAR, GAR, Genuine WDR and Imposter WDR on iris and fingerprint benchmark datasets considering various sizes of the secret cryptographic keys.
- The effect of noise and neighbourhood threshold have been assessed on the convergence stability of the objective function.
- Security analysis of the proposed method have been done by investigating the robustness of the method against brute force attack and correlation attack.

Details of related works which were recently reported, are illustrated in the next section.

3 Related work in the field of biometric cryptosystem

Protection of data has been recently investigated extensively due to proliferation of digital communication. Key binding based crypto systems have emerged as promising solution due to ease of usage and its adaptability. The scientific community all over the world have proposed various key binding mechanisms to secure the key from unauthorized persons using user biometrics.

The first method for biometric key binding 'Mytec1' was developed using fingerprint images [17]. This method was not very robust in providing security and accuracy. So, an enhanced version of Mytec 1 named as Mytec 2 was developed using a different filter function. Filter function was determined by finding the degree of similarity between a given biometric image and query image. Juels and Wattenberg introduced fuzzy commitment scheme based on binary biometric features to protect cryptographic keys [18]. In this method Reed-Solomon codes were used for error correction. Juels and Sudan proposed Fuzzy Vault scheme in which a cryptographic key was protected by binding it with fingerprint data [19]. In this scheme, a vault was created with the help of ECC and a polynomial based encoding method. Coefficients of the polynomial were taken from the secret-key that is to be secured. Additionally, some chaff points were randomly generated and merged with vault so that the original points could be secured. These chaff points should not overlap with the original points. Further, there are various methods given in the literature to generate distinct chaff points [20–22]. The first such method for generation of Chaff points were given by Juels and Sudan [19]. Clancy et al., proposed a method in which chaff points were generated in such a way that the Euclidean distances among themselves as well as with previously generated chaff points and original points, exceed a pre-defined threshold value [23]. Li et al., developed a fingerprint cryptosystem which was alignment-free [24]. In this, minutia structure, minutia descriptor and local features were fused by employing three fusion strategies. Volume of the minutia descriptor was compressed using Huffman coding. Marino et al., proposed a fuzzy extractor scheme in which key binding was done using iris template of the user [25]. Experimental results reveals that the most optimal size of the secret key that is to be secured is 192 considering FAR and FRR values.

M. Salas proposed elliptic curve cryptography based biometric encryption method for enabling biometric authentication in smart devices [26]. One of the main advantages of using ECC in providing security is that the memory requirement and execution time reduces significantly. Moreover, since instead of using user password it uses hash function which makes it quite resistant to several cryptographic attacks. A biometric based key authentication mechanism using ECC was developed by Yoon and Yoo for wireless sensor network [27]. This method claims to provide a secure and efficient wireless sensor networks. Liew et al. proposed a bio-cryptographic scheme in which chaotic encryption was done using Bernoulli-logistic mapping [28]. Absolute coefficients sum (ASC) of this approach was found to be quite low as compared to logistic map. This method got its wider applications in online biometric data network encryption and information transmission. Eskander et al., presented a fuzzy vault scheme in which offline signature images of the users were taken to resolve the key management issue [29]. Besides this, it can also be used for signature verification in different usage contexts. Another feature of this approach was that signatures could be revoked if they get compromised. Amirthalingam and Radhamani proposed a chaff point based fuzzy vault scheme [30]. In this method, optimal locations of the chaff points were found by employing particle swarm optimization algorithm. Chitra and Sujitha proposed a fuzzy vault scheme in which vault was created using pre-aligned minutia points and secret key [31]. This method was found to be secured against brute force and correlation attacks. Elrefaei et al., proposed a fuzzy commitment

method in which gait features of users were extracted through Machine Vision Sensor for providing security [32]. PCA was used for dimensionality reduction and BCH coding scheme was applied to encode the cryptographic key. Ponce-Hernandez et al., proposed a fuzzy vault scheme in which 15 global features of fixed-length signature template of the user were considered [33]. This method provides a robust solution against cryptanalytic attacks while maintaining a high level of accuracy. Asthana et al., proposed a multimodal biometric system wherein a robust template is generated by diffusion of individual transformed matrices using graph-based random walk cross-diffusion [34]. Walia et al., proposed a multimodal cancelable biometric system based on realtime Deep Feature Unification (DFU). For this, key images based generic feature extraction is introduced to achieve revocability and dimensionality reduction [35]. Asthana et al., proposed an adaptive fusion model to cater object rotation and scaling through a random walk state model and rotation invariant features [36]. Non-adaptiveness of multimodal systems to dynamic environment and their inability to distinguish between spoofing attack and the noisy input image was addressed by adaptively combining the scores from individual classifiers [37]

A large-scale high-speed retrieval through binary code has a certain degree of reduction in retrieval accuracy compared to traditional retrieval methods. Multi-view methods can well preserve the diverse characteristics of data to improve retrieval performance. Chenggang et al., introduced the multi-view deep neural network for the hash learning field, and designed an efficient and innovative retrieval model [38]. In this, authors proposed a supervised multi-view hash model which can enhance the multi-view information through neural networks. This was a completely new hash learning method that combines multi-view and deep learning methods. They also designed variety of multi-data fusion methods in the Hamming space to preserve the advantages of both convolution and multi-view. Further, Chenggang et al., studied the manifold learning method and devised an effective optimized learning strategy to obtain the graph Laplacian matrix, which reflects the topological structure of image, to further impose the smoothing priors to the denoised depth image [39]. A novel technique to automatically identify the layout topology of an input image, followed by a nonlinear optimization with equality constraints to estimate the final 3D layout of a scene was introduced in [40]. This is the first fully automatic technique to achieve single image-based 3D layout estimation of an indoor scene. Ouyang et al., developed a model which consists of an inference network to generate fine-grained flow distributions from coarse-grained inputs that uses a feature extraction module and a novel distributional upsampling module [41, 42]. They also proposed a general fusion subnet to further boost the performance by considering the influence of different external factors. This structure provides outstanding effectiveness and efficiency for small scale upsampling. Albakri and Mokbel proposed a convolutional neural network face recognition as a tool to extract biometric features that help in a key binding approach to protect the personal data in the wallet [43]. Uludag et al. discussed the challenges involved in biometric key generation primarily due to drastic acquisition variations in the representation of a biometric identifier and the imperfect nature of biometric feature extraction and matching algorithms [44].

In summary, although key binding based crypto system for data protection has extensively been studied. Most of the methods could not be adapted to different type and dimension of biometric data along with size of key. For instance, to augment the security of any cryptographic system, the secret key should be taken of a large size but an increase in key-size may deteriorate the performance of the system. Therefore, there is a requirement of developing such biometric cryptosystem for key-binding which should be able to bind a large key and retrieve the same efficiently. To address these issues, we have proposed a novel approach for protection of data. The details of proposed approach are described in the next section.

4 Proposed methodology for biometric cryptosystem

In this manuscript, we have introduced novel approach for protection of data using biometric crypto system. For this, we have bound the secret key with the biometric data of the legitimate user by minimizing the chosen objective function. New objective function is defined in such a way that if the cryptographic key is split in several parts then each part could be associated to one of the local minima of the objective function under certain conditions. These conditions are:

(i) Biometric traits should have low intra-class variability but high inter-class variability. Therefore, biometric templates for the same subject at multiple instances should not have much dissimilarity while the dissimilarity should be high if templates are taken from different subjects.
(ii) The starting point in the search space should be taken in such a manner that it should lead to convergence to one of the local minima of the objective function.

A block diagram of the proposed biometric crypto system based on key binding is shown in Fig. 1.

In the proposed approach, design of objective function plays a crucial role in convergence to local minima in finite number of steps. So, objective function should be highly regular so that the local minimum of the objective function

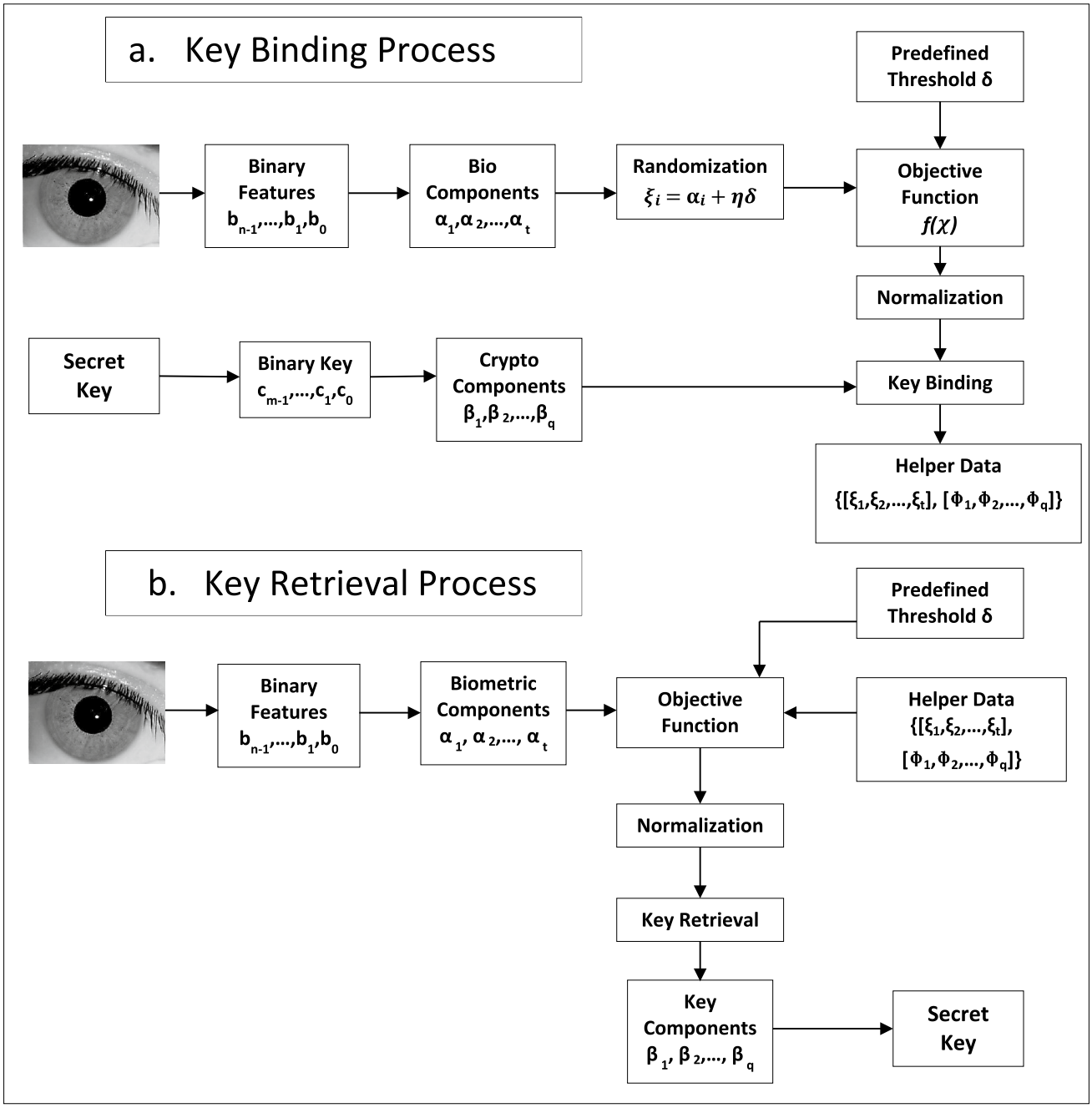

Fig. 1 Proposed biometric crypto system **a** Key binding process takes biometric

associated with any segment of biometric data should be indistinguishable from all other minima. These functions should also be numerically stable so that little deviations in the initial data should not lead to different local minimum than the desired one. Moreover, a very few parameters should be required to define the shape of the objective function. Also, biometric bit-stream is divided into several components. Corresponding to each of these components, there are separate objective function defined in such a way that each bit-stream segment will correspond to one of its local minima. This will happen only if the initial points are taken in proximity of the original biometric data. Otherwise, minimization procedure will lead to a different local minimum and an attacker would not be able to notice the error committed. In the proposed approach, we have designed the following objective function:

$$\varphi = f(\chi) = \frac{1}{\delta}\left[\chi - (\alpha + \eta\delta)\right] \sin\left[\frac{1}{\delta}\{\chi - (\alpha + \eta\delta)\}\right], \quad (1)$$

where 'α' represents a biometric component, 'η' a random value and 'δ' the neighbourhood threshold value for which the value of the function $\boldsymbol{f}$ converges to a local minimum. Since the value of local minima of $f(\chi)$ increases as χ increases, it is normalized using Eq. (2).

$$\psi_i = |\varphi_i|.10^{-\log_{10}(|\varphi_i|)}. \quad (2)$$

The following two main processes are involved in the proposed biometric cryptosystem:

A. Key binding process
B. Key retrieval process

4.1 Key binding process

In Key Binding process, secret cryptographic key is bound with the user biometric data. Consider the Secret key K which is to be protected is of length m and represented as m-bit sequence $K = c_{m-1}\, c_{m-2} \ldots c_0$. p and q are integers chosen in such a way that $m = p \times q$. Further, q sub-sequences K_i each of length p bits are formed by partitioning the key K. Therefore, the secret key is represented as $K = K_q, K_{q-1}, \ldots, K_1$ where each sub-sequence is of length p. By taking integer value β_i referred to as 'Crypto component' corresponding to each of these q sub-sequences we can form a set $\{\beta_1, \beta_2, \ldots, \beta_q\}$. This set may be referred to as 'Crypto Key'. If m is not multiple of q then the last crypto-component is padded with the required number of random bits to make its size p.

Similarly, consider B is a finite bit sequence of a particular biometric of the user of length n represented as $B = b_{n-1}\, b_{n-2} \ldots b_0$. s and t are integers chosen in such a way that $n = s \times t$. Biometric B could be partitioned into t subsequences each of length s bits. Therefore, the biometric may be represented as $B = B_t, B_{t-1}, \ldots, B_1$ where each sub-sequence is of length s. By taking integer value α_j referred to as 'Bio component' corresponding to each of these t sub-sequences we can form a set $\{\alpha_1, \alpha_2, \ldots, \alpha_t\}$. This set may be referred to as 'Biometric Key'. If n is not a multiple of s, then the last $(n - s \times t)$ bits of the biometric bit-sequence are discarded.

Therefore, we have Biometric Key $\{\alpha_1, \alpha_2, \ldots, \alpha_t\}$ and Crypto Key $\{\beta_1, \beta_2, \ldots, \beta_q\}$.

If α_i is a bio-component, then we can form

$$\xi_i = \alpha_i + \eta\delta \quad i \in \{1, 2, \ldots, t\}, \quad (3)$$

where 'η' is a random value and 'δ' is the neighbourhood threshold value for which the value of the function f converges to a local minimum.

For each α_i we compute the value φ_i of the objective function as given below

$$\varphi_i = f(\alpha_i) = \frac{1}{\delta}\left[\alpha_i - \xi_i\right] \sin\left[\frac{1}{\delta}\{\alpha_i - \xi_i\}\right] i \in \{1, 2, \ldots, t\}. \quad (4)$$

The values of the local minima increases in proportion to the value α_i, therefore the values ψ_i are normalized as follows

$$\psi_i = |\varphi_i| \cdot 10^{-\log_{10}(|\varphi_i|)}. \quad (5)$$

Number of bio-components are required to be equal to the number of crypto-components as each crypto-component is to be bound with a bio-component. In the case where the number of bio-components is larger than the number of crypto-components, methodology is required to form a subset of q bio-components which can be associated with each crypto-component. For this, we have taken the median value $\boldsymbol{\nu}$ of the t local minima ψ_i calculated using the above defined objective functions. Then the distance between each bio-component and the median is computed and sorted in the ascending order. From this, the first q bio-components which are termed as anchors.

If there are only fewer numbers of bio-components for binding the crypto-components, then the average value of the t local minima μ is computed. Then $\mu \cdot \psi_i$ are taken as the values of the anchors.

The normalized values of φ_i are then used to bind the secret key with the biometrics of the user in the following manner

$$\phi_i = \beta_i / \Upsilon_i, \quad (6)$$

where

$$\Upsilon_i = \psi_i \cdot \mu. \quad (7)$$

In this way, the secret key is bound with the biometric data of the user and a helper data $HD = \{[\xi_1, \xi_2, \ldots, \xi_t], [\Phi_1, \Phi_2, \ldots, \Phi_q]\}$ is formed which along with the pre-defined threshold value 'δ' is used to retrieve the secret cryptographic key.

A pseudocode of the proposed Key Binding Method is illustrated as Algorithm 1.

Algorithm 1 : Proposed Key Binding Method

1. **Function** Key_Binding (***B***, ***K***, **δ**)
2. $\{\alpha_1, \alpha_2, \ldots, \alpha_t\}$ = *Derive biocomponent* ***(B)***
3. $\{\beta_1, \beta_2, \ldots, \beta_q\}$ = *Derive biocomponent* ***(K)***
4. η = Generate random number (seed)
5. for (i = 1 to t)
   Randomize Bio-components α_i using Eq. (3)
   Determine φ_i by computing value of objective function $f(\alpha_i)$ using Eq. (4)
   Determine ψ_i by normalizing objective function output φ_i using Eq. (5)
   end
6. Determine μ = Mean (ψ_i), ν = Median (ψ_i)
7. Calculate L=sort($[\psi_1,\ldots,\psi_t]$ wrt $|\psi_i-\nu|$)
8. Determine T = truncate(L,t-q) to keep first q values
9. for (i = 1 to q)
   Compute Υ_i using Eq. (7)
   Compute ϕ_i using Eq. (6)
   end
10. *Generate Helper Data* ***HD*** = $\{[\xi_1,\xi_2,\ldots,\xi_t], [\Phi_1,\Phi_2,\ldots,\Phi_q]\}$
11. Return (***HD***)

4.2 Key retrieval process

In Key Retrieval process, this process, biometric keys $\{\alpha_1, \alpha_2, \ldots, \alpha_t\}$ of the user is used to retrieve the key from the helper data $HD = \{[\xi_1, \xi_2,\ldots, \xi_t], [\Phi_1, \Phi_2,\ldots, \Phi_q]\}$. For this, pre-defined value of threshold value 'δ' is chosen to ensure optimal retrieval of key.

The process is as follows: Using the user biometric and helper data values φ_i of the objective function are computed using Eq. (8).as given below

$$\varphi_i = f(\alpha_i) = \frac{1}{\delta}[\alpha_i - \xi_i] \sin\left[\frac{1}{\delta}\{\alpha_i - \xi_i\}\right] i \in \{1, 2, \ldots, t\}. \tag{8}$$

These values are then normalized as

$$\psi_i = |\varphi_i| \cdot 10^{-\log_{10}(|\varphi_i|)}. \tag{9}$$

In the case where the number of bio-components is larger than the number of crypto-components, methodology is required to form a subset of q bio-components which can be associated with each crypto-component. For this, we have taken the median value $\boldsymbol{\nu}$ of the t local minima ψ_i calculated using the above defined objective functions. Then the distance between each bio-component and the median is computed and sorted in the ascending order. From this, the first q bio-components which are termed as anchors.

If there are only fewer numbers of bio-components for binding the crypto-components, then the average value of the t local minima μ is computed. Then $\mu \cdot \psi_i$ are taken as the values of the anchors.

The normalized values of φ_i are then used to retrieve the secret key with the help of the helper data in the following manner

$$\beta_i = \phi_i \cdot \Upsilon_i, \tag{10}$$

where

$$\Upsilon_i = \psi_i \cdot \mu \tag{11}$$

From all the crypto-components thus computed, the secret cryptographic key K can be reconstructed back whenever required.

A pseudocode of the proposed Key Binding Method is illustrated as Algorithm 2.

Algorithm 2: Proposed Key Retrieval Method

1. **Function** Key_Retrieval (***HD***, ***B***, δ)
2. $\{\alpha_1, \alpha_2, \ldots, \alpha_t\}$ = *Derive biocomponent* ***(B)***
3.
4. for (i = 1 to t)

   Determine φ_i by computing value of objective function $f(\alpha_i)$ using Eq. (8)
   Determine ψ_i by normalizing objective function output φ_i using Eq. (9)

   end
5. Determine μ = Mean (ψ_i), ν = Median (ψ_i)
6. Calculate $L = sort([\psi_1, \ldots, \psi_t]\ wrt\ |\psi_i - \nu|)$
7. Determine $T = truncate(L, t - q)$ to keep first q values
8. for (i = 1 to q)

   Compute Υ_i using Eq. (11)
   Compute β_i using Eq. (10)

   end
9. *Generate Key* $\boldsymbol{K} = \{\beta_1, \beta_2, \ldots, \beta_q\}$
10. Return (***K***)

The proposed system is experimentally validated on benchmark datasets. Details of experimental analysis have been given follow in the following section.

5 Experimental validation

Proposed biometric crypto system has been evaluated both qualitatively and quantitatively on benchmark datasets for Iris and Fingerprint modalities. Proposed system is generic in nature and can be extended for any type and dimension of modality. Security analysis of the proposed method has been performed. Performance metrics which have been used for the evaluation of the performance of the proposed scheme include False Acceptance Rate (FAR), Genuine Acceptance Rate (GAR), Genuine Wrongly Decoded bit Rate (GWDR) and Imposter Wrongly Decoded bit Rate (IWDR). Proposed scheme has been implemented using MATLAB on a PC having 8 GB RAM and Intel i5 processor.

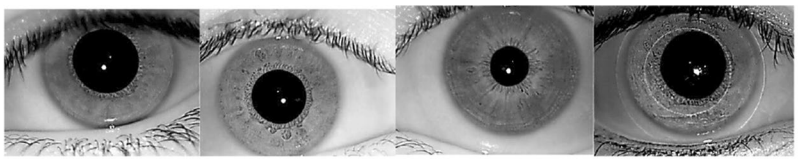

(a)

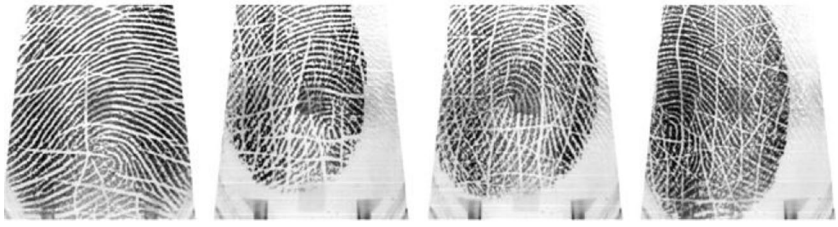

(b)

Fig. 2 **a** Sample images from IIT Delhi database. **b** Sample images from CASIA-FingerprintV5 database

5.1 Database for experimentation

Biometric data chosen for evaluation is benchmark datasets with low intra-class variability. Apart from this, chosen data is considered to be uniformly distributed over the feature space. John Daugman in his study showed that the Iris biometric possesses these two important characteristics [45]. For the experimental validation of the proposed method, we have considered iris biometric taken from IIT Delhi Iris database. This database has been created with iris biometrics of 224 persons IIT Delhi [46]. These images are in bitmap (*.bmp) format. Resolution of these images is 320×240 and all these images were acquired in the indoor environment. We have also taken fingerprint biometric database CASIA-FingerprintV5 for performance analysis of the proposed method [47]. CASIA Fingerprint Image Database Version 5.0 (or CASIA-FingerprintV5) contains 20,000 fingerprint images of 500 subjects. The fingerprint images of CASIA-FingerprintV5 were captured using URU4000 fingerprint sensor in one session. Each volunteer contributed 40 fingerprint images of his eight fingers (left and right thumb/second/third/fourth finger), i.e. 5 images per finger. The volunteers were asked to rotate their fingers with various levels of pressure to generate significant intra-class variations. All fingerprint images are 8 bit gray-level BMP files and the image resolution is 328 × 356. The sample images from these datasets are depicted in Fig. 2.

5.2 Performance evaluation metrics

The proposed scheme has been quantitatively analysed using following performance evaluation metrics:

False acceptance rate (FAR) It is the likelihood that an unauthorized user will be able to reconstruct the cryptographic key correctly [48]. If *FA* be the number of false accepts and *NI* be the number of impostor patterns, then

$$\mathrm{FAR} = \frac{\mathrm{FA}}{\mathrm{NI}}$$

Genuine acceptance rate (GAR) GAR expresses the likelihood that an authorized user will be able to reconstruct the cryptographic key correctly [49]. It is generally computed from the value of False Rejection Rate (FRR). Let FR represents the number of false rejects and NA be the number of authorized user patterns, then

$$\mathrm{FRR} = \frac{\mathrm{FR}}{\mathrm{NA}}$$

After calculating FRR we compute GAR by the given formula:

$$\mathrm{GAR} = 1 - \mathrm{FRR}$$

Genuine wrongly decoded bit rate (GWDR) This is the wrongly decoded bit rate between the actual secret key K and the reconstructed key K' by the genuine user. To calculate this the hamming distance between K and K' is considered as per the following formula [50]

$$\mathrm{GWDR} = \frac{\mathrm{HD}\left(K, K'\right)}{|K|}$$

Imposter wrongly decoded bit rate (IWDR) This is the wrongly decoded bit rate between the actual secret key K and the reconstructed key K' by an imposter. To calculate this the hamming distance between K and K' is taken into account as per the following formula

$$\mathrm{IWDR} = \frac{\mathrm{HD}\left(K, K'\right)}{|K|}$$

5.3 Performance analysis

Performance analysis is performed both qualitatively and quantitatively. The two main parameters of the proposed technique are neighbourhood threshold and random noise. The first experiment was carried out to study the effect of noise η_i and neighbourhood threshold δ on the convergence stability of the objective function. For this, noise η_i in the range [1, 40], neighbourhood threshold δ in the interval [1, 40] and biometric-components a_1, a_2,…, a_{128} in the range [0, 240] were taken. Secret key K of four different lengths viz., 256, 512, 1024 and 2048 were randomly generated for binding with the biometric data. The cryptographic key was bound with the biometric data through the proposed method and helper data was created. Then the cryptographic key was reconstructed using noisy bio-components ($\alpha_i + \eta_i$). This whole process was performed several times and the success rates of the proposed methodology were recorded. The results have been shown in the Fig. 3 for cryptographic keys of sizes 256, 512, 1024 and 2048 bits. The 3D plots of the success rate, amount of noise and neighbourhood threshold values have been shown.

The above results show that the proposed method consistently achieves good success rate even with some changes in the neighbourhood threshold values and some amount of randomization in the input values to the objective function. This means that the technique offers flexibility with regard to variation in the input biometric feature values, caused by different environmental and physical conditions. The two main parameters of the proposed technique are neighbourhood threshold and random noise. An assessment was done

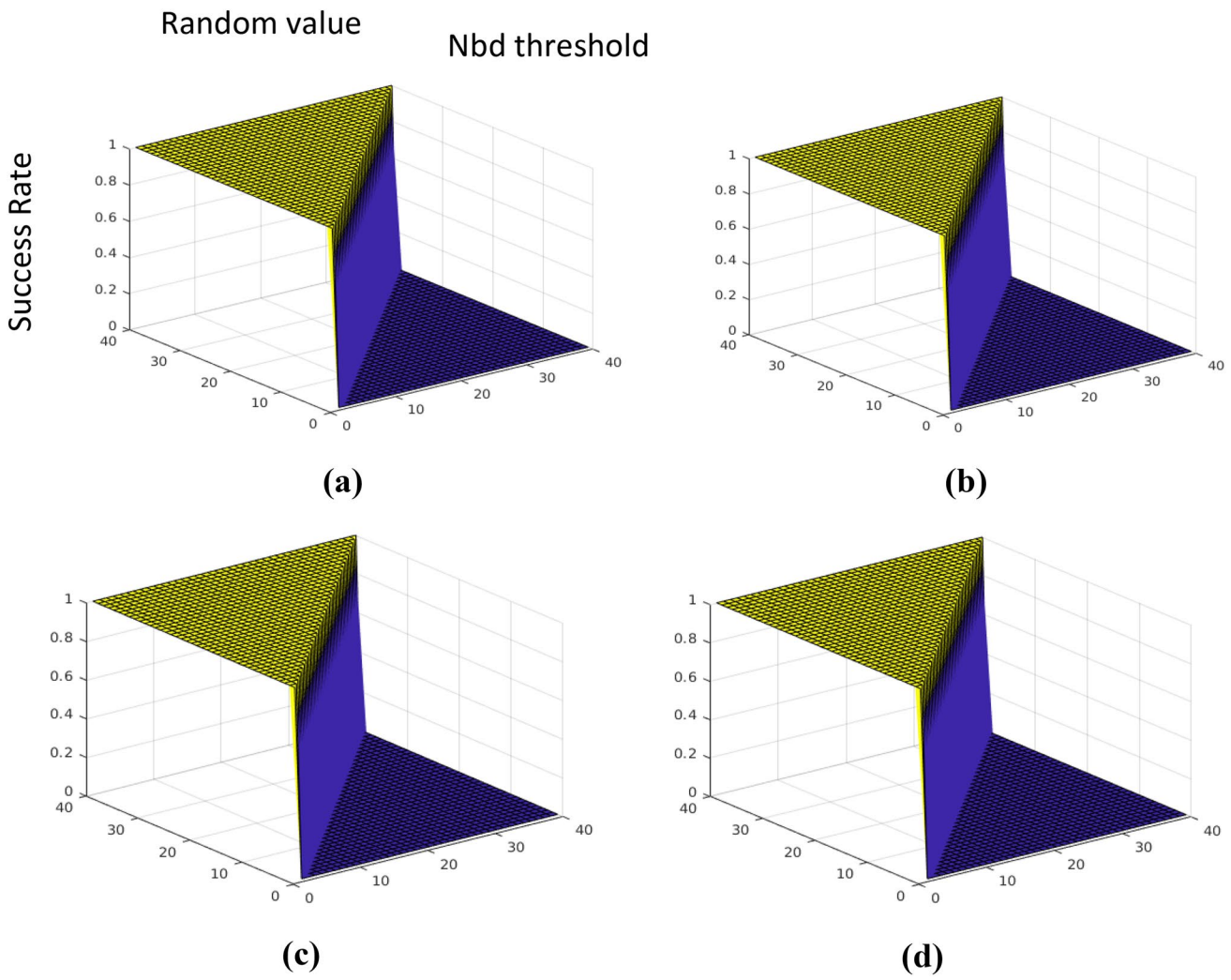

Fig. 3 Effect of change in neighbourhood threshold and random value on the success rate of the proposed method for key sizes of **a** 256 bits **b** 512 bits **c** 1024 bits and **d** 2048 bits

as to how these parameters affect the success rate of the biometric crypto system and the result is shown in the Fig. 3.

In the second experiment, the effect of the neighbourhood threshold values on the accuracy of the proposed method was studied for genuine users and impostors. Here, Chebyshev distances were computed for comparing each query template with all the available gallery templates. These comparisions were used for determining the optimum value of the threshold which helped in separating gennine from the imposters. Experimentation was performed on four key sizes viz., 256, 512, 1024 and 2048 bits. The results are shown in Fig. 4.

The results obtained in this experiment illustrates that the success rate for genuine user is unaffected upto a certain value of neighbourhood threshold and there is a clear separation of correct key retrieval between genuine user and imposter. Results demonstrate the fact that the proposed key binding method ensures that the secret key can be retrieved successfully by the genuine user whereas the imposter is unable to get the secret key which was bound with the biometrics of the authorized user.

In the third experiment, performance analysis of the proposed method was done with respect to various performance metrics like FAR, GAR, Genuine WDR and Imposter WDR for various sizes of the secret cryptographic keys viz., 256, 512, 1024 and 2048 bits. These performance metrics have been computed for various neighbourhood values δ ranging between 28 and 32. Performance results in terms of FAR, GAR, GWDR and IWDR plotted for secret key of size 256 bits have been shown in Fig. 5 for the IIT Delhi dataset.

The results obtained shows that there is not much variation in the FAR, GAR, GWDR and IWDR values if the neighbourhood threshold lies in the range [28, 32].

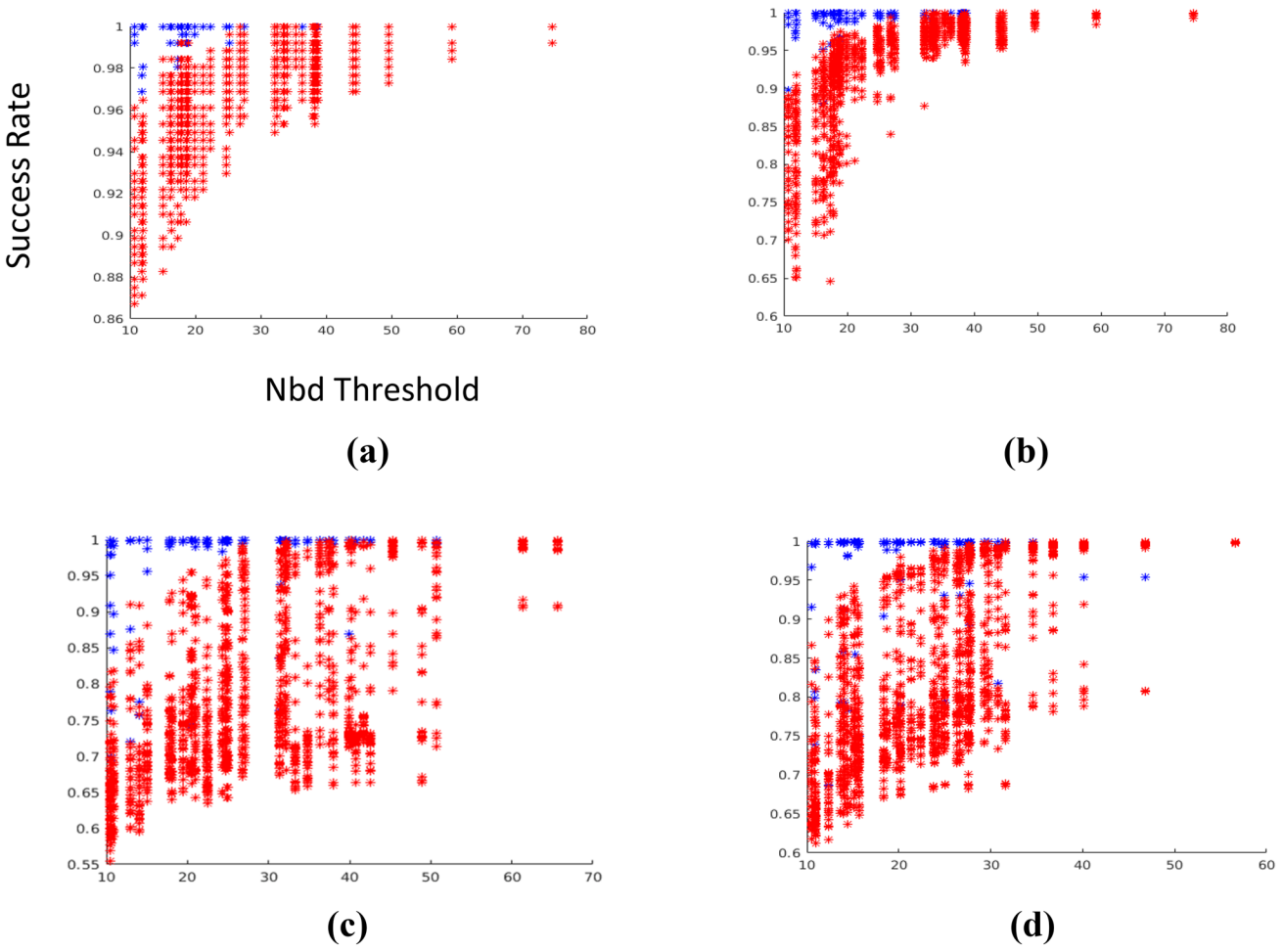

Fig. 4 Effect of change in neighbourhood threshold on success rate for genuine users (blue dots) and impostors (red dots) for key sizes of **a** 256 bits **b** 512 bits **c** 1024 bits and **d** 2048 bits (colour figure online)

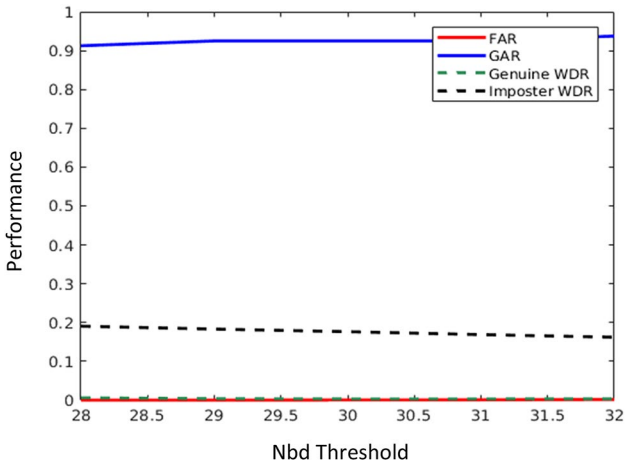

Fig. 5 Performance results: FAR, GAR, GWDR and IWDR for neighbourhood threshold in the range [28, 32] for 256 bits keysize

Table 2 Performance results on Iris datasets for different key sizes with δ fixed to 30

Key-size	GAR (%)	FAR (%)	Genuine WDR (%)	Imposter WDR (%)
256 bits	95.00	0.0475	0.0391	1.81
512 bits	91.25	0.210	0.1100	3.38
1024 bits	86.25	1.95	0.7900	10.61
2048 bits	86.25	7.83	0.9400	17.62

In the fourth experiment, the values of performance metrics like FAR, GAR, GWDR and IWDR were computed by fixing the neighbourhood threshold value δ to 30. These were computed for all the four key sizes and shown in the Table 2.

This experiment was also carried out on another fingerprint database namely, CASIA-V5. The values obtained for performance metrics like FAR, GAR, GWDR and IWDR by

Table 3 Performance results on Iris datasets for different key sizes with δ fixed to 30

Key-size	GAR (%)	FAR (%)	Genuine WDR (%)	Imposter WDR (%)
256 bits	94.00	0.0509	0.0407	2.17
512 bits	90.63	0.316	0.1403	3.96
1024 bits	87.34	2.09	0.8300	11.54
2048 bits	86.55	8.543	0.9614	18.13

fixing the neighbourhood threshold value δ to 30 are shown in the Table 3.

The result shows a high genuine acceptance rate and a very low false acceptance rate which is highly desired for such biometric cryptosystems. Moreover, wrongly decoded bit rate for genuine user is quite low which ensures retrieval of correct key.

Further, the heat maps were generated to assess how selection of gallery items i.e., templates stored in the database, affects reconstruction of secret key. For this, two cases were investigated. In the first case, five different bio-components were taken for each user. Out of these, one bio-component was used as gallery item whereas remaining four bio-components were used as probe items. The gallery item was used for binding the secret key whereas the probe items were used for reconstruction of secret key. The reconstructed key was compared with the original secret key. Heat map as shown in Fig. 6a represents the respective scores of the comparison made in the interval [0, 1]. Darker shade represents higher score. In this, each row represents a user's matching score for key regeneration using his 4 probe bio items. In the second case, five different bio-components for each user were taken. But unlike the first case, here gallery bio item was formed by taking mean of the five bio-components of the user. This gallery bio item was used to bind the key and all the five bio-components were used to reconstruct the secret key. The recovered key was compared with the original key and corresponding heat map was generated with the help of the respective scores as shown in Fig. 6b. As shown, darker shade depicts higher obtained score.

Results show that performance of the proposed system is better when the mean of the bio-components are taken as the gallery item i.e., representative template, in comparison to the case where an individual bio-component was taken as the gallery item. Hence, the proposed approach for mean value of bio-components is appropriate solution.

5.4 Security analysis

In security analysis of the proposed method, we have investigated the robustness of the method against brute force attack and correlation attack.

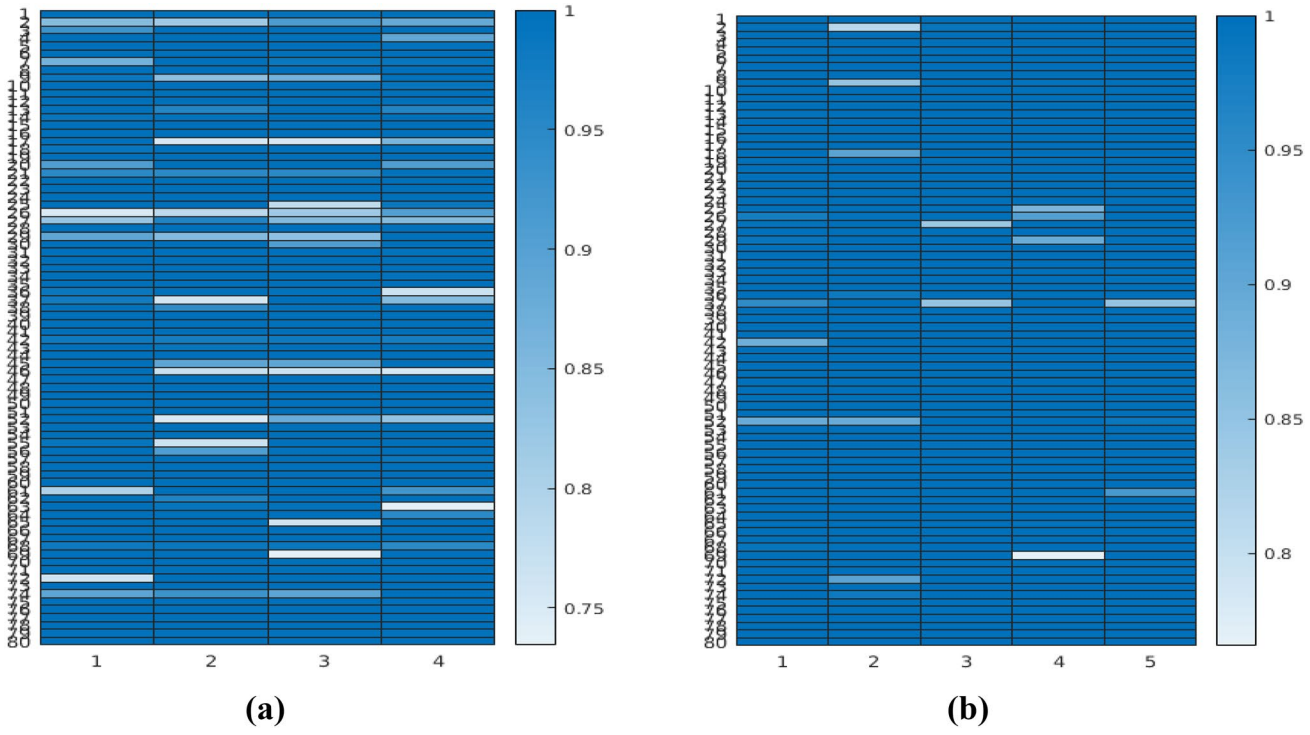

Fig. 6 **a** Heat maps when gallery item is the actual bio-component **b** Heat maps when gallery item is the mean of the bio-components

5.4.1 Resistance against brute force attack

From Eq. (3), it is quite evident that the random value $\boldsymbol{r}$ plays a significant role in the value of $\boldsymbol{h_i}$ which ultimately leads to formation of helper data HD. As the helper data is in public domain, the adversary tries to derive the cryptographic key with the help of the helper data. Attacker has access to values of $\boldsymbol{h_i}$ but in the absence of knowledge of random value $\boldsymbol{r}$, he would not be able to derive the values of bio-components $\boldsymbol{a_i}$ correctly. Values of $\boldsymbol{a_i}$ lies in the range [0, A], so the objective function has at least $n_{\min} = A/4\delta$ local minima in this range. But only a particular minimum out of those will be corresponding to actual $\boldsymbol{h_i}$. As described earlier the biometric data of a user is split into $\boldsymbol{t}$ bio-components. So, there will be exactly $\boldsymbol{t}$ objective functions each of them having $n_{\min} = A/4\delta$ local minima. Since the value of local minima increases as the value of x increases, there are values which would be some which would be more dominant than the others. Therefore, it is very essential that an attacker should arrive at correct local minimum for each of the $\boldsymbol{t}$ objective functions. This will require $\left(n_{\min}\right)^t$ trials. Therefore, brute force attack complexity will depend on the length of the biometric data of the user which is usually quite large. Hence, proposed approach exhibits strong resistance against brute force attack.

5.4.2 Resistance against correlation attack

In this attack, an adversary tries to derive crypto-components or bio-components by exploiting correlation if at all exists in multiple helper data created at multiple instances of protecting a secret key using a particular biometric data. Suppose $HD_1 = \{[\xi_{11}, \xi_{12},\ldots, \xi_{1t}], [\Phi_{11}, \Phi_{12},\ldots, \Phi_{1q}]\}$ and $HD_2 = \{[\xi_{21}, \xi_{21},\ldots, \xi_{2t}], [\Phi_{21}, \Phi_{22},\ldots,\Phi_{2q}]\}$ are two such helper data where in the same crypto-component is hidden in two different pairs $(\Phi_1 \cdot \Upsilon_1)$ and $(\Phi_2 \cdot \Upsilon_2)$. Therefore, corresponding bio-component is derived by identifying the correct local minima for which $\Phi_1 \cdot \Upsilon_1 = \Phi_2 \cdot \Upsilon_2$. But this is almost infeasible due to the following reasons:

(i) It is difficult to identify which q local minima out of total t local minima, are associated with the coefficients.
(ii) Attacker would not be able to test the condition $\Phi_1 \cdot \Upsilon_1 = \Phi_2 \cdot \Upsilon_2$. Y_{2i} for two different pairs $(\Phi_1 \cdot \Upsilon_1)$ and $(\Phi_2 \cdot \Upsilon_2)$, as q anchors in both the helper data HD_1 and HD_2 depend on the values of all the local minima.

The security analysis of the proposed method establishes the fact that the proposed approach is robust against brute force attack as well as correlation attack. Here, robustness means system is mathematically so strong that it can survive many cryptanalytic attacks mounted by the cryptanalysts.

6 Conclusion and future directions

In this manuscript, we have proposed a novel biometric cryptosystem which involves cryptographic key binding by minimizing the objective function. Secret key which is to be bound is split into a number of crypto-components. Similarly, the biometric data is also divided into several bio-components and distinct objective functions are defined corresponding to each bio-component. Key binding process has been devised using crypto-components, bio-components and objective functions. Process for reconstruction of secret key from the helper data is also designed. The proposed method is extensively evaluated for iris and fingerprint modalities. Also, robustness against cryptanalytic attacks have been assessed.

A detailed performance analysis in terms of FAR, GAR, GWDR and IWDR shows that this method is very efficient. Its performance does not get affected with change of length of secret key and upto a certain amount of noise induction in the user biometric data. Further, heat analysis illustrates that when the mean of the bio-components is taken as the gallery item i.e., representative template, the matching score is better in comparison to the case where individual bio-component is taken as the gallery item. Security analysis of the proposed method shows that it is quite robust against brute force attack and correlation attack.

The proposed scheme can further be studied for multimodal scenarios under dynamic environment. Adaptability of the biometric system to different types and dimension of the biometrics can also be investigated. Any biometric trait whose features can be extracted in binary form can be used in this methodology. There is no constraint on the type of biometric features that can be used for binding the secret key. Also, the issue of image quality may be studied as it plays an important role in the proposed key binding method. When some of the challenges like poor quality input images, improper sensor interaction, etc. are properly resolved, it enhances the adaptability of the system to the different type of user's environments. This will pave the way to make a highly reliable and robust biometric cryptosystem based on key binding method.

References

1. Dooley, J.F.: A Brief History of Cryptology and Cryptographic Algorithms. Springer, New York (2013)
2. Preneel, B.: Understanding Cryptography: A Textbook for Students and Practitioners. Springer, London (2010)
3. Schneier, B.: The Non-Security of Secrecy. Commun. ACM **47**(10), 120–120 (2004)
4. Piper, F., Murphy, S.: Cryptography: A Very Short Introduction. Oxford University Press, London (2002)

5. Stallings, W.: Cryptography and Network Security Principles and Practices. Prentice Hall, New York (2005)
6. Goldreich, O.: Foundations of Cryptography Basic Tools. Cambridge University Press (2004)
7. Callas, J.: The Future of Cryptography. Inf. Syst. Secur. **16**(1), 15–22 (2007)
8. Hirata, S., Takahashi, K.: Cancelable biometrics with perfect secrecy for correlation-based matching. In: Tistarelli, M., Nixon, M. (eds.) Advances in Biometrics, ser. Lecture Notes in Computer Science, vol. 5558, pp. 868–878. Springer, Berlin (2009)
9. Bolle, R.M., Connel, J.H., Ratha, N.K.: Biometrics perils and patches. Pattern Recogn. **35**(12), 2727–2738 (2002)
10. Sutcu, Y., Li, Q., Memon: Protecting biometric templates with sketch: theory and practice. IEEE Trans. Inf. Forensics Secur. **2**(3), 503–512 (2007)
11. Ratha, N.K., Connell, J., Bolle, R.M.: Enhancing security and privacy in biometrics-based authentication systems. IBM Syst. J. **40**(3), 614–634 (2001)
12. Katz, J., Lindell, Y.: Introduction to Modern Cryptography. Taylor & Francis Group LLC, London (2008)
13. Lincke, S.J., Hollan, A.: Network security: focus on security, skills, and stability. In: 37th ASEE/IEEE Frontiers in Education Conference, Milwaukee (2007).
14. Ratha, N.K.: Privacy protection in high security biometrics applications. In: Kumar, A., Zhang, D. (eds.) Ethics and Policy of Biometrics, ser. Lecture Notes in Computer Science, vol. 6005, pp. 62–69. Springer, Berlin (2010)
15. Jin, Z., Teoh, A.B.J., Goi, B.M., Tay, Y.H.: Biometric cryptosystems: a new biometric keybinding and its implementation for fingerprint minutiae based representation. Elsevier J. Pattern Recogn. **16**, 50–62 (2016)
16. Sadhya, D., Singh, S.K., Chakraborty, B.: Review of key-binding-based biometric data protection schemes. IET Biom. **5**(4), 263–275 (2016)
17. Soutar, C., Roberge, D., Stoianov, A., Gilroy, R., Kumar, B.V.K.V.: Biometric Encryption. Chapter 22 in ICSA Guide to Cryptography, pp. 1–28. McGraw-Hill (1999)
18. Juels, A., Wattenberg, M.: A fuzzy commitment scheme. In: Sixth ACM Conference on Computer and Communications Security, pp. 28–36. ACM Press (1999)
19. Juels, A., Sudan, M.: A fuzzy vault scheme. In: IEEE Int. Symp. On Information Theory, pp. 1–7 (2002)
20. Blanton, M., Aliasgari, M.: Analysis of reusability of secure sketches and fuzzy extractors. IEEE Trans. Inf. Forensics Secur. **8**(9), 1433–1445 (2013)
21. Al-Tarawneh, M. S., Woo, W.L., & Dlay, S.S.: Fuzzy vault crypto biometric key based on fingerprint vector features. In: 2008 6th International Symposium on Communication Systems, Networks and Digital Signal Processing, pp. 452–456 (2008)
22. Dang, T.K., Truong, Q.C., Le, T.T.B., Truong, H.: Cancellable fuzzy vault with periodic transformation for biometric template protection. IETBiometrics **5**(3), 229–235 (2016)
23. Clancy, T. C., Kiyavash N., & Lin, D. J.: Secure smartcard-based fingerprint authentication. In: Proc ACM SIGMM 2003 Multimedia, Biometrics Methods and Applications Workshop, pp. 45–52 (2003)
24. Li, P., Yang, X., Cao, K., Tao, X., Wang, R., Tian, J.: An alignment-free fingerprint cryptosystem based on fuzzy vault scheme. J. Netw. Comput. Appl. **33**(3), 207–220 (2010)
25. Marino, R.A., Alvarez, F.H., Encinas, L.H.: A crypto-biometric scheme based on iristemplates with fuzzy extractors. Inf. Sci. **195**, 91–102 (2012)
26. Salas, M.: A secure framework for OTA smart device ecosystems using ECC and biometrics. Springer Commun. Comput. Inf. Sci. **381**, 204–381 (2013)
27. Yoon, E. J., Yoo, K. E.: A biometric based authenticated key agreement scheme using ECC for wireless sensor networks. In: International Conference on Management and Service Science, Gyeongju, Korea, pp. 699–705 (2014)
28. Liew, C. Z., Shaw, R., Li, L., Yang, Y.: Survey on biometric data security and chaotic encryption strategy with bernoulli mapping. In: International Conference on Medical Biometrics, Shenzhen, China, pp. 174–180 (2014)
29. Eskander, G.S., Sabourin, R., Granger, E.: A bio-cryptographic system based on offline signature images. Inf. Sci. **259**, 170–191 (2014)
30. Amirthalingam, G., Radhamani, G.: New chaff point based fuzzy vault for multimodal biometric cryptosystem using particle swarm optimization. Elsevier J. King Saud Univ. Comput. Inf. Sci. **28**, 381–394 (2016)
31. Chitra, D., Sujitha, V.: Security analysis of prealigned fingerprint template using fuzzy vault scheme. Cluster Comput. **22**, 12817–12825 (2018)
32. Elrefaei, L. A., Al-Mohammadi, A. M.: Machine vision gait-based biometric cryptosystem using a fuzzy commitment scheme. J. King Saud Univ. Comput. Inf. Sci. 1–14 (2019)
33. Ponce-Hernandez, W., Blanco-Gonzalo, R., Liu-Jimenez, J., Sanchez-Reillo, R.: Fuzzy vault scheme based on fixed-length templates applied to dynamic signature verification. IEEE Access **8**, 11152–11164 (2020)
34. Asthana, R., Walia, G.S., Gupta, A., Rishi, S., Kumar, A.: A secure multimodal biometric system based on diffused graphs and optimal score fusion. J. IET Biom. **8**(4), 231–242 (2019)
35. Walia, G.S., Aggarwal, K., Singh, K., Kunwar, S.: Design and analysis of adaptive graph based cancelable multi-biometrics approach. IEEE Trans. Depend. Secure Comput. (2020). https://doi.org/10.1109/tdsc.2020.2997558
36. Asthana, R., Walia, G.S., Gupta, A., Raza, S.: A novel approach of multi-stage tracking for precise localization of target in video sequences. J. Expert Syst. Appl. (2017). https://doi.org/10.1016/j.eswa.2017.02.007
37. Walia, G.S., Gupta, K., Sharma, K.: Quality based adaptive score fusion approach for multimodal biometric system. J. Appl. Intell. **50**, 1086–1099 (2020)
38. Chenggang, Y., Gong, B., Yuxuan, W., Gao, Y.: Deep multi-view enhancement hashing for image retrieval. In: IEEE Transactions on Pattern Analysis and Machine Intelligence (2020)
39. Chenggang, Y., Zhisheng, L., Yongbing, Z., Yutao, L., Xiangyang, J., Yongdong, Z.: Depth image denoising using nuclear norm and learning graph model. ACM Trans. Multimed. Comput. Commun. Appl. **16**, 1–7 (2020)
40. Chenggang, Y., Shao, B., Zhao, H., Ning, R., Zhang, Y., Xu, F.: 3D Room layout estimation from a single RGB image. IEEE Trans. Multimed. **22**, 3014–3024 (2020)
41. Ouyang, K., Liang, Y., Liu, Y., Tong, Z., Ruan, S., Zheng, Y., Rosenblum: Fine-grained urban flow inference. IEEE Trans. Knowl. Data Eng. (2020)
42. Ouyang, K., Liang, Y., Jing, L., Ruan, S., Liu, Y., Zhang, J., Rosenblum, D. S., Zheng, Y.: UrbanFM: inferring fine-grained urban flows. In: Proceedings of the 25th ACM SIGKDD International Conference on Knowledge Discovery & Data Mining (KDD '19) (2019).
43. Alfaisal, A., Mokbel, C.: Convolutional neural network biometric cryptosystem for the protection of the Blockchain's private key. ScienceDirect Proc. Comput. Sci. **160**(2019), 235–240 (2019)
44. Uludag, U., Pankanti, S., Prabhakar, S., Jain, A.K.: Biometric cryptosystems: issues and challenges. Proc. IEEE **92**(6), 948–960 (2004)
45. Daugman, J.: How iris recognition works. IEEE Trans. Circuits Syst. Video Technol. **14**(1), 21–30 (2004)

46. https://www4.comp.polyu.edu.hk/~csajaykr/IITD/Database_Iris.htm
47. http://biometrics.idealtest.org/dbDetailForUser.do?id=7
48. Al-Waisy, A.S., Qahwaji, R., Ipson, S., Al-Fahdawi, S., Nagem, T.A.M.: A multi-biometric iris recognition system based on a deep learning approach. Pattern Anal. Appl. Springer **21**, 783–802 (2017)
49. Subban, R., Susitha, N., Mankame, D.P.: Efficient iris recognition using Haralick features based extraction and fuzzy particle swarm optimization. Clust. Comput. **21**(1), 79–90 (2017)
50. Ricco, D., Galdi, C., Manzo, R.: Biometric/cryptographic keys binding based on function minimization. In: 12th International Conference on Signal-Image Technology & Internet-based Systems, pp. 144–150 (2016)

Publisher's Note Springer Nature remains neutral with regard to jurisdictional claims in published maps and institutional affiliations.

2021 International Conference on Automation, Robotics and Applications

A Particle Swarm Optimization-Based Cooperation Method for Multiple-Target Search by Swarm UAVs in Unknown Environments

Aniket Gupta
Delhi Technological University
New Delhi, India
aniket.tcdav@gmail.com

Aman Virmani
Delhi Technological University
New Delhi, India
virmaniaman4@yahoo.com

Parth Mahajan
Delhi Technological University
New Delhi, India
mahajanparth0@gmail.com

Raghava Nallanthigal
Delhi Technological University
New Delhi, India
nsraghava@dtu.ac.in

***Abstract*—This paper presents a decentralized method for multi-target search problem using a swarm of unmanned aerial vehicles with the information available from the onboard sensors. The proposed method deals with three main objectives: Time optimized multi-target search, optimized payload drops and inter-UAV collision avoidance which is independent of the number of UAVs. The proposed controller uses a modified Particle Swarm Optimization for cooperative multi-target search and is called Multi-Target Particle Swarm Optimization (MTPSO). The controller's performance is evaluated on Ardupilot's SITL platform for realistic simulations in various case-scenarios. Moreover, the performance of the controller with various inertial functions is also analyzed for different case-scenarios. Finally, the effectiveness of the proposed algorithm is illustrated by comparison with existing search methods. 0**

Keywords—Swarm, Unmanned Aerial Vehicles, Multi-target Search, Multi-agent systems, Particle Swarm Optimization

NOMENCLATURE

UAV	Unmanned Aerial Vehicle
PSO	Particle Swarm Optimization
NED	North East Down
FOV	Field of View
FFOV	Frontal Field of View
v_i	Velocity of i^{th} UAV
p_i	Position of i^{th} UAV
W_{start}	Search Area Starting waypoint
W_{end}	Search Area Ending waypoint
D	Distance between two UAVs
D_C	Communication range of UAV
D_{end}	Distance between UAV and end waypoint
D_{wap}	Waypoint completion radius
D_{safe}	Minimum allowable inter-UAV distance
D_{max}	Maximum displacement range
R	Random Coefficient
C	Acceleration Coefficient
O_{min}	Minimum overlapping constant
N	Total number of UAVs
N_S	Sub-swarm size
α	Angle of FFOV
v_{max}	Maximum velocity for UAV
v_{min}	Maximum velocity for UAV

I. INTRODUCTION

Unmanned Aerial Vehicles are increasingly becoming popular for their contribution in civil and military applications. Rapid area coverage, better surveillance and efficient monitoring are some of the characteristics that gives UAVs and edge over other alternatives. Ground-target search problem is arguably one of the most important applications of UAVs. This problem becomes increasingly complex as the number of UAVs and targets increase. In scenarios such as target-following and search rescue missions, it is important to provide rapid response with the ability to detect multiple targets.

Traditional methods [1] for detecting multiple targets by swarm of UAVs include simple exhaustive search wherein UAVs simply scan the complete search area using pre-defined trajectories. Though successfully deployed for target search, this method lacks in several ways. First, since the trajectories are predefined, they are not optimal and thus fail to respond in the shortest time for both surveillance and payload drop. Second, since the UAVs are not making any decisions themselves, they always require multiple operators to coordinate the complete mission which is both time-consuming and expensive.

Other approaches include dividing the complete search area into small cells and associate each cell with a probability of existence of target in the cell. Thus, creating a complete probability map for the complete search area. As the UAVs continue to progress in the environment, the probability of cells with targets are updated continuously, the cells with the highest probability are finally accepted as the detected targets. This method requires a centralized probability map which stores data from all agents and thus requires a robust fully connected network [2][3].

In [4], a similar approach is presented for groups of UAVs with limited sensing and communication capabilities. The probability associated with each cell is modelled using Bernoulli distribution. Each agent keeps its individual probability map generated by fusing data from other agents in

2021 7th International Conference on Automation, Robotics and Applications (ICARA) | 978-1-6654-0469-3/21/$31.00 ©2021 IEEE | DOI: 10.1109/ICARA51699.2021.9376529

Authorized licensed use limited to: DELHI TECHNICAL UNIV. Downloaded on March 27,2021 at 05:23:44 UTC from IEEE Xplore. Restrictions apply.

its communication range. Though effective, this convergence of agents on the targets is slow and the method itself is computationally expensive. Thus, it is not suitable for modern UAVs which focus on minimalistic architecture and light hardware.

Particle Swarm Optimization algorithms have been proven to provide best search performance but its usage in multi-target search has been limited due to lack of proper structure, multi-UAV collision and poor navigation in the unknown search area. Through this paper, we aim to tackle these problems. The proposed controller follows a defined structure while incorporating smooth inter-UAV collision avoidance, flocking and multi-target search with optimized payload drop. The algorithm is scalable, fault-tolerant and computationally light- weight and thus can be deployed on very light hardware components which is often the key feature of a UAV swarm.

Inertial functions used in PSO algorithm control the exploration and exploitation characteristics of the algorithm and thus using different functions results in varying performances [5]-[11]. The paper also proposes different inertial functions which can be used in various different scenarios in the surveillance region such as when the difference between the number of targets and the agents is very high or if an immediate response is required for the targets.

The rest of the paper is organized as follows: Section II gives a short introduction to the original Particle Swarm Optimization algorithm and leads on for the mathematical formulation of our problem statement. Section III presents the structure and design of the cooperative navigational controller for a single UAV. The Simulation in the loop (SITL) experimental results are presented in Section IV. Section V provides a brief conclusion, with recommendations for future work.

II. Preliminaries

A. Particle Swarm Optimization Algorithm

Particle Swarm Optimization is a well-established optimization algorithm that iteratively tries to find the global optimum. The original algorithm uses a population of particles which move around the search space according to the PSO update rules. Each particle's movement is affected by its best-known position and the global best-known position. These values also get updated as better solutions are found by the particles. It is a metaheuristic algorithm and thus does not guarantee convergence to an optimal solution.

The PSO update rule is as follows:

$$v_i^{t+1} = \omega * v_i^t + R_1 * C_1 * (P_{best}^t - p^t) + R_2 * C_2 * (G_{best}^t - p^t) \quad (1)$$

B. Problem Formulation

We consider that a swarm of quadcopter UAVs have to navigate through a search area characterized by a starting waypoint W_{start}, ending waypoint W_{end} and the breadth B, searching for multiple targets scattered throughout the region. All the UAVs are assumed to be on the same height, thus moving in the same plane. The position vector for each agent can be denoted by $p_i^t = [x_i, y_i]^T$ and the velocity vector by $v_i^t = [\dot{x}_i, \dot{y}_i]^T$, for the UAV i (i = 1, 2, …, N) at time t, where N is the number of UAVs.

Each UAV is equipped with an onboard camera that can detect targets within its FOV and localize them using an onboard software stack*. The UAVs are also equipped with a single payload each and can drop it at any one target location. Thus, the complete mission UAVs is to scan the surveillance region, detect the maximum number of targets, drop maximum payloads and reach the end of the search area while avoiding inter-UAV collisions.

The network topology of all the agents is modelled by a partially connected ad-hoc network [12]. Mathematically the model can be represented by an undirected graph $G = (V, E), where\ V = \{1,2, \dots, N\}$ is the set of nodes and $E = \{(i,j): i,j \in V,\ ||p_i - p_j|| \leq D_C\}$ is the edge set. A single UAV directly connects only to its neighbouring agents denoted by $N_G = \{j \in V, (i,j) \in E\}$.

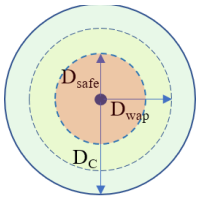

Fig. 1. Pictorial representation of D_{safe}, D_{wap} and D_C

Agents only share minimal data between themselves which includes their position data for collision avoidance, the position of the detected targets for cooperative convergence on target clusters and their payload state (see Table I) for cooperative payload delivery.

The algorithm is constrained by the following bounding conditions (in order of priority):

1. Avoid inter-UAV collision
2. Detect all the targets in the search area.
3. Drop the maximum number of payloads as soon as possible. (Rapid response)
4. Reach the end of the search area, so that no UAV wanders off.

III. Algorithm Design

A. Initialization of UAVS

To maximize the exploration, we start the target-search process in an exhaustive fashion, i.e. UAVs are arranged in a straight line at the start of the search area. The overlapping between the FOV of each UAV is kept at a minimum overlapping constant (Omin). If the search area is much larger, it can be divided into multiple parts for multiple consecutive runs.

B. Inertial Term

The Inertial velocity term as the name suggests helps maintain the original course of the swarm unit and prevents rapid changes in the trajectory of each UAV. It is the product

Authorized licensed use limited to: DELHI TECHNICAL UNIV. Downloaded on March 27,2021 at 05:23:44 UTC from IEEE Xplore. Restrictions apply.

of current velocity and the inertial function ω. Inertial function controls the exploration vs exploitation characteristics of the algorithm and is generally tuned to provide better exploration in the starting and exploitation as the swarm units become aware of the environment.

$$v_I^{t+1} = \omega * v^t \tag{2}$$

C. Personal Best

The personal best term is the best observation recorded by the swarm unit itself, it allows the units to explore the area under their current trajectory. While in traditional PSO, personal best is chosen out of all the observations, our algorithm follows a different approach. We only select the personal best from the current batch of observations, it provides the following two advantages:

1. It reduces the magnitude of the velocity vector offered by the personal best term and thus allows a stable trajectory for the UAVs.
2. It allows detecting multiple targets in the environment. Since each UAV follows the detect and drop method, the targets detected prior to the current observation can have one of the following three conditions only:
   a. UAV has dropped the payload to the target
   b. Neighbor UAV is coming to drop the payload to that target
   c. UAVs are out of payload and the target position is identified for further missions.

In each of these cases, the best strategy for multi-target detection is to choose the personal best from the current observations.

$$v_P^{t+1} = R_1 * C_1 * (P_{best}^t - p^t) \tag{3}$$

D. Global Best

To detect multiple targets in the environment all the swarm units are autonomously divided into sub-swarms of maximum size NS, which is a manually tunable parameter. UAVs are grouped into sub-swarms based on the inter-UAV distance if it is under Dmax.

The global best term represents the best observation detected by all of the UAVs in the sub-swarm. Similar to the personal best, MTPSO selects the global best term out of the current observations of the UAVs only.

$$v_P^{t+1} = R_2 * C_2 * (G_{best}^t - p^t) \tag{4}$$

E. Payload Optimization

Payload drop is the most important task in the rapid response strategy. For task assignment and optimized delivery, we start with assigning the following three states for the UAVs which helps in identifying which UAVs should continue search and which should go for payload drop:

TABLE I. PAYLOAD STATE

State	Meaning
State '1'	Payload available
State '0'	Going to the target position to drop the payload.
State '-1'	Payload unavailable

The position of the detected targets is continuously shared between the UAVs and the payload delivery task is assigned to the UAV nearest to the target within the constraint that target lies within the max displacement range.

$$v_{drop}^{t+1} = C_3 * \left(p_{drop} - p^t\right) \tag{5}$$

Further, if the UAV while going to drop payload on a target A, detects a target B which is closer than target A, it changes its drop location to target B, and target B becomes open for payload drop again. During payload drop, UAV continues to search for targets and sharing data with other UAVs. After dropping the payload, it does not retrace its path instead continues the search from drop point only.

F. Inter-UAV Collision Avoidance

Inter-UAV collision avoidance is necessarily required in any swarm system to ensure their safety. Thus, we utilize the concept of consensus equation to create an additional velocity term which can be vectorially added to the final velocity of each agent [13]. Avoidance is triggered if the distance between any nodes becomes smaller than Dsafe. This approach is easily integrable in our framework and can be represented as follows:

$$D = \left|\left|p_i - p^t\right|\right|_2$$

$$v_C^{t+1} = \begin{cases} C_4 * \sum_{i=1}^{N} (p_i - p^t) * \left(1 - \frac{D_{safe}}{D}\right), D \le D_{safe} \\ 0, D > D_{safe} \end{cases} \tag{6}$$

This approach only takes in account the agents approaching for collision and thus is suitable for our application. The Dsafe parameter is generally kept commensurate to the maximum swarm velocity and can be manually tuned if required.

G. Global Best and Personal Best Optimization

In the original PSO algorithm, Personal Best and Global best refers to the best personal value obtained and the best global value obtained over the entire iteration. This helps the particles to converge to a single optimum. In our case, we have modified this approach to dynamically update the Personal best and Global best.

We define a Frontal Field of View (FFOV) of each UAV with a front span of (-α, α). Each UAV constantly calculates the bearing of Personal best and Global best term wrt. To its position and if the bearing lies out of the frontal FOV range, both the terms are updated again. This is done to prevent the UAVs from settling on the pre-detected targets and continue the search for new targets. See Figure 2.

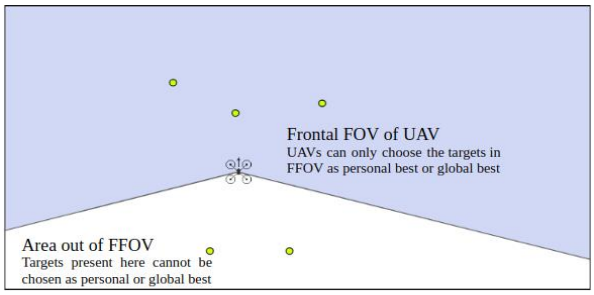

Fig. 2. Pictorial representation of FFOV

Authorized licensed use limited to: DELHI TECHNICAL UNIV. Downloaded on March 27,2021 at 05:23:44 UTC from IEEE Xplore. Restrictions apply.

H. Endpoint Velocity

The UAVs need to reach their desired end waypoint in order to successfully complete the mission, therefore, they need a heuristic term that can guide them towards the goal waypoint even when they are detecting the targets. To achieve this, we introduce another vectoral velocity term given by the following equation:

$$D_{end} = \left|\left|p_{end} - p^t\right|\right|_2$$

$$v_{end}^{t+1} = C_5 * (p_{end} - p^t) * \left(1 - \frac{D_{wap}}{D_{end}}\right) \quad (7)$$

Algorithm 1 Multi Target Search PSO

```
Initialize the swarm unit
Initialize hyper-parameters
while distance_from_end_waypoint > waypoint_radius do
    Collect data from neighbours
    Record the sensor readings
    Concatenate targets detected by all UAV's in target list
    Filter the target list for duplicates
    Remove all targets present outside the frontal FOV
    for target from Detected_targets_list do
        Find M nearest UAV's
        Update Personal best
        Update Global best
        Assign UAV's to the nearest detected targets
    end for
    if UAV has to drop payload then
        if Payload available then
            Calculate velocity vector to go to Drop Location
            if Distance from drop location < Drop_distance then
                Drop payload
            end if
        end if
    else
        Calculate Final velocity
    end if
    Limit Final velocity
end while
```

I. Net Equivalent Velocity

The vectoral sum of Eq. 2 to Eq.9 can be calculated to find the final velocity of each UAV *i* as follows:

$$v_{i,final}^{t+1} = \begin{cases} v_I^{t+1} + v_P^{t+1} + v_G^{t+1} + v_C^{t+1} + v_{end}^{t+1}, state \neq 0 \\ v_{drop}^{t+1} + v_C^{t+1} \quad , state = 0 \end{cases} \quad (8)$$

On top of this superposition, we introduce the maximum and minimum velocity cut-offs which keep the direction of the desired vector but limit its magnitude between the desired values. The final equation thus can be represented as:

$$v = \frac{v}{|v|} * \min(max(v_{min}, |v|), v_{max}) \quad (9)$$

IV. Simulation and Testing

In this section, we first describe our method of simulations. Then, we quantitatively compare the effects of different inertial functions with varying FOV. Lastly, we demonstrate the effectiveness of MTPSO by comparing them with other methods in various simulated scenarios.

A. Simulation Environment

We use Ardupilot's Simulation in the Loop (SITL) software for all the simulations. The targets were generated using a random function in the defined search area. These targets were then plotted on the SITL map module by using a separate custom made Mavlink module. Each UAV while in the search area, scans the area around it using a search function in the range of its Field of View. The SITL simulator uses GPS coordinates for localization and thus a conversion from GPS to UTM coordinates was performed for linearization of calculations. See Figure 4 in Appendix.

B. Quantitative Comparison with Various Hyperparameters

Since inertial functions can drastically alter the performance of the algorithm, 5 inertial functions were carefully chosen to test their convergence properties, advantages and disadvantages. These experiments were coupled with varying the FOV of the camera module. FOV values taken for the experiment were chosen by keeping in mind the minimum overlapping criteria (O_{min}).

Two types of objectives were kept in mind for the experiments. First, to identify the best inertial function which can provide a good balance between exploration and exploitation when the number of targets equals the number of UAVs. Second, to observe the performance of the algorithm with increasing FOV.

The results of experiments are summarized in Table II. data recorded clearly shows that increasing the FOV increases the exploration as most of the search area is completely scanned, this provides better results in the total number of detected targets but also increases the total time taken to completely scan the environment.

C. Quantitative Comparison with Other Approaches

We compare our method with the basic Exhaustive Search Approach and Probability Graph approach on various scenarios. Table III summarizes the values of hyper-parameters used in simulation tests for MTPSO.

TABLE II. Performance Metrics Evaluated for Different Inertial Functions with Different FOV's

Metrics	Method	FOV (in meters)			
		55x32	70x40	91x52	140x80
Targets Detected	Constant*	19	20	20	20
	Random Inertial*	19	20	20	20
	Squared Decreasing*	19	20	20	20
	Sigmoid Increasing*	20	19	20	20
	Chaotic Inertia Weight*	19	20	20	20
Payload Dropped	Constant	18	19	18	20
	Random Inertial	18	17	18	19
	Squared Decreasing	19	17	18	20
	Sigmoid Increasing	17	17	18	18
	Chaotic Inertia Weight	18	17	18	20
Time for mission	Constant	209	206	205	208
	Random Inertial	213	208	211	212
	Squared Decreasing	213	209	211	215
	Sigmoid Increasing	202	200	200	200
	Chaotic Inertia Weight	225	230	231	230

Authorized licensed use limited to: DELHI TECHNICAL UNIV. Downloaded on March 27,2021 at 05:23:44 UTC from IEEE Xplore. Restrictions apply.

Total area scanned	Constant	95.46	98.03	98.82	98.91
	Random Inertial	95.68	98.01	98.78	98.86
	Squared Decreasing	95.15	97.84	98.70	98.80
	Sigmoid Increasing	95.51	97.58	98.53	98.64
	Chaotic Inertia Weight	95.22	97.74	98.50	98.56

*Details of the mentioned inertial functions are given in Table V

TABLE III. HYPERPARAMETERS USED FOR SIMULATION

Hyperparameter	Value
R1	Rand (0,1)
R2	Rand (0,1)
C1	0.25
C2	0.25
C3	1
C4	0.3
C5	0.2
D_{safe}	15m
N	20

Hyperparameter	Value
D_{wap}	20m
D_C	500m
D_{max}	2.5*FOV
N_s	5
α	105°
v_{max}	15m/s
v_{min}	0m/s
ω	Squared decreasing

TABLE IV. PERFORMANCE METRICS EVALUATED FOR DIFFERENT APPROACHES WITH DIFFERENT FOV'S

Metrics	Method	FOV			
		55x32	70x40	90x52	140x80
Targets Detected	Exhaustive Search	19	**20**	**20**	**20**
	Probability Graph	**20**	**20**	**20**	**20**
	Our Approach	**20**	**20**	**20**	**20**
Payload Dropped	Exhaustive Search	**18**	17	18	19
	Probability Graph	**18**	18	18	18
	Our Approach	**18**	**19**	**20**	**20**
Time for mission	Exhaustive Search	393	402	401	412
	Probability Graph	288	296	301	278
	Our Approach	**204**	**203**	**200**	**207**
Total area scanned	Exhaustive Search	99.91	99.94	99.98	99.98
	Probability Graph	98.43	98.20	98.73	99.42
	Our Approach	**94.61**	**96.84**	**97.38**	**98.32**

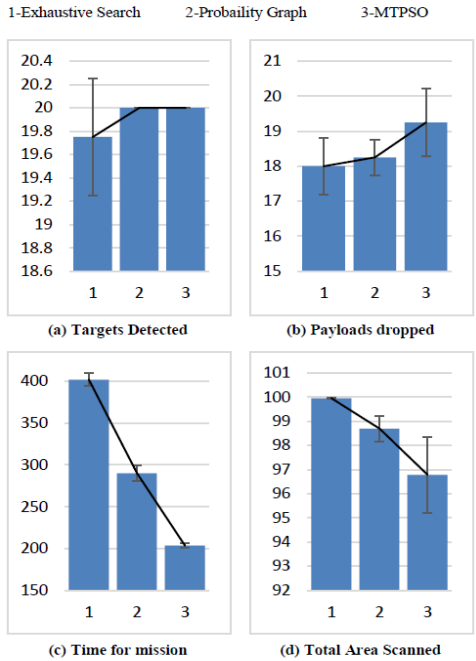

Fig. 3. Performance metrics for MTPSO, exhaustive search approach and probability graph approach

MTPSO offers a significant improvement over the other approaches in terms of response time. The complete mission time is almost half in comparison to Exhaustive Search. The algorithm is able to converge on multiple targets at a much faster rate and correctly identifies the most probable regions. It scans the least area in comparison to other approaches which is a direct consequence of discarding regions with low target probability. The computational power required for MTPSO is much less than the probability graph approach and it is easily implementable in a decentralized form on very light hardware platforms. Simulation videos can be found at link given in Reference [16].

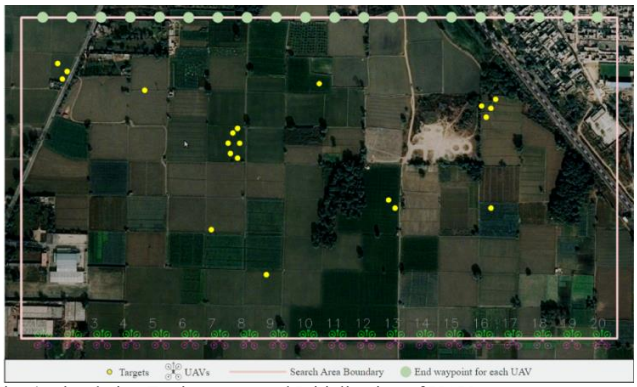

Fig. 4. Simulation Environment and Initialization of UAVs

Fig. 5. Convergence of UAVs on targets in search area pt. 1

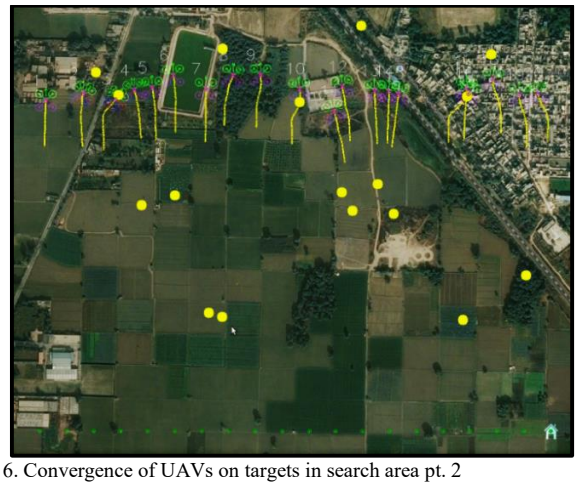

Fig. 6. Convergence of UAVs on targets in search area pt. 2

Authorized licensed use limited to: DELHI TECHNICAL UNIV. Downloaded on March 27,2021 at 05:23:44 UTC from IEEE Xplore. Restrictions apply.

TABLE V. Different Inertial Functions Used for Testing

Function	Mathematical Form	Advantage
Constant Function	$\omega = 0.7$	1. Facilitates Global search and Manual control over the exploration-exploitation criteria
Random Inertial Weight	$\omega = 0.5 + \frac{Rand(\ )}{2}$	1. Continuously exploits the data, ideal for situations with large numbers of targets.
Squared Decreasing	$\omega = w_{max} - \left(w_{max} - w_{min} \right) \cdot \left(\frac{iteration}{iteration_{max}} \right)^2$	1. High exploration in the beginning which gradually decreases over time. 2. Ideal for moderate number of targets
Sigmoid Increasing	$\omega = \frac{\left(w_{start} - w_{end} \right)}{\left(1 + e^{10(\log(gen) - 2) \cdot (k - n \cdot gen)} \right)} + w_{end}$	1. High exploration till no targets are found, exploration decreased when targets appear. 2. Ideal for small number of targets.
Chaotic Inertia Weight	$z = 4 \cdot z(1 - z)$ $\omega = \left(w_{start} - w_{end} \right) \cdot \frac{iteration_{max} - iteration}{iteration_{max}} + w_{end} \cdot z$	1. High exploitation when targets are found. Results in faster convergence to targets. 2. Ideal in cases where immediate response is required.

V. CONCLUSION

Through this paper, we address the problem of multi-target search in an unknown environment and optimized payload delivery for rapid response scenarios. Our decentralized PSO based controller and complete system architecture* allows a single operator on the Ground Control Station to control and monitor the entire swarm. It offers two major advantages which results in better performance over traditional approaches.

First, it provides rapid response to the detected targets and can be very useful in Disaster-Relief scenarios where human lives are at stake. Second, the UAVs follow a defined structure and aim to find target clusters which increases the intensity of regional searching.

The algorithm is tested in several experiments in various simulated scenarios with varying hyperparameters where it performs with high efficiency. Our future work aims to further improve the algorithm and study the effects of varying the value of FFOV over time. Further, we also want to investigate the efficiency of the same approach in multi-target tracking.

REFERENCES

[1] Cabreira, T.M.; Brisolara, L.B.; Ferreira Jr., P.R. Survey on Coverage Path Planning with Unmanned Aerial Vehicles. Drones 2019, 3, 4.

[2] L. Bertuccelli and J. How, “Robust UAV search for environments with imprecise probability maps,” in Proc. IEEE Conf. Decision Control, Dec. 2005, pp. 5680–5685.

[3] Y. Yang, A. Minai, and M. Polycarpou, “Decentralized cooperative search by networked UAVs in an uncertain environment,” in Proc. Amer. Control Conf., Jun.–Jul. 2004

[4] J. Hu, L. Xie, K. Lum and J. Xu, "Multiagent Information Fusion and Cooperative Control in Target Search," in IEEE Transactions on Control Systems Technology, vol. 21, no. 4, pp. 1223-1235, July 2013

[5] J. Kennedy and R. Eberhart. Particle swarm optimization. In Proceedings of IEEE International Conference on Neural Networks, pages 1942-1948, IEEE Press, Piscataway, NJ, 1995

[6] Y. Shi and R. Eberhart., “A modified particle swarm optimizer”, In Evolutionary Computation Proceedings, 1998. IEEE World Congress on Computational Intelligence., The 1998 IEEE International Conference on, pages 69–73.

[7] IEEE, 2002. R.C. Eberhart and Y. Shi., “Tracking and optimizing dynamic systems with particle swarms”, In Evolutionary Computation, 2001. Proceedings of the 2001 Congress on, volume 1, pages 94–100.

[8] IEEE, 2002. A.Nikabadi, M.Ebadzadeh , “Particle swarm optimization algorithms with adaptive Inertia Weight : A survey of the state of the art and a Novel method”, IEEE journal of evolutionary computation , 2008

[9] R.F. Malik, T.A. Rahman, S.Z.M. Hashim, and R. Ngah, “New Particle Swarm Optimizer with Sigmoid Increasing Inertia Weight”, International Journal of Computer Science and Security (IJCSS), 1(2):35, 2007.

[10] J. Xin, G. Chen, and Y. Hai., “A Particle Swarm Optimizer with Multistage Linearly-Decreasing Inertia Weight”, In Computational Sciences and Optimization, 2009. CSO 2009. International Joint Conference on, volume 1, pages 505–508. IEEE, 2009.

[11] Y. Feng, G.F. Teng, A.X. Wang, and Y.M. Yao., “Chaotic Inertia Weight in Particle Swarm Optimization”, In Innovative Computing, Information and Control, 2007. ICICIC’07.

[12] I. Bekmezci, O. K. Sahingoz, and Ş. Temel, “Flying AdHoc Networks (FANETs): A survey,” Ad Hoc Networks, vol. 11, no. 3.

[13] Anuj Agrawal, Aniket Gupta, Joyraj Bhowmick, Anurag Singh, Raghava Nallanthighal, “A Novel Controller of Multi-Agent System Navigation and Obstacle Avoidance”, Procedia Computer Science, Volume 171, 2020, Pages 1221-1230

[14] https://www.youtube.com/watch?v=rZYvWocTQGY

Authorized licensed use limited to: DELHI TECHNICAL UNIV. Downloaded on March 27,2021 at 05:23:44 UTC from IEEE Xplore. Restrictions apply.

2021 11th International Conference on Cloud Computing, Data Science & Engineering (Confluence) | 978-1-6654-1451-7/20/$31.00 ©2021 IEEE | DOI: 10.1109/Confluence51648.2021.9377083

A Study on Machine Learning Applied to Software Bug Priority Prediction

Ruchika Malhotra
Department of Computer Science & Engineering,
Delhi Technological University
Delhi, India.
ruchikamalhotra@dtu.ac.in

Ajay Dabas
Department of Computer Science & Engineering,
Delhi Technological University
Delhi, India.
se.dabasajay@gmail.com

Hariharasudhan A S
Department of Computer Science & Engineering,
Delhi Technological University
Delhi, India.
harimailbox99@gmail.com

Manish Pant
Department of Computer Science & Engineering,
Delhi Technological University
Delhi, India.
manishpant99@gmail.com

***Abstract*—Bugs are among the top problems faced by software developers. As the size and complexity of software projects increase so does the number of bugs and their complexity. Bug priority prediction helps software developers focus their efforts on the most critical bugs that affect the core functionality of a software. By automating the process of priority prediction, it is possible to reduce the time spent analyzing new bug reports. In this paper, we extract bug reports from the bug tracking software of six popular open-source projects Hadoop, HBase, HDFS, Mesos, Spark, and MapReduce and apply five machine learning classifiers Multinomial Naive Bayes, Decision Tree, Logistic Regression, Random Forest, AdaBoost to automatically predict bug priority using the title, description, and summary of the bug report. We use tf-idf to extract useful features from the bug reports and employ precision, recall, and F1-score for measuring the performance of the classifiers. A stratified 10-fold cross-validation technique is used for model evaluation and the results are averaged over all 10 folds. We find that machine learning applied to bug priority prediction provides excellent results and can be used to significantly reduce the time involved in the bug prioritization process. From our experiments, we observe that no single classifier consistently performs best on all priority levels and metrics across all datasets. However, trends from results show that Multinomial Naive Bayes gives well balanced performance and is also fast to train and test. Logistic Regression and AdaBoost also performed well and are potential alternatives.**

Keywords—Bug Priority Prediction, Mining Bug Repository, Text Classification, Machine Learning, Software Maintenance

I. Introduction

Software systems have grown complicated over the years with each software project spanning millions of Lines of Code (LOC) at times [1-3]. For popular software systems, the number of daily submitted bug reports is high. As the size of projects increase, we also see an increase in reported bugs due in part to the increase in complexity and distributed, collaborative nature of programming. Companies grapple with handling all these bug reports as the available manpower is limited. One way to deal with this problem is to deal with the important bugs at first and then move on to the not so necessary bug fixes or optional improvements. However, assigning priority to these incoming bugs manually is a time-consuming task. It can be automated by implementing a bug priority system that assigns a priority to each bug so that it can be resolved accordingly.

The present way of assigning priorities to a bug report is to manually assign it by a developer who is very familiar with the project. This is time, and effort consuming and robs valuable time from the developer. Automating this process has been tried by much past work [4-10]. By automating the bug priority assigning process, we can also alleviate the individual bias of the developer. The typical priority levels are Blocker, Critical, Major, Minor, and Trivial, ordered in descending order of priorities. Previous work in this field has focused on Eclipse and Firefox datasets. In this paper, we demonstrate bug priority prediction on six new datasets Hadoop, HBase, HDFS, Mesos, Spark, and MapReduce [11-16], collected from the bug tracking system JIRA. We apply five different machine learning techniques, namely Multinomial Naive Bayes, Decision Tree, Logistic Regression, Random Forest, AdaBoost to predict bug priority and compare their performance.

II. Related Work

Bug priority prediction is usually treated as a classification problem with the labels being the priority of the bug. Various studies have tried automatically assigning priority to bugs and some have tried machine learning methods to the problem as well. A significant contribution to the problem of automated bug priority prediction is from Yuan Tian et al.'s 'Automated prediction of bug report priority using multi-factor analysis' [4] which introduced the DRONE framework. DRONE used different properties of bug reports like temporal, textual, author, related-report, severity, and product information in order to predict bug priority. Like most papers in the area of automated bug priority prediction, DRONE used the Eclipse dataset which is highly imbalanced. The performance measure used in DRONE is F-Measure which is an appropriate metric for judging models on imbalanced datasets. Qasim Umer et al. [17] build upon DRONE and improve its performance by assigning an emotion value to each bug report based on emotion words presented in the bug report description. Our work introduces 6 new datasets that enable us to judge the generalization ability of our techniques. We also use the same F-Measure along with precision and recall as metrics because the datasets used in our paper are also imbalanced. It also makes our results comparable with previous work in the field.

Authorized licensed use limited to: DELHI TECHNICAL UNIV. Downloaded on March 27,2021 at 05:39:52 UTC from IEEE Xplore. Restrictions apply.

Uddin et al. [33] conducted a survey on automated bug prioritization using articles from the year 2000 to 2015. Their results showed that researchers mostly treated it as a classification problem and used techniques like Naive Bayes, Support Vector Machine, k-Nearest Neighbors, Decision Trees, Random Forest, etc. for classification. The top three commonly used evaluation metrics were Precision, Recall, and F-Measure, and the Eclipse and Mozilla datasets were found to be heavily used in previous studies. In our study, we also formulated bug priority prediction as a classification problem and employed the popular metrics and classifiers as mentioned in their study.

Wei Zhang et al. [5] treated priority prediction as a regression task and argued that the priority levels are ordered and the ordinal knowledge will be lost in a classification setting. Their dataset consisted of a total of 82,299 bugs from a software project, covering reports from 2004 to 2017. They extracted features from bug reports using topic modeling and trained a Deep Neural Network (DNN) to predict the priority of a bug. The study used Mean Absolute Error (MAE) between predictions and ground truth priorities to measure performance as they explain that MAE may be more aligned with the human viewpoint. They also used Precision, Recall, and F-Measure metrics to be more comparable with the previous studies and showed that their approach was effective in bug priority prediction.

Another closely related problem is that of bug triaging, which deals with assigning bugs to the relevant developer. Prior work in this field used bug reports, bug priority, severity, developer experience, etc to try and automate bug triaging. Plenty of past studies have dealt with this topic [19-26]. Automating both the task of bug triaging and bug priority prediction is of much use to the software developer community.

III. Proposed Approach and Experimental Design

A. Independent and Dependent Variables

Since the purpose here is to predict or assign a priority to a bug report, priority is the dependent variable in our experiment, also called the target variable. To predict the target variable, we select a set of features that are the contents of the bug report. We take the title of the report, its description, and the summary of the report as our features set. These are called independent variables in our experiment. We do not consider any other information such as the author of the bug report, project information, version, time, comments, etc. in this study.

B. Dataset Collection

For the sake of reproducibility and ease of access, we selected 6 popular open-source projects and collected bug reports from the issue and project tracking software JIRA [11-16]. We automated the extraction and storage of reports from JIRA using Python. Summary statistics of the collected reports from all projects are given in Table 1.

TABLE I. Summary Statistics of Bug Reports

Project Name	# bug reports
Hadoop	17,268
HBase	25,051
HDFS	15,445
Mesos	10,160
Spark	32,735
MapReduce	7,302

C. Dataset Preprocessing

The extracted raw reports need to be processed before they can be used in further steps of feature extraction and modelling. The raw reports are stored in the XML data format. Firstly, we extract the title, description, summary, and priority from all the reports. All 4 fields are of type string. We skip all the reports where priority is not given. Null values in the description and summary are filled with empty strings. A new column "reports" is created by concatenating title, description, and summary. We clean the reports by removing HTML tags, hex code, links, special characters, converting all text to lowercase. Stop words and punctuations are removed from the reports as they appear frequently and do not provide any useful information. Tokenization is the step of breaking up the text document into a sequence of words. We perform it with the help of Stanford's NLTK package [27]. The datasets in original form were pretty imbalanced with one priority level - "Major" being assigned to more than half of the reports in the dataset. Imbalanced datasets introduce bias in the models trained which leads to poor performance. [31] Some of the ways to solve this include oversampling and undersampling. To implement undersampling, we deleted some reports randomly making the target distribution balanced. The same sequence of steps is performed for each dataset independently.

D. Feature Extraction

Machine learning cannot work with text data directly. We need to encode it into some feature vectors of numbers. Two of the popular approaches to extract features from text data are Bag of Words (BOW) and Term frequency-inverse document frequency (tf-idf) [28]. The common issue with BOW is that commonly occurring but less important words will have very high counts and some less occurring but more important, for example, FileNotFoundException, RuntimeException, etc. words that are highly correlated to priority, will have low counts. tf-idf is robust to this effect and focuses on words that are frequent in documents but not across all documents. It is a quite popular option and we also chose tf-idf for our experiments. Previous studies [17, 29, 30] also used tf-idf in their experiments. When building the vocabulary using tf-idf, we ignored the terms that had a document frequency lower than 5. We also used unigrams and bigrams while building vocabulary. We experimented with different values of document frequency threshold and n-grams and found these to be working well.

E. Performance Measures

To evaluate the effectiveness of different machine learning classifiers, we chose the commonly used classification metrics - precision, recall, and f-measure. Accuracy was not chosen because of its poor performance on class imbalanced problems. A simple classifier predicting the majority class at all times would score the same accuracy percentage as the percentage of the majority class in the dataset. We also used the average of these metrics, weighted by the number of true instances for each label, or also called support.

Authorized licensed use limited to: DELHI TECHNICAL UNIV. Downloaded on March 27,2021 at 05:39:52 UTC from IEEE Xplore. Restrictions apply.

F. Training and Evaluation

We chose 5 of the popular machine learning classifiers from the Scikit-learn[18] library, namely Multinomial Naive Bayes, Decision Tree Classifier, Logistic Regression, Random Forest Classifier (bagging technique), and AdaBoost Classifier (boosting technique) for our experiments as they perform well in text classification tasks [32]. To evaluate our classifiers, we selected a k-fold cross-validation technique. The value of k was taken as 10, making it a 10-fold cross-validation procedure where each time we split the dataset into 10 sets or folds and hold out 1 set as test data and the remaining 9 sets as the training data. A rigorous cross-validation strategy gives us the confidence that the models are not overfitted and generalize well over unseen data. We also used stratification in k-fold instead of random sampling to make the class distribution - all 5 priority labels, similar in train and test data. It helped us to reduce the issues caused due to imbalance and worked well for all classifiers. We averaged the scores (precision, recall, f-measure, and weighted average) over all 10-folds and used them for evaluation.

IV. Results and Discussions

We obtained the results of running 5 different machine learning classifiers on 6 bug reports datasets and compiled them in Tables 2-7. Each table corresponds to a single dataset and contains scores achieved by each classifier on that dataset. The different classifiers are listed in the first column of each table. The reported scores are - precision, recall, and f-measure, for each priority level and also a weighted average is provided. The columns after the classifiers column of the table represent priority levels and at last is the weighted average column where we report the average of the metrics (precision, recall, and f-measure), weighted by support. The results for each dataset are averaged over stratified 10-folds cross-validation scores for each classifier.

The results tables may be read in the following manner - we select the priority level or weighted average, fix the evaluation metric (Precision, Recall, or F1-score), and then compare the values obtained by different classifiers. For instance, in Table 2, we can select the Major priority level and F1-score metric to compare and see that Multinomial Naive Bayes performs best among all classifiers. Similarly, for the weighted average and F1-score metric in Table 2, we notice that Logistic Regression outperforms other classifiers.

TABLE II. 10-fold Cross-validation Scores on Hadoop

		Blocker	Critical	Major	Minor	Trivial	Average
Logistic Regression	**Precision**	0	0	0.631	0.519	0.05	0.444
	Recall	0	0	0.731	0.69	0.002	0.545
	F1-score	0	0	0.653	0.568	0.003	0.47
Random Forest	**Precision**	0	0	0.625	0.503	0	0.432
	Recall	0	0	0.681	0.71	0	0.532
	F1-score	0	0	0.626	0.567	0	0.457
Decision Tree	**Precision**	0.131	0	0.596	0.446	0.292	0.432
	Recall	0.035	0	0.434	0.77	0.035	0.913
	F1-score	0.054	0	0.486	0.558	0.059	0.41
Multinomial NB	**Precision**	0.272	0	0.63	0.515	0	0.468
	Recall	0.013	0	0.742	0.676	0	0.54
	F1-score	0.023	0	0.654	0.553	0	0.46
AdaBoost	**Precision**	0.323	0.158	0.581	0.432	0.37	0.457
	Recall	0.045	0.028	0.454	0.723	0.107	0.459
	F1-score	0.077	0.047	0.49	0.535	0.161	0.411

TABLE III. 10-fold Cross-validation Scores on HBase

		Blocker	Critical	Major	Minor	Trivial	Average
Logistic Regression	**Precision**	0	0.438	0.517	0.481	0.3	0.442
	Recall	0	0.023	0.674	0.656	0.003	0.484
	F1-score	0	0.04	0.571	0.543	0.006	0.413
Random Forest	**Precision**	0	0.325	0.483	0.439	0	0.375
	Recall	0	0.014	0.511	0.721	0	0.451
	F1-score	0	0.028	0.491	0.544	0	0.381
Decision Tree	**Precision**	0.131	0	0.596	0.446	0.292	0.432

Authorized licensed use limited to: DELHI TECHNICAL UNIV. Downloaded on March 27,2021 at 05:39:52 UTC from IEEE Xplore. Restrictions apply.

	Recall	0.035	0	0.434	0.77	0.035	0.463
	F1-score	0.054	0	0.486	0.558	0.059	0.408
Multinomial NB	**Precision**	0.2	0.378	0.528	0.475	0.025	0.426
	Recall	0.002	0.038	0.654	0.663	0.001	0.485
	F1-score	0.004	0.065	0.571	0.543	0.002	0.413
AdaBoost	**Precision**	0.364	0.304	0.43	0.423	0.337	0.4
	Recall	0.094	0.051	0.422	0.674	0.081	0.418
	F1-score	0.144	0.088	0.426	0.518	0.131	0.38

TABLE IV. 10-FOLD CROSS-VALIDATION SCORES ON HDFS

		Blocker	**Critical**	**Major**	**Minor**	**Trivial**	**Average**
Logistic Regression	**Precision**	0	0	0.549	0.525	0.317	0.441
	Recall	0	0	0.681	0.665	0.01	0.527
	F1-score	0	0	0.599	0.577	0.02	0.46
Random Forest	**Precision**	0	0	0.501	0.513	0	0.398
	Recall	0	0	0.752	0.525	0	0.5
	F1-score	0	0	0.598	0.511	0	0.43
Decision Tree	**Precision**	0.114	0.19	0.445	0.47	0.394	0.407
	Recall	0.028	0.034	0.813	0.284	0.076	0.442
	F1-score	0.044	0.082	0.575	0.348	0.126	0.38
Multinomial NB	**Precision**	0	0.3	0.555	0.523	0.05	0.45
	Recall	0	0.006	0.697	0.655	0.002	0.529
	F1-score	0	0.009	0.609	0.572	0.004	0.46
AdaBoost	**Precision**	0.205	0.276	0.465	0.479	0.356	0.424
	Recall	0.046	0.064	0.694	0.421	0.16	0.458
	F1-score	0.076	0.097	0.557	0.445	0.214	0.42

TABLE V. 10-FOLD CROSS-VALIDATION SCORES ON MESOS

		Blocker	**Critical**	**Major**	**Minor**	**Trivial**	**Average**
Logistic Regression	**Precision**	0.2	0.2	0.546	0.484	0	0.425
	Recall	0.007	0.006	0.68	0.677	0	0.505
	F1-score	0.013	0.01	0.596	0.557	0	0.43
Random Forest	**Precision**	0.213	0.153	0.594	0.443	0	0.424
	Recall	0.018	0.011	0.52	0.782	0	0.484
	F1-score	0.032	0.019	0.541	0.565	0	0.42
Decision Tree	**Precision**	0.259	0.265	0.567	0.419	0.089	0.428
	Recall	0.123	0.138	0.339	0.769	0.017	0.435
	F1-score	0.163	0.176	0.435	0.542	0.027	0.39
Multinomial NB	**Precision**	0.267	0.25	0.618	0.453	0	0.454
	Recall	0.015	0.011	0.495	0.851	0	0.498
	F1-score	0.029	0.02	0.54	0.59	0	0.42
AdaBoost	**Precision**	0.322	0.261	0.507	0.422	0.185	0.416
	Recall	0.077	0.195	0.551	0.543	0.054	0.436
	F1-score	0.122	0.215	0.506	0.456	0.08	0.4

Authorized licensed use limited to: DELHI TECHNICAL UNIV. Downloaded on March 27,2021 at 05:39:52 UTC from IEEE Xplore. Restrictions apply.

TABLE VI. 10-FOLD CROSS-VALIDATION SCORES ON SPARK

		Blocker	Critical	Major	Minor	Trivial	Average
Logistic Regression	**Precision**	0.1	0	0.438	0.417	0	0.328
	Recall	0.001	0	0.577	0.558	0	0.421
	F1-score	0.002	0	0.49	0.465	0	0.354
Random Forest	**Precision**	0.45	0	0.421	0.421	0	0.321
	Recall	0.01	0	0.735	0.385	0	0.383
	F1-score	0.019	0	0.528	0.387	0	0.313
Decision Tree	**Precision**	0.142	0.156	0.385	0.402	0.243	0.332
	Recall	0.024	0.022	0.82	0.246	0.008	0.382
	F1-score	0.041	0.037	0.523	0.294	0.016	0.299
Multinomial NB	**Precision**	0.401	0.238	0.445	0.42	0	0.375
	Recall	0.012	0.006	0.577	0.565	0	0.426
	F1-score	0.024	0.01	0.489	0.468	0	0.359
AdaBoost	**Precision**	0.091	0.125	0.4	0.419	0.125	0.335
	Recall	0.018	0.009	0.821	0.239	0.015	0.398
	F1-score	0.027	0.015	0.535	0.293	0.026	0.314

TABLE VII. 10-FOLD CROSS-VALIDATION SCORES ON MAPREDUCE

		Blocker	Critical	Major	Minor	Trivial	Average
Logistic Regression	**Precision**	0.422	0	0.519	0.408	0	0.39
	Recall	0.036	0	0.859	0.448	0	0.481
	F1-score	0.063	0	0.647	0.418	0	0.392
Random Forest	**Precision**	0.223	0.312	0.481	0.386	0	0.379
	Recall	0.038	0.053	0.967	0.236	0	0.46
	F1-score	0.062	0.093	0.641	0.286	0	0.355
Decision Tree	**Precision**	0.248	0.233	0.487	0.374	0.224	0.379
	Recall	0.16	0.09	0.853	0.219	0.046	0.434
	F1-score	0.188	0.121	0.621	0.275	0.073	0.368
Multinomial NB	**Precision**	0.397	0.4213	0.526	0.419	0	0.437
	Recall	0.088	0.042	0.863	0.429	0	0.486
	F1-score	0.188	0.121	0.621	0.275	0	0.368
AdaBoost	**Precision**	0.297	0.326	0.509	0.345	0.286	0.397
	Recall	0.135	0.15	0.769	0.299	0.116	0.433
	F1-score	0.174	0.191	0.609	0.317	0.164	0.389

It can be observed from results that Logistic Regression and Multinomial Naive Bayes consistently outperforms other classifiers on weighted average of Precision, Recall, and F1-score. However, Logistic Regression does not perform well on "Blocker" and "Critical" priority levels which are generally considered as high priority. AdaBoost on the other hand performs better than other classifiers on "Blocker" and "Critical" levels. The classifiers that also perform well on these two priority levels are Multinomial Naive Bayes and Decision Trees. Random Forest performs badly for "Blocker", "Critical", and "Trivial" levels, as evident from precision, recall, and F1-score.

Among all classifiers, the Multinomial Naive Bayes classifier was the fastest to train and test on all datasets and it also achieves good metric scores. We find that the Multinomial Naive Bayes and Logistic Regression classifier performs best on weighted average scores. AdaBoost and Multinomial Naive Bayes give well balanced performance on all classes and are not just focused on some specific priority level. There's no single classifier that consistently performs best on all priority levels and metrics across all the datasets. However, from the general trends observed from experiment results, it is clear that Multinomial Naive Bayes is a good choice for bug prioritization as it gives well

Authorized licensed use limited to: DELHI TECHNICAL UNIV. Downloaded on March 27,2021 at 05:39:52 UTC from IEEE Xplore. Restrictions apply.

adjusted performance on all priority levels and metrics. It is also fast and easy to train.

V. Conclusion

In order to prioritize bugs, we need the bug priority assignee to be very familiar with the codebase and they end up spending a lot of time assigning priority. To relieve them of this time-consuming work and to avoid individual bias creeping into the process, we propose to automate the bug priority assignment using machine learning methods on bug reports of six open-source datasets. We collected the bug reports of these projects from bug tracking software and preprocessed them for use. Some useful features were extracted from the bug reports and five selected machine learning classifiers were chosen for modelling. Our validation strategy was a stratified 10-fold cross-validation technique and we averaged precision, recall, F1-score, and weighted averaged (weighted by support) over all 10 folds. After finding the experiment results, we conclude that no single classifier is best on all priority levels and metrics across all the datasets and each classifier performs differently. Some of them get better weighted scores while others perform well on individual priority levels. However, Multinomial Naive Bayes was found to be performing well on all priority levels and metrics across all datasets and it was also fast to train and test.

References

[1] E. Ng'ang'a and I. Tonui, "A Survey on Software Sizing for Project Estimation," International Journal of Software Engineering and Knowledge Engineering, vol. 5, p. 56, Jan. 2015.

[2] T. S. S. Angel, N. Snehalatha, S. Amutha, and J. T. M. Dhas, "IMPORTANCE OF SOFTWARE SIZING IN SOFTWARE PROJECT MANAGEMENT: A STUDY," p. 6.

[3] Z. Jiang, P. Naudé, and B. Jiang, "The Effects of Software Size on Development Effort and Software Quality," vol. 1, no. 4, p. 5.

[4] "Automated prediction of bug report priority using multi-factor analysis | SpringerLink." https://link.springer.com/article/10.1007/s10664-014-9331-y (accessed Nov. 09, 2020).

[5] W. Zhang and C. Challis, "Automatic Bug Priority Prediction Using DNN Based Regression," in Advances in Natural Computation, Fuzzy Systems and Knowledge Discovery, Cham, 2020, pp. 333–340, doi: 10.1007/978-3-030-32456-8_36.

[6] A. Lamkanfi, S. Demeyer, Q. D. Soetens, and T. Verdonck, "Comparing Mining Algorithms for Predicting the Severity of a Reported Bug," in 2011 15th European Conference on Software Maintenance and Reengineering, Mar. 2011, pp. 249–258, doi: 10.1109/CSMR.2011.31.

[7] Q. Umer, H. Liu, and Y. Sultan, "Emotion Based Automated Priority Prediction for Bug Reports," IEEE Access, vol. 6, pp. 35743–35752, 2018, doi: 10.1109/ACCESS.2018.2850910.

[8] "Information Retrieval Based Nearest Neighbor Classification for Fine-Grained Bug Severity Prediction - IEEE Conference Publication." https://ieeexplore.ieee.org/document/6385117 (accessed Nov. 09, 2020).

[9] P. A. Choudhary and D. S. Singh, "Neural Network Based Bug Priority Prediction Model using Text Classification Techniques," International Journal of Advanced Research in Computer Science, p. 5, 2017.

[10] A. Lamkanfi, S. Demeyer, E. Giger, and B. Goethals, "Predicting the severity of a reported bug," in 2010 7th IEEE Working Conference on Mining Software Repositories (MSR 2010), May 2010, pp. 1–10, doi: 10.1109/MSR.2010.5463284.

[11] Spark JIRA bug tracker https://issues.apache.org/jira/projects/SPARK/issues (Accessed Nov. 09, 2020).

[12] HBase JIRA bug tracker https://issues.apache.org/jira/projects/HBASE/issues (Accessed Nov. 09, 2020).

[13] HDFS JIRA bug tracker https://issues.apache.org/jira/projects/HDFS/issues (Accessed Nov. 09, 2020).

[14] MapReduce JIRA bug tracker https://issues.apache.org/jira/projects/MAPREDUCE/issues (Accessed Nov. 09, 2020).

[15] Mesos JIRA bug tracker https://issues.apache.org/jira/projects/MESOS/issues (Accessed Nov. 09, 2020).

[16] Hadoop JIRA bug tracker https://issues.apache.org/jira/projects/HADOOP/issues (Accessed Nov. 09, 2020).

[17] Umer, H. Liu, and Y. Sultan, "Emotion Based Automated Priority Prediction for Bug Reports," IEEE Access, vol. 6, pp. 35743–35752, 2018, doi: 10.1109/ACCESS.2018.2850910.

[18] F. Pedregosa et al., "Scikit-learn: Machine Learning in Python," MACHINE LEARNING IN PYTHON, p. 6.

[19] T. S. Gadge and N. Mangrulkar, "Approaches for automated bug triaging: A review," in 2017 International Conference on Innovative Mechanisms for Industry Applications (ICIMIA), Bengaluru, India, Feb. 2017, pp. 158–161, doi: 10.1109/ICIMIA.2017.7975592.

[20] P. Bhattacharya, I. Neamtiu, and C. R. Shelton, "Automated, highly-accurate, bug assignment using machine learning and tossing graphs," Journal of Systems and Software, vol. 85, no. 10, pp. 2275–2292, Oct. 2012, doi: 10.1016/j.jss.2012.04.053.

[21] J. Park, M.-W. Lee, J. Kim, S. Hwang, and S. Kim, "COSTRIAGE: A Cost-Aware Triage Algorithm for Bug Reporting Systems," p. 6.

[22] "Effective Bug Triage – A Framework," Procedia Computer Science, vol. 48, pp. 114–120, Jan. 2015, doi: 10.1016/j.procs.2015.04.159.

[23] M. Alenezi, K. Magel, and S. Banitaan, "Efficient Bug Triaging Using Text Mining," JSW, vol. 8, no. 9, pp. 2185–2190, Sep. 2013, doi: 10.4304/jsw.8.9.2185-2190.

[24] A. Tamrawi, T. T. Nguyen, J. Al-Kofahi, and T. N. Nguyen, "Fuzzy set-based automatic bug triaging: NIER track," in 2011 33rd International Conference on Software Engineering (ICSE), May 2011, pp. 884–887, doi: 10.1145/1985793.1985934.

[25] T. Zhang, G. Yang, B. Lee, and I. Shin, "Role Analysis-based Automatic Bug Triage Algorithm," Information Processing Society of Japan, p. 4.

[26] W. Zou, Y. Hu, J. Xuan, and H. Jiang, "Towards Training Set Reduction for Bug Triage," in 2011 IEEE 35th Annual Computer Software and Applications Conference, Jul. 2011, pp. 576–581, doi: 10.1109/COMPSAC.2011.80.

[27] E. Loper and S. Bird, "NLTK: the Natural Language Toolkit," in Proceedings of the ACL-02 Workshop on Effective tools and methodologies for teaching natural language processing and computational linguistics - Volume 1, USA, Jul. 2002, pp. 63–70, doi: 10.3115/1118108.1118117.

[28] R. Stohler, Document Embedding Models: A Comparison with Bag-of-Words. Zurich: University of Zurich, 2018.

[29] J. Xuan, H. Jiang, Z. Ren, and W. Zou, "Developer prioritization in bug repositories," in 2012 34th International Conference on Software Engineering (ICSE), Jun. 2012, pp. 25–35, doi: 10.1109/ICSE.2012.6227209.

[30] P. Bhattacharya and I. Neamtiu, "Fine-grained incremental learning and multi-feature tossing graphs to improve bug triaging," in 2010 IEEE International Conference on Software Maintenance, Sep. 2010, pp. 1–10, doi: 10.1109/ICSM.2010.5609736.

[31] N. Japkowicz and S. Stephen, "The class imbalance problem: A systematic study," Intell. Data Anal., vol. 6, no. 5, pp. 429–449, Oct. 2002.

[32] K. Kowsari, K. J. Meimandi, M. Heidarysafa, S. Mendu, L. E. Barnes, and D. E. Brown, "Text Classification Algorithms: A Survey," Information, vol. 10, no. 4, p. 150, Apr. 2019, doi: 10.3390/info10040150.

[33] J. Uddin, R. Ghazali, M. M. Deris, R. Naseem, and H. Shah, "A survey on bug prioritization," Artif. Intell. Rev., vol. 47, no. 2, pp. 145–180, Feb. 2017, doi: 10.1007/s10462-016-9478-6.

Authorized licensed use limited to: DELHI TECHNICAL UNIV. Downloaded on March 27,2021 at 05:39:52 UTC from IEEE Xplore. Restrictions apply.

EGU21-5033, updated on 06 Apr 2021
https://doi.org/10.5194/egusphere-egu21-5033
EGU General Assembly 2021
© Author(s) 2021. This work is distributed under
the Creative Commons Attribution 4.0 License.

Adaptation to climate change induced water stress in major glacierized mountain regions

Anubha Aggarwal[1], Holger Frey[2], Graham McDowell[2,3], Fabian Drenkhan[2,4], Marcus Nuesser[5], Adina Racoviteanu[6], and Martin Hoelzle[7]

[1]Civil Engineering Department, Delhi Technological University, New Delhi, India (agrawal.anubha@gmail.com)
[2]Department of Geography, University of Zurich, Zurich, Switzerland
[3]Canadian Mountain Assessment, University of Calgary, Calgary, Canada
[4]Department of Civil and Environmental Engineering, Imperial College London, London, United Kingdom
[5]South Asia Institute, Department of Geography, Heidelberg University, Germany
[6]Department of Geography and Earth Sciences, Aberystwyth University, Aberystwyth, UK
[7]Department of Geosciences, University of Fribourg, Fribourg, Switzerland

Mountains are a critical source of water and home to a large proportion of the world's population. Cryospheric and hydrological changes combined with increasing water demand are impacting water availability, livelihoods and cultural values, threatening long-term water security of downstream populations. Here, we present a global systematic review in which 83 peer-reviewed articles were critically evaluated to unravel and assess different types of adaptation measures that have been undertaken to manage water stress. We observe that changes in glacier extent and snowfall amount are the main cryospheric changes motivating adaptations. However, changes in precipitation patterns, such as increasing extremes or alterations of the rain-snow line, which lead to both increasing water stress and seasonal flooding or glacier lake outburst floods (GLOFs), and are also observed to be important motivators of adaptive actions. The main sectors affected by hydrological and cryospheric changes are agriculture, tourism, hydropower generation and health and safety. To reduce risks of water scarcity and water-related disasters, and to enhance the resilience of human and natural systems, a broad set of adaptation measures have been implemented in the world's mountain regions. Such adaptations include crop diversification, new irrigation practices, dams and water storage infrastructure, training programs and the establishment of Early Warning Systems, artificial snow making, shifts to non-snow-based tourism, and changes to cultural practices. We find that globally the most commonly used adaptation practices correspond to the improvement of water storage infrastructure, agricultural and irrigation practices, economic diversification and water governance and laws. However, our systematic review reveals these and other adaptation actions have strong regional variation. For example, adaptation in the agricultural sector is most prevalent in Africa, Asia and South America; while in Europe, Australia and New Zealand responses in the tourism sector are more common. Socio-ecological trade-offs associated with adaptations are often reported. For example, the promotion of snow-making reduces socio-economic vulnerability but adds pressure on water resources and environment.

However, successful implementation of adaptation measures are limited by a diverse set of factors. This includes reduced capacities and resources in infrastructure maintenance, mismanagement, conflicts and mistrust in government together with lack of funding and insufficient collaboration between stakeholders as well as delayed implementation of laws and mountain development programs. Moreover, extreme events and climate change impacts together with discontinuities and errors in climate data need to be considered. In order to address or overcome these limitations, it is important to raise awareness of local communities about climate change and to demonstrate the positive effects of adaptation measures and environmental laws; increase funding for mountain programs and motivate combined activities of governments and stakeholders to build their trust on each other.

ADAPTIVE MPPT ALGORITHM FOR SPV SYSTEM UNDER PARTIAL SHADING CONDITION

Pallavi Verma[a], Rachana Garg[b], Priya Mahajan[c]
[a,b,c] Electrical Engingeering Department,
Delhi Technological University, New Delhi

ABSTRACT

Partial Shading in Photovoltaic (PV) is a situation which has negative effect on the PV array output. It results in multiple peaks in non-linear Power Voltage (P-V) characteristic with only one peak having the maximum power i.e. Global Maximum Power Point (GMPP). Thus, an efficient controller needs to be implemented with fast tracking efficiency to track GMPP. In the present paper, Adaptive Neuro-Fuzzy Inference System (ANFIS) is designed, developed and validated for a solar PV system to detect maximum power under standard test condition (STC) and partial shading condition (PSC). Comparative analysis of ANFIS and Perturb & Observe (P&O) maximum power tracking algorithm is presented to establish the superiority of the ANFIS algorithm.

Keywords: Solar Photovoltaic system, Control algorithms (P&O and ANFIS), DC-DC Boost Converter

1. Introduction

Energy is required at every step of life and due to depletion of fossil fuels this demand is not fulfilled by conventional power generation system. To overcome this major concern, renewable resources such as solar, hydro, wind, hydrogen fuel cell, bio-gas etc. has taken the wide area of emerging technology. Also, renewable resources are abundant in nature, green and requires less maintenance. Amongst all, Solar PV cell has gained widespread acceptance [1,2]. Sunlight is a huge source of energy that can be converted into utilizable form with the help of solar PV cell.

The PV panel gives optimal output power at uniform shading and output power significantly reduces under non-uniform irradiation, termed as partially shading condition (PSC). PSC can be caused because of dense clouds, shadow of nearby building, tall trees, towers, dust and panel ageing or cracking [3]. Another major concern of shading is that it exhibits multiple peaks in Power-Voltage (P-V) and Current-Voltage (I-V) characteristics of solar PV system [4]. This may in turn accounts for the Maximum Power Point Tracking (MPPT) techniques converging in Local Maximum Power Point (LMPP) instead of GMPP, leading to notable power loss. Mitigating the effect of PSC's is a major practical challenge.

Several conventional MPPT techniques viz. perturb & observation (P&O), incremental conductance (INC), fractional open circuit voltage (FCOV) etc. have been reviewed and addressed in [5,6]. Among all these conventional methods, P&O is most widely used because of its ease of implementation and simplicity. But its reliability is low in PSC because the perturbation process makes the operating point lurch around the maximum power point (MPP), resulting into wastage of power. This challenge can be met by reducing the step size of perturbation, but small

perturbation size delays the MPP tracking [7,8]. Conventional MPPT tracking needs to think out of the box and explore for varying environmental condition.

The INC algorithm has been offered with improved tracking accuracy under steady state and variable environmental conditions. The main compensations provided by INC algorithm over the P&O algorithm have been dissected in [9]. The INC algorithm is founded on the fact that the rise of the PV module power curve is zero at the MPP, positive on the left side and negative on the right position of the MPP. It uses the derivative algorithm to find the MPP. This method takes more computation in the controller because the differentiation process involves a relatively complex decision-making procedure [10]. So, implementing INC algorithm increases the cost and complexity of the system and it may give unsatisfactory results at low insolation level. Shahbaz Tabish et al. [11] developed a MATLAB/Simulink model and validated the performance of system with experimental test bed under partial shading condition. On the other side, direct methods such as P&O, INC, FLC [12-13] based algorithms do not require prior knowledge of P-V characteristics and can track MPP under different weather condition. Ahteshamul Haque [15] developed and implemented a control circuit for MPPT. PSIM simulation software is used for simulation study. A prototype setup was tested under different irradiation levels provided through artificial light setup.

Ishaque et al. [16] presented impressive method based on particle swarm optimization (PSO) algorithm, but it is too complex to be commercially applied as some parameters needs to be set by the user. Karatepe et al. [17] applied artificial neural network (ANN). The problem faced in ANN based algorithm is that it is dependent on available training data under different environmental condition, so the data needs to be revised again when array configuration changes. In [18-20] genetic algorithms such as artificial bee, ant colony, flashing fireflies have been implemented for PV system. Genetic algorithm has better stability, its implementation is a major challenge as it involves complex calculation, equations and some data need to be set by the user.

FLC can incorporate a conventional design as they do not necessitate knowledge of exact model but on the other side FLC is costlier at the time implementation [21]. In [22] authors have compared P&O and intelligent FLC algorithm under partially shading condition for stand-alone PV system and simulation results shows that FLC can track maximum power with better tracking efficiency.

In the present study, authors have optimized the membership function by heuristic approach for ANFIS algorithm. ANFIS algorithm has been implemented as it is simple and easy and does not involve complex mathematical equations and calculations for their implementation. The simulation results of the proposed adaptive algorithm demonstrated their ability to track GMPP, with less fluctuation around MPP and minimum settling time.

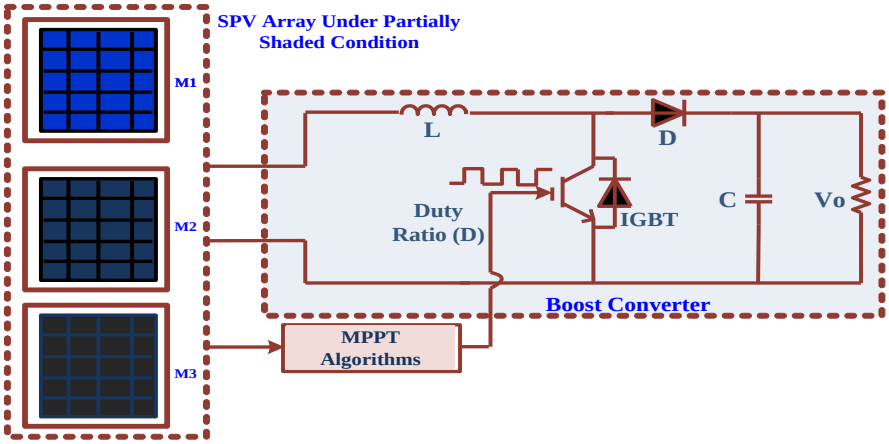

Fig.1 Block Diagram of Stand-alone SPV System under Partially Shaded Condition

Fig.1 presents the SPV system under PSC consists of a PV array source, MPPT algorithm and DC-DC converter (boost). The ANFIS algorithm which is combination of neural network and fuzzy inference system is designed, developed and validated to track the global peak from multiple peaks of P-V curve depicted under partially shaded condition which may not be tracked by conventional MPPT.

1.1 Organization of Paper

Equivalent circuit of SPV module has been discussed and its characteristics has been determined in section 2. Design of DC-DC Boost converter, which is a power interfacing device between source and the load, is discussed in section 3. MPPT algorithms P&O and adaptive neuro-fuzzy inference system for PV module are explained in section 4. In sections 5 and 6 the results and conclusions respectively of the proposed research work has been discussed.

2. Equivalent Circuit of SPV Module

Solar cell works on the principle of Photovoltaic effect. It is an active transducer which converts energy from sunlight (photons) into electricity (current). Voltage produced by solar cell is very small (0.5 to 0.8 V), to get appreciable power from solar PV cell they need to be connected in series. Solar cell connected in series makes PV module and PV module connected in series-parallel, as per power requirement, makes PV array. The ideal equivalent circuit of solar cell incorporates light generated current source with single anti-parallel diode. R_s and R_{sh} are series and shunt resistance of solar cell [23]. Fig.2 presents the equivalent circuit of single diode model used in the proposed system.

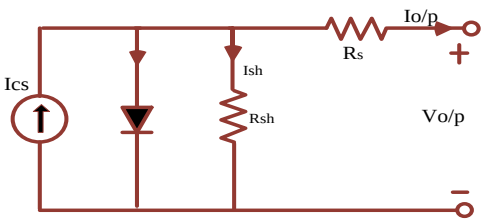

Fig.2 Equivalent circuit PV cell

2.1 Characterization of PV Cell

From the theory of semiconductors, following are mathematical equations between current and voltage relationship of photovoltaic cell.

(i) The output current $I_{o/p}$ of PV cell is given as

$$I_{o/p} = I_{cs} - I_{sat} * \left[exp\left(\frac{q\left(V_{o/p} + I_{o/p} * R_s\right)}{N_s\, AkT_{ac}}\right) - 1\right] \quad (1)$$

where, $I_{o/p}$ is the output current, I_{cs} is the photon current, I_{sat} is the diode saturation current, q is the elementary charge ($1.602*10^{-19}$ C), $V_{o/p}$ is the output voltage, R_s is the series resistance (Ω), N_s is the number of series cell, A is the ideal factor of the cell dependent on PV technology, K is the Boltzmann constant ($1.38*10^{-23}$ J), T_{ac} is the actual operating temperature.

(ii) The photon current I_{cs} directly depends on solar irradiation and very much influenced by temperature, which can be expressed as

$$I_{cs} = I_{scc} + \left(K_i\left(T_{ac} - T_{ref}\right)\right)\frac{I_{ac}}{I_{ref}} \quad (2)$$

where, I_{scc} is the short circuit current of the cell at temperature 25°C and solar insolation 1KW/m^2, Ki is the cell short circuit temperature coefficient , T_{ref} is the reference temperature of the cell, I_{ac} is the actual current of the cell, I_{ref} is the reference temperature of the cell.

(iii) The saturation current of diode I_{sat} varies with cell temperature, which is given by following equation

$$I_{sat} = I_{rs}\left(\frac{T_{ac}}{T_{ref}}\right)^3\left[exp\left(\frac{q* E_g}{Ak}\right) * \left(\frac{1}{T_{ref}}\right) - 1\right] \quad (3)$$

where, I_{rs} is the reverse saturation current of the cell at specified temperature and solar insolation, E_g is the energy band gap of the semiconductor material used in the cell.

(iv) The reverse saturation current I_{rsc} can be expressed as

$$I_{rsc} = \frac{I_{scc}}{\left(exp\left(\frac{q*V_{oc}}{N_s\ AkT_{ac}}\right) - 1\right)} \quad (4)$$

where, V_{oc} is the open circuit voltage of the cell.

In the present work, Sun Power Solar panel X22-360 PV modules is used. Table 1 shows the sun power solar panel specifications used in simulation and modeling of PV array. An array of (3X1) PV modules each of 360W simulated in MATLAB/Simulink. The maximum power obtained by the array is (360*3) 1.08kW.

Table.1 Specification of Sun Power PV Module	
SPR-X22-360	
Power Nominal(Max), P_{NOM}	360W
Rated Voltage, V_M	60.6V
Rated Current, I_M	5.94A
Open-Circuit Voltage, V_{ocv}	69.5V
Short-Circuit Current, I_{scc}	6.48A
Total Cell in Series, N_s	96

Fig.3(a) illustrates the electrical characteristics viz I-V and P-V characteristics of PV module under Standard Test Condition (STC) and partial shading condition. Fig.3(b) depicts the effect of shading on the I-V and P-V characteristics of the given SPV array showing multiple peaks having GMPP with side peaks LMPP.

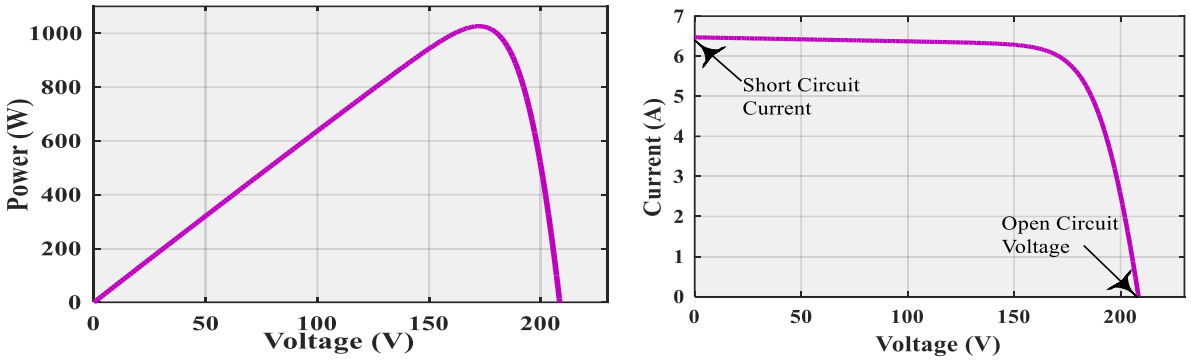

(a)

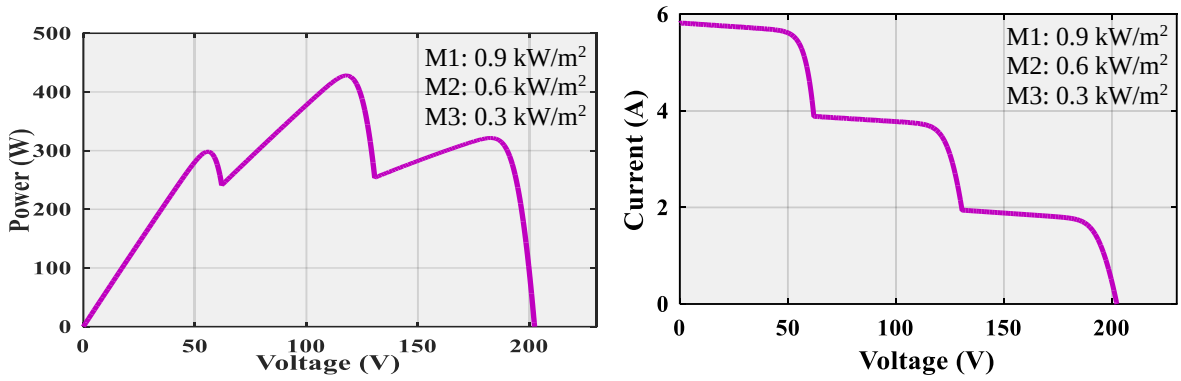

(b)

Fig.3 Power Vs Voltage and Current Vs Voltage curve of SPV system under two conditions
(a) Standard Test Condition (b) Partially Shaded condition.

3. DC-DC Converter

In the present study, boost converter is used as DC-DC converter which is also known as step-up converter (fig.1). The main components of boost converter along with IGBT switch are series inductor and shunt capacitor, which are passive components.
The inductor value (L) for boost converter can be expressed as:

$$L = \frac{V_o\,\alpha}{(\Delta I_1 f_{sw})} \tag{5}$$

Where α is the Duty Ratio and is defined as the ratio of ON time to the total period of the switching device.

$$\alpha = 1\text{-}\left(\frac{V_a}{V_o}\right) \tag{6}$$

The calculated value of α is between 0.5-0.7 and V_a is the average output voltage. ΔI_1 is output ripple current, and it is considered 10% of input current. The value of inductance L, as calculated from equation (6), is 1.1mH.

The value of output capacitor for the DC-DC Boost Converter is given as,

$$C = \frac{I_a\,\alpha}{(\Delta V f_{sw})} \tag{7}$$

Where I_a is the average output current. ΔV is the peak ripple voltage and the value of ΔV is taken 3% of output voltage. The value of capacitance calculated from equation (7) is 500μF.

4. Maximum Power Point Tracking Techniques

As the environmental conditions are ambiguous, so input voltage to the DC-DC converter by PV array varies and maximum power operating point changes. In order to ensure that during PSC the power tracked by the MPPT is GMPP not LMPP, intelligent MPPT algorithm is employed that can take into account the fluctuations around MPP and long settling time. MPPT finds the MPP and operates at optimal point by regulating the duty ratio of dc-dc converter. These adaptive MPPT algorithms are presented below.

4.1 Perturb & Observe Algorithm

The Perturb and Observe Maximum Power Point Algorithm is based on the criterion that on the right of the MPP, if voltage increases, power decreases then in this condition perturbation is made on the opposite direction whereas towards the left of MPP, if increasing the voltage, power also increases then perturbation should be made in same direction. The operation of P&O is given in table 2.

Table 2 The Operation of P&O Algorithm

S.No.	ΔP_{pv}	ΔV_{pv}	V_{pv}(ref.)	Duty Ratio
1.	>0	>0	↑	↓
2.	>0	<0	↓	↑
3.	<0	>0	↓	↑
4.	<0	<0	↑	↓

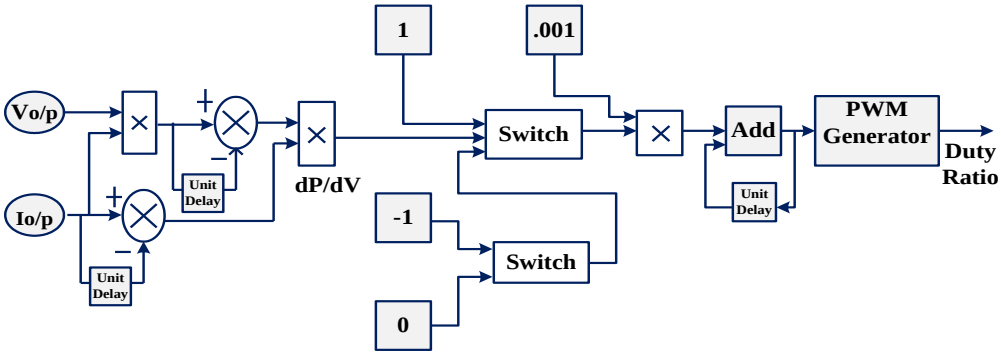

Fig.4 Block Diagram of P&O Algorithm

The main drawback of conventional MPPT algorithms is that they may not track GMPP and has larger settling time. The main drawback of the P&O algorithm is its lack of ability to track maximum power point due to the oscillations near MPP region under varying environmental conditions. To overcome these disadvantages, the membership functions are fine tuned to obtain greater sensitivity in the MPP region utilizing ANFIS algorithm.

4.2 Adaptive Neuro-Fuzzy Inference System (ANFIS)

Adaptive neuro fuzzy inference system (ANFIS) uses both FL and ANN in its process of mapping input and output [24]. ANFIS uses neural network to adjust membership function, its distribution and making fuzzy rules as all these parameters are obtained by heuristic approach. The block diagram of ANFIS MPP tracker for solar PV system is shown fig.5.

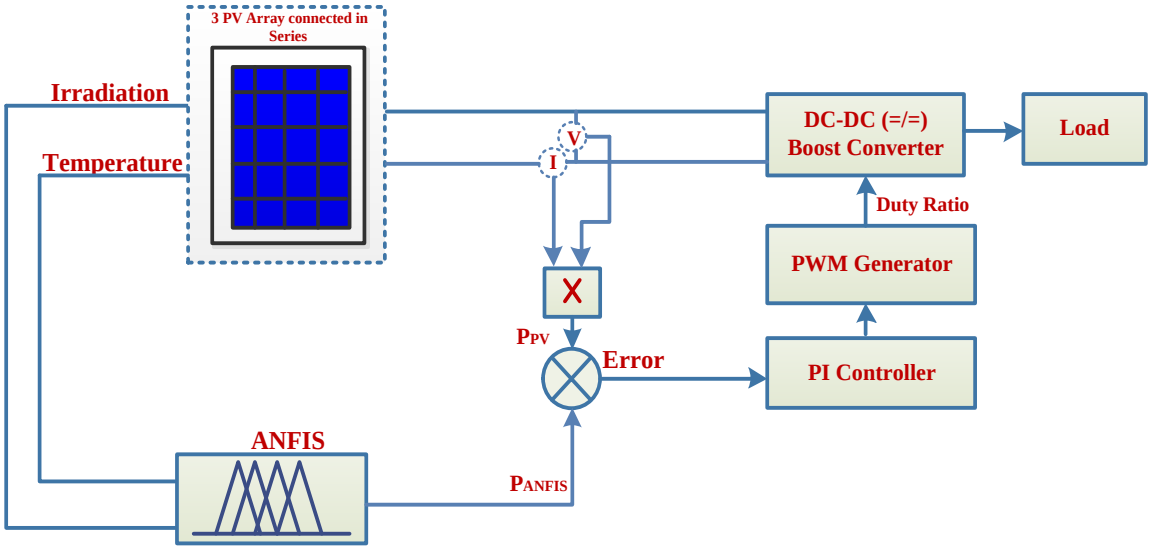

Fig.5 Block Diagram representation of ANFIS MPPT for SPV system under steady state and dynamic condition

Solar irradiation and temperature are used to generate the training data set for the ANFIS tracker. In the present work, to track the MPP in PSC, ANFIS has been implemented for each PV module. The training data set is taken for different environmental condition varied by changing irradiation

as well as temperature. The two inputs are irradiation and temperature and one output power. The actual power and power from trained data set are compared and error is given to the PI controller. The output generated from PI controller is compared with modulating signal having frequency 20 kHz.

4.2.1 ANFIS Tuning

To tune the ANFIS, firstly the training data set is required. To get this training data the MATLAB/Simulink of PV module is operated for solar irradiation variation from 0.1kW/m^2 to 1kW/m^2 at fixed step of 0.05kW/m^2 and similarly temperature is varied from 20°C to 60°C at a step of 5°C. The retrieved training data is saved in workspace of MATLAB. The ANFIS generates fuzzy inference system (FIS) by using loading training input and output data set. The ANFIS uses hybrid optimization technique for training, which is combination of least square type method and back propagation algorithm.

Fig.6 (a) shows training error v/s epoch waveform which has been reduced to approximately 4%. Fig.6 (b) shows the training data and ANFIS output, it is depicted from trained data that ANFIS data matches closely to actual data of PV module.

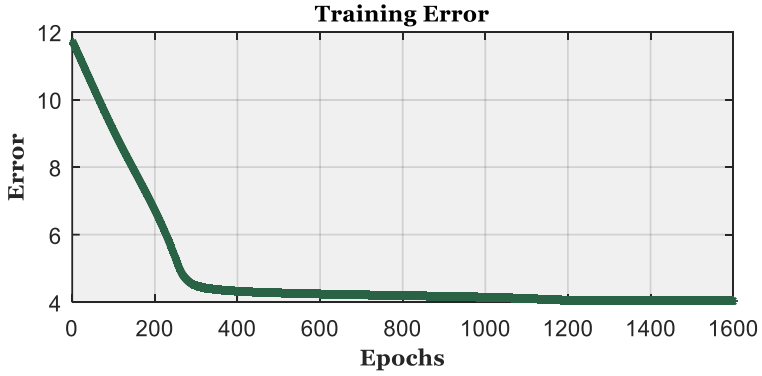

(a)

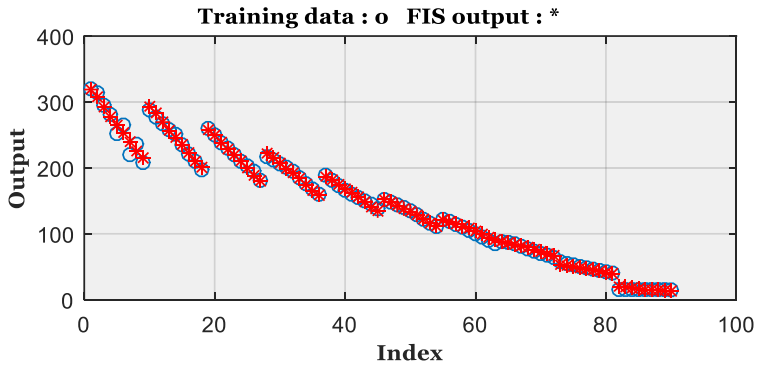

(b)

Fig.6 (a) Training error Vs Epoch waveform for ANFIS (b) Training Data and ANFIS output

Fig.7 shows the surface view generated by ANFIS. Fig.8 represents the structure of ANFIS. Input to ANFIS are irradiation and temperature and output is power. Inputmf, outputmf represents

membership function of input and output. In the present study, the membership function for both inputs learned by ANFIS is shown in fig.9. Nine fuzzy rules have been derived from two inputs each having three membership functions. The developed fuzzy rules derived according to input and output mapping.

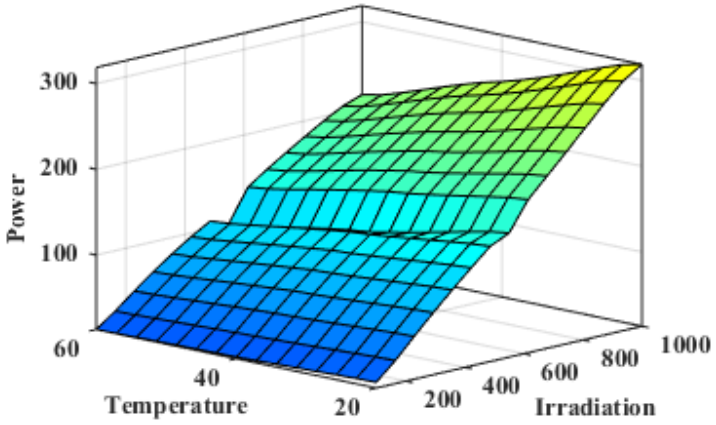

Fig.7 3-D surface view representation between two inputs (irradiation and temperature) and one output (Power) generated by ANFIS of proposed SPV system

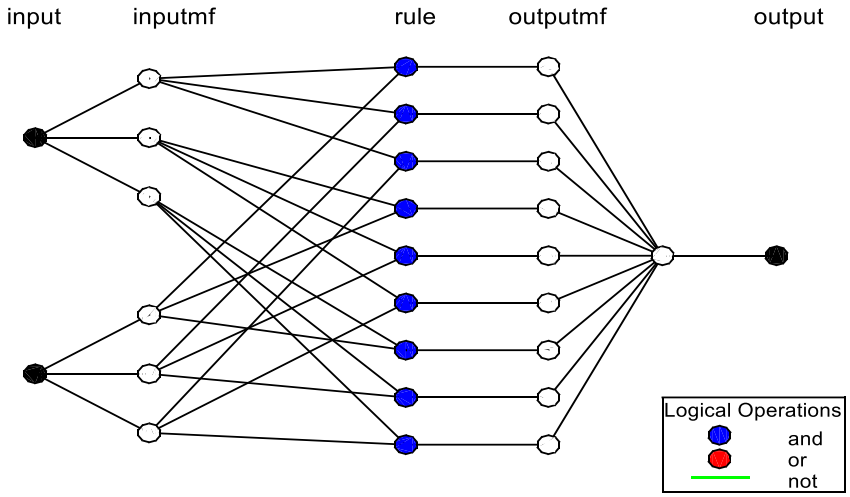

Fig.8 Structure of ANFIS

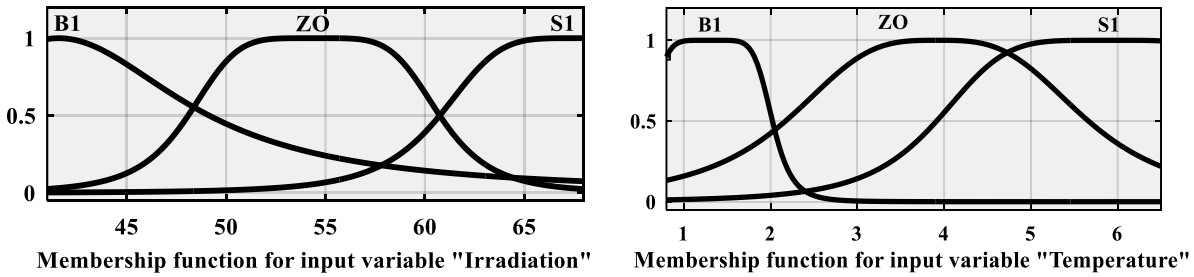

Fig.9 Membership functions for input variables ‘Irradiation’ and ‘Temperature’ after learning in ANFIS

5. Simulation and Results

The MATLAB/Simulink is used to develop SPV system. In the proposed SPV system, ANFIS algorithm has been implemented to trace maximum available power under varying environmental conditions.

The MATLAB/Simulink model for ANFIS algorithm and P&O has been designed, developed and validated under various conditions i.e. (i) STC (ii) PSC (iii) Dynamic condition.

In fig.10 (a) P-V characteristic achieved is at STC i.e. at insolation 1kW/m^2 and temperature 25°C. In fig.10 (b) P-V characteristic is obtained when module M1 given insolation 1kW/m^2, M2 0.9kW/m^2 and M3 0.5kW/m^2 and temperature 25°C.

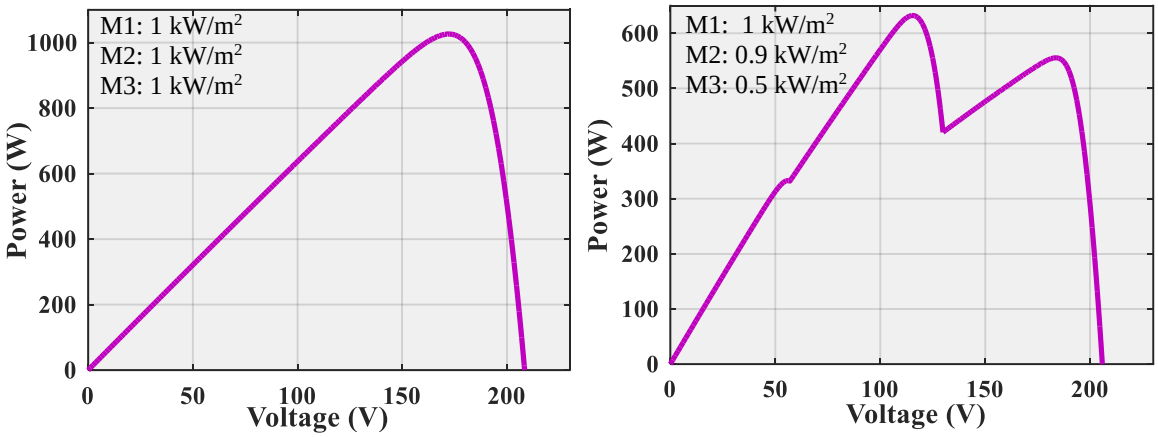

(a) (b)

Fig. 10 (a) PV characteristic achieved at STC (b) PV characteristic at PSC

As seen from fig.9 (b) P-V curve has multiple peaks depicted under partial shading condition, in which 2 lower peaks are LMPP and maximum peak is GMPP. In the present study, adaptive MPPT algorithm have been designed to track GMPP which may not be tracked by conventional MPPT algorithms. Results under STC, steady state condition as well as dynamic condition for both the algorithms i.e. P&O and ANFIS has been presented.

(i) Performance of P&O and ANFIS under STC

Fig.11 shows the power v/s time plot of PV module under uniform shading condition at STC. The power drawn by P&O and ANFIS is 920W and 967.5W with settling time 0.35s and 0.09s respectively.

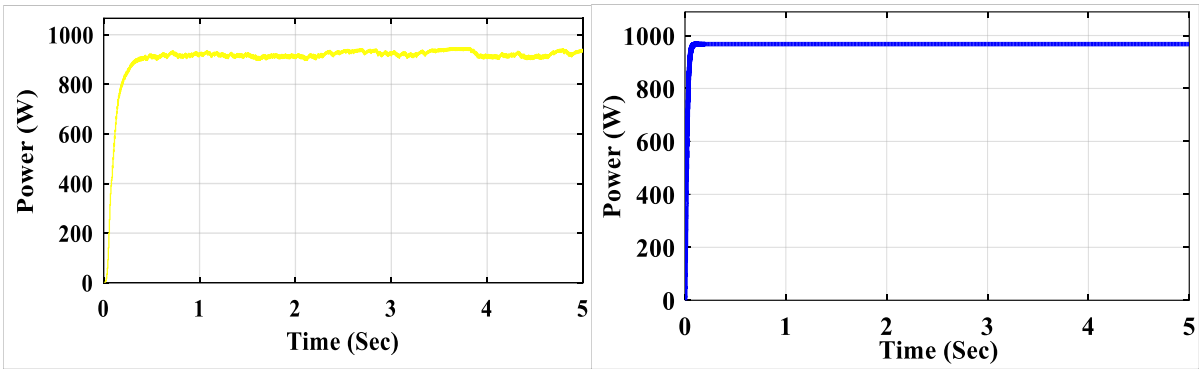

(a) (b)

Fig.11 Power v/s Time plot of (a) P&O and (b) ANFIS algorithm at STC

(ii) Performance of P&O and ANFIS under PSC

Fig.12 shows the power v/s time plot of PV module under partial shading condition. The PV modules have insolation levels as M1:1kW/m^{2,} M2:0.9kW/m^2 and M3:0.5kW/m^2 and temperature 25°C. In this condition the power drawn by P&O and ANFIS is 542 W and 576.6W with settling time 0.4s and 0.02s respectively.

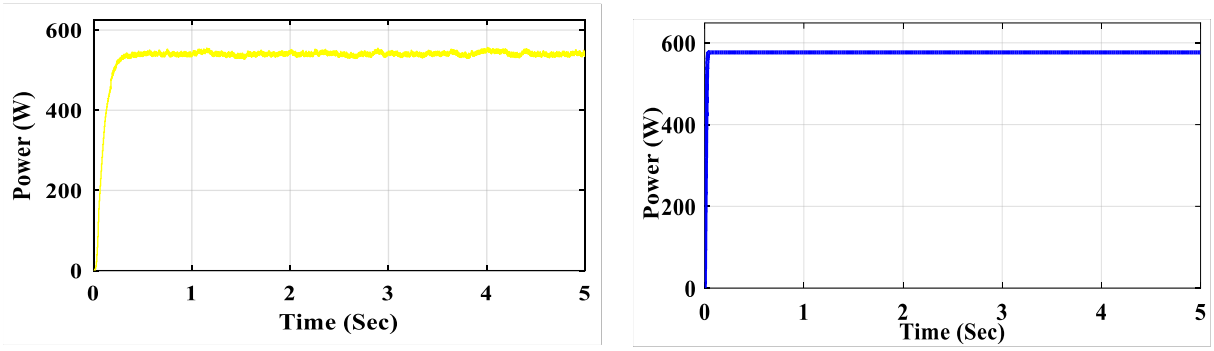

(a) (b)

Fig.12 Power v/s Time plot of (a) P&O and (b) ANFIS algorithm at PSC

(iii) Performance of P&O and ANFIS under Dynamic condition

Dynamic performances of both the MPPT algorithms are tested for rapidly changing irradiation level. Table.3 refers the shading pattern for each module under dynamic condition.

Table. 3 Shading Pattern of each PV Module

Pattern No.	Irradiation Level in W/m^2	Time
SP1	[M1:900, M2:700, M3:500]	0-2Sec
SP2	[M1:700, M2:500, M3:600]	2-4Sec
SP3	[M1:400, M2:300, M3:200]	4-5Sec

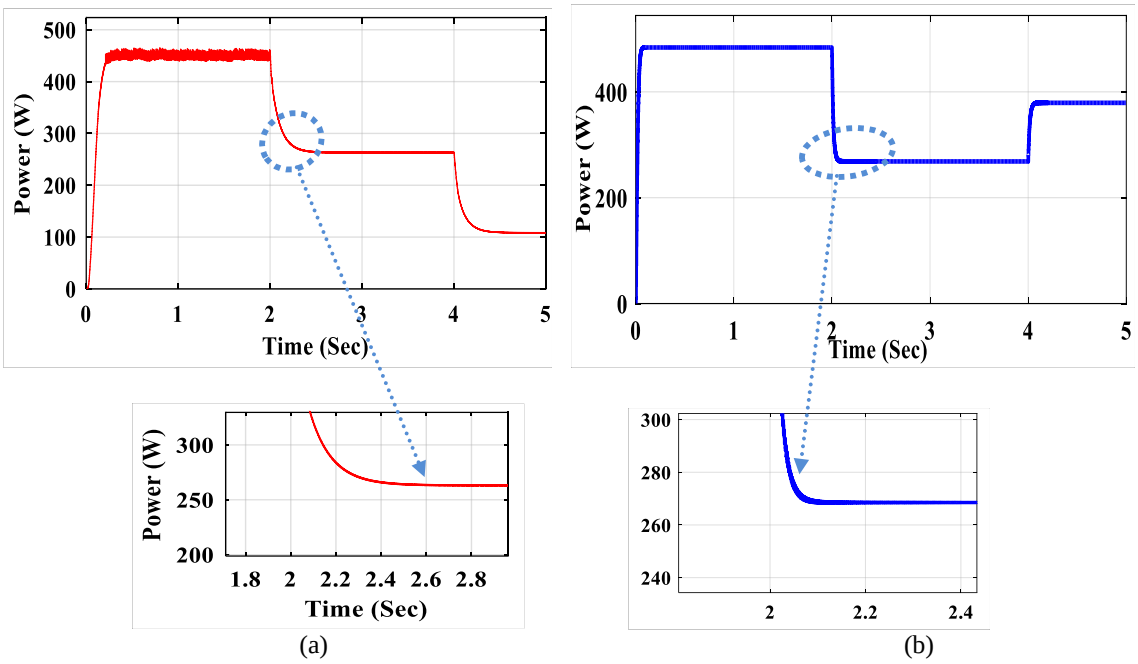

Fig.13 Dynamic performance of (a) P&O (b) ANFIS controllers during changing irradiation level and enlarged transient response of algorithms from 2-4 Sec.

It can be seen from fig.13 the performance of ANFIS is superior to P&O in terms of power tracking and settling time. Table 4 gives the comparative analysis of P&O and ANFIS algorithm under dynamic condition.

Table. 4 represents the power traced and settling time for each (P&O and ANFIS) algorithms.

Table. 4 Comparison of the dynamic behavior of P7O algorithm with proposed ANFIS algorithms

Pattern No.	P&O		ANFIS	
	Power	Settling Time	Power	Settling Time
SP1	450W	0.25 Sec	484W	0.07 Sec
SP2	263W	2.08 Sec	268W	2.08 Sec
SP3	102W	4.06 Sec	379 W	4.06 Sec

Fig.14 shows the power tracked by P&O and ANFIS algorithms and settling time on the bar chart. Comparative analysis of P&O and ANFIS algorithms shows that ANFIS has better tracking efficiency than P&O and power tracked is also more.

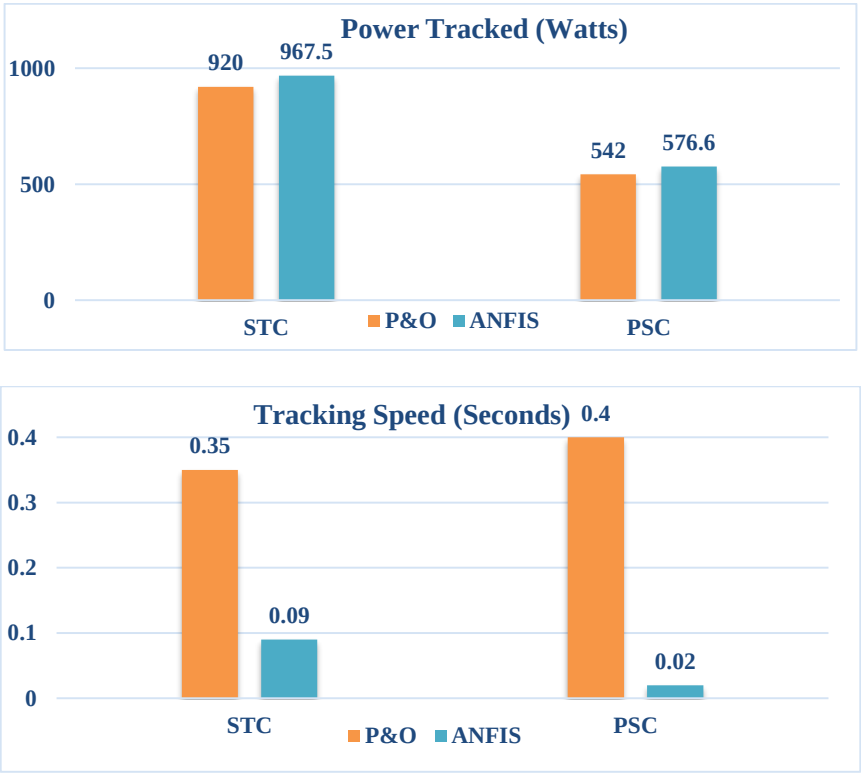

Fig.14 Comparison on bar chart basis of power tracked and tracking speed of P&O and ANFIS (a) STC (b) PSC

6. Conclusion

In the present work, Adaptive neuro fuzzy inference system based maximum power point trackers for PV system under PSC has been presented. The presented algorithm is simple and gives remunerative solution under varying environmental condition in residential applications. The proposed algorithm has been designed, developed and validated to track the maximum power under various shading scenarios viz standard test condition, partially shaded condition as well as dynamic condition. Simulation results demonstrated that ANFIS can track maximum power having lower settling time under different shading scenarios. Comparative analysis of ANFIS and P&O has established the superiority of the ANFIS algorithm as an efficient tool to track maximum power under steady state and transient condition for SPV system which makes it more suitable for residential applications.

Reference

[1] Esram T, Chapman PL "Comparison of photovoltaic array maximum power point tracking techniques", IEEE Trans Energy Convers, Vol. 22 (2),2007, pp.439–49.

[2] Dincer I, Acar C. "Review and evaluation of hydrogen production methods for better sustainability", Int J Hydrogen Energy, Vol. 40 (34), September 2015, pp. 11094-11111.

[3] Ahmed Nabil A, Miyatake M. "A novel maximum power point tracking for photovoltaic applications under partially shaded insolation condition", Electric Power System Res; Vol. 78, 2008, pp. 777–84.

[4] Ji YH, Jung DY, Kim JG, Kim JH, Lee TW, Won CY, "A real maximum power point tracking method for mismatching compensation in PV array under partially shaded conditions", IEEE Trans Power Electron; Vol. 26(4),m2011, pp.1001–9.

[5] Eltawil MA, Zhao Z. “MPPT techniques for photovoltaic applications”, Renew Sustain Energy Rev, 2013, Vol. 25, pp. 793–813.

[6] Li-qun L, Zhi-xin WA. “Rapid MPPT algorithm based on the research of solar cell's diode factor and reverse saturation current”, WSEAS Trans. Syst Vol. 7(5), 2008 pp. 1109-2777.

[7] Liu C, Wu B, Cheung R. Advanced algorithm for MPPT control of photovoltaic systems. In: Proceedings of the Canadian solar buildings conference. Montreal, , 2004, August20–24.

[8] Wu YE, Shen CL, Wu CY. Research and improvement of maximum power point tracking for photovoltaic systems. In: Proceedings of the 8th international conference on power electronics and drive systems. Taipei, Taiwan; November 2–5, 2009.

[9] Koutroulis E, Blaabjerg F. “A new technique for tracking the global maximum power”, Vol. 2(2), 2012, pp. 184–90.

[10] Abhishek Kumar Tripathi, M. Aruna, Ch. S.N. Murthy, “Performance of a PV panel under different shading strengths”, Int. Journal of Ambient Energy,2017, pp. 1-6.

[11] Shahbaz Tabish, Imtiaz Ashraf, “Simulation of partial shading on solar photovoltaic modules with experimental verification”, Int. Journal of Ambient Energy, pp. 161-170, 2015.

[12] Femia N, Petrone G, Spagnuolo G, Vitelli M. “Optimization of perturb and observe maximum power point tracking method”, IEEE Trans Power Electron; Vol. 20(4), 2005, pp:963–973.

[13] K. Sundareswarm, P. Sankar, P. S. R. Nayak, S. P. Simon, and S. Palani, “Enhanced energy output from a PV system under partial shaded conditions through artificial bee colony”, IEEE Trans. Sustain. Energy, Vol. 6 (1), 2015, pp. 198–09.

[14] Kumar P, Mahajan “A Soft computing technique for the control of an active power filter”, IEEE Trans Power Deliv; Vol. 24(1), 2009 pp.452-461

[15] Ahteshamul Haque, “Maximum Power Point Tracking (MPPT) Scheme for Solar Photovoltaic System. Energy Technology and Policy”, Vol. 1(1), 2014, pp. 115-122.

[16] Ishaque K, Salam Z, Syafaruddin “A comprehensive MATLAB Simulink PV system simulator with partial shading capability based on two-diode model”, Sol Energy; Vol. 85(9), 2011, pp. 2217–2227.

[17] Karatepe E, Boztepe M, Colak M. “Development of a suitable model for characterizing photovoltaic arrays with shaded solar cells”, Sol Energy; Vol. 81(8), 2005, pp. 977–92.

[18] Parlak KS “FPGA based new MPPT (maximum power point tracking) method for PV array system operating partially shaded conditions”, Energy; Vol. 68, 2014, pp. 399–10.

[19] Tajuddin MFN, Ayob SM, Salam Z “Tracking of maximum power point in partial shading condition using Differential Evolution (DE)”, In: Proceedings of the IEEE international conference on power energy (PECon), Vol. 384–89, 2012.

[20] Alajmi BN, Ahmed KH, Finney SJ, Williams BW “Fuzzy-logic-control approach of a modified hill climbing method for maximum power point in microgrid standalone photovoltaic system”, IEEE Trans Power Electron, Vol, 26,2011, pp. 1022–1030.

[21] Pallavi Verma, Priya Mahajan, Rachana Garg “Comparison of Intelligent and Conventional MPPT Algorithms for PhotoVoltaic system under Partially Shaded Condition”, In IEEE, International Conference, pp. 505-510, RDCAPE-2017. India.

[22] Casadei D “Single-phase single-stage photovoltaic generation system based on a ripple correlation control maximum power point tracking”, IEEE Trans Energy Convers, Vol. 21,2006, pp. 562–568.

[23] Nikita Gupta, Rachana Garg, Pramod Kumar “Characterization study of PV Module connected to microgrid”, In IEEE India, International conference JMI, 001:10. I 09/lNDICON.2015.7443360, India, 2015.

2021 11th International Conference on Cloud Computing, Data Science & Engineering (Confluence) | 978-1-6654-1451-7/20/$31.00 ©2021 IEEE | DOI: 10.1109/Confluence51648.2021.9377176

AlignPIN: Indirect PIN Selection For Protection Against Repeated Shoulder Surfing

Shreyans Jain
Department of Computer Engineering
Delhi Technological University
New Delhi, India
shreyansjain_2k17co331@dtu.ac.in

Shristi Dabola
Department of Computer Engineering
Delhi Technological University
New Delhi, India
shristidabola_2k17co333@dtu.ac.in

Shikhar Binjola
Department of Computer Engineering
Delhi Technological University
New Delhi, India
shikharbinjola_2k17co320@dtu.ac.in

Rajni Jindal
Department of Computer Engineering
Delhi Technological University
New Delhi, India
rajnijindal@dce.ac.in

***Abstract*—Authentication schemes need to be designed such that they can provide security against observational attacks. Many modern day services use Personal Identification Numbers (PINs) to authenticate their users. However, conventional PIN interfaces provide minimal to no security against observational attacks such as shoulder surfing. We propose AlignPIN, an Indirect PIN selection technique which is resistant to shoulder surfing. We present a detailed analysis to show that AlignPIN is effective in providing resistance against not only casual shoulder surfing, but also sophisticated shoulder surfing and repeated shoulder surfing. To test the usability of AlignPIN, we present a comprehensive usability analysis through data collected over the course of a twelve day usability study done with both young and old participants. The combined results of the security analysis and the practical usability study show that AlignPIN can be used as a PIN selection technique in public places.**

***Index Terms*—shoulder surfing, graphical authentication, personal identification number**

I. Introduction

We use different types of authentication schemes to securely access public services and personal information. Personal Identification number (PIN) is an authentication scheme which is widely used for the purpose of confirming user identity [1]. Most modern day services use a four digit PIN for authenticating their users. The shorter password length results in lower error rates and improved authentication times [2]. Although a PIN is strongly resistant to brute force entry, the conventional design of the PIN interface makes it highly susceptible to observational attacks such as shoulder surfing. The shoulder surfer may obtain the victim's PIN by observing their screen during the authentication process. De Luca et al. [3] found that 65% of users are inefficient in concealing their authentication process when other people are nearby. Apart from a direct observation, the shoulder surfer may also have the ability to record the authentication process. Such a recording would be highly efficient in revealing the victim's PIN. In one study, recording devices were found to be highly successful in capturing users' authentication process from distances as far as 144 feet away [4]. In another study, thermal cameras were found to be useful in situations where an opaque blockage made it infeasible to get an optical view of the victim's screen [5]. Clearly, there exists a need to develop an authentication scheme which is not only resistant to casual shoulder surfing, but also poses a great challenge to shoulder surfers employing sophisticated technology.

In this paper, we propose AlignPIN. The proposed scheme uses graphical authentication for indirect PIN selection. In addition to analysing security of the proposed scheme against casual shoulder surfing attacks, we provide a detailed analysis of its resistance against sophisticated shoulder surfing attacks. We also address the possibility of repeated shoulder surfing, and present a complete analysis of the effectiveness of the proposed scheme against such attacks. To test the usability of AlignPIN, we present a comprehensive usability analysis through data collected over the course of a twelve day usability study. We believe that a short usability study confined to a narrow time frame is ineffective in capturing the improvement which might be gained as a result of prolonged usage. A prolonged usability study is more probable to produce reliable results which are closer to the true value of usability metrics in the long run. In addition to testing the usability of AlignPIN amongst young adults, we also test its usability amongst older people.

II. Related Work

In the past few decades, a lot of research has been done towards developing PIN entry methods which are resistant to observational attacks [6]. The widespread adaptation of video surveillance systems, and frequent authentication in public settings, has made it necessary to develop anti-shoulder surfing PIN authentication schemes. PIN entry redesigns have mainly relied on cursor camouflage or indirect input. While cursor camouflage techniques have shown promise, they are incompatible with systems needing touch input. Still et al.

Authorized licensed use limited to: DELHI TECHNICAL UNIV. Downloaded on March 27,2021 at 05:36:52 UTC from IEEE Xplore. Restrictions apply.

Fig. 1: Graphical User Interface and Login Phase

[7] proposed Incognito, an authentication model which combines cursor camouflage and indirect input. Simpler distractor elements were used to eliminate the need of using dummy cursors. An input system based on eye tracking was also introduced, which may account for compatibility in systems needing touch input. However, the need of eye tracking technology posed a challenge to widespread adaptation.

Papadopoulos et al. [8] proposed IllusionPIN which used the concept of Hybrid Images to provide resistance against shoulder surfing. A virtual keypad was used which would appear differently when viewed from a point farther away from the screen. This would prevent shoulder surfers from determining the actual values of the digits selected by the user. While a thorough theoretical analysis was provided, the design relied heavily on the remoteness of the shoulder surfer.

Salman et al. [9] proposed a graphical authentication scheme resistant to shoulder surfing. The design involved the use of a 4x10 grid, in which each row could be shifted left or right. Each cell contained a single digit and each row consisted of all digits appearing exactly once. The registration consisted of setting a 4 digit PIN and a reference cell location. During authentication, the user was presented with a randomly generated grid. In Each row, the corresponding digit of the PIN was to be aligned to the digit given in the reference cell. However, Independent shifting in each row made it easier for adversaries to effect image based shoulder surfing. Also, The proposed design was susceptible to repeated shoulder surfing.

Roth et al. [10] proposed an indirect entry method to provide some level of shoulder surfing resistance. In the proposed design, The keypad digits were randomly distributed into two sets. Digits belonging to one set were shown in white and digits belonging to the other set were shown in black. The user would select the color to which the current PIN digit belonged. 4 such selections were required to confirm a single digit of the PIN and a total of 16 selections were required to confirm the whole PIN. Out of the three variants proposed, two were susceptible to recording based shoulder surfing. Though the third variant provided some level of security against observational attacks, it was still susceptible to repeated shoulder surfing.

Kwon et al. [11] proposed SteganoPIN which used the concept of indirect pin input to provide resistance against shoulder surfing. In SteganoPIN, the user was presented with two on screen keypads. While one keypad was ordered conventionally, the other keypad consisted of a random ordering of the digits. The former was termed response keypad and the latter was termed challenge keypad. The challenge keypad was presented only after the user had cupped their hand on a certain portion of the display. After this, the user was needed to derive an OTP on the challenge keypad using their long term PIN. The OTP was entered on the response keypad to complete authentication. Though SteganoPIN offered an elegant solution to resist shoulder surfing, it may be inconvenient to use with devices having smaller displays or with devices having displays with fixed orientation. The need of using both hands during authentication may also be unwanted by some users.

III. Proposed Work

The primary design objective was to reduce the effectiveness of shoulder surfing attacks while at the same time maintain an acceptable level of overall usability. Graphical authentication is used to introduce randomness in the authentication process. A randomly generated 4x10 grid is displayed at the time of login with each cell consisting of 4 digits. Each digit appears exactly 16 times and each row has all digits appearing exactly once as the leading digit. To improve security against image based shoulder surfing, each column is allotted a distinct color (discussed in section IV-C). To encourage open science, we have released a public repository containing the implementation details of the proposed algorithms [12].

A. Registration Phase

We assume that the user can perform registration in an isolated environment. In addition to a 4 digit PIN P, the user is required to register a reference grid cell $C = (row, col)$. To explain the next phase, we use 1234 as the PIN and 2,2 as the chosen grid cell. The cell location is "1 indexed" and is relative to the top left of the grid.

B. Login Phase

In this phase, a randomly generated grid G is presented to the user. Fig. 1 shows the grid used in this example. The user first checks the 4 digit number N, given in their chosen grid

Authorized licensed use limited to: DELHI TECHNICAL UNIV. Downloaded on March 27,2021 at 05:36:52 UTC from IEEE Xplore. Restrictions apply.

cell. Let's say that this is 2793. For successful authentication, the user must align in each row R_i, the i^{th} digit of their PIN with the i^{th} digit of the number in their chosen grid cell. For this, the user should use the arrow keys presented on either side of each row. For the scenario taken above, 1 needs to be aligned onto 2 in the first row. For this, the user needs to press the left arrow of the first row 4 times. The rows have been designed on top of circular arrays. Therefore, in the third row, the user can press the right arrow 3 times instead of pressing the left arrow 7 times. Fig. 1 explains the login process with this example. Fig. 2 outlines the general steps needed for successful authentication.

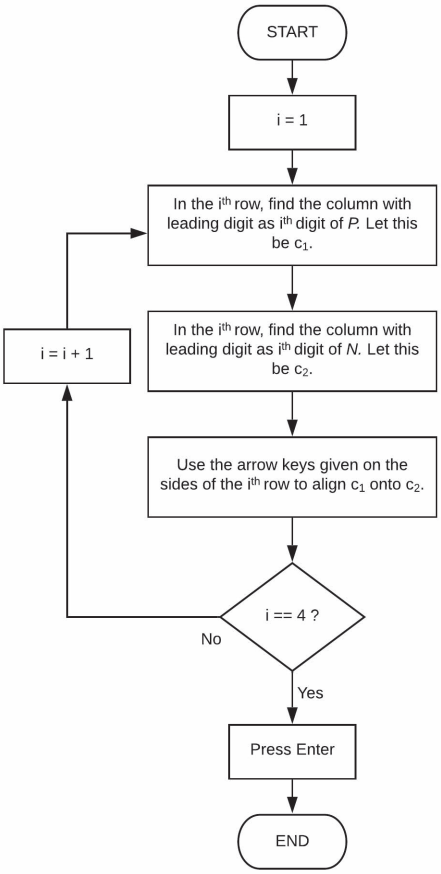

Fig. 2: Steps for successful authentication

User's input is recorded in the form of a move vector M. For example, the move vector generated in the example explained above is [-4, 2, 3, -5]. Here, $M[0] = -4$ indicates that user pressed left arrow in first row four times. Algorithm 1 is used to determine whether the authentication attempt was correct or incorrect. For each row R_i, first we find the column C having the i^{th} digit of the number in the chosen grid cell. Then it checked if the leading digit of the cell at position $C - M[i]$ is equal to the i^{th} digit of the PIN. If this is true for all rows, user is authenticated successfully.

Algorithm 1: Validating an authentication attempt

```
Function validate(G,M,C,P):
    row = C[0], col = C[1]
    for i ← 0 to 3 do
        c = 0
        while G[i][c][0] ≠ G[row][col][i] do
            c = c + 1
        c = c - M[i]
        c = (c + 10)%10
        if G[i][c][0] ≠ P[i] then
            return false
    return true
```

IV. Security Analysis

In this section we present a comprehensive security analysis of the proposed scheme. In addition to a thorough mathematical analysis, we present a novel technique for resisting repeated shoulder surfing. Before analysing security against different types of threats, we analyse the information gained by the adversary on successfully capturing a single authentication attempt. By successfully capturing a single authentication attempt A_i, the adversary can reproduce the corresponding grid G_i and the corresponding move vector M_i, which can then be used to generate a solution set S_i such that

$$S_i = \{X_i | X_i = (p_i, c_i)\}, |S_i| = 40 \quad (1)$$

$$X_0 = (p_0, c_0) \in S_i \quad (2)$$

where X_0 is the tuple consisting of the victim's credentials (p_0 = Registered PIN and c_0 = Registered Grid Cell). Given G_i and M_i, the set S_i can be generated by considering each cell as the victim's registered grid cell. Algorithm 2 explains this process.

Algorithm 2: Generating solution set S

```
Function solutions(G, M):
    S ← {}
    for i ← 0 to 3 do
        for j ← 0 to 9 do
            p = [-1, -1, -1, -1]
            for k ← 0 to 3 do
                c = 0
                while G[k][c][0] ≠ G[i][j][k] do
                    c = c + 1
                c = c - M[k]
                c = (c + 10)%10
                p[k] = G[k][c][0]
            S ← S ∪ (p, (i, j))
    return S
```


Authorized licensed use limited to: DELHI TECHNICAL UNIV. Downloaded on March 27,2021 at 05:36:52 UTC from IEEE Xplore. Restrictions apply.

Now we analyze the security of the proposed scheme against different types of attacks.

A. Incidental Entry Attack (IEA)

In this situation, the adversary does not have any information about the PIN or the registered grid cell of the user. Therefore, this involves entry by using a random move vector M. The theoretical probability of successful authentication is inversely proportional to the number of distinct move vectors possible

$$P_{IEA} = \frac{1}{10000} \tag{3}$$

B. Casual Shoulder Surfing Attack (C - SSA)

In this situation, the adversary relies only on their cognitive ability and natural memory for capturing an authentication attempt. To successfully capture an authentication attempt, the attacker must be able to remember the initial grid G, as well as the move vector M input by the user. This requires remembering a total of 164 data points. We hired 4 university final year students and trained them on the working of AlignPIN. 10 experiments were conducted in which one of the participants was asked to play the role of user and the remaining three were asked to play the role of shoulder surfers. In all 10 experiments, the shoulder surfing group failed to fully reproduce the grid G and the user's move vector M.

C. Image Based Shoulder Surfing Attack (I - SSA)

In this situation, the adversary can use a camera device to capture an authentication attempt. Now, we explain an important design component which helps in improving resistance against image based shoulder surfing attacks. When the user presses an arrow, corresponding feedback is provided through a shift in the column colors of the grid accordingly. Color shift takes place in every row irrespective of which arrow key is pressed. Therefore, at any time during the authentication, all cells in a single column have the same color. If a left arrow key is pressed, every column takes the color of the column to their right (the last column takes the color of the first column). If a right arrow key is pressed, every column takes the color of the column to their left (the first column takes the color of the last column). This design feature makes it necessary for the attacker to acquire at least 5 images (one for G and four for M) for the purpose of reproducing an authentication attempt.

D. Single Recording Shoulder Surfing Attack (S - SSA)

We analyse this situation with the assumption that the adversary has a clear recording of a single correct authentication attempt A_i by the user. Therefore, the adversary has complete information about G_i and M_i. As already discussed, the adversary can generate the corresponding solution set S_i. The probability of guessing the correct credentials is inversely related to the number of elements in the solution set.

$$P_{I-SSA} = \frac{1}{|S_i|} = \frac{1}{40} = 0.025 \tag{4}$$

E. Multiple Recording Shoulder Surfing Attack (M - SSA)

We analyse this situation with the assumption that the adversary has clear recordings of two consecutive and correct authentication attempts A_i and A_{i+1}. As discussed earlier, the adversary can generate the corresponding solution sets S_i and S_{i+1}. Clearly, both S_i and S_{i+1} contain $X_0 = (p_0, c_0)$ where X_0 is the tuple consisting of the victim's credentials (p_0 = PIN and c_0 = registered grid cell). Therefore,

$$|S_i \cap S_{i+1}| \geq 1 \tag{5}$$

Also, because G_i and G_{i+1} are generated randomly

$$P(|S_i \cap S_{i+1}| = 1) \simeq 1 \tag{6}$$

Therefore, if random grid generation is used, the adversary has a high probability of successfully determining X_0. To improve security against M - SSA, we introduce a semi random grid generation technique [12] which guarantees

$$|S_i \cap S_{i+1}| \geq 4 \tag{7}$$

The semi random grid generation method uses X_0 and G_i to generate G_{i+1} such that (7) holds true. Therefore, the semi random grid generation method can be used only if the user's credentials can be securely accessed by the authentication module. The relationship can be modelled as

$$G_{i+1} = g(G_i, X_0) \tag{8}$$

where g represents the algorithm used for semi random grid generation. Table I summarizes the probabilistic relationship between number of authentication attempts captured N and size of the solution set $|S_f|$ = $|S_1 \cap S_2 \cap S_3 ... \cap S_N|$ if semi random grid generation is used.

TABLE I: Probabilistic relationship between number of recordings and size of corresponding solution set

N	$\|S_f\| = 40$	$\|S_f\| = 4$	$\|S_f\| = 3$	$\|S_f\| = 2$	$\|S_f\| = 1$
1	1	-	-	-	-
2	-	1	-	-	-
3	-	$\simeq 0$	0.027	0.243	0.729

Table II summarizes the probability of a successful intruder break in using the information gained through multiple recording based shoulder surfing attacks.

TABLE II: Probability of determining victim's credentials

Number Of	**Number Of Authentication Attempts**			
Recordings	1	2	3	4
1	0.025	0.05	0.075	0.1
2	0.25	0.5	0.75	1
3	0.85	0.99	$\simeq 1$	1

Authorized licensed use limited to: DELHI TECHNICAL UNIV. Downloaded on March 27,2021 at 05:36:52 UTC from IEEE Xplore. Restrictions apply.

V. Usability Analysis

In addition to assuring high security, an authentication scheme should offer an acceptable level of usability. In this section we present a detailed usability analysis of AlignPIN based on the following metrics

- Authentication Time
- Authentication Accuracy

A. Study Methodology

For the purpose of collecting usability data, we created a working prototype using HTML, CSS and JavaScript. An online service was set up so that participants could easily access the prototype and register authentication attempts. Before starting the usability study, participants were required to register a correct attempt to verify their understanding of the system. Participants were required to register two successful attempts every day for a period of twelve days. Along with participant ID, The following data was collected for each authentication attempt

- Authentication Time (Accurate to three decimal places)
- Authentication Accuracy (Correct or Incorrect Login)

Only the attempts which resulted in a correct login were used for analyzing AlignPIN's usability with respect to authentication time. A MySQL based relational database was used for the purpose of storing data.

B. Participants

The usability study was conducted with two groups of participants. The age distribution of the two groups has been described in Table III.

TABLE III: Participant groups for usability study

	Size	Min Age	Max Age	Mean Age	Median Age
Group A	40	21	33	25	24
Group B	10	48	63	55	56

The usability study was conducted in two separate groups so that the usability amongst young users and relatively old users could be inferred separately. All participants were provided unique credentials for the purpose of accessing the working prototype. Data collected from participants of different groups was analyzed separately.

C. Analysis - Authentication Accuracy

Both groups registered a total of 27 incorrect attempts. Authentication accuracy was measured for each day of the usability study. Fig. 3 shows this data.

It can be seen that although accuracy is low on the initial day of the usability study, the final day records 98.76% accuracy for group A and 95.23% accuracy for group B. The general trend suggests a slightly higher error rate for participants in group B. Table IV summarizes the results based on analysis of authentication accuracy.

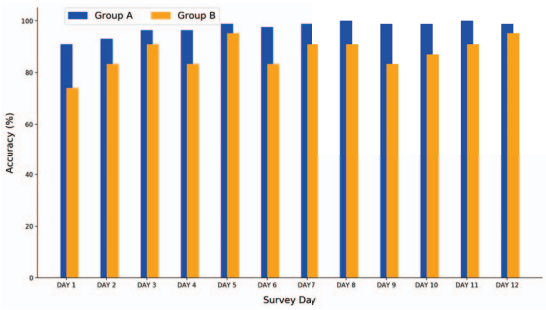

Fig. 3: Authentication Accuracy

TABLE IV: Results - Authentication Accuracy

	Authentication Accuracy		
	Initial	**Final**	**Overall**
Group A	90.90%	98.76%	97.34%
Group B	74.07%	95.23%	87.37%

D. Analysis - Authentication Time

A total of 960 correct attempts were recorded by participants in Group A. Participants in Group B recorded a total of 240 correct attempts. Authentication time was recorded accurately up to three decimal places. On each day of the twelve day usability study, the following metrics were used for analyzing authentication time

- Highest Login Time (Fig. 4)
- Mean Login Time (Fig. 5)
- Median Login Time (Fig. 6)

It was observed that all three metrics showed an overall decreasing trend. This proves that the participants adopted well to the proposed authentication method. As expected, participants belonging to group B showed much higher authentication times as compared to participants belonging to group A.

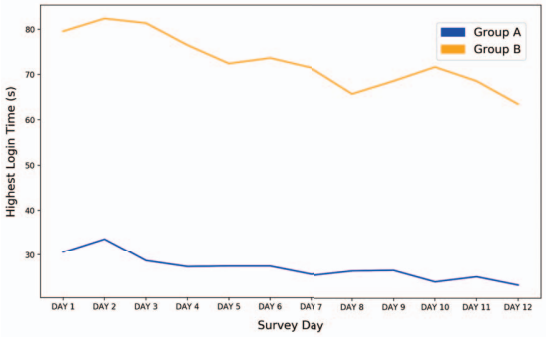

Fig. 4: Highest Authentication Time

Authorized licensed use limited to: DELHI TECHNICAL UNIV. Downloaded on March 27,2021 at 05:36:52 UTC from IEEE Xplore. Restrictions apply.

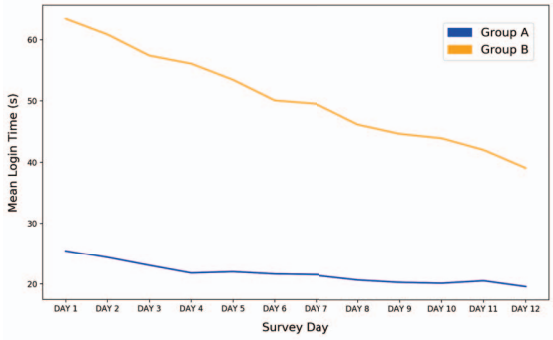

Fig. 5: Mean Authentication Time

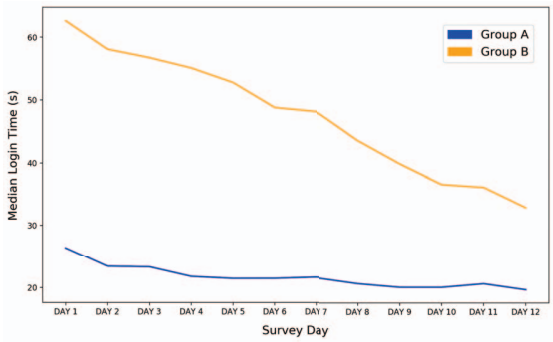

Fig. 6: Median Authentication Time

Table V summarizes the results based on analysis of authentication time.

TABLE V: Results - Authentication Time

	Authentication Time (s)					
	Highest		**Mean**		**Median**	
	Initial	Final	Initial	Final	Initial	Final
Group A	30.66	23.59	25.47	19.66	26.38	19.74
Group B	79.55	63.47	63.44	39.01	62.62	32.76

On the final day of the usability study, group A recorded a median login time of 19.74s and group B recorded a median login time of 32.76s. Given AlignPIN's effectiveness against sophisticated and repeated shoulder surfing attacks, it offers reasonable usability in terms of the expected time needed for successful authentication in both young and old people.

VI. Conclusion

In this paper, we proposed a AlignPIN, a PIN based authentication scheme which provides security against observational attacks such as shoulder surfing. The proposed scheme offers enhanced security as compared to the conventional PIN interface. In addition to resisting casual shoulder surfing attacks, AlignPIN is also effective in resisting sophisticated shoulder surfing and repeated shoulder surfing. Even with access to three clear recordings, the adversary cannot guarantee access through a single authentication attempt. We also conducted a comprehensive usability study for testing the usability of our scheme. The usability study was conducted over a period of twelve days. The results of this study show that both login time and login accuracy improve considerably through regular usage. Although the authentication times are considerably high amongst older people, we believe that this is fairly compensated by the enhanced security. It can be concluded that AlignPIN provides a rational balance between security and overall usability. It remains our future work to test usability of AlignPIN among uneducatd groups and on devices having relatively smaller screen sizes.

References

[1] J. Bonneau, C. Herley, P. C. v. Oorschot, and F. Stajano, "The quest to replace passwords: A framework for comparative evaluation of web authentication schemes," in 2012 IEEE Symposium on Security and Privacy, May 2012, pp. 553–567.

[2] M. Harbach, A. De Luca, and S. Egelman, "The anatomy of smartphone unlocking: A field study of android lock screens," in Proceedings of the 2016 CHI Conference on Human Factors in Computing Systems, ser. CHI '16. New York, NY, USA: ACM, 2016, pp. 4806–4817.

[3] De Luca A, Langheinrich M, Hussmann H. Towards understanding ATM security: a field study of real world ATM use. In: The proceedings of SOUPS; 2010. p. 1–10.

[4] Rigg J. Researchers crack iPad PINs by tracking fingers that enter them Retrieved from http://www.engadget.com/2014/06/25/ipad-PIN-snooping/?ncid=txtlnkusaolp00000595.

[5] Cluley G. This simple iPhone case can be used to steal ATM pins Retrieved from September http://www.intego.com/mac-security-blog/iphone-case-atm-pins/.

[6] Bošnjak, L. and Brumen, B., 2020. Shoulder Surfing Experiments: A Systematic Literature Review. Computers & Security, p.102023.

[7] Still, J.D. and Bell, J., 2018. Incognito: Shoulder-surfing resistant selection method. Journal of information security and applications, 40, pp.1-8.

[8] A. Papadopoulos, T. Nguyen, E. Durmus, and N. Memon, "Illusionpin: Shoulder-surfing resistant authentication using hybrid images," IEEE Transactions on Information Forensics and Security, vol. 12, no. 12, pp. 2875–2889, Dec 2017.

[9] M. Salman, Y. Li and J. Wang, "A Graphical PIN Entry System with Shoulder Surfing Resistance," 2019 IEEE 4th International Conference on Signal and Image Processing (ICSIP), Wuxi, China, 2019, pp. 203-207.

[10] V. Roth, K. Richter, and R. Freidinger, "A pin-entry method resilient against shoulder surfing," in Proceedings of the 11th ACM Conference on Computer and Communications Security, ser. CCS '04. New York, NY, USA: ACM, 2004, pp. 236–245.

[11] T. Kwon and S. Na, "Steganopin: Two-faced human-machine interface for practical enforcement of pin entry security," IEEE Transactions on Human-Machine Systems, vol. 46, no. 1, pp. 143–150, Feb 2016.

[12] Shreyans Jain, Shristi Dabola, Shikhar Binjola and Rajni Jindal. AlignPIN, v1.0. https://github.com/Shreyans365/AlignPIN, December 2020.

Authorized licensed use limited to: DELHI TECHNICAL UNIV. Downloaded on March 27,2021 at 05:36:52 UTC from IEEE Xplore. Restrictions apply.

Multimedia Tools and Applications
https://doi.org/10.1007/s11042-021-10750-1

An efficient image encryption scheme using elementary cellular automata with novel permutation box

Ashish Kumar[1] · N. S. Raghava[2]

Received: 10 August 2020 / Revised: 8 January 2021 / Accepted: 24 February 2021
Published online: 19 March 2021
© The Author(s), under exclusive licence to Springer Science+Business Media, LLC, part of Springer Nature 2021

Abstract

Digital image communication over public networks requires a high level of security to protect picture elements that represent information. Security is an important and challenging issue that can be solved using cryptography techniques. Generally, image encryption techniques are based on multiple rounds and iterations. In this paper, a secured lightweight cryptosystem is designed based on lookup table operations that reduce computational overhead, resource requirement and power consumption compared to traditional security mechanisms. In this context, one-dimensional elementary cellular automaton has been combined with Henon chaotic map to design a cryptosystem, which can produce unprecedented results in cryptography. Initially, state attractors for rule space are investigated and analyzed in Wolfram's cellular automata to extract the properties and functional abilities to perform cryptographic operations. A novel algorithm of keyed transposition cipher is applied to digital image in P-Box module to produce shuffled image. Then, the extracted properties of ECA are preserved in a tabular form and further used in the diffusion process. Based on the simulation and comparison with other existing mechanisms, it is evident that the proposed algorithm is promising and obstructive to all kinds of statistical attacks, and it yields security primacy in various areas of cryptography. Encryption/Decryption is based on indexed based lookup tables principal using ECA and can be easily implemented using logic gates. The proposed algorithm provides confidentiality and can be adopted in IoT networks that require lightweight cryptography modules. Experimental results of color and gray images demonstrate flourishing results in the real-time environment of cryptography.

Keywords Cellular automata · Chaotic map · Confusion · Diffusion · Image encryption

✉ Ashish Kumar
ashishkumar@dtu.ac.in

N. S. Raghava
nsraghava@dce.ac.in

Extended author information available on the last page of the article

1 Introduction

With the deployment of network-based technologies, the web world is more concerned about the privacy of multimedia-based information over the Internet [19, 28, 41]. In recent years, many devices such as mobiles, TV, smart meters, sensor nodes, and military surveillance devices, etc., can receive and transmit information over the Internet; users or inbuilt functions usually operate such devices.

Military data transfer and personal conversation between two people have equal importance and need to be confidential. When information is transmitted, ethically, it should reach its destination without any interference, which is taken care of by cryptography. Multimedia is an emerging field that deals with different forms of information such as text, images, audio, sensor data and videos in an integrated manner [41]. The advancement of devices to display multimedia and enabling them to transfer it from one location to another has increased their security issues. These security issues include confidentiality, integrity, availability [7, 23]. In a hostile environment, security services are required as per the need of organizations and individuals to protect their valuable information and resources. Because of this, secrecy is an essential critical component while transmitting or storing such information [20].

There are several standards that are designed to provide security services under ITU-T X.805 to individuals and organizations [30]. For each security service, security mechanisms are also standardized by ITU-T X.805, which are followed by all the countries. With the advancement of technologies, several attacks are also updated with time. Attackers apply cryptanalysis studies to understand the behavior of a system for unauthorized access. This study includes machine learning, neural network, CNN and deep neural network-based approaches, which are inspired by the human brain and also help in brute force attack [3, 14]. Hence comes the need for revised versions of mechanisms to resist such attacks.

Encipherment techniques are categorized into two categories: (1) Cryptography (2) Steganography. In steganography techniques, secret information is embedded in the cover object in such a way that it hardly modifies the cover object [2]. Billions of people are getting connected to each other through the Internet and exchange a large amount of personal information over the network. It becomes essential to secure such sensitive information from unauthorized users. In this context, over the past two decades, dynamic systems and other practices have emerged with cryptography in order to provide security services like confidentiality, authentication, integrity and non-repudiation [37]. In particular, chaotic maps are widely used in all aspects of cryptography to provide privacy and authentication. Effective extension policies of cellular automata systems and its properties are incorporated in cryptography due to randomness, unpredictability and dynamicity. Self-producing automata theory was given by J. Von Neumann and Stan Ulam in the year 1950. Besides, Stephen Wolfram extended the concept by adding generations and local transition rules concept, i.e., cellular automata (CA) theory; also, Wolfram was the first person to implement cellular automata-based stream cipher [32]. Meanwhile, various properties of cellular automata have been investigated and attention is given to their use in the privacy and other security models.

The proposed work is based upon the confusion and diffusion theory. The theory of confusion and diffusion was introduced by Shannon in 1945. The relationship between plaintext and ciphertext defines diffusion. In comparison, confusion is defined by the relationship between key and ciphertext [17]. In image encryption schemes, perfect diffusion is achieved when changing a single bit or a byte in the original image gives a different cipher image. Diffusion means a complex dependency of output bits on the input bits. Confusion is

achieved when a cipher image is dependent on the key. In particular, confusion and diffusion are used to make a robust cryptosystem that hides the statistical property of the original image and generates a cipher image, which is impossible to decode by intruder or eavesdropper in a specific time interval. Also, finding a key from the original image and its cipher image pair is almost impossible. Multimedia travels in the digital communication networks in different forms and each media has its own statistical properties and characteristics. For example, in the English language, 26 alphabets with some grammar rules are used to form the statement, and 'E' and 'T' are the most frequently used letters in the English language. When any scheme encrypts text, letters of the text are enciphered into different letters [11, 29]. In the hill cipher scheme, statistical attacks are not possible, whereas in the Vigenère cipher, some properties remain unchanged in the ciphertext. Therefore, a cryptanalyst can use this statistical information to break a cryptographic algorithm. According to NIST, industry and technology have emphasized the IoT based smart devices in recent times, which are deployed in RFID tags, sensing networks, cognitive area networks and embedded systems; such technology requires a lightweight cryptography algorithm [42].

Several methodologies are implemented based on symmetric and asymmetric key cryptography using different concepts. A.A. Abdo at el. [1] proposed an algorithm based on elementary cellular automata and a special kind of periodic boundary cellular automata with unity attractors is used. From the viewpoint of security, cellular automata attractor states are changed with respect to the encrypted image, and different key streams are used for encryption. The cellular neural network with chaotic properties is used as the generator of a pseudorandom keystream. Jun Jin [21] proposed a novel image encryption/decryption scheme, where the elementary cellular automata (ECA) of length 8 with periodic boundary conditions is investigated under rule 42. It is also found in the state-transition diagram that ECA rules in state attractors satisfy the essential requirement of the encryption/decryption scheme that can perform as S-Box to substitute the pixel values. Simulation results on some grayscale and color images show that the proposed image encryption method satisfies the properties of confusion and diffusion. In [40], cellular automata (CAs) are used to design a model based on Vernam cipher and CAs are applied to generate a pseudorandom number sequence (PNS), which is used during the encryption process. In [44], Wolfram introduced a cellular automata-based cryptographic scheme for symmetric encryption protocol using one-dimensional cellular automata. Rey [36] presented a secure protocol for message communication using finite cellular automata as a hash function, which results in different hash digest for different messages. Azza A.A. et al. [5] proposed a novel technique using cellular automata and multi-secret image sharing scheme based on steganography; in which unary attractors are used to sharing the secret images. Zheng et al. proposed a lightweight authentication scheme to protect the information of railway IoT cloud networks using S-box coupled lattice and obtained confidentiality and integrity services [45]. The information system must be designed on three basic parameters: security, availability, and correctness; In [5], the authors achieved these services in the cloud environment using data encryption and boundary maintenance according to the user's view of data to enable data sharing and maintain data storage. In paper [18], authors proposed an authentication protocol using ECC and random number generations and implemented it for tag, reader and server, and developed a model for IoT devices. In 2020, Babaei et al. [6] proposed cellular automata and DNA sequence based image encryption technique which require large memory space along with high computational cost. Enayatifar et al. [12] proposed an algorithm on the same concept using CA and DNA. Authors have worked on an indexed based technique that requires heavy computation due to DNA sequence.

Thus, the technique is unsuitable for those applications in which resources and memory spaces are limited. In [38], Roy proposed a programmable cellular automata (PCA) based block cipher, which utilizes the characteristics of programable cellular automata to encrypt the image by using the rule table of 8×256 values as a data structure.

The proposed algorithm is designed taking into account all the above statements. A lightweight mechanism is proposed based on the related work that can be implemented in IoT networks and cyber-physical systems. The proposed algorithm is based on the Lookup Table scheme, and most of the algorithms work on the principle of block and stream cipher [33, 39, 43]. It enables many low resources and constrained devices to communicate, compute, and make decisions in communication networks and executed with limited resource's capabilities. Therefore, state attractors/transitions are analyzed and extracted under elementary cellular automata (ECA) rule space, which is introduced as a table lookup for the cryptosystem. The objectives of this paper are as follow:

1) To propose a lightweight framework to be implemented with minimum hardware and software requirements. Rules are analyzed, and generations are found from the rule space to identify the specific property of the cryptography. Several rules are tested for eight-bit values and the generations are stored in a tabular form to operate the encryption/decryption module.
2) To design a permutation box, i.e., is governed by a key, unlike other traditional permutation schemes which are based on the algorithm; here, the key decides the shuffled location of the original pixel. Since the permutation box is solely dependent on the key, it can also be called a keyed transposition scheme. For this purpose, the Henon chaotic map is used, which is initiated by the initial key with a large keyspace.
3) To develop a novel cryptosystem using cellular automata to achieve confidentiality while sending images over the public networks.
4) To develop the encryption module based on substitution cipher (S Box), pixels are incorporated in the encryption procedure and work as a key for the neighboring pixels, making it resistible against cryptanalysis attacks. It is achieved with simple computation and mathematical operations.

2 Concept of the 2D chaotic map and elementary cellular automata

Elementary cellular automaton is widely used for various applications of science due to its properties. In this paper, we have identified and developed generations or transition of states by applying rules of cellular automata based upon periodic boundary conditions, which can be used to secure any multimedia information. To design a permutation box (P Box), Hénon chaotic map is associated with the proposed work to produce pseudorandom numbers. The properties of Henon chaotic map and ECA play a major role in leading the algorithm, which are discussed in this section. It is also explained how these rule tables are extracted from the rule space of ECA.

2.1 Henon chaotic map

Professor Edward Lopez derived a Chaos theory, which finds its existence in mathematical physics. A chaotic system based on confusion and diffusion was developed in 1989 [10, 34].

Chaotic systems are nonlinear, deterministic, highly sensitive and easy to reconstruct after filling in the image. Hénon chaotic map is one of the chaotic maps discovered in 1978 [8, 24], often used to generate pseudorandom sequences required for different mechanisms to provide security services in recent research. Two-dimensional discrete-time nonlinear dynamic Hénon chaotic map generates a pseudorandom binary sequence as described in Eq. (1):

$$\begin{aligned} X_{n+1} &= 1 + Y_n - aX_n^2 \\ Y_{n+1} &= bX_n \qquad\qquad n = 0, 1, 2, \ldots\ldots\ldots \end{aligned} \tag{1}$$

Here, the parameters a and b are of prime importance because they are responsible for the dynamic behavior of the system. The system is chaotic for the value of a and b equal to 1.4 and 0.3, respectively. Initial seeds X_1 and Y_1 works as a key for the Eq. (2) of chaotic map to produce pseudo random numbers, and used for encryption in most of the research literature. Since the Hénon chaotic system is deterministic, therefore deciphering the cipher image will reconstruct the original image at receiver's end with the same initial key values (X_1, Y_1). Thus, sensitivity of key and encipher algorithm together contribute to avoid all kinds of cryptanalysis attacks.

$$\begin{aligned} X_{n+1} &= 1 + Y_n - 1.4 \times X_n^2 \\ Y_{n+1} &= 0.3 \times X_n \qquad\qquad n = 0, 1, 2, \ldots\ldots\ldots \end{aligned} \tag{2}$$

2.2 Elementary cellular automata

Cellular automata (CAs) is a dynamical, physical, discrete-time computational model widely used in various fields of science and technology [8, 24, 44]. Pseudorandom number generation, pattern recognition, and developing games (Conway's Game of Life is a top-rated game based on cellular automata) are applications of CAs [16]. CA evolves on array of cells or lattice of neighboring sites. CA is classified into two categories based on the lattice structure of similar sites (cells). When CA is deployed over one-dimensional grid, it is known as one-dimensional cellular automata or elementary cellular automata. In two-dimensional cellular automata, CA spreads over a 2-D grid structure with several neighborhood configurations of cells. In 2-D cellular automata, Von-Neumann, Moore, Cole and smith models are popular in image processing and cryptography applications.

Elementary cellular automata (ECA) is a one-dimensional mathematical model based on discrete number of input and output [9, 31]. Automata based systems are constructed depending upon specific criteria, i.e., number of cells, state of a cell (0 or 1), participation of neighboring cells and choice of local rules. State values are binary values, either zero or one. Each cell is surrounded by its adjacent cells on both sides; if a cell integrates itself with its neighbors, this whole cell sequence can be called three neighborhoods. The selection of neighbors for the boundary cells can be decided by different conditions, as shown in Fig. 1.

Three-neighborhood cells with radius one and every cell having two states are also known as ECA, and in each iteration, a cell has two possible values, either 0 or 1. Accordingly, distinct neighborhood configurations will be $2 \times 2 \times 2 = 8$.

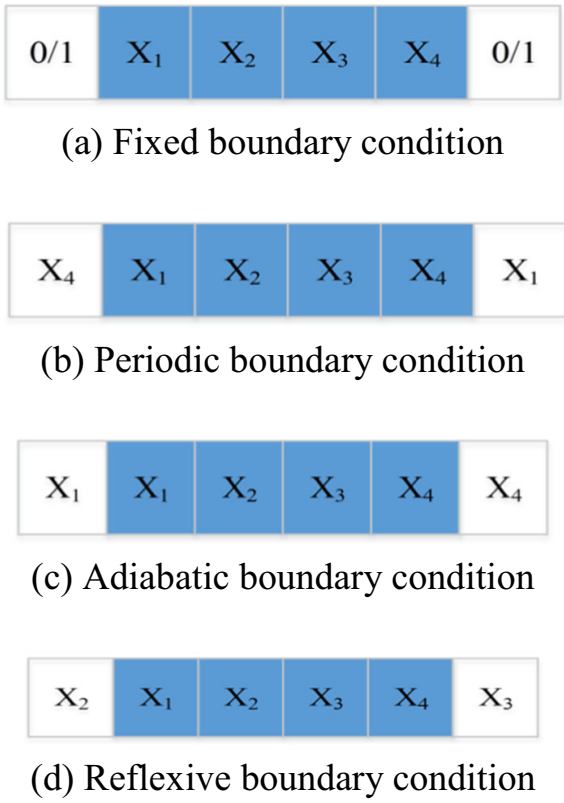

Fig. 1 Cellular automata boundary conditions

In Eq. (3), Let t , i represent the time and index of a cell, respectively. New state of a cell (x_i^{t+1}) depends upon the current state of its neighboring cells, i.e., x_{i-1}^t and x_{i+1}^t .

$$x_i^{t+1} = f\left(x_{i-1}^t, x_i^t, x_{i+1}^t\right) \tag{3}$$

Since $\boldsymbol{f}(\,)$ is a Boolean function of combinational logic, it produces a binary value depending upon the local rule of elementary cellular automata. Therefore, $x_i^{t+1} \in \{0, 1\}$. At every discrete time step (clock cycle), Boolean cellular automata sites update their state by using some rules (combination function or rule).

Table 1. exhibits the nature of local transition rules of ECA. Assume, S_0 represents $(000)_2$ binary block format, $S1$ represents $(001)_2$, ……$S7$ maps to $(111)_2$ binary block configuration. Now, these eight different binary block configurations can be evolved with discrete-time in 2^8 different possible ways. Therefore, the rule table of cellular automata has 256 distinct rules from rule 0 to rule 255. Each rule has its characteristics and pattern in elementary cellular automata, which influences the state of cells.

In setup, we have identified elementary rules which support stream cipher property. If the same rules are applied to entire cells of lattice, then it is called uniform cellular automata; otherwise, it is called hybrid cellular automata. Here, we have applied the same rule to the

Table 1 Ruleset for distinct cell compositions

S_7	S_6	S_5	S_4	S_3	S_2	S_1	S_0	RULE NUMBER
0	0	0	0	0	0	0	0	RULE 0
0	0	0	0	1	1	1	1	RULE 15
1	1	1	1	1	1	1	1	RULE 255

entire grid of cells. Among four boundary conditions, the periodic boundary condition is selected to generate the state attractor. In every iteration, when a rule is applied at time t and at time $t+1$, the state of a cell gets updated and this transition is known as an attractor.

To investigate the chaotic behavior of cellular automata rules, the periodic boundary condition is applied with all the 8- bit grayscale possible values and numerous rules are tested [22]. It is found that rule 15 has the ability to perform some cryptographic functions. Corresponding combination logic rule of 15 can be written as:

$$S_i^{t+1} = \overline{S_{i-1}^t}$$

Periodic boundary condition works as a ring for 8-bit value to determine the next state of the current state and we have recursively applied the same rules to the previous output at time $\{t+i \mid 0 \le i \le 7\}$ and this output has 256 distinct global states. We have tested up to nine generations for every value of D, where $0 \le D \le 255$.

Generations are further tested to accumulate the progress of the rules in such a way to be characterized by XOR and XNOR. We have determined and extracted two different tables, Tables 2 and 3. Table 2 is based on XOR property and Table 3. is based on XNOR property. These rule tables are used in the encryption module and are used as lookup tables. The lookup table (LUT) is employed when a pixel appears for the encryption.

$$Ruletable\ I = \begin{cases} D \oplus genration_1 \oplus genration_2 \ldots . \oplus genration_6 \oplus genration_7 = 0 \\ D \oplus genration_1 \oplus genration_2 \oplus genration_3 = 0 \end{cases} \quad (4)$$

$$Ruletable\ II = \begin{cases} D \oplus genration_1 \oplus genration_2 \ldots . \oplus genration_6 \oplus genration_7 = 255 \\ D \oplus genration_1 \oplus genration_2 \oplus genration_3 = 255 \end{cases} \quad (5)$$

Table 2 Elementary Cellular Automata based RULETABLE I

Row	Column								
	1	2	3	4	5	6	7	8	
1	0	0	0	0	0	0	0	0	0
2	3	126	192	159	48	231	12	249	0
3	5	125	65	95	80	215	20	245	0
4	6	252	129	63	96	207	24	243	0
5	9	123	66	222	144	183	36	237	0
6	10	250	130	190	160	175	40	235	0
7	15	120	195	30	240	135	60	225	0
8	18	246	132	189	33	111	72	219	0
9	23	116	197	29	113	71	92	209	0
10	27	114	198	156	177	39	108	201	0
11	43	106	202	154	178	166	172	169	0
12	45	105	75	90	210	150	180	165	0
13	46	232	139	58	226	142	184	163	0
14	51	102	204	153	0	0	0	0	0
15	53	101	77	89	83	86	212	149	0
16	54	228	141	57	99	78	216	147	0

Table 3 Elementary Cellular Automata based RULETABLE II

Row	Column								
	1	2	3	4	5	6	7	8	
1	1	127	64	223	16	247	4	253	255
2	2	254	128	191	32	239	8	251	255
3	7	124	193	31	112	199	28	241	255
4	11	122	194	158	176	167	44	233	255
5	13	121	67	94	208	151	52	229	255
6	14	248	131	62	224	143	56	227	255
7	19	118	196	157	49	103	76	217	255
8	21	117	69	93	81	87	84	213	255
9	22	244	133	61	97	79	88	211	255
10	25	115	70	220	145	55	100	205	255
11	26	242	134	188	161	47	104	203	255
12	35	110	200	155	50	230	140	185	255
13	37	109	73	91	82	214	148	181	255
14	38	236	137	59	98	206	152	179	255
15	41	107	74	218	146	182	164	173	255
16	42	234	138	186	162	174	168	171	255

This section investigates that attractors are updated in each iteration $(t+1)$. XOR operation is applied between iterated values after applying rule 15 using ECA. It yields either 255 or 0, as shown in Eqs. (4) and Eq. (5). In the proposed cryptosystem, state attractors tables have been extracted using the property of XOR XNOR logic operations generated by ECA; out of 33, 31 attractors are chosen with eight states. In Fig. 2. The flowchart of the procedure is illustrated with all the necessary steps.

3 Proposed algorithm

The proposed algorithm is designed in the context of sensitive information of digital color and gray images. The architecture of the proposed algorithm is exhibited in Fig. 3., where the permutation box and the encryption module operate as confusion and diffusion, respectively. The algorithm is performed in two iterative stages. In the first phase, confusion is performed, and after that diffusion process takes place. A shuffled image is obtained by the shuffling procedure (section 3.1), which is based on the property of keyed based transposition method. ECA is a vital core part of the second phase of the algorithm. A shuffled image is used as an input for the second phase of the encryption module. Let us consider a digital color image $\boldsymbol{I}$ with dimension $\boldsymbol{m \times n \times 3}$. (i.e., m rows and n columns) and its grayscale image is represented by $\boldsymbol{I_{m \times n}}$. Digital color image is decomposed into 2D channels, which are $\boldsymbol{Red_{m \times n}}$,$\boldsymbol{Green_{m \times n}}$ $\boldsymbol{Blue_{m \times n}}$. Since the proposed algorithm is designed for two-dimensional images, thus the dimension of 2D image **is** $\boldsymbol{I_{m \times n}}$. Each channel supports [0 255] decimal values represented in the 8-bit binary format of the computer system. The following subsections discuss the procedure for gray images, which can be performed on color images as well.

1) Keyed transposition method

Input: plain image I.
Output: shuffled image I′

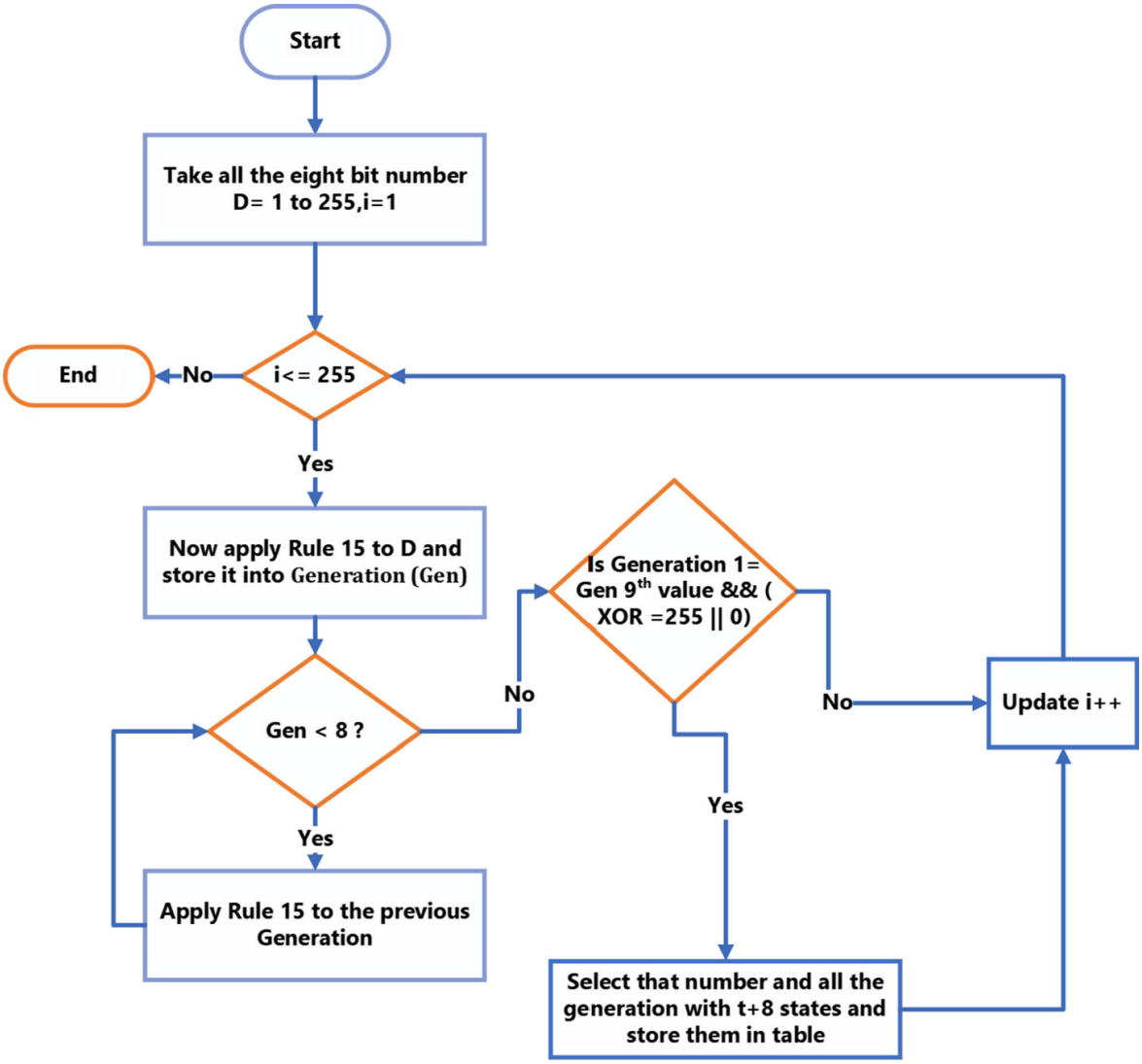

Fig. 2 Flowchart of rulespace investigation and extraction for rule tables

The correlation between pixels of the same region within an image is very high due to the similar properties. In contrast, an ideal cipher image should follow a low correlation among pixels. Therefore, shuffling is useful to disturb the relationship between adjacent pixels. In

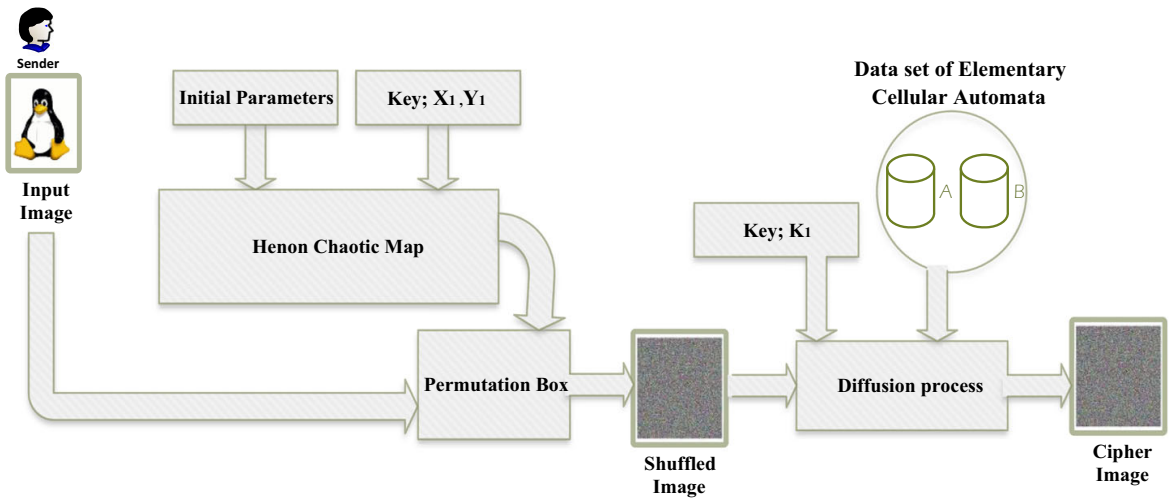

Fig. 3 The architecture of the proposed algorithm

traditional cryptography, most permutation boxes (P boxes) are designed for text information and, but they are not suitable for images and videos. In the spatial domain, an image is represented by mathematical function $\boldsymbol{f}(\boldsymbol{x},\boldsymbol{y})$, where $\boldsymbol{x}$ represents the horizontal axis, and $\boldsymbol{y}$ represents the vertical axis of an image. In the first phase, the shuffling process is done using Hénon chaotic map, which is based on keyed transposition property. Hénon chaotic map is a two-dimensional map where X_1 and Y_1 are used as a key to generate pseudorandom numbers. Using these numbers, a new pixel location $\boldsymbol{f}(\boldsymbol{x}',\boldsymbol{y}')$ is generated for every pixel $\boldsymbol{f}(\boldsymbol{x},\boldsymbol{y})$ of an original image, and as a result, a pixel is shifted to a newly updated location. Therefore, it is really hard to visualize the shuffled image to get sensitive information from it. Here, confusion is achieved by the shuffling method, whereas to achieve diffusion, a shuffled image is used as an input for the diffusion process. Fig. 4 demonstrates the working procedure of the method, where random integers 1 to n are generated.

Step 1: The Henon map is initialized with initial parameters a and b, and specific constant values of these parameters develop chaotic behaviors of the Henon map.

Step 2: X_1 and Y_1 referred to as a secret symmetric key for the shuffling procedure and chosen by the sender; these initial seeds are kept private by the user for privacy purposes.

Step 3: In the next step, Henon chaotic system is used as a keystream generator for the proposed cryptosystem. The size of the sequence depends upon the size of an image. If the input image size is $m \times n$, then the number of the sequence is produced of size $m \times n$. Thus, Sequence values are obtained by using Eq. (2), i.e., is iterated as per the size of an input image.

Step 4: Sequence values are obtained in signed float number format; $X \in \{-I, +I\}$. These generated sequences are used to design the P-Box.

Step 5: For all float numbers of X, the modular arithmetic concept is used to change the values of X under the range of [1 $m \times n$].

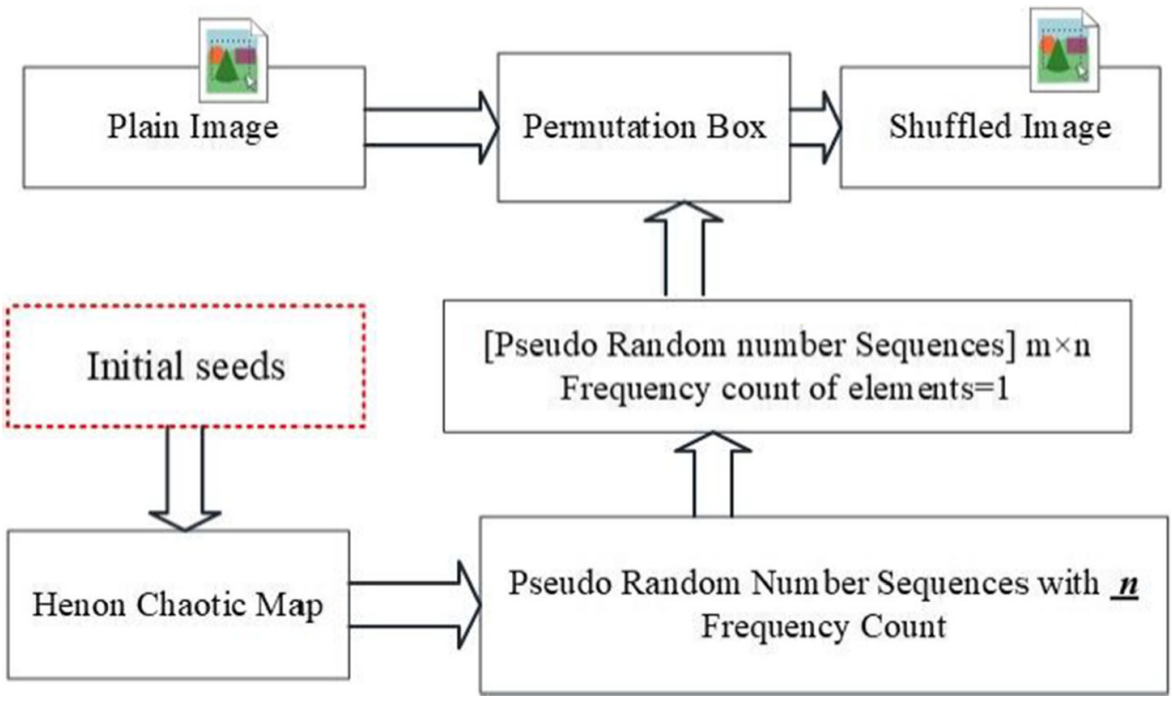

Fig. 4 Keyed Transposition Scheme

$$New_X = \lfloor (m \times n) \times X_{m \times n} \rfloor$$

$$New_matrix = (New_X \bmod N) + 1$$

It follows that $[New_matrix] \in [1, 2, 3 \ldots\ldots\ldots m \times n]$,

Frequency count of elements in $New_matrix \geq 1$

Step 6: Subsequently, *New _ matrix* stores duplicate values and for all the numerical values of *New _ matrix*, frequency count of all the elements (bin) and store it into *Frequency _ count*.

1. Initialize $i \leftarrow 1$
2. while $i \leq m \times n$
3. Count frequency of i in *New _ matrix* and it is represented by *Frequency _ count*;
4. *Frequency _ matrix*[i] = *Frequency _ count*;
5. $i = i + 1$;
6. While end

Algorithm 1. Permutation Box Generation Algorithm

1. **initialize i ← 1**
2. while **i to m × n do**
3. If **Frequency_matrix(i) == 0** then
4. **ptr = i + 1 until we find Frequency_matrix(i) > 0**
5. **Frequency_matrix(ptr) = Frequency_matrix(ptr) − 1;**
6. **search ptr value in New_matrix; where it is found out in New_matrix, that value is replaced by i and Frequency_matrix(i) is updated and it is increased by 1.**
7. else if **Frequency_matrix(i) > 1** Then
8. **ptr = i + 1 until we Find Frequency_matrix(i) == 0**
9. **update Frequency_matrix(ptr) = Frequency_matrix(ptr) + 1**
10. **Search *i* in New_matrix, wherever it is found in *New_matrix*, on that location value of ptr is copied.**
11. **Frequency_matrix(i) = Frequency_matrix(i) − 1;**
12. **Repeat this process until Frequency_matrix(i)==1**
13. else **Frequency_matrix(i) == 1** then
14. **Do nothing in this situation.**
15. endif
16. **Increment i**
17. while-end

Step 7: Now the next step after calculating *Frequency _ count* of the matrix is to remove all the duplicate numbers and create a matrix with a single frequency count. A detailed procedure is explained in **Algorithm 1.**

After applying step 7. of the shuffling procedure, $[New_matrix]_{m \times n} \in [1\ m \times n]$, where the frequency count of each element is one

Step 8: Image flattening is used to convert a two-dimensional image into a single-dimensional image [15]. The input image is converted into one-dimensional image and coordinate (x, y) of an image $I_{(x,y)}$ is shuffled and shifted to new location $F(x', y')$ using *New _ matrix*. Thus, the shuffled image I' is produced.

1. (Initialize) $i \leftarrow 1$
2. While i < =N
3. Shuffled image (New_matrix(i)) = image(i);
4. $i \leftarrow i + 1$
5. While-end

Furthermore, a one-dimensional shuffled image is converted into a two-dimensional image ***I′*** in a row ordered fashion.

2) Encryption algorithm based on elementary cellular automata

Input: shuffled image I′
Output: cipher Image Ω

In the second phase, elementary cellular automata become a significant component of the proposed cryptosystem, as shown in Fig. 5. Elementary cellular automata (ECA) operates on the shuffled image, where each pixel acts as a key for the next neighbor pixels, but for the first pixel of an image, a key ***KEY*1** is selected by a user. ***Ruletable I*** **and** ***Ruletable II*** are used for the encryption module. Each Table has sixteen distinct transition state attractors with a length of eight states and four states. These state attractors are based on the property of the XOR and XNOR scheme. Traditionally, encipherment techniques are based on pseudorandom numbers. However, CA has emerged with cryptographic techniques. Rule tables are divided into different parts on the basis of XOR and XNOR properties, which are discussed in Section 2.2. One more attractor is added in this list, where 0 decimal value is assigned to all eight states. Now, these state attractors are divided into two tables.

Step 1: First, we choose a key ***KEY*1** for the first pixel of an image, and any 8-bit binary number is chosen as key ***KEY*1**. Then for the second pixel, the first pixel of shuffled image behaves as a key and for the third pixel, the second pixel works as a key. The process is executed in a linear fashion to cover all the pixels of an image. Furthermore, this process is continued for the remaining pixel until the last pixel of an image is encrypted with the second last pixel of the shuffled image.

Step 2: Pixel plays an essential role as a key to encrypt an image. Pixel is broken into fixed-size blocks with a specific width to execute the encryption process. LSB bit of a key, ***Table number*** (***T***)**,** is used to reach the tables, ***Row number*** (***R***) and ***column number*** **(C)** are represented here by *R* and *C* respectively to trace the row and column index of the selected rule table. Pixel index (*i*, *j*) determines the length of EXOR and EXNOR operations. A detailed procedure of the encryption algorithm is discussed in Algorithm 2.

Step 3: After applying the encryption algorithm, **cipher Image Ω** is generated and transmitted to the receiver. Key ***KEY*1** is transmitted through the secure channel**.**

Algorithm 2 Encryption Algorithm

Encryption module (C, R, PTR)

1. while $\boldsymbol{PTR \neq 0}$ do
2. $\boldsymbol{Out = RULETABLE(R, C) XOR\ Out}$
3. C=C+1 in a modular fashion.
4. PTR=PTR-1
5. end

Encryption Algorithm (I', KEY1)

1. for $\boldsymbol{i = 1}$ ……$\boldsymbol{m}$ do
2. for $\boldsymbol{j = 1}$ ……$\boldsymbol{n}$ do
3. out= I' (i, j)
4. convert $\boldsymbol{Key1}$ in binary value with eight-bit representation.
5. $\boldsymbol{T = LSB(Key1)}$
6. $\boldsymbol{R = key1(Key1(7) to\ key1(4))}$
7. $\boldsymbol{C = key1(Key1(3) to\ key1(1))}$
8. $\boldsymbol{PTR = sum\ (i, j), summation\ in\ a\ modular\ airthmatic\ fashion\ with\ mod\ 8ight}$
9. **If** $\boldsymbol{T == 1}$
10. $\boldsymbol{Ruletable \leftarrow Ruletable\ I}$
11. Call Encryption module (C, R, PTR)
12. else T== **0** then
13. $\boldsymbol{Ruletable \leftarrow Ruletable\ II}$
14. Call Encryption module (C, R, PTR)
15. endif
16. $\boldsymbol{\Omega(i, j) \leftarrow out}$
17. $\boldsymbol{Key1 = I'\ (i, j)}$
18. end for
19. end for

Algorithm 3 Decryption Algorithm

Decryption Algorithm (I', KEY1)

1. for $\boldsymbol{i = 1}$ ……$\boldsymbol{..m}$ do
2. for $\boldsymbol{j = 1}$ ……$\boldsymbol{n}$ do
3. convert $\boldsymbol{Key1}$ in binary value with eight-bit representation.
4. $\boldsymbol{T = LSB(Key1)}$
5. $\boldsymbol{R = key1(Key1(7) to\ key1(4))}$
6. $\boldsymbol{C = key1(Key1(3) to\ key1(1))}$
7. $\boldsymbol{PTR = sum\ (i,j), summation\ in\ a\ modular\ airthmatic\ fashion\ with\ mod\ eight}$
8. $\boldsymbol{Temp \leftarrow \Omega(i,j)}$
9. **If** $\boldsymbol{T == 1}$
10. $\boldsymbol{Ruletable \leftarrow Ruletable\ I}$
11. Call Decryption module (C, R, PTR)
12. else T== **0** then
13. $\boldsymbol{Ruletable \leftarrow Ruletable\ II}$
14. Call Decryption module (C, R, PTR)
15. temp=255-temp
16. endif
17. $\boldsymbol{Key1 = Decrypted_image(i,j)}$ = temp
18. end for
19. end for

Decryption module (C, R, PTR)

1. **col= ((col+PTR-1)% 8)+1**
2. PTR=8-PTR
3. while $\boldsymbol{PTR \neq 0}$ do
4. $\boldsymbol{temp = RULETABLE(R,C) XOR\ (temp)}$
5. C=C+1 in a modular fashion.
6. PTR=PTR-1
7. end

3) Decryption Algorithm

Step 1: At the receiver's end, *KEY*1 and the initial seed of Henon chaotic map are transmitted through a secure channel.

Step 2: It is assumed that these rule tables are public and one who is connected to the network can access it. Therefore, security relies upon the key *KEY*1 and the P Box's initial seeds. A detailed procedure of the decryption process is explained in Algorithm 3. Which operates it first on the encrypted image $\boldsymbol{\Omega}$ to obtain the $\boldsymbol{I'}$. (that is still a shuffled image)

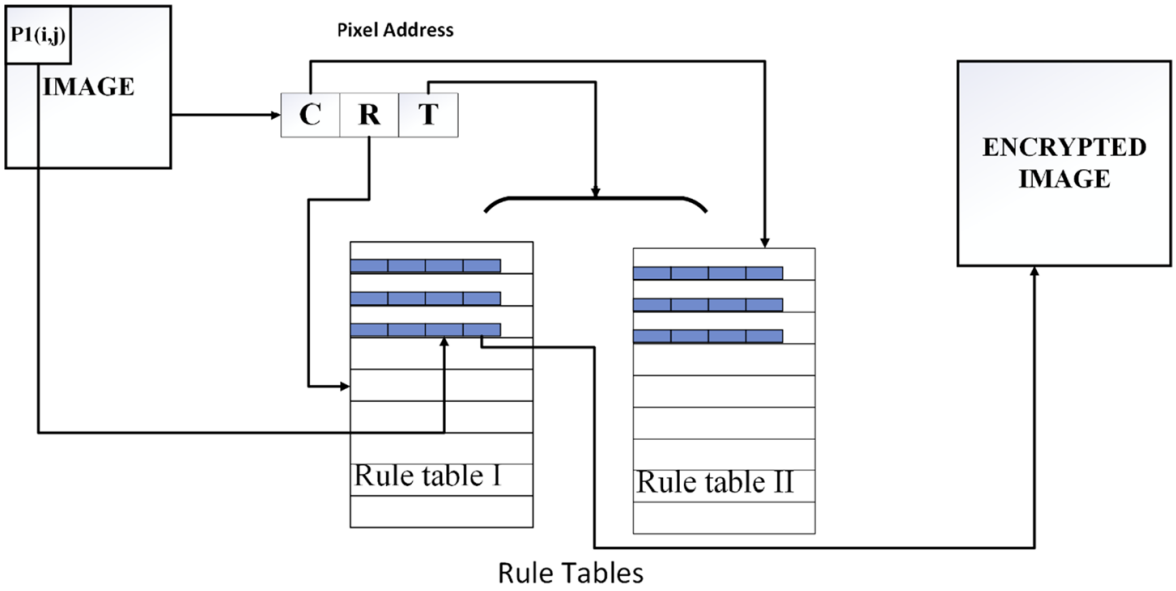

Fig. 5 Visual representation of encryption algorithm

Step 3: The second phase of the decryption algorithm is based on the keyed transposition algorithm. Since the chaotic system behavior is deterministic, so the reconstruction of an image using the same keys X_1 and Y_1 at decryption end gives the decrypted image. At the receiver end, pseudorandom numbers are generated with secret keys and henon map, which are further used to get back pixel values at their original positions. This shuffled image $\boldsymbol{I'}$ is further arranged in order exactly opposite of the way done for encryption. Further shuffling of pixels in the shuffled image in reverse direction produces the original image ($\boldsymbol{I}$).

4 Experimental results

In this section, the experimental results of the proposed image encryption algorithm are explained and discuss the efficiency and performance of the proposed algorithm. MATLAB R2015a software has been used for simulation and implementing the proposed algorithm. In the first phase, we have extracted rule tables by analyzing all eight-bit numbers using MATLAB. Standard input grayscale and color images of size $\mathbf{256 \times 256}$ are shown in Figs. 6 and 7. respectively. The secret symmetric key for encryption is $\boldsymbol{X_1 = 0.1231, Y_1 = 0.1231}$ is selected to initiate the P Box. Extracted State attractors tables, which are discussed in Section 2.2, are used for the encryption algorithm. The initial key $\boldsymbol{KEY1 = 15}$ is selected for the simulation process. The proposed algorithm is also applied to color images as well; here, standard Lena.jpeg is selected for that purpose. Similar mechanisms are applied to all three channels of a color image separately. Several test cases are performed to judge the efficiency of the proposed cryptosystem discussed in this section. In order to validate the correctness and efficiency of the proposed algorithm, we have compared the experimental results to existing algorithms given in [21, 26, 27, 38].

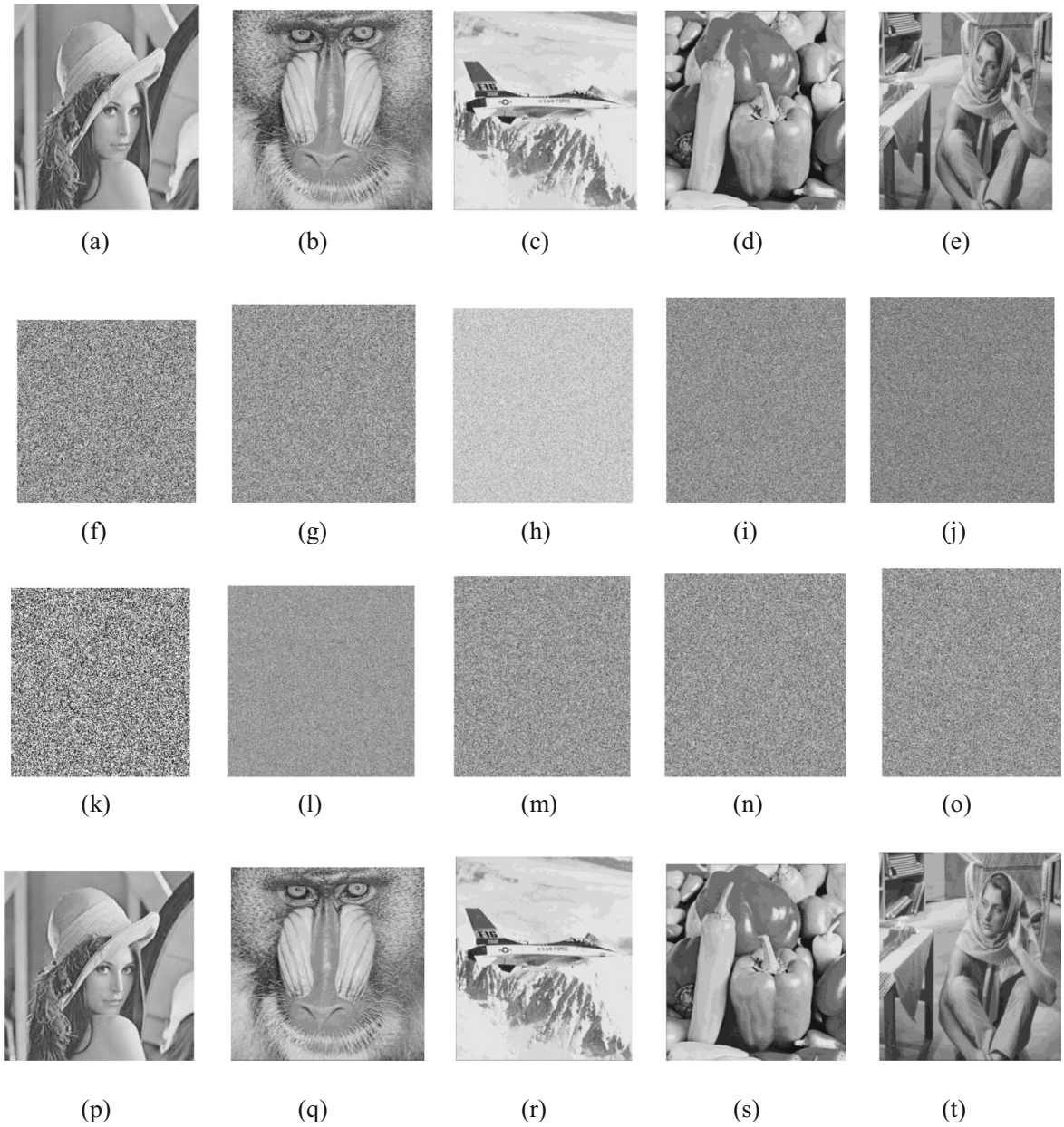

Fig. 6 visual illustration of plain images: (**a**) Lena (**b**) Baboon (**c**) Airplane (**d**) Peppers (**e**) Barbara; shuffled Images in the same order:: (**f**) Leena (**g**) Baboon (**h**) Airplane (**i**) Peppers (**j**) Barbara; Encrypted images:: (**k**) Leena (**l**) Baboon (**m**) Airplane (**n**) Peppers (**o**) Barbara; Decrypted images obtained by the proposed algorithm:: (**p**) Lena (**q**) Baboon (**r**) Airplane (**s**) Peppers (**t**) Barbara

4.1 Entropy analysis

In 1949, Shannon proposed a mathematical equation to calculate the uncertainty and randomness of the information source. Shannon entropy is also used as a primitive measure to check uncertainty within an image [13]. If Shannon entropy is calculated near to eight, it indicates that the encrypted image has uniformly distributed pixels with a high order of randomness and the texture of an image is so complex and unreadable; it is the ideal case of encryption. In permutation cipher, the entropy of a cipher image always remains the same as the original image because in permutation cipher, pixels are shifted to other ordinates within the image and the information could be accessible cipher images; Therefore, the entropy of encrypted image decides the ability of cryptosystem. Therefore,

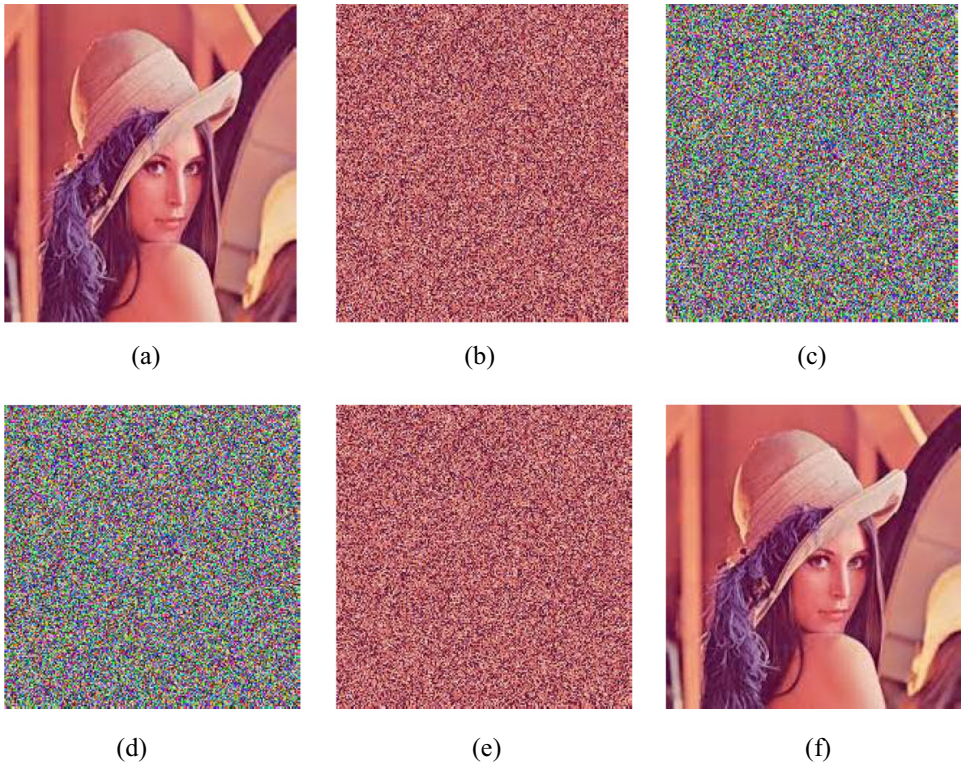

Fig. 7 Visual representation of color image at sender end (**a**) input test image :Lena , (**b**) Shuffled image of Lena after applying P BOX (**c**) Encrypted image of Lena. Visual representation of color image at receiver end by the proposed scheme: (**d**) Encrypted image (**e**) Image after applying CA based cryptosystem (**f**) Decrypted image

confusion is not the complete solution to encrypt an image; a combination of confusion and diffusion makes it more effective. Shannon entropy formula can be seen in Eq. (6), and the obtained values after the equation are demonstrated and compared with other techniques in Table 4.

$$H(X) = -\sum_{i=0}^{N-1} P_i \log_2 P_i \tag{6}$$

4.2 Keyspace analysis

The reliability of the cryptosystem is based on the keyspace. The keys X_1, Y_1 are used in this algorithm to carry forward the conformation originated from the Henon map according to the initial conditions. Which contributes to the confusion as well as the decryption process. The computational precision for 64-bit double-precision numbers is 10^{-15}; it is based on the IEEE floating-point standard format [33]. Thus, for henon chaotic map, the user can configure 64 ×

Table 4 Entropy analysis scores comparison

Test images	Entropy (original image)	Entropy (encrypted image) Proposed	Ref. [26]	Ref. [21]	Ref. [38]	Ref. [27]
Leena	7.4318	7.9922	7.9909	7.9927	7.9646	7.8232
Baboon	7.2283	7.9934	7.9912	7.9934	7.9823	7.4069
Airplane	6.8114	7.9830	–	7.9837	–	7.0227
Peppers	7.5807	7.9937	–	7.9961	–	7.5378
Barbara	7.3986	7.9922	–	7.9942	–	7.3056

(a) (b)

Fig. 8 Key sensitivity analysis (**a**) Lena (I), (**b**) cipher image with a wrong encryption key

64 bit keyspace. In addition, Key *KEY*1 is also used to initiate the encryption algorithm, and it needs an 8-bit space in memory. Therefore, the keyspace for the proposed algorithm reaches $64 \times 64 \times 8$. Interestingly for every pixel, a new key is selected; thus, it is also based on the size of an image; Thus, key length $\cong 64 \times 64 \times 8 \times m \times n$.

4.3 Key sensitivity test

It is assumed that the proposed system is public, and it is open for all the users; thus, security relies upon the key. The proposed system is sensitive to its keys. A slight change in the key generates a different result than applying the original key pair. We have replaced the key values from $\boldsymbol{X_1 = 0.1231, Y_1 = 0.1231}$ to $\boldsymbol{X_1{}' = 0.12310001, Y_1{}' = 0.1231000021,}$ and the obtained image is shown in Fig. 8. It can be observed that the generated image at the receiver end is entirely different from the original image (that was supposed to generate with the original key values).

4.4 Correlation analysis

It is a statistical measure to find the closeness of two variables or datasets. Correlation is also calculated to determine the pixel strength within an image; based on it, texture can be classified. When the correlation of plain image is calculated, it is found either positive or negative, whereas the correlation of encrypted image must be near to ≅0 as shown in Fig. 8. When correlation is

Table 5 Correlation analysis and comparison of colour image

Color Image	Orientation	Red Channel	Green Channel	Blue Channel
Plain Image (Lena)	Horizontal	0.962	0.9683	0.985
	Vertical	0.9015	0.9466	0.9621
	Diagonal	0.87	0.91	0.9402
Cipher (proposed)	Horizontal	0.0141	0.0304	−0.00278
	Vertical	−0.0094	0.0034	−0.0083
	Diagonal	0.0159	−0.00170	0.0014
Ref. [26]	Horizontal	−0.0463	0.04359	0.01369
	Vertical	−0.05877	−0.0682	−0.0688
	Diagonal	−0.0200	−0.0052	0.0127

Table 6 Correlation analysis of gray scale images

Color Image	Orientation	Test input image	Proposed algorithm
Lena	Horizontal	0.9457	0.0006
	Vertical	0.9751	−0.0227
	Diagonal	0.9102	0.0247
Baboon	Horizontal	0.8723	0.0135
	Vertical	0.8321	−0.0041
	Diagonal	0.7821	0.0107
Airplane	Horizontal	0.9301	0.0051
	Vertical	0.9632	−0.0150
	Diagonal	0.9.20	0.0185
Peppers	Horizontal	0.9615	−0.0164
	Vertical	0.9670	0.0297
	Diagonal	0.9408	−0.0146
Barbara	Horizontal	0.9393	0.0053
	Vertical	0.9515	−0.0035
	Diagonal	0.9061	−0.0111

found near to ideal value, it is considered that the encryption scheme is an effective scheme. Correlation analysis is conducted within an image on pixels with respect to their neighborhood pixels [25]. For the simulation of correlation analysis, we have selected 2000 random pixels along with their neighbor pixel in horizontal, vertical, and diagonal directions of original as well as encrypted images. The formula of correlation analysis is given in Eqs. (7), (8), (9). Correlation analysis of different schemes and the proposed algorithm are shown in Tables 5 and 6. correlation visual representation of Fig. 7a is illustrated in Fig. 9.

$$D(r) = \frac{1}{N}\sum_{i=1}^{N}[r_i - E(r)]^2 \tag{7}$$

$$Cov(r,s) = \frac{1}{N}\sum_{i=1}^{N}[r_i - E(r)][S_i - E(s)] \tag{8}$$

$$r_{r,s} = \frac{Cov(r,s)}{\sqrt{D(r)}\sqrt{D(s)}} \tag{9}$$

4.5 Histogram analysis

Histogram of an image is a visual representation of pixel intensity values. It is not the measurement to challenge any type of statistical attack [35]. However, obtaining authorized information from an encrypted image for an intruder is not easy, whose histogram is evenly distributed. The intensities of pixels are plotted on the scale of intensity level versus a count of pixel intensity. In gray test images, there are 256 distinct intensities plotted with the help of a histogram (Fig. 10).

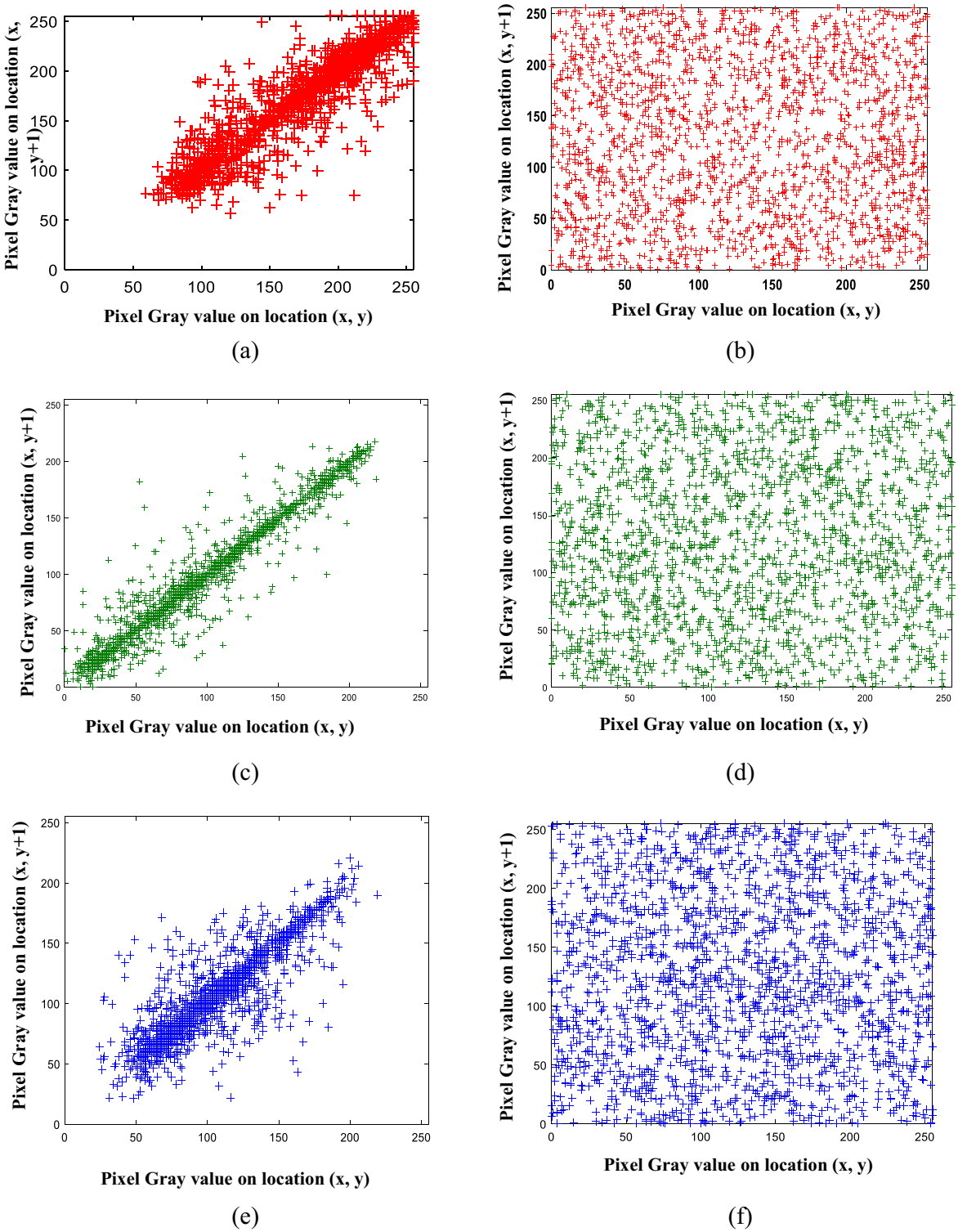

Fig. 9 Correlation plot of two adjacent plain-image pixels of Lena in horizontal direction for the (**a**) red channel, (**c**) green channel, and (**e**) blue channel. Correlation plot of two adjacent pixels of the cipher-image obtained by the proposed scheme: (**b**) red channel (**d**) green channel (**f**) blue channel

4.6 Differential attack

4.6.1 1) NPCR 2) UACI

The differential attack is an unethical way to disrupt the encryption algorithm. Intruders typically make little changes to the plain image (e.g., alter only one pixel or slight changes in a key) to

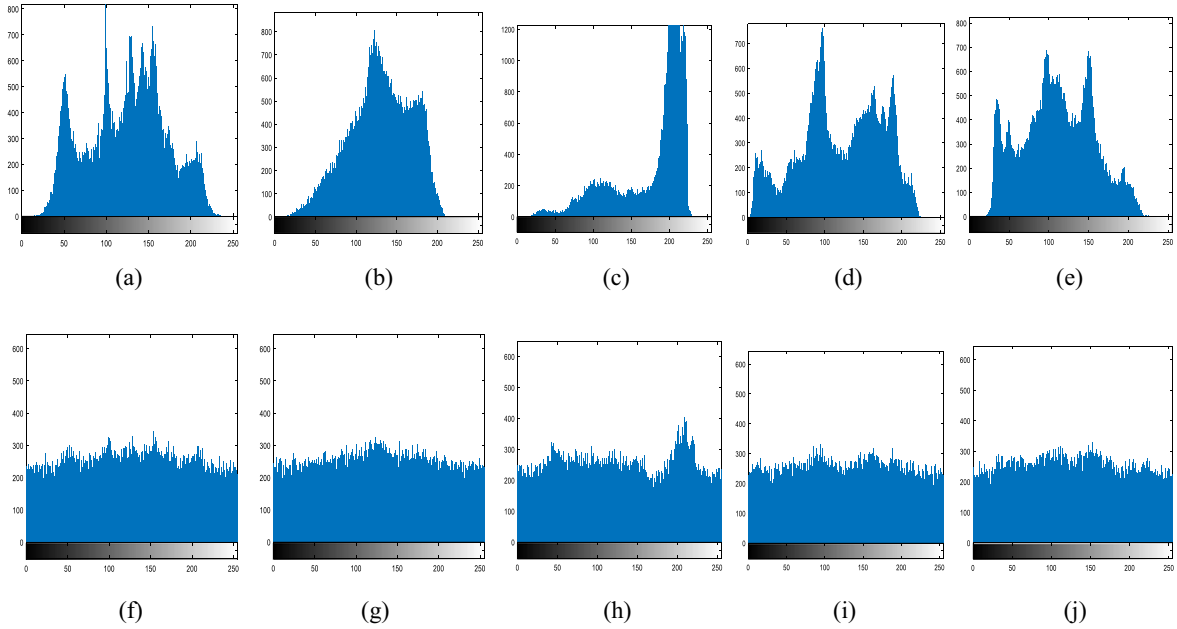

Fig. 10 Histogram plot of grayscale Images: (**a**) Leena (**b**) Baboon (**c**) Airplane (**d**) Peppers (**e**) Barbara; Histogram of encrypted images by the proposed scheme: (: (**f**) Leena (**g**) Baboon (**h**) Airplane (**i**) Peppers (**j**) Barbara

observe the working technique of the encryption algorithm. By comparing the differences, the cryptanalyst can detect the subtle relationship between the plain image and the resulting cipher image. The number of changing pixel rate (NPCR) and unified average changed intensity (UACI) tests are performed on two encrypted images [4]. Encrypted C image originates from the original image and the other Encrypted image C' is found by changing one pixel in the original image to determine the strength against differential attack. Theoretical ideal values of NPCR and UACI scores are 1 and 0.33, respectively (Tables 7).

$$NPCR = \frac{\sum_{(i,j)} D(i,j)}{m \times n} \times 100\% \tag{10}$$

$$where\ D(i,j) \begin{cases} 1 & if\ \left(C(i,j) \neq C'(i,)\right) \\ 0 & if\ \left(C(i,j) = C'(i,)\right) \end{cases}$$

$$UACI = \frac{1}{m \times n} \left(\sum_{i,j} \frac{|C\ (i,j) - C'(i,j)|}{255} \right) \times 100\% \tag{11}$$

Table 7 NPCR and UACI scores of the Test input image

position	Image	Original value	Modified Value	NPCR	UACI
(174,50)	Lena	234	235	0.992	0.334
(174,47)	Baboon	172	171	0.996	0.339
(200,200)	Airplane	79	80	0.993	0.331
(1,1)	Peppers	61	62	0.994	0.332
(187,245)	Barbara	237	238	0.998	0.331

Table 8 PSNR analysis and comparison

Test images	Proposed Scheme	Ref. [21]	Ref. [38]	Ref. [27]
Lena	27.60	28.50	65.12	28.46
Baboon	27.38	29.46	42.56	28.56
Airplane	25.9198	28.01	–	25.59
Peppers	27.7218	28.38	–	28.40
Barbara	28.1030	29.12	–	29.07

4.7 Perceptual security: peak signal-to-noise ratio (PSNR)

PSNR usually applies to signal to check the distortion level and the quality after retrieval at the other end. In cryptography, PSNR measures the perceptual security of the proposed algorithm, and it is calculated between the original image and its cipher image. Researchers suggest that the lower values of PSNR indicate that a proposed system encrypt the multimedia efficiently. Before calculating PSNR, the Mean square error (MSE) value is also calculated, and it must be on the higher side of the scale. Table 8 shows the PSNR test (original, cipher image) of grayscale images. The following equation calculates PSNR (in dB):

$$MSE = \frac{1}{m \times n} \sum_{i=0}^{m-1} \sum_{j=0}^{n-1} \left[(I(i,j) - \Omega(\mathrm{i},\mathrm{j}))^2 \right] \tag{12}$$

$$PSNR = 10\log_{10}\left(\frac{255^2}{MSE}\right) \tag{13}$$

Where $I(i,j)$ and Ω (i, j) represents the original image and cipher image, respectively.

5 Conclusion and future work

The proposed algorithm has been applied to color and grayscale images. Several test cases are applied to the test images to demonstrate the efficiency of the proposed cryptosystem. It can be observed that the proposed algorithm is lightweight in nature and resistant to all types of statistical attacks. The keyed transposition algorithm is designed for images to disturb the correlation among pixels with an excellent amount of keyspace. ECA is popular due to its implementation process, i.e., it takes minimum resources to be implemented either on software or hardware platforms. In this paper, ECA's dynamic properties are extracted and analyzed to obtain the rule tables using rule 15. These rule tables are used as a lookup table for each pixel of an image, and bitwise operations are performed on a pixel to generate a cipher pixel. Since IoT device's memory and computational abilities are limited, these rule tables can play a significant role in security algorithms to provide security with low computational complexity. It can also save device power consumption and reduce computational overhead in real-time computing. The other rules can be studied and analyzed for cryptography usage along with bulky sized multimedia format. Also, the cryptosystem can be implemented for the sensor's real-time data using steganography technique. It is evident based on experimental results that the proposed algorithm is reliable, robust, and adaptable in IoT and sensor networks and can protect digital images from active and passive attacks in the public communication channels.

References

1. Abdo AA, Lian S, Ismail IA, Amin M, Diab H (2013) A cryptosystem based on elementary cellular automata. Commun Nonlinear Sci Numer Simul 18(1):136–147. https://doi.org/10.1016/j.cnsns.2012.05.023
2. Abdulla AA (2015) Exploiting similarities between secret and cover images for improved embedding efficiency and security in digital steganography. Doctoral dissertation University of Buckingham. http://bear.buckingham.ac.uk/id/eprint/149
3. Ahlawat S, Choudhary A, Nayyar A, Singh S, Yoon B (2020) Improved Handwritten Digit Recognition Using Convolutional Neural Networks (CNN). Sensors 20(12):3344. https://doi.org/10.3390/s20123344
4. Ahmad J, Khan MA, Ahmed F, Khan JS (2017) A novel image encryption scheme based on orthogonal matrix, skew tent map, and XOR operation. Neural Comput & Applic 30(12):3847–3857. https://doi.org/10.1007/s00521-017-2970-3
5. Azza AA, Lian S (2020) Multi-secret image sharing based on elementary cellular automata with steganography. Multimed Tools Appl 79.29–30:21241–21264. https://doi.org/10.1007/s11042-020-08823-8
6. Babaei A, Motameni H, Enayatifar R (2020) A new permutation-diffusion-based image encryption technique using cellular automata and DNA sequence. Optik 203:164000. https://doi.org/10.1016/j.ijleo.2019.164000
7. Baek J, Wang L, Yang J (2018) A privacy preserving and fine-grained access control scheme in DaaS based on efficient DSP re-encryption. Int J High Perform Comput Networking 11(3):231. https://doi.org/10.1504/ijhpcn.2018.10012999
8. Bhattacharjee K, Naskar N, Roy S, Das S (2018) A survey of cellular automata: types, dynamics, non-uniformity and applications. Nat Comput 19(2):433–461. https://doi.org/10.1007/s11047-018-9696-8
9. Borriello E, Imari Walker S (2017) An Information-Based Classification of Elementary Cellular Automata. Complexity 2017:1–8. https://doi.org/10.1155/2017/1280351
10. Chai X (2017) An image encryption algorithm based on bit level Brownian motion and new chaotic systems. Multimed Tools Appl 76(1):1159–1175. https://doi.org/10.1007/s11042-015-3088-1
11. Dooley JF (n.d.) Cipher Mysteries," History of Cryptography and Cryptanalysis. Springer International Publishing, pp. 263–292, doi: https://doi.org/10.1007/978-3-319-90443-6_16.
12. Enayatifar R, Guimarães FG, Siarry P (2019) Index-based permutation-diffusion in multiple-image encryption using DNA sequence. Opt Lasers Eng 115:131–140. https://doi.org/10.1016/j.optlaseng.2018.11.017
13. Flores-Gallegos N (2016) A new approach of Shannon's entropy in atoms. Chem Phys Lett 650:57–59. https://doi.org/10.1016/j.cplett.2016.02.061
14. Gadekallu TR, Khare N, Bhattacharya S, Singh S, Maddikunta PKR, Srivastava G, (2020), "Deep neural networks to predict diabetic retinopathy," J Ambient Intell Humaniz Comput, doi: https://doi.org/10.1007/s12652-020-01963-7.
15. Gadekallu TR, Rajput DS, Reddy MPK, Lakshmanna K, Bhattacharya S, Singh S, Jolfaei A, Alazab M, (2020), "A novel PCA–whale optimization-based deep neural network model for classification of tomato plant diseases using GPU," J Real-Time Image Proc, doi: https://doi.org/10.1007/s11554-020-00987-8.
16. Gardner M (1970) Mathematical games. Sci Am 223(4):120–123. https://doi.org/10.1038/scientificamerican1070-120
17. Ghazanfaripour H, Broumandnia A (2020) Designing a digital image encryption scheme using chaotic maps with prime modular. Opt Laser Technol 131:106339. https://doi.org/10.1016/j.optlastec.2020.106339
18. Gupta BB, Tewari A (2019) A novel ECC-based lightweight authentication protocol for internet of things devices. Int J High Perform Comput Networking 15.1/2:106. https://doi.org/10.1504/ijhpcn.2019.10025215
19. Hussain S, Chaudhry SA (2019) Comments on 'Biometrics-Based Privacy-Preserving User Authentication Scheme for Cloud-Based Industrial Internet of Things Deployment. IEEE Internet Things J 6(6):10936–10940. https://doi.org/10.1109/jiot.2019.2934947
20. Jadhav R, VV (2017) Security issues and solutions in wireless sensor networks. Int J Comput Appl 162(2):14–19. https://doi.org/10.5120/ijca2017913256
21. Jin J (2012) An image encryption based on elementary cellular automata. Opt Lasers Eng 50(12):1836–1843. https://doi.org/10.1016/j.optlaseng.2012.06.002
22. Kamilya S, Das S (2018) A study of Chaos in cellular automata. Int J Bifurcation Chaos 28(03):1830008. https://doi.org/10.1142/s0218127418300082
23. Kaushik S, Gandhi C (2019) Ensure hierarchal identity based data security in cloud environment. Int J Cloud Appl Comput 9(4):21–36. https://doi.org/10.4018/ijcac.2019100102
24. Kemeny JG (1967) Theory of self-reproducing automata. John von Neumann. Edited by Arthur W. Burks. University of Illinois Press, Urbana, 1966. 408 pp., illus. $10. Science 157(3785):180. https://doi.org/10.1126/science.157.3785.180
25. Kumar A, Raghava NS (2020) Selective colour image encryption using Hénon chaotic system with a keyless substitution cipher. Eng Appl Sci Res 47(1):66–76

26. Li C, Luo G, Qin K, Li C (2016) An image encryption scheme based on chaotic tent map. Nonlinear Dyn 87(1):127–133. https://doi.org/10.1007/s11071-016-3030-8
27. Li Y, Wang C, Chen H (2017) A hyper-chaos-based image encryption algorithm using pixel-level permutation and bit-level permutation. Opt Lasers Eng 90:238–246. https://doi.org/10.1016/j.optlaseng.2016.10.020
28. Mayer RE (2002) Multimedia learning, in Psychology of learning and motivation, 41, Elsevier, pp. 85–139
29. McAndrew A (2016) Introduction to cryptography with open-source software. CRC Press, doi: https://doi.org/10.1201/9781439825716
30. McGee AR, Chandrashekhar U, Richman SH (2004) Using ITU-T X.805 for comprehensive network security assessment and planning, 11th International Telecommunications Network Strategy and Planning Symposium. NETWORKS,. IEEE, doi: https://doi.org/10.1109/netwks.2004.240993.
31. Moran A, Frasser CF, Roca M, Rossello JL (2020) Energy-efficient pattern recognition hardware with elementary cellular automata. IEEE Trans Comput 69(3):392–401. https://doi.org/10.1109/tc.2019.2949300
32. (2019), MSB based Cellular Automata for Edge Detection, Int J Innov Technol Explor Eng, 8.9, pp. 1354–1358, doi: https://doi.org/10.35940/ijitee.i7491.078919.
33. Murugan B, Nanjappa Gounder AG (2016) Image encryption scheme based on block-based confusion and multiple levels of diffusion. IET Comput Vis 10(6):593–602. https://doi.org/10.1049/iet-cvi.2015.0344
34. Parker AT, Short KM (2001) Reconstructing the keystream from a chaotic encryption scheme. IEEE Trans Circuits Systems I Fund Theory Appl 48(5):624–630. https://doi.org/10.1109/81.922466
35. Ravichandran D, Malayappan S, Manavalan R, Madhuri P, Amirtharajan R (2019) A 3D Key for Encrypting 2D Images - A DNA Melded Chaotic Approach, International conference on vision towards emerging trends in communication and networking (ViTECoN). IEEE, doi: https://doi.org/10.1109/vitecon.2019.8899349.
36. Rey AM (n.d.) Message Authentication Protocol Based on Cellular Automata, Lecture Notes in Computer Science. Springer Berlin Heidelberg, pp. 52–60, doi: https://doi.org/10.1007/978-3-540-71805-5_6.
37. Riahi Sfar A, Natalizio E, Challal Y, Chtourou Z (2018) A roadmap for security challenges in the internet of things. Digit Commun Netw 4(2):118–137. https://doi.org/10.1016/j.dcan.2017.04.003
38. Roy S, Rawat U, Sareen HA, Nayak SK (2020) IECA: an efficient IoT friendly image encryption technique using programmable cellular automata. J Ambient Intell Humaniz Comput 11:5083–5102. https://doi.org/10.1007/s12652-020-01813-6
39. Sanchez-Avila C, Sanchez-Reillol R (n.d.) The Rijndael block cipher (AES proposal): a comparison with DES," Proceedings IEEE 35th Annual 2001 International Carnahan Conference on Security Technology (Cat. No.01CH37186). IEEE, doi: https://doi.org/10.1109/ccst.2001.962837.
40. Seredynski F, Bouvry P, Zomaya AY (2004) Cellular automata computations and secret key cryptography. Parallel Comput 30.5–6:753–766. https://doi.org/10.1016/j.parco.2003.12.014
41. Shifa A, Asghar MN, Fleury M (2016) Multimedia security perspectives in IoT, in 2016 Sixth International Conference on Innovative Computing Technology (INTECH), pp. 550–555
42. Singh S, Sharma PK, Moon SY, Park JH (2017) Advanced lightweight encryption algorithms for IoT devices: survey, challenges and solutions, J Ambient Intell Humaniz Comput, doi: https://doi.org/10.1007/s12652-017-0494-4.
43. Sreelaja NK, Pai GAV (2012) Stream cipher for binary image encryption using ant Colony optimization based key generation. Appl Soft Comput 12(9):2879–2895
44. Wolfram S (n.d.) Cryptography with Cellular Automata, Lecture Notes in Computer Science. Springer Berlin Heidelberg, pp. 429–432, doi: https://doi.org/10.1007/3-540-39799-x_32.
45. Zheng Q, Wang X, Khurram Khan M, Zhang W, Gupta BB, Guo W (2018) A lightweight authenticated encryption scheme based on chaotic SCML for railway cloud service. IEEE Access 6:711–722. https://doi.org/10.1109/access.2017.2775038

Publisher's note Springer Nature remains neutral with regard to jurisdictional claims in published maps and institutional affiliations.

Affiliations

Ashish Kumar[1] · **N. S. Raghava**[2]

[1] Department of Information Technology, Delhi Technological University, Delhi, India

[2] Department of Electronics and Communication Engineering, Delhi Technological University, Delhi, India

Hindawi
Mathematical Problems in Engineering
Volume 2021, Article ID 6565841, 10 pages
https://doi.org/10.1155/2021/6565841

Research Article

An Intelligent PI Controller-Based Hybrid Series Active Power Filter for Power Quality Improvement

Arjun Baliyan,[1] **Majid Jamil**,[1] **M. Rizwan**,[2,3] **Ibrahim Alsaidan**,[2] **and Muhannad Alaraj**[2]

[1]*Department of Electrical Engineering, Jamia Millia Islamia, New Delhi 110025, India*
[2]*Department of Electrical Engineering, College of Engineering, Qassim University, Buraydah 52571, Qassim, Saudi Arabia*
[3]*Department of Electrical Engineering, Delhi Technological University, Delhi 110042, India*

Correspondence should be addressed to Arjun Baliyan; arjunbaliyaneee@gmail.com

Received 15 July 2020; Revised 10 January 2021; Accepted 15 February 2021; Published 28 February 2021

Academic Editor: Fotios Georgiades

Copyright © 2021 Arjun Baliyan et al. This is an open access article distributed under the Creative Commons Attribution License, which permits unrestricted use, distribution, and reproduction in any medium, provided the original work is properly cited.

The quality of power that is degrading day by day is an important issue for all the consumers. The important factor for this is harmonics in the voltage and current waveforms which can be resolved by the use of hybrid series active power filter. The combination consists of a series active power filter and a shunt passive filter connected in parallel to the load. The method used in this paper is for the purpose of achieving good harmonic compensation and reduced total harmonic distortion for various types of nonlinear loads as per the standards of IEEE 519. The proposed HSAPF technique uses the synchronous reference frame method for generating the compensating signal with an intelligent PI controller that uses particle swarm optimization (PSO) technique to obtain the required gain values needed to improve the steady state response of the system. The concept of vigorous HSAPF has been authenticated through MATLAB simulation analysis, and the results obtained validate the accuracy of the method for the different load conditions.

1. Introduction

In the recent times, due to the increase in the power demand, the quality of the power supply has deteriorated drastically at a very rapid rate. The main reason behind this is the use of nonlinear loads in the system which injects harmonics in the system, and therefore, it not only distorts the current and voltage waveform but also leads to poor power factor of the supply system [1].

Hence, it is required to compensate these harmonics generated due to nonlinear loads in the system. Conventionally, only passive filters were used for harmonic mitigation because of the simple advantage that they were cost effective and reliable, but on the other side, many drawbacks such as resonance and mistuning lead to their discontinuity in the system [2, 3]. These drawbacks were recently overcome by the use of shunt active power filters in the system which behaves as a current source and compensates the harmonics injected by the nonlinear loads in the system. Active power filters inject the same harmonics in the system as that of load, but they are opposite in phase to the load harmonics.

However, they were not preferable in the large systems due to cost limitations, and hence, series active power filter came in the late 80s as a possible solution to the existing APFs. The different combinations of these series and shunt active power filters have efficiently removed the harmonics in the source current as well as in the load voltage. However, they also have the demerit of being expensive and high inverter losses [4, 5]. Consequently, to overcome all these drawbacks and to have better harmonic mitigation with reduced overall cost, a novel hybrid series active power filter along with the artificial neural network-based PI controller [6] is proposed in the paper. Out of the different combinations of the hybrid filters that are used in the literature [7–11], the HSAPF is the most promising one [12]. The other evolutionary algorithms such as genetic algorithm [13], bacterial foraging [14], artificial bee colony [15], and

gravitational search [16] have also been recommended in the last decades, but particle swarm optimization with its simplicity has an edge over the existing techniques. The aim is to reduce the total harmonic distortion in both the load voltage as well as in the source current as per the IEEE standard 519. The first proposal was based on the instantaneous reactive power theory [17, 18]. Here, in case of nonideal supply (if $V_{sh}\neq 0$), the product of voltage and current will generate an average component which is not detachable; therefore, to overcome such difficulty, harmonic mitigation using the synchronous reference method is proposed in [19, 20]. This method requires the PLL block to keep the source voltage at the correct phase angle.

The paper is organized as follows. In Section 2, a brief description about the system topology, reference voltage generation technique, harmonic passive filter, and proposed PSO-based PI control strategy have been discussed. In Section 3, experimental results obtained from simulation are described in detail, and Section 4, finally, concludes the paper.

2. Description of System Topology

Hybrid series active power filter with the proposed PI controller that has been used here is the combination of series active power filter and a passive filter connected in parallel to the load. Figure 1 shows the proposed architecture of the above combination. The passive filters that have been used here are used to filter out the 5^{th} and 7^{th} harmonic components along with a high pass filter tuned for a specific frequency. The series APF is a combination of full bridge PWM, a three phase LC filter, and a DC link capacitor. This DC link capacitor provides the reactive energy that is needed to eliminate the harmonics. The LC filter used is to eliminate the ripples from the generated voltage of the inverter. The series APF as the name suggests is connected in series with the load. The artificial neural network-based PI controller used here is for the purpose of improving the steady state response of the system.

2.1. Reference Generation Voltage Technique. The synchronous reference frame method or *dq* method is used to transfer the load voltages from the stationary frame to the rotatory frame and is given as

$$\begin{bmatrix} V_d \\ V_q \end{bmatrix} = \frac{2}{3}\begin{bmatrix} \cos\theta & \cos\left(\theta-\frac{2\pi}{3}\right) & \cos\left(\theta+\frac{2\pi}{3}\right) \\ \sin\theta & \sin\left(\theta-\frac{2\pi}{3}\right) & \sin\left(\theta+\frac{2\pi}{3}\right) \end{bmatrix}\begin{bmatrix} V_{LA} \\ V_{LB} \\ V_{LC} \end{bmatrix}. \tag{1}$$

A PLL has been used to correct the source voltage phase angle which is very much needed for transformation. The V_d and V_q voltages obtained can be further divided into average and oscillating parts:

$$\begin{aligned} V_d &= \overline{V_d} + \widetilde{V_d}, \\ V_q &= \overline{V_q} + \widetilde{V_q}, \end{aligned} \tag{2}$$

where the load voltages are denoted by V_{LA}, V_{LB}, and V_{LC} which contain harmonic components in it. Furthermore, *dq* components are passed from the low-pass filters to eliminate the DC components present in it, and we get the net harmonic contents. After that, by doing the inverse transformation, we can obtain the harmonic components present in the load voltages after the compensation of the passive power filter:

$$\begin{bmatrix} V_{LAH} \\ V_{LBH} \\ V_{LCH} \end{bmatrix} = \begin{bmatrix} \cos\theta & \sin\theta \\ \cos\left(\theta-\frac{2\pi}{3}\right) & \sin\left(\theta-\frac{2\pi}{3}\right) \\ \cos\left(\theta+\frac{2\pi}{3}\right) & \sin\left(\theta+\frac{2\pi}{3}\right) \end{bmatrix}\begin{bmatrix} \widetilde{V_d} \\ \widetilde{V_q} \end{bmatrix}. \tag{3}$$

The same procedure is followed to transfer the source current into the rotating frame which is described below:

$$\begin{bmatrix} I_d \\ I_q \end{bmatrix} = \frac{2}{3}\begin{bmatrix} \cos\theta & \cos\left(\theta-\frac{2\pi}{3}\right) & \cos\left(\theta+\frac{2\pi}{3}\right) \\ \sin\theta & \sin\left(\theta-\frac{2\pi}{3}\right) & \sin\left(\theta+\frac{2\pi}{3}\right) \end{bmatrix}\begin{bmatrix} I_{SA} \\ I_{SB} \\ I_{SC} \end{bmatrix}. \tag{4}$$

In the same way, obtained components contain DC as well as AC quantities, and similarly, we will filter out the DC quantity by using the low-pass filter, so the left out is net harmonic content. Again, after doing the inverse transformation, we can obtain the harmonic content present in the source current described as

$$\begin{bmatrix} I_{SAH} \\ I_{LBH} \\ I_{SCH} \end{bmatrix} = \begin{bmatrix} \cos\theta & \sin\theta \\ \cos\left(\theta-\frac{2\pi}{3}\right) & \sin\left(\theta-\frac{2\pi}{3}\right) \\ \cos\left(\theta+\frac{2\pi}{3}\right) & \sin\left(\theta+\frac{2\pi}{3}\right) \end{bmatrix}\begin{bmatrix} \widetilde{I_d} \\ \widetilde{I_q} \end{bmatrix}. \tag{5}$$

The compensating signal is obtained by the combination of load voltage and the source current which is shown in Figure 2. From this figure, the error between the reference voltage and DC link capacitor voltage of the inverter is fed to the PI controller block, and the output of it is then subtracted from the oscillatory component. The oscillatory component mentioned here is obtained from the output of the low pass filter. Since the extra fundamental components such as ΔV_{caf}, ΔV_{cbf}, and ΔV_{ccf} also get added to the harmonic components, so the reference compensating voltage can be defined as

$$\begin{aligned} V_{ca}^{*} &= KI_{sah} - V_{Lah} + \Delta V_{caf}, \\ V_{cb}^{*} &= KI_{sbh} - V_{Lbh} + \Delta V_{cbf}, \\ V_{cc}^{*} &= KI_{sch} - V_{Lch} + \Delta V_{ccf}. \end{aligned} \tag{6}$$

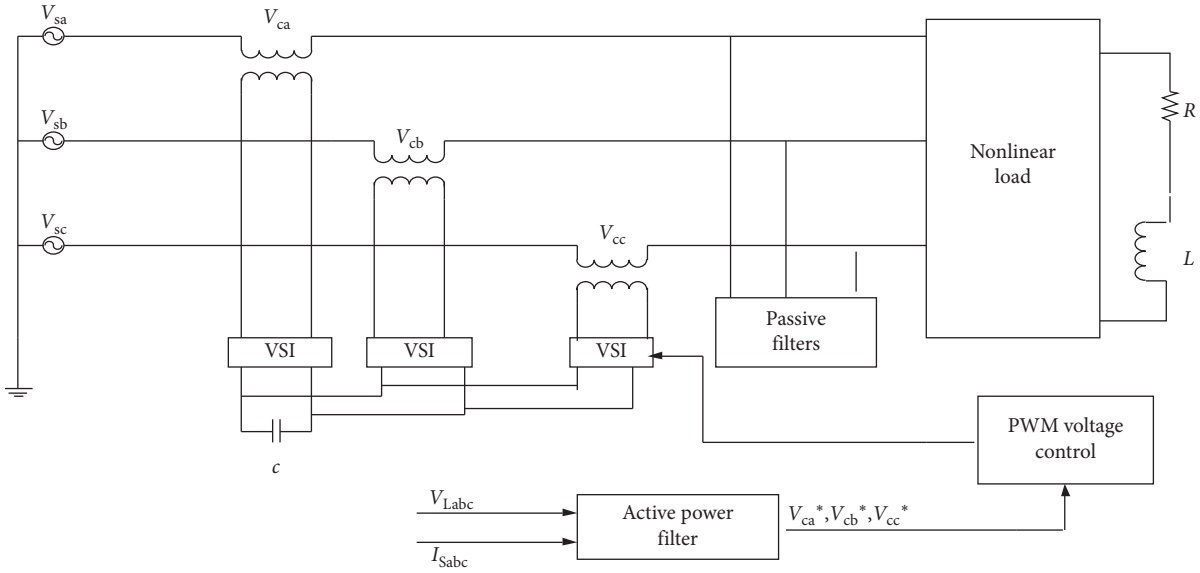

Figure 1: Hybrid series active power filter.

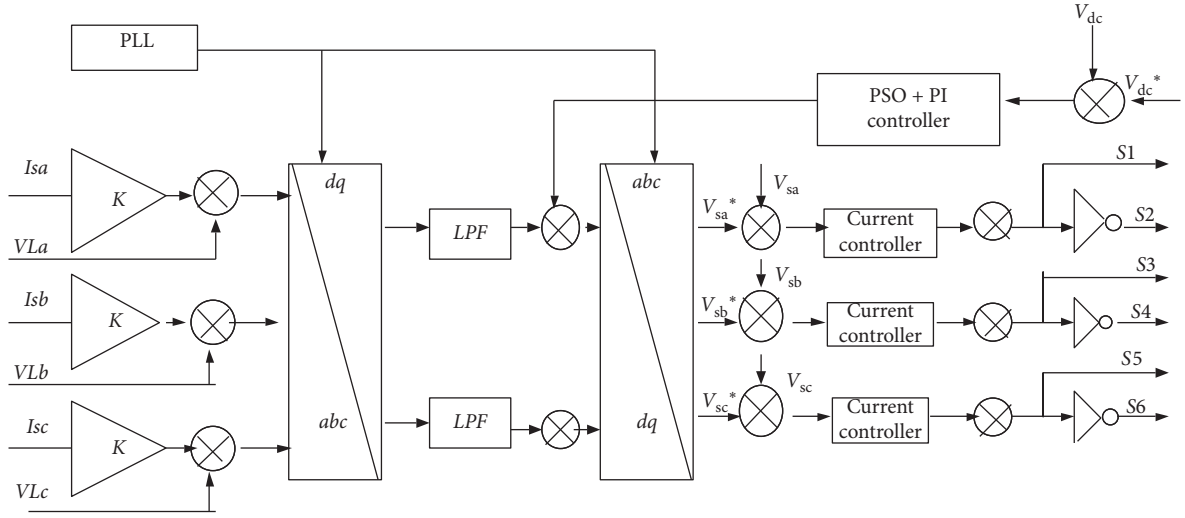

Figure 2: Block diagram for the proposed approach.

These currents I_{sah}, I_{sbh}, and I_{sch} are basically defined as the harmonic components of the source current, whereas V_{Lah}, V_{Lbh}, and V_{Lch} are defined as the harmonic components of the load voltages.

2.2. Harmonic Passive Filter. These filters are used to enhance the quality of the voltage waveform by diverting the current other than the fundamental current or we can say the high frequency component current into the low impedance path. They are usually connected in shunt and also used to provide the reactive power requisite by the load for the purpose of power factor improvement.

In this system, we are using four harmonic passive filters in order to eliminate the 5, 7, 11, and 13th order harmonics. To remove the high frequency component, we are also using the high-pass branch in the circuit. Using the technique recommended in [21], we have calculated the value of elements R, L, and C in such way that it optimizes the performance of the filter. Also, in order to remove the resonance problem, the filter is tuned at the frequency which is less than the harmonic frequency as we know most of the power system components are inductive in nature [22]. Figure 3 describes the passive harmonic filter, and Figure 4 represents the high pass filter or the damped filter.

2.3. Particle Swarm Optimization. In this paper, particle swarm optimization technique has been proposed to study the performance of the hybrid series active power filter. PSO is required here to obtain the optimal values of the gain constant that is required by the PI controller. The proposed algorithm updates the velocity and position of the particles till it reaches the desired objective. Each and every particle in

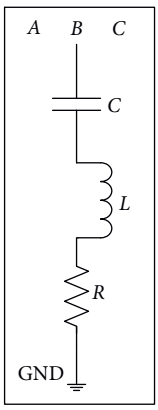

Figure 3: Harmonic passive filter.

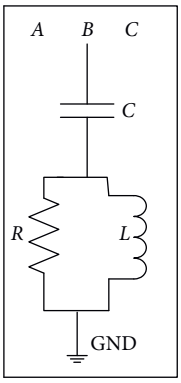

Figure 4: Damped filter.

the workspace is assigned with some arbitrary velocities. All particles search for optimal position in the global space by regularly updating their position and velocity. The particle optimizer checks for the best position attained so far [23]. Hence, based on the above concept tunes, the value of gain constant of the PI controller is such that the error between the V_{dc} and the reference voltage is minimized and it almost reaches the zero value.

The generalized equation for error can be given as

$$\text{Error} = \text{Reference Voltage} - V_{\mathrm{dc}}, \tag{7}$$

where V_{dc} is the DC link capacitor voltage.

The conventional PI controllers were not able to give the accurate results under unbalanced power supply voltage and also in case of severe load changing conditions. Hence, to overcome such issue, the PI controllers are tuned with different intelligent techniques to overcome the above existing issues. The output of the controller can be written as

$$\text{Output} = K_p \cdot e(t) + K_i \int_0^t e(t)\mathrm{d}t. \tag{8}$$

The PSO technique is widely used nowadays because of its simplicity, faster convergence rate, and greater accuracy. The DC link voltage has to be stabilized under severe load variations in the system. The tuning of PI controller parameters is a major challenge under the load changing conditions. Figure 5 represents the block diagram of the design of the PI controller using PSO.

3. Simulation Results

To examine the authenticity of the proposed controller, different types of loads have been taken for the purpose of analysis and are simulated in MATLAB using "Sims Power System Block set." The parameters taken are mentioned in Table 1. The aim of the simulation is to show the effectiveness of the proposed controller in reducing the THD of the system to a significant level. Figure 6 shows the circuit model for different loads taken for the analysis.

3.1. Case 1: Harmonic Compensation in Case of Battery Charger Load. The performance in this case is authenticated through a diode bridge rectifier with a battery charger load. It has been observed from the results that the THD of the load voltage has been reduced from 21.83% to 3.99% and THD in the source current is now reduced to 4.20% which justifies the IEEE standard 519. Figure 7 represents the steady state performance of source current I_s and the load voltage V_L. Figures 8–10 show the FFT analysis of the both source current and the load voltage.

Figure 11 gives the DC link voltage in case of battery charger load.

3.2. Case 2: Harmonic Compensation in Case of RL Load. In this case, the diode bride rectifier with RL load has been taken to see the effect on the THD of the source current and the load voltage. Similarly, Figure 12 represents the source

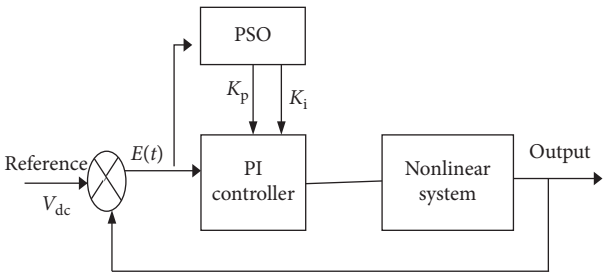

Figure 5: Block diagram representing the PI controller integrated with PSO.

Table 1: System parameters.

Parameters	Values
Line voltage & frequency	$V_s = 220\,\text{V (RMS)}, F_s = 50\,\text{Hz}$
Line impedance	$L_s = 0.5\,\text{mH}, R_s = 0.1\,\text{ohm}$
Nonlinear load	$L_L = 30\,\text{mH}, R_L = 25\,\text{ohm}, C_L = 50\,\mu\text{F}$
Battery charger load	$12\,\text{V}, R_L = 36.5\,\text{ohm}$
Series active filter parameter	$C_c = 60\,\mu\text{F}, L_c = 1.35\,\text{mH}$ $C_{dc} = 1200\,\mu\text{F}, V_{dc} = 85\,\text{V}$
Passive filter parameter	$L_f = 1.86\,\text{mH}, C_f = 60\,\mu\text{F}$
PI controller parameter	$K_p = 1.816, K_I = 1.1511$
T_s and switching frequency	$T_s = 50e-6, f_s = 1\,\text{kHz}$

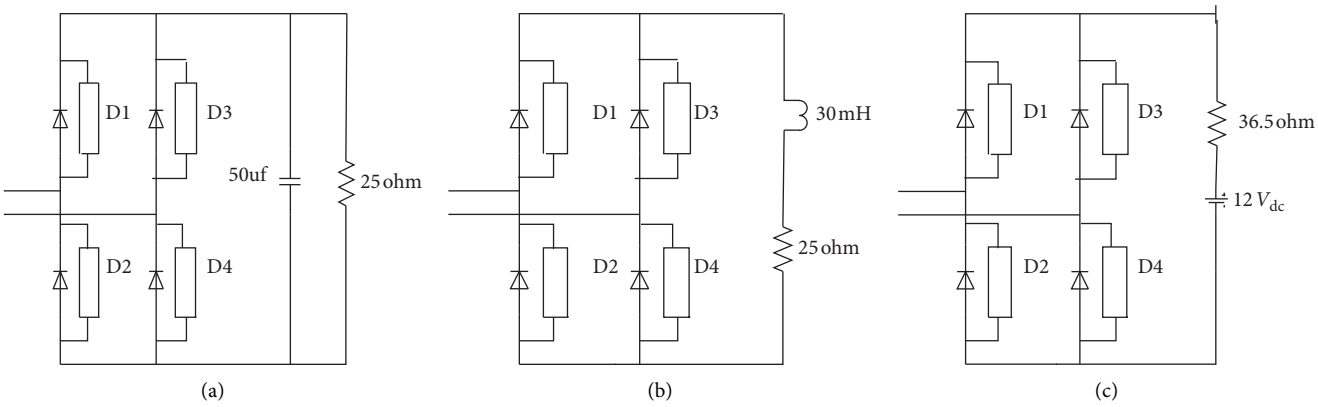

Figure 6: Different models of nonlinear loads: (a) RC load, (b) RL load, and (c) battery charger load.

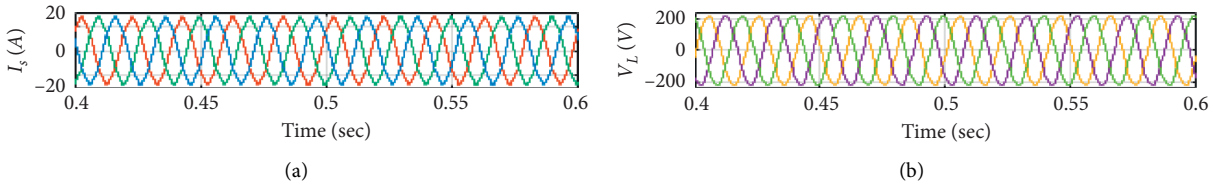

Figure 7: The steady state performance of (a) source current and (b) load voltage.

voltage, source current, and load voltage for this particular case. Finally, from Figures 13–15, we conclude that the THD of the source current has been reduced to 4.37% and the THD of the load voltage is reduced from 36.14% to 4.21% and both of them satisfy the IEEE standard 519. Figure 16 represents the error between the reference and the DC link voltage which is reduced to zero value.

3.3. Case 3: Harmonic Compensation in Case of Both Nonlinear Loads. In this case, the performance of HSAPF with the PI Controller for nonlinear load condition has been evaluated. Figure 17 shows steady state response of the supply current and the load voltage. The simulation results obtained as per Figures 18–20 show that the THD of the source current has been reduced to 4.54% and the THD of

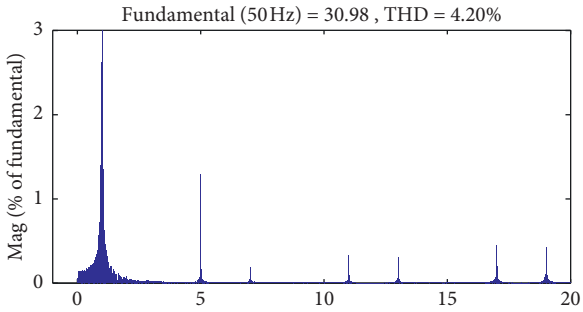

Figure 8: The THD in source current (after compensation).

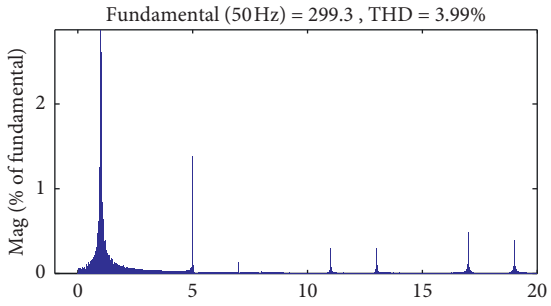

Figure 9: The THD in load voltage.

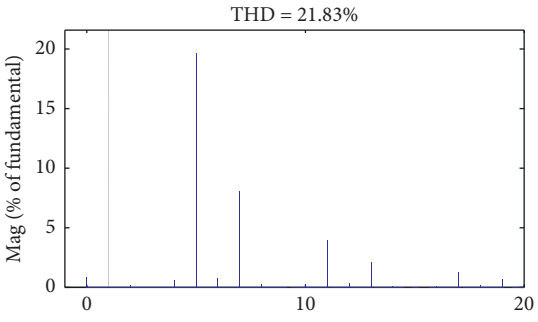

Figure 10: THD in load voltage (before compensation).

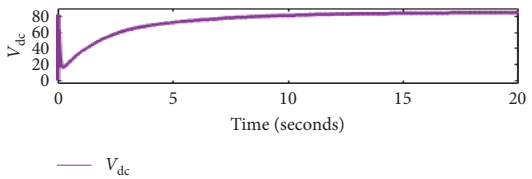

Figure 11: The DC link capacitor voltage.

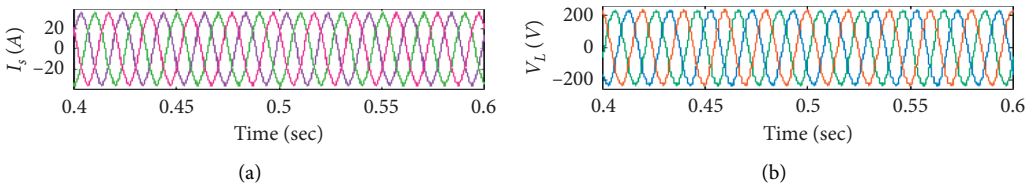

Figure 12: Steady state waveform of source current and the load voltage.

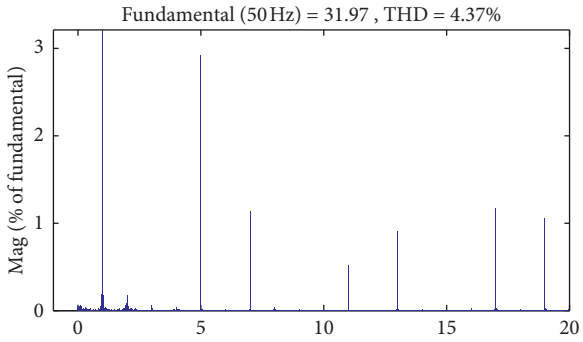

Figure 13: THD in source current.

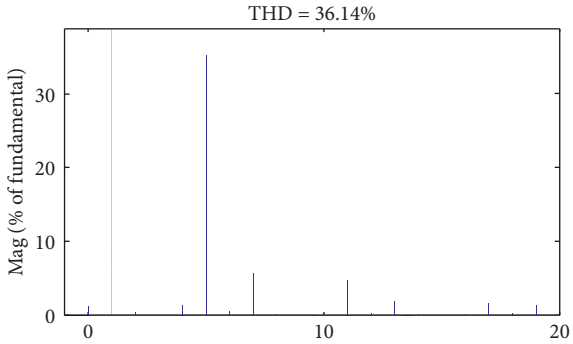

Figure 14: THD in load voltage (before compensation).

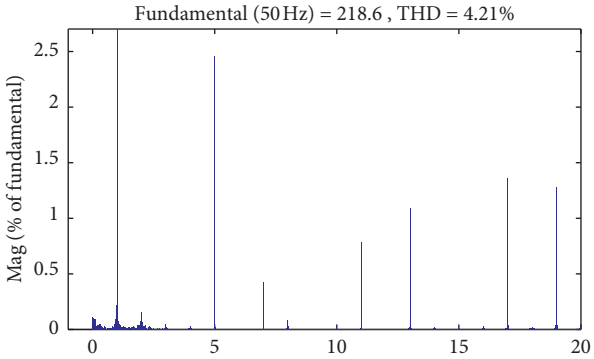

Figure 15: THD in load voltage (after compensation).

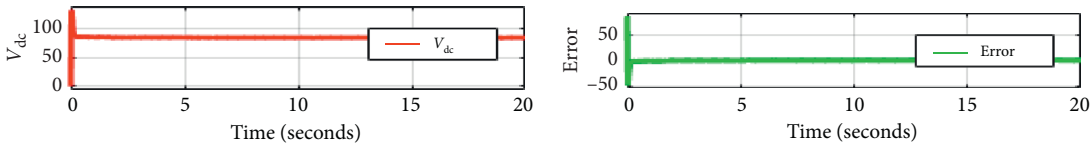

(a) (b)

Figure 16: Capacitor DC link voltage and the error between V_{dc} and the reference voltage.

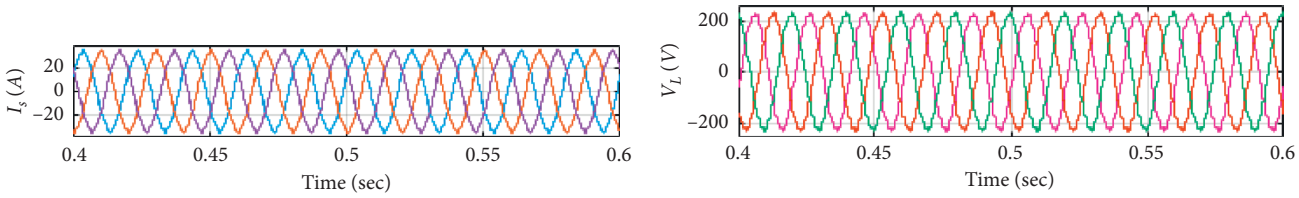

(a) (b)

Figure 17: Steady state performance of (a) source current and (b) load voltage.

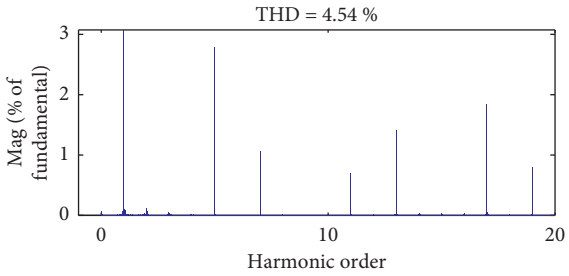

Figure 18: THD of source current (after compensation).

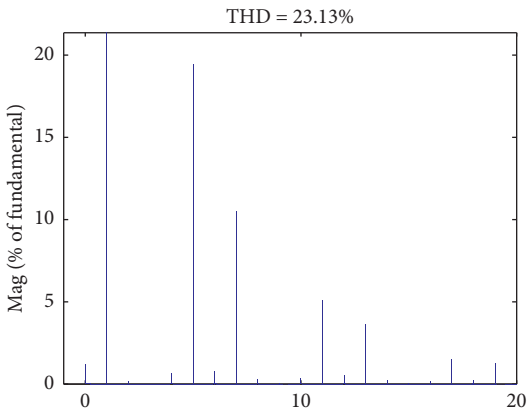

Figure 19: THD of load voltage (before compensation).

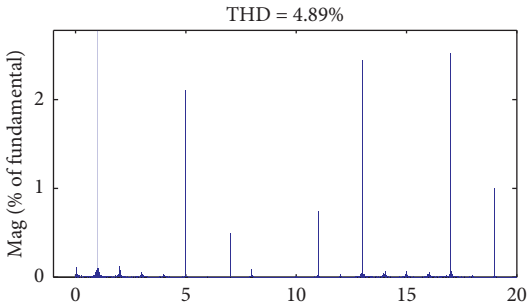

Figure 20: THD of load voltage (after compensation).

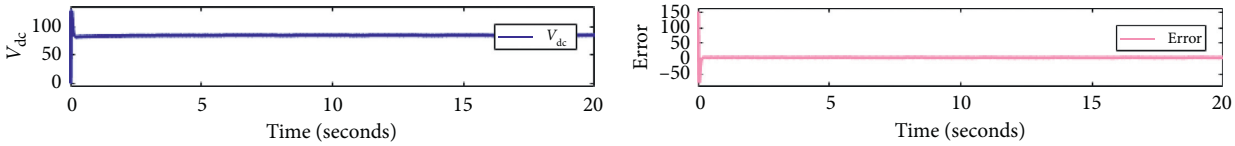

(a) (b)

Figure 21: DC link voltage and the error between reference and the capacitor voltage.

Table 2: THD (%) in different load conditions.

Loads	THD (before compensation) (%)	THD (after compensation) (%)
RL load	36.14	4.21
Battery charger load	21.83	3.99
(RC and RL) load	23.13	4.89

the load voltage is now 4.89%. Figure 21 shows the accuracy of the DC link capacitor voltage since it is stabilized at the required reference level.

Hence, from the three cases presented for different load variations, it is clear that the proposed method has better results in comparison to the existing intelligent techniques. Table 2 summarizes THD in load voltage for the different cases discussed in the paper.

4. Conclusion

The performance of HSAPF with the PI controller integrated with PSO is evaluated, and it is found better as compared to the amalgamation of other hybrid technique that uses series passive filter and shunt active power filter scheme. The hybrid control scheme is basically the coalition of source current and the load voltage detection approach. The proposed technique successfully compensates the harmonics in the source current and the load voltage under different loading conditions such as RL, both in nonlinear load as well as in case of battery charger load. The simulation results in various cases prove that the THD is in accordance with the IEEE standard 519, i.e., less than 5%. The proposed approach works well for different load variations in the system.

Data Availability

No data were used to support the findings of the study.

Conflicts of Interest

The authors declare that they have no conflicts of interest.

References

[1] Z. Zeng, H. Yang, S. Tang, and R. Zhao, "Objective-oriented power quality compensation of multifunctional grid-tied inverters and its application in microgrids," *IEEE Transactions on Power Electronics*, vol. 30, no. 3, pp. 1255–1265, 2015.

[2] H. Akagi and H. Fujita, "A new power line conditioner for harmonic compensation in power systems," *IEEE Transactions on Power Delivery*, vol. 10, no. 3, pp. 1570–1575, 1995.

[3] S. Rahmani, K. Al-Haddad, and F. Fnaiech, "Aseries hybrid power filter to compensate harmonic cureents and voltages," in *Proceedings of the IEEE 2002 28th Annual Conference IECON 02 Industrial Electronics Society*, pp. 644–649, Sevilla, Spain, November 2002.

[4] E. R. Ribeiro and I. Barbi, "Harmonic voltage reduction using a series active filter under different load conditionsfilter under different load conditions," *IEEE Transactions on Power Electronics*, vol. 21, no. 5, pp. 1394–1402, 2006.

[5] F. Z. Peng, H. Akagi, and A. Nabae, "A new approach to harmonic compensation in power systems-a combined system of shunt passive and series active filters," *IEEE Transactions on Industry Applications*, vol. 26, no. 6, pp. 983–990, 1990.

[6] S. Janpong, K. L. Areerak, and K. N. Areerak, "A literature survey of neural network applications for shunt active power filters," *International Journal of Electrical and Computer Engineering*, vol. 5, no. 12, 2011.

[7] B. Singh, G. Bhuvaneswari, and S. R. Arya, "Review on power quality solution technology," *Asian Power Electronics Journal*, vol. 6, no. 2, 2012.

[8] C. Kumar and M. K. Mishra, "An improved hybrid DSTATCOM topology to compensate reactive and nonlinear loads," *IEEE Transactions on Industrial Electronics*, vol. 61, no. 12, pp. 6517–6527, 2014.

[9] T.-L. Lee, Y.-C. Wang, J.-C. Li, and J. M. Guerrero, "Hybrid active filter with variable conductance for harmonic resonance suppression in industrial power systems," *IEEE Transactions on Industrial Electronics*, vol. 62, no. 2, pp. 746–756, 2015.

[10] Y. Jiang, J. Chang, and S. Tian, "Multi-objective optimal design of hybrid active power filter," in *Proceedings of the International Conference on Advanced Manufacture Technology and Industrial Application*, Shanghai, China, September 2016.

[11] Z. Shuai, A. Luo, R. Fan, K. Zhou, and J. Tang, "Injection branch design of injection type hybrid active power filter," *Automation of Electric Power Systems*, vol. 31, no. 5, pp. 57–60 + 75, 2007.

[12] S. Bhattacharya and D. Divan, "Synchronous frame-based controller implementation for a hybrid series active filter system," in *Proceedings of the Conference Record of the 1995 IEEE Industry Applications 30th IAS Annual Meeting*, pp. 2531–2540, Orlando, FL, USA, October 1995.

[13] Q. Long, "A constraint handling technique for constrained multi-objective genetic algorithm," *Swarm and Evolutionary Computation*, vol. 15, pp. 66–79, 2014.

[14] T. Sudhakar Babu, K. Priya, D. Maheswaran, K. Sathish Kumar, and N. Rajasekar, "Selective voltage harmonic elimination in PWM inverter using bacterial foraging algorithm," *Swarm and Evolutionary Computation*, vol. 20, pp. 74–81, 2015.

[15] R. Akbari, R. Hedayatzadeh, K. Ziarati, and B. Hassanizadeh, "A multi-objective artificial bee colony algorithm," *Swarm and Evolutionary Computation*, vol. 2, pp. 39–52, 2012.

[16] E. Rashedi, E. Rashedi, and H. Nezamabadi-Pour, "A comprehensive survey on gravitational search algorithm," *Swarm and Evolutionary Computation*, vol. 41, 2018.

[17] L. Asiminoaei, E. Aeloiza, P. N. Enjeti, and F. Blaabjerg, "Shunt active-power-filter topology based on parallel interleaved inverters," *IEEE Transactions on Industrial Electronics*, vol. 55, no. 3, pp. 1175–1189, 2008.

[18] S. Rahmani, N. Mendalek, and K. Al-Haddad, "Experimental design of a nonlinear control technique for three-phase shunt active power filter," *IEEE Transactions on Industrial Electronics*, vol. 57, no. 10, pp. 3364–3375, 2010.

[19] S. Hirve, K. Chatterjee, B. G. Fernandes et al., "PLL-less active power filter based on one-cycle control for compensating unbalanced loads in three-phase four-wire system," *IEEE Transactions on Power Delivery*, vol. 22, no. 4, pp. 2457–2465, 2007.

[20] M. C. Benhabib and S. Saadate, "New control approach for four-wire active power filter based on the use of synchronous reference frame," *Electric Power Systems Research*, vol. 73, no. 3, pp. 353–362, 2005.

[21] W. M. Grady, M. J. Samotyj, and A. H. Noyola, "Survey of active power line conditioning methodologies," *IEEE Transactions on Power Delivery*, vol. 5, no. 3, pp. 1536–1542, 1990.

[22] B. Singh, A. Chandra, and K. Al-Haddad, "Computer-aided Modeling and simulation of active power filters," *Electric Machines & Power Systems*, vol. 27, no. 11, pp. 1227–1241, 1999.

[23] S. S. Patnaik and A. K. Panda, "Real-time performance analysis and comparison of various control schemes for particle swarm optimization-based shunt active power filters," *International Journal of Electrical Power & Energy Systems*, vol. 52, pp. 185–197, 2013.

ResearchGate

See discussions, stats, and author profiles for this publication at: https://www.researchgate.net/publication/350054942

Analysis of Photovoltaic (PV) Power Technology

Article · March 2021

CITATIONS
0

READS
13

3 authors, including:

Harsh Mishra
Delhi Technological University
1 PUBLICATION **0** CITATIONS

SEE PROFILE

All content following this page was uploaded by Harsh Mishra on 14 March 2021.

The user has requested enhancement of the downloaded file.

Published by :
http://www.ijert.org

International Journal of Engineering Research & Technology (IJERT)
ISSN: 2278-0181
Vol. 10 Issue 03, March-2021

Analysis of Photovoltaic (PV) Power Technology

Harsh Kumar Mishra
Undergraduate Student,
Department of Mechanical Engineering
Delhi Technological University
New Delhi, India

Adarsh
Undergraduate Student,
Department of Mechanical Engineering
Delhi Technological University
New Delhi, India

Dr. Janardan Prasad Kesari
Professor, Department of Mechanical Engineering
Delhi Technological University
New Delhi, India

***Abstract*— The light from the sun is a renewable enerygy source that is not tainted by nature and noise. It can easily compensate for the energy taken from non-renewable energy sources such as fossil fuels and inland gasoline. Performance of solar cells have undergone a large number of developmental steps from one generation to the next. Silicon-based solar cells were first generation solar cells grown in Si Wafers, especially single crystals. Continous development in thin films, dye is sensitiveto solar cells and living solar cells improve cell performance. Development is basically hampered by its cost and efficiency. A PV cell is a specialized semiconductor diode that converts visible light into direct current (DC). Some PV cells can also convert infrared or ultraviolet (UV) radiation into DC electricity. Photovoltaic cells are an integral part of solar-electric energy systems. In this paper a deep analysis of Photovoltaic cell is done, focusing on PV functionality, working, environmental impact and overall photovoltaic system configuration**

Keywords-Photovoltaic system, Solar cell, PV Array, PV module

I. INTRODUCTION

When light shines on a photovoltaic (PV) cell – also called a solar cell – that light may be reflected, absorbed, or pass right through the cell. The PV cell is composed of semiconductor material; the “semi” means that it can conduct electricity better than an insulator but not as well as a good conductor like a metal. There are several different semiconductor materials used in PV cells. When the semiconductor is exposed to light, it absorbs the light’s energy and transfers it to negatively charged particles in the material called electrons. This extra energy allows the electrons to flow through the material as an electrical current. This current is extracted through conductive metal contacts – the grid-like lines on a solar cells – and can then be used to power your home and the rest of the electric grid. The efficiency of a PV cell is simply the amount of electrical power coming out of the cell compared to the energy from the light shining on it, which indicates how effective the cell is at converting energy from one form to the other. The amount of electricity produced from PV cells depends on the characteristics (such as intensity and wavelengths) of the light available and multiple performance attributes of the cell. An important property of PV semiconductors is the bandgap, which indicates what wavelengths of light the material can absorb and convert to electrical energy. If the semiconductor’s bandgap matches the wavelengths of light shining on the PV cell, then that cell can efficiently make use of all the available energy.

II. FUNCTIONALITY

When light shines on a photovoltaic (PV) cell – also called a solar cell – that light may be reflected, absorbed, or pass right through the cell. The PV cell is composed of semiconductor material; the “semi” means that it can conduct electricity better than an insulator but not as well as a good conductor like a metal. There are several different semiconductor materials used in PV cells. When the semiconductor is exposed to light, it absorbs the light’s energy and transfers it to negatively charged particles in the material called electrons. This extra energy allows the electrons to flow through the material as an electrical current. This current is extracted through conductive metal contacts – the grid-like lines on a solar cells – and can then be used to power your home and the rest of the electric grid. The efficiency of a PV cell is simply the amount of electrical power coming out of the cell compared to the energy from the light shining on it, which indicates how effective the cell is at converting energy from one form to the other. The amount of electricity produced from PV cells depends on the characteristics (such as intensity and wavelengths) of the light available and multiple performance attributes of the cell. An important property of PV semiconductors is the bandgap, which indicates what wavelengths of light the material can absorb and convert to electrical energy. If the semiconductor’s bandgap matches the wavelengths of light shining on the PV cell, then that cell can efficiently make use of all the available energy.

(This work is licensed under a Creative Commons Attribution 4.0 International License.)

International Journal of Engineering Research & Technology (IJERT)
ISSN: 2278-0181
Vol. 10 Issue 03, March-2021

III. WORKING OF PV CELL

PV cell is a semiconductor diode whose p–n junction is exposed to light. Photovoltaic cells made of several types of semiconductors using different manufacturing processes. The mono crystalline and polycrystalline silicon cells are the only found at commercial scale at the present time. Silicon Photovoltaic cells are composed of a thin layer of bulk Si or a thin Si film connected to electric terminals. One of the sides of the Si layer is doped to form the p–n junction. A thin metallic grid is placed on the Sun-facing surface of the semiconductor. Fig. 1 roughly illustrates the physical structure of a Photovoltaic cell. The incidence of light on the cell generates charge carriers that originate an electric current if the cell is short circuited. Charges are generated when the energy of the incident photon is sufficient to detach the covalent electrons of the semiconductor—this phenomenon depends on the semiconductor material and on the wavelength of the incident light.

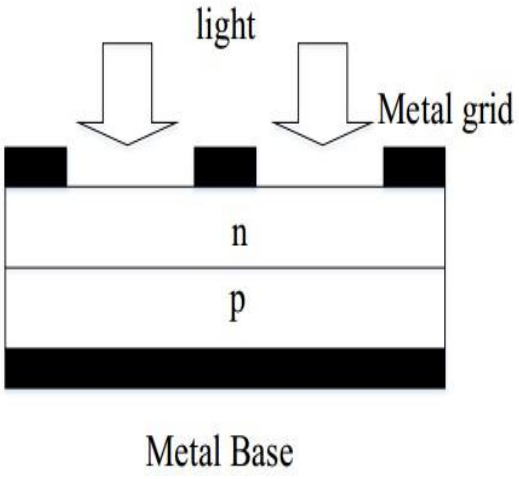

Fig. 1: Structure of a PV cell

Basically, the Photovoltaic phenomenon may be described as the absorption of solar radiation, the Generation and transport of free carriers at the p–n junction, and the collection of these electric charges at the terminals of the PV device. Generation rate of electric carriers depends on the incident light flux and the capacity of absorption of the semiconductor. The capacity of absorption depends mainly on the semiconductor band gap, on the reflectance of the cell surface (that depends on the shape and treatment of the surface), on the intrinsic concentration of carriers of the semiconductor, on the electronic mobility, on the recombination rate, on the temperature, and on several other factors. The solar radiation is composed of photons of different energies. Photons with energies lower than the band gap of the photovoltaic cell are useless and generate no voltage or electric current. Photons with energy superior to the band gap generate electricity, but only the energy corresponding to the band gap is used— the remainder of energy is dissipated as heat in the body of the PV cell. Semiconductors with lower band gaps may take advantage or a larger radiation spectrum, but the generated voltages are lower. Si is not the only, and probably not the best, semiconductor material for PV cells, but it is the only one whose fabrication process is economically feasible in large scale. Other materials can achieve better conversion efficiency, but at higher and commercially unfeasible costs. In a practical system, one PV cell will not be able to provid sufficient energy. Thus, several cells are grouped together to form a PV module, and several modules are grouped together to form a PV array. This combination of cells is what allows for a larger percentage of solar power to be absorbed due to a larger area of PV cells, and thus more current and voltage to be produced at the output. The solar PV array or module used has to be carefully designed to produce the right amount of power to charge the battery and also has to be designed to adhere to the charging characteristics of the battery as much as possible so as to minimize losses. Below epitomizes the formation of the PV module and array from the PV cell.

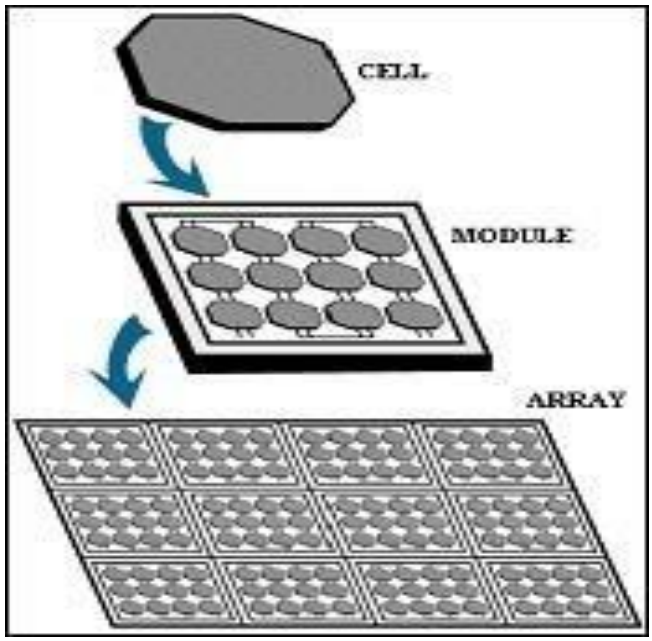

Fig 2: PV module and array formation from PV cells

PV MODULE

The solar module is normally connected in series sufficient number of solar cells to provide required standard output voltage and power. One solar module can be rated from 3 watts to 300 watts. Actually a single solar PV cell generates a very tiny amount that is around 0.1 watt to 2 watts. But it is not practical to use such a low power unit as the building block of a system. So required numbers of such cells are combined together to form a practical commercially available solar unit which is known as solar module or PV module. When needs higher voltage, connect PV cell in series and if load demand high current then connect PV cell in parallel A PV array is simply an interconnection of several photovoltaic modules in serial and/ or parallel.

PV ARRAY

The power generated by individual modules may not be sufficient to meet the requirement of trading applications, so

(This work is licensed under a Creative Commons Attribution 4.0 International License.)

International Journal of Engineering Research & Technology (IJERT)
ISSN: 2278-0181
Vol. 10 Issue 03, March-2021

the modules are secured in a grid form or as an array to gratify the load demand.

IV. PV CELL AS CURRENT SOURCE

A solar cell can be modeled as a current source which is parallel to a diode and an equivalent resistance. The equivalent resistance is comprised of a shunt (Rsh) and Series resistance(Rser). The series resistance factors in all the losses due to the resistive semiconductor material that the cell is made of, the resistance of the contacts, and other series losses. The shunt resistance is due to localized shorts in the silicon wafer that is the primary material of the cell.

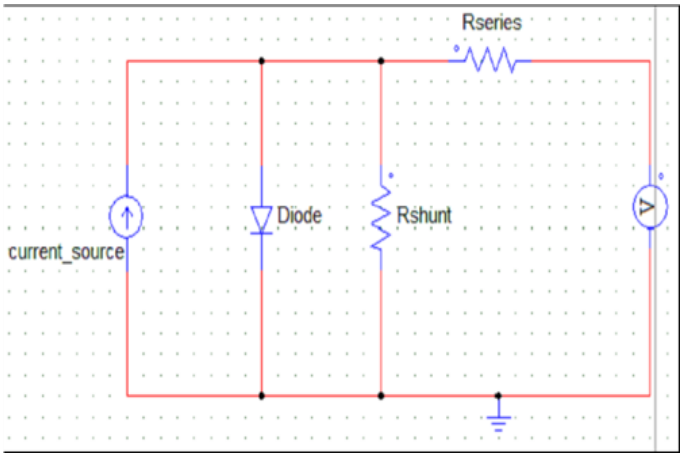

Figure 3: General circuit representation of a solar cell.

Generally, the series resistance is very small, and the shunt resistance is very large, making these losses almost negligible. Upon observation of the IV characteristics of a commercial solar panel such as the SQ150, it can be seen that changes in irradiance bring about significant changes in the panel short circuit current but barely affect the open circuit voltage. In effect, the short circuit current is approximately proportional to the irradiance. proposes that the current source used in the solar cell model be one that is dependent on a voltage; this voltage in turn is representative of the irradiance condition. Thus, the cell's characteristics can be made to vary with irradiance in a way that mimics the variations in the IV profile of a practical solar cell. A solar panel can be constructed out of series and parallel connections of the solar cell model given above. But, keeping in mind that the objective of the modeling process was to simply obtain a system whose IV characteristics are identical to that of a solar panel, another method was used: It was found that the open circuit voltage of the solar cell model is roughly proportional to the number of series-connected diodes that are in parallel to the short-circuit current source. Thus, by adding more diodes and increasing the shortcircuit current, the characteristics of the solar cell become more and more like that of a panel. A photovoltaic panel is constructed out of several cells in series and parallel combinations. This allows a panel to output an utilizable voltage and current. The figure below illustrates the typical Current-Voltage (I-V) characteristics of a PV panel.

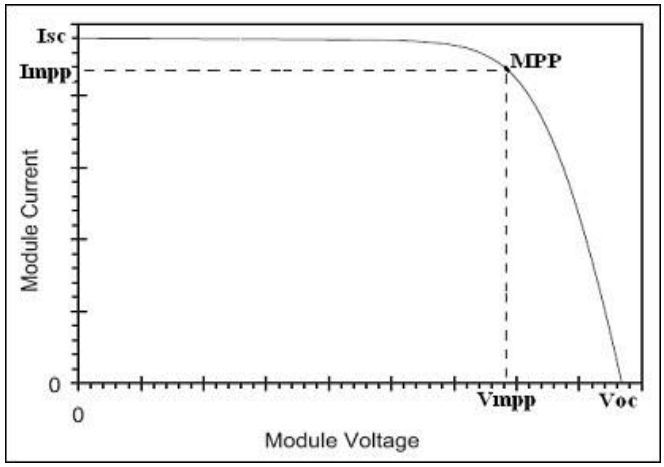

Figure 4: I-V characteristics of a PV panel

The curve shows how the current supplied by a PV panel varies with its voltage. The point of maximum power occurs at the knee of the curve and is called the maximum power point (MPP). The maximum power is given by Pmpp = Vmpp x Impp

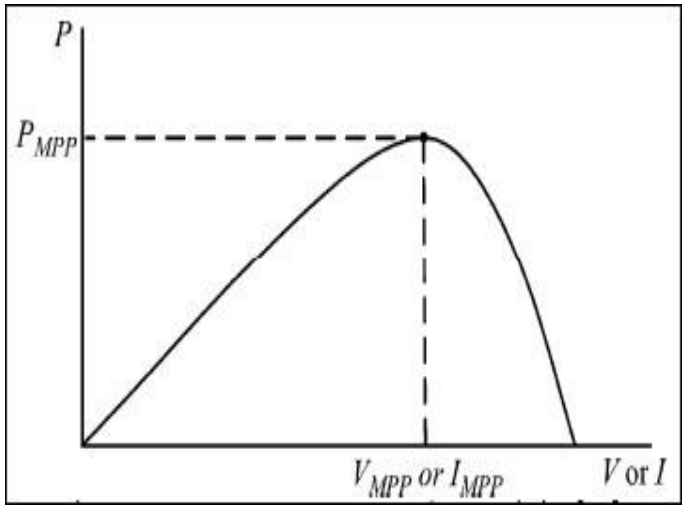

Figure 5: PV output power characteristics

In order for the PV panel to supply maximum power, it should supply a load of resistance (Rmpp): Rmpp = Vmpp / Impp If the load resistance as seen by the panel is below this value, the bias point would move to the left of the MPP, and to the right if the resistance is above this value.

(This work is licensed under a Creative Commons Attribution 4.0 International License.)

International Journal of Engineering Research & Technology (IJERT)
ISSN: 2278-0181
Vol. 10 Issue 03, March-2021

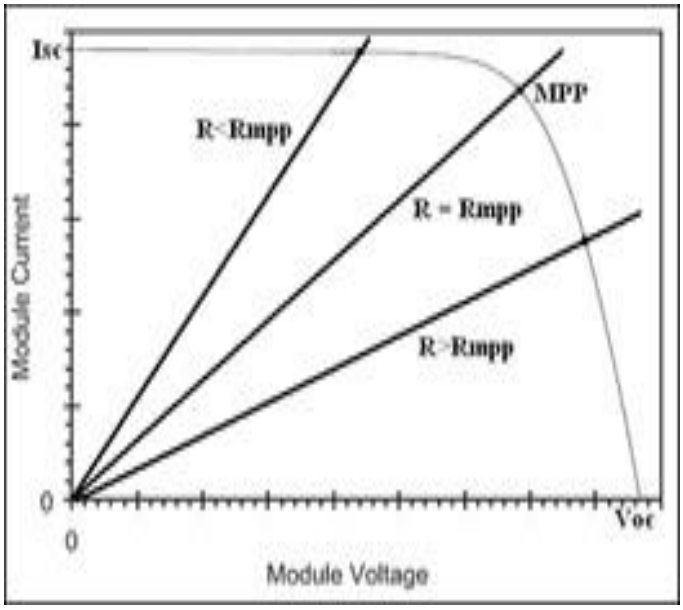

Figure 6: Bias points for various load resistances

V. ENVIRONEMENTAL IMPACTS OF PHOTOVOLTAIC SYSTEM

POSITIVE

1. **Using less water:** Water is one of our most precious natural resources. We live on the driest continent on the planet, and we run the risk of running out of fresh water in the future. Traditional electricity production can use thousands of litres of water each year. Water is used for cooling generators, processing and refining fuel and transporting fuel through pipes. Generating power through solar panels, however, uses no water whatsoever. The operation of solar photovoltaic cells doesn't require water at all to generate electricity, reducing the strain on this precious resource. The only water needed is rainwater to naturally clean the panels when they get a bit grubby. Using less water is a benefit to the environment of generating solar energy.

2. **Reducing air pollution:** the air we breathe can help or hinder our health and wellbeing. Electricity generation from fossil fuels can generate harmful carbon dioxide and methane gases that lower the quality of the air we breathe. Breathing poor quality air on a daily basis can have dire consequences for our health. Air pollution has been linked to asthma and allergies, bronchitis, pneumonia, headaches, anxiety, heart attacks and even some cancers. Using the sun to generate more and more of our power means less and less harmful emissions from burning fossil fuels. Generating electricity from solar panels produce no harmful emissions, and the more homes and businesses that rely on solar power means less toxic emissions from fossil fuels into our air.

3. **Help to slow climate change:** the release of toxic gases into the atmosphere, such as carbon dioxide, methane and nitrous oxide, doesn't just contribute to air pollution, but also contributes to the enhanced greenhouse effect. While the greenhouse effect is a natural process that warms the Earth's surface to a liveable temperature, human activities, such as the burning of fossil fuels, have increased the amount of greenhouse gases in our atmosphere. This has led to the enhanced greenhouse effect, which is warming our earth faster than ever before. In recent years, this has been linked to a number of catastrophic weather events, such as flooding, cyclones, storms, extreme heat and drought. Generating electricity from solar panels produce no greenhouse gases whatsoever, and so can help to reduce the effect of climate change if used widely. With solar energy powering a home or business, there is no burning of fuel and no emissions from energy production.

4. **Reducing your household's carbon footprint:** Solar energy is one of the cleanest sources of energy, and it's an extremely effective way of your household more efficient and sustainable. Solar panels don't use any water to generate electricity, they don't release harmful gases into the environment, and the source of their energy is abundant and, best of all, free. Using solar energy instead of the grid also means you reduce the need for carbon dioxide emitting energy to be produced for the grid on your behalf – for energy users on mainland Australia, you could offset anywhere between a half to one tonne of carbon dioxide for every megawatt-hour of solar energy you use. With even a small system installed on your home, you can help reduce your household's carbon footprint and contribute personally to the Australian Renewable Energy Target.

5. **Reducing our reliance on fossil fuels:** Solar energy supplies are massive; if we could harness all of the sunlight shining on the earth for just one hour, we could use that energy to power the entire world for a whole year. The sunshine used in solar energy production is free, and there's lots of it. On the other hand, fossil fuels are running out, and fast. Reducing our reliance on these finite resources and taking advantage of an abundant, free source of energy, such as sunlight, could mean lower energy prices, reduced greenhouse gas emissions and a stronger, more stable energy future.

NEGATIVE

Solar energy systems offer significant environmental benefits in comparison to the conventional energy sources, thus they greatly contribute to the sustainable development of human activities. At times however, the wide scale deployment of such systems has to face potential negative environmental implications. These possible problems may be a strong barrier for further advancement of these systems in some consumers. The potential environmental impacts associated with solar power can be classified according to numerous categories,

(This work is licensed under a Creative Commons Attribution 4.0 International License.)

International Journal of Engineering Research & Technology (IJERT)
ISSN: 2278-0181
Vol. 10 Issue 03, March-2021

some of which are land use impacts, ecological impacts, impacts to water, air and soil, and other impacts such as socioeconomic ones, and can vary greatly depending on the technology.

1. **Land Use and Ecological Impacts:** In the point of generating electricity at a utility-scale, solar energy facilities necessitate large areas for collection of energy. Due to this, the facilities may interfere with existing land uses and can impact the use of areas such as wilderness or recreational management areas. As energy systems may impact land through materials exploration, extraction, manufacturing and disposal, energy footprints can become incrementally high. Thus, some of the lands may be utilised for energy in such a way that returning to a pre-disturbed state necessitates significant energy input or time, or both, whereas other uses are so dramatic that incurred changes are irreversible.

2. **Impacts to Soil, Water and Air Resources:** The construction of solar facilities on vast areas of land imposes clearing and grading, resulting in soil compaction, alteration of drainage channels and increased erosion. Central tower systems require consuming water for cooling, which is a concern in arid settings, as an increase in water demand may strain available water resources as well as chemical spills from the facilities which may result in the contamination of the groundwater or the surface. As with the development of any large-scale industrial facility, the construction of solar energy power plants can pose hazards to air quality. Such threats include the release of soil-carried pathogens and results in an increase in air particulate matter which has the effect of contaminating water reservoirs.

3. **Heavy Metals:** Some have argued that the latest technologies introduced on the market, namely thin-film panels, are manufactured using dangerous heavy metals, such as Cadium Telluride. While it is true that solar panel manufacturing uses these dangerous material, coal and oil also contain the same substsances, which are released with combustion. Moreover, coal power plants emit much more ofthese

   toxic substances, polluting up to 300 times more than solar panel manufacturers.

VI. ECONOMICS OF A PV SYSTEM

Some important terms related to photovoltaic system economics are presented herein. The most important PV economic parameters are the total costs of installing a PV system, electricity price, Feed-In tariffs and the energy payback time - EPBT. Investments into renewable energies, particular into PV and wind technologies are another economics related area. The cost of a PV system is measured in price-per-peak-watt (€/Wp or US$/Wp for example). Peak watt is defined as the power at standard test conditions (solar irradiance 1000 W/m2, AM of 1.5 and temperature 25°C). Photovoltaic system costs encompass both module and BOS costs. Module costs typically represents only 40-60 % of total PV system costs. Typically the cost of installing a photovoltaic system having a power of 10 kW was about ₹ 70,000 /kWp and cost of 100 kW was about ₹ 60,000 /kWp in 2020. Approximately about half of this investment would be for the PV modules, and the inverter, PV array support structures, electrical cabling, equipment and installation would account for the rest. Please note that BOS and installation costs can vary significantly. For example: when costs for site preparation, laying a foundation, system design and engineering, permitting, as well as assembly and installation labour are higher, total installation costs are higher too. The life cycle cost (LCC) of a PV system may also include costs for site preparation, system design and engineering, installation labour, permits and operation and maintenance costs. Photovoltaic systems have an anticipated 25-year lifetime. For the most part, the commitment to renewable resources has come from individuals, big businesses and countries. Besides solar energy, companies such as Google (GOOG) and Amazon (AMZN) have committed to using wind to power company facilities. With big businesses, individuals and countries continuing to transition to renewable energy sources, adverse environmental effects from burning fossil fuels can hopefully be moderated.

VII. CONCLUSION

The sun is the most plentiful energy source for the earth. All wind, fossil fuel, hydro and biomass energy have their origins in sunlight. Solar energy falls on the surface of the earth at a rate of 120 petawatts, (1 petawatt =1015watt). This means all the solar energy received from the sun in one days can satisfied the whole world's demand for more than 20 years. We are able to calculate the potential for each renewable energy source based on today's technology. Future advances in technology will lead to higher potential for each energy source. However, the worldwide demand for energy is expected to keep increasing at 5 percent each year .olar energy is the only choice that can satisfy such a huge and steadily increasing demand. PV cells are a proven environmentally benevolent power source whose attractive characteristics will continue further photovoltaic research. Because current Dye sensitized solar systems are still inefficient and uncommon, they are not yet cost competitive with Silicon-based generators, the efforts to increase their potential are growing day by day. These solar devices are low-cost, sustainable and easier to fabricate. As efficiency increases, PV technology will attract a greater number of people, due to low cost. Because the sun delivers ten thousand times more energy than people currently consume, photovoltaic improvements will one day replace environmentally unfriendly power plants with a proven and clean energy source.

(This work is licensed under a Creative Commons Attribution 4.0 International License.)

International Journal of Engineering Research & Technology (IJERT)
ISSN: 2278-0181
Vol. 10 Issue 03, March-2021

VIII. REFERENCES

[1] https://energyeducation.ca/encyclopedia/Phot ovoltaic_cell
[2] https://en.wikipedia.org/wiki/Solar_cell
[3] https://www.energy.gov/eere/solar/solarphotovoltaic-cell-basics
[4] Manoj Kumar, "A Study of the characteristics of the PV Cell", November 2019, Research Gate
[5] Manoj Kumar, "A Study of the characteristics of the PV Cell", November 2019, Research Gate
[6] Vítězslav Benda, Ladislava Cerna, "PV cells and modules – State of the art, limits and trends", December 2020, Research Gate
[7] Swami, Rashmi "Solar cell" International Journal of Scientific and Research Publications, Volume 2, Issue 7, July 2012
[8] C Santhi Durganjali, Sameer Bethanabhotla, Satwik Kasina, Dr Sudha Radhika "Recent Developments and Future Advancements in Solar Panels Technology" International Conference on Multifunctional Materials (ICMM-2019)
[9] Ramesh Babu Kodati, Puli Nnageshwar Rao "A REVIEW OF SOLAR CELL FUNDAMENTALS AND TECHNOLOGIES" Advanced Science Letters
[10] Bartłomiej Milewicz, Magdalena Bogacka * and Krzysztof Pikoń "Influence of Solar Concentrator in the Form of Luminescent PMMA on the Performance of a Silicon Cell" Multidisciplinary Digital Publishing Institute.
[11] Ali Mohammad Hayder "Thermal performance of backflow solar air heating with integrated nanopracticle enhanced PCM absorber storage system" UTHM Tunku Tun Aminah Library
[12] Manoharan Premkumar, Chandrasekaran Kumar, Ravichandran Sowmya "Mathematical Modelling of Solar Photovoltaic Cell/Panel/Array Based on the Physical Parameters from the Manufacturer's Datasheet" International Journal of Renewable energy development
[13] MEHREEN GUL, YASH KOTAK, TARIQ MUNEER "REVIEW ON RECENT TREND OF SOLAR PHOTOVOLTAIC TECHNOLOGY"
[14] VINOD KUMAR, R.L. SHRIVASTAVA, S.P UNTAWALE "SOLAR ENERGY: REVIEW OF POTENTIAL GREEN & CLEAN ENERGY FOR COASTAL AND OFFSHORE APPLICATIONS"

(This work is licensed under a Creative Commons Attribution 4.0 International License.)

View publication stats

e-ISSN: 2582-5208
International Research Journal of Modernization in Engineering Technology and Science
Volume:03/Issue:03/March-2021 Impact Factor- 5.354 www.irjmets.com

ANALYSIS OF WAVE POWER TECHNOLOGIES

Dr JP Kesari*1, Siddharth Sharma*2, Chanda Singh*3

*1Professor, Department of Mechanical Engineering, Delhi Technological University, Bawana Road, New Delhi-110042, India.

*2,3Undergraduate Student, Department of Mechanical Engineering, Delhi Technological University, Bawana Road, New Delhi-110042, India.

ABSTRACT

This paper involves the study of significant wave power technologies and their applications. As the energy consumption of the world is increasing exponentially, there is a need for renewable energy resources. Wave energy (power) is one such alternative. Various Wave Energy Converters (WECs) are studied in this paper along with their characteristics. The current status of development of wave power technologies in India is also discussed. Given the depletion of traditional energy sources and their impact on climate, the authors emphasize to try adopting wave power technologies.

I. INTRODUCTION

Due to the depletion of the traditional sources of energy like fossil fuels and their harmful effects on the environment, there is a need for cleaner, safer and renewable energy sources. Since most of the earth is covered with water, wave energy is a promising renewable energy source. Wave energy (or wave power or ocean energy) is continuous (in the sense that waves are available 24 hours a day throughout the year), environmentally friendly, pollution free and predictable with high accuracy. Waves are formed on the ocean surface due to the interaction of wind with the water surface. Waves can store and transmit the kinetic energy which they carry from the wind thousands of kilometres with negligible loss. Wave power technologies have made remarkable progress in recent years but are still decades behind other renewable energy sources as huge amount of money is required for construction of structures in oceans and their maintenance. “A potential of 40,000 MW along the Indian coast has been concluded by a general research on wave nature.[1]”

II. WAVE ENERGY CONVERTERS

Wave Energy Converters (WECs) are used to transform potential and kinetic energy of a moving ocean wave into electrical or mechanical energy. WECs can be generally classified based on three types: location, operating principle and direction of wave propagation.

Location: Based on location, wave energy converter devices are classified into three types: onshore, nearshore and offshore devices.

1 Onshore Devices: Onshore devices are installed in the shallow water above sea. Waves are attenuated as they pass through shallow water. As a result, these devices are less prone to damage in severe weather conditions. They have less energy to utilise as shallow water results in reduced wave power. Since their location is mostly accessible, these are easy to install and maintain.

2 Nearshore Devices: Nearshore devices are installed in relatively shallow water “(there is lack of consensus for what defines shallow water). Nearshore constitutes an area within 2km from the coastline. [3]” Nearshore devices, like onshore devices, have reduced wave power due to shallow water.

3 Offshore Devices: Offshore devices are installed in deep water. As a result, they have higher amount of energy to exploit. Their installation and maintenance is difficult. Deep water waves have high energy content so offshore devices are designed to withstand extreme conditions which leads to higher cost.

e-ISSN: 2582-5208
International Research Journal of Modernization in Engineering Technology and Science
Volume:03/Issue:03/March-2021 Impact Factor- 5.354 www.irjmets.com

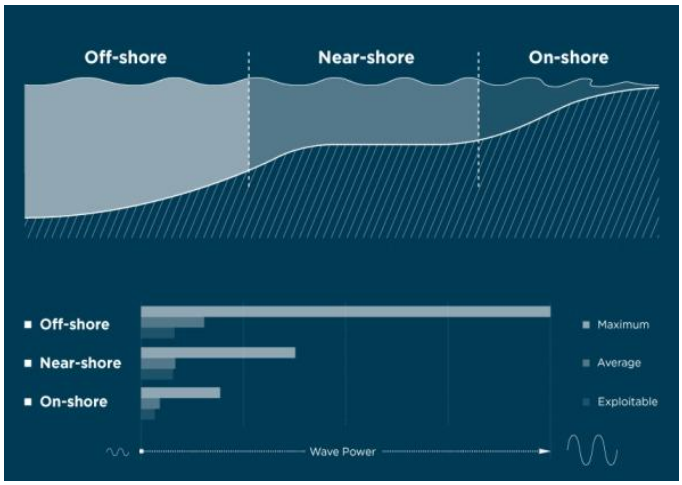

Figure-1: Wave power characteristics for off-shore, near-shore and on-shore WECs

Direction of Wave Propagation: Based on size and direction of wave propagation, wave energy converters are classified into three types: attenuator, point absorber and terminator.

1 Attenuator: These WECs are mounted parallel to the wave propagation direction. "They consist of a sequence of cylindrical sections in succession which are joined together by flexible hinged joints that allows the individual sections to rotate relative to each other.[2]" Pelamis which is developed by Ocean Power Delivery Ltd is a typical example. "The 750kW P2 (second generation) machine was successfully installed at the Billia Croo, Orkney wave test site for the first time in October 2010.[5]"

Figure-2: Pelamis (attenuator)

2 Point Absorber: These WECs are dimensionally considerably smaller relative to the incident wavelength. These devices generate electricity from the bobbing or pitching action of a device, by transforming the up-and-down pitching movement of the waves into rotary or oscillatory movements (depending on a particular device).They are able to generate power irrespective of the direction of wave propagation due to their small size. "150kW PowerBuoy technology developed by Ocean Power Delivery Ltd is an example of point absorber.[6]"

Figure-3: Power Buoy (point absorber)

e-ISSN: 2582-5208
International Research Journal of Modernization in Engineering Technology and Science
Volume:03/Issue:03/March-2021 Impact Factor- 5.354 www.irjmets.com

3 Terminator: A terminator is a near-surface floating device like a point absorber. However, it absorbs energy in only one direction. These WECs are placed perpendicular to the direction of wave propagation. As the name suggests, they terminate or end the wave action. An example of this type of WEC is the Salter's Duck which is developed at the University of Edinburgh.

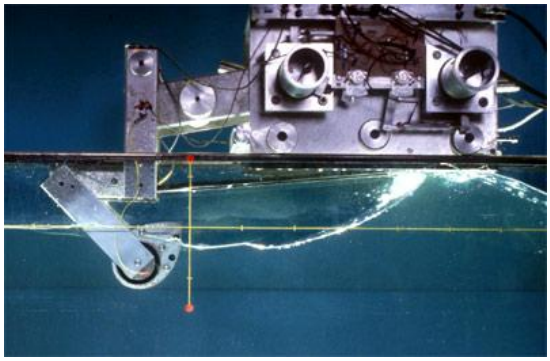

Figure-4: Salter's Duck (Terminator)

Mode of Operation: Based on mode of operation, some significant classifications are: submerged pressure differential, oscillating wave surge converter, oscillating water column and overtopping device.

1 Submerged Pressure Differential: This type of WEC is a completely submerged point absorber. It uses the pressure difference formed between the wave crests and troughs over the device. "It consists of a sea bed fixed air-filled cylindrical chamber with a moveable upper cylinder. When the crest of the wave travels over the device, the air within the cylinder is compressed by the water pressure above the device. As a result the upper cylinder moves down. When the trough of the wave travels over, the water pressure over the device is reduced and the upper cylinder rises.[8]" An example of this type of WEC is the Archimedes Waveswing submerged wave power buoy developed by AWS Ocean Energy Ltd. "The system is suitable for deployment in water depths in excess of 25m and can be configured for ratings between 25kW and 250kW by selecting the appropriate scale.[9]"

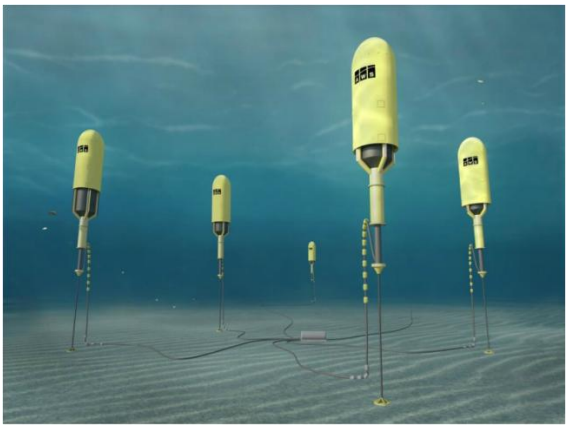

Figure-5: Archimedes Wave Swing (Submerged Pressure Differential)

2 Oscillating Water Column: "Oscillating water columns (or OWCs) generally comprise of a partially submerged fixed or floating hollow structure, which forms an air chamber, having an opening to the sea below the water surface. When water rises inside the chamber, the air volume inside the chamber is compressed and driven through a turbine. When the water level inside the chamber decreases, the air is drawn back through the turbine.[10]" OWCs have been used as point absorbers as well as being installed into the shoreline to serve as a terminator. An example of a shoreline mounted device is the Wavegen Limpet which is installed on the island of Islay, Western Scotland, and generates power for the national grid.

e-ISSN: 2582-5208
International Research Journal of Modernization in Engineering Technology and Science
Volume:03/Issue:03/March-2021 Impact Factor- 5.354 www.irjmets.com

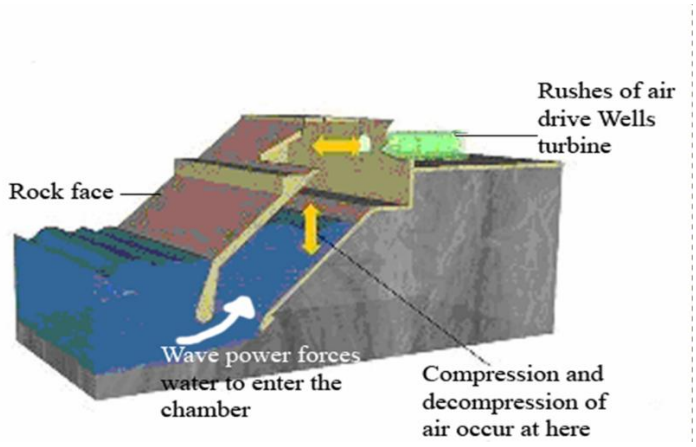

Figure-6: Limpet (Oscillating Water Column)

3 Overtopping Device: "Overtopping devices (OTDs) depend on the capture of water from waves. The incident waves would overtop the WEC's edge and be trapped in the reservoir, which is a few meters above sea level. The water is released to the sea from the reservoir through low-head turbines, which are responsible for generation of electricity. To increase the amount of energy captured by the WEC, an OTD can use collectors to concentrate incident waves and increase wave height. [12]." A typical example is the wave dragon. A pair of large curved reflectors collect waves in the central receiving section, where they flow up a ramp and over the top into a raised reservoir, from which the water is allowed to return to the sea through a number of low-head turbines.

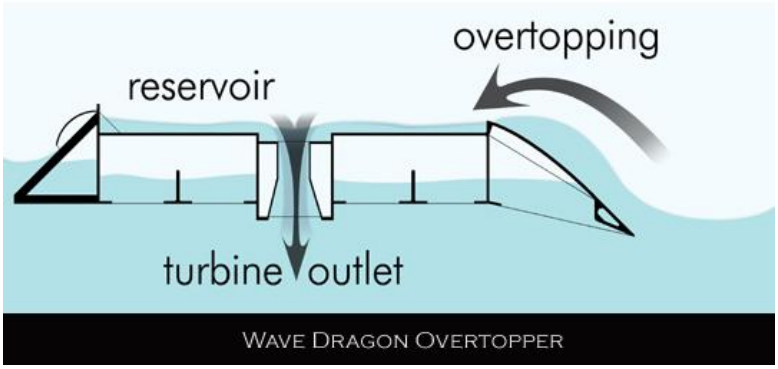

Figure-6: Wave Dragon (Overtopping Device)

4 Oscillating Wave Surge Converter: An oscillating wave surge converter generally consists of a hinged deflector which is positioned perpendicular to the wave direction (a terminator). The hinged deflector moves back and forth exploiting the horizontal particle velocity of the wave. "Aquamarine Power Oyster (a near-shore device) is a common example of an oscillating wave surge converter. In this device, the top of the deflector is above the water surface and is hinged from the sea bed.[14]"

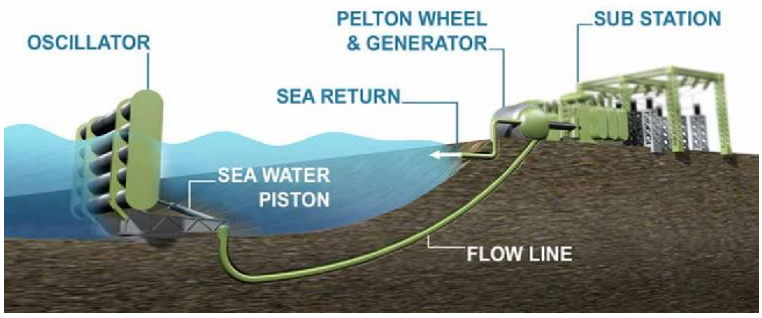

Figure-7: Aquamarine Power Oyster (Oscillating Wave Surge Converter)

III. STATUS OF WECS IN INDIA

"With the present state of technology, India's potential of wave energy is estimated to be 40-60 GW. The wave energy potential is estimated to be 5-15 MW/m along the coastline. Except for the pilot plant at Vizinjham Fisheries Harbour near Trivandrum in Kerala, India has no large wave energy plants. The Maharashtra Government has built a project which would lead to the generation of 15-20 kW of electricity located at Borya and Budhal villages in the coastal Ratnagiri district. The wave energy potential along the Indian coast was examined in depth in a report published by the Indian Renewable Energy Development Agency (2014). Their results depicted that higher wave power is available along the west coast which is likely due to strong waves during the south-west monsoon. However, due to very powerful winds, the highest wave power can be obtained at the southern tip of the Indian peninsula (Kanyakumari, Nagercoil district, Koodankulam). Based on wave statistics, five possible sites for the deployment of wave energy devices were identified. These locations and their wave power are shown in Table 1.[15], [16]"

Table-1: Favourable locations for WECs in India

State	Location	Wave power (in kW/m)
Andhra Pradesh	Kaviti	14.96
Tamil Nadu	Puducherry	10.59
Tamil Nadu	Kanyakumari	23.39
Kerala	Trivandrum	25.08
Maharashtra	Kudal	21.95

IV. CONCLUSION

Wave power has enormous potential in electricity generation. The ocean is an enormous resource and harnessing ocean wave energy is a significant step towards achieving the renewable energy targets. Wave power (or energy) conversion technologies have made significant progress over the past decade. Despite the remarkable progress, these technologies still remain immature as shown by a large number of different technologies and device sizes. Also the initial cost of construction is quite high for WECs. Currently, investment in wave power is considered risky due to lack of operational experience and high capital cost. A combination of focused research and the establishment of government incentives for an early adopter market would be required to move the technological progress forward.

ACKNOWLEDGEMENT

Authors wish to acknowledge Delhi Technological University for their complete support throughout the work.

V. REFERENCES

[1] https://www.mahaurja.com/meda/en/new_technologies/wave_power
[2] López, I., Andreu, J., Ceballos, S., Martínez de Alegría, I., & Kortabarria, I. (2013). Review of wave energy technologies and the necessary power-equipment. Renewable and Sustainable Energy Reviews, 27, 413–434.
[3] Blackledge, Jonathan & Coyle, Eugene & Kearney, Derek & McGuirk, Ronan & Norton, Brian. (2013). Estimation of Wave Energy from Wind Velocity. Engineering Letters. 21. 158-170.
[4] https://waveenergyconversiontamu15.weebly.com/theory-of-wave-energy--availability.html
[5] http://www.emec.org.uk/about-us/wave-clients/pelamis-wave-power/
[6] https://oceanpowertechnologies.com/pb3-powerbuoy/
[7] https://coastalenergyandenvironment.web.unc.edu/ocean-energy-generating-technologies/wave-energy/overtopping-terminator/
[8] Drew, B., Plummer, A. R., & Sahinkaya, M. N. (2009). A review of wave energy converter technology. Proceedings of the Institution of Mechanical Engineers, Part A: Journal of Power and Energy, 223(8), 887–902.

[9] https://tethys.pnnl.gov/organization/archimedes-wave-swing
[10] Alves, M. (2016). Frequency-Domain Models. Numerical Modelling of Wave Energy Converters, 11–30.
[11] http://wavesycys.blogspot.com/2008/05/case-study-limpet-wave-power-generator.html
[12] H. Polinder and M. Scuotto, "Wave energy converters and their impact on power systems," in Proc. Int. Conf. Future Power Systems, Nov. 18, 2005, pp. 9–18.
[13] https://tethys.pnnl.gov/project-sites/wave-dragon-pre-commercial-demonstration-project
[14] https://tethys-engineering.pnnl.gov/technology/oscillating-wave-surge-converter
[15] https://inpressco.com/wp-content/uploads/2016/10/Paper38179-182.pdf
[16] Khojasteh, D., Mousavi, S. M., Glamore, W., & Iglesias, G. (2018). Wave energy status in Asia. Ocean Engineering, 169, 344–358.

2021 11th International Conference on Cloud Computing, Data Science & Engineering (Confluence) | 978-1-6654-1451-7/20/$31.00 ©2021 IEEE | DOI: 10.1109/Confluence51648.2021.9377116

Application of Particle Swarm Optimization for Software Defect Prediction Using Object Oriented Metrics

Dr. Ruchika Malhotra
Department of Computer Science and Engineering
Delhi Technological University
New Delhi, India
ruchikamalhotra@dtu.ac.in

Nishant
Department of Computer Science and Engineering
Delhi Technological University
New Delhi, India
nishant_2k17co211@dtu.ac.in

Spandun Gurha
Department of Computer Science and Engineering
Delhi Technological University
New Delhi, India
spandungurha_2k17co342@dtu.ac.in

Vishal Rathi
Department of Computer Science and Engineering
Delhi Technological University
New Delhi, India
vishalrathi_2k17co378@dtu.ac.in

***Abstract*— With the growing number of software applications being developed for every small challenge, the importance of devising efficient software defect prediction models is imperative. Over the years, various machine learning techniques have been utilized to develop defect prediction model and have managed to achieve good results. In all defect prediction models, the task of correcting imbalanced data and feature selection has been of great significance. In this paper we have tried to analyze the working of the oversampling technique SMOTE along with feature selection using Particle Swarm Optimization on Object Oriented metrics. The selected features were then used to train the datasets one of the most popular classification techniques- Support Vector Machine to predict defects. The four datasets used for this study are of different Apache applications whose source code was obtained from open-source platforms and the raw data was pre-processed to obtain Object Oriented metrics. The performance measures used to record the results were Area Under ROC Curve, Recall and F-Measure values which showed that the Support Vector Classifier performed better on the dataset that had been balanced using SMOTE and acted upon by Particle Swarm Optimization for selecting feature set.**

Keywords—Support Vector Machine, Software Defect Prediction, Particle Swarm Optimization, SMOTE, Object Oriented metrics

I. INTRODUCTION

A widely researched area of study- software defect prediction finds its importance in software testing and debugging. [1] Defects arising can greatly affect the functioning of a complete software for which we require efficient defect prediction models. Various studies in the past have made use of class metrics and have predicted defects are the granular level.[2-4] Recent studies have shown the use of product and process metrics for defect prediction models. [5-6]

During the development of a defect prediction model, it is imperative to deal with imbalanced data as it may lead to faulty models that incorrectly classify defects. Various classifiers fail to classify defects accurately when trained on imbalanced datasets which could have catastrophic effects on the working of a software. Defect prediction models have used a number of machine learning techniques for classification, a study has shown that the classification technique of Support Vector Machine is counted as one of the most effective and popular techniques.[7]

While the problem of imbalanced data severely hampers the efficiency of a model, large number of attributes in a study also tends to have negative results. Selection of a suitable set of attributes is a crucial task that can greatly improve the performance of the model. In the past, various statistical tests as well as univariate and multi-variate analyses have been used to extract the optimum set of features from a dataset.

Through this study, we have tried to delve deeper into the possibility of using Synthetic Minority Oversampling Technique (SMOTE) to tackle the issue of imbalanced data and using a Random Forrest based Particle Swarm Optimisation technique to extract the optimal feature set on four Apache applications datasets which are then trained on the Support Vector Classifier to predict defects in a software. The results have been recorded under three performance measures namely- Area Under ROC Curve, Recall and F-Measure values. It was observed that the datasets after applying SMOTE and Particle Swarm Optimization fared much better than without it.

The rest of the study is divided into following sections: Abbreviations used in the study have been mentioned in section II, related work in III, the experiment design has been elaborated in section IV, V includes the proposed methodology, section VI explains the performance results, section VII highlights the experimental results, the conclusion of this study has been given in section VIII, acknowledgement in section IX and the references cited have been mentioned in section X.

II. ABBREVIATIONS

The following abbreviations have been used in this paper:

SMOTE	Synthetic Minority Oversampling Technique
SVM	Support Vector Machine
SVC	Support Vector Classifier
OO	Object Oriented
PSO	Particle Swarm Optimization

Authorized licensed use limited to: DELHI TECHNICAL UNIV. Downloaded on March 27,2021 at 05:37:33 UTC from IEEE Xplore. Restrictions apply.

ROC Receiver Operating Characteristics
AUC Area Under Curve
TP True Positive
TN True Negative
FP False Positive
FN False Negative

III. RELATED WORK

A number of studies have been conducted till date to study software defect prediction using classical machine learning techniques that included both supervised as well as unsupervised learning methods. A comparative analysis of 208 primary studies pertaining to defect prediction was carried out by Hall et al. [8]. Approximately 70% of the studies conducted till date have utilised the Eclipse datasets while there continues to be popularity of the NASA datasets available on the PROMISE repositories. [9] In more recent times studies have been made to ascertain the performance of machine learning techniques on the PROMISE repository datasets [10] which was further expanded on open-source datasets as well. [11] A systemic review of studies pertaining to application of machine learning for software fault prediction was carried out by Malhotra [12]. The open source platform provides a large amount of datasets for software defect prediction.

The types of attributes of a dataset greatly determine the performance of the predictive model. Previous studies have widely made use of complexity metrics [13] such as Lines of Code (LOC). However, it was stated by Bell et al. [14] that the Lines of Code metric fails to have the necessary predictive power and is overpowered by other performance metrics. Malhotra et al. [15] studied the application and efficiency of 22 OO metrics proposed over time by researchers. The validation of OO metrics in predicting software fault proneness was carried out by Singh et al. [16] The effect of OO metrics on classifying defects in open source software over multiple machine learning techniques has also been reported. [17] While building a model, the problem of imbalanced data persists quite often, various techniques of undersampling and oversampling have been tested by various researchers. The re-sampling technique of SMOTE was introduced by Chawla et al. [18] which introduced the concept of 'phantomtransduction' to create new instances in a dataset.

The selection of an optimal set of attributes to train the prediction model, several feature extraction techniques have been used in the past. V.A. Kumar and N. Elavarasan [19] conducted a study to analyse the various dimensionality reduction techniques suitable for classification models. Wahono et al. make use of Particle Swarm Optimisation and Bagging techniques to predict software defects. [20]
A wide range of trainable classifiers have used in defect prediction models, 22 such classifiers were studied by Lessman et al. [21]. The use of SVC for predicting defects has been reported by Akbani [22] while also stating the reasons for poor performance of SVC on imbalanced datasets.

IV. EXPERIMENT DESIGN

The datasets used in this study have been obtained from the source codes of four Apache applications built in Java language. Source codes were collected for multiple releases of all the applications, available publicly on GitHub, an open source software repository, owned by Microsoft. The Understand™ software by SciTools [23] was used to analyse the source code of all the applications through which 19 OO metrics were obtained, namely- 'CountLine' ,'CountLineCode', 'CountLineBlank', 'CountLineComment', 'CountClassBase', CountClassCoupled', 'CountClassDerived', 'CountDeclClassMethod', 'CountDeclClassVariable', 'CountDeclInstanceMethod', 'CountDeclInstanceVariable', 'CountDeclMethod', 'CountDeclMethodAll', 'CountDeclMethodDefault', 'CountDeclMethodPrivate',CountDeclMethodProtected', 'CountDeclMethodPublic', 'MaxInheritanceTree', 'PercentLackOfCohesion'.

The defect prediction dataset was formed by comparing successive versions of an application where by a defect in any functionality was noted. A binary classification was formed which marked the instances as defective (1) or non-defective (0). The redundancies in the data for different versions an application were removed before concatenation to achieve a master dataset for one application.

The datasets used in this study are:
1. Apache Beam
2. Apache Hive
3. Apache Geode
4. Apache Flink

Table 1: Summary of Instances of Apache Datasets

Dataset	Total No. of Instances	No.of defective instances	No. of non-defective instances
Beam	14353	1872	12481
Hive	15545	880	14665
Geode	45604	146	45458
Flink	35002	1569	33433

Figure 1 presents a summarized view of the steps involved in our study to construct a software defect prediction model.

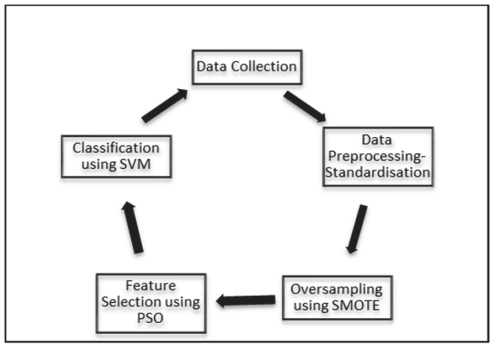

Fig 1: Flowchart of steps of the study

Authorized licensed use limited to: DELHI TECHNICAL UNIV. Downloaded on March 27,2021 at 05:37:33 UTC from IEEE Xplore. Restrictions apply.

V. PROPOSED METHODOLOGY

A. Data Preprocessing

In this study, four Apache application defect prediction datasets were taken which were checked for data imbalance, outliers and missing or inconsistent information. Since raw data tends to have a varied range of values, some objective functions in machine learning algorithms fail to produce good results without normalisation. To avoid such an error, we used the method of standardization to normalise our dataset. The StandardScaler function was used on the datasets which normalises the data points using their standard deviation. The standard score Z of a sample X is calculated by

$$Z = \frac{(X-U)}{S} \quad (1)$$

Where,
U: Mean of the training samples
S: Standard Deviation of training samples

On further analysing the data, it was noted that the number of non-defective instances in the dataset exceeded the number of defective instances making the dataset highly imbalanced. When classification is performed on an imbalanced dataset, the outcome is in the favour of the class having majority of the instances. To overcome this error, we have used SMOTE, an re-sampling method that performs oversampling on the minority classes and increases its instances, in this study the number of defective instances were oversampled to create a balance. The SMOTE uses K-Nearest Neighbour method to oversample the minority class in which the new instances that are generated are not the replica of the existing minority instances. The algorithm identifies and takes samples for every target class as well as its nearest neighbours, thus making the new samples more general.

B. Feature Selection

PSO(Particle Swarm Optimization) was formally introduced and popularized by Eberhart and Kennedy in 1995 [24] in which they proposed an optimization methodology based on the particle swarm theory. In PSO, a swarm of entities is placed in a definite search space defined for a particular problem in which every particle decides it path of movement by taking some consideration from past movements as well as the current best location (best fitness function value). An iteration is completed when every particle of the swarm has moved. This movement of the particles together in an iteration to the most optimum fitness location can be considered like the movement of a flock of birds as a swarm in search for food. All the particles in the swarm are comprised of three D-dimensional vectors, wherein D defines the dimensionality of the given problem's search space. These three vectors are, current position which is a set of coordinates defining the current location of a particle, the previous best position vector which defines the last value of the fitness function and the velocity vector which defines the particles velocity to move in the swarm. In every iteration, if the current location is better than the previous best fitness location, the best position vector is updated. This process continues till the best solution is not achieved or the limiting condition is not satisfied.

In this study, we have used a Random Forrest Classifier based Binary PSO model in order to retrieve the optimal set of features required for classification. In Binary PSO, the location of each particle in the swarm is denoted by 0 if absent and 1 if present. Every feature of the dataset is assigned as a dimension of every particle, hence for example if a dataset has 7 features, each particle of the swarm if going to be on 7-dimensions that is one dimension for every feature. Therefore for a dataset with P number of particles on D dimensions then the position of the particle can be defined In the form of

$P= [P_1, P_2, P_3,\ldots P_D]$ where $P_i \epsilon 0,1$

The values of P_i form a binary array from which determine whether a feature was selected or deselected by the swarm. The objective function used in binary PSO can be designed as per the requirements of a give problem however in this study we have used the equation given by Vieira et al. [25].

$$f(X)= \alpha(1-P)+(1- \alpha) \left(1-\frac{N_f}{N_t}\right) \quad (2)$$

Where,α is the hyperparameter that is used to determine a balance between the performance measure of classifier P, the size of subset of features N_f with respect to N_t, total number of features. The measure of classifier performance can be accuracy, precision, recall among others. In our study we have used the Random Forest Classifier and have used the G-1 Mean values of the classifier to measure its performance.

Since the total size of the feature set in the dataset was 19, the dimensions of each particle were also 19. The other optimization parameters of the weights, constant c_1, c_2, number of particles and iterations were decided by a hit and trial method so as to get the best cost and along with it an optimal subset of features to be used. On applying binary PSO, a feature subset of 10 OO metrics was obtained that was chosen by all the four Apache datasets, which were

1. CountLine
2. Count LineCode
3. CountLineComment
4. CountClassCoupled
5. CountClassDerived
6. CountDeclClassMethod
7. CountDeclInstanceMethod
8. CountDeclMethod
9. CountDeclMethodPublic
10. MaxInheritanceTree

These selected features were then used to train the SVM classifier to predict defects on the test data.

C. Classification

Over the years, a number of machine learning techniques have been used as classifiers in software defect prediction models but it has been observed that the SVM technique of classification continues to be a very popular classification method. Introduced formally in 1995 by Vapnik and Cortes [26] the SVM algorithm works on the principle that all the data points in an n-dimensional space are a set of vectors. It has a vector plane referred to as the hyperplane which is

Authorized licensed use limited to: DELHI TECHNICAL UNIV. Downloaded on March 27,2021 at 05:37:33 UTC from IEEE Xplore. Restrictions apply.

created equidistant from the closest identifiable and distinguishable vectors. The location of each data point with respect to the hyperplane determines the category of the data point. All the data points are either labelled as +1 or -1 which are useful for dividing them into their respective categories. The main aim of the algorithm is to establish maximum distance between the two classes present in the feature space. SVM states that given a training dataset of total n data points in the form of

$$(\vec{x1}, y1), (\vec{x2}, y2) \ldots\ldots (\vec{x_n}, y_n)$$

Where, every vector $\vec{x_i}$ is a d- dimensional vector and each y_i carries the values of either +1 or -1 which is an indication of the class to which the vector belongs. The priority is to create a maximum margin hyper plane that will divide the instances belonging to the +1 class farthest away from the instances belonging to the -1 class.

The equation of the hyperplane can be defined over a set of points $\vec{x}$

$$\vec{w}.\vec{x} - b = 0 \quad (3)$$

Wherein, $\vec{w}$ is the normal vector to the given hyper-plane.

This concept of the hyperplane introduced by Vapnik in 1995 was successful in building a linear classifier. Boser et al. [27] suggested the use of kernel functions in the same model to build non-linear classifiers. The resulting algorithm introduces a kernel function in every dot product. In our study we have made use of the Gaussian Radial Basis Function as the kernel function to build a non-linear classifier. While using the SVM classifier for a defect prediction model, an imbalance in the number of data points results the shifting of the hyperplane towards the majority class which pushes the minority class instances far away from the hyperplane. Thus it is imperative to balance the data points in a dataset before training the SVM classifier. We have tried to draw a comparison in the efficiency of the SVM classifier before and after the use of SMOTE and PSO for defect prediction.

VI. Performance Measures

Three performance measures have been used in this study to record the results of SVM classifier in predicting defects in four Apache datasets- Area Under Curve (AUC) value of the Receiver Operating Characteristics (ROC) curve, recall and F-Measure values.

The most common and primarily used measure is the ROC-AUC values for our given dataset. These values are a depiction of the degree of independence achieved during classification along with the degree to which the classes can be separated. In classification models, these values generally range between 0 and 1, where a greater ROC-AUC value indicated better performance of the classification technique. The ideal value of 1 indicated that the prediction model is capable of classifying all classes correctly whereas a value of 0.5 indicates that the model fails to distinguish between two classes and is of no use. The ROC curve is a graphical representation of the relationship between the True Positive Rate (TPR) and the False Positive Rate (FPR) both of which are calculated using the confusion matrix metrics.

$$\text{TPR} = \frac{TP}{TP+FN} \quad (4)$$

$$\text{Specificity} = \frac{TN}{TN+FP} \quad (5)$$

$$\text{FPR= 1- Specificity=} \frac{FP}{TN+FP} \quad (6)$$

The second performance measure used is the Recall values. Recall is defined as the ratio of all the correctly classified instances to the total actually correct instances in a dataset.

$$\text{Recall=} \frac{\text{TP}}{\text{TP+FN}} \quad (7)$$

The third performance measure used is the F1-Measure which is determined using the harmonic mean of precision and recall values. The F1-score determines how accurate and precise our classifier is at the same time also showcases the robustness of the model. The greater the value of the F1-score the higher is the efficiency of the defect prediction model.

$$\text{F1-Measure= } 2 * \frac{Precision * Recall}{Precision + Recall} \quad (8)$$

VII. Experimental Results

The four Apache datasets were standardized to achieve values that would not give errors during classification. Since the data was highly imbalanced, we used SMOTE to achieve a balance between the two classes. After the data had been balanced, PSO was applied to get an optimal set of features needed for classifications which were then trained on the SVM classifier and results were recorded in the above mentioned three performance measures.

Through the means of this study we have tried to bring out a comparative analysis between the performance of the SVM classifier when trained on an imbalanced dataset without feature selection with the performance of the SVM classifier on a balanced dataset with the features being selected using PSO.

Table 2 presents the comparative analysis of SVM classifier in terms of ROC-AUC values of the four Apache datasets. It is observed that prior to the feature selection method, imbalanced datasets were incapable of classifying data accurately. Apache Geode turned out to be the most promising dataset with an ROC-AUC value of 0.873.

Authorized licensed use limited to: DELHI TECHNICAL UNIV. Downloaded on March 27,2021 at 05:37:33 UTC from IEEE Xplore. Restrictions apply.

Table 2: ROC-AUC values for SVM classifier

Dataset	Without SMOTE and PSO	With SMOTE and PSO
Apache Beam	0.52	**0.71**
Apache Hive	0.50	**0.72**
Apache Geode	0.70	**0.873**
Apache Flink	0.50	**0.72**

Table 3 presents a comparative analysis of SVM classifier using Recall values of the four Apache datasets. Since recall gives a measure of the correctly classified instances, a high recall value is preferred for more accurate results. Apache Geode gives the best recall value of 0.952, indicating that the dataset was successful in classifying almost all of the instances accurately.

Table 3: Recall values for SVM classifier

Dataset	Without SMOTE and PSO	With SMOTE and PSO
Apache Beam	0.382	**0.776**
Apache Hive	0.50	**0.751**
Apache Geode	0.716	**0.952**
Apache Flink	0.50	**0.715**

Table 4 presents the comparative analysis of SVM classifier in terms of F1-Meaure values of the four Apache datasets. A high F1-Measure signifies that a classification model is efficient and robust in predicting defects. In this case as well, Apache Geode outperforms other datasets and has the maximum F1 score.

Table 4: F1-Score values for SVM classifier

Dataset	Without SMOTE and PSO	With SMOTE and PSO
Apache Beam	0.305	**0.702**
Apache Hive	0.484	**0.705**
Apache Geode	0.722	**0.844**
Apache Flink	0.48	**0.715**

Thus, we observe that all the datasets give significantly better results when combined with SMOTE and PSO and Apache Geode outperforms all the other datasets in predicting defects.

VIII. CONCLUSION

Through this study we have tried to depict the various steps involved in constructing an efficient software defect prediction model. It was observed that classification techniques do not work well on imbalanced data and this study aims to tackle that problem using the oversampling technique of SMOTE. While building a prediction model for software defect, it is observed that not all features and attributes of the dataset contribute equally to the classification process and hence a subset of optimal features needs to be selected for better performance of the model.

Tables 2-4 showcase the different ROC-AUC, recall and F1-measure values for the SVM classifier. It was observed through the numerical values obtained that an SVM classifier performs much more efficiently when the problem of data imbalance was solved using SMOTE and important features were selected for classification using PSO. Hence, we can conclude that the oversampling technique of SMOTE when combined with PSO for feature selection can be used for building efficient software defect prediction models.

IX. ACKNOWLEDEGMENT

We extend our sincerest gratitude to the Department of Industrial Research & Development, Delhi Technological University for providing grant and constant support and guidance throughout our research without which this study would not have been possible.

X. REFERENCES

[1] X. Yang, D. Lo, X. Xia, Y. Zhang, & J. Sun, "Deep learning for just-in-time defect prediction." In Proceedings of International Conference on Software Quality, Reliability and Security, pp. 17-26, 2015.

[2] M. DAmbros, M. Lanza, and R. Robbes, "Evaluating defect prediction approaches: a benchmark and an extensive comparison," Empirical Software Engineering, vol. 17, no. 4-5, pp. 531–577, 2012.

[3] T. Zimmermann and N. Nagappan, "Predicting defects using network analysis on dependency graphs," in ICSE, 2008, pp. 531–540.

[4] B. Turhan, T. Menzies, A. B. Bener, and J. Di Stefano, "On the relative value of cross-company and within-company data for defect prediction," Empirical Software Engineering, vol. 14, no. 5, pp. 540–578, 2009.

[5] R, Jayanthi & Florence, Lilly & Arya, Arti. (2017). A Review on Software Defect Prediction Techniques Using Product Metrics. International Journal of Database Theory and Application. 10. 163-174. 10.14257/ijdta.2017.10.1.15.

[6] L. Madeyski, M. Jureczko, Which process metrics can significantly improve defect prediction models? An empirical study. Software Qual J 23, 393–422 (2015). https://doi.org/10.1007/s11219-014-9241-7

[7] A. Kalsoom, M. Maqsood, M.A.Ghazanfar et al. A dimensionality reduction-based efficient software fault prediction using Fisher linear discriminant analysis (FLDA). J Supercomput 74, 4568–4602 (2018). https://doi.org/10.1007/s11227-018-2326-5

[8] T. Hall, S. Beecham, D. Bowes, Gray, D., & Counsell, S. (2012). A systematic literature review on fault prediction performance in software engineering. IEEE Transactions on Software Engineering, 38(6), 1276–1304.

[9] http://promise.site.uottawa.ca/SERepository/

[10] D. Bowes, T. Hall, & J. Petri´c "Different classifiers find different defects although with different level of consistency." In Proceedings of the 11th International Conference on Predictive Models and Data Analytics in Software Engineering, PROMISE '15, pp 3:1–3:10. doi:10.1145/2810146.2810149. (2015)

[11] D. Bowes, T. Hall, & J. Petri´c "Software defect prediction: do different classifiers find the same defects". Software Qual J 26, 525–552 (2018). https://doi.org/10.1007/s11219-016-9353-3

[12] R. Malhotra "A systematic review of machine learning techniques for software fault prediction." Appl Soft Comput, 27(C), 504–518. doi:10.1016/j.asoc.2014.11.023. (2015)

[13] Y. Zhou, B. Xu, & H. Leung, "On the ability of complexity metrics to predict fault-prone classes in object-oriented systems". Journal of Systems and Software, 83(4), 660–674. (2010)

Authorized licensed use limited to: DELHI TECHNICAL UNIV. Downloaded on March 27,2021 at 05:37:33 UTC from IEEE Xplore. Restrictions apply.

[14] R. Bell, T. Ostrand, & E. Weyuker, Looking for bugs in all the right places. In Proceedings of the 2006 international symposium on Software testing and analysis, ACM, pp 61–72. (2006).

[15] K. Aggarwal, Y. Singh, A. Kaur and R. Malhotra. "Empirical Study of Object-Oriented Metrics." *J. Object Technol.* 5 (2006): 149-173.

[16] Y. Singh, A. Kaur & R. Malhotra,. Empirical validation of object-oriented metrics for predicting fault proneness models. Software Qual J 18, 3 (2010). https://doi.org/10.1007/s11219-009-9079-6

[17] T. Gyimothy, R. Ferenc, and I. Siket, "Empirical validation of object-oriented metrics on open source software for fault prediction," IIEEE Trans. Software Eng., vol. 31, no. 10, pp. 897–910, Oct. 2005.

[18] Chawla, V. Nitesh, K. Bowyer, L. Hall and W. P. Kegelmeyer. "SMOTE: Synthetic Minority Over-sampling Technique." *J. Artif. Intell. Res.* 16 (2002): 321-357.

[19] V. Arul Kumar, N. Elavarasan, , " A Survey on Dimensionality Reduction Technique " , International Journal of Emerging Trends & Technology in Computer Science (IJETTCS), Volume 3, Issue 6, November - December 2014 , pp. 036-041 , ISSN 2278-6856.

[20] Wahono, Romi & Suryana, N.. (2013). Combining Particle Swarm Optimization based Feature Selection and Bagging Technique for Software Defect Prediction. International Journal of Software Engineering and Knowledge Engineering. 7. 153-166. 10.14257/ijseia.2013.7.5.16.

[21] S. Lessmann, B. Baesens, C. Mues, & S. Pietsch, Benchmarking classification models for software defect prediction: A proposed framework and novel findings. IEEE Transactions on Software Engineering, 34(4), 485–496. (2008)

[22] Akbani, Rehan & Kwek, Stephen & Japkowicz, Nathalie. (2004). Applying Support Vector Machines to Imbalanced Data Sets. Lecture Notes Artif. Intell.. 3201. 39-50. 10.1007/978-3-540-30115-8_7.

[23] www.scitools.com/

[24] R.C. Eberhart, & J. Kennedy, A new optimizer using particle swarm theory. In Proceedings of the sixth international symposium on micro machine and human science (pp. 39–43), Nagoya, Japan. Piscataway: IEEE. (1995)

[25] M. Susana, Vieira, F. Luís, Mendonça, J. Gonçalo, Farinha, João M.C. Sousa,'Modified binary PSO for feature selection using SVM applied to mortality prediction of septic patients',Applied Soft Computing,Volume 13, Issue 8,2013, Pages 3494-3504, ISSN 1568-4946, https://doi.org/10.1016/j.asoc.2013.03.021.

[26] Cortes, Corinna and V. Vapnik. "Support-Vector Networks." *Machine Learning* 20 (2004): 273-297.

[27] Boser, Bernhard & Guyon, Isabelle & Vapnik, Vladimir. (1996). A Training Algorithm for Optimal Margin Classifier. Proceedings of the Fifth Annual ACM Workshop on Computational Learning Theory. 5. 10.1145/130385.130401.

Authorized licensed use limited to: DELHI TECHNICAL UNIV. Downloaded on March 27,2021 at 05:37:33 UTC from IEEE Xplore. Restrictions apply.

Eco. Env. & Cons. 26 (November Suppl. Issue) : 2020; pp. (S174-S181)
Copyright@ EM International
ISSN 0971–765X

Assessment of elemental Carbon, Nitrogen, Hydrogen and Sulphur in alluvial sediments of River Yamuna in Delhi region

Vivek Chopra[1] and Jai Gopal Sharma[2*]

[1]Department of Biotechnology, [1]Department of Botany,
Hindu College, University of Delhi, Delhi 110 007, India
[2]Department of Biotechnology, Delhi Technological University, Delhi 110 042, India

(Received 8 April, 2020; Accepted 18 May, 2020)

ABSTRACT

River Yamuna a major wetland on which significant portion of the population of Delhi depends for the daily requirements of water usage has been analyzed for elemental Carbon (C), Hydrogen (H),Nitrogen (N)and Sulphur(S) as well as the ratio of Nitrogen and Hydrogen with Carbon. Total of 18 samples were collected from 2 different sites of the Yamuna. Site APalla village where Yamuna enters in Delhi. Nine samples were collected from river bed vertically from 3 different locations with 3 samples from each location at varying depths. Same set of sampling was done at Site 2 Okhla barrage and 9 samples were collected from 3 various locations at different depths of river bed. Average percentage concentration of C, H, N and S at site A on the surface (0-2 cm) of river was 0.256, 0.223, 0.173 and 0.012 while at depth range of 26-32 cm and 59-80 cm was 0.3, 0.22, 0.2, 0.02 and 0.303, 0.189, 0.146 and 0.011 respectively. Average percentage concentration of C, H, N, and S at site B at the surface (0-2 cm) of river bed was measured as 0.216, 0.176, 0.15, and 0.024 and at depth range of 26-32 cm it was 0.52, 0.22, 0.16, and 0.061 while it was 0.33, 0.284, 0.19, and 0.0495 at an average depth of 62-69cm. C/N and C/H ratio ranged from 1.461 to 3.0769 and 1.194 to 2.1769 respectively at both the sites. The analysis of above data helps to determine the difference in concentration and deposition of elements at different vertical levels of strata of the river bed which ultimately increases our understanding about complex aquatic ecosystems and helps in conservation.

Key words*: River Yamuna, Carbon, Hydrogen, Nitrogen, Sulphur, CHNS analysis*

Introduction

River Yamuna travels a distance of 1376 km from its source near Yamunotri glacier to its convergence with Ganga River at city Prayagraj. 70% population of Delhi depends for daily usage of water on 48km stretch which passes through it (CPCB, 2006). River Yamuna which is an important wetland ecosystem of Delhi is facing a great threat of pollution from industrialization, unplanned urbanization, extensive agricultural practices and a very deprived waste water treatment and drainage system. Many studies have been done on various aspects of the river like heavy metal contaminants in river water and soil (Sehgal *et al*., 2012; Said *et al*., 2019), microbial communities (Sharma *et al.,* 2017) but comparatively less data is available for elemental CHNSin the sediments of the river bed. The aim of this study is to investigate the amount of CHNS at various depths of soil sediments and correlation of ratio of Nitrogen and Hydrogen with Carbon at different sites of river Yamuna in Delhi region. It is necessary

to identify the distribution and concentration of soil elements to study systematic conditions within sediments and how it affects the physicochemical nature of the soil which can ultimately help in conservation of such vital aquatic ecosystems.

Materials and Methods

A total of 18 samples were collected from two sites (Fig. 1) of River Yamuna in Delhi region. Site A was Palla village (28°85′61.7"N 77°20′80.2"E) which is located at north of Delhi and the point where river Yamuna enters in Delhi. Site B was near Okhla barrage (28°32′10.5"N 77°19′29.6"E) which is almost located at the last stretch of river Yamuna in Delhi.

Site 1 is comparatively free from pollutants and other anthropogenic activities beside agriculture in vicinity. Multiple samples were collected for better and authentic interpretation of results. Nine samples were collected at site A (Palla village) from 3 different locations on river and from each location 3 samples were taken at different depths of river bed. At location 1 samples were taken from surface (0-2 cm) and at the depth of 30-32 cm and 78-80 cm depth of the river bed. Again 3 samples were taken from location 2 and location 3 at the surface (0-2 cm) and depths of 30-32 cm, 74-76 cmand 26-28 cm, 59-61 cm respectively. Same set of sampling was done at Site B (Okhla barrage) with 9 samples in total from three different locations i.e. location 4, 5 and 6 at the surface (0-2 cm) and various depths of 30-32 cm, 76-78 cm and 30-32 cm, 67-69 cm and 26-28 cm and 62-64 cm respectively. The geographical location was taken by Garmin GPSMAP 76CSX global positioning system. 5–10 mg sub-samples were homogenized and dried in an oven at 105ºC (Relic *et al.*, 2010) and concentration Percentage of Carbon, Hydrogen, Nitrogen and Sulphur were analyzed by elementar EL cube CHNS elemental analyzer.

Statistical analysis

In this study, we have performed statistical analysis using the Statistical Package for Social Sciences (SPSS 19.0) software package in direction to understand the relationship and interaction of elements with each other.

Results

Per cent concentration of total Carbon, Hydrogen,

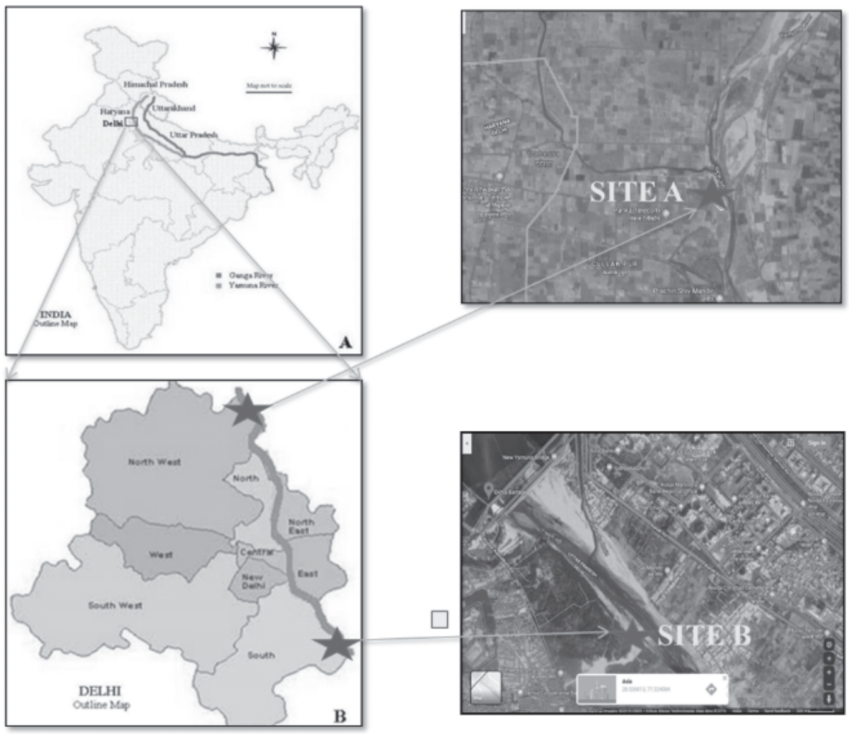

Fig. 1. Location of Site A (Palla village) and Site B (Okhla barrage) of River Yamuna in Delhi

Nitrogen and Sulphur in all 18 samples from both the sites is shown in Tables 1-2 and Figs. 2-3.

Total Carbon at Site A ranged from 0.11 to 0.45 % while Hydrogen, Nitrogen and Sulphur ranged between 0.132-0.299 %, 0.09-0.28 % and 0.01-0.024 % respectively. Site B percentage range varied from 0.17 to 0.33% in case of Carbon and from 0.126-0.371%, 0.09-0.29% and 0.017-0.104% of Hydrogen, Nitrogen and Sulphur respectively. [Results of Sample taken from depth 76-78 cm at location 4 was not recorded because of technical error]

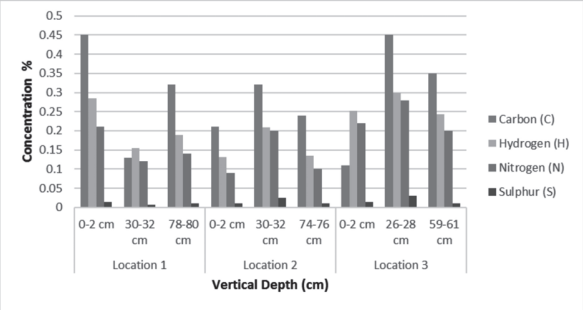

Fig. 2. Elements Concentration % of Three Locations at Site A (Palla Village)

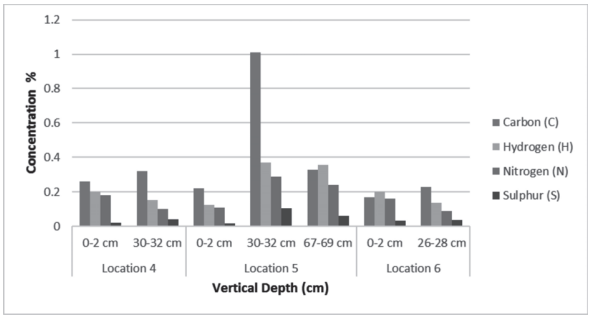

Fig. 3. Elements Concentration % of Three Locations at Site B (Okhla barrage)

The C/N and C/H ratios of both the sites are shown in Tables 3-4 and Figures 4-5.

The variation between the ratio of Nitrogen and Hydrogen with Carbon has been also recorded. C/N ratio ranged from 0.494-2.1254 and from 0.433-1.7838 in case of C/H at Site A while C/N and C/H ratio at Site B varied from 1.0237-3.472 and 0.8223-2.7341 respectively.

Table 1. Elements Concentration % of Three Locations at Site A (Palla village)

Elements	Depths at Location 1 (cm)			Depths at Location 2 (cm)			Depths at Location 3 (cm)		
	0-2 cm	30-32	78-80	0-2	30-32	74-76	0-2	26-28	59-61
	Concentration %								
Carbon (C)	0.45	0.13	0.32	0.21	0.32	0.24	0.11	0.45	0.35
Hydrogen (H)	0.284	0.155	0.189	0.132	0.209	0.135	0.253	0.299	0.243
Nitrogen (N)	0.21	0.12	0.14	0.09	0.2	0.1	0.22	0.28	0.2
Sulphur (S)	0.013	0.007	0.011	0.01	0.024	0.01	0.013	0.03	0.011

Table 2. Elements Concentration % of Three Locations at Site B (Okhla barrage)

Elements	Depths at Location 4 (cm)			Depths at Location 5 (cm)			Depths at Location 6 (cm)		
	0-2 cm	30-32	76-78	0-2	30-32	67-69	0-2	26-28	62-64
	Concentration %								
Carbon (C)	0.26	0.32	E	0.22	1.01	0.33	0.17	0.23	0.33
Hydrogen (H)	0.202	0.153	E	0.126	0.371	0.358	0.202	0.136	0.21
Nitrogen (N)	0.18	0.1	E	0.11	0.29	0.24	0.16	0.09	0.14
Sulphur (S)	0.022	0.04	E	0.017	0.104	0.06	0.033	0.039	0.039

[E-Shows error]

Table 3. C/N and C/H Ratios of Three Locations at Site A (Palla village)

Ratio (%)	Depths at Location 1 (cm)			Depths at Location 2 (cm)			Depths at Location 3 (cm)		
	0-2	30-32	78-80	0-2	30-32	74-76	0-2	26-28	59-61
C/N	2.1254	1.1501	2.2375	2.19	1.62	2.3089	0.494	1.613	1.7171
C/H	1.5808	0.8669	1.7143	1.5696	1.5326	1.7838	0.433	1.4954	1.4376

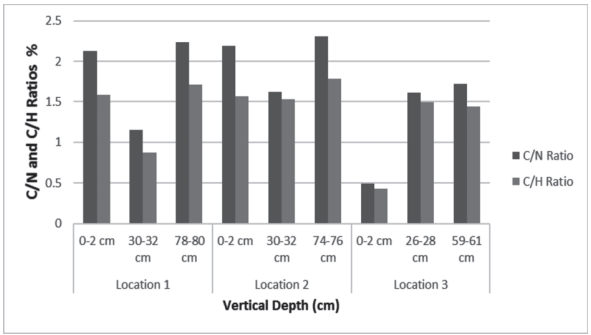

Fig. 4. C/N and C/H Ratios % of Three Locations at Site 1 (Palla Village)

Different descriptive statistics have been calculated as shown in Table 5 and Table 6 for Site A and Site B. We observed that all elements concentrations have less variations at Site A (Table 5) in comparison to Site B (Table 6).

To reveal the correlation between different elements we have conducted Pearson correlation test. From Table 7, the correlation analysis suggests significant positive correlation between Nitrogen and Hydrogen ($p < 0.01$) and between Sulphur and Nitrogen ($p < 0.05$) at site A.

Table 8 shows significant positive correlation between N and C ($p < 0.05$) and between N and H (p

Table 4. C/N and C/H Ratios of Three Locations at Site B (Okhla barrage)

Ratio (%)	Depths at Location 4 (cm)			Depths at Location 5 (cm)			Depths at Location 6 (cm)		
	0-2	30-32	76-78	0-2	30-32	67-69	0-2	26-28	62-64
C/N	1.4516	3.1508	E	2.0066	3.472	1.38	1.0237	2.6081	2.3696
C/H	1.2698	2.0713	E	1.7178	2.7341	0.9184	0.8223	1.7254	1.5812

[E-Shows error]

Table 5. Elements concentrations Descriptive Statistics for Site A (Palla village)

Elements	Minimum	Maximum	Average	Std. Deviation	Variance
Carbon (C)	.110	.450	.287	.124	.015
Hydrogen (H)	.132	.299	.211	.063	.004
Nitrogen (N)	.090	.280	.173	.064	.004
Sulphur (S)	.007	.030	.014	.007	.000

Table 6. Elements concentrations Descriptive Statistics for Site B (Okhla barrage)

Elements	Minimum	Maximum	Average	Std. Deviation	Variance
Carbon (C)	.170	1.010	.359	.270	.073
Hydrogen (H)	.126	.371	.220	.095	.009
Nitrogen (N)	.090	.290	.164	.071	.005
Sulphur (S)	.017	.104	.044	.027	.001

Table 7. Correlations of different Elements at Site A (Palla village)

Elements	Correlation	Carbon	Hydrogen	Nitrogen	Sulphur
Carbon	Pearson Correlation	1			
	Sig. (2-tailed)				
Hydrogen	Pearson Correlation	.617	1		
	Sig. (2-tailed)	.077			
Nitrogen	Pearson Correlation	.549	.958**	1	
	Sig. (2-tailed)	.126	.000		
Sulphur	Pearson Correlation	.568	.595	.755*	1
	Sig. (2-tailed)	.111	.091	.019	

* Correlation is significant at the $p < 0.05$ level (2-tailed)
** Correlation is significant at the $p < 0.01$ level (2-tailed)

Table 8. Correlations of different Elements at Site B (Okhla barrage)

Elements	Correlation	Carbon	Hydrogen	Nitrogen	Sulphur
Carbon	Pearson Correlation	1			
	Sig. (2-tailed)				
Hydrogen	Pearson Correlation	.706	1		
	Sig. (2-tailed)	.050			
Nitrogen	Pearson Correlation	.744*	.961**	1	
	Sig. (2-tailed)	.034	.000		
Sulphur	Pearson Correlation	.920**	.832*	.787*	1
	Sig. (2-tailed)	.001	.010	.020	

* Correlation is significant at the $p < 0.05$ level (2-tailed)
** Correlation is significant at the $p < 0.01$ level (2-tailed)

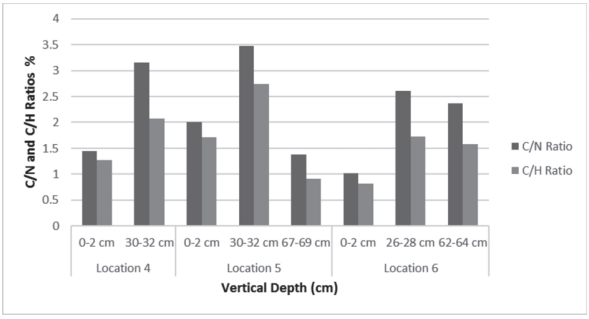

Fig. 5. C/N and C/H Ratios % of Three Locations at Site B (Okhla barrage)

< 0.01). We also observed that S is significantly correlated with C ($p < 0.01$), N ($p < 0.05$) and H ($p < 0.05$) at Site B.

Discussion

The concentration of Carbon, Hydrogen, Nitrogen and Sulphur with other trace elements susceptible to many reactions like nitrification, denitrification, co-precipitation, sulfide oxidation and hence directly affects pH (Relic *et al.,* 2010). Combined amounts of C in the atmosphere and vegetation is lesser Than the total amount of 1500 Pg carbon (1Pg= 1015 g) present in top soil up to 1 m depth and the soil carbon normally falloffs alongside depth of sediments (Jobbagy and Jackson 2000; Goidts and Wesemael, 2007). Total organic carbon is comparatively well studied as compared to total Carbon in sediments. Soil Organic Carbon (OC) is vital for plant nutrients and in conserving the soil integrity (Solanki and Chavda, 2012). Soils with <0.20% organic carbon indicates very less amount; 0.21%-0.40% indicates low OC; 0.41%-0.80% as medium and > 0.80% is considered as high OC (Jaiswal, 2006). During present study, the Carbon % results at Site A showed the higher concentration of carbon at all the locations as compared to site B. This factor is positively correlated with available Nitrogen and Sulphur which confirm that high amount of OC increases nutrient availability (Prusty *et al.,* 2009). Even hydrogen shows a close link between hydrogen and carbon cycles (Paul *et al.,* 2016). The amount of Hydrogen affects pH and the accessibility of other elements in soil andat high and low pH valuesnutrient deficiencies can be observed; Therefore, Hydrogen plays an important role in the development of plants. The percentage of Hydrogen kept varying with depths at both the site A and site B. Site A has the higher amount of Hydrogen % in almost all the three locations as compared to site B. Nitrogen concentration of the sediments critically influencesthe productivity and biodiversity of an aquatic system (Kumar *et al.,* 2012). In the present study, Site A has the higher amount of Nitrogen % in soil as compared to site B. Percentage amount of Nitrogen kept varying with depth at both the site A and site B. Organic matter presents in the soil affects the proportion of Nitrogen in the soil (Baruah, 1997). Due to diverse heterogeneity of soil it is very challenging to perceive the changes in soil N and C contents exactly (Mitsch and Gosselink, 2000). Nitrogen is one of the important limiting elements of wetland ecosystem and plays a significant role in primary productivity (Song *et al.,* 2012; Jobbagy and Jackson, 2000). Transport of sulphate from the water column into the sediments is influenced by Evapotranspiration induced advection (Choi *et al.,* 2006). Oxidation of Fe-Sulfides can lead to decreased total S content in sediments (Relic *et al.,* 2010). It could be a possible reason for low concentration of S at Site A. Sulphur showed higher values at site B as compared to site A. This may be as a result of the accumulation of sewage and industrial pollutants at this site.

A very preliminary study revealing the inorganic elements and pollutants in the Yamuna River bank soil in Delhi was studied by Farago *et al.,* (1989). Carbon content as well as organochlorine pesticides in fluvial sediments of river Yamuna was studied by Parween *et al.* (2014). Das *et al.* (2018) explained about the available Nitrogen and Sulphur by using K-jeldahl method in River Yamuna in Allahabad city. Organic Carbon and available nitrogen in different horizons of Yamuna River Bank at Prayagraj was studied by Dogo *et al.* (2019). Total Carbon (TC) and Total Nitrogen (TN) concentrations in dried sediment of Meenachil river basin in Kerala is studied by George & Joseph, (2017). Comparatively less emphasis has been given on CHNS studies on Indian river sediments while it has been extensively done all over the world on many rivers. Organic carbon and nitrogen with C/N ratios of river sediments were discussed by Dinelli *et al.* (2005) in Arno river, Italy. CHN analysis on sediments of São Francisco River basin in Brazil was done by Rezende *et al.* (2011). Relic *et al.* (2010) explained distribution of total CHNS content in relation to other heavy metals at different depths of alluvial sediments of Danube River, Serbia. The ratio of C/N and total N content in various depths of Yellow River was studied by Li *et al.* (2014). CHNS distribution in Sediments of the River Horna´d, Slovakia was explained by Findora´kova *et al.* (2017) and C and N content in comparison to Heavy-Metal from surface sediments of the Minho River Estuary, Spain by Homens *et al.*, (2013).

Ratio of Total Organic Carbon and Nitrogen can increase during diagenesis (Hunt *et al.,* 2000). Sometime high value of Carbon and Nitrogen ratio is associated with lower N content and not because of large proportions of Carbon (Remon *et al.*, 2005, Trembaly and Gagne 2007). Less than 1.0 % value of Hydrogen and total Organic Carbon ratio indicates aromatic character of the organic matter and values greater than 1.0% indicate a lower content of organic matter and shows the aliphatic nature of organic matter which can be possibly contributed by bacterial and algal organic matters (Meyers and Ishiwatari, 1995). According to Steelink (1985) the presence of non-humic substances represented by values greater than 1.3 %. Exposure to air or by inorganic oxidation can also decline these values (Ortiz *et al.,* 2004). In the present study significant relationships between elements demonstrate that they have good paragenetic association. Similar statistical analysis has been done by Li *et al.,* (2014) in Yellow River, China and by Relic *et al.,* (2010) in Danube River in Serbia.

Conclusion

The river Yamuna is a very dynamic ecosystem which is different from any static system like of ponds and lakes and facing high threat of pollution in many parts of Delhi. Percentage concentration of CHNSin River bed soil varies at different depths at both the sites. River bed mainly consists of sand therefore less concentration of C, H, N, S elements as compared to any other type of soil. Site A is having higher amounts of Carbon, Hydrogen, Nitrogen concentration except Sulphur as compared to Site B at various depths of river bed. This can be a result of heavy domestic and industrial pollution at site 2 which interferes with the chemical composition of the soil and effects its quality and adds extra amount of Sulphur in river soil through polluted water. The concentrations of CHNS with other trace elements susceptible to many physicochemical reactions and hence directly affect pH and quality of soil. Present study could be useful for researchers working on the river sediments which can ultimately help in conservation of rivers and other wetlands.

Acknowledgements

We would like to thank Dr Neel Ratan, Mr Jogender Singh, Mr Virender Kumar and Mr Lalit Yadav for their kind help in collection of soil samples. A kind thanks to Mr Sandeep Kataria for his assistance during CHNS analysis at University Science Instrumentation Centre, University of Delhi, Delhi. A special thanks to Dr. M. Sharma for her support in statistical analysis of data.

References

Baruah, T.C. and Barthakur, H. P. 1997. *A Textbook of Soil Analysis.* Vikas Publishing House Pvt. Ltd.

Choi, J.H., Park, S.S. and Jaffe, P.R. 2006. The effect of emergent macrophytes on the dynamics of sulfur species and trace metals in wetland sediments. *Environmental Pollution*. 140(2) : 286-293.

CPCB, 2006. Assesment and development of the River Basin Series, Water Quality Status of Yamuna River 1999-2005, eds. Sengupta, B. Central Pollution Control Board, Delhi, India.

Das, A., David, A.A., Swaroop, N., Thomas, T., Rao, S. and Hasan, A. 2018. Assessment of physico-chemical properties of river bank soil of Yamuna in Allahabad city, Uttar Pradesh. *IJCS*. 6(3) : 2412-2417.

Dinelli, E., Cortecci, G., Lucchini, F. and Zantedeschi, E. 2005. Sources of major and trace elements in the stream sediments of the Arno river catchment (northern Tuscany, Italy). *Geochemical Journal*. 39(6): 531-545.

Dogo, S., Swaroop, N., Smitri Rao, P. and Thomas, T. 2019. Morphology and Physico-Chemical Properties of Lowland Area of Yamuna River Bank, Mahewa Village of Prayagraj. *International Journal of Current Microbiology and Applied Sciences*. ISSN: 2319-7706, 8(5) : 452-461.

Farago, M.E., Mehra, A. and Banerjee, D.K. 1989. A preliminary investigation of pollution in the River Yamuna, Delhi, India: metal concentrations in river bank soils and plants. *Environmental Geochemistry and Health*. 11(3-4) : 149-156.

Findoráková, L., Šestinová, O. and Kováèová, M. 2017. Assessment of potential sediment contamination using screening methods (XRF, TGA/MS) taking into account principles of green chemistry, Eastern Slovakia. *Environmental Earth Sciences*. 76(3) : 119.

George, P. and Joseph, S. 2017. Appraisal of nutrient distribution in the surface water and bed sediments of a small mountainous river. *Environmental Monitoring and Assessment*. 189(4) : 183.

Goidts, E. and Wesemael, B. 2007. Regional assessment of soil organic carbon changes under agriculture in Southern Belgium (1955–2005). *Geoderma*. 141(3-4) : 341-354.

Homens, M., Costa, A.M., Fonseca, S., Trancoso, M.A., Lopes, C., Serrano, R. and Sousa, R. 2013. Characterization of heavy-metal contamination in surface sediments of the Minho River Estuary by way of factor analysis. *Archives of Environmental Contamination and Toxicology*. 64(4) : 617-631.

Hunt, A.P., Parry, J.D. and HamiltonTaylor, J. 2000. Further evidence of elemental composition as an indicator of the bioavailability of humic substances to bacteria. *Limnology and Oceanography*. 45(1) : 237-241.

Jaiswal, P. C. 2006. *Soil, Plant and Water Analysis.* Kalyani publishers.

Kumar, N.R., Solanki, R. and Kumar, J.I. 2012. Geochemistry of Sabarmati River and Kharicut Canal, Ahmedabad, Gujarat. *International Journal of Environmental Sciences*. 2(4) : 1909-1919.

Li, Y., Zhang, H., Chen, X., Tu, C., Luo, Y. and Christie, P. 2014. Distribution of heavy metals in soils of the Yellow River Delta: concentrations in different soil horizons and source identification. *Journal of Soils and Sediments*. 14(6) : 1158-1168.

Meyers, P.A. and Ishiwatari, R. 1995. Organic matter accumulation records in lake sediments. In *Physics and Chemistry of Lakes* (279-328). Springer, Berlin, Heidelberg.

Mitsch, W. J., Gosselink, J. G. Wetlands, Van Nostrand Reinhold Company Inc., New York 2000, 89–125–200.

Ortiz, J. E., Torres, T., Delgado, A., Julia, R., Lucini, M, Llamas, F.J., Reyes, E., Solar, V. and Valle, M. 2004. The paleoenvironmental and paleohydrological evolution of Padul Peat Bog (Granada, Spain) over one million years, from elemental, isotopic and molecular organic geochemical proxies. *Org Geochem.* 35 : 1243–1260.

Parween, M., Ramanathan, A.L., Khillare, P.S. and Raju, N.J. 2014. Persistence, variance and toxic levels of organochlorine pesticides in fluvial sediments and the role of black carbon in their retention. *Environmental Science and Pollution Research*. 21(10) : 6525-6546.

Paul, A., Hatté, C., Pastor, L., Thiry, Y., Siclet, F. and Balesdent, J. 2016. Hydrogen dynamics in soil organic matter as determined by 13C and 2H labeling experiments. 13 : 6587–6598.

Prusty, B.A.K., Chandra, R. and Azeez, P.A. 2009. Distribution of carbon, nitrogen, phosphorus, and sulfur in the soil in a multiple habitat system in India. *Soil Research*. 47(2) : 177-189.

Relic, D., Dordevic, D. and Popovic, A. 2010. Assessment of the pseudo total metal content in alluvial sediments from Danube River, Serbia. *Environmental Earth Sciences*. 63(6) : 1303-1317.

Remon, E., Bouchardon, J.L., Cornier, B., Guy, B., Leclerc, J.C. and Faure, O. 2005. Soil characteristics, heavy metal availability and vegetation recovery at a former metallurgical landfill: Implications in risk assessment and site restoration. *Environmental Pollution*. 137(2) : 316-323.

Rezende, P.S., Moura, P.A., DurãoJr, W.A., Nascentes, C.C., Windmöller, C.C. and Costa, L.M. 2011. Arsenic and mercury mobility in Brazilian sediments from the São Francisco River Basin. *Journal of the Brazilian Chemical Society*. 22(5) : 910-918.

Said, S. and Hussain, A. 2019. Pollution mapping of Yamuna River segment passing through Delhi using high-resolution GeoEye-2 imagery. *Applied Water Science*. 9(3) : 46.

Sehgal, M., Garg, A., Suresh, R. and Dagar, P. 2012. Heavy metal contamination in the Delhi segment of Yamuna basin. *Environmental Monitoring and Assessment*. 184(2) : 1181-1196.

Sharma S., Singh, K. and Singh, D. K. 2017. Microbial community composition in contaminated soil samples of the Yamuna river. *International Journal of Microbiology Research.* 9(3) : 874-877.

Solanki, H.A. and Chavda, N.H. 2012. Physico-chemical analysis with reference to seasonal changes in soils of victoria park reserve forest, bhavnagar (gujarat).

Life Sciences Leaflets. 30 : 62-68.

Song, B., Niu, S., Zhang, Z., Yang, H., Li, L. and Wan, S. 2012. Light and heavy fractions of soil organic matter in response to climate warming and increased precipitation in a temperate steppe. *PloS One*. 7 (3).

Steelink, C. 1985. Elemental characteristics of humic substances. In : Aiken GR, McKnight DM, Wershaw RL, MacCarthy P. (eds) *Humic Substances in Soil, Sediment, and Water*. Wiley-Interscience, New York, 457–476.

Tremblay, L. and Gagné, J.P. 2007. Distribution and biogeochemistry of sedimentary humic substances in the St. Lawrence Estuary and the Saguenay Fjord, Québec. *Organic Geochemistry*. 38(4) : 682-699.

Multimedia Tools and Applications
https://doi.org/10.1007/s11042-021-10612-w

Bag-of-Visual-Words codebook generation using deep features for effective classification of imbalanced multi-class image datasets

Manisha Saini[1] · Seba Susan[1]

Received: 20 May 2020 / Revised: 14 November 2020 / Accepted: 25 January 2021
Published online: 10 March 2021
© The Author(s), under exclusive licence to Springer Science+Business Media, LLC part of Springer Nature 2021

Abstract

Classification of imbalanced multi-class image datasets is a challenging problem in computer vision. Most of the real-world datasets are imbalanced in nature because of the uneven distribution of the samples in each class. The problem with an imbalanced dataset is that the minority class having a smaller number of instance samples is left undetected. Most of the traditional machine learning algorithms can detect the majority class efficiently but lag behind in the efficient detection of the minority class, which ultimately degrades the overall performance of the classification model. In this paper, we have proposed a novel combination of visual codebook generation using deep features with the non-linear Chi^2 SVM classifier to tackle the imbalance problem that arises while dealing with multi-class image datasets. The low-level deep features are first extracted by transfer learning using the ResNet-50 pre-trained network, and clustered using k-means. The center of each cluster is a visual word in the codebook. Each image is then translated into a set of features called the Bag-of-Visual-Words (BOVW) derived from the histogram of visual words in the vocabulary. The non-linear Chi^2 SVM classifier is found most optimal for classifying the ensuing features, as proved by a detailed empirical analysis. Hence with the right combination of learning tools, we are able to tackle classification of multi-class imbalanced image datasets in an effective manner. This is proved from the higher scores of accuracy, F1-score and AUC metrics in our experiments on two challenging multi-class datasets: Graz-02 and TF-Flowers, as compared to the state-of-the-art methods.

Keywords ResNet-50 · Bag-of-Visual-Words · Imbalanced dataset · Image classification · Chi^2 SVM · Multi-class datasets

✉ Manisha Saini
manisha.saini44@gmail.com

[1] Delhi Technological University, New Delhi, India

1 Introduction

In the real-world scenario, imbalanced datasets are found in various situations in sectors such as the health care, telecommunication, credit card fraudulent detection, etc. [34]. There exist various challenges while dealing with imbalanced datasets since the distribution of samples in each class is in a disproportionate ratio [49]. In the imbalanced datasets, identification of the minority class is generally more difficult. Even though sometimes model accuracy is high, there is huge probability that it might lead to inappropriate classification results. There are chances that sometimes results get biased towards the majority class because of the imbalanced distribution of data in different classes. As the majority class has a greater number of samples, this creates a bias in the learning of minority classes because it is given less importance in comparison to the majority class [27]. The problem becomes more challenging and complex while dealing with multi-class imbalanced datasets [36]. In case of multi-class datasets there are more than two classes while in binary-class datasets there are only two classes. There is difficulty in addressing the multi-class imbalance problem because of the random and haphazard manner in which samples are distributed into multiple classes. Since many classifiers like Support Vector Machines (SVM) are binary classifiers, hence the question of how to define the majority and minority classes in a multi-class scenario, also arises. According to literature, several solutions for tackling class-imbalance exist that are broadly grouped into the three categories that we discuss next. 1) The first type of approach is the data level method that involves under-sampling of the majority class or over-sampling of the minority class, and their variants [31]. However, it was observed that over-sampling commonly causes over-fitting, whereas under-sampling generally results in valuable loss of information. 2) The second approach is related to cost-sensitive algorithms that counter class-imbalance by modifying the existing algorithms so as to give more importance to the minority class while optimizing the cost function [47]. 3) The third approach is to create a hybrid technique of data and algorithmic-level change [23]. But the computational cost involved in creating the hybrid technique is much more in comparison to the other methods. Recent advancements in deep learning were observed in various fields of computer vision ranging from object detection [22], image classification [4], image segmentation [19], human pose detection [54] to visual tracking [58]. This is made possible because of the availability of high-performance computational machines nowadays, in comparison to the previous decades. The graphical processing units (GPU's) and cloud computing have made real-time processing possible.

In this paper, we have utilized the deep features extracted from pre-trained deep convolutional neural networks (CNN) by transfer learning. The extracted features are used for codebook generation in the Bag-of-Visual-Words (BOVW) model that traditionally creates a visual dictionary from handcrafted features. Features extracted using the transfer learning approach with pre-trained models [41] have certain benefits over the handcrafted features. The pre-trained networks are already trained on the large-scale ImageNet dataset [11] which overall reduces the training time required to train the model and also leads to the extraction of the most relevant low-level features for codebook generation. Furthermore, the non-linear Chi^2 SVM using the one-versus-all scheme is found to be an optimal choice of classifier, from our experiments, while dealing with the multi-class imbalanced datasets.

Image classification is a supervised learning task to classify images into distinct categories. Suh et al. (2017) describe an approach for distinguishing between sugar beet

and volunteer potato under natural and daylight conditions using a Bag-of-Visual-Words model [43]. The low-level features used for constructing the visual dictionary are Scale-Invariant Feature Transform (SIFT) and Speeded-Up Robust Feature (SURF) features with Out-of-Row Regional Index (ORRI). From the experiments, it was found that that the highest accuracy was obtained for the combination of SIFT with SVM, in the case of the traditional Bag-of-Visual-Words approach. Wang et al. (2020) proposed a novel technique to resolve any feature redundancy which is certain while dealing with deep convolutional neural networks that comprise of multiple layers. The approach is well designed to apply pruning at each level of the deep network such that redundant features generated by convolutional filters or even repeated kernel matrices can be eliminated by pruning to accelerate scenarios of image retrieval. Pruning of the excessive redundant filters at each step ensures that complexity is reduced while these intermediate features are passed onto the next layer of the deep network [56]. Cheng et al., (2017) proposed a novel approach for scene classification, defined as bag of convolutional features (BoCF) [8]. In which the visual words are extracted from deep convolutional features obtained from convolutional neural networks. Feng et al. (2017) performed geographical scene classification by incorporating the spatial features extracted from CNN in the BOVW approach. They initially trained a ten-layer CNN on ten selected classes of ImageNet and used a convolution dictionary to extract local features from the CNN. The dictionary is used to construct a histogram vector representation that is used to train the classifier [16]. Brendel, and Bethge (2019) had proposed the BagNet model which was a simple variation of the ResNet-50 pre-trained network architecture, that considers bag of local image features without considering their spatial ordering [5]. SIFT features are handcrafted features that have been proved to be successful for various image classification tasks ranging from object and place recognition to face recognition [46]. The conventional BOVW utilizes SIFT as the low-level features based on which the visual codebook is constructed. Georgescu et al. (2020) presented an improvisation recently, where they combined the handcrafted SIFT features with the features extracted using convolutional neural networks (CNN) in the BOVW model. They performed facial expression recognition on various datasets such as the Facial Expression Recognition (FER) challenge dataset, the FER+ dataset and the AffectNet dataset [17]. However, the addition of handcrafted features with deep learning features increases the computational complexity of the classification pipeline.

Various works in literature have compared the BOVW model with CNN for different applications. Okafor et al. (2016) in their work have compared the CNNs and BOVW variants using the wild-animal dataset (Wild-Anim) [29]. For BOVW, they have used the HOG features and regularized L2 SVM. In the case of CNN, they modified the pre-trained CNN and the CNN network created from scratch. From the experimental analysis, it was found that CNN methods work significantly well in comparison to the BOVW approach and its variants [29]. Kumar et al. (2017) have also done a comparative study for the image classification of histopathological images using local binary patterns (LBP), deep features extracted using AlexNet and VGG16 models, and BOVW, on the KIMIA Path960 biomedical multi-class dataset. Their investigations revealed that the BOVW approach has higher accuracy in comparison to the LBP and deep features for the biomedical dataset [24]. In [37], the authors have compared deep learning, data augmentation and BOVW for image classification using Ant and Plane imbalanced image categories from the Caltech-101 dataset. From the experimental analysis, it was found

that using deep learning, higher accuracy is obtained in comparison to data augmentation and BOVW approaches. From the studies conducted, it is concluded that both the approaches (CNN and BOVW) work well based upon the type of the datasets used for the classification task.

A brief set of works that have addressed the class-imbalance issue for computer vision tasks are discussed next. The authors had previously proposed data augmentation of the minority class to counter-balance the class-imbalance in medical datasets while learning with the InceptionV3 pre-trained network in [38] and a hybrid model containing pre-trained VGG16 layers at the lower level and 2D convolutional layers at the higher level in [39]. Buda et al. (2017) thoroughly explained the effect of the class-imbalance on CNN architecture [6]. The authors focused on the evaluation of over-sampling and under-sampling techniques using well–known popular datasets MNIST, CIFAR-10, and ImageNet, by altering them into imbalanced datasets. From their experimental works, it was concluded that the imbalanced dataset has an adverse effect on the class performance of the model. Moreover, it was also observed that over-sampling emerged as the most prevailing method to tackle the class-imbalance issue, whereas under-sampling performed better when the imbalance was partially removed. In data mining, the most conventional solution to imbalanced learning is over-sampling the minority class and under-sampling the majority class for which several hybrid strategies are available [44, 45]. Lessmann (2004) determined that the SVM classifier is proficient in dealing with class-imbalance in comparison to various resampling methods [25]. Eitrich and Lang (2017) discussed and reviewed the role of various learning parameters, kernels, and hyper parameters performance of SVM for handling imbalanced datasets. Also adjusting and tuning the SVM parameters by grid search has an overall impact on the performance of the SVM classifier. They have performed various experiments on the breast cancer dataset and have also presented the framework for automatically tuning the hyperparameters of SVM [14]. Therefore, it is inferred from previous works that SVM has intrinsic properties to tackle class-imbalance problem as it relies on large margin classification on the basis of support vectors computed from each class. The number of support vectors is not connected with the population of the class, making it an optimal classifier for imbalanced datasets. This motivated us to use SVM for classifying the BOVW feature vectors extracted from the imbalanced image datasets in our experiments. Kernel machines (like SVMs) employ effective learning strategies by transforming data points into higher dimensions in such a way that these machines are able to exhibit very high generalization performance. The kernel transformation step comes at the additional computational cost of calculating kernel matrices. In general, SVM performs quadratic convex optimization which is less data hungry and more robust to data changes. Yet, these methods do not usually adapt well to large scale settings where scalability of such algorithms pose quite a challenge. Hence, we generally use a suitable approximation technique to apply kernel transformation on larger datasets and provide support for online learning (where it would not be possible to compute a large N x N kernel matrix, due to the very large number of N samples). Empirically, it has been shown in the work done by Rahimi, and Recht (2018) [35], that Random Fourier Features are able to approximate better shift-invariant kernels with respect to other techniques. Also, it is shown that Random Fourier Features are more suitable for use with large scale kernel machines viz. neural networks that are used to approximate kernelized support vector machines. Neural networks are generally trained using the backpropagation rule

combined with advanced optimization techniques that work on stochastic mini-batches; online learning can be quite well supported with the help of Random Fourier Features (RFF) as the kernel approximation step.

In summary, this paper has the following contributions: (i) Successfully applied transfer learning approach to extract deep features using pre-trained models, for generating the visual codebook in our improved Bag-of-Visual-Words model (ii) Conducted an extensive empirical analysis to find the optimal set of deep features for codebook generation and the appropriate classifier to tackle the class imbalance problem prevalent in two of the benchmark datasets (iii) Analyzing the role of chi-squared Kernelized SVM as an effective classifier for the histogram features. Further, the rest of the paper is divided into the following sections. In Section 2, the proposed methodology of visual codebook generation using deep features followed by classification using Chi-square (Chi^2) SVM classifier is discussed in detail. Additionally, we experiment with a set of neural networks that are used to approximate linear as well as kernel SVMs to investigate an alternative learning methodology for dealing with large scale settings [35, 51].The experimental settings and results are presented in Section 3. Finally, the conclusions are drawn in Section 4.

2 Proposed Bag-of-Visual-Words codebook generation using deep features with chi-square SVM classification

BOVW is an effective and well–known technique for image classification inspired by the bag-of-words (BOW) model which is widely used for text processing. The complete process of BOVW can be categorized into the following steps [43, 12]: (1) Low-level feature extraction (2) Feature clustering and quantization for the generation of the visual vocabulary (3) Classification using a suitable classifier. Initially, from each image, 128-dimensional keypoint descriptors are extracted. This procedure pertains to the most commonly used feature descriptor for BOVW namely, the Scale-Invariant Feature Transform (SIFT) which are classified as handcrafted features, a genre that preceded deep learning. The keypoint descriptors are then clustered. The cluster centers are interpreted as visual words, and in this manner, a visual vocabulary is formulated. The feature vectors for classification are derived from the normalized frequency of occurrences of the visual words in an input image. It is noted that the Support Vector Machine (SVM) classifier is popularly used for classifying the BOVW features. The proven success of the BOVW model motivated us to explore the incorporation of deep features derived from pre-trained networks into the existing scheme for efficient classification, with a special focus on improving the class-wise performance of imbalanced multi-class datasets. We have performed extensive experiments to find out the optimal choice of low-level deep features to be integrated into the BOVW approach, along with the optimum choice of classifier, to overcome the biasness problem that arises due to unequal class distribution. Through our work, we have proposed a novel combination of visual codebook generation using deep features with the non-linear Chi^2 SVM classifier to tackle the imbalance problem that arises while dealing with multi-class image datasets. The low-level deep features are first extracted by transfer learning using the ResNet-50 pre-trained network, and clustered using k-means. The center of each cluster is a visual word in the codebook. Each image is then translated into a set of features called the Bag-of-Visual-Words

(BOVW) which is the normalized count of visual words in the vocabulary. Our end-to-end approach is further detailed in Algorithm 1 and illustrated in Fig. 1.

The various steps of the algorithm are explained below.

Algorithm 1: ResNet-50 Deep Feature Extraction for Bag-of-Visual-Words codebook generation with Chi² SVM Classification

Input :
Dataset, D (IMAGES, LABELS)
Output:
Performance metrics for Test set after classification by Chi² SVM classifier (CLF)

1. Construct a model V_f using all layers from pre-trained ResNet-50 model V except final GAP and Dense layer
2. Create an empty list for storing deep features of all images, X_{deep}
3. Create an empty list for storing class labels, Y
4. M ← Number of classes in D
5. **for each** (IMAGE, LABEL) in D **do**
6. IMG ← Preprocess IMAGE (using mean normalization)
7. FV ← Use model V_f to extract 3D feature of dimension 7 x 7 x 2048 from IMG
8. Append list X_{deep} with FV
9. Append list Y with LABEL
10. **end for**
11. X ← Concatenate the feature vectors X_{deep} into 2D matrix of size 49 x 2048
12. Create an empty list for storing visual word features, X_{bovw}
13. KM ← Apply k-means clustering algorithm on X using *k* number of clusters
14. **for each** FEATURE in X **do**
15. NC ← Determine which cluster each vector in FEATURE belong to using KM
16. Create empty array F of size *k*
17. **for** I in [1….*k*] **do**
18. F[I] ← 0
19. Increment F[I] with number of occurrences of I in NC
20. **end for**
21. Append list X_{bovw} with the histogram features F, and normalize the value in each feature column to [0,1] using MaxAbsScaler
22. **end for**
23. Instantiate a Chi² SVM classifier, CLF, and divide X_{bovw} into X_{train} and X_{test}, and create corresponding target vectors Y_{train} and Y_{test} from Y
24. X_{chi^2} ← $K_{chi^2}(X_{train}, X_{train})$, according to Eq. (3)
25. Fit support vector machine CLF using (X_{chi^2}, Y_{train}), according to Eq. (2)
26. Create an empty list Y_{pred}
27. **for each** F in X_{test} **do**
28. C_{pred} ← Use support vectors from trained CLF to predict class label of F
29. Append list Y_{pred} with C_{pred}
30. **end for**
31. ACC ← Calculate accuracy using (Y_{test}, Y_{pred})
32. Create lists for storing precision, recall, and F1-score: P, R, F1
33. **for each** class J in [1..M] **do**
34. P[J], R[J], F1[J] ← Calculate precision, recall, and F1-score using (Y_{test}, Y_{pred})
35. **end for**

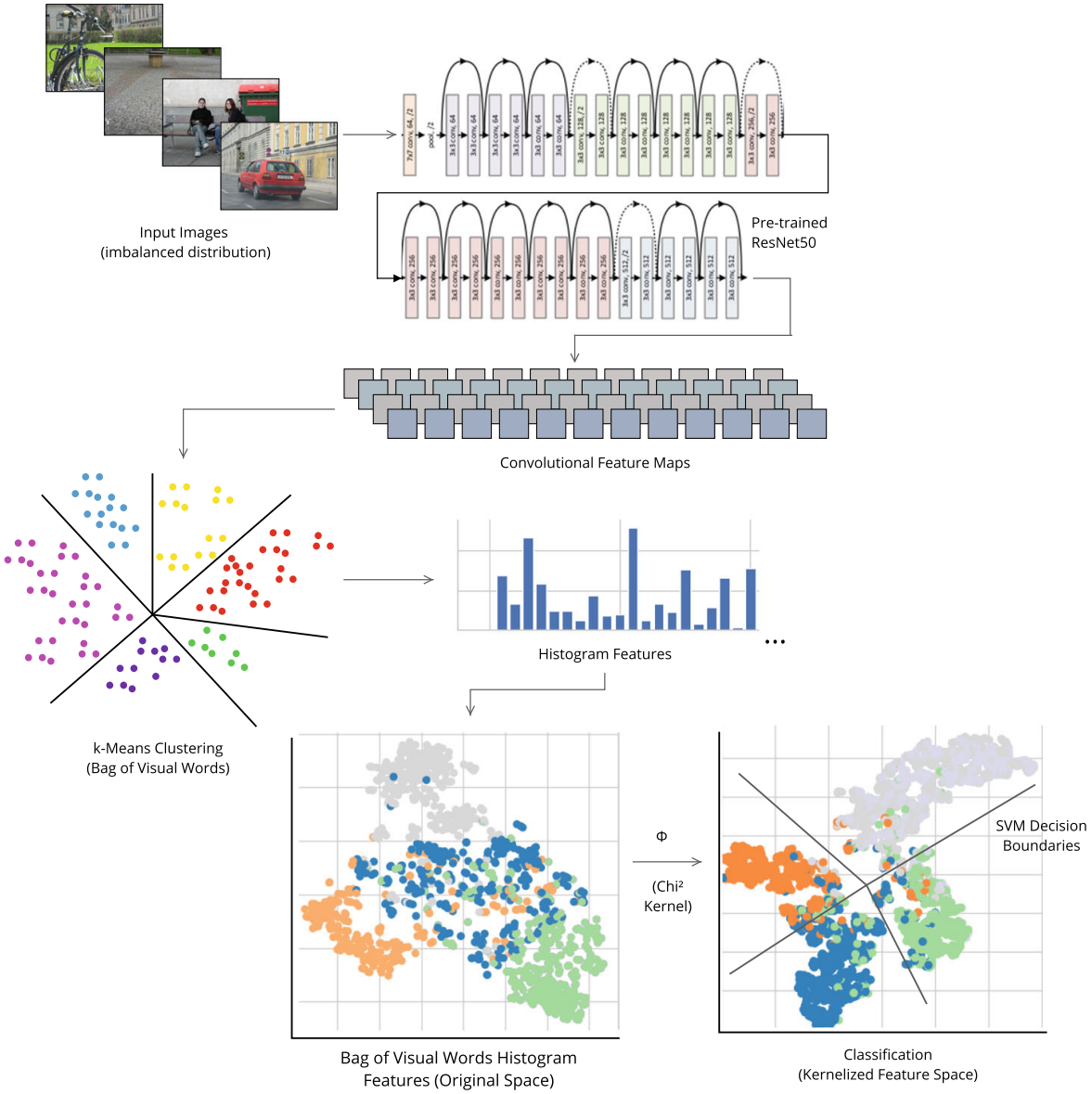

Fig. 1 Proposed Bag-of-Visual Word codebook generation from deep features and subsequent classification using Chi-square SVM

2.1 Deep feature extraction using pre-trained models

Traditional BOVW uses handcrafted features such as scale-invariant feature transform (SIFT) as the low-level features. In the last decade, deep learning became one of the most sought-after technique for image classification while traditional approaches like BOVW were almost pushed into obsolescence. Computational challenges have not deterred the deep convolutional networks to advancing to the state of the art today in the form of pre-trained deep networks that have been trained on millions of images [21, 42, 57]. We seek to incorporate the deep features extracted from the latest state-of-the-art pre-trained networks into the traditional BOVW approach for constructing the visual codebook or dictionary. Specifically, we focus on the features extracted from the last residual block of the fifth convolutional layer just preceding the global average pooling and dense layer of the pre-trained model ResNet-50 [21], defined as the Res5c features in [28]. The 3D features are of the form H x W x C for an input image, where H and W are the height and width of the 2D feature maps and C denotes the number of channels in the last residual block of the fifth convolutional layer that is used for feature extraction. The

set of features are converted into two-dimensional (H x W) feature vectors, each with the dimension of C. From the ResNet-50 architecture in [28], we see that $H = 7$, $W = 7$ and $C = 2048$. Thus 49 deep feature vectors each of dimension 2048 are extracted from each input image. The total number of feature vectors extracted from the training set are *No. of training images* × *49*, with each feature vector having dimension of 2048. The deep features are used for constructing the visual vocabulary associated with the Bag-of-Visual-Words model.

ResNet is a fast network (faster at train time and same or improved speed at inference time) having residual connections or skip connections, which provides significant contributions to the computer vision domain. These skip connections help to learn the identity function well and also mitigate the effect of the vanishing gradient problem effectively. Introduction of the skip connections in the ResNet architecture leads to efficient propagation of the gradients in the network architecture from the output to the input. So the advantage of using residual networks would be the effective propagation of the gradients (moving backwards). One of the most prevalent problems faced in the previous ConvNet architectures such as VGG16, AlexNet etc. was the inability to effectively propagate gradients due to the lack of identity mappings and the increasing depth of the architectures. Another advantage of the ResNet is that it is an ensemble of different networks of varied depths which definitely provides extra edge over other networks. The presence of batch normalization layer inside every convolutional block in the ResNet architecture also improves gradient backpropagation to a great extent. ResNet architectures are usually very deep, which overall achieves good performance without degrading the performance of the network due to their increased depth. So we can state that very deep network with residual connections can achieve significantly lower training error than its non-residual counterparts. [9, 21].

2.2 Visual codebook generation and feature engineering

The first step in codebook generation is clustering. The 2048-dimensional deep features ensuing from all the images in the training set are clustered into k groups based on the similarity between the feature vectors. K-means is an unsupervised clustering algorithm [48] that is popularly used in the Bag-of-Visual-Words model for grouping the low-level features into distinctive clusters. Choosing an appropriate value of the number of clusters k plays a crucial role in k-means clustering. Silhouette analysis is an approach that determines the optimal number of clusters [18]. We chose a local maximum value of silhouette score in the silhouette plot as the value of k for the two benchmark datasets used in our experiments. As noted from the local maxima of silhouette score plots in Fig. 2, the optimum value of k is determined to be 60 for the Graz-02 dataset and 100 for the TF-Flowers dataset.

For all the experiments we have used the widely adapted k-means++ algorithm to initialize the cluster centroids. The k-means++ technique is a cluster center initialization strategy. In comparison to the traditional approach it leads to the smarter initialization of the centroids which automatically helps to enhance the clustering quality. In the k-means++ clustering initialization strategy, firstly the random centroids are selected from the available data points. Then the distance of all the available data points are calculated from the nearest centroid. After the first iteration phase, the next set of centroids are selected on the basis of the calculation of the distance from the farthest available data point. This procedure is repeated till the k centroids have been sampled. The choice of this popular initialization strategy is solely in favour of improving the performance and it is known to act as a robust method for variety of scenarios to

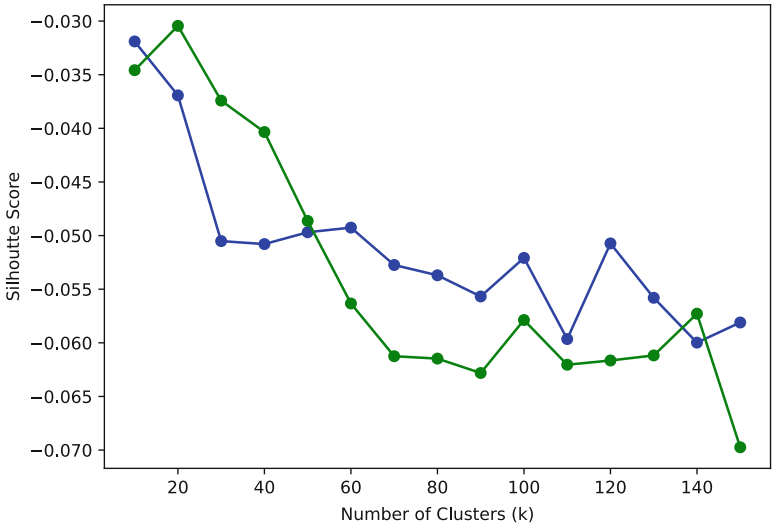

Fig. 2 Silhouette score plot to find the optimum value of k for Graz-02 and TF-Flowers dataset

improve k-means convergence. After clustering, the cluster centers form the bins of a histogram, and are defined as the visual words in the codebook generated. The next task is to find which of these visual words are present in each image. The histogram over the visual codebook is generated next for each image in the training and the test sets. This is achieved by considering each of the 49 × 2048 deep feature vector of the image, and considering which of the binscluster centroid it is closest to in terms of smallest Euclidean distance. The frequency of this bin is then increased by one. The histogram features are then normalized by scaling, using a procedure explained in section 2.3, and the resulting feature vectors are learned by a suitable classifier. While performing clustering using the k-means model, in our experiments, the number of instances is much larger than the dimensionality of features.

The cumulative histograms of deep features are shown in the case of the Graz-02 and TF-Flowers datasets in Fig. 3.

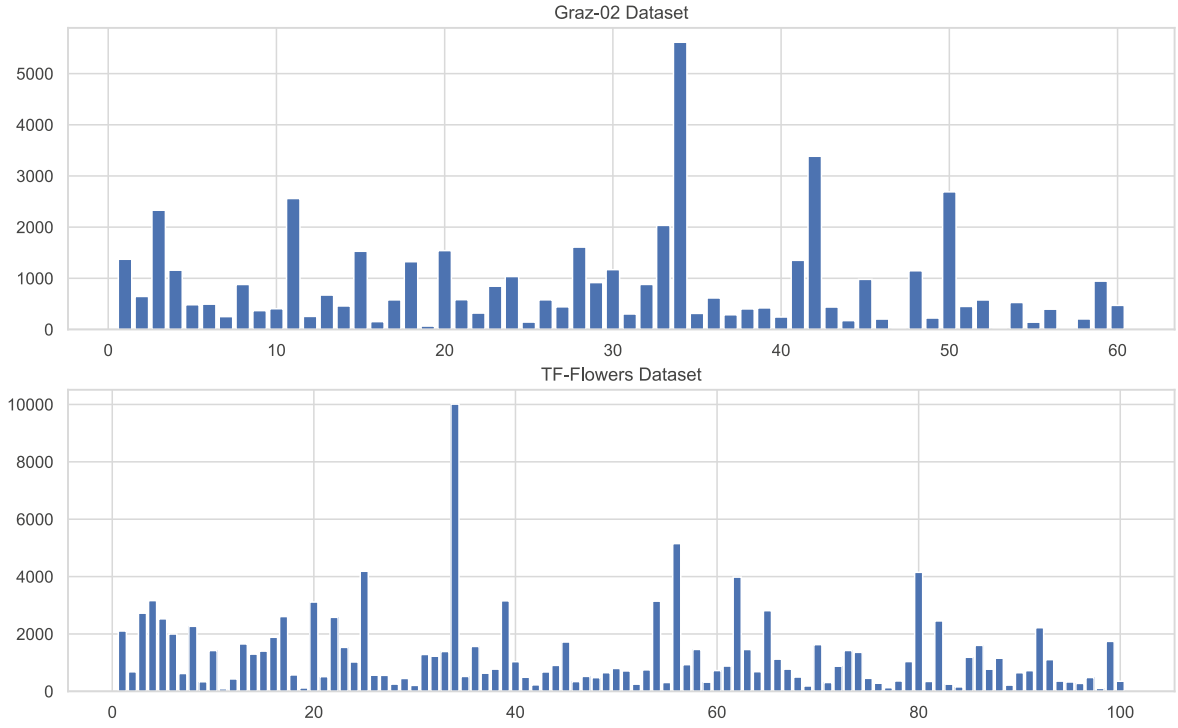

Fig. 3 Histogram representation for Graz-02 and TF-Flowers dataset

2.3 Scaling of histogram features

The resulting histogram features, which we now call as BOVW features, are normalized using maximum absolute scaling (MaxAbsScalar) [52], wherein we scale each feature column by dividing it with the maximum absolute value present in the respective feature column. Equation 1 illustrates the scaling technique, where *X[i]* denotes the ith feature and X_{max} *[i]* denotes the maximum value in the ith feature column of the BOVW feature matrix. Thus, the normalized feature *x[i]* is confined to a range of [0, 1]. Chi-Square (Chi^2) SVM kernel, used in the next phase of experiments, is a positive semi-definite kernel which expects the input to be in a non-negative range.

$$x[i] = \frac{X[i]}{X_{max}[i]} \tag{1}$$

2.4 Chi^2 SVM classifier for classification of multi-class imbalanced datasets

We have conducted extensive experiments using various classifiers in the evaluation phase to find the perfect choice of the classifier for our BOVW features. From the empirical analysis, the results of which are presented in section 3, it is found that the Chi^2 SVM classifier [26] results in better generalization performance and works effectively for classifying the under-represented classes in imbalanced multi-class datasets. We review, in this section, some of the theoretical aspects of the SVM kernels that we investigated in our study to understand their suitability for resolving the class-imbalance problem in multi-class datasets.

SVM classification for a multi-class problem is solved using the one-vs-rest approach [10]. Equation 2 discusses the generalized function h, which shows the optimization problem associated with a kernelized SVM by applying a kernel function ϕ on the original input data $\boldsymbol{x}$.

$$\begin{aligned} h_{\boldsymbol{w},b}\left(\phi(\boldsymbol{x}^{(n)})\right) &= \boldsymbol{w}^T\phi(\boldsymbol{x}^{(n)}) + b = \left(\sum_{i=1}^{m}\alpha^{(i)}t^{(i)}\phi(\boldsymbol{x}^{(i)})\right)^T\phi(\boldsymbol{x}^{(n)}) + b \\ &= \sum_{i=1}^{m}\alpha^{(i)}t^{(i)}\left(\phi(\boldsymbol{x}^{(i)})^T\phi(\boldsymbol{x}^{(n)})\right) + b \\ &= \sum_{\substack{i=1 \\ \alpha^{(i)}>0}}^{m}\alpha^{(i)}t^{(i)}K(\boldsymbol{x}^{(i)},\boldsymbol{x}^{(n)}) + b \end{aligned} \tag{2}$$

For our proposed methodology, we have used a chi-squared kernel [26] which is known to measure similarities of data points using a weighted exponential method. Equation 3 defines the chi-squared kernel function for the data points x and y with the help of gamma term γ.

$$k(x,y) = e^{-\gamma\sum_{i=0}^{n}\frac{(x[i]-y[i])^2}{x[i]+y[i]}} \tag{3}$$

For our experimental setup, the value of $\gamma = 1$ and the kernel is of the form $e^{-\gamma d(x,y)}$ as given in eq. 3. The value of $d(x,y)$ which is calculated based on affinity, is 0 for a pair of similar feature vectors and tends to ∞ for highly dissimilar feature pairs such that $e^{-1.0} = 1$ and $e^{-1.\infty} = 0$, respectively. Thus, the Chi-squared kernel when applied on histogram feature vectors produces a pairwise distance matrix in the range[0, 1]. The exponent of the exponential term in Eq. (3) is

a non-linear squaring function that brings similar points closer and dissimilar points farther apart akin to theoretical concept of distance metric learning (DML) which is a transformation of the input space [2, 3]. The feature transformation as a result of the kernel dot product, in case of Chi^2 SVM, is able to capture the correlation between pairs of features. The weighted pairwise feature distance used in chi-square allows it to internally calculate the similarities between combinations of samples from the majority as well as minority classes. As a result, the class imbalance problem has been tackled to an extent such that classifier is able to give almost equal results in case of minority as well as majority classes.

Additionally, we conducted another set of experiments to support larger scale use cases. A simple fully connected neural network is used that is trained with the help of hinge loss instead of logistic loss (softmax) which is generally used in most artificial neural networks with terminal fully-connected layers for classification problems. These neural networks are termed as Quasi-SVMs, and the work done is inspired from [51] (the neural network remains completely the same besides only the loss function is replaced). The choice of hinge loss for training our artificial neural networks used in the proposed approach is due to hinge loss being better suited to deal with the imbalanced datasets. It was motivated by the fact that SVMs as well as Quasi-SVMs are able to deal with different datasets better than softmax classifiers due to their property of robustness, these classifiers are able to learn features distinctively and it does help the gradients to propagate well enough making it easy to generalize on a wider range of datasets. Apart from the Quasi-SVMs being trained in linear mode, we also train them in kernelized mode. In kernelized mode, we add another RFF (Random Fourier Features) layer, as per work done in [35] which is used to provide a simple yet effective kernel transformation directly inside the neural network allowing us to construct a true Quasi-SVM that deals with the kernel approximation internally and making our approach highly suitable for larger datasets also. This technique is basically used to kernelize the linear model using a non-linear transformation such that it approximates a kernel SVM with hinge loss providing us with the added advantage of online learning for use with our proposed approach which is generally not supported by generic SVMs.

3 Results and discussions

For the experiments, the proposed mechanism was implemented as per the procedure outlined in section 2. For the purpose of our experiments, we have used various network architectures pre-trained on the large scale ImageNet dataset which is constructed using tf.keras (TensorFlow Keras) framework [1]. The pre-trained weights are available from keras_applications repository hosted by Francois Chollet. The deep feature extraction phase has been accelerated by the use of NVIDIA Tesla T4 GPU. The k-means clustering and SVM classification that are a part of the BOVW approach have been performed using Scikit-Learn package [32] with Python 3.6 version on a Google Compute Engine VM with 16 GB RAM and quad-core Intel Xeon CPU. The imbalanced multi-class datasets: Graz-02, TF-Flowers are used in the experimental tasks. Each class is split into 70:30 train test ratio using the stratified shuffle-split technique. The same is repeated over 10 folds to evaluate all the classifiers using a cross-validation based approach. The observed metrics are aggregated over all folds and the reported results include their mean and standard deviation.

For our analysis, we compare our proposed approach with VGG16, InceptionV3 and ResNet-50 pre-trained networks. The VGG16 network architecture consists of 3 fully connected layers whereas the InceptionV3 and the ResNet-50 architectures uses a single fully connected layer. For

our experimental task, we use these network architectures primarily using pre-trained weights, except that all of the dense layers use weights randomly initialized from a Glorot uniform distribution while the biases are initially set to zeros. All the dense layers in the respective architectures have been trained in order to adapt the network to the new classification task (instead of ImageNet classification) which is the procedure followed in several deep learning experiments [50]. In case of VGG16 network, we train the FC1, FC2 and final classification output layer which provides the softmax predictions of the various classes. For the InceptionV3 and ResNet-50, we train only the last fully connected layer in order to adapt the network to the new classification task. For all of these experiments, we train the network for a total of 20 epochs to minimize the categorical cross entropy loss using Adam optimizer, with a learning rate of 0.01. Similar to our other experiments, we train these models over 10 stratified folds.

Additionally, with the help of a few experiments we demonstrate another variant of our proposed Bag-of-Visual-Words approach. Our proposed approach with minor modifications and the learned BOVW features, can be made suitable for large scale classification tasks as well. We make use of neural networks that work like Quasi SVMs with and without kernel approximation. Kernel approximations have been done with the help of Random Fourier Features as per work done in [35]. The following experimental settings have been used while conducting the experiments for Quasi-SVM (which approximates a Linear SVM) and Kernelized Quasi-SVM (which approximates a kernel SVM). We make use of the Adam optimizer combined with hinge loss. We noticed that the choice of hinge loss function significantly improved the convergence of our classifiers to a noticeable extent. We apply L2 regularization penalty of 1e-4 on all the trainable network weights and biases. Initially, we set the learning rate as 5e-4 which is inversely time decayed by a factor of 1e-5 and all the experiments are carried out till 1000 epochs. We have also analysed the role of adding various hidden layers to these neural networks (which are used to approximate large scale support vector machines). For the experiments, input layers consist of 60 or 100 nodes (based upon the number of clusters and the dataset as discussed in other sections of the paper related to BOVW features) and the output layers are adjusted based on the number of classes in the target dataset. Further, the addition of hidden (fully connected) layers leads to the formation of complex neural networks but it's important to analyse the effect in each scenario to observe how the addition of hidden layers affect the working on large scale settings. We added three hidden layers to the Quasi-SVM i.e. with 64, 128 and 256 hidden units respectively. In case of Kernelized Quasi-SVM, Random Fourier Features are used (as the kernel approximation step) with 1024 feature dimensions. Also, we consider adding two dense layers with 256 and 512 hidden nodes respectively. In case of a larger scale setting it is recommended to use mini-batch k-means [40] instead of the standard k-means implementation used earlier in our experiments. This would ensure that the clustering for codebook generation can be conducted easily on more samples at lesser computational complexity.

3.1 Datasets

3.1.1 Graz-02 dataset

Graz-02 dataset [30] is one of the two benchmark datasets used for the experimental task. It consists of four classes: class 0 (Bike), class 1 (Car), class 2 (None) and class 3 (Person) with a total 1476 images. Figure 4 depicts the class-imbalance in Graz-02 dataset. The number of samples in class 1 (Cars) is higher in comparison to other classes. Figure 5 shows various samples taken from the original Graz-02 dataset to depict the inter and intra-class similarities.

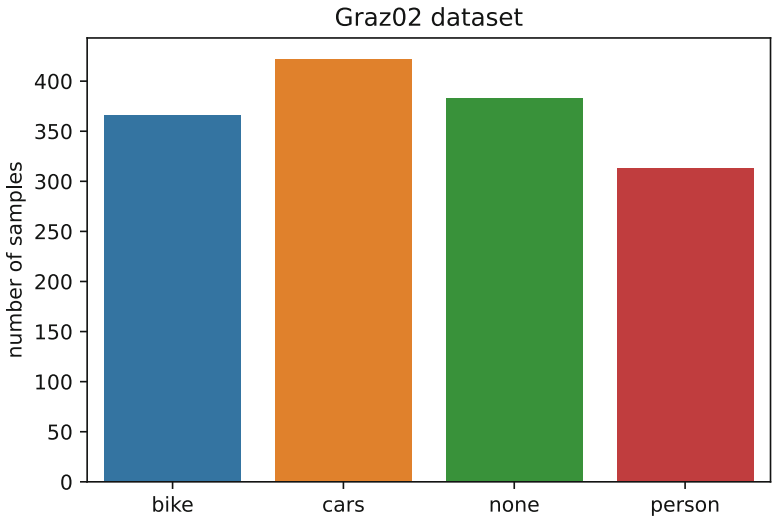

Fig. 4 Distribution of the number of samples present in each class of Graz-02 dataset

3.1.2 TF-flowers dataset

The TF-flowers dataset [53], samples of which are shown in Fig. 6, is an imbalanced challenging dataset that consists of images from five different categories of flowers. It contains high-quality images of flowers of different sizes and aspect ratios, which makes this dataset more challenging to tackle for the image classification task. All the images were collected specifically for deep learning workloads. The imbalanced multi-class dataset consists of different classes: Class 0 (Daisy), Class 1(Dandelion), Class 2 (Tulips), Class 3 (Roses) and Class 4 (Sunflowers) classes respectively, with the class-distributions shown in Fig. 7.

3.2 Performance evaluation metrics

The imbalanced multi-class datasets contain an uneven class-distribution of images. In this situation, accuracy by itself cannot be an appropriate measure for predicting the performance of the model. Other metrics that need to be considered while measuring the efficiency of the model includes (a) precision and recall (b) F1-Score, which can be calculated from the confusion matrix [33]; the metrics are summarized in Table 1. We have also done the ROC analysis. The AUC metric obtained from the ROC curve is also indicative of class-wise performance.

3.3 Discussions on results

The experiments are conducted on the Graz-02 and TF-Flowers datasets using the proposed approach with comparisons to the state-of-the-art methods. The detailed discussion is given below.

3.3.1 Graz-02 dataset results

In Table 2, the comparison has been done using different deep features extracted using pre-trained models (VGG16, InceptionV3, ResNet-50) along with the traditional SIFT descriptor, for the BOVW codebook generation, in combination with the different variants of SVM

Fig. 5 Samples of the four classes in Graz-02 dataset

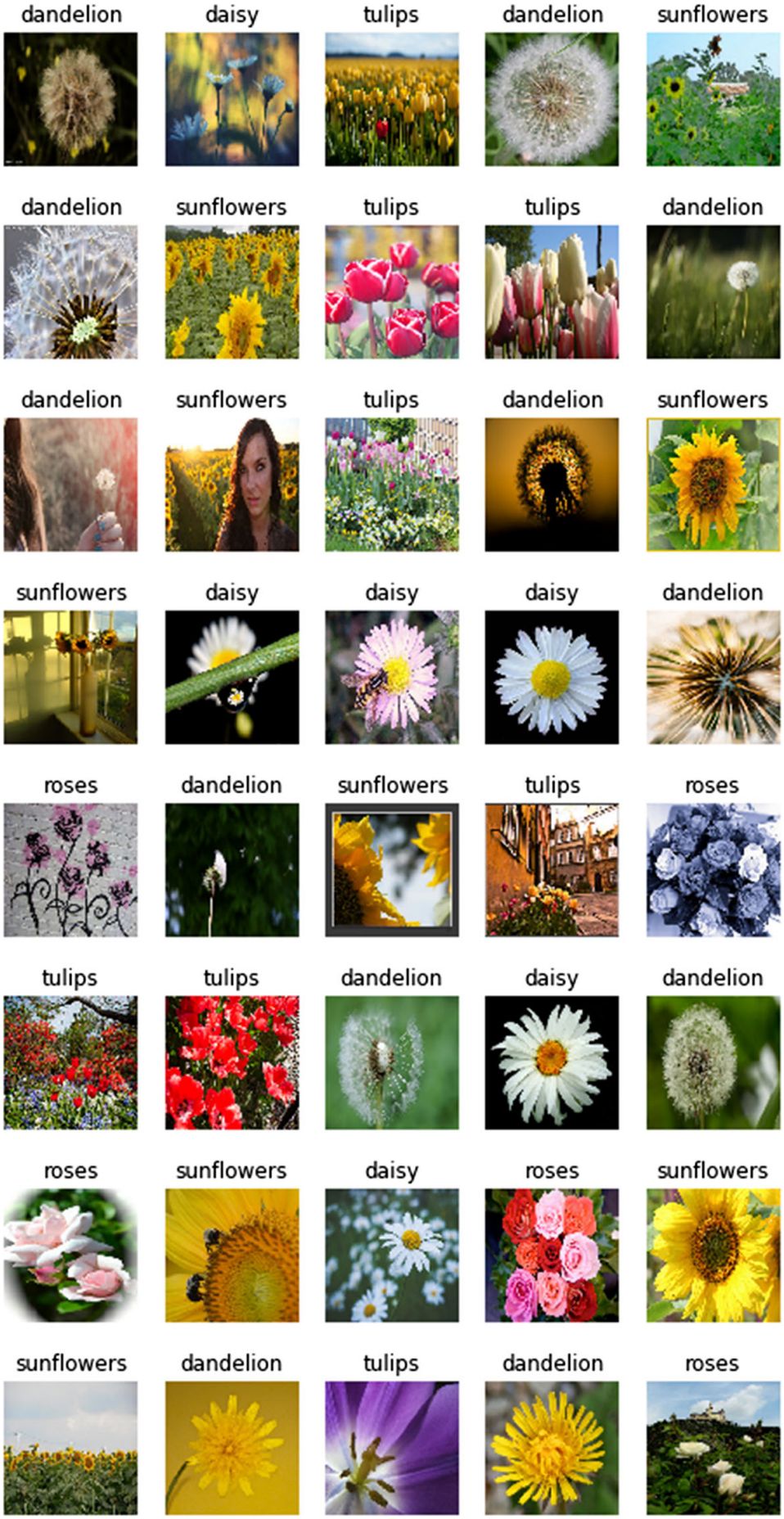

Fig. 6 Samples of the five classes in TF-Flowers dataset

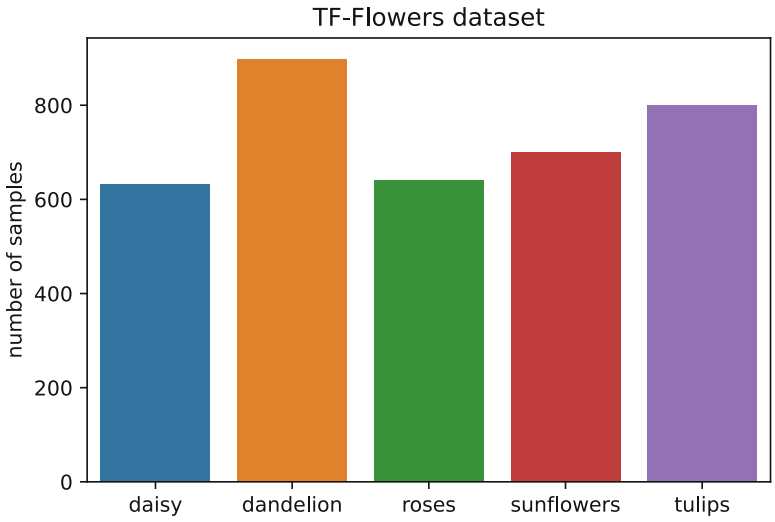

Fig. 7 Distribution of the number of samples present in each class of TF-Flowers dataset

classifier (Linear, RBF, Chi^2 SVM using scalar and without using scalar approach). From the analysis, it was found that the deep features extracted using ResNet-50 pre-trained model in combination with Chi^2 SVM classifier works best for our BOVW model, since it shows high accuracies for all the four classes present in the Graz-02 dataset. Another observation that was inferred from the result analysis is that scaling operation plays a very crucial role because avoiding the scaling of features would have an adverse impact on the overall performance of the classifier as some minority classes were not detected. The same pattern is observed in a few approaches such as in SIFT + BOVW and ResNet-50 + BOVW as shown in Table 2. A third observation which was inferred from the analysis is that Chi^2 SVM exhibits an overall better performance since it is able to identify all the classes separately and more efficiently in comparison to other variants of SVM (linear and RBF SVM).

Further, experiments were conducted for the Graz-02 dataset in Tables 3 and 4 to validate the proposed combination of ResNet-50 + BOVW approach with the Chi^2 SVM classifier. The analysis drawn from Table 3 proves that the proposed combination for BOVW works well in comparison to direct deep learning using state-of-the-art pre-trained approaches (VGG16, Inception V3 and ResNet-50). Five different supervised classifiers are evaluated and analyzed in Table 4 for our BOVW features. A comparative experimental analysis of various popularly used classifiers such as Logistic Regression, Linear Discriminative Analysis, K-Nearest Neighbors, Decision Tree and Gaussian Naïve Bayes classifiers was conducted with the Chi^2 SVM classifier, for the proposed approach. From the classification scores in Table 4, it is noted that the other classifiers have not performed sufficiently well in comparison to the Chi^2 SVM classifier. Therefore, Chi^2 SVM proves to be a better choice of the classifier in comparison to other classifiers, for the imbalanced multi-class dataset.

Table 1 Various performance metrics used for the evaluation

Evaluation parameters	
Accuracy	$Accuracy = \frac{TP+TN}{TP+TN+FP+FN}$
Precision	$Precision = \frac{TP}{TP+TN}$
Recall	$Recall = \frac{TP}{TP+FN}$
F1-score	$F1{-}score = \frac{2*(Precision*Recall)}{(Precision+Recall)}$

Table 2 Performance evaluation of different low-level features for BOVW codebook generation and choice of classifier for Graz −02 dataset

	Classifier	None (F1)	Person (F1)	Car (F1)	Bike (F1)	Accuracy
SIFT + BOVW	Chi^2 SVM	0.530±0.0218	0.4414±0.0270	0.5331±0.0246	0.7115±0.0174	0.5616±0.0123
	Chi^2 SVM (without scalar)	0.0±0.0	0.0±0.0	0.4447±0.0012	0.0423±0.0270	0.2898±0.0035
	Linear SVM	0.4403±0.0328	0.4150±0.0328	0.4774±0.0317	0.6906±0.0141	0.5076±0.0184
	RBF SVM	0.0234±0.0185	0.0±0.0	0.4848±0.0076	0.5432±0.0344	0.3844±0.0110
VGG16+BOVW	Chi^2 SVM	0.8303±0.0212	0.9187±0.0131	0.8926±0.0146	0.9407±0.0096	0.8918±0.0119
	Chi^2 SVM (without scalar)	0.069±0.0085	0.0021±0.0131	0.4451±0.0012	0.0423±0.0270	0.2909±0.0037
	Linear SVM	0.7959±0.0188	0.9061±0.0187	0.8774±0.0136	0.9416±0.093	0.8742±0.0118
	RBF SVM	0.6851±0.0179	0.8050±0.0212	0.8234±0.0105	0.8203±0.0249	0.7717±0.0130
InceptionV3 + BOVW	Chi^2 SVM	0.7992±0.0208	0.8848±0.0399	0.8781±0.0225	0.9360±0.0568	0.8702±0.0138
	Chi^2 SVM (without scalar)	0.0156±0.0480	0.03291±0.0321	0.4693±0.0074	0.3372±0.0568	0.3584±0.0145
	Linear SVM	0.7839±0.0181	0.875±0.0245	0.8692±0.0189	0.3372±0.0568	0.8586±0.0116
	RBF SVM	0.6988±0.0259	0.7324±0.0535	0.8563±0.0171	0.8730±0.0254	0.7857±0.0219
ResNet-50+BOVW	**Chi^2 SVM**	**0.8509±0.142**	**0.9405±0.0141**	**0.9013±0.0184**	**0.9609±0.117**	**0.9097±0.0106**
	Chi^2 SVM (without scalar)	0.0±0.0	0.0±0.0	0.4461±0.0012	0.0731±0.0268	0.2939±0.0036
	Linear SVM	0.8399±0.0184	0.9318±0.0158	0.8969±0.0139	0.9592±0.108	0.9029±0.0116
	RBF SVM	0.7263±0.0185	0.8347±0.0258	0.8381±0.0268	0.8935±0.2069	0.8124±0.0155

Table 3 Performance evaluation of various state-of-the-art pre-trained networks for Graz-02 dataset

Pre-trained Networks	None (F1)	Person (F1)	Car (F1)	Bike(F1)	Accuracy
VGG16 [42]	0.788±0.0313	0.9046±0.0244	0.8585±0.0215	0.9367±0.0262	0.8693±0.0167
InceptionV3 [57]	0.4301±0.0574	0.8338±0.165	0.7711±0.0301	0.8946±0.0453	0.7568±0.0109
ResNet-50 [21]	0.670±0.1136	0.8981±0.0228	0.8350±0.0302	0.9471±0.0186	0.8460±0.0302

3.3.2 TF-Flowers dataset results

The experiments are done, on similar lines, in the case of TF-Flowers dataset. It was also validated from the result analysis of TF-Flowers dataset that the proposed Bag-of-Visual-Words model constructed with deep features and integrated with the Chi^2 SVM classifier works well in comparison to all other combinations, as shown in Table 5. It is noted that the deep features work well in comparison to the handcrafted SIFT features, for the BOVW model. Further observations from Table 5 led us to the conclusion that ResNet-50 features integrated with the BOVW approach proves to be the best amongst the other features extracted using different pre-trained networks, and the Chi^2 SVM classifier emerges as the optimal choice of the classifier in this combination. Comparisons to other variants of SVM such as RBF and Linear SVMs proves the efficacy of our learning model, as observed from Table 5.

The comparison of the proposed combination of BOVW approach with Chi^2 SVM classifier and the state-of-the-art pre-trained networks (VGG16, InceptionV3 and ResNet-50) is shown in Table 6, and from the analysis, it was found that the proposed BOVW approach works well in comparison to the other state-of-the-art pre-trained networks. To validate our approach, we have shown a comparative analysis of various supervised machine learning classifiers combined with deep features for the BOVW model. Hence, we have also presented the comparative analysis of the performance of various machine learning classifiers for classifying the ResNet-50 based BOVW features. It is noted that the Chi^2 SVM classifier works well in comparison to the other five supervised classifiers as per the classification scores in Table 7.

We have also applied various resampling techniques which are known to be baseline methods that are applied to imbalanced distributions to balance out the number of samples in each class. These strategies involve either over-sampling or under-sampling approaches,

Table 4 Performance evaluation of various supervised classifiers on our BOVW features (ResNet-50 + BOVW approach) for Graz-02 dataset

Classifiers	None (F1)	Person (F1)	Car (F1)	Bike(F1)	Accuracy
Logistic Regression	0.8294± 0.0177	0.9330± 0.0164	0.8938± 0.0165	0.9532± 0.0127	0.8979± 0.0133
Linear Discriminative Analysis	0.8245± 0.0169	0.9224± 0.0196	0.8933± 0.0174	0.9503± 0.0116	0.8925± 0.0124
K-nearest Neighbors Classifier	0.7803± 0.0154	0.8953± 0.0160	0.8452± 0.0143	0.9324± 0.0137	0.8580± 0.0079
Decision Tree	0.7852± 0.0213	0.8911± 0.0153	0.8609± 0.0152	0.9167± 0.0200	0.8623± 0.0079
Gaussian Naïve Bayes	0.3763± 0.2451	0.9264± 0.0138	07720±0.0630	0.9112± 0.0365	0.7785± 0.0594

Table 5 Performance evaluation of different low-level features for BOVW codebook generation and choice of classifier for TF-Flowers dataset (Best performance highlighted by gray cells)

		Dandelion (F1)	Daisy (F1)	Sunflowers (F1)	Roses (F1)	Tulips (F1)	Accuracy
SIFT + BOVW	Chi^2 SVM	0.6571±0.0244	04871±0.0375	0.5891±0.0262	0.3737±0.0314	0.4841±0.0239	0.5364±0.0192
	Chi^2 SVM (without scalar)	0.3930±0.0002	0.0±0.0	0.0075±0.056	0.0±0.0	0.0±0.0	0.2450±0.0005
	Linear SVM	0.6962±0.0111	0.5092 ± 0.0195	0.6169±0.0195	0.4188±0.0222	0.4567±0.0123	0.5405±0.0082
	RBF SVM	0.4625±0.085	0.1615±0.0243	0.4765±0.0271	0.0378 ± 0.0140	0.3218 ± 0.0230	0.3722±0.0108
VGG16+ BOVW	Chi^2 SVM	0.8961±0.0115	0.8610±0.02	0.8511±0.00092	0.8114±0.0211	0.8211±0.0117	0.8503±0.0087
	Chi^2 SVM (without scalar)	0.3931±0.0001	0.0041±0.051	0.0075±0.0056	0.0010±0.031	0.0008±0.002	0.2455±0.0004
	Linear SVM	0.8757±0.0185	0.8380±0.0248	0.8144±0.0202	0.7786±0.0215	0.7760±0.0164	0.8190±0.0150
	RBF SVM	0.7853±0.0166	0.6622±0.0278	0.6202±0.0435	0.2573±0.0823	0.6012±0.0188	0.6292±0.0196
InceptionV3 + BOVW	Chi^2 SVM	0.8651±0.0122	0.8414±0.0174	0.7477±0.0220	0.7162 ± 0.0283	0.7120±0.0205	0.7836±0.0124
	Chi^2 SVM (without scalar)	0.4185±0.0044	0.3135±0.0606	0.1014±0.0247	0.0636±0.0165	0.1476±0.0447	0.3103±0.0121
	Linear SVM	0.8585±0.0115	0.8392±0.0146	0.7327±0.0140	0.6996±0.0341	0.7246±0.0212	0.7729±0.0151
	RBF SVM	0.7932±0.0209	0.8064±0.0204	0.6102±0.0435	0.2141±0.1519	0.6269±0.0229	0.6552±0.0226
ResNet-50+BOVW	**Chi^2 SVM**	**0.9162±0.0141**	**0.9159±0.0136**	**0.8883±0.0133**	**0.8335±0.0141**	**0.8492±0.0147**	**0.8816±0.0084**
	Chi^2 SVM (without scalar)	0.3931±0.0003	0.004±0.0051	0.0075 ± 0.0056	0.0041±0.0050	0.8008±0.0241	0.2457±0.0004
	Linear SVM	0.9070±0.0115	0.9059±0.171	0.8648±0.0177	0.8054±0.0135	0.8211±0.0101	0.8619±0.0053
	RBF SVM	0.8206±0.0271	0.7425±0.0249	0.7934±0.0355	0.4089±0.0901	0.6700±0.0275	0.7127±0.0190

Table 6 Performance evaluation of various state-of-the-art pre-trained networks for TF-Flowers dataset

Pre-trained networks	Dandelion (F1)	Daisy (F1)	Sunflowers (F1)	Roses (F1)	Tulips (F1)	Accuracy
VGG16 [42]	0.9108± 0.0149	0.8761± 0.0236	0.8752± 0.0299	0.8343± 0.0245	0.8395± 0.0254	0.8689± 0.0196
InceptionV3 [57]	0.7413± 0.0378	0.6331± 0.250	0.5199± 0.0179	0.6201± 0.0629	0.7651± 0.0156	0.6640± 0.0190
ResNet-50 [21]	0.8901± 0.210	0.8394± 0.0369	0.8509± 0.0190	0.6504± 0.0797	0.8031± 0.0203	0.8203± 0.0176

such as ADASYN, SMOTE, random over-sampling, random under-sampling [45]. The aim was to investigate the effect of these balancing tools, popular in data mining, in our classification scheme. These resampling strategies have been applied directly at the feature-level after the first phase of our deep feature based BOVW scheme. We did not observe any significant improvement in the classification results even by applying the well-known sampling techniques in the proposed combination, as evident from the scores in Tables 8 and 9 for the two datasets respectively. In the case of deep learning-based approaches, we popularly use affine transformations to randomly augment the data samples. It significantly increases the total number of samples used to train the deep learning network and is known to improve classification performance on the smaller dataset through regularization. For our proposed approach, we have used ResNet-50 network to extract deep features, that is in turn pre-trained on the million-scale ImageNet dataset. Thus, applying random data augmentation at image level before the feature extraction step would not effectively improve the clustering step in the Bag-of-Visual-Words model.

From the experimental results in Tables 10 and 11, it was found that both Quasi-SVM and Kernelized Quasi-SVM were able to achieve acceptable classification performance on our studied datasets. The addition of hidden (fully connected) layers in these combinations have affected the performance of the classifier to some extent but their role is quite stochastic in nature. So, it is recommended that the use of this alternate approach (large scale kernel machines) on larger datasets would require us to perform some hyperparameter tuning with respect to the target dataset.

Table 7 Performance evaluation of various supervised classifiers on our BOVW features (ResNet-50 + BOVW approach) for TF-Flowers dataset

Classifiers	Dandelion (F1)	Daisy (F1)	Sunflowers (F1)	Roses (F1)	Tulips(F1)	Accuracy
Logistic Regression	0.9052± 0.0096	0.9027± 0.0160	0.8618± 0.0100	0.8055± 0.0197	0.8288± 0.0120	0.8621± 0.0044
Linear Discriminative Analysis	0.8603± 0.082	0.9054± 0.0131	0.8628± 0.0156	0.8171± 0.0176	0.8171± 0.0129	0.8603± 0.0082
K-Nearest Neighbors Classifier	0.8707± 0.0190	0.8537± 0.0241	0.8179± 0.0139	0.7714± 0.0291	0.7714± 0.0217	0.8153± 0.0135
Decision Tree	0.8274± 0.0115	0.8208± 0.0252	0.7564± 0.0162	0.7259± 0.224	0.7522± 0.0230	0.7791± 0.0082
Gaussian Naïve Bayes	0.8619± 0.0277	0.884± 0.0141	0.8105± 0.0328	0.7447± 0.505	0.7960± 0.0207	0.8214± 0.0187

Table 8 Performance evaluation of our BOVW model with different sampling techniques applied at the feature-level for Graz-02 dataset

Sampling technique	None (F1)	Person (F1)	Car (F1)	Bike (F1)	Accuracy
ADASYN [20]	0.8478 ± 0.0128	0.9315±0.0157	0.9003±0.0192	0.9609±0.0117	0.9069±0.0094
SMOTE [7]	0.8528±0.0128	0.9389±0.0142	0.9020±0.0183	0.9623±0.0106	0.9103±0.0100
Random Over-sampling [13]	0.8508±0.0130	0.9390±0.0129	0.9002±0.0177	0.9624±0.0116	0.9094±0.0100
Random Under-sampling [15]	0.8495±0.0137	0.9405±0.0141	0.8985±0.0212	0.9599±0.0137	0.9081±0.0126
None (Proposed Approach)	0.8509±0.0142	0.9405±0.0141	0.9013±0.0184	0.9609±0.0117	0.9097±0.0126

To further prove the validity of the proposed BOVW approach for imbalanced datasets, analysis has been shown using the Receiver Operating Curve (ROC). In Table 12, the Average Area Under the Curve (AUC) scores are recorded for both Graz-02 and TF-Flowers datasets, to validate the performance of the proposed BOVW model. It was observed from the analysis in Table 12 that the Chi^2 SVM with ResNet-50 BOVW features combination yields higher Macro average ROC AUC readings in comparison to other classifiers with the same combination of ResNet-50 BOVW features. Further, the Macro average ROC AUC reading was recorded in case of different pre-trained deep features and handcrafted SIFT features with static Chi^2 SVM classifier as shown in Table 13. The AUC scores indicate that the ResNet-50 deep features prove to be superlative in comparison to other combinations in BOVW model, in the case of both Graz-02 and TF-Flowers datasets.

The ROC curves for various features and classifiers are presented in Fig. 8 to prove the significance of the proposed combination. Figure 8 (Top row) inclusive of Fig. 8 (a) and (b) illustrate that the deep features extracted from the ResNet-50 pre-trained model is the best choice in comparison to the other handcrafted and deep features infused into the proposed BOVW approach. The Chi^2 SVM classifier is considered while performing all the experiments with a different combination of deep and traditional handcrafted features. Figure 8 (Bottom row) inclusive of Fig. 8 (c) and (d) prove that Chi^2 SVM, in the proposed BOVW approach, is

Table 9 Performance evaluation of our BOVW model with different sampling techniques applied at the feature-level for TF-Flowers dataset

Sampling technique	Dandelion (F1)	Daisy (F1)	Sunflowers (F1)	Roses (F1)	Tulips (F1)	Accuracy
ADASYN [20]	0.9164± 0.0117	0.9190± 0.0117	0.8900± 0.0130	0.8339± 0.0151	0.8502± 0.0141	0.8829± 0.0073
SMOTE [7]	0.9190± 0.0127	0.9158± 0.0118	0.8892± 0.0120	0.8363± 0.0105	0.8502± 0.0125	0.8831± 0.0070
Random Over-sampling [13]	0.9165± 0.0145	0.149± 0.0136	0.8859± 0.0127	0.8363± 0.0129	0.8509± 0.0141	0.8800± 0.0064
Random Under-sampling [15]	0.9174± 0.0128	0.9170± 0.0137	0.8886± 0.0134	0.8324± 0.0136	0.8405± 0.0150	0.8800± 0.0064
None (Proposed Approach)	0.9162± 0.0141	0.9159± 0.0136	0.8883± 0.0133	0.8335± 0.0141	0.82±0.0147	0.8816± 0.0084

Table 10 Performance evaluation of ResNet-50 BOVW features combined with Quasi SVM and its variants for Graz-02 dataset

Classifier	None (F1)	Person (F1)	Car (F1)	Bike (F1)	Accuracy
Quasi-SVM	0.8186±0.0166	0.9234±0.0167	0.8833±0.0144	0.9497±0.0152	0.8826±0.0130
Quasi-SVM (w/ 1 hidden layer)	0.8490±0.0116	0.9322±0.0157	0.8958±0.0110	0.9011±0.0080	0.9063±0.085
Quasi-SVM (w/ 2 hidden layers)	0.8474±0.0164	0.9331±0.0139	0.8985±0.0178	0.9617±0.0077	0.9072±0.0105
Quasi-SVM (w/ 3 hidden layers)	0.8506±0.0188	0.9298±0.0178	0.8966±0.0149	0.96630±0.012	0.9081±0.0125
Kernelized Quasi-SVM	0.8383±0.0148	0.9338±0.0164	0.8911±0.0147	0.95966±0.085	0.9018±0.0112
Kernelized Quasi-SVM (w/ 1 hidden layer)	0.8382±0.0174	0.9318±0.0147	0.8903±0.0167	0.9588±0.0080	0.9090±0.0109
Kernelized Quasi-SVM (w/ 2 hidden layers)	0.8393±0.0175	0.9241±0.0219	0.8905±0.0203	0.9606±0.0096	0.9004±0.0123

the best choice of the classifier by analysing from the experiments conducted using various classifier options, while keeping ResNet-50 deep features as static.

From our extensive experiments and analysis, it is summarized that the deep features extracted using ResNet-50 pre-trained CNN when integrated with the BOVW approach, with the combination of the Chi^2 SVM classifier, proved to be optimal for the image classification task when dealing with multi-class imbalanced datasets. The same pattern is observed for both the benchmark datasets: Graz-02 and TF-Flowers, as validated by the experimental results on the basis of various evaluation measures: ROC curve and its AUC, F1-score, and accuracy. The proposed learning model is able to detect all the classes (Majority and Minority classes) equally and effectively. Application of resampling strategies had little or no effect on the learning model that makes it a distinctive approach.

In the case of the TF-Flowers dataset there are 3670 images, out of which 70% images are taken for training i.e. 2569 image samples. From each image present in the dataset, ResNet-50 features are extracted. The dimension of features extracted from training set is (2569, 7, 7, 2048) which is converted to 2-dimensional matrix of size (2569 * 7 * 7, 2048) as in (125881, 2048). The 2-dimensional matrix X was passed to k-means algorithm. So in this particular case of TF-Flowers dataset, N is 125881 (number of instances) and D is equal to 2048 (number of features) as $X \in \mathbb{R}^{N \times D}$ (matrix X has N x D dimension). Similarly for Graz-02 dataset, out of 1476 images 70% images are taken i.e. 1033 image samples for training set. So (1, 60) features are obtained and subsequently passed to SVM classifier. Therefore, it can be inferred that even after applying k-means for BOVW codebook generation, each image yields k number of features only ($k = 100$ for TF-Flowers dataset, $k = 60$ for Graz02 dataset). Therefore, we did not experience any issues related to the curse of dimensionality problem as N is sufficiently greater than D ($N >> D$) in the proposed BOVW approach.

4 Conclusion

In this paper, we have proposed a novel combination of visual codebook generation using deep features with the non-linear Chi^2 SVM classifier, to tackle the imbalance problem that arises while dealing with multi-class image datasets. The low-level deep features are first extracted by transfer learning using the ResNet-50 pre-trained network, and clustered using k-means.

Table 11 Performance evaluation of ResNet-50 BOVW features combined with Quasi SVM and its variants for TF-Flowers dataset

Classifier	Dandelion (F1)	Daisy (F1)	Sunflowers (F1)	Roses (F1)	Tulips (F1)	Accuracy
Quasi-SVM	0.8942±0.0160	0.8880±0.0204	0.8491±0.0205	0.7882±0.0177	0.8047±0.0163	0.8459±0.0106
Quasi-SVM (w/ 1 hidden layer)	0.9075±0.0124	0.9239±0.0122	0.8661±0.0159	0.8095±0.0161	0.8251±0.0153	0.8643±0.0051
Quasi-SVM (w/ 2 hidden layers)	0.7957±0.2022	0.6910±0.3504	0.6746±0.3394	0.4555±0.3735	0.6103±0.3089	0.6958±0.2321
Quasi-SVM (w/ 3 hidden layers)	0.9006±0.0162	0.9028±0.0132	0.8678±0.0143	0.8065±0.0223	0.8290±0.0095	0.8630±0.0061
Kernelized Quasi-SVM	0.9022±0.0119	0.9044±0.0135	0.8646±0.0173	0.8034±0.0210	0.8206±0.0108	0.8603±0.0062
Kernelized Quasi-SVM (w/ 1 hidden layer)	0.9075±0.0124	0.9074±0.0120	0.8661±0.0159	0.8095±0.0161	0.8095±0.0161	0.8643±0.0051
Kernelized Quasi-SVM (w/ 2 hidden layers)	0.7957±0.2022	0.6910±0.3504	0.6746±0.3394	0.4555±0.3735	0.6103±0.3089	0.6958±0.2321

Table 12 Macro average ROC AUC readings for different classifiers and ResNet-50 deep features for Graz-02 dataset and TF-Flowers dataset

Features	Classifier	Macro average ROC AUC	
		Graz-02 dataset	TF-flowers dataset
ResNet-50 BOVW features	**Chi^2 SVM**	**0.9837**	**0.9824**
	Logistic Regression	0.9828	0.9806
	Linear Discriminative Analysis	0.9822	0.9788
	K Nearest Neighbors Classifier	0.9549	0.9482
	Decision Tree	0.9166	0.8796
	Gaussian Naïve Bayes	0.9552	0.9517

Table 13 Macro average ROC AUC readings for different features for Chi^2 SVM classifier for Graz-02 dataset and TF-Flowers dataset

Features	Classifier	Macro average ROC AUC	
		Graz-02 dataset	TF-flowers dataset
ResNet-50 BOVW features	**Chi^2 SVM**	**0.9837**	**0.9824**
InceptionV3 BOVW features		0.9651	0.9457
VGG16 BOVW features		0.9758	0.9705
SIFT BOVW features		0.8017	0.8275

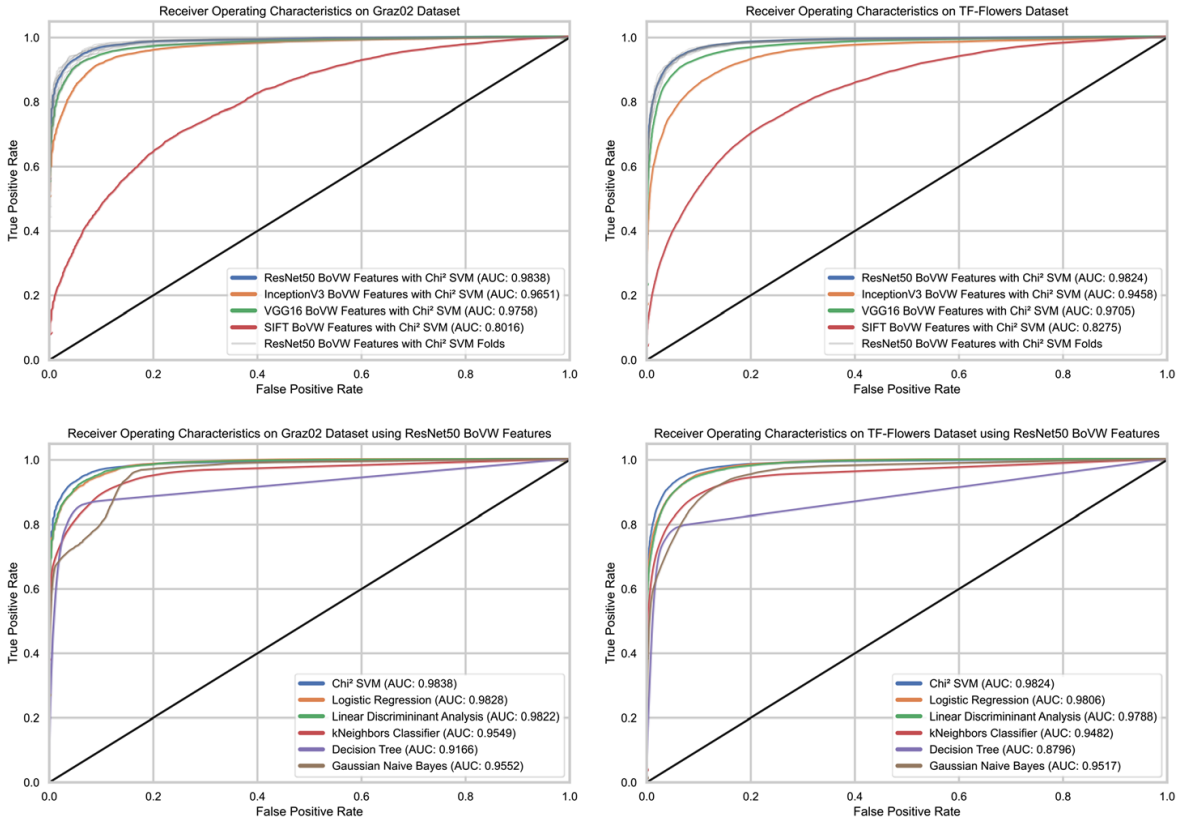

Fig. 8 (Top row left to right) ROC curve depicting different features in comparison with Chi^2 SVM classifier in case of Graz-02 and TF-Flowers dataset respectively. (Bottom row left to right) ROC curve depicting different classifiers in combination with ResNet−50 deep features in case of Graz-02 and TF-Flowers dataset respectively

The center of each cluster is a visual word in the codebook. Each image is then translated into a set of features called the Bag-of-Visual-Words (BOVW) which is the histogram representation over the visual words in the vocabulary. The non-linear Chi^2 SVM classifier is found most optimal for classifying the ensuing features, as proved by a detailed empirical analysis. In this paper, we have performed extensive experiments on two imbalanced multi-class datasets: Graz-02 and TF-Flowers, to validate the proposed BOVW approach with Chi^2 SVM using ResNet-50 deep features for visual codebook generation. The choice of ResNet-50 (ImageNet pre-trained model) deep features over traditional handcrafted features helps improve overall classification performance of BOVW. The role of feature scaling is also highlighted which significantly improves classification of the histogram representation. The significance of Chi^2 kernel transformation has been analysed to be an effective similarity metric for classifying histogram based features using one-vs-rest Support Vector Machines. The proposed model has been evaluated in comparison to various state-of-the-art techniques using evaluation measures like F1-score, accuracy, ROC curve and its AUC. All the experiments have been performed on a total of 10 folds (cross-validation strategy) for both the datasets. The analysis of experimental results, depicts that the presented BOVW approach using ResNet-50 deep features and Chi^2 SVM is able to surpass the baseline methods while dealing with imbalanced datasets. Additionally, we have shown results with an alternate approach suitable for large scale settings with the help of Quasi SVMs constructed using neural networks. This is especially useful to vouch for the scalability of our BOVW based approach on data expensive scenarios as well. An added advantage of using this alternate approach for kernel SVM approximation would be the support for online learning which could be highly desirable for many applications. In future work, we shall evaluate the proposed approach on other multi-class imbalanced datasets and explore similar techniques for improving classification performance of larger datasets as well as using other adaptive clustering techniques [55] in the proposed Bag-of-Visual-Words model.

References

1. Abadi M, Barham P, Chen J, Chen Z, Davis A, Dean J, ... & Kudlur M (2016). Tensorflow: A system for large-scale machine learning. In 12th {USENIX} symposium on operating systems design and implementation ({OSDI} 16) (pp. 265–283).
2. Bellet A, Habrard A, Sebban M (2013) A survey on metric learning for feature vectors and structured data. arXiv preprint arXiv:1306.6709
3. Bellet A, Habrard A, Sebban M (2015) Metric learning. Synthesis Lectures on Artificial Intelligence and Machine Learning 9(1):1–151
4. Bosch A, Zisserman A, Munoz X (2007, October) Image classification using random forests and ferns. In 2007 IEEE 11th international conference on computer vision (pp. 1-8). IEEE.
5. Brendel W, Bethge M (2019) Approximating cnns with bag-of-local-features models works surprisingly well on imagenet. arXiv preprint arXiv:1904.00760
6. Buda M, Maki A, Mazurowski MA (2018) A systematic study of the class imbalance problem in convolutional neural networks. Neural Netw 106:249–259
7. Chawla NV, Bowyer KW, Hall LO, Kegelmeyer WP (2002) SMOTE: synthetic minority over-sampling technique. J Artif Intell Res 16:321–357
8. Cheng G, Li Z, Yao X, Guo L, Wei Z (2017) Remote sensing image scene classification using bag of convolutional features. IEEE Geosci Remote Sens Lett 14(10):1735–1739
9. Convolutional Neural Networks (CNNs / ConvNets) (2019) The Stanford CS class notes, Spring 2019 Assignments, http://cs231n.github.io/convolutional-networks/, Accessed 28 August 2020.
10. Cortes C, Vapnik V (1995) Support-vector networks. Mach Learn 20(3):273–297

11. Deng J, Dong W, Socher R, Li LJ, Li K, Fei-Fei L (2009) Imagenet: a large-scale hierarchical image database. In 2009 IEEE conference on computer vision and pattern recognition (pp. 248-255). IEEE
12. Deselaers, T., Pimenidis, L., & Ney, H. (2008, December). Bag-of-visual-words models for adult image classification and filtering. In 2008 19th International Conference on Pattern Recognition (pp. 1-4). IEEE.
13. Dittman DJ, Khoshgoftaar TM, Wald R, Napolitano A (2014, May). Comparison of data sampling approaches for imbalanced bioinformatics data. In The twenty-seventh international FLAIRS conference.
14. Eitrich T, Lang B (2006) Efficient optimization of support vector machine learning parameters for unbalanced datasets. J Comput Appl Math 196(2):425–436
15. Estabrooks A, Jo T, Japkowicz N (2004) A multiple resampling method for learning from imbalanced data sets. Comput Intell 20(1):18–36
16. Feng J, Liu Y, Wu L (2017) Bag of visual words model with deep spatial features for geographical scene classification. Computational intelligence and neuroscience 2017:1–14
17. Georgescu MI, Ionescu RT, Popescu M (2019) Local learning with deep and handcrafted features for facial expression recognition. IEEE Access 7:64827–64836
18. Géron A (2019) Hands-on machine learning with Scikit-learn, Keras, and TensorFlow: concepts, tools, and techniques to build intelligent systems. O'Reilly Media
19. Haralick RM, Shapiro LG (1985) Image segmentation techniques. Computer vision, graphics, and image processing 29(1):100–132
20. He H, Bai Y, Garcia EA Li S (2008) ADASYN: adaptive synthetic sampling approach for imbalanced learning. In 2008 IEEE international joint conference on neural networks (IEEE world congress on computational intelligence) pp 1322–1328 IEEE
21. He K, Zhang X, Ren S, Sun J (2016). Deep residual learning for image recognition. In Proceedings of the IEEE conference on computer vision and pattern recognition (pp. 770-778).
22. Hou Q, Cheng MM, Hu X, Borji A, Tu Z, Torr PH (2017) Deeply supervised salient object detection with short connections. In Proceedings of the IEEE Conference on Computer Vision and Pattern Recognition pp 3203–3212
23. Kotsiantis SB, Pintelas PE (2003) Mixture of expert agents for handling imbalanced data sets. Annals of Mathematics, Computing & Teleinformatics 1(1):46–55
24. Kumar MD, Babaie M, Zhu S, Kalra S, Tizhoosh HR (2017) A comparative study of CNN, BoVW and LBP for classification of histopathological images. In 2017 IEEE Symposium Series on Computational Intelligence (SSCI) pp 1–7. IEEE
25. Lessmann S (2004) Solving imbalanced classification problems with support vector machines. In IC-AI 4: 214–220
26. Li P, Samorodnitsk G, Hopcroft J (2013) Sign cauchy projections and chi-square kernel. In Advances in Neural Information Processing Systems pp 2571–2579
27. López V, Fernández A, García S, Palade V, Herrera F (2013) An insight into classification with imbalanced data: empirical results and current trends on using data intrinsic characteristics. Inf Sci 250:113–141
28. Mahmood A, Bennamoun M, An S, Sohel F (2017) Resfeats: residual network based features for image classification. In 2017 IEEE international conference on image processing (ICIP) pp 1597–1601 IEEE
29. Okafor E, Pawara P, Karaaba F, Surinta O, Codreanu V, Schomaker L, Wiering M (2016, December). Comparative study between deep learning and bag of visual words for wild-animal recognition. In 2016 IEEE Symposium Series on Computational Intelligence (SSCI) (pp. 1-8). IEEE.
30. Opelt A, Fussenegger M, Pinz A, Auer P (2004) Weak hypotheses and boosting for generic object detection and recognition. In European conference on computer vision Springer, Berlin, Heidelberg pp. 71–84
31. Oskouei RJ, Bigham BS (2017) Over-sampling via under-sampling in strongly imbalanced data. International Journal of Advanced Intelligence Paradigms 9(1):58–66
32. Pedregosa F, Varoquaux G, Gramfort A, Michel V, Thirion B, Grisel O, Vanderplas J (2011) Scikit-learn: Machine learning in Python. the Journal of machine Learning research, 12:2825–2830
33. Powers DM (2011) Evaluation: from precision, recall and F-measure to ROC, informedness, markedness and correlation
34. Provost F (2000) Machine learning from imbalanced data sets 101. In Proceedings of the AAAI'2000 workshop on imbalanced data sets 68(2000):1–3 AAAI press
35. Rahimi A, Recht B (2008) Random features for large-scale kernel machines. In Advances in neural information processing systems pp. 1177–1184
36. Sáez JA, Krawczyk B, Woźniak M (2016) Analyzing the over-sampling of different classes and types of examples in multi-class imbalanced datasets. Pattern Recogn 57:164–178
37. Saini M, Susan S (2018) Comparison of deep learning, data augmentation and bag of-visual-words for classification of imbalanced image datasets. In International Conference on Recent Trends in Image Processing and Pattern Recognition Springer, Singapore pp. 561–571

38. Saini M, Susan S (2019) Data augmentation of minority class with transfer learning for classification of imbalanced breast Cancer dataset using inception-V3. In Iberian Conference on Pattern Recognition and Image Analysis Springer, Cham pp. 409–420
39. Saini M, Susan S (2020) Deep transfer with minority data augmentation for imbalanced breast cancer dataset. Appl Soft Comput 97:106759
40. Sculley D (2010) Web-scale k-means clustering. In Proceedings of the 19th international conference on World wide web pp. 1177–1178
41. Shin HC, Roth HR, Gao M, Lu L, Xu Z, Nogues I, Yao J, Mollura D, Summers RM (2016) Deep convolutional neural networks for computer-aided detection: CNN architectures, dataset characteristics and transfer learning. IEEE Trans Med Imaging 35(5):1285–1298
42. Simonyan K, Zisserman A (2014) Very deep convolutional networks for large-scale image recognition. arXiv preprint arXiv:1409.1556
43. Suh HK, Hofstee JW, IJsselmuiden J, van Henten EJ (2018) Sugar beet and volunteer potato classification using Bag-of-Visual-Words model, scale-invariant feature transform, or speeded up robust feature descriptors and crop row information. Biosyst Eng 166:210–226
44. Susan S, Kumar A (2018, December). Hybrid of intelligent minority over-sampling and PSO-based intelligent majority under-sampling for learning from imbalanced datasets. In International Conference on Intelligent Systems Design and Applications (pp. 760-769). Springer, Cham.
45. Susan S, Kumar A (2019) SSOMaj-SMOTE-SSOMin: three-step intelligent pruning of majority and minority samples for learning from imbalanced datasets. Appl Soft Comput 78:141–149
46. Susan S, Jain A, Sharma A, Verma S, Jain S (2015) Fuzzy match index for scale-invariant feature transform (SIFT) features with application to face recognition with weak supervision. IET Image Process 9(11):951–958
47. Susan S, Sethi D, Arora K CW-CAE: pulmonary nodule detection from imbalanced dataset using class-weighted convolutional autoencoder. In International Conference on Innovative Computing and Communications (pp. 825-833). Springer. Singapore.
48. Syarif, I., Prugel-Bennett, A., & Wills, G. (2012, April). Unsupervised clustering approach for network anomaly detection. In International conference on networked digital technologies (pp. 135-145). Springer, Berlin, Heidelberg.
49. Tahir MA, Kittler J, Yan F (2012) Inverse random under sampling for class imbalance problem and its application to multi-label classification. Pattern Recogn 45(10):3738–3750
50. Tajbakhsh N, Shin JY, Gurudu SR, Hurst RT, Kendall CB, Gotway MB, Liang J (2016) Convolutional neural networks for medical image analysis: full training or fine tuning? IEEE Trans Med Imaging 35(5): 1299–1312
51. Tang Y (2013) Deep learning using linear support vector machines. arXiv preprint arXiv:1306.0239
52. Tax DM, Duin RP (2000) Feature scaling in support vector data descriptions. Learning from Imbalanced Datasets, 25–30
53. The TensorFlow Team (2019) January. Flowers, TensorFlow Datasets http://download.tensorflow.org/example_images/flower_photos.tgz
54. Voulodimos A, Doulamis N, Doulamis A, Protopapadakis E (2018) Deep learning for computer vision: a brief review. Computational intelligence and neuroscience 2018:1–13
55. Wang XD, Chen RC, Yan F, Zeng ZQ, Hong CQ (2019) Fast adaptive K-means subspace clustering for high-dimensional data. IEEE Access 7:42639–42651
56. Wang X, Zheng Z, He Y, Yan F, Zeng Z, Yang Y (2020) Progressive local filter pruning for image retrieval acceleration. arXiv preprint arXiv:2001.08878
57. Xia X, Xu C, Nan B (2017) Inception-v3 for flower classification. In 2017 2nd International Conference on Image, Vision and Computing (ICIVC) pp. 783–787 IEEE
58. Yang H, Shao L, Zheng F, Wang L, Song Z (2011) Recent advances and trends in visual tracking: a review. Neurocomputing 74(18):3823–3831

Publisher's note Springer Nature remains neutral with regard to jurisdictional claims in published maps and institutional affiliations.

Proceedings of the Sixth International Conference on Inventive Computation Technologies [ICICT 2021]
IEEE Xplore Part Number: CFP21F70-ART; ISBN: 978-1-7281-8501-9

Car Traffic Sign Recognizer Using Convolutional Neural Network CNN

Abhay Lodhi
Computer Science Department
Delhi Technological University
Delhi, India
abhaylodhi3@gmail.com

Sagar Singhal
Electronics and Communication Department
Delhi Technological University
Delhi, India
sgrsinghal16@gmail.com

Massoud Massoudi
Software Engineering Department
*Assistant Professor,*Delhi Technological University
Delhi, India
massoud.massoudi@hotmail.com

Abstract—Acknowledgment of traffic signs vary significantly in numerous applications, for example, in self-driving vehicle/driverless vehicle, traffic planning and traffic observation. Traffic Sign Recognition (TSR) framework is a segment of Driving Assistance System (ADAS). The TSR framework helps the drivers in safe driving as street signs give significant data of the street. The car business has built up a great deal and a portion of the organizations are attempting to assemble self-sufficient vehicles and in which traffic sign acknowledgment is one of the significant factors to be thought of. To perceive the traffic signs, a model utilizing convolutional neural network is fabricated and this model will perceive the traffic signs. This model can likewise be utilized in typical vehicles to caution the driver about traffic signs through content identification.

Keywords—Convolution neural network, Adam optimizer, Traffic Sign.

I. INTRODUCTION

For the most part, traffic sign acknowledgment (TSR) frameworks comprise two phases of recognition and arrangement; for some TSR frameworks, a following stage is planned among detection and Classification for managing video successions[1].Deep learning emerges to be the most successful subset of machine learning in solving problems related to image classification and identification. The achievement of deep learning in the field of self-driving cars is unequivocal. For example, DNNs have been utilized in scene semantic division [2], traffic signal recognition [3], crosswalk arrangement [4], [5], traffic sign location [6], walker investigation [7], vehicle heading course assessment [8] and numerous different applications.

The proposed research work focuses around traffic sign detection. A traffic in alone can convey a whole lot of information to the street clients. It is significantly important to develop a reliable automatic traffic sign detection system. Apart from the advantages of Deep learning there are few concerns related to it as .Deep learning requires expensive annotation, a large balanced data set which in result requires high computational cost in training.

To achieve this task, a dataset that contains almost all the information about traffic is required as there are some traffic signs, which are rarely seen and uncommon under normal driving scenarios.

There are basically three techniques to identify traffic signs: (i) 'AdaBoost based detection', (ii) 'Support Vector Machine (SVM), and (iii) 'Neural Network (NN) based detection'.

German Traffic Sign Detection Benchmark (GTSDB) [9] is used as these images are taken from real scenarios of German street.

II. CONVOLUTION NEURAL NETWORK

A CNN is a supervised learning procedure which needs both information and target yield information to be provided. These are grouped by utilizing their marks to give a scholarly model to future information investigation.

Normally a CNN has three principles constitutes- a convolutional Layer, a Pooling Layer and a fully associated Dense Network. The Convolutional layer takes the info picture and applies m number of nxn channels to get a component map. The element map is next taken into the maximum pool layer which is basically utilized for dimensionality decrease, it picks simply the best highlights from the component map. At last, all the highlights are smoothed and sent as contribution to the completely associated thick neural organization which learns the loads utilizing backpropagation and gives the characterization yield.

The inspiration driving the CNN is that it depends in transit the visual cortex capacities, where one item in the scene is in center while the rest is obscured, comparably the CNN takes one segment/window of the info picture at once. Each time the CNN will deliver a component map for each part, in the convolutional layer. In the Pooling layer it eliminates the overabundance highlights and takes just the main highlights for that part, consequently performing highlight extraction. Subsequently, with the utilization of CNNs and don't need to play out an extra component extraction procedure.

CNNs require lesser pre-preparing when contrasted with other comparative characterization calculations. While customary MLP (Multi Layer Perceptron) calculations have critical exactness for picture

2021 6th International Conference on Inventive Computation Technologies (ICICT) | 978-1-7281-8501-9/21/$31.00 ©2021 IEEE | DOI: 10.1109/ICICT50816.2021.9358594

Authorized licensed use limited to: DELHI TECHNICAL UNIV. Downloaded on March 03,2021 at 06:02:52 UTC from IEEE Xplore. Restrictions apply.

acknowledgment, they experience the ill effects of the scourge of dimensionality because of the hubs being completely associated, and subsequently can't be scaled to high goal pictures. CNNs beat these difficulties presented by MLP by abusing the spatial relationship of a picture. This is finished by implementing an example of neighborhood network between nearby neuron layers. Subsequently, CNNs end up being unrivaled at Image order, Video Analysis, Natural Language Processing and wide scope of different applications when contrasted with different methods.

III. RELATED WORK

In earlier times traffic sign detection used only shapes and colors and it was not that efficient and robust. Due to increase in computational prowess of mankind and advent of large data sets, deep convolutional datasets have demonstrated their capabilities that has led to increase in accuracy of traffic sign recognition. Traffic sign recognition mainly includes detection and recognition. Yuga hatolkar et al [10] proposed a method for traffic sign recognition in which the fuzzy classification module acts as an optimizer module for results obtained by CNN. It measured accuracy and Loss. In the last decade Convolutional Neural Networks (CNN) have shown remarkable progress in increasing the accuracy and reliability of the traffic detection system. Wu et al. [11] began employing CNNs to address traffic sign detection as a candidate region classifier. Zhu et al. [12] proposed a novel framework in which a fully convolutional network generated the region CNN for Small Traffic Sign Recognition proposals and CNNs was used for classification. Jain A et al [13] optimized detection using CNN they applied convolutional neural network domain transfer learning and genetic algorithm to calculate accuracy, precision, recall percentage. Zhang J [14] used CNN and knowledge distillation to calculate accuracy however pruning a model to 70% decreased its accuracy.S.Mehta [15] used CNN softmax activation function, RELU activation function and Adam optimizer to test and train accuracy and loss. Jin et al [16] proposed Traffic Sign Recognition implementing Hinge Loss method in Neural Networks that achieved a 99.65% accuracy on the GTSRB dataset. In recent times a new technique R-CNN is being proposed by the scholars. RBG [17] proposed an R-CNN framework. Recent developments in deep learning have increased recognition and detection capabilities of the systems using different layers in the convolutional networks. Inspired by these works we aim to develop an effective traffic sign detection framework following the similar philosophy of using different features of layers of CNN.

IV. METHODOLOGY

1) Dataset

In this paper German traffic sign dataset (GTSDB)[9] is utilized as an information base which has been widely used in the majority of the research work for ordering and identifying traffic signs.31367 samples of images are used for training purpose, 7842 for validations and 12630 for testing .The dataset contains 43 classes i.e. ,{ 1:'Speed limit (20km/h)', 2:'Speed limit (30km/h)', 3:'Speed limit (50km/h)', 4:'Speed limit (60km/h)', 5:'Speed limit (70km/h)', 6:'Speed limit (80km/h)', 7:'End of speed limit (80km/h)', 8:'Speed limit (100km/h)', 9:'Speed limit (120km/h)', 10:'No passing', 11:'No passing veh over 3.5 tons', 12:'Right-of-way at intersection', 13:'Priority road', 14:'Yield', 15:'Stop', 16:'No vehicles', 17:'Veh > 3.5 tons prohibited', 18:'No entry', 19:'General caution', 20:'Dangerous curve left', 21:'Dangerous curve right', 22:'Double curve', 23:'Bumpy road',24:'Slippery road', 25:'Road narrows on the right', 26:'Road work', 27:'Traffic signals', 28:'Pedestrians', 29:'Children crossing', 30:'Bicycles crossing', 31:'Beware of ice/snow', 32:'Wild animals crossing', 33:'End speed + passing limits', 34:'Turn right ahead', 35:'Turn left ahead', 36:'Ahead only', 37:'Go straight or right', 38:'Go straight or left', 39:'Keep right', 40:'Keep left', 41:'Roundabout mandatory', 42:'End of no passing', 43:'End no passing veh > 3.5 tons' }.

Figure 1: Preview of German Dataset

Below are the three histograms representing the class wise samples of images taken for (i) training, (ii) validation and (iii) testing. We had taken 80% of the dataset for training purpose and 20% for testing.

Authorized licensed use limited to: DELHI TECHNICAL UNIV. Downloaded on March 03,2021 at 06:02:52 UTC from IEEE Xplore. Restrictions apply.

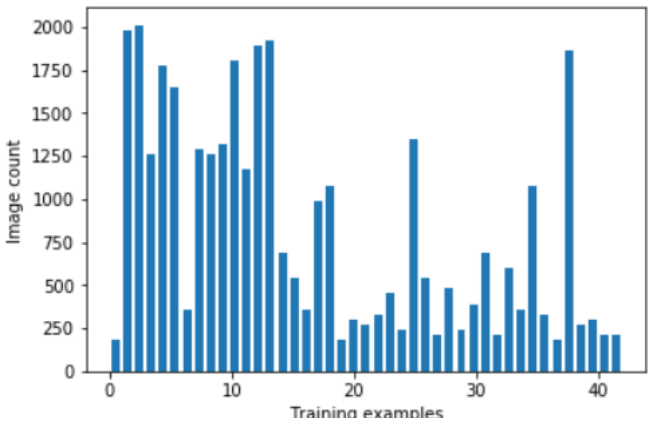

Figure 2: Class wise visualization of samples taken for Training

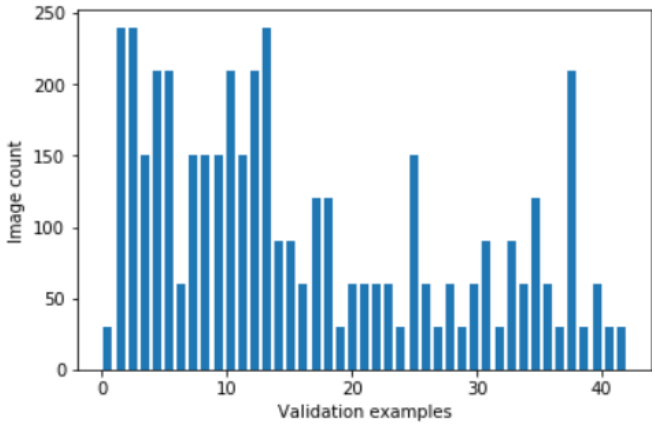

Figure 3: Class wise visualization of samples taken for Validation

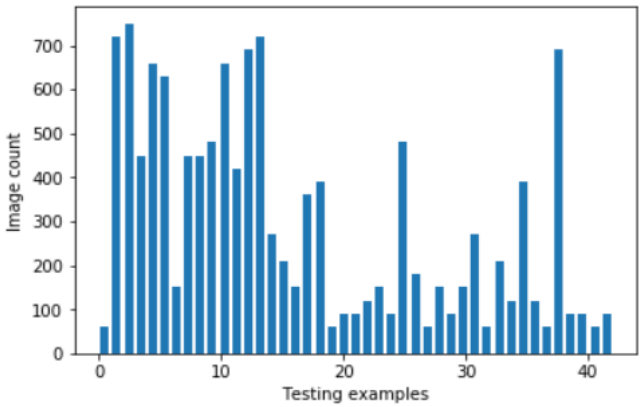

Figure 4: Class wise visualization of samples taken for Training

2. *Experimental Setup*

Proposed work is implemented with the help of tensorflow and keras library. The system is backed with Intel core i7 7th Gen, Nvidia Geforce GTX 1050Ti, 8 GB ram and 64 bit operating system. We had used pillow library for opening, manipulating and saving images and had used OS module for iterating the dataset because of its redundancy, portability, safety. It provides faster execution of images with respect to other module.

3. *CNN Architecture*

Figure 6, showed the proposed CNN architecture which we had developed for classification and recognition of German Traffic Sign. The proper number of filter size is subjected to experimental tries. The number of filter size must be chosen considering calculation costs. The first three layers of CNN network is constructed with 32 filters and a kernel size of (5x5).Kernel is slided over the input dataset performing the dot product with the sub area of input images and gives matrix representation of the dot product as a output. ReLu Activation function is used in each layer. The output of the convolutional layer was made to go through the ReLU initiation function each time. This function basically chooses the output that must be shipped to the neurons of the next layer. This function gives zero as an output for all the values less than zero. Graphical representation of ReLU function is given below.

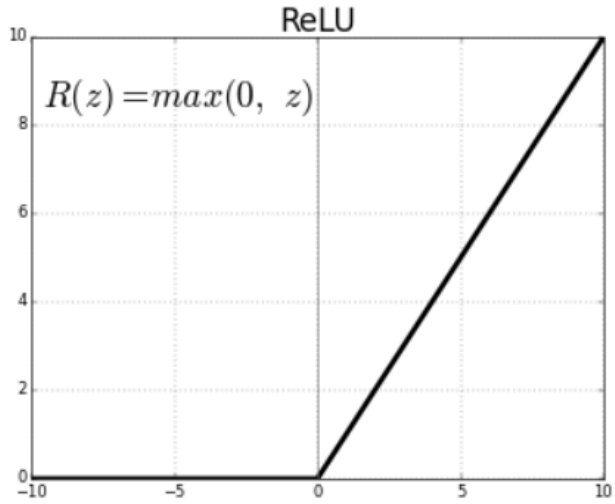

Figure 5: Graphical representation of ReLU Function

Authorized licensed use limited to: DELHI TECHNICAL UNIV. Downloaded on March 03,2021 at 06:02:52 UTC from IEEE Xplore. Restrictions apply.

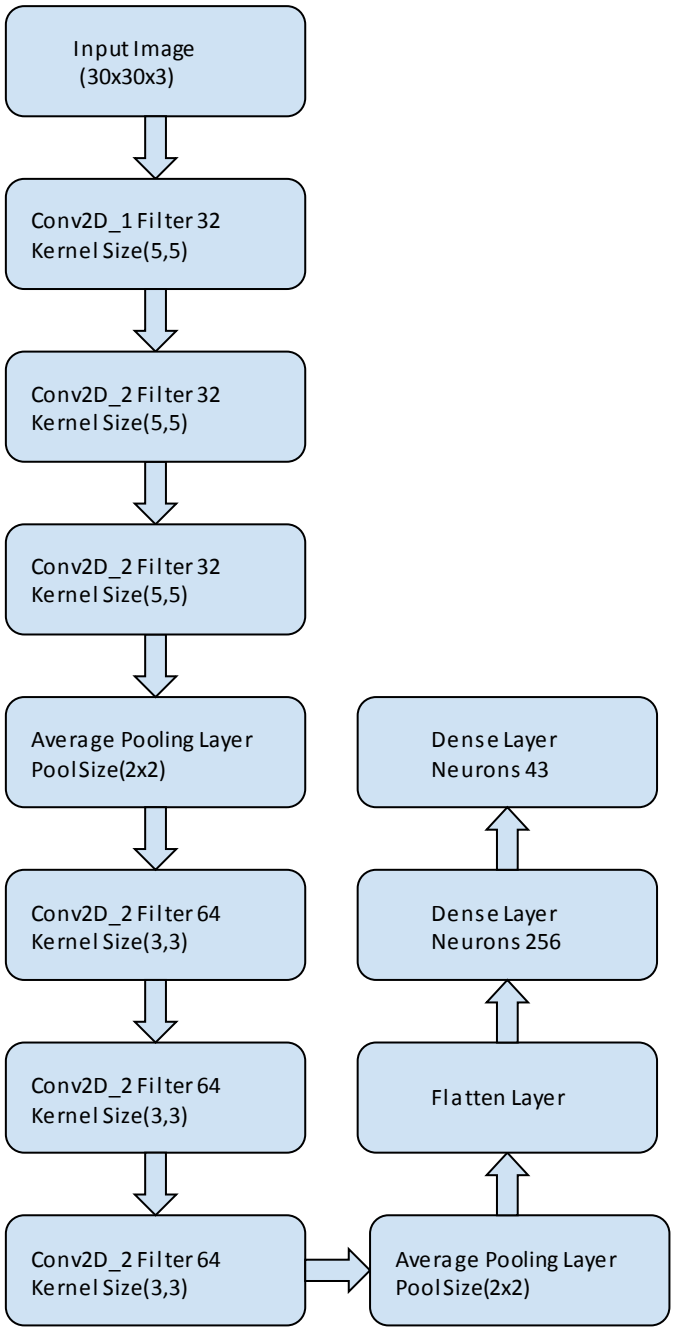

Figure 6: Flow Diagram Of CNN Architecture.

To choose the correct pooling layer is next big step to build a successful neural network, as it help us in reducing the spatial size and reduce the complexity of the input images[18],deducting some parameters to reduce the computational complexity of the input images. The sizes of images are controlled by three parameters (i) how many filters we have used, (ii) stride, (iii) zero padding. The proposed model is tested with average pooling layer and max pooling layer results were prominent from both side. The average pooling layer help us in bringing the smoothness in image, so finally we build our model with average pooling layer.

We first thought of using dropout layer, but after experimental result we were motivated not use dropout layer as dataset we had used was less prone to overfitting and we were getting better training and validation accuracy by dropping dropout layer. Training accuracy which was around 96% jumps to touching 100% (99.06) and there was also slight increase in the validation accuracy but the final testing accuracy were more and less similar. Table I shows the experimental result of our model with and without dropout layer.

Table I shows the comparison of the model with and without dropout layer.

With And Without Dropout layer	Training Accuracy	Training Loss	Validation Accuracy	Validation Loss
With Dropout layer	0.9602	0.1462	0.988	0.0477
Without Dropout Layer	0.9906	0.0366	0.987	0.0637

Output from the dropout layer is sent as an input to the flatten layer which is useful in fast feeding the forward execution,reducing parameters especially weights of neural network is taken into consideration at high exent.

After passing images through linear layers (y=wx+c) , we passed our model to the nonlinear layer(Dense layer) to modulate the nonlinear properties of our model and we finally aggregate this model with Adam optimizer which performs well in categorical cross entropy as we had various classes of traffic signs to classify.To achieve high accuracy it is important to choose correct optimizer with right parameter.

V. EXPERIMENTAL RESULT

We first preprocess the data set to improve the training and testing results.we resize them to 30x30x3 format.After that we observe that data augmentation done improves the accuracy.

Table II shows the accuracy of the model with different optimizers.

Optimi-zer	Training Accuracy	Training Loss	Validation Accuracy	Validation Loss
SGD	0.020	0.022	0.022	0.022
AdaGra	0.038	0.024	0.061	0.022

Authorized licensed use limited to: DELHI TECHNICAL UNIV. Downloaded on March 03,2021 at 06:02:52 UTC from IEEE Xplore. Restrictions apply.

d				
Adam	0.958	0.150	0.986	0.055

We tested our model with different optimizer results depicted in table I.Model was performing poorly with SGD(Stochastic Gradient Descent), AdaGrad as these optimizers were not able to learn weights adaptively.Most prominent results were with Adam optimizer.

Taking into account this comparison Table I we finally decided to use Adam optimizer as its training cost was much lower than others optimizer and we were able to achieve higher accuracy.There were several pros for using this optimizer , as it not only reduce the computational cost but was also faster than the other optimizer [19].

To choose the correct pooling layer is an important decision to build a better CNN architecture , we were getting slightly better results with the average pooling layer,so we finally decided to use it.We finally used 3 convolution layer with ReLU as an activation function in each layer,followed by average pooling layer , repeating this pattern one more time and finally passing it to flatten layer followed by two dense layers.

Table III shows the performance measure of the model with different pooling layers.

Performance Measure	Score (Max_Pooling_layer)	Score (Average_Pooling_layer)
Training Accuracy	95.87%	99.06%
Validation Accuracy	98.62%	98.71%
Testing Accuracy	96.00%	96.19%
F1 Score	0.9600	0.9619
Precision Score	0.9487	0.9619
Cohen Kappa Score	0.9584	0.9605
Training Loss	0.1501	0.1462
Validation Loss	0.0552	0.0477

This paper presents a good approach to recognise traffic signs , on training the model on 15 epochs with a batch size of 62 we were able to get an accuracy of 99.06% on training model.The accuracy on validation was about 98.71% and the final testing accuracy was 96.19%. The accuracy and loss on training and validation dataset are shown in fig 6 and fig 7.

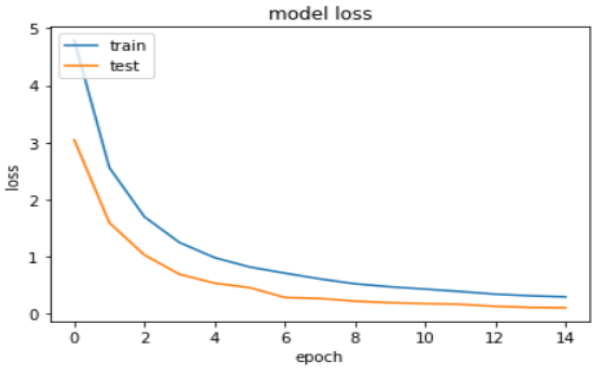

Figure 6: Model loss vs epoch

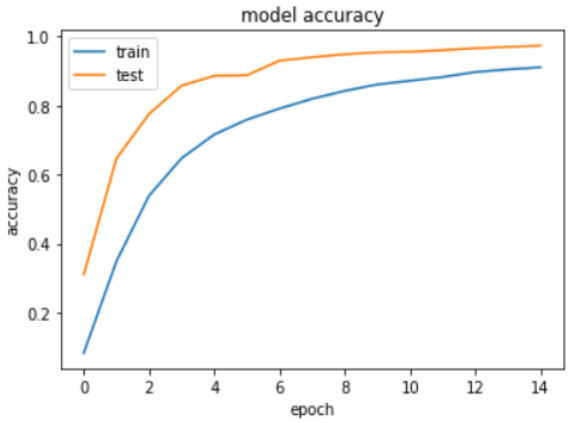

Fig 7. Accuracy vs epoch

VI. CONCLUSION

In this paper we proposed a Traffic Sign recognition system using Convolutional Neural Networks(CNN) with State of art results having 96.19% accuracy on the German dataset(GTSDB) used. The CNN framework integrates multiple levels of convolution feature and multiple levels of contextual information. At the detection stage, the region proposals are generated from the fused feature map with sufficient information. ADAM optimizer was used to decrease the computational and training cost which helped in achieving the given accuracy.

In the future we would like to increase the accuracy and efficiency of our project by visualizing remaining errors and using further optimization techniques.

REFERENCES

[1] C. Liu, S. Li, F. Chang and Y. Wang, "Machine Vision Based Traffic Sign Detection Methods: Review, Analyses and Perspectives," in *IEEE Access*, vol. 7, pp. 86578-86596, 2019, doi: 10.1109/ACCESS.2019.2924947.

[2] L.-C. Chen, Y. Zhu, G. Papandreou, F. Schroff and H. Adam, "Encoder-Decoder with Atrous Separable Convolution for Semantic Image Segmentation", *European Conference on Computer Vision (ECCV)*, 2018.

[3] K. Behrendt, L. Novak and R. Botros, "A deep learning approach to traffic lights: Detection tracking and classification",

Authorized licensed use limited to: DELHI TECHNICAL UNIV. Downloaded on March 03,2021 at 06:02:52 UTC from IEEE Xplore. Restrictions apply.

International Conference on Robotics and Automation (ICRA), pp. 1370-1377, 2017.

[4] R. F. Berriel, F. S. Rossi, A. F. de Souza and T. Oliveira-Santos, "Automatic Large-Scale Data Acquisition via Crowdsourcing for Crosswalk Classification: A Deep Learning Approach", *Computers & Graphics*, vol. 68, pp. 32-42, 2017

[5] R. F. Berriel, A. T. Lopes, A. F. de Souza and T. Oliveira-Santos, "Deep Learning-Based Large-Scale Automatic Satellite Crosswalk Classification", *Geoscience and Remote Sensing Letters*, vol. 14, no. 9, pp. 1513-1517, 2017.

[6] Z. Zhu, D. Liang, S. Zhang, X. Huang, B. Li and S. Hu, "Traffic-Sign Detection and Classification in the Wild", *Conference on Computer Vision and Pattern Recognition (CVPR)*, 2016

[7] R. Guidolini, L. G. Scart, L. F. Jesus, V. B. Cardoso, C. Badue and T. Oliveira-Santos, "Handling Pedestrians in Crosswalks Using Deep Neural Networks in the IARA Autonomous Car", *International Joint Conference on Neural Networks (IJCNN)*, 2018.

[8] R. F. Berriel, L. T. Torres, V. B. Cardoso, R. Guidolini, C. Badue, A. F. D. Souza, et al., "Heading direction estimation using deep learning with automatic large-scale data acquisition", *International Joint Conference on Neural Networks IJCNN*, 2018.

[9] S. Houben, J. Stallkamp, J. Salmen, M. Schlipsing and C. Igel, "Detection of Traffic Signs in Real-World Images: The German Traffic Sign Detection Benchmark", *International Joint Conference on Neural Networks (IJCNN)*, 2013.

[10] Hatolkar, Yuga & Agrawal, Poorva & Patil, Seema. (2018). A Survey on Road Traffic Sign Recognition System using Convolution Neural Network. International Journal of Current Engineering and Technology. 8. 10.14741/ijcet/v.8.1.21.

[11] Y. Wu, Y. Liu, J. Li, H. Liu and X. Hu, "Traffic sign detection based on convolutional neural networks," The 2013 International Joint Conference on Neural Networks (IJCNN), Dallas, TX, 2013, pp. 1-7, doi: 10.1109/IJCNN.2013.6706811.

[12] Y zhu,C zhang "Traffic sign detection and recognition using fully convolutional network".

[13] Jain, A., Mishra, A., Shukla, A. et al. A Novel Genetically Optimized Convolutional Neural Network for Traffic Sign Recognition: A New Benchmark on Belgium and Chinese Traffic Sign Datasets. Neural Process Lett 50, 3019–3043 (2019).

[14] Zhang, J., Wang, W., Lu, C. et al. Lightweight deep network for traffic sign classification. Ann. Telecommun. 75, 369–379 (2020).

[15] S. Mehta, C. Paunwala and B. Vaidya, "CNN based Traffic Sign Classification using Adam Optimizer," 2019 International Conference on Intelligent Computing and Control Systems (ICCS), Madurai, India, 2019, pp. 1293-1298, doi: 10.1109/ICCS45141.2019.9065537.

[16] J. Jin, K. Fu and C. Zhang, "Traffic Sign Recognition With Hinge Loss Trained Convolutional Neural Networks," in IEEE Transactions on Intelligent Transportation Systems, vol. 15, no. 5, pp. 1991-2000, Oct. 2014, doi: 10.1109/TITS.2014.2308281.

[17] R. Girshick, J. Donahue, T. Darrell and J. Malik, "Region-Based Convolutional Networks for Accurate Object Detection and Segmentation," in IEEE Transactions on Pattern Analysis and Machine Intelligence, vol. 38, no. 1, pp. 142-158, 1 Jan. 2016, doi: 10.1109/TPAMI.2015.2437384.

[18] C.Martin Navas, F. J. Navas Gonzalez, V. Castillo Lopez, L.Payers Capella, M. Gomez Fernandez , and J. V. Delgado Bernejo , "Impact of breeding for coat and spotting patterns on the population structure and genetic diversity of an islander endangered dog breeds' ', Res. vet. Sci.,vol.131,no.April,pp.117-130,2020,doi:10.1016/j.rvsc.2020.04.003.

[19] R. Girshick, J. Donahue, T. Darrell and J. Malik, "Rich Feature Hierarchies for Accurate Object Detection and Semantic Segmentation," 2014 IEEE Conference on Computer Vision and Pattern Recognition, Columbus, OH, 2014, pp. 580-587, doi: 10.1109/CVPR.2014.81.

Authorized licensed use limited to: DELHI TECHNICAL UNIV. Downloaded on March 03,2021 at 06:02:52 UTC from IEEE Xplore. Restrictions apply.

Proceedings of the Sixth International Conference on Inventive Computation Technologies [ICICT 2021]
IEEE Xplore Part Number: CFP21F70-ART; ISBN: 978-1-7281-8501-9

Comparison of ECC and RSA Algorithm with DNA Encoding for IoT Security

Malti Bansal, Shubham Gupta, Siddhant Mathur
Department of Electronics and Communication Engineering
Delhi Technological University, Delhi-110042, India
maltibansal@gmail.com

2021 6th International Conference on Inventive Computation Technologies (ICICT) | 978-1-7281-8501-9/21/$31.00 ©2021 IEEE | DOI: 10.1109/ICICT50816.2021.9358591

Abstract— **IoT is still an emerging technology without a lot of standards around it, which makes it difficult to integrate it into existing businesses, what's more, with restricted assets and expanding gadgets that essentially work with touchy information. Thus, information safety has become urgent for coders and clients. Thus, painstakingly chosen and essentially tested encryption calculations should be utilized to grow the gadgets productively, to decrease the danger of leaking the delicate information. This investigation looks at the ECC calculation (Elliptic Curve Cryptography) and Rivest-Shamir-Adleman (RSA) calculation. Furthermore, adding the study of DNA encoding operation in DNA computing with ECC to avoid attackers from getting access to the valuable data.**

Keywords— IoT , RSA , ECC , DNA Sequencing , Cryptography

I. INTRODUCTION

IoT (Internet of things) is a overpowered global organization establishment self-planning limits dependent on traditional and interoperable communication protocols in which the physical and virtual things have real objects or physical identities and also the virtual personalities and use shrewd interface and are entirely dependent to get into the data organization [14]. Registering gadgets, for example, cell phones, embedded system, sensors, personal digital assistant (PDA), and smart watches, rings have assumed a prime function in our today's evolving technology These are becoming a basic piece of present-day individual's reality. These gadgets are carefully limited computing force, space and power storing capacity and other assets; So, this limitation may convert the gadget Prone to numerous security assaults. What's more, the trust and unwavering quality they give is getting increasingly more consideration when they should be related with touchy information like in IoT gadgets. In a nutshell, IoT is portrayed by the real world of smart objects with restricted storage and processing power [1]. The danger of trading off client information or admittance to private frameworks, the exertion to make sure about IoT gadgets is as significant as making IoT gadgets accessible for use. This study will compare elliptical curves cryptography (ECC) algorithm which is based of the curves and Rivest-Shamir-Adleman (RSA) which is based of large factorization of co-prime numbers. This comparison is based on the analysis of the data from case studies and separated data of specialized reports. The result of this investigation will be valuable for additional examination and additional work. This shall be useful to discover an answer to defeat existing Limitations in IoT security. This prompts an expansion in execution with a similar degree of security in gadgets with restricted assets. Since chips and microchips are turning out to be increasingly littler, it is imperative to make cryptographic ideas, so that they should not be costly and should be reliable and faster.

II. LITERATURE REVIEW

A. RSA

RSA is a generally utilized Public-Key calculation. RSA was initially depicted in 1977. In our proposed work, we are utilizing RSA calculation to scramble the information to give security so that just the concerned client can get to it. RSA calculation includes these steps:

1. Key Generation
2. Encryption
3. Decoding

Moreover, some steganography analyses have affirmed RSA to be a dependable method throughout a long term. This exhibits features which are like; this algorithm has a surprising measure of dependability, trouble of considering enormous possibilities that happen to be a central part in RSA's safety. The proficiency of RSA should be destroyed only when the factoring the large co-prime numbers would be easy. In like manner, RSA research centers gave the term of 'permutational assault' to be a test in 1989. [2] has told about the different major assaults about the cycling assault on RSA programs and also the major time assault on it .

B. ECC

This cryptography technique was brought to the world by Neal Koplitz and Miller Victor in 1979 [16][V.S. Miller, 1985].ECC is the most proficient encoded public key encipher strategy dependent on the idea of elliptic bend which is utilized for improved cryptography techniques. ECC assists with furnishing most elevated security with low power processing gadgets. Elliptic Curve Cryptography is utilized to contrast with the public hash key scrambling frameworks like RSA which involves large factorization and the oldest technique Diffie-Hellman encryptions method which involves key exchange. The DNA sequencing and elliptic curve cryptography are the recent methods of cryptography. Hence, for better security, functionalities of both the frameworks might be consolidated to build exceptionally secure IoT devices.

Authorized licensed use limited to: DELHI TECHNICAL UNIV. Downloaded on March 03,2021 at 06:08:36 UTC from IEEE Xplore. Restrictions apply.

Trouble of elliptical bend discrete algorithm issue (ECDLP) assumes a significant function for the safety of ECC which is the issue that can be settled in much large time [6].

III. ECC AND RSA COMPARISON

Elliptical Cure Cryptography technique's performance is dependent on the efficiency of computation algorithm of matrix multiplication (kH) [12]. String length of 180-bit ECC is same as safety feature of a 512-bit RSA/DSA [10]. [10] Found about RSA efficiency needed 512 bits for usage and 1024 bits for highly good efficiency for a secure key. Additionally, the supremacy of this steganography over RSA is evident because with a undersized length of string, Elliptical Curve Technique can give much more certainty. Figure given depicts the key lengths used in RSA and ECC. The base string area required for a made sure about steganographic system of ECC is 180 bits and even much more. The experiment was led [11] for discovering time lapses during scrambling, unscrambling/decoding by RSA and ECC on three different information of 16 bits, 32 bits, 512 bits as example with arbitrary generated string dependent on NIST suggestion. In light of experimentation, it was reasoned that ECC was far better than RSA for the security and computational efficiency with lesser attributes. An Elliptical Curve Cryptography is mainly very much suitable for computing power constraint gadgets. Among the largest essential perspectives of steganography's methods is computational force prerequisite. Productive elliptic bend mathematical calculations that are essential to ensure if it may work on asset obliged contraptions as FPGA [9] where FPGA is a field programmable gate array and reconfigurable exhibit which has a capacity is not pre-decided and would be easily modified in any framework. Particularly in asset compelled contraptions, need to not exclusively be secure but also practical and uncostly. In light of the figure below, ECC has more modest price proportion. Moreover, to augment the exhibition of the recently planned chips, ECC itself needs predictable upgraded version. [10].

TABLE I: SECURITY LAYERS (BITS) AND DIVISON OF PRICE FOR RSA/DSA AND ECC WITH SIMILAR SECURITY LAYERS [10]

Key Size		Security Level (bits)	Ratio of Cost
RSA	ECC		
1024	160	80	3:1
2048	224	112	6:1
3072	256	128	10:1
7680	384	192	32:1
15360	521	256	64:1

IV. DNA ENCODING FOR ECC

A. Elliptical Curve Cryptography

Elliptic curves are not essentially elliptic in form. They happen to be named so as they are represented with cubic equations. Weierstrass equation also known as three degree equations of elliptic bends are of the structure [17].

$$m_{xy} + y^2 + b_y = x^3 + px + q + nx^2$$

The first step in this system is encoding of simple text string that is to be given as a point on elliptical curve depicted by H_M. This is the point that is then encoded as the cipher text and will be sent and after being received has to be decrypted. A point G and an elliptic group Eq(e,f) as parameters are required for an encryption/ decryption system for the key exchange system. A private key n_E is then selected by each user E and then generates a $H_E=n_E$ x G which is the public key . [15] To encode and convey a string H_M to F, E selects any arbitrary positive whole number z and creates the mystery text C_M which contains the two points:

$$C_m = zG, H_m + kH_F$$

Here F's public key H_F is used by E. So as to unscramble the ciphertext, the principal value in the pair is multiplied by F's mystery string and the outcome is then deducted from the other point:

$$H_M + zH_F - n_F(kG) = H_M + z(n_FG) - z(n_FG) = H_M$$

As an instance of the encryption process (taken from [16]), Let p=282, E_P (-2,141) that is equal to the curve $y^2 - x^3 = x+522$; and G=(0,321).
Suppose that E desires to send a text to F that is encoded in the point on cure as H_M= (923,725) and that E chooses the random number z=557.
F's public key equals H_F= (725,7). We have 469(-1,291) = (393,992), and (562,725) + 368(201,5) = (385,328).
Thus, the encrypted message [(393,992), (472,439)] is sent by E.

B. DNA ENCODING

To safeguard personal communication and keep it exclusive from everyone except the intended receivers, cryptography is used. To ensure security of IoT devices and other electronic gadgets, proper usage of cryptographic technique is crucial. Evidently, any key will in theory be overwhelmed by a brute-force attack with adequate evaluating power. The practical outlook to contemporary steganography is using a key of sufficient enough length so that it can't be broken without a remarkable amount of evaluating power that would be notably more than the value of the contents that the cryptosystem preserves. IoT product developers have no rational excuse to continue to disregard IoT security threats because the contemporary cryptographic ICs make IoT security reasonably inexpensive.

The 3 methods mentioned in [5] for DNA steganography are used generally. These 3 methods are
1. Insertion method
2. Substitution Method

Authorized licensed use limited to: DELHI TECHNICAL UNIV. Downloaded on March 03,2021 at 06:08:36 UTC from IEEE Xplore. Restrictions apply.

3. Pair Complementing approach.

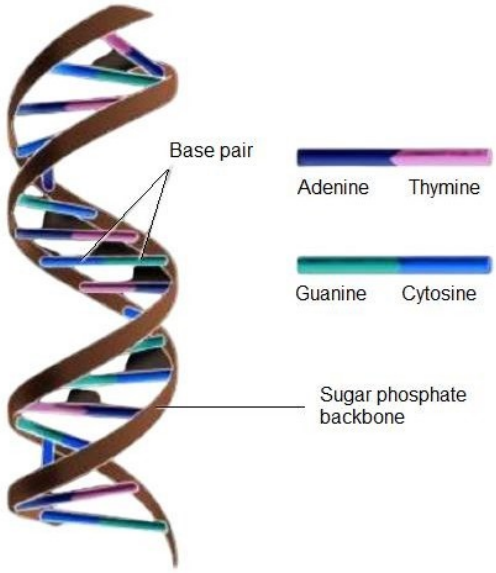

Fig. 1: DNA STRUCTURE.

A typical strategy for encoding and decoding is utilized in the entirety of the previously mentioned methods. The plain text is changed to twofold numbers (2's power representation numbers). The changed twofold numbers are then additionally changed into comparable DNA nucleotides pattern [5]. For encryption or decoding, A algorithm from the DNA steganography's strategies of [5] are utilized. DNA is the genetic matter of eukaryotes. It has a twofold helical sub-atomic structure and 2 single strands corresponding to one other. DNA is known as a polymer and made out of numerous little nucleotides. A nucleotide comprises of 3 sections:

a. The bases which are Nitrogenous
b. Phosphate
c. Deoxyribose

DNA is known as the condensing of deoxy-ribo nucleic acid that is considered as the plasma of every living thing's germ. Deoxy-ribo nucleic acid is a sort of organic full-scale atom and comprises of nucleotide. All of the nucleotides involve only one base and other are 4 types of bases commonly known as Adenine and Thymine or Cytosine and Guanine equivalent to four kinds of nucleotides represented as ATCG. The encrypted points on the elliptic curve are called cipher text points. The receiver is sent this point. The receiver will derive the plain text message in the reverse process.[14]

$$[\, zG, Hm + k H_F \,]$$

Here , G – The generated points
z – Chosen by user (Random number)

Hm – Points of Plain text
H_F - Another user's Public key

$$H_M + zH_F - n_F(kG) = H_M + z(n_FG) - k(n_FG) = H_M$$

TABLE II. NUCLEOTIDE TO BINARY NUMBER CONVERSION TABLE

DNA Nucleotide Base	Equivalent in Binary
A	00
T	01
G	10
C	11

The DNA sequence is then transformed into binary following Table -2. Then the binary DNA sequence is broken into smaller slots where each slot of DNA sequence consists of a arbitrary chosen number of bits. The number of bits chosen at random should be greater than two. Binary plain text's each bit is after that placed in the starting of fragmented 2's power representations of DNA string. The allocated bit patterns are then joined together to generate a new encrypted binary text as a sequence. [14] A new virtual (not achieved actually, only found from calculations) binary string is achieved by changing the encrypted binary string into nucleotide using Table -2.

The first given sequence is a fragment of Litmus's DNA sequence, where as its original length was 2856 long and security taken from [5]:
ATCGAATTCGCGCTGAGTCACAATTCGCGCTGAGTC
ACAATTCGCGCTGAGTCACAATTGTGACTCAGCCGC
GAATTCCTGCAGCCCCGAATTCCGCATTGCAGAGAT
AATTGTATTTAAGTGCCTAGCTCGATACAATAAACGC
CATTTGACCATTCACCACATTGGTGTGCACCTCCAAG
CTCGCGCACCGTACCGTCTCGAGGAATTCCTGCAGG
ATATCTGGATCCACGAAGCTTCCCATGGTGACGTCAC
C.

V. FUTURE WORK

With reason to improve the robustness and dependability of the administrations in urban communities, it requires a tough IoT system which is fit to respond and self-design after unpredictable events. This significant prerequisite includes resilience in IoT framework, which is one of the open issues in the IoT field that should be handled.
DNA Encoding with Elliptic curve steganography has various advantages over traditional systems, such as increased speed, smaller key size and less memory. There is an immediate connection between factor key lengths and activeness of security in uneven codification calculations. A safer calculation is the one which is having greater key string length. However, then again, more prominent key length needs more and more force of computers and assets.

Authorized licensed use limited to: DELHI TECHNICAL UNIV. Downloaded on March 03,2021 at 06:08:36 UTC from IEEE Xplore. Restrictions apply.

Furthermore, normally some essentials shall bring down the method's efficiency. The requirement to make this method more better is that the ECC algorithm can be fulfilled by progress in matrix multiplication calculation as the elementary mathematical tool of ECC algorithm. To accomplish this, we have to plan a productive calculation that can improve both scalar arithmetic and point calculations. Moreover, many security estimation investigations should be done to guarantee the safety of calculation from the famous attacks like side channel assaults. This calculation is better with regards to the expense with the adequacy and shall outperform the other founded calculation in term of productivity or viability [8].

VI. CONCLUSION

In this paper we reviewed a cryptographic algorithm by mixing DNA Encoding with ECC algorithm and its correlation with customary RSA algorithm. As indicated by above in the figure, in examination with additional regular steganography's like RSA, a similar level of safety for modest key lengths can be ensured by ECC.

DNA Encoding with Elliptic Curve cryptography has different points of interest over customary frameworks, in the structure of time, less space and more modest key lengths. Additionally, the given framework has two layer security, where the first layer is DNA encoding and second one corresponds to ECC steganography. Cryptographic plan particularly in resource constrained gadgets, should be not just secure but also pragmatic and uncostly. Moreover, to boost the execution of the recently planned chips, ECC itself needs consistent upgrade [7].

REFERENCES

[1] Rodrigo Roman, Pablo Najera and Javier Lopez, Securing the Internet of Things in IEEE Computer, Volume 44, Number-9,51-58, (2011) Jon Oltsik, "The Internet of Things: A CISO and Network

[2] Security Perspective", ESG White Paper was commissioned by Cisco Systems, (2014).'

[3] Majid Bakhtiari, Mohd Aizaini Maarof. "Serious Security Weakness in RSA Cryptosystem" IJCSI International Journal of Computer Science Issues, Vol. 9, Issue 1, No 3, 2012.

[4] Hemant Kumar and Archana Singh, Internet of Things: A Comprehensive Analysis and Security Implementation through Elliptic Curve Cryptography, International Journal of Current Engineering and Technology,Vol{6, No.-2, 498-502, (2016)

[5] H. Z. Hsu and R. C. T. Lee, DNA Based Encryption Methods, The 23rd workshop on Combination Mathematics and Computation Theory, 145- 150 European Bioinformatics Institute, URL: http://www.ebi.ac.uk.

[6] Ansari, B.; Hasan, M.A. "High-Performance Architecture of Elliptic Curve Scalar Multiplication," Computers, IEEE Transactions, vol.57, no.11, pp.1443, 1453, 2008. 502, (2016)

[7] Koblitz, N. Elliptic curve cryptosystems. Mathematics of computation. No. 48, pp. 203- 209,1987.

[8] Roshan Duraisamy; Salcic, Z.; Morales-Sandoval, M.; Feregrino-Uribe, C. "A Fast Elliptic Curve Based Key Agreement Protocol-on-Chip (PoC) for Securing Networked Embedded Systems," Embedded and Real-Time Computing Systems and Applications. Proceedings. 12th IEEE International Conference, pp.154, 2006.

[9] Securing the Internet of Things: A Proposed Framework,http://www.cisco.com/c/en/us/about/security-center/secure-iot-proposedframework.html

[10] Hankerson, D., L`opez Hernandez, J. and Menezes, A., Software implementation of elliptic curve cryptography over binary fields. Cryptographic Hardware and Embedded Systems, CHES'00. LNCS, 1965:1–24, 2000.

[11] Bafandehkar, Mohsen & Yasin, Sharifah & Mahmod, Ramlan & Zurina, Mohd Hanapi. (2013). Comparison of ECC and RSA Algorithm in Resource Constrained Devices. 2013 International Conference on IT Convergence and Security, ICITCS 2013. 1-3. 10.1109/ICITCS.2013.6717816.

[12] Mahto, D., & Yadav, D. K. (2017). RSA and ECC: a comparative analysis. *International journal of applied engineering research*, *12*(19), 9053-9061.

[13]] Yong Wang; Streff, K.; Raman, S., "Smartphone Security Challenges," Computer , vol.45, no.12, pp.52,58, Dec. 2012.

[14] Barman, P., & Saha, B. (2019). DNA encoded elliptic curve cryptography system for IoT security. *International Journal of Computational Intelligence & IoT*, *2*(2).

[15] Stallings, W. (2011). Cryptography and Network Security Principles and Practice Fifth Edition

[16] Koblitz, N A - Course In Number Theory And Cryptography (Springer,1994 2Ed)

[17] P. K. Sahoo, Dr. R. K. Chhotray, Dr. Gunamani Jena, Dr. S. Pattnaik, 2013, An Implementation Of Elliptic Curve Cryptography, INTERNATIONAL JOURNAL OF ENGINEERING RESEARCH & TECHNOLOGY (IJERT) Volume 02, Issue 01 (January 2013),

Authorized licensed use limited to: DELHI TECHNICAL UNIV. Downloaded on March 03,2021 at 06:08:36 UTC from IEEE Xplore. Restrictions apply.

Journal of ELECTRONIC MATERIALS
https://doi.org/10.1007/s11664-021-08793-z
© 2021 The Minerals, Metals & Materials Society

Comparison of Ferroelectric Photovoltaic Performance in BFO/BTO Multilayer Thin Film Structure Fabricated Using CSD & PLD Techniques

SAVITA SHARMA,[1,5] ANJALI SHARMA,[2] VINAY GUPTA,[1] NITIN K. PURI,[3] and MONIKA TOMAR [4,6]

1.—Department of Physics and Astrophysics, University of Delhi, Delhi, India. 2.—Physics Department, Atma Ram Sanatan Dharma College, University of Delhi, Delhi, India. 3.—Department of Applied Physics, Delhi Technological University, Delhi, India. 4.—Physics Department, Miranda House, University of Delhi, Delhi, India. 5.—Physics Department, Kalindi College, University of Delhi, Delhi, India. 6.—e-mail: monikatomar@gmail.com

Multilayer thin film structures of BFO/BTO possessing a distinct count of layers were prepared by chemical solution deposition and pulsed laser deposition techniques. These two different deposition techniques have been explored to investigate the effect of deposition technique on ferroelectric-photovoltaic properties of the BFO/BTO system in detail. Multilayers prepared using both the techniques exhibit pure perovskite structure showing the tetragonal and rhombohedral phases of BTO/BFO respectively obtained using XRD analysis. The multilayer thin film of BTO/BFO structures possessed enhanced ferroelectric and ferromagnetic properties, which is found to be increasing as the number of layers increases. The maximum values of P_s = 99.80 μC/cm^2 and M_s = 94.70 emu/cm^3 were obtained for the six-layer system prepared using the PLD technique. The six-layer PLD-grown PV cell upon irradiation with 405-nm wavelength light with 160 mW/cm^2 intensity, showed a large increase in photocurrent from 4.5 $\times$ 10^{-7}A to 3.84 $\times$ 10^{-4}A as compared to the PV cell grown using CSD. The obtained magnitudes of short-circuit photocurrent density (J_{sc}) and open circuit voltage (V_{oc}) were 0.384 mA/cm^2 and $-$ 0.40 individually with 0.098% light-to-electricity conversion efficiency for a six-layer PLD-grown PV cell.

Key words: Ferroelectric, ferromagnetic, photovoltaic, multilayer, thin film

INTRODUCTION

Researchers worldwide are working very hard to find alternate options for the generation of sustainable energy to meet the expanding requirements for abundant energy and clean fuel resources.[1–5] For the last few decades, efforts have been continuously made to harness solar energy using silicon-based photovoltaic (PV) technology which is a substitute to the diminishing energy sources. Typically, the PV effect involves two processes, creation of electron-hole pairs as the electrical charge carriers, and formation of electric current due to the motion of separated electrons and holes. The internal electric field that splits the charge carrier prevails in really limited space charge region across p-n junction in the case of junction-based photovoltaic effect. The radiation-provoked charge bearers are swept away from the depletion width exclusive of internal field in the material extent.[6] Therefore, there is a limited charge transportation in the junction-based photovoltaics due to this process of diffusion. For Si, the junction barrier height is ordinarily less than 1 V which cannot be run over by the open circuit

(Received April 24, 2020; accepted January 28, 2021)

Published online: 02 March 2021

photovoltage (V_{oc}).[6–8]. Moreover, a p–n junction is not a prerequisite for the photovoltaic effect. The photovoltaic effect can emerge from a diversity of other processes such as a built in potential[7] or spin polarization.[8] Another mechanism called the bulk photovoltaic effect (BPVE) came into the picture, in non-centro-symmetric materials (like ferroelectrics), which was in contrast to the traditional photovoltaic effect in semiconductors involving the junction effect[9]. Large photo-voltage, with photocurrent proportionate to the ferroelectric–polarization intensity and charge barrier segregation is an exclusive feature of this alluring bulk ferroelectric photovoltaic effect (BFPVE) phenomenon.[9] In BFPVE, the remnant polarization and the polarization-driven internal electric field prevails in the entire extent of the ferroelectric instead of the narrow interfacial depletion layer. Here, the charge transportation is not bounded by diffusion, and V_{oc} is not barred by the energy band gap[10,11]. Therefore, the photo-voltage obtained in this case is substantially greater than the E_g (band gap).[11] The ferroelectric photovoltaic effect (FE-PV) was primarily inspected in different ferroelectric materials including $BaTiO_3$,[12,13] $PbTiO_3$,[14] $Pb(Zr,Ti)O_3$,[15] and PLZT[16]. A brief summary of the photovoltaic application of ferroelectric material is presented in Table I.

Oxide materials are cheap, abundant, stable, highly light absorbing and their characteristics can be methodically integrated via element replacements, making them favorable for thin film ferroelectric photovoltaics.[9,17] High motivation was achieved because of the exceptionally high open circuit photo-voltage (in some cases, $V_{oc} > 10^2$ V), which is obtained when crystal was subjected to illumination.[18–22]

However, the light-to-electricity conversion efficiency (power conversion efficiency) of the bulk PV effect in ferroelectric thin film-based solar cells is reported to be significantly lower ($< 10^{-4}$) than that of silicon-based solar cells available in the market.[2,10] Moreover, the large energy band gap of ferroelectric materials allows strong absorption of light in the UV region only. Recently, a different mechanism for the ferroelectric photovoltaic phenomenon is proposed for BFO, where the observed high photovoltaic voltage is related to the domain wall mechanism in the ferroelectric material instead of the bulk which contributes substantial vision to the photovoltaic effect in BFO.[23–33] Yang et al. (2010) was able to achieve above band-gap photo-voltages.[31]

The output of the ferroelectric-based solar cell can be adjusted by different other means including magnetic, electrical and mechanical functionality.

Table I. Brief summary on photovoltaic study carried out on ferroelectric samples

S. No.	Sample type	Deposition technique	Light source	Important results	References
1.	BFO/SRO/(111) STO, (110) DSO	PLD	λ = 550 nm with (100 mW/cm^2)	J_{SC} = 13.4 μA/cm^2	Basu et al.[17]
2.	BFO/SRO/(001) STO	MOCVD	White light (285 mW/cm^2)	V_{OC} = 0.9 V J_{SC} = 1.5 mA/cm^2 η = 10%	Yang et al.[2]
3.	BFO/SRO/(001) STO	RF magnetron sputtering	Incident light (λ = 435 nm) with (750 mW/cm^2)	V_{OC} = 0.3 V $\eta = 7 \times 10^{-4}$%	Ji et al.[9]
4.	BFO/SRO/(111), (100) STO	RF magnetron sputtering	λ = 435 nm with (20 mW/cm^2)	Five order large bulk photovoltaic tensor coefficient β_{22}	Ji et al.[18]
5.	BFO/(001) Nb-STO	Laser molecular-beam epitaxy	He-Cd laser (λ = 325 nm) and pulsed Nd:YAG laser (λ = 355 nm)	V_{OC} = 136 mV	Wang et al.[19]
6.	ITO/BFO ceramic/ Au	Solid state reaction	Diode lasers (λ = 373, 532 nm)	J_{SC} = 1.2 μA/cm^2	Hung et al.[20]
7.	BFO/FTO	Modified CSD	Solar simulator (100 mW/cm^2)	$J_{sc} = 0.13 \times 10^{-3}$ A/cm^2 Voc = 0.65 V $\eta = 5.34 \times 10^{-3}$%	Dong et al.[21]
8.	BFO/Pt/Ti/SiO_2/ Si(100)	Sputtering	λ = 405 nm laser	J_{SC} = 11.7 μA/cm^2	Chang et al.[22]
9.	In_2O_3-SnO_2/ $BiFe_{0.6}Sc_{0.4}O_3$/ $LaNiO_3$ (ITO/ BFSO/LNO)	RF magnetron sputtering		BFSO film in a negatively poled state, efficiency is improved fivefold with an enhanced switchable V_{oc} up to 0.6 V	Fan et al.[23]

The foundation of strain management can be engaged for the engineering of materials [multilayers and superlattices (SLs)] with improved magnetoelectric (ME) properties. Towards this aspect, numerous multilayer structures encompassing alternating ferromagnetic and ferroelectric layers have recently been studied, including $Pb(Zr,Ti)O_3/CoFe_2O_4$,[32,33] $(Pr_{0.88}Ca_{0.15}MnO_3)/(Ba_{0.6}Sr_{0.4}TiO_3)$,[34] $CoFe_2O_4/BaTiO_3$,[35] $BiFeO_3/BaTiO_3$,[36] $BiFeO_3$ and $BiMnO_3$[37] and were found useful in observing the enhanced ME properties. Upon investigation of $BiFeO_3/BaTiO_3$ SLs, it was concluded that structures with less modulation periods exhibited higher magnetic polarization and ME effect owing to increment in respective interfaces.[36–39]

Usage of appropriate ferroelectric materials with limited band gap in the visible region are encouraging towards the potential application in innovative solar energy devices. The lower optical band gap (2.2–2.8 eV) of multiferroic $BiFeO_3$ (BFO) has attracted recent interest of the research community because of its co-existing ferroelectricity, ferromagnetism and ferroelasticity. The interaction between these ferroic orderings may be adopted to endow next-generation photovoltaic cells with an appended range of capabilities. The physical mechanism of the photovoltaic effect in the multiferroic BFO system is not completely understood yet. It is clearly evident from Table I that the ferroelectric photovoltaic phenomenon was detected in BFO in various forms including single crystal,[40] thin films[23] and ceramics.[24,41–44] It is evident that the thin films are highly useful over single crystal or ceramics towards the device applications, because the poling voltage necessary in thin films is significantly low. However, the main limitation while using BFO thin film towards the ferroelectric photovoltaics is high leakage current deteriorating its ferroic and thus, PV properties. Along with this, BTO is another attractive ferroelectric material useful towards energy and charge storage, memories etc. owing to its extra-ordinary dielectric, piezoelectric and ferroelectric characteristics.[45] Nonetheless, BTO has a wide band gap ($\sim$ 3.3 eV) and, therefore, its use in the visible region photovoltaics is not possible. Researchers are making continuous attempts to decrease the energy band gap of BTO preserving its valuable ferroelectric characteristics towards the photovoltaic application in the visible region[46].

Reportedly, multilayer thin film-based structures occupy remarkable ferroic properties in comparison to respective thin film materials such as large ferroelectric and magnetic polarization, large dielectric constant with comparatively low losses.[47] Also, various other researchers have made efforts to modify the structure of ferroelectric materials or utilize different patterns of photovoltaic cells to obtain the improved ferroelectric–photovoltaic response but they have not achieved much success.[41–43] Hence, by depositing BFO and BTO multilayer structures, enhanced ferroelectric properties in BFO along with a lower band gap of BTO can be achieved. There are several reports along with of BFO and BTO, where band-gap adjustments have been displayed by producing multilayered structures.[48,49] However, efforts have not been made to study the ferroelectric-based photovoltaic output of BFO/BTO thin film-based multilayer structures. Therefore, in this work, BFO/BTO thin film-based multilayer structures were deposited by chemical solution deposition (CSD) and its multiferroic characteristics have been inspected with focus on the ferroelectric photovoltaic applications.

The PV cell with six consecutive layers of BFO and BTO exhibited the improved PV response characteristics (V_{oc} = 1.806 V and J_{sc} = 17.76 μA/cm^2), in comparison to the other prepared multilayer PV cells. In order to further enhance the PV characteristics, it was important to improve the quality of BTO and BFO thin films. It has been reported that the multicomponent oxide thin films with superior quality can be easily fabricated using physical deposition techniques such as pulsed laser deposition (PLD). PLD is superior in stoichiometric composition of multicomponent oxide thin films with convoluted components, especially BFO which has high volatility of bismuth. Since composition is a key factor in determining the crystal structure and defect profile in the deposited films, PLD has attractive advantages which can be used to control the desirable quality and structure of BTO and BFO thin films by adjusting the substrate temperature, laser fluence, deposition rate and time.[50] PLD also extends flexibility towards depositing different multilayer heterostructures of oxide materials with even high melting point. Therefore, in the second part of the present work, the BFO/BTO thin film-based multilayer structures have been prepared by PLD on different substrates and their structural, electrical, ferroelectric and ferromagnetic characteristics were studied. Thus, the BFO/BTO structure fabricated using two different deposition techniques has been studied for the ferroelectric–photovoltaic application and discussed in detail.

In conclusion, in the present work, BFO/BTO thin film-based multilayer structures have been deposited using CSD and PLD and its multiferroic characteristics have been investigated with focus on the ferroelectric–photovoltaic applications.

EXPERIMENTAL PARTICULARS

Multilayer structures containing respective BFO and BTO layers were fabricated utilizing both PLD and CSD techniques. The number of constituent layers (BFO and BTO) was varied from two to seven while keeping the entire thickness of the structure at 350 nm.

Deposition of Multilayer BFO/BTO Structures by the PLD Technique

The ceramic targets of $BiFeO_3$ and $BaTiO_3$ of 1-inch diameter were made for growing respective thin films in the multilayer system. Conventional co-precipitation was employed to prepare the $BiFeO_3$ ceramic target with 20% surplus bismuth and stoichiometric $BaTiO_3$ target.[51] BFO and BTO thin films were fabricated by Nd:YAG pulsed laser with fourth harmonic (λ = 266 nm) using PLD. The PLD chamber is thoroughly cleaned and evacuated to a base pressure of about 1.33×10^{-5} kPa to remove any unwanted impurities that might contaminate the deposited thin films. The critical processing parameters for the deposition of thin film using PLD include gas pressure, substrate temperature, laser energy density, target to substrate distance and the repetition rate of the laser pulse. The deposition parameters used in the present work to deposit BFO and BTO layers are summarized elsewhere.[51,52]

Before multilayer structure fabrication, a platinum (Pt) metal thin layer of 70 nm thickness was deposited over the passivated Si (i.e. SiO_2/Si) substrate by E-beam evaporation; a buffer layer of Ti (20 nm) was deposited in situ over SiO_2/Si prior to Pt deposition to improve the adhesion of Pt on SiO_2/Si substrate.

Since film crystallinity is greatly affected by the kinetics of atomic arrangements on the substrate surface during film deposition, substrate temperature was kept fixed at 750°C. Multilayer structures deposited on platinum-coated passivated silicon (Pt/Ti/SiO_2/Si) substrate were used for electrical, ferroelectric and photovoltaic measurements in MFM configuration with Au circular dots (200 μm dia) as the top electrodes. The Au top electrode was deposited using thermal evaporation.

Multilayer structures deposited under similar growth conditions on fused quartz substrate were used for XRD and surface morphology studies while the magnetic properties were studied using the Si substrate.

Deposition of Multilayer BFO/BTO Structures by the CSD Technique

The multilayer structure of BFO and BTO were grown on different substrates including Pt/Si, fused quartz and Si. Barium acetate and titanium *n*-butoxide were dissolved in 2-methoxyethanol and acetic acid with 1 ml of acetylacetone to prepare the BTO precursor solution. Bismuth nitrate and iron nitrate were dissolved in 2-methoxyethanol and 1 ml acetic acid to prepare the BFO precursor solution. The prepared solutions were blended well to obtain the final respective homogenous solutions. Solution spin casting was done to fabricate the BFO/BTO thin film multilayer system containing interspersed layers of BFO and BTO assemblage onto Pt/Ti/SiO_2/Si substrate. The BTO thin film was fabricated on Pt-coated Si substrate as the starting layer with BFO thin film as next layer respectively to get the final BFO/BTO multilayer system.

The number of layers (consecutively BTO and BFO) were changed from two, four and six while maintaining BTO as the first layer [BFO/BTO/Pt/Ti/SiO_2/Si (two-layer system), BFO/BTO/BFO/BTO/Pt/Ti/SiO_2/Si (four-layer system), and so on. The final prepared samples were annealed at 700°C. Thickness of respective BFO and BTO layers in the multilayer system were kept equal with the total thickness of the system at 350 nm. Thus, BFO/BTO bilayer structure had 175 nm thin BFO as well as BTO thin films, 87 nm for a four-layer (BFO/BTO/BFO/BTO) structure, respectively, and so on. The effect of number of constituent layers (BFO and BTO) in the multilayer structures on structural, optical, electrical, ferroic and photovoltaic properties had been studied.

RESULTS AND DISCUSSION

Structural Analysis: X-ray Diffraction

Figure 1 shows the XRD (θ–2θ) diffraction patterns of the prepared six-layer BFO/BTO multilayer system using both CSD and PLD techniques fabricated on Pt/Ti/SiO_2/Si substrates. It is inferred from XRD graphs that multilayer structures prepared using both techniques are polycrystalline with pure perovskite structure of BTO and BFO confirming the formation of explicit phase with an absence of

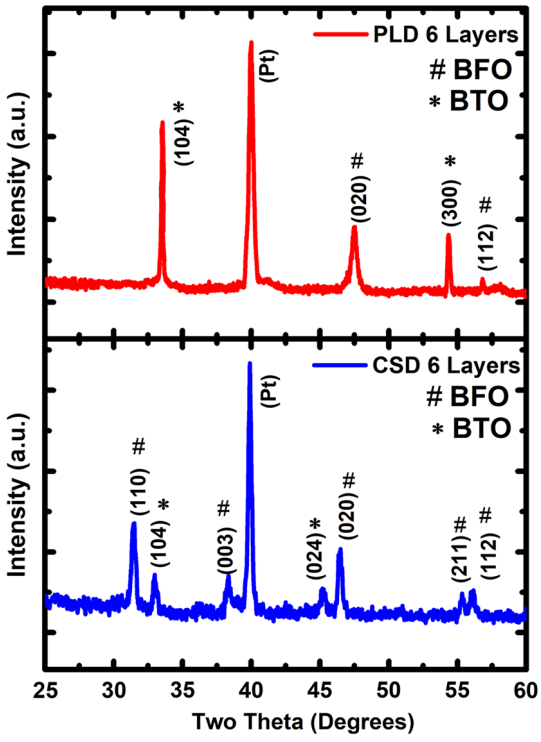

Fig. 1. XRD pattern of BFO/BTO multilayer systems with variation in constituent layers of BFO and BTO.

impurity (Fig. 1). The obtained XRD pattern conforms to respective tetragonal and rhombohedral structures of BTO and BFO. Le-Bail fitting was used to calculate the lattice parameters of BFO and BTO in the multilayer thin film structure. Table II summarizes the lattice parameters (a, c), c/a distortion ratio including induced strain along 'c' axis calculated from XRD data in BTO and BFO thin films, respectively, in the multilayer system. For comparison, data reported for bulk BTO and BFO has also been inserted in Table II. The variation in the lattice parameters, stress and c/a distortion (Table II) for multilayer structure prepared by PLD are similar to those observed earlier for the BFO/BTO multilayer structure prepared by CSD techniques and is attributed to the variation in the unit cell dimension of the constituent layers of BTO and BFO.[51,52] The lattice parameters values, a and c were approximated as 4.372 Å and 4.078 Å for BTO and 5.424 Å and 13.315 Å for BFO, respectively, for the six-layer BFO/BTO system prepared using CSD (Table II). However, the values of lattice specifications a and c were found to be 4.252 Å and 4.079 Å for BTO and 5.528 Å and 13.603Å for BFO, respectively, for the six-layer BFO/BTO system for the PLD grown films. The obtained parameters are marginally inferior than the analogous bulk values for BFO and slightly higher in the case of BTO [JCPDS card No. 01-072-0138 and 01-072-2035],[51] indicating the presence of stress in the BFO/BTO multilayered structures. It can also be observed from Table III that the stress modulus in BTO and BFO thin films grown using PLD is very low as compared to CSD grown films, indicating the growth of crack free and uniform films using PLD. Moreover, the value of c/a distortion ratio is higher in PLD grown films resulting in better ferroelectric properties which is needed for higher photovoltaic response.

Optical Properties: UV–Visible Transmittance

The inset of Fig. 2 shows the optical transmittance graph of the six-layer BFO/BTO multilayer structures fabricated using CSD and PLD. Both multilayer structures are deposited over fused quartz substrate for the optical study and are found to be transparent (> 60%) over a wide range of wavelengths from 600 nm to 1100 nm (Fig. 2). A explicit and sharp absorption edge is observed at about 600 nm for BFO/BTO multilayer structures prepared using both techniques. The absorption edge in the PLD prepared multilayer structure is seen to be shifting towards lower wavelength as compared to that prepared using CSD. The obtained results clearly indicate that the prepared multilayer structures are suitable for the photovoltaic applications over the wavelength range 350–600 nm. Figure 2 also depicts Tauc plot of the fabricated six-layer BFO/BTO multilayer structures to estimate the band gap. It can be observed from Fig. 2 that the band gap of the PLD-grown BFO/BTO multilayer system is obtained as 2.67 eV which is lower than the band gap of the CSD-grown multilayer structure, i.e. 2.88 eV, resulting in higher photovoltaic response of PLD-grown six-layer BFO/BTO multilayer structure.

Ferroelectric Property: P-E Hysteresis Loop

Figure 3 shows the P–E hysteresis loops for the BFO/BTO multilayer structures prepared using CSD and PLD techniques, measured at 1 kHz frequency and room temperature under metal-ferroelectric-metal (MFM) capacitor configuration. It is seen from Fig. 3 that the fabricated multilayer systems exhibit explicit and saturated PE hysteresis curves. The obtained result indicates that all prepared multilayer structures possess good ferroelectric property. Figure 3 shows ferroelectric hysteresis loops for the CSD-prepared BFO/BTO multilayer sample and the PLD-prepared BFO/BTO multilayer sample, exhibiting a transition from square loop to classic hysteresis loop. Classic hysteresis loop exhibited by the PLD-grown sample manifest a substantial change in polarization after the applied electric field is around the value of coercive field, depicting that maximum domains are swapped with the applied field with an amount equal to the coercive field. However, the hysteresis loop around E_c is not completely at 90 degrees with the x-axis, implying that swapping of domain walls

Table II. Summarized Lattice parameters of the BTO and BFO layers in BFO/BTO multilayer systems fabricated by CSD and PLD techniques.

	BTO				BFO			
	Lattice parameter		Stress modulus (%)	c/a distortion ratio	Lattice parameter		Stress modulus (%)	c/a distortion ratio
	a (Å)	c (Å)			a (Å)	c (Å)		
Six-layer CSD	4.372	4.078	1.115	0.9327	5.424	13.315	3.980	2.4548
Six-layer PLD	4.252	4.079	1.140	0.9586	5.528	13.603	1.903	2.4607
Bulk	3.999	4.033	–	1.0085	5.876	13.867	–	2.3599

Table III. Comparison of photovoltaic properties of BFO/BTO multilayer structure prepared by PLD and CSD techniques

Parameters	Six-layer BFO/BTO by PLD	Six-layer BFO/BTO by CSD
Saturation polarization (P_s)	99.80 μC/cm^2	95.85 μC/cm^2
Remnant polarization (P_r)	72.14 μC/cm^2	54.60 μC/cm^2
Saturation magnetization (M_s)	94.70 emu/cm^3	90.10 emu/cm^3
Remnant magnetization (M_r)	35.32 emu/cm^3	20.21 emu/cm^3
Open circuit voltage (V_{oc})	0.40 V	1.80 V
Short circuit current density (J_{sc})	132 μA/cm^2	17.73 μA/cm^2
On to Off ratio (I_{on}/I_{off})	8.53 $\times$ 10^3	2.95 $\times$ 10^3
Efficiency (η) (%)	0.098	0.067

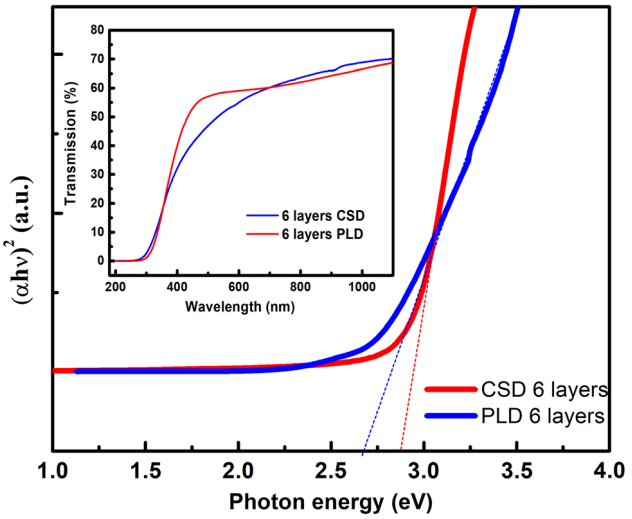

Fig. 2. UV–Visible Tauc plots of the BFO/BTO multilayer system fabricated over quartz substrates using CSD and PLD. Inset shows the transmission graphs of the BFO/BTO multilayer system.

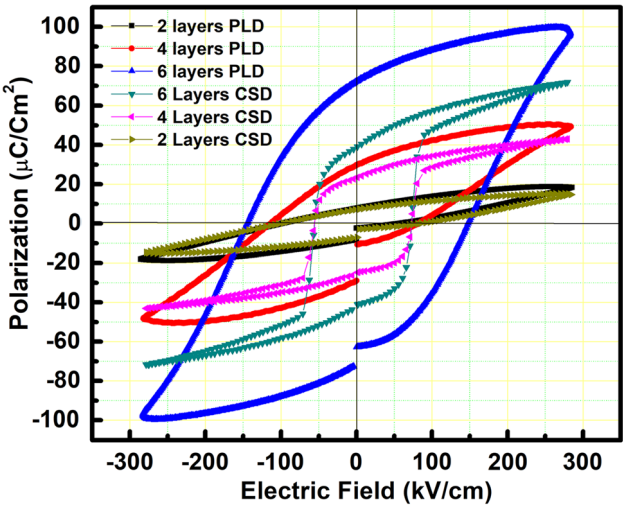

Fig. 3. Ferroelectric polarization versus applied electric field (P–E) curves obtained in the BFO/BTO multilayered structures with varying number of constituent layers.

is still present over the coercive field. This experience is associated with the clamping of domain walls, that may be induced electrically, mechanically, or chemically, whereas the CSD sample can be considered with larger grain without grain boundary. Thus, this clamping phenomenon due to the surrounding grains is absent in CSD samples[44].

The value of remnant polarization was seen to increase with an increase in the number of layers (Fig. 3) and exhibited a maximum value for both the CSD- and PLD-grown six-layer BFO/BTO structure. The observed improvement in remnant polarization of the BFO/BTO multilayer structure with advancing constituent layers may be attributed to several factors including the low leakage current, interface coupling between the constituent layers, the (110) preferred orientation of BFO crystallites and induced interfacial strain.[51–53] The observed magnitudes of remnant polarization ($2P_r$), saturation polarization (P_s) and coercive field ($2E_c$) for the fabricated multilayer systems are compiled in Table III and it can be inferred that the PLD-grown BFO/BTO multilayer thin film structures yield higher values of all ferroelectric parameters. This may result in higher photovoltaic response in PLD-grown BFO/BTO multilayer systems. The value of $2P_r$ of PLD-grown BFO/BTO multilayer structures increases from 19.33 μC/cm^2 to 108.12 μC/cm^2 (Table III) with an increase in respective layers from two (with each BFO and BTO layer of about 175 nm thickness) to six (with each layer of about 58 nm thickness), respectively, and the coercive field is also found to be increasing from 126.80 kV/cm to 195.22 kV/cm with number of stacking layers up to six layers. Gradual increase in the polarization with stacking layers may be attributed to the relative increase in interface coupling between layers (BTO and BFO). This is due to an increase in (110) preferred orientation of BFO crystallites and induced interfacial strain resulting into significant distortion in the ABO_3 perovskite structure of both BTO and BFO layers. The observed magnitudes of saturation polarization 23.77 μC/cm^2 to 95.85 μC/cm^2 for the two- and six-layered BFO/BTO systems, respectively, are found to be superior in comparison to previous reports for respective BTO and BFO thin films,[54] indicating the advantage of multilayer BFO/BTO structure over bare constituent layers.

Magnetic Study

Figure 4 shows the magnetization versus magnetic field (M–H) hysteresis loops obtained at room temperature of the fabricated BFO/BTO thin film multilayer systems prepared using both PLD and CSD. Well-saturated M-H hysteresis graphs are obtained for all the BFO/BTO multilayer systems of total thickness 350 nm (Fig. 4). The saturation magnetization (M_s) for the BFO/BTO multilayer system is observed to gradually increase with an increase in the constituent layers of BFO and BTO while maintaining a constant total thickness at 350 nm (Fig. 4) for BFO/BTO multilayer structures prepared using both PLD and CSD. The values of saturation magnetization (M_s) obtained for the prepared multilayer BFO/BTO systems with a distinct number of layers are presented in Table III for comparison. The value of M_s obtained for the BFO/BTO multilayer system is higher in contrast to the corresponding values published for bare BFO thin films (~ 13 emu/cm^3) grown by PLD. The variation in the value of M_s obtained for the multilayer system as a function of the number of stacking layers is shown in Fig. 4. It can be inferred that the PLD-grown BFO/BTO multilayer structures produce higher values of all ferromagnetic parameters. This may be attributed to the lower stress obtained in PLD-grown BFO/BTO thin film multilayer structures. It may be seen that the M_s value gradually increases from 25.65 to 90.10 emu/cm^3 with increasing layers from two to six in the BFO/BTO multilayer system grown using PLD. The maximum value of M_s = 90.10 emu/cm^3 is obtained for the six-layer structure (Table III). This may be attributed to the fact that the thickness of constituent layers (BFO and BTO) gradually decreases from 175 nm to 58 nm for two- to six-layer structures. The thickness of constituent layers (~58 nm) for BFO/BTO multilayer structures with six layers

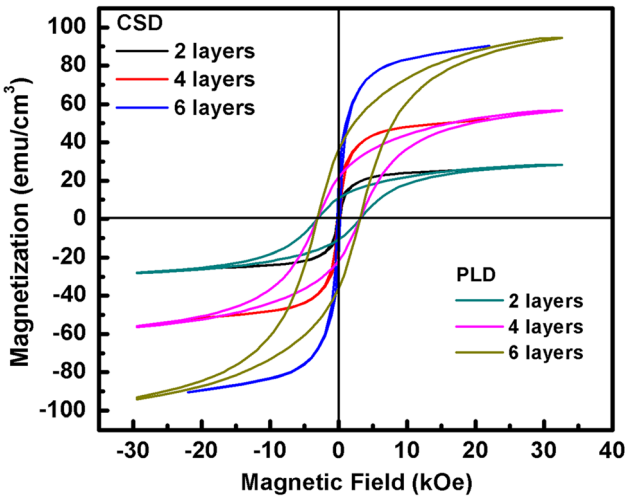

Fig. 4. Magnetization versus applied magnetic field (M–H) curves obtained for the BFO/BTO multilayered structures with varying number of constituent layers.

becomes comparable to the characteristic cycloid spin spiral modulation periodicity of 62 nm reported for BFO[53], and results in a higher value of M_s (Table III) in the present work. Such observation is found to be consistent with the other reports available in the literature[54–62]. As given in literature, coercive field (M_C) values depends on practical polarization switching affected by nucleation and growth of domains[54]. In an obliquely deposited ferromagnetic film, the coercive field increases sharply as the deposition angle becomes more and more tilted resulting in square hysteresis loop. Thus, PLD has an advantage over CSD to grow highly aligned thin films. Nevertheless, the magnetic characteristics of the BFO/BTO multilayers fabricated by PLD in the current article are superior in contrast to previous reports for the BTO/BFO multilayer structure fabricated by PLD[58,59]. The observed enhancement in the ferroelectric polarization along with the improvement in magnetization for the six-layer BFO/BTO structure, suggests a strong interface coupling between the constituent layers (BFO and BTO) and induced interfacial strain in the stacking layers.

Ferroelectric-Photovoltaic Studies

Figure 5 illustrates the comparison of current density–voltage (J–V) properties acquired for the six-layer BFO/BTO multilayer system fabricated using CSD and PLD techniques in dark and radiance conditions (λ = 405 nm). The J–V graph in radiance conditions (Fig. 5) showed a conventional ferroelectric photovoltaic phenomenon. The open-circuit voltage (V_{oc}) and short-circuit current density (J_{sc}) were approximated as − 0.40 V and − 1.80 V, 17.73 μA/cm^2 and 0.384 mA/cm^2 , respectively, for PLD- and CSD-fabricated six-multilayer systems, respectively, as calculated using intercepts of the horizontal and the vertical axes (Fig. 5a and b). The values of various photovoltaic response parameters at zero bias for both multilayer systems are listed in Table III. It may also be noted from Table III that the magnitude of J_{sc} is much higher in the case of the PLD-grown BFO/BTO multilayer system as compared to that grown by CSD due to the superior ferroelectric properties in the PLD-grown BFO/BTO multilayer system.

From Fig. 5a it can be seen that the value of J_{sc} for PLD-grown BFO/BTO multilayer structure increases from 16 μA/cm^2 to 132 μA/cm^2 with increase in the number of layers from two to six. This enhancement in J_{sc} must be credited to high polarization intensity owing to improved interfusion strain in the six-layered BFO/BTO multilayer system fabricated using PLD. However, the obtained value of J_{sc} for the four-layered BFO/BTO multilayer system was low in comparison to the six-layered multilayer system because of its relatively lower polarization magnitude and higher leakage current density. Enhanced (~8.533 × 10^3) ON to

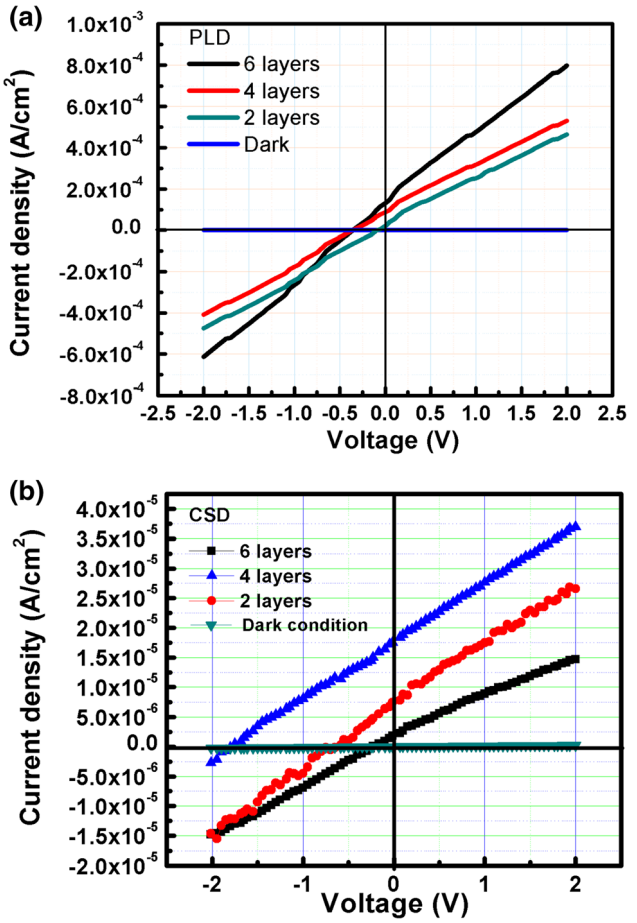

Fig. 5. (a) J–V plots obtained in fabricated multilayer BFO/BTO system deposited by PLD with two, four and six layers in dark and radiance conditions. (b) *J–V* plots obtained in the multilayer BFO/BTO system deposited by CSD with two, four and six layers in dark and radiance conditions.

OFF ratio was obtained for the PLD six-layer BFO/BTO multilayer system in comparison to the four-layer system. This was because of the origin and dispersion of additional light-caused charge barriers in radiance for the six-layer structure.

Figure 6 illustrates the transient response graphs of current density determined at zero applied voltage for two, four and six constituent layered BFO/BTO multilayer system fabricated using PLD and CSD in regular on and off radiance conditions (λ = 405 nm) at continuous 20-s intervals. From Fig. 6 it can be noted that the value of J_{sc} for the PLD-grown BFO/BTO multilayer system is higher than the J_{sc} for the CSD-grown BFO/BTO multilayer system. This observation is consistent with the enhanced ferroelectric polarization intensity owing to improved interfusion strain in the PLD fabricated BFO/BTO multilayer system as discussed in previous sections. When the radiance is switched off, the radiance generated current declines swiftly and achieves its initial value. Also, it is evident form the Fig. 6 that fabricated BFO/BTO multilayer system reciprocated immediately towards the incident

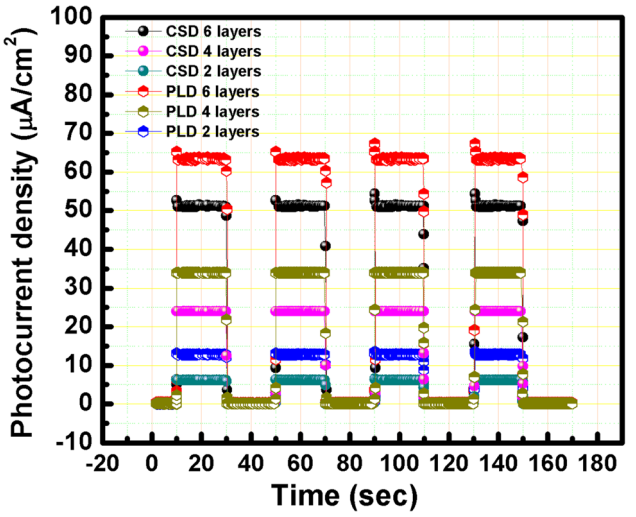

Fig. 6. Transient responses of short circuit current density of multilayer BFO/BTO structures having five and six layers at different radiance conditions.

radiance and no deterioration in response could be seen in regular ON and OFF radiance conditions. Thus, it can be concluded that the ferroelectric domains inside the multilayer system switches swiftly. The observed outcome distinctly point towards the substantial utilization of fabricated multilayer BFO/BTO system for energy conservation.

Comparison Between CSD-Grown and PLD-Grown BFO/BTO Multilayer PV Cells

Table III tabulates the comparison of the six-layer BFO/BTO multilayer structure prepared by PLD with that of the multilayer structure prepared by CSD. The six-layer BFO/BTO structure prepared by PLD was identified to be the best suited for ferroelectric–photovoltaic applications with high I_{on}/I_{off} ratio and enhanced multiferroic properties as compared to the corresponding (six-layer) multilayer structure prepared by CSD.

It is interesting to note that a slight decrease in V_{oc} from 1.8 to 1.52 V was observed for the PLD-derived PV cell, but a significant increase in J_{sc} from 18 to 384 μA/cm^2 signifies the importance of the PV cell prepared by PLD. This was attributed to the formation of a sharp juncture amidst BFO and BTO layers by PLD in comparison to that of CSD, resulting in generation of maximum induced interface polarization due to large interfacial coupling. Furthermore, an increase in efficiency from 0.067% to 0.098% has been obtained for the PLD-derived PV cell which is ascribed to the efficient origination and dispersion of charge barriers.

SUMMARY

In the current article, multilayer BFO/BTO structures with two, four and six alternating layers were fabricated by both CSD and PLD and the effect of

these two deposition techniques have been investigated towards the ferroelectric–photovoltaic properties. X-ray diffraction analysis confirms the production of perfect phase and polycrystalline structures of BTO and BFO thin films. Ferroelectric and ferromagnetic (multiferroic) characteristics of the multilayer BFO/BTO thin films improved with the advancement in respective BFO/BTO layers up to six layers. The leakage current density in the multilayer system exhibited a similar pattern holding minimal value 3.18 x10^{-7} A/cm^2 for the six layered structure. The six-layer thin film multilayer structures exhibited an outstanding growth in current density from 4.50×10^{-7} A/cm^2 to 3.84×10^{-4} A/cm^2 upon radiance condition. The PLD prepared six-layer BFO/BTO system showed large value of V_{oc} = 0.40 V, $J_{ON/OFF} = 8.53 \times 10^3$ and responsivity (R) = 2.40 mAW^{-1} owing to its enhanced ferroelectric properties associated with momentous juncture coupling among six respective interfaces of BFO and BTO. The relatively high efficiency (η = 0.098 %) estimated at 405 nm for the fabricated multilayer BFO/BTO PV system using the PLD technique features its achievable realistic utilization in energy harvesting and multifunctional systems.

ACKNOWLEDGEMENTS

The authors are thankful to the Department of Science & Technology (DST) for financial support and the Department of Physics and Astrophysics, University of Delhi, for providing the research facility to carry out this work.

FUNDING

This study was funded by the Department of Science & Technology (DST) (Grant Number EMR/2017/000194).

CONFLICT OF INTEREST

Author Monika Tomar, Principal Investigator of the project, has received research grants from the Department of Science & Technology (DST). Authors Vinay Gupta and Anjali Sharma are Co-Principal Investigators of the project.

REFERENCES

1. B.T. Marquis, and J.F. Vetelino, *Sens. Act. B*, 2001, **77**, p 100–110.
2. S.Y. Yang, L.W. Martin, S.J. Byrnes, T.E. Conry, S.R. Basu, D. Paran, L. Reichertz, J. Ihlefeld, C. Adamo, A. Melville, Y.-H. Chu, C.-H. Yang, J.L. Musfeldt, D.G. Schlom, J.W. Ager III., and R. Ramesh, *Appl. Phys. Lett.*, 2009, **95**, p 062909.
3. J. Zhang, X. Su, M. Shen, Z. Dai, L. Zhang, X. He, W. Cheng, M. Cao, and G. Zou, *Nat. Sci. Rep.*, 2013, **3**, p 2109.
4. B. Chen, M. Li, Y. Liu, Z. Zuo, F. Zhuge, Q.F. Zhan, and R.W. Li, *Nanotechnology*, 2011, **22**, p 195201.
5. W. Cai, C. Fu, J. Gao, Q. Guo, X. Deng, and C. Zhang, *Phys. B*, 2011, **406**, p 3583.
6. M. Qin, K. Yao, and Y.C. Liang, *Appl. Phys. Lett.*, 2008, **93**, p 122904.
7. A. Shah, P. Torres, R. Tscharner, N. Wyrsch, and H. Keppner, *Photo. Tech.*, 1999, **285**, p 692.
8. P. Peumans, S. Uchida, and S.R. Forrest, *Nature*, 2003, **425**, p 158.
9. B.W. Ji, K. Yao, and Y.C. Liang, *Adv. Mater.*, 2010, **22**, p 1763.
10. A.M. Glass, D. von der Linde, and T.J. Negran, *Appl. Phys. Lett.*, 1974, **25**, p 233.
11. S.Y. Yang, J. Seidel, S.J. Byrnes, P. Shafer, C.H. Yang, M.D. Rossell, P. Yu, Y.H. Chu, J.F. Scott, J.W. Ager III., L.W. Martin, and R. Ramesh, *Nat. Nanotech.*, 2010, **5**, p 143.
12. A.G. Chynoweth, *Phys. Rev.*, 1956, **102**, p 705.
13. P.S. Brody, and F. Crowne, *J. Elect. Mater.*, 1975, **4**, p 955–961.
14. V.M. Fridkin, *Photoferroelectrics* Springer, New York, 1979.
15. A. Kholkin, O. Boiarkine, and N. Setter, *Appl. Phys. Lett.*, 1998, **72**, p 130.
16. M. Qin, K. Yaoa, Y.C. Liang, and S. Shannigrahi, *J. Appl. Phys.*, 2007, **101**, p 014104.
17. S.R. Basu, L.W. Martin, Y.H. Chu, M. Gajek, R. Ramesh, R.C. Rai, X. Xu, and J.L. Musfeldt, *Appl. Phys. Letts.*, 2008, **92**, p 091905.
18. W. Ji, K. Yao, and Y.C. Liang, *Phys. Rev. B*, 2011, **84**, p 094115.
19. W. Mao, Q. Yao, Y. Fan, Y. Wang, X. Wang, Y. Pu, and X. Li, *J. Alloys Comp*, 2019, **784**, p 117–124.
20. Y. Zhou, R. Zhang, Y. Fan, Z. Wang, W. Mao, J. Zhang, Y. Min, J. Yang, Y. Pu, and X. Li, *Solid State Commun.*, 2018, **270**, p 12–16.
21. R. Zhang, Y. Zhou, Y. Zhu, Y. Li, L. Chu, Y. Min, J. Zhang, J. Yang, and X. Li, *Mod. Phys. Lett. B*, 2017, **31**(32), p 1750304.
22. W. Zhang, X. Zhu, L. Wang, X. Xu, Q. Yao, W. Mao, and X. Li, *J. Supercond. Nov. Magn.*, 2017, **30**, p 3001–3005.
23. Y. Wang, *J. Appl. Phys.*, 2011, **109**, p 124105.
24. C.M. Hung, C.-S. Tu, W.D. Yen, L.S. Jou, M.-D. Jiang, and V.H. Schmidt, *J. Appl. Phys.*, 2012, **111**, p 07D912.
25. W. Dong, Y. Guo, G. Bing, L. Hongyan, H. Li, and L. Hezhou, *Mater. Lett.*, 2012, **88**, p 140–142.
26. H.W. Chang, F.T. Yuan, Y.C. Yu, P.C. Chen, C.R. Wang, C.S. Tu, and S.U. Jen, *J. Alloys Comp.*, 2013, **574**, p 402–406.
27. F. Fan, C. Changle, L. Bingcheng, and J. Kexin, *J. Appl. Phys.*, 2011, **109**, p 073716.
28. M. Alexe, and D. Hesse, *Nat. Commun.*, 2011, **2**, p 256.
29. A. Kumar, R.C. Rai, N.J. Podraza, S. Denev, M. Ramirez, Y.H. Chu, L.W. Martin, J. Ihlefeld, T. Heeg, J. Schubert, D.G. Schlom, J. Orenstein, R. Ramesh, R.W. Collins, J.L. Musfeldt, and V. Gopalan, *Appl. Phys. Lett.*, 2008, **92**, p 121915.
30. J. Allibe, K.B. Robin, E. Jacquet, I.C. Infante, S. Fusil, C. Carretero, J.L. Reverchon, B. Marcilhac, D. Crete, J.C. Mage, A. Barthelemy, and M. Bibes, *Appl. Phys. Lett.*, 2010, **96**, p 182902.
31. S.Y. Yang, J. Seidel, S.J. Byrnes, P. Shafer, C.H. Yang, M.D. Rossell, P. Yu, Y.H. Chu, J.F. Scott, J.W. Ager III., L.W. Martin, and R. Ramesh, *Nat. Nanotech.*, 2010, **5**, p 143–147.
32. N. Ortega, A. Kumar, R.S. Katiyar, and C. Rinaldi, *J. Mater. Sci.*, 2009, **44**, p 5127–5142.
33. J.P. Zhou, H. He, Z. Shi, and C.W. Nan, *Appl. Phys. Lett.*, 2006, **88**, p 013111.
34. P. Murugavel, M.P. Singh, W. Prellier, B. Mercey, C. Simon, and B. Raveau, *J. Appl. Phys.*, 2005, **97**, p 103914.
35. H. Zheng, J. Wang, S.E. Lofland, Z. Ma, L. Mohaddes-Ardabili, T. Zhao, L. Salamanca-Riba, S.R. Shinde, S.B. Ogale, F. Bai, D. Viehland, Y. Jia, D.G. Schlom, M. Wuttig, A. Roytburd, and R. Ramesh, *Nano. Sci.*, 2004, **303**, p 661–663.
36. H. Toupet, V.V. Shvartsman, F. Lemarrec, P. Borisov, W. Kleemann, and M. Karkut, *Integ. Ferro.*, 2008, **100**, p 165–176.
37. A. Chen, H. Zhou, Z. Bi, Y. Zhu, Z. Luo, A. Bayraktaroglu, J. Phillips, E.-M. Choi, J.L. MacManus-Driscoll, S.J. Pennycook, J. Narayan, Q. Jia, X. Zhang, and H. Wang, *Adv. Mater.*, 2013, **25**, p 1028.

38. V. Yang, K.M. Kim, J.Y. Lee, J. Zhu, and H.Y. Lee, *Int. Ferro.*, 2010, **113**, p 26–30.
39. G. Catalan, and J.F. Scott, *Adv. Mater.*, 2009, **21**, p 2463–2485.
40. M. Alexe, and D. Hesse, *Nat. Commun.*, 2011, **256**, p 1.
41. R.K. Katiyar, P. Misra, S. Sahoo, G. Morell, and R.S. Katiyar, *J. Alloys Comp.*, 2014, **609**, p 168–172.
42. H. Liu, K. Zhao, N. Zhou, H. Lu, M. He, Y. Huang, K.J. Jin, Y. Zhou, G. Yang, S. Zhao, A. Wang, and W. Leng, *Appl. Phys. Lett.*, 2008, **93**, p 171911.
43. Z. Fan, K. Yao, and J. Wang, *Appl. Phys. Lett.*, 2014, **105**, p 162903.
44. R. Yu, D.S. Shin, K. Jang, Y. Guo, H.M. Noh, B.K. Moon, B.C. Choi, J.H. Jeong, and S.S. Yi, *J. Am. Ceram. Soc.*, 2014, **97**(1), p 1–27.
45. W. Jiang, W. Cai, Z. Lin, and C. Fu, *Mater. Res. Bull.*, 2013, **48**, p 3092–3097.
46. R. Nechache, C. Harnagea, S. Li, L. Cardenas, W. Huang, J. Chakrabartty, and F. Rosei, *Nat. Photon.*, 2015, **9**, p 61–67.
47. N.M. Murari, A. Kumar, R. Thomas, and R.S. Katiyar, *Appl. Phys. Let.*, 2008, **92**, p 132904.
48. H.K. Yadav, K. Sreenivas, and V. Gupta, *Appl. Phys. Let.*, 2010, **96**, p 223507.
49. M. Lorenz, V. Lazenka, P. Schwinkendorf, F. Bern, M. Ziese, H. Modarresi, A. Volodin, M.J.V. Bael, K. Temst, A. Vantomme, and M. Grundmann, *J. Phys. D: Appl. Phys.*, 2014, **47**, p 135303.
50. K. Jiang, J.J. Zhu, J.D. Wu, J. Sun, Z.G. Hu, and J.H. Chu, *ACS Appl. Mater. Interfaces*, 2011, **3**, p 4844–4852.
51. S. Sharma, M. Tomar, A. Kumar, N.K. Puri, and V. Gupta, *J. Phys. Chem. Solids*, 2016, **93**, p 63–67.
52. S. Sharma, M. Tomar, A. Kumar, N.K. Puri, and V. Gupta, *Phys. B*, 2014, **448**, p 125–127. https://doi.org/10.1016/j.physb.2014.03.089.
53. S. Gupta, M. Tomar, and V. Gupta, *J. Appl. Phys.*, 2014, **115**, p 014102.
54. G. Qeemat, H. Wei, L. Yan, S. Rui, L. Na, Y. Xu, L. Yang, G.Z. Zhao, X. ZongKai, Z.X. Qun, and C.Z. Hua, *Chin. Phys. B*, 2018, **27**(9), p 097504.
55. M. Kumar, A. Srinivas, and S.V. Suryanarayana, *J. Appl. Phys.*, 2000, **87**, p 855–862.
56. J. Wu, W. John, X. Dingquan, and Z. Jianguo, *Appl. Surf. Sci.*, 2011, **257**, p 7226–7230.
57. K. Jiang, J.J. Zhu, J.D. Wu, J. Sun, Z.G. Hu, and J.H. Chu, *ACS Appl. Mater. Interfaces*, 2011, **3**, p 4844–4852.
58. P. Yang, K.M. Kim, J.Y. Lee, J. Zhu, and H.Y. Lee, *Int. Ferro.*, 2009, **113**, p 26–30.
59. Y.X. Yang, G.L. Yuan, Z.B. Yan, Y.J. Wang, X.B. Lu, and J.M. Liu, *Adv. Mater.*, 2017, **29**, p 1700425.
60. Z.A. Xiao, J.H. Zhao, C. Lu, Z.Y. Zhou, H. Wang, L. Zhang, J.J. Wang, X.Y. Li, K.Y. Wang, and Q.L. Zhao, *Appl. Phys. Lett.*, 2018, **113**, p 223501.
61. C.H. Yang, Y.J. Han, J. Qian, P.P. Lv, X.J. Lin, S.F. Huang, and Z.X. Cheng, *ACS Appl. Mater. Inter.*, 2019, **11**, p 12647–12655.
62. C.F. Ding, W.T. Hsiao, and H.T. Young, C.F. Ding, W.T. Hsiao, and H.T. Young, *Ceram. Int.*, 2019, **45**(13), p 16387–16398.

Publisher's Note Springer Nature remains neutral with regard to jurisdictional claims in published maps and institutional affiliations.

2021 11th International Conference on Cloud Computing, Data Science & Engineering (Confluence) | 978-1-6654-1451-7/20/$31.00 ©2021 IEEE | DOI: 10.1109/Confluence51648.2021.9377185

Computational Analysis of Machine Learning Algorithms to Predict Heart Disease

1st Kunal Rao
University School of Management and Entrepreneurship
Delhi Technological University
Delhi, India
kunalrao_2k19bmba22@dtu.ac.in

2nd Pawan Raj Gopal
University School of Management and Entrepreneurship
Delhi Technological University
Delhi, India
pawanrajgopal_2k19bmba12@dtu.ac.in

3rd Kusum Lata
University School of Management and Entrepreneurship
Delhi Technological University
Delhi, India
kusumlata@dtu.ac.in

***Abstract*—: Heart disease is one of the most common problems and also a disease whose rate of increase has been higher in recent years. The complex task associated is exploitation of hidden patterns for effective and accurate prediction. There is plenty of data generated every year from various health institutes. This research focuses on development of supervised machine learning models for prediction of target heart disease. We have used publicly available heart disease datasets from University of California, Irvine (UCI) data repository for Cleveland, Switzerland, Hungarian and Long Beach. Various forms of preprocessing steps such as handling the missing values and null values, removal of duplicate entries is employed on these datasets in order to use it for developing effective models. The correlation between the features set and the target variable is studied. The prediction models are developed using effective machine learning techniques like Logistic Regression, Decision Trees, Naive Bayes, K-nearest neighbors, ensembles AdaBoost and XGBoost. The predictive performance of the developed models is compared with the help of stable accuracy measures like accuracy, precision, recall, F1-score, Cohen's kappa and Area Under the Curve score. K-nearest neighbors was the best model for the Cleveland dataset with 86.81% accuracy. AdaBoost algorithm gave us the highest accuracy of 98% for Switzerland dataset. Bernoulli Naive Bayes predicted the heart diseases for Hungarian dataset with 84.26% accuracy. XGBoost gave better accuracy of 82.20% for VA Long Beach dataset. The results of the study advocate the applicability of machine learning techniques to predict heart disease.**

Keywords—heart disease, data mining, machine learning, XG-Boost

I. INTRODUCTION

Heart diseases have always been a major problem and the rate of increase in people having cardiovascular problems has increased in recent years. Heart disease is one of the leading causes of death in many countries. According to the Centers for Disease Control and Prevention (CDC) in the United States, one in every four deaths occur due to cardiovascular problems. So, it is very important and useful to predict the Heart disease occurrence more accurately. Machine learning (ML) has played an important role in development of an efficient heart attack prediction model. Many Researchers have applied various algorithms and techniques to predict heart diseases. In this study, we have used ML techniques on four different datasets belonging to different locations and try to develop effective models that predict heart diseases with higher accuracy. We have also applied Boosting algorithms such as AdaBoost and XGBoost in order to compare the performance of traditional ML techniques with these Boosting approaches to predict heart diseases more effectively. XGBoost has been more in use in predictive modeling in recent years. XGBoost is simply the implementation of gradient boosted decision trees which are especially designed for speed and performance. In our Study XGBoost is one of the important algorithms that we have used. The four datasets from Cleveland Clinic Foundation, Hungarian Institute of Cardiology (Budapest), V.A. (Veterans Affairs) Medical Center (Long Beach, California), University Hospital (Zurich, Switzerland) were taken from UCI data repository for experimentation. After extensive study, data preprocessing steps are applied on the datasets, before developing the models with the ML techniques. In order to analyze the performance of the models, we have used various stable performance evaluation metrics. The rest of the paper is organized as follows; Section II describes the literature work done before in this area of study; Section III describes our research framework which explains various steps that we followed while conducting this study; Section IV introduces the experimental setup including modeling using ML techniques and evaluation metrics used in this research; Section V includes all the experiments we performed and their respective results, and finally Section VI presents conclusions and future work.

II. RELATED WORK

Machine learning has played an important role in development of efficient heart attack prediction models. Researchers have applied various ML techniques in this domain and they come up with various models for this problem.

Ananey-Obiri and Sarku [1] deployed ML techniques linear regression, decision tree (DT), Gaussian Naïve Bayes (GNB) to develop models for heart disease prediction. The models were developed using k-fold cross validation approach and receiver operator characteristic (ROC) curves were used for assessing the performance of the models. The UCI dataset of patients with heart diseases was used for analysis in this research. Accuracy for DT classifier model was 79.31%, GNB was 76% accurate and LR was 82.75% accurate.

Chaurasia et al. [2] proposed a model using data mining algorithms like Classification and Regression Trees and ID3 for generating classification models. The data used in this study was Cleveland Clinic Foundation available at UCI data repository. This dataset consists of 76 attributes with 303 rows. CART predicts the best with 83.49%, ID3 with around 73% accuracy. Further using Chi-squared, Info-Gain, and Gain Ratio the important variables were identified.

Marimuthu et al. [3] has applied DTs, Support Vector Machine, NB and KNN for heart disease prediction. They have utilized the past medical data of patients and took into consideration the factors such as Blood Pressure, Cholesterol etc. Various models were applied on the accounted dataset after proper pre-processing. They compared the performance of the models based on performance metric accuracy.

III. RESEARCH FRAMEWORK

The Framework for the entire study consists of following steps.

Authorized licensed use limited to: DELHI TECHNICAL UNIV. Downloaded on March 27,2021 at 05:40:50 UTC from IEEE Xplore. Restrictions apply.

A. Data preprocessing

In this step, we gathered the heart diseases datasets from the UCI data repository. Next we employed various forms of preprocessing on the data such as removing all the duplicate entries, dealt with the missing values from each dataset in order to remove data redundancy and get unbiased results. Finally we labelled our target variable by assigning it values like 0 or 1 where 0 signifies the absence of the disease and 1 specifies the presence of the disease.

B. Machine learning model deployment process

In this step, we developed models using different machine ML techniques.

C. Evaluation of the best Model

For selection of the best ML model compared the performance of all models using the classification model evaluation metrics.

IV. EXPERIMENTAL SETUP

This section describes the various elements of our experimental setup.

A. Dataset Description

The dataset used in this research study is retrieved from UCI data repository. Four different datasets of Cleveland, Switzerland, Hungarian and VA long beach are collected. The original dataset consisted of 76 attributes but a sub-string of 14 of them have been used in analysis after correlation analysis. The features are:
age of patient in years; patient's gender; patient's chest pain type; patient's resting blood pressure(in mm Hg); patient's serum cholesterol (in mg/dl); fasting blood sugar level is measured across the threshold value of 120 (in mg/dl); patient's resting electrocardiographic (ECG) value is checked to be normal or not; patient's heart rate; exercise induced angina for a patient; patient's depression level induced by exercise relative to rest; the slope of the peak exercise ST segment for the patient; patient's count of major vessels colored by fluoroscopy; patient's thalassemia disorder; target: diagnosis of heart disease where value '0' means less than 50% of diameter narrowing and value '1' means more than of 50% diameter narrowing .
The predictors being the first 13 attributes and the target is the y-feature vector in the heart diseases prediction. The Switzerland dataset contains 123 records. The Cleveland dataset contains 303 records. The Hungarian dataset contains 294 records. The VA long beach dataset contains 200 records**.**

B. Data Pre-Preprocessing

Cleveland: The Cleveland dataset consisted of 303 non-duplicate instances. The preliminary analysis included studying the missing values. It was noticed that all attributes contained non-null values. It was also seen that the attributes are not correlated with other attributes so we concluded that there is not much multicollinear in our dataset. We moved to further steps of pre-processing. As, the target attribute had 5 different values so the values with 0 label were regrouped as 0 only while the values with labels equal to more than 1 values were regrouped as 1 value label. Finally, we had more than 160 instances for 0 labeled class and less than 140 instances for 1 labeled class.

Switzerland: The Switzerland dataset consisted of 123 non-duplicate instances. The preliminary analysis included studying the missing values. It was noticed that attributes like fbs, ca, thal consisted of majority of null values and other attributes of chol consisted of the same value of 0 across all instances, so all these 4 attributes were dropped. It has been seen that the attributes are not correlated with other attributes so we concluded that there is not much multicollinear in our dataset. we moved to further steps of pre-processing. Next the Target attribute had 5 different values so the values with 0 label were regrouped as 0 only while the values with labels equal to more than 1 values were regrouped as 1 value label. Finally, we had 26 instances of 0 label and 97 of 1 label. To deal with this we did the oversampling using Synthetic Minority Oversampling Technique (SMOTE) [11] created synthetic instances for 0 labels and now had a total of 194 instances, equally (97) for both labels.

Hungarian: The Hungarian dataset consisted of 294 non-duplicate instances. The preliminary analysis included studying the missing values. It was noticed that all attributes contained non-null values. It was also seen that the attributes are not correlated with other attributes so we can conclude that there is not much multicollinear in our dataset. we can move to further steps of pre-processing. Next the Target attribute had 5 different values so the values with 0 label were regrouped as 0 only while the values with labels equal to more than 1 values were regrouped as 1 value label. Finally, we had 188 instances of 0 label and 106 of 1 label. Now our dataset is ready for the model building process.

VA long beach: The VA long beach dataset consisted of 200 non-duplicate instances. The preliminary analysis included studying the missing values. It was noticed that attributes like exang, slope, ca and thal consisted of the majority of null values so all these 4 attributes were dropped. It was seen that the attributes are not correlated with other attributes so we can conclude that there is not much multicollinear in our dataset. we can move to further steps of pre-processing. Next the Target attribute had 5 different values so the values with 0 label were regrouped as 0 only while the values with labels equal to more than 1 values were regrouped as 1 value label. Finally, we had 51 instances of 0 label and 149 of 1 label. To deal with this we did the oversampling using SMOTE learning and created synthetic instances for 0 labels and now had a total of 298 instances, equally (149) for both labels.

C. Model Building

After preprocessing all of the datasets the final datasets were splitted up into training - test dataset in the ratio of 70:30. The numerical attributes in the dataset consisted of age of patient in years, patient's gender, patient's chest pain type, patient's resting blood pressure, patient's resting electrocardiographic value, patient's heart rate, exercise induced angina for a patient, patient's depression level, the slope of the peak exercise. These were standardized using the StandardScaler function in the sklearn package on the scale from -3, 3, having mean of 0 and standard deviation of 1. ML techniques used in this study are: logistic regression (LR), K-nearest neighbor (KNN), Bernoilli Naive Bayes (BNB), Decision tree (DT), Gaussian Process Classifier (GPC), AdaBoost Classifier (ADA), Extreme Gradient Boost Classifier (XGB). KNN was introduced by Cover et al. [4] to classify the datasets. Quinlan [5] was the first

Authorized licensed use limited to: DELHI TECHNICAL UNIV. Downloaded on March 27,2021 at 05:40:50 UTC from IEEE Xplore. Restrictions apply.

to demonstrate the idea of building Decision Tree (DT) from the examples in a robust way. Chen and Guestrin [6] proposed XGB to fasten up the executing speed of the model training and it holds a significant advantage in performance as compared to other classification and regression algorithms. Freund and Schapire [7] proposed the ADA. Herbrich et al [8] have proposed a complete framework for sparse Gaussian Process methods that uses forward selection. Rish [9] has used Monte Carlo simulations to understand the data characteristics which affects the performance of Bernoulli Naive Bayes (BNB). Berkson [10] proposed the Logistic Ruling and also introduced the Logit function for the classification problem We employed all above techniques for prediction of heart disease in this study.

D. Evaluating the performance of models

The study employed following performance metrics for analyzing the performance of the developed models.

Confusion Matrix: A confusion matrix is a table/matrix that is often used to elaborate the performance of a classification model based on a set of test data for which all the true values are known. This confusion matrix itself is relatively simple to understand.

Table I: Confusion Matrix

	Actual Positive (1)	Actual Negative (0)
Predicted Positive (1)	TP	FP
Predicted Negative (0)	FN	TN

In our study we have calculated all the metrics based on this confusion matrix. The various entries of the confusion matrix are TP (true positive), FP (false positive), TN (true negative), and FN (false negative). TP→ Person having a heart disease and being tested Positive, FP→ Person having no heart disease and being tested Positive, FN→ Person having no heart disease and being tested Negative, FP→ Person having a heart disease and being tested Negative. We derived the following metrics from the confusion matrix.

(i) Accuracy: Accuracy is one of the metrics for evaluating classification models. It signifies the percentage of number of correctly classified data instances upon in a dataset. If the dataset is imbalanced, accuracy may not be a good measure to evaluate the predictive capability of the models. Informally, accuracy represents the fraction of predictions that were rightly classified in our model.

(ii) F1-Score: The F-score or F1-score, is an important measure to evaluate the classification accuracy. The F-score enables to select a prediction model that is having a balance of the precision and recall values as F1-score is based on the harmonic mean of the recall and precision values.

(iii) Recall: The recall measures the model's accuracy in terms of predicting True Positive data points correctly. For instance, the patients who truly have heart disease, recall states how many patients are correctly predicted as suffering from heart disease by the model. Recall measures how precisely the model is able to recognize the class of interest i.e., the patients having heart disease. It is also termed as Sensitivity or True Positive Rate. For example, if a patient is suffering from heart disease, but no treatment given to him/her because he or she is predicted as not having heart disease, we would like to evade from this situation. Mathematically, Recall is given as:

$$Recall = \frac{True\ Positive\ (TP)}{True\ Positive\ (TP)\ +\ False\ Negative\ (FN)} \quad (i)$$

(iv) Precision: is the ratio of the predicted True Positive data points and the total actual Positive data points. In our study, precision is a measure of patients that are correctly predicted as having heart disease out of all the patients really having it. Mathematically. Precision is given by the following formula.

$$Precision = \frac{True\ Positive\ (TP)}{True\ Positive\ (TP)\ +\ False\ Positive\ (FP)} \quad (ii)$$

(v) Cohen's kappa (κ): Cohen's kappa is defined as a performance metric that generally tells you on how much better our classifier is performing when compared to that of a classifier that performs simply by classifying randomly or based on guesses according to the frequency of each class.

$$\kappa = \frac{Po\ -\ Pe}{1\ -Pe} = 1 - \frac{1\ -\ Po}{1\ -Pe} \quad (iii)$$

where po is the observed agreement, and pe is the expected agreement. The value of Cohen's kappa measure can have a maximum value of 1. If its values are less than 0 then it means that the classifier performance is not good.

(vi) AUC - ROC (Area Under the Curve - Receiver Operating Characteristic) curve is considered as one of the most important performance measures for problems related to classification at different thresholds values. ROC is nothing but a probability curve. AUC also tells the extent to which the parameters are separable.

V. EXPERIMENTAL SETUP

In this section we present the result of our study. In order to develop the models, we applied ML techniques discussed in section V on each of our datasets. For training the models, we used a stratified validation method in which we divided our dataset into two partitions containing 70% and 30% instances respectively. Table II-V describes the results of the models developed on each of four datasets. It is to be noted that in Tables II-V A*refers to as Accuracy score, P* refers to as Precision

Authorized licensed use limited to: DELHI TECHNICAL UNIV. Downloaded on March 27,2021 at 05:40:50 UTC from IEEE Xplore. Restrictions apply.

score, R* refers to as Recall score, F1* refers to as F1 score, κ refers to Cohen's Kappa score and AUC refers to AUC-ROC.

Table II: ML algorithms on Cleveland dataset

ML	A*	P*	R*	F1*	κ	AUC
LR	0.80	0.80	0.76	0.78	0.60	0.80
KNN	**0.86**	**0.87**	**0.83**	**0.85**	**0.73**	**0.85**
BNB	0.84	0.85	0.79	0.82	0.67	0.83
DT	0.74	0.75	0.69	0.72	0.49	0.74
GPC	0.83	0.87	0.77	0.81	0.66	0.83
ADA	0.80	0.80	0.76	0.78	0.60	0.80
XGB	0.78	0.79	0.72	0.75	0.55	0.77

Table III: ML algorithms on Switzerland dataset

ML	A*	P*	R*	F1*	κ	AUC
LR	0.96	1.00	0.93	0.96	0.93	0.96
KNN	0.93	0.96	0.90	0.93	0.86	0.93
BNB	0.81	0.80	0.83	0.82	0.62	0.81
DT	0.96	1.00	0.93	0.96	0.93	0.96
GPC	0.96	1.00	0.93	0.96	0.93	0.96
ADA	**0.98**	**1.00**	**0.96**	**0.98**	**0.96**	**0.98**
XGB	0.94	1.00	0.90	0.94	0.89	0.95

Table IV: ML algorithms on Hungarian dataset

ML	A*	P*	R*	F1*	κ	AUC
LR	0.82	0.76	0.65	0.70	0.57	0.77
KNN	**0.84**	**0.85**	0.62	0.72	0.61	0.78
BNB	**0.84**	0.75	**0.75**	**0.75**	**0.64**	**0.82**
DT	0.76	0.64	0.62	0.63	0.45	0.72
GPC	0.83	0.79	0.65	0.71	0.59	0.78
ADA	0.83	0.75	0.72	0.73	0.61	0.80
XGB	0.82	0.71	**0.75**	0.73	0.59	0.85

Table V: ML algorithms on VA Long Beach dataset

ML	A*	P*	R*	F1*	κ	AUC
LR	0.74	0.73	0.75	0.74	0.48	0.74
KNN	0.76	0.83	0.66	0.74	0.53	0.76
BNB	0.60	0.58	0.66	0.62	0.20	0.60
DT	0.81	0.81	0.80	0.80	0.62	0.81
GPC	0.78	0.85	0.67	0.75	0.56	0.78
ADA	0.77	0.81	0.68	0.74	0.53	0.77
XGB	**0.82**	**0.83**	**0.80**	**0.82**	**0.64**	**0.82**

For the Cleveland dataset, we found that KNN algorithm is the best model as it gives the highest accuracy of 86.81%. All the other metrics are also comparatively higher for KNN algorithm like Precision-87%, Recall-83%, F1 score-85%, Cohen's kappa-73% and AUC-ROC of 85%. In the case of the Switzerland dataset we find ADA algorithm to be having the highest accuracy of 98.30%. Other algorithms have comparatively low testing accuracy. Each and every metric is better in ADA algorithm like Precision- 100%, Recall-96%, F1 score-98%, Cohen's kappa-96% and ROC-AUC - 98%. On applying various algorithms on Hungarian dataset, we found BNB giving a higher testing accuracy of 84.26% compared to other algorithms. Also, except Precision some other metrics were better for Naive Bayes algorithms like Recall-75%, F1 score-75%, Cohen's kappa-64% and ROC-AUC - 82%. The testing accuracies of all algorithms applied on VA Long Beach Dataset have been less compared to that of other datasets. Compared to other algorithms XGB is having a higher testing accuracy of 82.2%. with also other metric scores to be comparatively higher when seen with the other algorithms like Precision- 83%, Recall-80%, F1 score-82%, Cohen's kappa-64% and AUC-ROC-82%.

VI. CONCLUSIONS AND FUTURE WORK

We collected four datasets belonging to different locations from UCI data repository and preprocessed each of them accordingly. We applied various algorithms like LR, KNN, BNB, DT, GPC, ADA, and XGB on all four datasets and found the best model for each dataset. For the Cleveland dataset KNN was giving higher accuracy of 86.81% compared to other algorithms. In the case of the Switzerland dataset the highest accuracy of 98.30% was achieved through ADA algorithm. For Hungarian Dataset the best accuracy of 84.26% was achieved through Bernoulli Naive Bayes. In the case of VA Long Beach Dataset, the accuracies achieved through various models were similar with the XGB algorithm giving the highest accuracy and AUC of 82.20%. As AUC is one of the most stable performance measures to evaluate the performance of classification models, and for our four datasets, all of the ML techniques exhibited good AUC values. For all datasets and ML techniques combinations, AUC values are greater than 70%. Therefore, the results of the study indicate the applicability ML techniques for developing successful models that can be employed to predict heart disease. In future, we plan to extend this study using such evolutionally and search-based classification techniques on more datasets.

REFERENCES

[1] D. Ananey-Obiri and E. Sarku, "Predicting the Presence of Heart Diseases using Comparative Data Mining and Machine Learning Algorithms". International Journal of Computer Applications, 2020, pp. 975.

[2] V. Chaurasia and S. Pal, "Early prediction of heart diseases using data mining techniques". Caribbean Journal of Science and Technology, vol 1, 2013, pp. 208-217.

[3] M. Marimuthu, S. Deivarani and R. Gayathri, "Analysis of heart disease prediction using various machine learning techniques". In Advances in Computerized Analysis in Clinical and Medical Imaging, 2019, pp. 157-168.

[4] T. Cover and P. Hart, "Nearest neighbor pattern classification". IEEE transactions on information theory, vol 13, no. 1, 1967, pp. 21-27.

[5] J. R. Quinlan, "Induction of decision trees". Machine learning, vol 1, no. 1, 1986, pp. 81-106.

[6] T. Chen and C. Guestrin, "Xgboost: A scalable tree boosting system". In Proceedings of the 22nd acm sigkdd

Authorized licensed use limited to: DELHI TECHNICAL UNIV. Downloaded on March 27,2021 at 05:40:50 UTC from IEEE Xplore. Restrictions apply.

international conference on knowledge discovery and data mining, 2016, pp. 785-794.

[7] Y. Freund, R. Schapire and N. Abe, "A short introduction to boosting". Journal-Japanese Society for Artificial Intelligence, vol. 14, no. 5, 1999, pp. 771-780.

[8] R. Herbrich, N. Lawrence and M. Seeger, "Fast sparse Gaussian process methods: The informative vector machine". Advances in neural information processing systems, vol 15, 2002, pp. 625-632.

[9] I. Rishi, "An empirical study of the naive Bayes classifier". In IJCAI 2001 workshop on empirical methods in artificial intelligence, vol. 3, no. 22, 2001, pp. 41-46.

[10] J. Berkson, "Why I prefer logits to probits. Biometrics", vol 7, no. 4, 1951, pp. 327-339.

[11] N. V. Chawla, K. W. Bowyer, L. O. Hall, & W. P. Kegelmeyer, "SMOTE: synthetic minority over-sampling technique. Journal of artificial intelligence research, vol. 16, 2002, 321-357.

Authorized licensed use limited to: DELHI TECHNICAL UNIV. Downloaded on March 27,2021 at 05:40:50 UTC from IEEE Xplore. Restrictions apply.

Conceptual Design of Localized Vibration Proximity Belt for the Visually Impaired

Ayan Ahmad
Department of Applied Physics
Delhi Technological University
Delhi, India
ayanscholar@gmail.com

***Abstract*—To design a wearable technology using digital electronics that detects obstacles around the reference (person) and informs them via feedback mechanism. This wearable technology will be able to provide assistance to the visually impaired by warning them of any obstacle close by. Initially we had planned our feedback mechanism to be in audio form, informing the reference by announcing when an obstacle is present and its direction, either by speaker or earphone. But we realised, speaker announcements can be inappropriate when in public and earphone can be a hassle. For this reason we switch to vibration motor and worked on the placement of each HC-SR04 and vibration motor using mathematical analysis of ideal angles and distances. The placement of vibration motors determine where the reference will feel the vibration will give an intuitive and quick sense of direction of obstacle.**

***Index Terms*—arduino – ultrasonic sensor – visually impaired**

I. Introduction

To build a wearable device (belt) that uses digital (and in general) electronics hardware (ultrasonic sensors, Arduino uno R3, LED, vibration motors etc.) to detect proximity in multiple directions, creating a map of a certain limited volume in front of the reference/visually impaired person. If the obstacle lies/enters the volume, the reference will be informed via a feedback mechanism that does not require visual communication - local vibrations around the belt/waist of reference. The location of vibration communicates the direction of obstacle to the reference.

II. Mathematical Analysis

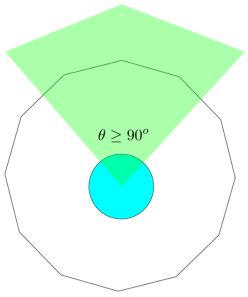

Fig. 1.

Figure 1: We do not want the person's arm beign detected as an obstacle, for this reason we create a 0.2m horizontal blindspot halo around the person so that the arms are not taking into account as obstacle.

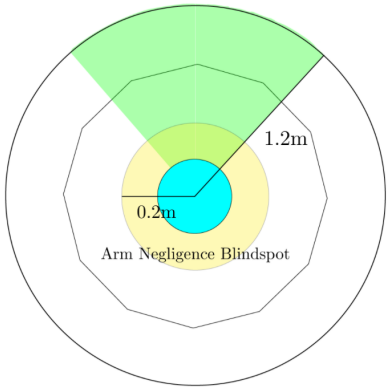

Fig. 2.

Figure 2: We do not want the person's arm beign detected as an obstacle, for this reason we create a 0.2m horizontal blindspot halo around the person so that the arms are not taking into account as obstacle.

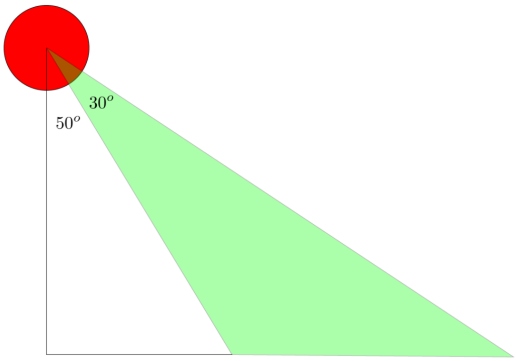

Fig. 3.

Figure 2: The fourth sensor which detects ground changes will be put 50^o off perpendicular for reasons we will mention in next figure.

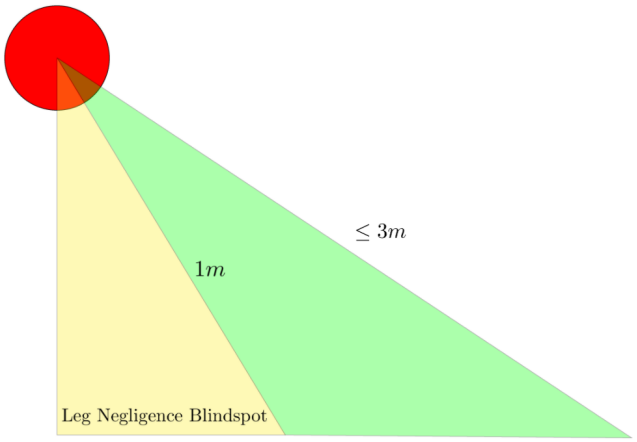

Fig. 4.

Figure 4: We don't want the legs to be taken as an obstacle either. For this reason, we orient the down sensor 50^o off to create a leg neglegence area. The maximum distance limit for a sensor here is 4m but we take 3m as the upper bound.

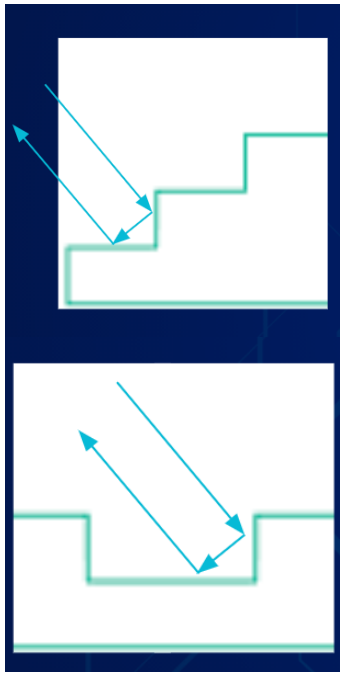

Fig. 5.

Figure 5: ([Left] Stairs [Right] Dips) Here we see a very intuitive understanding of how the down sesnsor will detect impulsive changes in ground level. The arrows represent the path of trigger generated pulses which travel pack into the echo.

III. Conceptual Design

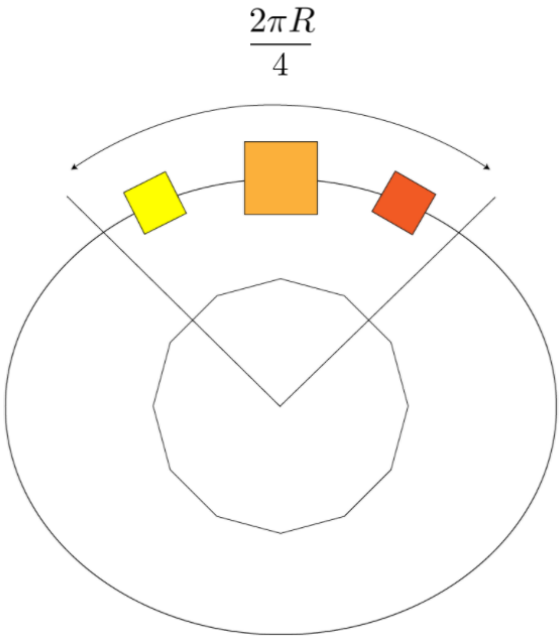

Fig. 6.

Figure 9: [Made by us on Adobe Illustrator and LaTeX] Top view of the belt. If we assume a circular belt for ease of calculation, the active length of the belt will approximately be $\frac{2\pi R}{4}$ as the angular coverage is approximately 90^o

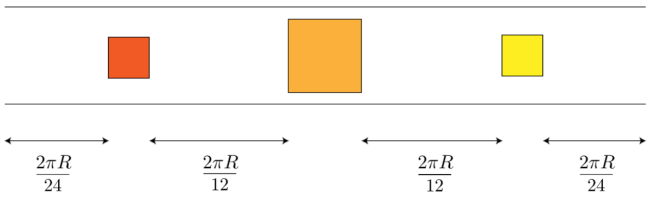

Fig. 7.

Figure 7: [Made by us on Adobe Illustrator and LaTeX] Front view of the belt. The separation of the sensors ([Left] Right sensor [Center] Front and down sensor [Right] Left sensor) will be as shown in the figure. This will ensure minimal unwanted blindspots and maximum horizontal angular coverage using three sensors.

IV. Simulation

Our arduino code is shown in Appendix VI. For simulation of our circuit, we used mainly two softwares:

- Arduino IDE (for coding)
- Tinkercad Arduino (for life-like simulation)

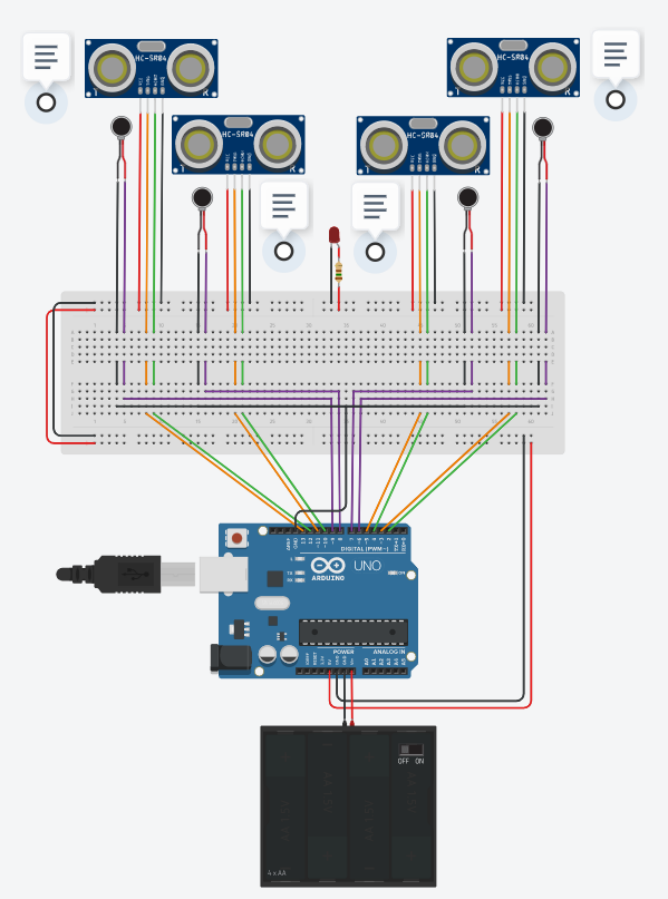

Fig. 8.

Figure 8 shows the finalized circuit (made in TinkerCad Arduino)

V. Conclusions & Discussion

A. Detection of Obstacle and Impulsive Ground Changes

Using all four sensors, we were able create a 3D volume ahead of the reference/visually impaired person and help not just detect upcoming obstacles but also inform them in a way that is very intuitive.

Using our down sensor, we can detect impulsive ground changes such as upward stairs/escalators and dips. That although is not the end of it. Using the orientation of our down sensor using the mathematical analysis we did and distance limits, we will also be able to detect any object that may be lying on the ground in front of the reference as even that can cause the reference to trip and fall.

B. Local Vibration Method

The boxes on the elliptical belt denote not just the placement of the sensors but also the vibration motors alongside those sensors ([Yellow] Left sensor and vibration motor [Orange] Front/Down sensor and vibration motor [Red] Right sensor and vibration motor). If an obstacle were detected on the left

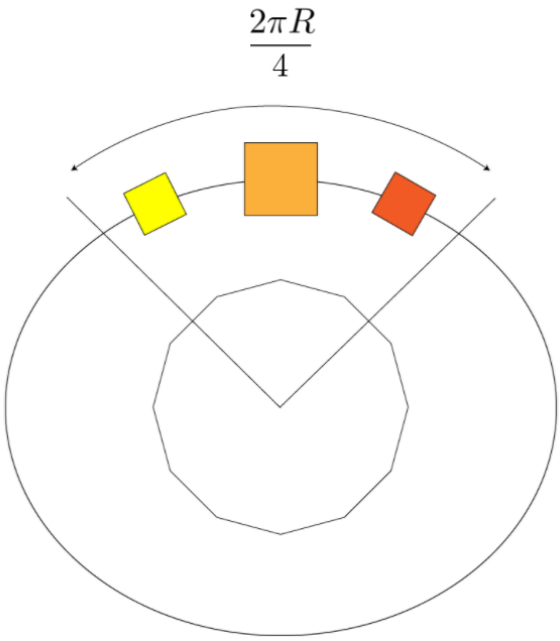

Fig. 9.

side, the left sensor would detect it and the left vibration motor would vibrate. The reference/visually impaired person would sense the vibration on the left side of their waist/belt and would intuitively get to know the direction of detected obstacle. This is a huge improvement (mentioned in previous sections) over our first draft which had one piezoelectric actuator speaker instead of four vibration motors placed in a way that they produce local vibrations.

References

[1] HAFIZUL ALIEF BIN ABU BAKAR. Dc motor speed control using measured distance by ultrasonic sensor.

[2] G Balakrishnan, G Sainarayanan, R Nagarajan, and Sazali Yaacob. Wearable real-time stereo vision for the visually impaired.Engineering Letters, 14(2), 2007.

[3] John L Barth and Emerson Foulke. Preview: A neglected variable in orientation and mobility.Journal of Visual Impairment & Blindness, 1979.

[4] Shripad S Bhatlawande, Jayant Mukhopadhyay, and Manjunatha Mahadevappa. Ultrasonic spectacles and waist-belt for visually impaired and blind person. In2012 National Conference on Communications (NCC), pages 1–4. IEEE, 2012.

[5] Allan G Dodds, David D Clark-Carter, and C Ian Howarth. The sonic pathfinder: an evaluation.Journal of Visual Impairment & Blindness, 78(5):203–206, 1984.

[6] H Hamid Hadwan and YP Reddy. Smart home control by using raspberry pi and arduino uno.Int. J. Adv. Res. Comput.Commun. Eng, 5(4):283–288, 2016.

[7] AD Heyes. A ‘polaroid’ ultrasonic travel aid for the blind?Journal of Visual Impairment Blindness, 76(5):199–201, 1982.

[8] Amit Kumar, Rusha Patra, M Manjunatha, Jayanta Mukhopadhyay, and Arun K Majumdar. An electronic travel aid for navigation of visually impaired persons. In2011 Third International Conference on Communication Systems and Networks(COMSNETS 2011), pages 1–5. IEEE, 2011.

[9] Tom H Margrain. Helping blind and partially sighted people to read: the effectiveness of low vision aids.British Journal of Ophthalmology, 84(8):919–921, 2000.

[10] Peter BL Meijer. An experimental system for auditory image representations.IEEE transactions on biomedical engineering,39(2):112–121, 1992.
[11] G Sainarayanan.On intelligent image processing methodologies applied to navigation assistance for visually impaired. PhD thesis, Universiti Malaysia Sabah, 2002.
[12] Shraga Shoval, Johann Borenstein, and Yoram Koren. The navbelt-a computerized travel aid for the blind based on mobile robotics technology.IEEE Transactions on Biomedical Engineering, 45(11):1376–1386, 1998.
[13] Iwan Ulrich and Johann Borenstein. The guide cane-applying mobile robot technologies to assist the visually impaired.IEEE Transactions on Systems, Man, and Cybernetics-Part A: Systems and Humans, 31(2):131–136, 2001

SIMULATION CODE SHOWN IN THE NEXT PAGES

VI. Arduino IDE Code for our Device

```
//  CONCEPTUAL DESIGN OF LOCALIZED VIBRATION PROXIMITY BELT FOR THE VISUALLY IMPAIRED
//  by Ayan Ahmad


int LeftSensor, FrontSensor, DownSensor, RightSensor;

int duration = 0;

int i = 0;

long readUltrasonicDistance(int triggerPin, int echoPin)
{
  pinMode(triggerPin, OUTPUT);  // Clear the trigger
  digitalWrite(triggerPin, LOW);
  delayMicroseconds(2);
  // Sets the trigger pin to HIGH state for 10 microseconds
  digitalWrite(triggerPin, HIGH);
  delayMicroseconds(10);
  digitalWrite(triggerPin, LOW);
  pinMode(echoPin, INPUT);
  // Reads the echo pin, and returns the sound wave travel time in microseconds
  return pulseIn(echoPin, HIGH);
}

void setup()
{
  Serial.begin(9600);

  pinMode(9, OUTPUT);
  pinMode(8, OUTPUT);
  pinMode(7, OUTPUT);
  pinMode(6, OUTPUT);
}

void loop()
{
  // Sound takes 29.155 microseconds per cm
  // Distance in cm = ( duration / 29 ) / 2 = 0.01723 * duration

  LeftSensor = 0.01723 * readUltrasonicDistance(13, 12);

  FrontSensor = 0.01723 * readUltrasonicDistance(11, 10);

  DownSensor = 0.01723 * readUltrasonicDistance(5, 4);

  RightSensor = 0.01723 * readUltrasonicDistance(3, 2);

  if (LeftSensor <= 120 && LeftSensor >= 20) {
    Serial.print("Obstacle Left: ");
    Serial.print(LeftSensor); // Print distance on serial monitor
    Serial.println("cm");
    digitalWrite(9, HIGH);
```

```
    delay(100); // Wait for 100 milliseconds
  } else {
    Serial.print("No obstacle Left: ");
    Serial.print(LeftSensor); // Print distance on serial monitor
    Serial.println("cm");
    digitalWrite(9, LOW);
    delay(100); // Wait for 100 milliseconds
  }
  if (FrontSensor <= 120 && FrontSensor >= 20) {
    Serial.print("Obstacle Front: ");
    Serial.print(FrontSensor); // Print distance on serial monitor
    Serial.println("cm");
    digitalWrite(8, HIGH);
    delay(100); // Wait for 100 milliseconds
  } else {
    Serial.print("No obstacle Front: ");
    Serial.print(FrontSensor); // Print distance on serial monitor
    Serial.println("cm");
    digitalWrite(8, LOW);
    delay(100); // Wait for 100 milliseconds
  }
  if (DownSensor <= 300 && DownSensor >= 100) {
    Serial.print("Obstacle Below: ");
    Serial.print(DownSensor); // Print distance on serial monitor
    Serial.println("cm");
    digitalWrite(7, HIGH);
    delay(100); // Wait for 100 milliseconds
  } else {
    Serial.print("No obstacle Below: ");
    Serial.print(DownSensor); // Print distance on serial monitor
    Serial.println("cm");
    digitalWrite(7, LOW);
    delay(100); // Wait for 100 milliseconds
  }
  if (RightSensor <= 120 && RightSensor >= 20) {
    Serial.print("Obstacle Right: ");
    Serial.print(RightSensor); // Print distance on serial monitor
    Serial.println("cm");
    digitalWrite(6, HIGH);
    delay(100); // Wait for 100 milliseconds
  } else {
    Serial.print("No obstacle Right: ");
    Serial.print(RightSensor); // Print distance on serial monitor
    Serial.println("cm");
    digitalWrite(6, LOW);
    delay(100); // Wait for 100 milliseconds
  }
}
```

ResearchGate

See discussions, stats, and author profiles for this publication at: https://www.researchgate.net/publication/349290249

Contrast Analysis of TTV-TDV Phase Difference Induced by Possible Exomoons

Preprint · October 2020

DOI: 10.13140/RG.2.2.16760.16649

CITATIONS
0

READS
6

3 authors:

Ayan Ahmad
Delhi Technological University
3 PUBLICATIONS **0** CITATIONS
SEE PROFILE

Binayyak Bhusan Roy
University of Delhi
6 PUBLICATIONS **12** CITATIONS
SEE PROFILE

Pulkit Ojha
National Institute of Science Education and Research
1 PUBLICATION **0** CITATIONS
SEE PROFILE

Some of the authors of this publication are also working on these related projects:

Magnetism View project

Exomoon Hypothesis View project

All content following this page was uploaded by Ayan Ahmad on 13 February 2021.

The user has requested enhancement of the downloaded file.

MNRAS **000**, 1–10 (2020) Preprint 13 February 2021 Compiled using MNRAS LATEX style file v3.0

Contrast Analysis of TTV-TDV Phase Difference Induced by Possible Exomoons

Ayan Ahmad,[1†§★] Binayyak B. Roy,[2§] Aayushi Rajgor[3§] Charmi Bhatt[4§] Kedar Kulkarni[5†] Pulkit Ojha[6†§]

[1]*Department of Applied Physics, Delhi Technological University, Delhi*
[2]*Department of Physics, St. Stephen's College, University of Delhi, Delhi*
[3]*Department of Electrical Engineering, K. J. Somaiya College of Engineering, Mumbai*
[4]*Department of Physics, Swarrnim Startup and Innovation University, Gandhinagar, Gujarat*
[5]*Department of Aerospace Engineering, Priyadarshini College of Engineering, Nagpur*
[6]*School of Physical Sciences, NISER, Bhubaneswar, Odisha*

[†]*Theoretical and Mathematical Analysis*
[§]*Data Collection and Analysis*

In original form 17 October 2020

ABSTRACT

In our short duration research project, our team worked upon a target of understanding using the theoretical model of the gravitational effects due to the presence of a satellite in the exo-planetary system using variations in the transit signals (TTV and TDV) of the target exoplanet, developed back in 2009. Using the model, we derived the expressions for the instantaneous variations of the signals and used them to confirm theoretically that the phase difference between the above mentioned signals for the possible exomoon candidates should be $\frac{\pi}{2}$. Further, we used this criteria along with some other parametric constraints like SNR value and the standard deviation to short-list the candidates to check for the further possibility of the presence of an exomoon. Working with 2016 data set shows that only 1.9% of the candidates have the quoted phase difference, we've tried to draw some theoretical conclusions which can be used to further analyse the reason behind the discrepancy between the prediction and the data-analysis. We're also eagerly waiting to try the data-analysis process with the latest dataset to gain better insights in the outcome.

Key words: exomoons – transit variations – orbital phase

1 INTRODUCTION

Till date there has been no concrete evidence for the existence of Exomoon candidates. There are multiple ways to look for them: the major one being photometric observations but they produce extremely faint signal making it invisible to detectors. So we turn towards the signal produce by gravitational effects of Exomoon on Exoplanets.

The observations are mostly made via the NASA's Kepler space telescope, which was designed to detect a photometric signal corresponding to a transit depth of 85 ppm—equal to the Earth-Sun analog. Here, we target on possible Exomoons which are not detectable directly, but by these indirect signals.

The signals that we have focused on are the Transit Timing Variations and the Transit Duration variations. Our aim is to provide a better version of the theoretical model and sinusoidal fitting of TTV and TDV signals that can set well together, explaining the discrepancies which will be discussed in following sections.

★ E-mail: ayanscholar@gmail.com

2 METHODOLOGY

2.1 Theoretical modelling

The aim of modifying the theoretically modeled transit timing and duration variations is to analyse the possible theoretical sources that give rise to the discrepancy down to have mainly three possible explanations:

- **Theoretical assumptions which hinder theoretical accuracy**

There are constants in Kipping (2008) and our mathematical model (1, 4), denoted by C^T and C^D, can change considerably if given a long enough epoch. This can complicate mathematical modelling by a significant amount so considering the time constraint of the project, we will be taken them as constants, while mentioning the possibility of their modification in future scopes section.

- **Sensitive parameters not taken into account for theoretical modelling**

There is always a possibility of sensitive and unnoticed parameters when we talk about far-away systems such as exoplanets. We will be analyzing each non-intrinsic parameter in order to see what role they play in varying transit timing variations and transit duration variations. If we do not see a parameter that can cause a change

© 2020 The Authors

of phase difference from $\frac{\pi}{2}$, it would indicate the existence of an additional parameter/s.

- **Change of reference epoch to match limitations for data analysis**

This will be the main focus of theoretical modelling for this report. Change of reference indicates not one but two modifications to previously known theoretical models. Let us discuss the two in brief below.

2.1.1 *Epoch unit*

The previous models use transit number as their discrete epoch unit as it is only at certain time intervals that we are able to notice the exoplanet transit in front of its host star. This is what we mean by limitations for data analysis. It is favorable that we have a continuous epoch rather than a discrete one so as to really be able to map the change in TTV and TDV over the epoch.

The true anomaly of the wobble orbit is what causes the phase of TTV and TDV to shift (equally, therefore phase difference is maintained). It also describes the orientation of the exoplanet with respect to the planet-moon barycenter (our reference for the C component of $O-C$). This suits our conditions for epoch unit very well as it is related to the physical orientation of exoplanet and is also the main factor in changing the phase of transit variations.

2.1.2 *Equations of variations*

The previous models use RMS equations of variations given by

$$\delta TTV = \sqrt{\frac{1}{2\pi}\int_0^{2\pi} [TTV(f_W)]^2 df_W}$$

$$\delta TDV = \sqrt{\frac{1}{2\pi}\int_0^{2\pi} [TDV(f_W)]^2 df_W}$$

The integration of the square of $TTV(f_W)$ and $TDV(f_W)$ are non-trivial and require certain assumptions to be taken in order to get an approximate RMS value as done by Kipping (2008) and Kipping (2009). The above expressions also assume one wobble orbit in the transit duration as the integration is being done form $0 \rightarrow 2\pi$.

To overcome these assumptions we must derive a set of variation equations that do not require such assumptions and yet compliment the epoch unit as discussed above. In 2.1.3, we will derive our modified instantaneous variation equations which are a function of our selected epoch, true anomaly of exoplanet on wobble orbit.

2.1.3 *Instantaneous variations*

The most generalized theoretical model of potentially exomoon-induced transit timing variations and transit duration variations up-to-date comes from Kipping (2008) and Kipping (2009). In order to analyze theoretically, the source of the aforementioned discrepancy in phase difference for the six exomoon candidates considered in Fox & Wiegert (2020), we must first find an absolute epoch with respect to the planet-moon barycentre as variations are expected to occur from the model of an exoplanet without an exomoon.

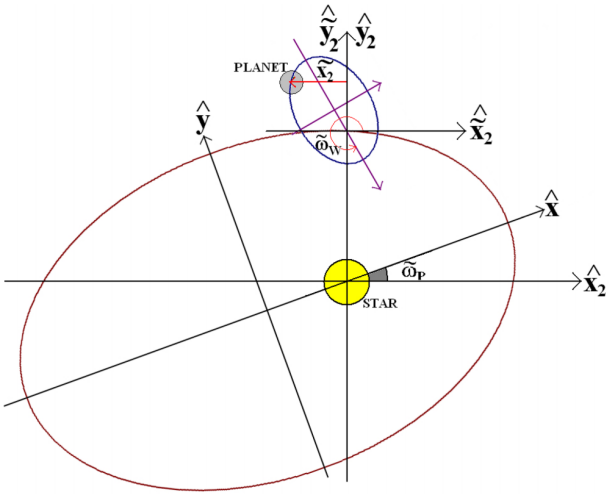

Figure 1. Reference diagram for our derivation - from Kipping (2008)

As the TTV and TDV phase is the main focus of our project, we have taken true anomaly, the orientation phase of the exoplanet w.r.t. planet-moon barycenter as the to be the absolute epoch for the theoretical model. Unlike the model used by Kipping (2020) and Fox & Wiegert (2020), we do not use the RMS value of TTV and TDV to check for phase as integrating the square of instantaneous variation equations we obtain in the appendix is non-trivial without assumptions that can hinder the theoretical accuracy.

2.1.4 *Transit timing variations*

The transit timing variation can be expressed as a function of true anomaly as follows

$$TTV(f_W) = \frac{C_1^T}{C_2^T + v_{W\perp}} \frac{cos(f_W + \bar{\omega}_W)}{1 + e_W cos(f_W)} \tag{1}$$

where

$$C_1^T = a_W(1-e_W^2) \qquad C_2^T = v_{B\perp} = \Upsilon(e_P, \bar{\omega}_P)\sqrt{\frac{G(M_{\rm PRV} + M_*)}{a_P}} \tag{2}$$

$$\Upsilon(e_P, \bar{\omega}_P) = \cos\left[\arctan\left(\frac{-e_P\cos(\bar{\omega}_P)}{1 + e_P\sin(\bar{\omega}_P)}\right)\right]\sqrt{\frac{2(1 + e_P\sin(\bar{\omega}_P))}{\left(1 - e_P^2\right)} - 1} \tag{3}$$

where f_W represents the true anomaly of the planet in wobble orbit and $M_{ps} = M_p + M_s$.

The above expression gives the same result as that given by the expressions in Kipping (2008). Hence for TTV, we obtain the same phase and magnitude in our modelling as predicted and used in the paper.

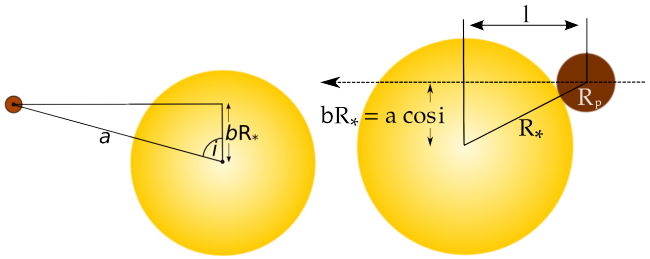

Figure 2. Reference diagrams for impact parameter - from paulanthonywilson.com

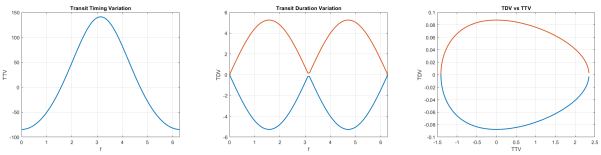

Figure 3. [Left: TTV plot] ; [Center: OB TDV plot] ; [Right: $O_2O_1B_4B_3$ Phase plot]

2.1.5 *Transit duration variations*

The transit duration variation can be expressed as a function of true anomaly as follows

$$TDV(f_W) = C^D \left(\frac{l_r}{1 + v_{r\perp}} - 1 \right) \tag{4}$$

where

$$C^D = \frac{l_B}{v_{B\perp}} = \frac{\sqrt{(R_* + R_P)^2 - (bR_*)^2}}{v_{B\perp}} \tag{5}$$

$$l_r = \frac{l_W}{l_B} = \left(\frac{(R_* + R_P)^2 - (bR_*)^2(1 + \frac{1}{r_P})^2}{(R_* + R_P)^2 - (bR_*)^2} \right)^{\frac{1}{2}} \tag{6}$$

$$v_{r\perp} = \frac{v_{W\perp}}{v_{B\perp}} \tag{7}$$

where b represents the impact parameter as shown in 2.

The above expression deviates from the formula derived by Kipping (2009). Here, we have not taken transit duration as a parameter as it cannot be considered as a replacement for transit duration of a planet transmitting without an exomoon. So instead, we have replaced it with a theoretical expression for the transit duration of planet lacking moon.

Note that the phase of our TDV does not deviate from Kipping (2009)'s TDV expression, hence our theoretical model too predicts a phase difference of $\frac{\pi}{2}$. The change in magnitude can play a key role in RMS expressions for sinusoidal functions, hence further effecting the plots for TDV.

2.1.6 *Diagrammatic role of parameters*

We will set a nomenclature for TDV graphs as we are obtaining a symmetric two point graphs which must be resolved into one per domain using theoretical understanding.

(i) **TDV plots**: Separated by node, described by first letter of color, left to right

(ii) **Phase plots**: Separated by quadrant, described by first letter of color, chronological

Let us look at our reference/starting diagram 3 and explain the nomenclature using that.
To be able to interpret different data plots and find a possible phase shift causing sensitive parameter, we must first identify the role of reach parameter diagrammatically. In this section we will individually look at the diagrammatic role of non-intrinsic parameters such as the following. The first three plots for each parameter represent a low value taken for it, the next three represent higher, both relative to the reference plot 3.

2.2 Data Analysis

2.2.1 *Systems shortlisting*

For shortlisting candidates we went forward with the conditions mentioned in Fox and Wiegert's paper:

- Imposing a cut-off of standard deviation less than 40 minutes for the fitted TTV signals.
- Transit depth of 85 ppm or less.
- Finally selecting the ones with the best SNR values greater than 1.0

Using these points we reconfirmed the results as reported in paper. We got similar results as were reported in the paper. Next, we tried to add a condition which checks how many systems do show a phase difference of $\frac{\pi}{2}$.

We expected to see a majority of candidates with the required phase difference (excluding the SNR condition) as Kipping's theory doesn't assume anything else which could have been eliminated in our shortlisting conditions and therefore most of them (if exomoons) should be showing such a phase difference.

Next, we shortlisted candidates with just a phase difference of $\frac{\pi}{2}$ and SNR value greater than 1.0 since we did not want to look at systems with noise greater than signal. Even then we did not get a considerable number of candidates. We decided to look at candidates which showed a standard deviation of less than 40 minutes and showed $\frac{\pi}{2}$ phase difference with a tolerance of 0.1. Using these conditions we got 12 candidates (table A1) with which we would be using to find a common link as to why these are the ones which show the required phase difference.

2.2.2 *Plot fitting*

For fitting the TTV and TDV data points we went with the least χ-square fit i.e., global minimisation. We used the SciPy $curve_fit$ function module to fit the data points using a general function of the form $A\sin(Bx + C)$. We fit the TTV and TDV datapoints against the transit number. And calculate the difference in the value of C for both the fits to give the phase difference. Regarding the number data points we started out with just 5 and then increased it to 10 in order to minimise random noise. If the number of data points were to be higher than that then because of lack of observations some candidates get eliminated. In order to make sure the least χ-square fit was working properly we first matched the results with that in Fox and Weigert's paper. We got the same results for the KOI mentioned in their paper.

The module was providing certain erroneous results when the dataset provided had a shifted mean in different sections then the module failed to fit it properly because of an optimization error. For this we started considering more number of data points (as mentioned before). Next, we also started facing error with some datasets that could not be properly fitted using the default settings of the module such that maximum number of calls to the function being 800. This was changed to 5000 to get the best fit (most converged) result.

3 DISCUSSION & CONCLUSIONS

3.1 Theoretical

There were mainly two theoretical modifications made in order to compensate for the limitations that hinder data analysis (such as being able to observe the state of TTV and TDV only on transit rather than having continuous observations so as to be able to measure the true changes in TTV and TDV):

- Use of instantaneous variation equations rather than RMS variation so as to remove the assumptions made for integration.

- True anomaly of exoplanet on its wobble orbit being the measure of epoch unit rather than transit numbers which can be discrete.

These modifications show four merits over previously used theoretical methods:

- The method make sure the TTV and TDV have the same frequency so as to avoid change of phase difference by assuming a common, shorter epoch - true anomaly of exoplanet on its wobble orbit.

- On analysis, it gives out more candidates with a phase difference of $\frac{\pi}{2}$ than found using previous methods of analysis.

- It gets us a step closer to removal of discrepancy between the theoretical model for exomoon-induced TTV-TDV and data analysis methods.

- The period of exomoon orbit P_s is taken as a parameter, the factor of which can be obtained after fitting the instantaneous variations on modified epoch.

3.2 Data Analysis

On having modified the shortlisting conditions used by Fox and Weigert we got 53 candidates with an epoch of $\frac{\pi}{2}$ (excluding the standard deviation and SNR condition). The following table provides the list of KOIs that showed an epoch of approximately $\frac{\pi}{2}$. (Now the precision is to 0.5 because the SD condition has been removed and we also need to account for the noise in the low SNR candidates and that's why the tolerance level has been increased) (table 1)

All of these candidates can be looked into further as they do not vary significantly from Kipping's theory and might stand out to be probable exomoon candidates. Better curve fitting methods maybe used to do the analysis other wise these can also be used as a part of the neural network method explained in future scope.

The other conclusions based on just the data analysis are:

- Through the datasets till 2016 there were only 1.9% of the candidates which did show a phase difference comparable to $\frac{\pi}{2}$.

- Initially for the curve fitting module for less number of data points the graph had concentrated data points leading to a shifted mean and therefore the least χ^2 method ended up giving logically erroneous results or the module for curve fit in SciPy was not converging even when the maximum calls to the function was increased to 9000. Therefore there must be a pattern in the variation of TTV which must be periodic (although the order of variation maybe small but overtime accumulates).

- A high frequency plotting was also tried as described earlier while that did considerably decrease the phase difference variation for our shortlisted candidates it also gave rise to newer candidates. This could have been possible because of the fact that some candidates start out with a phase difference not close to $\frac{\pi}{2}$ and then the high frequency plot actually accounts for this change.

- In order to comment or confirm Kipping's theory a more independent and rigorous curve fitting analysis has to be undertaken. Using any sort of pre-defined functions to fit the data points would be a bit biased and therefore using convoluted neural networks would be the best way to go forward.

- The change in phase difference shown in the plots actually hint towards the fact that the ω_p and ω_s variables which were assumed to be constant by Kipping's theory aren't actually constant, they do vary somewhat. A better way to plot the theoretical models would have been to just do a numerical integration and for that the form of the function describing the previous 2 variables have to be known, which as of yet we do not.

In the end the fact stands that using any module with pre-defined curve fitting methods might not work here as we do not want to bias our fitting. The plots of the TTV and TDV might give better results with more results (as that might reduce the error because of random noise).

4 RESULTS

4.1 Theoretical Modelling

The results for checking the role of non-instrinsic parameters in TTV, TDV and phase plots are given below and hyperlinked by their title in the previous section.

4.1.1 Parameter 1: Barycenter eccentricity (e_P) - (A2)

Result 1:
The amplitude of TTV and TDV are directly proportional to e_P^n.
Result 2:
The phase of TTV and TDV are independent of e_P^n.

4.1.2 Parameter 2 and 3: Wobble eccentricity ($e_W = e_S$) - (A4)

Result 1:
The amplitude of TTV and TDV are directly proportional to e_W^n and e_S^n.
Result 2:
The phase of TTV and TDV are independent of e_W^n and e_S^n.

[h]

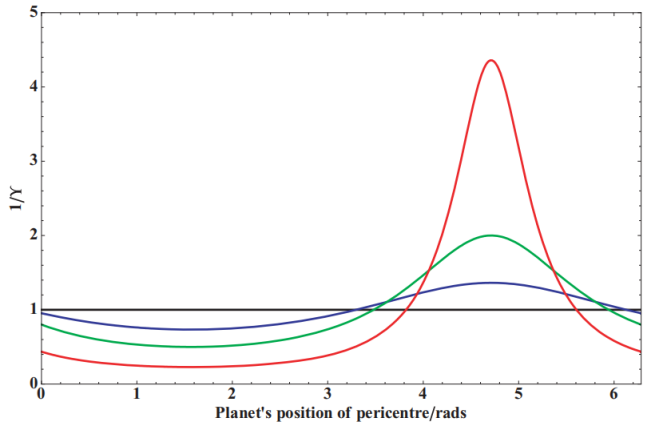

Figure 4. Υ^{-1} dependency on $\bar{\omega}_P$ for different e_P - from Kipping (2008)

Result 3:
The rate of change of TTV changes with e_W^n and e_S^n.

4.1.3 Parameter 4: Barycentre semi-major axis (a_P) - (A6)

Result 1:
The amplitude of TTV and TDV are directly proportional to a_P^n.
Result 2:
The phase of TTV and TDV are independent of a_P^n.

4.1.4 Parameter 5 and 6: Wobble semi-major axis ($a_S \propto a_W$) - (A8)

Result 1:
The amplitude of TTV is directly and TDV is inversely proportional to a_S^n and a_W^n.
Result 2:
The phase of TTV and TDV are independent of a_S^n and a_W^n.
Result 3:
The proportionality varifies the relations: $TTV \propto M_s a_S$ and $TDV \propto M_s a_S^{-\frac{1}{2}}$.

4.1.5 Parameter 7: Position of barycenter pericenter ($\bar{\omega}_P$) - (4)

Dealing with proportionality of angles can be tricky as for their often symmetric nature. To represent the effect of $\bar{\omega}_P$ we refer to Kipping (2008) so as to see the change in value of Υ^{-1}, the function that absorbs barycenter orbit properties, w.r.t. $\bar{\omega}_P$. Higher its value, higher the value for both TTV and TDV.

4.1.6 Parameter 8: Position of wobble pericenter ($\bar{\omega}_S$) - (A10, A11)

Result 1:
The amplitude of TTV is independent of $\bar{\omega}_S$.
Result 2:
The amplitude of TDV is altered per π cycle due to $\bar{\omega}_S$.
Result 3:
The phase of TTV and TDV is shifted equally by $\bar{\omega}_S$, maintaining phase difference.

4.1.7 Parameter 9 : Impact parameter (b) - (A13)

Result 1:
The amplitude of TTV is independent of b.
Result 2:
The amplitude of TDV is inversely proportional to b^n.
Result 3:
The phase of TTV and TDV are independent of b.

4.1.8 Parameter 10 : True anomaly (f_W)

The true anomaly is the argument against which we plot TTV and TDV in our theoretical model. Hence it is trivial that
Result 1:
The TTV and TDV follow sinosoid-like curves as a function of f_W.
Result 2:
The phase of TTV and TDV is shifted equally by $\bar{\omega}_S$, maintaining phase difference.

4.2 Data analysis

The data analysis done in Fox & Wiegert (2020) was very detailed and therefore we considered to work with that as our basis. Going by our objective, we would have modified the code a bit after having reconfirmed the results in their paper, to shortlist candidates with a $\frac{\pi}{2}$ phase difference. Since Kipping (2008) already suggests that TTV and TDV signals must have a phase difference of $\frac{\pi}{2}$ for exomoon systems. This would help us not only detect probable exomoon candidates but also inspect the fact as to why Fox and Weigert did not find the required phase difference.

4.2.1 Data Analysis of Exoplanetary Systems

From our shortlisted candidates we fit the TTV and TDV signals upto 10 data points and their results are presented below. A14
The fitting in all of these cases seem reasonable as when other methods are used like fitting using higher order polynomials, different algebraic and geometric iterative methods as well, give fairly similar results.

Since the fitted curves have different frequencies for TTV and TDV the phase keeps on changing, looking at the magnitude of this change and the speed would give us some information regarding the parameters in the theoretical model that controls it. A15
In order to look at a constant phase difference we tried to fit the observations of TTV using the least χ^2 method and use the frequency of that plot to fit TDV but that would be a biased fitting which would lead to wrong results. We also tried to do a high frequency fitting as the TTV would vary between transits, and going from the theory of the ratio

$$\frac{P_s}{P_p} \tag{8}$$

the frequency should be greater than or equal to 9 (Kipping (2008)). Therefore we tried to fit using the function

$$A \sin\{(|B| + 9)x + C\} \tag{9}$$

While this does lead to a lesser variation in the phase difference but it also brings up newer candidates. The best fitting function would be to use a composite form of the formulas provided by Kipping's theory but that wouldn't be for confirming his theory since we aren't considering any formula independent of his theory, it would just be

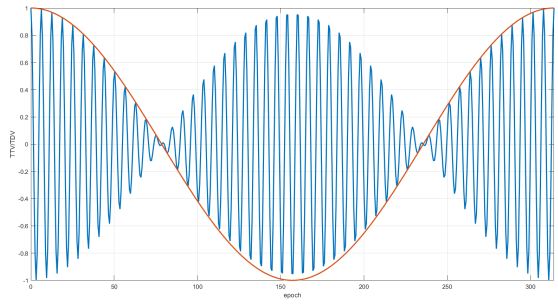

Figure 5. Exaggerated evolution of TTV/TDV (blue line) over long transit epoch interval

helpful to find out exomoons given his theory works out fine.
There are a lot of other factors in the curve fitting that can be explored.

5 FUTURE WORK

5.1 Modifications of theoretical constants

For a long epoch interval, the parameters considered constant in both our and Kipping (2008) can change considerably enough so as to play a role in changing the magnitude of TTV and TDV. Parameters such as $\bar{\omega}_S$, $\bar{\omega}_S$, a_P and a_S can change slightly over the course of a single planetary orbit. For a confirmed hypothesis, we need observations from multiple transits usually in the order of 10^1. So it is pretty evident that in this order of transit numbers, the constants mentioned above are bound to change by some amount. If not taken into account, they can result in discrepancies between the theoretical models and data analysis. Figure 5 is an exaggerated description of how the evolution of the aforementioned constants can have an effect on the magnitude of TTV and TDV over long epoch interval. Note that a sinosoidal magnitude change is assumed in the figure and is only for providing a rough idea for the evolution. In reality, the change can be of any arbitrary functions which can change the values of TTV and TDV seperately. Such a function (figure 5) will require further mathematical modelling. Fourier transform can be a promising method to find close-to analytical solution as our epoch - true anomaly - changes with time depending on other parameters and it would be useful to express transit timing and duration variations as sinosoidal frequency domain function.

$$TV(\omega) = \int_{-\infty}^{+\infty} TV(f_W(t))e^{j\omega t}dt \tag{10}$$

where TV (transit variation) can be TTV and TDV in compact form

$$TTV(f_W) = \frac{C_1^T}{C_2^T + v_{W\perp}} \frac{cos(f_W + \bar{\omega}_W)}{1 + e_W cos(f_W)} \tag{11}$$

$$TDV(f_W) = C^D \left(\frac{l_r}{1 + v_{r\perp}} - 1 \right) \tag{12}$$

Although the current models are very general, they can be be further generalized if this change in constants is taken into account so as to be able to expand the range of applicability of our model to any given epoch interval. It is almost certain that for the above generalization, analytical solutions can be quiet difficult to obtain and for this reason, we will need computational analysis to play an important role alongside theoretical and mathematical analysis.

5.2 Modelling using Convoluted Neural Networks

A completely independent and unbiased way of confirming Kipping (2008) theory would be to train a convoluted Neural Netwrok using the latest dataset possible. There are already well developed models for analyzing lightcurves of different TTV and TDV signals from possible exomoon candidates. One easy model Alshehhi et al. (2020) to set up would be to consider a binary classification where a false positive would be 0 and an exomoon candidate would mean 1. Considering a dataset going from 0<n<N. The loss function can be defined as follows,

$$L_err(\Phi) = \frac{1}{N}\Sigma_0^{N-1}|C(X_m;\Phi) - c_m| \tag{13}$$

where each term can only take values 1 or 0. For getting the required convoluted neural network (CNN) one is required to minimise this function (The number of data should be more than the number of Φ parameters). In fitting the data points there might be noise generated by more (unnecessary) parameters and even more the weights associated with them. In order to smoothen out the last convoluted layer i.e., to eliminate noise one would have to take up a convolution with a centered Gaussian Kernel G of the form,

$$S_m(p) = \Sigma_{j=0}^{l} Y(p-j)G(j) \tag{14}$$

where Y is the final layer and l denotes the last layer number.
Using these modifications one can easily define a preliminary neural network to analyse the dataset and form one with well-defined variables and weights associated with each. Once we have a neural network one can work with all different sorts of activation functions to check how the fitting changes. Once we have converging results we can then do a missing variable analysis by comparing the variables of the CNN with that of Kipping's theory. This will help us exactly confirm his theory and also have a well-defined code to check for exomoons.

5.3 Testing exomoon hypothesis

The aforementioned theoretical and data analysis models are made from scratch, purely for exomoon-induced TTV and TDVs. To confirm an exomoon, we collect data and try fitting it with our theoretical model, and we do so for multiple transits as mentioned in 5.1. Considering the assumptions made in theoretical model for TTV and TDV instantaneous equations, such as periodic values for TTV and TDV, and so on, it is very unlikely for a system to follow the model accurately for multiple transits. With the fitted values of $\frac{M_S}{M_P}$, $\frac{a_S}{a_P}$, $\frac{P_S}{P_P}$ and other satellite-planet ratio parameters taken into account as well. If we obtain a fitting for the ratio parameters that describe a satellite-planet ratio and do so consistently for multiple transits, it is likely to be an exomoon-candidate.

REFERENCES

Alshehhi R., Rodenbeck K., Gizon L., Sreenivasan K. R., 2020, arXiv preprint arXiv:2005.13035
Fox C., Wiegert P., 2020, arXiv preprint arXiv:2006.12997
Huber D., et al., 2013, The Astrophysical Journal, 767, 127
Jontof-Hutter D., et al., 2016, The Astrophysical Journal, 820, 39

Kipping D. M., 2008, Monthly Notices of the Royal Astronomical Society, 392, 181
Kipping D. M., 2009, Monthly Notices of the Royal Astronomical Society, 396, 1797
Kipping D., 2020, An Independent Analysis of the Six Recently Claimed Exomoon Candidates (arXiv:2008.03613)
Kipping D., Teachey A., 2020, arXiv preprint arXiv:2004.04230
Kipping D. M., Schmitt A. R., Huang X., Torres G., Nesvornỳ D., Buchhave L. A., Hartman J., Bakos G. Á., 2015, The Astrophysical Journal, 813, 14
Mazeh T., Holczer T., Faigler S., 2016, Astronomy & Astrophysics, 589, A75
Mills S. M., Mazeh T., 2017, The Astrophysical Journal Letters, 839, L8
Nesvornỳ D., Morbidelli A., 2008, The Astrophysical Journal, 688, 636
Pál A., Kocsis B., 2008, Monthly Notices of the Royal Astronomical Society, 389, 191
Rodenbeck K., Heller R., Gizon L., 2020, Astronomy & Astrophysics, 638, A43
Sengupta S., Marley M. S., 2016, The Astrophysical Journal, 824, 76
Simon A., Szabó G. M., Szatmáry K., 2009, Earth, Moon, and Planets, 105, 385
Sucerquia M., Alvarado-Montes J. A., Zuluaga J. I., Cuello N., Giuppone C., 2019, Monthly Notices of the Royal Astronomical Society, 489, 2313
Sucerquia M., Ramírez V., Alvarado-Montes J. A., Zuluaga J. I., 2020, Monthly Notices of the Royal Astronomical Society, 492, 3499
Teachey A., Kipping D., Burke C. J., Angus R., Howard A. W., 2020, The Astronomical Journal, 159, 142

APPENDIX A: DERIVATION OF GENERALIZED INSTANTANEOUS VARIATIONS

A1 Frame switch operators

A general linear translation of magnitude x_0, from α to β frame can be expressed as

$$x_\beta = x_\alpha - x_0 \tag{A1}$$

A general 2-D rotational transform of magnitude θ, from α to β frame can be expressed as

$$\begin{pmatrix} x_\beta \\ y_\beta \end{pmatrix} = \begin{pmatrix} cos\theta & -sin\theta \\ sin\theta & cos\theta \end{pmatrix} \begin{pmatrix} x_\alpha \\ y_\alpha \end{pmatrix} \tag{A2}$$

$\hat{\tilde{x}}_1 - \hat{\tilde{y}}_1$ to $\hat{\tilde{x}} - \hat{\tilde{y}}$ frame
This is a purely rotational frame switch and hence can be expressed in rotation matrix form.

$$\begin{pmatrix} \tilde{x}_1 \\ \tilde{y}_1 \end{pmatrix} = \begin{pmatrix} cos(\bar{\omega}_W) & -sin(\bar{\omega}_W) \\ sin(\bar{\omega}_W) & cos(\bar{\omega}_W) \end{pmatrix} \begin{pmatrix} \tilde{x} \\ \tilde{y} \end{pmatrix} \tag{A3}$$

$\hat{\tilde{x}}_2 - \hat{\tilde{y}}_2$ to $\hat{\tilde{x}}_1 - \hat{\tilde{y}}_1$ frame
This is a purely translational frame switch and hence can be expressed as seperate linear equations.

$$\tilde{x}_2 = \tilde{x}_1 - a_W e_W \cos(\bar{\omega}_W) \tag{A4}$$

$$\tilde{y}_2 = \tilde{y}_1 - a_W e_W \sin(\bar{\omega}_W) \tag{A5}$$

$\hat{x} - \hat{y}$ to $\hat{x}_2 - \hat{y}_2$ frame
This is a combination of rotational and translational frame switch and hence can be expressed as

$$\begin{pmatrix} x \\ y \end{pmatrix} = \begin{pmatrix} cos(-\bar{\omega}_W) & -sin(-\bar{\omega}_W) \\ sin(-\bar{\omega}_W) & cos(-\bar{\omega}_W) \end{pmatrix} \begin{pmatrix} x_2^0 \\ y_2 \end{pmatrix} \tag{A6}$$

$$x_2 = x_2^0 - a_P e_P \tag{A7}$$

$\hat{\tilde{x}} - \hat{\tilde{y}}$ to $\hat{\tilde{x}}_2 - \hat{\tilde{y}}_2$ frame
This is a combination of rotational and translational frame switch and hence can be expressed as

$$\begin{pmatrix} \tilde{x} \\ \tilde{y} \end{pmatrix} = \begin{pmatrix} cos(-\bar{\omega}_W) & -sin(-\bar{\omega}_W) \\ sin(-\bar{\omega}_W) & cos(-\bar{\omega}_W) \end{pmatrix} \begin{pmatrix} \tilde{x}_2^0 \\ \tilde{y}_2 \end{pmatrix} \tag{A8}$$

$$\tilde{x}_2 = \tilde{x}_2^0 - a_W e_W \tag{A9}$$

A2 Barycenter terms

The distance of any point on the ellipse from the foci is given by

$$r(f) = \frac{a\left(1 - e^2\right)}{1 + e\cos(f)} \tag{A10}$$

The above equation when applied to orbital motion of barycenter around the star, takes the following form

$$r_P(f_P) = \frac{a_P\left(1 - e_P^2\right)}{1 + e_P\cos(f_P)} \tag{A11}$$

where r_P is roughly the distance between star and exoplanet.

Assuming $\lim_{\Delta t \to \tau_0}(\Delta f_P) \to 0$, we obtain the expression $f_P = \frac{\pi}{2} - \bar{\omega}_P$, a constant as the barycenter must roughly lie on the line joining star and observer for an observable transit. That gives us the constant expression for position of barycenter during transit.

$$r_P = \frac{a_P\left(1 - e_P^2\right)}{1 + e_P\sin(\bar{\omega}_P)} \tag{A12}$$

As we have seen in Kipping (2008), the apparent velocity of barycenter around the star is given by

$$v_{B\perp} = \Upsilon(e_P, \bar{\omega}_P)\sqrt{\frac{G(M_{\rm PRV} + M_*)}{a_P}} \tag{A13}$$

where

$$\Upsilon(e_P, \bar{\omega}_P) = \cos\left[\arctan\left(\frac{-e_P\cos(\bar{\omega}_P)}{1 + e_P\sin(\bar{\omega}_P)}\right)\right] \sqrt{\frac{2(1 + e_P\sin(\bar{\omega}_P))}{\left(1 - e_P^2\right)} - 1} \tag{A14}$$

A3 Wobble terms

Equation A10 when applied to wobble motion of exoplanet around the planet-moon barycenter, takes the following form

$$r_W(f_W) = \frac{a_W\left(1 - e_W^2\right)}{1 + e_W\cos(f_W)} \tag{A15}$$

where r_W is the distance between barycenter and exoplanet. The perpendicular distance of the exoplanet from line joining star, barycenter and observer will be given by

$$\tilde{x}_2 = r_W cos(f_W + \bar{\omega}_W) \tag{A16}$$

$$\tilde{x}_2 = a_W(1-e_W^2)\frac{cos(f_W+\bar{\omega}_W)}{1+e_W cos(f_W)} \tag{A17}$$

Once again, we will consider Kipping (2008) for the wobble velocity of the exoplanet on its wobble orbit, given by

$$v_W(f_W) = \mu_W^{\frac{1}{2}}\left(\frac{2}{r_W(f_W)} - \frac{1}{a_W}\right)^{\frac{1}{2}} \tag{A18}$$

where

$$\mu_W = \frac{GM_S^3}{M_{PRV}^2} \tag{A19}$$

This is not the final expression for the apparent wobble velocity. We must now take the component perpendicular to line joining star and observer

$$v_{W\perp}(f_W) = v_W(f_W)\cos\left[\tilde{\theta}(f_W)\right] \tag{A20}$$

$$\tilde{\theta}(f_W) = \arctan\left(\frac{d\tilde{y}_2}{d\tilde{x}_2}\right) \tag{A21}$$

The expression for $\tilde{\theta}(f_W)$ is obtained by differentiating (w.r.t. $\tilde{x}_2$) equation of ellipse in the $\tilde{x}_2 - \tilde{y}_2$ frame after replacing them with $\tilde{x} - \tilde{y}$ by performing the inverse frame switch operator A8. Doing so, we get

$$\tilde{\theta}(f_W) = \arctan\left(\frac{\tilde{y}\sin(\bar{\omega}_W) - \left(1-e_W^2\right)\tilde{x}\cos(\bar{\omega}_W)}{\tilde{y}\cos(\bar{\omega}_W) + \left(1-e_W^2\right)\tilde{x}\sin(\bar{\omega}_W)}\right) \tag{A22}$$

A4 Transit timing variation

Transit timing variations by definition is the magnitude of lag or lead in the observed transit time of the exoplanet from the calculated one. Our reference for calculations is the barycenter which represents the motion of exoplanet without an exomoon. So it is trivial now, that the lag or lead in transit time will depend on the apparent distance between exoplanet and barycenter, and also will depend on the total apparent velocity of the exoplanet on its orbit.

$$TTV(f_W) = TTV_O - TTV_C = \frac{\tilde{x}_2}{v_{B\perp}+v_{W\perp}} - 0 \tag{A23}$$

$$TTV(f_W) = \frac{\tilde{x}_2}{v_{B\perp}+v_{W\perp}} \tag{A24}$$

Substituting in the above equation from equations A13, A17 and A20, we obtain the expression for instantaneous TTV, as a function of true wobble anomaly.

Writing the purely constant TTV terms as C^T, we get

$$TTV(f_W) = \frac{C_1^T}{C_2^T + v_{W\perp}}\frac{cos(f_W+\bar{\omega}_W)}{1+e_W cos(f_W)} \tag{A25}$$

A5 Impact parameter

The impact parameter plays a huge role in determining the magnitude of the theoretical TDV value. The larger the impact parameter, the shorter will be the distance the exoplanet has to travel in order to fully transit the star.

In this section we will be deriving expressions for relative lengths and velocities, in the case of any general impact parameter (zero or non-zero). For this purpose, we use 2 as our reference. We can notice the following relations from the diagram-

$$bR_* = r_P cos(i) \tag{A26}$$

where r_P is position of exoplanet w.r.t. star, given by A12 and b is the impact parameter.

$$l_B = \sqrt{(R_*+R_P)^2 - (bR_*)^2} \tag{A27}$$

In the case of exoplanet containing exomoon, the apparent length is altered due to perturbation by an amount Δl, given by Kipping (2009)

$$\Delta l = cos(i) r_W sin(f_W + \bar{\omega}_W) \tag{A28}$$

We now substitute our relation A26 in the above formula to get

$$\Delta l = \frac{bR_*}{r_P} r_W sin(f_W + \bar{\omega}_W) \tag{A29}$$

Therefore the apparent length in presence of an exomoon will be given by

$$l_W = \sqrt{(R_*+R_P)^2 - (bR_*)^2(1+\frac{1}{r_P})^2} \tag{A30}$$

A6 Transit duration variation

Transit duration variations by definition is the magnitude of lag or lead in the observed transit duration (time taken for the exoplanet to complete its transit). Our reference for calculations is again, a barycenter which represents motion of exoplanet without an exomoon. So it is trivial now, that the lag or lead in transit duration will depend upon both the length of transit distance and on the total apparent velocity.

$$TDV(f_W) = TDV_O - TDV_C = \frac{l_w}{v_{B\perp}+v_{W\perp}} - \frac{l_b}{v_{B\perp}} \tag{A31}$$

$$TDV(f_W) = \left(\frac{\frac{l_W}{l_b}}{1+\frac{v_{W\perp}}{v_{B\perp}}} - 1\right)\frac{l_B}{v_{B\perp}} \tag{A32}$$

We define the ratios as $\frac{l_W}{l_b} = l_r$ and $\frac{v_{W\perp}}{v_{B\perp}} = v_{r\perp}$ which denote relative apparent length and velocity.

$$TDV(f_W) = \left(\frac{l_r}{1+v_r} - 1\right)\tau_0 \tag{A33}$$

Here, τ_0 represents the transit duration if the exomoon were to be absent, or in other words our reference transit duration.
Writing the purely constant TDV terms as C^D, we get

$$TDV(f_W) = C^D\left(\frac{l_r}{1+v_{r\perp}} - 1\right) \tag{A34}$$

Serial No.	KOI	Phase Difference
1	2.01	-2.0156
2	12.01	1.27826
3	20.01	1.42405
4	46.01	-2.0634
5	70.01	1.4444
6	82.01	-1.4825
7	82.02	-1.4335
8	103.01	1.5966
9	108.01	-1.4314
10	110.01	1.2680
11	111.01	1.14898
12	116.01	-1.9258
13	116.02	1.6313
14	127.01	1.9293
15	128.01	1.5973
16	137.01	1.13160
17	142.01	-1.5763
18	149.01	1.7468
19	152.02	1.4184
20	162.01	-1.0878
21	165.01	1.1309
22	197.01	-1.526
23	203.01	1.8189
24	227.01	1.8297
25	249.01	1.6505
26	252.01	-1.94436
27	254.01	2.0503
28	255.01	-1.1239
29	257.01	1.1589
30	260.02	-1.6505
31	275.01	-2.035
32	282.01	-1.373
33	288.02	1.7280
34	304.01	-1.419
35	306.01	-1.8629
36	314.02	-1.3976
37	315.01	1.2489
38	354.01	1.6941
39	398.01	1.94631
40	456.01	-1.1332
41	657.02	-1.3819
42	723.02	1.8721
43	841.02	-1.5054
44	921.02	-1.9889
45	984.01	-1.6896
46	1074.01	1.5429
47	1299.01	1.62746
48	1426.01	-1.26108
49	1573.01	-1.8433
50	1781.01	-1.25435
51	1805.01	2.03585
52	2577.01	1.630129
53	2672.02	-1.9235

Table 1. KOIs showing a phase difference of $\frac{\pi}{2}$ within a 30% agreement

KepId	Kepoi Name	Kepler Name	Phase Difference	SNR
10187017	K00082.01	Kepler-102 e	-1.4825	2.38507
4914423	K00108.01	Kepler-103 b	1.5966	2.15896
8359498	K00127.01	Kepler-77 b	1.6313	3.2644
8644288	K00137.01	Kepler-18 c	1.5974	2.64098
5735762	K00148.02	Kepler-48 c	-1.57637	2.25042
2987027	K00197.01	Kepler-489 b	-1.52618	2.940218
9390653	K00249.01	Kepler-504 A b	1.6505	2.04999
8292840	K00260.02	Kepler-126 d	-1.65055	1.9133
5792202	K00841.02	Kepler-27 c	-1.505414	2.06893
10272640	K01074.01	Kepler-762 b	1.54297	2.003461
10864656	K01299.01	Kepler-432 b	1.6275	2.0652
12257999	K02577.01		1.63013	1.521138

Table A1. Shortlisted Candidates

Figure A1. *

[1^{st} row: Low value for e_P] [2^{nd} row: High value for e_P]

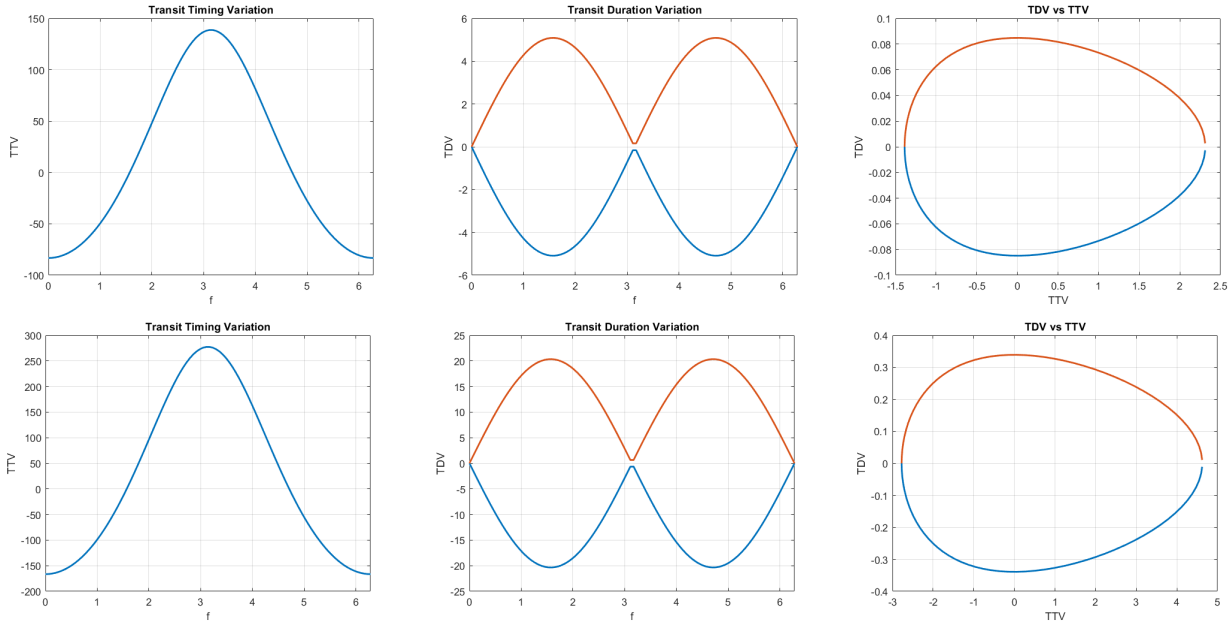

Figure A2. [Left: TTV plot] ; [Center: OB TDV plot] ; [Right: $O_2O_1B_4B_3$ Phase plot]

Figure A3. *

[1^{st} row: Low value for e_S] [2^{nd} row: High value for e_S]

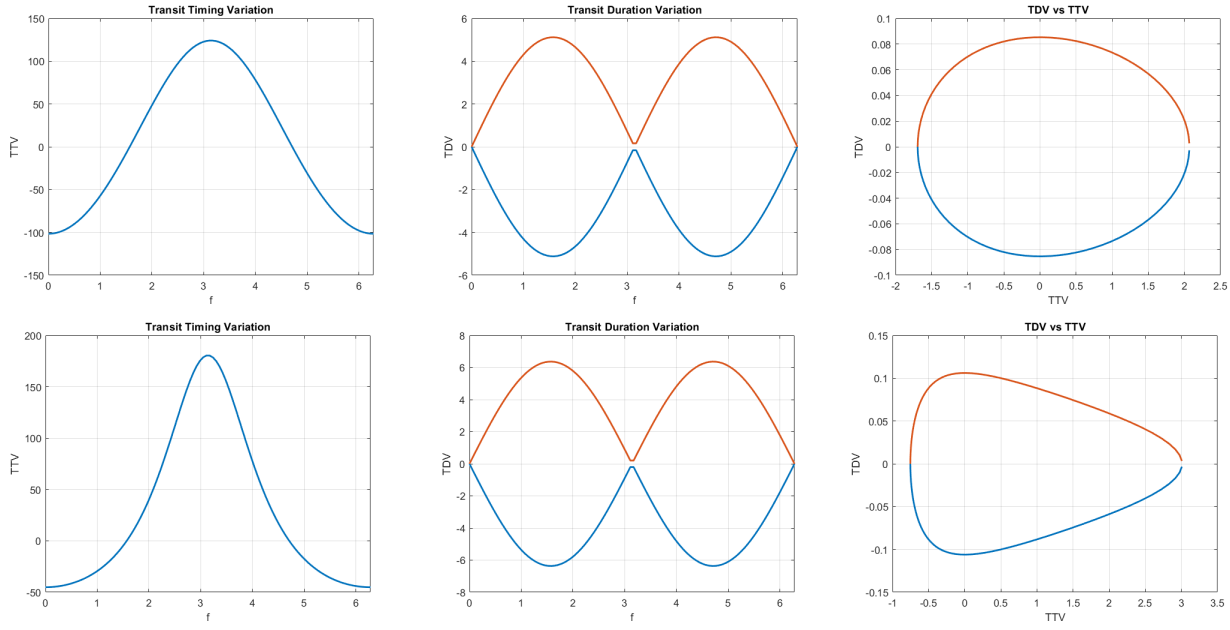

Figure A4. [Left: TTV plot] ; [Center: OB TDV plot] ; [Right: $O_2O_1B_4B_3$ Phase plot]

This paper has been typeset from a TEX/LATEX file prepared by the author.

Figure A5. *

[1^{st} row: Low value for a_P] [2^{nd} row: High value for a_P]

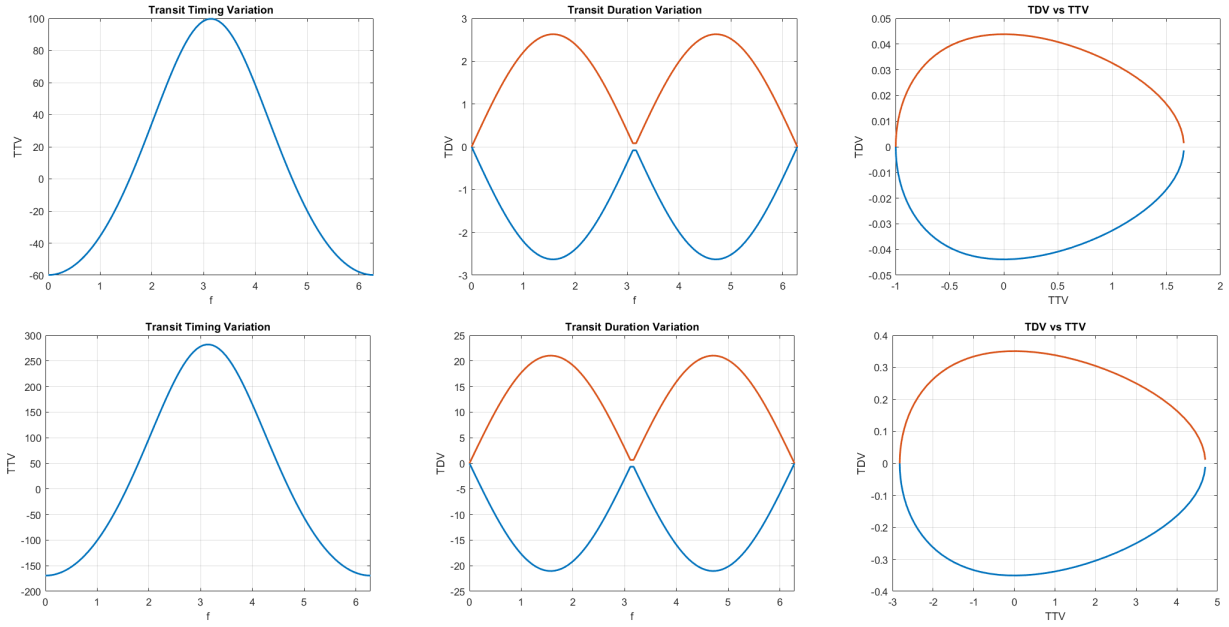

Figure A6. [Left: TTV plot] ; [Center: OB TDV plot] ; [Right: $O_2O_1B_4B_3$ Phase plot]

Figure A7. *

[1^{st} row: Low value for a_S] [2^{nd} row: High value for a_S]

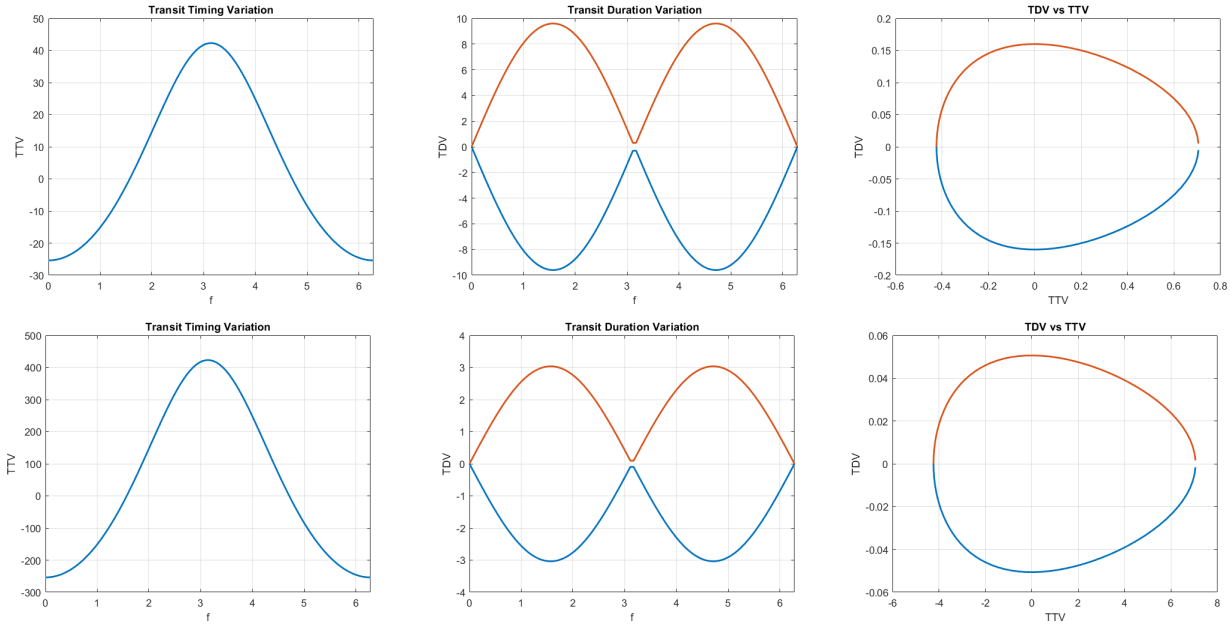

Figure A8. [Left: TTV plot] ; [Center: OB TDV plot] ; [Right: $O_2O_1B_4B_3$ Phase plot]

Figure A9. *

[1^{st} row: $\bar{\omega}_S = \frac{\pi}{4}$] [$2^{nd}$ row: $\bar{\omega}_S = \frac{3\pi}{4}$]

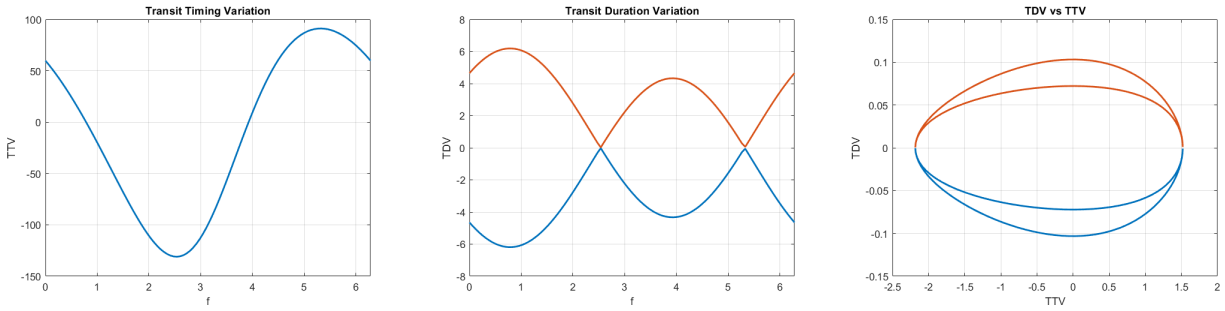

Figure A10. [Left: TTV plot] ; [Center: BOB TDV plot] ; [Right: $B_{4H}O_{1L}O_{2L}B_{3H}B_{4H}$ Phase plot]

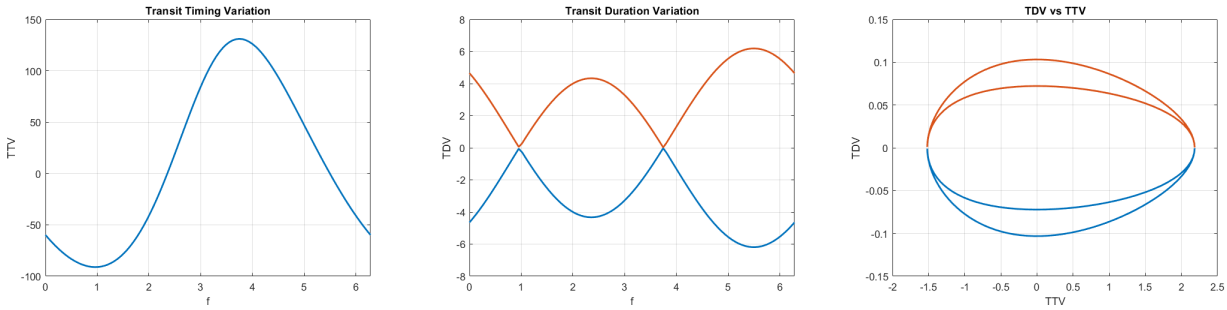

Figure A11. [Left: TTV plot] ; [Center: OBO TDV plot] ; [Right: $O_{2H}B_{3L}B_{4L}O_{1H}O_{2H}$ Phase plot]

Figure A12. *

[1^{st} row: Low value for b] [2^{nd} row: High value for b]

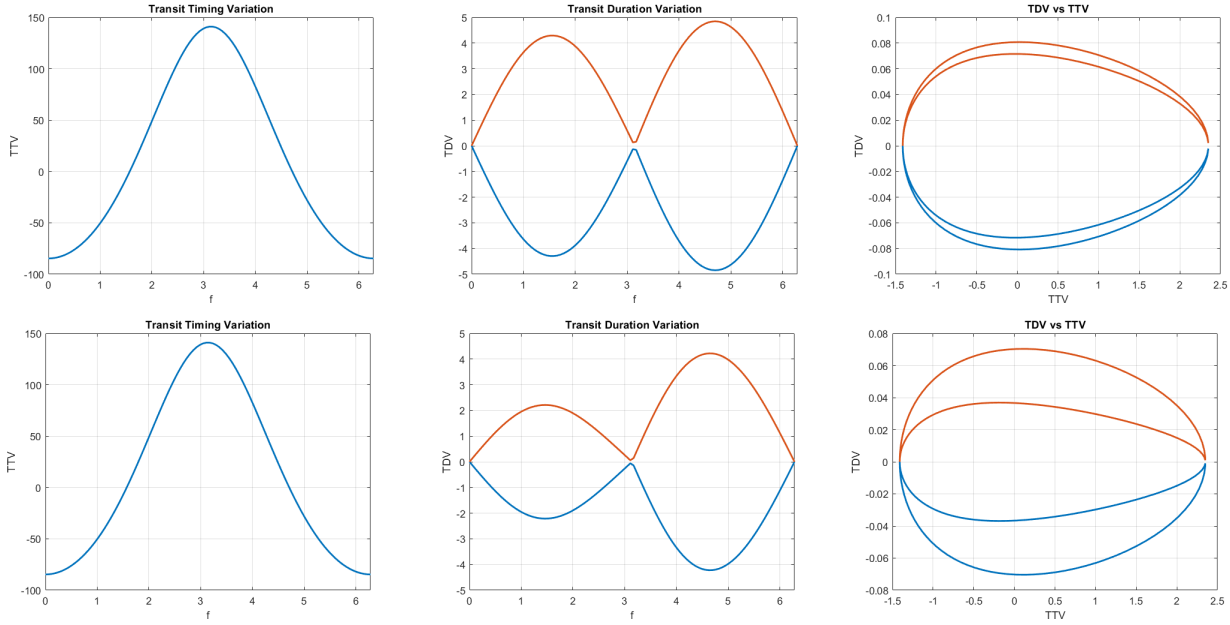

Figure A13. [Left: TTV plot] ; [Center: OB TDV plot] ; [Right: $O_{2L}B_{3H}B_{4H}O_{1L}$ Phase plot]

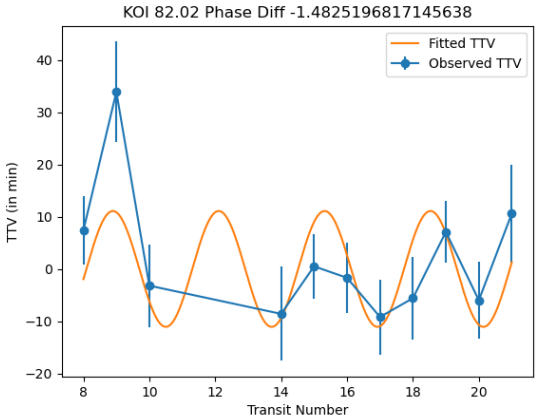
KOI 82.02 Phase Diff -1.4825196817145638
Fitted TTV
Observed TTV
TTV (in min)
Transit Number

[]

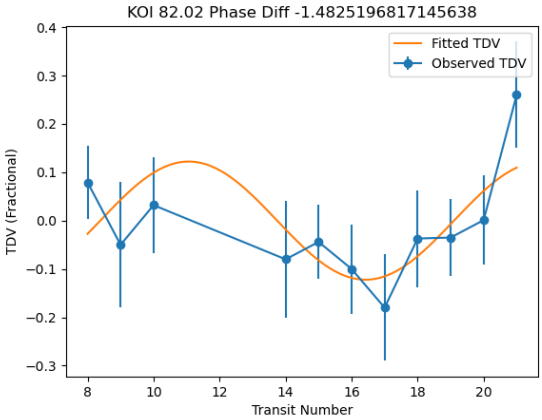
KOI 82.02 Phase Diff -1.4825196817145638
Fitted TDV
Observed TDV
TDV (Fractional)
Transit Number

[]

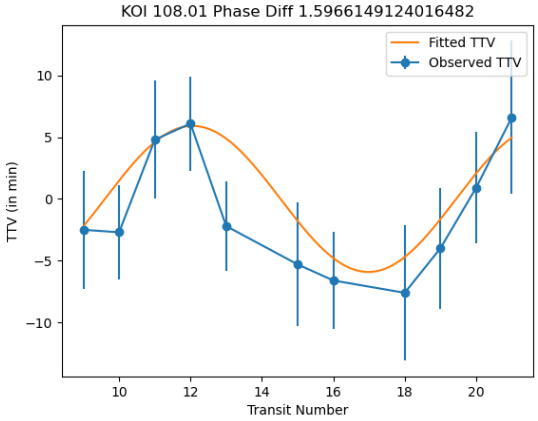
KOI 108.01 Phase Diff 1.5966149124016482
Fitted TTV
Observed TTV
TTV (in min)
Transit Number

[]

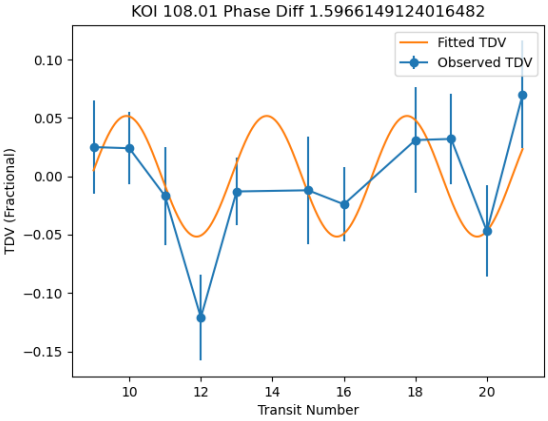
KOI 108.01 Phase Diff 1.5966149124016482
Fitted TDV
Observed TDV
TDV (Fractional)
Transit Number

[]

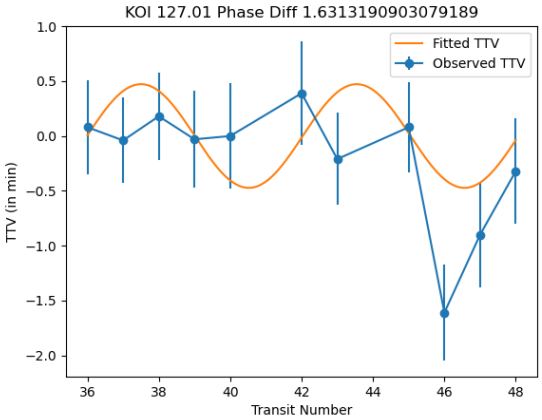
KOI 127.01 Phase Diff 1.6313190903079189
Fitted TTV
Observed TTV
TTV (in min)
Transit Number

[]

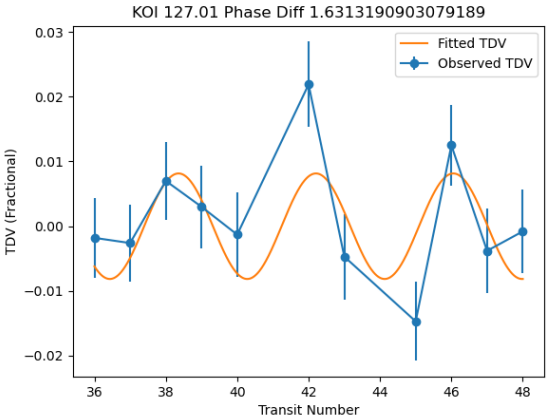
KOI 127.01 Phase Diff 1.6313190903079189
Fitted TDV
Observed TDV
TDV (Fractional)
Transit Number

[]

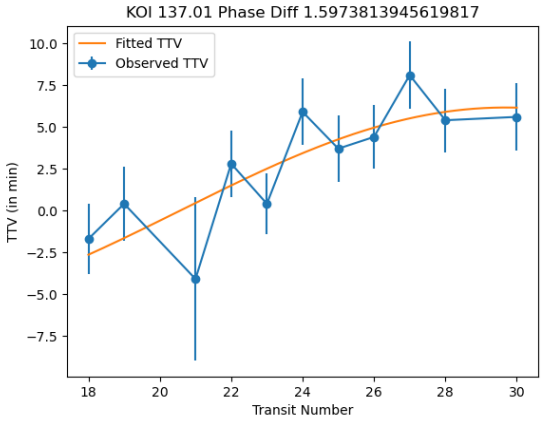
KOI 137.01 Phase Diff 1.5973813945619817
Fitted TTV
Observed TTV
TTV (in min)
Transit Number

[]

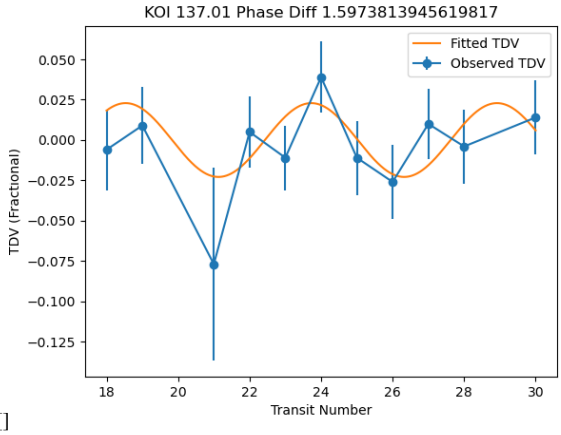
KOI 137.01 Phase Diff 1.5973813945619817
Fitted TDV
Observed TDV
TDV (Fractional)
Transit Number

[]

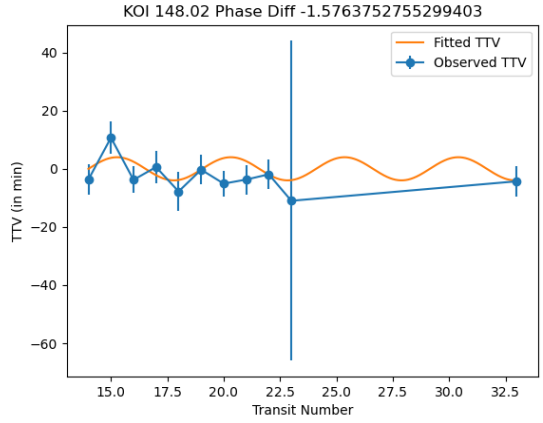
KOI 148.02 Phase Diff -1.5763752755299403
Fitted TTV
Observed TTV
TTV (in min)
Transit Number

[]

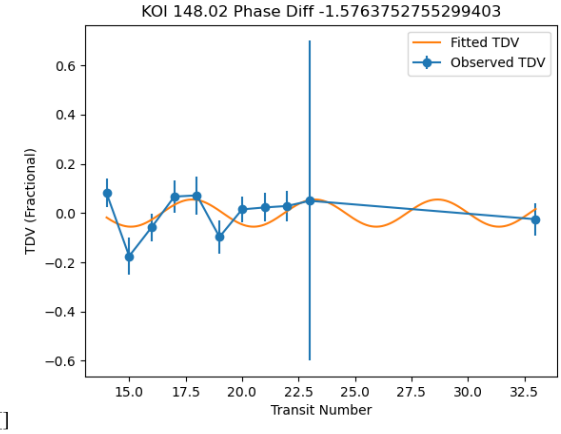
KOI 148.02 Phase Diff -1.5763752755299403
Fitted TDV
Observed TDV
TDV (Fractional)
Transit Number

[]

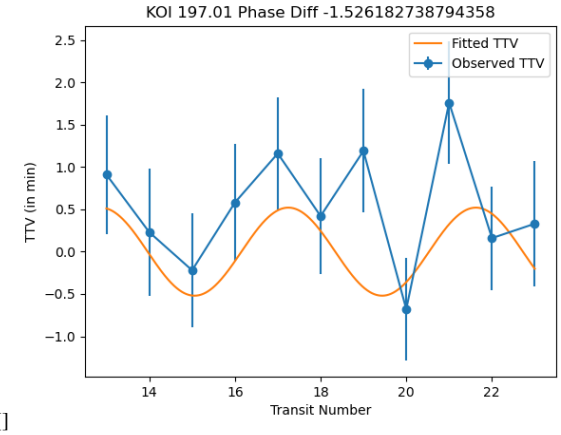
KOI 197.01 Phase Diff -1.526182738794358
Fitted TTV
Observed TTV
TTV (in min)
Transit Number

[]

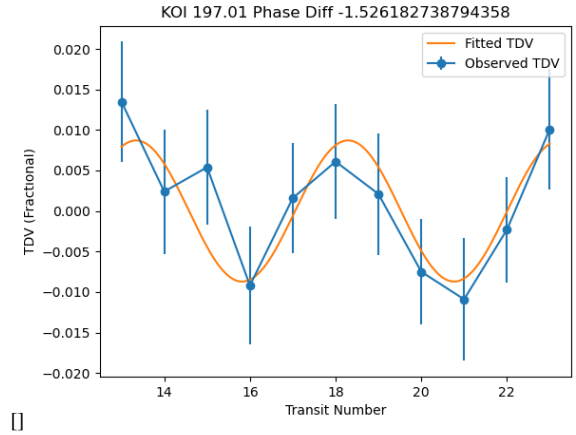
KOI 197.01 Phase Diff -1.526182738794358
Fitted TDV
Observed TDV
TDV (Fractional)
Transit Number

[]

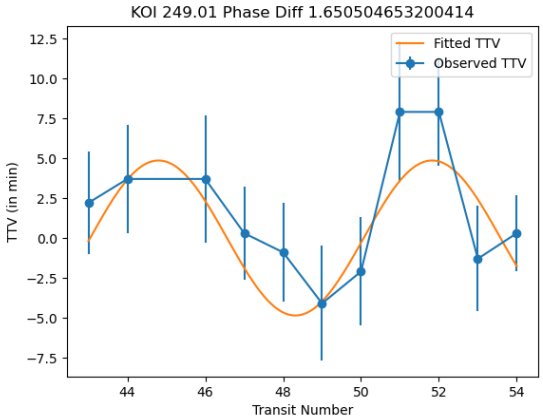
KOI 249.01 Phase Diff 1.650504653200414
Fitted TTV
Observed TTV
TTV (in min)
Transit Number

[]

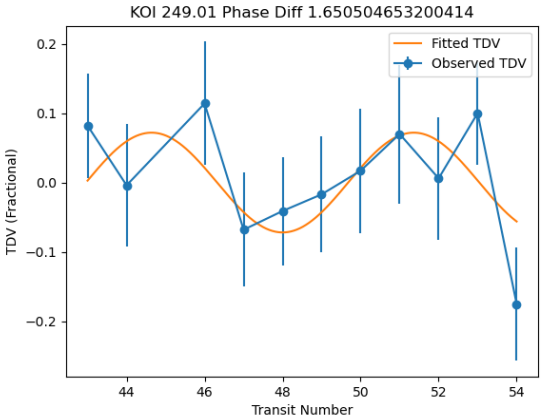
KOI 249.01 Phase Diff 1.650504653200414
Fitted TDV
Observed TDV
TDV (Fractional)
Transit Number

[]

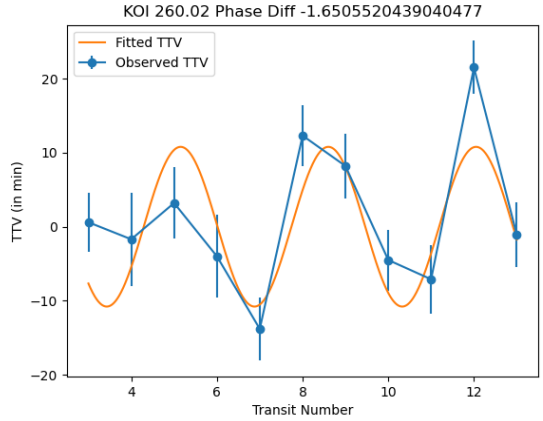
KOI 260.02 Phase Diff -1.6505520439040477
Fitted TTV
Observed TTV
TTV (in min)
Transit Number

[]

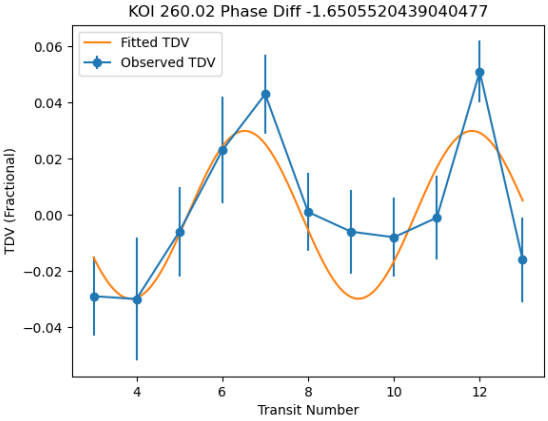
KOI 260.02 Phase Diff -1.6505520439040477
Fitted TDV
Observed TDV
TDV (Fractional)
Transit Number

[]

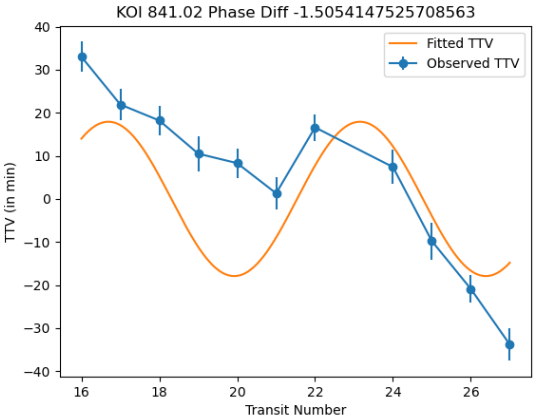
KOI 841.02 Phase Diff -1.5054147525708563
Fitted TTV
Observed TTV
TTV (in min)
Transit Number

[]

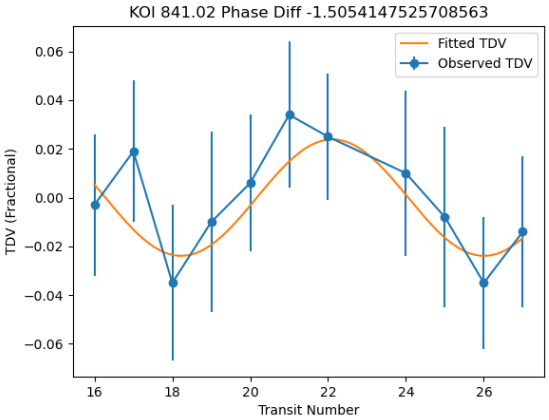
KOI 841.02 Phase Diff -1.5054147525708563
Fitted TDV
Observed TDV
TDV (Fractional)
Transit Number

[]

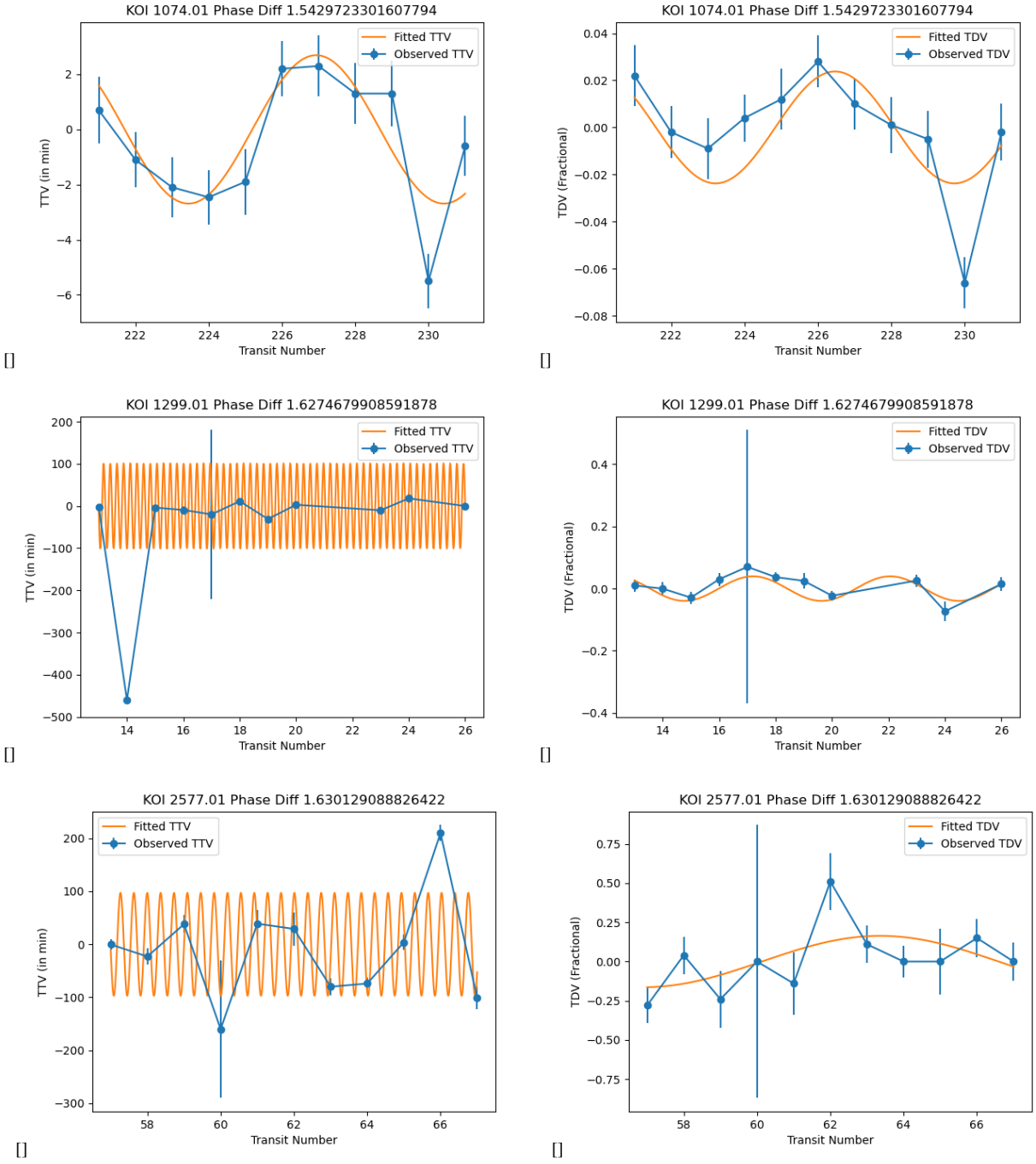

Figure A14. (a) Fitted TTV signals (Y) against Transit number (X) (orange) and data points along with errorbars (blue) (b) Fitted TDV signals (Y) against Transit number (X) (orange) and data points along with errorbars (blue)

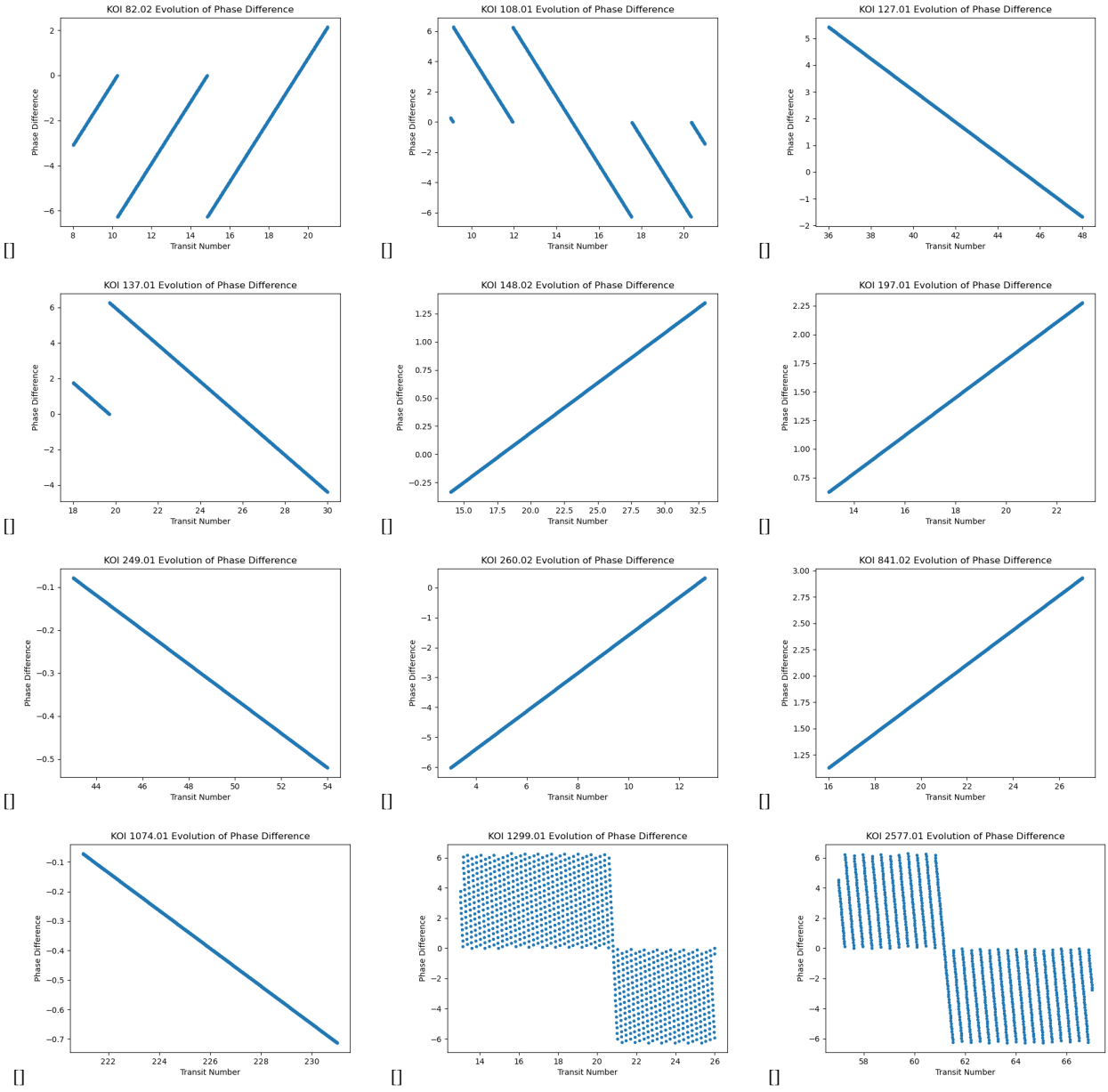

Figure A15. Variation of Phase Difference between TTV and TDV over Transit Number

View publication stats

2021 1st International Conference on Power Electronics and Energy (ICPEE-2021).

Control of Two-Stage OFF-Board Electric Vehicle Charger

Aakash Kumar Seth*
Electrical Engineering Department
Delhi Technological University
Delhi, India
akrseth@gmail.com

Mukhtiar Singh
Electrical Engineering Department
Delhi Technological University
Delhi, India
smukhtiar_79@yahoo.co.in

2021 1st International Conference on Power Electronics and Energy (ICPEE) | 978-1-7281-8774-7/21/$31.00 ©2021 IEEE | DOI: 10.1109/ICPEE50452.2021.9358732

Abstract— **Due to the population rise of EV, numbers of off-board electric vehicle (EV) chargers are increasing in worldwide. The larger quantity of EV chargers connected to utility grid may affect the supply quality if operate by improper control. This paper shows a control development of two stage OFF board EV charger which can work in all possible active (*P*)-reactive (*Q*) power cases. The performance of controller is evaluated in eight modes including charging and reactive power compensation. The charger charges the battery pack as per desired by user and compensate the reactive power if requested by utility grid. The charger comprises of two bidirectional stages i.e. first (AC to DC) and second (DC to DC) conversion stages. A simulation based study has been presented of a 12.5 KVA EV charger using MATLAB/Simulink toolbox. Further, the claims are verified in real time using *dSPACE 1104*.**

Keywords— **Battery Charger controller, Reactive Power Compensation, Proportional Integral Controller, AC-DC power Conversion.**

I. INTRODUCTION

Electric vehicles have gained lot of popularity in last two decades because of increasing pollution and greenhouse emissions from burning of fossil fuels and also to deal with growing energy needs. EVs provide an alternative to reduce fossil fuel consumption. Several researches have been done but EV has yet to gain wide acceptance [1]-[4].

Battery and its charging technology is an important part for EV [5]. To overwhelmed from the issue of short driving range, fast charging is adopted during short stops that charge battery from 20-80% of nominal capacity [6]. However, fast charging suffers from the cost of charger, battery technology and their effects on grid power quality [7].

There are several classifications for charging topologies presented in literature [8]-[9]. Firstly, charging can be two types i.e. OFF board and ON board [4]. The infrastructure installed on EV itself is known as ON board charging and used for lower power levels whereas OFF board charging is installed separately and can support fast charging up to hundreds of kiloWatts (kW). Further based on charging power levels, charging can be level-1, 2 and 3 [8]. Level-1 charging is low power charging and can be done through power outlets available in our houses. Level-2 charging is used for both public and private and it takes less time to charge the battery pack than level-1. Level-3 charging is fastest method of charging and used commercially. Charging systems can be unidirectional or bidirectional. Also they can be two-stage or single stage [9]. In two-stage EV charger, two converters i.e. AC to DC (first stage) and DC to DC (second stage) are connected in cascade. The second stage converter reduces the ripple at battery side and provides galvanic isolation between grid and battery pack [10].

978-1-7281-8774-7/21/$31.00 ©2021IEEE

Unidirectional topology of charger can only transfer power from utility grid to vehicle (G2V) whereas, bidirectional chargers have additional advantage of operation of vehicle to grid (V2G) mode in which power can be transferred from vehicle to grid whenever required [11]. Apart from active power transfer, a bidirectional EV charger can provide reactive power support in lagging or leading operation. If EVs are used to compensate reactive power, cost of compensators like capacitor banks and static VARs will go down. This mode of EV charger is called vehicle for grid (V4G) [12].

Large numbers of EVs connected to grid may create fluctuations in voltage and frequency because of improper control. Therefore, suitable control techniques are required. Regarding the control of power converters, various types of control strategies have been presented in literature and mainly these are based on model predictive control (*MPC*), proportional plus integral (*PI*), hysteresis, direct power control (*DPC*), proportional resonant (*PR*) control [13]-[19]. *PI* control is simple to design and desired values can be attained accurately with removal of steady state error.

Among the various control techniques, a controller based on conventional *PI* regulator for two-stage OFF board EV charger is presented here. The charger comprises of a fully controlled three-phase AC to DC converter trailed by a buck boost DC to DC converter which is bidirectional. Both the conversion stages can work in positive as well as negative side of *P-Q* power plane. In presented control strategy, four quantities are controlled namely, real-reactive power (*P-Q*), battery current (I_{bat}) and DC link voltage (V_{dc}). Therefore, two separate controllers have been included each for both stages. The control

Authorized licensed use limited to: DELHI TECHNICAL UNIV. Downloaded on March 03,2021 at 06:04:43 UTC from IEEE Xplore. Restrictions apply.

of AC-DC converter consist two loops i.e. outer (P and Q) control and inner one for AC side current control. In outer loop, active and reactive power is regulated by utilizing two individual *PI* controllers. The outputs of outer power loop will generate reference of active (I_d^*) and reactive current component (I_q^*), respectively. These reference currents are in *dq* domain. Furthermore, these two current components are compared with the actual active and reactive current components of grid current and two *PI* controllers are employed to minimize the mismatch between them in inner current loop. The decoupling terms i.e. ($-I_d \cdot \omega L + V_q$) and ($I_q \cdot \omega L + V_d$) are added in output of reactive and active current control loop, respectively. To produce the active and reactive duty ratios, both the quantities are divided by DC link voltage. A *dq-abc* transformation is done to develop the duty cycle for all three phases, after that pulses of first stage are generated by recognized pulse width modulation (PWM) technique. In the control design of DC to DC (second stage) converter, two quantities are regulated i.e. battery current (I_{bat}) and DC-link voltage (V_{dc}). This controller also has two loops, where in outer loop the reference and actual DC link voltage (V_{dc}^*) is compared and error is minimized by *PI* controller. The outer loop generates the reference battery current (I_{bat}^*) and equated with actual value and controlled in inner loop by *PI* controller. Therefore, four reference quantities, P, Q, V_{dc} and I_{bat} are commanded to the controller. Furthermore, the MATLAB software is utilized to simulate EV charger model and total eight modes have been executed to examine the performance of controller. Moreover, a real time system is also made to verify the performance of controller.

II. System Configuration and Modes of Operation

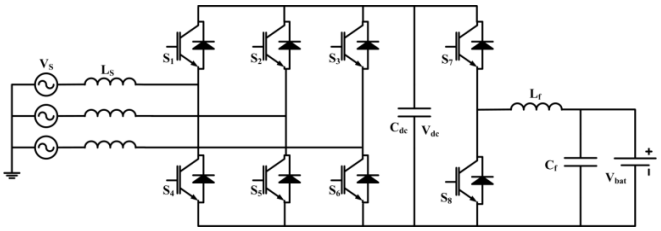

Fig. 1. Two-Stage EV Charger.

Fig. 1 shows the system architecture having AC-DC (first) and DC-DC (second) power alteration stages. Both the converters are based on insulated gate bipolar transistor (IGBT). The AC-DC stage consist six IGBTs and two in DC-DC stage. Each switch has voltage blocking limit is V_{dc}. The first stage is directly linked to the three-phase grid and battery is connected across the second stage. The charger architecture is capable to operate in all possible active-reactive power commands cases as shown in Fig. 2.

Here, charging/discharging of battery is shown in mode 1 and 2 respectively, where positive active power means power is transfer to the battery and vice versa. The current is in and out of phase while charging and discharging, respectively. Mode 3 and 4 shows reactive power operation only, where the current is lagging and leading, respectively. Similarly, the power factor depends upon the simultaneously operation of EV charger as discussed in rest four modes.

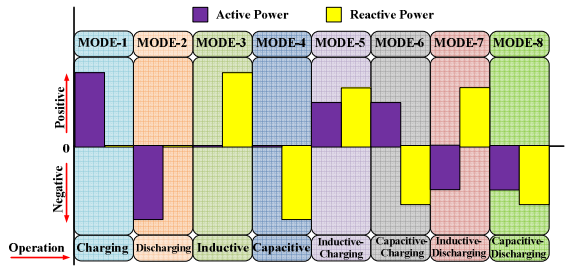

Fig. 2. Possible Operation of bidirectional EV Charger.

III. Controller Development

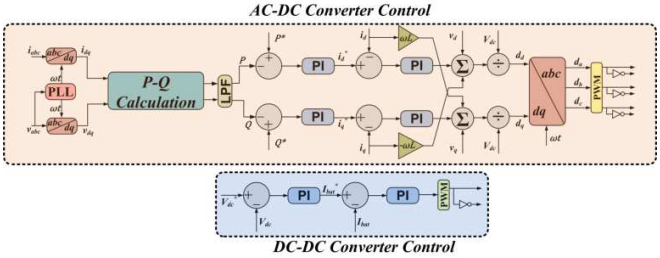

Fig. 3. EV Charger Controller.

AC-DC Converter Control

Here, the first task is to calculate active-reactive power at the AC side of EV charger in *dq* domain. For this, transformation from *abc* to *dq* domain is done through the park transformation. This is given as [20]:

$$\begin{bmatrix} V_d \\ V_q \end{bmatrix} = \begin{bmatrix} \sin(\omega t) & \sin(\omega t - 2\frac{\pi}{3}) & \sin(\omega t + 2\frac{\pi}{3}) \\ \cos(\omega t) & \cos(\omega t - 2\frac{\pi}{3}) & \cos(\omega t + 2\frac{\pi}{3}) \end{bmatrix} \times \begin{bmatrix} V_a \\ V_b \\ V_c \end{bmatrix} \quad (1)$$

$$\begin{bmatrix} I_d \\ I_q \end{bmatrix} = \begin{bmatrix} \sin(\omega t) & \sin(\omega t - 2\frac{\pi}{3}) & \sin(\omega t + 2\frac{\pi}{3}) \\ \cos(\omega t) & \cos(\omega t - 2\frac{\pi}{3}) & \cos(\omega t + 2\frac{\pi}{3}) \end{bmatrix} \times \begin{bmatrix} I_a \\ I_b \\ I_c \end{bmatrix} \quad (2)$$

The P and Q are calculated directly from *dq* component of grid current and voltage as follows:

$$P = \frac{3}{2}\left(V_d I_d + V_q I_q\right) \quad (3)$$

$$Q = \frac{3}{2}\left(V_q I_d - V_d I_q\right) \quad (4)$$

Now, these P and Q are compared with reference active (P^*)-reactive (Q^*) power and the errors are minimized by *PI* regulators. Theses *PI* regulators will generate the references of active (i_d^*)-reactive (i_q^*) current components in *dq* domain respectively as follows.

$$i_d^* = \left(K_{p1} + \frac{K_{i1}}{s}\right) \times (P^* - P) \quad (5)$$

$$i_q^* = \left(K_{p2} + \frac{K_{i2}}{s}\right) \times (Q^* - Q) \quad (6)$$

Here, K_{p1}, K_{p2}, K_{i1} and K_{i2} are proportional and integral constants for controllers tracking real and reactive powers respectively.

Further, similar *PI* loops are obtained for current control in inner loop. In this, two separate *PI* regulators are utilized to track i_d^* and i_q^*. The output of *PI* regulators are added in decoupling terms (±ωL) and after that divided by V_{dc}. Finally, duty ratio is obtained in *dq* frame as follows:

Authorized licensed use limited to: DELHI TECHNICAL UNIV. Downloaded on March 03,2021 at 06:04:43 UTC from IEEE Xplore. Restrictions apply.

$$\begin{bmatrix} d_d \\ d_q \end{bmatrix} = \frac{1}{V_{dc}} \begin{bmatrix} e_d + v_d + 3\omega L_s \times i_q \\ e_q + v_q - 3\omega L_s \times i_d \end{bmatrix} \quad (7)$$

To generate the pulses for AC-DC conversion stage, the duty ratios are converted into *abc* frame and passed through the well-known PWM technique.

$$\begin{bmatrix} D_a \\ D_b \\ D_c \end{bmatrix} = \sqrt{\frac{2}{3}} \begin{bmatrix} \sin \omega t & \cos \omega t \\ \sin\left(\omega t - \frac{2\pi}{3}\right) & \cos\left(\omega t - \frac{2\pi}{3}\right) \\ \sin\left(\omega t + \frac{2\pi}{3}\right) & \cos\left(\omega t + \frac{2\pi}{3}\right) \end{bmatrix} \begin{bmatrix} d_d \\ d_q \end{bmatrix} \quad (8)$$

DC-DC Converter Control

The quantities to be controlled in second stage of EV charger are battery pack current (I_{bat}) and DC-link voltage (V_{dc}). To design this control, two *PI* regulators are utilized. In outer loop, DC-link voltage is equated with desired reference value and regulated by *PI* controller. This *PI* controller produces the reference battery current and regulated in inner control loop. Now, this inner loop controller produces the duty cycle and pulses are generated through PWM technique.

$$i^*_{bat} = \left(K_{p5} + \frac{K_{i5}}{s}\right) \times (V^*_{dc} - V_{dc}) \quad (9)$$

$$d_{DC-DC} = \left(K_{p6} + \frac{K_{i6}}{s}\right) \times (i^*_{bat} - i_{bat}) \quad (10)$$

IV. Simulation Results

The system discussed above is designed in MATLAB/Simulink toolbox and parameters are enumerated in below Table I. Here, 600 V reference of DC-link voltage is selected and nominal voltage of EV battery pack is taken as 350 V. To claim the performance of controller, a simulation with different *P* and *Q* commands has been developed as listed in table II. In this, the initial two modes are related with charge-discharge of EV battery and next two modes are showing reactive power operation only. Rest four modes are related with both active-reactive operations simultaneously.

TABLE I
System Parameters

PARAMETER	SYMBOL	VALUE
kVA rating of charger	S	12.5 kVA
Grid voltage	V_s	400V
Supply frequency	f	50 Hz
Line inductors	L_s	4 mH
DC link capacitor	C_{dc}	1100 µF
Battery voltage	V_{bat}	370V

TABLE II
Simulation Situation

# Mode	P (KW)	Q (KVAR)	S (KVA)	PF	Time (sec)
1	12.5	0	12.5	1	0-3
2	-12.5	0	12.5	-1	3-6
3	0	12.5	12.5	0	6-9
4	0	-12.5	12.5	0	9-12
5	10	7.5	12.5	+ 0.8	12-15
6	7.5	-10	12.5	- 0.6	15-18
7	-5.5	11.2	12.5	+ 0.44	18-21
8	-11.2	-5.5	12.5	- 0.89	21-24

Battery voltage (V_{bat}), Battery current (I_{bat}), V_{dc}, grid side current and Real-reactive powers are shown in Fig 4 during all the modes. The run time of each operating mode is three seconds. The negative value of battery current shows charging and positive value shows discharging while battery voltage is positive for all cases.

In mode 1, reactive power is zero and it shows charging operation as battery current is negative. In mode 2, reactive power is still zero and battery current is positive, thus it is discharging case. The real power is zero in mode 3 and 4 and reactive powers are positive and negative respectively, thus they show reactive-inductive/capacitive operations. Mode 5 shows inductive charging operation and mode 6 shows capacitive charging operation. The mode 7 and 8 shows inductive and capacitive discharging operation respectively.

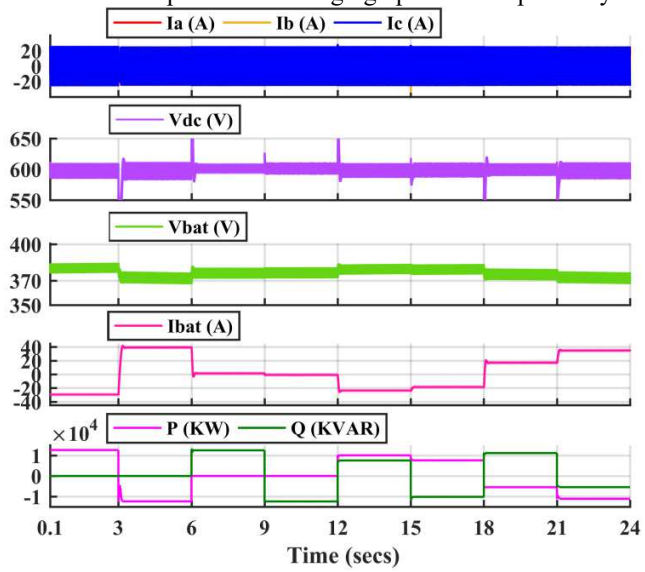

Fig. 4. Simulation results of *P-Q*, battery current (I_{bat}), battery voltage (V_{bat}) and DC-link voltage (V_{dc}), grid current.

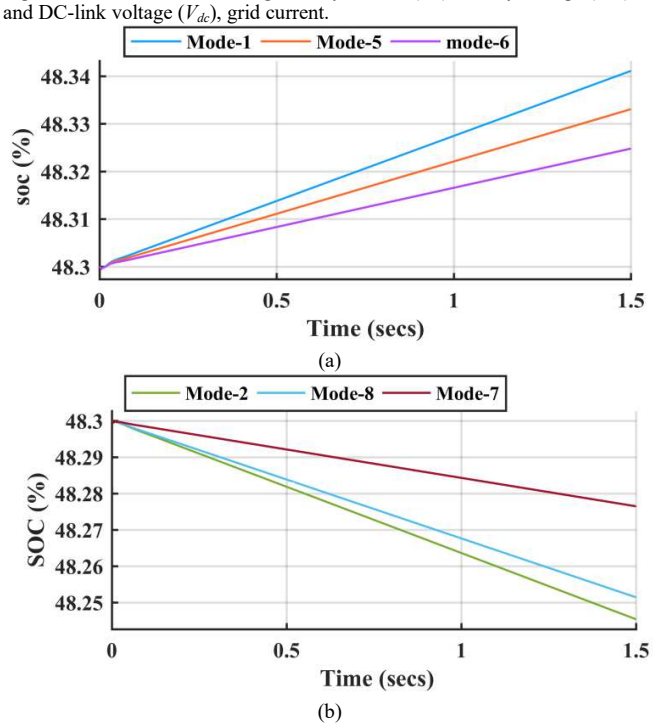

Fig. 5. SOC during (a) mode-1, 5 and 6, and (b) mode-2, 7 and 8.

Authorized licensed use limited to: DELHI TECHNICAL UNIV. Downloaded on March 03,2021 at 06:04:43 UTC from IEEE Xplore. Restrictions apply.

The variations of SOC with different charging-discharging rate are shown in Fig 5 (a) and (b). It can observe that the SOC increases faster in mode-1 and slower in mode-6 as the active power supply to EV battery pack is higher in mode-1. Similarly, SOC decreases faster in mode-2 and slower in mode-7 as amount of active power supplied by battery is higher in mode-2.

During mode 1, current and voltage of phase *a* are in same phase as presented in Fig 6. As charger shifts from mode 1 to mode 2, current I_a becomes completely out of phase with voltage V_a as shown in Fig. 6. As charger shifts from mode 2 to mode 3, current I_a changes from out of phase of voltage V_a to 90 degrees lagging behind voltage as indicted in Fig. 6. In the course of changeover from mode 3 to 4, current I_a transpose from 90 degrees lagging behind voltage V_a to 90 degrees leading as shown in Fig. 7. This indicates that charger shifts from reactive-inductive to reactive-capacitive operation. In mode 5, charger is in inductive charging state, and thus current I_a lags voltage V_a by some angle as indicated in Fig. 8. In transition from mode 5 to 6, current I_a changes from lagging to leading the voltage V_a. This indicates capacitive charging in mode 6. In transition from mode 6 to 7, current I_a shifts to lagging behind Voltage V_a by an angle greater than 90 degrees as shown in Fig. 8. In transition from mode 7 to 8, current changes to lagging behind voltage by an angle greater than 180 degrees as depicted in Fig. 9.

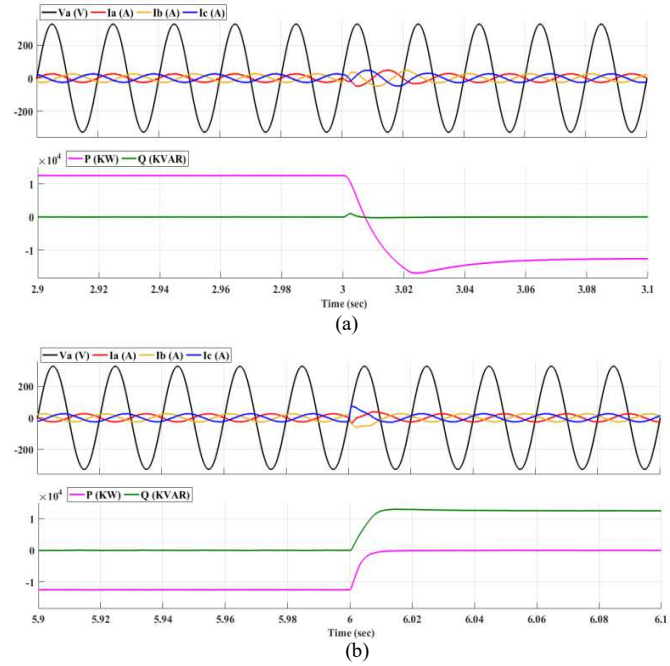

(a)

(b)

Fig. 6. Changeover (a) Mode 1 to 2 and (b) Mode 2 to 3.

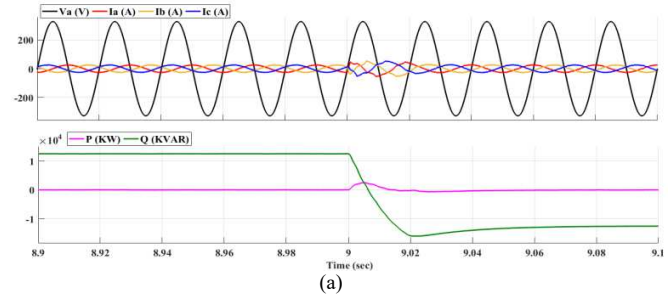

(a)

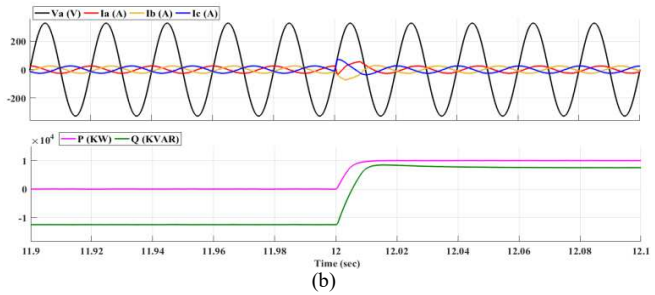

(b)

Fig. 7. Changeover (a) Mode 3 to 4 and (b) Mode 4 to 5.

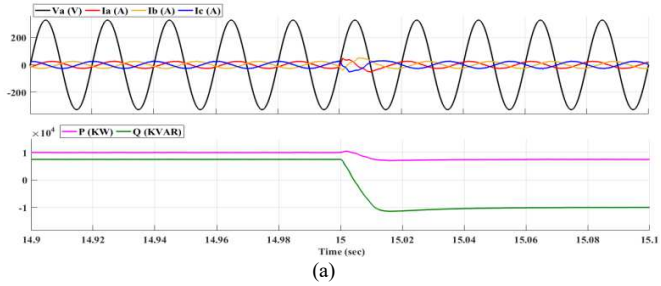

(a)

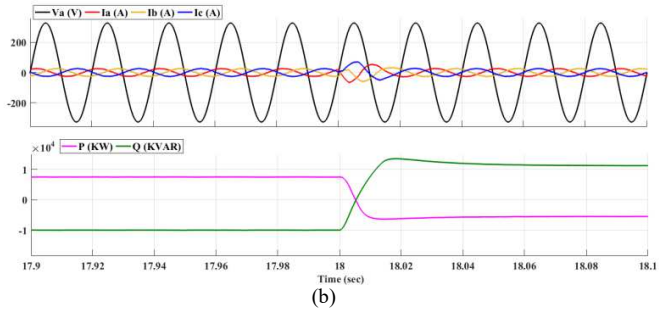

(b)

Fig. 8. Changeover (a) Mode 5 to 6 and (b) Mode 6 to 7.

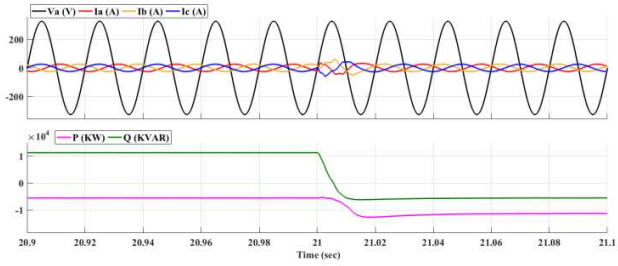

Fig. 9. Changeover from Mode 7 to 8.

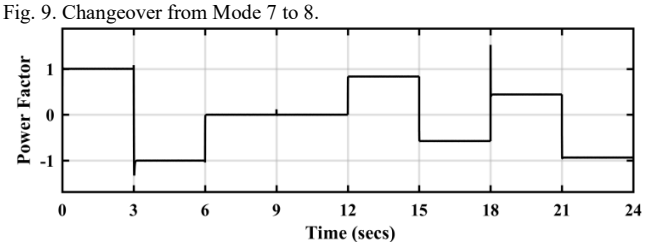

Fig. 10. Power Factor During All Modes.

Fig. 10 shows the power factor during all the working modes. The positive and value shows the lagging and leading power factor, respectively.

The results of proposed controller shows fast dynamics and zero steady state error. Moreover, it can be seen from the results that the charger operation will not affect grid power quality in any of working mode.

Authorized licensed use limited to: DELHI TECHNICAL UNIV. Downloaded on March 03,2021 at 06:04:43 UTC from IEEE Xplore. Restrictions apply.

V. Experimental Results

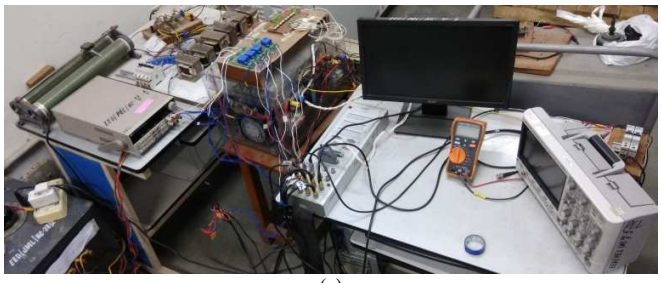

(a)

(b)

Fig. 10. (a) Hardware Prototype and (b) Battery Pack

Fig. 10 depicts the experimental setup of a 500 VA two stage OFF-board charger. Both the converters are made up of semikron IGBT leg which having skyper gate driver circuit. A *dSPACE 1104* is utilized to generate the pulses for both converters, however a TLP-350 optocoupler is used for providing isolation between *dSPACE* and converters. A 96 V battery pack is build up by connecting eight 12 V battery in series.

TABLE III
Hardware Scenario

# Mode	P (W)	Q (VAR)	S (VA)	PF
1	500	0	500	1
2	-500	0	500	-1
3	0	500	500	0
4	0	-500	500	0
5	400	300	500	+0.8
6	300	-400	500	-0.6
7	-200	458.3	500	+0.4
8	-458.3	-200	500	-0.9

Fig. 11 shows the hardware prototype results of above discussed controller with the variations as listed in Table III. The Fig. 11 (a) shows the changeover between mode 1 and 2. The phase angle is zero and 180° in mode 1 and 2 respectively. This shows that in mode 1 the charger works under battery charging mode and discharging in mode-2. Since, the phase angle is exactly 90° lagging and leading in mode 3 and 4 respectively, there is only reactive power operation occurs as depicted in Fig. 11 (b). Mostly, the EV charger works under mode 5 and 6 in which charger is supply reactive power and simultaneously charge the battery pack. The power factor in these modes depends on amount of active-reactive power supplied by charger. Here, the P is 400 W and Q is 300 VA in mode-5 and 300 W, 400 VA in mode-6 and the changeover is shown in Fig. 11 (c). Similarly, battery is discharging at the rate of 200 W in mode-7 while compensating 458.3 VA inductive reactive power. In mode-8, the active-reactive operation is swapped and battery is discharging at the rate of 458.3 W while compensating 200 VA of capacitive reactive power. The changeover between the mode-7 and 8 is depicted in Fig. 11 (d).

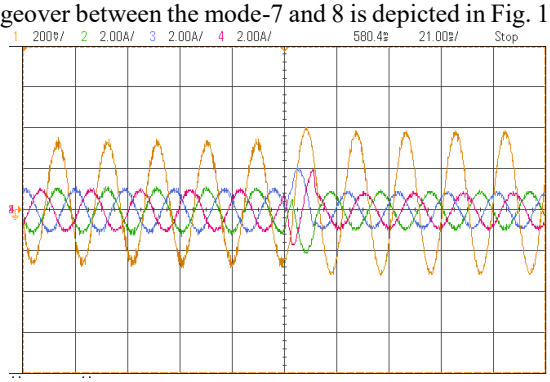

(a)

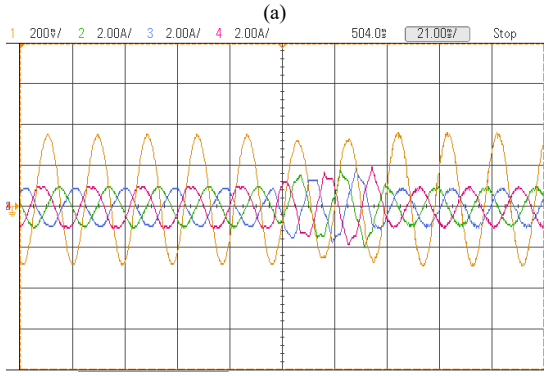

(b)

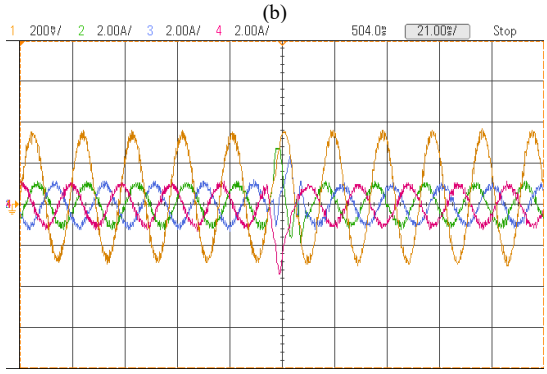

(c)

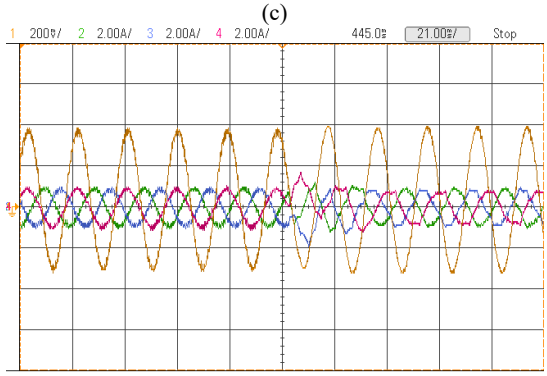

(d)

Fig. 11. Changeover between mode (a) 1 to 2, (b) 3 to 4, (c) 5 to 6, and (d) 7 to 8.

VI. Conclusion

This paper presents the control design of dual stage OFF board EV charger. This EV charger controller receives active and reactive command and work at desired power factor. The

Authorized licensed use limited to: DELHI TECHNICAL UNIV. Downloaded on March 03,2021 at 06:04:43 UTC from IEEE Xplore. Restrictions apply.

performance has been verified in all possible modes in *P-Q* plane where it is found that the controller works very-well in all modes. The charger is capable to compensate reactive power within the limit of charger's rating along with fast charging ability. A 12.5 KVA EV charger is simulated in MATLAB where the battery SOC is taken 50% so that charging/discharging operation can be observed. Consequently, the paper shows the optimal utilization of an EV charger and reduces line losses by compensating reactive power at the load end.

REFERENCES

[1] D. Gautam, F. Musavi, M. Edington, W. Eberle, and W. G. Dunford, "A zero voltage switching full-bridge dc-dc converter with capacitive output filter for a plug-in-hybrid electric vehicle battery charger," in Proc. IEEE Applied Power Electronics Conf. and Expo., 2012, pp. 1381-1386.

[2] P. Ramadass, B. Haran, R. White, and B. Popov, "Performance study of commercial LiCoO2 and spinel-based Li-ion cells," Journal of Power Sources, vol. 111, no. 2, pp. 210–220, April 2002.

[3] P. A. Cassani and S. S. Williamson, "Feasibility analysis of a novel cell equalizer topology for plug-in hybrid electric vehicle energy-storage systems," IEEE Trans. on Vehicular Technology, vol. 58, no. 8, pp. 3938-3946, Oct. 2009.

[4] A. K. Rathore and U. R. Prasanna, "Comparison of soft-switching voltage-fed and current-fed bi-directional isolated dc/dc converters for fuel cell vehicles," in Proc. IEEE International Symp. on Industrial Electronics, 2012, pp. 252-257.

[5] F. R. Salmasi, "Control strategies for hybrid electric vehicles: Evolution, classification, comparison, and future trends," IEEE Trans. Veh. Technol., vol. 56, no. 5, pp. 2393–2404, Sep. 2007.

[6] C. C. Chan, "The state of the art of electric, hybrid, and fuel cell vehicles," Proc. IEEE, vol. 95, no. 4, pp. 704–718, Apr. 2007.

[7] A. Khaligh and Z. Li, "Battery, ultracapacitor, fuel cell, and hybrid energy storage systems for electric, hybrid electric, fuel cell, and plug-in hybrid electric vehicles: State of the art," IEEE Trans. Veh. Technol., vol. 59, no. 6, pp. 2806–2814, Jul. 2010.

[8] M. Yilmaz and P. T. Krein, "Review of battery charger topologies, charging power levels and infrastructure for plug-in electric and hybrid vehicles," *IEEE Trans. Power Electron.*, vol. 28, no. 5, pp. 2151–2169, May 2013.

[9] P. Asthana and V. Verma, "PV Fed Current Controlled Low Stress High Gain Converter for Battery Charging Applications," 2020 IEEE International Conference on Power Electronics, Smart Grid and Renewable Energy (PESGRE2020), Cochin, India, 2020, pp. 1-4.

[10] S. S. Williamson, A. K. Rathore and F. Musavi, "Industrial Electronics for Electric Transportation: Current State-of-the-Art and Future Challenges," in *IEEE Transactions on Industrial Electronics*, vol. 62, no. 5, pp. 3021-3032, May 2015.

[11] C. C. Chan, A. Bouscayrol, and K. Chen, "Electric, hybrid, and fuel-cell vehicles: Architectures and modeling," IEEE Trans. Veh. Technol., vol. 59, no. 52, pp. 589–598, Feb. 2010.

[12] K. Clement-Nyns, E. Haesen, and J. Driesen, "The impact of charging plug-in hybrid electric vehicles on a residential distribution grid," *IEEE Trans. Power Syst.*, vol. 25, no. 1, pp. 371–380, Feb. 2010.

[13] A. Khaligh and S. Dusmez, "Comprehensive topological analysis of conductive and inductive charging solutions for plug-in electric vehicles," *IEEE Trans. Veh. Technol.*, vol. 61, no. 8, pp. 3475–3489, Oct. 2012.

[14] D. B. Wickramasinghe Abeywardana, P. Acuna, B. Hredzak, R. P. Aguilera and V. G. Agelidis, "Single-Phase Boost Inverter-Based Electric Vehicle Charger With Integrated Vehicle to Grid Reactive Power Compensation," in IEEE Transactions on Power Electronics, vol. 33, no. 4, pp. 3462-3471, April 2018.

[15] A. K. Seth and M. Singh, "Resonant controller of single-stage off-board EV charger in G2V and V2G modes," in *IET Power Electronics*, vol. 13, no. 5, pp. 1086-1092, 8-4-2020.

[16] P. Cortés, J. Rodríguez, P. Antoniewicz, and M. Kazmierkowski,"Direct power control of an AFE using predictive control," *IEEE Trans. Power Electron.*, vol. 23, no. 5, pp. 2516–2523, Sep. 2008.

[17] T. He, J. Zhu, D. D. Lu and L. Zheng, "Modified Model Predictive Control for Bidirectional Four-Quadrant EV Chargers With Extended Set of Voltage Vectors," in *IEEE Journal of Emerging and Selected Topics in Power Electronics*, vol. 7, no. 1, pp. 274-281, March 2019.

[18] X. Zhou, S. Lukic, S. Bhattacharya and A. Huang, "Design and control of grid-connected converter in bi-directional battery charger for Plug-in hybrid electric vehicle application," 2009 IEEE Vehicle Power and Propulsion Conference, Dearborn, MI, pp. 1716-1721, 2009.

[19] M. C. Kisacikoglu, B. Ozpineci, and L. M. Tolbert, "Examination of a PHEV bidirectional charger for V2G reactive power compensation," in Proc. IEEE APEC Expo., Palm Springs, CA, USA, Feb. 21–25, pp. 458–465, 2010.M. Hartmann, T. Friedli, and J.W. Kolar, "Three-phase unity power factor mains interfaces of high power EV battery charging systems," in *Proc. ECPE Workshop Power Electron. Charging Elect. Veh.*, Valencia, Spain, Mar. 21–22, 2011, pp. 1–66.

[20] Amirnaser Yazdani, Reza Iravani, "Voltage-Sourced Converters in Power Systems : Modeling, Control, and Applications," Wiley-IEEE Press, Feb. 2010.

Authorized licensed use limited to: DELHI TECHNICAL UNIV. Downloaded on March 03,2021 at 06:04:43 UTC from IEEE Xplore. Restrictions apply.

Polymer Bulletin
https://doi.org/10.1007/s00289-021-03634-9

ORIGINAL PAPER

Controlled release and release kinetics studies of boron through the functional formulation of carboxymethyl tamarind kernel gum-based superabsorbent hydrogel

Khushbu[1] · Sudhir G. Warkar[1] · Nandkishore Thombare[2]

Received: 30 November 2020 / Revised: 30 January 2021 / Accepted: 27 February 2021
© The Author(s), under exclusive licence to Springer-Verlag GmbH Germany, part of Springer Nature 2021

Abstract

The novel Boron micronutrient-loaded superabsorbent hydrogel (BSH) was synthesized via *in situ* mechanism having carboxymethyl tamarind kernel gum (CMTKG) as its principle component. The synthesis was established by thermal gravimetric analysis examination, scanning electron microscopy micrographs studies, and Fourier transform infrared analysis. The influence of various solvents, such as standard saline solution, different pH solutions (4, 9, 12), and distilled water on the swelling degree of BSH, was examined. Out of all the mentioned solvents, the highest swelling degree was noticed by the distilled water (465 g/g). The BSH was also examined for the agricultural application to assess the release of the boron micronutrient. It was established by studying and calculating the release behavior pattern along with the release kinetics of BSH in water, and as well in soil. It is significant to note that in soil, BSH exhibited 20.07% for the 1st day which notably increased to 76.17% on the 80th day. Release kinetic studies suggested that the Korsmeyer–Peppas model fitted the best out of all the models used, in the case of water, which also revealed that the release of boron from BSH was independent of the polymeric network as it followed Fickian diffusion mechanism. However, in the case of soil, the release was observed to follow the Higuchi model. The half-life and time period for the release of 95% and 99% were calculated as per the Olson's single exponential model, to predict the pattern of boron release from developed BSH formulation. Release time for 99% boron in the soil, 274 days (with a half-life of 38 days), was found higher than in water, 9.33 days (with a half-life of 1.29 days). Thus, moisture-retaining BSH also successfully revealed slow boron release behavior.

Keywords Boron · Micronutrient · Agriculture · Release kinetic · Soil conditioner · Superabsorbent hydrogel

✉ Sudhir G. Warkar
sudhirwarkar@gmail.com

Extended author information available on the last page of the article

Published online: 09 March 2021

Introduction

With increasing inhabitants on the surface of the earth, demands for the resurgence of resources are on a very high scale. One of the consequences of this demand is from the areas of arid regions. These regions tend to receive less water than expected, as we witness the wearing out of fluid resources from our earth. Agriculture holds the top priority of problems as a civilization grows around areas rich in agriculture. Adequate water supply is a must for plant growth [1–4]; however, only water is not sufficient as micronutrients can promote the growth of plants [5–8]. Therefore, water and micronutrient are two essential necessity of plant growth [9].

Micronutrients are the vital input substances for the continuous growth of crop production and play a significant role in food security [10]. Boron is one such micronutrient critical to the health and growth of all crops [11–14]. It plays a vital role in a diverse range of plant functions including cell wall formation and stability, maintenance of structural and functional integrity of biological membranes, movement of sugar or energy into growing parts of plants, and pollination and seed set. Adequate boron is also required for effective nitrogen fixation [15–17]. Studies showed that adequate boron nutrition improves the root uptake of phosphorous and potassium. Since it is required in small amounts, traditional fertilizer blends containing boron struggle to achieve uniform nutrient distribution. Despite the need for this critical nutrient, boron is the second most widespread micronutrient deficiency problem worldwide after Zinc [18, 19].

Coming up with a solution to provide water along with boron micronutrient to those needy areas, we introduced superabsorbent hydrogels [20]. Superabsorbent hydrogels, as a carrier of micronutrients, have lately been used for the controlled release of nutrients to the plants in the soil [21].

A superabsorbent hydrogel is a tridimensional cross-linked polymeric network. They are highly absorbent structural units that can imbibe more than three hundred times of its weight in water [22]. Based on their special properties, they have been triumphantly applied in the horticulture and agriculture field to improve the physical properties of soil and reduce irrigation frequency [23, 24]. The combination of hydrogels and boron micronutrients could make the products have both water retaining properties and release of Boron. Also, limited literature is available regarding the work dealing with hydrogels as boron vehicle [25]. According to the research gaps and urgent need to supply boron micronutrient to the crops, and to our best information, CMTKG based hydrogel is being utilized for the time as a matrix for the controlled release of boron [26].

This research talks about the transformation of Carboxymethyl Tamarind Kernel Gum (CMTKG)-based superabsorbent hydrogels by in situ incorporations of boron source and its accomplishment as a carrier vehicle for boron micronutrient for the applications in the field of agriculture. The objectives of this research work were to examine through BSH: (i) the swelling degree at different media of pHs, distilled water, and saline solution; (ii) the release studies of boron in water; (iii) the release studies of boron in the soil; (iv) the release kinetics studies of both water and soil.

Materials and methods

Materials

Acrylic acid (AAc, CDH, New Delhi), boric acid (BA, Merck, Germany), EDTA (Sigma-Aldrich), 0.9% azomethine-H (Sigma-Aldrich) solution in 2% ascorbic acid (Merck, Germany), ammonium acetate (Sigma-Aldrich), acetic acid (Sigma-Aldrich), sodium hydroxide (Fischer Scientific, Mumbai), potassium persulfate (KPS, Fischer Scientific, Mumbai), and N,N'-methylenebisacrylamide (MBA, Merck, Germany) were used as received. CMTKG (0.20°) was graciously gifted by Hindustan Gum and chemicals ltd., Haryana, India. Distilled water was used for the preparation of solutions.

The SAS data was subjected to a one way analysis of variance (ANOVA) along with a post hoc LSD test to test the difference between treatments at 5% significance level.

Synthesis of BSH

The in situ technique was used to incorporation boron into CMTKG polymer based superabsorbent hydrogel. All the polymerization and cross-linking reactions took place at 25 °C. To start with, a beaker having distilled water (33.3 mL) along with CMTKG (1 gm) and sodium acrylate (399.9 mmol) was kept to stir for an hour on a magnetic stirrer. To this, a prefixed quantity of boric acid (183.2 mmol) was added followed by MBA (0.369 mmol), and KPS (1.22 mmol) which was further allowed to stir constantly for another one hour. Afterward, the whole mixture was then poured into the polypropylene tubes which were kept in a hot water bath oven for 2 h at 60 °C. Later on, the polypropylene tubes were cut and BSH was cut into small discs for further use [27]. These discs were first made to dry at room temperature for four days followed by drying at 55 °C in a vacuum oven (Fig. 1).

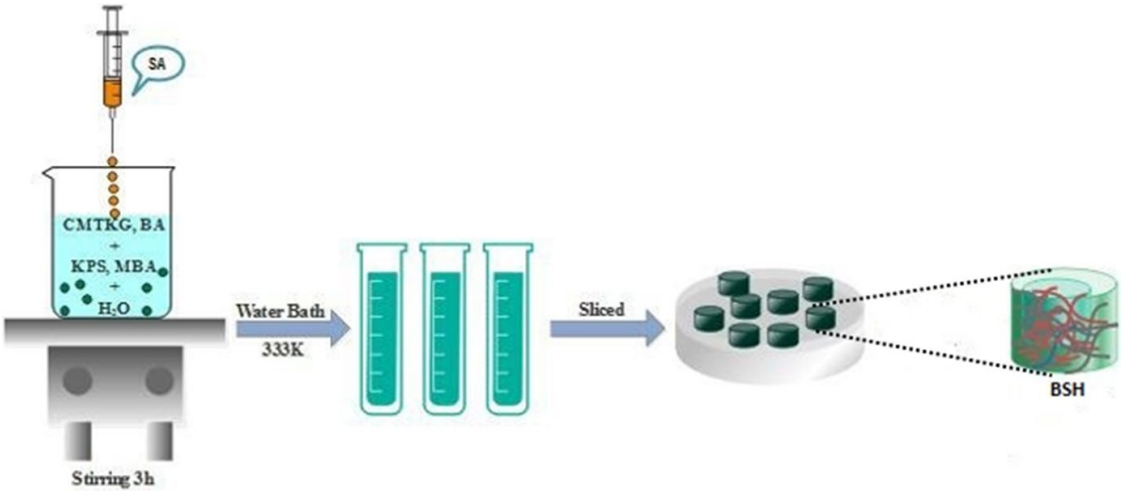

Fig.1 Pictorial representation of the synthesis of BSH

Characterization

FTIR spectroscopy

The FTIR (Fourier-transform Infrared) spectra of CMTKG, boric acid and BSH were recorded with the KBr pellet method. FTIR spectrophotometer of Model: PerkinElmer spectrum version 10.5.3 was used and the sample was taken in the solid phase.

Scanning electron microscopy (SEM)

The morphological investigation of CMTKG and BSH was performed by Scanning Electron Microscopy (SEM) (Model: JEOL JSM-6610LV).

Thermal analysis

The thermogravimetric analysis (TGA) of CMTKG and BSH was performed by the PerkinElmer TGA. The study was carried out with 10 °C/min of uniform heating rate and inert N_2 atmosphere (25–900 °C).

Swelling studies

Swelling studies of the synthesized BSH were done in triplicates. Completely dried BSH samples (0.2 g) were weighed and soaked in various media such as distilled water, 0.9% NaCl solution (standard saline solution), and pH solutions of 12, 9, and 4 (all the solutions were made by adding NaOH or HCl in dilute form).

After a prefixed time interval, once wiping off the surface water using a filter paper, the swollen BSH were weighed.

The calculation of the swelling degree was done using the following equation [28].

$$\text{Swelling degree} = \left(W_{sg} - W_{dg}\right) / W_{dg}$$

where, W_{sg} = weight of equilibrium swollen BSH, W_{dg} = initial weight of the dried BSH.

Applications of BSH as a boron micronutrient carrier

The BSH synthesized was examined for the agricultural application in order to study the controlled release of the boron micronutrient. It was established by calculating and studying the release behavior pattern along with the kinetics of BSH in water and as well in the soil for 72 h and 80 days, respectively. The composition of soil showed particle density 2.625 g/cm^3, bulk density 1.32 g/cm^3, and

carried slit & clay 0.7%, sand 89%, which was gathered from Delhi Technological University, New Delhi, India.

Release study of boron in water

A precisely weighed BSH was taken in nylon sieve bags (0.2 g, particle size: 150–200 mesh) and put into beakers carrying 1 L of water. At a regular interval of time namely, 0.5, 1, 3, 6, 9, 12, 24, 36, 48, and 72 h, 2 mL of solution was taken out. To this 2 mL solution, 0.5 mL of buffer solution (comprising EDTA, ammonium acetate, and acetic acid), and 0.5 mL of azomethine-H solution were added uniformly. It was then allowed to rest in a dark chamber for almost 30 min so as to attain total boron complexation [29]. This prepared sample solution, with the help of UV–vis spectrophotometer (Systronics UV–VIS spectrophotometer-117), was then analyzed for Boron concentration. The results were then compiled with respect to time in the form of a graph. All the release data were collected in triplicates.

Release study of boron in soil

In the plastic pots containing 0.2 kg soil (20 mesh), each non-woven bag carrying an accurately weighed BSH (200 mg, particle size: 150–200 mesh) were buried 5 cm below the surface of the soil. Throughout the study, samplings were done periodically (1, 3, 5, 10, 15, 20, 30, 40, and 80 days) while maintaining the moisture of the soil. The soil samples were taken out, post removing the non-woven bags, one by one at definite incubated time intervals. These soil samples then dried in an oven at 100 °C overnight and weighed. 10 g of each soil samples were treated with 20 ml of distilled water along with 0.25 g of activated charcoal and filtered through Whatman No. 42 filter paper once it was boiled for 5 min on a hot plate [30]. For UV–VIS measurements, the above-extracted solution along with buffer solution, and azomethine-H solution were used. All the release data of boron concentrations were collected in triplicates.

Release kinetic studies of BSH in water and soil

Several mathematical models including the Korsmeyer–Peppas Model have been reported over the period of time for estimating the release of an active agent from superabsorbent hydrogel as a function of time.

Boron release data, in case of water studies as well as in case of soil studies, were fitted to different forms of mathematical kinetic models for understanding boron-slow release mechanism namely, Korsmeyer–Peppas model [31], first-order equation [32], and Higuchi model [33, 34], Olson model [35]. All these models' data are tabulated in Table 1, 2. The coefficient of determination (R^2) was kept as the grounds for differentiating the data for the best fit model. The model having the highest R^2 value is considered as the best fit model.

Table 1 Mathematical models used for the released kinetics from BSH

Model	Proposed Mechanism	Equation	Water		Soil		Ref
			n	R^2	n	R^2	
Korsmeyer–Peppas	Fickian Diffusion ($n < 0.5$) Non-Fickian Diffusion ($0.89 \geq n \geq 0.45$) Super case II	$\frac{M_t}{M_\infty} = kt^n$ k = kinetic constant n = diffusion exponent	0.35	0.99	0.31	0.88	[31]
First Order	Rate is dependent on the concentration of one reactant only	$\log\left(1 - \frac{M_t}{M_0}\right) = k_1 \cdot \frac{t}{2{\cdot}303}$ K_1 = release rate constant	–	0.89	–	0.82	[32]
Higuchi	Fickian Diffusion	$\frac{M_t}{M_\infty} = k_H t^{\frac{1}{2}}$ k_H = kinetic constant	–	0.98	–	0.94	[33, 34]

Table 2 Relative time period (days) for the released amount of boron from BSH

	Olson equation	R^2	k	T_{50}	T_{95}	T_{99}
Water	$y = 17.618e^{0.527x}$	0.80	0.0224	1.29	5.60	9.33
Soil	$y = 21.813e^{0.018x}$	0.88	0.0183	38.08	164.84	274.72

Results and discussion

Synthesis of novel BSH

In an effort to fabricate BSH, CMTKG based cross-linked network (SH) was used to incorporate boron via the *in-situ* mechanism, in the form of boric acid. The hypothetical incorporation of boric acid in the three-dimensional network of SH is illustrated through Fig. 2.

Characterization

FTIR spectroscopy

FTIR spectra of CMTKG, boric acid, and BSH are shown in Fig. 3. CMTKG showed symmetric vibrations (1415 cm^{-1}) and asymmetric vibrations (1631 cm^{-1}) for $–COO^-$ group. It also showed significant and broad band (3428 cm^{-1}) for –OH stretching. In BSH FTIR spectrum, –OH stretching vibration was at around 3418 cm^{-1}, while symmetric vibrations and asymmetric vibrations for $–COO^-$ group around 1410 cm^{-1} and 1568 cm^{-1}, respectively [36]. Also, sharp peak (1568 cm^{-1}) was observed for the C=O bond related to SA, whereas CMTKG skeleton validated by the peaks shown at 627 cm^{-1} and 1039 cm^{-1}. The cross-linked took place between CMTKG and SA by MBA can be attributed to the broad band at 627 cm^{-1} (O=C–N bond) and a peak at 1317 cm^{-1} (C–N bond) [37]. It is significant to mention that no notable peak was observed in the FTIR spectra of BSH related

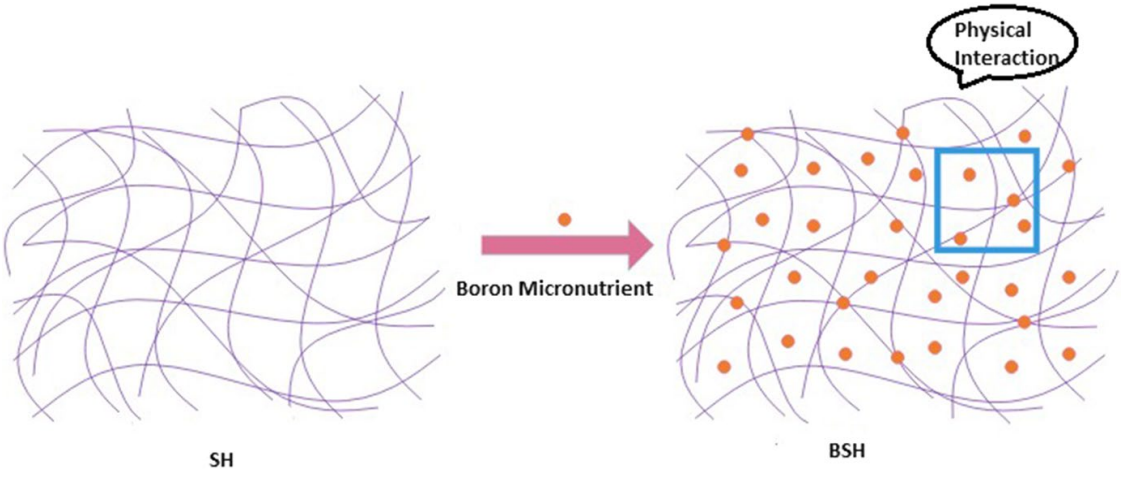

Fig.2 Pictorial representation of the formation of BSH

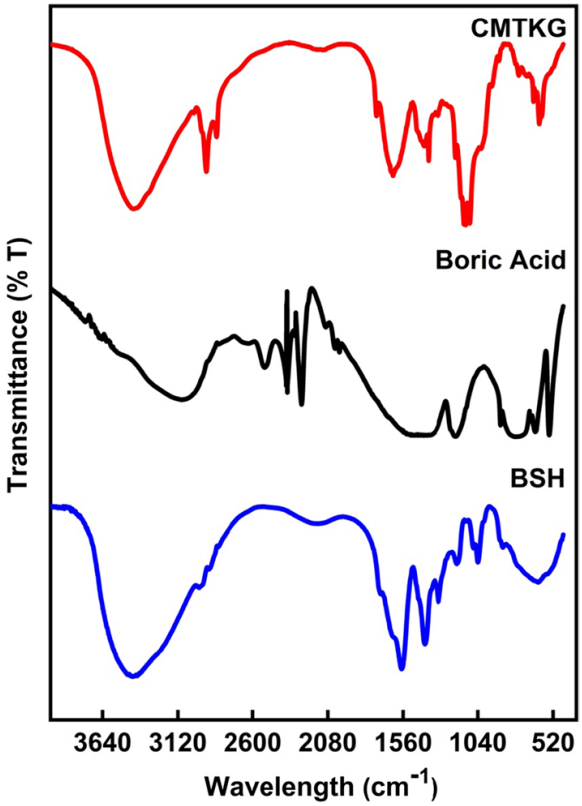

Fig. 3 FTIR spectra of CMTKG, boric acid, and BSH

to boric acid as noticeable from the absence of any peak shifts related to boric acid. Interpreting this behavior, it can be inferred that only weak interactions (physical interactions) took place between CMTKG-based cross-linked network and boron micronutrient.

Scanning electron microscopy (SEM)

The morphological examination of CMTKG and BSH was done to see the morphological alterations in BSH as an effect of boron incorporation. SEM micrographs of BSH is shown in Fig. 4b. For a comparative study, SEM of CMTKG has also been shown in Fig. 4a. This analysis of CMTKG showed rough, non-porous and compact surface, while BSH showed spongy surface, distinct boundaries, and interspatial voids. Although, the morphology of BSH seemed to have influenced by the addition of boron in the form of slightly fractured appearance of BSH. The reason being is that the intercalation of boron into the CMTKG based cross-linked network's matrix [38].

Thermal analysis

Figure 5 showed thermogravimetric analysis (TGA) thermograms of CMTKG and BSH which was done in order to establish its thermal stability. Weight loss pattern for CMTKG was observed in three different zones. The first zone showed a weight loss of 13.31% for 30–240 °C which is simply due the burning of moisture present in CMTKG polymer. The second zone (240–602 °C) observed prominent weight

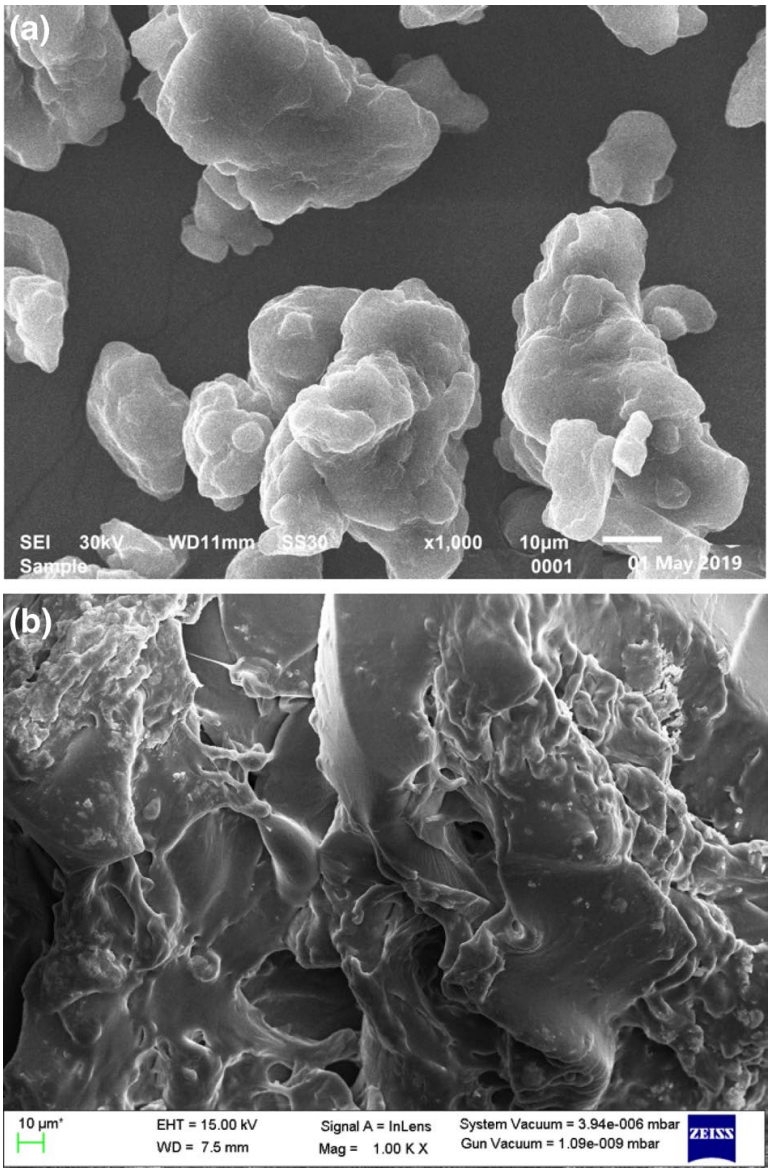

Fig. 4 SEM micrographs of **a** CMTKG and **b** BSH

loss of 47.38% due to the breakdown of CMTKG's polymeric backbone which was followed by the 602 °C-900°C (third zone) with weight loss of 21.49% [39].

However, in case of BSH, weight loss was found in four distinct zones. The weight loss of 19.38%, at an initial zone of 30–295 °C, is due to moisture removal from the polymeric network of BSH. The second zone of 295–465°C showed a major weight loss of 24.95% which was due to the degradation of the polymeric backbone [40]. Weight loss of 11.86% was observed for the third zone (465–698 °C). The reason for this weight loss may be the degradation of crosslinker and cross-linked bonds between hydroxyl groups of the polymer backbone present in the network of BSH. This was lastly followed up with 11.37% weight loss by the fourth zone of complete combustion from 698 to 900 °C. It can be clearly seen that 50% of CMTKG degraded at 365 °C, whereas for BSH, 50% degradation was observed at 481 °C. Moreover, the residual mass of BSH came out to be more than 32% in comparison

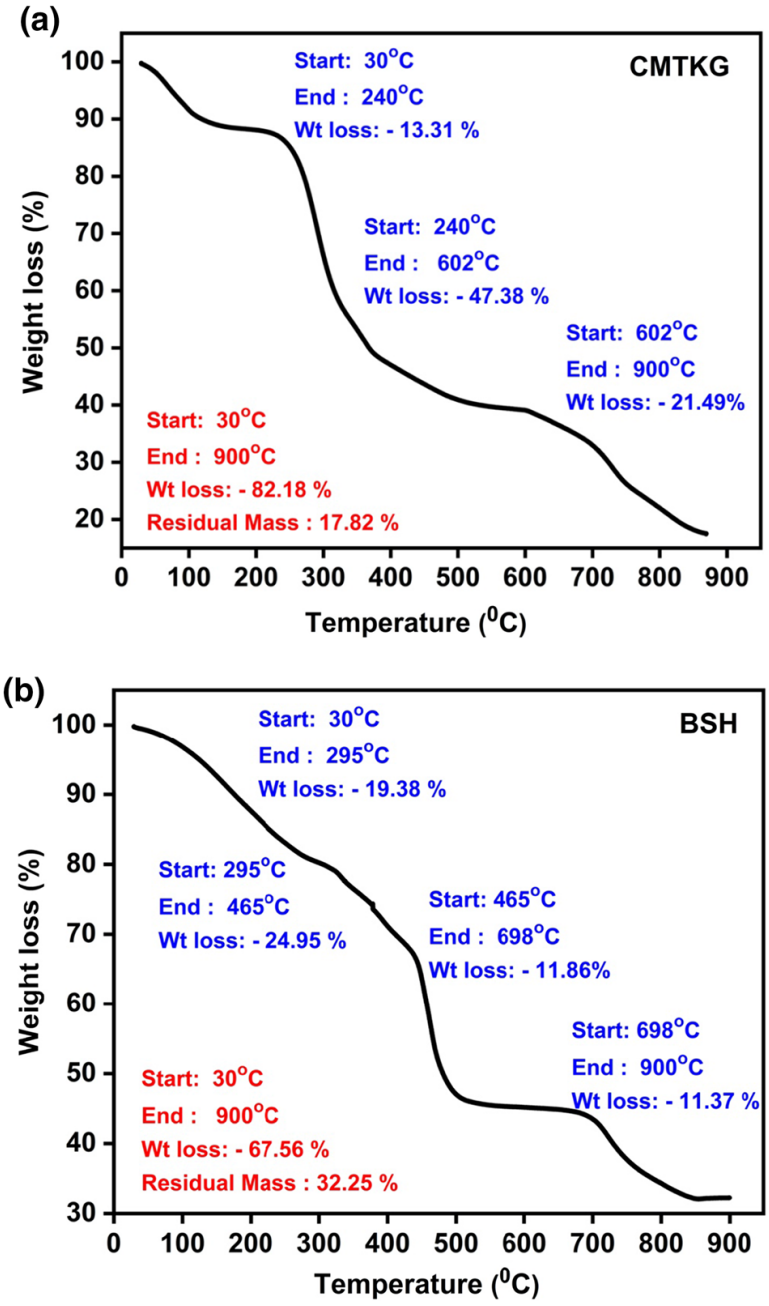

Fig. 5 TGA thermogram of **a** CMTKG, **b** BSH

to the residual mass of CMTKG (17.82%), and henceforth, it can be concluded that BSH is more thermally stable than CMTKG, even at 900 °C.

Swelling studies

Swelling studies of BSH showed its immense range to swell by soaking water into its polymeric porous framework. The swelling degree of BSH for various solvents such as standard saline solution (0.9% NaCl), pH 12, 9 and 4, and distilled water all have been compiled in Fig. 6. BSH took 42 h in order to attain swelling equilibrium.

and out of all used solvents, the highest swelling degree of 466 g/g was shown by distilled water.

For solutions at diverse pHs media, the water absorption capacity reduced significantly from pH 12–4. At pH 12, 402 g/g swelling degree was observed by BSH which at pH 9 declined to 310 g/g and it got further lessened to 83 g/g at pH 4. The spaces present in the polymeric network of BSH might have broadened in alkaline conditions because of amplification in electrostatic repulsions produced by the carboxylate (COO^-) anions in BSH [41]. However, the least swelling was observed for acidic medium, the reason being is that the protonation of COO^- anions decreases the anionic–anionic repulsion which results in the shrinkage of polymeric framework of BSH, whereas water absorbency of BSH was found to be fallen off significantly in 0.9% NaCl (49 g/g) solution case. This can be attributed to the existence of high ionic concentration which produced disparity in the surroundings of inner and outer phases of osmotic pressure and consequently entry of free water got obstructed inside the tri-dimensional network of BSH [42].

Moreover, statistical analysis of swelling data indicated a significant difference between the treatments. Post hoc test showed that all the treatments were different from each other ($P < 0.05$).

Agricultural applications of BSH

Boron plays a key role in a diverse range of plant functions including maintenance of functional and structural integrity of biological membranes, cell wall formation, and pollination to name a few. Despite the importance and need of boron, boron is still the second most widespread micronutrient deficiency problem. In this work, BSH was synthesized in order to supply boron to the plants. Figure 7 depicts the release rate of boron with respect to time, whereas Fig. 8 depicts the release kinetics of BSH.

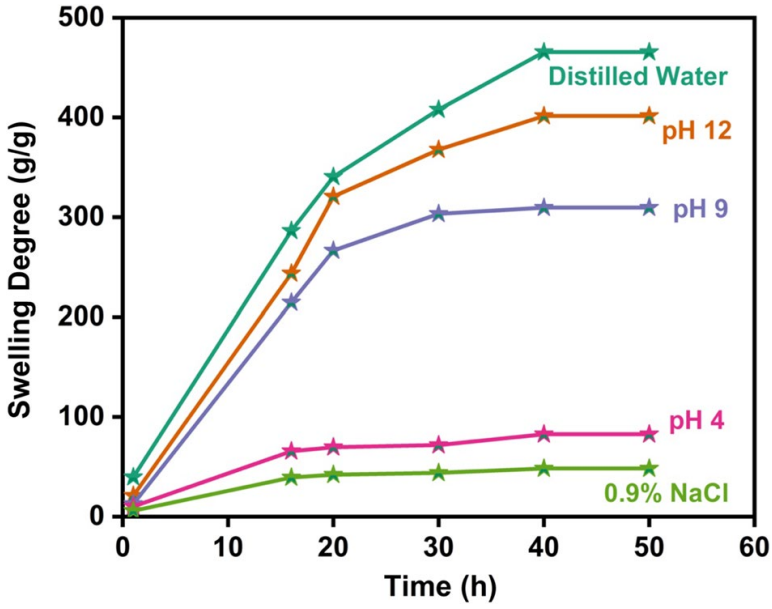

Fig. 6 Swelling studies of BSH

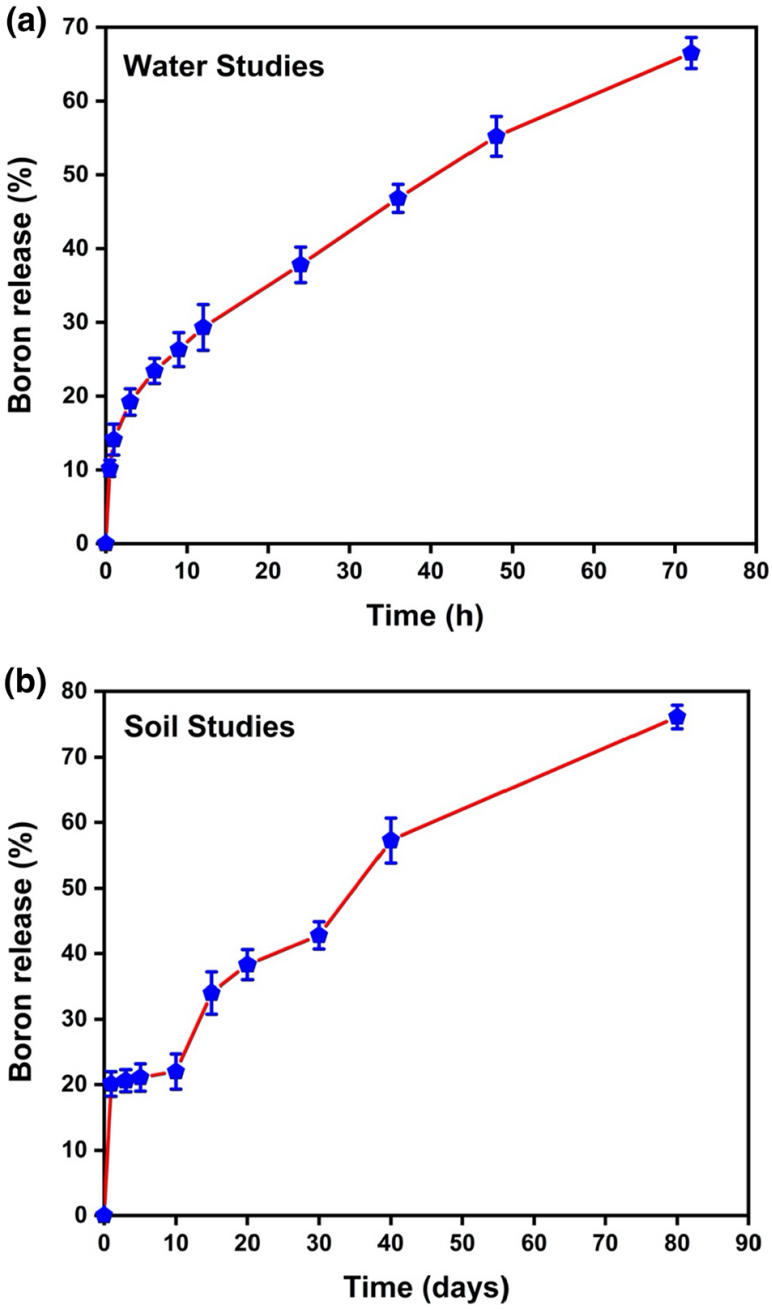

Fig. 7 Cumulative release percentage of Boron with respect to time **a** in water **b** in soil

Release study of boron in water and soil

The recurrent release of boron from BSH in water is shown in Fig. 7a. This study was done for the time span of 72 h where a linear trend was noticed to be followed in releasing boron from BSH. To start with 60 min, the boron release percentage was observed to be 14.1%. However, the release percentage got amplified with time and in 72 h, the release percentage notably hiked up to 66.5%.

In the case of soil also, the recurrent release was noticed to see the release of boron from BSH as depicted in Fig. 7b. This study was done for the time span of

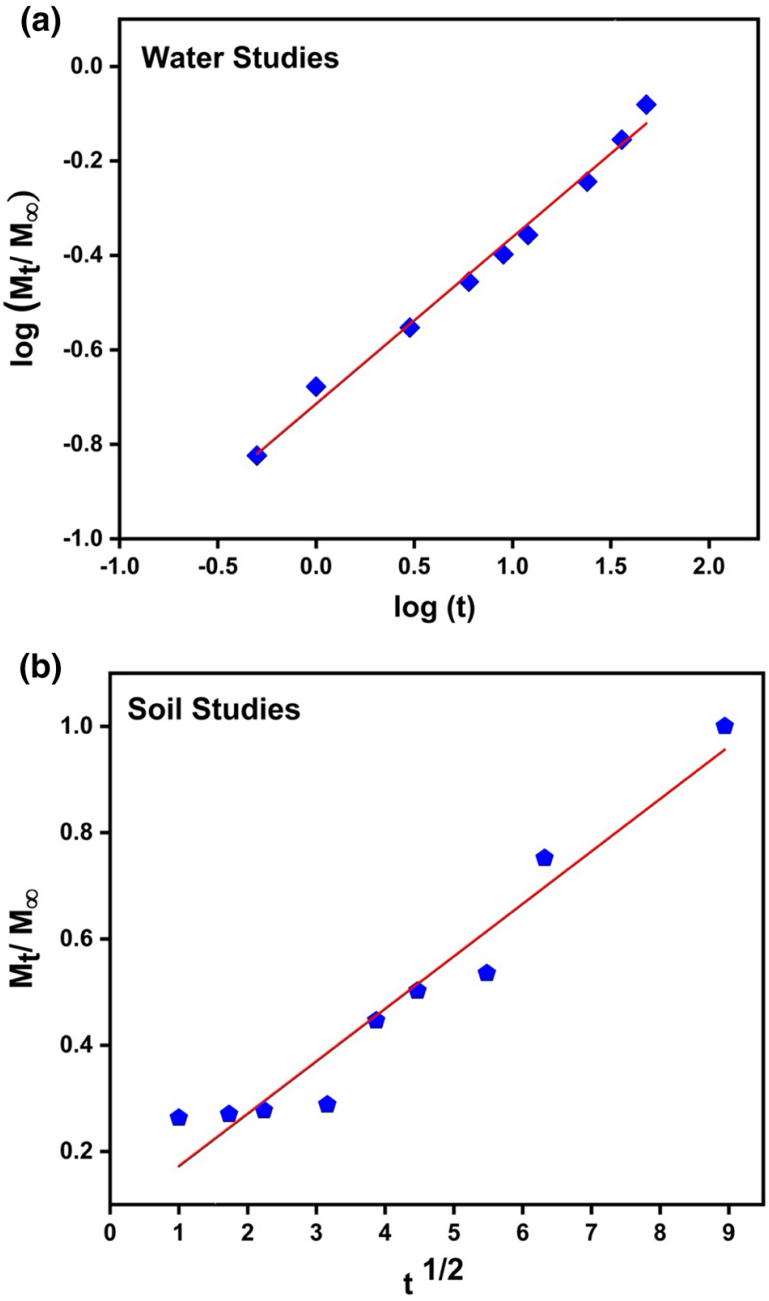

Fig. 8 Release kinetics of Boron as per **a** Korsmeyer–Peppas model in water **b** Higuchi model in soil

80 days. In this case, also, a linear trend was observed in releasing boron from BSH. In soil, BSH exhibited 21.07% for the 5th day to further 40.77% for the 30th day, which significantly augmented on the 80th day to 76.17%. This slow release of boron in the soil can be discussed through three phases as visible in Fig. 7b. Initially, the release happened because of the wetting time of BSH while later on, diffusion of boron occurred from the outer layers of BSH and consequently, boron diffused through inner layers by setting equilibrium with the outer matrix of BSH. Hence, it can be concluded, in the case of soil also, the BSH showcased a moderate increase in the pattern of releasing boron.

Release kinetics study of boron in water and soil

In order to elucidate the kinetics of boron release from the BSH, release data were carefully examined as per the various kinetic equations. The release data for water observed with the coefficient of determination values (R^2) nearer to one and hence it followed the Korsmeyer–Peppas model. However, for the release of boron, BSH followed the Higuchi model, with 0.94 as R^2, in the case of soil (Table 1).

As per the value of R^2 given in Table 1, in case of water, the Korsmeyer–Peppas model was observed to be the best fit model which narrated the release kinetic behavior of boron from BSH (Fig. 8a). Boron release in the water had 0.99 as R^2, and 0.35 as diffusion exponent value (n) which distinctly demonstrated solely Fickian diffusion taking place which happens via the simple method of diffusion through the hydrogel polymeric network [43].

However, the release of boron from BSH in soil showed its maximum R^2 to be 0.94 and that too for the Higuchi model (Fig. 8b). This clearly indicated that the release mechanism was through Fickian diffusion, which suggested that boron could be considered to be diffused through the hydrogel framework network plainly by diffusion processes [33].

The predicted time (in days), as per the Olson equation [35] to release 50%, 95%, and 99%, i.e. (T_{50}, T_{95}, and T_{99}), of boron from developed BSH formulation, are listed along with other parameters in Table 2. Boron release in soil from BSH had higher T_{50}, T_{95}, and T_{99} values, 38.08, 164.84, and 274.72 days, respectively, than the release of boron in water (1.29, 5.60, and 9.33 days in the same order). This difference can be attributed to the fact that in case of water, water is a limiting factor for release, whereas in soil, soil moisture is responsible for the release.

Conclusion

Novel BSH was synthesized by doping boron into the CMTKG's cross-linked network by using the *in-situ* technique. The effect of different solutions like pH 4, 9, 12, distilled water, and standard saline solution, on the water capacity of BSH, was studied. The highest swelling degree was shown in the case of distilled water, up to 466 g/g. Release and kinetics studies of boron were observed in water and as well as in soil, and studied with respect to time. It is significant to note that in soil, BSH exhibited 21.07% boron release for the 5th day which notably enhanced to 76.17% on the 80th day. Release kinetic studies were also analyzed in both water and soil in which the Korsmeyer–Peppas model fitted the best, in case of water, as its R^2 values were nearer to one. However, in the case of soil, the Higuchi model was found out to be the best fit. It also revealed that the release of boron from BSH, in water, was highly independent of the structure of the polymeric network as it followed the Fickian diffusion mechanism. The half-life (T_{50}), T_{95}, and T_{99} values have also been determined using the Olson model, which clearly showed the boron release in soil (38.08, 164.84, and 274.72 days, respectively) had higher values than the release of boron in water (1.29, 5.60, and 9.33 days in the same order).

These attractive qualities of BSH make it a powerful competitor in the field of horticulture as a water-rationing operator as well as above all as a boron micronutrient transporter.

Acknowledgment The authors would like to thank the senior management of Delhi Technological University for constant encouragement and support.

Authors' contributions All authors equally helped to conceive the study and helped draft the final manuscript. All authors gave approval for publication.

Funding No funding has been received for the research work.

Data accessibility This article has no additional data.

Declaration

Conflict of interest We declare we have no competing interests.

References

1. An Z, Yan J, Sha J, Ma Y, Mou S (2021) Dynamic simulation for comprehensive water resources policies to improve water-use efficiency in coastal city. Environ Sci Pollut Res. https://doi.org/10.1007/s11356-020-12191-z
2. Dhakal MP, Ali A, Khan MZ, Wagle N, Shah GM, Maqsood MM, Ali A. 2021 Agricultural water management challenges in the Hunza River Basin: Is a solar water pump an alternative option?*. *Irrig. Drain.* , ird.2563. https://doi.org/10.1002/ird.2563
3. He G, Geng C, Zhai J, Zhao Y, Wang Q, Jiang S, Zhu Y, Wang L (2021) Impact of food consumption patterns change on agricultural water requirements: An urban-rural comparison in China. Agric Water Manag 243:106504. https://doi.org/10.1016/j.agwat.2020.106504
4. He L, Du Y, Wu S, Zhang Z (2021) Evaluation of the agricultural water resource carrying capacity and optimization of a planting-raising structure. Agric Water Manag 243:106456. https://doi.org/10.1016/j.agwat.2020.106456
5. Baroni-nezhad H, Karimi M, Motaghian H, Direkvand-moghadam F (2021) Response of stevia (stevia rebaudiana) to copper, iron and zinc. J Plant Nutr. https://doi.org/10.1080/01904167.2021.1871753
6. Mohammed S, Alsafadi K, Enaruvbe GO, Harsányi E (2021) Assessment of soil micronutrient level for vineyard production in southern Syria. Model Earth Syst Environ 1:3. https://doi.org/10.1007/s40808-021-01104-9
7. Suhr N, Widdowson M, Kamber BS (2021) The role of pedogenesis and natural fertiliser as vectors for essential metal content in agricultural topsoils. Central India SN Appl Sci 3:40. https://doi.org/10.1007/s42452-020-03982-7
8. El-Desouky HS, Islam KR, Bergefurd B, Gao G, Harker T, Abd-El-Dayem H, Ismail F, Mady M, Zewail RMY (2021) Nano iron fertilization significantly increases tomato yield by increasing plants' vegetable growth and photosynthetic efficiency. J Plant Nutr. https://doi.org/10.1080/01904167.2021.1871749
9. Zhong K, Lin ZT, Zheng XL, Jiang GB, Fang YS, Mao XY, Liao ZW (2013) Starch derivative-based superabsorbent with integration of water-retaining and controlled-release fertilizers. Carbohydr Polym 92:1367–1376. https://doi.org/10.1016/j.carbpol.2012.10.030
10. Xie L, Liu M, Ni B, Zhang X, Wang Y (2011) Slow-release nitrogen and boron fertilizer from a functional superabsorbent formulation based on wheat straw and attapulgite. Chem Eng J 167:342–348. https://doi.org/10.1016/j.cej.2010.12.082
11. Tadayon MS (2020) 2021 Effect of foliar nutrition with calcium, boron, and potassium on amelioration of aril browning in pomegranate (Punica granatum cv. 'Rabab'). J Hortic Sci Biotechnol. https://doi.org/10.1080/14620316.2020.1846467

12. Jia Z, Bienert MD, Wirén N, Bienert GP (2021) Genome-wide association mapping identifies HvNIP2 2/HvLsi6 accounting for efficient boron transport in barley. Physiol Plant. https://doi.org/10.1111/ppl.13340
13. Demircivi P (2021) Application of Adsorption Methods for Boron Uptake. Springer, Cham, pp 313–322. https://doi.org/10.1007/978-3-030-47400-3_12
14. Zhao Z, Wang Y, Shi J, Wang S, White PJ, Shi L, Xu F (2021) Effect of balanced application of boron and phosphorus fertilizers on soil bacterial community, seed yield and phosphorus use efficiency of Brassica napus. Sci Total Environ 751:141644. https://doi.org/10.1016/j.scitotenv.2020.141644
15. Shorrocks VM (1997) The occurrence and correction of boron deficiency. Plant Soil 193:121–148. https://doi.org/10.1023/A:1004216126069
16. Marschner H. 1995 *Mineral nutrition of higher plants*. 2nd edn
17. Gupta U, Solanki HA (2013) Impact of boron deficiency on plant growth. Int J Bioassays 2:1048–1050
18. Brown PH, Bellaloui N, Wimmer MA, Bassil ES, Ruiz J, Hu H, Pfeffer H, Dannel F, Römheld V (2002) Boron in plant biology. Plant Biol 4:205–223. https://doi.org/10.1055/s-2002-25740
19. Cakmak I, Römheld V (1997) Boron deficiency-induced impairments of cellular functions in plants. Plant Soil 193:71–83. https://doi.org/10.1023/A:1004259808322
20. Das D, Prakash P, Rout PK, Bhaladhare S (2021) Synthesis and characterization of superabsorbent cellulose-based hydrogel for agriculture application. Starch-Stärke 73:1900284. https://doi.org/10.1002/star.201900284
21. Thombare N, Mishra S, Shinde R, Siddiqui MZ, Jha U (2021) Guar gum based hydrogel as controlled micronutrient delivery system: Mechanism and kinetics of boron release for agricultural applications. Biopolymers. https://doi.org/10.1002/bip.23418
22. Thombare N, Mishra S, Siddiqui MZ, Jha U, Singh D, Mahajan GR (2018) Design and development of guar gum based novel, superabsorbent and moisture retaining hydrogels for agricultural applications. Carbohydr Polym 185:169–178
23. Mo C, Shu-quan Z, Hua-Min L, Zhan-bin H, Shu-qin L (2006) Synthesis of poly(acrylic acid)/sodium humate superabsorbent composite for agricultural use. J Appl Polym Sci 102:5137–5143. https://doi.org/10.1002/app.24661
24. Abedi-Koupai J, Sohrab F, Swarbrick G (2008) Evaluation of hydrogel application on soil water retention characteristics. J Plant Nutr 31:317–331. https://doi.org/10.1080/01904160701853928
25. Bortolin A, Serafim AR, Aouada FA, Mattoso LHC, Ribeiro C (2016) Macro-and micronutrient simultaneous slow release from highly swellable nanocomposite hydrogels. J Agric Food Chem 64:3133–3140. https://doi.org/10.1021/acs.jafc.6b00190
26. Khushbu WSG (2020) Potential applications and various aspects of polyfunctional macromolecule-carboxymethyl tamarind kernel gum. Eur Polym J 140:110042. https://doi.org/10.1016/j.eurpolymj.2020.110042
27. Khushbu WSG, Kumar A (2019) Synthesis and assessment of carboxymethyl tamarind kernel gum based novel superabsorbent hydrogels for agricultural applications. Polymer (Guildf) 182:121823. https://doi.org/10.1016/j.polymer.2019.121823
28. Warkar SG, A.P. G. (2015) Synthesis, characterization and swelling properties of poly (Acrylamide-cl-carboxymethylguargum) hydrogels. Int J Pharma Bio Sci 6:516–529
29. Wolf B (1974) Improvements in the azomethine-H method for the determination of boron. Commun Soil Sci Plant Anal 5:39–44. https://doi.org/10.1080/00103627409366478
30. Singh D, Chhonkar PK, Dwivedi BS. 2005 *Manual on soil, plant and water analysis.* Westville Publishing House. See https://www.cabdirect.org/cabdirect/abstract/20073118818.
31. Korsmeyer RW, Von Meerwall E, Peppas NA (1986) Solute and penetrant diffusion in swellable polymers. II. Verification of theoretical models. J Polym Sci Part B Polym Phys 24:409–434. https://doi.org/10.1002/polb.1986.090240215
32. Serra L, Doménech J, Biomaterials NP (2006) U. 2006 Drug transport mechanisms and release kinetics from molecularly designed poly (acrylic acid-g-ethylene glycol) hydrogels. Biomaterials 27:5440–5451
33. Siepmann J, Peppas NA (2011) Higuchi equation: Derivation, applications, use and misuse. Int J Pharm 418:6–12. https://doi.org/10.1016/j.ijpharm.2011.03.051
34. Higuchi T (1963) Mechanism of sustained-action medication. Theoretical analysis of rate of release of solid drugs dispersed in solid matrices. J Pharm Sci 52:1145–1149. https://doi.org/10.1002/jps.2600521210

35. Olson JS (1963) Energy Storage and the Balance of Producers and Decomposers in Ecological Systems. Ecology 44:322–331. https://doi.org/10.2307/1932179
36. Trivedi JH (2013) Synthesis, characterization, and swelling behavior of superabsorbent hydrogel from sodium salt of partially carboxymethylated tamarind kernel powder- g -PAN. J Appl Polym Sci 129:1992–2003. https://doi.org/10.1002/app.38910
37. Reddy BV, Rao GR (2008) Vibrational spectra and modified valence force field for N. N'-methylenebisacrylamide Indian J Pure Appl Phys 46:611–616
38. Sarkar DJ, Singh A, Mandal P, Kumar A, Parmar BS (2015) Synthesis and Characterization of Poly (CMC-g-cl-PAam/Zeolite) Superabsorbent Composites for Controlled Delivery of Zinc Micronutrient: Swelling and Release Behavior. Polym - Plast Technol Eng 54:357–367. https://doi.org/10.1080/03602559.2014.958773
39. Pal S, Sen G, Mishra S, Dey RK, Jha U (2008) Carboxymethyl tamarind: synthesis, characterization and its application as novel drug-delivery agent. J Appl Polym Sci 110:392–400. https://doi.org/10.1002/app.28455
40. Dias RJ, Havaldar VD, Mali KK, Dhawale SC, Kavitake PR. 2017 sustained delivery of aceclofenac Interpenetrating networks of carboxymethyl tamarind gum and chitosan for sustained delivery of aceclofenac. https://doi.org/10.12991/mpj.2017.20
41. Chang C, Duan B, Cai J, Zhang L (2010) Superabsorbent hydrogels based on cellulose for smart swelling and controllable delivery. Eur Polym J 46:92–100. https://doi.org/10.1016/j.eurpolymj.2009.04.033
42. Zhao Y, Kang J, Tan T (2006) Salt-, pH- and temperature-responsive semi-interpenetrating polymer network hydrogel based on poly(aspartic acid) and poly(acrylic acid). Polymer (Guildf). https://doi.org/10.1016/j.polymer.2006.08.056
43. Ritger P, Release NP (1987) A simple equation for description of solute release I. Fickian and non-fickian release from non-swellable devices in the form of slabs, spheres, cylinders or discs. J Control Release 5:23–26

Publisher's Note Springer Nature remains neutral with regard to jurisdictional claims in published maps and institutional affiliations.

Authors and Affiliations

Khushbu[1] · Sudhir G. Warkar[1] · Nandkishore Thombare[2]

[1] Department of Applied Chemistry, Delhi Technological University, Delhi 110042, India

[2] Processing and Product Development Division, ICAR- Indian Institute of Natural Resins and Gums, Namkum, Ranchi 834010, India

2021 11th International Conference on Cloud Computing, Data Science & Engineering (Confluence) | 978-1-6654-1451-7/20/$31.00 ©2021 IEEE | DOI: 10.1109/Confluence51648.2021.9377060

ConvNet Based Single Image Deraining Methods: A Comparative Analysis

Anil Singh Parihar*, Chirag Jasuja †, Devanshu Gupta‡, Harshit Gupta§
*†‡§ Computer Science and Engineering Department
Delhi Technological University, Delhi, India
* anil@dtu.ac.in † chiragjasuja_2k17co96@dtu.ac.in
‡ devanshugupta_2k17co103@dtu.ac.in § harshitgupta_2k17co132@dtu.ac.in

***Abstract*—Deraining essentially is removing the visual effect of rain from the captured video or image. It is broadly classified into two fields video deraining and image deraining. Rainy images are a complex blend of base image layer and rain layer. Captured images having drops of rain suffer from uneven brightness where regions occupied by rain are overexposed compared to other regions. After the advent of deep learning, there has been a renewed interest in developing more effective approaches. Many deep CNN-based approaches have been devised to effectively derain images. We have summed up these approaches while focusing on the ConvNet based ones to establish part by part comparison of each phase of the rain removal process: image preparation, model design, basic blocks, training. In this paper, we have analyzed the performance of the considered approaches on both qualitative and quantitative grounds.**

***Index Terms*—Single Image Deraining, Convolutional Neural Network**

I. Introduction

Rain significantly reduces visibility, which weakens several computer vision applications. Removing such degradations can substantially boost the capabilities of many computer vision applications that are not trained to perform in bad weather conditions.

In traffic surveillance, clarity of captured images is vital for analyzing road user behavior, accident investigations, and crime scene evaluation. Improvements in camera hardware will not translate to captured images/videos if the weather is bad. Similarly, rain can severely hamper object and lane detection accuracy in self-driving cars, making them ineffective during harsh weather. With deraining, they can be as efficient in the rain as in typical weather.

The deraining problem as a whole has two branches video deraining and image deraining. While the latter is suitable for applications requiring low computational power since the former processes multiple frames simultaneously. In video deraining, there is a high correlation among the subsequent video frames. In contrast, single image deraining is very different as here the rainy images are contextually detached, thus making it more complicated than the former. This method is relatively easy as, in a video, one has a lot of spatial information to regenerate pixels hidden by rain droplets. Video deraining is useful when one has to reanalyze captured footage, e.g., in surveillance footage, etc. We define the scope of this paper as image deraining. Images captured during rain have significant degradation due to the blurring and hazing effects, specifically variably localized magnification, hue shifts, irregular reflections, and clarity degradation. In long depth images, the rain gets collected in a single shot, which causes a haze-like effect, thus significantly reducing the image's sharpness. In short-depth images, the scintillating effect of rain droplets is very prominent. Thus, rain covered pixels are overexposed, hence brighter than the neighboring ones. Single image deraining techniques aim to use these images to remove and rebuild rain-affected regions, restoring the image's quality. Deraining problem's traditional solutions are based on a Gaussian mixture model [9], which performed decently but smoothened the images. Other earlier methods include low-rank representation [24], discriminative sparse coding [23]. Various image enhancement techniques have been used to improve image contrast [15], [18]–[20], which can further contribute to detail maintenance.

This paper analyzes the performance of works by Fu *et al.* [2], Yang *et al.* [3], Zhang *et al.* [1], Li *et al.* [4], Wang *et al.* [5] on both qualitative and quantitative grounds.

II. Literature Review

A. Image Decomposition

Image decomposition is a crucial step in the process of deraining an image. Each rainy image can be split into two layers called base and detail. The detail layer comprises of all the brightness and hue changes caused due to reflective and refractive components of light added by droplets of rain.

$$Image = Base + Detail \tag{1}$$

Every approach tries to maximize its performance by getting the most out of this step. Fu *et al.* [2] splits the image into a base and detail layer. The former is obtained by applying a guided filter [22] on the input image, while deducting this from the rainy image gives the sparse detail layer. Zhang *et al.* [1] uses a two-staged technique. Firstly, they classify the input image into one of three categories : light, medium, or heavy rain. This is used along with a multi-layered convolutional network to capture various shapes and sizes of rain droplets. The image thus obtained is fused with the density information to form a final image.

Authorized licensed use limited to: DELHI TECHNICAL UNIV. Downloaded on March 27,2021 at 05:47:39 UTC from IEEE Xplore. Restrictions apply.

TABLE I: Analysis of Compared Models.

Method	*Network Type*	*Advantages*	*Disadvantages*
DerainNet [2]	3-layer CNN arranged sequentially.	It avoids too much of network complexity and is much faster as compared to other competitive methods.	It suffers in heavy rainfall and also produces undesirable results when the object is aligned with the rain streaks.
JORDER [3]	Multi-staged CNN based Contextualized Dilated Network.	More information is preserved while splitting layers, it is very effective in heavy rainfall.	Sometimes, it leaves fine rain impressions in the output image.
DID-MDN [1]	Multi-Stream Densely Connected Convolutional Networks (DenseNet).	It has better training speed on small datasets and is very effective in removing rainfall from low rain images.	It involves a classifier model, so the dataset needs to be split into low, medium and heavy rain, which is a time consuming process. Moreover, the network is heavy, so it has considerable GPU requirements.
RESCAN [4]	Multi-staged Context Aggregation Network with Multiple Full-Convolutional Layers.	Batch Normalization is not used in RESCAN, this saves up to 40 percent GPU memory.	It leaves faint impressions of heavy rain streaks.
SPANet [5]	Convolutional Neural Network Architecture with RNN inspired blocks.	It performs exceptionally well on low depth photographs that have large rain droplets with a significant amount of scattered light. It uses an extensive real-world dataset for testing so it produces consistent results in all real conditions.	SPANet uses an extensive network, it is very deep and has many parameters to train. This requires significant GPU power which hampers its usage in real life.

Yang *et al.* [3] decomposes the image by carefully handling streak and non-streak features of the input image. Further, to address issues like fogging effects due to streak accumulation and blurring in open-world distant images, they variably localize the rainy regions. The rain model is transformed, taking into account global atmospheric light, atmospheric transmission, layerwise separation of rain streak layer according to different directions. Doing this preserves sharpness in the resulting image plus also restricts deraining tasks only to affected areas. Rather than using the popular two-layer decomposition as we have seen in earlier models. JORDER [3] decomposes the whole streak layer into several, each having comparable shape streaks together. Thus, it transforms the basic formula into $O = B + \sum R$. Further to handle issues like - scattering, attenuation creating a haze in the image, imaging constraints and fine streaks not occupying an entire pixel, the formula is transformed into:

$$O = \alpha \left(B + \sum_{t=1}^{s} \tilde{S}_t R \right) + (1 - \alpha) A \tag{2}$$

α = atmospheric transmission, S_t = a directional streak layer, s = total sparse rainy layers, A = global atmospheric light.

Instead of using pre-existing decomposition methods, the RESCAN [4] approach decomposes the image by learning a neural network-based function to map a rainy image to a rain streak layer. The generalized equation modeling rain is as follows:

$$O = \left(1 - \sum_{i=0}^{n} \alpha_i \right) B + \alpha_0 A + \sum_{i=1}^{n} \alpha_i R^i, s.t \alpha_i \geq 0, \sum_{i=0}^{n} \alpha_i \leq 1 \tag{3}$$

A = global atmospheric light, α_0= scene transmission, α_i = brightness of a particular streak layer.

SPANet [5] does not use image decomposition but tries to utilize spatial information of an image using a capable network, which is explained in the next section.

B. Architectures

In our study, we found three patterns in network design with variations in basic units. Starting with DerainNet [2], ConvNet units were arranged in a sequential fashion. So understandably, being one of the most straightforward approaches, this was relatively faster to train and work.

JORDER [3] introduced a task-based dilation network to learn the main features and then progressively removes the rain hence this way recurrency is introduced in the network. DID-MDN splits derain tasks into two parallel branches, a classification one which calculates the density of rain. The output of the classifier is used in deciding how much deraining is to be applied based on the output of the classifier branch. However, any misclassification may drastically affect the results. Branching in these two approaches assist in learning different types of information, which can then be used accordingly.

RESCAN [4] uses a complex network where each unit is represented by a SCAN block [13]. These units are then further interconnected at the feature layer level and the output of one block being fed into another. This type of architecture helps collect contextual information about rain, which helps improve the quality of the deraining process. SPANet [5] uses a capable set of blocks inspired by recurrent neural networks (RNN). These blocks collect and use spatial information from the input image. This information plays an essential role in the

Authorized licensed use limited to: DELHI TECHNICAL UNIV. Downloaded on March 27,2021 at 05:47:39 UTC from IEEE Xplore. Restrictions apply.

rain removal process as there is no prior image decomposition performed on the input image.

C. Objective Function

In our study, we found different loss functions and strategies used to train the model which significantly improved the performance of the models. In this subsection, we list various types of functions utilized in these approaches.

RESCAN [4] employs an elaborate method utilizing streak layers to calculate their loss function for training the recurrent network and similarly JORDER [3] uses a loss function based on decomposed layer and intermediate variables. DID-MDN [1] uses the Euclidean loss of residual component and cross-entropy loss to train its classifier which can be formalized as:

$$L = L_{E,r} + L_C \tag{4}$$

Here, $L_{E,r}$ represents the approximate Euclidean loss in residual component, whereas L_C represents the cross-entropy loss in classification. It utilizes a multi-layered, dense network to approximate the location of rain droplets using different kernels for each layer in the segment. The rain intensity detected by the classifier is used to rebuild the final image. Here the last layer of a dense network utilizes the classifier result to reduce rain, and this image is combined with the rained image. It is tweaked using image transformation to form a final derained image. This method achieves a better convergence rate due to fewer parameters for training. The loss function to train dense network is :

$$L = L_{E,r} + L_{E,d} + \lambda_F L_F \tag{5}$$

where $L_{E,d}$ is Euclidean loss in reconstructing the derained image, L_F is a feature-based loss in the derained image, which is formulated as:

$$L_F = \frac{1}{CWH} \left|\left| F\left(\hat{x}\right)^{c,w,h} - F\left(x\right)^{c,w,h} \right|\right|_2^2 \tag{6}$$

where F represents a Convnet transformation, and $\hat{x}$ is the recovered derained image. Here h, w, c are the dimensions of the image matrix.

DerainNet [2] minimizes the following function:

$$L = \frac{1}{N} \sum_{n=1}^{N} ||f_w\left(I^n_{detail}\right) - J^n_{detail}||_F^2 \tag{7}$$

where I , J represent the rainy and clean images respectively, $f_w(I^n_{detail})$ is the network output for the rainy image's detail layer.

SPANet [5] uses L_1 loss for regeneration accuracy with SSIM loss to limit similarities and attention loss given as:

$$L_{att} = ||A - M||_2^2 \tag{8}$$

M = binary map (rain covered pixel represented by one),
A = attention map.

III. Testing Process

A. Dataset

Most of the pre-existing works utilize synthetic datasets, the reason being this allows training of high capacity models which can detect rain streaks of various shapes, sizes, directions. However, it should be noted that natural rainy images are quite different from the synthetic ones, so it is common to test the trained models on real-world images to get an idea of how versatile the approach is. We used two datasets, Rain100L [3] and Rain12 [9] datasets for our comparative study.

Rain100L [3] consists of 200 synthetically produced images with light rainfall streaks. All the images are of either 481x321 or 321x481, making this dataset easy to use without much image pre-processing. The dataset also provides us with the ground truth images, making it easier to evaluate our models on the selected metrics.

Rain12 [9] is also a dataset containing synthetically produced images. There are 12 images in this dataset and are widely used for comparison purposes. This dataset also contains the ground truth of the images along with the rain streak patterns. In our comparative analysis Rain100L is used for comparing the average performance of the models using SSIM [6] and PSNR [7] . Some Images from Rain12 [9] are individually used for comparing the model performance where we will be showing the output (derained) image from each model followed up by SSIM [6], PSNR [7] and BRISQUE [8] values.

B. Metrics

SSIM [9] stands for "Structural Similarity Index Measure" and is a regularly used metric to quantify image quality. SSIM calculates the image quality based on the clear image and the distorted image. SSIM is based on the fact that there is a strong inter-dependency between the pixels which is preserved even after distortion to the original image. These inter-dependencies carry essential information about the structure which can be used to calculate the structural dependency between two images. While calculating SSIM, three factors are taken into calculation structure, luminance and contrast. The output value of SSIM ranges from -1 to 1. Two images are identical if SSIM value is 1, whereas -1 means that images are dissimilar. Following expression can be used to calculate SSIM for two MXN sized images represented by x and y:

$$SSIM(x,y) = \frac{(2\mu_x\mu_y + c_1)(2\sigma_{xy} + c_2)}{(\mu_x^2 + \mu_y^2 + c_1)(\sigma_x^2 + \sigma_y^2 + c_2)} \tag{9}$$

μ_x = mean(x), μ_y = mean(y), ${\sigma^2}_x$ = variance(x),
${\sigma^2}_y$ = variance(y), σ_{xy} = co-variance(x,y),
c_1 , c_2 = weak denominator stabilizers

PSNR [7] ("Peak Signal to Noise Ratio") is defined as the ratio between the power of an image (maximum possible) to that of corrupting noise that affects the representational quality. Since signals have a dynamic range, PSNR uses a decibel scale for results. PSNR is used to assess the compression quality of

Authorized licensed use limited to: DELHI TECHNICAL UNIV. Downloaded on March 27,2021 at 05:47:39 UTC from IEEE Xplore. Restrictions apply.

TABLE II: Performance Metrics for above tested images

Image	*Metric*	*DerainNet [2]*	*JORDER [3]*	*DID-MDN [1]*	*RESCAN [4]*	*SPANet [5]*
cat	***SSIM***	0.86	0.92	0.85	0.88	0.87
	PSNR (in dB)	31.36	32.37	29.31	31.83	28.49
	BRISQUE	17.93	18.15	18.88	20.64	21.38
boat	***SSIM***	0.88	0.96	0.89	0.91	0.87
	PSNR (in dB)	30.69	36.83	28.43	34.42	29.96
	BRISQUE	4.64	4.23	4.41	4.62	4.63

TABLE III: Average Values of Performance Metrics for 100L Image Dataset

dataset	*Metric*	*DerainNet [2]*	*JORDER [3]*	*DID-MDN [1]*	*RESCAN [4]*	*SPANet [5]*
100L Image Dataset	***SSIM***	0.86	0.95	0.90	0.89	0.92
	PSNR (in dB)	31.69	36.21	34.55	33.95	35.61

(a) Ground Truth (b) Rainy (c) DerainNet [2] (d) JORDER [3]

(e) DID-MDN [1] (f) RESCAN [4] (g) SPANet [5]

Fig. 1: Outputs of all the networks on Cat image

image compression algorithms. In this case, the original image is compared with a compressed image analogous to a noisy image. PSNR value is analogous to the human eyes' perception of reconstructing the image. The PSNR (in dB) is defined as:

$$PSNR = 10X \log_{10}\left(\frac{MAX_I^2}{MSE}\right) \tag{10}$$

$$= 20X \log_{10}(MAX_I) - 10X \log_{10}(MSE)$$

BRISQUE [8] stands for "Blind Referenceless Image Spatial Quality Evaluator" and is a no-reference method for Image Quality Assessment (IQA). BRISQUE provides a value that determines how an image is compared to a natural image. The BRISQUE value of an image is calculated with reference to natural scenes with the same features. Results obtained from BRISQUE are really competitive to other Image Quality Assessment models. The computation complexity is much lesser than other latest approaches, making it much suitable for referenceless IQA. The BRISQUE value of an image ranges from 0 to 100, where a lower value refers to a much more natural image whereas a higher value means that the image is distorted.

IV. Experimental Results

With the idea of keeping a common baseline for comparing the approaches, we chose two specific images from the Rain12 dataset and calculated SSIM [6], PSNR [7] and BRISQUE [8] values. The first image, 'cat' has many blended textures to test local-detail preserving in the output image. The second image, 'boat' is a distant image with fewer background intricacies. To test the overall effectiveness, we calculated the average values of metrics except for BRISQUE on the 100L dataset.

Authorized licensed use limited to: DELHI TECHNICAL UNIV. Downloaded on March 27,2021 at 05:47:39 UTC from IEEE Xplore. Restrictions apply.

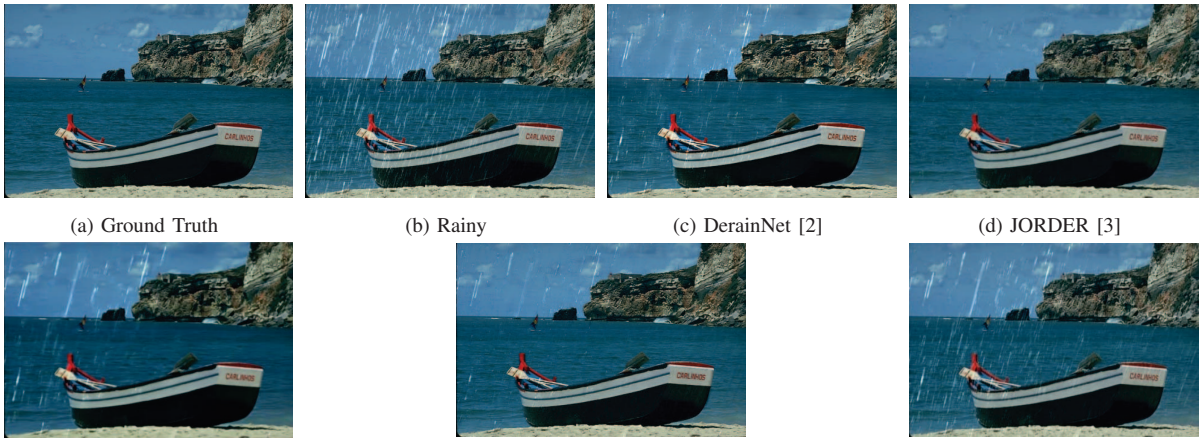

(a) Ground Truth (b) Rainy (c) DerainNet [2] (d) JORDER [3]

(e) DID-MDN [1] (f) RESCAN [4] (g) SPANet [5]

Fig. 2: Outputs of all the networks on Boat image

A. Qualitative Evaluation

On visual evaluation, JORDER [3] performed relatively well on both test images excelling in removal effectiveness and maintaining original sharpness. RESCAN [4] produced decent results on the 'boat' image where only the impression of some strong streaks remained in the final image, but there were many faint streaks in the 'cat' image. DID-MDN [1], although derained the 'cat' image better than RESCAN [4], the faint impressions in the latter's 'boat' image were much prominent. It also exhibits much loss of original sharpness and darker tint, clearly evident from the ocean color in the 'boat' image. DerainNet held the original color, sharpness with multiple finer streaks in both the image, indicating lesser overall effectiveness. SPANet [5] seems only to handle light streaks as the stronger ones exhibit minimal change.

B. Quantitative Evaluation

Numerically as we know, higher PSNR [7], SSIM [6] values, and lower BRISQUE [8] values are desirable. JORDER [3] seems to excel in both test image values and averages over 100L dataset except in BRISQUE value of 'cat' image. Tables II and III mention the calculated values of metrics. While DID-MDN [1] and DerainNet [2] are closely matched in single image values, the former has an edge in average values. SPANet [5] exhibits great improvements in average values.

V. Conclusion

In this paper, we presented an in-depth comparison of various ConvNet based deraining models, which have been prevalent and used for establishing improvements by other deep-learning models in single image deraining. An initial step, like image decomposition and its generalization for more effective rain modeling can significantly impact model effectiveness, ease of training. Since the advances in model performance may saturate depending on the data used. There scope for improving the image decomposition and post-processing stages by utilizing fuzzy image enhancement methods [14], [16], [17], [21]. Although these approaches are driven by data and have improved significantly in the last few years, they still lack the ability to generalize well on various rain scenarios, mainly due to their suitability to a type of data. So, there is still ground to cover before they can be deployed for real-life applications.

References

[1] H. Zhang and V. M. Patel, "Density-aware single image de-raining using a multi-stream dense network," in CVPR, 2018, pp. 695–704

[2] X. Fu, J. Huang, X. Ding, Y. Liao, and J. Paisley, "Clearing the skies: A deep network architecture for single-image rain removal," IEEE TIP, vol. 26, no. 6, pp. 2944–2956, 2017.

[3] W. Yang, R. T. Tan, J. Feng, J. Liu, Z. Guo, and S. Yan, "Deep joint rain detection and removal from a single image," in CVPR, 2017, pp. 1357–1366.

[4] X. Li, J. Wu, Z. Lin, H. Liu, and H. Zha, "Recurrent squeeze-and excitation context aggregation net for single image deraining," in ECCV, 2018, pp. 262–277.

[5] T. Wang, X. Yang, K. Xu, S. Chen, Q. Zhang, and R. W. Lau, "Spatial attentive single-image deraining with a high quality real rain dataset," in CVPR, 2019, pp. 12 270–12 279.

[6] Zhou Wang, A. C. Bovik, H. R. Sheikh and E. P. Simoncelli, "Image quality assessment: from error visibility to structural similarity," in IEEE Transactions on Image Processing, vol. 13, no. 4, pp. 600-612, April 2004, doi: 10.1109/TIP.2003.819861.

[7] Q. Huynh-Thu and M. Ghanbari, "Scope of validity of PSNR in image/video quality assessment," in Electronics Letters, vol. 44, no. 13, pp. 800-801, 19 June 2008, doi: 10.1049/el:20080522.

[8] A. Mittal, A. K. Moorthy and A. C. Bovik, "No-Reference Image Quality Assessment in the Spatial Domain," in IEEE Transactions on Image Processing, vol. 21, no. 12, pp. 4695-4708, Dec. 2012, doi: 10.1109/TIP.2012.2214050.

[9] Y. Li, R. T. Tan, X. Guo, J. Lu and M. S. Brown, "Rain Streak Removal Using Layer Priors," 2016 IEEE Conference on Computer Vision and Pattern Recognition (CVPR), Las Vegas, NV, 2016, pp. 2736-2744, doi: 10.1109/CVPR.2016.299.

[10] H. Zhang, V. Sindagi and V. M. Patel, "Image De-Raining Using a Conditional Generative Adversarial Network," in IEEE Transactions on Circuits and Systems for Video Technology, vol. 30, no. 11, pp. 3943-3956, Nov. 2020, doi: 10.1109/TCSVT.2019.2920407.

Authorized licensed use limited to: DELHI TECHNICAL UNIV. Downloaded on March 27,2021 at 05:47:39 UTC from IEEE Xplore. Restrictions apply.

[11] X. Fu, J. Huang, D. Zeng, Y. Huang, X. Ding and J. Paisley, "Removing Rain from Single Images via a Deep Detail Network," 2017 IEEE Conference on Computer Vision and Pattern Recognition (CVPR), Honolulu, HI, 2017, pp. 1715-1723, doi: 10.1109/CVPR.2017.186.
[12] R. Li, L. Cheong and R. T. Tan, "Heavy Rain Image Restoration: Integrating Physics Model and Conditional Adversarial Learning," 2019 IEEE/CVF Conference on Computer Vision and Pattern Recognition (CVPR), Long Beach, CA, USA, 2019, pp. 1633-1642, doi: 10.1109/CVPR.2019.00173
[13] Hu, J., Shen, L., Sun, G.: Squeeze-and-excitation networks. arXiv preprint arXiv:1709.01507 (2017)
[14] A. S. Parihar, O. P. Verma and C. Khanna, "Fuzzy-Contextual Contrast Enhancement," in IEEE Transactions on Image Processing, vol. 26, no. 4, pp. 1810-1819, April 2017, doi: 10.1109/TIP.2017.2665975.
[15] A. S. Parihar and O. P. Verma, "Contrast enhancement using entropy-based dynamic sub-histogram equalisation," in IET Image Processing, vol. 10, no. 11, pp. 799-808, 11 2016, doi: 10.1049/iet-ipr.2016.0242.
[16] O. P. Verma, A. S. Parihar and M. Hanmandlu, "Edge Preserving Fuzzy Filter for Color Images," 2010 International Conference on Computational Intelligence and Communication Networks, Bhopal, 2010, pp. 122-127, doi: 10.1109/CICN.2010.35.
[17] A. S. Parihar, "Fuzzy adaptive gamma correction for contrast enhancement," 2017 International Conference on Intelligent Sustainable Systems (ICISS), Palladam, 2017, pp. 625-629, doi: 10.1109/ISS1.2017.8389246.
[18] K. Singh and A. S. Parihar, "A comparative analysis of illumination estimation based Image Enhancement techniques," 2020 International Conference on Emerging Trends in Information Technology and Engineering (ic-ETITE), Vellore, India, 2020, pp. 1-5, doi: 10.1109/ic-ETITE47903.2020.195.
[19] Parihar A.S., Verma O.P., Yadav D. (2018) Image Contrast Enhancement Using Differential Evolution. In: Bera R., Sarkar S., Chakraborty S. (eds) Advances in Communication, Devices and Networking. Lecture Notes in Electrical Engineering, vol 462. Springer, Singapore. https://doi.org/10.1007/978-981-10-7901-6_57.
[20] Parihar A.S., "Entropy-based adaptive gamma correction for content preserving contrast enhancement," Int J Pure Appl Math 117(20), 2017, pp. 887–893.
[21] A. S. Parihar, O. P. Verma and S. Tyagi, "An optimal fuzzy filter for Gaussian noise in color images using bacterial foraging algorithm," 2013 Annual International Conference on Emerging Research Areas and 2013 International Conference on Microelectronics, Communications and Renewable Energy, Kanjirapally, 2013, pp. 1-6, doi: 10.1109/AICERA-ICMiCR.2013.6576022.
[22] K. He, J. Sun and X. Tang, "Guided Image Filtering," in IEEE Transactions on Pattern Analysis and Machine Intelligence, vol. 35, no. 6, pp. 1397-1409, June 2013, doi: 10.1109/TPAMI.2012.213.
[23] Luo, Y., Xu, Y., Ji, H.: Removing rain from a single image via discriminative sparse coding. In: IEEE ICCV. (2015) 3397–3405.
[24] Chang, Y., Yan, L., Zhong, S.: Transformed low-rank model for line pattern noise removal. In: IEEE ICCV. (2017) 1726–1734.

Authorized licensed use limited to: DELHI TECHNICAL UNIV. Downloaded on March 27,2021 at 05:47:39 UTC from IEEE Xplore. Restrictions apply.

Applied Intelligence
https://doi.org/10.1007/s10489-021-02345-y

ConvNet frameworks for multi-modal fake news detection

Chahat Raj[1] · Priyanka Meel[1]

Accepted: 10 March 2021
© The Author(s), under exclusive licence to Springer Science+Business Media, LLC, part of Springer Nature 2021

Abstract
An upsurge of false information revolves around the internet. Social media and websites are flooded with unverified news posts. These posts are comprised of text, images, audio, and videos. There is a requirement for a system that detects fake content in multiple data modalities. We have seen a considerable amount of research on classification techniques for textual fake news detection, while frameworks dedicated to visual fake news detection are very few. We explored the state-of-the-art methods using deep networks such as CNNs and RNNs for multi-modal online information credibility analysis. They show rapid improvement in classification tasks without requiring pre-processing. To aid the ongoing research over fake news detection using CNN models, we build textual and visual modules to analyze their performances over multi-modal datasets. We exploit latent features present inside text and images using layers of convolutions. We see how well these convolutional neural networks perform classification when provided with only latent features and analyze what type of images are needed to be fed to perform efficient fake news detection. We propose a multi-modal Coupled ConvNet architecture that fuses both the data modules and efficiently classifies online news depending on its textual and visual content. We thence offer a comparative analysis of the results of all the models utilized over three datasets. The proposed architecture outperforms various state-of-the-art methods for fake news detection with considerably high accuracies.

Keywords Fake news detection · Multimodal combination · Weighted average fusion · Convolutional neural networks · Deep learning

1 Introduction

Visual data attracts viewers more quickly than words do. A Human brain captures and rapidly analyzes a news item and often flags it as fake or real by just a glance of its title, image, or a small segment of it, mostly without going through the entire textual content. It does this based on the preexisting knowledge in our conscience. Even if it does go through a whole text, there are very few references and not enough time to check for the authenticity of the content we come across. Various content creators exploit these drawbacks of the human brain and behavior. There is a need for technological state of the art methods to assess the credibility of content, textual or visual, and authenticate it as fake or real. Online media emerged as a platform to share ideas, views, news. With the advancement of mobile devices and the internet, news became easily accessible to people who were either deprived of or uninterested in official news sources such as television and newspapers. The long and seemingly tedious to read texts became easy to understand as images and videos now accompany them. In the same process, it also became challenging to detect the truth in such content.

In the present scenario, online media is losing its charm and credibility as content creators lure users to gain popularity and money using the content they post online. In this process, they do not pay heed to the authenticity of the information, ignore the verification process, and mix up misleading or tampered images or clips with the texts. Content creators focus on posting catchy and attractive content that bags them many likes, comments, and dollars. Sometimes both the text and graphic content are intentionally made erroneous to spread fake news, making the entire content even more unrealistic. Hence there is an urgent need to design and develop a new classification method to assess the credibility of content, textual or visual, and segregate it as fake or real. If textual and visual factors are taken collectively, fake news detection methods have proved to provide higher accuracies than unimodal detection

✉ Priyanka Meel
priyankameel86@gmail.com

Chahat Raj
chahatraj58@gmail.com

[1] Department of Information Technology, Delhi Technological University, Delhi, India

Published online: 26 March 2021

methods. Machine learning and deep learning-based detection mechanisms depend on fake or real news by analyzing the text's features and visual data. Users consuming information play an essential part in stopping the spread of fake content at the root level or circulating to reach a great mass affecting political, social, and economic lives. The algorithms so far used depend upon news data collected from websites and social media platforms, which are later classified into binary (real and fake) or multiple (ranging according to their severities) labels by crowdsourcing or third-party authenticators.

With the advent of massive data and news content online, the intricacies add up when multiple data forms are available. Despite being beneficial in terms of easy transmission and news consumption, multi-modal data also presents a strenuous task for detecting fake news amongst them. The modalities prevalent on online media include text, image, audio, video, and hyperlinks. With the vast accompaniment of text with visual data, the effectiveness of news rises. A large amount of visual data makes verification difficult as multi-modal data does not guarantee the credibility and attracts more attention than pure text contents. Multi-modal features are expected to be more beneficial in detecting fake news as compared to unimodal features. Few of the excellent quality datasets available for scientific research include binary labeled datasets and multi-label datasets such as Mediaeval, Sina Weibo, PolitiFact, Emergent, and Resized_V2 [1].

Figures 1 and 2 represent critical knowledge predominantly available in text and image parts of information circulating online. We propose that online social media images consist of three features: latent features, explicit features, and contextual features. Latent features are extracted using layers of convolutions. Deep convolutional networks are capable of learning kernel values that are utilized to extract latent features. According to Yang et al. [1], explicit features are handcrafted features such as the resolution of an image and the number of faces in the picture. Apart from these two intrinsic features, contextual features are based on semantic relationships between the text and the image. We have executed convolutional neural networks for text and image classifications. CNNs provide an advantage to extract features directly from raw input without any pre-processing required. CNNs reduce input data on various layers such that only required information is preserved and worked upon to make essential

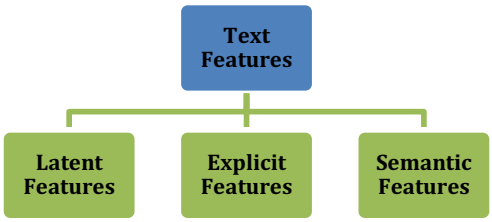

Fig. 1 Text features

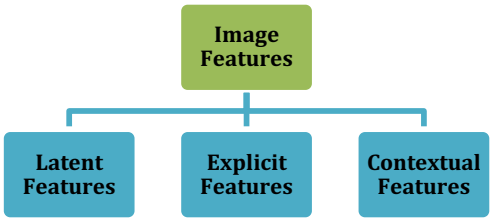

Fig. 2 Image features

predictions. In this work, we propose a novel fake news detection framework. It is based on two-stream convolutional neural networks for text and image input streams. This novel architecture consists of individual text and image classification modules, which are fused at a later stage post-training of convolutional models. The experiments performed resulted in ~3–6% higher scores than the established state-of-the-art methods. The proposed architecture is capable of detecting fake news based on both textual and visual information. The usage of Text-CNN increases the overall efficiency of the architecture. Simultaneously, the combination of Image-CNN has resulted in an additive accuracy for the detection task. The use of convolutional models that we propose with introduced Text-CNN and Image-CNN models outperform the existing state-of-the-art.

The contributions of this work include:

- Web scraping, creating clean-image datasets from two previously available datasets that contained news URLs.
- We have proposed a new Coupled ConvNet architecture that constitutes proposed Text-CNN and Image-CNN modules for multi-modal fake news detection.
- We have implemented CNN models on TI-CNN, Emergent, and MICC-F220 dataset on textual and visual data.
- We have performed a comparative analysis of various CNN models' efficiencies on real-world datasets for fake news detection.
- We have analyzed the performance of deep learning on latent textual and visual features for fake news detection.
- We have provided new deep learning pathways to better fake news detection.

The paper's organization is as follows: Section 1 introduces the problem statement, the need for multi-modal fake news detection, datasets available, and modality features. Section 2 discusses the previous works performed on fake news classification and detection using various CNN and RNN models. In section 3, we present the mathematical background of CNN architectures we have utilized. Section 4 explains the proposed Coupled ConvNet architecture, its constituent modules, namely, Text-CNN and Image-CNN, and our methodology. Section 5 describes the datasets, experiments, results analysis,

and baseline comparison of our work. In section 6, we discuss potential research directions and concludes.

2 Related works

Fake news detection challenges include the usage of multimal data to classify real and fake news. Present methodologies include fake news detection on textual content [2–4]. Research shows that the incorporation of visual data improves fake news detection. With the rise of multi-modal content on users' posts and news contents, studies involving detection using visual data have rapidly increased.

Previous research [2, 5] includes studying image features of visual data like accompanying images, type of image, etc. Other investigations include learning forensic features [6, 7]. Text information is fused by Jin et al. [8] to get better detection using attention mechanism with RNN on image and LSTM on the text and social context to obtain features and perform rumor detection on microblogs. Qi et al. [9] combined Recurrent Neural Networks to detect and interpret real and fake photos semantically. They introduced a novel approach called Multi-domain Visual Neural Network (MVNN). It uses CNN to extract frequency-domain patterns and CNN-RNN to extract pixel domain patterns and fuses using an attention mechanism outperforming state-of-the-art methods by 9.2%. Researchers have provided various forensics tools and techniques to identify image manipulations. Mostly used methods include detecting physical cues within the image.

Recent works have traversed towards deep learning techniques rather than using available prior knowledge about the data. Using labeled training data is specifically advanced for fake news detection. Previous studies focused on linguistic and textual data to study fake news characteristics and semantics of the data. Deep Neural Networks have been utilized to check tweets for temporal-linguistic traits [3]. Attention mechanisms have also been used with RNNs for fusion [10]. Liu and Wu [11] modeled the classification with a combination of CNNs and RNNs. Less focus has been given to the credibility of multi-modal data on the web. Text and images can be well represented using deep neural networks. Jin et al. and Wang et al. [8, 12] applied it to fake news detection.

To overcome the limitation of learning shared representation of multi-modal data, Khattar et al. [13] proposed a Multimodal Variational AutoEncoder. It is coupled with binary classifier features of text and image modalities with three components in the model, an encoder, decoder, and a fake news detection module. The model leverages state-of-the-art techniques with ~6% accuracy. Ajao et al. [14] used a hybrid of CNNs and LSTM-RNNs to identify fake news-related features without prior knowledge, achieving 82% accuracy. Jindal et al. [15] presented two novel datasets containing fake news text and image, using data augmentation to increase fake news data. Singhal et al. [16] perform fake news detection by introducing the SpotFake framework that exploits textual and visual features of news posts without considering subtasks such as event discriminator and modality correlations. The model increases the accuracy from previous approaches by 3.27% and 6.83% on Twitter and Sina Weibo datasets. TI-CNN has been proposed for fake news detection by Yang et al. [1] using Convolutional Networks on both textual and visual data. They have incorporated both explicit and latent features extracted for both the modalities using CNN layers.

A new challenge emerged to detect fake or computer-generated images with technological advancement in Generative Adversarial Networks. GANs pose a threat by allowing the creation of fake images and manipulations in existing images. Marra et al. [17] studied the performance of existing detectors that use conventional and deep learning methods, concluding higher efficiencies by deep learning detectors with 89% accuracy. They compared the performances of traditional and deep learning image forgery detectors on a dataset of 36,302 images under compression and without compression, concluding that high accuracies are obtained on compressed data using deep networks like XceptionNet, InceptionV3, and DenseNet. In recent years, the yearly trend of published articles using deep networks for credibility analysis is represented in Fig. 3. Figure 4 offers the percentage of fine-tuned CNN models in similar tasks.

By extracting event-invariant features, proposing event adversarial neural networks, Wang et al. [17] performed fake news detection on newly arrived events. Three tasks are completed, namely feature extraction, detection, and event discrimination. The study is conducted by ignoring features that are event-specific and considering just the shared features. It provides accuracies of 71.5% and 82.7% on Twitter and Weibo, respectively. Sabir et al. [18] detected image repurposing, i.e., manipulations in image meta-data on a self-proposed MEIR dataset that consists of real-world Flickr data. It proposes a multi-modal deep learning method that utilizes metadata and image information to identify modifications.

Pomari et al. [19] came up using CNNs and illumination maps in images to detect splicing in fake images with a colossal accuracy of more than 96%. Another approach used diverse modalities, including text, image, and source, to detect hoaxes [20]. Bayar and Stamm [21] developed a new convolutional layer that learns features from training data suppressing image features and highlighting manipulation features. This new approach can detect image manipulations with an accuracy of 99.10%. Lago et al. [22] performed the task using image forensics algorithms to see tampered images and a verification mechanism to check if the images are rightly mapped to textual news. In 2019, Cui et al. [23], a detection framework named SAME, exploits user comments and latent sentiments and uses an adversarial mechanism. Volkova et al.

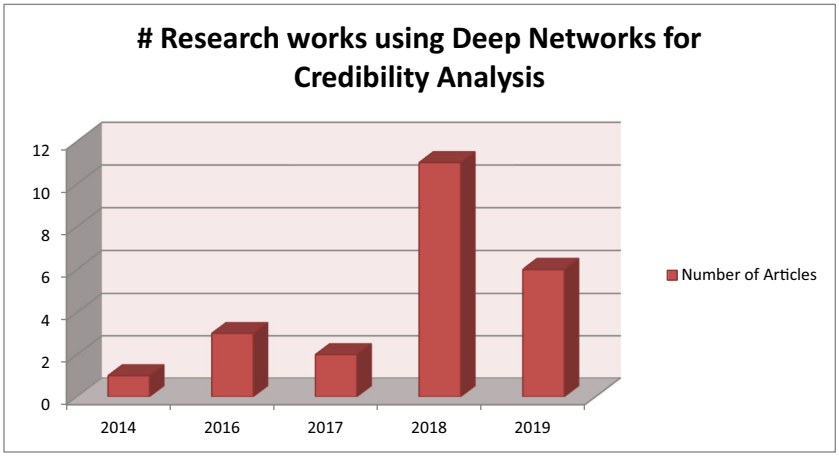

Fig. 3 Yearly trend of research works

[24] performed a qualitative and quantitative analysis of fake news classification models, proposing a qualitative analysis tool ERRFILTER. Modalities analyzed are text, lexical and image inputs, and their combinations.

In image classification, Tariq et al. [27] detected fake face images generated by humans and machines using CNN-based models including VGG16, VGG19, ResNet, DenseNet, NASNet, XceptionNet, ShallowNet, and their ensembles. These neural networks detected GANs and human-generated fake face images without using their metadata. The highest accuracies on various image sizes were obtained with Ensemble ShallowNet (V1& V3).

Sabir, Cheng, et al. [25] performed the detection in manipulations of faces in videos using recurrent convolutional models. These models have proved beneficial in utilizing temporal information in still images to detect tampered images improving the existing accuracies by up to 4.55%. Fake video detection has been performed by Guera and Delp [26], using a convolutional LSTM model on a large dataset of deep fake videos in which face swaps have been done. Papadopoulou et al. [30] verified real-time, user-generated online videos, YouTube videos taking their context into account. The information exploited includes video comments for textual data and metadata like video description, likes, dislikes, and uploader information.

3 Methodology

3.1 Overview

This section elaborates on the architectures of the classification models utilized in this task. Proposed Coupled ConvNet is composed of Text-CNN module for textual fake news classification and Image-CNN module for visual fake news classification. We pre-process input data at their earlier stages in both modules and feed them to convolutional neural networks. This section explains the architectures and mathematical background of Text-CNN and other CNN models utilized in this work. Table 1 summarizes different Neural Network architectures used for the credibility analysis of data in various modalities.

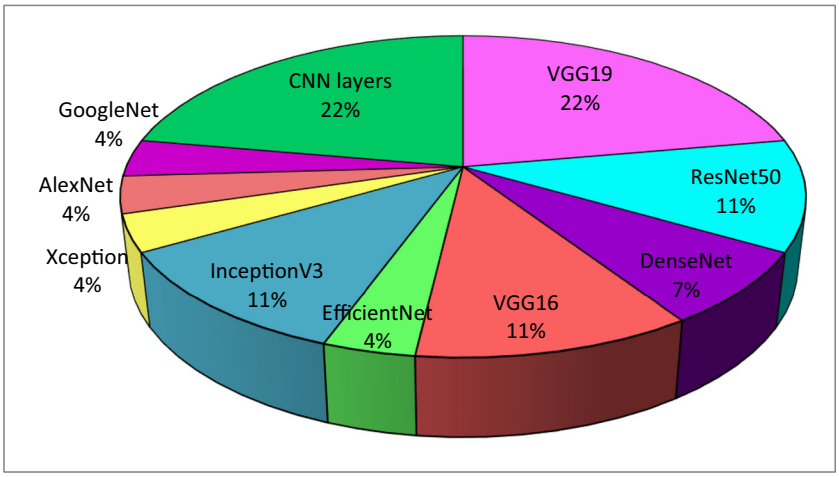

Fig. 4 CNN architectures used in previous research

Table 1 ConvNet architectures for credibility analysis of different data modalities

References	Modality	Task	Network	Model
[13]	Text, Image	Fake News Detection using MVAE	RNN, CNN	Bi-LSTM, VGG19
[14]	Text, Image	Fake News Detection on Twitter	Hybrid CNN, RNN	LSTM, CNN
[25]	Video	Face Manipulation Detection	RNN, CNN	ResNet50, DenseNet
[16]	Text, Image	Fake News Detection	RNN, CNN	BERT, VGG19
[1]	Text, Image	Fake News Detection	CNN	Bi-LSTM, CNN
[17]	Image	GAN-generated Fake Image Detection	CNN	DenseNet, InceptionV3, Xception
[12]	Text, Image	Fake News Detection	EANN	Text-CNN, VGG19
[18]	Image	Image Repurposing Detection	CNN	VGG19
[26]	Video	Fake Video Detection	RNN, CNN	LSTM, InceptionV3
[19]	Image	Image Splice Detection	CNN	ResNet50
[20]	Text, Image, Source	Hoax Detection	CNN	Deep CNN [1]
[21]	Image	Image Manipulation Detection	CNN	Proposed CNN
[22]	Text, Image	Image Trustworthiness Assessment in Online News	CNN	
[23]	Text, Image	Fake News Detection	CNN	LSTM, VGG16
[27]	Image	Classifying Computer-generated and Photographic Images	Modular CNN	VGG19
[8]	Text, Image, Video	Rumor Detection on Microblogs	Att-RNN	LSTM, VGG19
[28]	Image	Tampered Face Detection	Two Stream Neural Networks	GoogleNet, InceptionV3
[29]	Image	Classifying Computer Graphics and Natural Images	CNN	MLP

3.2 Text-CNN

CNNs are widely used for visual tasks. For image classification, pixel information extracted from images is propagated as pixel values to consequent convolutional layers. Words are needed to be processed to make them understandable by a machine. A computing machine treats visual and textual data in the same manner as numeric data. The idea is to serve the machines with text in numeric data in the same way visible data is treated using pixel values. This task is performed by embedding words into vectors. Figure 5 details the various layers of text-CNN architecture.

A fixed vector can thus represent each word in the sentence. These embedded vectors are then propagated through convolutional layers in the same way image data moves through the deep network. The consequent layers are of the same structure incorporating max-pooling, padding, activation function, fully connected layers, and dropout. It is mathematically represented in the form of a k-dimensional vector as $x_i \in R^k$, where x_i is the i^{th} word in a sentence.

Then, $x_{1:n} = x_1 \oplus x_2 \oplus \ldots \oplus x_n$, ($x_{1:n}$ is a sentence of length n) and $\oplus$ represents concatenation. The series of words $x_i, x_{i+1}, \ldots, x_{i+j}$ are concatenated as $x_{i:i+j}$. If h is the number of words, a filter w that is applied to the text generates a feature c_i from a word window $x_{i:i+h-1}$ where filter $w \in R^{hk}$and $c_i = f(w \cdot x_{i:i+h-1} + b)$ given b as a bias term and f, a non-linear function. The filter w is applied to every word window, producing a feature map $c = [c_1, c_2, \ldots, c_{n-h+1}]$ where $c \in k^{n-h+1}$. A max-pooling layer is applied next. It extracts the feature with maximum value in the feature map c which is expressed as $\widehat{c} = \max\{c\}$. These features with maximum values are propagated further to fully connected layers passing them to a softmax layer for classification.

3.3 Image-CNN

The fine-tuned CNN architectures provide good accuracies when it comes to extracting hidden image features and patterns. We implemented eight different CNN architectures AlexNet, Xception, VGG16, VGG19, ResNet50, MobileNetV2, InceptionV3, and DenseNet, for visual fake news detection. The designs of all fine-tuned image CNN models used in this work are described in the following section and represented in Fig. 6.

AlexNet AlexNet is a Convolutional Neural Network designed by Alex Krizhevsky in 2012 and won the ILSVRC challenge. The model displayed that depth in the network is necessary for efficient applications. Depth in the model contributed to providing high performance and became computationally costly, sufficed by using multiple GPUs. AlexNet architecture consists of 8 layers. The first five are convolutional layers, with each layer optionally being followed by a pooling layer and

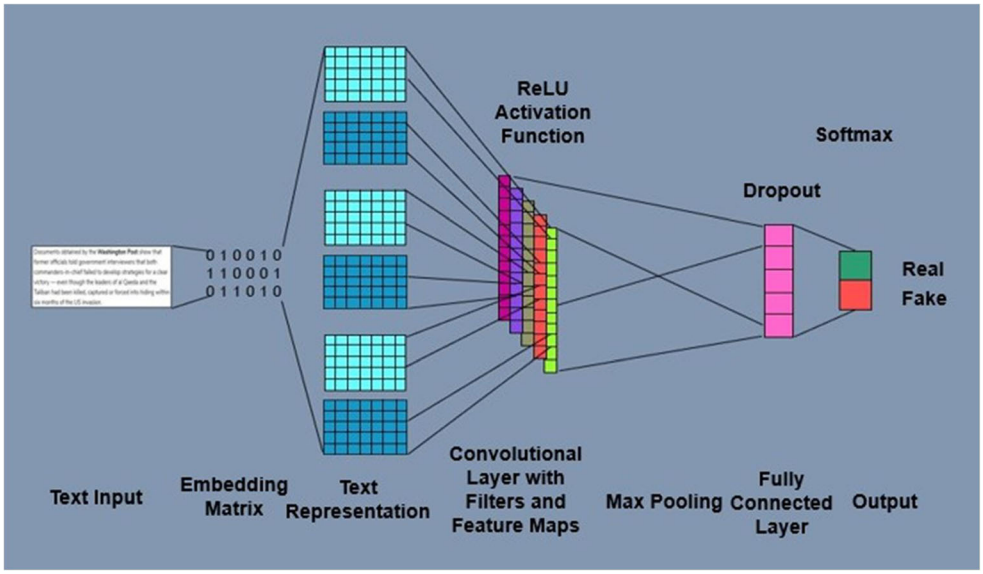

Fig. 5 Text-CNN architecture

the last three layers are fully connected layers. The model prefers the ReLU activation function, owing to its advantage in training time over tanh or sigmoid functions. Overfitting encountered in AlexNet was reduced by data augmentation and using Dropouts that turn off neurons with a specified probability of 0.5.

VGG Visual Geometry Group (VGG) won the ILSVRC 2014 competition. The group members, Karen Simonyan and Andrew Zisserman, experimenting with multiple numbers of layers in the deep network, released two versions of their model, VGG16 and VGG19, with 16 and 19 deep network layers each. They displayed that deeper networks with a more significant number of layers result in higher accuracy for image classification tasks. They replaced large kernel-sized filters of sizes 11×11 and 5×5 with smaller filters of size 3×3. Three fully-connected layers follow the convolutional layers following a softmax layer. ReLU is used as the non-linear activation function for hidden layers. The number of channels increases with a twice-factor from 64 in the first layer to 512 in the last layer. The increased depth makes VGG a network slower to train.

ResNet Residual Neural Network is a network simplified by skipping layers introduced by Kaiming He in 2015. ResNet makes double and triple layers skips jumping across the network. This network makes training more comfortable and faster and reduces the vanishing gradient problem as there is a lesser number of layers in the network. It uses the ReLU activation function and Batch Normalization. Activations are reused from a previous layer until the current layer learns the weights.

Layers are indexed as $l-2$ to l for single skips in backward propagation and as l to $l+2$ for forward propagation. Given $k-1$ as the skip number, this can be generalized as $l-k$ for a backward skip and $l+k$ for a forward skip. A residual network building block with residual function $F(x)$ can be defined by the equations:

For equal dimensions of x and F,

$$y = F(x, \{W_i\}) + x \tag{1}$$

and

For unequal dimensions,

$$y = F(x, \{W_i\}) + W_s x \tag{2}$$

Here x is the input vector, and y is the output vector, $F(x, \{W_i\})$ is the residual mapping and W_s is a linear projection used for mapping dimensions.

Inception V3 The inception V3 model by Google for image classification was presented in ILSVRC 2015, providing a low error rate due to a 42-layer deep network. This model uses the factorization method to factorize a 5×5 convolution into two 3×3 convolutions. It reduces the parameters by 28%. Similarly, a set of one 1×3 and one 3×1 convolution can be replaced by a 3×3 convolution. The auxiliary loss tower in Inception V1 is used only on the last 17×17 layer as a regularizer in Inception V3. Inception V3 is observed to be much efficient than VGGNet in terms of computation cost.

Xception Xception stands for "Extreme Inception," Its architecture is entirely based on depthwise separable convolutional layers. Its architecture consists of 36 convolutional layers (as 14 modules) followed by fully connected layers and a logistic regression layer. Except for the first and last modules, all convolutional layers have residual connections. The weight decay rate or L2 regularization of the Inception V3 model was improved to $1e-5$, and the dropout layer used a

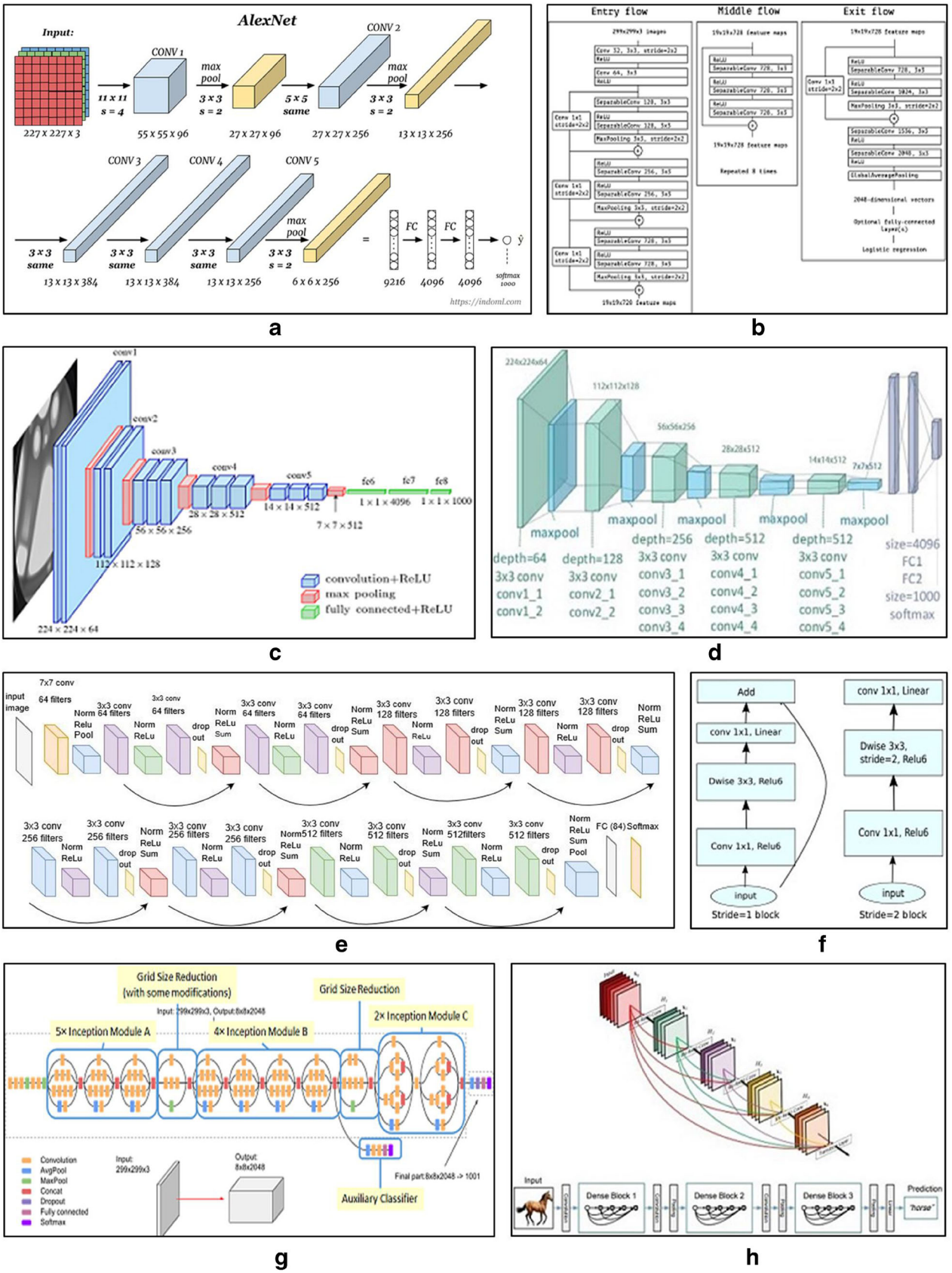

Fig. 6 CNN model architectures: (**a**) AlexNet, (**b**) Xception, (**c**) VGG16, (**d**) VGG19, (**e**) ResNet50, (**f**) MobileNetV2, (**g**) InceptionV3, (**h**) DenseNet

probability of 0.5. The model does not incorporate the 'Auxiliary loss tower' that is optionally used in Inception V3 architecture.

DenseNet DenseNets, introduced in 2018, are residual networks with various parallel skips. Each layer in a DenseNet is connected in a feed-forward manner to every other layer. The expression gives the total number of direct connections between the layers $\frac{L(L+1)}{2}$, where L is the number of layers. DenseNets do not require the learning of repeated feature maps and require a lesser number of parameters. They perform concatenation of feature maps instead of sum. Its equation can be stated as:

$$x_l = H_l([x_0, x_1, \ldots, x_{l-1}]) \tag{3}$$

Here x_l is the output of l^{th} layer and H_l is a non-linear transformation.

MobileNet V2 MobileNet V2, a type of CNN, was specially designed in 2019 for mobile devices based on inverted residual connections and bottleneck light-weight depthwise separable convolution layers. The first layer of MobileNet V2 is a convolutional layer with 32 filters. Nineteen residual bottleneck layers follow it. The kernel size used is 3×3, and the non-linear activation function used is ReLU6. The residual layers are used to make the model memory efficient. The bottleneck block operator used can be expressed as:

$$F(x) = \sum_{i=1}^{t} (A_i \circ N \circ B_i)(x) \tag{4}$$

where, A_i is a linear transformation, N is a non-linear transformation and B_i is a linear transformation to the output domain.

4 Proposed Coupled ConvNet

The proposed approach to fake news detection extends the utilization of convolutional neural networks to a broader scale to automate fraudulent content detection on the web. Most of the existing literature is flooded with singular modality tasks where one of the present features are exploited. Most of the approaches are based on machine learning algorithms, while others use deep learning such as GRU, LSTM, Bi-LSTM, and other RNNs for text classification. We leverage this task by introducing a new text classification model using a convolutional neural network. With the onset of using visual features, pre-trained CNN networks are in wide use. The proposed image classification model is based on the usage of a pre-trained model with fine-tuning. Fake news detection tasks can be combined based on data modalities. Hence, the Coupled ConvNet introduced in this work is a hybrid two-stream convolutional architecture (based on text stream and image stream) is proposed, which are then combined using a late fusion technique. The architecture comprises of two streams (modules): Text Module (for textual classification) and Image Module (for visual classification). The architectures of these modules are explained in sections 4.1 and 4.2. The combination mechanism used in the proposed Coupled ConvNet is provided in section 4.3. The series of operations performed in both the modules is depicted in Fig. 7. Figure 8 represents the proposed Coupled ConvNet architecture.

4.1 Text module

A raw text dataset undergoes several refinements and analysis procedures before being affirmed for its realness. The first of those processes is pre-processing the text information. Then the word embeddings are generated for the textual content. Upon completion of this step, the embedded vectors are fed to a one-dimensional convolutional model. We then utilize the CNN model on textual data by applying convolutions on text vectors. A series of layers of convolution and pooling are generated to analyze the data features. Finally, all these layers are conjectured to provide a binary output of the data's information's authenticity. The results are obtained after training the data under multiple iterations of the proposed Text-CNN model.

We use only the 'title,' 'text,' and 'label' columns from the versatile information present in the datasets. Textual pre-processing involves the following steps: lowercase conversion, punctuation removal, URL removal, numeric value removal, data tokenization, stop-word removal, and stemming/lemmatization. In the next step, we perform Array Padding. Padding is done by calculating the maximum length from the most extended news item present in the array data. The text, which is shorter in length than the full content length, is padded with zeroes. The data is further split into the train, test, and validation sets. This processed data is now encoded, and text and title inputs are embedded using Glove embeddings. These embeddings are added next to the 1-D input layer. We then feed this data to the proposed CNN model. The proposed text classification model consists of three one-dimensional convolutional layers with ReLU activation function, each followed by a max-pooling layer. Subsequent layers are fully connected Dense and Dropout layers. After experimentation with different dropout values ranging between 0.2 to 0.8, the best results were portrayed by setting the value to 0.4 for both the dropout layers. A binary Sigmoid classifier is deployed to generate the predictions.

4.2 Image module

CNNs have shown considerable performance for various image classification tasks. They identify latent features without demanding any extra information. These latent features are present inside an image and are described as resolution, objects, pixel parameters, size of an image, etc. When the image

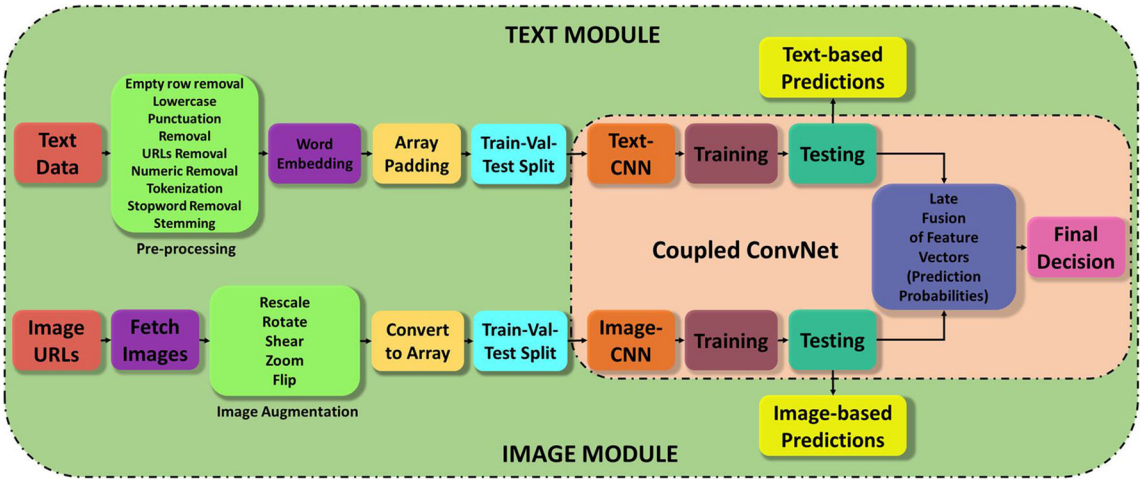

Fig. 7 Sequence of operations performed

data under examination is combined with other modalities such as text, it classifies real and fake news. For Image Analysis, the available image datasets are created as explained. The datasets consist of URLs of news pages. We use these URLs present in the database to scrape URLs of images present in those news pages, using BeautifulSoup. We download and then zip the fake and real photos from those newly obtained URLs into separate directories to our local access. These image URLs are also added to the datasets corresponding to their respective news. Data folders are uploaded to Google Drive, and the drive is mount to Google Colab. We use the split-folders module to divide the dataset into train, test, and validation sets with 80%, 10%, and 10% fake and real images, respectively, for TI-CNN and EMERGENT datasets. MICC-F220 dataset is split into 60%, 20%, and 20% for training, validation, and testing sets, respectively. A different proportion is used for MICC-F220. This difference in splitting ratios consists of 220 images, with 110 real and 110 fake images. Splitting this dataset into 8:1:1 leads to a minimal number of images in the validation and test sets. It creates a bias in the classification results. To avoid this bias and generate normalized results, this dataset has been split in a proportion that keeps a good number of images for validation and testing. After this, we perform Image Augmentation using ImageDataGenerator. Operations performed during augmentation include rescaling, rotation, shear, zoom, and flipping of images, which improves the quality of the datasets for usage. Image data is then fed to various mentioned CNN models for classification. The CNN training sequence is similar to that of the text convolution sequence except that in this case, two-

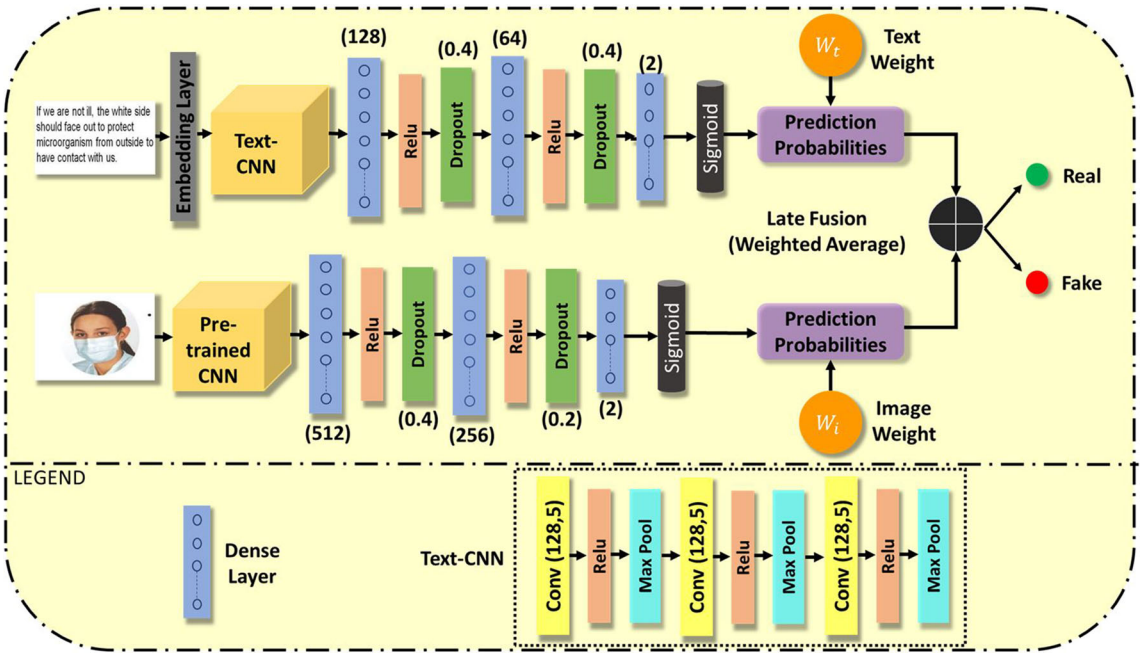

Fig. 8 Proposed Coupled ConvNet architecture

dimensional convolutions are performed on visual (image) data. We feed visual data to various CNN models separately. The list of multiple models experimented with our data includes AlexNet, ResNet50, MobileNet, DenseNet, XceptionNet, InceptionV3, VGG16, and VGG19 [31–34]. Accuracy is determined after training the models for a specified number of epochs, and the result trends for training, test, and validation are observed.

The proposed Image-CNN module uses one of the above-mentioned pre-trained models for each experiment. After adding a pre-trained model, a Dense layer of shape 512 with ReLU activation is added. Next, a Dropout layer of probability 0.4 is used. Another dense layer with shape 256 is used next. Subsequent layers incorporate a dropout layer of value 0.2 and a binary classification layer with a sigmoid activation function. The dense and dropout values are chosen decreasingly to avoid the immediate transition to the final classification layer. It allows the input to travel smoothly through the fully connected layers rather than directly jumping to the last layer. As observed during the experiments, using two dropout layers of value 0.4 and 0.2 reduces overfitting considerably and reduces the loss during the training phase, thereby increasing accuracy.

4.3 Text-image fusion

Post-implementation of text and image classification modules separately, this segment fuses the outputs obtained. Prediction probabilities from both the modules are forwarded to a late fusion operation. Late fusion, a scalable and straightforward method, combines the features from multiple streams after the training phase. The decision vectors from each stream are combined using a suitable combinatorial operation. The proposed method uses a weighted fusion approach in which each modality is assigned a weight that determines the contribution of that modality in the final classification decision. Weights are chosen in a way such that maximum classification accuracy is obtained. For a fusion function $f : P_t, P_i \rightarrow P_c$ where P_t *and* P_i are two different sets of prediction probabilities that denote the decisions of each stream, the combined probabilities indicated by P_c gives the output decisions after late fusion. P_c is calculated by adding the products of text and image prediction probabilities with their assigned weights W_t (text-weight) and W_i (image-weight). It is expressed as:

$$P_c = P_t{*}W_t + P_i{*}W_i \tag{5}$$

Choice of weights is made by experimenting with all possible combinations, varying the weight values between 0.1 to 0.9, with a difference of 0.1 unit. Text and image weights vary inversely. The variety of probabilities that produce the best result are used for each experiment. These weights have been described in Table 2 in section 5.2.

Table 2 Fusion weights that provided maximum classification accuracies

Model	TI-CNN		EMERGENT	
	Text	Image	Text	Image
ResNet50	0.5	0.5	0.8	0.2
VGG16	0.5	0.5	0.5	0.5
VGG19	0.7	0.3	0.6	0.4
InceptionV3	0.8	0.2	0.7	0.3
DenseNet	0.5	0.5	0.8	0.2
Xception	0.5	0.5	0.5	0.5
AlexNet	0.6	0.4	0.7	0.3
MobileNet	0.5	0.5	0.5	0.5

5 Experimental result analysis

This section discusses the datasets utilized in each of the performed experiments. We also describe the results obtained for various experiments on different models and compare their efficiencies obtained for the mentioned datasets that we have used. Results are observed in terms of accuracy score, precision, recall, and F1-score. For efficient baseline comparison of our model's performance on the MICC-F220 dataset, we calculate TPR (True Positive Rate) and FPR (False Positive Rate). We further compare our work with existing fake news classification tasks performed in the past on the datasets we have used and demonstrate that our model beats all established baselines in textual and visual fake news detection.

5.1 Datasets

Ti-CNN With the availability of only a few good quality multimodal datasets, we utilize the already collected dataset that is available online,[1] used by Yang et al. [1] for a similar fake news classification task. This dataset contains 20,015 news items from websites, with 11,941 items being fake and 8074 being real. The dataset is rich in terms of the wide range of details that it covers. We use all of these news items for the Text-CNN module using their title, text, and label information. For the Image-CNN module, we use image URLs obtained from the dataset in the 'main_img_url' column to scrape images from the web. The total number of images extracted from TICNN is 5733, constituting 2612 real news images and 3121 fake news images. The remaining URLs redirected to corrupted web pages or pages removed left us with an image dataset of a smaller size than their corresponding text items. TI-CNN dataset is used for experimentation in both Text-CNN and Image-CNN modules and later in the proposed Coupled ConvNet architecture.

[1] https://drive.google.com/file/d/0B3e3qZpPtccsMFo5bk9Ib3VCc2c/view

Table 3 Performance of Text-CNN module on TI-CNN and EMERGENT

Dataset	Accuracy	Precision	Recall	F1-Score
TI-CNN	96.26	95.77	96.00	95.89
EMERGENT	93.56	94.07	89.35	93.12

Emergent Another dataset experimented with is the EMERGENT (FNC) dataset created by Ferreira et al. [35], consisting of a total of 300 claims and 2595 associated articles. We polish this dataset by discarding duplicate news items and removing blank spaces. For the Image-CNN module, we use post URLs to extract image URLs and then scrape images from EMERGENT datasets' web-pages that led to a clean dataset of 1338 fake and 791 real images. We have made both of these image datasets publicly available. This dataset is also used in both the proposed individual modules and then in the proposed Coupled ConvNet architecture.

MICC-F220 Further, we used the MICC-F220 dataset by Amerini et al. [36] that consists of only real and tampered images, without any other form of data present. We use it with CNN models to identify whether an image is tampered with or original, in short, fake or real. Due to the lack of textual information, this dataset is solely employed in the proposed Image-CNN module. It is used to compare the efficiencies of utilized pre-trained CNN models within the proposed architecture.

5.2 Implementation settings

All experiments have been performed on Google Colab that provides up to 13.53 GB of RAM. It also allocated us 12 GB NVIDIA Tesla K80 GPU hardware accelerator and python version 3. In Text-CNN, we employed RegexTokenizer to extract tokens from news titles and news texts. To reduce the words into their root forms, we used Porter Stemmer and WordNet Lemmatizer. We have utilized Glove representations for word embeddings used in Text-CNN. We have also applied one-dimensional convolutions on title and text and concatenated their layers. We used 0.4 and 0.8 as subsequent dropout values in the experiments. We used a batch size of 64 and have trained the model upon running for 250 epochs. For Image-CNN, we take the image input in size 224*224. Upon setting the dropout value to 0.2, the experiments exhibited a considerable increase in training accuracy. We have used Adam optimizer for all the given models. The batch size is set to 64 instances. The value of batch-size affects the training time of the model. The aim is to maximize the performance of classification models and minimize computation time. Choosing a batch-size less than 64 resulted in higher training time, which made the process slower. Whereas Google Colab did not accommodate a value greater than 64. Therefore, 64 is the perfect fit and is used as the batch size for both text and image modules. We have used binary cross-entropy loss for classifying the item into two categories: real and fake. In the final merging phase, different weights for text and image features as detailed in (Table 2) have been taken for providing the best precision and accuracy of classification.

Table 5 Performance of Image-CNN module on MICC-F220

Image Model	MICC-F220			
	Accuracy	Precision	Recall	F1-Score
ResNet50	61.36	61.37	59.52	60.43
VGG16	95.05	95.15	78.26	85.88
VGG19	91.97	92.02	83.33	87.46
InceptionV3	91.01	91.01	90.63	90.82
DenseNet	89.63	89.61	92.00	90.79
Xception	100.00	100.00	93.75	96.78
AlexNet	91.54	91.52	95.00	93.22
MobileNet	82.82	82.73	100.0	90.55

Table 4 Performance of Image-CNN module on TI-CNN and EMERGENT

Image Model	TI-CNN				EMERGENT			
	Accuracy	Precision	Recall	F1Score	Accuracy	Precision	Recall	F1Score
ResNet50	77.54	58.22	88.57	70.25	**51.26**	**58.59**	**76.82**	**66.26**
VGG16	82.72	63.49	97.65	77.26	45.18	51.29	58.56	54.77
VGG19	81.04	59.77	88.98	71.32	41.90	48.42	42.45	45.00
InceptionV3	58.76	09.18	100.00	16.81	43.54	50.28	54.41	52.89
DenseNet	60.00	11.40	97.96	20.43	48.65	52.93	63.71	57.25
Xception	62.57	10.51	97.62	18.98	**51.26**	57.19	68.42	62.59
AlexNet	59.44	48.32	91.69	59.87	43.62	50.71	48.64	49.71
MobileNet	73.37	55.66	79.46	65.46	46.93	55.18	52.53	53.48

Table 6 Performance of Coupled ConvNet model on TI-CNN and EMERGENT

Text Model	Image Model	TI-CNN				EMERGENT			
		Accuracy	Precision	Recall	F1Score	Accuracy	Precision	Recall	F1Score
Text-CNN	ResNet50	96.90	96.48	96.71	96.59	91.47	91.90	88.95	87.96
	VGG16	98.93	98.21	99.22	98.71	94.05	90.08	86.72	86.12
	VGG19	98.40	97.18	98.96	98.06	89.12	89.11	85.80	85.49
	InceptionV3	97.65	97.65	97.19	97.42	89.88	89.63	86.44	85.88
	DenseNet	97.86	98.34	96.96	97.64	90.64	90.35	87.39	86.73
	Xception	97.22	94.36	98.92	96.59	90.98	91.77	88.02	87.97
	AlexNet	96.91	96.26	96.94	96.60	89.66	89.80	86.09	86.02
	MobileNet	97.54	97.41	97.18	97.29	93.98	91.48	86.22	86.55

5.3 Result analysis

This section presents the performance comparisons of all models used in our work for fake news classification on each of the three datasets. The scores are presented as accuracy, precision, recall, and F1-scores. The compared results are shown in Tables 3, 4, 5, 6 and 7.

Table 3 provides comparison values of the Text-CNN module on two datasets, TI-CNN and EMERGENT. The values indicate that CNNs exhibited an outstanding performance for classifying text-based fake news with 96.26% accuracy on TI-CNN and 93.56% accuracy on EMERGENT. Better scores were obtained on the TI-CNN dataset when compared to EMERGENT in all Text-CNN performance scores. It accounts for the larger size of TI-CNN data. More data aids in better training and hence produces better results. Table 4 portrays performance comparison values for eight Image-CNN modules on TI-CNN and EMERGENT. VGG16 and VGG19 performed the best with 82.72% and 81.04% scores, respectively, on the TI-CNN dataset, followed by ResNet50 and MobileNet with 77.54% 73.37% accuracy, respectively. Other Image-CNN models scored below 63% accuracy on the TI-CNN dataset. The top four in terms of precision and F1 score were in the same order as the accuracy on the TI-CNN dataset with VGG16, VGG19, ResNet50, and MobileNet top four best performing models. In Recall scores, Inception V3 bagged 100%, followed by DenseNet, VGG16, and Xception, on the TI-CNN dataset. For the EMERGENT dataset, in terms of accuracy scores, ResNet50 and Xception secured 51.26% each (highest accuracy), followed by DenseNet and MobileNet with 48.65% 46.93%, respectively. VGG16 performed better on TI-CNN, whereas ResNet50 and Xception on the EMERGENT dataset indicate varying importance and reliance on different Image-CNN models regarding variations in the dataset. Table 5 shows the performance of the eight Image-CNN models on the Image-only dataset MICC-F220. Xception with 100% accuracy, followed by VGG16 with 95.05% accuracy, VGG19 with 91.97%, and AlexNet with 91.54% accuracy, lead the table.

Table 6 provides the final output performance figures of the proposed Coupled ConvNet framework on the two datasets. Comparisons based on Accuracy, Precision, Recall, and F1 scores can be inferred from the table. To eliminate complexity in deciphering the best model or the most relevant text and Image multi-modal fake news detection, let us analyze the Accuracy score comparisons between the TI-CNN and EMERGENT datasets. The combination of Text-CNN with VGG16 performed the best on each of these datasets with 98.93% and 94.05% scores, respectively. While Text-CNN and VGG19 combination performed with 98.4% accuracy on TI-CNN as the second best, Text-CNN and MobileNet coupled ConvNet produced 93.98% accuracy on the EMERGENT dataset, being the second-best. Third and fourth-best performance on TI-CNN was observed with DenseNet and InceptionV3 with 97.86% and 97.65% accuracy, respectively, and on EMERGENT, ResNet50, and Xception produced 91.47% and 90.98% accuracy, respectively.

As inferred from Table 2, weights produced the best classification results can be concluded to be 0.5 for both text and image. Text and image both offer an equal contribution to

Table 7 Accuracy comparison of Image-CNN models on all datasets

Image Model	TI-CNN	EMERGENT	MICC-F220
ResNet50	77.54	51.26	61.36
VGG16	82.72	45.18	95.05
VGG19	81.04	41.90	91.97
InceptionV3	58.76	43.54	91.01
DenseNet	60.00	48.65	89.63
Xception	62.57	51.26	100.00
AlexNet	59.44	43.62	91.54
MobileNet	73.37	46.93	82.82

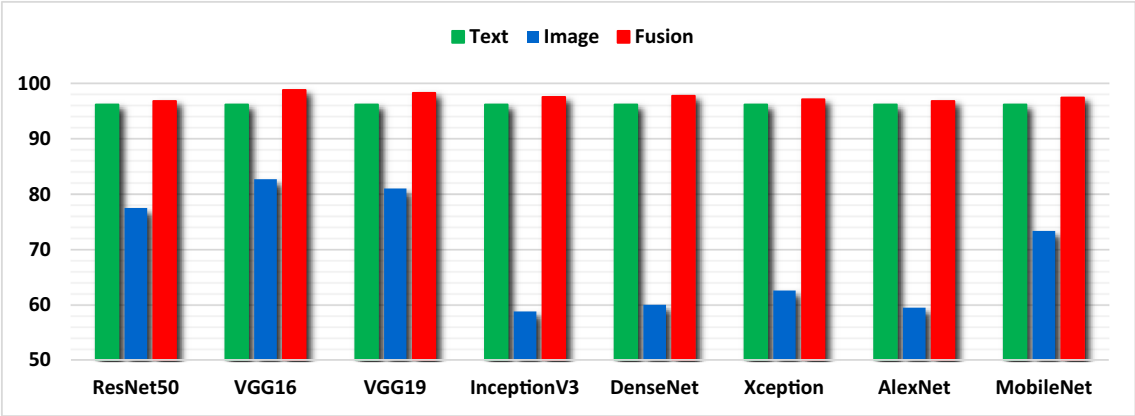

Fig. 9 Accuracy comparison on TI-CNN dataset

detecting fake news efficiently. In some cases, the participation can be discovered to be 7:3 for text and image data modalities. It highlights text being a necessary component for fake news detection. It is also evident that exploring visual modality is equally essential.

The MICC-F220 dataset consists of tampered and unaltered images. Images under the unaltered category have not been edited in any form, and thus it serves the purpose of efficiently distinguishing between real and fake images. We deduce that CNN models are highly accurate in detecting fake news where the text is classified based on their vector embeddings and images have been tampered with or edited. We propose using combinations of text and image CNN models to detect fake news using multiple textual and visual modalities. Hence, we provide performance comparisons of these models to make a witty selection for counterfeit news detection tasks. The accuracy obtained with the MICC-F220 dataset is as high as 100% using XceptionNet, and the lowest is 59.52% with the ResNet50 model. Other models have also demonstrated outstanding performance with high accuracy values. This performance highlights the need for larger visual and multi-modal datasets with distinguishable latent features.

Table 7 is provided for ease of comparison of accuracy scores of Image-CNN models across the three datasets. It can be concluded that VGG16 is a consistent performer. Xception and MobileNet are observed to be the next best performers. Despite achieving 100% result with the MICC-F220 dataset, Xception displays average performance with the other two datasets. It can be regarded as being slightly inconsistent with varying datasets. Figures 9, 10, and 11 graphically represent achieved comparative accuracy using proposed architectures to aid more straightforward visual understanding.

We conclude that CNNs perform better when the dataset is comprised of all tampered images. Data with fake images where fake corresponds to false, tampered, old, misleading, and unrelated images perform somewhat lower as CNNs could detect only latent features. For utilizing features contained in all types of fake photos, multi-modal frameworks are needed which can incorporate elements contained in all kinds of counterfeit images. The above best performing models are likely to show better performance over larger training datasets.

5.4 Baseline comparisons

We validate our results with both single modality textual and visual methods and multi-modal methods for a fair comparison of our proposed work with established baselines. We

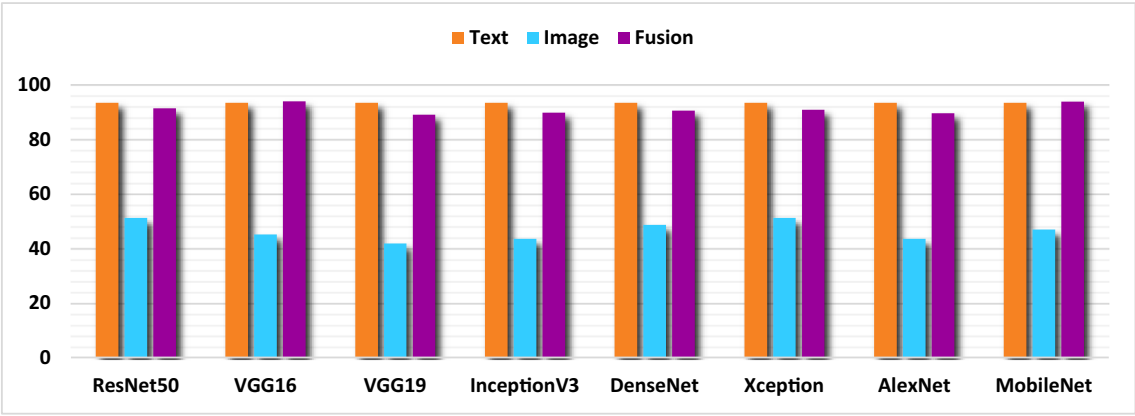

Fig. 10 Accuracy comparison on Emergent dataset

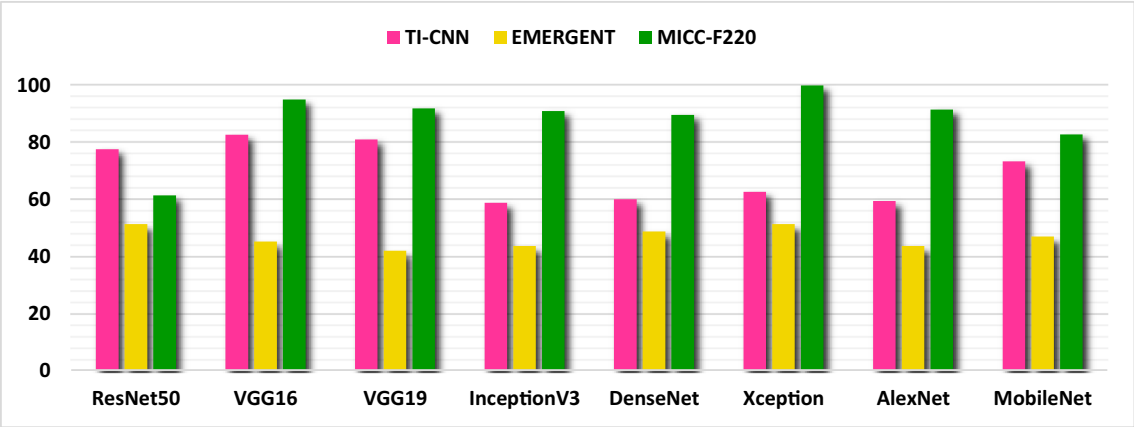

Fig. 11 Accuracy comparison of Image-CNNs on three datasets

compare the results for each dataset separately in Tables 8, 9, and 10. The proposed task being the first to examine Emergent on a visual basis, we establish a baseline for visual and multimodal fake news detection on this dataset. Due to the absence of work performed in the visual domain, our work stands first to do so. The methods used for comparison have been re-implemented by reproducing the works of established baselines. All experiments have been performed by providing an environment similar to as mentioned in the existing research. For unimodal tasks, individual comparisons of results are obtained by using a single-stream model individually. Existing works, where a combination of two-stream networks has been proposed, are compared with the results of proposed Coupled ConvNet.

Ti-CNN On this dataset, Yang et al. experimented with multiple text classification methods: Logistic Regression, GRU, LSTM, and Text-CNN [1]. For the visual domain, Yang et al. used image-CNN with a proposed architecture of convolutional layers. They created a TI-CNN dataset and

Table 8 Baseline comparison of TI-CNN dataset

Modality	Baseline	Method	P	R	F1
Textual	(Yang et al.) [1]	LR	55.08	40.45	46.22
		GRU	88.75	86.43	87.58
		LSTM	90.67	87.44	88.87
		Text-CNN	87.22	90.79	88.97
	Proposed Method	Text-CNN	**95.77**	**96.00**	**95.89**
Visual	(Yang et al.) [1]	CNN-image	53.87	42.15	47.29
	Proposed Method	ResNet50	58.22	88.57	70.25
		VGG16	63.49	97.65	**77.26**
		VGG19	**59.77**	88.98	71.32
		InceptionV3	09.18	**100.00**	16.81
		DenseNet	11.40	97.96	20.43
		Xception	10.51	97.62	18.98
		AlexNet	48.32	91.69	59.87
		MobileNet	55.66	79.46	65.46
Textual and Visual (Combined)	(Yang et al.) [1]	TI-CNN	92.20	92.77	92.10
	Proposed Method	ResNet50	96.48	96.71	96.59
		VGG16	**98.21**	**99.22**	**98.71**
		VGG19	97.18	98.96	98.06
		InceptionV3	97.65	97.19	97.42
		DenseNet	98.34	96.96	97.64
		Xception	94.36	98.92	96.59
		AlexNet	96.26	96.94	96.60
		MobileNet	97.41	97.18	97.29

Table 9 Baseline comparison on EMERGENT (FNC) dataset

Modality	Baseline	Method	Acc%
Textual	(Conforti et al.) [37]	Bi-LSTM	33.00
	(Bourgonje et al.) [38]	LR	87.59
	(Thorne et al.) [39]	Ensemble Method	90.89
	Our Method	Text-CNN	**93.56**

performed text classification using the embedding layer and one-dimensional convolutional layer. Image convolution is achieved by using a model that contains three convolutional layers. Filter size is kept as 3 × 3. Thirty-two filters have been used, and the layers inculcate the ReLU activation function. All of our text and image models surpass the scores obtained by Yang et al. [1]. Individual text and image models proposed by us provide accuracies higher than those observed by Yang et al. In the multi-modal aspect, our approach obtains the highest F1-score of 98.71% using a combination of Text-CNN and VGG-16, which outperforms the state-of-the-art result by ~6%. It establishes the proposed work as a new baseline for multi-modal fake news detection.

Emergent Experiments previously performed by researchers used FNC (FakeNewsChallenge) dataset, which has been derived from Emergent. We compare text-classification results of our model with the LSTM model used by Conforti et al. [37], Logistic Regression applied by Bourgonie et al. [38], and an ensemble of multiple methods deployed by Thorne et al. [39]. Usage of the Text-CNN classification model beats these established baselines, providing an accuracy of 93.56%. Visual fake news detection on this dataset has not been performed previously as the dataset was limited to textual information only. We leverage the task to a visual analysis by adding images extracted from page websites and provide a maximum of 51.26% accuracy using ResNet50 and Xception models.

Table 10 Baseline comparison of MICC-F220 dataset

Modality	Baseline	Method	TPR%	FPR%
	(Uliyan et al.) [40]	Hessian Method	92.00	08.00
	(Uliyan et al.) [41]	Blur Detection	96.50	02.86
	(Doegar et al.) [42]	AlexNet	100.0	12.12
	(Amerini et al.) [36]	SIFT	100.0	08.00
	Our Method	ResNet50	59.52	**0.00**
		DenseNet	78.26	**0.00**
		AlexNet	83.33	**0.00**
		InceptionV3	90.63	83.33
		VGG16	92.00	**0.00**
		MobileNet	93.75	25.00
		VGG19	95.00	12.50
		Xception	**100.0**	**0.00**

MICC-F220 Earlier tasks on this dataset have incorporated image forgery detection techniques with Amerini et al. [36] demonstrating 100% TPR and 8% FPR. Most of our proposed model methods have displayed 0% False Positive Rate, and XceptionNet provides 100% True Positive Rate outperforming all other baselines. 0% FPR demonstrates that no fake samples were wrongly classified as real during the testing phase, and 100% TPR shows that all unaltered samples in the test set were classified into the correct class. A model that achieves 0% FPR and 100% TPR is a perfect classifier. With the proposed approach, the Xception model is the ideal classifier for this dataset, classifying all test samples into correct classes.

6 Conclusion and future work

A novel Coupled ConvNet architecture is proposed comprising of Text-CNN and Image-CNN modules. This work accomplishes fake news detection using several convolutional models on text and image data. Our first contribution provides image datasets for counterfeit news detection, which we have publicly available on Kaggle[2,3]. We compare the performances of image classification models, namely AlexNet, ResNet50, DenseNet, MobileNet, Xception, InceptionV3, VGG-16, and VGG-19, on three real-world datasets TI-CNN, EMERGENT, and MICC-F220. Text-CNN module has been used over TI-CNN and EMERGENT and Image-CNN module on all of the above datasets. We have trained these models and obtained their training, validation, and testing accuracy scores. We utilized latent features for fake image classification and analyzed how well classification can be performed, comparing various efficiencies. All of our models have surpassed fake news detection baselines with high results. The proposed architecture provides a new fake news detection method using convolutional neural networks and establishes a new baseline in this domain. Our proposed model would function more efficiently on larger datasets. We intend to apply these models to larger datasets further. We are also motivated to tune further the parameters used in these models to enhance classification accuracy. Additionally, we focus on coming up with an efficient classification model based on CNN's with fine-tuned hyperparameters serving greater accuracies and better fake news detection.

[2] https://www.kaggle.com/chahatraj/ticnn-extracted-images
[3] https://www.kaggle.com/chahatraj/emergent-extracted-images

References

1. Yang Y, Zheng L, Zhang J, Cui Q, Li Z, Yu, PS (2018) TI-CNN: Convolutional Neural Networks for fake news detection
2. Wu K, Yang S, Zhu KQ (2015) False rumors detection on sina weibo by propagation structures. In: 2015 IEEE 31st international conference on data engineering, pp 651–662
3. Ma J, Gao W, Mitra P, Kwon S, Jansen BJ, Wong KF, Cha M (2016) Detecting rumors from microblogs with recurrent neural networks
4. Ma J, Gao W, Wong KF (2019) Detect rumors on twitter by promoting information campaigns with generative adversarial learning. In: The world wide web conference, pp 3049–3055
5. Jin Z, Cao J, Zhang Y, Zhou J, Tian Q (2016) Novel visual and statistical image features for microblogs news verification. IEEE Transactions on Multimedia 19(3):598–608
6. Boididou C, Andreadou K, Papadopoulos S, Dang-Nguyen DT, Boato G, Riegler M, Kompatsiaris Y (2015) Verifying multimedia use at MediaEval 2015. MediaEval 3(3):7
7. Boididou C, Papadopoulos S, Dang-Nguyen D-T, Boato G, Riegler M, Middleton SE, Petlund A, Kompatsiaris Y et al (2016) Verifying multimedia use at MediaEval 2016. MediaEval
8. Jin Z, Cao J, Guo H, Zhang Y, Luo J (2017) Multi-modal fusion with recurrent neural networks for rumor detection on microblogs. In: Proceedings of the 25th ACM international conference on multimedia, pp 795–816
9. Qi P, Cao J, Yang T, Guo J, Li J (2019) Exploiting multi-domain visual information for fake news detection. In: 2019 IEEE International Conference on Data Mining (ICDM), pp 518–527
10. Chen T, Li X, Yin H, Zhang J (2018) Call attention to rumors: deep attention based recurrent neural networks for early rumor detection. In: Pacific-Asia conference on knowledge discovery and data mining, pp 40–52
11. Liu Y, Wu YFB (2018) Early detection of fake news on social media through propagation path classification with recurrent and convolutional networks. Thirty-Second AAAI Conference on Artificial Intelligence
12. Wang Y, Ma F, Jin Z, Yuan Y, Xun G, Jha K et al (2018) Eann: event adversarial neural networks for multi-modal fake news detection. In: Proceedings of the 24th acm sigkdd international conference on knowledge discovery & data mining, pp 849–857
13. Khattar D, Goud JS, Gupta M, Varma V (2019) Mvae: multi-modal variational autoencoder for fake news detection. In: The world wide web conference, pp 2915–2921
14. Ajao O, Bhowmik D, Zargari S (2018) Fake news identification on twitter with hybrid cnn and rnn models. In: Proceedings of the 9th international conference on social media and society, pp 226–230
15. Jindal S, Sood R, Singh R, Vatsa M, Chakraborty T (2020) NewsBag: a multi-modal benchmark dataset for fake news detection
16. Singhal S, Shah RR, Chakraborty T, Kumaraguru P, Satoh SI (2019) SpotFake: a multi-modal framework for fake news detection. In: 2019 IEEE fifth international conference on multimedia big data (BigMM), pp 39–47
17. Marra F, Gragnaniello D, Cozzolino D, Verdoliva L (2018) Detection of Gan-generated fake images over social networks. In: 2018 IEEE conference on multimedia information processing and retrieval (MIPR), pp 384–389
18. Sabir E, AbdAlmageed W, Wu Y, Natarajan P (2018) Deep multi-modal image-repurposing detection. In: Proceedings of the 26th ACM international conference on multimedia, pp 1337–1345
19. Pomari T, Ruppert G, Rezende E, Rocha A, Carvalho T (2018) Image splicing detection through illumination inconsistencies and deep learning. 2018 25th IEEE International Conference on Image Processing (ICIP):3788–3792
20. Maigrot C, Claveau V, Kijak E, Sicre R (2016) Mediaeval 2016: a multi-modal system for verifying multimedia use task
21. Bayar B, Stamm MC (2016) A deep learning approach to universal image manipulation detection using a new convolutional layer. In: Proceedings of the 4th ACM workshop on information hiding and multimedia security, pp 5–10
22. Lago F, Phan QT, Boato G (2019) Visual and textual analysis for image trustworthiness assessment within online news. Security and Communication Networks
23. Cui L, Wang S, Lee D (2019) SAME: sentiment-aware multi-modal embedding for detecting fake news. In: Proceedings of the 2019 IEEE/ACM international conference on advances in social networks analysis and mining, pp 41–48
24. Volkova S, Ayton E, Arendt DL, Huang Z, Hutchinson B (2019) Explaining multi-modal deceptive news prediction models. In: Proceedings of the international AAAI conference on web and social media, vol 13, pp 659–662
25. Tariq S, Lee S, Kim H, Shin Y, Woo SS (2018) Detecting both machine and human created fake face images in the wild. In: Proceedings of the 2nd international workshop on multimedia privacy and security, pp 81–87
26. Sabir E, Cheng J, Jaiswal A, AbdAlmageed W, Masi I, Natarajan P (2019) Recurrent convolutional strategies for face manipulation detection in videos. Interfaces (GUI) 3(1)
27. Güera D, Delp EJ (2018) Deepfake video detection using recurrent neural networks. In: 2018 15th IEEE international conference on advanced video and signal based surveillance (AVSS), pp 1–6
28. Papadopoulou O, Zampoglou M, Papadopoulos S, Kompatsiaris Y (2017) Web video verification using contextual cues. In: Proceedings of the 2nd international workshop on multimedia forensics and security, pp 6–10
29. Zhou P, Han X, Morariu VI, Davis LS (2017) Two-stream neural networks for tampered face detection. In: 2017 IEEE conference on computer vision and pattern recognition workshops (CVPRW), pp 1831–1839
30. Rahmouni N, Nozick V, Yamagishi J, Echizen I (2017) Distinguishing computer graphics from natural images using convolution neural networks. In: 2017 IEEE workshop on information forensics and security (WIFS), pp 1–6
31. He K, Zhang X, Ren S, Sun J (2016) Deep residual learning for image recognition. In: Proceedings of the IEEE conference on computer vision and pattern recognition, pp 770–778
32. Huang G, Liu Z, Van Der Maaten L, Weinberger KQ (2017) Densely connected convolutional networks. In: Proceedings of the IEEE conference on computer vision and pattern recognition, pp 4700–4708
33. Chollet F (2017) Xception: deep learning with depthwise separable convolutions. In: Proceedings of the IEEE conference on computer vision and pattern recognition, pp 1251–1258
34. Szegedy C, Liu W, Jia Y, Sermanet P, Reed S, Anguelov D et al (2015) Going deeper with convolutions. In: Proceedings of the IEEE conference on computer vision and pattern recognition, pp 1–9
35. Ferreira W, Vlachos A (2016) Emergent: a novel dataset for stance classification. In: Proceedings of the 2016 conference of the north American chapter of the association for computational linguistics: human language technologies, pp 1163–1168
36. Amerini I, Ballan L, Caldelli R, Del Bimbo A, Serra G (2011) A sift-based forensic method for copy–move attack detection and transformation recovery. IEEE Transactions on Information Forensics and Security 6(3):1099–1110
37. Conforti C, Pilehvar MT, Collier N (2018) Towards automatic fake news detection: cross-level stance detection in news articles. In: Proceedings of the first workshop on fact extraction and VERification (FEVER), pp 40–49

38. Bourgonje P, Schneider JM, Rehm G (2017) From clickbait to fake news detection: an approach based on detecting the stance of headlines to articles. In: Proceedings of the 2017 EMNLP workshop: natural language processing meets journalism, pp 84–89
39. Thorne J, Chen M, Myrianthous G, Pu J, Wang X, Vlachos A (2017) Fake news stance detection using stacked ensemble of classifiers. In Proceedings of the 2017 EMNLP Workshop: Natural Language Processing meets Journalism, pp 80–83
40. Doegar A, Dutta M, Gaurav K (2019) CNN based image forgery detection using pre-trained AlexNet model. Int J Comput Intell & IoT 2(1)
41. Uliyan DM, Jalab HA, Wahab AWA (2015) Copy move image forgery detection using hessian and center symmetric local binary pattern. In: 2015 IEEE Conference on Open Systems (ICOS), pp 7–11
42. Uliyan DM, Jalab HA, Wahab AWA, Shivakumara P, Sadeghi S (2016) A novel forged blurred region detection system for image forensic applications. Expert Syst Appl 64:1–10

Publisher's note Springer Nature remains neutral with regard to jurisdictional claims in published maps and institutional affiliations.

Chahat Raj received B.Tech. in Computer Science and Engineering from Indira Gandhi Delhi Technical University for Women, India in 2019 and is currently pursuing M.Tech. with research-centered curriculum in Information Systems from Delhi Technological University, India. Her research interests include Deep Learning, Machine Learning, Computer Vision and Cyber Security. She is oriented towards social network analysis and the development of AI-based solutions towards real-world social media ailments.

Priyanka Meel is an Assistant Professor in Information Technology department of Delhi Technological University, New Delhi India. She completed her B. Tech. and M.Tech degree from Indian Institute of Information Technology and Management, Gwalior. Her current research interests include social media mining, information credibility analysis, AI in medical field, deep learning and machine learning.

Materials Today: Proceedings xxx (xxxx) xxx

Contents lists available at ScienceDirect

Materials Today: Proceedings

journal homepage: www.elsevier.com/locate/matpr

Critical assessment on application of software for designing hybrid energy systems

Khemshika Ram, Prasanna Kumar Swain, Ruchita Vallabhaneni, Anil Kumar *

Department of Mechanical Engineering, Delhi Technological University, Delhi 110042, India

ARTICLE INFO

Article history:
Available online xxxx

Keywords:
Hybrid
Renewable energy
Technical analysis
PV
Optimization

ABSTRACT

HRES (hybrid renewable energy systems) are an amalgamation of traditional and renewable sources that strive to overcome the intermittent nature of renewable energy production sources. The paper aims to provide a critical analysis of the capabilities and limitations of various software to assess HRES. The analysis cycle from design to optimization is an extremely complex task due to the many parameters being considered and has to be done thoroughly. Thus, the use of correct software to obtain comprehensive analysis is critical as it leads to minimal limitations in terms of cost, implementation, and maintenance of the system. When compared to traditional systems, hybridization can reduce costs and emissions by an estimated 20%. The software reviewed are the most widely used and comprehensive for HRES. Yet, they all come with their limitations. For example, HOMER is incapable of conducting a thermal analysis while only HOMER and IHOGA can conduct hydro energy sources analysis. As such, the paper aims to provide an in-depth review of the capabilities and limitations of various software regarding HRES, so that users can decide which software (both individually and in combination with each other) would be most appropriate for their HRES.
© 2021 Elsevier Ltd. All rights reserved.
Selection and peer-review under responsibility of the scientific committee of the International Conference on Advancement in Materials, Manufacturing and Energy Engineering (ICAMME-2021).

1. Introduction

The use of energy is so much integrated with our lives that the energy demand is increasing day by day. Fossil fuels are still supplying around 80% of the world's current energy.[1]. Non-renewable, also known as dirty energy, are sources of energy available in reserved amounts and take a considerable amount of time to plenish again. On the flip side, clean energy, the other name of renewable energy, emanate from naturally occurring sources or natural actions and is continually being replenished. A hybrid energy system generally comprises multiple clean energy sources used in conjunction to develop more system efficiency, a more effective system, and a greater balance in energy supply. They can be integrated with several types of equipment, including energy generation, energy storage, etc.

Software tools have been used considerably in many projects to optimise HRES (Hybrid Renewable Energy System) in various projects and papers worldwide. Software tools can analyse the various parameters present and accordingly give the optimal solution required for the analysis. In the following section, these software tools have been analysed and review for further use.

A major limitation to HRES has been that there is no one ideal configuration for the hybrid energy system. Optimization depends on the accessibility of renewable and non-renewable resources, available energy infrastructure, construction costs, and incentive programs. Hence planning a hybrid system requires a detailed study of the proposed project site and policies and resources. While designing a system that incorporates several different renewable energy sources, it is extremely crucial to model and simulate the design, after which it can be optimized. To optimize the hybrid system, the most common software tools which been analyzed are available. However, in the present analysis, it becomes apparent that while these software have many features and are the most popular software today, they have certain limitations. It is important to be aware of the limitations and work on methods to minimize errors in the calculations. Also, these software analyze different aspects such as the environmental impact of the system, a feature some software currently do not cover. Modelling production costs accurately is key for determining the economics of hybrid energy systems. As application increases,

* Corresponding author.
E-mail address: anilkumar76@dtu.ac.in (A. Kumar).

https://doi.org/10.1016/j.matpr.2021.02.452
2214-7853/© 2021 Elsevier Ltd. All rights reserved.
Selection and peer-review under responsibility of the scientific committee of the International Conference on Advancement in Materials, Manufacturing and Energy Engineering (ICAMME-2021).

Please cite this article as: K. Ram, Prasanna Kumar Swain, R. Vallabhaneni et al., Critical assessment on application of software for designing hybrid energy systems, Materials Today: Proceedings, https://doi.org/10.1016/j.matpr.2021.02.452

markets expand and the systems become more complex as a whole, it is vital to minimise any uncertainties of modelling the systems energy production.

Even though various studies have been carried out on the optimization of HRES, the authors could not find a paper on applying software for the analysis of hybrid energy systems. This review article aims to throw light on the contemporary software applied in HRES, various optimization techniques, and simulation procedures for the investigators, researchers, and scientists working on this.

2. Overview of software tools

Designing, analysing, and optimising hybrid systems is a complex task and calculates their various impacts such as economic, environmental etc. As such requires software tools that can provide, analyse, simulate, economical and optimization planning, and design and modelling. Several software has been created to conquer issues about presenting the ideal design, optimisation, and analysis. This is crucial to ensure the minimisation of installation costs and awareness of the various impacts before starting.

2.1. Homer

HOMER (hybrid optimization model for electric renewable energy software is one of the most predominantly used software globally. Its main purpose is to design and model power or energy systems. In the USA, the national renewable energy laboratory has been credited with creating HOMER [2]. It uses Visual C++ as a programming language. HOMER is a micropower optimization model [2]; whose main aim is to assess the models of grid-connected systems as well as systems not connected to the grid, for a multitude of purposes. This software has also proved useful in optimising and analysing HRES. Examples would include generators, wind power, PV cells for solar sources, cogeneration, biomass, water generated power, batteries, and many other varying sources [3].

HOMER energy features for analysis included economic, solar power, generators, storage devices, water-induced power generation, and other renewable energy sources [3,4]. The core capabilities of HOMER fall into three major categories, as shown in Fig. 2. As shown in Fig. 1, the outputs obtained through these analysis capabilities are comprehensive and provide the user with information across multiple aspects to assess their system.

Rohani et al. used HOMER to design and optimise a renewable HRES, where most of the energy generated from the HRES comes from wind generators and PV panels (fuel cells or batteries are kept as backup). The system is designed to produce electricity for a remote village. The aim was to design a dependable and independent system by optimizing the design and its scope and aiming to minimise the cost incurred. In addition to both the technical design and economic analysis the paper also reviews the environmental impact of the system based solely on the annual emissions [5].

Ramli et al. devised an HRES using PV and diesel components to be used in Saudi Arabia. Arrangement's dependability was boosted by energy-storing mechanisms such as battery and flywheel energy. The performance of both the system as well as the storage mechanism was analyzed using HOMER software. The analysis was focused on the economic and environmental impact based on fuel consumption and carbon emission reductions. The paper also covered the impact of using the flywheel for energy cost, power generation, and NPC (net present cost) [6].

Alam et al. suggested an HRES which would be appropriate even for isolated area applications. Their system consists of an energy installation powered by wind, photovoltaic panels, and a battery cell. The design and analysis were carried out by HOMER and based on the simulation results; the system was a feasible solution. Along with the renewable energy resources, the system also features an electrolyser and a reformer for the making of and providing a consistent source of H2 gas for the battery. HOMER was used to analyse the economic feasibility to determine the starting price, yearly replacement price, yearly capital price, annual maintenance, and operation prices [7].

Kumar et al. present an idea that discusses the optimisation, modelling, and evaluation of an independent system that uses clean energy resources suitable for HRES. This paper aims to provide an ideal answer that alleviates the world power crunch problem, especially so in locations that do not have access to the grid. The HOMER software was used to perform an economic, energy balance and sensitivity analysis of the system [8].

2.2. Retscreen

RETScreen is a software that provides access to renewable energy modelling and analysis. It allows users to identify and analyse potential power efficacy, clean power, and combined production projects. It has been extensively utilized to assess and validate the various power performances of houses, plants, and other structures worldwide, including actual, predicted, and ongoing performances, and to handle the files of multiple projects [9]. The Canadian government has created the software in collaboration with various global affiliates and is used by approximately 7 lakh people worldwide [10]. The software boasts many features that allow for a thorough analysis of the system to be designed. Some include a virtual energy analyser, a 5-star benchmarking system, an entire project life analysis and an expert decision engine [9]. As shown in Fig. 3, the outputs obtained through the analysis capabilities of RETscreen are thorough and especially useful while analysing a combination of both conventional and renewable energy sources in their system.

Chowdhury et al. have proposed a hybrid system containing photovoltaics (PV) and biomass in conjunction with extra storage.

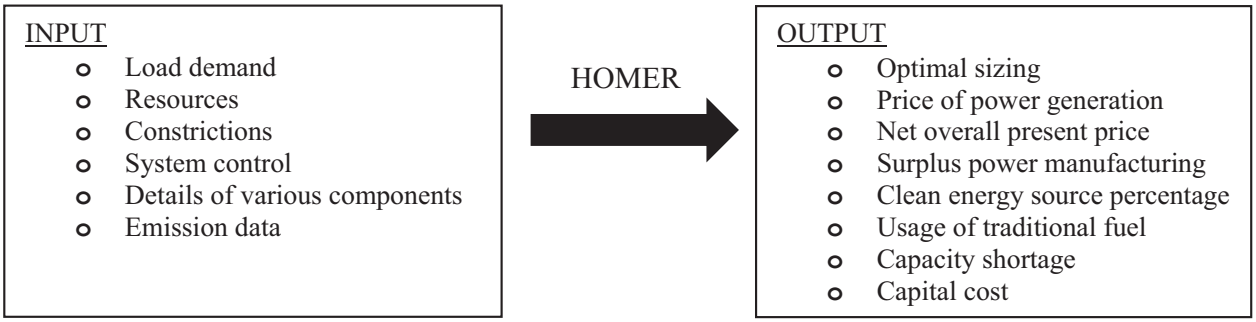

Fig. 1. The respective inputs and outputs generated in a HOMER analysis [4].

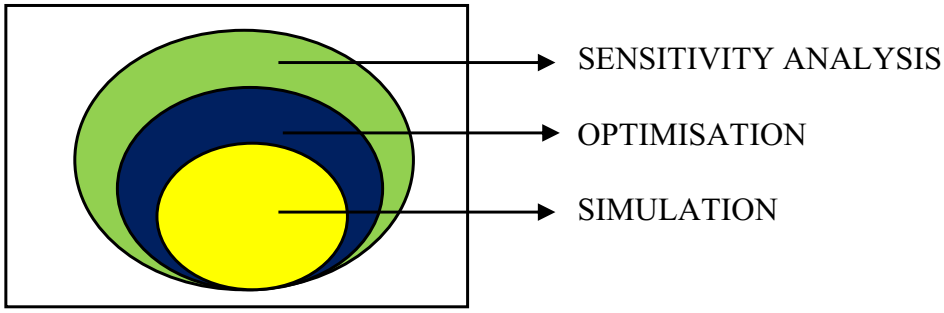

Fig. 2. The core capabilities of the HOMER software [3].

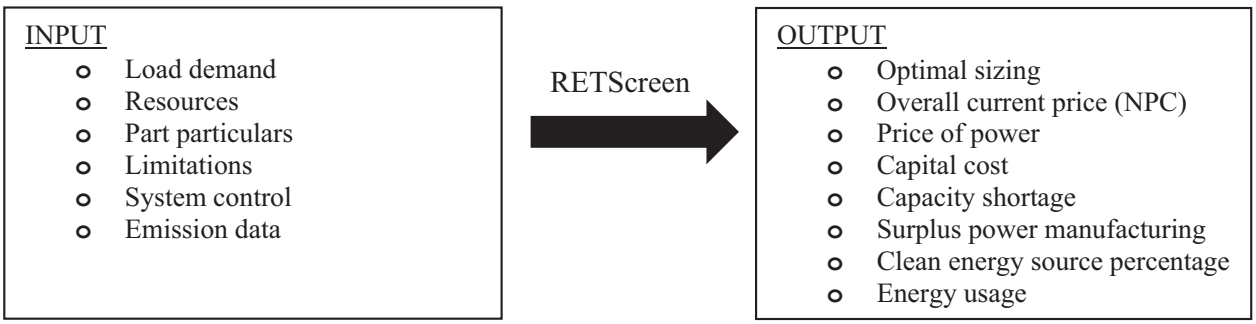

Fig. 3. The respective inputs and outputs generated in a RETScreen analysis [4].

The paper gauges the viability of the system to be used with an off-grid power system in the remote localities of Bangladesh. RETScreen model software has been used to assess pollutant emissions and measure the cost parameters. The fiscal evaluation has been conducted by considering the annual earnings of the end-user along with the payback periods. The analysis aims to cover all aspects of the system and contain the environmental impacts of setting up the proposed system. RETScreen software bases its analysis on the contrast between the proposed design and the conventional design. The conventional system here is a kerosene-based system. Through the simulation and analysis, the payback of the project had been estimated to be 6.9 years.

Furthermore, this model can reduce CO_2 emissions by nearly 3.81 tonnes per year. In this hybrid energy model, the simulation results show that 81.2% is produced by PV and the remaining from the biomass generator. As a result, the findings are significantly in favour of the proposed system. The proposed system has proven to be more dependable, environmentally friendly, and less expensive than the traditional kerosene-based system [11]. Fig. 4. shows the core capabilities and features of RETScreen and the flowchart associated with a typical technical evaluation in system analysis.

2.3. iHOGA

iHOGA (Improved Hybrid Optimization by Genetic Algorithms) is a computer program made in computer coding language C++ by scientists from the University of Zaragoza to improve hybrid electrical power systems that supported renewable energy sources. This program can simulate and optimize the systems of many different sizes. It can simulate systems connected to the grid and for different cases of Net Metering and Net Billing [13]. It uses thorough control strategies which enables it to consider both the types of algorithm (Main Algorithm and Secondary Algorithm) for simulating any set of results. This is the main reason the required time for analysis using iHOGA is slightly longer than other software. Fig. 5 shows the various parameters that that be set in iHOGA and their respective output.

Shezan used iHOGA to estimate and reduce COE (cost of energy), NPC and CO_2 emissions for conducting a feasibility analysis on an isolated hybrid microgrid system with power and voltage response. This would have helped establish it for offshore islands. The author had displayed a practical and useful design for a hybrid wind-diesel energy system to get the results which fulfilled the

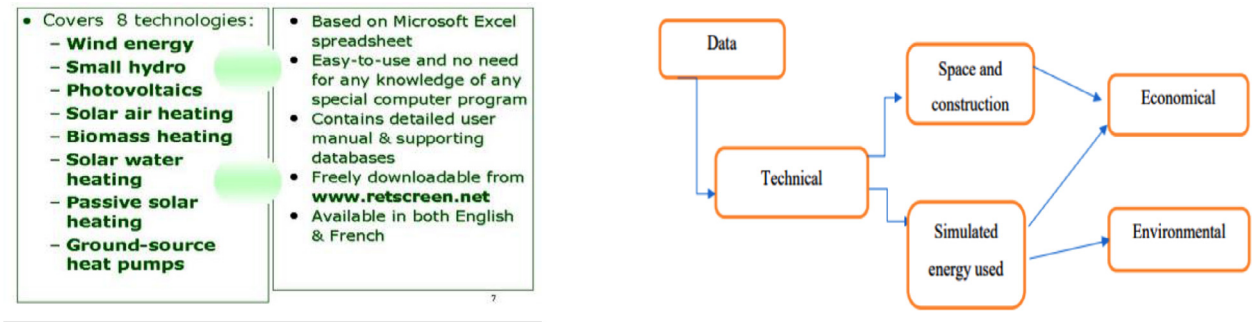

Fig. 4. (a) The core capabilities and salient features of RETScreen software [12], (b) RETScreen technical evaluation structure flowchart [11].

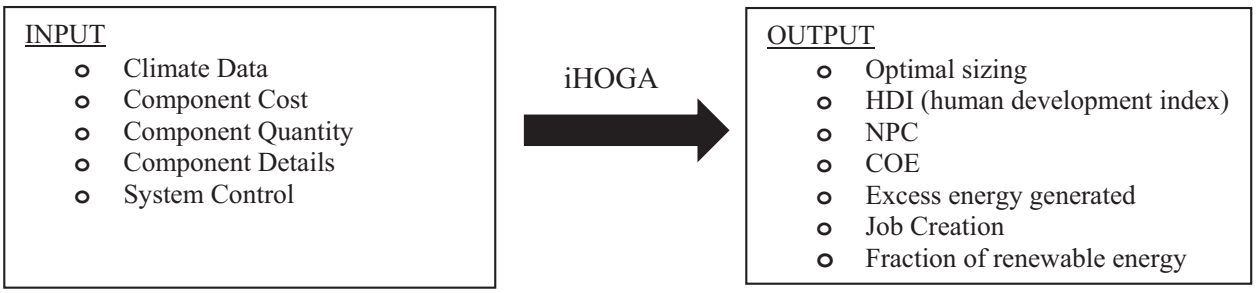

Fig. 5. The respective inputs and outputs generated in an iHOGA analysis.

demand load requirement for a small town in Malaysia. Shezan considered meteorological data and technical specs of each module to conduct the optimization process in iHOGA [14].

Fulzele and Daigavane designed and optimized a hybrid wind-PV renewable energy system for rural electrification in countries like India, which is a developing nation. They used iHOGA to perform mono-objective functions only. The objective was to minimize NPC for the user defined constraints such as maximum unmet load allowed and maximum levelized cost of energy. While designing the hybrid system, economic viability had to be the top priority because the system is meant for rural areas, where the actual users are not supposed to be in a condition to pay the high costs of electricity due to their unstable and impoverished economic state [15].

Zubi et al. utilized iHOGA to generate outputs for the optimal solution. Different battery banks were considered and a variety of PV generators with diverse power ratings were taken into account for iHOGA to perform the simulation for all the combinations possible. The NPC was estimated and least cost solution was provided. The lifetime for the complete installation was considered to be 25 years and the simulation was done in time steps of 1 h for the same [16].

Simple Ah model [17], Kinetic model [18] Copetti et al's model [19] or advanced weighted Ah-throughput model [20]. These are the few models that iHOGA can use to calculate the state of charge in the battery and its voltage.

Tawfik et al. worked on providing desalinated water to people in a remote area somewhere in Egypt. To minimize the cost of desalinated water, the NPC for electricity consumption of the desalination unit needed to be reduced.The research aimed to select such HSES components that would be most suitable for the energy supply to the desalination unit. It was accomplished by optimizing and managing the loads to find the best scenario possible.iHOGA software was used to simulate and optimize the system. The optimization of HSES showed COE to be around 12.46 INR/kWh and NPC was 1.19 crore INR. However, 1.3% of total energy requirements remained unmet and 75% was renewable proportion [21].

2.4. Insel

INSEL (Integrated Simulation Environment Language) is a graphical programming language for a common objective. It can solve any of the simulation problems for PV systems. It presents a block diagram to simulate electrical constituents, meteorological data and thermal/heat energy. It helps to understand, visualize, plan, and monitor energy systems by working as a modular simulation environment. It has the capability of simulating PV systems, including sun-tracking impact and shading analysis. INSEL offers users, ready-made simulation models, also. The software tool works for grid-connected systems and standalone systems both. MATLAB and Simulink compatible databases for PV devices, thermal systems and meteorological specifications are also provided for the user [22,23].

Gürlich et al. modelled the technical system for a European building with the simulation environment INSEL (version 8.2.0.779) in one-minute time steps for a PVT (photovoltaic-thermal) hybrid system for trigeneration. They followed the idea of hybrid generation but extended the conversion of heat and electricity: added the longwave radiative cooling in a PVT panel operation, allowing the direct generation of cooling in times of no heating operation [24].

Beringer et al. performed theoretical calculations using INSEL. To show the comparison between tilted and normal panels, calculating the solar irradiation data on tilted surface was required. For this, INSEL was needed to find the cumulative irradiances on the various tilted surfaces, as per the solar cells [25].

Gerstmaier et al. described an approach of making FLATCON® CPV (Concentrating PV) technology compatible with standard photovoltaic simulation software like INSEL. Curve fitting using INSEL was done for two-diode model with high accuracy [26].

2.5. Hybrid2

With a commendation from the National Renewable Energy Laboratory, Hybrid2 software was launched by RERL (Renewable Energy Research Laboratory) of the University of Massachusetts Amherst, USA (1996), after the development of Hybrid1(1994). The software package of Hybrid2 is an easily manageable tool for users to carry out in-depth output and economic study over a long-time span on a plethora of hybrid power systems. Moreover, Hybrid2 is based on computer models that use probabilistic series. It requires data for loads for those time series, wind velocity, radiation from the sun, temperature, and the hybrid power model considered by the designer to forecast the output of the model while considering variations in wind velocity and load for each time step. Hybrid2 was designed to deliver a reliable platform for assessing the performance of a variety of hybrid power systems [27,28]. Fig. 6 shows the various parameters that that be set in Hybrid2 and their respective output.

In Chicago, IL, a hybrid system based on hydrogen as fuel was designed, and its simulation was run using renewable resources available on a probabilistic model developed for Hybrid2. The system was integrated using 6.5 kWp solar array, 2-kW fuel cell joined to a 12kWp wind turbine, an electrolyser of 8 kW and a hydrogen gas compressor of 3 kW comply with a fluctuating load having an average of 1 kW. According to a paper published by McGowan et al., over one year, the energy produced by the system was over the required capacity by 160% and no additional hydrogen or fossil [30]. Genec's hybrid system was simulated using Hybrid2. Some precise parameters, such as the number of modules per string, the MPPT, the consumption and threshold value for when the Genset resumes, have been considered. The influence of these parameters on the system's performance has been analysed [31].

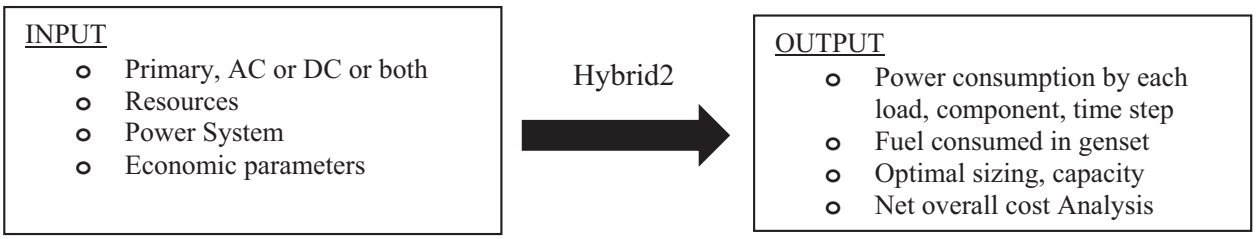

Fig. 6. Overview of various input parameters hybrid2 requires and the output that it gives [29].

McGowan et al. (1995) showed that using proper computational techniques, the key performance parameters for determining the size and designing renewable energy system were recognized, where HYBRID2 tries to give output according to the load [32].

Hybrid2 is also thorough enough to be used by skilled hybrid system designers as an instrument to design a preliminary system [33]. However, the software tool has still paid access. There are also some limitations to the configuration of the software tool. For instance, PV and diesel cannot be used on different buses simultaneously. Moreover, no additional diesel may be used if a rotary converter is running [32].

2.6. Trnsys

TRNSYS is simulation software used mainly for transient systems that has been available for commercial purposes since 1975. It was founded by the University of Wisconsin and the University of Colorado. The program is now being handled by the Thermal Energy System Specialists (United States) and the Solar Energy Laboratory of the University of Wisconsin along with a collaboration with Centre Scientifique et Technique du Bâtiment (France), as well as TRANSSOLAR Energie Technik (Germany) [34,35]. TRNSYS has an array of users globally ranging from scientists to engineers, building simulation experts to consultants, as well as students to designers, owing to its flexible nature and many areas of application [35].

An emergency container, a small energy reservoir, is demonstrated for use in rural areas. In this paper, the model is a hybrid PV/wind/engine system that generates electricity and can provide potable water for around 1000 individuals during natural disaster periods. For the hybrid PV/wind/engine energy system, a transient model employed in TRNSYS for two different sites, Nairobi (Kenya), and Nyala (Sudan). A control algorithm has been employed to make the system more reliable and for higher power accessibility. The simulation shows that the power generated in Nairobi is 63% and in Nyala is 80% of solar energy. For wind power, the share holds up to 27% and 12%, for Nairobi and Nyala, respectively, implying that around 90% of the energy demand could be supplied by renewable resources [36].

Saleem et al. simulated a solar hydrogen cogeneration system, which comprised photovoltaics, an electrolyser component, a fuel cell part, a battery for storage, a unit for storing hydrogen, and a controller, using TRNSYS for locations in Lahore, Pakistan and Fargo, North Dakota (USA). The system generated hydrogen. The overall energy improvements are very promising for warmer temperatures, demonstrating that this model holds future renewable energy alternatives. The system was 7.8% efficient in Fargo North Dakota state's low temperature environment as it receives lower solar irradiance. In comparison, the higher temperature climatic conditions of Lahore led to the system being 11.8% efficient. The output report showed that the system could cover 85% and 53% (due to lower solar irradiance present) of the water demand in summer and winter, respectively [37].

Lamrania et al. proposed a numerical system model for evaluating the output of an indirect hybrid solar dryer for wood by using TRNSYS software, where solar compound parabolic concentrator (CPC) was utilised for producing heat (thermal energy). A comparative study between theory and experimentation was carried out and the mean relative error was 3.9%. An environmental analysis showed that the collector led to lower CO_2 emissions by 34% at the auxiliary heater system [38].

Liu et al. performed a techno-economic. Four different renewable application setups were considered to be applied on a regular high-rise structure in Hong Kong using simulation and optimisation on two software namely TRNSYS and jEPlus + EA. Their experimentation confirmed that the RMS (root mean square) deviations present between the established and simulated battery for TRNSYS are 1.49% and 0.94% for jEPlus + EA. Moreover, it was shown that a supplementary battery improved the yearly mean load cover ratio, and the self-consumption ratio improved by 14.08% for TRNSYS and 16.56% for jEPlus + EA, for the optimal PV-wind-battery system covers 81.29% of the annual load. It concluded that techno-economic studies of diverse typical situations can provide a pedestal for applying renewable resources in high-rise structures and resulting in an additional decrease of carbon footprint in urban areas [39].

TRNSYS helps users when the standard models do not closely represent the actual performances as they are not sufficiently comprehensive or when new technologies are to be dealt with. Moreover, through TRNSYS, users can work beyond the boundaries of the simulation where numerous factors are required. Moreover, TRNSYS makes it easier to add mathematical models, accessible supplementary parts, as well as the capability to work along with other simulation software in case of any requirements. However, for environmental analysis, an estimate of CO_2 emission is not available in the basic version of TRNSYS [40].

3. Overview of software tools

Software tools have proven to be of paramount importance while designing, analysing, and optimising hybrid renewable energy systems. Table 1. presents an analysis of each software by going through their unique advantages and limitations. This overview provides the user with a detailed compilation of information which would then further allow them to be well informed and pick out an appropriate software to analyse their hybrid system. It would also help them be aware of any limitations or pitfalls that the respective software may have.

An overview of the different analysis capabilities, more precisely techno-economic and renewable energy generator parameters, of the various available software tools used for the design and analysis of hybrid energy system, are compared in Table 2. Besides the reviewed software tools in this paper, thirteen additional software have been included.

Table 1
An overview of the comparison of advantages and limitations of the various software.

Software	Advantages	Limitations
HOMER	- Homer models off-grid and grid connected power systems, comprising wind, solar, hydro, biomass, and conventional power sources [7] - It can analyse economic impact based on the emissions of the proposed system [5] - It can provide the initial cost, annualized capital cost, annualized replacement cost, annual operation and maintenance cost are first evaluated through homer and then compared with the cost analysis. [6] - This model can analyse stand-alone wind-PV-fuel cell system [7] - It can do sensitivity analysis, which determines varying factors such as wind speed, fuel cost [8]	- The software only allows imperial units. [4] - Any time-series data in the form of daily average cannot be imported. [4] - It cannot analyse thermal systems. - It does not consider depth of discharge (DOD) of batteries. This plays an important role in optimizing the hybrid system since in real life the factor of both life and size of battery bank decreasing is a significant factor. - Allows only single objective function for minimizing the net present cost. This means that the multi-objective problems cannot be formulated using this software. - It does not rank the hybrid systems as per the cost of energy. - Does not consider the factor of intra-hour variability [41].
RETScreen	- RETScreen hosts a diverse range of both traditional and non-traditional sources of clean energy as well as conventional energy sources and technologies [9] - Allows for the instant and precise estimation and analysis of energy production and energy savings potential for any location worldwide [42]. - RETScreen Expert has analysis capabilities that can cover the entire life cycle of a project life, making the software unique and useful [42].	- Data or files cannot be imported [4] - Lots of limitations for search [28]-Less data input [28]-Not capable of the generator, hydro energy [4]
Hybrid2	- It has a user-friendly interface [33] - Short-term fluctuations in the load and renewable resources are accounted for by the probabilistic method [33] - It allows for a remarkably diverse system architecture - It provides a detailed economic analysis [31]	- There are limitations to its configuration; for example, PV and diesel cannot be used at the same time [32] - It is incompatible with Windows versions updated after Windows XP [43] - The software is not flexible in defining the various components [31].
iHOGA	- It makes use of advanced optimization algorithms and hence in-depth optimization is feasible in iHOGA - iHOGA could simulate Net- metering of any case [13]. - It has multi-objective optimization and probability analysis [44]. - Advanced battery aging models and auto optimization of PV panels slope are plus [44]. - It allows to select "evaluate all combination" which produces 100% population.	- EDU version has limited use; plenty of the options or features are not accessible. - The advanced algorithm is relatively time-taking [13]. - It does not have analysis capability for Bio-energy system [43].
INSEL	- Synthesis of Meteorological Time Series. [22] - Dynamic Building Simulation. - It can be combined with all MATLAB & Simulink. [22] - Offers users ready-made simulation models [22] - single-axis tracking, double-axis tracking, as well as losses for fixed angles can be seen.	- It cannot be used for systems where PV is not included - Economic analysis is not available [43] - Costs around 1100 US $ [45]
TRNSYS	- It has good flexibility and wide-spread areas of application [35]. - It is helpful to users when details are missing to represent the real-world performance clearly - Users can work beyond the boundaries of the simulation where numerous parameters are required [40].	- For environmental analysis, an estimate of CO_2 emission is not available in the basic version [40]. - It cannot perform analysis of hybrid systems which include biofuel or hydropower [43].

Table 2
Overview of the analysis capabilities of the software tools [43].

Software Tools	Economic Analysis	Technical Analysis	PV System	Wind System	Generator set	Storage device	Bioenergy	Hydro energy	Tidal Power	Fuel cell	Thermal System
HOMER	✓	✓	✓	✓	✓	✓	✓	✓	✓	✓	X
RETScreen	✓	✓	✓	✓	X	✓	✓	X	✓	✓	✓
iHOGA	✓	✓	✓	✓	✓	✓	X	✓	X	✓	X
Hybrid2	X	✓	✓	✓	✓	✓	X	X			✓
INSEL	X	✓	✓	✓	✓	✓	X	X			✓
TRNSYS	✓	✓	✓	✓	✓	✓	X	X			✓
HYBRIDS	X	✓	✓	X	X	✓	X	X			X
SOMES	✓	✓	✓	✓	X	✓	X	X			X
RAPSIM	X	✓	✓	✓	✓	✓	X	X			X
SOLSIM	✓	✓	✓	✓	✓	✓	✓	X			X
ARES-I&II	X	✓	✓	✓	✓	✓	X	X			X
HYSYS	X	✓	✓	✓	✓	✓	X	X			X
HybSim	✓	✓	✓	X	✓	✓	X	X			X
Dymola/ Modelica	✓	X	✓	✓	X	✓	X	X			X
SOLSTOR	✓	✓	✓	✓	✓	X	X	X			X
HySim	✓	✓	✓	X	✓	✓	X	X			X
IPSYS	X	✓	✓	✓	✓	✓	X	✓			X
Hybrid Designer	✓	X	✓	✓	✓	✓	X	X			X
GRHYSO	✓	✓	✓	✓	X	✓	X	✓			X

4. Conclusion

Software tools are widely used to design hybrid renewable energy systems. The following concluding remarks can be drawn from the comparative study and critical assessment made:

- The use of software tools in the design and optimization of hybrid renewable energy systems help in minimising capital investment, determining the optimal capacity of the system and forecasting its long-term performance.
- HOMER is the most commonly used software as it can handle a wider range of hybrid system analysis, from photovoltaics to fuel cells. Therefore, extensively customizable projects can be produced.
- Moreover, HOMER produces results in an extremely clear, focused, well-organised manner.
- HOMER and RetScreen are two of the most widely used software and hence have the most extensive databases for facilities and their specifications.
- RETScreen can perform both thermal and techno-economic analysis on all hybrid systems except for hydropower. Additionally, it has one of the most extensive databases for facilities and specifications.
- iHOGA can perform techno-economic analysis along with multi-objective and in-depth optimization using advanced optimization algorithms.
- Hybrid2 and INSEL can handle hybrid PV systems or solar systems, including generator set and power storage devices, to perform technical and thermal analysis. INSEL also includes a sun-tracking analysis and it is compatible with MATLAB and Simulink.
- TRNSYS is able to perform a techno-economic and thermal analysis on the hybrid systems that include wind and PV. Simulations, where multiple parameters and/or details are missing, can be carried out on TRNSYS.

The present commonly used software tools are all unique because they have been configured with different parameters and complexities. However, they are limited in their features and analysis capabilities. The software cannot make a thorough analysis of the hybrid renewable energy systems in all aspects, that is while techno-economic analysis can be performed in some, a thermal analysis cannot be executed. Some software do not include features to support analysis of hybrid systems for all renewable energy sources available. HOMER can execute a techno-economic analysis for hybrid systems including PV, wind, hydro, tidal and bio-energy but a thermal analysis is not supported in the software. RETScreen's and TRNSYS's configuration supports both techno-economic and thermal analysis. Yet RETScreen cannot optimise systems that include a generator or hydro-power while TRNSYS's features do not include hydro- and bio-energy. Similarly, INSEL and Hybrid2 are both limited to economic and thermal analysis on hybrid systems that include photovoltaics and wind power. iHOGA can execute only techno-economic analysis for hybrid systems excluding bioenergy and tidal power.

It is therefore recommended to identify thoroughly the components of a hybrid renewable energy system before choosing a software tool for its design and analysis. Additionally, the renewable energy sources included in the system should be supported in the software's feature. It is therefore more suitable to use a combination of software tools or software tools and algorithms in the design of a hybrid renewable energy system to complement a complete and thorough design, analysis, and optimisation.

CRediT authorship contribution statement

Khemshika Ram: Data curation, Conceptualization, Writing - original draft. **Prasanna Kumar Swain:** Methodology, Writing - original draft. **Ruchita Vallabhaneni:** Visualization, Investigation, Writing - original draft. **Anil Kumar:** Writing - original draft, Supervision.

Declaration of Competing Interest

The authors declare that they have no known competing financial interests or personal relationships that could have appeared to influence the work reported in this paper.

Acknowledgment

The authors are highly thankful to Centre for Energy and Environment, Delhi Technological University, Delhi (India), for providing the basic facility in compiling this manuscript.

References

[1] https://www.forbes.com/sites/rrapier/2020/06/20/bp-review-new-highs-in-global-energy-consumption-and-carbon-emissions-in-2019/. [Accessed 02 01 21].
[2] https://www.homerenergy.com/products/pro/index.html. [Accessed 01 12 20].
[3] https://openjicareport.jica.go.jp/pdf/12265039_03.pdf. [Accessed 07 10 20].
[4] A.P. Kumar, Analysis of hybrid systems: software tools, Electronics, Information, Communication and Bio-Informatics (AEEICB) (2016) 327–330.
[5] A. Rohani, K. Mazlumi, H. Kord, Modeling of a hybrid power system for economic analysis and environmental impact in HOMER, in 2010 18th Iranian Conference on Electrical Engineering, 2010.
[6] Ramli, AM Makbul, Ayong Hiendro, Twaha Ssennoga, Economic analysis of PV/diesel hybrid system with flywheel energy storage, Renewable Energy 78 (2015) 398–405.
[7] M.S. Alam, D.W. Gao, Modeling and Analysis of a Wind/PV/Fuel Cell Hybrid Power System in HOMER, 2nd IEEE Conference on Industrial Electronics and Applications (2007) 1594–1599.
[8] Kumar Prashant, Pukale Rahaul, Kumabhar Nilesh, Optimal Design Configuration Using HOMER, Procedia Technology 24 (2016) 500–504.
[9] https://www.nrcan.gc.ca/maps-tools-publications/tools/data-analysis-software-modelling/retscreen/7465. [Accessed 17 12 20].
[10] https://openei.org/wiki/RETScreen_Clean_Energy_Project_Analysis_Software.. [Accessed 17 12 20].
[11] Nusrat Chowdhury, Chowdhury Akram Hossain, Michela Longo, Wahiba Yaïci, "Feasibility and Cost Analysis of Photovoltaic-Biomass," MDPI, pp. 3-12, 2020.
[12] https://present5.com/retscreen-an-evaluation-tool-for-renewable-energy-projects/. [Accessed 02 01 21].
[13] https://ihoga.unizar.es/Desc/iHOGA%202.5%20User%20manual.pdf," [Online]. [Accessed 30 01 20].
[14] S.K.A. Shezan, Feasibility analysis of an islanded hybrid wind-diesel-battery microgrid with voltage and power response for offshore Islands, Journal of Cleaner Production 288 (2020).
[15] B. Fulzele Ms. Jyoti, Daigavane M. B., Design and Optimization of Hybrid PV-, Wind Renewable Energy, Mater. Today no. 2018 (5) 810–818..
[16] Ghassan Zubi, Rodolfo Dufo-López, Guzay Pasaoglu, Nicolás Pardo, Techno-economic assessment of an off-grid PV system for developing regions to provide electricity for basic domestic needs: A 2020–2040 scenario, Appl. Energy 176 (2016) 309–319.
[17] Joachim Luther, INSEL—A simulation system for renewable electrical energy supply systems." Tenth EC Photovoltaic, in: Solar Energy Conference, Springer, Dordrecht, 1991, pp. 457–460.
[18] Manwell, F. James, G.McGowan. Jon, Lead acid battery storage model for hybrid energy systems, Solar energy 50 (5) (1993) 399–405.
[19] J.B. Copetti, E. Lorenzo, F. Chenlo, A general battery model for PV system simulations, Progress in Photovoltaics: research and applications 1 (4) (1993) 283–292.
[20] Julia Schiffer, Dirk Uwe Sauer, Henrik Bindner, Tom Cronin, Lundsager Per, Kaiser Rudi, Model prediction for ranking lead-acid batteries according to expected lifetime in renewable energy systems and autonomous power-supply systems, Power Sources 168 (2007) 66–78.
[21] T.M. Tawfik, M.A. Badr, E.Y. El-Kady, Optimization and energy management of hybrid standalone energy system: a case study, Renewable Energy Focus 25 (00) (2018) 48–56.
[22] https://insel.eu/files/public/inselFlyer.pdf, [Online]. [Accessed 08 01 21].

[23] G. Ganesan, R. Sagayaraj, A.Ali. Nazar, Investigations on Review of Software Tools for the Integration of Renewable Energy Systems for Sustainable Energy Development, International Journal for Research in Engineering Application & Management (IJREAM) 04 (04) (2018) 705–710.
[24] Gürlich Daniel, Antoine Dalibard, Ursula Eicker, Photovoltaic-thermal hybrid collector performance for direct trigeneration in a European building retrofit case study, Energy and Buildings 152 (2017) 701–717.
[25] S. Beringer, H. Schilke, I. Lohse, G. Seckmeyer, Case study showing that the tilt angle of photovoltaic plants is nearly irrelevant, Solar Energy 85 (2011) 470–476.
[26] Tobias Gerstmaier, Sascha van Riesen, Andreas Gombert, André Mermoud, Thibault Lejeune, and Eric Duminil, "Software Modelling of FLATCON© CPV Systems, American Institute of Physics, Maryland, 2010.
[27] I. Baring-gould, H.J. Green, V.A.P.van Dijk, J.F. Manwell, Hybrid2: The Hybrid System Simulation Model, National Renewable Energy Laboratory NREL, Colorado, USA, 1996.
[28] Daljeet Kaur, PS Cheema, Software tools for analyzing the hybrid renewable energy sources:-A review, International Conference on Inventive Systems and Control, (ICISC), 2017, pp. 1–4.
[29] H. Manwell, J. Green, HYBRID2- A versatile model of the performance of Hybrd Power Systems, National. Renewable Energy Laboratory (1995).
[30] Andrew Mills, Said Al-Hallaj, Simulation of hydrogen-based hybrid systems using Hybrid2, International Journal of Hydrogen Energy 29 (10) (2004) 991–999.
[31] H. Colin, P. Boulanger, Photovoltaic Hybrid System Modelling with Hybrid2 Software, Consommation 6000 (2000) 6500.
[32] J. McGowan, J. Manwel, Hybrid wind/pv/diesel hybrid power systems modeling, Renewable Energy Laboratory, Department of Mechanical and Industrial Engineering 9 (1) (1996) 836–847.
[33] Green, H. J., and Manwell, J. HYBRID2–A versatile model of the performance of hybrid power systems (No. NREL/TP-441-7807; CONF-950309-1). National Renewable Energy Lab., Golden, CO (United States) (1995)
[34] U. o. Wisconsin-Madison, A TRaNsient SYtems Simulation program, http://sel.me.wisc.edu/trnsys/, [Accessed 04 01 2021].
[35] http://www.trnsys.com/#2. [Accessed 04 01 21].
[36] S.G. Sigarchian, A. Malmquista, T. Fransson, Modeling and control strategy of a hybrid PV/Wind/Engine/Battery system to provide electricity and drinkable water for remote applications, Energy Procedia (2013) 1401–1410.
[37] M.S. Saleem, N. Abas, A.R. Kalair, S. Rauf, A. Haider, M.S. Tahir, M. Sagir, Design and optimization of hybrid solar-hydrogen generation system using TRNSYS, Int. J. Hydrogen Energy 45 (32) (2019) 15814–15830.
[38] B. Lamrani, A. Khouya, A. Draoui, Energy and environmental analysis of an indirect hybrid solar dryer of wood, Solar Energy 183 (2019) 132–145.
[39] J. Liu, M. Wang, J. Peng, C. Xiu, S. Cao, Techno-economic design optimization of hybrid renewable energy applications for high-rise residential buildings, Energy Conversion Management 213 (2020) 112868.
[40] H. Sharma, É. Monnier, G. Mandil, P. Zwolinski, S. Colasson, Comparison of environmental assessment methodology in hybrid energy system simulation software, Procedia CIRP 80 (2019) 221–227.
[41] Kenneth OkeduEloghene, Uhunmwangho Roland, Optimization of renewable energy efficiency using HOMER, International Journal of Renewable Energy Research (IJRER) 4 (1) (2014) 421–427.
[42] https://www.softwaresuggest.com/us/retscreen.. [Accessed 27 12 20].
[43] Sunanda Sinha, S.S. Chandel, Review of software tools for hybrid renewable energy systems, Renewable and Sustainable Energy Reviews 32 (2014) 192–205.
[44] https://ihoga.unizar.es/en/caracteristicas/. [Accessed 06 01 21].
[45] https://photovoltaic-software.com/pv-softwares-calculators/pro-photovoltaic-softwares-download/insel. [Accessed 09 01 21].

International Journal of Policy Sciences and Law
Volume 1, Issue 3

International Journey of Policy Sciences and Law

Volume 1, Issue 3

Cultural Exploitation of Rural Women Subjected to Menstrual Exile: A Review of Nepal and India

Pearl Khurana[1] and Ankita Singh Gujjar[2]

This Article is brought to you for "free" and "open access" by the International Journal of Policy Sciences and Law. For more, visit http://ijpsl.in/
To submit your manuscript, email it to us at editorial.ijpsl@gmail.com or click here.

[1] *B.A. Hons. Economics, Delhi Technological University, India*

[2] *B.A. Hons. Political Science, Lady Shri Ram College for Women, University of Delhi, India*

International Journal of Policy Sciences and Law
Volume 1, Issue 3

Abstract

Menstrual exile is an exploitative custom observed in the tribal communities of developing nations across the world, where menstruating women are banished from their own homes. This paper explores the impacts of menstrual exile on the physical, psychological and reproductive health of women. This stigma around menstrual exile interferes with their liberty, bodily integrity and violates the right not to be discriminated against based on sex. The authors have performed a complete review of Chhaupadi and Gaokor in Nepal and India with the help of existing quantitative data, journal articles, international and national reports and case studies. Finally, the authors have highlighted the areas which can be worked upon, and have left room for further discussion as the scope for research is immense. This paper is the authors' contribution to a cause with minimal representation in the mainstream development agendas.

Keywords: *Menstruation, menstrual exile, Chhaupadi, myths and beliefs, awareness campaigns, policy non-compliance, mental health, reproductive health, Nepal, India*

1.0 Introduction

Menstruation, commonly known as a 'Period', is a natural process where the uterus lining sheds, resulting in vaginal bleeding once every 21-40 days, and the bleeding usually continues for 5-7 days. The origin of menstrual myths dates back to the Vedic times. For centuries, menstruation has been so firmly doused in taboos, deeming women impure, polluting, and somehow capable of cursing through their touch. These socio-cultural beliefs have long normalised Menstrual Exile, often known as 'Chhaupadi' in Nepal and 'Gaokor' in India; 'Chau' meaning menstruation, and 'Padi' for women.

In both of these practices, women and young girls are required to spend their entire menstrual duration away from home, typically in isolated huts or livestock sheds, as a centuries-long custom. It is a tradition for these women to give birth in these very sheds, where they risk their pregnancy, due to lack of access to a midwife and proper nutrition. These women are expected to live with no toilet facilities, minimal sustenance, and in poorly ventilated spaces, leading to frequent casualties. Despite the outlaw of Chhaupadi in 2005 and a subsequent criminalization in 2017, menstrual exile continues to prevail.

Women, too, are reluctant to let go of their traditional beliefs, almost afraid of upsetting their deities, some of them even believing their 'sins' could bring ill-health to their households. Lack of education and awareness has left generations of these women vulnerable and in desperate need of carving out space for themselves within their culture and society. Menstrual exile is a deeply-rooted public health issue, one that comes in the way of more than 5 Sustainable Development Goals (SDGs) and hence the overarching objective of this paper is to know the underlying reasons for the persistence of this evil. The authors of this paper have reviewed the policy implications and laws already in place in Nepal and India and the various reasons for their non-compliance. There has been an attempt to fully understand the conditions these women are subjected to and the perceptions of the locals on a menstruating woman. The authors have used case studies and secondary data for the same.

2.0 Background of Countries

Nepal:

Women make up about 54% of the population of The Federal Democratic Republic of Nepal. (*Population, Female (% of Total Population) - Nepal | Data*, n.d.) These women are affected by poverty differently than men, mostly due to their occupation, daily chores, biological differences, childbirth and the need to meet societal expectations. Menstruation is one such factor that worsens the social exclusion of women in Nepal.

School education on Menstrual Hygiene Management(MHM) is very important since most girls experience menstruation for the first time in their adolescent years. Even though the Ministry of Education in Nepal has made certain efforts towards including sexual and reproductive health in their curriculum, the ideal situation is nowhere near. Based on a survey done by World Vision, a Non-governmental Organisation, and the National Health Research Council (NHRC), it was found that mothers continue to be the bearers of information regarding periods, while also being the ones imposing several restrictions on their children during their menstrual cycle. (World Vision, 2020)

The gaps in MHM of Nepal are manifold, especially in the Sudurpaschim Province of Nepal, where menstrual exile is most diligently followed. Key findings of World Vision's and NHRC's survey included:

a. 47.4% of Sudurpaschim residents knew of menstruation before menarche, while 71.7% of adolescent girls knew of periods before their first menstruation cycle.
b. Due to the unavailability of proper disposal mechanisms and lack of facilities, only 45% of the girls could change sanitary materials at school.
c. 59.2% of girls knew Chhaupadi was illegal, 10% didn't, and 22.5% wished for these practices to continue. 21.2% of adolescent girls had spoken up against the practice in their community. (World Vision, 2020)

Figure 1

Source: World Vision, 2020b

(Key findings of NHRC's and World Vision's survey)

India:

The menstrual experience of 120 million adolescent girls (10-19 years) in India varies between states, cities, villages, and the rich and poor. According to national estimates, 58% of adolescents use hygienic methods of menstrual management. This is not the case in Uttar Pradesh, where the figure is at a low of 43% (Chatterjee, 2020)

Even though rural girls are more aware now than they were a few years ago, menstruation continues to be tabooed and stigmatised, often talked about with long uncomfortable silences.

Many girls even believe it to be a god-given disease, instead of a natural bodily function. This inadequate knowledge of periods makes them fall prey to various exploitative customs. It appears that in rural India, the main issue to date is to tackle the shame around vaginal bleeding. (Karki & Espinosa, 2018, p. 7)

Key findings:

The National Family Health Survey (NFHS) 2015-16 revealed that the number of women using either sanitary napkins or tampons during periods was 78% in urban areas, 48% in rural areas, and 58% overall. (The Logical Indian, 2017)

a. A 2016 study on menstrual hygiene found that roughly out of 1,00,000 girls, 50,000 did not know of menstruation until they reached menarche, some of them assuming they had caught a disease instead. (Upadhyay, 2019)
b. A 2014 report showed that around 23 million girls drop out of school annually once they start menstruating, due to the lack of access to sanitation facilities while in school. (Upadhyay, 2019)

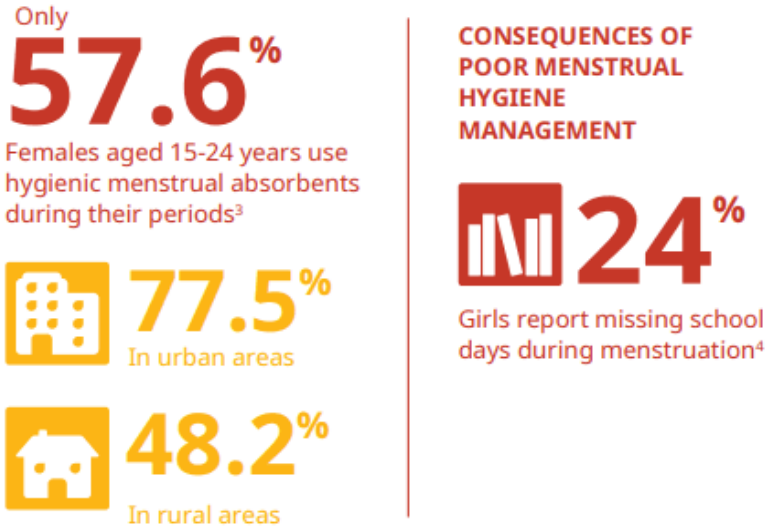

Figure 2.

Source: World Vision. (2020b, December 10)

Status of Menstrual Health and Hygiene Management among Adolescent Girls in Nepal

3.0 Comparative Analysis of Menstrual Exile in Nepal and India based on Ethnicity and Region

a. Ethnicity

A study surveyed a sample of the girls subjected to menstrual exile and/or menstrual taboos at their homes in **Nepal.** 72% of the girls practised menstrual exile, while 28% followed menstrual taboos at home. Based on their findings, 20% of the women were Dalit and the remaining 80% belonged to Upper Caste. (Amatya, 2018) Upper Caste households, having more facilities, can afford the costs of building sheds and can provide other basic facilities to their wives and daughters. Upper caste men also tend to put stricter restrictions to follow the customs as it is also a matter of pride for them. (Jun & Jang, 2018) Also, another study revealed that the women who identified as Janajati have less knowledge about menstruation than the women who identify as Brahman/Chhetri. (Baumann et al., 2019)

In **India**, Gaokor is common in the Gond and Madiya ethnic groups. Another study revealed that those belonging to general castes in India were 1.9 times more likely to adopt safe menstrual practices than those belonging to scheduled castes or scheduled tribes. (Baumann et al., 2019)

b. Regions

In **Nepal,** menstrual exile is mainly practised in the midwest and far-west regions of Nepal. It is deeply rooted in the migrated communities of Accham, Dailekh, Bajhang, which are often known as the source of Chhaupadi culture. In comparison with Kailali, Bardiya has lesser migration from those districts. As a result, reproductive health problems are significantly lower in Bardiya. (Ranabhat et al., 2015, p. 790) It is also prevalent in Doti, Baitadi, Dadheldhura, Darchula, Jumla, Humla, Mugu, Surkhet and Kanchanpur. (Singh, 2020, pp. 6) Low menstrual knowledge was observed in girls living in hill districts are compared to those living in Tarai (lowland). (Baumann et al., 2019)

In **India,** Gaokor is practised in the states of Uttarakhand, Maharashtra, Andhra Pradesh, Orissa, Chhattisgarh, Tamil Nadu. The practice is very common in Sitatola village in Maharashtra and the Pindar Valley in Uttarakhand.

4.0 Poor Condition of Women and its Subsequent Impact on their Physical Health

As stated earlier, menstrual exile is the banishment of young girls and women from their homes for the entire duration of their menstruation and childbirth. It had led to the suffering of thousands of women in the past and continues to do so, making it a prominent public health issue in Nepal and India. Away from their family, these women often find themselves facing several physical and psychological hardships, along with health issues. Even during menstruation, these women are expected to work, most spending their time cleaning, mopping, and cutting grass. Moreover, girls experiencing menstruation for the first time are made to stay in their "Chhau sheds" for at least 14 days. (United Nations Resident and Humanitarian Coordinator's Office, 2011) Casualties caused by menstrual exile tend to make the headlines in Nepal now and then yet there's very little that's been done about it.

Women on their period, often known as 'Chhau girls', are often left with no supplies and no sanitary protection or washing facilities. Action Aid, an international charity working for underprivileged girls, conducted a study where they questioned young girls in Nepal about their menstrual exile experiences. A few of them reported that their journey to the nearest river was almost a two-hour journey, which made them skip baths very frequently. These girls expressed their dislike for these practices. Their sheds were built without windows, and they feared the night time. (ActionAid, 2021)

Barred from consuming milk, yoghurt, butter, meat and other nutritious food, these women are expected to survive on a diet of dry foods, salt, and rice. Even carrying a blanket along is prohibited, and they're only provided with a small rug which these women fold as a pillow during the day. (WikiGender, n.d.) So, without a blanket in freezing temperatures, they resort to lighting fires in their sheds, risking suffocation due to poor ventilation. Many of these women, like Parbati Buda Rawat, were suffocated to death by smoke inhalation. (Vaughn, 2019) Apart from this, these women are also at risk of animal attacks, such as snakebites and physical assault by men wandering around the sheds. Mothers are scared about the well being of their children who're sent away for menstrual exile to "Chau Goths", especially because drunk men sexually assault or rape these girls while they're away from their homes. (ActionAid, 2021)

In Sitatola village in Maharashtra, it becomes extremely difficult for women to practice Gaokor since the roof often leaks. In Gaokor, the customs expects women to live alone on the edge of forests. In Gaokor, menstruating women are often not allowed to cook, hence increasing their dependency on their male partners who provide them with food. Out of 223 Gaokors in tribal areas, nearly 98% lacked proper blankets and beds and had temporary bamboo made bathrooms around the huts. Electricity and other basic amenities will be out of the reach of these women for years to come. (The Guardian, 2020) Both Gaokor and Chhaupadi prohibit young girls from going to school, and from even bathing.

These women risk hypothermia and dehydration, by staying in freezing temperatures without proper facilities. Belonging from poor families, these women don't take help even after contracting painful urinary infections due to the use of rags to soak up the blood. (Amatya, 2018) They perform hard labour, such as digging and collecting wood despite the lack of a nutritious and whole diet, which makes them vulnerable to diseases such as pneumonia, respiratory disorders, and diarrhoea. The health status of children was poorer in Chhaupadi-affected areas when compared to the national average because mothers tend to take their small children along with them to the menstrual huts. Also, Anemia and underweight (body mass index<18) was higher in these women. (Ranabhat et al., 2015, p. 790) According to a report by the National Human Rights Commission, 18 deaths have been reported since 2005, 13 of them in Achham district alone, while most other cases have been left unreported. (Shrestha, 2019)

4.1 Impact on Mental Health

The mental health of these women is severely impacted, due to feelings of abandonment, guilt, isolation, humility and insecurity of being polluting and impure. (Karki & Espinosa, 2018) Having to coexist with animals in sheds reduces their respect for themselves, and these women hardly view themselves as equals to other humans. Staying in livestock sheds, these women are forced to share living and eating spaces with cattle. Some lived experiences show that these animals often urinate in these very sheds (ActionAid, 2021), which over time makes these women accepting of whatever conditions they're subjected to.

The mental health effects are manifold. Isolation leads to depression in particular. The trauma of being sexually assaulted while away from home is something these women carry with themselves for years. More often than not, most of the rape cases are also not even revealed, or reported, due to the shame of being the victim, and to protect the future of their daughters who're yet to marry. These women are angry and hurt for being considered impure for something so fundamentally natural to their being, and beyond their control. Being embarrassed due to a process as natural as vaginal bleeding has severely affected the self-esteem of these women.

This perception of women being dirty affects their sense of identity and lowers their self-esteem. Feeling inferior to their male peers, young girls often develop a dislike for their body and its natural functions. They learn to internalise the notion of being subordinate to men, and often become submissive and dependent. (Karki & Espinosa, 2018) There's often a lack of communication between mothers and daughters regarding these customs, which could lead to feelings of loneliness in an adolescent girl. Due to isolation and stigmatisation, these women also tend to fall prey to negative behaviours such as smoking and alcohol consumption throughout their Chhaupadi stay. (Ranabhat et al., 2015, p. 790)

4.2 Impact of Menstrual Exile on Reproductive Health

The reproductive health facilities in Nepal and India consists of the following:

a. Antenatal Care(ANC)

Regular checkups from trained professionals are necessary for a healthy pregnancy. These checkups are called Antenatal Care (ANC) or visits, meaning pre-birth. For most women, at least 4 visits to trained providers are important to detect any early signs of complications.

(Pradhan & Pant, 2007)

b. Institutional Deliveries

Births taken in the presence of a midwife, a doctor, a nurse or a skilled birth attendant (SBA) are called Institutional deliveries. To lower the pregnancy-related health risks, it is important to increase the number of babies delivered under the supervision of health professionals, and in a health facility. (Pradhan & Pant, 2007) Factors such as region, education and income level affect Institutional delivery to a great extent.

c. Nutritional Status

For both the child and the mother to be healthy, maternal nutritional status is very important. There's a greater risk of adverse pregnancy in mothers with poor nutritional status, thereby giving birth to unhealthy and stunted children. The Body Mass Index (BMI) is defined as the weight in kilograms divided by the height squared in metres (kg/m^2), and a healthy BMI ranges from 18.5 kg/m^2 to 25 kg/m^2. (Pradhan & Pant, 2007)

Childbirth during menstrual exile doesn't let these women receive the above- mentioned facilities, thereby increasing the overall risk of their pregnancy. Most of these women are underweight, with a body weight less than 18.5 kg/m^2, and according to the 2006 National Demographic and Health Survey (NDHS), one in three women in Nepal is anaemic. (Pradhan & Pant, 2007)

Menstruating women often have very poor hygiene due to the limited access to water and the constant use of leaves, mud, rugs and paper in place of sanitary pads, which leads to Reproductive Tract Infections (RTI) and uterovaginal prolapse. Symptoms include backache, painful intercourse, white watery and foul-smelling discharge, itching, burning micturition and difficulty in walking, standing and sitting. (Ranabhat et al., 2015, p. 790) Despite all complications, these women are expected to wait till after their menstruation to receive medical care. (Amatya, 2018)

Delivery is also required to take place in unhygienic sheds, and women along with their fragile newborns are compelled to stay in their sheds for 10-14 days post-delivery. Menstrual exile during childbirth can lead to the deaths of both mother and the child, arising from septic shock, excessive bleeding and sometimes even minor unresolved health complications due to lack of access to health care. Often, these reproductive tract infections are transferred to the child by the pregnant mother. Severe bleeding and lower abdominal pain are very common in weak and feeble postpartum mothers who have a newborn to look after. Chronic pelvic pain, cervical and uterus cancers are extremely common in these women due to recurring human papillomavirus and heavy working. (Ranabhat et al., 2015, p. 790)

The maternal morbidity and neonatal mortality rates are incredibly high in regions where menstrual exile is common, owing to poor nutrition and inhumane living conditions. Infection and hypothermia are two significant factors leading to neonatal death in Nepal. (Kadariya & Aro, 2015) Infant Mortality rate is the number of deaths of children under one year of age per 1,000 live births. India's infant mortality rate was about 28.3 deaths per 1,000 live births in 2019, whereas the infant mortality rate of Nepal in 2019 was at about 25.6 deaths per 1,000 live births. (Pradhan & Pant, 2007)

5.0 Myths around menstruation

Throughout history, menstruation has either been worshipped or looked down upon. There was a time when a menstruating woman was anything but impure and polluting. To date, menstruation is an auspicious event in many states of India. In Assam, young girls are pampered for achieving menarche, at a ceremony called Ritushuddhi, also called Ritu *Kala Samskara*. These girls are bestowed with gifts and love from their family and friends, in an attempt to alleviate her to the status of a goddess. In some states of South India, girls are bathed in turmeric and gifted Saris from their dear ones. The ceremony is grand, with invitation cards being distributed to friends, neighbours and relatives.

However, from a more general perspective, in the 21st century, menstruation is steeped in stigma and taboo and is almost an event of sin. This notion of women significantly changed with the manifestation of menstrual taboo in the Rig Veda. Indra, the king of all gods, slays Vitras, a water demon. Upon learning that Vitras was a Brahmana, an upper caste in the Indian society, Indra is consumed with guilt. He requests the womankind to take up his guilt, in the form of a recurring cycle of repentance. This cycle of vaginal bleeding soon became a punishment forced onto women for eternity, and menstruation came to be associated with guilt and sin. Famous Sanskrit texts such as Vasistha Dharmasutra declared "For month by month the menstrual excretion takes away her sins. A woman in her courses is impure during three days and nights.", , "A female who neither goes naked nor is temporarily unclean is paradise," and "A woman is not independent; the males are her masters" and had various other notions about the status of women in society. (Desai, 2019)

In Hindu culture, a woman is prohibited from participating in her normal activities for the entire duration of menstruation since they need to be purified before she is allowed to return to her family and the chores of life. Most Hindu states follow the culture of 'Ritual Cleansing' to free women of their uncleanliness, especially before the worship of a deity. Ritual uncleanliness is often not identical to ordinary physical impurity, such as dirt stains. Here, a bodily fluid, such as vaginal blood, is what makes a woman ritually impure. (Wikipedia contributors, n.d.) It is believed that all women, regardless of their social status, are polluted by the bodily processes of menstruation and childbirth, and therefore in need of purification. There is also a practice in Judaism called 'Mikvah'. It consists of ritual bathing at the end of a menstrual period to attain ritual purity. This custom has been known to harm women's health. (Ranabhat et al., 2015, p. 790)

This' impurity' of a menstruating woman forces restrictions on her which deny her from entering a temple during her period, or even the 'Puja room' at her home. Entering the kitchen, praying, attending guests and touching holy books are a few other acts a menstruating woman can't perform. Sour food like curd, tamarind, and pickles are usually not given to menstruating girls, and neither are they allowed to cook since their impurity is believed to contaminate the food, or that the smell of a menstruating woman can turn food bad. (Anand & Garg, 2015) Water, which is considered to be the most common medium of purification, ought to be protected from menstruating women according to some religions. This is the very reason why menstruating women are not allowed to bathe for the first few days of their period. It is also believed that if a cow comes in contact with a menstruating woman, it would be deemed infertile, further associating menstruation with sin and guilt.

These socio-cultural beliefs have impacted the physical and psychological health of women for years past and have excluded them from society from a very young age. These taboos associate periods with evil spirits, shame and create embarrassment around even the mention of sexual reproduction. Women are taught to bury their clothes used during their bleeding to prevent them from the use of 'evil spirits'. The period cloth is considered by some to be "the most vulnerable object and a potent agent which might be used for casting evil eyes/magic on someone."

In Surinam, period blood is often treated as dangerous, and the woman is taken to be weak, that a malevolent person could use black magic to bring harm to her during her cycle. These women are also known to impose their will over men during their menstruation and hence simply avoiding the lady is preferred. (Anand & Garg, 2015)

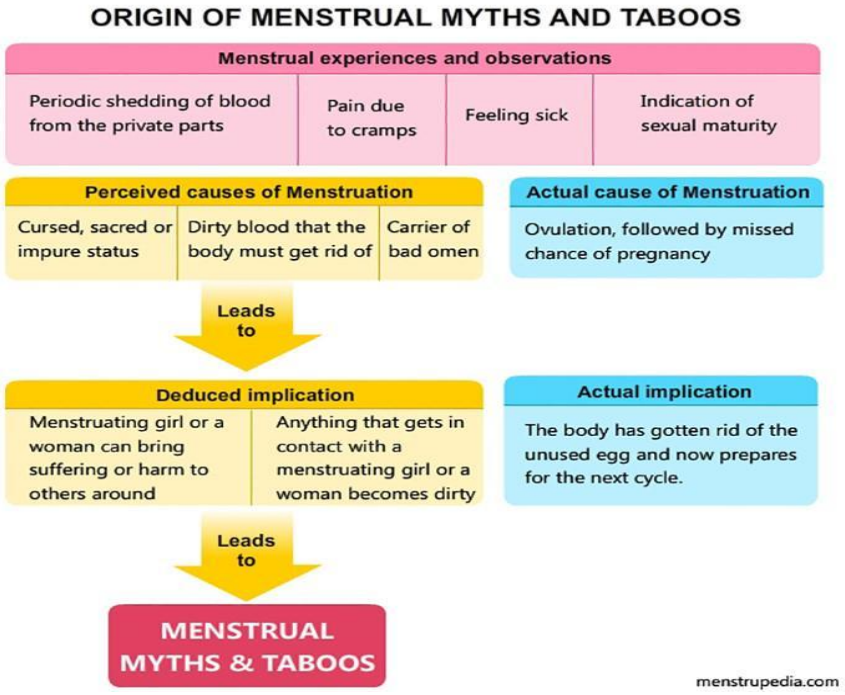

Figure 3

Source: (Gupta, 2012)

Along with violating women's rights, these taboos also affect their right to bodily integrity, equality, health, right to privacy and freedom from inhuman treatment. These myths and taboos have become a substitute for appropriate sex education in the adolescent years.

5.1 Sabarimala Temple Protests (2019)

The Sabarimala Temple is a hill shrine in Kerala, where devotees from all across the country visit between November and January. The presiding deity, Lord Ayyapa was worshipped as a Naishtika Brahmachrior- a celibate, so on the account of 'purity', women of menstruating age, that is from 10 to 50, were hitherto barred from entering the temple. (Jacob, 2018)

On 28th September 2018, the Supreme Court bench with Chief Justice Dipak Misra as the head ruled in a verdict that by not allowing women between 10 and 50 years of age into the temple, Article 21 of the Constitution of India, that is, 'Protection of life and personal liberty was being violated. (Jacob, 2018) This ban on the entry of women also violated Article 51A(e), which states that any such restriction based on women's biological features is fundamentally derogatory.

The Bharatiya Janata Party (BJP), The Congress, conservative Hindus and certain political groups were all critical of the judgement, believing it disregarded their traditional and religious beliefs. However, The Communist government in Kerala instructed the Travancore Devaswom Board to ensure that women were not restricted from entering the premises. For several continuous days after the verdict, numerous protestors attempted to prevent women from entering the temple shrine on 17th October. As protests intensified, a lot of women journalists and innocent people were attacked by the opposing parties. (Jacob, 2018) This interlinkage of traditional beliefs with religious beliefs is so deeply rooted that a major proportion of the protesters were women, who accepted their exclusion to honour their customs.

5.2 Fear of Gods- Nepal and India

Menstrual taboos in Nepal and India are "most keenly enforced" by elder family members, including mothers, grandmothers and other senior women, as well as religious leaders and traditional healers. (Vaughn, 2019) Along with Menstrual Exile, women are prohibited from having milk and encouraged to eat and drink only when food and water are offered to them. These women are forbidden from touching men, especially the ones who have performed the rituals of 'Bratabandha'. They're provided with limited access to essentials and made to stay away from plants, kitchen, children, cattle and fruit-bearing trees. (Robbinson, 2015) This perception of menstruation is so firmly doused in Chhaupadi culture that a yearly festival called "Rishi Panchami" is observed in August by young girls and women, where they 'purify' themselves with water, fasting and prayer for all the 'sins' they committed while menstruating. (Hodal, n.d.)

If the practices of Chhaupadi and Gaokor are not followed, it is believed that harm and ill-health will be brought to the whole household. People think that contact with a menstruating woman would make them sick and bad things would start happening to them. In Gaokor, women aren't even allowed to move around the village, because if they do, they would 'contaminate' the others. Even on seeing a menstruating woman, locals have to bathe to purify themselves. (Press Trust of India, 2013)

In most rural communities, people tend to rely on their harvested crops and reared animals for their livelihood. If the menstruating women stop practising menstrual exile or even disregard any of the restrictions, then Gods will be angered, as a result of which the crops will fail and other casualties might occur. Further, some women have seen blood in their buffalo milk after consuming it regularly during their menstrual cycle. When questioned, these women expressed this act as an expression of the anger of their gods. Ideas like these strengthen their belief in Chhaupadi and the fear of upsetting their deities. (ActionAid, 2021)

Nursing mothers believe that they would be punished for taking their babies outside after childbirth, or for going outside, cooking, or touching anyone during their period. If ever something bad happens in the village, these poor women will be blamed for their defiance to follow the customs of Chhaupadi. (WikiGender, n.d.) There's a traditional belief that girls touching books while menstruating would upset their gods, making a huge disparity between the education level of men and women. This linkage of culture and traditional beliefs to religion stops these issues from being widely explored, thereby affecting the status of women in this male-dominated society.

6.0 Laws criminalizing Menstrual Exile

Nepal

The evil of Chhaupadi violates several articles of The Constitution of Nepal such as:

a. Article 18 of the Constitution provides its citizens with the right to equality. It states that
    i. All citizens shall be equal before the law. No person should be denied the protection of the law

ii. There shall be no discrimination in the application of general laws on the grounds of origin, religion, race, caste, tribe, sex, physical conditions, disability, health condition, matrimonial status, pregnancy, economic condition, language or geographical region, or ideology or any other such grounds. (Global Gender Equality Constitutional Database, n.d.)

b. Article 29(2), which states that "No one shall be exploited in the name of any custom, tradition and usage or any other manner whatsoever" (Global Gender Equality Constitutional Database, n.d.)
c. Article 38, which states that "Every woman shall have the right relating to safe motherhood and reproductive health." (Global Gender Equality Constitutional Database, n.d.)

Keeping these in mind, Chhaupadi gives rise to several legal concerns. The Supreme Court of Nepal passed a significant piece of legislation in 2005, in which a directive was issued to the Government of Nepal for the formulation of laws that help curb the practice of Chhaupadi. In the year 2008, the Ministry of Child and Women welfare laid down certain guidelines to eliminate the practice. Chhaupadi got outlawed in 2005, but the system lacked a defined set of rules which imposed a ban on the practice.

In the wake of a rise in deaths of women practising Chhaupadi, the Parliament of Nepal enacted a new law, criminalizing the practice of Chhaupadi in August 2017. Any person found forcing menstrual exile on a woman would either be punished with a jail sentence of three months or would be charged a fine of 3,000 rupees. Despite a ban on the practice, the implementation process is proceeding at a prolonged rate, especially in far-western Nepal, where the first arrest was made only a few years ago. (Shrestha, 2019)

India

Gaokor violates the following articles of the Indian Constitution:

a. Article 15, which states that "The State shall not discriminate against any citizen on grounds only of religion, race, caste, sex, place of birth or any of them." (George, 2020)

b. Article 21 of the Indian Constitution provides women with the right to make reproductive choices, as a part of personal liberty. (George, 2020)

Despite Gaokor violating these constitutional rights, no legislation has yet been passed to outlaw this practice.

6.1 Loopholes in the implementation process

Despite all the efforts of the Government, the practice of Chhaupadi has been able to sustain itself. The ban put by the supreme court lacked the adequate mechanism to enforce the act. With the first arrest being made just a few years ago since the 2005 Outlaw of Chhaupadi, the indifference of the Government towards violation of rights shines through. A government-led social change campaign engaged in the practice of destroying huts built specifically for Chhaupadi, and though it was well-intended, knocking down sheds wasn't enough to bring about real change. (Amatya, 2018) Rather, it proved to be counter-productive, since most of these sheds were primarily built for food storage. A few lucky women were provided with new sheds, others exiled to places even more unhygienic and dangerous, co-existing with livestock in a primal state. Also, for the law to work, a woman would have to file a complaint, most likely against a family member, which seems next to impossible in Nepal's patriarchal system. (Preiss, 2017)

6.2 Policy non-compliance and the Role of Social Capital

The traditional beliefs are so deeply rooted that locals rarely question the exact rationale behind the customs, hence leading to policy non-compliance. Policy non-compliance is the modification of behaviours accepted by the government or society. (Jun & Jang, 2018) This non-compliance is encouraged by the following situations:

a. When the instruction is somewhat vague, inconsistent and abstract.
b. When the law is considered to be undesirable or not fully understood by the target groups. The affected population is less likely to comply if the policies in effect somehow disturb their traditions and customs.

c. When the government has no incentive to implement, either due to fewer resources, or a notion that the policy is outside the bubble of the government's interests. (Jun & Jang, 2018) When one wants to avoid becoming a deviant by justifying the unlawful behaviour of the people around. More weight is given to being a deviant in one's community, and the fear of being a lawbreaker lessens.

Shared norms, values, beliefs, networks, social relations, trust, along with the institutions that facilitate cooperation and collective action are together referred to as the Social Capital.

A high level of bonding social capital, that is the level of solidarity in a group, could be a potential obstacle for national governance. According to Putnam, in any community, a high level of social capital will have better governance. For him, social capital has a direct relationship with the public good and he considered trust to be the aggregate indicator of social capital. His theory, however, has been criticized by many. (Jun & Jang, 2018)

A study conducted by (Jun & Jang, 2018) targeting over 400 residents in South-Eastern Nepal proved that the case of Chhaupadi is completely the opposite of what Putnam conceptualised., that is, the social capital in Nepal led to policy non-compliance.

Following are the results:

a. Women with strong social capital are more likely to adhere to cultural practices such as Chhaupadi. According to some disaster studies, the more solidarity in a group, the more it tries to build a self-regulatory system. (Jun & Jang, 2018) In such a system, behaviours which favour the maintenance of traditional values and practices are encouraged.
b. Individuals with a strong perception of policies associated with Chhaupadi have a negative opinion of this practice.
c. The social capital of higher caste individuals is greater than that of the lower caste, hence they're more likely to follow Chhaupadi.

The results confirmed that the bonding social capital is strongly associated with a positive perspective on practices like Chhaupadi, which results in policy non-compliance by the community.

6.3 Menstrual Hygiene Campaigns and Social Initiatives

Several Social Initiatives have been started in India and Nepal to spread menstrual awareness. Some of them are:

a. 'No Chhaupadi Shed' is a campaign aimed at reducing menstrual exile. It started as a partnership between the local units and various NGOs. A very far-fetched aim of theirs is to eliminate Chhhaupadi by the end of 2021. (Budha, 2019)
b. In India, there are several projects aimed at educating young girls about menstruation and sexual health. Lok Biradari Prakalp is one such organisation that has collaborated with the government to educate the villagers in Maharashtra. By visiting Gaokors, they've helped in improving the hygiene of some menstruating women. (The Guardian, 2020)
c. An NGO 'Sparsh' urged the National Human Rights Commission (NHRC) to intervene and prevent the evil of Gaokor, as it makes the lives of tribal women miserable. (Press Trust of India, 2013)
d. Young girls have started organising themselves in self-help groups, and have also started campaigns, despite being discouraged by their parents for the same. In 2021 itself, girls in Raskot and Khanda Chakra have started campaigns against practices that are discriminatory against girls and women.
e. Social media campaigns to spread menstrual awareness have also been started. The Kachra Project launched a 'Period of Change' campaign. Many celebrities in India also trended the hashtag 'Happy to Bleed' after the controversial comments made by the head priest of a Hindu temple.
f. The national focus on Menstrual Hygiene Management (MHM) gained momentum after the 2015 Gorkha Earthquake, as the need for reproductive health services increased in affected areas. (Maverick Collective, 2017)
g. Ideas of sanitary napkin vending machines and sustainable menstruation have begun to grow in India, with urban people preferring biodegradable pads to support green consumerism. Various NGOs are providing rural girls with affordable, yet safe alternatives, with the hopes of reducing severe infections.

6.4 Violations of International Agreements

Since menstrual exile violates the rights of women as humans and as a reproductive group, it violates the following International agreements:

a. Article 25 of the Universal Declaration of Human Rights states "Everyone has the right to live a standard life with adequate care, food, clothing, housing and necessary social services." (Kadariya & Aro, 2015)
b. Vienna Declaration and paragraph 38 of the Program of Action commands "The eradication of any conflict which may arise between the rights of women and the harmful effects of certain traditional or customary practices, cultural prejudices and religious extremism." (Kadariya & Aro, 2015)
c. The Beijing Declaration, World Conference on Women's Rights and the Platform for Action have agreed that "Women and girls' human rights are an inalienable, integral and indivisible part of all human rights and fundamental freedom" (Kadariya & Aro, 2015)
d. International human rights treaties, including the International Convention on the Elimination of all Forms of Discriminations Against Women, guarantees the right to be free from gender discrimination and gender-based violence. (The Office of the High Commissioner for Human Rights (UN Human Rights), n.d.)

6.5 Liberalism vs. Universalistic Communitarianism

According to a study, menstrual exile, or Chhaupadi, could be seen as the case of individual rights and personal liberty from the standpoint of Liberalism versus the enforced traditional beliefs from the standpoint of Universalistic Communitarianism.

Liberalism is that branch of philosophy that proposes that if human beings have the will and ability to develop and implement decisions about their well being, then they should have the right to do so. These women from mid and far-western Nepal are banished from their homes against their will, violating their liberty. Deciding to cook, fetch water, mop, cut grass, teach, go to school, eat food are all matters of personal choice for these women, and to be able to decide your environment during your menstruation and childbirth should be too. (Kadariya & Aro, 2015)

Communitarianism focuses on highlighting the goals of the community as a whole over those of individuals. Universalistic Communitarianism is based on the belief that there is a single true form of good society, and hence only one pre-defined way for that society to function. These principles are in direct disagreement with those of liberalism, which focus on the freedoms of an individual over the unifying beliefs of a society. (Kadariya & Aro, 2015) Chhaupadi, therefore, seems like an excuse for spreading ignorant beliefs in the name of tradition and custom, dehumanizing women and young girls and depriving them of respect for something as natural as a period in attempts of keeping a community of people and their forsaken deity at peace. Illiteracy, backwardness and a total lack of genuine reasoning is what perpetuates centuries-old customs like that of menstrual exile, and leaves minimum to no room for change. The fear of the wrath of their Gods and the people in their community makes these women somewhat accepting of social exclusion and everything else they're subjected to.

7.0 Recommendations

a. Education

i. Education will help de-stigmatize menstruation. Using social beliefs as a way to oppress women and violate their liberty will significantly reduce proper literacy in the form of primary and secondary education. The linkage of culture with religion induces the fear of facing the wrath of their Gods and other villagers, which is why even after the outlaw of menstrual exile, some women willingly participate in these derogatory customs.

ii. Individual freedom is given less importance than what the community deems crucial. (Kadariya & Aro, 2015) With appropriate schooling, the youth has an opportunity to analyse the role of social capital and cultural bonding in policy non-compliance, and to make better choices, together as a community.

iii. Education will help break gender hierarchies. Lack of education makes women internalise the notion of being inferior to men, leading to gender disparity and male domination of society. Being less aware than men leaves these women in a subordinated position, as they let biological differences define their worth. (Karki & Espinosa, 2018)

b. Mass awareness

i. A proactive approach to awareness campaigns and community education needs to be taken. (Shrestha, 2019) Prolonged multi-sectoral involvement of the government and NGOs is necessary to increase social awareness. (Kadariya & Aro, 2015)

ii. Appropriate Menstrual Hygiene Management will reduce the risk of urinary tract infections and would lead to healthy menstrual cycles and pregnancy. Special programs could be set for sexual and reproductive health awareness. Special focus is required on the Health and Water, Sanitation and Hygiene (WASH) initiative.

iii. The goal is to make the target communities realise the fault in their patterns, and for that, the change has to start with the campaigners. The campaigners have to let go of the embarrassment, secrecy and shame associated with menstruation. (Karki & Espinosa, 2018)

c. Enforcement

i. Despite the outlaw and the ban, the implementation has been very slow. There needs to be better enforcement since change requires more than just the establishment of policies.

ii. All the campaigns, laws, and policy measures need to be analysed and reconceptualised. The policies should uphold the defiance of the locals.

d. Global Effort

i. There needs to be an increase in the number of policymakers and researchers working on the practices of Chhaupadi and Gaokor.

ii. There has been invisibility of menstruation within the main development agenda (Karki & Espinosa, 2018) International and National organisations aligned with the promotion of the Sustainable Development Goals (SDGs) need to bring their focus on menstrual taboos and practices in developing countries.

8.0 Conclusion

Patriarchy and gender hierarchies have subjected women to years of suffering. Menstrual exile is a development and public health issue which needs to be tackled on a larger scale. It has become evident that without proper enforcement, the establishment of laws will only lead to policy non-compliance. Despite attempts at social awareness, deeply-rooted beliefs keep the locals ignorant. The secrecy and embarrassment of being a menstruating woman have kept Chhaupadi and Gaokor cultures alive for centuries. Adolescent minds, however, can be trained to think differently, which is why menstruation needs to be de-stigmatised at the primary and secondary school level.

Gender disparity conditions women to be subordinate to men. It perpetuates negative perceptions of their bodies, which is why women associate shame and guilt with menstrual bleeding. Economic participation through small businesses and self-help groups will instil some confidence in young girls, making them not as accepting of everything society forces on them. Without the empowerment of women, there will be no radical change.

To actualise Sustainable Development Goals of No Poverty, Quality Education, Gender Equality and Reducing Inequality, menstrual exile and the silence around it needs to be overcome. The scope for research is broad, but the attention this issue gets from policymakers, researchers and government officials is inadequate for these practices to come to an end.

References

ActionAid. (2021, January 15). *Chhaupadi and menstruation taboos*. ActionAid UK. https://www.actionaid.org.uk/about-us/what-we-do/womens-economic-empowerment/chhaupadi-and-menstruation-taboos

Amatya, P. (2018, December 10). *Practice and lived experience of menstrual exiles (Chhaupadi) among adolescent girls in far-western Nepal*. National Center for Biotechnology Information. https://journals.plos.org/plosone/article?id=10.1371/journal.pone.0208260

Anand, T., & Garg, S. (2015). Menstruation related myths in India: Strategies for combating it. *Journal of Family Medicine and Primary Care*, *4*(2), 184. https://doi.org/10.4103/2249-4863.154627

Baumann, S., Lhaki, P., & Burke, J. (2019). Assessing the Role of Caste/Ethnicity in Predicting Menstrual Knowledge, Attitudes, and Practices in Nepal. *Global Public Health*, *14*(9), 1288–1301. https://doi.org/10.1080/17441692.2019.1583267

Budha, D. B. (2019, December 13). *Campaign against Chhaupadi practice*. My Republica. https://myrepublica.nagariknetwork.com/news/campaign-against-chhaupadi-practice/

Chatterjee, P. (2020, June 1). *Improving menstrual hygiene among adolescent girls in India*. ScienceDirect. https://linkinghub.elsevier.com/retrieve/pii/S2352464220301425

Desai, R. (2019, May 29). *From Riches to Rags: The Evolution of Menstrual Taboos in India*. The Swaddle. https://theswaddle.com/from-riches-to-rags-the-evolution-of-menstrual-taboos-in-india/#:%7E:text=Indra%20is%20consumed%20with%20guilt,cycle%20of%20repentence%20%E2%80%94%20aka%20menstruation

George, A. A. (2020, March 23). *Constitution of India: List of All Articles (1-395) and Parts (1-22)*. ClearIAS. https://www.clearias.com/constitution-of-india/

Global Gender Equality Constitutional Database. (n.d.). *Constitution of Nepal 2006, as amended to 2015*. Retrieved January 29, 2021, from https://constitutions.unwomen.org/en/countries/asia/nepal

Gupta, A. (2012, November 20). *Origin of Menstrual Myths and Taboos* [Photograph]. Menstrupedia. https://menstrupedia.com/blog/menstrual-myths-time-to-let-go-of-that-burden/origin-of-menstrual-myths-and-taboos/

Hodal, K. (n.d.). *Nepal's bleeding shame: menstruating women banished to cattle sheds*. The Guardian. Retrieved January 29, 2021, from https://www.theguardian.com/global-development/2016/apr/01/nepal-bleeding-shame-menstruating-women-banished-cattle-sheds

Jacob, J. (2018, October 19). *Equality vs Faith: The Sabarimala Stand-Off Explained In 10 Points*. NDTV.Com. https://www.ndtv.com/kerala-news/sabarimala-temple-protests-kerala-equality-vs-faith-the-sabarimala-stand-off-explained-in-10-points-1934690

Jun, M., & Jang, I. (2018). The Role of Social Capital in Shaping Policy Non-compliance for Chhaupadi Practice in Nepal. *Asian Women*, *34*(3), 47–70. http://e-asianwomen.org/xml/16248/16248.pdf

Kadariya, S., & Aro, A. R. (2015). Chhaupadi practice in Nepal – analysis of ethical aspects. *Medicolegal and Bioethics*, 53. https://doi.org/10.2147/mb.s83825

Karki, R., & Espinosa, C. (2018). Breaking Taboos: Menstruation, Female Subordination and Reproductive Health, the Case of India. *Insights of Anthropology*, *2*(2), 4–13. https://heller.brandeis.edu/gds/pdfs/working-papers/gds-wp-2019-1-breaking-taboos-3.pdf

Maverick Collective. (2017). *Menstrual Health and Hygiene Management in Nepal*. https://menstrualhygieneday.org/wp-content/uploads/2017/09/PSI_Scoping-Review-and-Preliminary-Mapping-of-Menstrual-Health-in-Nepal-Final.pdf

Population, female (% of total population) - Nepal | Data. (n.d.). World Bank Group. Retrieved January 28, 2021, from https://data.worldbank.org/indicator/SP.POP.TOTL.FE.ZS?locations=NP

Pradhan, A., & Pant, P. D. (2007). *Trends in Demographic and Reproductive Health Indicators in Nepal*. https://dhsprogram.com/pubs/pdf/TR5/TR5.pdf

Preiss, D. (2017, August 10). *Law In Nepal Sets Penalties For Forcing A Woman Into A Menstrual Shed*. NPR. https://www.npr.org/sections/goatsandsoda/2017/08/10/542585664/law-in-nepal-sets-penalties-for-forcing-a-woman-into-a-menstrual-shed

Press Trust of India. (2013, September 9). *NHRC asks Maha to file a report on sexist practice among tribals*. Business Standard. https://www.business-standard.com/article/pti-stories/nhrc-asks-maha-to-file-report-on-sexist-practice-among-tribals-113091900875_1.html

Ranabhat, C., Kim, C.-B., Choi, E. H., Aryal, A., Park, M. B., & Doh, Y. A. (2015). Chhaupadi Culture and Reproductive Health of Women in Nepal. *Asia Pacific Journal of Public Health*, *27*(7), 785–795. https://doi.org/10.1177/1010539515602743

Robbinson, H. (2015, December). *Chaupadi: The affliction of menses in Nepal*. ScienceDirect. https://www.sciencedirect.com/science/article/pii/S2352647515000623?via%3Dihub

Shrestha, E. (2019, December 11). *Everything you need to know about Chhaupadi, the taboo ritual of banishing women to period huts*. The Kathmandu Post. https://kathmandupost.com/national/2019/12/11/everything-you-need-to-know-about-chhaupadi-the-taboo-ritual-of-banishing-women-to-period-huts

Singh, D. (2020). *Factors associated with Chhaupadi Pratha and its impact on the health of the women in Khaptad Channa Rural Municipality-05, Thakuri Community, Bajhang* (1st ed., Vol. 1). Grin Verlag.

The Guardian. (2020, October 15). *Banished for menstruating: the Indian women isolated while they bleed*. https://www.google.co.in/amp/s/amp.theguardian.com/global-development/2015/dec/22/india-menstruation-periods-gaokor-women-isolated

The Logical Indian. (2017, May 2). *A Reality Check Of Menstruation In Rural India*. https://thelogicalindian.com/health/menstruation-in-rural-india/?infinitescroll=1

The Office of the High Commissioner for Human Rights (UN Human Rights). (n.d.). *OHCHR | Convention on the Elimination of All Forms of Discrimination against Women*. Retrieved January 29, 2021, from https://www.ohchr.org/en/professionalinterest/pages/cedaw.aspx

United Nations Resident and Humanitarian Coordinator's Office. (2011, April). *FIELD BULLETIN Chaupadi In The Far-West*. https://www.ohchr.org/Documents/Issues/Water/ContributionsStigma/others/field_bulletin_-_issue1_april_2011_-_chaupadi_in_far-west.pdf

Upadhyay, A. (2019, May 29). *Menstrual Hygiene Day Facts: Only 36 Percent Of The Women In India Use Sanitary Pads During Periods*. NDTV-Dettol Banega Swasth Swachh India. https://swachhindia.ndtv.com/menstrual-hygiene-day-facts-26-percent-use-sanitary-pads-periods-34309/

Vaughn, E. (2019, December 17). *Menstrual Huts Are Illegal In Nepal. So Why Are Women Still Dying In Them?* NPR. https://www.npr.org/sections/goatsandsoda/2019/12/17/787808530/menstrual-huts-are-illegal-in-nepal-so-why-are-women-still-dying-in-them

WaterAid India. (2019). [The National Family Health Survey (NFHS) 2015-16 revealed that the number of women using either sanitary napkins or tampons during periods was 77.5% in urban areas, 48.2% in rural areas, and 57.6% overall.]. https://www.wateraidindia.in/sites/g/files/jkxoof336/files/informed-product-choice-and-disposal_1.pdf

WikiGender. (n.d.). *Chhaupadi: Confinement and Female Uncleanliness | Wikigender*. Retrieved January 28, 2021, from https://www.wikigender.org/wiki/chhaupadi-confinement-and-female-uncleanliness/

Wikipedia contributors. (n.d.). *Ritual purification*. Wikipedia. Retrieved January 29, 2021, from https://en.wikipedia.org/wiki/Ritual_purification

World Vision. (2020a, December 10). *The national survey of menstrual health and hygiene management of adolescent girls in Nepal - Nepal*. ReliefWeb. https://reliefweb.int/report/nepal/national-survey-menstrual-health-and-hygiene-management-adolescent-girls-nepal

World Vision. (2020b, December 10). *Status of Menstrual Health and Hygiene Management among Adolescent Girls in Nepal* [Photograph]. World Vision. https://reliefweb.int/sites/reliefweb.int/files/resources/MHM_OnePager_updated.pdf

PAPER • **OPEN ACCESS**

Current-mode Positive and Negative Rectifier based on DDCC suitable for Higher Frequency operations

To cite this article: Sweta Kumari and Deva Nand 2021 *IOP Conf. Ser.: Mater. Sci. Eng.* **1084** 012079

View the article online for updates and enhancements.

This content was downloaded from IP address 14.139.251.100 on 27/03/2021 at 09:20

Current-mode Positive and Negative Rectifier based on DDCC suitable for Higher Frequency operations

*Sweta Kumari[1], Deva Nand[2]
[1,2]Deptt. of Electronics and Communication
Delhi Technological University
Delhi, India
[1*]sweta.sma30@gmail.com
[2]devkamboj07@gmail.com

* Corresponding Author

Abstract. In the present proposal current-mode (CM) full-wave rectifiers (FWR) using a differential-difference current conveyor (DDCC) block, two MOS-based diodes and three grounded resistors. Two proposals of rectifiers are presented, the first is CM FW positive rectifier and the second is CM FW negative rectifier. The value 200MHz was observed in the operating frequency of the simulated designs. The SPICE simulations with 180 nm TSMC CMOS technology model file has been used to ensure the proper functioning of both of the proposals.

Keywords: Analog Building Block, Current Mode, Differential Difference Current Conveyor, Full-Wave Rectifier.

1.INTRODUCTION

A full-wave rectifier that is extensively used in signal processing, instruments and measurements, communications, RF modulators and demodulators, AC voltmeters, ammeters, watt-meters, signal polarity detection, peak detection, function fitter, absolute value computation, in-floor detector used in ultra-sonic, average finder, clipper circuits and frequency doubler [1-10]. The MOS based diodes [3,5,6,8,9] and DDCC have been used in rectifiers but offer a low-frequency range of operations. In some literature shows only diodes [2,4,7,10], Current mode (CM) circuits are more versatile nowadays because of more accuracy, high-frequency performance and wide dynamic range [2,3,7,9]. The second generation of current conveyors (CCII) was introduced in 1970 and its applications are summers, differentiators, integrators, amplifiers, filters, oscillation and controllers [11-14].

The differential difference amplifier (DDA) was first reported in 1987 which has two differential input voltage signals and somehow it behaves like Op-Amp [15-16]. The DDCC was introduced in 1996 and it is a combination of DDA and CCII for high input impedance and arithmetic operations [14,17,18]. Table. 3 shows a comparison of the proposed rectifier to existing rectifiers with different analog building blocks (ABB). The salient features of proposed FWRs:

- Employment of only one ABB.
- Used grounded passive components.
- Used MOS based diodes.
- No matching condition is required.
- Eligible for low power and low voltage systems.
- Suitable for high-frequency operations (MHz).

In the proposal, single DDCC based current-mode positive and negative types of full-wave rectifiers

Content from this work may be used under the terms of the Creative Commons Attribution 3.0 licence. Any further distribution of this work must maintain attribution to the author(s) and the title of the work, journal citation and DOI.
Published under licence by IOP Publishing Ltd

have been reported. The three sections are reported including the current section. The circuits structure is defined in Section 1, Section 2 includes the analysis of the proposed circuits and verification using simulations, followed by a conclusion in Section 3.

2. CIRCUIT DESCRIPTION

2.1 Differential difference current conveyor

The DDCC symbol is reproduced in Figure 1. It has three Y-ports with differential inputs, one X-port and one Z-port. The low and the high impedance at input ports X and Y respectively and the high output impedance at Z-port. The matrix characteristic is as follows:

$$\begin{bmatrix} I_{Y1,2,3} \\ V_X \\ I_Z \end{bmatrix} = \begin{bmatrix} 0 & 0 & 0 & 0 \\ 1 & -1 & 1 & 0 \\ 0 & 0 & 0 & \pm 1 \end{bmatrix} \begin{bmatrix} V_{Y1} \\ V_{Y2} \\ V_{Y3} \\ I_X \end{bmatrix} \quad (1)$$

$$I_{Y1} = I_{Y2} = I_{Y3} = 0 \quad (2)$$

$$V_X = V_{Y1} - V_{Y2} + V_{Y3} \quad (3)$$

$$I_Z = \pm I_X \quad (4)$$

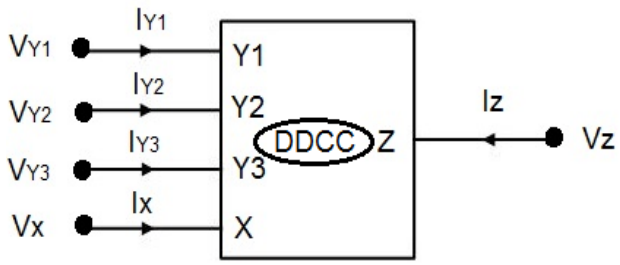

Figure 1. Symbol of the plus-type DDCC [17]

In equation (2) it shows the current at all Y-port is zero, the X-port voltage is proportional and varies with the Y-port voltage in equation (3), and current at X-port varies with Z-port either inward or outward direction in equation (4). The CMOS structure of plus-type DDCC is shown in Figure 2.

2.2 MOS based implementation of DDCC

The (M6 and M7) and (M8 and M9) are two input differential stages. By considering the large gain stage, (M1 and M2) a current mirror transforms the differential signal current to the single-ended output signal current (M3). The M4 is copying the current from M3. Figure 3 and Figure 4 show a full-wave rectifier for positive-type and negative-type respectively.

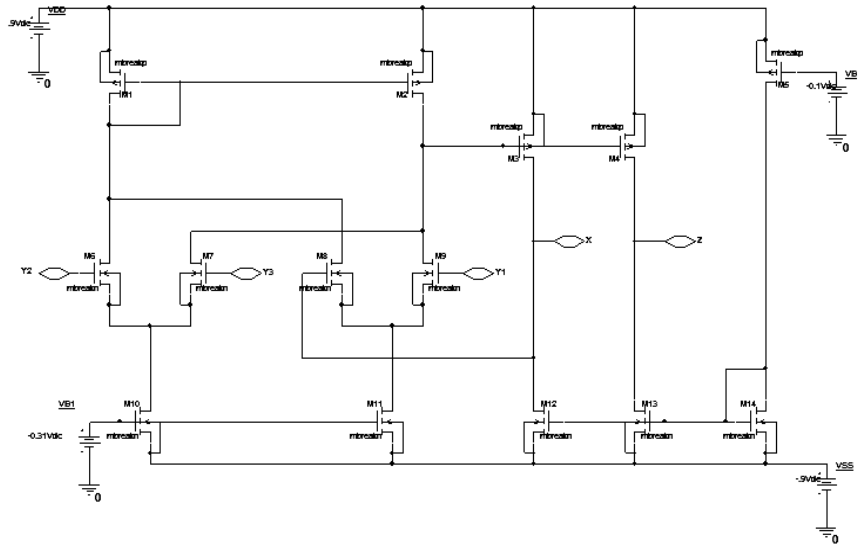

Figure 2. CMOS structure of plus-type DDCC [17]

2.3 Proposed rectifiers

One DDCC block and two MOS can be seen in the designed full-wave rectifier. Here, M1 and M2, two NMOS based diodes are behaving like switches. Equation (5) reveals the output current of the implemented rectifiers. Table 1 is shown the working of rectifiers and resulting outputs.

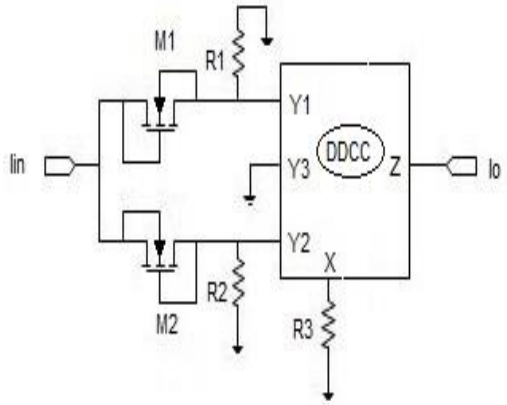

Figure 3. Proposed positive full-wave rectifier

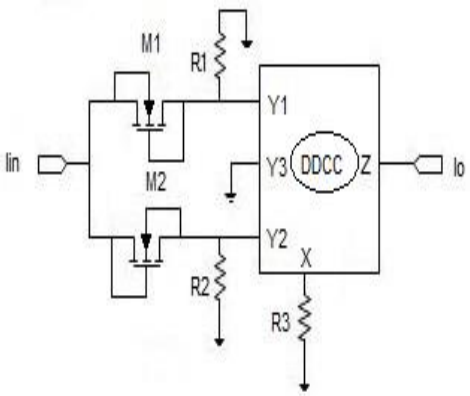

Figure 4. Proposed negative full-wave rectifier

Table 1: Working principle of full-wave rectifiers

For positive FWR:

Input current signal (I_{in})	Half cycle	M1	M2	Output
Sine wave	Positive	ON (FB*)	OFF (RB*)	I_{in} (R_1/R_3)
	Negative	OFF (RB)	ON (FB)	$-I_{in}$ (R_2/R_3)
Triangular wave	Positive	ON (FB)	OFF (RB)	I_{in} (R_1/R_3)
	Negative	OFF (RB)	ON (FB)	$-I_{in}$ (R_2/R_3)

*RB- Reverse bias, FB- Forward bias

For negative FWR:

Input current signal (I_{in})	Half cycle	M1	M2	Output
Sine wave	Positive	OFF (RB*)	ON (FB*)	$-I_{in}$ (R_2/R_3)
	Negative	ON (FB)	OFF (RB)	I_{in} (R_1/R_3)
Triangular wave	Positive	OFF (RB)	ON (FB)	$-I_{in}$ (R_2/R_3)
	Negative	ON (FB)	OFF (RB)	I_{in} (R_1/R_3)

*RB- Reverse bias, FB- Forward bias

The output current equation of the proposed FWR would be:

$$I_O = I_{in} \frac{(R_1 - R_2)}{R_3} \tag{5}$$

3 SIMULATION RESULTS

The DC transfer characteristic of the implemented FWR is presented in Figure 5 with a dynamic range -300 µA to 300 µA of the current. Figure 6 shows simulated rectified outputs on the transient response of FWR for different amplitudes 100 µA, 200 µA and 300 µA at 1 KHz. The maximum operating frequency is 200 MHz and the respective simulation result is shown in Figure 7 for positive FWR and negative FWR. Figure 8 shows the transient response of the triangular output current for the peak to peak -100 µA to 100 µA triangular input current. The PSPICE simulation results verified using 180 nm TSMC CMOS model file with the supply voltages V_{DD} and V_{SS} is ± 0.9 V and two bias voltages of V_B = - 0.1 V and V_{B1} = - 0.31 V. The values of all resistors are 1 kΩ. The power dissipation of the implemented rectifiers is 2.94 mW. Table 2 illustrates the aspect ratio or Width/Length values for various transistors.

Table 2: Transistor's sizes for DDCC [18]

Transistors	Transistor's Size W(um)/L(µm)
All PMOS	10/0.4
All NMOS	05/0.4

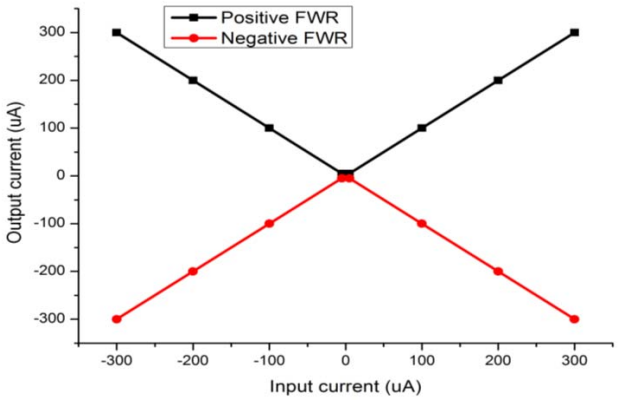

Figure 5. DC Transfer characteristics of the proposed FWRs

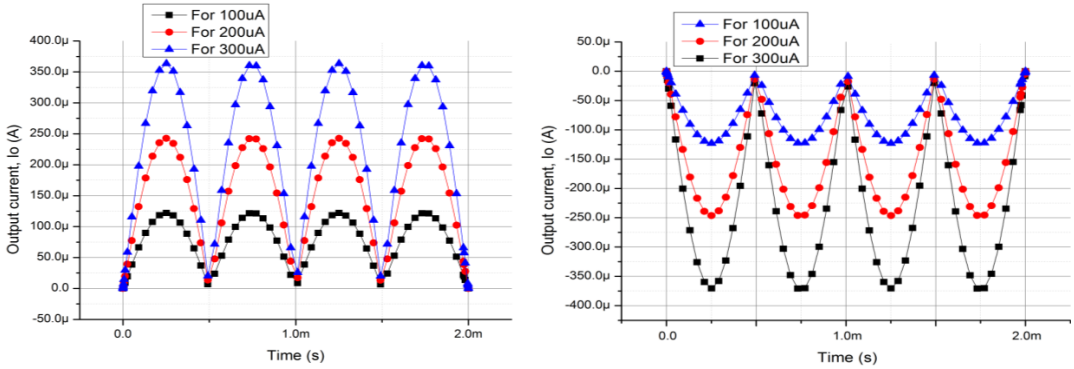

Figure 6. Transient responses of (a) positive FWR (b) negative FWR

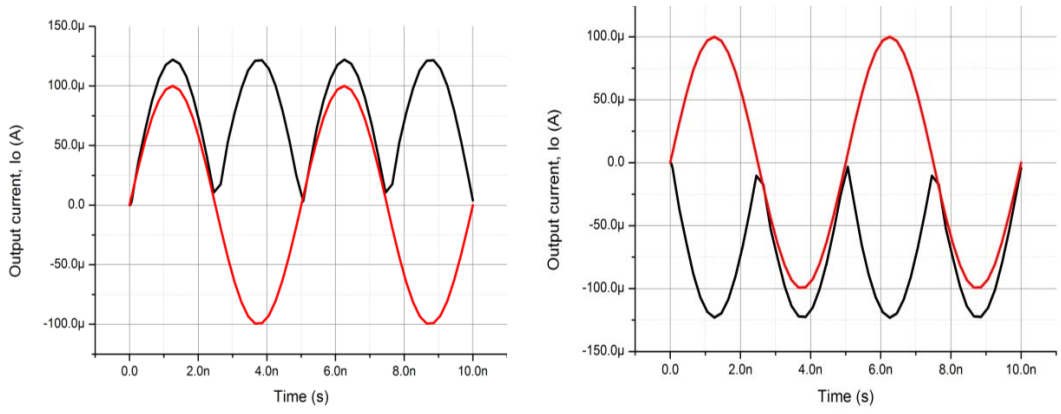

Figure 7. The output current of (a) Positive FWR (b) Negative FWR for sine input at 200 MHz

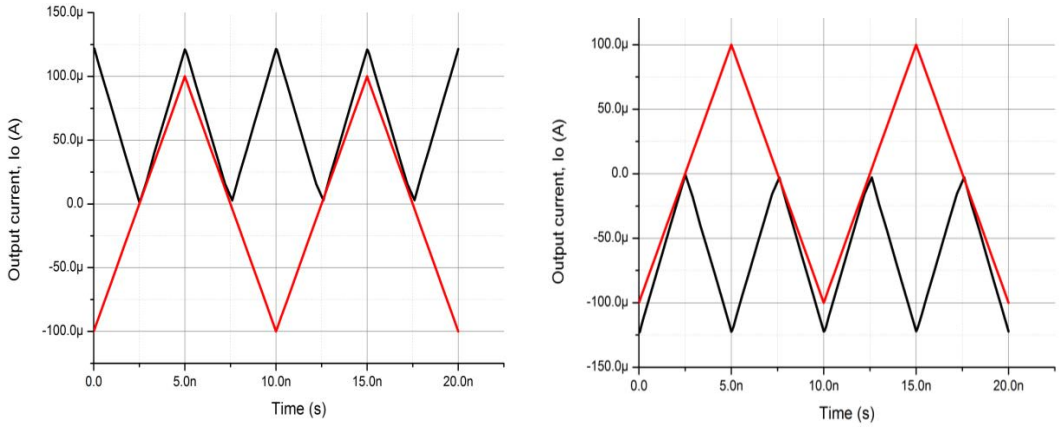

(a) (b)

Figure 8. The output current of (a) Positive FWR (b) Negative FWR for triangular input

Table 3: A comparison of proposed FWR.

Ref. No.	No. of ABB	Mode of Operation	No. of R	Diode/ MOS	Output Impe-dance	Operating Frequency (Hz)	P. Diss. (mW)	CMOS Techno-logy	Supply Voltage (V)
1	1 CCII	VM	0	0/0	H	100 M	5.200	0.18 µm	±1.2
2	1 OTA	CM	2	2/0	L	1.00 M	NA	0.25 µm	±1.5
2	1 DVCC	CM	3	2/0	H	1.00 M	NA	0.25 µm	±1.5
3	1 EXCCII	CM	0	0/2	H	125 M	0.690	0.18 µm	±1.2
4	1 DXCCII	VM	2	2/0	H	10.0 M	NA	0.35 µm	±2.5
5	1 CDTA	MIXED	3	0/2	H	10.0 M	1.12	0.18 µm	±1.5
6	1 Op-amp	VM	1	0/2	H	5.00 M	2.050	3.00 µm	-2 to 8
7	1 CDBA	CM	0	2/0	L	1.00 M	NA	0.25 µm	±1.5
8	1 OTRA	VM	8	0/6	L	1.00 K	NA	0.18 µm	±2
9	1 OFCC	CM	0	0/2	H	300 K	0.432	0.18 µm	±1.8
10	2 VC	MIXED	1	2/0	L	1.00 M	0.700	0.35 µm	±1.65
Proposed	1 DDCC	CM	3	0/2	H	200 M	2.940	0.18 µm	±0.9

H: High, L: Low, CM: Current Mode, VM: Voltage Mode, CCII: Second-generation current-conveyor, OTA: Operational Transconductance Amplifier, DVCC: Differential voltage current-conveyor, EXCCII: Extra-X Current Conveyor, DXCCII: Dual-X Current Conveyor, CDTA: Current Differencing Trans-conductance Amplifier, Op-amp: Operational Amplifier, CDBA: Current Differencing Buffered Amplifier, OTRA: Operational Transresistance Amplifier, OFCC: Operational Floating Current Conveyor, VC: Voltage Conveyor.

4 CONCLUSION

In this work, the DDCC based current mode positive and negative types full-wave rectifiers are proposed. The proposed circuits consist of one single active building block, two MOS based diodes and three grounded resistors suitable from the monolithic implementation point of view. The proposed

circuit has a high impedance at the input as well as output terminals, so best from cascadability point of view. This circuit is useful for a higher frequency, low power consumption, low supply voltage, higher and wider input dynamic range. The PSPICE simulations have been performed using TSMC 180 nm CMOS technology parameters and the supply voltage of ± 0.9V. The full-wave rectifiers output can be achieved for the operating frequency of 200 MHz.

References

[1] Kumngern, M.: New versatile precision rectifier. IET Circuits, Devices & Systems. 8, 141–151 (2014).

[2] Minaei, S., Sagbas, M., Ayten, U.E.: Component reduced current-mode full-wave rectifier circuits using single active component. IET Circuits, Devices & Systems. 10, 1–11 (2016).

[3] Das, R., Paul, S.K.: Resistorless current mode precision rectifier using EXCCII. Analog Integrated Circuits and Signal Processing. 103, 511–522 (2020).

[4] Koton, J., Vrba, K., Herencsar, N.: Voltage-mode full-wave rectifier based on DXCCII. Analog Integrated Circuits and Signal Processing. 81, 99–107 (2014).

[5] Kaçar, F., Başak, M.E.: A new mixed mode full-wave rectifier realization with current differencing transconductance amplifier. Journal of Circuits, Systems and Computers. 23, 1450101 (2014).

[6] Wang, Z.: Full-Wave Precision Rectification that is Performed in Current Domain and Very Suitable for CMOS Implementation. IEEE Transactions on Circuits and Systems I: Fundamental Theory and Applications. 39, 456–462 (1992).

[7] Erkan, S., Ayten, U.E., Sagbas, M.: Current-mode full-wave rectifier circuits using current differencing buffered amplifier. In: 2015 38th International Conference on Telecommunications and Signal Processing (TSP). pp. 344–348. IEEE (2015)

[8] Oruganti, S., Gilhotra, Y., Pandey, N., Pandey, R.: New topologies for OTRA based programmable precision half-wave and full-wave rectifiers. In: 2017 Recent Developments in Control, Automation & Power Engineering (RDCAPE). pp. 327–331. IEEE (2017).

[9] Pandey, N., Pandey, R., Nand, D., Kumar, A.: Current-mode rectifier configuration based on OFCC. In: 2014 International Conference on Signal Propagation and Computer Technology (ICSPCT 2014). pp. 533–536. IEEE (2014).

[10] Safari, L., Barile, G., Stornelli, V., Ferri, G.: A new versatile full wave rectifier using voltage conveyors. AEU - International Journal of Electronics and Communications. 122, 153267 (2020).

[11] Sedra, A., Smith, K.: A second-generation current conveyor and its applications. IEEE Transactions on Circuit Theory. 17, 132–134 (1970).

[12] Abdalla, K.K., Bhaskar, D.R., Senani, R.: Configuration for realising a current-mode universal filter and dual-mode quadrature single resistor controlled oscillator. IET Circuits, Devices & Systems. 6, 159 (2012).

[13] Yuce, E., Minaei, S.: New CCII-based versatile structure for realizing PID controller and instrumentation amplifier. Microelectronics Journal. 41, 311–316 (2010).

[14] Abdalla, K. K., Bhaskar, D. R., Senani, R.: A review of the evolution of current-mode circuits and techniques and various modern analog circuit building blocks. Nature science. 10, pp. 1-13. (2012).

[15] J.S. Sakthi Suriya Raj, P. Sivaraman, P. Prem, A. Matheswaran, Wide Band Gap semiconductor material for electric vehicle charger, Materials Today: Proceedings, 2020, ISSN 2214-7853, https://doi.org/10.1016/j.matpr.2020.02.916.

[16] Huang, S.-C., Ismail, M.: Design and applications of a CMOS analog multiplier cell using the differential difference amplifier. Analog Integrated Circuits and Signal Processing. 6, 209–217 (1994).

[17] Chiu, W., Liu, S.I., Tsao, H.W., Chen, J.J.: CMOS differential difference current conveyors and their applications. IEE Proceedings: Circuits, Devices and Systems. 143, 91–96 (1996).

[18] Lee, C.N.: Independently tunable plus-type DDCC-based voltage-mode universal biquad filter with MISO and SIMO types. Microelectronics Journal. 67, 71–81 (2017).

Decentralized Multi-agent Formation Control via Deep Reinforcement Learning

Aniket Gutpa[1,*] and Raghava Nallanthighal[2,†]
[1]Department of Electrical Engineering, Delhi Technological University, New Delhi, India
[2]Department of Electronics and Communication Engineering, Delhi Technological University, New Delhi, India

Keywords: Multi-agent Systems, Swarm Robotics, Formation Control, Policy Gradient Methods.

Abstract: Multi-agent formation control has been a much-researched topic and while several methods from control theory exist, they require astute expertise to tune properly which is highly resource-intensive and often fails to adapt properly to slight changes in the environment. This paper presents an end-to-end decentralized approach towards multi-agent formation control with the information available from onboard sensors by using a Deep Reinforcement learning framework. The proposed method directly utilizes the raw sensor readings to calculate the agent's movement velocity using a Deep Neural Network. The approach utilizes Policy gradient methods to generalize efficiently on various simulation scenarios and is trained over a large number of agents. We validate the performance of the learned policy using numerous simulated scenarios and a comprehensive evaluation. Finally, the performance of the learned policy is demonstrated in new scenarios with non-cooperative agents that were not introduced during the training process.

1 INTRODUCTION

Multi-agent systems are rapidly gaining momentum due to their several real-world applications in disaster relief scenarios, rescue operations, military operations, warehouse management, agriculture and many more. All these tasks require the teams of robots to cooperate autonomously to produce the desired results as displayed by many animals and insects in nature which emulate swarming behaviour.

One of the major challenges for multi-agent systems is autonomous navigation while adhering to the three rules of Reynolds (Reynolds and Craig, 1987). Modern control theory presents numerous solutions, supported with rigorous proofs, to this problem and demonstrates the feasibility of multi-agent formation control and obstacle avoidance. (Marko and Stiepan, 2012), (Anuj et al., 2020), (Egerestedt, 2007) present an artificial potential field approach and have demonstrated stable autonomous navigation of a swarm of unmanned aerial vehicles (UAVs). While this approach does the work, it neglects the non-linearities in the system dynamics and thus fails to demonstrate optimal behaviour in conjunction with the vehicle dynamics. Further, these approaches require extensive tuning to provide desired performance.

Further, in (Hung and Givigi, 2017), a Q-learning based controller is presented for flocking of a swarm of UAVs in unknown environments using a leader-follower approach. This approach does not yield an optimal solution as state space and action space is discretized to limit the size of the Q-table. As the number of states increases, computing the Q-table becomes increasingly inefficient. Another disadvantage of this approach is the single point of failure offered by the leader agent.

In (Johns and Rasmus, 2018), Reinforcement learning is utilized to improve the performance of a behaviour-based control algorithm which serves as both a baseline from which the RL algorithm compares with and a base from which the RL algorithm starts training. This approach produces significant results but is not an end to end solution which can be directly applied to any kind of system. Appropriate tuning of the behaviour-based control algorithm is still required for the efficient performance of the complete controller.

[*] http://www.dtu.ac.in/Web/Departments/Electrical/about/
[†] http://www.dtu.ac.in/Web/Departments/Electronics/about/

Gutpa, A. and Nallanthighal, R.
Decentralized Multi-agent Formation Control via Deep Reinforcement Learning.
DOI: 10.5220/0010241302890295
In *Proceedings of the 13th International Conference on Agents and Artificial Intelligence (ICAART 2021) - Volume 1*, pages 289-295
ISBN: 978-989-758-484-8
Copyright © 2021 by SCITEPRESS – Science and Technology Publications, Lda. All rights reserved

The contribution of this paper is to propose a decentralized, end-to-end framework that is scalable, adaptive, and fault-tolerant which directly maps the sensor data to optimal steering commands. To overcome the problems offered by discrete state space and discrete action space controllers, we propose a policy gradient-based controller, which utilizes a Deep neural network map the continuous state space directly to a continuous action space. The effectiveness of policy learned from the proposed method is demonstrated through a series of simulation experiments where it is able to find the optimal trajectories in complex environments.

The rest of the paper is organised as follows: Section II gives a short introduction to Policy Gradient methods and leads on for the mathematical formulation of our problem statement in the context of RL. Section III introduces the proposed algorithm and the underlying structure of the complete controller for decentralized implementation. Subsequently, section IV describes the simulation environment, the computational complexity of our approach and presents the quantitative results obtained. Further, it also provides the experimental results in unknown environments to demonstrate the generalization capability of the learned policy. Finally, Section V concludes the paper with recommendations for future work.

2 PRELIMINARIES

2.1 Markov Decision Process

A Markov decision process (Bellman and Richard, 1957) is a finite transition graph which satisfies the markov property. For a single agent MDP can be represented by a tuple $Z = (S, A, R)$ where $S = \{s_1, \dots, s_T\}$ is the set of states, $A = \{a_1, \dots, a_{T-1}\}$ is the set of actions and $R = \{r_1, \dots, r_{T-1}\}$ is the set of rewards obtained by through transition between states (s_T represents the terminal state). The objective is to find the solution of this MDP to maximize the expected sum of rewards by finding the optimal policy, value function or action-value function.

2.2 Deep Q-learning

Deep Q-learning (Mnih et al., 2015) is one of the well-known methods in Deep RL and has been shown to provide extremely efficient results. It uses deep neural networks for estimating the action-value function for a given problem to identify the optimal action in any state. The estimator function can be described as:

$$Q^{\pi}(s,a) = E_{s'\sim P}\left[r(s,a) + \gamma \max_{a'} Q^{\pi}(s',a')\right] \quad (1)$$

where, E is the denotes the expectation operator. Therefore, if the neural network representing the Q function is given by parameters φ, the loss function can be given by:

$$L(\varphi, D) = E_{(s,a,r,s')\sim P}[(Q^{\pi}(s,a) - y)^2] \quad (2)$$

$y = (r + \gamma(1-d)\max_{a'} Q^{\pi'}(s',a')$ is called the temporal difference and is calculated using target network Q^π' which is updated with the same parameters as main Q-function periodically. This method stores the set of experiences generated over time into the Replay buffer which is used to randomly sample data for training the loss function given above.

2.3 Policy Gradient Algorithms

Policy gradient algorithms explicitly denote the policy as $\pi_{\theta}(a|s)$ represented by a deep neural network with parameter θ. These parameters can be trained by maximizing the objective function $J(\pi_{\theta}) = E_{s'\sim P, a\sim\pi_{\theta}}(R)$, where R is the reward function. Thus, to update the policy parameters, gradient ascent can be used by calculating the gradient of the objective function.

$$\theta_{k+1} = \theta_k + \alpha \nabla_{\theta} J(\pi_{\theta})|_{\theta_k} \quad (3)$$

Where,

$$\nabla_{\theta} J(\pi_{\theta}) = E_{s\sim P, a\sim\pi_{\theta}}\left[\sum_{t=0}^{T} \nabla_{\theta} \log \pi_{\theta}(a_t|s_t) R\right]$$

These methods can be used for both stochastic as well as deterministic policies and thus are suitable for problems with continuous action spaces.

2.4 Algebraic Graph Theory

A complete multi-agent system can be mathematically represented by a weighted undirected graph $G = (V, E)$ where $V = \{1,2, \dots, N\}$ is the set of agents and $E = \{(i,j): i,j \in V, i \neq j\}$ is the edge set. The adjacency matrix of graph G represented by $A(G)$ is a standard matrix in graph theory which represents the weights of the edges. This matrix can be used to represent the relationship between agents.

3 PROBLEM FORMULATION

In this paper, the task of formation flocking is defined in the context of holonomic agents moving on the Euclidean plane. The position vector for each agent can be denoted by $p_i^t = [x_i, y_i]^T$ and the velocity vector by $v_i^t = [\dot{x}_i, \dot{y}_i]^T$, for the UAV i (i = 1, 2, …, N) at time t, where N is the number of UAVs. The goal of the agents is to attain the desired formation using the adjacency matric A_{FM} of the formation matrix graph G_{FM} (where the weight of each edge (i, j) of the graph corresponds to the desired distance between the agents i and j) and navigate to the goal position $p_g^t = [x_g, y_g]^T$ while avoiding inter-agent collisions. To maintain the formation at the goal position, another adjacency matrix A_{GFM} of graph G_{GFM} (where the weight of each edge (i, p_g) of the graph corresponds to the desired distance between the agent i and goal position p_g.

Thus, the problem statement can be modelled as a sequential MDP defined by a tuple $Z = (S, A, R, O)$ where, $S = \{S_1, \dots S_N\}, A = \{A_1, \dots, A_N\}$, $R = \{R_1, \dots, R_N\}$, $O = \{O_1, \dots, O_N\}$ is the set of sets of states, actions, rewards and observations of all agents.

At time step t, agent i is present in state s and has access to an observation o, which is used to calculate action a. As a consequence of this action, the agent reaches a new state s', receives a reward r and has access to new observation o'. The goal of the agent is to learn the optimal policy $\pi_\theta^*(a|s)$ where θ denotes the policy parameters which maximizes the sum of obtained rewards. This process continues until all the agents reach the goal position where the episode terminates.

The sequence of the tuple (o, a, r, o') made by the robot i can be considered as a trajectory denoted by τ. The set of these trajectories collected by all the agents is denoted by D and is stored in memory as the Replay buffer. B denotes the minibatch of experiences randomly samples from D for training the model.

4 APPROACH

4.1 Environmental Setup

To solve the sequential MDP defined in Section III, an environmental model with appropriately defined observation space, action space and reward function is required.

4.1.1 Observation Space

The observation space o consists of the planar position of each agent given by p_i^t along with the goal position p_g^t. These values are flattened and passed to a fully connected input layer of the policy network to calculate the action values. Thus, the size of input layer varies with the number of agents which also increases the training time for the policy network.

4.1.2 Action Space

The holonomic agents considered for the problem statement have an action space that consists of a set of permissible velocities in the continuous space. The output action is the two-dimensional velocity vector $v_i^t = [\dot{x}_i, \dot{y}_i]^T$. The output layer is constrained by the hyperbolic tangent ($tanh$) activation function which limits the output value in the range of (-1,1). This output value is then multiplied by v_{max} parameter to limit the action value, which is then directly passed to the navigation controller of the agent.

4.1.3 Reward Function

To achieve the target of formation control and navigation in the minimum time possible, the reward function is designed as follows:

$$r_i^t = (r_G)_i^t + (r_F)_i^t + (r_C)_i^t \tag{4}$$

where, the total reward r_i^t is the sum of goal reward (r_G), formation reward (r_F) and inter-agent collision penalty (r_C) of an agent i at timestep t.

The goal reward $(r_G)_i^t$ is awarded for the agent i for reaching the goal position as:

$$d_g = \|p_g^t - p_i^t\|$$
$$(r_G)_i^t = \begin{cases} r_{goal} & , \left|d_g - A_{GFM}^{i,p_g}\right| < d_{wp} \\ \frac{C_g}{N}\left(\left|d_g - A_{GFM}^{i,p_g}\right|\right), otherwise \end{cases} \tag{5}$$

To maintain the desired formation as governed by the formation graph G_{FM}, the agents are penalized for deviating from their desired relative position with other agents as:

$$(r_F)_i^t = \frac{C_f}{N} \sum_{j=1, j\neq i}^{N} \left|\|p_i^t - p_j^t\| - A_{FM}^{i,j}\right| \tag{6}$$

Finally, to avoid inter-agent collisions, the agents are penalized as follows:

$$(r_C)_i^t = \sum_{j=1, j\neq i}^{N} \begin{cases} r_{collision}, \|p_i^t - p_j^t\| < d_{safe} \\ 0, otherwise \end{cases} \tag{7}$$

Algorithm 1: Multi-agent TD3.

Initialize policy network with parameters θ, Q-functions with parameters φ_1, φ_2. Empty the replay buffer D

Set target network parameters equal to main parameters

$$\theta_{target} \leftarrow \theta, \varphi_{target,1} \leftarrow \varphi_1, \varphi_{target,2} \leftarrow \varphi_2$$

for number of episodes **do**

  for robot $i = 1,2, \dots N$ **do**

    Take observation o^t select action

$$a = clip\left(\mu_{\theta_{target}}(s') + \varepsilon, a_{Low}, a_{High}\right)$$

    Execute action a in the environment

    Observe next state o', reward r and done signal d to indicate whether o′ is terminal.

    Store (o, a, r, o', d) in replay buffer D

    If o' is terminal, reset environment state.

  end for

  if memory can provide minibatch **then**

    Randomly sample a batch of transitions,

$$B = \{(o, a, r, o', d)\} \text{ from } D$$

    Compute target actions

$$a'(o') = clip\left(\mu_{\theta_{target}}(o') + q, a_{Low}, a_{High}\right)$$

$$q = clip(\varepsilon, -c, c)$$

    Compute Bellman target

$$y(r, o', d) = r + \gamma(1 - d) \min_{k=1,2} Q_{\varphi_{target,k}}(o', a'(o'))$$

    Update Q-functions by one step of gradient descent using lr_ϕ

$$\nabla_{\varphi_k} \frac{1}{|B|} \sum_{(o,a,o',d) \in B} \left(Q_{\varphi_k}(o, a) - y(r, o', d)\right)^2 \quad k = 1,2$$

    if time to update policy **then**

      Update policy by one step of gradient ascent using lr_θ

$$\nabla_\theta \frac{1}{|B|} \sum_{o \in B} Q_{\varphi_1}(o, \pi_\theta(o))$$

      Update target networks with

$$\theta_{target} \leftarrow \rho\theta_{target} + (1 - \rho)\theta$$

$$\varphi_{target,k} \leftarrow \rho\varphi_{target,k} + (1 - \rho)\varphi_k \quad k = 1,2$$

    end if

  end if

end for

4.2 Algorithm Design

The algorithm used in this paper is an extended version of the state-of-the-art Twin Delayed Deterministic Policy Gradient algorithm (Fujimoto et al., 2018), (Lillicrap et al., 2015)) commonly known as TD3. TD3 concurrently learns two Q-functions and a policy and uses the smaller out of the two Q-values to calculate the loss function. We use the paradigm of centralized training with decentralized execution, which means that the data collected by all the agents is used for training the policy network $\pi_\theta(a|s)$, but each agent takes action in a decentralized fashion by using this policy.

During each episode of the training process, there are two major steps. First, all the agents exploit the same policy to calculate their actions and record their new observations which are then stored in the replay buffer. Second, random batches of experiences are sampled from the replay buffer to calculate the Bellman target which is used to calculate the loss function as given in eq.2. This loss is optimized using Adam optimizer (Kingma et al., 2014). Further, for policy training, the problem statement requires a deterministic policy $\pi_\theta(a|s)$ which gives the action that maximizes the Q-function. Therefore, the objective function can be modified as

$$J(\pi_\theta) = \max_\theta E_{o \sim B}\left[Q_\varphi(o, \pi_\theta)\right] \quad (8)$$

and therefore, the policy gradient can be calculated as

$$\nabla_\theta J(\pi_\theta) = \nabla_\theta \frac{1}{|B|} \sum_{o \in B} Q_{\varphi_1}(o, \pi_\theta(o)) \quad (9)$$

The target networks in the algorithm are updated periodically using the Polyak averaging method as follows:

$$\theta_{target} \leftarrow \rho\theta_{target} + (1 - \rho)\theta \quad (10)$$

$$\varphi_{target,k} \leftarrow \rho\varphi_{target,k} + (1 - \rho)\varphi_k \quad ; k = 1,2 \quad (11)$$

where $\rho \ll 1$.

4.3 Network Architecture

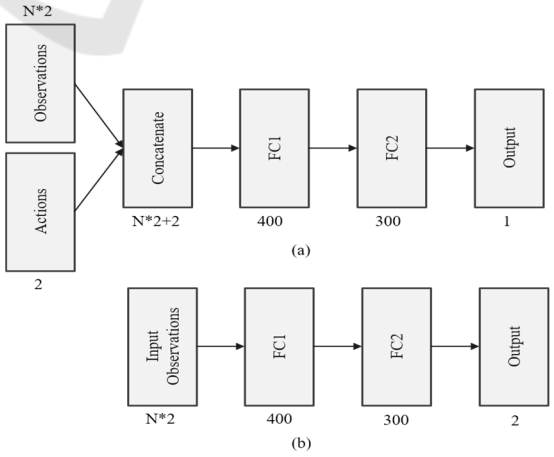

Figure 1: Network architecture of the (a) critic and (b) actor neural networks.

TD3 algorithm utilizes six neural networks in total, three main and three target networks. The target networks are employed to stabilize the training process. The observation o with dimensions $(N * 2 * 1)$ directly acts as the input for the policy network and outputs the action value. While for the Q-network, observation o and action a are concatenated to form the input layer and the output is a single Q-value which gives the quality of that action. The network architecture for both policy network and the Q-network is given in Figure.1. RELU activation function is used for the hidden layers while the output layer utilizes a 'tan h' activation function to limit the output velocity by a maximum limit.

5 SIMULATION AND TESTING

In this section, first the method of simulation is explained. Then, the computational complexity of the algorithm and training resources utilized is described. Lastly, the quantitative results of various simulations in varying environments are demonstrated.

5.1 Simulation Environment

The simulation environment is a custom developed GUI using Matplotlib library in python. The blue circles represent the agents, the red circle is the goal and the black circles are the obstacles.

The start position of the agents, goal position and all the obstacles are randomly generated after each episode is over. This approach was found to prevent the policy from exploiting the errors in the Q-function and thus improved the performance of the algorithm substantially.

5.2 Training Configuration

The complete implementation was carried out using TensorFlow 2 on a computer with a Nvidia GTX 1060 GPU and an Intel i7-8750 CPU with the set of hyper-parameters as mentioned in Table 1. The complete training process took about 22 hours for the learned policy to achieve robust performance in a complete simulation of 10 agents.

During the execution, since only the actor network is required, the computational resources required are minimal and thus the same architecture can be used on single-board computers like the Nvidia Jetson nano and Raspberry Pi.

Table 1: Hyperparameters used for simulation.

Hyperparameter	Value	Hyperparameter	Value
B	1000	ε	0.1
γ	0.99	c	0.5
lr_θ	0.0001	r_{goal}	10
lr_ϕ	0.001	$r_{collision}$	-50
ρ	0.995	d_{wap}	0.5
D	1000000	d_{safe}	1
a_{Low}	-2	C_f	-0.1
a_{High}	2	C_g	-0.1

5.3 Experiments and Results

Since, the observation space consists of the planar positions of all the agents and the goal position, the training time increases rapidly as the number of agents scale up. Figure 3 shows the training time required for training the policy on three, five, seven and ten agents respectively.

Further, Figure 3 shows the average reward received as training progresses. Figure 4-6 shows the performance of the learned policy on a varying number of agents for different formations.

To test the generalization capabilities of the learned policy, we introduced non-cooperative agents [agents travelling directly towards the goal position in a straight line with constant velocity] which were not used during the entire training process. But the learned policy was able to generalize well with these agents as demonstrated in Figure 7. (Non-cooperative agents are shown by square boxes)

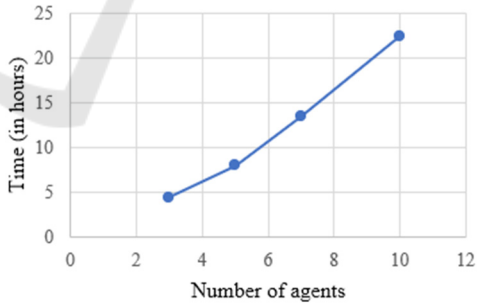

Figure 2: Increase in training time with increment in number of agents.

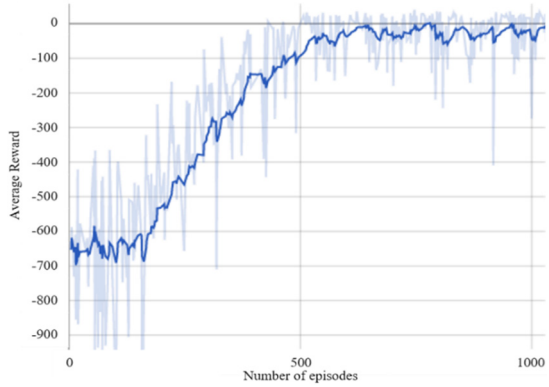

Figure 3: Average rewards progression with increasing episodes during training process.

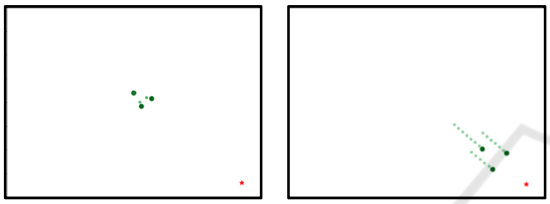

(a) (b)

Figure 4: V-formation using 3 agents.

(a) (b)

Figure 5: X-formation using 5 agents.

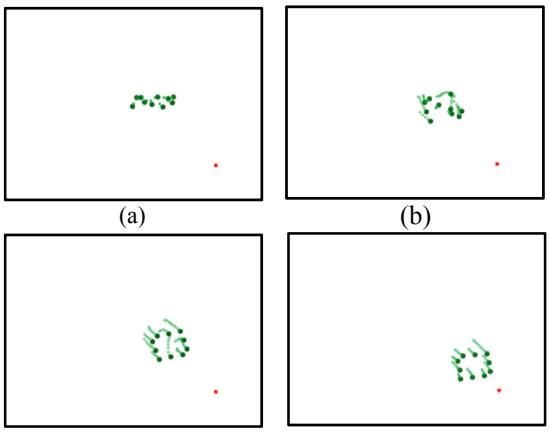

(a) (b)

(c) (d)

Figure 6: Diamond-formation using 10 agents.

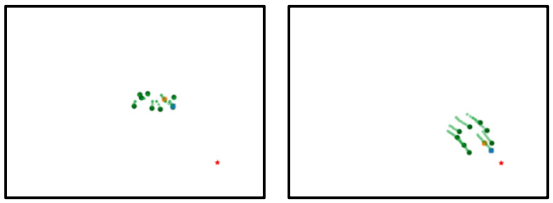

(a) (b)

Figure 7: Diamond-formation using 8 cooperative and 2 non-cooperative agents.

6 CONCLUSIONS

In this paper, we addressed the problem of Multi-agent formation control and navigation in unknown environments by using an end-to-end Deep Reinforcement Learning framework. The learned policy demonstrates several advantages over the existing methods in terms of maintaining the desired formation, collision avoidance performance, adaptability to the environments and generalized performance.

Multi-agent systems are the future of the robotics industry and as they become more prevalent, these systems will require adaptive controllers which can execute the tasks effectively in unfamiliar situations. Thus, integration of Reinforcement Learning with multi-agent systems is a step towards developing truly intelligent systems which can perform efficiently in real-world. We hope that our work can serve as the starting step in developing swarming systems for future applications.

Our future work in this area will be aimed towards following two goals:

1. Developing an efficient approach to solve the problem of extended training time with increase in number of agents.
2. Applying DRL to mission-specific problems such as target search and area coverage and to apply better exploration techniques to improve the learning time of the policy.

REFERENCES

Reynolds, Craig, 1987. Flocks, herds and schools: A distributed behavioural model. SIGGRAPH '87: Proceedings of the 14th Annual Conference on Computer Graphics and Interactive Techniques. Association for Computing Machinery. pp. 25–34.

Marko Bunic, Stjepan Bogdan, 2012. Potential Function Based Multi-Agent Formation Control in 3D Space, IFAC Proceedings Volumes, Volume 45, Issue 22, Pages 682-689.

Anuj Agrawal, Aniket Gupta, Joyraj Bhowmick, Anurag Singh, Raghava Nallanthighal, 2020. “A Novel Controller of Multi-Agent System Navigation and Obstacle Avoidance”, Procedia Computer Science, Volume 171, Pages 1221-1230.

M. Egerestedt, 2007. “Graph-theoretic methods for multi-agent coordination” in ROBOMAT.

S. Hung and S. N. Givigi, 2017. "A Q-Learning Approach to Flocking with UAVs in a Stochastic Environment," in IEEE Transactions on Cybernetics, vol. 47, no. 1, pp. 186-197.

Johns, Rasmus, 2018. “Intelligent Formation Control using Deep Reinforcement Learning.”.

Mnih, V., Kavukcuoglu, K., Silver, D. et al, 2015. Human-level control through deep reinforcement learning. Nature 518, 529–533.

Fujimoto, Scott & Hoof, Herke & Meger, Dave, 2018. Addressing Function Approximation Error in Actor-Critic Methods.

Lillicrap, Timothy & Hunt, Jonathan & Pritzel, Alexander & Heess, Nicolas & Erez, Tom & Tassa, Yuval & Silver, David & Wierstra, Daan, 2015. Continuous control with deep reinforcement learning. CoRR.

Kingma, Diederik and Ba, Jimmy, 2014. “Adam: A method for Stochastic Optimization.”

Bellman, Richard, 1957. “A Markovian Decision Process.” *Journal of Mathematics and Mechanics*, vol. 6, no. 5, pp. 679–684., www.jstor.org/stable/24900506.

SCITEPRESS
SCIENCE AND TECHNOLOGY PUBLICATIONS

2021 11th International Conference on Cloud Computing, Data Science & Engineering (Confluence) | 978-1-6654-1451-7/20/$31.00 ©2021 IEEE | DOI: 10.1109/Confluence51648.2021.9377172

Deep Neural Architecture for Veracity Analysis of Multimodal Online Information

Priyanka Meel
Biometric Research Laboratory
Department of Information Technology
Delhi Technological University
New Delhi, India-110042
priyankameel86@gmail.com

Dinesh Kumar Vishwakarma
Biometric Research Laboratory
Department of Information Technology
Delhi Technological University
New Delhi, India-110042
dvishwakarma@gmail.com

***Abstract*— The extensive digital communication among users around the world in various fields such as politics, sports, religious beliefs, product promotions, celebrities, etc. has given rise to a huge volume of unauthenticated and unverified information. So, it has become imperative in the current scenario to design methods for veracity analysis of online information in various data formats mainly text and images. This work introduces a novel automatic fake news detection framework by utilizing the capabilities of Deep Neural Networks namely VGG16 for Image, Bi-LSTM for Text and Title part of online news. The designed model is intended to be robust enough for handling the forgeries present in the online news articles. Finally, the three parallel architectures for each part of the news are combined using the late fusion approach by some sets of normalized weights. Effective experimental analysis has been carried out on two different real-world news datasets which comprise of real and fake news articles. The highest classification accuracy achieved is 97.74% on the All Data dataset. The state-of-the-art comparison advocates the advantages of the proposed model over other contemporary techniques.**

Keywords—Visual Geometry Group, Recurrent Neural Network, Late Fusion, Word Embedding, Multimodal

I. INTRODUCTION

According to the Oxford Dictionary News means 'newly received or noteworthy information, especially about recent events [1]. So, the news contains happening around the world which can be statements, claims, speeches, weather information, information related to government bodies and various types of information related to public figures and organizations. We rely on different sources such as newspapers, news channels, news websites, etc. to obtain information. In the current scenario, the dependency on social media to obtain news has tremendously increased. News propagation may lead to the involvement of a huge number of platforms like Facebook, twitters, and other popular news apps to report the same observation rapidly in the online social world. Fake news can be narrowly defined as a piece of news article whose content is not verifiable and its primary intention is to mislead its consumer [2].

There could be various aspects and impacts of fake news articles. The spams in our emails may have a small impact on the smaller number of audiences; however, spams of fake news via social networks platform can hugely affect the people because a huge number of people are reading online articles globally. Sometimes user shares news information which even they are unaware whether it is fake or not. To identify the fake news in itself is a challenging task. It requires some concrete evidence, fact-checking and other comparable news articles present in the public domain. Table I highlights few instances of fake news circulation about Indian politics in recent times.

Researchers are trying hard to propose solutions for classifying fake articles from genuine ones using different machine learning, rule-based and artificial intelligence techniques. The main objective of the proposed work is to carry out fake news detection of online available news contents in multimodal format by considering the forgeries involved in both images and text part of the news, as pictures are integral and effective means of communication. The key contributions of the proposed work are as follows:

- A CNN based VGG16 model is used to detect hidden distortion and forgeries in news images.
- The Bi-LSTM approach is used to perform pattern analysis of writing style in the text and title part of the news.
- The three parallel streams of image, text and title are fused using weighted averaging of the three independent predictions.
- The framework is tested on two different datasets and performance is compared with baseline methods.

The work is organized into five different sections. Section 1 introduces the problem with some real-life examples and facts. The literature survey is presented in section 2. Section 3 details the architectural specifications of the proposed model and section 4 deals with experimentation as well as result analysis. Finally, the conclusion and future research directions are highlighted in section 5.

II. RELATED WORKS

The research for analyzing the credibility of online information is a very trendy topic and attracts the attention of the scientific community. The work [2], [3], [4] provides an extensive survey of the available fact-checking platforms, fake news detection methods, challenges and opportunities in the field of rumor, misinformation, disinformation, spam, propaganda and fake news analysis. Yang et al. [5] developed an approach of stance detection of online news articles using CNN. They divided the approach into implicit and explicit feature engineering. They had extracted the implicit features of text and image from convoluting the data through a CNN architecture. These features obtained are then merged with the external features of the text and images to obtain a final features vector. Then they have passed the final

Authorized licensed use limited to: DELHI TECHNICAL UNIV. Downloaded on March 27,2021 at 05:38:09 UTC from IEEE Xplore. Restrictions apply.

features vector through a deep CNN architecture for designing fake news detection framework.

TABLE I. FAKE NEWS EXAMPLES IN INDIA

News	Reported By/Spread By	Identified as Fake!
A startup by IIT-Delhi named Sanfe claimed that they have FDA approval and AYUSH ministry certificate for their pain relief roll-on [6].	This was reported by several news outlets such as TOI, NDTV, The Economic Times, India Today, Indian Express, DNA India as per the Official IIT Delhi website's release.	Fact-checked and published by altnews.in on 7th April 2019. They cross-checked via email to the FDA CDER which confirmed that no such approval was sanctioned.
	This particular image was shared on various social media such as Twitter, WhatsApp, Facebook, etc. claiming that it is a 'new trick for fake voting' by using fake fingers for casting vote in the 2019 Lok Sabha election. Among various users who believed in this image was Former CEC S.Y. Quraishi [6].	The rumor was debunked by Altnews on 12th April 2019. The fake fingers shown in the image is a prosthetic finger for Yakuza members. This image also went viral during the 2017 legislative assembly election and was fact-checked by BBC in 2017.
Pakistan Flag waved at Rahul Gandhi's Wayanad rally [6].	Several people shared photos and videos of people waving Pakistan's National Flag in Rahul Gandhi's rally in Wayanad during the Lok Sabha polls of 2019. Among these users was a public figure, Koena Mitra. Some of them also claimed it was an Islamic flag.	Altnews on 4th April 2019 clarified that the flag that was claimed as Pakistan's National Flag or Islamic Flag was IUML, Indian Union Muslim League Flag.
Several WhatsApp and Facebook posts being shared saying that the NRI voters can cast their vote online in the 2019 Lok Sabha Polls [6].	This piece of the fabricated message was shared in various WhatsApp groups and social media platforms.	Altnews on 25th March 2019 checked this message and found out to be partially true. The NRIs can register themselves online but needs to be physically present in the polling booth to cast their votes.
President Kovind earns 3.25 million followers within minutes of becoming India's 14th President [6].	It was tweeted by the official Twitter handle of Zee News. The same was tweeted by the official Twitter handle of other news channels such as Republic, TOI India, Financial Express, Economic Times.	This information was debunked by altnews.in and India Today on 26th July 2018. The follower count was of the President of India's official Twitter account which was passed on to President Ram Nath Kovind from Former President Pranab Mukherjee.

Kumar et al. [7] developed a fake news detection approach using various combinations of CNNs and LSTMs. Initially, they tried only CNN but the results from that architecture were not promising, so they switched to LSTMs. LSTM and Bi-LSTM gave a much better result than CNN and finally, they aggregated the architectures of CNN and LSTM; so that they can have the best features from both methods and hence can have better results. Drif et al. [8] implemented veracity analysis by using a combination of CNN-LSTM architectures on the text part of the news dataset and the results are 62.3% for the Liar dataset and 72.5% for the news article dataset. Gangireddy et al. [9] proposed a graph-based unsupervised model and Abonizio et al. [10] designed a language-independent framework for the classification of untrustworthy news articles.

The parallel computing approach of Yang et al. [5] is quite interesting and the different variants of RNNs used by Kumar et al. [7] and Drif et al. [8] are also promising. To incorporate the best features of available methods and improve the results by avoiding their shortcomings we develop our novel framework based on late fusing the results after parallel predictions from three neural architectures that are trained using three different parts of online news articles. Thus, we have obtained more accurate and precise predictions than state-of-the-arts.

III. PROPOSED MODEL

The proposed framework consists of three parallel predictions being accumulated into one final overall classification by using the weighted averaging late fusion method as represented in figure 1. Pre-trained VGG16 followed by one hidden layer ANN is used for the training image model. Text and title models are being trained using Bi-LSTM architecture. The framework is being experimented and tested on two different datasets for establishing higher validity of results.

A. Pre-processing

The text and title part of the datasets are first pre-processed and tokenized to convert them into a format that can be passed into the neural network. Stop words and punctuations are removed, whole corpus is transformed into lower case then it is converted into a sequence matrix using 100-dimensional word2vec embedding vectors, to retrieve the latent hidden sequential pattern so that the Bi-LSTM

Authorized licensed use limited to: DELHI TECHNICAL UNIV. Downloaded on March 27,2021 at 05:38:09 UTC from IEEE Xplore. Restrictions apply.

method can do the pattern classification on the dataset by its own.

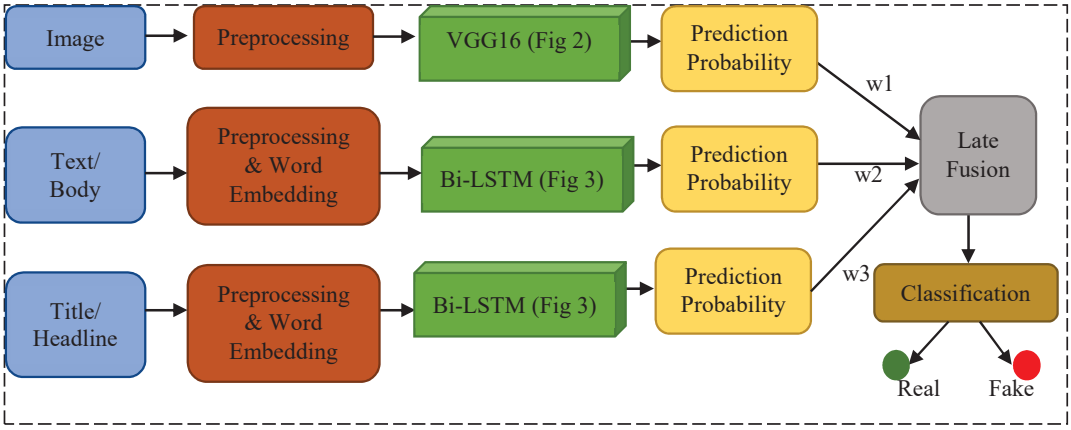

Fig.1: Proposed Multimodal Architecture

Word2vec makes use of vector arithmetic to capture the various depth of similarity in words with each other. Hence the deep neural network can easily find semantic as well as the syntactic relationship between the given words. The embedding word vector is passed as an input to the Bi-LSTM network. In the image part of the All Data dataset, the images are obtained from URLs and converted to (128x128x3) pixel array. Jruvika and Emergent datasets do not have images in them, therefore we used site URL to perform web scraping and extracted image URLs from there. Images are downloaded from respective URLs and finally converted into (128x128x3) pixel array.

B. Visual Geometry Group(VGG16)

VGG16 also known as OxfordNet is a deep CNN based architecture. The salient feature that makes VGG16 stand out of crowd is that it has 3x3 filter that too with a stride 1 and often tries using the same padding alongside with max pool layers which are of 2x2 filter having stride 2. The input image in the VGG16 model is passed through a stack of convolutional layers with filters of small receptive field 3×3 with a fixed stride of 1 pixel. The spatial pooling in the VGG16 model is carried out by 5 max-pooling layers. Max-pooling on other hand is performed over a 2×2-pixel window with stride equal to 2. There is a total of 16 layers in VGG16.

Initially, the convolution layer extracts some lower-level features such as color, points, edges, etc. After adding each new layer, we get more robust features or high-level feature and finally gives a better understanding of images in datasets. Figure 2 represents overall VGG16 architecture that we have used in our proposed framework in figure 1 including pre-trained and customized parts. A neural network model is built with VGG16 blocks (without top layer) which takes the training images as an input of (128x128x3) dimensional vector and produces a flattened one-dimensional feature vector of dimension(1x8192). The feature vector (8192 units) extracted out of the pre-trained

VGG16 model is then allowed to pass through a fully connected neural network of 1 hidden layer (512 units) with Relu activation, batch normalization and dropout probability 0.5. The final output is obtained with a sigmoid activation function. The complete model is then run for 100 epochs with a batch size of 16, adam optimizer and binary cross-entropy loss function. Each epoch takes 5 seconds of CPU time to complete. The validation is done with validation data of size 10% from the original dataset.

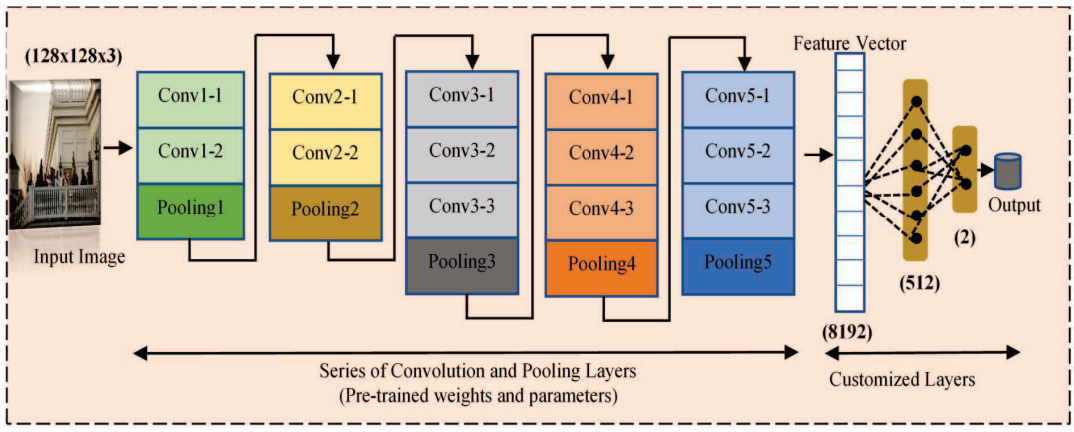

Fig.2: VGG16 Architecture

Authorized licensed use limited to: DELHI TECHNICAL UNIV. Downloaded on March 27,2021 at 05:38:09 UTC from IEEE Xplore. Restrictions apply.

C. Bi-Directional LSTM

The primary idea behind the recurrent neural network is that the system's past state influences its next state. Nodes in the Recurrent Neural Network are like neurons organized into successive manners. Each node in the previous layer is connected to all the nodes in the next layer and each neuron contains a time-varying activation function or real-valued function. These nodes are of three types: input nodes, output nodes and hidden nodes. In supervised learning, a sequence of real-valued or time-variant input vector arrives at the input nodes, one vector at a time. After this, every non-input node computes its current results and pass it to the next node in the network.

LSTM is a recurrent neural network that is free from vanishing gradient problems and also helps to prevent the back-propagated errors from being lost. Input gate, forget gate and output gate are three main building blocks of LSTM. The input gate is used for updating the cell states. Information from the current and previous state is passed through a sigmoid function to the input gate. Forget gate retains only required information and throws away unnecessary content. The output gate will decide the next hidden state. This hidden state contains information of previous inputs.

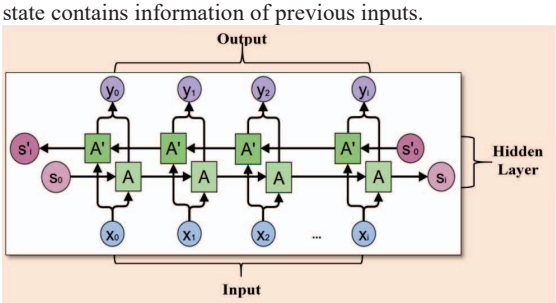

Fig. 3: Bi-Directional LSTM Architecture

Bi-LSTMs are an extended version of traditional LSTMs. This version of LSTM can boost model performance on sequence classification applications. Bi-Directional LSTMs consists of two unbiased RNNs put together. The idea behind the Bi-Directional RNN is that it splits the neurons into 2 directions of which one is for positive time direction known as forward state and the other is moved to negative time direction also called backward state. This type of model permits the network layers to both forward and backward approximation about the sequence on each time step. The inputs can run in both the direction from past to future and from future to past. With the combined use of 2 hidden states Bi-LSTM networks can preserve information from both the future and past in any time frame as represented in figure 3.

A Bi-LSTM model is built with 1 embedding layer which takes the text as an input of dimension (1x200) and produces an output of dimension (1x200x100) after using 100-dimensional Word2Vec embedding. This vector is allowed to pass through a neural network of 1 hidden layer (128 units) with batch normalization and dropout probability of 0.2. The final output is obtained by the sigmoid activation function. The complete model is run for 100 epochs with a batch size of 64, RMSprop optimizer and binary cross-entropy loss function. Each epoch takes 11 seconds of CPU time to complete. The validation is done with validation data of size 10% from the original dataset. The same process is repeated for the title Bi-LSTM model with input of dimension (1x25) into the embedding layer and identical hyperparameter settings.

D. Late Fusion

To combine the predictions done by three independent parallel features images, text and title; first, each of the features is separately used to train three different models:

- A pre-trained VGG16 followed by a hidden layer is used to train the image model.
- A Bi-LSTM model with an embedding layer is used to train the text model.
- A Bi-LSTM model with an embedding layer is used to train title mode.

After training all three independent models, the predicted arrays obtained from all of them are combined using the weighted averaging late fusion method and three normalized weights (w1, w2, w3) are used to make an overall prediction. The final prediction is performed according to the following equation (1); where x_i is the probability of i^{th} feature and w_i is the corresponding assigned weight. The weights assigned for image classifier is w1, for text classifier is w2 and for title classifier is w3.

$$Final\ prediction = \frac{\sum_{i=1}^{n} w_i x_i}{\sum_{i=1}^{n} w_i} \quad (1)$$

IV. Experiments

To validate the effectiveness of our work we implemented the proposed model in python programming language on Windows 10 operating system. We trained our model using NVIDIA TESLA P100 GPU and 13 GB RAM on the Kaggle Notebooks Platform. The architecture is being trained, validated and tested independently on each of the two datasets. The ratio of the dataset used for training, validation and testing is 80:10:10 respectively. Performance is being evaluated in terms of precision, recall, accuracy and F1 score. A comparative analysis of the proposed approach is being done with other contemporary models on the same datasets being used.

A. Datasets

The framework proposed in section 3 is tested on two different datasets. Table II highlights the details of the datasets.

1) All Data

The dataset All Data [11] contains 54 different attributes title, text, image URL, site URL, comments, likes, replies, shares, spam scores, sentiment scores etc. We preprocessed the dataset to extract only useful attributes news headline/title, news text/body, image URL and Label (Real/Fake). After preprocessing, deleting rows with missing values and cleaning of corrupted image links 5000 news articles are extracted out of which 2600 are true and 2400 are false news instances. This 5k dataset is divided into 3 subsets in the ratio of 80:10:10 to get training, validation and testing parts. This dataset contains images in the form of URLs that are retrieved and converted to (128x128x3) size pixel array.

Authorized licensed use limited to: DELHI TECHNICAL UNIV. Downloaded on March 27,2021 at 05:38:09 UTC from IEEE Xplore. Restrictions apply.

TABLE II. DATASET DETAILS

Sr. No.	Dataset Name	Details	# Instances after pre-processing	# Real News	# Fake News
1.	All Data [11]	Dataset contains 54 attributes including site URL, Headline, Body, Image URL, Label	5000	2600	2400
2.	Jruvika [12] +Emergent [13]	Jruvika is hosted on Kaggle, contains site URL, Headline, Body and Label Emergent is hosted on Kaggle, contains 15 attributes including source URL, Title, Body, Label	2150	1400	750

2) Jruvika+Emergent

Jruvika [12] and Emergent [13] both datasets are hosted on the Kaggle platform. Jruvika contains four attributes and Emergent contains 15 different attributes including site URL, title, text and Label. Both of these datasets did not have images preloaded or image URLs, so we performed web scraping to extract image URLs from website URLs of the news article and modified the dataset by adding a new field. After extraction of image_url, we use urllib library to fetch images and download them on our local system. The images are converted into (128x128x3) size pixel array to save processing time when running the code. After pre-processing the dataset, deleting rows with missing attribute values, scraping of images and loading it into the system; the size of two of the datasets became small, hence we merged the two datasets Jruvika and Emergent into a single dataset. This combined final dataset contains a total of 2150 news instances, out of which 1400 are real and 750 are fake news articles. The dataset is divided into 3 subsets in the ratio of 80:10:10 to get training, validation and testing parts.

B. Result Analysis

The performance of the proposed architecture is tested on two datasets for accuracy, precision, recall and F1-score parameters. Extensive analysis of the results is being done initially for independent models on image, text and title and then using late fusion with weighted averaging. Three different combinations of weights (w1, w2, w3) are being tested and concluded that both the datasets contributed their best performance for (w1, w2, w3) = (0.20,0.50,0.30) combination. Table III and Table IV highlights the details of results obtained for All Data and Jruvika + Emergent datasets respectively.

TABLE III. RESULT ANALYSIS OF ALL DATA DATASET

Feature	Accuracy (%)	Precision (%)	Recall (%)	F1-Score (%)
Independent Feature Accuracy				
VGG16 on Images	73.32	73.04	72.85	72.94
Bi-LSTM on Text	96.30	97.91	94.80	96.32
Bi-LSTM in Title	86.58	86.00	86.28	86.14
Overall Accuracy after Late Fusion/ Weighted Averaging				
(w1, w2, w3) = (0.33,0.34,0.33)	93.22	94.06	93.44	93.75
(w1, w2, w3) = (0.25,0.45,0.30)	94.07	94.65	95.92	95.28
(w1, w2, w3) = (0.20,0.50,0.30)	**97.74**	**97.84**	**97.29**	**97.56**

TABLE IV. RESULT ANALYSIS OF JRUVIKA+EMERGENT DATASET

Feature	Accuracy (%)	Precision (%)	Recall (%)	F1-Score (%)
Independent Feature Accuracy				
VGG16 on Images	70.71	70.21	71.56	70.88
Bi-LSTM on Text	94.15	95.62	94.91	95.26
Bi-LSTM in Title	84.65	85.92	83.13	84.50
Overall Accuracy after Late Fusion/ Weighted Averaging				
(w1, w2, w3) = (0.33,0.34,0.33)	92.90	90.18	92.33	91.24
(w1, w2, w3) = (0.25,0.45,0.30)	93.28	93.60	94.19	93.89
(w1, w2, w3) = (0.20,0.50,0.30)	**95.40**	**95.10**	**93.42**	**94.25**

TABLE V. PERFORMANCE COMPARISON OF ALL DATA AND JRUVIKA+EMBERGENT DATASETS WITH BASELINES

Method	Modality	Description	All Data Accuracy (%)	Jruvika + Emergent Accuracy (%)
Karimi and Tang [14]	Text	Hierarchical Discourse level Structure using Bi-LSTM	86.32	83.09
Ajao et al. [15]	Text	Hybrid CNN and RNN	84.80	86.00

Authorized licensed use limited to: DELHI TECHNICAL UNIV. Downloaded on March 27,2021 at 05:38:09 UTC from IEEE Xplore. Restrictions apply.

Yang et al. [6] (TI CNN)	Text and Image	CNN	92.00	92.91
Lago et al. [16]	Text and Image	TF-IDF, cosine and Jaccard's similarity, Classical and advanced image forensics, CNN, Logistic Regression, Random Forest	92.13	90.26
Our Method	**Text and Image**	**VGG16 and Bi-LSTM with Late Fusion**	**97.74**	**95.40**

C. State-of-the-art Comparison

The outcomes of the state-of-the-art comparison of the proposed framework with other contemporary methods on identical datasets are being highlighted in Table V. The reference methods are tested on All Data and Jruvika + Emergent dataset for identical training, validation, testing split (80:10:10) with the same experimental conditions and the proposed architecture in corresponding research. The following baselines are used for state-of-the-art comparison:

• To identify structure-related properties of fake news articles Hierarchical Discourse Level Structure using Bi-LSTM is proposed by Karimi and Tang [14] .

• Ajao et al. [15] designed Hybrid CNN and RNN deep models for classifying real and fake news instances.

• Text-Image Convolutional Neural Network (TI CNN) by Yang et al. [5] is simultaneously trained with explicit and latent features of text and images for designing a robust credibility analysis system.

• Classical and advanced image forensics architecture for textual and visual fake news detection is designed by Lago et al. [16].

V. Conclusion and Future Works

Information is an integral part of human life and plays a major role in decision making. The problem of veracity analysis of online information is highly important and needs to be taken care of seriously. The experimentation shows that the combined result of all the three classifiers with weighted averaging is much better than the individual result of each classifier for both the datasets. We also tested with different weights of individual classifiers for deeper analysis. These results signify that during news veracity prediction if the text classifier is going wrong the other two classifiers have helped it out to gain weight to remove the chances of false positives in combined results. The work can also be further extended by incorporating the use of transformers, natural language processing techniques and language-independent frameworks. Deep fake videos are also a prevalent format of forgery, hence must also be addressed.

VI. References

[1] "news | Definition of news in English by Oxford Dictionaries," [Online]. Available: https://en.oxforddictionaries.com/definition/news.

[2] P. Meel and D. K. Vishwakarma, "Fake news, rumor, information pollution in social media and web: A contemporary survey of state-of-the-arts, challenges and opportunities," *Expert Systems with Applications,* p. 112986, 2019.

[3] X. Zhang and A. A. Ghorbani, "An overview of online fake news: Characterization, detection, and discussion," *Information Processing and Management,* vol. 57, no. 2, pp. 1020-1025, 2020.

[4] A. Bondielli and F. Marcelloni, "A survey on fake news and rumour detection techniques," *Information Sciences,* vol. 497, pp. 38-55, 2019.

[5] Y. Yang, L. Zheng, J. Zhang, Q. Cui, Z. Li and P. S. Yu, "TI-CNN: Convolutional Neural Networks for Fake News Detection," *arXiv preprint arXiv:1806.00749,* 2018.

[6] "Alt News," [Online]. Available: https://www.altnews.in/topics/news/.

[7] S. Kumar, R. Asthana, S. Upadhyay, N. Upreti and M. Akbar, "Fake news detection using deep learning models :A novel approach," *Transactions on Emerging Telecommunications Technologies,* vol. 31, no. 2, 2020.

[8] A. Drif, Z. F. Hamida and S. Giordano, "Fake News Detection Method Based on Text-Features," in *The Ninth International Conference on Advances in Information Mining and Management (IMMM)*, Nice, France, 2019.

[9] S. C. R. Gangireddy, D. P, C. Long and T. Chakraborty, "Unsupervised Fake News Detection: A Graph-based Approach," in *Proceedings of the 31st ACM Conference on Hypertext and Social Media*, New Yark, USA, 2020.

[10] H. Q. Abonizio, J. I. d. Morais, G. M. Tavares and S. B. Junior, "Language-Independent Fake News Detection: English, Portuguese, and Spanish Mutual Features," *Future Internet,* vol. 12, no. 5, 2020.

[11] "All Data," [Online]. Available: https://drive.google.com/file/d/0B3e3qZpPtccsMFo5bk9Ib3VCc2c/view.

[12] "Fake News Detection," [Online]. Available: https://www.kaggle.com/jruvika/fake-news-detection..

[13] "Who starts and who debunks rumors," [Online]. Available: https://www.kaggle.com/arminehn/rumor-citation#emergent.csv.

[14] H. Karimi and J. Tang, "Learning Hierarchical Discourse-level Structure for Fake News Detection," in *The 2019 Conference of the North American Chapter of the Association for Computational Linguistics: Human Language Technologies*, Minneapolis, Minnesota, 2019.

[15] O. Ajao, D. Bhowmik and S. Zargari, "Fake news identification on twitter with hybrid cnn and rnn models," in *Proceedings of the 9th International Conference on Social Media and Society*, Copenhagen, Denmark, 2018.

[16] F. Lago, Q.-T. Phan and G. Boato, "Visual and Textual Analysis for Image Trustworthiness Assessment within Online News," *Security and Communication Networks,* pp. 1-14, 2019.

Authorized licensed use limited to: DELHI TECHNICAL UNIV. Downloaded on March 27,2021 at 05:38:09 UTC from IEEE Xplore. Restrictions apply.

e-ISSN: 2582-5208
International Research Journal of Modernization in Engineering Technology and Science
Volume:03/Issue:02/February-2021 Impact Factor- 5.354 www.irjmets.com

DETAILED ANALYSIS OF WIND ENERGY TECHNOLOGY AND ITS FUTURE IN INDIA

Dr. J.P Kesari*1, Aditya Vikram Kochar*2, Anand Kumar Jha*3

*1 Professor, Department of Mechanical Engineering, Delhi Technological University Bawana Road, Delhi 110042, India.

*2,3 Undergraduate Student, Department of Mechanical Engineering, Delhi Technological University Bawana Road, Delhi 110042, India.

ABSTRACT

India has a vast population that is why energy demand is increasing day by day to make this happen through a sustainable route, the Indian government decided to achieve 60 GW of power from wind by 2022. India has the 4th largest in terms of wind power after China, U.S, and Germany. Fossil fuel-based thermal power plants predominate India's electricity sector, but now we are shifting towards inexhaustible energy resources to arrest GHG emissions. Solar and wind energy supply us with clean and green energy. The present paper tries to explain the structure of windmill and also determine the role of wind energy in reducing cost and harmful gas emissions and the equipment required to establish wind energy plants. Here we try to estimate the total production of wind energy in India by 2050.

Keywords: Inexhaustible, vast, emission, GHG.

I. INTRODUCTION

Wind energy has now become one of the most economical renewable energy technology in recent years. Today, electricity-generating wind turbines are tested technology and provide a secure and sustainable energy supply. At right, windy sites, wind energy can already successfully compete with conventional energy production.

The technological development in recent years brings more efficient and reliable turbines, is making wind power cheaper. In general, the specific energy costs per annual kWh decrease with the turbine's size, notwithstanding existing supply difficulties.

Developing countries and emerging economies had faced the challenge of meeting additional energy needs for their social and economic development with traditional energy supply structures. Overcoming supply demands through fossil fuels, i.e., coal, oil, and gas increases dependency on volatile markets and eats up their valuable foreign currency reserves. Simultaneously, there is growing pressure on emerging economies like India to combat climate change and limit their pollutant emissions.

II. UNDERSTANDING THE WINDMILL

A windmill is a structure used to covert wind's power for purposes like grinding grain, pumping water, and generating electricity. They consisted of vanes called blades that convert the wind energy into rotational energy.

An anemometer is an instrument used to measures the wind speed and transmits the data to the controller. The wind produces a torque that rotates the blades around the rotor, connected to the central shaft that spins the generator to create electricity.

e-ISSN: 2582-5208
International Research Journal of Modernization in Engineering Technology and Science
Volume:03/Issue:02/February-2021 Impact Factor- 5.354 www.irjmets.com

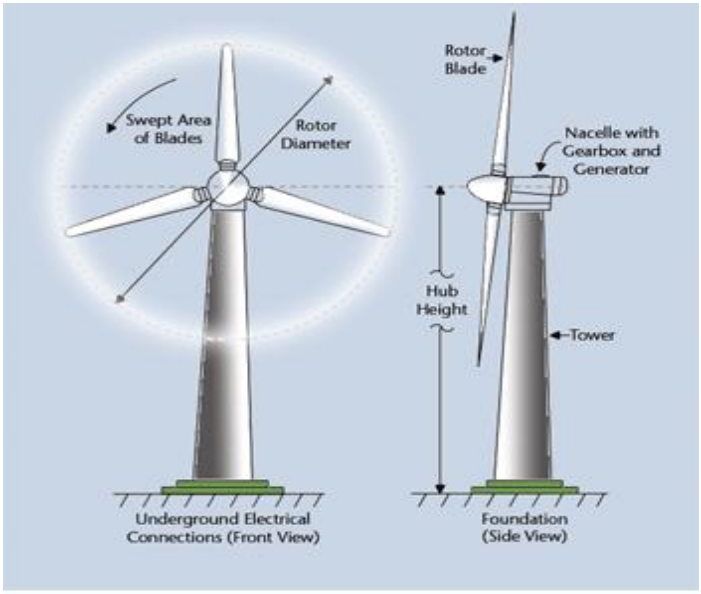

Drawing of the rotor and blades of a wind turbine, courtesy of ESN

Today's turbines also consist of a brake system(that can mechanical, electrical, hydraulic) that help us to stop the rotor in emergencies, and a controller that starts the machine up at wind speeds that are between 6 to 14 mph and shuts the machine off when wind speed is above 56 mph to prevent overloading to the generator.

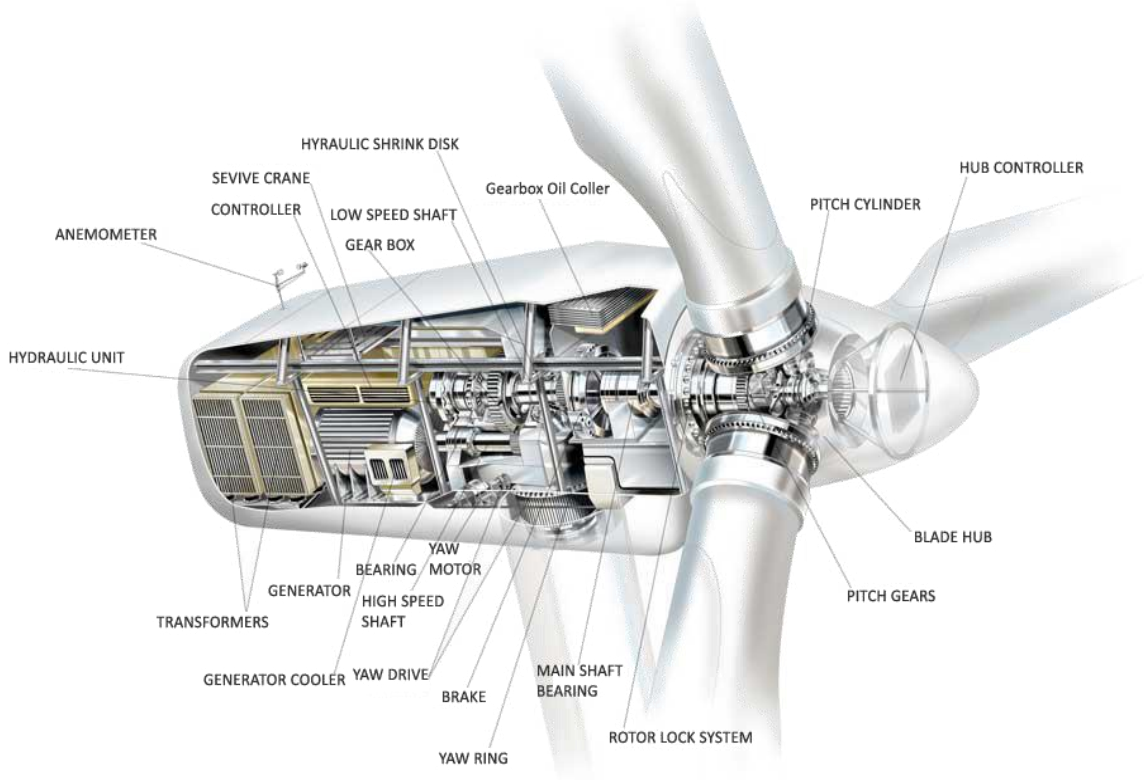

The power generated by the windmill is directly proportional to the rotor area, and the rotor area is directly proportional to square of the diameter. If we increase turbine size by 2 times then it produces energy 4 times more energy.

e-ISSN: 2582-5208
International Research Journal of Modernization in Engineering Technology and Science
Volume:03/Issue:02/February-2021 Impact Factor- 5.354 www.irjmets.com

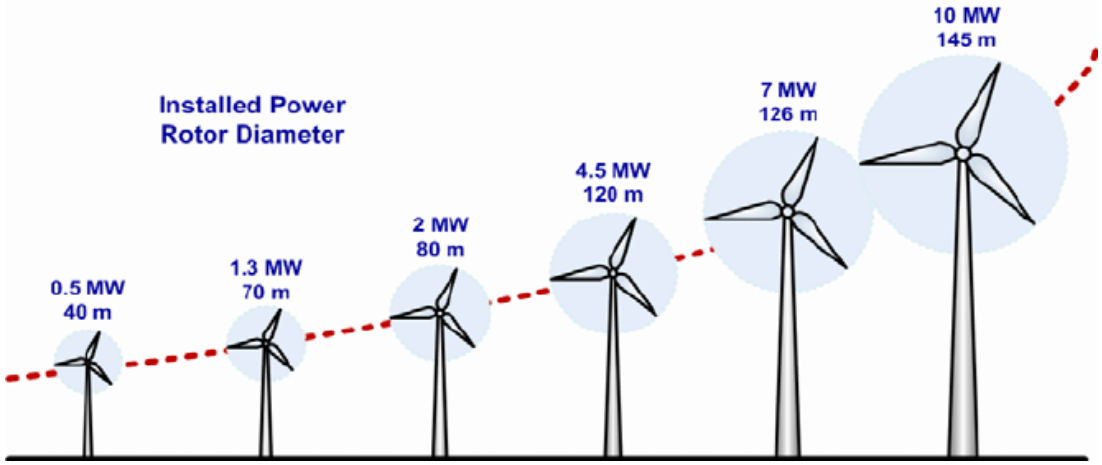

III. FUTURE OF WIND ENERGY IN INDIA

With the push of the Atmanirbhar Bharat mission, more manufacturing companies are setting their production unit in India, and this will cause a boom in electrical energy demand. With this demand, now the government is also focussing on ways to utilize inexhaustive natural resources to meet this energy requirement. After the jerk caused by COVID 19 to our economy IMF projected the growth rate of 11.5% for 2021. It is impressive growth that India will register, and we are expecting this growth will continue as the Government of India is stressing upon "Make in India," "Ease of Doing Business," "land, and "labor reforms." It will further push the demand for electricity in almost all the sectors, i.e., household, agriculture, commercial, institutional and industrial sectors.

The International Renewable Energy Agency revealed that increasing inexhaustible natural resources as power sources to about 36 % would bring the goal of reducing greenhouse gases significantly closer in the coming future. Before looking into the future of wind energy in India, let us discuss the factors favorable to wind energy. These are the following factors that will be held favourable for the development of wind energy.

IV. WIND ENERGY POTENTIAL OF A COUNTRY

Any country needs to have natural resources for renewable energy potential. Proper wind velocity and availability of wasteland are essential for the wind energy potentials. There is a wide gap in accessing the country's wind energy potential by different organizations.

Jeremy Rifkin, an economist and activist right when he said in New Delhi in January 2012: "India is the Saudi Arabia of renewable energy."

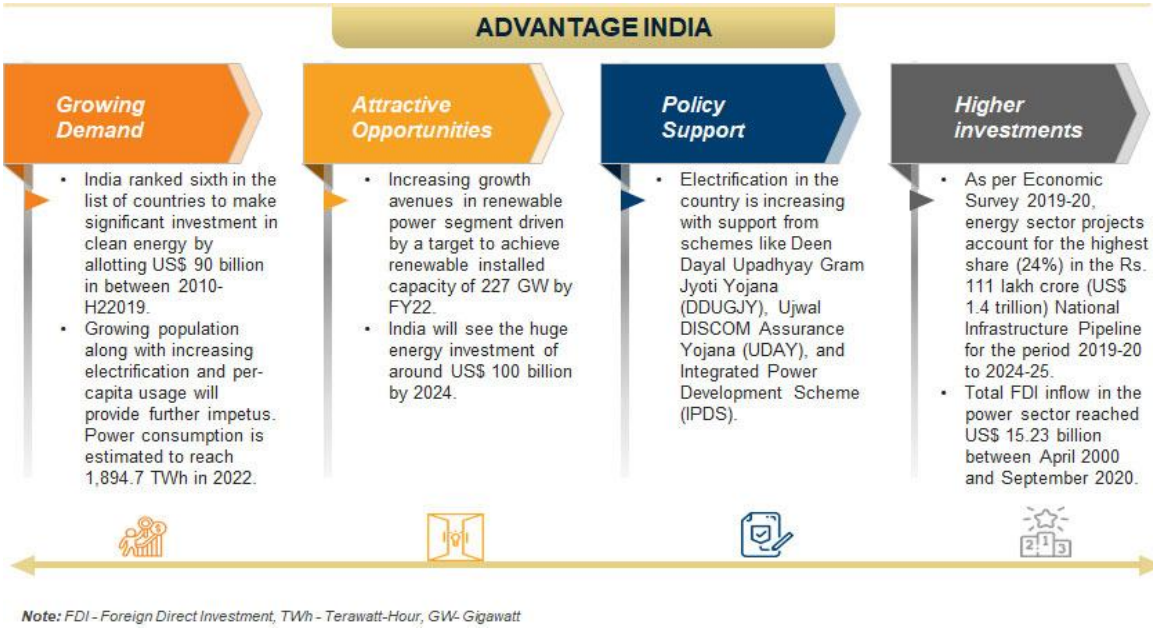

Note: *FDI - Foreign Direct Investment, TWh - Terawatt-Hour, GW- Gigawatt*

e-ISSN: 2582-5208
International Research Journal of Modernization in Engineering Technology and Science
Volume:03/Issue:02/February-2021 Impact Factor- 5.354 www.irjmets.com

"The Centre of Wind Energy Technology recently announced that the total onshore wind energy potential in India is about 302 GW. The new estimates are six-times the wind energy potential determined at a 50-meter hub height and three-times the potential estimated at a hub height of 80 meters. Of the total estimated value of 302 GW potential, 153 GW is available in the wasteland, 146 GW in cultivated land, and 3 GW in the forest area. (Mittal, 2015). The new Berkeley Lab study has found the total techno-economic wind potential to range from 2,006 GW for 80-meter hub heights to 3,121 GW for 120-meter hub heights. Only 25% of potential realization allows us to double the present total installed capacity. All of the above pieces of information show the enormous potentials of wind energy in India.

V. STATE WISE DISTRIBUTION OF WIND POTENTIAL IN INDIA

Wind Energy, which can be useful for producing electricity, is available across India's South, West and North regions. We will find wind energy's potential across these states Andhra Pradesh, Gujarat, Karnataka, Madhya Pradesh, Maharashtra, Rajasthan, Tamil Nadu, Telangana. With the country's highest installed capacity, Tamil Nadu produces about 7.5 GW, and its state regulations are very much favorable to wind power development. Maharashtra has the second-highest installed capacity of about 5 GW, followed by Gujarat with the third-highest installed capacity of around 4 GW.

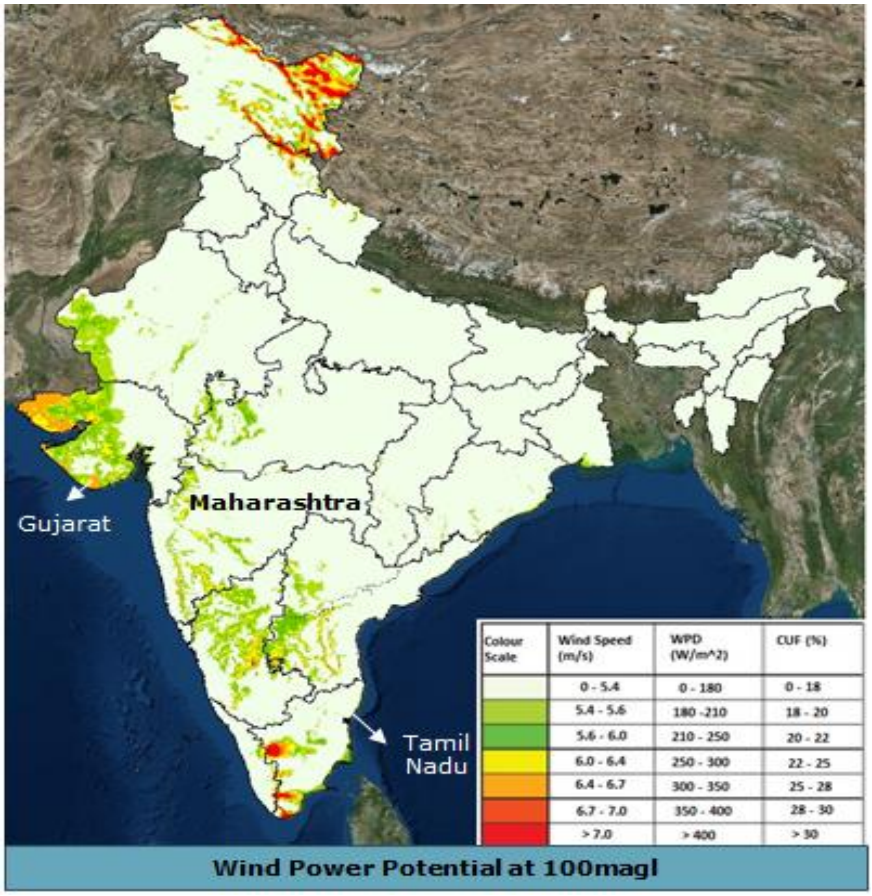

VI. GW OFFSHORE WIND ENERGY PROJECT

The offshore wind energy project of 1.0 GW capacity is planned in the identified zone-B off Gujarat's coast to bring the economy of scale and localization of necessary ecosystem for the offshore wind energy sector. In principle (stage-I), clearance per the National offshore wind energy policy from relevant Ministries/Departments for a 1.0 GW offshore wind energy project in Zone –B off Gujarat coast has already been obtained. Further, stage-II clearances required to carry out critical studies/surveys for the selected areas have already been obtained by NIWE and NIWE to collect geophysical and geotechnical data. Expression of Interest (EoI) for the first offshore wind project of 1.0 GW capacity off Gujarat coast has been floated on 10.04.18 by

NIWE. Thirty-five International/Multinational and Indian Developers/OEMs have participated in the EoI and subsequent consultation process, which provided their inputs for the bidding process.

VII. CONCLUSION

Wind energy has a bright future, and we can expect a 25-30% contribution of wind energy in the total generation of electricity in India by 2050. Wind energy has its problems of noise and loss of birds' life, yet it can be minimized by focussing more on offshore wind power and shifting to bladeless windmills that have no visible moving part and almost noise-free. Wind power is an alternative to fossil fuels, is plentiful, renewable, widely distributed, clean, produces no greenhouse gasses emissions during operation, consumes no water, and but uses little land. Windmill's efficiency is increasing day by day with improvement in the technology involve in it.

ACKNOWLEDGEMENT

The authors wish to acknowledge Dr. J.P Kesari and Delhi Technological University for their complete support throughout their work.

VIII. REFRENCES

[1] Ministry of Power, GOI https://mnre.gov.in/wind/offshore-wind/#:~:text=Ministry%20set%20a%20targetof%205.0,project%20developers%20in%20India%20market

[2] Denmark in India (MFA) https://indien.um.dk/en/innovation/sector-updates/renewable-energy/wind-energy-in-india/#:~:text=India%20has%20the%204th%20largest,m%20hub%2Dheight%20in%20India.

[3] Image credit https://www.google.com/search?q=power+aafected+by+blade+size+of+wind+mill&tbm=isch&ved=2ahUKEwj6la-6iYXvAhWUkksFHSQTBOYQ2-cCegQIABAA&oq=power+aafected+by+blade+size+of+wind+mill&gs_lcp=CgNpbWcQAzoGCAAQCBAeOgIIADoFCAAQsQM6BggAEAUQHlD60AZYq9EHYMHTB2gBcAB4AIABkQKIAe86kgEGMC40Ny4zmAEAoAEBqgELZ3dzLXdpei1pbWfAAQE&sclient=img&ei=_pw3YPqeJJSlrtoPpKaQsA4&bih=657&biw=1366&rlz=1C1CHBF_enIN931IN931#imgrc=giAgWkttIQHJFM

[4] Gifford, G. (2016, January 24). Renewable Energy To Solve 2030 Emission Reduction Targets. Retrieved from Renewable Energy World.com: http://blog.renewableenergyworld.com/ugc/blogs/2016/01/renewable_energyto.html

[5] Goswami, D. (2014, May 08). Can India Go 100 Percent Renewable by 2050? Retrieved August 08, 2015, from Triple Pundit: People, Planet, Profit: Can India Go 100 Percent Renewable by 2050?

[6] Marloes Caduff, M. A.-J. (2012). Wind Power Electricity: The Bigger the Turbine, The Greener the Electricity? Environmental Science & Technology, 46(9), 4725-4733. doi:10.1021/es204108

Journal of Contemporary Issues in Business and Government Vol. 27, No. 1, 2021
P-ISSN: 2204-1990; E-ISSN: 1323-6903
https://cibg.org.au/

Devising a Knowledge Culture

Nishant Gaur[1], Dr. Vikas Gupta[2]

[1]*Associate Professor, USME, East Delhi Campus, Delhi Technological University*

[2]*Research Scholar, Delhi School of Management,Delhi Technological University*

E mail id: nishantgaur2006@gmail.com, vikasguptadtu@gmail.com

Abstracts

Purpose: The paper aims to explore the literature on culture facilitating knowledge management (KM) in an organisation. The paper deliberates on various attributes, components, framework and classification of culture that stimulates KM.

Design/methodology/approach: A systematic review of peer-reviewed journal articles has been carried out to understand the culture that fosters KM from Pro-Quest, Emerald and EBSCO host. Various attributes, components, framework and classification of culture have been extracted from the literature that impacts KM processes, knowledge assets, Knowledge conversion cycles and types of knowledge sharing.

Findings: The literature reveals a positive impact of cultural attributes, components of culture, various cultural frameworks and various classification of culture on KM processes, knowledge assets, knowledge conversion cycles and types of knowledge sharing.

Research implications: This paper is an output of extensive literature review studying all the attributes, components, framework and classification of culture that impacts KM. However, it would have been better to go for a precise study deliberating on a particular dimension of culture amongst framework, attributes or classification which impacts a specific KM dimension amongst KM processes, knowledge assets, KM conversion cycle and types of knowledge sharing. Also, a longitudinal study would have given long term data to understand how organisational culture would have influenced KM.

Research limitations: This paper is an output of extensive literature review studying all the attributes, components, framework and classification of culture that impacts KM. However, it would have been better to go for a precise study deliberating on a particular dimension of culture amongst framework, attributes or classification which impacts a specific KM dimension amongst KM processes, knowledge assets, KM conversion cycle and types of knowledge sharing. Also, a longitudinal study would have given long term data to understand how organisational culture would have influenced KM.

Originality/value: This paper contributes to knowledge culture literature by adding the fact that culture not only affects human resource activities but also plays a prominent role in KM.

Keywords: Knowledge Management, Organisational Culture, Knowledge Culture

1. INTRODUCTION:

In this era of continuous and rapid changes in the economy, competition is getting fierce where organisations fully utilise all the resources and assets to maximise the return on investments. But it is most difficult to exploit the intellectual capital; the resource which is embedded within individuals and groups of individuals in the form of knowledge. Knowledge is considered to be the most valuable asset of the company (Stankosky, 2005; Albors-Garrigos et al., 2010). The organisations struggling for sustainable competitive advantage should fully utilise their intellectual assets (Machua et al., 2012). Knowledge is the most relevant source of competitive advantage (Ramadani and Dana, 2016). The world economy is experiencing a transition as companies are now competing to provide value addition to customers, suppliers and employees. This change has led to a paradigm shift that signals a shift from the industrial era to the knowledge era (Charles Savage, 1996). Knowledge era is an era where products and services constitute more of intellect level then capital, material and labour. The agenda in KM era is to create an organisation with the culture and structure that can unlock the potential of the intellectual assets. The survival of organisations is entirely dependent on the capacity to unlock and exploit the intellect and creativity of its employees and its ability to further create knowledge. KM recognises intellectual capital as the most treasured resource. The intellectual capital is aggregate and integral of knowledge, tacit or explicit of everyone in the organisation.

Information technology plays an important role in KM but is facilitated by the culture in the organisation. Information and communication technology open avenues for innovation and experimentation (Gupta and Jain, 2017). As technology helps in gathering, analysing and disseminating information; humans can use, exploit and implement it for betterment. The state of art technology will not guarantee organisational competencies as there is no correlation between investment in technology and business performance. Information technology should enable the culture by being an integral part and utilising creative and innovative strength of human resource. Expert systems contribute to knowledge culture as it captures the tacit knowledge of experts for sharing and reuse. Although KM is not limited only to tapping the expertise of intellects in expert systems or building databases it involves creating a framework and structure for communication, sharing and transfer of knowledge. In knowledge sharing, culture programmable information systems play a vital role (Banks, 1999). The tasks which are routine and repetitive in nature can be delegated to the information systems and the people can utilise their time in value addition by performing analytical and interpretative tasks. Simple technologies like e-mail and video conferencing are allowing individuals to share their knowledge. The major outcome of the dependence of KM on organisational culture is the creation of knowledge culture. This dependence is studied through the extensive literature survey.

The structure of this paper is as follows: In the first section, we have analysed the literature pertinent to KM and organisational culture. The next section deliberates on research methodology for the paper. In the third section, the linkage between KM and organisational culture is established through pieces of evidence from the literature itself. The fourth section

proposes a conceptual model integrating organisational culture with KM. Finally, we have concluded with some reflections and lessons extracted from the literature.

2. LITERATURE REVIEW

2.1 Organisational Culture

Culture is referred to as a composite entity of values, beliefs, ethics, conduct and behavioural models (HO, 2009). Culture results from the continuous negotiations about values, beliefs and conduct among the members of the organisations (Douglas, 1985; Barney, 1986). In the organisations which are categorised as knowledge-driven organisations, it is the value system that drives what knower views, understands and interprets from his observations (King, 2008; Machua et al., 2012). The power of knowledge for perceiving, organising, interpreting and learning is more attributed to the values than data, information and analytical ability (Mas et al., 2004).

The culture rests on value pillars of storytelling, trust, continuity, loyalty, top management support and reward (Zamantili et al., 2008). The storytelling refers to retelling stories about the founding years and hardship of the company. The storytelling is an effective tool to teach management values, establish principles and generate beliefs (Edwards et al., 1994; Zamantili Nayir et al., 2008). Continuity refers to the lifetime employment of employees and promotion within the company. Continuity of employment results in people cooperating and coordinating with each other as they understand and know each other well. Loyalty refers to emotional commitment which can be achieved by investing in employees training, seminars, life workshops giving lessons on life, marriage, relationships, child upbringing (Zamantili Nayir et al., 2008). Trust and openness are values that promote KM behaviour (Van Krogh, 1998; Lee et al., 2006). The trust should be visible in employee's relations (O'Dell et al., 2001). Top management support and commitment encourages knowledge acquisition, sharing and utilisation (Smith and Mckeen, 2003). The organisations reward and incentive scheme increase the effectiveness of knowledge flow in organisation (Leonard, 1995; Alavi et al.,2006).

There are five dimensions of organisational culture given by "The Great Place to Work Institute" (GPTW). The survey conducted by GPTW provides a baseline to evaluate various elements of organisational culture. The GPTW survey categorises cultural attributes into five dimensions: respect, fairness, credibility, pride and camaraderie. Respect, fairness and credibility collectively form the Trust Index (GPTW, 2011). The GPTW survey is developed with the intention that great place to work is environment and surrounding where employees trust the people they work for, have pride in what they do and enjoy the people they work with.

2.1.1 Classification of organisational culture

Organisational culture like a human being is unique, complex and elusive. Understanding culture involves assessing the difference between the formal and informal rules, way of

carrying out the tasks. There is a diverse classification of cultures on a different basis. One of the classifications constitutes entrepreneurial culture, task-goal-accomplished culture and smooth-running culture (Wallach, 1983; Cameron, 1985; Ogbonna and Harris, 2000). An entrepreneurial culture is attributed to flexibility and innovation. People who are a risk taker and ambitious thrive in these organisations. Tasks-goal-accomplished cultures are well suited for production-oriented firms. This type of culture emphasises achievement and competitive actions. The smooth-running culture is based on control and power. This type of culture can be characterised as bureaucratic, power-oriented, regulated, structured, procedural and hierarchical.

There are four types of organisational culture depicted by Chang and Lin's (2007) which have been derived from Quinn's competing value model (1988). These cultures are cooperativeness culture, innovativeness culture, consistency culture and effectiveness culture. Cooperativeness culture is characterised by internal orientation and flexibility (Chang and Lin, 2007). The innovativeness culture is characterised by external orientation and flexibility (Cameron and Quinn, 1999). The consistency culture is characterised by internal orientation and control. Effectiveness culture is characterised by environmental orientation and control (Cameron and Quinn, 1999).

Based on Hofstede et al. (1990) behavioural perspective, there are five types of culture: result versus process-oriented culture, tightly controlled versus loosely controlled culture, job-oriented versus employee-oriented culture, closed system versus open system culture, professional versus parochial culture. Process-oriented culture constitutes of individuals who are risk averse and result-oriented culture constitute of individuals who are risk taker (Hofstede et al., 1990; Kayworth and Leidner, 2003; Wei, 2005; Ajmal and Koskinen, 2008). The loosely controlled organisation constitutes of negligible written or verbal codes of behaviour and tightly controlled organisations have strict written and unwritten policies (Hofstede et al., 1990; Ajmal and Koskinen, 2008; Shih and Huang, 2010). Job oriented culture emphasises on concern for getting the task done and employee-oriented culture emphasises on concern for people (Hofstede et al., 1990; Eskerdo and Skriver, 2007; Ajmal and Koskinen, 2008, Woodman and Zade, 2011). Open system culture provides the environment for clear communication channels whereas closed system culture is secretive in nature. The professional culture refers to those units where people are loyal to their profession and parochial culture refers to those units where people remain loyal to their organisation.

Quinn and Spreitzer (1991) conceptualised organisational culture into four typologies-development culture, group culture, hierarchical culture and rational culture. The development culture emphasises on flexibility and external environment. The development culture is characterised by resource acquisition, creativity and growth. The group culture emphasises on flexibility and internal environment. The group culture is characterised by trust, belongingness and participation. The hierarchical culture emphasises on stability and internal environment. This culture is characterised by uniformity and efficiency. The rational culture emphasises on stability and external environment. This culture is characterised by productivity and achievement. The four cultures can coexist within the same organisation. It

is also noted that a high rating on one culture may not exclude a high rating on other culture (Dension and Spreitzer, 2001; Iivari and Huisman, 2007; Cameron and Quinn, 2011).

2.1.2 Competing value framework of organisational culture

The competing value framework was research based on identifying indicators of organisational effectiveness (Quinn and Rohrbaugh, 1983). The four culture types in competing for value framework are termed as a clan, adhocracy, market and hierarchy culture (Quinn and Rohrbaugh, 2006 and Yu and Wu, 2009). The clan refers to human relation perspective and is characterised by flexibility, collabouration, teamwork, empowerment, interpersonal relationships, information sharing, participative decision making. The adhocracy culture refers to an open system perspective and is characterised by innovation, creativity, flexibility, articulating the future vision, entrepreneurship, growth, adaptation and transformational change (Yu and Wu, 2009). The market culture refers to rational goal perspective and is characterised by competitiveness, decisiveness, goal clarity, goal achievement, driving through barriers, efficiency and control. The hierarchy culture refers to internal process perspective and is characterised by routine work processes, structuring, documentation, evaluation, measurement, centralisation, control, continuity and efficiency.

2.1.3 Corporate Culture

Culture tends to create loyalty and motivation in employees with high potential; which leads to knowledge sharing in organisation (Bresman et al. 1999; Kotter and Heskett, 1992). The organisation should develop a knowledge-creating culture before adopting KM strategy (Sivan, 1999). According to McDermott and O'Dell (2001), corporate culture does not only reflect mission and values but also reflects employee's behaviour and their expectations. There are four orientations in corporate culture which includes power, role, achievement and support (Harrison, 1990). In power culture, all power and authority reside with the boss and employees get motivated through a carrot and stick approach of motivation and their willingness to be associated with a powerful leader. In role culture, there are clearly defined rules, regulations and expectations rather than direct supervision and continuous monitoring. In achievement culture employees are trusted and given freedom by the management to take decisions. Support culture is characterised by employees looking for mutual respect, trust, and support and deriving satisfaction from relationship.

2.1.4 Culture at different levels

Culture is defined as a collective phenomenon as it is shared with the individuals who have lived within the same socio-cultural environment where it was learned (Hofstede, 1980). The culture is present at different levels: national culture, organisation culture and professional culture (Schein, 2004; Trompenaars, 1998). The culture at each level is a multidimensional embracing sense of belongingness, achievement, sense of security and self-esteem (Kahle et al., 1988). The organisational culture is determined by various factors which include history, ownership, leadership, the technology employed, size, market and type of business activity. Organisational culture reflects universally held assumptions about the organisation. A

professional culture is developed when a group of likeminded professionals is employed. The professional culture is a subculture which co-exists with primary organisational culture. This can be best understood as interlocking "nested subcultures" (Martin and Siehl, 1983).Culture propagates through various institutions or parts of society which includes family, school, community and workplace. The years spent with family and school shapes the underlying values that make national culture. To establish harmony among different levels of culture, an organisation requires strong directional culture for the synthesis of all culture in an attempt to unify various levels or layers of cultures (Ajmal and Koskinen, 2008).

2.1.5 Cultural dimensions

Culture has a significant impact on knowledge creation as it impacts interaction, knowledge exchange and perceived value of members (Tseng, 2010). Pillania (2006) mentioned that culture about an organisation is the main reason behind the failure of KM and is also crucial for the success of KM. To gather deep insight into the culture, Hofstede (1980) identified five major dimensions of culture; individualism-collectivism, uncertainty avoidance, power distance, masculinity-femininity, time horizon (Hofstede, 2001). Individualism refers to the state where individual interests are considered as more superior to group interests. Whereas Collectivism refers to the state where the group's interest takes precedence over individual interest and desires (Wagner, 1995). Individualism is attributed to independence and collectivism is attributed to interdependence (Chen et al., 1998; Wuyts and Geyskens, 2005). Uncertainty avoidance refers to the state where a member of a particular culture feels threatened and tries to avoid uncertain situations (Hofstede, 2001). Power distance is that dimension of culture which focuses on power and authority distribution in a culture. (Hofstede, 1980). It is the tolerance from low to high for power disparity in the society. Masculinity- femininity refers to the distinction between emotional gender roles. Time horizon refers to the goal orientation of an individual as short term or long term based on period. The long-term orientation is dynamic and future-oriented with values such as ordered relationship by status and perseverance (Hamilton and Dana, 2008). The short-term orientation is past-oriented and traditional in nature with values such as personal stability (Hamilton and Dana, 2008).

2.1.6 Multi-level attributes of organisational culture

The organisational culture is assessed as a multi-level construct comprising artefacts, espoused beliefs and values and underlying assumptions (Said Abdullah Al Saifi, 2014). Artefacts refer to a visible expression of a culture which constitutes organisational aspects like structure, practices, processes, technology, language and dress code (Barrios, 2013). This is the initial level attribute which depicts what individuals in an organisation are doing but do not explain the reason behind it (Boggs, 2002). The reason behind any Artefacts is espoused beliefs and values (Schein, 2004). The espoused values and beliefs are not visible to workers. These values constitute creativity, problem-solving and working with others (Hibbard, 1998; White, 1998). These beliefs and values do not depict identical behaviour and working style on every occasion (McDermott and O'Dell, 2001). Thus, to comprehend close examination of basic underlying assumption is needed. The underlying assumptions are unconscious in

nature and do not change easily and frequently (Schein, 1990). The underlying assumptions constitute perceptions, thoughts and feelings.

2.2 KM

Knowledge is referred to as information residing with the individuals (Alaviand Leidner, 2001). Knowledge can also be defined as the high-value form of information available with the individual that can be immediately applied to take decisions and actions (Davenport and Prusak, 2000). KM is managing of organisation's knowledge both explicit and tacit for value creation and meeting operational and strategic objectives. KM constitutes of initiatives, systems and strategies to create, maintain, upgrade, store, transfer and disseminate knowledge source Nonaka and Konno, 1998). Organisations are busy creating a tremendous amount of data and information for pursuing routine activities. This routine business information is needed to be managed to augment its value and for its reuse to solve new problems.

2.2.1 KM Process

KM process is defined as a sequence of stages involved in capturing, storing, sharing and applying knowledge (Chang et al., 2015). KM is the process of generating, representing, storing, sharing, transforming, applying and embedding organisation's knowledge (Massey and Montoya-Weiss, 2006).

There are four constituents in the KM process: knowledge creation, knowledge storage, knowledge transfer and knowledge application (Kayworth and Leidener, 2003; Chang and Lin, 2015). Knowledge creation is developing new content or modifying existing content and replacing it with organisations tacit and explicit knowledge. Knowledge can be created from operational systems, local abilities and know-how that are essential for carrying out routine tasks and solving routine problems (Ramadani and Dana, 2016). Knowledge can be created, transferred, amplified and enlarged through an individual's cognitive process (Ajmal and Koskinen, 2008). Knowledge acquired by individuals and group of individuals can be stored in an explicit and tacit form (Heisig, 2009). Knowledge transfer is the dissemination of knowledge to various locations where it is needed and is to be applied (Pirkkalainen and Pawlowski, 2013). Knowledge application is the actualisation of knowledge to settle down novel problems, to provide strategic directions and to offer optimised utilisation of resources (Newell et al. 2004).

2.2.2 Explicit and tacit knowledge sharing

Knowledge resides with individuals, knowledge sharing depends on the willingness of the individual to share the knowledge that they acquired or created (Kuo et al., 2014). Knowledge can be classified as explicit and tacit knowledge. And on similar basis knowledge sharing can be classified. Explicit knowledge is formal, systematic and tangible in nature. This form of knowledge can be articulated easily. The explicit knowledge sharing can be done easily through documented books, manuals constituting text, images, graph etc. Although sharing depends on the willingness of the knowledge owner. Tacit knowledge is

highly personal as they are present in the form of views, ideas, experience. Tacit knowledge sharing is difficult in comparison to explicit knowledge as it is difficult to verbalise and communicate because it is present in the form of evaluations, viewpoint and motivation.

There are two processes of knowledge sharing: Knowledge donation and knowledge collection (Van den Hooff and Van Weenen, 2004). Knowledge donation refers to sharing and transferring of intellectual capital by the individual willingly. And knowledge collection refers to persuading an individual to share his knowledge.

Many stakeholders in the firm are involved in knowledge sharing (Guadamillas and Mario j., 2011). The various stakeholders to a firm who are involved in knowledge exchange constitute customers, suppliers, employees, shareholders. The knowledge exchange with customers in the form of feedback can provide the company with ad-hoc solutions to their problems. The organisations should make an effort to gather knowledge about customers need and should develop extranets for this exchange. There should be a knowledge exchange to advance supply chain management. The firms should reward employees with incentives to motivate them for sharing their tacit knowledge. Also, there should be transparency in exchange of knowledge with shareholders as a commitment.

2.2.3 Knowledge Assets

Knowledge assets are very are critical for knowledge-creating processes as they are inputs, outputs and moderating factors for these knowledge-creating processes (Rai,2011). The knowledge assets are categorised as experiential, conceptual, systematic and routine (Nonaka et al. 2000). The experiential knowledge asset constitutes of shared tacit knowledge amongst the member of organisation and other stakeholders. Conceptual knowledge asset constitutes of explicit knowledge that is tangible and can be documented and expressed through images, symbols and languages. Systemic knowledge asset constitutes of systematised packages of knowledge like product specification, manuals, documented information about customer and suppliers. Routine knowledge asset constitutes of tacit knowledge that can be found in routine activities and practices of employees. This asset is embedded in day to day operations carried out in organisation.

2.2.4 Knowledge conversion: The SECI process

The knowledge creation in an organisation is carried through interactions between explicit and tacit knowledge. The interaction that is carried out between these two forms of knowledge is referred to as knowledge conversion (Nonaka and Takeuchi, 1995). The SECI process refers to socialisation, externalisation, combination and internalisation of knowledge (Nonaka et al., 2000). The socialisation mode of knowledge conversion refers to the sharing of tacit knowledge where individual share experiences with each other. The externalisation mode of knowledge conversion refers to documentation of tacit knowledge held by customers or experts into explicit and tangible form. The combination mode of knowledge conversion refers to articulating, sharing and reconfiguring of existing explicit knowledge into the new understandable form of explicit knowledge. The internalisation mode refers to the process where explicit knowledge is internalised through self-understanding and interpretation of knowledge into tacit knowledge.

2.2.5 Ba: Shared context in motion for knowledge creation

"Ba" is the key to knowledge creation, generation and regeneration as it moves along the knowledge spiral and also provides a place to perform individual conversions (Nonaka and Konno, 1998). Ba is classified into four types: originating, dialoguing, systemising and exercising (Nonaka et al., 2000). Originating Ba offers a place where individuals socialise face to face and share their experiences, feelings and emotions. This is important in sharing tacit knowledge. Dialoguing Ba offers a place for externalisation. The face to face interactions are shared and the knowledge gathered is converted into concepts and are documented at a later stage. Systemising Ba offers a place for a combination where explicit knowledge can be disseminated at a larger scale through online modes and groupware technologies. Exercising Ba offers a place for internalisation. The explicit knowledge is communicated through written manuals and is then embedded in individuals based on their understanding.

3. RESEARCH APPROACH

To study the impact of organisational culture on KM, required data is gathered from the literature. This study has performed a detailed analysis of literature and articles to develop a deeper understanding of the concepts. Data for this research was gathered until April 2019 through a series of searches through extant literature. Research papers concerning Organisational culture, KM and knowledge culture were accessed utilising social sciences databases. The databases used for research are Emerald, ProQuest Central, Business source complete (EBSCO).

The searches were conducted using these keywords: KM, organisational culture, knowledge culture, organisational culture, KM, knowledge sharing and knowledge sharing culture. These searches were repeated using the above-mentioned search strings in these databases. A systematic literature review was carried and a selection criterion for papers was well specified. The research papers selected for the study used the term: knowledge culture or knowledge sharing or KM and/or organisational culture in their title. Moreover, references for all research papers selected were scanned to identify relevant research on the topic. All research papers were analysed from the perspective of the theme of the study. This is followed by the abstract scanning of all the papers. If the abstract didn't match the theme of the study, they were excluded from further study. This has led to 473 papers. Next step was a detailed examination of papers. After the thorough examination, 91 papers were finalised and were further analysed and summarised. After conducting this process, various components of organisational culture and KM were identified (Refer table 1).

4. CULTURE: LINKING ORGANISATION CULTURE AND KM

Knowledge culture refers to making knowledge sharing as the norm in organisation (Gurteen, 1999). The leading-edge firms practice collective sharing of knowledge and collective decision making for success (Dana et al., 2005). The factors contributing towards the success of knowledge sharing are rewards, recognition and appreciation for knowledge sharing (Al-Alawi et al., 2007). The individual does not offer knowledge for free, there is trading expect

in which employee expects pecuniary and non-pecuniary components which include rewards, incentives, recognition and appreciation. The ability to learn and relearn, willingness to share tacit knowledge, accepting change, flexibility, creativity, motivation and tolerance to mistakes are attributes of knowledge culture that stimulate knowledge sharing and creation in an organisation. The effective KM practices combined with unique corporate culture enables a company to have a long-lasting KM culture (Zamantili Nayir et al., 2008). Researchers have focused on exploring the culture that promotes KM implementation in an organisation (Jennex and Olfman, 2006; King, 2007; Suppiah and Sandhu 2010).

Motivation is the key driver for KM as it is a necessity for KM initiatives and is required throughout the KM implementation (Malhotra and Galletta, 2003; Fernandes, 2007). All the members of the organisations should be highly motivated to carry out and implement KM (Sedziuviene, 2009). There is a significant relationship between motivation and knowledge creation (Nirwan, 2015). It has been identified that sharing of information, team-oriented work and cohesive groups are essentials for successful implementation of KM (Park 2005). The knowledge sharing and KM success depend on organisational culture which encompasses components like trust, freely sharing of information, working closely with others and making friends at workplace. These four components together are known as organisational culture profile (Heejun Park et al., 2004).

Culture is most important in achieving the success of KM initiatives. The values identified as trust, transparency, flexibility, collabouration, commitment, honesty and professionalism have a positive impact on the success of KM implementation leading to innovation, employee satisfaction, enhanced quality, productivity and capability (Machua, 2011). These values result in a knowledge friendly culture. The high level of trust encourages knowledge sharing. Sharing values and mission with employees create a sense of belongingness leading to collabouration of employees for knowledge creation and sharing. The company high in values like trust and collabouration lead to sharing of expertise and insights with each other (De Long and Fahey, 2002). The personal commitment is important for sharing knowledge within organisation (Malhotra and Galletta, 2003). The commitment to work and organisation ensures sharing and usage of knowledge. To carry out day to day activities, employees require autonomy and flexibility which further leads to knowledge creation. The organisation that is transparent in communication and exchange of documents and information creates a culture of knowledge sharing. The professionalism is reflected from the level of customer satisfaction. The satisfied customers give feedback for the advancement of products and services leading to knowledge creation.

The cultural attributes including openness to change, innovation, trust, teamwork, morale, information flow, employee involvement, customer service and reward orientation have an impact on knowledge exchange process (Al-Adaileh and Al-Atawi, 2010). The openness to change refers to out of box thinking (Davenport and Prusak, 1998; Stankosky, 2005). Innovation refers to creating novel products and extraordinary solutions leading to competitive advantage. The new class of companies with a continuous drive for innovation is emerging (Sinha et. al, 2009). In team working employees are willing to learn from each other which results in knowledge sharing (Sheng et al., 2004; Schein, 2004). Morale is the

cultural attribute which refers to the extent to which employees feels motivated to be productive and efficient (Schein, 2004; Senge, 1990). Information flow refers to open communication and smooth flow helping in knowledge exchange (Sheng et al., 2004). Involvement refers to employee participation in decision making (Glaser and Associated Inc., 2008). The customer orientation refers to continuously improving service to customer group (Glaser and Associated Inc., 2008). Customer orientation helps organisations to improve their product and services leading to knowledge creation and its application. The KM practices have a positive impact on organisational performance in terms of customer service perspective (Gupta and Chopra, 2018). Trust represents the culture in which people trust each other (Stankosky, 2005; Figallo, 2002; Cohen and Prusak, 2001). Rewards encourage knowledge-sharing culture in organisations (Davenport and Prusak, 2000).

The orientation of human resource management also contributes to the culture of an organisation. The way various functions of human resource are carried out shapes the culture of organisation. The five areas of human resource which includes training, decision making, performance appraisal, compensation and reward impacts KM processes; encouraging knowledge creation, knowledge sharing, knowledge storage and knowledge application (Salleh Yahya and Wee-Keat Goh,2002). The people are the main drivers of KM (Civi, 2000; Gooijer, 2000; Robertson and Hammersley, 2000; Soliman and Spooner, 2000). KM has been evolved from human resource management using information technology as a medium for interactions and collabouration (Salleh Yahya and Wee-Keat Goh, 2002). The main task of human resource management is to monitor and measure knowledge creation, knowledge storage, knowledge dissemination and knowledge application (Clarke and Staunton, 1989; Armstrong, 2000; Garavan et al., 2000; Soliman and Spooner, 2000).

The KM enablers play an important role in carrying out KM activities (Hsieh et al., 2002; Bose, 2004; Rowley, 2004). The KM enabler refers to key factors for achieving effective execution of KM in the organisation. The KM enablers constitute of strategy and leadership, organisational culture, people and information technology. The strategy and leadership constitute top management support; organisational cultural constitutes culture of sharing; people enablers constitute training and incentives; information technology constitutes digitisation of documents and speedy search of information (Chase, 1997; Demarest, 1997; Davenport et al., 1998; Plan and Scarbrough, 1998, Von Krogh, 1998; Hendriks, 1999; Liebowitz, 1999;Holsapple and Joshi, 2000; Martensson, 2000; Smith et al., 2001; Alavi and Leidner, 2001; Gold et al., 2001; Lee and Hong, 2002; Hedelin and Allwood, 2002; Bose, 2004; Wong, 2005; Yeh et al., 2006).

4.1Organisational cultures and KM process

There are diverse classifications of organisational culture. One of the significant classifications of organisational culture constitutes result-oriented culture versus process-oriented culture, tightly-controlled culture versus loosely-controlled culture, job-oriented culture versus employee-oriented culture, closed-system versus open-system and professional-oriented culture versus parochial-culture. The research carried out by Ling-hsing and Lin in 2015 has provided very useful insights on the impact of diverse culture on KM processes. The process-oriented culture encourages knowledge storage (Markus et al., 2002).

The result-oriented culture encourages sharing of knowledge, favours knowledge transfer and knowledge application practices (Schein, 2000; Jarvenpaa and Staples, 2000; Bhatt, 2001; Kayworth and Leidner, 2003; Wasko and Faraj, 2005; Wei, 2005; Alavi et al., 2006 Ajmal and Koskinen, 2008). Tightly-controlled organisations facilitate knowledge storage whereas loosely controlled culture introduces knowledge creation strategies (Brockman and Morgan, 2003; Kayworth and Leidner, 2003; Norman, 2004, jacks et al., 2012). In job-oriented culture, individuals are willing to share their knowledge with colleagues to create new knowledge and to store this knowledge for the organisations (Woodman and Zade, 2011). Employee-oriented culture facilitates knowledge transfer as they are concerned for employees (Hofstede et al., 1990; Wasko and Faraj, 2005, Eskerod and Skriver, 2007; Ajmal and Koskinen, 2008). Open-system culture facilitates knowledge application as it encourages communication and interactions between knowledge contributors and receivers. Closed-system culture hurts absorption and application of knowledge as it resists and discourages communication with outsiders (Kayworth and Leidner, 2003; Alavi et al., 2006). Parochial-culture facilitates knowledge transfer as employees believe it is for the betterment of the company and gets rewarded for the same (Janz and Prasarnphanich, 2003).

The research carried out by Li and Lee in 2007 studied the impact of entrepreneurial culture, tasks-goal-accomplished culture and smooth-running culture on KM processes. The knowledge developing, sharing, coordinating, recycling takes place in entrepreneurial culture as they allow and encourage employees to be driving, enterprising, risk-taking and creative. Task-goal-accomplished culture negatively affects knowledge process as in this type of cultural knowledge is regarded as power. Smooth-running culture also negatively affect knowledge activities as they have bureaucratic setup based on control and power where there is no space for flexibility, creativity and open communication.

The research carried by Akhavan et al., in 2014 studied the impact of cooperativeness culture, innovativeness culture, consistency culture and effectiveness culture on KM activities. The cooperativeness and innovativeness culture creates an atmosphere where the human resource has peer learning through knowledge creation and knowledge exchange. On the other side, consistency-culture harms knowledge creation and knowledge sharing. Effectiveness culture has a neutral impact on KM.

4.2Competing value framework of organisational culture and SECI model:

here is a linkage observed between competing value framework of organisational culture (which constitutes clan-culture, adhocracy-culture, market-culture and hierarchical-culture) and SECI model of knowledge conversion (Rai, 2011). Clan-culture in an organisation focuses on knowledge creation and conversion occurs through socialisation mode. Organisations with an adhocracy-culture focus on knowledge creation and conversion occur through externalisation mode. An organisation with market-culture focuses on knowledge creation and conversion occurs through externalisation mode. Organisations with a hierarchical-culture focus on knowledge creation and conversion occur through internalisation mode. The organisations which adapt through four modes of SECI framework have more effective KM systems.

4.3 Organisational culture and knowledge sharing

The empirical research carried out by Shao et. al. (2015) to study the impact mechanism of organisational culture on explicit and tacit knowledge sharing behaviour has provided important insights. There is explicit knowledge sharing in hierarchical culture as the employees at various levels send and receive data in the form of manuals and documents (Jones et al., 2006). The group-culture facilitates tacit knowledge sharing as this particular culture emphasises on strong human relations, affiliations and internal organisation (Liu et al. 2011). The development-culture is directly related to knowledge creation as it emphasises flexibility, change and external environment (Quinn and Spreitzer, 1991; Nonaka and Von, 2009). Rational-culture is positively related with explicit as well as tacit knowledge sharing (Shao et al. 2015).

4.4Corporate Culture and KM

The research by Sabri (2005) established a relationship between corporate culture and KM. The power and role-oriented culture do not lead to knowledge sharing as it reflects bureaucratic organisations that work on tasks which are simple and routine in nature. These cultures avoid KM as they are centrally coordinated and have limited information processing capability and managers are isolated and have more of political orientation. The achievement and support culture facilitate knowledge creation in an organisation. These types of corporate culture indulge knowledge sharing and transfer as they are open, highly participative, risk-taking, outward-oriented, creative and innovative.

4.5Cultural Dimension and KM:

The impact of cultural dimensions on KM studied by Wong et. al. (2011) has a great contribution to the field of research linking organisational culture and KM. The collectivism has a positive effect on knowledge creation as it facilitates cooperation and teamwork (Wagner, 1995; Chen et al., 1998). The impact of uncertainty avoidance on knowledge creation is negative. Organisations that are high in uncertainty avoidance do not pursue new knowledge creation (Bochner and Hesketh, 1994) and organisations that are low in uncertainty avoidance take risks and accept challenges to pursue new knowledge creation (Cakar and Erturk, 2010). Power distance hurts knowledge creation. High power distance organisation has a strong control mechanism on individual inhibiting knowledge creation (Shane, 1995). Low power organisations participate in knowledge sharing and exchange as knowledge is easier to diffuse as members feel comfortable in interactions with others.

The research by Remy Magnier-Watanabe et.al (2010) has also studied the impact of cultural dimensions on KM. High power-distance societies focus on knowledge acquisition because of power disparity. Individualistic societies focus on knowledge storage (Nahapiet and Ghoshal, 1998; Smith et al., 2005). Masculine societies encourage knowledge diffusion and high uncertainty avoidance society focus on exploitative knowledge application.

Table 1: KM Culture: Linking Organisational culture and KM

S.No	Organizational culture	Knowledge Management	Literature Support

1	Flexible Adaptable Creativity Innovation	Knowledge sharing	Eric Banks(1999)
2	Innovation	Knowledge processes	Darroch, J. and McNaughton (2002)
3	**Human Resource Management** Training Decision making Performance appraisal Compensation and reward	Knowledge acquisition Knowledge documentation Knowledge transfer Knowledge creation Knowledge application	Salleh Yahya and Wee-Keat Goh (2002)
4	**Organisational Culture Profile** Trust Sharing information freely Working closely with others Developing friends at work	Knowledge sharing KM technology implementation success	Heejun Park,Vncent Ribiere and D. Schulte Jr (2004)
5	Collabourative culture	Knowledge management	Susana Perez Lopez, Jose Manuel Montes Peon and Ordas (2004)
6	Power culture Role culture Achievement Support culture	Knowledge management	Hala Sabri (2005)
7	**Cultural enablers for KM** Organisational culture (atmosphere and culture of sharing) People (training course, employee incentive program) Information technology Strategy & leadership (obtaining top management support)	Knowledge management	Ying-Jung Yeh, Sun-Quae Lai and Chin-Tsang Ho (2006)
8	Entrepreneurial culture Task-goal-accomplish culture	Transferring Diffusing Storing	Ming-Fong Lai and Gwo-Guang Lee (2007)

	Smooth-running culture	Innovating	
9	Motivation	Knowledge management Knowledge asset	Adji Achmad Rinaldo Fernandes and Haris Maupa (2007)
10	Business transaction theory Motivators Rewards	Knowledge sharing Knowledge creation	Franz Barachini (2009)
11	Story telling Continuity Loyalty Trust Top management support Reward structure of organisation	Knowledge acquisition Knowledge sharing Knowledge utilisation	Dilek Zamantili Nayir and Ulku Uzuncarsili(2008)
12	Innovativeness Customer service	Information technology support KM culture	Ching-Chiao Yang, Peter B. Marlow, Chin-Shan Lu (2009)
13	National culture Organisational culture Professional culture	Knowledge management	Mian M. Ajmal, Tauno Kekale and Josu Takala (2009)
14	**National culture** High power distance Individualism Masculinity High uncertainty avoidance	Knowledge acquisition Knowledge storage Knowledge diffusion Knowledge application	Remy Magnier-Watanabe and Dai Senoo(2009)
15	Clan culture Adhocracy culture Hierarchy culture	Knowledge Conversion Socialisation Externalisation Combination Internalisation	Shu-Mei Tseng (2009)
16	Clan culture Adhocracy culture Hierarchy culture Market culture	Tacit knowledge sharing behaviour Organisational communication Personal interactions Mentoring Willingness to share knowledge freely	Visvalingam Suppiah and Manjit Singh Sandhu (2010)

17	Trust Collabouration Learn	Socialisation Externalisation Internalisation Combination	Honolulu Hawaii (2011)
18	Innovation Ethical leadership Legitimacy	Knowledge exchange with stakeholders Knowledge creation KM strategy	Fatima Guadamillas-Gomez and Mario J. Donate-Manznares (2011)
19	Openness to change Innovation Trust Teamwork Morale Information flow Employee involvement Customer service Reward orientation	Knowledge exchange	Raid. M. Al-Adaileh and Muawad S. Al-Atawi (2011)
20	**Competing value framework** Clan culture Adhocracy culture Market culture Hierarchical culture	**SECI process** Socialisation Externalisation Combination Internalisation **Ba** Originating Dialoguing Systemising Exercising **Knowledge assets** Experiential Conceptual Systematic Routine	Rajnish Kumar Rai (2011)
21	Organisational culture	KM practices	Hai Nam Nguyen and Sherif Mohamed (2011)
22	Collectivism Uncertainness Avoidance Power distance	Knowledge creation capability	Dong Wang, Zhongfeng Su and Dongtao Yang (2011)

23	Hierarchy culture	**Knowledge conversion** Socialisation Externalisation Combination Internalisation **KM processes** KM strategy KM plan KM plan implementation	Shu-Mei Tdseng (2011)
24	Creativity Innovation Strategic flexibility	Knowledge processes	Kianto,A. (2011)
25	**Great place to work** Credibility Respect Fairness Pride Camaraderie	Knowledge processes	Herbert A. Nold III (2012)
26	**Strategies** Organisation structure Education and training Reward and incentives Open communication Worker involvement Worker flexibility	Knowledge accumulation Knowledge sharing Knowledge utilisation	Sachin K. Patil and Ravi Kant (2012)
27	Trust Transparency Flexibility Collabouration Commitment Honesty Professionalism	KM initiatives	Marta Mas Machua and Carme Martinez Costa (2012)
28	Adhocracy culture Clan culture	Knowledge sharing Knowledge dissemination Knowledge donation Knowledge collection	Lu Trong Tuan (2012)
29	Innovativeness culture Cooperativeness culture Consistency culture	**Knowledge management** Generate &	Peyman Akhavan, Mohamad Ebrahim Sanjaghi, Jalai Rezaeenour, Hamed Ojaghi

	Effectiveness culture	Acquisition Organising & saving Dissemination & sharing Application	(2014)
30	Hierarchical Culture Rational Culture Group Culture Development Culture	**Knowledge Sharing** Explicit Knowledge sharing Tacit Knowledge sharing	Zhen Shao, Tienan Wang and Yuqiang Feng (2015)
31	Result oriented culture Tightly controlled culture Job oriented culture Closed system culture Professional oriented culture	Knowledge creation Knowledge storage Knowledge transfer Knowledge application	Christina Ling-hsing Chang and Tung-Ching Lin (2015)
32	Artefacts Espoused beliefs and values Underlying assumptions	Knowledge creation Knowledge sharing Knowledge application	Said Abdullah Al Saifi (2015)
33	Innovation Level of trust Culture that value knowledge sharing Sharing of knowledge by experienced employees Effective values system and culture intended to promote knowledge sharing Publicly recognising people for their contribution to KM Tolerance for mistakes	Knowledge management	Neena Sinha, N.K. Kakkar and Vikas Gupta (2015)
34	Culture change	Knowledge sharing	Alison Corfield Rob Paton (2016)
35	**Organisational culture** Communication Leadership Motivation & reward Trust Organisational structure	Knowledge sharing	Dr. Santosh Areekkuzhiyil(2016)
36	Corporate culture	Knowledge sharing	Buckova Jarosalva(2017)

37	Continuous learning Dialogue Team learning Empowerment	Acquire Creation Sharing Utilising	Wadha Wadha (2017)
38	Organisational culture	Acquiring knowledge Storing knowledge Diffusing knowledge Applying knowledge	Paliszkiewicz Joanna,Svanadze Salome,Jikia Mariam (2017)
39	**Cultural attribute** Artefacts Espoused beliefs & values Underlying assumptions	Tacit knowledge Explicit knowledge	Lehman, Dwayne W. (2017)
40	Collabouration Trust Learning IT	Knowledge management	Muhammad Zaidie Bardan, Mazwani Ayu Mazlan (2018)
41	Practices Norms Values	Effective use of KMS KM Outcomes	Thierno Tounkara (2018)
42	Trust Communication Rewards Organisational leadership Learning development Organisation socialisation	Knowledge transfer	Mohammad Habibur Rahman, Immanuel Azzad Moonesar, Md Munir Hossain, Md Zahidul Islam (2018)
43	Process leadership Organisation Technology Learning	Knowledge storage (Product Prototyping)	Abdi Suryadinata Telaga, Anggun Fadhlin Librianti, Putri Ayu Rahayu (2018)
44	Collectivism Uncertainty avoidance Masculinity Feminity Short and long-term orientation Power distance Individualism	Knowledge sharing Collabourative work done virtually Intention to adopt KM	Abel Usoro & Bridget Abaigam (2018)
45	Organisation culture	Knowledge seeking via socialisation (from peers) Knowledge contributing via	Ali M. Baker (2018)

		socialisation (to peers) Knowledge seeking via socialisation (from managers) Knowledge contributing via socialisation (to managers)	
46	Culture	Creation of knowledge Sharing community Creation of a KM	Taylor, Andy K. (2019)

5. CONCEPTUAL FRAMEWORK

A holistic view of organisational culture and its linkage with KM is presented. The proposed model reveals a possible relationship between organisational culture and KM. The culture drives the success of an organisation as KM initiatives will fail if the company's culture does not reflect the creation and exchange of knowledge. In this paper, authors have tried to identify various constituents in organisational culture from the literature that provides a platform for knowledge processes, knowledge conversion, knowledge assets and knowledge sharing. The suggested framework tries to derive the linkage between organisational culture and KM so that they can develop a knowledge culture.

The proposed framework studies the impact of organisational culture which is an independent variable on KM in an organisation which is a dependent variable. The critical success factor for implementing KM is organisational culture (Chase, 1997; Dalkir, 2005; Hung et al., 2005). Knowledge culture involves establishing structure and process for knowledge sharing, knowledge transfer and knowledge advancement from existing knowledge. The multi-level characteristics of organisational culture including Artefacts espoused beliefs and values and underlying assumptions can develop an organisation which values knowledge creation and knowledge sharing. The core values of culture which include storytelling, continuity, loyalty, trust, top management support and reward system can lead to huge success in KM (Zamantili Nayir and Ulku Uzuncaasili, 2008). The values identified by Machua (2012) deliberate on knowledge friendly culture; these values include trust, transparency, flexibility, collabouration, commitment, honesty and professionalism. Innovation, information flow, trust, reward system, teamwork, morale, openness to change, employee involvement and customer service are important cultural attributes considered for the success of KM (Al-Adaileh et al., 2011). Promoting a culture which worships these values enhances knowledge exchange between workers. There are various enablers in a culture which facilitates KM, known as KM enablers. These enablers include strategy and leadership, organisational culture, people and information technology. There are various levels in a culture which individually and collectively impacts KM. These levels include organisational culture,

professional culture and national culture. There are several dimensions in a culture which dominates KM in an organisation. These dimensions include collectivism, low uncertainty avoidance and low power distance. The human resource management activities of an organisation also shape the culture-specific to KM. Various components of organisation cultural profile including trust, sharing information freely, working closely with others and developing friends at work also encourages KM activities. The literature has identified various cultures which are suitable for carrying KM in an organisation efficiently: process-oriented culture, result-oriented culture, loosely controlled culture, tightly controlled culture, job oriented culture, employee-oriented culture, open system culture, parochial culture, entrepreneurial culture, cooperativeness culture, innovativeness culture, clan culture, adhocracy culture, market culture, hierarchical culture, rational culture, group culture, development culture, achievement culture and support culture. When all these components of culture are embedded in the fabric of an organisation, it fosters knowledge creation and sharing.

The authors have integrated and compiled all suitable organisational culture for KM with cultural dimensions, organisational cultural profile, KM enablers, cultural attributes, levels of culture and cultural values to study its impact on KM processes, KM assets, Knowledge conversion cycle and different types of knowledge sharing (Figure 1).

Figure1: KM dependence on Culture (Compiled by authors)

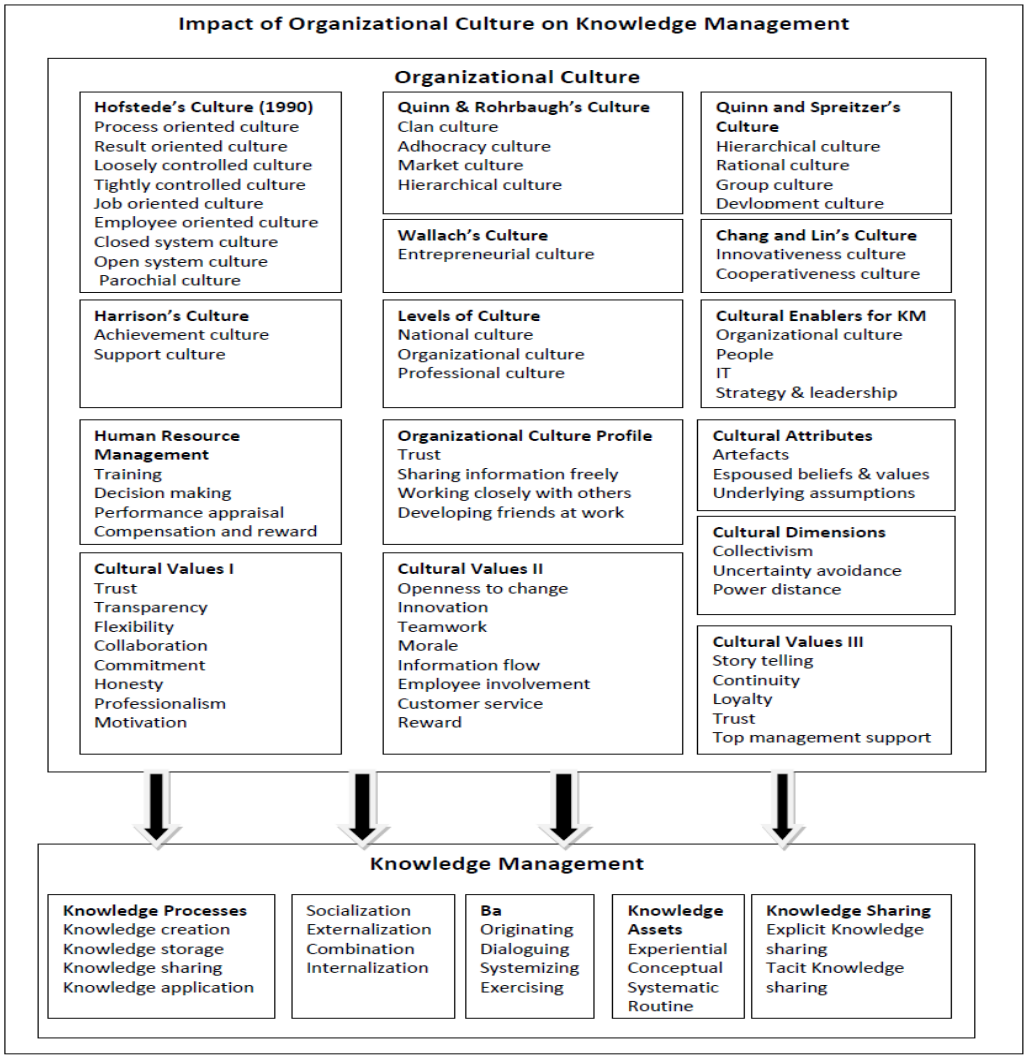

6. CONCLUSION

This paper concludes that culture and KM are inextricably linked in an organisation. The scrutiny of literature presents the significant impact of organisational culture on KM. The existing body of knowledge is not sufficient to provide an integrated and holistic view of the impact of organisational culture on KM. This paper deals with the gap found in the literature relative to the impact of KM on organisational culture. The paper attempts to develop knowledge culture from the prevailing organisational culture which fosters and facilitates KM activities in the organisation. In earlier researches it was emphasised KM involves understanding and commitment to IT but it could be possible only when organisation nurtures a culture where knowledge creation, sharing is a norm. It is overemphasised that technologies-built KM in an organisation but software alone cannot solve KM problems specifically knowledge sharing. Now managers need to recognise and acknowledge that no technology can facilitate KM activities without having a proper culture for KM activities. It has been quoted that 80 per cent of KM is concerned with people and culture and only 20 per

cent is concerned with technology (Liebowitz, 1999). Technology is only the enabler for knowledge sharing through internet, intranet and virtual communities (Love et al., 2005). Technology has a limited role in KM activities; behaviour and attitude of people play a driving role in KM. This paper focuses on the concept of knowledge as a cultural issue rather than a sophisticated information technology infrastructure. The important aspect of KM is concerned with people and culture. It is important to acknowledge that knowledge sharing is influenced by the cultural values of the organisation as a whole as well as individual members (Wei et al., 2008). Thus, authors have tried to explore various factors in a culture that can lead to successful knowledge creation, sharing, application and reuse.

An organisation should focus on execution of managerial action as its KM evolves. The drivers for KM come from trust, collabouration, openness to change, information flow, sharing information freely, working closely with others, top management support, strategic flexibility, creativity, innovation, employee involvement, rewarding policies, team building, morale and managerial commitment. Recognition and providing rewards for knowledge creation and sharing should be exercised to encourage people to participate in KM activities. These activities like sharing learning, exchanging ideas, sharing expertise, application of knowledge should be built into daily work routines. The moral support, as well as budgetary support, is needed from top management for the success of KM (Anantatmula, 2008). The management can support KM by having tolerance for mistakes, allocating time and resources for KM. The management can also document the KM failures to learn from them and avoid them in the future. This paper conveys that culture lays down the foundation for transforming individual knowledge of employees into the synergy of knowledge in an organisation. This paper has tried to fill up the gap in the literature linking organisational culture and KM. The authors had a realisation that literature acknowledges the importance of culture in KM but a comprehensive framework linking the two concepts is not presented in the literature. The conceptual framework proposed in the paper deliberates specifically on cultures that have an impact on knowledge process, knowledge assets, knowledge conversion cycle and knowledge sharing. The culture that supports KM in an organisation results in organisational success. If organisations can increase the level of key elements of organisational culture that act as KM enablers then the organisation may gain greater access to a major portion of knowledge base residing in the mind of employees in the tacit form of knowledge. Effective KM processes result in creating intangible assets and intellectual capital for organisations contributing towards operating performance, value and growth (Herbert A. Nold, 2012). Thus, it is a necessity to now shift from knowledge is the power to knowledge sharing is powerful.

7. STUDY IMPLICATIONS, LIMITATIONS AND FUTURE RESEARCH

The current research paper deliberates on developing a conceptual framework in which culture impacts KM. This study contributes to the theoretical arena of KM in many ways. One of the theoretical contributions to research is a proposed conceptual framework which has been heavily influenced by academic literature. The significant output of the research is bridging the gap in previous literature and giving a comprehensive view to the reader. The significance of this model can be noticed from the fact that despite the popularity of extensive

research on organisational culture and KM there is no integrative model studying all the dimensions of variables under study. The implication of this paper is the utilisation of the model when executing KM. Organisations can consider a specific type of culture into a plan to carry out KM initiatives. This is important as KM involves investments in terms of time, money and personnel (Becerra-Falezernandez et al., 2004; Parikh, 2001). The conceptual model proposed in the paper can guide an organisation in developing a robust KM plan. The model can also guide organisations to interrogate the reasons for KM failure. By focusing on different aspects mentioned in the model, organisations can work towards enhancement of knowledge-centric culture. Most of the studies have discussed KM as an IT problem, this paper focuses on KM as a cultural issue.

This paper provides a deep insight into the culture required for successful knowledge creation and sharing in an organisation. This research can have managerial as well as theoretical implications. Establishing and implementing the link between culture and KM will lead to the conceptualisation of knowledge culture. Managerial implications can be initiated by developing an understanding in managers, that KM won't lead to success until supported by the culture. Managers should realise that knowledge creation and sharing need a culture that is open and flexible; motivates the employees for knowledge sharing by rewarding and recognising; acceptance for mistakes; giving space for creativity and innovation. The theoretical implication implies contribution to literature, especially for the research scholars. The conceptual model proposed in the current research can be further tested empirically. The research findings can provide a deeper understanding of individuals as well as organisations. KM can be successful in organisations if supported by enabling culture. In the future, managers can assess the role of culture in the success of KM in organisations. Our study offers an effective approach for managers to promote suitable organisational culture to enhance employee confidence and facilitate knowledge sharing behaviour. This research paper provides guidelines for top executives to establish clear goals and inspire employees to achieve KM goal by effective organisational culture. The managers should also know various types of culture to foster knowledge sharing behaviour.

The KM activities like knowledge creation, sharing, dissemination relies on the behaviour and attitude of people (Ajmal et al., 2009). Thus, it is necessary to check the alignment between culture and KM of an organisation. Managers should work on creating a knowledge-centric culture. A knowledge friendly culture is one that values knowledge and its creation, sharing and application (Migdadi, 2009). The current research may lead to the new shape in the company's culture that values knowledge. There were some limitations which include the difficulty in establishing a relationship between various dimensions of organisational culture and KM based on literature. There was also difficulty in generalising conclusion from the conceptual model reflecting the dependence of KM on organisational culture. Also, this research is limited to the conceptual model and is not tested empirically. The statistical tests are needed to assess and operationalise the variables and test the linkages between them. A better approach would be to study a particular sector, organisation or industry in particular and to establish empirical data about the interrelationship. This paper is an output of extensive literature review studying all the attributes, components, framework and

classification of culture that impacts KM. However, it would have been better to go for a precise study deliberating on a particular dimension of culture amongst framework, attributes or classification which impacts a specific KM dimension amongst KM processes, knowledge assets, KM conversion cycle and types of knowledge sharing. This could result in the assessment of the role that particular cultural dimension plays in particular KM activities. Also, a longitudinal study would have given long term data to understand how organisational culture would have influenced KM.

8. REFERENCES:

[1] Abel Usoro and Bridget Abiagam (2018), "Culture effect on knowledge management adoption in Nigerian hospitality industry".

[2] Aimal, M.M.kekale, T. and Takala, J. (2009),"Cultural impacts on knowledge management and learning in project-based firms", VINE: The Journal of Information and Knowledge Management Systems, Vol.39 No. 4, pp. 339-52.

[3] Ajmal, M.M. and Koskinen, K.U. (2008),"Knowledge transfer in project-based organizations: an organizational culture perspective" , Prefect Management Journal, Vol. 39 No. 1, pp. 7-15.

[4] Akhavan, P. and Sanjaghi, M.E., " Examining the relationships between organizational culture, knowledge management and environmental responsiveness capability", The journal of information and knowledge management systems, Vol. 44 No. 2, 2014, pp 228-248.

[5] Al- Adaleih, and Al-Atawi, M.S. (2011), "Organizational culture impact on knowledge exchange: Saudi Telecom context", Journal of knowledge Management, Vol.15 No. 2, pp.212-30.

[6] Al-Saifi, S. (2014), "The nature of the relationship between social networks, interpersonal trust, management support and knowledge sharing", Unpublished PhD Thesis, University of Waikato, Hamilton.

[7] Alave, M. and Leidner, D.E. (2001), "Review: Knowledge management and knowledge management systems: conceptual foundations and research issues", MIS Quarterly, Vol. 25 No. 1, pp. 107-136.

[8] Alavi, M. and Leidner, (1999), "Knowledge management systems: issues, challenges benefits"' Communication of Association for Information Systems, Vol.1 No.7, pp.1-37.

[9] Alavi, M. Kayworth, T.R and Leidner, D.E. (2005-2006), "An empirical examination of influence of organizational culture on knowledge management practices", Journal of management information systems, vol. 22 No. 3, pp. 191-224.

[10] Alavi ,M., Timonthy, R.K. and Leidner, D.E.(2005-2006), " An empirical examination of the influence of organizational culture on knowledge management practices"' Journal of Management Information Systems, Vol.22 No.3, pp.199-204.

[11] Albros-Garrigos, J., Ramos, J.C. and Mas-Machuca, M. (2010), "Actionable intelligence, a critical competence for innovation performance: a research multi-case

analysis", International Journal of Technology Intelligence and planning, Vol.6 No. , pp. 210-225.

[12] Alison Corfield Rob Paton (2016), "Investigating Knowledge Management: Can KM really change organizational culture?" Journal of knowledge management, Vol. 20.

[13] Anantatmula, V.S. (2008), "Leadership role in making effective use of KM", VINE: The Journal of information and knowledge Management Systems, Vol. 38 No. 4 pp. 445-60.

[14] Armstrong, M. (2000), "The name has changed but has the game remained the same?", Employee Relations, Vol. 22. No. 6, pp. 5767-93.

[15] Arthur Anderson Business Consulting (1999), Zukai Knowledge Management, TOKYO Keizai, Inc., Tokyo.

[16] Banks, E. (1999), Creating a Knowledge culture", Work Study, Volume 48, Number 1, pp. 18-20.

[17] Barney, J.B. (1986), "Organizational culture: can it be a source of sustained competitive advantage?", Academy of Management Review, Vol. 11 No. 3, pp. 656-665.

[18] Barrios, J. (2013), The impact of mandated change on a hierarchical subculture: a mixed-methods using the competing values framework", Unpublished Ph.D thesis, Capella University, Minneapolis, M.N.

[19] Bhatt, G.D. (2001), "Knowledge management in organizations; examining the interaction between technologies, techniques and people", Journal of knowledge management, Vol. 5 No. 1, pp. 68-75.

[20] Becerra-Falezernandez, I., Gonzalez, A. and Sabherwal, R. (2004), Knowledge management challenges, solutions and technologies, Prentice Hall, upper saddle river, NJ.

[21] Bresman, H.B.J., & Nobel, R. (199). Knowledge transfer in international acquisition Journal of International Business Studies, 30(3): pp439-462.

[22] Bryne, R. (2001), "Employees: capital or commodity?", The Learning Organization, Vol. 8 No. 1, pp. 44-50.

[23] Bochner, S. and Hesketh, B. (1994), "Power distance, individualism/collectivism, and job oriented attitude in a culturally diverse work group", Journal of cross- cultural psychology, Vol. 25 No. 2, pp. 233-57.

[24] Boggs, B. (2002), "An exploratory study of the relationship between organizational culture types and a balance scorecard of effectiveness measure in church ", Unpublished Ph.D Thesis, Regent University, VA.

[25] Bose, R. (2004), "Knowledge management metrics", Industrial Management & Data Systems, Vol. 104 No. 6, pp. 457-68.

[26] Brockman, B.K. and Morgan, R.M. (2003), "The role of existing knowledge in new product innovativeness and performance", Decision science, Vol. 34 No. 2, pp 385-419.

[27] Byosiere, P. and Luethge, D.J (2004), "Realizing vision through envisioning reality: strategic leadership in building knowledge spheres", in Bruke, R.J and Cooper, C. (Eds), Leading in trubulent times: Managing in new world of work, Blackwell publishing, Maiden, MA pp 243-58.

[28] Cakar, N.D. and Erturk, A. (2010), "Comparing innovation capability of small and medium sized enterprises: examining the effects of organizational culture and empowerment", Journal of small business management, Vol. 48 No. 3, pp. 325-59.
[29] Cameron, K.S. and Quinn, R.E (1999), Diagnosing and changing organizational culture, Addison-Wesley, Reading, MA.
[30] Cameron, K.S. and Quinn, R.E (1999), Diagnosing and changing organizational culture: Based on competing vale framework, John Wiley Sons, San Francisco, CA.
[31] Civi, E. (2000) "Knowledge management as a competitive asset: a review", Marketing Intelligence & Planning, Vol. 18 No. 4, pp. 166-74
[32] Clarke, P. and Staunton, N. (1989), Innovation in Technology and Organization, Routledge, London.
[33] Chang, S.E, and Lin., C.S.(2007), "Exploring organizational culture for information security management.
[34] Chang, C. L. and Tung-Ching-Lin, "The role of organizational culture in the knowledge management process", Journal of knowledge management, Vol. 19 No. 3, 2015, pp. 433-455.
[35] Chase, R.L. (1997),"The knowledge-based organization: an international survey"' Journal of knowledge management, Vol.1 No. 1, pp. 29-45.
[36] Chakravorti, S. (2011), "Managing organizational culture change and knowledge to enhance customer experience: analysis and framework", Journal of strategic management, Vol. 19 No. 2, pp. 123-151.
[37] Chen, C.C., Chen, X.P. and Meindl, J.R. (1998), "How can cooperation be fostered? The cultural effects of individualism-collectivism", Academy of management review, Vol. 23 No. 2, pp. 285-304.
[38] Cohen, D. and Prusak, L. (2001), "In good company: How social capital makes organization work", Harvard Business School Press, Boston, MA.
[39] Dana L.P. and Korot Len and Tovstiga George (2005), "A cross- national comparison of knowledge management practices", International Journal of manpower, Emerald group publishing limited, vol. 26, Issue 1, pp. 10-22.
[40] Dalkir, K. (2005), Knowledge Management in Theory and Practice, Elsevier, Oxford.
[41] Dalkir, K. (2011), Knowledge Management in Theory and Practice, MIT, Cambridge, MA.
[42] Davenport, T.H., De Long, D.W. and Beers, M.C. (1998), "successful knowledge management projects" , Sloan Management Review, Vol. 39 No. 2, pp. 43-57
[43] Demarest, M. (1997) , " Understanding knowledge management", Long Range Planning, Vol. 30 No. 3, pp. 374-84
[44] De Long, D.W. and Fahey, L. (2000), Diagnosing cultural barriers to knowledge management', Academy of Management Executive, Vol. 14 No. 4, pp. 113-27.
[45] Denison, D.R. and Spreitzer, G.M. (2001), "Organizational culture and organizational development: a competing values approach ", Research in organizational change and development, Vol. 5 No. 1, pp. 1-21.

[46] Edwards, V. and Sienkewicz, T.J. (1994), Oral Cultures: Past and Present, Human Resources Development, Boston, MA.
[47] Eskerod, P. and Skriver, H.J. (2007), "Organizational culture restraining in-house knowledge transfer between project managers-a case study", Project management journal, Vol. 38 No. 1, pp. 110-122.
[48] Figallo, C. (2002), Building the knowledge management network: Best Practices, tools, and techniques for putting conversation to work, John Wiley, New York. NY.
[49] Fernandes, A. A. R. and Maupa, H. (2007), "The effect of Organization culture and technology on motivation, knowledge asset and knowledge management".
[50] Garavan, T.N., Gunnigle, P. and Morley, M. (2000), "Contemporary HRD research: a triarchy of theoretical perspectives and their prescriptions for HRD", Journal of European Industrial Training, Vol. 24 No. 2/3/4, pp. 65-93.
[51] Glaser & Associated Inc. (2008), "Organizational Culture Survey", available at www.theglassers.com/service-survey.html#OCS1.
[52] Gooijer, F.D. (2000), "Designing a knowledge management performance framework", Journal of knowledge Management, Vol. 4 No. 4, pp. 3030-3050.
[53] Gruber, H. and Duxbury, L.(2000), "Does organizational culture affect the sharing of knowledge: the case of a department in a high technology company", paper presented at 28th Annual ASAC Conference, Technology and Innovation Management Division, Montreal, 9 July.
[54] Gold, H., Malhotra A. and Segars, A. (2001), "Knowledge management: an organizational capabilities perspective', Journal of Management Information Systems, Vol.18 No. 1, pp. 185-214.
[55] Great Place to Work Institute (2011), available at www.greatplacetoworkinstitute.com/what_we_do/employee_srvey.php.
[56] Griffith, T.L, Sawyer, J.E. and Neale, M.A. (2003), "Virtualness and knowledge in teams: managing the love triangle of organizations, individuals, and information technology", MIS Quarterly, Vol. 27 No. 2, pp. 265-288.
[57] Guadamillas-Gomez, F. and Donate-Manzanares, M. J., "Ethics and corporate social responsibility integrated into knowledge management and innovation technology", Journal of management development, Vol. 30 No. 6, 2011, pp. 569-581.
[58] Gupta, B., Iyer, L.S. and Aronson, J.E (2000), "Knowledge management practices and challenges", Industrial management and data systems, Vol. 100 No. 1, pp. 17-21.
[59] Gupta, V. & Chopra, M (2018) 'Gauging the impact of knowledge management practices on organizational performance – a balanced scorecard perspective', VINE *Journal of Information and Knowledge Management Systems* 48(1), pp.21-46.
[60] Gupta, V., Jain, N. (2017), "Harnessing information and communication technologies for effective knowledge creation: shaping the future of education", Journal of enterprise information management Vol. 30 (5), pp. 831-855.
[61] Gurteen, D., Knowledge Management Magazine, Volume 2, Issue 5, February 1999.
[62] Hedelin, L. and Allwood, C.M (2002), "IT and strategic decision making", Industrial Management &Data Systems, Vol. 102 No. 3, pp. 125-39.

[63] Hendriks, P. (1999), "Why share knowledge? The influence of ICT on motivation for knowledge sharing" Knowledge and Process Management, Vol. 6 No. 2, pp. 91-100.
[64] Hibbard, J. (1998), "Cultural breakthrough", Information Week, Vol. 21 No. 701, pp. 44-55.
[65] Holsapple, C.W and Joshi, K.D. (2000), "An investigation of factors that influence the management of knowledge in organizations", Journal of Strategic Information Systems, Vol. 9 Nos 2/3, pp. 235-61.
[66] Hsieh, C.T., Yang, H. and Lin, B. (2002), "roles of knowledge management in online procurement systems", Industrial Management & Data Systems, Vol. 102 No. 7 pp. 365-70.
[67] Hai Nam Nguyen and Sherif Mohamed,"Leadership behaviors, organizational culture and knowledge management practices an empirical investigation", Journal of management development, Vol. 30 No. 2, 2011, pp 206-221.
[68] Heejun Park, Vincent Ribiere and William D. Schulte (2004), "Critical attributes of organizational culture that promote knowledge management technology implementation success" Vol. 8No. 3 2004, pp. 106-117.
[69] Heisig, P. (2009), "Harmonisation of knowledge management-comparing 160 KM frameworks around the globe", Journal of knowledge management, Vol. 13 No. 4, pp. 4-31.
[70] Herbert A. Nold III, "Linking knowledge processes with firm performance: organizational culture", Journal of intellectual capital, Vol. 13 No. 1, 2012, pp. 16-38.
[71] Ho, C.T. (2009), "The relationship between knowledge enablers and performance", Industrial Management & Data Systems, Vol. 109 No. 1, pp. 98-117.
[72] Ho, L.A. (2008), "What affects organizational performance? The linking of learning and knowledge management", Industrial Management & Data Systems, Vol. 108 No. 9, pp. 1234-54.
[73] Hofstede, G. (1980), Cultures consequences: International differences in work related values, Sage publications, Beverly Hills, CA.
[74] Hofstede, G. (2001), Cultures Consequences, 2nd ed., Sage Publications, Thousand Oaks, CA.
[75] Hofstede, G. and Hofstede, G. J. (2005), cultures and organizations: Software of the mind, McGraw-Hill, New York, NY.
[76] Hofstede, G., Neijen, B., Ohyay, D.D and Sander, G. (1990), "Measuring organizational cultures: a qualitative and quantitative study across twenty cases", Administrative Science Quarterly, Vol. 35 No. 2, pp. 286-316.
[77] Hung,Y., Huang, S., Lin, Q. and Tsai, M.(2005), "Critical factors in adopting a knowledge management system for the pharmaceutical industry", Industrial Management & Data Systems, Vol. 105 No. 2, pp. 164-83.
[78] Iivari, J. and Huisman, M.(2007), " The relationship between organizational culture and deployment of systems development methodologies", MIS Quarterly, Vol. 31 No.1, pp. 35-58.

[79] Jacks, T., Wallace, S. and Nemti, H. (2012), "Impact of culture on knowledge management: a meta analysis and framework", Journal of global information technology management, Vol. 15 No. 4 pp. 8-42.
[80] Janz, B.D. and Prasarnphanich, P. (2003), "Understanding the antecedents of effective knowledge management: the importance of knowledge oriented culture", Decision Science, Vol. 34 No. 2, pp. 351-384.
[81] Jarvenpaa, S.L. and Stples, D.S. (2001), "Exploring perceptions of organizational ownership of information and expertise", Journal of management information systems, Vol. 18 No. 1, pp. 151-183.
[82] Jennex, M.E. and Olfman, L. (2004), "Assessing knowledge management success/effectiveness models"' Proceedings of the 37th Hawaii International conference on system sciences, Big Island, HI, USA.
[83] Jennex, M.E. and Olfman, L. (2006), "A model of knowledge management success", International journal of Knowledge Management, Vol. 2 No. 3, pp. 51-68.
[84] Jones, M.C., Cline, M. and Ryan, S. (2006), "Exploring knowledge sharing in ERP implementation: an organizational culture framework ", Decision support systems, Vol. 41 No. 2, pp. 411-434.
[85] Kahle, L.R., Best, R.J. and Kennedy, P.F. (1998), "An alternative method for measuring value-based segmentation and advertisement positioning", Current Issues Research in Advertising, Vol. 11, pp. 139-55.
[86] Kayworth, T. and Leidner, D. (2003), "Organizational culture as knowledge resource", in Holsapple, C.W. (Ed.), Handbook on knowledge management: Knowledge matters, springer-verlag, Heidelberg, pp. 235-252.
[87] Kim, S. and Lee, H. (2006), "The impact of organizational context and information technology on employee knowledge sharing capacities", Public Administration Review, Vol. 66 No. 3, pp. 370-385.
[88] King, W.R. (2007), "A research agenda for relationships between culture and knowledge management", Vol. 14 No. 3, pp. 51-68.
[89] King, W.R. (2008), "Questioning the conventional wisdom: culture- knowledge management relationships", Journal of Knowledge Management, Vol. 12 No. 3, pp. 35-47.
[90] Ko, D., G., Kirsch, L.J. and King, W.R. (2005), "Antecedents of knowledge transfer from consultants to clients in enterprise system implementations", MIS Quarterly, Vol. 29 No. 1, pp. 59-85.
[91] Kotter, J.P. & Heskett. J.L. (1992). Corporate culture and performance. Free Press.
[92] Kuo, Y.K., Kuo, T.H. and Ho, L.A (2014), "Enabling innovative ability: knowledge sharing as mediator", Industrial Management and Data systems, Vol. 114 No. 5, pp. 696-710.
[93] Lee, S.M. And Hong, S. (2002), "An enterprise-wide knowledge management system infrastructure", Industrial Management & Data systems, Vol. 102 No. 1, pp. 17-25.

[94] Lee, J.-H., Kim, Y,-G, and Kim, M.-Y (2006),"Effects of managerial drivers and climate maturity on knowledge-management performance: empirical validation", Information Resources Management Journal, Vol. 19 No. 3, pp. 48-61.

[95] Leidner, D.E., Alavi, M. and Kayworh, T. (2006), The role of culture in knowledge management: a case study of two global firms", International Journal of e-collaboration, Vol. 2 No. 1, pp. 17-40

[96] Leonard, D. (1995) Wellsprings of Knowledge: Building and sustaining the source of innovation, Harvard Business School Press, Boston, MA.

[97] Li, M. and Lee, G., "Relationships of organizational culture toward knowledge activities", Business process management journal, Vol. 13, No. 2, 2007, pp. 306-322.

[98] Liebowitz, J. (1999), "Key ingredients to the success of an organization's knowledge management strategy", Knowledge and process Management, vol. 6 No. 1, pp. 37-40.

[99] Liebowitz, J. (2008),"'Think of others' in knowledge management: making culture work for you",Knowledge Management Research & Practice, Vol.6 No. 6, pp. 47-51.

[100] Liu, L.N., Feng, Y.Q., Hu, Q. and Huang, X.J. (2011), "From transactional user to VIP: how organizational and cognitive factors affect ERP assimilation at individual level", European journal of information systems, Vol. 20 No.2, pp 186-200.

[101] Li, W., Ardichvili, A., Maurer, M. Wenting,T. and stedemann, R. (2007)", Impact of Chinese culture values on knowledge sharing through online communities of practice", International journal of knowledge management, Vol.3 No. 3, pp. 46-59.

[102] Long, D.D. (1997), "Building the knowledge-based organization: how culture drives knowledge behaviors", working paper of the Center for Business Innovation, Ernst & young LLP, Cambridge, MA.

[103] Louis, M.R (1980), "Surprise and sense making: what newcomers experience in entering unfamiliar organizational settings", Administrative science quarterly, Vol 25 pp. 226-51.

[104] Luu Trong Tuan "Behind Knowledge Transfer", Management Decision Vol. 50 No. 3, 2012, pp 459-478.

[105] Luu Trong Tuan (2012)," Behind knowledge transfers", Management Decision Vol. 50 No. 3, pp 459-478.

[106] Machua, M.M and Costa, C.M (2012), "A study of knowledge culture in the consulting industry", Industrial Management & Data Systems, Vol. 112 No. 1, pp. 24-41.

[107] McDermott, R. and O'Dell, C. (2001), "Overcoming cultural barriers to sharing Knowledge", Journal of Knowledge Management, Vol. 6 No. 1, pp. 76-85.

[108] Magnier-Watanabe, R. (2009), "Congruent knowledge management behaviors as discriminate sources of competitive advantage", Journal of workplace learning, Vol. 21 No. , pp. 109-24.

[109] Malhotra, Y. and Galleta, D.F. (2003), "Role of commitment and motivation in knowledge management systems implementation: theory, conceptualization, and measurement of success", Proceedings of the 36th Hawaii International Conference on System Sciences, Los Alamitos, CA, USA.

[110] Markus, M.L, Majchrzak, A. and Gasser, L. (2002), "A design theory for system that support emergent knowledge processe" MIS quarterly, Vol. 26 No. 3, pp. 179-212.
[111] Martin, J. and Siehl, C. (1983), Organizational culture and counter-culture: an easy symbiosis", organizational dynamics, Vol. 12, pp. 52-65.
[112] Marwick. A.D. (2001), "Knowledge management technology", IBM Systems Journal, Vol. 40 No. 4, pp. 814-830.
[113] Mas, M., Corrales, A. and Velaz, I. (2004), "Direccion de Empresas en la Economia del Conocimiento"' Cuadernos de Empresa y Humanismo, Vol. I, May, pp. 3-56.
[114] Massey, A.P., Montoya,-Weiss, M. and O' Driscoll, T. (2002), "Knowledge management in pursuit of performance: insights from Nortel networks", MIS Quarterly, Vol. 26 No., pp. 269-289.
[115] McDermott, R. & O'Dell, C. (2001). Overcoming cultural barriers to sharing-knowledge. Journal of Knowledge Management.
[116] Mianm. Ajmal, Tauno Kekale and Josu Takala, " Cultural impacts on knowledge management and learning in project-based firms", The journal of information and knowledge management systems, Vol. 39No. 4, 2009, pp. 339-352.
[117] Migdadi, M. (2009), "Knowledge management enablers and outcomes in small-and-medium sized enterprises" Industrial Management and Data Systems, Vol. 109 No. 6, pp. 840-58.
[118] Mertensson, M. (2000), "A critical review of knowledge management as a management tool", Journal of Knowledge Management, Vol. 4 No. 3, pp. 204-16
[119] Nahapiet, J. and Ghoshal, S. (1998), "Social capital, intellectual capital, and the organizational advantage", Academy of management review, Vol. 23 No. 2, pp. 242-66.
[120] Sinha, N., Kakkar, N. K., & Gupta, V. (2009). 'Unleash the power of creativity and innovation', *International Journal of Sustainable Strategic Management, 1*(4), 417-433.
[121] Sinha, N., Kakkar, N. K., & Gupta, V. (2015), "Harnessing the power of knowledge management for innovation", International journal of knowledge and learning, Vol. 10.No. 2, 2015.
[122] Newwell, S., Huang, J.C., Galliers, R.D. and Pan, S.L. (2003), "Implementing enterprise resource planning and knowledge management systems in tandem/; fostering efficiency and innovation complementarily", Information and organization, Vol. 13 No. 1, pp 25-52.
[123] Newell, S., Tansley, C. and Huang, J. (2004), "Social capital and knowledge integration in ERP project team: the importance of bridging and bonding ", British journal of management, Vol. 15, S43-S57.
[124] Nirwan. (2015). Model Development of Knowledge Management System at Hanasuddin University. Hasanuddin University, Doctoral Dissertation, Not Published.
[125] Nonaka, I. and Takeuchi, H. (1995), The Knowledge-Creating Company, Oxford university Press, Inc., New York, NY.
[126] Nonaka, I. and Konno, N. (1998), "The concept of 'ba': building a foundation for knowledge creation", California management review, Vol. 40 No. 3, pp. 40-54.

[127] Nonaka, I.., Toyama, R. and Konno, N. (2000), "SECI, ba and leadership: a unified model of dynamic knowledge creation", Long Range Planning, Vol. 33 No. 1, pp. 5-34.
[128] Nonaka, I. and Von, K.G. (2009), "Perspective tacit knowledge and knowledge conversion: controversy and advancement in organizational knowledge creation theory", Organization science, Vol. 20 No. 3, pp 635-652.
[129] Norman, P.M. (2004), "Knowledge acquisition, knowledge loss, and satisfaction in high technology alliances", Journal of Business research, Vol. 57 No. 6, pp. 610-619.
[130] Ogbonna, E. and Harris, L.C. (2000). "Leadership style, organizational culture and performance: empirical evidence from UK companies", International Journal of Human Resource Management, Vol. 11 No. 4, pp. 766-88.
[131] O'Dell, C., Grayson, J.C. and Essaides, N.(2001), Si tan solo supieramos lo que sabemos, Griker and Asociados, Madrid.
[132] Orlikowski, W.J. (2002), "Knowing in practice: enacting collective capability in distributed organizing", Organization Science, Vol. 10 No. 1, pp. 92-108.
[133] Park, H. (2005), "Critical attributes of organizational culture promoting successful KM implementation", Computational Science and its Applications-ICCSA 2005 Vol. 3482, Sringer, Berlin, pp. 1316-25.
[134] Pan, S.L and Scarbrough, H. (1998), "A socio-technical view of knowledge-sharing at Buckman Laboratories", journal of Knowledge Management, Vol. 2 No. 1, pp. 55-66.
[135] Pawlowski, J. and Bick, M. (2012), "The global knowledge management framework: towards a theory for knowledge management in globally distributed settings", Electronic Journal of Knowledge Management, Vol. 10 No. 1, pp. 92-108.
[136] Pankh, M. (2001), "Knowledge management framework for hi-tech research and development", Engineering management journal, Vol. 13 No. 3, pp. 27-33.
[137] Pieris, C., David, L. and William, M. (2003), "Excellence in knowledge management: an empirical study to identify critical factors and performance measures", Measuring Business Excellence, Mol. 7 No. 2, pp. 29-45.
[138] Pillania, R.K (2006), "State of organizational culture for knowledge management in Indian industry", Global business review, Vol. 7 No. 1, pp. 119-135.
[139] Pirkkalainen, H. and Pawlowski, J. (2013), "Global social knowledge management from barriers to the selection of social tools", Electronic Journal of knowledge Management, Vol. 11 No. 1, pp. 3-17.
[140] Quinn, R.E. and Rohrbaugh, J. (1983b), "A spatial model of effectiveness criteria: towards a competing vale approach to organizational analysis", Management Science, Vol. 29 No. 3, pp 363-377.
[141] Quinn, R.E and Spreitzer, G.M (1991), "The psychometrics of the competing value culture instrument and analysis of the impact of organizational culture on quality of life", Research in organizational change and development, vol. 5, pp. 115-142.
[142] Rai, R. K., "Knowledge management and organizational culture: a theoretical integrative framework", Journal of knowledge management, Vol. 15 No. 5, 2011, pp. 779-801.

[143] Ramadani V., Abazi-Alili H., Dana L.P., Rexhepi Gadaf and Ibraimi Sadudin (2016), "The impactof knowledge spillovers and innovation on firms performance: findings from Balkans countries, International entrepreneurship and management journal, Vol. 13, Issue 1, pp. 299-325.

[144] Remy Magnier-Watanbe and Dai Senoo, "Shaping knowledge management: organization and national culture", Journal of knowledge management, Vol 14 No. 2 2010, pp. 214-227.

[145] Hamilton Robert and Dana L.P. and Benfell Camilla (2008), "Changing cultures: an international study of migrant entrepreneurs",Journal of enterprising culture, World scientific publishing company, Vol. 16, Issue 1, pp. 89-105.

[146] Robertson, M. And Hammersley, G.M. (2000), "Knowledge management practices within a knowledge-intensive firm; the significance of the people management dimension", Journal of European Industrial Training, vol. 24 No. 2/3/4, pp. 241-53.

[147] Rowley, J. (2004), "Partnering paradigms? Knowledge management and relationship marketing', Industrial Management & Data Systems, Vol. 104 No. 2, pp. 149-57.

[148] Sabri, H., "Knowledge management in its context: Adapting structure to knowledge creating culture, IJCM Vol. 15(2), 2005.

[149] Sachin K. Patil and Ravi Kant, " The organizational culture as HR strategy for successful knowledge management, Strategic HR Review, Vol. 6 No. 4, 2012, pp. 322-328.ement research", Journal of knowledge management, Vol. 19 No. 2, 2015, pp. 164-189.

[150] Said Abdullah Al Saifi, "Positioning organizational culture in knowledge management research", Journal of knowledge management, Vol. 19 No. 2, 2015, pp. 164-189.

[151] Salleh yahya and Wee-Keat Goh, "Managing human resource toward achieving knowledge management", Journal of knowledge management, Vol. 6 No. 5, 2002, pp. 457-468.

[152] Schein, E. 2004, Organizational culture and leadership, Jossey-Bass, San Francisco,CA.

[153] Schein, E.H. (2000), "Sense and nonsense about culture and climate", in Ashkanasy, N.M., Widerom, C.P.M. and Peterson, M.F. (Eds), Handbook of organizational culture and climate, Sage Publications, Thousand Oaks, CA, pp. 23-30.

[154] Schultze, U. and Leidner, D. (2002), "Studying knowledge management in information systems research: discourses and theoretical assumptions", MIS Quarterly, Vol. 26 No. 3, pp. 213-242.

[155] Sedziuviene, Natalija & Jolita Vveinhardt (2009), "The Paradigm of Knowledge Management in Higher Educational Institutions". Inzinerine Ekonomika-Engineering Economics (5), 111-115.

[156] Senge, P. (1990), "The fifth discipline: The art and practice of the learning organization", Double day, New York, NY.

[157] Shane, S. (1995), "Uncertainty avoidance and the preference for innovation championing roles", Journal of international business studies, Vol. 26 No. 1, pp. 47-68.

[158] Shao, Z., Wing, T. and Feng, Y., "Impact of ofrganizational culture and computer self-efficacy on knowledge sharing"' Industrial management & data systems, Vol. 115No. 4, 2015, pp. 590-611.

[159] Sheng, Y., Pearson, M. and Crosby, J.L. (2004), An Empirical examination of the Impact organizational culture has on employees' Computer Self efficacy, Ide Group, Hershey, PA.

[160] Shih, C.C. and Huang, S.J. (2010), "Exploring the relationship between organizational cult ure and software process improvement deployment", Information & management, Vol. 47 Nos 5/6, pp. 271-281.

[161] Shu-Mei Tseng, "The correlation between organizational culture and knowledge conversion on corporate performance", Vol. 14 No.2, 2010, pp. 269-284.

[162] Shu-Mei Tseng, "The effects of hierarchical culture on knowledge management process", Management Research Review, Vol. 34, No. 5, 2011, pp. 595-608.

[163] Smith, K.G, Collins, C.J. and Clark, K.D (2005), "Existing knowledge, knowledge creation capability and the rate of new product introduction in high technology firms", Academy of management journal, Vol. 48 No. 2, pp. 346-57.

[164] Smith, L., Campbell, F., Sbramanian, A., Bird, D. and Nelson, A. (2001), "Strategic planning for municipal information systems: some lessons from a large U.S city", American Review of Public Administration, Vol. 31 No. 2, pp. 139-57

[165] Soliman, F. and Spooner, K. (2000), "Strategies for implementing knowledge management: role of human resources management", Journal of Knowledge Management, Vol .4 No. 4, pp. 337-45

[166] Smith, H.A. and McKeen, J.D. (2003), "Instilling a knowledge-sharing culture", available at: http://is.Ise.ac.uk//Support/OKLC_2002/pdf_files/ID25.pdf (accessed May 31, 2004).

[167] Snowdn, D. (2000), "The social ecology of knowledge management", in Despres, C. and Chauvel, D. (Eds), The Present and the Promise of Knowledge Management, Butterworth-Heinemann, New York, NY, pp. 237-65

[168] Sveiby, K. (1997), "The New Organizational Wealth: Managing and Measuring Knowledge-Based Assets".

[169] Stankosky, M. (2005), "Creating the Discipline of Knowledge Management: The latest in University Research", Butterworth-Heinemann, New York, NY.

[170] Suppiah, V. and Sandhu, M.S. (2011), "Organizational culture's influence on tacit knowledge-sharing behavior"' Journal of Knowledge Management, Vol. 15 No. 3, pp. 462-77.

[171] Susana Perez Lopez, Jose Manuel Montes Peon and Camilo Jose Vazquez Ordas," Managing knowledge: the link between culture and organizational learning", Vol. 8No. 6, 2004, pp 93-104.

[172] Tan, N.-L., Lim, Y. –S. and Ng, T,-H. (2009), "Trust: facilitator of knowledge sharing culture", Journal of communication of the IBIMA, Vol. 7 No. 15, pp. 137-142.

[173] Trompenaars, F. (1998), Riding the waves of culture, The Economist Books, London.

[174] Tohidinia, Z. and Mosakhani, M. (2010), "Knowledge sharing behavior and its predictors", Industrial management and data systems, Vol. 110 No. 4, pp. 611-631.
[175] Tseng, S.M. (2010), "The correlation between organizational culture and knowledge conversion on corporate performance", Journal of knowledge management, Vol. 14 No. 2, pp. 103-17.
[176] Van Kroh, G. (1998),"Care in knowledge creation", California Management Review, Vol. 40 No. 3, pp. 133-53.
[177] Von Krogh, G. (1998), "Care in knowledge creation", California Management Review, Vol. 40 No. 3, pp. 133-53
[178] Wasko, M.M. and Faraj, S. (2005), "Why should I share? Examining knowledge contribution in networks of practice" MIS Quarterly, Vol. 29 NO. 1, pp. 35-57.
[179] Wallach, E.J. (1983), "Individuals and organizations; the cultural match", Training & Development Journal, February, pp. 29-36.
[180] Wagner, J.A III (1995), "Studies of individualism-collectivism: effects on cooperation", Academy of Management Journal, Vol. 38 No. 1, pp. 152-172.
[181] Wei, J., Stankosky, M., Calabrese, F. and Lu, L. (2008), "A framework for studying the impact of national culture on knowledge sharing motivation in virtual teams", VINE: The journal of information and knowledge management systems, vol. 38 No. 2, pp. 221-231.
[182] Wei, Z. (2005), The impact of organizational culture, structure and strategy on knowledge management effectiveness and organizational effectiveness, UMI dissertation services, Proquest, Minneapolis, MN.
[183] Wenger, E.C. and Schneider, W.M. (2000), "Communities of practice: the organizational frontier", Harvard Business Review, pp. 139-145.
[184] Woodman, M. and Zade, A. (2011), "Five grounded principles for developing knowledge management systems", Electronic journal of management, vol. 10 No. 2, pp. 328-339.
[185] Wong, K.Y. (2005),"Critical success factors for implementing knowledge management in small and medium enterprises", Industrial Management & Data Systems, Vol. 104 No. 9, pp. 735-773.
[186] Wong, D., Su., Z. and Yang, D., "Organizational culture and knowledge creation capability", Vol. 15 No. 3 2011, pp. 363-373.
[187] Wuyts, S. and Geyskens, I. (2005), "The formation of buyer-supplier relationships: detailed contract drafting and close partner selection", Journal of Marketing, Vol. 69 No. 4, pp. 103-17.
[188] Yeh, Y., Lai, S. and Ho, C., "Knowledge management enablers: a case study", Industrial management and data systems, Vol. 106 No. 6, 2006, pp. 793-810.
[189] Young, M. and Post, J. (1993), "Managing to communicate, communicating to manage: how leading companies communicate with employees", Organizational Dynamics, Vol. 22 No.1, pp. 31-43
[190] Yu, T. and W, N. (2009), "A review of study on the competing value framework" International journal of business and management, Vol 4 No. 7, pp 37-42.

[191] Yuvan, Y.C., Gay, G. and Hembrooke, H. (2006), "Focused activities and the development of social capital in distributed learning community", The information society, vol. 22 No. 1, pp. 25-39.

[192] Zamantili Nayr, D. and Uzuncarsili, U. " A cultural perspective on knowledge management: the success story of sarkuysan company", Journal of knowledge management, Vol. 12 No. 2, 2008, pp. 141-155.

International Journal of Trend in Scientific Research and Development (IJTSRD)
Volume 5 Issue 2, January-February 2021 Available Online: www.ijtsrd.com e-ISSN: 2456 – 6470

Diagnosing Covid-19 by CRISPR Technology

Vijay Pratap Singh

M Tech, Department of Biotechnology, Delhi Technological University, New Delhi, India

ABSTRACT

In December 2019, a series of patients with symptoms resembling viral pneumonia with unknown etiology detected in Wuhan, China. A novel coronavirus is identified by the disease symptoms which resembles two families of coronavirus and known as COVID-19. COVID-19 is a disease which is associated with the infection of SARS-CoV-2. It becomes a pandemic disease globally because it spreads. CRISPR is a technology can be used for the diagnosis, which is a rapid, easy to implement and an accurate technology. CRISPR -Cas protein-based assay is used for the detection of SARS-CoV-2 infection. CRISPR based assay is an alternative method for other diagnostic techniques like RT-PCR assay because it is faster and more accurate than other techniques.

KEYWORDS: *COVID-19, SARS-CoV-2, CRISPR, RT-PCR, nCoV, ICTV, MERS-CoV, ACE2, Cas Protein, Cas9, IGIB*

How to cite this paper: Vijay Pratap Singh "Diagnosing Covid-19 by CRISPR Technology" Published in International Journal of Trend in Scientific Research and Development (ijtsrd), ISSN: 2456-6470, Volume-5 | Issue-2, February 2021, pp.303-307, URL: www.ijtsrd.com/papers/ijtsrd38400.pdf

IJTSRD38400

Copyright © 2021 by author(s) and International Journal of Trend in Scientific Research and Development Journal. This is an Open Access article distributed under the terms of the Creative Commons Attribution License (CC BY 4.0) (http://creativecommons.org/licenses/by/4.0)

INTRODUCTION

Beginning in December 2019, a series of patients with symptoms resembling viral pneumonia with unknown etiology detected in Wuhan, China. China has first reported to the WHO country office in China on 31 December 2019. However, the cause of disease with a clinical manifestation of infected patients include fever (77-98%), cough (59-81%), fatigue (38-98%) Malaga (11-34%), sputum production (28-56%), and headache (6-33%) and it spread rapidly throughout China. In the month of January 8, 2020, eventually novel coronavirus (nCoV) was identified as the seventh member of the Coronaviridae by the Chinese Centers for Disease Control and Prevention and disease symptoms resemble the other two families of coronavirus. A study group of the international committee of Taxonomy of Viruses (ICTV) proposed the name as severe acute respiratory syndrome coronavirus 2 (SARS-CoV-2) and the resulting disease termed 2019 novel coronavirus (2019-nCoV). On 30 January 2020 WHO declared it as an international public health emergency and 11 February 2020, WHO announced the name of the new coronavirus disease COVID-19.

In November 2002, the first cases of the coronavirus family reported as severe acute respiratory syndrome coronavirus (SARS-CoV) emerge in Guangdong, China that infected 8000 people and 774 deaths. Second reported, in 2012, known as Middle East respiratory syndrome coronavirus (MERS-CoV) which was first detected in Saudi Arabia. However, these pathogenic viral strains isolated from camels have affected 2494 individuals and caused 858 mortalities.

According to an epidemiological report severe acute respiratory syndrome coronavirus (SARS- CoV), Middle East respiratory syndrome coronavirus (MERS-CoV), and SARS-CoV-2 share many similar clinical symptoms. The most severe type of coronavirus can affect the respiratory tract in immunocompetent hosts and can cause viral pneumonia. It may also affect the gastrointestinal system, body organs such as heart, kidney, liver and central nervous system leading to multi-organ failure. However, patients infected with SARS and MERS have gastrointestinal symptoms (one third) than COVID19 patients. A recent study reported that male reproductive systems are susceptible to infection and dramatic changes in sex hormones have been Observed in patients suggesting gonadal function impairment. Different phases of the epidemic condition have also influenced the clinical characteristics of COVID-19.

The epidemiologic study by another group has reported the surface stability of SARS-CoV-2 and SARS CoV-1 under the experimental circumstances and both are similar. Similarly, an indication was made that the epidemiologic characteristic feature of these viruses probably arises from other factors. Thus, the result of the virus can remain viable and contagious in aerosols for several hours and days on surfaces (depending on the inoculum shed). As seen that more pathogenic viruses that are well transmitted between humans can usually be contained effectively implicated through syndromic (high fever) surveillance and contact tracing, for example, SARS-CoV-2 and, more recently, Ebola virus.

1. Evolution of 2019-nCoV:

Coronavirus is a class of genetically diverse viruses found in a wide range of host species, including birds and mammals. Coronaviruses are members of the subfamily Coronavirinae in the family *Coronaviridae* and the order Nidovirales. Based on their phylogenetic relationship, this subfamily consists of four genera Alphacoronavirus, Betacoronavirus, Gammacoronavirus and Deltacoronavirus. The

alphacoronaviruses and betacoronaviruses cause infection in gastroenteritis of human. The gamma coronaviruses and delta coronaviruses infect birds, but some of them can also be responsible to infect mammals. However, based on current sequence databases, domestic animals may have important roles as intermediate hosts that enable virus transmission from natural hosts to humans. Also, domestic animals themselves can suffer a disease caused by bat-borne or closely related coronaviruses. A study reported that 4 out of 9 betacoronavirus species were identified only in bats.

Structure and pathogenic mechanism:

COVID-19 is a spherical or pleomorphic enveloped particle containing single-stranded RNA positive-sense RNA viral genome, encodes several structural proteins, including the spike and glycosylate protein (S). This S protein mediates host cell invasion by SARS-CoV-2 via binding to a receptor protein called angiotensin-converting enzyme 2 (ACE2) located on the surface membrane of host cells inducing host immune responses. To complete the entry of into the host cell Following initial process, the interaction between viral S protein use the cellular attachment factor ACE2 and the cellular protease TMPRSS2 for their activation is of significant interest since it initiates the infection process.

There are many other viral proteins in the membrane and the most abundant structural protein is the membrane glycoprotein. The 3D structure of viral S protein determines by Cryogenic Electron Microscopy has revealed that the binding affinity of SARS-CoV-2 S protein to ACE2 is about 10–20 times higher than that of SARS-CoV S protein. It is speculated that this may contribute to the reported higher transmissibility and contagiousness of SARS-CoV-2 as compared to SARS- CoV.

Researchers identified that the COVID19 geometrical similarity differs from SARS-CoV about 79% and MERS-CoV about 50%. Sequence alignment and homology modelling show that SARS-CoV and SARS-CoV-2 share a highly conserved receptor-binding domain (RBD). Current evidence reported that S protein of SARS-CoV-2 functionally divides into two subunits which consist of 1253aa and these amino acid shares 75% of identity. These two subunits S1 and S2 play an important role in binding to the receptor and cell membrane fusion activity, respectively. S1 is further divided into two domains: first, N-terminal domain (NTD) and the C-terminal domain (CTD). Each domain has a different function like CTD functions as the RBD and is responsible for binding ACE2 and entering cells. Whereas the NTD display a structural fold as human galectins, galactose-binding lectins, and hence, in other caves, a carbohydrate present at the cell surface assist as an attachment factor. After binding to ACE2 receptor, viral S protein catalyses fusion of the viral and cellular membrane to allow access of the viral genome to the cytosol, starts replication and infect host.

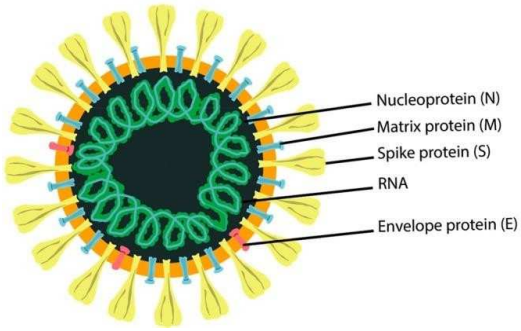

Fig Structure of COVID -19

2. CRISPR:

CRISPR (**C**lustered **R**egularly **I**nterspaced **S**hort **P**alindromic **R**epeats) is a technique of gene editing in which the Cas9 protein and several other Cas proteins are utilized along with the specific guide RNAs and used to either disrupt host genes or insert sequences of interest. Initially this technique is used in bacteria as an adaptive immunity response, then CRISPR have been utilized in the various biological fields as a new alternative to genome engineering. As compared to other diagnosis technique, CRISPR is a cheaper alternative to other gene editing techniques such as zinc fingers and is quickly being adopted as the best technique for gene editing and diagnosis.

About Cas:

Cas (**C**RISPR **as**sociated protein) is a naturally occurring enzyme found in some bacteria that is used for immunity. Cas protein works by using guide RNA with short sequences complementary to potential foreign DNA, combating infection. This mechanism has similarities to RNA interference found in many eukaryotes. Because of its capabilities, Cas9 has been used recently in experiments to serve as a genome editing tool.

How CRISPR works:

1. First, the Cas protein with designing guide RNA [s] are injected into developing embryos.
2. Once they get inside the cell body, Cas protein searches for the targeted DNA sequence that is complementary to the sequence in the designed guide RNA.
3. The DNA helix is unwinding by Cas protein when the sequence is recognized.
4. After the DNA has been unwound, Cas9 creates a double stranded breaks in the cell's DNA.
5. After that, the double-stranded break is repaired by the repair enzyme along with the integration of new experimental DNA.

3. CRISPR as a Diagnosis Technique for COVID-19:

There is various diagnosis method for COVID-19 based on the symptoms, the techniques are chest CT (Computed tomography scan) scans and QRT-PCR (Quantitative reverse transcription polymerase chain reaction). Currently, the QRT - PCR technique is the standard molecular detection method for COVID-19 (SARS-CoV-2), approved by the CDC and World Health Organization (WHO). Recently, a coronavirus rapid detection method is proposed by the researchers which is based on CRISPR/Cas system with the advantages of sensitivity, specificity, rapidity, and simplicity.

CRISPR/Cas (Clustered Regularly Interspaced Short Palindromic Repeats) is an adaptive immune system in archaea and bacteria against foreign genetic elements such as phages. Recently, CRISPR/Cas is used as a powerful gene editing tool and treatment for genetic diseases and cancers. In this technique, we used a protein linked with the guide RNA, which helps it attaches to the target site by a guide RNA and cleaved of the target sequence. There are several types of Cas proteins that have different properties. Among them, Cas9 protein has received more attention for gene editing whereas, Cas12a and Cas13a have been more efficient in diagnosis of diseases. Cas12a is DNA-specific, but Cas13a works with RNA, which makes it convenient in the detection of SARS-CoV-2.

Diagnosis

Recently, Zhang *et al* reported specific high-sensitivity enzymatic reporter unlocking (SHERLOCK) technology,

which is a CRISPR/Cas13 based nucleic acid detection technique for rapid detection of SARS-CoV-2.

In this diagnostic technique, the ORF 1ab and S protein genes in the genome of coronavirus are targeted. This SHERLOCK technique uses ssRNA or ssDNA reporter used is labelled with a quenched green fluorescent molecule.

- First, the RNA is purified from the patient sample as in the other diagnostic techniques.
- Cas 12a/ Cas 13 proteins identifies the targeted sequence that is ORF 1ab and S protein genes in the genome of corona virus and binds to it.
- An ssDNA reporter labelled with a quenched green fluorescent molecule was introduced, which will be cleaved by Cas protein when there is a nucleic acid of SARS-CoV-2 in the detection system.
- When the fluorescent molecule is cleaved, this results in the emission of green fluorescence can be seen with the naked eye under 485 nm light.
- The viral genome is detected at attomolar concentration using this technology.

To improve the sensitivity of the reaction, targeted DNA or RNA can be amplified by Recombinase Polymerase Amplification (RPA) or reverse transcriptase-RPA (RTRPA). Application of CRISPR/Cas13 based diagnosis or SHERLOCK for SARS-CoV-2 detection is much faster than detection by QRT-PCR and has high sensitivity. So, it can replace QRT-PCR technique.

4. PROCEDURE:

RNA is isolated and purified from the patient sample.

↓

After purification of RNA, RT-RAA is performed which is reverse-transcription recombinase- aided amplification assay. It takes approx. 30 min at 39 degree Celsius.

↓

Add ssDNA reporter labelled with fluorescent to the amplified sample and incubate for 15 min. At 37 degree Celsius.

↓

Then observe the sample, if there is emission of green fluorescence then it will be a positive sample and if there is no fluorescence then it will be a negative sample.

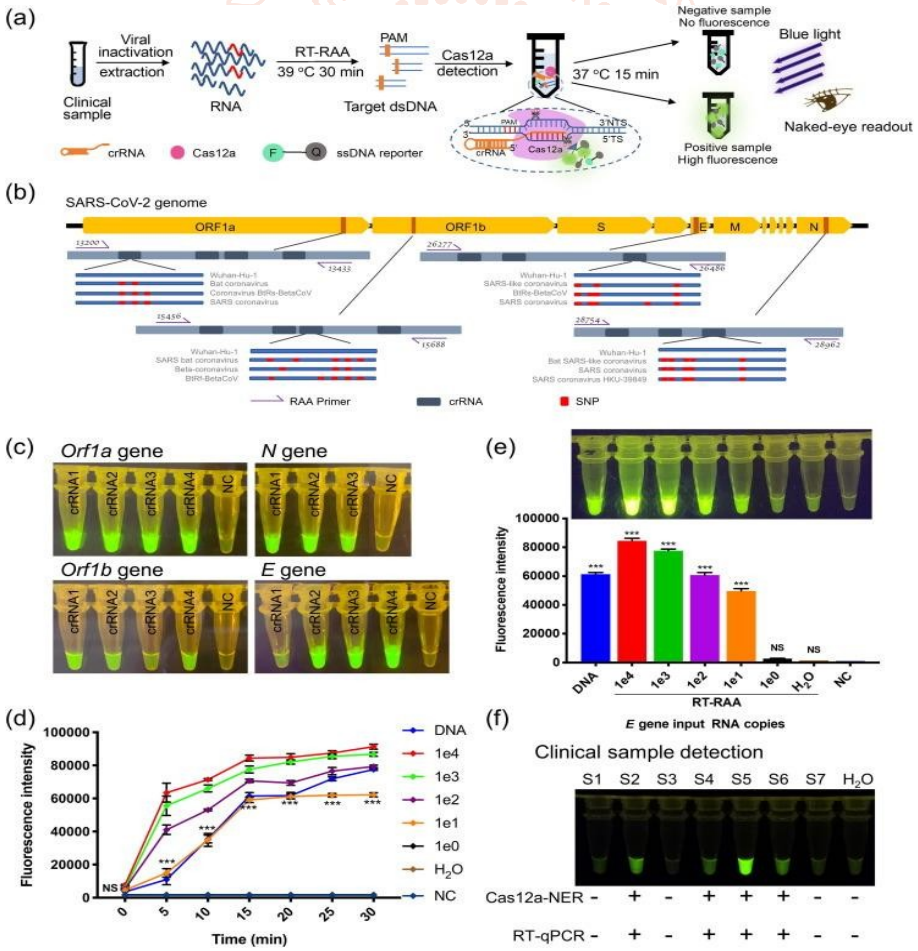

CRISPR/Cas12a-based detection with naked eye readout (CRISPR/Cas12a-NER) of SARS-CoV-2. (a) Schematic of Cas12a-based assay for rapid and visual nucleic acid detection. After 30 min of RT-RAA reaction, the Cas12a enzyme targets cleavage for an additional 15 min. The green fluorescent signals can be observed by the naked eye under blue light with a wavelength of 485 nm. (b) Four target gene fragments and SARS-CoV-2-specific crRNAs location on the genome. (c) Validation of crRNA specifically reacts with the target gene. (d) Time course of *E* gene detection with *E*-crRNAmix on gradient diluted input RNAs from 1e4 to 1e0 copies. (e) Sensitivity assay using *E*-crRNAmix to detect gradient diluted *E* gene RNA from 1e4 to 1e0 copies. (f) Diagnostic accuracy of CRISPR/Cas12a-NER on the diagnosis of COVID-19 clinical samples. ***: statistical significance; NS: not significance.

5. INDIA'S CRISPR BASED COVID -19 TEST- 'FELUDA'

On 19 SEP 2020, the Tata CRISPR (Clustered Regularly Interspaced Short Palindromic Repeats) test, powered by CSIR-IGIB **(*Institute of Genomics and Integrative Biology*)** FELUDA, received regulatory approvals today from the Drug Controller General of India (DCGI) for commercial launch, as per ICMR guidelines, meeting high quality benchmarks with 96% sensitivity and 98% specificity for detecting the novel coronavirus.

This test is developed which uses cutting-edge CRISPR technology for detection of the genomic sequence of SARS-CoV-2 virus.

The Tata CRISPR test is the world's first diagnostic test to deploy a specially adapted Cas9 protein to successfully detect the virus causing Covid-19. This marks a significant achievement for the Indian scientific community, moving from R&D to a high-accuracy, scalable and reliable test in less than 100 days. The Tata CRISPR test achieves accuracy levels of traditional RT-PCR tests, with quicker turnaround time, less expensive equipment, and better ease of use. Moreover, CRISPR is a futuristic technology that can also be configured for detection of multiple other pathogens in the future. The effort is the result of a fruitful collaboration between the scientific community and industry. The Tata Group has worked closely with CSIR-IGIB and ICMR to create a high- quality test that will help the nation ramp up Covid-19 testing quickly and economically, with a 'Made in India' product that is safe, reliable, affordable, and accessible. Scientists from Delhi based - Institute of Genomics and Integrative Biology (IGIB) would work together with Tata Sons to develop India's first paper-strip test for rapid diagnosis of Covid-19.

RESULT AND CONCLUSION:

COVID-19 is a pandemic disease, and in this report we introduce a rapid detection method of coronavirus which is CRISPR-based technology. This assay can detect the viral gene in 45 min. and does not need any special instrument and professional operations. Also, the result of CRISPR assay can be observed by naked eye because a fluorescent light is emitted in the positive sample. CRISPR based technology is more advantageous than qPCR and other detection techniques in sensitivity, specificity, rapidity, and simplicity. So, CRISPR based assay provides a simple and reliable on-site detection method.

REFERENCES:

[1] Agrebi S, Larbi A. Use of artificial intelligence in infectious diseases. Artificial Intelligence in Precision Health. 2020: 415-438. DOI: 10. 1016/B978-0-12-817133- 2. 00018

[2] Battegay M, Kuehl R, Tschudin-Sutter S, Hirsch HH, Widmer AF, Neher RA. 2019-novel Coronavirus (2019-n CoV): estimating the case fatality rate-a word of caution. Swiss Med Wkly 2020; 150:w20203. [PubMed] [Google Scholar]

[3] Broughton JP, Deng W, Fasching CL, Singh J, Chiu CY, Chen JS. A protocol for rapid detection of the 2019 novel coronavirus SARS-CoV-2 using CRISPR diagnostics: SARS- CoV-2 DETECTR.

[4] Chen J. S., Ma E., Harrington L. B. Crispr-cas12a target binding unleashes indiscriminate single-stranded dnase activity. Science. 2018; 360:436–439. [PMC free article] [PubMed] [Google Scholar]

[5] Chu D. K. W., Pan Y., Cheng S. M. S. Molecular diagnosis of a novel coronavirus (2019- ncov) causing an outbreak of pneumonia. Clin Chem. 2020; 66:549–555. [PMC free article] [PubMed] [Google Scholar]

[6] Control CfD, Prevention. Frequently Asked Questions and Answers: Coronavirus Disease 2019 (COVID-19) and Pregnancy. Accessed; 2020.

[7] Creutzburg S. C. A., Wu W. Y., Mohanraju P. Good guide, bad guide: spacer sequence- dependent cleavage efficiency of cas12a. Nucleic Acids Res. 2020; 48:3228–3243. [PMC free article] [PubMed] [Google Scholar]

[8] Cui, J., Li, F. & Shi, Z. Origin, and evolution of pathogenic coronaviruses. *Nat Rev Microbiol* 17, 181–192 (2019). https://doi.org/10.1038/s41579-018-0118-9

[9] Gootenberg J. S., Abudayyeh O. O., Lee J. W. Nucleic acid detection with crispr- cas13a/c2c2. Science. 2017; 356:438–442. [PMC free article] [PubMed] [Google Scholar]

[10] Gorbalenya AE. Severe acute respiratory syndrome-related coronavirus–The species and its viruses, a statement of the Coronavirus Study Group. BioRxiv 2020.

[11] Hryhorowicz M, Lipiński D, Zeyland J, Słomski R. CRISPR/Cas9 immune system as a tool for genome engineering. Arch Immunol Ther Exp (Warsz) 2017; 65(3):233–240. [PMC free article] [PubMed] [Google Scholar]

[12] https://global.infervision.com/

[13] https://robotics.sciencemag.org/content/5/40/eabb5589

[14] https://www.futurithmic.com/2020/03/27/how-ai-might-help-diagnose-track-covid-19/

[15] https://www.nejm.org/doi/full/10.1056/NEJMc2004973?query=recirc_mostViewed_railB_article

[16] https://www.who.int/emergencies/diseases/novel-coronavirus-2019

[17] hYang Z, Zeng Z, Wang K, et al. Modified SEIR and AI prediction of the epidemics trend of COVID-19 in China under public health interventions. J Thorac Dis. 2020; 12(3):165– 174. doi:10. 21037/jtd. 2020. 02. 64

[18] Jin Y. H., Cai L., Cheng Z. S. A rapid advice guideline for the diagnosis and treatment of 2019 novel coronavirus (2019-ncov) infected pneumonia (standard version) Mil Med Res. 2020; 7:4. [PMC free article] [PubMed] [Google Scholar]

[19] Jin YH, Cai L, Cheng ZS, Cheng H, Deng T, Fan YP, et al. A rapid advice guideline for the diagnosis and treatment of 2019 novel coronavirus (2019-nCoV) infected pneumonia (standard version). Mil Med Res 2020; 7(1):4. [PMC free article] [PubMed] [Google Scholar]

[20] Jiumeng Sun., Wan-Ting He., et al., COVID-19:

Epidemiology, Evolution, and Cross- Disciplinary Perspectives, Trends in Molecular Medicine, 2020,

[21] Juan A. Siordia, Epidemiology and clinical features of COVID-19: A review of current literature, Journal of Clinical Virology, Volume 127, 2020, 104357, ISSN 1386-6532,

[22] Kellner MJ, Koob JG, Gootenberg JS, Abudayyeh OO, Zhang F. Author Correction: SHERLOCK: nucleic acid detection with CRISPR nucleases. Nat Protoc 2020; 15(3):1311. [PubMed] [Google Scholar]

[23] Kim H. K., Song M., Lee J. *In vivo* high-throughput profiling of crispr-cpf1 activity. Nat Methods. 2017; 14:153–159. [PubMed] [Google Scholar]

[24] Lai CC, Shih TP, Ko WC, Tang HJ, Hsueh PR. Severe acute respiratory syndrome coronavirus 2 (SARS-CoV-2) and corona virus disease-2019 (COVID-19): the epidemic and the challenges. Int J Antimicrobial Agents 2020; 55(3):105924. [PMC free article] [PubMed] [Google Scholar]

[25] Li SY, Cheng QX, Wang JM, Li XY, Zhang ZL, Gao S, et al. CRISPR-Cas12a-assisted nucleic acid detection. Cell Discov 2018; 4(1):20. [PMC free article] [PubMed] [Google Scholar]

[26] Li Y, Glass Z, Huang M, Chen ZY, Xu Q. Ex vivo cell based CRISPR/Cas9 genome editing for therapeutic applications. Biomaterials 2020; 234:119711. [PMC free article] [PubMed] [Google Scholar]

[27] Lu R., Zhao X., Li J. Genomic characterisation and epidemiology of 2019 novel coronavirus: implications for virus origins and receptor binding. Lancet. 2020; 395:565–574. [PMC free article] [PubMed] [Google Scholar]

[28] Metsky HC, Freije CA, Kosoko-Thoroddsen T-SF, Sabeti PC, Myhrvold C. CRISPR- based COVID-19 surveillance using a genomically-comprehensive machine learning approach. BioRxiv 2020.

[29] Myhrvold C, Freije CA, Gootenberg JS, Abudayyeh OO, Metsky HC, Durbin AF, et al. Field-deployable viral diagnostics using CRISPR- Cas13. Science 2018; 360 (6387):444–448. [PMC free article] [PubMed] [Google Scholar]

[30] Rasmussen SA, Smulian JC, Lednicky JA, Wen TS, Jamieson DJ. Coronavirus Disease 2019 (COVID-19) and Pregnancy: What obstetricians need to know. Am J Obstet Gynecol 2020. [Epub ahead of print]. [PMC free article] [PubMed]

[31] Sexton NR, Smith EC, Blanc H, Vignuzzi M, Peersen OB, Denison MR. Homology-based identification of a mutation in the coronavirus RNA-dependent RNA polymerase that confers resistance to multiple mutagens. J Virol 2016; 90(16):7415–7428. [PMC free article] [PubMed] [Google Scholar]

[32] Shan F, Gao Y, Wang J, Shi W, Shi N, Han M, et al. Lung Infection Quantification of COVID-19 in CT Images with Deep Learning. arXiv preprint arXiv: 200304655. 2020.

[33] Wang D, Hu B, Hu C, Zhu F, Liu X, Zhang J, et al. Clinical characteristics of 138 hospitalized patients with 2019 novel coronavirus-infected pneumonia in Wuhan, China. JAMA 2020; 323(11):1061–1069. [PMC free article] [PubMed] [Google Scholar]

[34] World Health Organization Coronavirus disease 2019 (COVID-19): situation report, 45. 2020. https://www.who.int/docs/default-source/coronaviruse/situation-reports/20200305-sitrep-45-covid-19. pdf?sfvrsn=ed2ba78b_4

[35] Wu F., Zhao S., Yu B. A new coronavirus associated with human respiratory disease in China. Nature. 2020; 579:265–269. [PMC free article] [PubMed] [Google Scholar]

[36] Wu Z, McGoogan JM. Characteristics of and important lessons from the coronavirus disease 2019 (COVID-19) outbreak in China: summary of a report of 72 314 cases from the Chinese Center for Disease Control and Prevention. JAMA 2020; 323(13):1239–1242. [PubMed] [Google Scholar]

[37] Zhang F, Abudayyeh OO, Jonathan SG. A protocol for detection of COVID-19 using CRISPR diagnostics. https://www.broadinstitute.org/files/publications/special/COVID- 19%20detection%20(updated).pdf.

JOURNAL OF MECHANICAL ENGINEERING AND SCIENCES (JMES)
ISSN: 2289-4659 e-ISSN: 2231-8380
VOL. 15, ISSUE 1, 7894 – 7906
DOI: https://doi.org/10.15282/jmes.15.1.2021.23.0623

ORIGINAL ARTICLE

Effect of layering pattern and fiber hybridization on viscoelastic properties of PALF/COIR hybrid epoxy composites

Mohit Mittal[1] and Rajiv Chaudhary[1]

[1] Department of Mechanical Engineering, Delhi Technological University, Delhi – 110042, India
Phone: +91-7988368530

ABSTRACT – To design and develop a hybrid biocomposite material for structural applications, it becomes necessary to determine the optimum fibers layering pattern. Therefore, in this research work, the different layered hybrid biocomposite boards i.e. bilayer pineapple/coir (P/C), trilayer (PCP, CPC), and intimately mixed (IM) were developed and characterized for viscoelastic properties. The composites were made by hand lay-up method, keeping the volume ratio of PALF and COIR 1:1 and the total fiber volume fraction is 0.40 volume of composite. Dynamic mechanical thermal analysis test was employed to characterize the viscoelastic behavior in terms of storage modulus, loss modulus, loss damping factor, and the glass transition temperature. Amongst all the different layered hybrid composites, the trilayer CPC has lowest value (0.635) of effectiveness coefficient with highest stiffness and activation energy (40.54 kJ/mole). It confirms the better fiber-matrix interaction at the interfacial region. The glass transition temperature of CF-EP and PF-EP was increased by 8.74% and 13.15% respectively by the synergistic hybridization of cellulosic fibers. The PCP layered composite possesses lowest value of phase transition energy (9.17 kJ/mole) and this was because of the poor fiber-matrix interfacial adhesion.

ARTICLE HISTORY
Received: 20th Oct 2019
Revised: 07th May 2020
Accepted: 07th Aug 2020

KEYWORDS
Pineapple leaf fiber;
coconut husk fiber;
polymer composite;
dynamic mechanical thermal analysis;
glass transition temperature

INTRODUCTION

The increased awareness towards sustainability, product recyclability, and depletion of fossil fuels leads to the progressive utilization of green bio-based product and processes in various applications such as automotive, building and construction, railways, marine, and packaging. The lignocellulosic plant based fibers and their composites are active and feasible solution to replace non-renewable synthetic materials and it was due to their wide verities of profitable properties such as low cost, low density, high specific strength and stiffness, energy and ecological balance, and problem-free disposal at the end of use [1]. Amongst all the cellulosic strands, the pineapple leaf fiber (PALF) and coconut husk fiber (COIR) are enjoying a lot of attention for industrial and household applications and it was attributed to their superior physical, thermal, and mechanical properties. B.T. Mulyo et al. [2] have also proved the positive attributes of PALF based material as an alternative material for Indonesia National Standard (SNI) helmet. The COIR and PALF can be obtained from the fibrous husk (mesocarp) of coconut palm and the leaves of the pineapple fruit respectively using the biological and mechanical retting process. According to the report (2016) of Food and Agriculture Organization (FAO) entitled as "The State of Food and Agriculture", the total production of pineapple (Ananas-comosus) and coconut (Cocos-nucifera) in India is 1.9 and 11.1 million tonnes respectively.

PALF and COIR are multi-cellular fibers that consist of high cellulose (70-82%) and high lignin (40-45%) content respectively. Due to the presence of high cellulosic and low lignin content in PALF, it exhibits better tensile and flexural strength than the most commonly used natural fibers. As compared to PALF, the COIR is tougher, resilient, and highly durable in nature. Therefore, to combine their properties synergistically, it becomes necessary to incorporate them in the same polymeric matrix. The hybridization of stiffer fiber with the high strain to failure one leads to the improvement in impact energy absorbing capacity of material [3]. The combination of COIR and PALF may lead to the improved quality of performance. In most of the cases, the hybrid biocomposites have better or comparable performance than the glass fiber reinforced composites (GFRCs). The key benefits of hybrid composites over the single fiber reinforced ones are that they possess better impact strength, fatigue strength, and fracture toughness with significant amount of weight saving [4]–[12]. In order to make composites for various structural applications, it is desirable to test them in oscillating load, frequency, and dynamic thermal conditions.

Dynamic mechanical thermal analysis (DMTA) is a potent technique to interpret the structure/property relationship of a composite material. It can be used to analyze the effect of hybridization, fiber-resin volume fraction, fiber geometrical parameters and fiber orientation on the thermo-mechanical performance of a composite. The stiffness and damping behavior of a polymer and polymer based composites can be determined in terms of storage modulus (E' or G'), loss modulus (E"), and loss damping factor (tan δ). S.K Saw et al. [13] examined the effect of layering pattern on dynamic mechanical properties of Jute/Bagasse hybrid composites. C. Capela et al. [14] studied the effect of fiber length on the dynamic mechanical properties of carbon fiber reinforced composites. A. Chafidz et al. [15] investigated the effect of

*CORRESPONDING AUTHOR | M. Mittal | ✉ mohit.30mittal@gmail.com

© The Authors 2021. Published by Penerbit UMP. This is an open access article under the CC BY license.

date palm fiber loading on the thermal and rheological properties of HDPE based composites. Q. Ahsan et al. [16] declared the positive impact of nano fibrillated kenaf fiber addition on the tensile properties of PLA based composites. Y. Nishitani et al. [17] investigated the viscoelastic properties of untreated and treated hemp fiber filled polyamide 1010 composites. W.S. Widodo et al. [18] examined the influence of ramie fiber addition on the sealing characteristics of silicon rubber gaskets and reported that the composite has better sealing performance than the pure silicon. J. Alexander et al. [19] reported that the storage modulus (E') of sisal/basalt/epoxy composite is higher than the sisal/glass/epoxy. S.S Chee et al. [20] evaluated the viscoelastic properties of kenaf/epoxy, bamboo/epoxy, and bamboo charcoal/epoxy composites and found that the kenaf/epoxy has higher E' and lower tan δ than the other composites. Y.S. Song et al. [21] examined the viscoelastic behavior of twill and plain woven Hemp/PLA composites and observed that the twill woven has higher stiffness and damping ability than the plain woven. S. Rwawiire et al. [22] examined the effect of bark cloth ply angle arrangement on viscoelastic properties of Bark/Epoxy composites. M. Idicula et al. [23] have examined the effect of layering pattern on the thermo-mechanical properties of Banana/Sisal/Polyester hybrid composites. R. Murugan et al. [24] reported that the Carbon/Glass/Carbon reinforced hybrid composite has higher storage and loss moduli than the single carbon, single glass, and hybrid Glass/Carbon/Glass-Epoxy composites. M. Jawaid et al. [25] analyzed the effect of layering pattern on dynamic mechanical characteristics of Jute/EFB filled epoxy based composites. They found that the Jute/EFB/Jute layered composite has higher stiffness than the EFB/Jute/EFB.

After reviewing the above mentioned work, it can be concluded that the relative arrangement of fibers significantly affect the overall performance of a hybrid composite. Therefore, this work considered the effect of different layering pattern on the viscoelastic properties of PALF/COIR hybrid composites. Moreover, the effect of fiber hybridization on the thermo-mechanical behavior of composites was also examined.

EXPERIMENTAL

Materials

The cellulosic fibers (PALF and COIR) were obtained from M/s Go Green Products, Chennai (India). Their physical properties and surface morphology are reported in Table 1 and Figure 1 respectively. The SEM micrographs revealed the network like structure that contains longitudinally oriented unit cells held together by lignin and fatty-waxy substances. The morphology of PALF is much smoother and continuous than the COIR and it is due to the presence of higher cellulose content and low fibril orientation angle (14^{O}). The epoxy resin [diglycidyl bisphenol-A (DGEBA)] and curing agent [tri-ethylene tetra-amine (TETA)] were obtained from M/s Sakshi Dies and Chemicals, Delhi (India). The typical properties of epoxy thermoset are mentioned in Table 2.

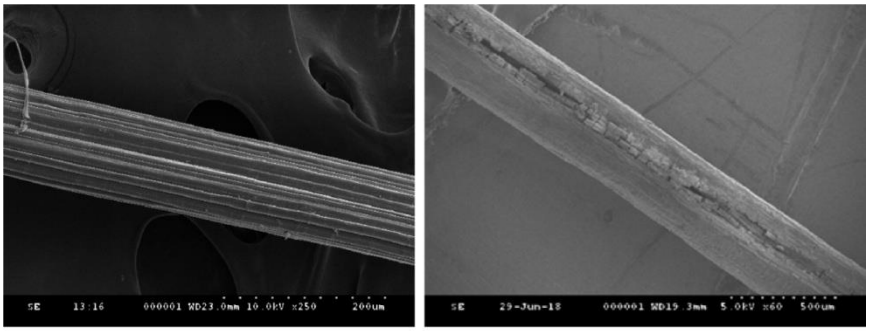

(a) (b)

Figure 1. Surface morphology of (a) PALF and (b) COIR

Table 1. Physical properties of PALF and COIR

Physical properties	PALF	COIR
Density (g/cm^3)	0.98	1.2
Cellulose (%)	70-82	32-43
Hemicellulose (%)	18.8	0.15-0.25
Lignin (%)	5-12.7	40-45
Pectin (%)	1.1	3-4
Moisture content (%)	11.8	8

Table 1. Physical properties of PALF and COIR (cont.)

Physical properties	PALF	COIR
Microfibrillar angle (deg)	14	30-49
Diameter (µm)	20-80	100-460
Tensile strength (MPa)	413-1627	131-220
Young's modulus (GPa)	34.5-82.5	4-6
Elongation at break (%)	1.6	15-40

Table 2. Typical properties of epoxy thermoset

The appearance of liquid resin	A clear pale yellow
Density (Kg/m^3)	1200-1250
Viscosity at 25^{O}C (cps)	550
Tensile strength (MPa)	11-15
Tensile modulus (GPa)	0.45-0.52
Flexural strength (MPa)	23-28
Flexural modulus (GPa)	1.3-1.7
Max. Elongation (%)	4.2-5.6
Flashpoint	> 2000C

Preparation of Composites

The randomly oriented dried and chopped fibers of length 20 mm were impregnated with medium viscosity epoxy resin in a glass mold cavity of dimensions 70 mm X 10 mm X 2 mm. The different layered composite specimens [bilayer {pineapple/coir (P/C)}; trilayer {pineapple/coir/pineapple (PCP), coir/pineapple/coir (CPC)}; and intimately mixed (IM)] were made by hand lay-up technique, keeping the volume ratio of PALF and COIR 1:1 and V_f equal to 0.40 V_c. Figure 2 illustrates the various layering pattern for PALF/COIR hybrid composites. In all composite samples, the volume ratio of epoxy resin (DGEBA) with hardener (TETA) was fixed as 2:1(v/v). Before using the thermoset matrix for molding, ensure that the resin was completely mixed with hardener and no air bubbles were present. To accomplish this, the mixing was done in a necked round glass flask through mechanical stirrer at room temperature for 20 minutes. The curing of composite was performed at room temperature for 24 h under the dead weight of 35 kg. The DMA test specimens (Figure 3) of dimensions 35 X 10 X 2 mm^3 were cut from the molded sheets and their designation are recorded in Table 3.

Table 3. Designation of DMTA test specimens

Designation	Details
EP	Neat Epoxy resin
CF-EP (1)	Coir fiber-Epoxy composite (frequency 1 Hz)
PF-EP (1)	Pineapple leaf fiber-Epoxy composite (frequency 1 Hz)
CPC (1)	COIR/PALF/COIR hybrid composite (frequency 1 Hz)
PCP (1)	PALF/COIR/PALF hybrid composite (frequency 1 Hz)
Bilayer (P/C) (1)	Bilayer (PALF/COIR) hybrid composite (frequency 1 Hz)
IM (1)	Intimately mixed hybrid composite (frequency 1 Hz)
CPC (5)	COIR/PALF/COIR hybrid composite (frequency 5 Hz)
PCP (5)	PALF/COIR/PALF hybrid composite (frequency 5 Hz)
Bilayer (P/C) (5)	Bilayer (PALF/COIR) hybrid composite (frequency 5 Hz)
IM (5)	Intimately mixed hybrid composite (frequency 5 Hz)

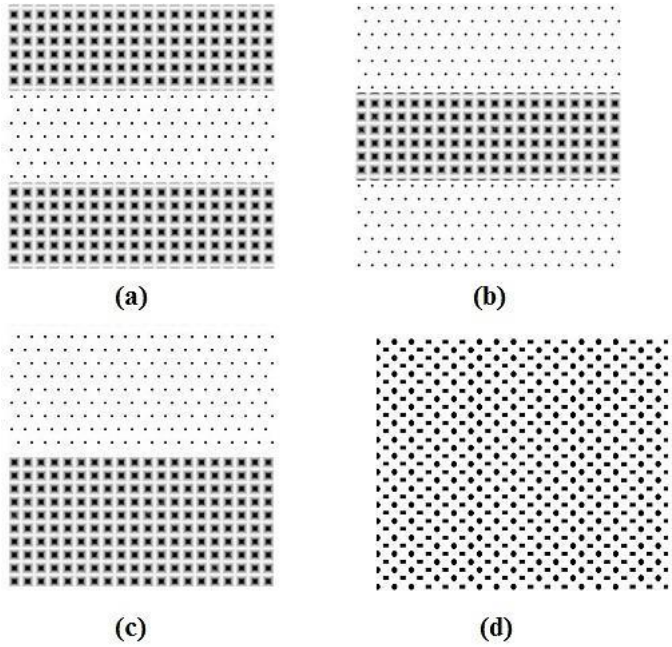

Figure 2. Different layering pattern of hybrid composites (a) PCP, (b) CPC, (c) Bilayer (P/C) and (d) IM

Figure 3. DMTA test specimens

Dynamic Mechanical Thermal Analysis (DMTA)

DMTA is a powerful technique in the development of composites aiming to establish a significant relationship between microscopic structure and thermo-mechanical properties. The comprehensive knowledge of viscoelastic properties such as stiffness, damping, thermal transition, melting & degradation, and crystallization is important for manufacturing a high-performance polymeric material. DMTA method has enormous potential to analyze the elastic and viscous response of polymer composites over a range of temperature, frequency, and time. The thermo-mechanical properties of a composite were determined using DMTA, Q800 instrument (Figure 4) which is supplied by Anamatrix Instrument Technologies Pvt. Ltd., Bangaluru (India). The specimens are of rectangular in shape having dimensions 35mm X 10mm X 2mm. They were used in double cantilever mode over a temperature range of 25-140^{O}C with the heating rate of 3^{O}C/min. The effect of frequency on storage modulus (E'), mechanical damping factor (tan δ), and glass transition temperature (T_g) has also investigated at two different frequencies, namely 1Hz and 5 Hz.

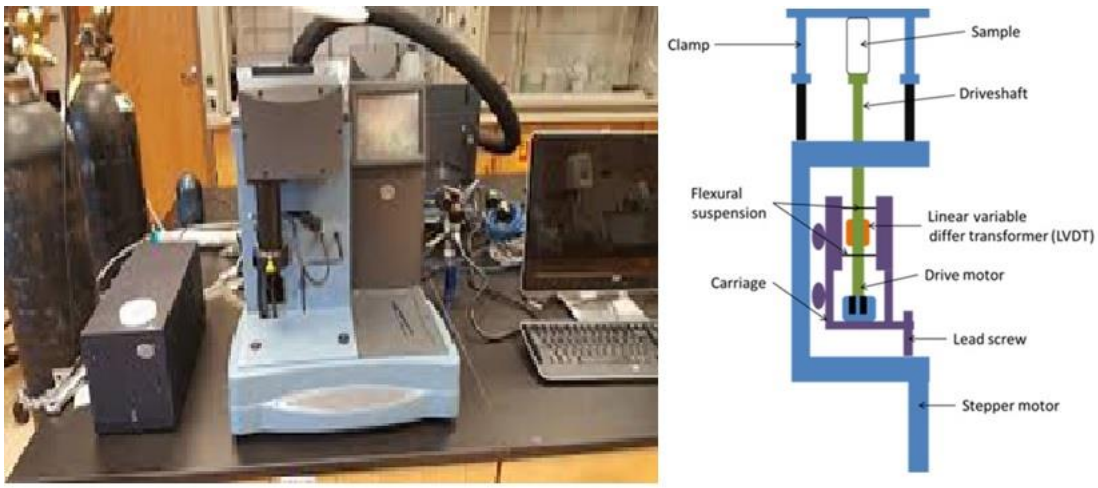

Figure 4. DMTA Q800 test instrument

RESULTS AND DISCUSSION

The thermo-mechanical behavior of a composite can be accurately assessed using the DMTA technique. DMTA is one of the most reliable and widely acceptable thermal analysis techniques that can record the viscoelastic response of polymer based composites under the sinusoidal load, temperature, and oscillation frequency. The test results which are reported in this section concerns the effect of layering pattern and fiber hybridization on the dynamic mechanical behavior of PALF/COIR hybrid composites in terms of storage modulus (E'), loss modulus (E''), and loss damping factor (tan δ).

Effect of layering pattern and fiber hybridization on the storage modulus (E')

The modulus curve provides the information about the viscoelastic rigidity and energy storage ability of a composite material. Figure 5 illustrates the effect of layering pattern and fiber hybridization on the storage modulus (E') of composites. The reinforced fibers and fillers play an active role to enhance the modulus of polymeric materials. The stiffness of thermoset resin was increased considerably by the incorporation of stronger and stiffer cellulosic fibers and this was attributed to the higher restriction of chain movements. The cross-linking density of epoxy polymer was increased after the loading of PALF and COIR. The E' curve approaches to lower values with the increase of temperature. Above the glass transition temperature (T_g), the E' of thermoset matrix was dropped sharply. The reinforcing fibers contribute much more for modulus at higher temperatures, above T_g than below it. It was due to the hydrodynamic mechanical action of reinforced fibers to impart constraints against the mobility, deformability, and relaxation of the macromolecular chain segments in viscoelastic medium. Irrespective of the fibers layering pattern, the stiffness of CF-EP was improved significantly by the incorporation of PALF. This was because of the synergistic compatibility between PALF and COIR. Among all the different layered hybrid composites, the bilayer (P/C) and trilayer CPC exhibits the higher E' below and above T_g (70^OC) respectively. The effectiveness of each fibers layering arrangement in regard to the increase of modulus can be determined by a coefficient 'C'.

$$C = \frac{{E'_G}/{E'_R}^{\text{Composite}}}{{E'_G}/{E'_R}^{\text{Resin}}} \quad (1)$$

where E'_G and E'_R are the storage modulus in the glassy and rubbery phase respectively.

The higher value of constant C signifies the poor effectiveness of fiber in regard to the increase of modulus. Usually, the filled systems have lower C value than the unfilled matrix polymer. Table 4 revealed that the CPC has lower 'C' value ($30\text{-}120^OC$) as compared to the other hybridized composites. This was due to the higher wettability of coir fiber, less void content, and the formation of more covalent bond at the interface. The 'C' value of CF-EP (0.7048) was reduced after the loading of PALF and it confirms the synergistic compatibility between reinforcing fibers. It was observed that the bilayer (P/C) and intimately mixed (IM) composites have approximately same modulus at T_g. But at higher temperature (above T_g), the E' of bilayer composite was significantly greater than the intimately mixed one.

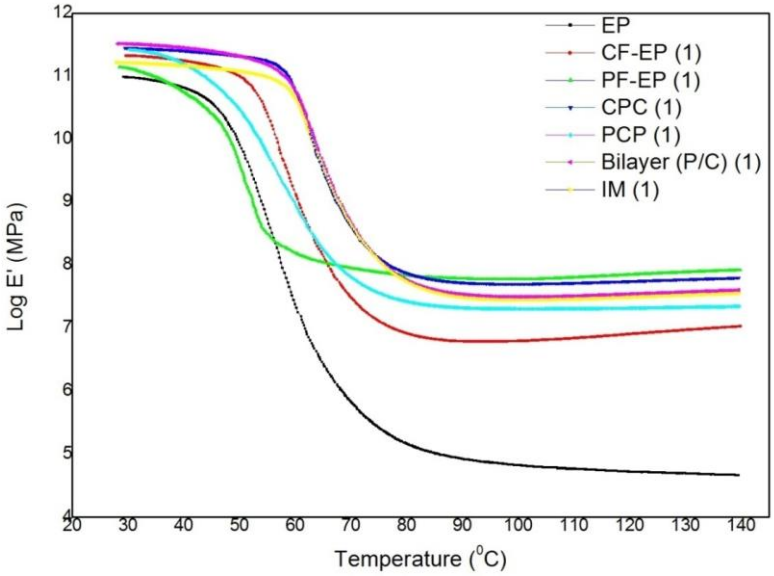

Figure 5. Effect of layering pattern and fiber hybridization with temperature on the storage modulus of fabricated composites at a frequency of 1 Hz

Effect of Layering Pattern and Fiber Hybridization on the Damping Loss Factor (tan δ)

The tan δ curve revealed the damping ability of a material. It provides indirect information about the stiffness, internal structure, interfacial characteristics, and the morphology of a composite. The damping ability of a composite depends on the orientation and distribution of fibers; fiber to matrix volume ratio; fiber/matrix interfacial interaction; and the concentration of void content. Figure 6 shows the tan δ curve of unhybridized and hybridized composites as a special reference of temperature. In all specimens, the tan δ curve goes on increasing and attains a peak value (phase transition region) followed by the reduction with the increase of temperature. The increment in tan δ peak corresponds to the greater mobility of small groups and chain segments. Table 4 revealed that the virgin epoxy occupies a higher tan δ_{max} value than the reinforced polymer composites. This was attributed to the hindrance in molecular motion induced by the reinforced fibers. Among all the hybrid composites, the trilayer PCP possesses shorter and wider tan δ peak. However, it occupies lower value of E' and T_g (62^{O}C) with higher coefficient 'C'. It confirms that the 'PCP' shows poor interfacial interaction with thermoset matrix and it was due to the presence more hydroxyl (-OH) group on the surface of PALF.

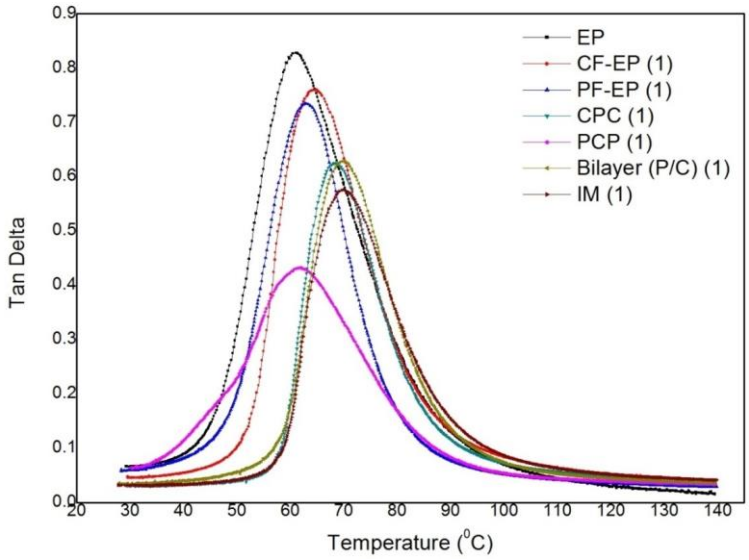

Figure 6. Effect of layering pattern and fiber hybridization with temperature on the loss damping factor (tan δ) of fabricated composites at a frequency of 1 Hz

The hybridization effect can be better understood in terms of T_g. The glass transition temperature (T_g) of CF-EP was increased from 64.9^{O}C to 68.51^{O}C and 70^{O}C in CPC and bilayer (P/C) arrangements respectively. The CF-EP exhibits

higher T_g than the PF-EP and it was due to the better interaction between COIR and epoxy matrix at the interfacial region. In comparison to the CPC, the bilayer and intimately mixed have higher value of glass transition temperature (T_g). Furthermore, they (Bilayer and IM) possess higher peak width with lower peak height than the CPC. This was due to the better distribution of fibers and effective stress transfer from matrix to fibers without the matrix cracking. The shifting of T_g to a higher value revealed the reinforcement effectiveness of fiber. In this context, the intimately mixed (IM) has higher reinforcing ability than the others. The better performance of intimately mixed banana/sisal composite was also reported by M. Idicula et. al [23].

Effect of Layering Pattern and Fiber Hybridization on the Loss Modulus (E'')

The loss modulus (E'') represents the ability of a material to dissipate mechanical energy as heat per cycle of sinusoidal viscoelastic deformation. Figure 7 shows the E'' curves of developed composites as a function of temperature. The E" of epoxy thermoset was increased significantly by the incorporation of cellulosic fibers (PALF and COIR). It confirmed the prominent effect of fibers to increase the frictional force at the fiber-matrix interface. The peak value of E'' corresponds to the glass transition temperature (T_g). Beyond T_g, the loss modulus curve drop down to lower values and it was due to the free movement of polymer chain segments. Table 4 revealed that the T_g (obtained from E'' curve) of epoxy matrix was increased after the loading of reinforcing fibers. It was attributed to the inhibition in chain relaxation process, rigidity of polymer chain segments, and elevation in heterogeneity within the composite material. The phase transition temperature (T_g) of CF-EP and PF-EP was positively shifted to a higher value after the synergistic hybridization. The glass transition temperature obtained from E'' curves is lower as compared to the values resulted from tan δ curve. The intimately mixed composite possesses highest value of T_g, followed by bilayer, CPC, and PCP.

Table 4. Values of the effectiveness coefficient 'C', tan δ peak height and width, glass transition temperature (T_g), E'' peak height, E' and E'' values at different temperature for virgin epoxy, pure coir fiber-epoxy, pineapple leaf fiber-epoxy, and the different layered hybrid composites

Composites	C	T_g from Tan δ_{max} (^OC)	Tan δ peak width	Tan δ peak height	T_g from E'' (^OC)	Log E'' Peak height (MPa)	Log E' (30^OC)	Log E' (50^OC)	Log E' (70^OC)	Log E' (90^OC)	Log E' (120^OC)	Log E'' (50^OC)	Log E'' (70^OC)
EP	-	61.2	23.66	0.83	44.3	8.79	10.98	9.6	5.83	4.93	4.72	8.78	5.29
CF-EP	0.70	64.9	20.39	0.76	55.88	9.14	11.33	10.99	7.45	6.79	6.91	8.71	7.02
PF-EP	0.61	62.9	19.08	0.73	52.17	9.21	11.12	9.9	7.95	7.79	7.85	9.16	7.02
CPC	0.64	68.51	17.12	0.63	61.56	9.21	11.45	11.32	8.61	7.73	7.75	8.12	8.12
PCP	0.67	62	27.52	0.43	49.24	9.14	11.42	10.46	7.81	7.33	7.32	8.99	6.71
Bilayer	0.66	70	18.64	0.63	62	9.13	11.51	11.33	8.68	7.54	7.54	8.46	8.22
IM	0.64	70	20.13	0.58	62.23	8.93	11.22	11.08	8.64	7.49	7.49	7.92	8.09

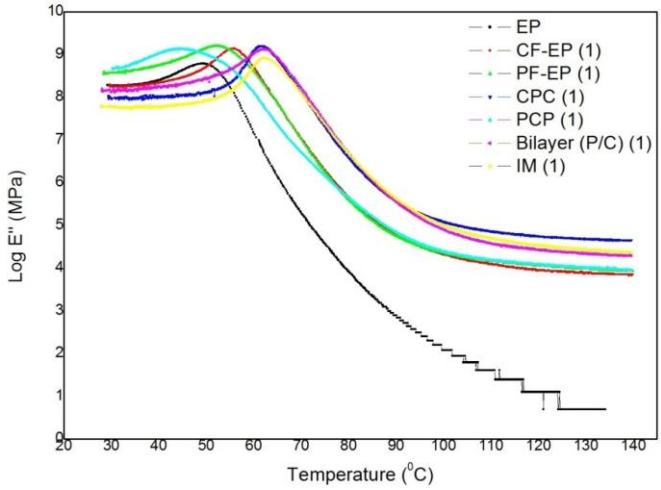

Figure 7. Effect of layering pattern and fiber hybridization with temperature on the loss modulus of fabricated composites at a frequency of 1 Hz

Effect of Frequency

The dynamic behavior of a material depends on the time, temperature, and frequency of oscillation. To characterize the viscoelastic behavior of polymer-based composites, it becomes necessary to analyze the effect of frequency on storage modulus (E'), loss modulus (E''), loss damping factor (tan δ), and the glass transition temperature (T_g). Figure 8 shows the variation in E' as a special reference of frequency and temperature. In all cases, the E' was increased with the increase of frequency of oscillation from 1 Hz to 5 Hz. It follows the same line of action as in the previous research works [Idicula et. al [23], Pothan et. al [26], Romanzini et. al [27], Mittal et al. [28]]. The static and dynamic moduli were found to be decreased over a long period of time and this may be due to the rearrangement of molecules in order to overcome the localized stresses. It was observed that the E' was decreased dramatically with the increase of temperature from 55^{O}C to 110^{O}C and it was due to the breakage of covalent bonding between the fibers and matrix resin.

The damping ratio (tan δ) is also influenced by the frequency of oscillation (Figure 9). At a higher frequency (5 Hz), the composites have higher value of tan δ_{max} and T_g. This behavior assured the higher degree of cross-linkage between polymeric chain segments. The tan δ peak and its corresponding temperature (T_g) is linked with the process of partial loosening of the polymeric structure and the cross-linkage density. Table 5 shows that the peak width of tan δ curve becomes broader by the increase of frequency from 1 Hz to 5 Hz. Similar to tan δ curve, the peak of E'' was shifted to the higher value with the increase of frequency (Figure 10 and Table 5). The response of the viscoelastic materials may vary with temperature and oscillation frequency. Therefore, it becomes significant to plot a three-dimensional thermogram (Figure 11) which represents the combined effect of frequency and temperature on the damping ratio of developed composites.

Table 5. Effect of frequency on viscoelastic properties of hybrid composites

Composite	T_g from tan δ_{max} (^{O}C)	Tan δ peak height	Tan δ peak width	T_g from E'' (^{O}C)	Log E'' peak height (MPa)
CPC (1)	68.51	0.63	17.12	61.56	9.206
CPC (5)	70.1	0.656	20.91	62.55	9.577
PCP (1)	62	0.43	27.52	49.24	9.138
PCP (5)	68.16	0.528	25.99	54.5	9.35
Bilayer (P/C) (1)	70	0.63	18.64	62	9.130
Bilayer (P/C) (5)	73.7	0.622	22.88	63.08	9.212
IM (1)	70	0.58	20.13	62.23	8.928
IM (5)	73.36	0.619	24.19	62.35	9.28

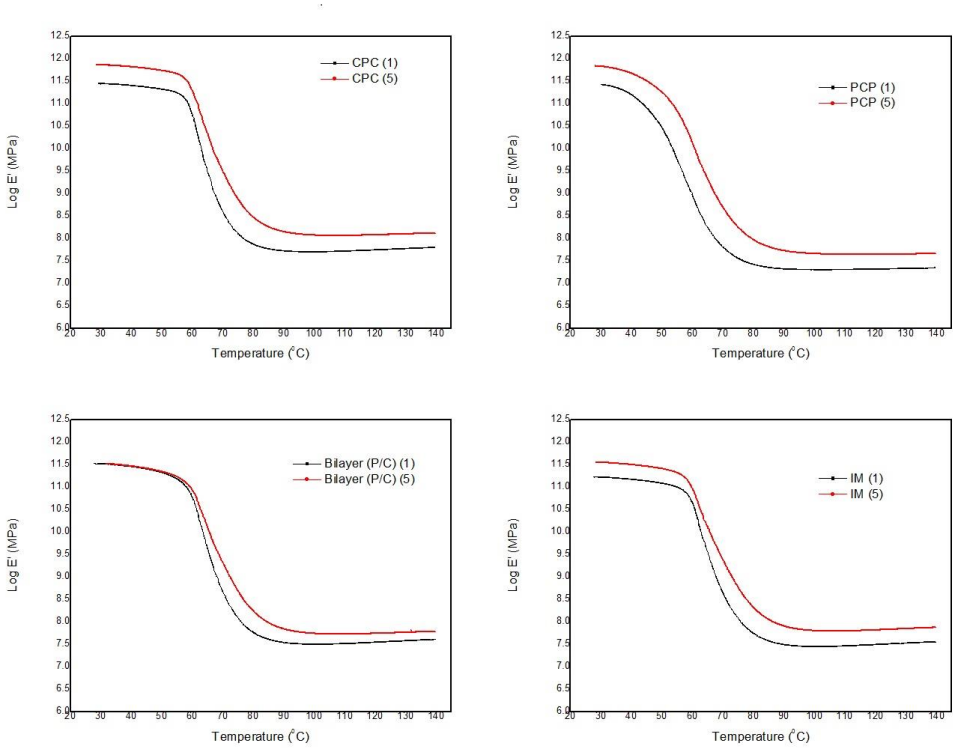

Figure 8. Effect of frequency with temperature on the storage modulus of fabricated hybrid composites

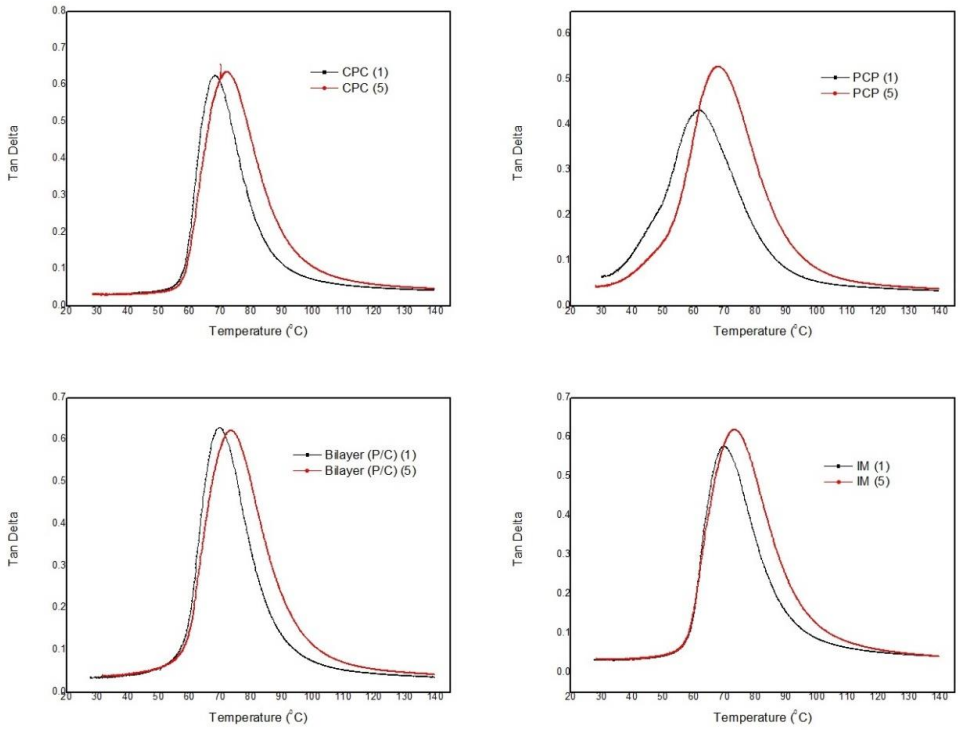

Figure 9. Effect of frequency with temperature on the damping ratio (tan δ) of fabricated hybrid composites

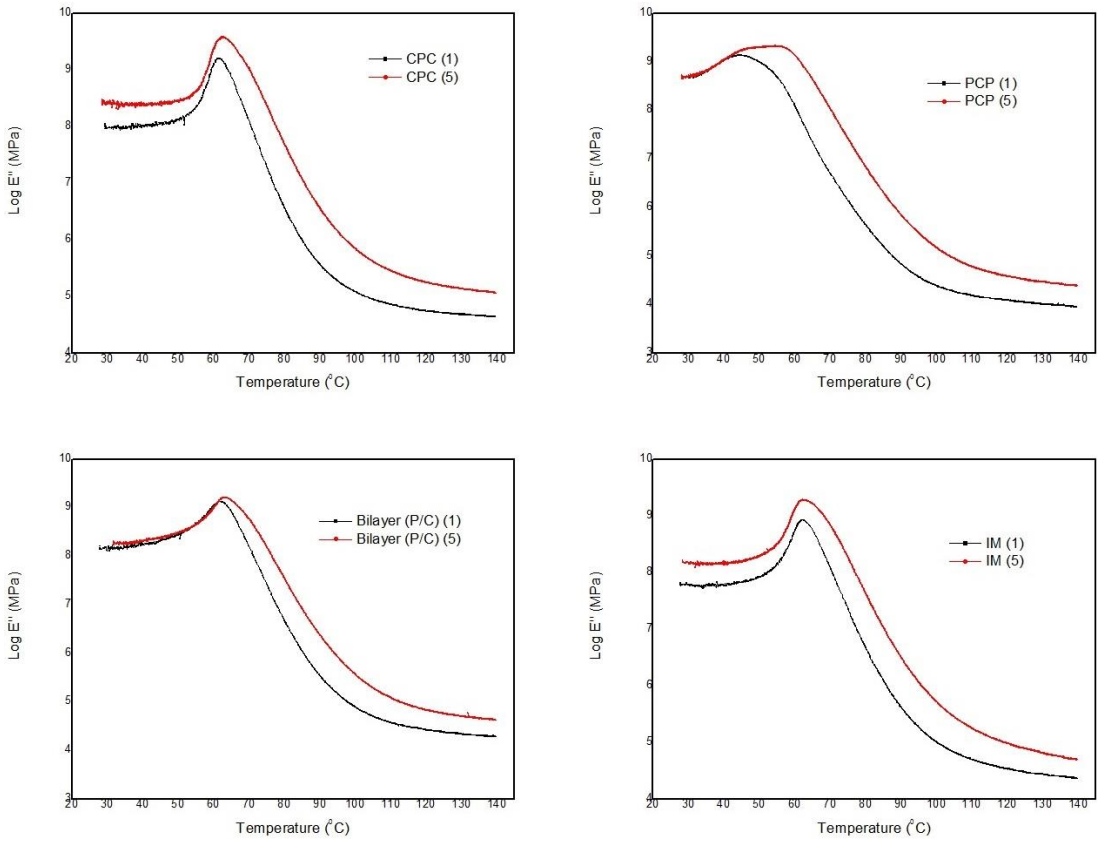

Figure 10. Effect of frequency with temperature on the loss modulus of fabricated hybrid composites

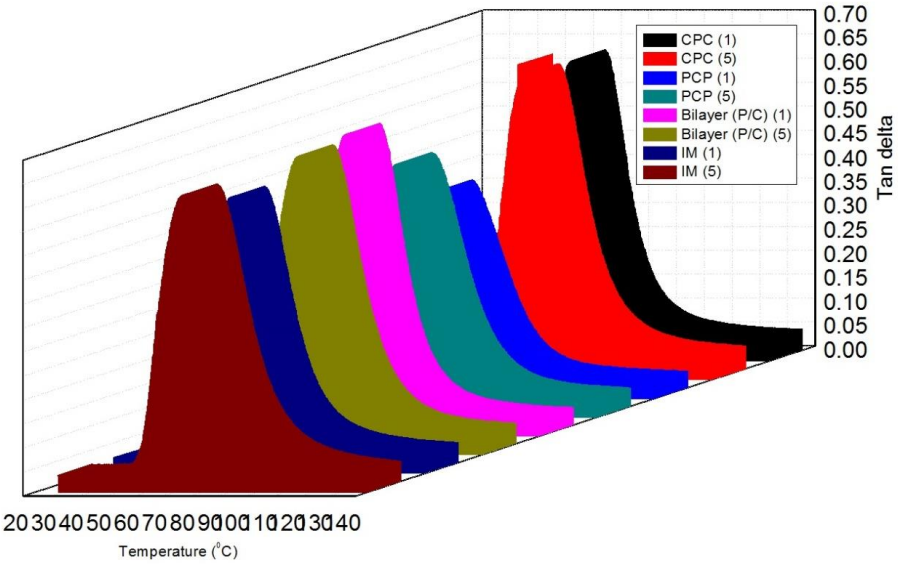

Figure 11. Three dimensional thermogram of different layered PALF/COIR hybrid epoxy composites

The Energy of Activation for Phase Transition

The energy required for phase transition from the glassy state to rubbery state can be easily and accurately determined using the Arrhenius equation:

$$f = f_0 \exp\left(-\frac{E}{RT}\right) \quad (2)$$

where f is the measuring frequency, fo is the frequency when T approaches infinity, T is the glass transition temperature obtained from tan δ curve analysis, E is the activation energy, and R is the gas constant. The calculated activation energy for the different layered hybrid composites is mentioned in Table 6. It was observed that the CPC and PCP have highest and least value of activation energy. This outcome is in favor of the extent of reinforcement.

Table 6. The activation energy for the different layered hybrid composites

Hybrid composites	Activation energy (kJ/mole)
CPC	40.54
PCP	9.179
Bilayer (P/C)	18.65
IM	20.45

Cole-Cole Plots

The Cole-Cole plot is an effective and valuable tool to fully characterize the viscoelastic properties of polymer-based materials. It represents the relationship between loss modulus (E'') and the storage modulus (E'). It signifies the fiber-matrix interaction and the heterogeneity or non-uniform dispersion of fibers in the matrix system. The Cole-Cole plot of a homogenous system is reported as a smooth semi-circular arc whereas the heterogeneous system displays irregular or imperfect semicircles. The dielectric relaxation and viscoelastic response can never be predicted by a single tan δ peak. Therefore, it is particularly important to understand the structure-property relationship using the Cole-Cole method. The Cole-Cole plot of hybrid composites at a frequency of 1 Hz and 5 Hz are reported in Figures 12-13. The Cole-Cole plot of EP was significantly changed and leads to a higher degree of imperfection by the addition of reinforcing fibers. The curve of PCP shows less heterogeneity and proposed the poor fiber-matrix interfacial adhesion. The shape of curves for IM, CPC, and bilayer was pointed towards the good fiber-matrix interfacial adhesion.

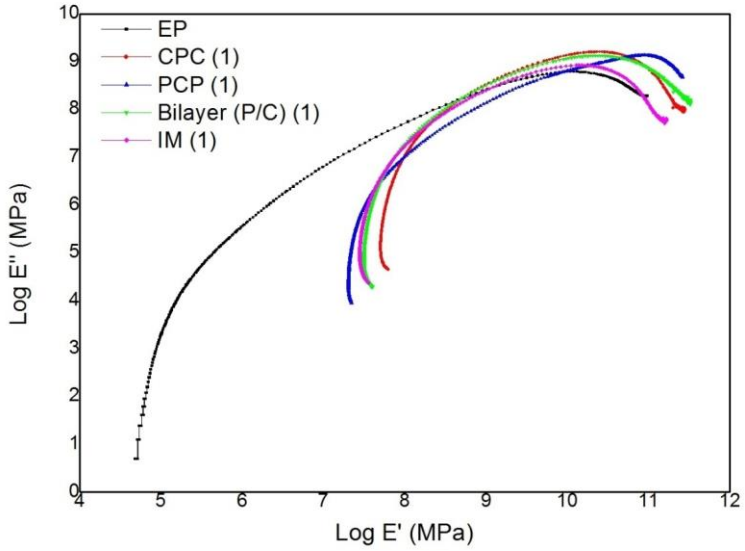

Figure 12. Cole-Cole plots of neat epoxy and hybrid composites at a frequency of 1 Hz

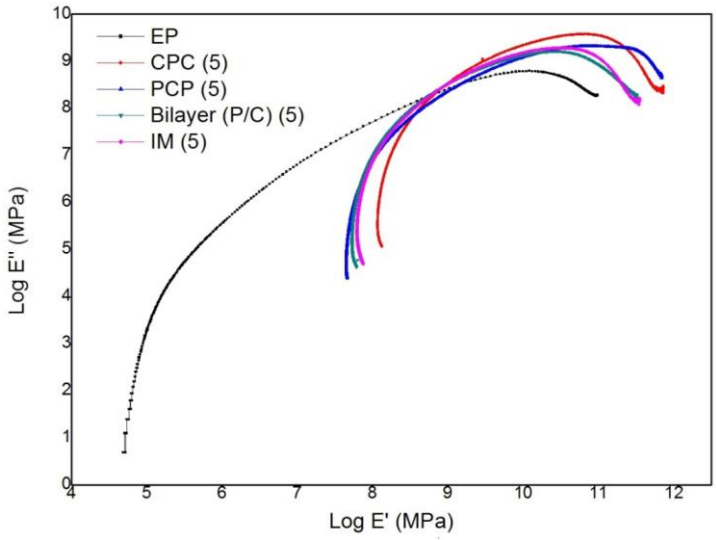

Figure 13. Cole-Cole plots of neat epoxy and hybrid composites at a frequency of 5 Hz

CONCLUSIONS

The viscoelastic properties of a composite material are significantly influenced by the hybridization and fibers layering pattern. In this regard, the different layered hybrid composites were made and characterized. Based on the experimental work, the following conclusions can be made:

1. The dynamic modulus and the glass transition temperature of single fiber reinforced composites (CF-EP and PF-EP) were increased by the synergistic hybridization of cellulosic fibers. After the incorporation of PALF and COIR in a single matrix resin, the shortcomings of each type of fiber was cracked which results in the formation of synergistic hybrid material.
2. Amongst all the different layered hybrid composites, the trilayer CPC possesses lowest value of effectiveness coefficient ‘C' which results that it occupies maximum stiffness and higher activation energy for transition glassy phase to rubbery phase.
3. The bilayer (P/C) and intimately mixed hybrid composites have approximately same modulus (E’) and the glass transition temperature. However, the intimately mixed one has lower value of coefficient ‘C’ and it was due to the effective and uniform stress transfer from matrix to fiber and fiber to fiber

4. The stiffness and phase transition temperature (T_g) of the epoxy resin were increased considerably by the loading of PALF and COIR.

5. The storage modulus (E'), glass transition temperature (T_g), and width of tan δ curve were increased with the increase of frequency from 1 Hz to 5 Hz. This behavior proved the better fiber-matrix interaction at a higher frequency (short time).

Overall we can conclude that the fibers layering patterns significantly affect the performance of a hybrid composite material. The incorporation of PALF and COIR in a single matrix medium result the high performing material having significant potential to be used in various engineering applications.

ACKNOWLEDGMENTS

The authors extend their gratitude to the Delhi Technological University, Delhi (India) for supporting this research work.

REFERENCES

[1] A. Atiqah, M. A. Maleque, M. Jawaid, M. Iqbal, "Development of kenaf-glass reinforced unsaturated polyester hybrid composite for structural applications," *Composite Part B: Engineering*, vol. 56, pp. 68-73, 2014, doi.org/10.1016/j.compositesb.2013.08.019.

[2] B. T. Mulyo and H. Yudiono, "Toughness analysis of pineapple leaves fiber composite as alternative material for SNI helmet," *J. Mech. Eng. Sci.*, vol. 13, no. 4, pp. 5961–5972, Dec. 2019, doi: 10.15282/jmes.13.4.2019.16.0472.

[3] A. Shahzad, "Impact and fatigue properties of hemp-glass fiber hybrid biocomposites," *J. Reinf. Plast. Compos.*, vol. 30, no. 16, pp. 1389–1398, Aug. 2011, doi: 10.1177/0731684411425975.

[4] M. Jawaid, H. P. S. A. Khalil, A. Hassan, and E. Abdallah, "Bi-layer Hybrid Biocomposites," *BioResources*, vol. 7, no. 2, pp. 2344-2355, 2012.

[5] M. Haq, R. Burgueño, A. K. Mohanty, and M. Misra, "Hybrid bio-based composites from blends of unsaturated polyester and soybean oil reinforced with nanoclay and natural fibers," *Compos. Sci. Technol.*, vol. 68, no. 15–16, pp. 3344–3351, Dec. 2008, doi: 10.1016/j.compscitech.2008.09.007.

[6] V. S. Chevali, B. A. Nerenz, C. A. Ulven, and E. Kandare, "Mechanical Properties of Hybrid Lignocellulosic Fiber-Filled Acrylonitrile Butadiene Styrene (ABS) Biocomposites," *Polym. - Plast. Technol. Eng.*, vol. 54, no. 4, pp. 375–382, Mar. 2015, doi: 10.1080/03602559.2014.961078.

[7] N. Ranganathan, K. Oksman, S. K. Nayak, and M. Sain, "Structure property relation of hybrid biocomposites based on jute, viscose and polypropylene: The effect of the fibre content and the length on the fracture toughness and the fatigue properties," *Compos. Part A Appl. Sci. Manuf.*, vol. 83, pp. 169–175, Apr. 2016, doi: 10.1016/j.compositesa.2015.10.037.

[8] M. R. Kaiser, H. Anuar, and S. B. A. Razak, "Improvement in thermomechanical properties of injection molded nano-modified hybrid biocomposite," *J. Thermoplast. Compos. Mater.*, vol. 27, no. 7, pp. 992–1009, 2014, doi: 10.1177/0892705712461518.

[9] M. M. Davoodi, S. M. Sapuan, D. Ahmad, A. Aidy, A. Khalina, and M. Jonoobi, "Concept selection of car bumper beam with developed hybrid bio-composite material," *Mater. Des.*, vol. 32, no. 10, pp. 4857–4865, Dec. 2011, doi: 10.1016/j.matdes.2011.06.011.

[10] M. S. Sreekala, J. George, M. G. Kumaran, and S. Thomas, "The mechanical performance of hybrid phenol-formaldehyde-based composites reinforced with glass and oil palm fibres," *Compos. Sci. Technol.*, vol. 62, no. 3, pp. 339–353, Feb. 2002, doi: 10.1016/S0266-3538(01)00219-6.

[11] S. Panthapulakkal and M. Sain, "Injection-molded short hemp fiber/glass fiber-reinforced polypropylene hybrid composites—Mechanical, water absorption and thermal properties," *J. Appl. Polym. Sci.*, vol. 103, no. 4, pp. 2432–2441, Feb. 2007, doi: 10.1002/app.25486.

[12] M. M. Davoodi, S. M. Sapuan, D. Ahmad, A. Ali, A. Khalina, and M. Jonoobi, "Mechanical properties of hybrid kenaf/glass reinforced epoxy composite for passenger car bumper beam," *Mater. Des.*, vol. 31, no. 10, pp. 4927–4932, Dec. 2010, doi: 10.1016/j.matdes.2010.05.021.

[13] S. K. Saw, G. Sarkhel, and A. Choudhury, "Effect of layering pattern on the physical, mechanical, and thermal properties of jute/bagasse hybrid fiber-reinforced epoxy novolac composites," *Polym. Compos.*, vol. 33, no. 10, pp. 1824–1831, Oct. 2012, doi: 10.1002/pc.22313.

[14] C. Capela, S. E. Oliveira, J. Pestana, and J. A. M. Ferreira, "Effect of fiber length on the mechanical properties of high dosage carbon reinforced," *Procedia Struct. Integr.*, vol. 5, pp. 539–546, 2017, doi: 10.1016/j.prostr.2017.07.159.

[15] A. Chafidz, M. Rizal, R. M. Faisal, M. Kaavessina, D. Hartanto, and S. M. AlZahrani, "Processing and properties of high density polyethylene/date palm fiber composites prepared by a laboratory mixing extruder," *J. Mech. Eng. Sci.*, vol. 12, no. 3, pp. 3771–3785, Sep. 2018, doi: 10.15282/jmes.12.3.2018.2.0333.

[16] Q. Ahsan, T. S. S. Carron, and Z. Mustafa, "On the use of nano fibrillated kenaf cellulose fiber as reinforcement in polylactic acid biocomposites," *J. Mech. Eng. Sci.*, vol. 13, no. 2, pp. 4970–4988, 2019, doi: 10.15282/jmes.13.2.2019.15.0412.

[17] Y. Nishitani, T. Yamanaka, T. Kajiyama, and T. Kitano, "Thermal Properties of Hemp Fiber Reinforced Plant-Derived Polyamide Biomass Composites and their Dynamic Viscoelastic Properties in Molten State," in *Viscoelastic and Viscoplastic Materials*, InTech, 2016.

[18] W. S. Widodo, R. Soenoko, M. A. Choiron, and A. A. Sonief, "Sealing performance analysis of composite gaskets made of silicone rubber filled with ramie natural fibers," *J. Mech. Eng. Sci.*, vol. 13, no. 4, pp. 6178–6194, Dec. 2019, doi: 10.15282/jmes.13.4.2019.28.0484.

[19] J. Alexander and S. J. Elphej Churchill, "Mechanical Characterization of Baslat Based Natural Hybrid Composites for Aerospace Applications," in *IOP Conference Series: Materials Science and Engineering*, 2017, vol. 197, no. 1, doi: 10.1088/1757-899X/197/1/012008.

[20] S. S. Chee, M. Jawaid, and M. T. H. Sultan, "Thermal stability and dynamic mechanical properties of kenaf/bamboo fibre reinforced epoxy composites," *BioResources*, vol. 12, no. 4, pp. 7118–7132, Nov. 2017, doi: 10.15376/biores.12.4.7118-7132.

[21] Y. S. Song, J. T. Lee, D. S. Ji, M. W. Kim, S. H. Lee, and J. R. Youn, "Viscoelastic and thermal behavior of woven hemp fiber reinforced poly(lactic acid) composites," *Compos. Part B Eng.*, vol. 43, no. 3, pp. 856–860, Apr. 2012, doi: 10.1016/j.compositesb.2011.10.021.

[22] S. Rwawiire, B. Tomkova, J. Militky, B. M. Kale, and P. Prucha, "Effect of Layering Pattern on the Mechanical Properties of Bark Cloth (Ficus natalensis) Epoxy Composites," *Int. J. Polym. Anal. Charact.*, vol. 20, no. 2, pp. 160–171, Feb. 2015, doi: 10.1080/1023666X.2015.988534.

[23] M. Idicula, S. K. Malhotra, K. Joseph, and S. Thomas, "Effect of layering pattern on dynamic mechanical properties of randomly oriented short banana/sisal hybrid fiber-reinforced polyester composites," *J. Appl. Polym. Sci.*, vol. 97, no. 5, pp. 2168–2174, Sep. 2005, doi: 10.1002/app.21980.

[24] R. Murugan, R. Ramesh, and K. Padmanabhan, "Investigation on static and dynamic mechanical properties of epoxy based woven fabric glass/carbon hybrid composite laminates," in *Procedia Engineering*, Jan. 2014, vol. 97, pp. 459–468, doi: 10.1016/j.proeng.2014.12.270.

[25] M. Jawaid, H. P. S. Abdul Khalil, and O. S. Alattas, "Woven hybrid biocomposites: Dynamic mechanical and thermal properties," *Compos. Part A Appl. Sci. Manuf.*, vol. 43, no. 2, pp. 288–293, Feb. 2012, doi: 10.1016/j.compositesa.2011.11.001.

[26] L. A. Pothan, Z. Oommen, and S. Thomas, "Dynamic mechanical analysis of banana fiber reinforced polyester composites," *Compos. Sci. Technol.*, vol. 63, no. 2, pp. 283–293, Feb. 2003, doi: 10.1016/S0266-3538(02)00254-3.

[27] D. Romanzini, A. Lavoratti, H. L. Ornaghi, S. C. Amico, and A. J. Zattera, "Influence of fiber content on the mechanical and dynamic mechanical properties of glass/ramie polymer composites," *Mater. Des.*, vol. 47, pp. 9–15, May 2013, doi: 10.1016/j.matdes.2012.12.029.

[28] M. Mittal, R. C.-M. R. Express, and undefined 2018, "Effect of fiber content on thermal behavior and viscoelastic properties of PALF/Epoxy and COIR/Epoxy composites," *Materials Research Express*, vol. 5, no. 12, 2018.

Communications in Mathematics and Statistics
https://doi.org/10.1007/s40304-020-00217-4

Effects of Nonmonotonic Functional Responses on a Disease Transmission Model: Modeling and Simulation

Abhishek Kumar[1] · **Nilam**[1]

Received: 18 September 2019 / Revised: 18 March 2020 / Accepted: 13 April 2020
© School of Mathematical Sciences, University of Science and Technology of China and Springer-Verlag GmbH Germany, part of Springer Nature 2021

Abstract

In this article, a novel susceptible–infected–recovered epidemic model with nonmonotonic incidence and treatment rates is proposed and analyzed mathematically. The Monod–Haldane functional response is considered for nonmonotonic behavior of both incidence rate and treatment rate. The model analysis shows that the model has two equilibria which are named as disease-free equilibrium (DFE) and endemic equilibrium (EE). The stability analysis has been performed for the local and global behavior of the DFE and EE. With the help of the basic reproduction number (R_0), we investigate that DFE is locally asymptotically stable when $R_0 < 1$ and unstable when $R_0 > 1$. The local stability of DFE at $R_0 = 1$ has been analyzed, and it is obtained that DFE exhibits a forward transcritical bifurcation. Further, we identify conditions for the existence of EE and show the local stability of EE under certain conditions. Moreover, the global stability behavior of DFE and EE has been investigated. Lastly, numerical simulations have been done in the support of our theoretical findings.

Keywords Monod–Haldane functional · Basic reproduction number · Local and global stability · Bifurcation

Mathematics Subject Classification 34D20 · 92B05 · 37M05

✉ Nilam
rathi.nilam@gmail.com

Abhishek Kumar
abhishek.dtu14@gmail.com

[1] Department of Applied Mathematics, Delhi Technological University, Delhi 110042, India

Published online: 02 March 2021

1 Introduction

Mathematical modeling is an effective tool to understand the dynamics of infectious diseases/epidemics from over a century. In mathematical epidemiology, many mathematical models have been proposed for disease transmission dynamics such as SIR [15, 7, 19, 10, 28, 8, 2], SIRS [26, 23], SEIR [6], and SVEIR [12] (where S, E, V, I, and R denote the susceptible, exposed, vaccinated, infected, and recovered individuals, respectively). In the disease transmission model, the rate of a new infection mainly depends on the incidence rate. The number of people who become infected per unit of time is defined as the incidence rate [10]. In the pioneering work of Kermack and McKendrick [14], the incidence rate is in the bilinear form (βSI), which was unrealistic for a large population because if the number of susceptibles increases, then the incidence rate also increases. So this unreasonable bilinear incidence rate is needed to be modified. Due to this unrealistic situation, many researchers [15, 7, 19, 8, 16, 1, 11, 17] have proposed various nonlinear functional forms such as Holling type II, Beddington–DeAngelis type, and Crowley–Martin type, since these functional forms incorporate inhibitions measures either by susceptibles or by both susceptibles and infectives, thus making the model more realistic for a large population. In 1986, to include the effect of behavioral changes, Liu et al. [20] proposed the nonlinear saturated incidence rate of the form:

$$f(I)S = \frac{\beta I^l S}{1 + \alpha I^h}, \tag{1.1}$$

where $\beta I^l S$ measures the infection force of the disease, $\frac{1}{1+\alpha I^h}$ describes the inhibition effects from the behavioral changes of susceptibles individuals when the number of infected individuals increases, β, l, and h are positive constants, and α is a nonnegative constant [3, 23, 21]. Note that bilinear incidence (βSI) is a particular case of (1.1) with $l = 1$ and $\alpha = 0$. The case when $l = 1$ and $h = 1$ in (1.1), i.e., $f(I) = \frac{\beta I}{1+\alpha I}$, was proposed by Capasso and Serio [1] to describe the crowding effect in modeling the cholera epidemic in Bari in 1973. The function $f(I) = \frac{\beta IS}{1+\alpha I}$ is also known as the Holling type II function. The case when $l = 1$ and $h = 2$ in (1.1), i.e., $f(I) = \frac{\beta I}{1+\alpha I^2}$, represents a nonmonotonic incidence function which can be used to interpret the "psychological effects" [23]. The function $f(I) = \frac{\beta IS}{1+\alpha I^2}$ is also known as the simplified Monod–Haldane (M–H) function. In M–H incidence function, for a large number of infectious individuals, the infection force may decrease as the number of infectious individuals increases, because in the presence of a large number of infectious individuals the population may tend to reduce the number of contacts per unit time, as seen with the spread of SARS [15].

It is well known that the treatment rate always plays a crucial role in preventing and controlling the spread of infectious diseases. We know that the treatment resources of any community are limited. Therefore, it is essential to choose an effective treatment rate to control the spread of the disease. In 2004, Wang and Ruan [25] considered an SIR epidemic model with a constant treatment rate given as follows:

$$T(I) = \begin{cases} r, & I > 0 \\ 0, & I = 0. \end{cases}$$

They performed a stability analysis and showed that their model exhibits various bifurcations. Later, in 2010, Zhang and Sao [27] modified the constant removal rate into the Holling type II:

$$T(I) = \frac{aI}{1+bI}, \quad I \geq 0; \quad a, b > 0.$$

They analyzed the stability behavior of equilibria and investigated that the model exhibits various bifurcations such as Bogdanov–Takens bifurcation, Hopf bifurcation, and Homoclinic bifurcation. In 2013, Dubey et al. [6] proposed an SEIR model with Holling type III and IV treatment rates for disease dynamics. Motivated by these important works, we have considered the simplified Monod–Haldane (M–H) function type treatment rate in the present epidemic model. In the M–H treatment rate, the treatment rate initially rises with the increase in infectives and achieves the greatest, and after that begins decaying. Such a circumstance may emerge due to the limited availability of treatment for a highly infected population. When the availability of treatment is exhausted (due to the fewer medicines, doctors, and medical staff in hospitals, immunization, etc.), at that point, regardless of the high number of infectives, the accessible medicines turn out to be exceptionally low.

The present article aims to study the transmission and control of infectious diseases when psychological effects and nonmonotonic treatment of infected individuals exist simultaneously in the community. Therefore, to model this situation, we propose an SIR epidemic model with M–H type incidence rate and treatment rate. For the dynamics of the proposed model, we derive the basic reproduction number [5] of the model and study the dynamical behavior through the stability analysis. We give a precise indication of the bifurcation phenomenon using center manifold theory, which ensures the occurrence of the forward bifurcation. We prove the uniform persistence of the system and show the local and global stability of the equilibria under certain conditions. The existence of the limit cycle has also been shown, which shows the occurrence of Hopf bifurcation, regarding the transmission rate as a bifurcation parameter.

The rest of this paper is structured as follows: in Sect. 2, an SIR mathematical model is formulated. In Sect. 3, the basic properties of the model are studied. The local and global stability behaviors of equilibria are discussed in Sect. 4. The model is numerically simulated in Sect. 5. Finally, a brief discussion and conclusion of the work are presented in Sect. 6.

2 Mathematical Model

In this section, we propose a mathematical disease transmission model with an assumption that the total population size (P) is constant. We divide the total population into three subpopulations or classes, which are named as: susceptible $S(t)$, infected I

Table 1 Summary of symbols

Symbol	Description
S	Susceptible population
I	Infected population
R	Recovered population
A	The constant recruitment rate of susceptibles
μ	Natural death rate
β	Transmission rate
α	Rate of inhibitory or psychological effect
d	Disease-induced death rate
δ	Recovery rate
a	Cure rate
b	Limitation rate in treatment availability
R_0	Basic reproduction number
P	Total constant population
$Q\left(\frac{A}{\mu}, 0\right)$	Disease-free equilibrium
$Q^*\left(S^*, I^*\right)$	Endemic equilibrium
β^*	Bifurcation parameter
$G(S, I)$	M–H type incidence rate
$h(I)$	M–H type treatment rate

(t), and recovered $R(t)$. These subpopulations may vary with respect to the time t, but ultimately the sum of subpopulations is fixed, i.e., $S(t)+I(t)+R(t) = P =$ constant. Further, it is assumed that a disease can spread due to the direct contact between susceptibles and infectives only. It is also assumed that recovered individuals are immune to their entire life, and they will not reinfect in their rest of life. Let A be the constant recruitment rate of susceptibles, μ be the natural death rate of the population, β be the transmission rate of a disease, α be the rate of psychological effects or behavioral changes due to the susceptibles, d be the death rate due to the disease, δ be the recovery rate of infected individuals, a be the cure rate to disease, and b be the limitation rate in treatment availability. These assumptions lead to the following nonlinear system of ordinary differential equations:

$$\begin{aligned}
\frac{\mathrm{d}S(t)}{\mathrm{d}t} &= A - \mu S - \frac{\beta SI}{1+\alpha I^2},\\
\frac{\mathrm{d}I(t)}{\mathrm{d}t} &= \frac{\beta SI}{1+\alpha I^2} - (\mu + d + \delta)I - \frac{aI}{1+bI^2},\\
\frac{\mathrm{d}R(t)}{\mathrm{d}t} &= \frac{aI}{1+bI^2} + \delta I - \mu R,
\end{aligned} \tag{2.1}$$

where

$$S(0) > 0, I(0) \geq 0, R(0) \geq 0. \tag{2.2}$$

In model (2.1), the term $G(S, I) = \frac{\beta SI}{1+\alpha I^2}$, represents the Monod–Haldane (M–H) functional type incidence rate, which describes a nonmonotonic behavior of incidence rate due to the psychological effect or behavioral changes of susceptibles in case of the high density of infectives in the community. Here, βIS measures the infection force of the disease and $\frac{1}{1+\alpha I^2}$ describes the inhibition effects of the behavioral changes of susceptible individuals when the number of infected individuals increases. The rate of inhibitory effect α may be affected by government interference. The term $h(I) = \frac{aI}{1+bI^2}$ represents the M–H functional type treatment rate, which describes the nonmonotonic behavior of the treatment rate due to the limitation in the treatment availability of infectives. A summary of the symbols used in the proposed model is given in Table 1.

3 Basic Properties of the Model

For biological reasons, it is assumed that all state variables (S, I, R) and parameters $(A, \beta, \alpha, \mu, d, \delta, a, b)$ of model (2.1) are nonnegative. We now show that the model solutions always lie in a compact region D as follows:

Theorem 3.1 *All solutions of model (2.1) starting in $\mathbb{R}^3_+$ with initial conditions (2.2) are bounded and enter the positively invariant region $D = \left\{(S, I, R) \in \mathbb{R}^3_+ : S(t) + I(t) + R(t) \leq \frac{A}{\mu}\right\}$ for all time $t \geq 0$.*

Proof Note that

$$\begin{aligned}
&\frac{\mathrm{d}S}{\mathrm{d}t} + \frac{\mathrm{d}I}{\mathrm{d}t} + \frac{\mathrm{d}R}{\mathrm{d}t} = \frac{\mathrm{d}}{\mathrm{d}t}(S + I + R)\\
\Rightarrow &\frac{\mathrm{d}}{\mathrm{d}t}(S + I + R) = \frac{\mathrm{d}P}{\mathrm{d}t} = 0, \ (\because\ S + I + R = P)\\
\Rightarrow &\frac{\mathrm{d}S}{\mathrm{d}t} + \frac{\mathrm{d}I}{\mathrm{d}t} + \frac{\mathrm{d}R}{\mathrm{d}t} = 0\\
\Rightarrow &A - \mu P - \mathrm{d}I = 0\\
\Rightarrow &\mu P + \mathrm{d}I = A\\
\Rightarrow &P \leq \frac{A}{\mu}.
\end{aligned}$$

Therefore,

$$\lim_{t\to\infty} (S(t) + I(t) + R(t)) \leq \frac{A}{\mu}.$$

It follows that all the solutions of model (2.1) lie in the invariant set $D = \left\{(S, I, R) \in \mathbb{R}^3_+ : S + I + R \leq \frac{A}{\mu}\right\}$.

It is noticed that the right-hand side of model (2.1) is completely continuous and locally Lipschitzian on D. Thus, it follows that the solution of model (2.1) exists and is unique. It completes the proof of the theorem. □

Under the assumption that the total population size P is constant, model (2.1) may be reduced to a two-dimensional system. The third equation (equation of R) of model (2.1) is traditionally omitted; this equation is decoupled from the first two equations of model (2.1). The condition $P = S(t) + I(t) + R(t) =$ Constant may be used to find $R(t)$. Therefore, the following reduced system is considered for further mathematical analysis:

$$\begin{aligned} \frac{\mathrm{d}S}{\mathrm{d}t} &= A - \mu S - \frac{\beta SI}{1+\alpha I^2}, \\ \frac{\mathrm{d}I(t)}{\mathrm{d}t} &= \frac{\beta SI}{1+\alpha I^2} - (\mu + d + \delta)I - \frac{aI}{1+bI^2}. \end{aligned} \tag{3.1}$$

4 Equilibria and Their Stability Analysis

System (3.1) has two nonnegative equilibria, obtained by equating the derivatives of the system to zero. These are given as follows:

i. Disease-free equilibrium (DFE) $Q\left(\frac{A}{\mu}, 0\right)$.
ii. Endemic equilibrium (EE) $Q^*(S^*, I^*)$.

4.1 Local Stability Analysis of Disease-Free Equilibrium

To investigate the local stability behavior of disease-free equilibrium, we need to compute the basic reproduction number (R_0) [7, 5]. Therefore, using the next-generation matrix method [5, 4], the basic reproduction number is computed as follows.

Let

$$\dot{\boldsymbol{x}} = Z(x) - V(x),$$

where $x = (I, S)^T$, $Z(x)$ is the matrix of new infection term, and $V(x)$ is the matrix of transfer terms into compartments and out of compartments. The Jacobian matrices of $Z(x)$ and $V(x)$ at $Q\left(\frac{A}{\mu}, 0\right)$ are given by

$$Z = \begin{pmatrix} \frac{\beta A}{\mu} & 0 \\ 0 & 0 \end{pmatrix}, V = \begin{pmatrix} \mu + d + \delta + a & 0 \\ \frac{\beta A}{\mu} & \mu \end{pmatrix}.$$

Now,

$$ZV^{-1} = \begin{pmatrix} \frac{\beta A}{\mu} & 0 \\ 0 & 0 \end{pmatrix} \begin{pmatrix} \frac{1}{a+d+\delta+\mu} & 0 \\ -\frac{\beta A}{\mu^2(a+d+\delta+\mu)} & \frac{1}{\mu} \end{pmatrix} = \begin{pmatrix} \frac{A\beta}{\mu(a+d+\delta+\mu)} & 0 \\ 0 & 0 \end{pmatrix}.$$

By using the concept of [5], the basic reproduction number is the spectral radius of the next-generation matrix ZV^{-1}. Therefore, the basic reproduction number (R_0) for our model is

$$R_0 = \rho\left(ZV^{-1}\right) = \frac{A\beta}{\mu(a+d+\delta+\mu)}.$$

Hence, by the above basic reproduction number and theorem 2 of [5], we propose the following theorem:

Theorem 4.1 *The disease-free equilibrium* $Q\left(\frac{A}{\mu}, 0\right)$ *is locally asymptotically stable (LAS) when* $R_0 < 1$ *and unstable when* $R_0 > 1$.

Biologically, Theorem 4.1 says that the disease will die out from the society whenever the basic reproduction number is less than unity, and a positive equilibrium will exist if $R_0 > 1$.

4.1.1 Analysis of $R_0 = 1$

In this section, we analyze the local stability behavior of disease-free equilibrium when R_0 is equal to one. For this, first, we redefine $S = x_1$ and $I = x_2$. Then, system (3.1) can be rewritten as

$$\begin{aligned}
\frac{\mathrm{d}x_1}{\mathrm{d}t} &= A - \mu x_1 - \frac{\beta x_1 x_2}{1+\alpha x_2^2} \equiv f_1, \\
\frac{\mathrm{d}x_2}{\mathrm{d}t} &= \frac{\beta x_1 x_2}{1+\alpha x_2^2} - (\mu + d + \delta)x_2 - \frac{a x_2}{1+b x_2^2} \equiv f_2.
\end{aligned} \tag{4.1}$$

Now, the linearized matrix of system (4.1) at $Q\left(\frac{A}{\mu}, 0\right)$ and at the bifurcation parameter $\beta = \beta^* = \frac{\mu(\mu+d+\delta+a)}{A}$ is given by

$$J = \begin{pmatrix} -\mu & -\frac{\beta^* A}{\mu} \\ 0 & \frac{\beta^* A}{\mu} - \mu - d - \delta - a \end{pmatrix} = \begin{pmatrix} -\mu & -\frac{\beta^* A}{\mu} \\ 0 & 0 \end{pmatrix}.$$

The matrix J has a simple zero eigenvalue at $R_0 = 1$, and another eigenvalue of the matrix has a negative real part. Thus, the linearization technique fails to determine the behavior of system (4.1) [7, 8]. Therefore, we adopt the center manifold theory [22] to analyze the behavior of disease-free equilibrium at $R_0 = 1$. Using Theorem 4.1 of [2], the bifurcation constants a_1 and b_1 can be computed as

$$a_1 = \sum_{k,i,j=1}^{2} u_k w_i w_j \left(\frac{\partial^2 f_k}{\partial x_i \partial x_j}\right)_Q,$$

and

$$b_1 = \sum_{k,i=1}^{2} u_k w_i \left(\frac{\partial^2 f_k}{\partial x_i \partial \beta^*}\right)_Q,$$

where $w = (w_1, w_2)^T$ and $u = (u_1, u_2)$ are the right and the left eigenvectors of the matrix J corresponding to a zero eigenvalue, respectively. Then, we have

$$u_1 = 0, u_2 = 1 \text{ and } w_1 = -\frac{\beta^* A}{\mu^2}, w_2 = 1.$$

The nonzero partial derivatives of the functions $f_i's$ $(i = 1, 2)$ of system (4.1) at $R_0 = 1$ and $\beta = \beta^*$ are

$$\left(\frac{\partial^2 f_2}{\partial x_1 \partial x_2}\right)_Q = \beta^*, \left(\frac{\partial^2 f_2}{\partial x_2 \partial x_1}\right)_Q = \beta^* \text{ and } \left(\frac{\partial^2 f_2}{\partial x_2 \partial \beta^*}\right)_Q = \frac{A}{\mu}.$$

Therefore,

$$\begin{aligned} a_1 &= u_2\left(w_1 w_2 \beta^* + w_1 w_2 \beta^*\right) \\ &= -2\frac{\beta^{*2} A}{\mu^2} < 0, \end{aligned}$$

and

$$\begin{aligned} b_1 &= u_2\left(w_2 \frac{A}{\mu}\right) \\ &= \frac{A}{\mu} > 0. \end{aligned}$$

It can be seen that a_1 is negative and b_1 is positive. Hence, bifurcation is forward. Therefore, we propose the following theorem:

Theorem 4.2 *System (3.1) exhibits a forward transcritical bifurcation at* $Q\left(\frac{A}{\mu}, 0\right)$, $R_0 = 1$ *and bifurcation parameter* $\beta = \beta^*$.

This theorem implies that a positive equilibrium will always exist whenever R_0 slightly crosses the unity.

The forward transcritical bifurcation is illustrated in Fig. 1.

4.2 Existence of Endemic Equilibrium

For the existence of an endemic equilibrium $Q^*(S^*, I^*)$, system (3.1) is rearranged to get S^* and I^*, which gives:

$$S^* = \frac{A\left(1 + I^{*2}\alpha\right)}{I^*\beta + \mu + I^{*2}\alpha\mu},$$

where I^* is given by the equation

$$C_1 I^{*4} + C_2 I^{*3} + C_3 I^{*2} + C_4 I^* + C_5 = 0, \tag{4.2}$$

where

$$
\begin{aligned}
C_1 &= b\mu\alpha(\mu + d + \delta),\\
C_2 &= \beta b(\mu + d + \delta),\\
C_3 &= (\mu\alpha(\mu + d + \delta + a) + b\mu(\mu + d + \delta) - \beta Ab),\\
C_4 &= \beta(\mu + d + \delta + a),\\
C_5 &= (\mu(\mu + d + \delta + a) - \beta A) = \mu(\mu + d + \delta + a)(1 - R_0).
\end{aligned}
$$

Now, for $R_0 > 1$, using the Descartes' rule of signs [24], the biquadratic Eq. (4.2) has a unique positive real root I^* if the following condition holds:

$$C_1 > 0, C_2 > 0, C_3 > 0, C_4 > 0 \text{ and } C_5 < 0.$$

After getting the value of I^*, we can obtain the value of S^*. Hence, there exists a unique endemic equilibrium $Q^*(S^*, I^*)$ if the above condition holds. Hence, we state the following theorem:

Theorem 4.3 *If* $R_0 > 1$, *system* (3.1) *admits a unique endemic equilibrium* $Q^*(S^*, I^*)$.

Now, we show the uniform persistence of system (3.1). Let D_1 denote the interior of D_r $\left(\text{where, } D_r = \left\{(S, I) \in \mathbb{R}^2_+ : S + I \leq \frac{A}{\mu}\right\}\right)$ and ∂D_r denote the boundary of D_r. Epidemiologically, persistence means that the subpopulation always exists and will not lead to elimination if initially, they exist. For this, the following theorem has been proved:

Theorem 4.4 *If* $R_0 > 1$, *system* (3.1) *is uniformly persistent*, *which means that there exists a positive constant* K *such that every solution* (S, I) *of system* (3.1) *with the initial data* $(S(0), I(0)) \in D_1$ *satisfies*

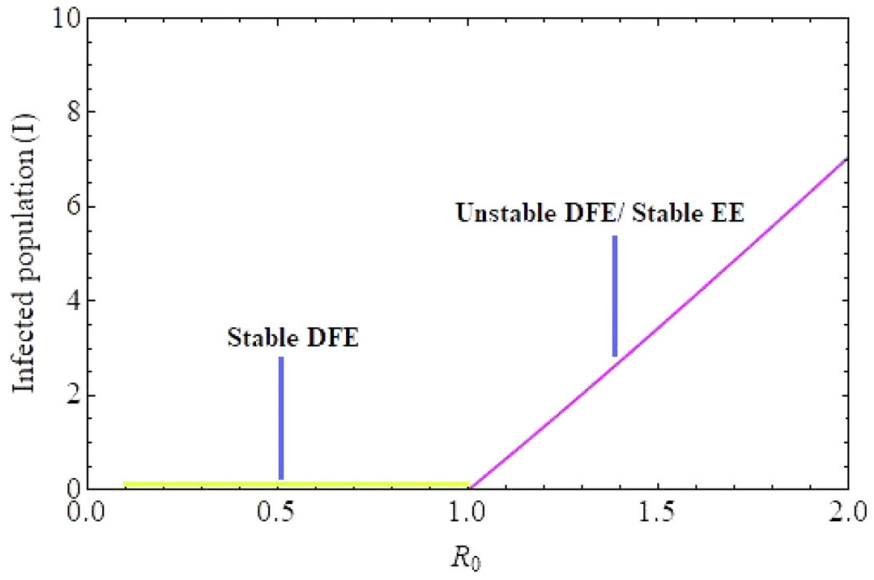

Fig. 1 Forward transcritical bifurcation graph in support of theorem (3.1) with numerical data as given in Table 2

$$\lim_{t\to\infty} \inf S(t) \geq K, \lim_{t\to\infty} \inf I(t) \geq K,$$

where K is independent of initial data in D_1.

Proof From Theorem 4.3, for $R_0 > 1$, there exists a unique endemic equilibrium Q^*. From Theorem 4.1, we know that $R_0 > 1$ implies that the DFE (Q) is unstable. By theorem 4.3 in [9], the instability of Q, together with $Q \in \partial D_r$, implies the uniform persistence of the state variables of system (3.1). Therefore, there exists a positive constant K such that every solution (S, I) of system (3.1) with the initial data $(S(0), I(0)) \in D_1$ satisfies

$$\lim_{t\to\infty} \inf S(t) \geq K, \lim_{t\to\infty} \inf I(t) \geq K,$$

where K is independent of initial data in D_1. □

The uniform persistence, together with the boundedness of D_r, is equivalent to the existence of a compact set in the interior of D_r which is absorbing for system (3.1) [13]. So, we have

Theorem 4.5 *If $R_0 > 1$, then there exists a compact absorbing set $B \subset D_1$.*

4.3 Local Stability Analysis of Endemic Equilibrium

The local stability of the endemic equilibrium $Q^*(S^*, I^*)$ is explored as follows.

The variational matrix J_{Q^*} corresponding to $Q^*(S^*, I^*)$ of system (3.1) is given by

$$J_{Q^*} = \begin{pmatrix} -\frac{I\beta}{1+I^2\alpha} - \mu & \frac{2SI^2\alpha\beta}{(1+I^2\alpha)^2} - \frac{S\beta}{1+I^2\alpha} \\ \frac{I\beta}{1+I^2\alpha} & -d + \frac{2abI^2}{(1+bI^2)^2} - \frac{a}{1+bI^2} - \frac{2SI^2\alpha\beta}{(1+I^2\alpha)^2} + \frac{S\beta}{1+I^2\alpha} - \delta - \mu \end{pmatrix}.$$

The characteristic equation of the variational matrix $\left(J_{Q^*}\right)$ is given as:

$$\varepsilon^2 + p_1\varepsilon + p_2 = 0, \tag{4.3}$$

where

$$p_1 = l_a - l_b,\ p_2 = m_a - m_b,$$

where

$$l_a = \frac{a\left(1+I^{*2}\alpha\right)^2 + \left(1+bI^{*2}\right)^2\left(d\left(1+I^{*2}\alpha\right)^2 + \delta + 2\mu + I^*\left((1+I^*(S^*+I^*)\alpha)\beta + I^*\alpha\left(2+I^{*2}\alpha\right)(\delta+2\mu)\right)\right)}{\left(1+bI^{*2}\right)^2\left(1+I^{*2}\alpha\right)^2},$$

$$l_b = \frac{\left(ab\left(I^*+I^{*3}\alpha\right)^2 + S^*\left(1+bI^{*2}\right)^2\beta\right)}{\left(1+bI^{*2}\right)^2\left(1+I^{*2}\alpha\right)^2},$$

$$m_a = \frac{a(1+I^{*2}\alpha)(\mu+I^*(\beta+I^*\alpha\mu))+(1+bI^{*2})^2\left(I^*(1+I^{*2}\alpha)\beta(d+\delta)+\left(d(1+I^{*2}\alpha)^2+I^*(1+I^*(S^*+I^*)\alpha)\beta+(1+I^{*2}\alpha)^2\delta\right)\mu+(\mu+I^{*2}\alpha\mu)^2\right)}{(1+bI^{*2})^2(1+I^{*2}\alpha)^2},$$

$$m_b = \frac{\left(S^*(1+bI^{*2})^2\beta\mu+abI^{*2}(1+I^{*2}\alpha)(I^*\beta+\mu+I^{*2}\alpha\mu)\right)}{(1+bI^{*2})^2(1+I^{*2}\alpha)^2}.$$

The eigenvalues of the matrix $\left(J_{Q^*}\right)$ have a negative real part if and only if $p_1 > 0$ and $p_2 > 0$. Thus, by Routh–Hurwitz criterion, the following results are proposed in the form of theorems given as follows:

Theorem 4.6 *Endemic equilibrium $Q^*(S^*, I^*)$ is*

i. *locally asymptotically stable if the conditions $l_a > l_b$ and $m_a > m_b$ hold simultaneously.*
ii. *a saddle point if the conditions $l_a > l_b$ and $m_a < m_b$ hold simultaneously.*
iii. *unstable if $l_a < l_b$ and $m_a > m_b$.*

Biologically, Theorem 4.6 says that when disease persists in society, it can be controlled under condition (i); otherwise, the disease will continue to spread, under conditions (ii) and (iii), respectively.

Theorem 4.7 *System (3.1) exhibits a Hopf bifurcation near to the endemic equilibrium $Q^*(S^*, I^*)$ if the conditions $l_a = l_b, m_a > m_b$ and $I \leq \frac{1}{\sqrt{b}}$ hold simultaneously.*

Proof The condition $l_a = l_b$ implies that $p_1 = 0$ in Eq. (10), and the condition $m_a > m_b$ implies that $p_2 > 0$. Thus, Eq. (4.3) has purely imaginary roots. From Theorem 4.6(i) and (ii), it follows that the equilibrium $Q^*(S^*, I^*)$ changes its behavior from stable to instability as the parameter β crosses the critical value $\beta = \beta^*$, where

$$\beta^* = -\left(\frac{\left(1+I^2\alpha\right)^2\left(d-\frac{a(-1+bI^2)}{(1+bI^2)^2}+\delta+2\mu\right)}{-S+I+I^2(S+I)\alpha}\right).$$

Again, we have

$$\begin{aligned}\frac{\mathrm{d}}{\mathrm{d}\beta}\left[tr\left(J_{Q^*}\right)\right]_{\beta=\beta^*} &= -\left(\frac{-S+I+I^2(S+I)\alpha}{\left(1+I^2\alpha\right)^2}\right)\\ &= \frac{1}{\beta^*}\left(d-\frac{a\left(-1+bI^2\right)}{\left(1+bI^2\right)^2}+\delta+2\mu\right)\\ &= \frac{1}{\beta^*}\left(\frac{a-abI^2}{\left(1+bI^2\right)^2}+d+\delta+2\mu\right)\neq 0.\end{aligned}$$

Hence, system (3.1) shows a Hopf bifurcation near $Q^*(S^*, I^*)$ when $\beta = \beta^*$.

Theorem 4.7 says that if model (3.1) undergoes a Hopf bifurcation under the conditions mentioned above, then (from the Poincare and Bendixson theorem) every solution initiating the limit cycle must approach a stable limit cycle. □

Next, we derive the condition for the nonexistence of a periodic solution in the interior of the positive quadrant of the S–I plane. For this, we prove the following theorem:

Theorem 4.8 *If $\alpha \geq b$, then system (3.1) does not have any periodic solution in the interior of the positive quadrant of S–I plane.*

Proof We take a real-valued function in the interior of the S–I plane given as follows:

$$H(S, I) = \frac{1 + \alpha I^2}{SI}$$

Let us consider,

$$h_1(S, I) = A - \mu S - \frac{\beta SI}{1 + \alpha I^2},$$
$$h_2(S, I) = \frac{\beta SI}{1 + \alpha I^2} - (\mu + d + \delta)I - \frac{aI}{1 + bI^2}.$$

Then,

$$\begin{aligned}\operatorname{div}(Hh_1, Hh_2) &= \frac{\partial}{\partial S}(Hh_1) + \frac{\partial}{\partial I}(Hh_2) \\ &= -\frac{A + AI^2\alpha}{S^2 I} - \frac{2I\left(a(-b + \alpha) + \left(1 + bI^2\right)^2 \alpha(d + \delta + \mu)\right)}{S\left(1 + bI^2\right)^2}.\end{aligned}$$

It can be seen that the above expression can never be equal to zero when $\alpha \geq b$, and also, its sign will be unchanged in the positive quadrant of the S–I plane. Thus, using Dulac's criterion [22], it can be said that system (3.1) does not have any periodic solution in the interior of the positive quadrant of the S–I plane. Epidemiologically, this theorem says that if the given condition holds, the disease will not reappear in the society.

Since the set D defined in Theorem 3.1 is a positively invariant set, the following theorem is a direct result of the Poincare–Bendixson theorem [22] showing the existence of a limit cycle in the interior of the positive quadrant of the S–I plane. □

Theorem 4.9 *If either the conditions $l_a > l_b \& m_a < m_b$ or $l_a \langle l_b \& m_a \rangle m_b$ are satisfied simultaneously, system (3.1) has at least one limit cycle in the interior of the positive quadrant of the S–I plane.*

Epidemiologically, the above theorem implies that if an endemic equilibrium is a saddle point or unstable, then disease may re-occur in society in the future.

4.4 Global Stability Analysis

In this section, we discuss the global stability behavior of disease-free and endemic equilibria by Lyapunov functions.

4.4.1 Global Stability of Disease-Free Equilibrium

In this subsection, the global stability behavior of disease-free equilibrium $Q\left(\frac{A}{\mu}, 0\right)$ is discussed by Lyapunov function given as follows:

Theorem 4.10 *The disease-free equilibrium $Q\left(\frac{A}{\mu}, 0\right)$ is globally asymptotically stable when $R_0 \leq 1$ and the condition $ab \leq \alpha(\mu + d + \delta)$ hold simultaneously.*

Proof Let L_1 be the Lyapunov function defined as:

$$L_1 = S - S_0 - \int_{S_0}^{S} \lim_{I \to 0^+} \frac{G(S_0, I)}{G(\omega, I)} \mathrm{d}\omega + I,$$

where $S_0 = \frac{A}{\mu}$.

Differentiating L_1 with respect to t, we get

$$\begin{aligned}
\frac{\mathrm{d}L_1}{\mathrm{d}t} &= \left(1 - \frac{S}{S_0}\right).\frac{\mathrm{d}S}{\mathrm{d}t} + \frac{\mathrm{d}I}{\mathrm{d}t} \\
&= -\frac{\mu\,(S - S_0)^2}{S} + \frac{\beta I S_0}{1 + \alpha I^2} - (\mu + d + \delta)\, I - \frac{aI}{1 + bI^2} \\
&= -\frac{\mu\left(S - \frac{A}{\mu}\right)^2}{S} + \frac{(\mu + d + \delta + a)\,(R_0 - 1)\, I}{1 + \alpha I^2} \\
&\quad + \left(\frac{ab - \alpha\,(\mu + d + \delta) - b\alpha\,(\mu + d + \delta)\, I^2)}{\left(1 + \alpha I^2\right)\left(1 + bI^2\right)}\right) I^3.
\end{aligned}$$

Since all parameters of the model are positive, it follows that $\frac{\mathrm{d}L_1}{\mathrm{d}t} < 0$ if $R_0 \leq 1$ and $\frac{ab}{\alpha(\mu+d+\delta)} \leq 1$ hold simultaneously, and $\frac{\mathrm{d}L_1}{\mathrm{d}t} = 0$ if $S = S_0 = \frac{A}{\mu}$ and $I = I_0 = 0$. Hence, L is a Lyapunov function on $D_r = \left\{(S, I) : 0 < S + I \leq \frac{A}{\mu}\right\}$.

It implies that the largest compact invariant set in $\left\{(S, I) \in D_r : \frac{\mathrm{d}L_1}{\mathrm{d}t} = 0\right\}$ is the singleton set $\{Q\}$. From LaSalle's invariance principle [22, 18], DFE is globally asymptotically stable. □

4.4.2 Global Stability of Endemic Equilibrium

To prove the global stability of an endemic equilibrium $Q^*(S^*, I^*)$, we consider the following hypothesis:

H(1) $\frac{aI}{1+b(I^*)^2} + \frac{(1+I)\beta S^* I^*}{I+I\alpha(I^*)^2} + \frac{a}{1+bI^2} \leq \frac{aI}{1+bI^2} + \frac{\beta(S^*)^2}{S+S\alpha(I^*)^2} + I^*\left(\frac{S\beta}{1+I^2\alpha} + \frac{a}{I+bI(I^*)^2}\right)$ for all $S, I \geq 0$.

Theorem 4.11 *Under hypothesis $H(1)$, endemic equilibrium $Q^*(S^*, I^*)$ is globally asymptotically stable.*

Proof Let L_2 be the Lyapunov function defined as:

$$L_2 = S - S^* - \int_{S^*}^{S} \frac{G(S^*, I^*)}{G(\emptyset, I^*)} \mathrm{d}\emptyset + I - I^* - I^* \ln \frac{I}{I^*}.$$

Differentiating L_2 with respect to t, we get

$$\begin{aligned} \frac{\mathrm{d}L_2}{\mathrm{d}t} &= \left(1 - \frac{G(S^*, I^*)}{G(S, I^*)}\right).\frac{\mathrm{d}S}{\mathrm{d}t} + \left(1 - \frac{I^*}{I}\right).\frac{\mathrm{d}I}{\mathrm{d}t} \\ &= \left(1 - \frac{S^*}{S}\right).\frac{\mathrm{d}S}{\mathrm{d}t} + \left(1 - \frac{I^*}{I}\right).\frac{\mathrm{d}I}{\mathrm{d}t}. \end{aligned}$$

Note that

$$A - \mu S^* = \frac{\beta S^* I^*}{1 + \alpha I^{*2}}, \frac{\beta S^* I^*}{1 + \alpha I^{*2}} = (\mu + d + \delta) I^* + \frac{a I^*}{1 + b I^{*2}}.$$

Therefore,

$$\begin{aligned} \frac{\mathrm{d}L_2}{\mathrm{d}t} = {} & \frac{aI}{1 + b\,(I^*)^2} + \frac{(1 + I)\,\beta S^* I^*}{I + I\alpha\,(I^*)^2} + \frac{a}{1 + bI^2} \\ & - \left(\frac{aI}{1 + bI^2} + \frac{\beta\,(S^*)^2}{S + S\alpha\,(I^*)^2} + I^* \left(\frac{S\beta}{1 + I^2\alpha} + \frac{a}{I + bI\,(I^*)^2} \right) \right). \end{aligned}$$

Hence, by $H(1)$, we see that $\frac{\mathrm{d}L_2}{\mathrm{d}t} \leq 0$ for all $S, I \geq 0$. It is easy to verify that the largest invariant in $\left\{(S, I) \in \mathbb{R}^2_+ : \frac{\mathrm{d}L_2}{\mathrm{d}t} = 0\right\}$ is singleton $\{Q^*\}$. By the Lyapunov–LaSalle asymptotic stability theorem [22, 18], $Q^*(S^*, I^*)$ is globally asymptotically stable. □

5 Numerical Simulations

In this section, system (3.1) is simulated numerically using Mathematica 11 (Table 2). The following numerical experimental values of parameters are taken for the simulation:

The initial values of populations are as follows:

$$S(0) = 90, I(0) = 7, R(0) = 3.$$

Table 2 Parameters and their numerical values

Parameter	P	A	μ	β	α	d	δ	a	b
Numerical value	100	2	0.02	0.003	0.0005	0.02	0.002	0.02	0.005

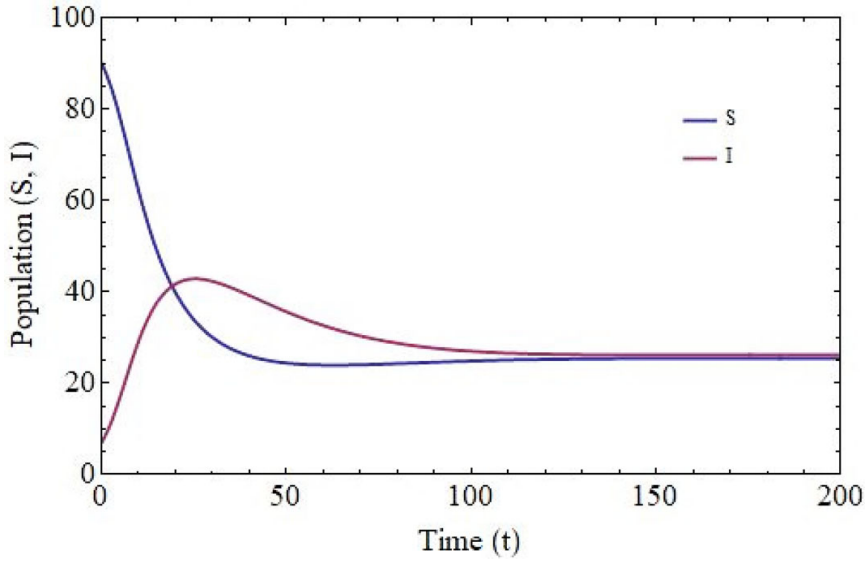

Fig. 2 Combined population of susceptibles and infectives

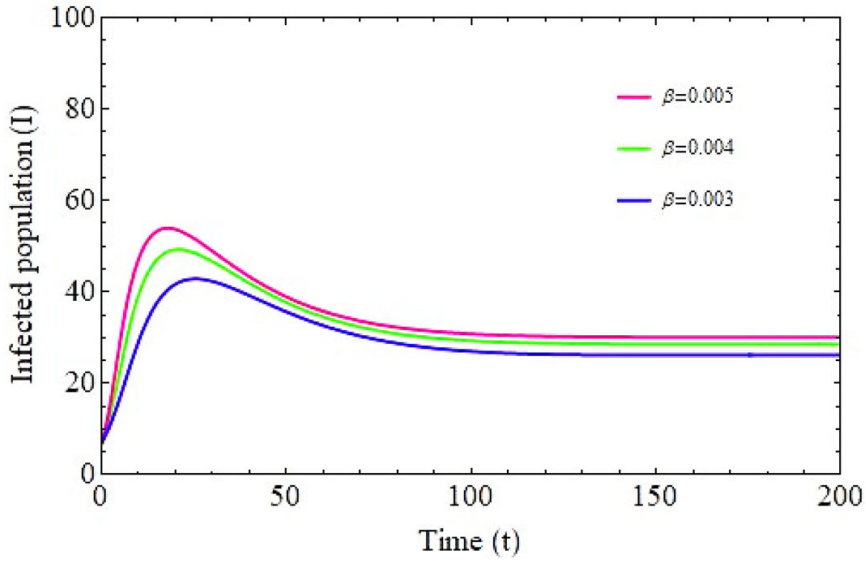

Fig. 3 Infected population at increased values of transmission rate (β)

At the above parameters values, the endemic equilibrium point of system (3.1) is calculated as $Q^*(S^*, I^*) = (25.4721, 26.2010)$. Therefore, R^* of system (1) can be calculated as $R^* = P - S^* - I^* = 48.3269$.

Figure 2 shows the combined population of susceptible and infected individuals. From this figure, it can be observed that as time passes, the number of susceptibles is decreasing, the number of infectives is increasing, and finally, both populations are approaching the endemic equilibrium Q^* with respect to the time.

Figures 3 and 4 show the infected population at various values of transmission rate (β) and psychological effects (α), respectively. Figure 3 shows that the number of infected individuals increases with the increase in transmission rate, and Fig. 3 shows that the number of infected individuals decreases with the increase in the

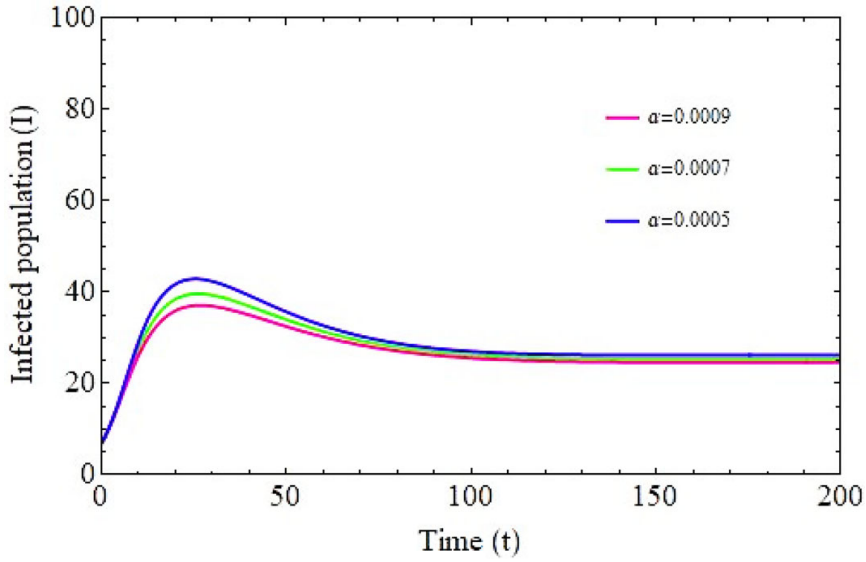

Fig. 4 Infected population at increased values of psychological effects (α)

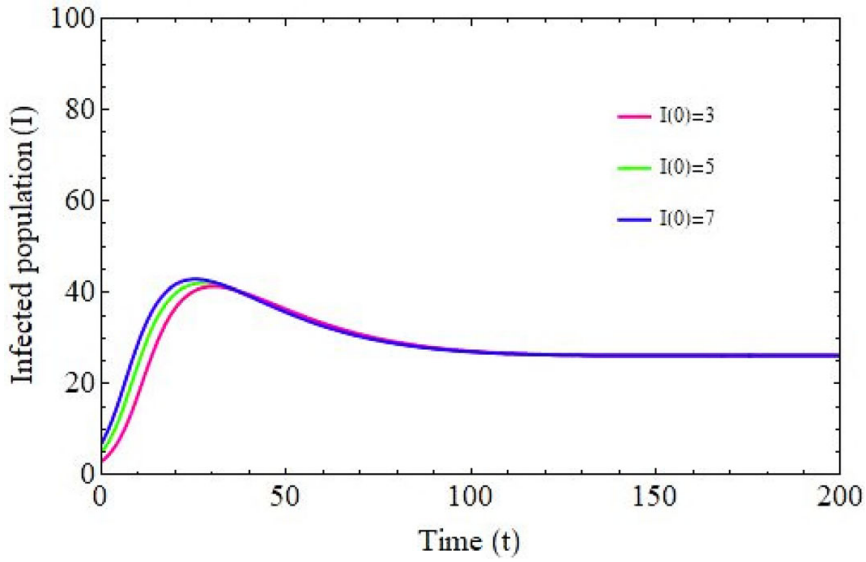

Fig. 5 Infected population with different values of the initially infected individuals ($I(0)$)

psychological or inhibitory effect. In both figures, the infected population is initially increasing, and as time passes, the infected population approaches their steady state.

Figure 5 shows the infected population with different values of the initially infected individuals $I(0)$. It can be observed from the figure that the infected population approaches the same steady state at any value of $I(0)$ with respect to the time.

Figure 6 shows the infected populations with and without M–H treatment rate. It can be observed from the figure that when the treatment to the infected population is given according to M–H treatment rate, the total number of infected individuals is less, while the total number of infected individuals is high when M–H treatment rate

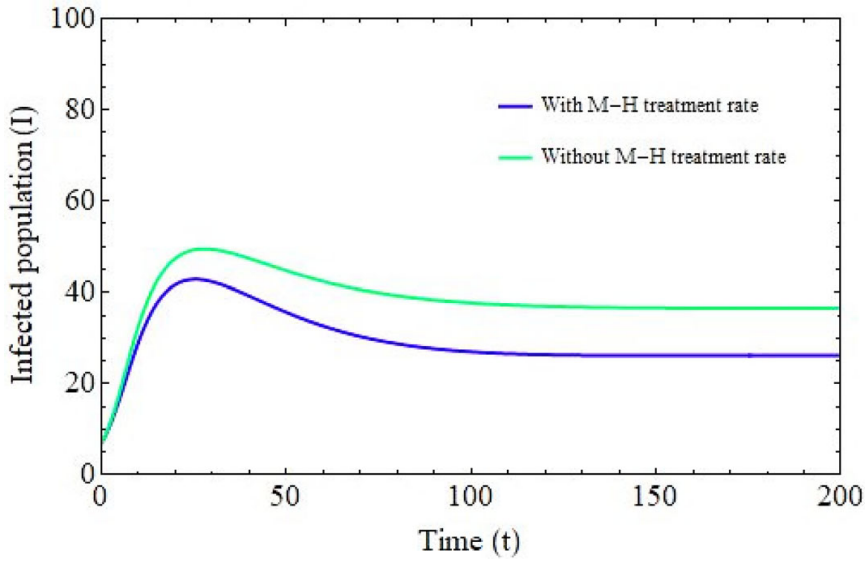

Fig. 6 Infected individuals with and without M–H treatment rate

is not considered. Thus, the M–H treatment rate plays a vital role in the control of the spread of infection in society.

Figure 7 shows the difference in the number of infected individuals when different types of incidence rates, namely Holling type I (H-I), Holling type II (H-II), and Monod–Haldane (M–H), are considered. It shows the effect of incidence rates on the number of infected individuals. It can be seen that, in comparison with the H-I and H-II incidence rates, the number of infectives is less when we consider the M–H type incidence rate for disease dynamics, which has an essential role in disease prevention. Reducing incidence is one of several possible strategies to prevent the spread of infectious disease. Thus, the M–H incidence rate has a vital role in the study of disease dynamics.

To obtain the numerical result in support of Theorem 4.7, we consider the following values of the parameters (Table 3).

Figure 8 shows the occurrence of the limit cycle and confirms the existence of Hopf bifurcation. Clearly, this figure shows the stable limit cycle with an equilibrium point $E^* = (47.87, 1.29)$.

6 Discussion and Conclusion

In this study, we proposed and analyzed a mathematical SIR disease transmission model to investigate the role of psychological effects and the limitation in treatment availability. We considered the nonmonotonic Monod–Haldane functional as the incidence rate and the treatment rate. From the mathematical analysis, we obtained that our model has two equilibria, namely disease-free and endemic. Further, we investigated that the disease-free equilibrium is locally asymptotical stable when the basic reproduction number (R_0) is less than unity. For $R_0 = 1$, we

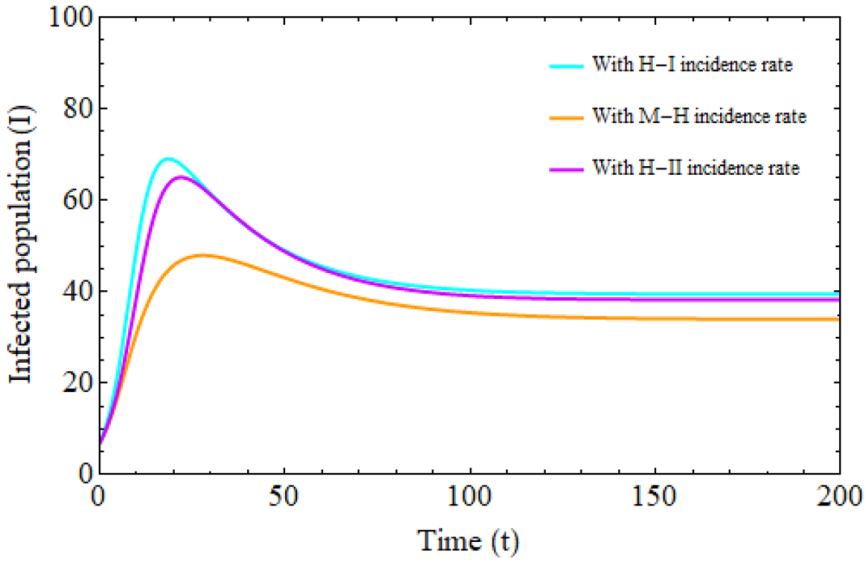

Fig. 7 The behavior of the infected population for different incidence rates

Table 3 Parameters and their numerical values

Parameter	P	A	μ	β	α	d	δ	a	b
Numerical value	100	2	0.02	0.043	0.0005	0.02	0.002	2	0.005

obtained that disease-free equilibrium exhibits a forward transcritical bifurcation which implies that a positive equilibrium will always exist whenever R_0 slightly crosses the unity. We checked the existence of the endemic equilibria and obtained that the endemic equilibrium is locally asymptotically stable, a saddle point, and unstable when the conditions in Theorem 4.6 satisfied, respectively. Further, we investigated that system (3.1) exhibits a Hopf bifurcation under the conditions, as stated in Theorem 4.7. We also investigated that system (3.1) is uniformly persistent under the conditions, stated in Theorem 4.4. Moreover, global stability behavior of disease-free and endemic equilibria has been analyzed and obtained that disease-free equilibrium is globally asymptotically stable when $R_0 \leq 1$ and endemic equilibrium is globally asymptotically stable under the hypothesis $H(1)$, when $R_0 > 1$.

From numerical simulations, we observed that the number of infected individuals increases when the transmission rate increases (Fig. 3), while the number of infected individuals decreases when the psychological effect increases (Fig. 4). Further, we observed that the number of infected individuals is low when the treatment rate of the infected individuals is managed according to the M–H treatment rate (Fig. 6). We also portray the various bifurcations through numerical simulation, such as forward transcritical and Hopf bifurcations.

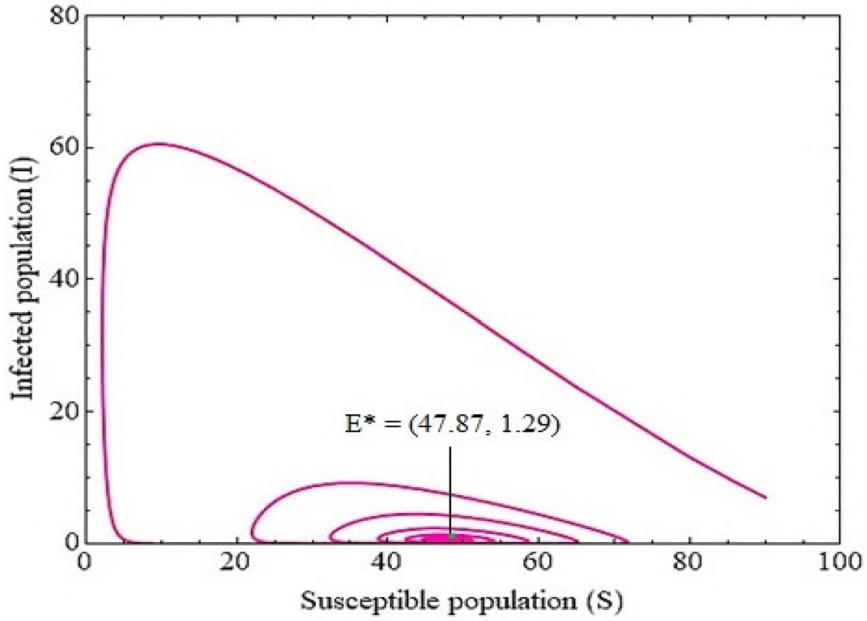

Fig. 8 Limit cycle in S–I plane

In conclusion, we find that the SIR model with a combination of Monod–Haldane incidence rate and treatment rate is capable of successfully addressing the dynamics of such diseases where the psychological effects and limitation rate in treatment availability are significantly available.

Acknowledgements The authors are gratefully acknowledged to Delhi Technological University for providing monetary support for this research. The authors are also thankful to the handling editor and anonymous reviewers for their constructive comments and suggestions which enhance the quality of the paper.

Compliance with Ethical Standards

Conflict of interest The authors declare that they have no conflict of interest.

References

1. Capasso, V., Serio, G.: A generalization of the Kermack–McKendrick deterministic epidemic model. Math. Biosci. **42**(1–2), 43–61 (1978)
2. Chavez, C.C., Song, B.: Dynamical models of tuberculosis and their applications. Math. Biosci. Eng. **1**(2), 361–404 (2004)
3. Cui, Q., Qiu, Z., Liu, W., Hu, Z.: Complex dynamics of an SIR epidemic model with nonlinear saturate incidence and recovery rate. Entropy **19**(7), 305 (2017)
4. Diekmann, O., Heesterbeek, J.A.P., Metz, J.A.: On the definition and the computation of the basic reproduction ratio R_0 in models for infectious diseases in heterogeneous populations. J. Math. Biol. **28**(4), 365–382 (1990)
5. Driessche, P.V.D., Watmough, J.: Reproduction numbers and sub-threshold endemic equilibria for compartment models of disease transmission. Math. Biosci. **180**(1–2), 29–48 (2002)
6. Dubey, B., Patara, A., Srivastava, P.K., Dubey, U.S.: Modelling and analysis of a SEIR model with different types of nonlinear treatment rates. J. Biol. Syst. **21**(3), 1350023 (2013)

7. Dubey, B., Dubey, P., Dubey, U.S.: Dynamics of n SIR model with nonlinear incidence and treatment rate. Appl. Appl. Math. **10**(2), 718–737 (2015)
8. Dubey, P., Dubey, B., Dubey, U.S.: An SIR model with nonlinear incidence rate and Holling type III treatment rate. Appl. Anal. Biol. Phys. Sci. **186**, 63–81 (2016)
9. Freedman, H.I., Ruan, S., Tang, M.: Uniform persistence and flows near a closed positive invariant set. J. Differ. Equ. **6**(4), 583–600 (1994)
10. Goel, K., Nilam: A mathematical and numerical study of a SIR epidemic model with time delay, nonlinear incidence and treatment rates. Theory Biosci. (2019). https://doi.org/10.1007/s12064-019-00275-5
11. Goel, K., Kumar, A., Nilam: A deterministic time-delayed SVIRS epidemic model with incidences and saturated treatment. J. Eng. Math. (2020). https://doi.org/10.1007/s10665-020-10037-8
12. Gumel, A.B., Mccluskey, C.C., Watmough, J.: An SVEIR model for assessing the potential impact of an imperfect anti-SARS vaccine. Math. Biosci. Eng. **3**(3), 485–494 (2006)
13. Hutson, V., Schmitt, K.: Permanence and the dynamics of biological systems. Math. Biosci. **111**(1), 1–71 (1992)
14. Kermack, W.O., McKendrick, A.G.A.: A contribution to the mathematical theory of epidemics. Proc. R. Soc. A Math. Phys. Eng. Sci. **115**(772), 700–721 (1927)
15. Kumar, A., Nilam: Mathematical analysis of a delayed epidemic model with nonlinear incidence and treatment rates. J. Eng. Math. **115**(1), 1–20 (2019)
16. Kumar, A., Nilam, Kishor, R.: A short study of an SIR model with inclusion of an alert class, two explicit nonlinear incidence rates and saturated treatment rate. SeMA J. (2019). https://doi.org/10.1007/s40324-019-00189-8
17. Kumar, A., Goel, K., Nilam: A deterministic time-delayed SIR epidemic model: mathematical modeling and analysis. Theory Biosci. **139**, 67–76 (2020)
18. LaSalle, J.P.: The Stability of Dynamical Systems. SIAM, Philadelphia (1976)
19. Li, G.H., Zhang, Y.X.: Dynamic behavior of a modified SIR model in epidemic diseases using nonlinear incidence and recovery rates. PLoS ONE **12**(4), e0175789 (2017)
20. Liu, W., Hetchote, H.W., Levin, S.: Influence of nonlinear incidence rates upon the behavior of SIRS epidemiological model. J. Math. Biol. **23**(2), 187–204 (1986)
21. Ruan, S., Wang, W.: Dynamical behavior of an epidemic model with a nonlinear incidence rate. J. Differ. Equ. **188**(1), 135–163 (2003)
22. Sastry, S.: Analysis, Stability and Control. Springer, New York (1999)
23. Tang, Y., Huang, D., Ruan, S., Zhang, W.: Coexistence of limit cycles and homoclinic loops in a SIRS model with a nonlinear incidence rate. SIAM J. Appl. Math. **69**(2), 621–639 (2008)
24. Wang, X.: A simple proof of Descartes's rule of signs. Am. Math. Mon. (2004). https://doi.org/10.2307/4145072
25. Wang, W., Ruan, S.: Bifurcation in an epidemic model with constant removal rates of the infectives. J. Math. Anal. Appl. **291**(2), 775–793 (2004)
26. Xu, R., Ma, Z.: Stability of a delayed SIRS epidemic model with a nonlinear incidence rate. Chaos Solitons Fractals **41**(5), 2319–2325 (2009)
27. Zhang, Z., Sao, Y.: Qualitative analysis of a SIR epidemic model with saturated treatment rate. J. Appl. Math. Comput. **34**(1–2), 177–194 (2010)
28. Zhou, L., Fan, M.: Dynamics of a SIR epidemic model with limited medical resources revisited. Nonlinear Anal. RWA **13**(1), 312–324 (2012)

e-ISSN: 2582-5208
International Research Journal of Modernization in Engineering Technology and Science
Volume:03/Issue:02/February-2021 Impact Factor- 5.354 www.irjmets.com

ELECTRICITY GENERATION FROM SOLAR ENERGY

Dr. J.P Kesari*1, Prashant Meena*2, Pankaj Garhwal*3

*1 Professor, Department of Mechanical Engineering, Delhi Technological University Bawana Road, Delhi 110042, India.

*2,3 Undergraduate Student, Department of Mechanical Engineering, Delhi Technological University Bawana Road, Delhi 110042, India.

ABSTRACT

Power is the most predominant ingredient of infrastructure for growth in the social science and welfare of a nation. The expansion of Indian economy in terms of development is crucial within the current infrastructure. The facility sector of Bharat is one of the most essential dilated power sectors within the world. Because of the increase in demand of electricity rising every day, the Indian power sector is interfacing some hurdles to keep up the balance between energy supplied and demand with plagued by offer constraints and shortages in Power. Maintaining the quantitative relation of age and need for Power, the choice of moving from traditional methods to conventional method was not a sole option. The importance of mistreatment star as an energy supply in India's views is not exclusively to extend power generation but also to expand energy dependability when the social and environmental issues were concerned. The article conjointly tries to mentioned operating, solar array types; focuses on the varied application s and strategies to market solar power advantages.

Keywords: infrastructure, sustaining, increment.

I. INTRODUCTION

Nowadays, with the renewable resources getting depleted being very less in number, the last ten years have become necessary for the per watt value of solar power devices. It had to be economically viable within the coming years and growing as higher technology in each matter and application. Every day, the earth receives daylight higher than (1366W approx.); this is often a vast supply of energy accessible at no value. The most important advantage of solar Power over different types of power generators is that the daylight is directly born-again into solar Power to utilize the smallest electrical phenomenon (PV) star cells. An excessive quantity of analysis activities to mix the sun's energy method by developing star cells/panels/modules with high changing types. The biggest blessings of solar Power is that it's free to access to people and obtainable in giant quantities unlike fossil fuels which produce far less than this in the past few years. Moreover, solar Power needs significantly lower men's expenses over standard energy production technology.

II. SOLAR ENERGY

The amount of energy within the style of heat and radiation is said to be Solar Power. It's bright, lightweight, and warm which is coming from the sun, a natural supply of energy victimization. It varies from ever-changing and developing technology such as star thermal energy, star design, star heating, liquified salt powerhouse, and artificial chemical processes. The immense magnitude of star power accessible makes an extremely appealing supply of electricity. It was calculated that approximately half an hour of radiation is back to the area whereas the other part is absorbed by the ocean clouds and land.

III. WORKING OF SOLAR ENERGY

PV cells is generally used to convert daylight to electricity (DC) electricity. Charge Controller works as a facility manager from an electrical device that reverses back to the electrical device to explain panel injury. Battery Systems act as storage of electrical Power is employed once daylight not accessible (i.e., night). This technique is connected to an electrical converter to convert electricity (DC) into electricity (AC).

IV. MODELING OF PV PANEL

A. Solar Cell (Photovoltaic Cell)

The cell is used to convert the radiation directly into electricity. It consists of various sorts of semiconductor materials. It is of two types: charge and charge. This cell technology area unit wont to style star cells with low

value, similarly to high conversion potency. Once the cell absorbed photons from daylight, certain amount of electron is released from the semiconductors , and these electron was drawn off by a grid of metal conductors, this causes a flow of electricity. Electric cell PV is created of several chemicals.

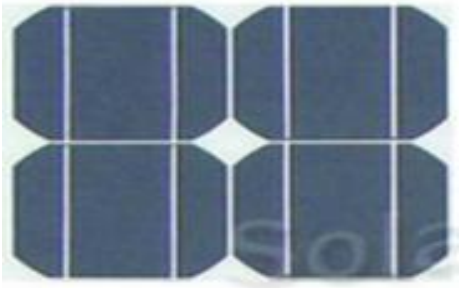

Figure 1: Photovoltaic Cell (4 cells)

B. Photovoltaic Module

A PV module generally consists the circuit of photovoltaic cell sealed in Associate in environmentally protecting laminate and are the main building block of the system. Usually, sizes from 60W to 170W. Typically the variety of PV modules are organized nonparallel and parallel to satisfy the energy demand.

Figure 2: Photovoltaic Module (Multiple cells)

C. Photovoltaic Panel

It includes one or additional PV modules which are assembled as a pre-wind, unstable field unit. During this panel, PV cell is series connections. Star panels are made of separate PV cells which are connected along each other.

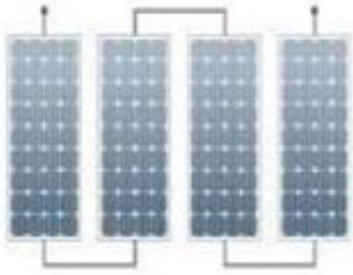

Figure 3: Photovoltaic Panel

D. Photovoltaic Array

It contains many PV cells, asynchronous and parallel connections. Series affiliations square measure is responsible for the increment of the module's voltage, whereas the responsibility of parallel connection is to expand the present within the array. It produces around 180W of full sunshine. Major portion of the whole extent of the array's world, a huge amount of star electricity it'll manufacture.

e-ISSN: 2582-5208
International Research Journal of Modernization in Engineering Technology and Science
Volume:03/Issue:02/February-2021 Impact Factor- 5.354 www.irjmets.com

Figure 4: Photovoltaic Arrays (Multiple Modules)

V. SOLAR CONCRETE COLLECTOR

A. PARABOLIC TROUGH REFLECTORS

It contains a linear paraboloid reflector that concentrates lightweight to a receiver on the focal line of the reflector. It consists of a receiver that could possibly be a tube which is such that it is directly above the centre of the paraboloid reflector and fluid with operating fluid. An operating fluid is generally heated around in the temperature range of 150°-350°C as it flows, although in such case the receiver had to be used as a heat supply in order to influence the generation system.

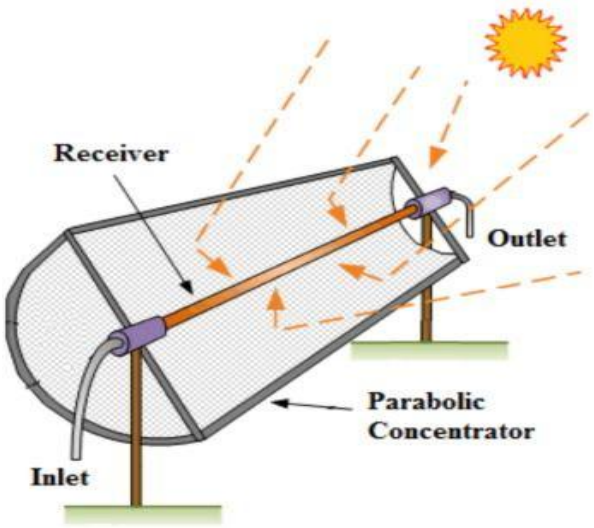

Figure 5: Parabolic Trough Reflectors

B. Fresnel

In a lens, the refraction happens to supply within the surface, whereas the material between the two surface is negligible or is not suitable for the refraction. It'll use raise a lot of temperature than the standard one and conjointly used in chamber heating. Its Installation could be used for the modifications of surface of argentiferous materials. This instrumentality is applying alternative energy within the field of high temperatures. These temperatures unit are achieved in just a matter of few seconds. Around 34 % of reduction in the reflective area is achieved by then physicists as compared to the parabolic reflector both having the same diameter, the twenty minutes is required for the action of the performance of the reflector in order to manually adjust to trace the sun is also considers to be its major disadvantage

e-ISSN: 2582-5208
International Research Journal of Modernization in Engineering Technology and Science
Volume:03/Issue:02/February-2021 Impact Factor- 5.354 www.irjmets.com

Figure 6: Fresnel Reflector

C. Parabolic Dish

It is similar in look to an outsized satellite dish; however, it has a mirror-like reflector and absorbent material to put the concentration. It uses a twin axial for following the sun. It is the result of half-hour obtained. By this dish is produces at the MW level in the star plant. It is considered to be the highest conversion performance of the concentrating alternative energy technology.

VI. MERITS OF SOLAR ENERGY

It saves up to twenty of energy prices. It will use in Remote Locations. Straightforward Installation (i.e., does not need any wires, cords, etc.). Rooftop, which suggests no new area is required & each domestic and commercial people could be able to produce their own electricity with the help of solar energy. It's broad on the market of daylight with freed from value, eco-friendly, renewable resources There is no need to provide any separate power source or any kind of other source i.e., fuel in order to run solar energy. No one would like water and energy.

VII. DEMERITS OF SOLAR ENERGY

No generation of energy once the sun isn't shining. The initial value is high. Large amount of extra space is required for such an immense production of power. For electrical energy (AC) application needed of the electrical converter and additionally storage in the dark. Production PV systems single semiconductor crystals is technically tricky, energy, time intense.

VIII. ISSUES IN SOLAR POWER DEVELOPMENT

- Potential land is needed mainly for developers/manufacturers.
- The deficiency within the relationship between the govt and business.
- The want for distinct, goals-driven, and cooperative R&D pro-jects to assist Asian countries to accomplish technology governance in the field of electric availability.
- Training and evolution of human amenities to control business enlargement and electrical phenomenon acquisition.
- The demand for intra-industry cooperation in growing the PV offer chain, by victimization the technical enlightenment, sharing through the workshops and conferences, in alliances with 'balance of systems' makers and collecting and correct business trends, market information, and projections.
- The got to construct shopper consciousness regarding the star technology, its usage, and social science.
- There is complexity of structure of grant and implication of too several organizations or agencies like MNRE, SECI, IREDA, restrictive electricity commission, and electricity board makes the enlargement of star electrical phenomenon comes terribly.
- Land allocation and Power purchase contract (PPA) linguistic communication could become a long method below the GBI (Generation primarily based Incentive) theme.
- Manufacturers square measure chiefly shopping for their all instrumentation for solar energy generation, from the foreign market thanks to the low costs compared to the native Indian market. So, the native market is facing losses thanks to importing solar energy generation instrumentation from foreign.

IX. APPLICATIONS OF SOLAR ENERGY

It is utilized in several applications including production of electricity, evaporation of water for various purposes, heating water for different task, heating and cooling of buildings, cooking of food, pumping of water, etc.

X. TARGET AND ACHIEVEMENTS IN SOLAR POWER PLANT IN INDIA

1. The world's largest floating 600 MW alternative energy project to be created at Omkareshwar dam on Narmada stream in the Khandwa district of Madhya Pradesh will begin power generation by the year 2022-23. The derived investment throughout this project stands at Rs 3,000 crore.

2. Bhadla star Parka

3. Shakti Sthala energy project

4. extremist Megastar Park – 1000MW

5. Rewa energy Project – 750MW

6. Kamuthi energy plant – 648MW

XI. CONCLUSION

Most of the source of major energy is completely reliable upon the non-renewable source of energy Alternative energy has become additional increase standard thanks to its economic advantages. On Battery Backup, alternative energy will even offer Electricity 24x7, even on cloudy days and at midnight. This is conjointly used with an inter-grid System with incessantly Power provides. It has additional advantages compared to different kinds of energy like fossil fuels and fossil fuel deposits. It's an alternate that is the promise and consistent with satisfying the high energy demand. Analysis of photovoltaic cells and alternative energy is promising contains a future worldwide.

ACKNOWLEDGEMENT

The authors wish to acknowledge Dr. J.P Kesari and Delhi Technological University for their complete support throughout their work.

XII. REFERENCES

[1] Shruti Sharma, Kamlesh Kumar Jain, Ashutosh Sharma's a review on "Solar Cell: Research and Applications," Material Sciences and Applications, 2015, 6, 1145-1155 Published in December 2015 http://dx.doi.org/10.4236/msa.2015.612113

[2] Askari Mohammad Bagher , Mirzaei Mahmmoud Abadi Vahid, Mirhabibi Mohsen. "Types of Solar Cells and Application." American Journal of Optic and Photonic. Vol. 3, No. 5, 2015, pp. 94-113. DOI: 10.11648/j.ajop.20150305.17

[3] Book of "Wind and Solar Power Plant" by Mukund Patel, CRC Press .

[4] N. Gupta, G. F. Alapatt, R. Podila, R. Singh, K.F. Poole, (2009). "Prospects of Nanostructure-Based Solar Cells for Manufacturing Future Generations of Photovoltaic Modules." International Journal of Photo energy 2009: 1. doi:10.1155/2009/154059.

[5] Book of "Solar Energy" by Dr. S.P. Sukhatme. Tata McGraw Hill Publication.

[6] Gaurav A. Madhugiri, S. R. Karale, "High solar energy concentration with a Fresnel lens: A Review" Vol.2, Issue.3, May-June 2012 pp-1381-1385 ISSN: 2249

Exploring the Effects of Different Embedding Algorithms and Neural Architectures on Early Detection of Alzheimer's Disease

Minni Jain, Rishabh Doshi, Vibhu Sehra and Divyashikha Sethia

Department of Computer Engineering, Delhi Technological University, Delhi, India

Abstract

Alzheimer's Disease (AD) is an irrecoverable, progressive neurodegenerative disorder that deteriorates the cognitive and linguistic abilities of a person over time. Ample research has been done on the early detection of AD; it remains a challenging task. Doctors use the patient's history, laboratory tests, and change in behaviour to diagnose the disease. Natural Language Processing(NLP) techniques can help automate the detection of AD, as Language impairments accompany this disease. This work aims to analyze the effect of different Embedding models on the DementiaBank dataset in order to detect the disease. The work uses both Generic and domain-specific Word Embeddings on the three deep learning models - CNN, Bidirectional LSTM(BLSTM), and CNN+BLSTM. Results indicate that for a specific picture description task like cookie theft description, domain-specific Word Embeddings tend to work better. Lastly, it is discussed how results are affected by the use of different Embedding models (Fasttext, Word2Vec, GloVe).

Keywords

Alzheimer's Disease, Natural Language Processing, Word Embeddings, Deep Learning, Cookie theft Description task

1. Introduction

Alzheimer's Disease(AD) is a brain disorder that slowly damages the nerve connections in the Brain. It is the most common type of dementia and symptoms of AD include communication difficulties, memory loss, poor judgment, and changing mood and personality[1]. More than 50 million people are diagnosed with Alzheimer's Disease every year [2]. This challenge has grown substantially over the years with the ageing of the population and the agerelated nature of many dementia-producing neurodegenerative diseases [1]. This number of cases for Alzheimer's Disease will continue to grow in the coming years. There is no proven health care method to cure AD. Hence, it is necessary to develop a new method to detect AD in a patient. Around 50 to 90% of dementia cases are left undiagnosed by standard clinical examinations [1]. Early detection of Alzheimer's Disease is still a massive issue in the current scenario. Alzheimer's Disease progresses over the years, and sometimes patients can have the disease for 20 years before showing symptoms. At this point, medical treatment is not very useful after the diagnosis of the disease. Hence the early detection of Alzheimer's is still a challenge in medical science. There have been many attempts to diagnose the disease with the help of neuroimaging techniques, but non-imaging techniques are essential to personalize the treatment for a patient and monitor disease progression. Machine learning can detect the language deficits that often accompany dementia and therefore can be used for ealry detection of Alzheimer's Disease. Previously, many Natural Language Processing (NLP) techniques were proposed to help in early detection of Alzheimer's Disease. These techniques treat the problem as a supervised learning problem. Previous research works like [2, 3, 4] made use of transcripts obtained from interviews with patients to detect Alzheimer's disease by using various machine learning and deep learning algorithms. Further, other studies like [5, 6, 7] used acoustic features obtained from the audio recordings of the interviews for the classification task. Our study aims to explore the effect of various Word Embeddings and neural architectures on transcripts obtained from the cookie theft description task of DementiaBank.

This paper makes use of both generic and domain-specific Word Embeddings that are trained on the transcripts. Out of all the presented models, the CNN + Bidirectional LSTM models that make use of Fasttext domain-specific Word Embeddings provides the best results. Sentences obtained from the transcripts are input to the models, and the output is the predicted label (Healthy or Alzheimer's), no feature engineering

ISIC'2021: International Semantic Intelligence Conference, Feb 25–27, 2021, New Delhi, Delhi , India

minnijain@dtu.ac.in (M. Jain); doshirishabh26@gmail.com (R. Doshi); vibhusehra@gmail.com (V. Sehra); divyashikha@dtu.ac.in (D. Sethia)

© 2020 Copyright for this paper by its authors. Use permitted under Creative Commons License Attribution 4.0 International (CC BY 4.0).

CEUR Workshop Proceedings (CEUR-WS.org)

[1] https://www.alz.org/alzheimers-dementia/10_signs

[2] https://www.alz.org/alzheimers-dementia/facts-figures

CEUR-WS.org/Vol-2786/Paper46.pdf

was involved in the process. Hence, this paper investigates how the task of detecting Alzheimer's Disease is affected by the use of various domain-specific and generic Embeddings on different neural architectures.

The rest of the paper comprises section 2, which consists of the Related works followed by our proposed work and experimental setup in sections 3 and 4, respectively. Then we present our results and discussion in sections 5 and 6, respectively, which is followed by the conclusion and future work in section 7.

2. Related Work

This section discusses the previous research, done in the field of Alzheimer's detection using the various machine learning and deep learning techniques.

2.1. Machine Learning Techniques

Existing research found on early detection of Alzheimer's Disease using Natural language processing made use of various machine learning techniques. [8] used three different machine learning algorithms - namely Decision trees, Support Vector Machine, and K-Nearest neighbours on a sample of 80 conversations to achieve the best accuracy of 79.5% using their Decision tree model. [9]proposed a model using Support Vector machine making use of 14 lexical features, nine syntactic features, and n-grams extracted from the Pitt Corpus in Dementia Bank Dataset by using 99 dementia transcripts and 99 control transcripts from the dataset. They used Area Under Curve (AUC) metric to test the performance of the algorithm achieving a maximum AUC score of 0.93 by using the top 1000 features obtained using a Leave Pair Out Cross-Validation (LPOCV) crossvalidation technique.

Further, [7] used the DementiaBank dataset to extract the acoustic measures and semantic measures to predict the clinical scores of the patients by making use of the bivariate dynamic Bayes network. [5] extracted acoustic features from the DementiaBank dataset and created a regression model to predict clinical scores (MMSE) used for dementia prediction. [6] made use of acoustic features on various Machine Learning models like Logistic Regression, KNN, Naive Bayes, Dummy classifier, Random Forests, and achieved the best accuracy of 78% with Logistic regression classifier.

2.2. Deep Learning Techniques

[10] had made use of Deep-Deep neural networks and had achieved an accuracy of 87.5% using the sparse vector representations of 4, 5 n-grams. The dataset was equally divided by making use of 99 dementia transcripts and 99 control transcripts from the dataset. Recently, [2] proposed the use of 3 different deep learning algorithms- 2D-CNN, LSTM, and 2D CNN - RNN models by making use of the complete Dementia bank dataset which consists of 1017 Alzheimer's transcripts and 243 control transcripts. They used each utterance as a separate data sample, therefore obtaining 14362 utterance samples. They achieve the best accuracy of 91.1% using the CNN-RNN model by using Word Embeddings along with POS tagged data to the classifier. [3] used a Hierarchical attention network (HAN) on the transcripts obtained from DementiaBank Dataset. They made use of Word Embeddings along with demographic features for the prediction task obtaining an accuracy of 86.9%. [11] proposed a model that combined bidirectional hierarchical recurrent neural network with an attention mechanism for dementia detection. [12] showed that fine tuned BERT model outperformed the models that used hand crafted feature engineering. Table.4 summarizes the approach used by previous research works.

3. Proposed Work

3.1. Preprocessing

This work uses the transcripts in the Dementia Bank dataset [13], which are available in the form of CHAT transcription [14]. The transcripts are passed through a series of steps as given below and illustrated in Fig. 1. PyLangAcq library [15], which is a powerful library that can handle CHAT data, reads the transcripts. We then convert all obtained utterances to lower text and remove all punctuations. We use 99 transcripts from each set (Dementia and Control) from the Cookie Theft task as suggested by [9, 10] where they made use of an equal number of dementia and control patients.

3.2. Word Embeddings used for early detection of Alzheimer's Disease

This work uses three types of Word Embeddings- Word2Vec [16], Glove [17] and, Fasttext [18]. These embeddings are chosen because they are widely used and have different architechtures which may tell us the best way to proceed with the problem in hand. All the Word Embeddings have a 300-dimensional vector representation for each Word. For each of the types mentioned above, two-Word Embeddings are used, Domain-

specific and generic Word Embeddings. All the transcripts from DementiaBank are used to create the domain specific Word Embeddings stated above. The maximum size of a transcript was 498 words. Hence, we keep the size of the Word Embedding as (500,300).

3.2.1. Domain-Specific Word Embeddings

Domain-Specific Word Embeddings are Embeddings that are trained on a specific corpus that contains data from the interested domain. They are highly effective for a specific domain but require extra training time. Gensim library [19] is used to create Word2vec [16] and Fasttext [18] Word Embeddings from the corpus. Glove[3] library is used to create the GloVe Embeddings [17].

3.2.2. Generic Word Embeddings

Generic Word Embeddings are Embeddings that are trained on vast generic corpora. Hence these Embeddings reduce training time and often give outstanding results. The work trains the pretrained Glove [17] Embeddings on 6 billion words. It trains Word2vec Embedding, which includes word vectors for a vocabulary of 3 million words and phrases on roughly 100 billion words from a Google News dataset. It also trains Fasttext [18] Embedding, which contains vectors for 1 million words, on Wikipedia 2017, UMBC web base corpus, and statmt.org news dataset having a total of 16 billion tokens.

3.3. Deep Learning Models Used

This section explains the deep learning models that are used for the classification of control and dementia patients. Keras functional API [20] is used to create all the deep learning models explained below. To address the concern of overfitting, we use L2 regularizer [21] as the kernel initializer. Due to the small size of the dataset, the research makes use of 10-fold cross-validation on each model. The model atempts to capture the language impairments that are often seen in the ealry phases of dementia. The Annexure provides the details of the model architecture.

3.3.1. CNN Model

In this work, the CNN model consists of a combination of 1DConvolution layers with an increasing number of kernels followed by MaxPool layers. A Dense network follows this. We use the Tanh activation for the 1D Convolution layer, ReLU [22] as the activation function for the Dense layers, and Softmax for classification.

3.3.2. Bi-Directional LSTM Model

The model has a series of the Bidirectional LSTM layer and Dropout [23] layer; further layers consist of a Dense network for classification. The Dropout layers are added to prevent overfitting in the model and dropout rate is kept at 30%. All the layers use default Tanh activation except the last one, which uses Softmax for classification.

3.3.3. Hybrid CNN + Bi-Directional LSTM Model

This model is a combination of the above two models. We pass the Embeddings through a series of 1D-convolutional layers followed by a MaxPooling layer, with two bidirectional LSTM layers stacked over the Maxpool layer. A dense network follows this. Fig. 2. illustrates the proposed model. The Activations used for CNN and bidirectional LSTM is Tanh, while we use ReLU [22] activation for dense layers followed by a SoftMax function for classification.

3.4. Training Details

The above-stated models are trained using the Adam Optimizer [24] for 30 epochs, each using Binary cross-entropy as the loss function. L2 regularization [21] is applied in each layer has $\lambda = 10^{-5}$

4. Experimental Details

This work uses Pitt Corpus, which is the largest English dataset available in DementiaBank [13]. DementiaBank is a part of the TalkBank project initiated by Carnegie Mellon University. The National Institute of Aging funds it. The project encourages research for human communication. It uses the Codes for the Human Analysis of Transcripts (CHAT) system [14], which provides automatic analysis and testing. The CHAT system is commonly used in many datasets to provide uniformity and easy usage. Various participants from each group (Control and dementia) visited annually for the interview. Pitt Corpus [13] is a collection of transcripts and audio files that were collected as a part of a longitudinal study conducted by Alzheimer's and Related dementia at the University of Pittsburgh School of Medicine. This dataset contains interviews

[3] https://github.com/JonathanRaiman/glove

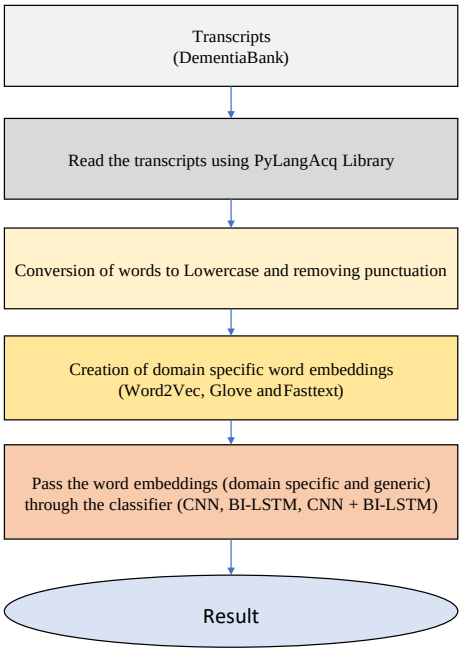

Figure 1: Proposed Approach for early detection of Alzheimer's Disease

of patients with possible Alzheimer's along with control patients, containing transcripts of 104 control patients and 208 dementia patients. The patient's ages range from 49-90 years in the dataset. It comprises of four different tests on the patients:

- Cookie Theft: Patients see an image provided by the Boston Diagnostic Aphasia Examination, and then the patients (Control and Dementia) recall the events taking place in the image (Fig. 3).
- Fluency: This task is done only for dementia patients where they respond to a word Fluency task.
- Recall: The Dementia Patients undergo a story recall test.
- Sentence: The Dementia Patients perform a Sentence construction task.

The work uses the Cookie theft part of the corpus as it contains the maximum number of participants, and previous researchers have used it.

5. Results

All the three neural models - 1D CNN, Bidirectional LSTM(BLSTM), and 1D CNN + Bidirectional LSTM (CNN + BLSTM) use the generic and domain-specific Word Embeddings of each Embedding model. For domain-specific Word Embeddings, we achieved maximum accuracies of 89.9%, 85%, and 90.6% with Fasttext Embedding for CNN, BLSTM, and CNN + BLSTM models, respectively. While for pre-trained Word Embeddings, maximum accuracies obtained were 85.2% with Glove for both CNN and BLSTM, and 85.5% with Fasttext for CNN + BLSTM. The baseline model used is constant label classifier which gives the same result for any input which achieved an accuracy of 50% since we have two classes. Tables 1, 2, and 3 summarize the results obtained by using the three Embedding models (Glove, Word2Vec, Fasttext) for the three given deep learning models. Fig. 4. compares the F1 scores achieved by these models which makes clear that Domain Specific Fasttext embeddings outperform all the other embeddings.

Accuracy, precision, recall, and F1-score are used as the evaluation metrics. Previous works using deep learning techniques such as [2] used accuracy, [10] used AUC (Area Under Curve), and [3] used precision, recall and F1 score as the evaluation metrics. Generally, the performance of the domain-specific Word Embeddings was better than that of Generic Word Embeddings. The probable causes are discussed further in the next section.

6. Discussions

The paper aims to explore how the different Word Embedding models and types of Embeddings perform on different neural models. It uses both the domain specific and the generic Word Embeddings to classify the transcripts. However, since the domain-specific Word Embeddings have been trained on the same corpus being used, it generally provides better results. As the cookie theft data comprises of explaining a particular image, the vocabulary found in the transcripts is limited, and as a result, it is easier to understand the relationship between words. Using Domain-specific, Fasttext, and Word2vec provides better results than their Generic counterparts. Results indicate that Glove Embeddings provide similar results on both types of Word Embeddings.

If we had a combination of different tasks (not only cookie theft) having a larger corpus and vocabulary, Generic Embedding might perform better.

Results indicate that Word2vec has the lowest accuracy amongst the three Embedding models. This is possible because domain-specific Word2vec requires a larger corpus to develop the semantic relation as it

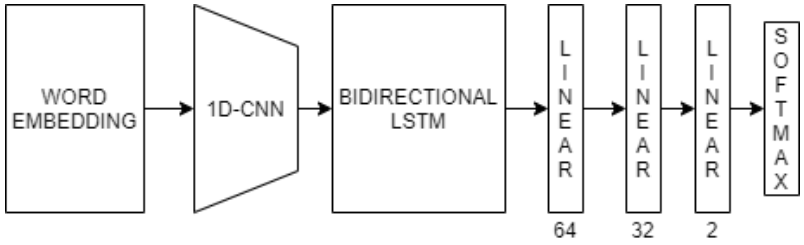

Figure 2: Pictorial Representation of the CNN+BLSTM used

Table 1
Results obtained for the CNN model

Word Embedding	Accuracy	Precision	Recall	F1-score
Fasttext				
Generic	0.85	0.86	0.85	0.85
Domain-specific	0.90	0.92	0.90	0.91
GloVe				
Generic	0.85	0.85	0.85	0.85
Domain-specific	0.83	0.83	0.81	0.82
Word2Vec				
Generic	0.77	0.78	0.77	0.77
Domain-specific	0.80	0.80	0.80	0.80

only captures local word relations. The domain specific Fasttext Embedding gives the best result since it does not require a large corpus as it breaks each word into character n-grams, thereby increasing the vocabulary size.

Results also indicate that the hybrid CNN + BLSTM model achieves the highest accuracy of 90.6%. The CNN + BLSTM model works better than any single use of either of the model, because:

- CNN model captures the short-term dependencies in text.
- LSTM model captures long term dependencies in the text. Bidirectional LSTM is better than the LSTM as it trains on two LSTM cells instead of one cell in a single input sequence.

Compared to similar previous works like [2] and [3] use a Word Embeddings layer that is trained along with the neural architecture, this study uses three Word Embedding models and from each Embedding model, a domainspecific and pre-trained Embedding is created to identify how different Embedding models and the type of data on which the Embeddings are trained affects the performance of detecting Alzheimer's Disease. [2] breaks down each transcript into utterances and considers them as separate data samples thereby

Table 2
Results obtained for the BLSTM model

Word Embedding	Accuracy	Precision	Recall	F1-score
Fasttext				
Generic	0.80	0.85	0.80	0.82
Domain-specific	0.85	0.86	0.85	0.85
GloVe				
Generic	0.85	0.88	0.85	0.86
Domain-specific	0.84	0.85	0.84	0.84
Word2Vec				
Generic	0.74	0.75	0.74	0.74
Domain-specific	0.80	0.80	0.80	0.80

Table 3
Results obtained for the CNN+BLSTM model

Word Embedding	Accuracy	Precision	Recall	F1-score
Fasttext				
Generic	0.86	0.86	0.85	0.85
Domain-specific	0.91	0.91	0.91	0.91
GloVe				
Generic	0.84	0.85	0.83	0.84
Domain-specific	0.87	0.88	0.87	0.87
Word2Vec				
Generic	0.77	0.79	0.78	0.78
Domain-specific	0.80	0.80	0.80	0.80

Table 4
Comparision of proposed work with results and techniques of existing work

Author	Accuracy	Model	Technique
Orimaye et al. (2018) [10]	87.5%	Neural Network	4-5 n-grams
Karlekar et al. (2018) [2]	82.8%	2D-CNN	Word Embeddings
Karlekar et al. (2018) [2]	83.7%	RNN	Word Embeddings
Karlekar et al. (2018) [2]	91.1%	2D-CNN + RNN	Word Embeddings along with POS tagged data
Kong et al. (2019) [3]	86.9%	Hierarchical Attention Network	Word Embeddings
Proposed work	90.6%	1D-CNN + BLSTM	Doamin-Specific Fasttext Word Embedding

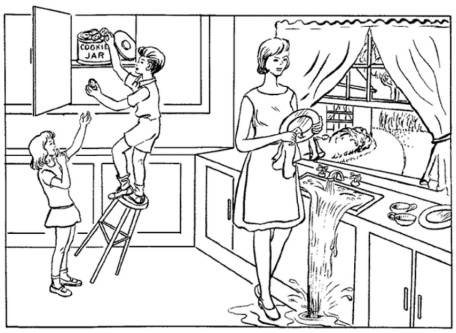

Figure 3: Boston cookie theft description task

creating 14362 samples as compared to our 198 samples which are complete transcripts of a patient.

7. Conclusion and Future Work

This study employs three Word Embedding algorithms on three different Neural Models that make use of CNN and Bidirectional LSTM for Alzheimer's Disease Classification. For each word embedding algorithm 2 different types of word embeddings were used - Domain Specific and Generic Embeddings, where it was found that Domain Specific word embeddings performed better than Generic Word Embeddings. This work was limited by the small amount of dataset available. In future, we may gather a larger dataset that may help in creation of a more generalized embedding. Further, we can also extend the dataset for people speaking different languages.

A. Appendix

A.1. Neural Model Details

We used the following neural models. The batch size was kept at 10. In the last dense layer of each model softmax activation function was used. Other dense layers use a rectified linear activation function.

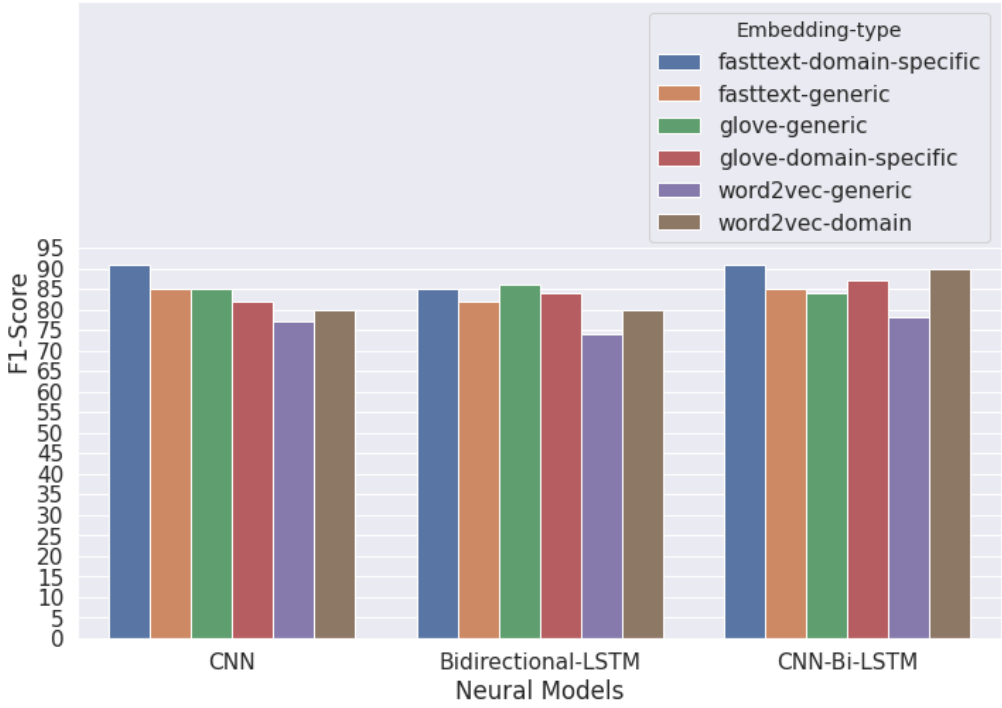

Figure 4: Comparsion of F1-scores achieved by different neural models and Word Embeddings

A.1.1. CNN Model

Each CNN-1D layer in brackets represents(no-of-filters , kernel-size)
CNN-1D(8,3) ⟶ CNN-1D(10,3) ⟶ MaxPool-1D(3) ⟶ CNN-1D(12,3) ⟶ CNN-1D(14,3) ⟶ MaxPool-1D(3) ⟶ Flatten() ⟶ Dense(20,Relu) ⟶ Dense(10,Relu) ⟶ Dense(2,Softmax)

A.1.2. BLSTM

Each LSTM layer in brackets represents(no-of-lstm-cells-in-that-layer)
Bidir(LSTM(16)) ⟶ Dropout(0.3) ⟶ Bidir(LSTM(8)) ⟶ Bidir(LSTM(4)) ⟶ Bidir(LSTM(2)) ⟶ Dropout(0.2) ⟶ Dense(8) ⟶ Dense(2,Softmax)

A.1.3. CNN+BLSTM

CNN-1D(8,3) ⟶ CNN-1D(10,3) ⟶ MaxPool-1D(3) ⟶ CNN-1D(16,3) ⟶ CNN-1D(20,3) ⟶ MaxPool-1D(3) ⟶ Bidir(LSTM(8)) ⟶ BatchNorm() ⟶ Bidir(LSTM(16)) ⟶ Dense(64,Relu) ⟶ Dense(32,Relu) ⟶ Dense (2,Softmax)

References

[1] M. W. Bondi, E. C. Edmonds, D. P. Salmon, Alzheimer's disease: past, present, and future, Journal of the International Neuropsychological Society 23 (2017) 818–831.

[2] S. Karlekar, T. Niu, M. Bansal, Detecting linguistic characteristics of Alzheimer's dementia by interpreting neural models, arXiv preprint arXiv:1804.06440 (2018).

[3] W. Kong, H. Jang, G. Carenini, T. Field, A neural model for predicting dementia from language, in: Machine Learning for Healthcare Conference, 2019, pp. 270–286.

[4] S. O. Orimaye, J. S.-M. W. K. J. Golden, Learning Predictive Linguistic Features for Alzheimer's Disease and related Dementias using Verbal Utterances, in: Proceedings Workshop on Computational Linguistics and Clinical Psychology: From Linguistic Signal to Clinical Reality, 2014, pp. 78–87.

[5] S. Al-Hameed, M. Benaissa, H. Christensen, Sim-

ple and robust audio-based detection of biomarkers for alzheimer's disease, in: 7th Workshop on Speech and Language Processing for Assistive Technologies (SLPAT), 2016, pp. 32–36.

[6] V. Masrani, Detecting dementia from written and spoken language, Ph.D. thesis, University of British Columbia, 2018.

[7] M. Yancheva, F. Rudzicz, Vector-space topic models for detecting Alzheimer's disease, in: Proceedings Annual Meeting of the Association for Computational Linguistics, 2016, pp. 2337–2346.

[8] C. Guinn, A. Habash, Language analysis of speakers with dementia of the Alzheimer's type, in: AAAI Fall Symposium Series, 2012, pp. 8–13.

[9] S. O. Orimaye, J. S.-M. Wong, K. J. Golden, C. P. Wong, I. N. Soyiri, Predicting probable Alzheimer's disease using linguistic deficits and biomarkers, BMC Bioinformatics 18 (2017).

[10] S. O. Orimaye, J. S.-M. Wong, C. P. Wong, Deep language space neural network for classifying mild cognitive impairment and alzheimer-type dementia, PloS one 13 (2018).

[11] Y. Pan, B. Mirheidari, M. Reuber, A. Venneri, D. Blackburn, H. Christensen, Automatic hierarchical attention neural network for detecting ad, 2019, pp. 4105–4109. doi:10.21437/Interspeech.2019-1799.

[12] A. Balagopalan, B. Eyre, F. Rudzicz, J. Novikova, To bert or not to bert: Comparing speech and language-based approaches for alzheimer's disease detection, 2020. arXiv:2008.01551.

[13] J. T. Becker, F. Boller, O. L. Lopez, J. Saxton, K. McGonigle, The natural history of Alzheimer's disease. Description of study cohort and accuracy of diagnosis., Archives of Neurology 51 (1994) 585–594.

[14] B. Macwhinney, The CHILDES project: tools for analyzing talk, Child Language Teaching and Therapy 8 (2000).

[15] J. L. Lee, R. Burkholder, G. B. Flinn, E. R. Coppess, Working with CHAT transcripts in Python, Technical report TR-2016-02, Technical Report, Department of Computer Science, University of Chicago, 2016.

[16] T. Mikolov, et al., Efficient Estimation of Word Representations in Vector Space, in: Proceedings International Conference on Learning Representations, 2013.

[17] Pennington, Jeffrey, R. Socher, C. D. Manning, Glove: Global vectors for word representation, in: Proceedings International Conference Empiricial Methods in Natural Language Processing, 2014.

[18] P. Bojanowski, E. Grave, A. Joulin, T. Mikolov, Enriching Word Vectors with Subword Information, arXiv:1607.04606 (2016).

[19] R. Rehurek, P. Sojka, Software framework for topic modelling with large corpora, in: Proceedings International Workshop on New Challenges for NLP Frameworks, 2010.

[20] Keras, Deep learning for humans, https://github.com/fchollet/keras, 2015. Last accessed on Nov 2019.

[21] J. Schmidhuber, Deep learning in neural networks: An overview, Neural Networks 61 (2015) 85–117.

[22] A. F. Agarap, Deep Learning using Rectified Linear Units (ReLU), arXiv:1803.08375 (2018).

[23] N. Srivastava, et al., Dropout: A Simple Way to Prevent Neural Networks from Overfitting, Journal of Machine Learning Research 15 (2014) 1929–1958.

[24] D. P. Kingma, J. Ba, A Method for Stochastic Optimization, ?arXiv:1412.6980 (2014).

[25] L. Hebert, P. A. Scherr, J. L. Bienias, D. A. Bennett, D. A. Evans, Alzheimer disease in the US population: prevalence estimates using the 2000 census, Arch Neurol 60 (2003) 1119–1122.

Facial Expression Recognition from 3D Facial Landmarks Reconstructed from Images

2020 IEEE International Symposium on Sustainable Energy, Signal Processing and Cyber Security (iSSSC) | 978-1-7281-8880-5/20/$31.00 ©2020 IEEE | DOI: 10.1109/iSSSC50941.2020.9358815

Limysh Kalapala, Harshit Yadav, Himanshu Kharwar, Seba Susan
Delhi Technological University, Shabad Daulatpur, Bawana Road, Delhi, India-110042
seba_406@yahoo.in

***Abstract*—Direct classification of normalized and flattened 3D facial landmarks reconstructed from 2D images is proposed in this paper for recognizing eight types of facial expressions depicting the emotions of- *sadness, anger, contempt, disgust, fear, happiness, neutral* and *surprised*. The first stage is the 3D projection of 2D facial landmarks. The pre-trained convolutional Face Alignment Network (FAN) proposed recently for 2D/3D face alignment is used for the purpose. The 3D cartesian coordinates are translated to the spherical coordinate system prior to the classification stage. A variety of classifiers are tried and tested for classifying the 68 facial landmarks, for both the coordinate systems. The benchmark CK+ video dataset is used for the experimentation; the last frame of each video that depicts the peak of each emotion is used as the input image. The experimental results indicate that direct classification of normalized and flattened 3D facial landmarks in the spherical coordinate system yields the highest accuracy for the support vector machine classifier with grid search for determining optimal parameters.**

Keywords—Facial expression recognition, Face alignment network, Support Vector Machine, 3D facial landmarks, Spherical coordinate system

I. INTRODUCTION

Facial expression recognition has always been a trending and popular research topic. It has a wide range of applications such as security and electronic surveillance for human-computer interaction (HCI) [1], in the medical field for treating patients [2, 3], and also in the entertainment field [4]. In the area of electronic surveillance, the malicious intentions of thieves or mischief-makers can be detected by automated analysis of their facial expressions [5]. The first step in a facial expression recognition pipeline is accurate face segmentation and cropping. The accurate and automated segmentation of human faces from videos and images is a challenging problem by itself. Face recognition [6, 7], eye movement tracking [8, 9] and facial expression analysis [10] are some of the applications that involve face segmentation. Facial expressions are a non-verbal mode of interaction for human beings. Human emotions impact our daily routines and describe our social behaviour. Our face is the biggest indicator of our emotions. Computer-based facial expression recognition is a complex task to deal with. Practically there are numerous emotions, but during the 1970s, the psychologist Eckman identified six basic emotions: *happiness*, *surprise*, *disgust*, *fear*, *sadness* and *anger* [11]; these being the basic emotions experienced by all human beings. Facial expression cues are usually gathered from images [12] or videos [13] of frontal-view faces. Spatio-temporal features [14] are extracted from videos for dynamic texture analysis. Facial emotion depicted in videos can also be interpreted as a dynamic texture [15].

Facial landmarks are a set of keypoints on a human face that convey important information about shape and pose information. Detection of landmarks is an intermediary task in many computer vision tasks such as face recognition, registration, expression analysis, and face tracking [16]. Initially researchers were focused on facial expression recognition using 2D facial landmarks [17]. These 2D points are a set of cartesian coordinates detected from a single image. In a recent work, Khan [18] used intra-landmark distances as the feature vector for the classification of facial expressions. Facial expressions of drivers were detected with the help of 2D facial landmarks by Jeong and Ko for the purpose of safe driving [19]. 2D facial landmarks are more popular than 3D facial landmarks due to the ease of availability of 2D images. However, 2D data is not sufficient for accurate facial expression analysis due to sensitivity to illumination and pose.

Subsequent to the success of 2D facial landmarks, researchers were next drawn towards the problem of facial emotion recognition using 3D facial landmarks. Facial emotion recognition using 3D feature points can be achieved by adopting two different approaches: - firstly, extracting the 3D points using 3D scanner devices, and secondly, using 3D projection of 2D facial points extracted from an image. Berretti *et al.* [20] used 3D face scanner for real-time recognition of facial expressions. Yang and Yin used CNN based 3D facial expression recognition model that makes use of masking and landmark features [21]. Several other researches on 3D facial emotion recognition [22, 23, 24] also use similar techniques. The processing of 3D facial data is computationally expensive. In [25], the geometric face deformations of multiple subjects are transferred to a single standard model, and a generalized expression manifold is built for the standard model. In a recent work [26], the 3D facial expression modelling is performed from a single image. The Kendall shape space is used for modelling the facial expressions. Likewise, in [27], 3D facial modelling was achieved from 2D images by using texture and mesh analysis. Similar to the second line of approach, our work takes a single 2D facial image as input and reconstructs 3D facial landmarks from the 2D image using the pre-trained convolutional Face Alignment Network (FAN) proposed recently for 2D/3D face alignment. We present a simple, fast and reliable classification approach by translating all the landmark points into the spherical coordinate system and using an appropriate classifier for direct classification of the normalized and flattened 3D facial landmarks. The remainder of this paper is organized as follows: Section II details the proposed model of facial emotion detection using

978-1-7281-8880-5/20/$31.00 ©2020 IEEE

Authorized licensed use limited to: DELHI TECHNICAL UNIV. Downloaded on March 03,2021 at 06:09:18 UTC from IEEE Xplore. Restrictions apply.

the reconstructed 3D landmarks, section III analyses the results and section IV summarizes the conclusions.

II. Proposed Method

3D facial landmark points yield important information regarding the facial expression, pose and shape, that yields improved recognition results [28]. Usually, the 3D landmark points are used for face pre-processing operations such as face cropping and normalizing the face to a standard size [29]. They are seldom used directly as features, a possibility that we have explored through our experiments on facial expression recognition. Most of the related research revolves around the development of complex learning models that accept as input the projected 3D face model. Masi *et al*. for instance, proposed pose-aware CNNs in 2016 that used the 3D facial model as the input for face recognition [30]. Features extracted from a pre-trained facial landmark localization network along with landmark heatmaps were integrated in [31] with features from the face recognition network for efficient classification. In our proposed model, we treat the normalized and flattened 3D landmark points projected from 2D images as features for classification. Both cartesian and spherical coordinate systems are tested for the purpose, and a variety of classifiers are used. The steps in our proposed method comprise of: - (i) face detection (ii) 3D-facial landmark extraction (iii) feature normalization and (iv) flattening. Facial expression classification is achieved by creating the feature set and training these on various classifiers. The process flow for our method is shown in Fig. 1. The steps are explained below in more detail.

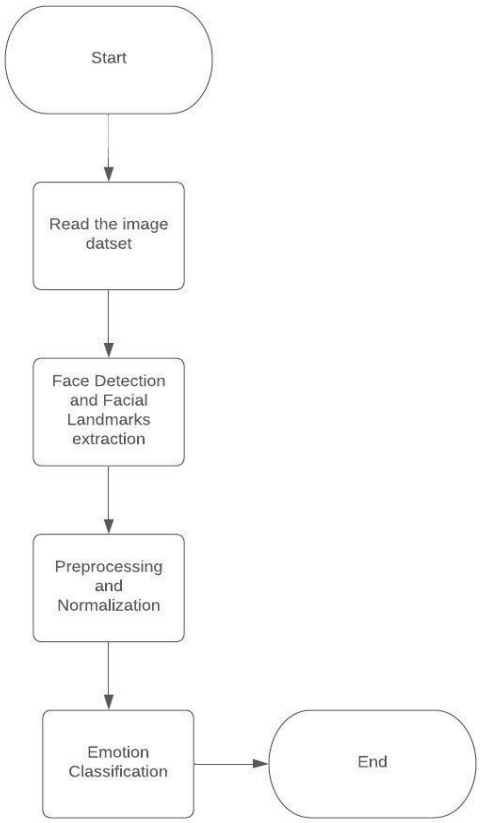

Fig. 1. Workflow of proposed Model.

A. Face Detection and 3D Facial Landmarks Extraction

The standard pre-trained python library face-alignment 1.1.1 [32] was used to extract 3D facial landmarks from a 2D image dataset. The pre-trained model used is the convolutional Face Alignment Network (FAN) proposed by Bulat and Tzimiropoulos in [32], which is an improvisation of the stacked hour glass model [33]. There are 68 unique 2D landmarks that are projected onto 3D by the pre-trained FAN model. The facial distribution of the 68 landmarks is summarized in Table I. An example of the facial landmarks shown superimposed on a facial image is shown in Fig. 2. The corresponding 3D projection is shown in Fig. 3. The 3D landmark points are stored in a 68x3 matrix format.

Fig. 2. 68 x 3 Facial landmarks extracted

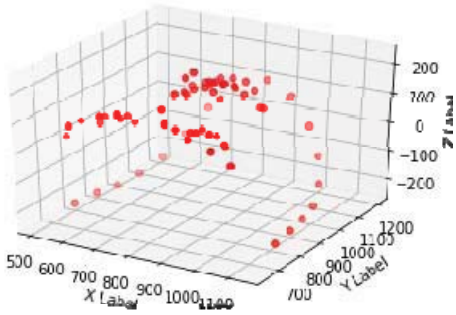

Fig. 3. Facial landmarks plotted in 3D

TABLE I. Facial Landmarks and their Facial Location

Face Feature	Facial Landmarks
Left eye	42-47
Mouth	48-67
Left Eyebrow	22-26
Nose	27-35
Right Eyebrow	17-21
Right Eye	36-41
Jaw	0-16

B. Feature Pre-Processing and Normalization

We convert the cartesian coordinates into the equivalent spherical coordinates. In object tracking experiments in computer vision, the polar (2D) or spherical coordinates (3D) yield a better representation of the positional and angular displacements than the cartesian coordinate system [34].

Authorized licensed use limited to: DELHI TECHNICAL UNIV. Downloaded on March 03,2021 at 06:09:18 UTC from IEEE Xplore. Restrictions apply.

The inter-relationship between cartesian coordinate system (x, y, z) and the spherical coordinate system (ρ, θ, ϕ) is shown in (1). The normalization procedure is shown in (2) for the cartesian coordinate system.

$$
\begin{aligned}
x &= \rho \cos\theta \sin\theta \\
y &= \rho \sin\theta \sin\phi \\
z &= \rho \cos\phi \\
&where: \\
\rho &= \sqrt{x^2 + y^2 + z^2}, \\
\theta &= \arctan\frac{y}{x}, \\
\phi &= \arctan\frac{\sqrt{x^2 + y^2}}{z}
\end{aligned}
\tag{1}
$$

We normalized all features by

$$
\begin{aligned}
x &= \frac{(x - x_{mean})}{x_{std}} \\
y &= \frac{(y - y_{mean})}{y_{std}} \\
z &= \frac{(z - z_{mean})}{z_{std}}
\end{aligned}
\tag{2}
$$

where,

$x_{std}, y_{std}, z_{std}$ are standard deviations of x, y, z.

$x_{mean}, y_{mean}, z_{mean}$ are mean value of x, y, z

A similar normalization operation is performed for the spherical coordinates (ρ, θ, ϕ).

C. Facial Emotion Classification

The normalized features are then flattened or linearized. The 68x3 feature matrix is transformed into a linear list in both formats: - {XYZXYZXYZ..} that we term as row-wise representation, and {XXXYYYZZZ..} that we term as column-wise representation. The procedure was repeated for the spherical coordinates.

TABLE II. CLASS DISTRIBUTION OF CK+ DATASET

Emotion	Classes	No. of samples
Sadness	0	28
Anger	1	45
Contempt	2	18
Disgust	3	59
Fear	4	25
Happiness	5	69
Neutral	6	593
Surprise	7	83

We then created a labeled dataset consisting of our pre-processed features and emotion labels, the class distribution of which is shown in Table II. Next, the emotions were predicted using various classifiers such as: KNN, Naive Bayes, Logistic Regression, Decision Tree, fully connected neural network, and Support Vector Machines (SVM) (with and without grid search that is used to determine the optimal SVM parameters).

III. RESULTS AND DISCUSSION

In our experiments, we have used the extended Cohn-Kanade Plus dataset [35]. It is a dataset with 123 subjects and 593 videos, out of which 327 videos depict a person going from neutral to one of the emotions (*sadness, anger, contempt, disgust, fear, happiness,* and *surprised*). In each video, the last frame has the highest-level depiction of the emotion. The last frame of the dataset is extracted from all the 327 videos and extra 593 images of *neutral* emotion are added to the dataset as it is harder for classification models to classify *neutral* emotion. The classification is performed on 8 emotions (classes) of *sadness, anger, contempt, disgust, fear, happiness, neutral,* and *surprised.* Table II gives the class-wise distribution of the samples for the eight emotions.

The experiments were performed using python version 3.8.5 software; python is the language of choice because it has a plethora of machine learning libraries and APIs which makes it very fast and easy to use. The following libraries were used for the implementation: - *Sci-kit Learn, TensorFlow, NumPy, Pandas, Matplotlib, Seaborn, face-alignment.* The experiments were conducted on an i7-7700HQ processor with 4 cores and 8 threads, and a GTX 1060 graphics card with 1280 CUDA cores. 3D facial landmarks were extracted from all 920 images in the dataset using *face-Alignment* pre-trained library [32] which gave us 68 3D facial landmarks, each of the landmark has three coordinates (the x, y, and z coordinates), and a feature matrix of size 68x3 for every image in the dataset. To pass these features into a machine learning classifier, we need to flatten or transform the 68x3 image into a linear 1D vector. A couple of approaches were used for converting the 68x3 data into a 1D vector.

1) 68x3 matrix is flattened row-wise i.e. if an image has facial landmarks (x1, y1, z1), (x2, y2, z2) … (x68, y68, z68) then our resulting vector will be (x1, y1, z1, x2, y2, z2… x68, y68, z68) which gives us 204 features.

2) 68x3 matrix is flattened column-wise i.e. if an image has facial landmarks (x1, y1, y1), (x2, y2, z2) … (x68, y68, z68) then our resulting vector will be (x1, x2, x3…x68, y1, y2, y3…y68, z1, z2, z3…z68) which has 204 features.

3) Transforming 68x3 matrix into spherical coordinates as explained in the previous section, and then flattening the resulting matrix row-wise and column-wise as stated in approaches (1) and (2), resulting in feature vectors of dimension 204. The results on all the classifiers for (1) and (2) approaches are similar, but in case of (3) we get significantly better results than the first two approaches.

Several supervised machine learning classification models namely Logistic Regression (LR), Support Vector Machines, Fully Connected Neural Networks, Decision

Authorized licensed use limited to: DELHI TECHNICAL UNIV. Downloaded on March 03,2021 at 06:09:18 UTC from IEEE Xplore. Restrictions apply.

Trees, K-Nearest Neighbors (KNN), and Naïve Bayes Classifier were used for evaluating the proposed method. A summary of the mean accuracy scores of all the classifiers is given in Table III. Out of all the classification algorithms, the best performance was that of the Support Vector Machine (SVM). Using grid search for SVM parameter selection gave us the best recognition results. The parameters for grid search were c= [100,10000], gamma = [0.0000005, .0001], and kernel = ['linear','rbf'], out of which best parameters were c = 1000, gamma= 1e-5, and kernel = 'rbf'. A 70-30 Train-Test split was used to train the dataset along with 5-fold cross-validation for performance comparison of all the classifiers. The experimental results indicate that direct classification of normalized and flattened 3D facial landmarks in the spherical coordinate system yields the highest accuracy for the support vector machine classifier, with grid search for determining optimal SVM parameters.

TABLE III. COMPARISON OF TEST ACCURACIES OF ALL CLASSIFICATION MODELS

	Spherical Coordinates normalized (column-wise)	**Spherical Coordinates normalized (row-wise)**	**Cartesian Coordinates normalized (column-wise)**	**Cartesian Coordinates normalized (row-wise)**
SVM	0.8261	0.8385	0.8354	0.8214
SVM (Grid Search)	0.8695	0.8850	0.8648	0.8602
LR	0.8820	0.8276	0.8007	0.8152
FCNN	0.7835	0.8152	0.8007	0.8151
Decision Tree	0.7748	0.7638	0.7717	0.7810
KNN	0.8043	0.7779	0.7701	0.7748
Naïve-Bayes	0.4855	0.5133	0.4565	0.4413

IV. CONCLUSION

Direct classification of normalized and flattened 3D facial landmarks projected from 68 2D landmark points is proposed in this paper for recognizing eight categories of facial expressions. 3D facial landmarks are projected from the 2D points using a recently proposed pre-trained convolutional neural network called Face Alignment Network. The spherical coordinate system is found to yield the best results for row-wise flattening of features. The support vector machine classifier with grid search for optimal parameters proves to be the best classifier. Results on the CK+ facial expression recognition prove the veracity of our claim.

REFERENCES

[1] Abdat, Faiza, Choubeila Maaoui, and Alain Pruski. "Human-computer interaction using emotion recognition from facial expression." In *2011 UKSim 5th European Symposium on Computer Modeling and Simulation*, pp. 196-201. IEEE, 2011.

[2] Fuchs-Lacelle, Shannon, and Thomas Hadjistavropoulos. "Development and preliminary validation of the pain assessment checklist for seniors with limited ability to communicate (PACSLAC)." *Pain Management Nursing* 5, no. 1 (2004): 37-49.

[3] Surguladze, Simon A., Andrew W. Young, Carl Senior, Gildas Brébion, Michael J. Travis, and Mary L. Phillips. "Recognition accuracy and response bias to happy and sad facial expressions in patients with major depression." *Neuropsychology* 18, no. 2 (2004): 212.

[4] Hazlett, Richard L. "Measuring emotional valence during interactive experiences: boys at video game play." In *Proceedings of the SIGCHI conference on Human Factors in computing systems*, pp. 1023-1026. 2006.

[5] Al-modwahi, Ashraf Abbas M., Onkemetse Sebetela, Lefoko Nehemiah Batleng, Behrang Parhizkar, and Arash Habibi Lashkari. "Facial expression recognition intelligent security system for real time surveillance." In *Proc. of World Congress in Computer Science, Computer Engineering, and Applied Computing*. 2012.

[6] Susan, Seba, Abhishek Jain, Aakash Sharma, Shikhar Verma, and Siddhant Jain. "Fuzzy match index for scale-invariant feature transform (SIFT) features with application to face recognition with weak supervision." *IET Image Processing* 9, no. 11 (2015): 951-958.

[7] Susan, Seba, and Roni Chakre. "3D-difference theoretic texture features for dynamic face recognition." In *2016 International conference on computational techniques in information and communication technologies (ICCTICT)*, pp. 227-232. IEEE, 2016.

[8] Susan, Seba, Ankur Agarwal, Chetan Gulati, Sunpreet Singh, and Vaibhav Chauhan. "Human Attention Span Modeling using 2D Visualization Plots for Gaze Progression and Gaze Sustenance." In *Proceedings of the 2019 3rd International Conference on Artificial Intelligence and Virtual Reality*, pp. 42-46. 2019.

[9] Susan, Seba, and Pooja Kadyan. "A supervised fuzzy eye pair detection algorithm." In *2013 5th International Conference and Computational Intelligence and Communication Networks*, pp. 306-310. IEEE, 2013.

[10] Susan, Seba, Nandini Aggarwal, Shefali Chand, and Ayush Gupta. "Image coding based on maximum entropy partitioning for identifying improbable intensities related to facial expressions." *Sādhanā* 41, no. 12 (2016): 1393-1406.

[11] Ekman, Paul. "Basic emotions." *Handbook of cognition and emotion* 98, no. 45-60 (1999): 16.

[12] Susan, Seba, and Gitin Kakkar. "Decoding facial expressions using a new normalized similarity index." In *2015 Annual IEEE India Conference (INDICON)*, pp. 1-6. IEEE, 2015.

[13] Liu, Mengyi, Shiguang Shan, Ruiping Wang, and Xilin Chen. "Learning expressionlets on spatio-temporal manifold for dynamic facial expression recognition." In *Proceedings of the IEEE conference on computer vision and pattern recognition*, pp. 1749-1756. 2014.

[14] Susan, Seba, Minni Mittal, Srishti Bansal, and Prachi Agrawal. "Dynamic texture recognition from multi-offset temporal intensity co-occurrence matrices with local pattern matching." In *Computational Intelligence: Theories, Applications and Future Directions-Volume II*, pp. 545-555. Springer, Singapore, 2019.

[15] Zhao, Guoying, and Matti Pietikainen. "Dynamic texture recognition using local binary patterns with an application to facial expressions." *IEEE transactions on pattern analysis and machine intelligence* 29, no. 6 (2007): 915-928.

[16] Ouanan, Hamid, Mohammed Ouanan, and Brahim Aksasse. "Facial landmark localization: Past, present and future." In *2016 4th IEEE International Colloquium on Information Science and Technology (CiSt)*, pp. 487-493. IEEE, 2016.

[17] Taheri, Sima, Pavan Turaga, and Rama Chellappa. "Towards view-invariant expression analysis using analytic shape manifolds." In *Face and Gesture 2011*, pp. 306-313. IEEE, 2011.

[18] Khan, Fuzail. "Facial expression recognition using facial landmark detection and feature extraction via neural networks." *arXiv preprint arXiv:1812.04510* (2018).

[19] Jeong, Mira, and Byoung Chul Ko. "Driver's facial expression recognition in real-time for safe driving." *Sensors* 18, no. 12 (2018): 4270.

[20] Berretti, Stefano, Alberto Del Bimbo, and Pietro Pala. "Automatic facial expression recognition in real-time from dynamic sequences of 3D face scans." *The Visual Computer* 29, no. 12 (2013): 1333-1350.

[21] Yang, Huiyuan, and Lijun Yin. "CNN based 3D facial expression recognition using masking and landmark features." In *2017 Seventh International Conference on Affective Computing and Intelligent Interaction (ACII)*, pp. 556-560. IEEE, 2017.

Authorized licensed use limited to: DELHI TECHNICAL UNIV. Downloaded on March 03,2021 at 06:09:18 UTC from IEEE Xplore. Restrictions apply.

[22] Godil, Afzal, Sandy Ressler, and Patrick Grother. "Face recognition using 3D facial shape and color map information: comparison and combination." In *Biometric Technology for Human Identification*, vol. 5404, pp. 351-361. International Society for Optics and Photonics, 2004.

[23] Vezzetti, Enrico, and Federica Marcolin. "3D human face description: landmarks measures and geometrical features." *Image and Vision Computing* 30, no. 10 (2012): 698-712.

[24] Chen, Hui, Jiangdong Li, Fengjun Zhang, Yang Li, and Hongan Wang. "3D model-based continuous emotion recognition." In *Proceedings of the IEEE conference on computer vision and pattern recognition*, pp. 1836-1845. 2015.

[25] Chang, Ya, Marcelo Vieira, Matthew Turk, and Luiz Velho. "Automatic 3D facial expression analysis in videos." In *International Workshop on Analysis and Modeling of Faces and Gestures*, pp. 293-307. Springer, Berlin, Heidelberg, 2005.

[26] Lv, Chenlei, Zhongke Wu, Xingce Wang, and Mingquan Zhou. "3D facial expression modeling based on facial landmarks in single image." *Neurocomputing* 355 (2019): 155-167.

[27] Moeini, Ali, Karim Faez, Hamid Sadeghi, and Hossein Moeini. "2D facial expression recognition via 3D reconstruction and feature fusion." *Journal of Visual Communication and Image Representation* 35 (2016): 1-14.

[28] Deng, Jiankang, Anastasios Roussos, Grigorios Chrysos, Evangelos Ververas, Irene Kotsia, Jie Shen, and Stefanos Zafeiriou. "The menpo benchmark for multi-pose 2d and 3d facial landmark localisation and tracking." *International Journal of Computer Vision* 127, no. 6-7 (2019): 599-624.

[29] Berretti, Stefano, Alberto Del Bimbo, Pietro Pala, Boulbaba Ben Amor, and Mohamed Daoudi. "A set of selected SIFT features for 3D facial expression recognition." In *2010 20th International Conference on Pattern Recognition*, pp. 4125-4128. IEEE, 2010.

[30] Masi, Iacopo, Stephen Rawls, Gérard Medioni, and Prem Natarajan. "Pose-aware face recognition in the wild." In *Proceedings of the IEEE conference on computer vision and pattern recognition*, pp. 4838-4846. 2016.

[31] Yang, Jing, Adrian Bulat, and Georgios Tzimiropoulos. "FAN-Face: a Simple Orthogonal Improvement to Deep Face Recognition." In *AAAI*, pp. 12621-12628. 2020.

[32] Bulat, Adrian, and Georg. s Tzimiropoulos. "How far are we from solving the 2d & 3d face alignment problem?(and a dataset of 230,000 3d facial landmarks)." In Proceedings of the IEEE International Conference on Computer Vision, pp. 1021-1030. 2017.J. Clerk Maxwell, A Treatise on Electricity and Magnetism, 3rd ed., vol. 2. Oxford: Clarendon, 1892, pp.68–73.

[33] Newell, Alejandro, Kaiyu Yang, and Jia Deng. "Stacked hourglass networks for human pose estimation." In *European conference on computer vision*, pp. 483-499. Springer, Cham, 2016.

[34] Susan, Seba, Samdisha Chaurawat, Vinay Nishad, Mayank Sharma, and Sonali Sahay. "Speed and trajectory based sports event categorization from videos." In *2016 International Conference on Signal Processing and Communication (ICSC)*, pp. 496-501. IEEE, 2016.

[35] Lucey, Patrick, Jeffrey F. Cohn, Takeo Kanade, Jason Saragih, Zara Ambadar, and Iain Matthews. "The extended cohn-kanade dataset (ck+): A complete dataset for action unit and emotion-specified expression." In *2010 ieee computer society conference on computer vision and pattern recognition-workshops*, pp. 94-101. IEEE, 2010.

Authorized licensed use limited to: DELHI TECHNICAL UNIV. Downloaded on March 03,2021 at 06:09:18 UTC from IEEE Xplore. Restrictions apply.

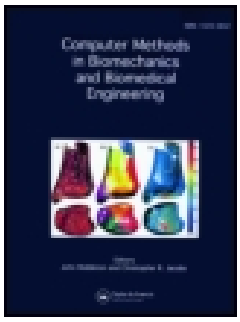

Computer Methods in Biomechanics and Biomedical Engineering

ISSN: (Print) (Online) Journal homepage: https://www.tandfonline.com/loi/gcmb20

Genetic particle filter improved fuzzy-AEEMD for ECG signal de-noising

Rajiv Kapoor & Rajesh Birok

To cite this article: Rajiv Kapoor & Rajesh Birok (2021): Genetic particle filter improved fuzzy-AEEMD for ECG signal de-noising, Computer Methods in Biomechanics and Biomedical Engineering, DOI: 10.1080/10255842.2021.1892659

To link to this article: https://doi.org/10.1080/10255842.2021.1892659

Published online: 05 Mar 2021.

Submit your article to this journal

Article views: 10

View related articles

View Crossmark data

Full Terms & Conditions of access and use can be found at
https://www.tandfonline.com/action/journalInformation?journalCode=gcmb20

COMPUTER METHODS IN BIOMECHANICS AND BIOMEDICAL ENGINEERING
https://doi.org/10.1080/10255842.2021.1892659

Taylor & Francis
Taylor & Francis Group

Check for updates

Genetic particle filter improved fuzzy-AEEMD for ECG signal de-noising

Rajiv Kapoor and Rajesh Birok

Department of ECE, Delhi Technological University, Delhi, India

ABSTRACT

With the aid of ensemble empirical mode decomposition (EEMD), de-noising of the electrocardiogram (ECG) signal based on the genetic particle filter and fuzzy thresholding is proposed in this paper, which effectively eliminates noise from the ECG signal. This paper proposes a two-phase scheme for removing noise from ECG signal. In the first phase, noisy signal is decomposed into true intrinsic mode functions (IMFs) with the help of EEMD. Adaptive EEMD (AEEMD) is better than EMD because it removes the mode-mixing effect. In the second phase, IMFs which are corrupted by noise are obtained by using spectral flatness of each IMF and fuzzy thresholding. Corrupted IMFs are filtered using genetic particle filter to remove the noise. Finally, the signal is reconstructed with the processed IMFs to get the de-noised ECG. The proposed algorithm is analyzed for different databases and it gives better signal-to-noise ratio and root mean square error than other existing techniques.

ARTICLE HISTORY
Received 13 August 2020
Accepted 16 February 2021

KEYWORDS
Genetic particle filter; adaptive ensemble empirical mode decomposition; fuzzy thresholding; ECG de-noising; SNR; RMSE

Introduction

Electrocardiogram (ECG) signal records the electrical conduction activity of heart. These are very small signals in strength with narrow bandwidth of 0.05–120 Hz. Physicians especially cardiologists use these signals for diagnosis of the heart's condition or heart diseases. ECG signal is contaminated with various artifacts such as power-line interference (PLI), Patient-electrode motion artifacts, electrode-pop or contact noise, and baseline wandering and electromyographic (EMG) noise during acquisition. Analysis of ECG signals becomes difficult to inspect the cardiac activity in the presence of such unwanted signals. So, de-noising of ECG signal is extremely important to prevent misinterpretation of patient's cardiac activity. Various methods are available for de-noising the ECG signal such as hybrid technique (Pradeep Kumar et al. 2009), empirical mode decomposition (Chacko and Ari 2012), un-decimated wavelet transform (Naga Prudhvi Raj and Venkateswarlu 2011), Hilbert-Hung transform (Zhang et al. 2010), morphological filtering (Liu et al. 2011), noise invalidation techniques (Nikvand et al. 2010), non-local means technique (Tracey and Miller 2012), S-transform (Alarka et al. 2012), adaptive filtering (Ying and An 2011), and FIR filtering (Ying and An 2011), etc.

Pradeep Kumar et al. (2009) proposed a hybrid technique that combined empirical mode decomposition and wavelet thresholding. EMD for decomposing the noisy ECG signal into sequences of intrinsic mode functions (IMF). Wavelet thresholding is used for removing the noise from decomposed signal. Hybrid technique has been improved the performance of de-noising signal. The hybrid technique also provides improved signal-to-noise ratio (SNR) than wavelet transform approach. It removes both power-line noise and baseline wander noise. Naga Prudhvi Raj and Venkateswarlu (2011) proposed a de-noising approach that contains un-decimated wavelet transform. This transform is used to decompose the raw ECG signal. In this method, the shrinkage action is used to eliminate the noise from the noisy ECG signal. In the shrinkage phase, semi-soft and stein thresholding are used with traditional soft and hard thresholding. It confirmed the suitability of different wavelets for ECG signals de-noising. It provided better smoothness, stability, and accuracy as compared to discrete wavelet transform (DWT). The wavelet transform technique has the following limitations as a de-noising method for ECG signal: (i) the hard thresholding may lead to the oscillation of the reconstructed ECG signal, (ii) soft thresholding method may reduce the amplitudes of the ECG waveforms and especially reduce the amplitudes of the R-waves which is more important to diagnose the heart diseases (Chacko and Ari 2012). Liu et al. (2011) proposed a morphological methodology to eliminate the noise of

CONTACT Rajiv Kapoor rajivkapoor@dce.ac.in
© 2021 Informa UK Limited, trading as Taylor & Francis Group

the ECG signals. The structuring elements exist in different sizes. These structuring elements are used to process the different environments of ECG signal and noise. This filter is very effective in removing noise and correct baseline drift only. Zhang et al. (2010) proposed an algorithm for ECG signal de-noising based on Hilbert-Huang transform. This transform presents two phases for signal processing. Firstly, original dataset is converted into an 'n' number of IMF through EMD method and then these IMFs components are passed through Hilbert transforms. It is a simpler approach as compared to wavelet de-noising method. Zhang et al. (2019) used the grid search approach to select the optimal parameters which generated the minimal multi-scale complexity, but the calculation of multi-scale complexity was complicated and it was not suitable for small sample data. Another application of ensemble empirical mode decomposition (EEMD) is given by Xiang and Zhong (2017) which introduced RDT (random decrement technique)-based EEMD approach that helps in detecting faults to extract the feature frequencies that occur from the vibrations of gears and bearings. Meng et al. (2015) developed a hybrid approach on fault diagnosis to discover faults that arise in rolling bearings. To extract fault characteristics, EEMD is introduced.

Chacko and Ari (2012) proposed de-noising approach for ECG signals built on empirical mode decomposition. The noisy ECG signal is initially decomposed into sequences of IMFs with the help of EMD method. The IMFs which are ruled by noise are spontaneously determined through spectral flatness (SF). These noisy IMFs are filtered with the help of Butterworth filters to eliminate noise. It performs better SNR and lower root mean square error (RMSE) as compared to wavelet transform de-noising technique. The major shortcoming of EMD is the mode-mixing consequence. Mode-mixing indicates that oscillations of different time scales co-exist in a given IMF or oscillations with the similar time scale have been allocated to different IMFs. All these techniques have some limitations such as mode-mixing problem, oscillation in the reconstructed signals, reduced amplitude of the ECG signal and problem of degeneracy, etc. To overcome the above-mentioned limitations, a new technique is proposed for de-noising of ECG signal based on genetic algorithms (GA) and AEEMD with the help of fuzzy thresholding.

AEEMD methods are used to decompose the ECG signal into true IMFs. Then the IMFs which are ruled by noise are automatically determined using fuzzy thresholding and then filtered using genetic particle algorithms to remove the noise. The use of genetic particle filter mitigates the sample degeneracy of particle filter. AEEMD is used in this manuscript instead of EMD because it solves the EMD mode-mixing problem. AEEMD represents a major improvement with great versatility and robustness in noisy ECG signal filtering.

The paper is organized as follows. The second section explains the theoretical background on genetic particle filter, EEMD, and AEEMD. The third section explains our proposed method for de-noising of ECG signal. The fourth section shows the results of applying the proposed algorithm with different databases. Finally, the conclusion is drawn in the fifth section.

Theoretical background

The ECG is frequently contaminated through noise and artifacts.

Various artifacts are:

1. Power-line interference: PLI or artifact consists of 50–60 Hz power-line frequencies and bandwidth of less than 1 Hz. The amplitude of PLI fluctuates up to 50% of full scale deflection (FSD) level.
2. Baseline wander: Baseline wander artifact occurs mainly due to respiration at the drifting frequencies between 0.15 Hz and 0.3 Hz. Baseline wander artifact is also known as baseline shift or drift.
3. Muscle noise/electromyographic artifact: Electrical bio-potential due to EMG or muscle contraction adulterates the ECG signal. The amplitude of muscle noise fluctuates up to 10% of FSD level with a frequency of 10 KHz.
4. Motion artifact: Motion artifacts are produced due to motion of electrode or change in impedance between electrodes when it is superimposed on the ECG activity then it is known as motion artifact.
5. Electrode contact noise: Contact noise originates due to loss of contact between the subject's skin and the electrodes.
6. Data-gathering device and electrosurgical noises: It is generated through medical apparatus and signal processing hardware at frequencies between 100 kHz and 1 MHz.

Ensemble EMD

Ensemble EMD (EEMD) (Wu and Huang 2009) is used to eliminate the mode-mixing consequence. It overcomes mainly the mode-mixing problem of the

original EMD through the addition of white noise into the targeted signal frequently. It is also known as a noise-assisted data analysis (NADA) system. EEMD consists of EMD and taking corresponding IMFs ensemble average of 'n' number of trials. These ensemble averages output treats as final result of EEMD. Ensemble EMD methods are used to decompose the ECG signal into true IMFs.

The process of decomposition using EEMD can be done in the following steps (Tabrizi et al. 2015):

i. Random white noise signal is added to the developed original signal:

$$x_j(t) = x(t) + A \cdot n_j(t) \quad j = 1, 2, .., M,$$

where A denotes the amplitude of added white noise and M is the preset number of trials.

ii. Obtained signal ($x_j(t)$) is decomposed into IMFs using EEMD:

$$x_j(t) = \sum_{i=1}^{N_j} c_{ij} + r_{Nj}, \tag{1}$$

Here c_{ij} denotes the ith IMF of the jth trial, r is the residue, and N_j represents IMF number of the jth trial.

iii. Repeat these steps till the predefined ensemble trial number is attained also add dissimilar random noise signal every time.

iv. For evaluating ensemble mean of the resultant IMFs of the decompositions is denoted as (c_i):

$$c_i(t) = \frac{\sum_{j=1}^{M} c_{ij}}{M} i = 1, 2, \ldots, \mathrm{K}, \tag{2}$$

where K denotes the minimum number of IMFs in the trial.

The mode-mixing problem is one of the key drawbacks of the original EMD, meaning that multiple decomposition components appear in the same frequency waveform or a plurality of different frequency waveforms are found in some decomposition components. A NADA system called EEMD was proposed by Wu and Huang (2009) and Zhang et al. (2019). EEMD avoids the problem of mode mixing by applying white noise to the initial data in several cases. The EEMD method is a big advance in EMD development and increases the reliability of the EMD algorithm significantly. The GA was implemented to improve the self-adaptiveness of the EEMD method.

EMD also suffers the end effect issue in which, at the time of EMD process, the signal envelopes determined by the extreme points can reflect its appearance which filter out the higher frequency component and only represents signal's lower frequency component. However, all the data between them should cover the upper and lower envelopes. The end points having extremes are difficult to recognize very exactly. To resolve this problem, Zhang et al. (2009) proposed an end shifting method to resolve the end effect issue from EMD.

Adaptive EEMD (AEEMD)

The added white noise must influence the extrema of the original signal to reduce or decrease the irregularity as much as possible. However, the extrema are influenced (and as a consequence decreases the current mode of mixing) by a random noise in a predetermined constant amplitude value, which does not effectively alter any extrema.

Instead, an adaptive approach (AEEMD) (Zhang et al. 2019) is proposed and many signals are used to test its efficiency and applicability.

$$SNR_j(t) = 20 \log \left(\frac{x(t)}{Amp_j n_j(t)} \right) \tag{3}$$

$$Amp_j(t) = 10^{-(SNR/20)} \left(\frac{x(t)}{n_j(t)} \right) \tag{4}$$

where $j = 1,2,3, \ldots, \mathrm{M}$.

After adding a random white noise, by applying the SNR in Equation (3), the amplitude rate for each data point of a sample is acquired from Equation (4). Given the required value of SNR, there will be confident that the extrema of the initial signal are adequately affected.

In Figure 5, a noisy ECG signal contaminated with various artifacts is shown. A suggested fixed value (0.3) multiplied by standard deviation of the original signal creates a predefined constant value along with the whole signal. Thus, affecting the extrema depends on value of random noise at the location of the extrema. Using the proposed algorithm, an adaptive value is generated to preserve the SNR. It means that, for any randomly created noise, the amplitude will be high enough to affect the extrema. Investigating the result of adding noise to the vibration signal shows how the proposed amplitude acts more efficiently on the extrema as shown in Figures 17 and 18.

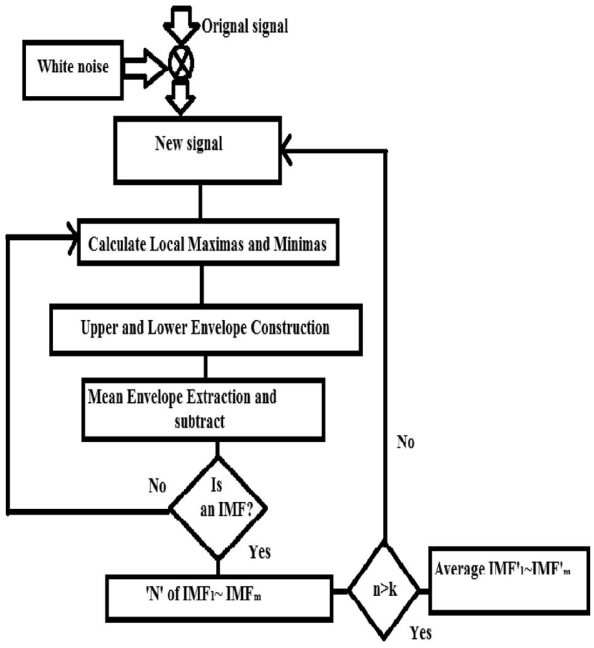

Figure 1. Flow chart of EEMD method.

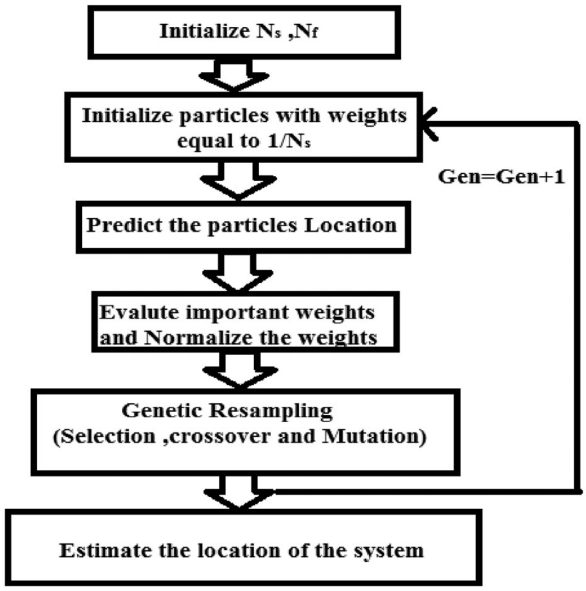

Figure 2. Block diagram of the GA-PF method.

Fuzzy thresholding

Fuzzy rules are well defined in terms of statistical properties which determine the required range of thresholds is known as fuzzy thresholding (Üstündağ et al. 2012).

Genetic particle filter

A GA is embedded into the standard particle filter (S-PF) is known as GA-PF (Li et al. 2012) which is used to overcome the degeneracy problem. It improves the self-evolution and self-adaptation.

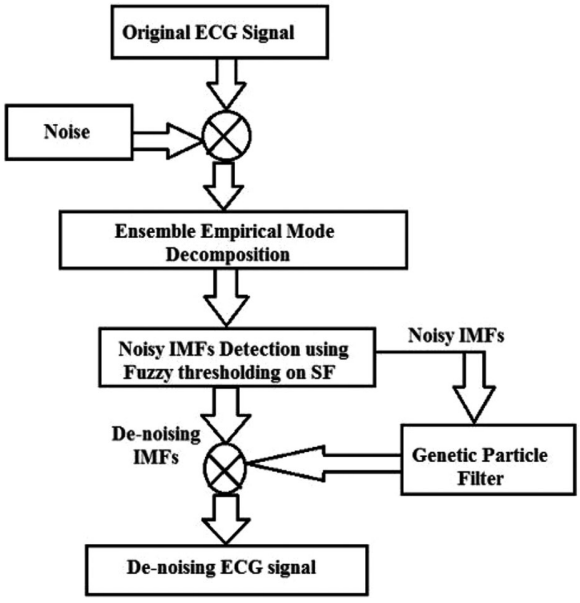

Figure 3. Block diagram of the proposed ECG de-noising method.

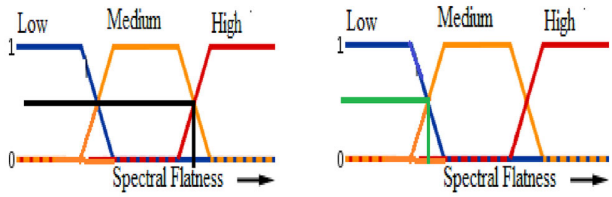

Figure 4. Membership function lies between medium and high or low and medium.

Proposed algorithm

In this proposed approach, programming of MATLAB software has been utilized to develop an algorithm for de-noising of ECG signal. AEEMD methods are used to decompose the ECG signal into IMFs. Then IMFs which are dominated by noise are automatically determined using Fuzzy Thresholding and then filtered using genetic particle algorithms to remove the noise and improve the computational efficiency of adaptive processing.

The ECG signals have been taken from the hospital databases. The noisy signal $n(t)$ is acquired as $n(t) = y(t) + m(t)$ where $y(t)$ is the original ECG and $m(t)$ is the noise signal. The $n(t)$ signal is decomposed into IMFs using AEEMD process. Noisy signal is passed through EMD method to obtain the IMFs. True IMFs taken as targeted signal is obtained by ensemble means of corresponding IMFs.

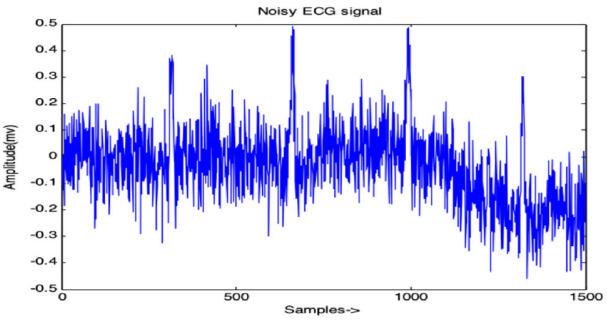

Figure 5. Noisy ECG signal.

The number of noisy IMFs is acquired by using the SF of individual IMF. The SF is the relationship between the geometric mean (GM) and arithmetic mean (AM). It is defined as the ratio of GM to its AM of the power spectrum.

$$\text{Spectralflatness(SF)} = \text{GM}/\text{AM} \tag{5}$$

SF measure is fuzzied to detect whether the IMFs are noisy or not. Linguistic variables used are low, medium, and high membership functions for SF.

The rules for SF are:

Rule 1: If SF is in high range then IMF is clean

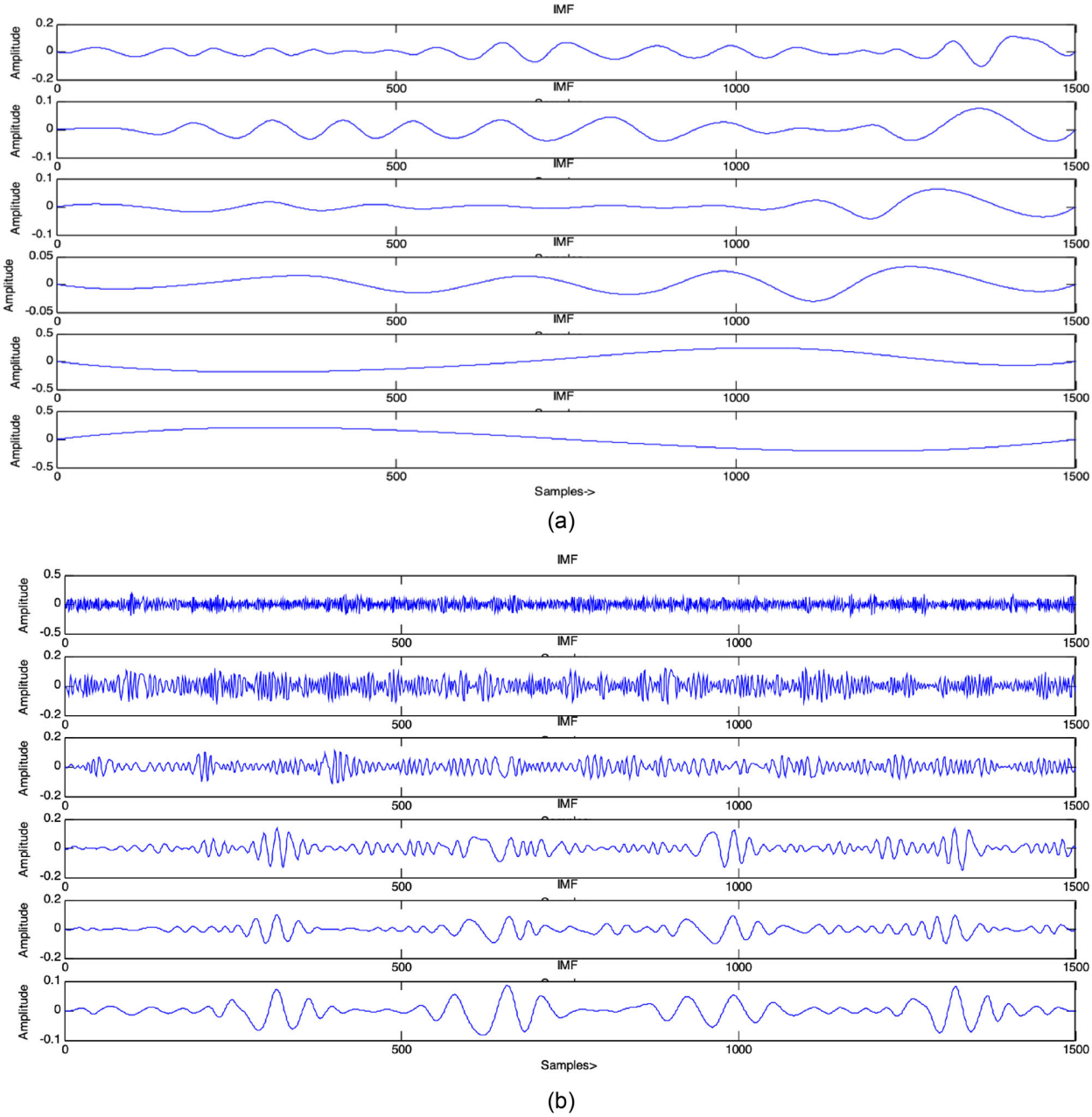

Figure 6. (a, b) Twelve improved intrinsic mode functions.

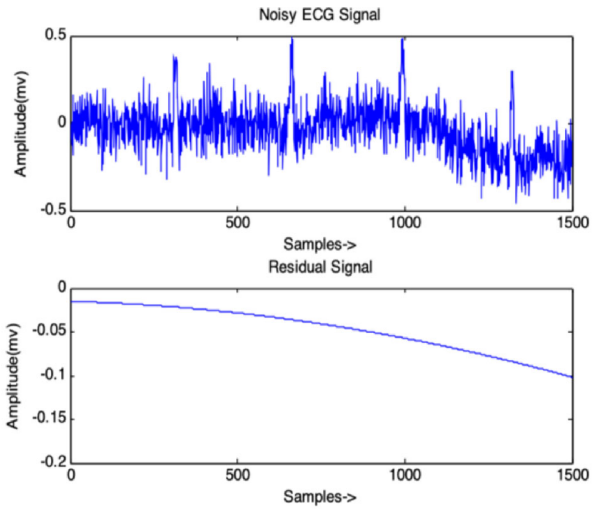

Figure 7. Noisy ECG signal and residual signal.

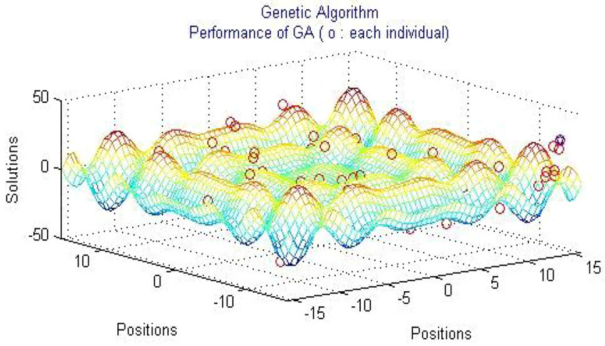

Figure 8. Performance of GA (o: each individual).

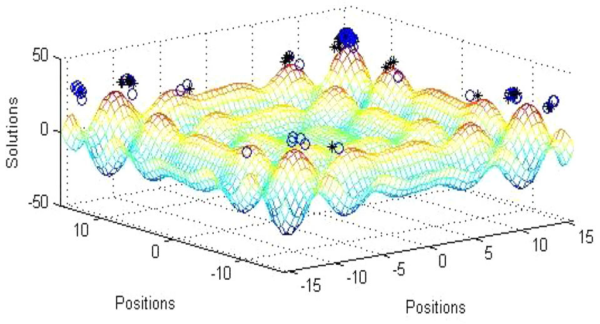

Figure 9. Best solution by GA (: o) and RS (:*) in each generation.

Rule 2: If SF is in medium range then IMF is noisy

Rule 3: If SF is in low range then IMF is very noisy.

Now applying Rule 1,

Take minimum of membership of SF

Noisy = min (0.09, 0.08) = 0.08

Now applying Rule 2,

Take minimum of membership of SF

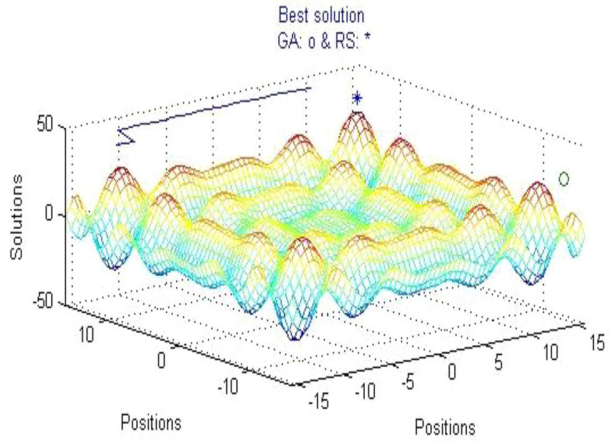

Figure 10. Best solution by GA (: o) and RS (: *) for overall.

Noisy = min (0.03, 0.05) = 0.03

For combining the rules, according to fuzzy max–min implication, 'min' membership is noisy. Automatic determination of noisy IMFs is done using SF. The noisy IMFs are cleaned using genetic particle filter to remove the noise.

Methodology

The goal of this study is to evaluate the performance measures of the proposed algorithm (AEEMD) for the different conditions of the ECG signal.

The ECG signal de-noising method is given as:

a. To collect ECG signals and add random white noise.
b. To apply the EEMD with different amplitude of added white noise to decompose the signals into some IMFs. The first IMFs including the most dominant information are chosen to extract the feature.
c. To calculate the total energy E_i of the first m IMFs:

$$E_i = \int_{-\infty}^{\infty} |c_i(t)|^2 dt \tag{6}$$

d. To create a feature vector with the energies of the m selected IMFs:

$$FV = [E_1, E_2, \ldots, E_m] \tag{7}$$

e. To normalize the feature:

$$FV = \left[\frac{E_1}{E}, \frac{E_2}{E}, \ldots, \frac{E_m}{E}\right] \tag{8}$$

where, $E = (\sum_{i=1}^{m} |E_i|^2)^{1/2}$

Simulation results

The performance of the proposed algorithm is tested against five different local hospital databases. De-noising of ECG signal is done in a way so that suppress impulsive noises at several levels while conserving the preferred ECG signal. It is not possible to remove noise completely but it eliminates as much as possible. The performance of our proposed algorithm is analyzed by SNR and RMSE values.

Parameters (Li et al. 2012) of proposed algorithm listed as follows:

Number of particles = 100

Crossover probability = 0.8

Mutation probability = 0.1

Maximal acceptable generation T = 20.

Figure 1 explains the process flow of EEMD and Figure 2 provides the detailed flow of GA-PF based ECG understanding techniques so that the proposed technique given in Figure 3 could be compared .Membership function has been shown in Figure 4, which will be used in the proposed technique and to the noisy data shown in Figure 5.

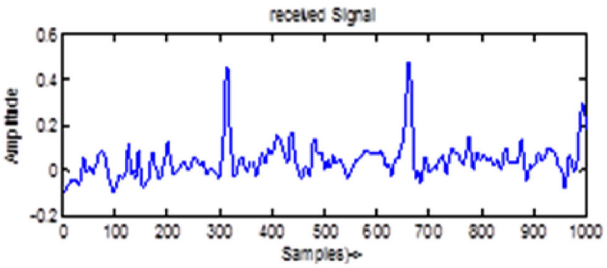

Figure 11. De-noised ECG signal.

Figure 5 shows the noisy ECG signal which is contaminated with various artifacts. Figure 6(a,b) show the decomposition of ECG signals into IMF components which are obtained by AEEMD method. Thus, only the first 12 IMFs are used for further processing. The number of noisy IMFs is acquired by using SF of individual IMF. In other words, SF is fuzzied to detect whether the IMFs are noisy or not.

The number of noisy IMFs is acquired by using SF of individual IMF. In other words, SF is fuzzied to detect whether the IMFs are noisy or not. Figure 7 shows the residual component of ECG signal. These signals do not have any maxima and minima.

Figure 8 indicates the performance of GA which shows the individual's weight as fitness function of the particle. Figure 9 shows the highest fitness function which is obtained with the help of Roulette wheel selection method in each generation. The individual highest fitness function is directly reserved for the coming generation.

Figure 10 indicates the highest fitness function among all generations. The noisy IMFs are filtered by using genetic particle filter. Then, ECG signal is reconstructed by adding the filtered IMFs and the remaining signal IMFs. The de-noised ECG signal is obtained which is shown in Figure 11.

The performance of our approach is estimated based on the SNR and RMSE. SNR and RMSE stand for signal to noise ratio and root mean square error, respectively. These parameters are used to compare existing method with proposed method.

Table 1. Comparison of SNR values for different databases of existing methods with proposed method.

Database	Wavelet-based techniques (SNR in dB)	EMD-based techniques (SNR in dB)	Particle filter method (SNR in dB)	Proposed method (SNR in dB)	Percentage improvement with particle filter method
Database1	10.9142	12.9997	14.0853	17.7205	25.80
Database2	11.1984	13.8093	15.2512	18.8058	23.30
Database3	10.1845	13.8138	15.9588	19.9987	25.31
Database4	10.4252	14.0839	16.0254	18.5141	15.52
Database5	11.9732	14.3374	14.8569	17.3418	16.72
Average	10.9391	13.8088	15.2355	18.4761	21.33

Table 2. Comparison of RMSE values for different databases of existing methods with proposed method.

Database	Wavelet-based techniques (RMSE in dB)	EMD-based techniques (RMSE in dB)	Particle filter method (RMSE in dB)	Proposed method (RMSE in dB)	Percentage improvement with particle filter method
Database1	0.299	0.224	0.198	0.131	−33.83
Database2	0.271	0.215	0.179	0.112	−37.43
Database3	0.310	0.212	0.162	0.105	−35.18
Database4	0.302	0.199	0.152	0.119	−21.71
Database5	0.255	0.191	0.187	0.137	−26.73
Average	0.287	0.208	0.175	0.120	−30.97

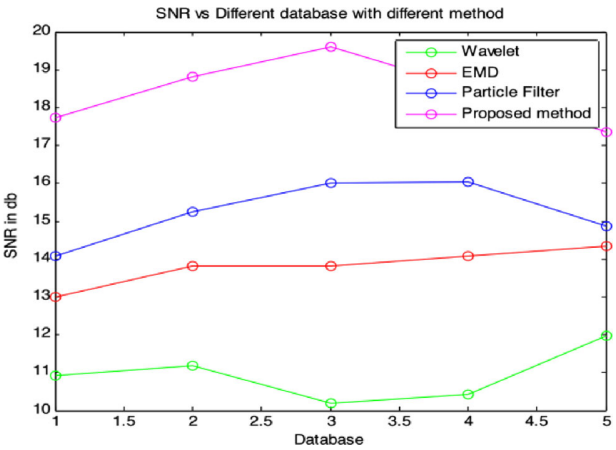

Figure 12. SNR vs. different databases with different methods and proposed method.

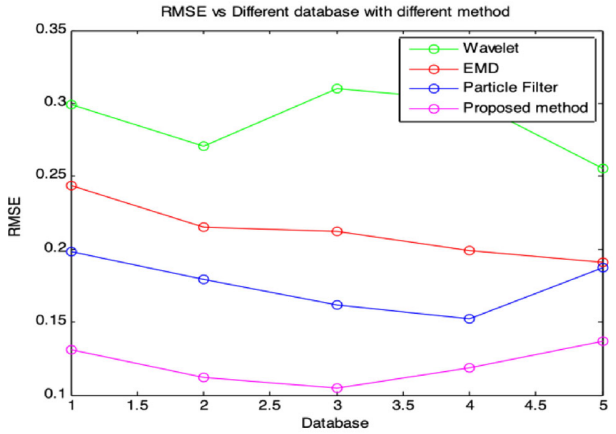

Figure 13. RMSE vs. different databases with different methods and proposed method.

The SNR can be calculated as follows:

$$\mathrm{SNR} = 10 \times \log 10(\mathrm{output}^2/(\mathrm{input}-\mathrm{output})^2)$$

The RMSE can be calculated as follows:

$$\mathrm{RMSE} = \sqrt{\sum_{t=0}^{L-1}\left[(\text{original signal} - \text{reconstructed signal})^2\right]/L}$$

Table 1 represents the values of SNR measure for the results of various existing approaches with proposed method. Existing approaches are EMD-based technique, genetic particle filtering, etc., with five different databases.

Table 2 represents the values of RMSE measure for the results of various existing approaches with proposed method.

Wavelet methods have shown popular and superior performance over the earlier methods (Nikolaev et al. 2000). Daubechies-4 (dB4) wavelet used along with

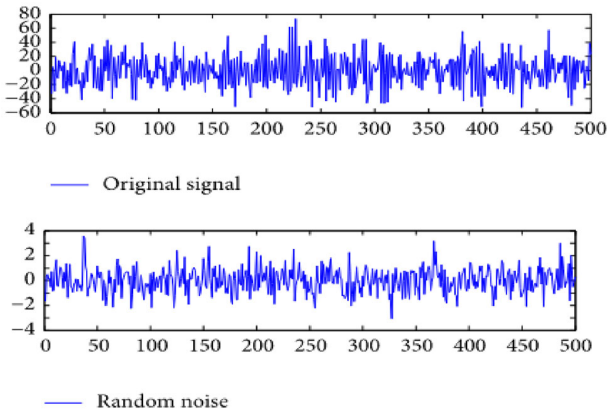

Figure 14. Original signal and added random noise.

soft thresholding is the best de-noising method so far among all wavelet families. Wavelet methods characterize both the time and frequency information simultaneously. They can enhance the ECG signals when thresholding methods are used. This is the reason for the popularity of wavelet-based ECG de-noising methods. But, the wavelet transform technique has certain limitations: (i) the reconstructed ECG signal shown oscillations because of the use of hard thresholding, (ii) using soft thresholding can reduce the ECG signal amplitude especially the R-waves amplitude which is a major concern because R-wave is important to diagnose heart disease (Zhang et al. 2010). These limitations have led the researchers to use empirical mode decomposition (EMD)-based method to de-noise ECG signal (Nikvand et al. 2010; Liu et al. 2011; Joshi et al. 2013). A signal is decomposed into a set of oscillatory functions known as IMFs. In one EMD-based method, ECG signal is partially reconstructed by removing noisy IMFs (Nikvand et al. 2010; Liu et al., 2011). The limitations of this method are the removing of the signal information along with noise. In another method, a measure known as SF is used to detect noisy IMFs. Noisy IMFs are then filtered out to get de-noised ECG signal. However, the EMD technique has major limitations for de-noising method for ECG signal: (i) the mode-mixing consequence and (ii) end effect and unstable are also a problem with EMD (Chacko and Ari 2012). In this proposed method, all the limitations discussed above have been overcome. From Tables 1 and 2 and Figures 12, 13, 17, and 18, it is evident that the performance of the presented algorithm is better than the existing algorithms with different types of artifacts. The SNR results of the proposed algorithm show better results and lower RMSE compared to EMD, wavelet, and particle filter-based

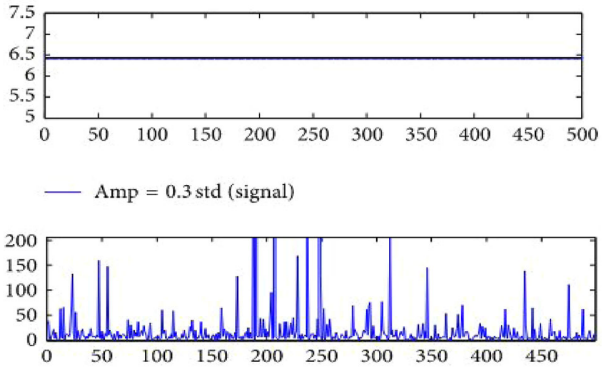

Figure 15. Original signal multiplied by SD (0.3), AEEMD with SNR 10.

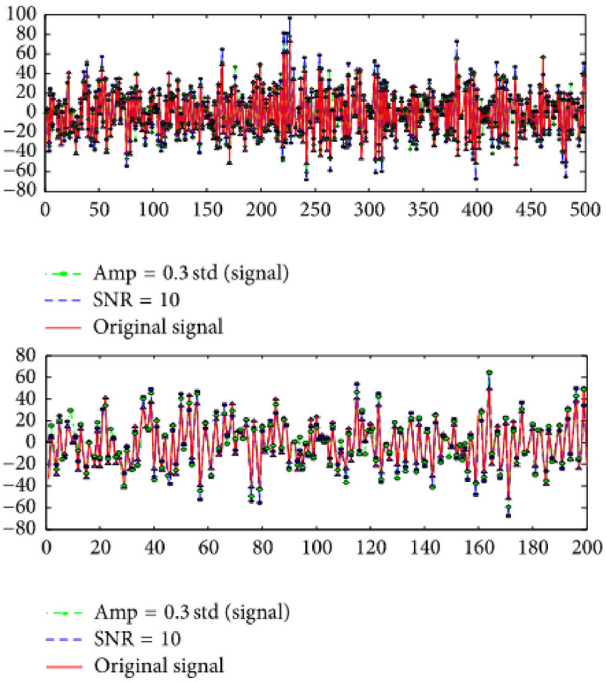

Figure 16. The effect of using constant amplitude 0.3 SD and the AEEMD process (simulation result).

techniques which are usually used as an ECG signal de-noising method with five different types of databases. The average SNR and RMSE improvement of the results de-noised by the proposed method has been improved by 21.33% and −30.97%, respectively, to particle filter method.

Digital storage oscilloscope output has been shown in Figure 17. Raspberry Pi board was used to embed the AEEMD implementation. It works very well in real time. Figures 14–16 provide signal to be analyzed having different noise levels.This analysis provides a better view of the proposed technique.

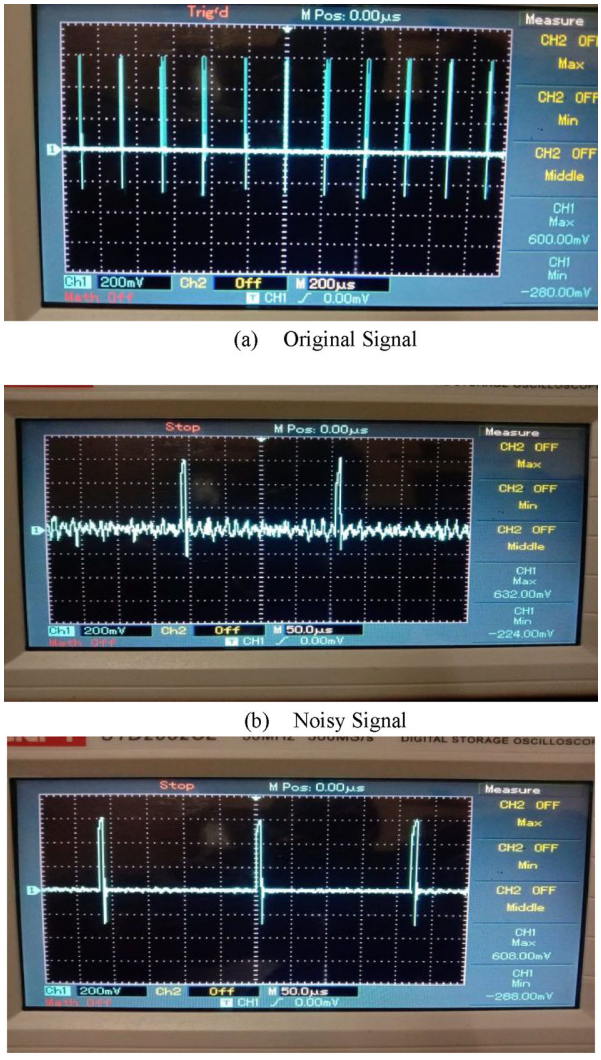

Figure 17. DSO output acquired through the proposed algorithm (AEEMD).

Conclusion

In this paper, de-noising of ECG signal based on genetic particle filter and fuzzy thresholding with the help of AEEMD gives better performance in comparison with EMD-based technique and other existing noise removal algorithms in terms of SNR. The AEEMD methods are used to split the ECG signal into IMFs. The adaptive ensemble EMD (AEEMD) symbolizes a major improvement with great adaptability, flexibility, versatility, and robustness in noisy ECG signal filtering method. The AEEMD is better than EMD because it removes the mode-mixing effect from the signal. The fuzzy thresholding is used for automatic detection of IMFs (noisy) using SF. The remaining noisy IMFs are filtered using genetic

particle filter to obtain clean ECG signal. The GA particle filter improves the self-evolution and self-adaptation process. By using advantages of the AEEMD over EMD technique and genetic particle filter over the particle filter, de-noising performance has been improved. The experimental output results showed that our proposed method to de-noise the signal is better both in terms of qualitative and quantitative measures. When the proposed method is compared with best existing method, it shows marked improvement in terms of average SNR (21.33%) and RMSE (−30.97%) than other techniques with good quality output ECG signal. Overall, the proposed method provides the better accuracy compared to other methods.

Disclosure statement

No potential conflict of interest was reported by the authors.

ORCID

Rajiv Kapoor http://orcid.org/0000-0003-3020-1455

References

Alarka S, Arijit B, Abhijit L. 2012. Application of S-transform for removing baseline drift from ECG. Paper presented at: 2012 2nd National Conference on Computational Intelligence and Signal Processing (CISP); Mar 2–3; Guwahati, India.

Chacko A, Ari S. 2012. Denoising of ECG signals using empirical mode decomposition based technique. Paper presented at: IEEE International Conference on Advances in Engineering, Science and Management (ICAESM-2012); Mar 30–31; Nagapattinam, India.

Joshi SL, Vatti RA, Tornekar RV. 2013. A survey on ECG signal denoising techniques. Paper presented at: 2013 International Conference on Communication Systems and Network Technologies; Apr 6–8; Gwalior, India.

Li G, Zeng X, Lin J, Li G, Zhou X. 2012. Genetic particle filtering for denoising of ECG corrupted by muscle artifacts. Paper presented at: 2012 8th International Conference on Natural Computation; May 29–31; Chongqing, China.

Liu Z, Wang J, Liu B. 2011. ECG signal denoising based on morphological filtering. Paper presented at: 2011 5th International Conference on Bioinformatics and Biomedical Engineering; May 10–12; Wuhan, China.

Meng L, Xiang J, Wang Y, Jiang Y, Gao H. 2015. A hybrid fault diagnosis method using morphological filter–translation invariant wavelet and improved ensemble empirical mode decomposition. Mech Syst Sig Process. 50: 101–115.

Naga Prudhvi Raj V, Venkateswarlu T. 2011. ECG signal denoising using undecimated wavelet transform. Paper presented at: 2011 3rd International Conference on Electronics Computer Technology; Apr 8–10; Kanyakumari, India.

Nikolaev N, Nikolov Z, Gotchev A, Egiazarian K. 2000. Wavelet domain wiener filtering for ECG denoising using improved signal estimate. Paper presented at: 2000 IEEE International Conference on Acoustics, Speech, and Signal Processing. Proceedings (Cat. No.00CH37100); Jun 5–9; Istanbul, Turkey.

Nikvand N, Bagherzadeh Rafsanjani H, Khalilzadeh MA. 2010. ECG signal denoising using noise invalidation. Paper presented at: 2010 17th Iranian Conference of Biomedical Engineering (ICBME); Nov 3–4; Isfahan, Iran.

Pradeep Kumar B, Balambigai S, Asokan DR. 2009. ECG de-noising based on hybrid technique. Adv Adapt Data Anal. 1(1):1–41.

Tabrizi AA, Garibaldi L, Fasana A, Marchesiello S. 2015. Performance improvement of ensemble empirical mode decomposition for roller bearings damage detection. Shock Vib. 2015:1–10.

Tracey BH, Miller EL. 2012. Nonlocal means denoising of ECG signals. IEEE Trans Biomed Eng. 59(9):2383–2386.

Üstündağ M, Gökbulut M, Şengür A, Ata F. 2012. Denoising of weak ECG signals by using wavelet analysis and fuzzy thresholding. Netw Model Anal Health Inform Bioinforma. 1:135–140.

Wu Z, Huang NE. 2009. Ensemble empirical mode decomposition: a noise-assisted data analysis method. Adv Adapt Data Anal. 1(1):1–41.

Xiang J, Zhong Y. 2017. A fault detection strategy using the enhancement ensemble empirical mode decomposition and random decrement technique. Microelectron Reliab. 75:317–326.

Ying Y, An X. 2011. ECG signals denoising using neighbouring coefficients. Paper presented at: 2011 5th International Conference on Bioinformatics and Biomedical Engineering; May 10–12; Wuhan, China.

Zhang C, Li X, Zhang M. 2010. A novel ECG signal denoising method based on Hilbert-Huang transform. Paper presented at: International Conference on Computer and Communication Technologies in Agriculture Engineering; Jun 12–13; Chengdu, China.

Zhang D, Cai C, Chen S, Ling L. 2019. An improved genetic algorithm for optimizing ensemble empirical mode decomposition method. Syst Sci Control Eng. 7(2):53–63.

Zhang L, Chen H, Li J, Chen W. 2009. New method to solve the end effect of empirical mode decomposition. Paper presented at: 2009 2nd International Congress on Image and Signal Processing; Oct 17–19; Tianjin, China.

Appendix

Algorithm for proposed method

1. $y^i[n] = y[n] + w^i[n]$
   where $w^i[n], i.e. i = 1, 2 \ldots \ldots \ldots \ldots I$ are different realization of white Gaussian.
2. Each $y^i[n] i = 1,\ 2 \ldots \ldots \ldots \ldots \ldots I$ is decomposed into modes using EMD.
   $\mathrm{IMF}_k{}^i[n]$ where $k = 1,\ \ 2 \ldots \ldots \ldots .. K$ indicates the modes.

3. Assign IMF_k as the kth mode of $y[n]$. Obtained as average of the corresponding $IMF_k{}^i$

$$\overline{IMF_k}(n) = 1 \Big/ I \sum_{i=1}^{I} IMF^k[n]$$

   a. Residue $R[n] = y[n] - \overline{IMF_k}[n]$
   b. The number of noisy intrinsic mode functions is acquired by using the spectral flatness (SF) of individual IMF.

$$\text{Spectral flatness measure} = \sqrt{\prod_{n=0}^{L-1} G(n)i} \div \left(\sum_{n=0}^{L-1} G(n) \right) / L$$

4. Fuzzification: three trapezoidal membership functions 'low', 'medium', 'high'.
   Rule base:
   1. If S-PF is high range then IMF is noiseless.
   2. If S-PF is medium range then IMF is noisy.
   3. If S-PF is low range then IMF is very noisy.
   Condition:
   Take min of membership function of SF.
   Noisy = min (0.09, 0.08) = 0.08
   Take min of membership function of SF.
   Noisy = min (0.03, 0.05) = 0.03
   For combining the rules, according to fuzzy max–min implication, 'min' membership is noisy.
5. Defuzzification method
6. Output: 2 output: one for noisy
   second for noiseless
7. Noisy IMFs are passed through the GA-PF algorithms.
   - Set (initialize) particles and their weights:
     $K = 0$, make particles $\{y_0{}^i\}_{i\ =\ 1}{}^{\mathrm{Ns}}$ based on the prior probability density p_{y0} and Ns = 100.
   - Evaluate the importance weights are 1/Ns.
   - Predict the particle location

$$U_k{}^i = U_{k-1}{}^i p\left(Z_k | y_k{}^i\right)$$
$$i = 1, 2 \ldots\ldots\ldots\ldots\ldots\text{Ns.}$$

   - Normalize importance weights.

$$U_k{}^i = U_k{}^i / \sum\nolimits_{i=1}{}^{\mathrm{Ns}} U_k{}^i$$

   - Output of PF
   - Genetic resample:
     Starting generation = 0 and maximal acceptable generation $T = 20$.
     - Selection: Compute the individual's weight as fitness function of the particles and then choose the individuals through high fitness function with the help of Roulette Selection. The individual greatest fitness is directly reserved for the coming generation.
     - Crossover: Within mutation probability 'Pc', stochastically pick two individuals from beyond particles to create two recombinants using the recombination principle.
     - Mutation: Pick certain individuals stochastically from the population within slight mutation probability. Then it mutates them as $y_k{}^{\mathrm{new}} = y_k{}^{\mathrm{A}} + \mathfrak{y}$
       - New particles, the succeeding repetition are determined until evolving generation T.
       - Update the valuation of system state is the final output.
8. ECG signal is reconstructed by adding clean IMFs and the remaining signal IMFs.

This article has been accepted for publication in a future issue of this journal, but has not been fully edited. Content may change prior to final publication. Citation information: DOI 10.1109/TMM.2021.3060951, IEEE Transactions on Multimedia

GPS2Vec: Pre-trained Semantic Embeddings for Worldwide GPS Coordinates

Yifang Yin, Ying Zhang, Zhenguang Liu, Sheng Wang,
Rajiv Ratn Shah, and Roger Zimmermann, Senior Member, IEEE

***Abstract*—GPS coordinates are fine-grained location indicators that are difficult to be effectively utilized by classifiers in geo-aware applications. Previous GPS encoding methods concentrate on generating hand-crafted features for small areas of interest. However, many real world applications require a machine learning model, analogous to the pre-trained ImageNet model for images, that can efficiently generate semantically-enriched features for planet-scale GPS coordinates. To address this issue, we propose a novel two-level grid-based framework, termed GPS2Vec, which is able to extract geo-aware features in real-time for locations worldwide. The Earth's surface is first discretized by the Universal Transverse Mercator (UTM) coordinate system. Each UTM zone is then considered as a local area of interest that is further divided into fine-grained cells to perform the initial GPS encoding. We train a neural network in each UTM zone to learn the semantic embeddings from the initial GPS encoding. The training labels can be automatically derived from large-scale geotagged documents such as tweets, check-ins, and images that are available from social sharing platforms. We conducted comprehensive experiments on three geo-aware applications, namely place semantic annotation, geotagged image classification, and next location prediction. Experimental results demonstrate the effectiveness of our approach, as prediction accuracy improves significantly based on a simple multi-feature early fusion strategy with deep neural networks, including both CNNs and RNNs.**

***Index Terms*—GPS, semantic embedding, neural networks, geo-aware applications**

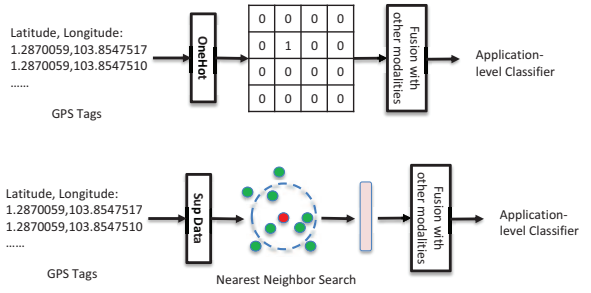

Fig. 1: Illustration of existing GPS encoding techniques.

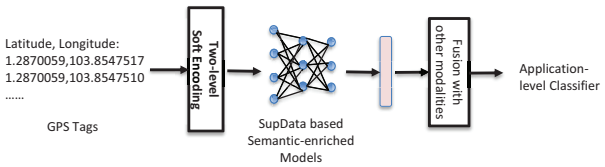

Fig. 2: Illustration of our proposed GPS2Vec approach.

I. Introduction

With the ubiquity of sensor-equipped smartphones it is common that multimedia documents, uploaded to the Internet from all over the world, have GPS coordinates associated with them. Such geotags can provide rich contextual information that is crucial for, *e.g.*, information understanding, document retrieval, and personalized recommendations [1]–[3]. For instance, a photo of clouds and a photo of a field of snow can be quite similar in their visual appearances. If a geotag is available, it could tell us that the photo was taken at a location where it never snows and so it is more likely to depict clouds [1]. Despite the significant importance of geotags, previous research has focused on extracting hand-crafted features from GPS locations that are tailored for specific applications, often targeting small areas of interest. A global method that can handle worldwide geotags is preferred as it can be applied to both global and regional applications. Conversely, extending a regional method to global applications is usually difficult. Moreover, constructing an end-to-end pre-trained model for geospatial feature extraction would be superior to existing hand-crafted feature engineering techniques. First, such an approach can provide a lightweight mobile solution to extract geo-aware features in real-time for locations worldwide and second, it would enable a more straightforward fusion between GPS coordinates and features from other modalities (*e.g.*, visual and textual features) in machine learning applications.

Figure 1 illustrates the existing two types of GPS encoding techniques which both generate manually crafted GPS embeddings in small areas of interest. The first type, as shown in Figure 1, is the OneHot encoding approach [4]. This type typically segments the 2D space into grid cells, thus recording into which cell each GPS coordinate falls into. These methods have been widely adopted due to their simplicity. However, they do not encode any semantic information of the locations and only work well for small areas of interest. A difference of one degree in latitude or longitude at the equator equals approximately 110 km. Therefore, segmenting

Y. Yin and R. Zimmermann are with the National University of Singapore (e-mail: idsyin@nus.edu.sg; rogerz@comp.nus.edu.sg).

Y. Zhang is with the Northwestern Polytechnical University, Xi'an, China (e-mail: yingz118@gmail.com).

Y. Yin and Y. Zhang contributed equally to this work.

Z. Liu is with the Zhejiang Gongshang University, China (e-mail: liuzhenguang2008@gmail.com). He is the corresponding author.

S. Wang is currently with the Alibaba Group, Singapore (e-mail: sh.wang@alibaba-inc.com). This work was done while he was at the National University of Singapore.

R. Shah is with the IIIT-Delhi, India (e-mail: rajivratn@iiitd.ac.in).

1520-9210 (c) 2021 IEEE. Personal use is permitted, but republication/redistribution requires IEEE permission. See http://www.ieee.org/publications_standards/publications/rights/index.html for more information.
Authorized licensed use limited to: DELHI TECHNICAL UNIV. Downloaded on March 27,2021 at 09:52:40 UTC from IEEE Xplore. Restrictions apply.

This article has been accepted for publication in a future issue of this journal, but has not been fully edited. Content may change prior to final publication. Citation information: DOI 10.1109/TMM.2021.3060951, IEEE Transactions on Multimedia

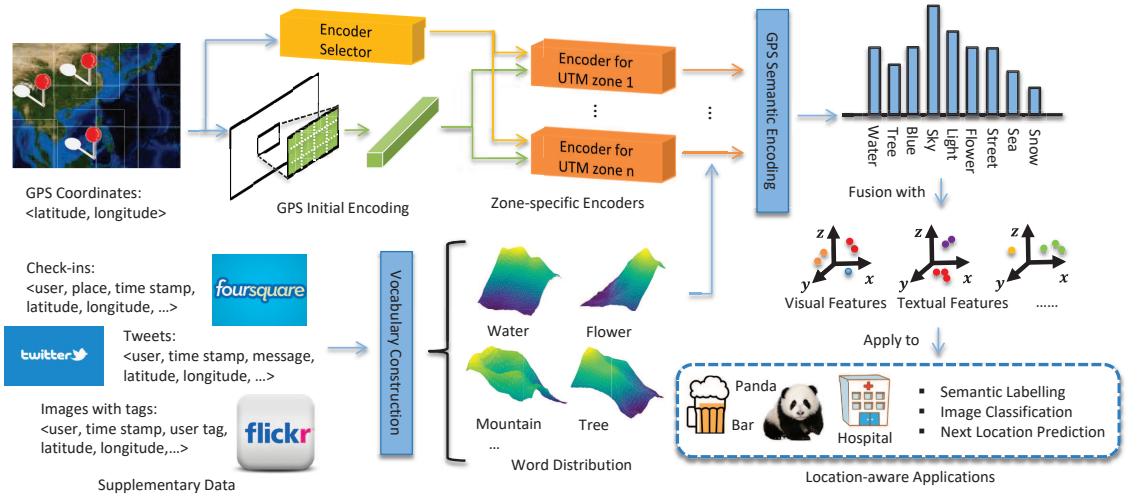

Fig. 3: The system overview of our proposed GPS semantic feature extraction and its use in location-aware applications.

the entire planet with a coarse-grained grid of $0.1° \times 0.1°$ cells (*i.e.*, a cell length at the equator of approximately 11 km) would result in a large 1800×3600 encoding. This would be significantly larger than the common input size of neural networks, *e.g.*, 224×224 pixels for images, and this might exhaust computational resources such as system or GPU memory.

The second type of GPS encoding technique uses supplementary data. Such additional data refers to large-scale datasets of geotagged documents or objects, from which we can extract surrounding information of a given GPS coordinate. For example, Joshi and Luo [5] proposed to utilize GeoNames [6] to retrieve nearby place entities at a specific location. Tang *et al.* [1] proposed to utilize geotagged images to extract both hashtag and visual context features for locations within the United States. To encode a GPS coordinate, these methods perform a nearest neighbor search to obtain a list of nearby objects from the supplementary data, from which a semantic vector is generated as the GPS representation. Though spatial indexing methods such as the KD-tree and the ball-tree [7] can be adopted to perform real-time spatial queries in 2D space, their efficiency declines when handling high dimensional features in the visual space [2]. Moreover, GPS encoding still relies on the supplementary dataset even with spatial indexing. To encode worldwide locations, the supplementary dataset must densely cover the whole world. The costs to maintain such a large-scale dataset are prohibitive. For mobile applications, the system efficiency will be further degraded by network communication delays between mobile devices and a server.

To address these issues we present our novel lightweight GPS2Vec approach which is able to extract geo-aware semantic features in real-time during inference for large-scale areas without dependence on supplementary datasets. As shown in Figure 2, we first propose a two-level soft encoding approach to extend the idea of one hot encoding to work smoothly with worldwide locations. Next, we use the semantic information extracted from supplementary data as labels to train neural networks that map the initial soft encoding (input) to a semantically-enriched encoding (output). We refer to these neural networks as the *SupData*-based semantically-enriched models. These models need to be trained only once for them to capture and summarize the semantic information of the supplementary data. Thus they can be used as a replacement to generate semantically-enriched GPS encodings. Moreover, our proposed models are lightweight and can be deployed in mobile devices, which enables true real-time response even without Internet connection.

Figure 3 illustrates the overall architecture of our system. For our method to handle GPS coordinates worldwide, we introduce a two-level grid-based approach to strike a balance between information loss and computation cost. On the first level, we adopt the Universal Transverse Mercator (UTM) coordinate system to divide the Earth's surface into 60 longitude zones and 20 latitude bands. On the second level, we encode GPS coordinates into grid-based features and train a neural network to learn the semantic embeddings separately in each UTM zone. While one hot encoding is widely used in previous work [1], [4], we present a new soft GPS encoding method that relaxes the requirements on the cell size, and thus is able to generate descriptive encoding features using a grid with fewer cells. As choice for the supplementary data source we can utilize any large-scale geotagged dataset such as tweets, check-ins, or images that are available from social media sharing platforms. Given a specific location, we generate a normalized histogram in its vicinity by calculating the weighted sum of the semantic words in a pre-defined vocabulary. For example, semantic words can be keywords in tweets, user tags associated with Flickr images, or venue types in Foursquare check-ins. Intuitively, we aim to use neural networks to predict the distribution of semantic words at a specific location, which can be a good semantically-enriched representation for GPS coordinates. The key contributions of this work are summarized as follows:

- We present the first machine-learning-based lightweight solution that generates semantically-enriched embeddings

1520-9210 (c) 2021 IEEE. Personal use is permitted, but republication/redistribution requires IEEE permission. See http://www.ieee.org/publications_standards/publications/rights/index.html for more information.
Authorized licensed use limited to: DELHI TECHNICAL UNIV. Downloaded on March 27,2021 at 09:52:40 UTC from IEEE Xplore. Restrictions apply.

This article has been accepted for publication in a future issue of this journal, but has not been fully edited. Content may change prior to final publication. Citation information: DOI 10.1109/TMM.2021.3060951, IEEE Transactions on Multimedia

for worldwide GPS coordinates. It achieves real-time responses with minimal computational resources that can be easily satisfied on mobile devices.
- We propose a novel two-level grid-based approach to learn global GPS semantic embeddings. Considering the surface area of the Earth, earlier methods have struggled to achieve a balance between computational cost and information loss during GPS encoding.
- The GPS2Vec models, once trained on supplementary data, can be used as pre-trained models for feature extraction from GPS coordinates. Transfer learning can be applied even when the domain of the supplementary data is different from that of an application.
- Extensive experiments have been conducted on place semantic labeling, image classification, and next location prediction. Our method significantly improves the prediction accuracy, and overall provides new insights into the challenges and opportunities in GPS encoding tasks.

The rest of this paper is organized as follows. Section II reports important related work. Section III introduces our proposed GPS2Vec system framework. Section IV presents the utilization of our GPS semantic embeddings in three location-aware applications. Experimental comparisons with state-of-the-art methods are reported in Section V. Finally, Section VI concludes and suggests future work.

II. Related Work

Geo-clustering and Geo-filtering: With the ubiquity of sensor-equipped cellphones, it is common for multimedia documents such as tweets and images posted on the Internet to be associated with GPS coordinates (*i.e.*, latitude and longitude) [8], [9]. The availability of geo-location context has opened up new opportunities in a variety of applications such as landmark recognition [10]–[12], image classification [1], [2], semantic annotation [13], [14], *etc.* The early utilization of geo-location context associated with documents can be roughly classified into the following two scenarios: geo-clustering and geo-filtering. These methods compute and leverage the geographical distance between documents calculated based on their associated geotags, rather than analysing the geotags directly. For example, Zheng *et al.* [10] proposed to discover landmarks worldwide by first performing geo-clustering. Moxley *et al.* [15] proposed to annotate an image based on its k-nearest geo neighbors. Kleban *et al.* [16] further proposed to weigh the geo neighbors of an image based on their visual similarity.

GPS Encoding without Supplementary Data: Since a GPS coordinate is a tuple of only two values, namely latitude and longitude, its integration with existing high dimensional textual and visual features in geo-based application is difficult. In recent years, several efforts have attempted to encode GPS coordinates at the feature level based on one hot encoding [1], [17]. Tang *et al.* [1] proposed to divide an area of interest (AOI) into 25×25 km^2 square cells and construct an indicator vector that records into which grid cell a GPS coordinate falls. Yao *et al.* [17] further proposed to transform the sparse indicator vector into a dense embedding vector by introducing an embedding layer in their system architecture. However, the number of cells to encode GPS coordinates is always limited by the computational cost and memory. In an extreme example, geotagged documents are spread all over the world [4]. The authors adopted UTM zones for GPS encoding, resulting in significant information loss, as the granularity of UTM is too coarse.

GPS Encoding with Supplementary Data (Regional): When supplementary data sources are available, it is possible to encode GPS coordinates into feature vectors with semantics. However, under many circumstances, such a geotagged supplementary dataset is only available in a limited number of regions around the world [1], [18]. For example, Tang *et al.* [1] proposed to extract geographic map features and ACS features for a given GPS coordinate using Google Maps [19] and American Community Survey (ACS) [20], respectively. Joshi and Luo [5] proposed to encode GPS coordinates by retrieving nearby place entities from GeoNames [6], which is a freely available geographic information system (GIS) database. Recently, Spruyt [21] presented a triplet network to learn a metric space that captures semantic similarity between different geographic location coordinates. Given a location and a radius, they queried their GIS database to obtain a large set of geographic information, and then rasterized it into image tiles for the triplet network training. As mentioned earlier, one major drawback of these approaches lies in their difficulties to generalize to worldwide applications, due to the limited availability of the required supplementary data sources in less populous areas around the world.

GPS Encoding with Supplementary Data (Global): One promising data source to generate worldwide GPS embeddings can be large-scale user generated and geotagged documents that are available online (*e.g.*, check-ins, images, and tweets) [22], [23]. Towards this direction, Liao *et al.* [2] proposed to extract geo-aware tag features by tag propagation from both the geo and visual neighbors of a given geotagged image. Tang *et al.* [1] proposed a hashtag context feature by capturing the distribution of hashtags associated with Instagram images in the vicinity of a given image. However, the aforementioned methods are tailored for geotagged image classification only. Moreover, it is time-consuming to query geo and visual neighbors from a large collection of supplementary images, which significantly hinders the use of such methods in real-time applications.

Image Geolocalization: Image geolocalization aims to predict the geotag of an image either by matching it to a large-scale georeferenced image dataset [24] or by directly classifying it to a pre-defined set of geographic cells [25]. A key component of image geolocalization is to model the distance between the query image and worldwide locations. To obtain a better distance metric, Salem *et al.* proposed to construct a global-scale, dynamic map of visual appearance attributes using geotagged images [26]. The distance can thus be computed by comparing the visual attributes of a query image with the visual attributes of a location predicted by their model. Similarly, though our GPS2Vec model was originally designed for geotag encoding, it has the potential to be utilized to support image geolocalization as well. The distance metric

1520-9210 (c) 2021 IEEE. Personal use is permitted, but republication/redistribution requires IEEE permission. See http://www.ieee.org/publications_standards/publications/rights/index.html for more information.
Authorized licensed use limited to: DELHI TECHNICAL UNIV. Downloaded on March 27,2021 at 09:52:40 UTC from IEEE Xplore. Restrictions apply.

This article has been accepted for publication in a future issue of this journal, but has not been fully edited. Content may change prior to final publication. Citation information: DOI 10.1109/TMM.2021.3060951, IEEE Transactions on Multimedia

could possibly be improved by additionally considering the difference between the semantic features of a query image and the semantic features of a location predicted by our model.

Multimodal Feature Fusion: The semantic embedding features extracted from GPS coordinates aim to capture high-level semantics that are complementary to the raw GPS coordinates and the existing textual/visual descriptors. Therefore, multimodal fusion techniques can be applied to obtain performance gains by combining different types of features [27]. To incorporate location features into existing neural networks, a concatenation layer is usually introduced to combine multiple features before passing them to a fusion network for more robust predictions [1]. More advanced fusion techniques, *e.g.*, bilinear CNN models [28] and multiplicative fusion methods [29], have also been proposed recently and significant improvements were reported.

III. Learning Worldwide GPS Semantic Embeddings

We propose a general solution that encodes a GPS coordinate into a semantic descriptor based on a neural network (NN) and is capable of handling locations worldwide rather than focusing on specific small areas of interest. Leveraging neural networks enables the extraction of GPS semantic embeddings in real-time. More importantly, our generated GPS semantic embeddings can easily be applied in a variety of location-aware applications to obtain significant performance gains. Next, we introduce the technical details of our proposed approach in the rest of this section and discuss its use in three location-aware applications in Section IV.

A. GPS Initial Encoding

It is difficult to directly use GPS coordinates as inputs to a neural network. Therefore, we transform the low-dimensional GPS coordinates into high-dimensional distributed vector representations before passing them to our proposed neural network to learn the semantic embeddings [30]. Additionally, none of the existing GPS encoding methods have ever been investigated for or extended to deal with locations worldwide. Thus we present a novel two-level grid based GPS encoding approach. On the first level, we adopt the Universal Transverse Mercator (UTM) coordinate system and divide the Earth into 60 longitude zones and 20 latitude bands. Each UTM zone is referenced by a longitudinal zone number (*i.e.*, 1 to 60) and a latitudinal zone letter (*i.e.*, C to X, omitting O). A location in a zone is represented by the projected easting and northing planar coordinate pair. Considering that the granularity of the UTM zones might be too coarse, we further divide each zone into $m \times m$ grid cells on the second level to perform the initial GPS encoding. Formally, let $Z = \{g_{ij} | i, j = 1, 2, ..., m\}$ denote the set of cells in zone Z. Let $c_{ij} = (x_{ij}, y_{ij})$ denote the center UTM coordinate of cell g_{ij}. Then for any GPS coordinate in the same zone Z, we first represent it by the corresponding UTM coordinate $l = (x, y)$. Next, we compute its initial encoding $E^l = \{e^l_{ij} | i, j = 1, 2, ..., m\}$ as,

$$e^l_{ij} = \exp(-\frac{\|l - c_{ij}\|_2}{\sigma}) \quad (1)$$

where $\|l - c_{ij}\|$ denotes the Euclidean distance between the UTM coordinates l and c_{ij}, and σ represents a constant attenuation coefficient.

Existing grid-based GPS encoding methods mostly use a one-level grid to construct an indicator vector that records which grid cell a GPS coordinate falls into, resulting in a sparse feature vector with only one entry set to 1 [1], [4], [17]. The grid granularity is required to be very fine in order to reduce the information loss as GPS coordinates that fall into the same cell will be assigned the same encoding feature. When it comes to the scale of the entire planet, the use of a single grid level may result in great information loss as the number of cells is always limited by the system's computational resources. Comparatively, our approach processes each UTM zone individually by introducing a second grid level to improve the system's scalability. The advantages of our proposed two-level grid-based GPS encoding method are twofold. First, multiple models can be more efficiently retrieved and updated locally in each UTM zone compared to a single model representing the entire planet. Second, the information loss during GPS encoding is majorly controlled by the cell size of the second-level grid. Therefore, the choice of the first-level grid in our method has more flexibility in terms of its granularity. Here we adopt the UTM coordinate system as the first-level grid, for ease of converting a latitude and longitude pair into a planar coordinate in meters. Other projection models such as the ECEF (Earth-centered Earth-fixed) [31] and Google's S2 geometry [25] can be adopted, but we choose UTM as it is a grid-based projection that is widely used in many geo-based applications [4].

Moreover, our soft encoding approach using Eq. 1 can better discriminate GPS coordinates since the distance $\|l - c_{ij}\|$ is more sensitive to the location change in the corresponding UTM coordinate l. With a proper setting of σ, we are able to generate a dense encoding E^l with few zero entries, leading to effective learning by the neural network presented in Section III-C. Later in the experiments, we will demonstrate that representative semantic embeddings can be extracted by neural networks from the initial GPS encoding generated with a simple 20×20 grid in each UTM zone.

B. Vocabulary-based Semantic Feature

Given GPS coordinates' initial encoding features, we aim to learn GPS semantic embeddings based on neural networks. The labels for training can be automatically generated by extracting semantic contexts from supplementary data sources such as Flickr, Twitter, and Foursquare. Formally, let $V = \{t_1, t_2, ..., t_n\}$ denote a vocabulary consisting of n words. The construction of vocabulary V will be discussed in Section III-D. Our goal is to automatically generate a vocabulary-based feature for a GPS coordinate based on vocabulary V. The resulting n-dimensional feature, denoted as $S^l = \{s^l_i | i = 1, 2, ..., n\}$, will be used as a set of labels for the training of the neural networks.

Let o be a multimedia document in the supplementary dataset, and $l(o)$ and $T(o)$ be the geotag and semantic words associated with sample o, respectively. For example, $T(o)$ can

1520-9210 (c) 2021 IEEE. Personal use is permitted, but republication/redistribution requires IEEE permission. See http://www.ieee.org/publications_standards/publications/rights/index.html for more information.
Authorized licensed use limited to: DELHI TECHNICAL UNIV. Downloaded on March 27,2021 at 09:52:40 UTC from IEEE Xplore. Restrictions apply.

This article has been accepted for publication in a future issue of this journal, but has not been fully edited. Content may change prior to final publication. Citation information: DOI 10.1109/TMM.2021.3060951, IEEE Transactions on Multimedia

be the user tags associated with an image, the texts of a tweet, or the venue type in a check-in record where o is an image, a tweet, or a check-in record, respectively. For each multimedia document, we compute its semantic encoding $S(o)$ based on vocabulary V as,

$$s_i(o) = \begin{cases} 1 & t_i \in T(o) \\ 0 & t_i \notin T(o) \end{cases} \quad (2)$$

where $s_i(o)$ is the i-th element in vector $S(o)$. This semantic encoding can be quite sensitive to both GPS noise and semantic keyword uncertainty, and therefore cannot be directly used as the vocabulary-based semantic feature. For instance, images that are geographically close to each other can sometimes have completely different user tags. This can be caused by human mistakes, or more commonly by the difference between the image content location and the camera location. To reduce noise, we smooth the geographic distribution of semantic words by taking the geo neighbors into consideration as well. Given a location l, we first retrieve the k-nearest geo neighbors $NN(l)$ of location l from the geotagged supplementary dataset in terms of the geographic distance. Next, we compute the weighted sum of the semantic encodings in the geo neighborhood,

$$\tilde{s}_i^l = \sum_{o \in NN(l)} w_i^l(o) \cdot s_i(o) \quad (3)$$

and apply l_1 normalization to obtain our vocabulary-based semantic feature S^l

$$s_i^l = \frac{\tilde{s}_i^l}{\sum_j \tilde{s}_j^l} \quad (4)$$

where j iterates over the words in the vocabulary V, and s_i^l represents the i-th element in S^l.

Weight $w_i^l(o)$ is formulated based on the geographic distance between locations l and $l(o)$ as [2],

$$w_i^l(o) = \exp(-\frac{\|l - l(o)\|_2}{\sigma_w}) \quad (5)$$

where $\|l - l(o)\|_2$ computes the Euclidean distance between the UTM coordinates l and $l(o)$, and σ_w is a constant attenuation coefficient.

The generated feature vector S^l captures the distribution of semantic words around location l, which provides rich contextual information about events that occur in the real world. The l_1 normalization is applied to reduce the impact caused by the unbalanced geographic distribution of the geotagged documents.

C. Neural Network Architecture

In each UTM zone we propose to train a neural network, which is able to transform the GPS initial encoding (introduced in Section III-A) into the vocabulary-based semantic feature (introduced in Section III-B). We map the zone-level GPS initial encodings into the shared global semantic embeddings by training separate models in each UTM zone. It is noteworthy that though the GPS coordinates in different UTM zones may have the same initial encodings, the extracted semantic embeddings will be different as they will be processed by different neural networks. Compared with traditional unsupervised methods, the advantages of our proposed machine based solution are twofold. First, our method divides the GPS encoding into two stages: offline training and online extraction. The offline training executes time-consuming nearest neighbor queries from large-scale supplementary datasets, while online extraction generates GPS semantic embeddings in real-time using only pre-trained models. Second, we adopt a relatively simple neural network architecture to prevent overfitting, based on experiments, which makes our solution more robust than unsupervised methods to both GPS noise and semantic keyword uncertainty. Though multiple models are trained to cover the entire Earth's surface, these models can be efficiently retrieved and updated locally in each UTM zone. The maintenance costs of our pre-trained models are much smaller than that of the supplementary dataset. Moreover, the inference of our model is performed simply by passing an input location to a neural network that outputs the semantic embedding, which can be executed highly efficiently in milliseconds.

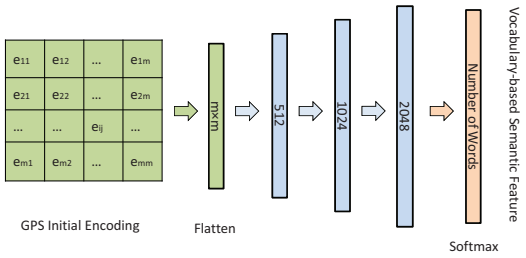

Fig. 4: Illustration of the proposed neural network for GPS semantic encoding.

As shown in Figure 4, we adopt a neural network that consists of three hidden layers and one output layer. A ReLU (Rectified Linear Unit) activation is applied to each hidden layer and a softmax activation is applied at the end to transform the network output into the prediction space. The size of the three hidden layers are set to 512, 1024, and 2048 neurons based on experiments. Algorithm 1 illustrates the preparation of a training dataset from a worldwide supplementary dataset, and the training of the GPS2Vec models in each UTM zone. The size of the output layer equals the size of vocabulary V, whose construction will be discussed in the next section. The input to our neural networks is the GPS initial encoding E^l as introduced in Section III-A. During learning, we aim to use the vocabulary-based semantic features S^l as labels to train our set of neural networks $f(E^l)$ to estimate the normalized word frequency in the vicinity of location l. Let θ be the model parameters to be learned, then the loss function for the network training is given as,

$$L(\theta) = \sum_l D_{KL}(S^l || f(E^l; \theta)) \quad (6)$$

where $D_{KL}(P||Q) = \sum_i P_i \log \frac{P_i}{Q_i}$ represents the Kullback Leibler (KL) divergence. As the semantic feature S^l can be interpreted as a distribution of the semantic words in vocabulary V, the KL divergence, which measures how one probability distribution is different from another, reference probability

1520-9210 (c) 2021 IEEE. Personal use is permitted, but republication/redistribution requires IEEE permission. See http://www.ieee.org/publications_standards/publications/rights/index.html for more information.
Authorized licensed use limited to: DELHI TECHNICAL UNIV. Downloaded on March 27,2021 at 09:52:40 UTC from IEEE Xplore. Restrictions apply.

This article has been accepted for publication in a future issue of this journal, but has not been fully edited. Content may change prior to final publication. Citation information: DOI 10.1109/TMM.2021.3060951, IEEE Transactions on Multimedia

Algorithm 1: GPS2Vec Model Training

Input: A worldwide large-scale supplementary dataset *SupData* and a vocabulary V consisting of n semantic words
Output: Pre-trained GPS2Vec models in each UTM zone
List $list_E$, $list_S$;
Dictionary $models$;
for *each* o, $l(o)$, $T(o)$ *in SupData* **do**
  /* o is a multimedia document, $l(o)$ and $T(o)$ are the geo and semantic tags associated with o */
  $l = l(o)$;
  compute the initial GPS encoding E^l using Eq. 1;
  add E^l into $list_E$;
  compute the normalized semantic feature S^l using Eq. 4;
  add S^l into $list_S$;
for *each utm in UTM zones* **do**
  $list'_E, list'_S$=filtering($list_E$,$list_S$);
  /* filter $list_E$ and $list_S$ based on locations */
  train a neural network $model$ as shown in Fig. 4 with $list'_E$ being the input and $list'_S$ being the output;
  $models[utm] = model$
return $models$;

Algorithm 2: Semantic Embedding Extraction

Input: GPS2Vec pre-trained models $models$ and a GPS coordinate l
Output: The semantic embedding of the GPS coordinate l
$model$=select($models$,l);
/* select the correct GPS2Vec model representing the UTM zone that contains location l */
compute the initial GPS encoding E^l using Eq. 1;
return $model(E^l)$;

distribution, can be a good choice for the loss function. During training, we optimize $\arg\min_\theta L(\theta)$ using stochastic mini-batch gradient descent based on back-propagation with momentum. The mini-batch size and the momentum were set to 32 and 0.9, respectively. The learning rate was set to 0.001.

Algorithm 2 illustrates the process of GPS semantic embedding extraction based on our pre-trained GPS2Vec models. Given a GPS coordinate l, we first compute its initial GPS encoding E^l using Eq. 1. Next, we pass E^l to the correct GPS2Vec model, selected according to l. Finally, the model output is returned as the semantic embedding of location l.

D. Vocabulary Construction

Ideally, the vocabulary construction should be application-specific, as applications in different domains may require different words. For example, Flickr, Twitter, Foursquare, Strava, *etc.*, record different user activities and therefore depict a place from inherently different perspectives. In this initial attempt to learn worldwide GPS semantic embeddings, we start by building the vocabulary from one data source. Fortunately, the extension to leverage multiple data sources for embedding learning is straightforward. For example, multiple vocabularies can be built with different data sources and the most appropriate one can be selected based on the application domain. Moreover, the embeddings learnt from one data source (*e.g.*, images) are also helpful when they are applied to other data sources (*e.g.*, tweets or check-ins) based on transfer learning. This is reasonable as correlations exist between words from different domains. For example, a user tag "beer" associated with an image may have a high correlation with venues of type "pub" and "bar", and a tag "food" tends to appear more frequently near "restaurants."

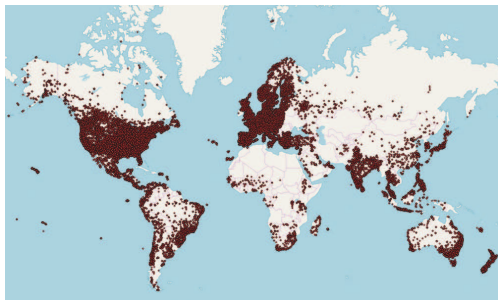

Fig. 5: Geographical distribution of the one million Flickr images.

By considering both the data availability and application popularity, for vocabulary construction and semantic embedding learning we chose geotagged images and leveraged the one million Flickr images collected by Li *et al.* [22], which were taken by 145,000 distinct users in over 100 countries. As seen in Figure 5, this dataset is quite diverse in terms of its geographical distribution. To ensure that high frequency tags are included in the semantic embedding learning, we constructed the vocabulary V by selecting the top 2,000 most frequent tags in the one million Flickr dataset, excluding stop words, camera brands, and non English words [2], [32]. Thus, both the vocabulary-based semantic feature and the output of our neural network have a dimensionality of 2,000. For feature normalization, in addition to the l_1 norm that we adopted in Eq. 4, it would also be possible to consider the tag frequency in the future [1].

One issue of the supplementary dataset that we used in this study might be the uneven distribution of the geotagged images. The GPS embeddings generated in regions with only a few geotagged images can be sparse. Fortunately, when used in applications, the GPS embeddings will be fused with features from other modalities such as the visual features in image classification and the check-in-based features in place annotation. Thus, locations with sparse embeddings can still be distinguished based on multi-modal feature fusion.

IV. Enriching Geo-applications with Semantics

Next we introduce the use of our proposed GPS semantic embeddings not only in image classification, but also in place semantic annotation and in next location prediction with transfer learning.

A. Semantic Annotation of Places

Semantic place annotation refers to the process of assigning a meaningful name to a location. For example, with GPS data from government diary studies, the semantic labels may be "home," "work," and "school," given to geographic locations where a person spends time [14]. With check-in data collected from location-based social networking (LBSN) services such as Foursquare, the semantic labels may be "restaurant," "hotel," and "hospital," given to places of interest (*i.e.*, venues) in LBSN [13]. Such semantic labels are important for people to

1520-9210 (c) 2021 IEEE. Personal use is permitted, but republication/redistribution requires IEEE permission. See http://www.ieee.org/publications_standards/publications/rights/index.html for more information.
Authorized licensed use limited to: DELHI TECHNICAL UNIV. Downloaded on March 27,2021 at 09:52:40 UTC from IEEE Xplore. Restrictions apply.

This article has been accepted for publication in a future issue of this journal, but has not been fully edited. Content may change prior to final publication. Citation information: DOI 10.1109/TMM.2021.3060951, IEEE Transactions on Multimedia

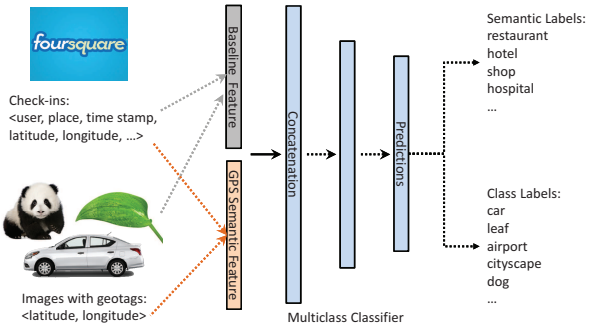

Fig. 6: Integration of our GPS semantic feature with other application-related features in place annotation and image classification.

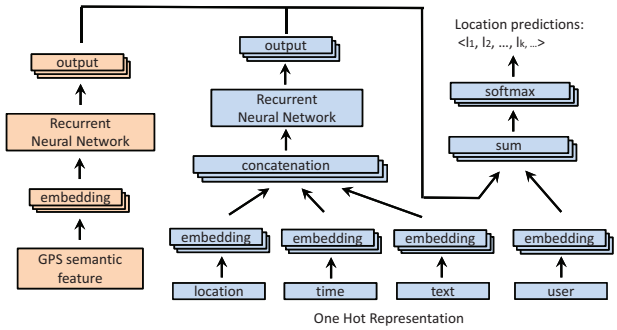

Fig. 7: Integration of our GPS semantic feature in the recurrent model for next location prediction.

infer activities, explore new places, and develop recommendation services [33], [34].

The semantic place annotation can be formulated as a multi-class classification problem based on features generated for each place. For example, in LBSN, users are likely to behave differently at different venues due to the nature of the services and functions offered by these places [13]. Therefore, different behavior patterns of visitors can be extracted from the check-in data at each venue to depict the place. Some baseline features that are proposed in previous work are as follows:

- total number of visits,
- total number of unique visitors,
- maximum number of check-ins by a single visitor,
- distribution of visit time in a week, and
- distribution of visit time in a day.

Such baseline features can be easily integrated with our proposed GPS semantic embeddings that are extracted based on the geo-coordinates of the places to be labeled. As illustrated in Figure 6, one way to achieve this goal is to concatenate different features to form a final feature vector through early fusion. The concatenated feature vector is next passed to a multi-class classifier for label prediction. The advantage of this early fusion strategy not only lies in its effectiveness, but also its generalization capability to any geo-aware classification problem with little modifications required.

B. Image Classification with Location Context

Nowadays it is common for online images to be associated with GPS coordinates, due to the availability of sensor-equipped smartphones. Such geotags can be leveraged to obtain rich contextual information that is of great importance to help predict what is captured in an image. Though several efforts have been made in this direction, drawbacks exist in some methods, *e.g.*, tailoring for specific AOIs [1], GPS encodings that are computationally expensive [2], and significant information loss with coarse-grained encodings [4]. Our work differs in that we are interested in efficient and fine-grained GPS semantic embeddings extraction that is not tailored to particular tasks or AOIs. Our method can be applied to a wide range of geo-aware applications with sufficient performance gains, in terms of both effectiveness and efficiency, achieved.

The use of our GPS semantic embeddings in image classification is illustrated in Figure 6. In this case, the baseline features refer to image visual features varying from hand-crafted low-level features such as HOG [35] and SIFT [36] to the most recent CNN-based deep features for object and scene recognition [37], [38]. Moreover, the class labels can cover a wide range of concepts without limitations to particular types of objects and scenes. For the classifier, we adopt a neural network with one hidden layer of 512 units and one output layer for both semantic annotation of places and image classification. Other classifiers such as SVM [39] would also suffice.

C. Next Location Prediction in Semantic Trajectories

Predicting the next location that a user tends to visit is a challenging and crucial task for applications such as tour recommendations and traffic planning [40]. For example, given a user's historical check-in data, we may be able to predict where the user will go next by jointly analyzing multiple factors including time, location, texts, and user preferences [17]. Recently, Yao *et al.* [17] proposed a unified framework, termed SERM, which is capable of jointly learning the embeddings of the aforementioned multi-factors and the transition parameters of a recurrent neural network (RNN) for next location prediction. The architecture of their proposed semantics-enriched recurrent model (SERM) is illustrated in Figure 7. First, one hot representations are generated for all inputs, where the category of each factor is defined as follows:

- **Time:** one hot vector generated based on timestamp by discretizing one week's time into 48 equal sized time slots
- **Location:** one hot vector generated based on location by discretizing the AOI into a $500\ \text{m} \times 500\ \text{m}$ grid
- **Text:** one hot vector generated based on bag-of-keywords
- **User:** one hot vector generated based on user id

Next, embedding vectors are generated and concatenated from one hot representations of time, location, and text to train a recurrent neural network, and fused with the user embedding that describes the user preferences, at the RNN's output layer. To make use of pre-trained models and reduce RNN training time, we propose to first train an individual RNN with the same architecture based on our GPS semantic embeddings, and then fuse its output with pre-trained SERM for fine-tuning as shown

1520-9210 (c) 2021 IEEE. Personal use is permitted, but republication/redistribution requires IEEE permission. See http://www.ieee.org/publications_standards/publications/rights/index.html for more information.
Authorized licensed use limited to: DELHI TECHNICAL UNIV. Downloaded on March 27,2021 at 09:52:40 UTC from IEEE Xplore. Restrictions apply.

This article has been accepted for publication in a future issue of this journal, but has not been fully edited. Content may change prior to final publication. Citation information: DOI 10.1109/TMM.2021.3060951, IEEE Transactions on Multimedia

TABLE I: Venue categories and their percentages (z%) in the evaluation dataset.

Category	z%	Category	z%
Restaurant & Food	40.4%	Shop	19.8%
Hotel	3.5%	Pub & Bar	13.1%
Store	20.7%	Hospital	2.5%

in Figure 7. Finally, we derive the probability distribution over all the locations at each step by applying the softmax function. In addition to CNN-based models such as the aforementioned image classification, this application demonstrates the use of our proposed GPS semantic embeddings in RNN-based models, and its effectiveness in sequential data modeling.

V. Experiments

We first evaluate the effectiveness of our proposed GPS semantic embeddings learning method in three location-aware applications. The venue semantic annotation and the geotagged image classification are global applications based on world-wide Foursquare check-in records and Flickr images, respectively. The next location prediction is a regional application based on city-scale semantic trajectory data (*i.e.*, check-ins and tweets) in New York and Los Angeles. We evaluate our proposed approach on both global and regional applications to verify its effectiveness. Throughout the experiments, the parameter m that controls the grid size in each UTM zone is set to 20. The attenuation coefficient σ is set to 20 km. The number of geo neighbors k is set to 150 as suggested by Liao *et al.* [2]. We adopt the output of the softmax layer in our proposed neural network as the generated GPS semantic embedding. Next, we perform an ablation analysis on the model parameter settings and discuss their impact in our proposed framework.

A. Evaluation on Venue Semantic Annotation

1) Experimental Setup: We conduct experiments on a global-scale check-in dataset collected from Foursquare [41], [42]. Each check-in records the user id, venue id, visit time, latitude, longitude, and venue category name. We choose six popular categories as shown in Table I to form an evaluation dataset. The semantic labeling of places can be formulated as a multi-label classification problem. For example, a place associated with tag "restaurant" can also be annotated with "bar." Therefore, we apply sigmoid activation at the output layer, and choose binary cross-entropy as the loss function. The network was trained using stochastic mini-batch gradient descent based on back-propagation. The learning rate and mini-batch size were set to 0.001 and 32, respectively.

2) Performance Comparison: We adopt the following three metrics: hamming loss, coverage error, and average precision as the evaluation metrics. The hamming loss measures the fraction of labels that are incorrectly predicted, while the other two metrics measure the ranking performance of the predictors [43]. The coverage error evaluates how far we need to travers the ranked list of predicted tags in order to cover all the ground-truth tags associated with the venue. The average precision is a measure that combines recall and precision for ranked retrieval venues given a tag, and is computed as the mean of the precision scores after each ground-truth venue is retrieved. We extract the five baseline features as introduced in Section IV-A, and concatenate them into a feature vector, which we refer to as the baseline feature.

TABLE II: Performance comparison on place semantic labeling based on GPS embedding, baseline feature (B), and their fusion.

Method	Hamming loss	Coverage error	Average precision
Baseline [13]	0.159	2.129	0.298
OneHot [4]	0.165	2.235	0.210
HashTag [1]	0.164	2.200	0.249
GPS2Vec$_{onehot}$	0.165	2.224	0.220
GPS2Vec	0.164	2.189	0.243
OneHot [4] + B	0.152	2.045	0.337
HashTag [1] + B	0.153	2.060	0.335
GPS2Vec$_{onehot}$ + B	0.151	2.034	0.340
GPS2Vec + B	**0.151**	**2.029**	**0.344**

We report the overall hamming loss, coverage error, and average precision in Table II, with the **best** result highlighted in bold, and the place semantic labeling results per venue category in Figure 8. We compared our GPS2Vec to the OneHot encoding [4] and the GPS2Vec$_{onehot}$ which is a variation of GPS2Vec by using the one hot encoding instead of our proposed soft encoding approach in generating the initial GPS encoding. As is illustrated, GPS2Vec outperforms OneHot and GPS2Vec$_{onehot}$ by 3.3% and 2.3% in terms of the average precision, respectively. Please note that the GPS2Vec embeddings are learnt from geotagged images. By being applied to an application in a different domain (*i.e.*, check-in records), our proposed GPS2Vec+B is still able to achieve the best classification result, outperforming Baseline and OneHot+B by 4.6% and 0.7% in terms of the average precision. This indicates that the GPS2Vec embeddings learnt from one data source have the potential to work reasonably well with applications in different domains. Generally speaking, the baseline features depict different user behavior patterns at different places in terms of population and temporal duration. The vocabulary-based GPS2Vec embeddings, on the other hand, provide contextual information about events that occur in the real world at each place. The distribution of user tags in the vicinity can be closely related to the place category. For example, the tag "beer" can have a high correlation with places such as pubs and bars, and the tag "food" tends to appear more frequently near restaurants.

Next, we compare our proposed method to the HashTag context feature proposed by Tang *et al.* [1]. Given a GPS coordinate to be encoded, the authors define a set of radii R, and for each $r \in R$, they pool over a circle of radius r around that GPS coordinate and count the number of images tagged with tag t that falls within the radius. We normalize the generated feature vector and set $R = \{1,000, 2,000, ..., 10,000\}$ as described in their original paper. To perform a fair comparison, we generated a 2,000-D feature by setting the tag collection to be the top 50 most frequent tags in our one million Flickr dataset. As shown in Table II, GPS2Vec+B outperforms HashTag+B by 0.9%. Moreover, the computation of the HashTag context

1520-9210 (c) 2021 IEEE. Personal use is permitted, but republication/redistribution requires IEEE permission. See http://www.ieee.org/publications_standards/publications/rights/index.html for more information.
Authorized licensed use limited to: DELHI TECHNICAL UNIV. Downloaded on March 27,2021 at 09:52:40 UTC from IEEE Xplore. Restrictions apply.

This article has been accepted for publication in a future issue of this journal, but has not been fully edited. Content may change prior to final publication. Citation information: DOI 10.1109/TMM.2021.3060951, IEEE Transactions on Multimedia

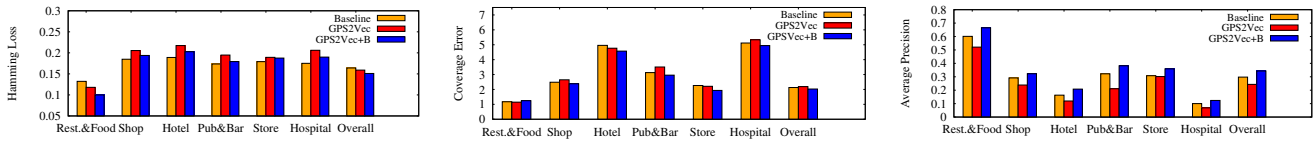

(a) Hamming loss (b) Coverage error (c) Average precision

Fig. 8: Performance comparison per concept on place semantic labeling based on GPS embedding, baseline feature, and their fusion.

feature relies on the supplementary Flickr image dataset, while our proposed method generates GPS semantic embeddings based on pre-trained models during inference without relying on any large-scale supplementary dataset.

B. Evaluation on Image Classification

1) Experimental Setup: For image classification, we evaluate our method using the NUS-WIDE dataset [44], which is a benchmark dataset that is widely used for image annotation and classification. As the location context is required in our experiments, we use the geotagged images in NUS-WIDE and form a training set with 41,173 images and a test set with 27,401 images. Ignoring rare concepts, we test on 75 concepts covering objects, scenes, and events. In terms of the visual feature, we adopt the BovW representation based on SIFT descriptors that is used in previous work [2] to make it a fair comparison.

Since an image is mostly associated with more than one tag, we formulate this problem as a multi-label classification, apply sigmoid activation at the output layer, and choose binary cross-entropy as the loss function. The network was trained using stochastic mini-batch gradient descent based on back-propagation. The learning rate and mini-batch size were set to 0.001 and 32, respectively. We report the Average Precision (AP) per concept, and the mean Average Precision (mAP) as the evaluation criteria.

2) Performance Comparison: We first compare our proposed method to the state-of-the-art geo-based and fusion-based image classification systems in Table III with the **best** and second best results highlighted. Our GPS2Vec obtained the best mAP among the geo-based methods. Moreover, the GPS2Vec+V outperforms the OneHot+V, HashTag+V, and GPS2Vec$_{onehot}$+V by 6.2%, 3.9%, and 2.3%, respectively. The results verify the effectiveness of our proposed GPS2Vec embeddings and its complementarity to image visual features. When comparing to other fusion approaches, our method achieves significant improvements over the approaches that utilize the GPS coordinates in a traditional manner for geo neighbor search [8], [16], [22]. Wang *et al.* [32] and Liao *et al.* [2] both proposed to fuse a visual classifier with a textual classifier built upon tag features generated by conjunctively considering geo and visual neighbors from a supplementary image dataset. The method proposed by Liao *et al.* [2] was able to achieve the best classification result due to the following reasons. First, this method searches for visual neighbors of test images, which is tailored for image classification and cannot be applied to other geo-aware applications. Second, the authors leverage a much larger supplementary dataset that consists of 10 million geotagged images to generate a more descriptive tag-based feature. Comparatively, our method is more general, and at the same time, is able to obtain the second best mean average precision of 0.3 in image classification. Moreover, our method moves the time-consuming nearest neighbor queries to the offline training stage, in order to achieve a real-time response in the testing stage of extracting semantic embeddings from GPS coordinates.

TABLE III: Comparison with the state-of-the-art location-aware image classification approaches.

Method	Classifier	mAP
Visual	visual	0.234
OneHot [4]	geo	0.066
HashTag [1]	geo	0.163
GPS2Vec$_{onehot}$	geo	0.130
GPS2Vec	geo	0.182
OneHot [4] + V	fusion	0.238
HashTag [1] + V	fusion	0.261
GPS2Vec$_{onehot}$ + V	fusion	0.277
GPS2Vec + V	fusion	<u>0.300</u>
Kleban *et al.* [16]	fusion	0.080
Qian *et al.* [8]	fusion	0.113
Li *et al.* [22]	fusion	0.251
Wang *et al.* [32]	fusion	0.236
Liao *et al.* [2]	fusion	**0.347**

TABLE IV: Mean average precision comparison per UTM zone on image classification based on GPS embedding, visual feature, and their fusion.

UTM Zones	30U	31U	18T	10S	32T
Visual	0.254	0.238	0.256	0.283	0.291
GPS2Vec	0.166	0.189	0.156	0.197	0.174
GPS2Vec + V	0.293	0.282	0.278	0.351	0.322

Next, we compare the average precision per UTM zone and per concept obtained by different classifiers trained with GPS semantic embedding (GPS2Vec), image visual feature (Visual), and their fusion (GPS2Vec+V). The results are illustrated in Table IV and Figure 9, respectively. We select the top five most popular UTM zones based on the number of testing images each zone contains. Some UTM zones contain areas of only one country (*e.g.*, 10S is within the United States), while others contain more than one (*e.g.*, 32T overlaps with multiple European countries including Italy, Switzerland, and France). By fusing our proposed GPS2Vec embeddings with image visual features, a consistent performance gain was observed among different UTM zones. Similarly in Figure 9, the fusion method achieves the best average precision with most of the concepts. The geo method outperformed the visual method in

1520-9210 (c) 2021 IEEE. Personal use is permitted, but republication/redistribution requires IEEE permission. See http://www.ieee.org/publications_standards/publications/rights/index.html for more information.
Authorized licensed use limited to: DELHI TECHNICAL UNIV. Downloaded on March 27,2021 at 09:52:40 UTC from IEEE Xplore. Restrictions apply.

This article has been accepted for publication in a future issue of this journal, but has not been fully edited. Content may change prior to final publication. Citation information: DOI 10.1109/TMM.2021.3060951, IEEE Transactions on Multimedia

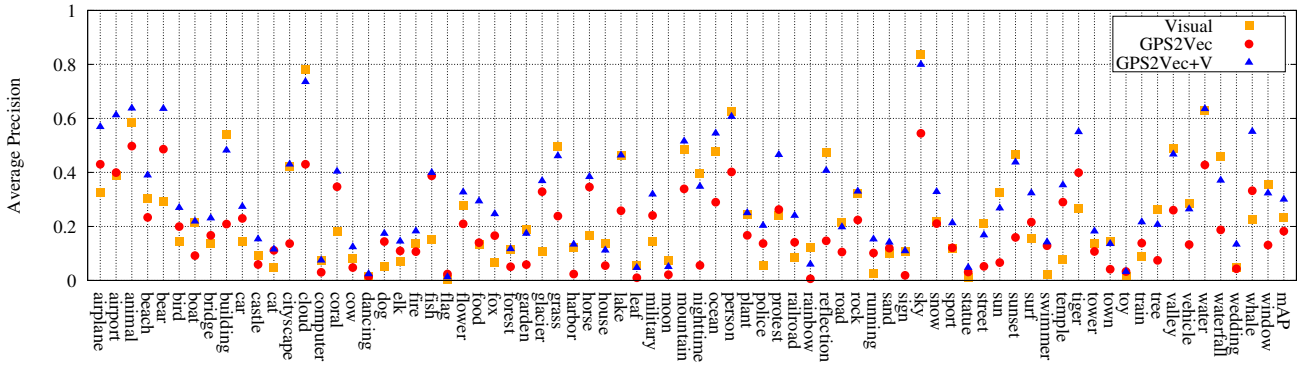

Fig. 9: The average precision comparison per concept on image classification based on GPS embedding, visual feature, and their fusion.

TABLE V: Comparison to the state-of-the-art next location prediction methods on the New York dataset.

Method	HR@1	HR@5	HR@10	HR@20	δ_d/m
NL	0.1630	0.2455	0.2998	0.4386	2903
MF [45]	0.1690	0.4326	0.5013	0.5358	1963
HMM [46]	0.1763	0.4298	0.5251	0.5518	1952
ST-RNN [40]	0.1942	0.4421	0.5381	0.6053	1602
SERM [17]	0.2535	0.4507	0.5433	0.6237	1457
HashTag + S	0.2575	0.4889	0.6036	**0.6861**	1253
GPS2Vec + S	**0.2716**	**0.5131**	**0.6097**	0.6841	**1193**

TABLE VI: Comparison to the state-of-the-art next location prediction methods on the Los Angeles dataset.

Method	HR@1	HR@5	HR@10	HR@20	δ_d/m
NL	0.3745	0.4516	0.4704	0.4911	6061
MF [45]	0.3646	0.5810	0.6354	0.6877	2647
HMM [46]	0.3921	0.5935	0.6331	0.6732	2521
ST-RNN [40]	0.4311	0.6013	0.6521	0.6980	2384
SERM [17]	0.4625	0.6265	0.6670	0.7026	2177
HashTag + S	0.4625	0.6343	0.6709	**0.7055**	2154
GPS2Vec + S	**0.4654**	**0.6344**	**0.6729**	0.7036	**2135**

concepts such as “coral,” “whale,” “surf,” and “temple,” that are sensitive to locations. For example, “coral,” “whale,” and “surf” can have a strong correlation with seas and oceans. On the other hand, the visual method outperforms the geo method in concepts such as “sun,” “cloud,” “sky,” “grass,” and “tree” that can be easily recognized based on their visual appearance.

C. Evaluation on Next Location Prediction

1) Experimental Setup: For next location prediction, we conducted experiments on two semantic trajectory datasets collected in two cities, namely New York City and Los Angeles. Records are segmented into semantic trajectories with a time gap constraint of $\Delta t = 10\ h$. Users with fewer than 50 records and trajectories with a length shorter than three are removed [17]. After data preprocessing, the New York dataset [47] consists of 3,103 trajectories from 235 users and the Los Angeles dataset [48] consists of 7,826 trajectories from 244 users. We apply softmax activation at the output layer, and choose categorical cross-entropy as the loss function. The two evaluation datasets are divided into 80%–20% splits for training and testing. Two metrics are adopted for method comparison: 1) the hit ratio at k, which examines whether the ground-truth location appears in the top-k predictions, and 2) the prediction error in the distance, which computes the minimum geographical distance from the ground-truth location to the top-5 predictions. We train the network architecture using stochastic mini-batch gradient descent based on back-propagation. The learning rate and mini-batch size were set to 0.001 and 200, respectively.

2) Performance Comparison: We compare our method to SERM, HashTag+S, and four other next location prediction methods. HashTag+S is a variation of our method GPS2Vec+S by using the HashTag context feature [1] instead of our proposed GPS2Vec feature. Here “S” refers to method SERM as we integrate the proposed GPS2Vec feature into the original SERM architecture. The results are reported in Tables V and VI, with the **best** results highlighted. The NL (Nearest Location) method chooses the nearest neighbor to the user’s current location as the prediction. We show it as a straightforward baseline method for comparison.

As can be seen, our method outperforms its competitors on both datasets. The MF method casts the location prediction as a recommendation problem without modeling the transition of the sequential input. The HMM method considers the sequential transition but it only models the first-order dependency of the semantic trajectories. Comparatively, RNN-based methods, ST-RNN and SERM, are capable of capturing long-term dependencies of people’s movements, and therefore turn out to be the strongest baseline methods. SERM outperforms ST-RNN as it captures the spatiotemporal dynamics by jointly learning the embeddings of location and time. Additionally, SERM leverages the textual information such as tweets in its modeling, while ST-RNN only focuses on the next location prediction for GPS trajectories without a user’s textual messages. Next, we compare GPS2Vec and HashTag features in the next location prediction. As Tables V and VI show, GPS2Vec+S outperforms HashTag+S on both datasets, which indicates that the GPS semantic embeddings generated by

1520-9210 (c) 2021 IEEE. Personal use is permitted, but republication/redistribution requires IEEE permission. See http://www.ieee.org/publications_standards/publications/rights/index.html for more information.
Authorized licensed use limited to: DELHI TECHNICAL UNIV. Downloaded on March 27,2021 at 09:52:40 UTC from IEEE Xplore. Restrictions apply.

This article has been accepted for publication in a future issue of this journal, but has not been fully edited. Content may change prior to final publication. Citation information: DOI 10.1109/TMM.2021.3060951, IEEE Transactions on Multimedia

our pre-trained models are more descriptive than the HashTag context features generated from the supplementary data.

By integrating the GPS semantic embeddings, our method improves the SERM method in the following two aspects. First, the vocabulary-based semantic feature extracted from GPS makes it possible to measure the high-level similarity between places, which is crucial for the next location prediction problem. For example, people tend to frequent similar venues due to personal preferences. This may be one of the reasons why our method obtained more significant improvements with the New York check-in dataset compared to the Los Angeles tweets dataset. Compared with tweets, locations of check-ins more likely correlate with the semantic similarities of places. Second, the SERM method encodes locations into one hot representations by discretizing the area of interest into 500 m $\times$ 500 m grid cells. Comparatively, our GPS encoding method is able to generate a more generalized and semantically-enriched representation that can be applied to locations anywhere in the world.

D. Parameter Tuning

We first study the impact of the grid size controlled by parameter m for the GPS initial encoding. As mentioned before, each UTM zone is divided into an $m \times m$ grid. Let m be $\{10, 20, 30\}$, respectively. We report the mean average precision on venue semantic labeling and image classification in Table VII with the **best** result highlighted in each row. The GPS2Vec method uses our GPS semantic embeddings as the only feature. The GPS2Vec+B method concatenates the GPS semantic embeddings and the base line features extracted from the check-in data, while the GPS2Vec+V method concatenates the GPS semantic embeddings and the image visual features to train a classifier. As Table VII shows, GPS2Vec obtains the best mean average precision with $m = 30$ on both venue semantic labeling and image classification. Generally speaking, the GPS semantic embeddings tend to be more descriptive with a smaller grid cell size, *i.e.*, larger m. This is because a grid with fine granularity has a better resolution to discriminate GPS coordinates that are located close to each other. However, with the number of grid cells increasing, the input size of the neural network will rise quadratically, leading to high computational costs and delay. On the other hand, GPS2Vec+B and GPS2Vec+V obtain competitive classification results with $m = 20$ and 30, which indicates that the GPS2Vec embeddings and the baseline/visual features are complementary to each other so that the influence of the grid cell size on the system effectiveness has been reduced. We consider that $m = 20$ can be a good trade-off, and use this as the optimal setting in the rest of the experiments.

Next, we study the impact of the attenuation coefficient in Eq. 1 on the classification results in venue semantic labeling and image classification. We set σ to 10 km, 20 km, and 30 km, respectively, and report the mean average precision in Table VIII with the **best** result highlighted in each row. As can be seen, all three methods obtain their best mean average precision with $\sigma = 20$ km. The calculation of the GPS initial encoding is parameterized together by m and σ. With a moderate-sized grid where $m = 20$, a small change in σ is unlikely to have a significant impact on the classification results. Therefore, we set σ to 20 km throughout the experiments.

The results shown indicate that our proposed method has the advantage of not being sensitive to the parameters m and σ within a large range. This is a good property as the parameters of our proposed method can be effectively tuned when being applied to different applications.

E. Ablation Analysis

1) Comparison of layers: We analyze the discriminative performance of each layer in our proposed neural network. In the previous experiments, we adopted the output of the softmax layer in our proposed neural network as the GPS semantic embedding. However, more generally, the output of intermediate layers can also be used as GPS semantic embeddings in downstream applications. We compare the GPS semantic embeddings extracted from different layers and report the mean average precision in Table IX. As illustrated in Figure 4, the feature dimensions extracted from fc1, fc2, fc3, and output layers are 512, 1,024, 2,048, and 2,000, respectively. For all three methods, the mean average precision increases when using features extracted from layers closer towards the output. Therefore, we adopt the features extracted from the output layer, which tend to encode more semantic information, as the GPS semantic embedding in our proposed framework.

2) Comparison of first-level grid: In our current work, we have adopted the UTM coordinate system as the first-level grid, due to its popularity and the ease of converting a latitude and longitude pair into a planar coordinate in meters. We now compare it to a density-based grid partitioning method using Google's S2 geometry library [25]. More specifically, starting at the root S2 cell, we recursively descend each quad-tree and subdivide cells until no cell contains more than 15,000 images. Subsequently, sparsely populated areas are covered by larger cells and densely populated areas are covered by finer cells. We further divide each cell into a 16×16 second-level grid[1] for the GPS initial encoding. The results are reported in Table X. Recall that m controls the granularity of the second-level grid. Therefore, $m = 16$ in Google's S2 cells causes a slight mAP decrease compared to $m = 20$ in UTM zones (please refer to Table VII). Google's S2 geometry has the advantage of partitioning the Earth's surface into fewer cells in a balanced way. However, the UTM grid can perform competitively well in terms of accuracy as long as the model capacity is sufficient to capture the data characteristics in each zone.

3) Comparison of training sample distribution: In the training phase of our proposed GPS2Vec method, we use the geotags of the images in the supplementary dataset as the training locations in each UTM zone. Table XI shows the comparison of our sampling strategy to a uniform sampling strategy where the training samples are evenly distributed in

[1]As Google's S2 follows a quadtree partitioning, a second-level grid of 16×16 is the closest to the one of 20×20 used in each UTM zone.

1520-9210 (c) 2021 IEEE. Personal use is permitted, but republication/redistribution requires IEEE permission. See http://www.ieee.org/publications_standards/publications/rights/index.html for more information.
Authorized licensed use limited to: DELHI TECHNICAL UNIV. Downloaded on March 27,2021 at 09:52:40 UTC from IEEE Xplore. Restrictions apply.

This article has been accepted for publication in a future issue of this journal, but has not been fully edited. Content may change prior to final publication. Citation information: DOI 10.1109/TMM.2021.3060951, IEEE Transactions on Multimedia

TABLE VII: Mean average precision comparison on venue semantic labeling and image classification based on GPS semantic embeddings generated with different grid sizes.

Task	Method	10×10	20×20	30×30
Venue Semantic Labeling	GPS2Vec	0.2349	0.2435	**0.2441**
	GPS2Vec+B	0.3399	**0.3435**	0.3431
Image Classification	GPS2Vec	0.1754	0.1824	**0.1853**
	GPS2Vec+V	0.2971	**0.2999**	0.2987

TABLE VIII: Mean average precision comparison on venue semantic labeling and image classification based on GPS semantic embeddings generated with different σ settings in Eq. 1.

Task	Method	10 km	20 km	30 km
Venue Semantic Labeling	GPS2Vec	0.2422	**0.2435**	0.2405
	GPS2Vec+B	0.3408	**0.3435**	0.3415
Image Classification	GPS2Vec	0.1779	**0.1824**	0.1747
	GPS2Vec+V	0.2947	**0.2999**	0.2986

TABLE IX: Mean average precision comparison of extracting GPS embeddings at different layers on venue semantic labeling and image classification.

Task	Method	fc1	fc2	fc3	output
Venue Semantic Labeling	GPS2Vec	0.2319	0.2332	0.2409	**0.2435**
	GPS2Vec+B	0.3336	0.3341	0.3397	**0.3435**
Image Classification	GPS2Vec	0.1708	0.1718	0.1762	**0.1824**
	GPS2Vec+V	0.2853	0.2950	0.2960	**0.2999**

TABLE X: GPS2Vec mAP comparison of first-level grid choices: UTM zones vs. Google's S2 cells.

Task	UTM	Google's S2
Venue Semantic Labeling	0.243	0.238
Image Classification	0.182	0.179

TABLE XI: GPS2Vec mAP comparison of training sample distribution: data-driven vs. uniform.

Task	data-driven	uniform
Venue Semantic Labeling	0.243	0.229
Image Classification	0.182	0.149

TABLE XII: GPS2Vec mAP comparison of distance metric: Euclidean vs. Haversine.

Task	Euclidean	Haversine
Venue Semantic Labeling	0.243	0.243
Image Classification	0.182	0.185

TABLE XIII: GPS2Vec mAP comparison of supervision: supervised vs. unsupervised.

Task	supervised	unsupervised
Venue Semantic Labeling	0.243	0.247
Image Classification	0.182	0.161

each UTM zone[2]. As can be seen, our data-driven sampling outperforms the uniform sampling by a significant margin. The vocabulary-based semantic features generated at geotag locations can be more accurate as they are directly associated with user tags. Moreover, the image distribution in the supplementary dataset tends to be consistent with the distribution of the testing images. Thus, an improved mAP can be obtained by paying more attention to densely populated areas.

4) Comparison of distance metric: We use the Euclidean distance in this work as the UTM coordinate system naturally converts a latitude and longitude pair into a planar coordinate in meters. Table XII shows the mAP comparison by using the alternative Haversian distance. On one hand, the calculation of the Euclidean distance is more efficient. On the other hand, the Haversian distance is more accurate when computing the distance between two geo-coordinates on the spherical Earth's surface. Moreover, the Euclidean distance can only be used within UTM zones, while the Haversian distance should be adopted together with other projection models such as the Google's S2 cells.

[2]The training locations are obtained by dividing each UTM zone into 1000×1000 cells.

5) Comparison of supervision: Finally, we compare our proposed supervised method with existing unsupervised geotag encoding approaches. For example, the vocabulary-based semantic feature introduced in Section III-B can be used directly as an unsupervised geotag encoding approach. The advantages of the supervised method are twofold. First, unsupervised methods require access to the supplementary dataset during inference, leading to potential computational costs and processing delays. Second, as Table XIII shows, the supervised method outperforms the unsupervised method as the latter requires hand-crafted features that are sensitive to data noise. Comparatively, our supervised method generates learnt features that are more smooth and robust to data noise.

VI. Conclusions and Future Work

We have presented a novel framework, GPS2Vec, to learn GPS semantic embeddings in support of location-aware applications. The generated semantic embeddings can be easily integrated with existing high dimensional descriptors, *e.g.*, image visual features, by early fusion, based on which a new classifier can be trained to obtain more robust predictions. To divide the Earth's surface into smaller areas of manageable scale, we adopt the UTM coordinate system and train a neural

1520-9210 (c) 2021 IEEE. Personal use is permitted, but republication/redistribution requires IEEE permission. See http://www.ieee.org/publications_standards/publications/rights/index.html for more information.
Authorized licensed use limited to: DELHI TECHNICAL UNIV. Downloaded on March 27,2021 at 09:52:40 UTC from IEEE Xplore. Restrictions apply.

This article has been accepted for publication in a future issue of this journal, but has not been fully edited. Content may change prior to final publication. Citation information: DOI 10.1109/TMM.2021.3060951, IEEE Transactions on Multimedia

network for each UTM zone to generate location semantic embeddings. We have conducted extensive experiments using tweets, check-ins, and images with three location-aware applications. Our generated GPS semantic embeddings are complementary to the textual and visual features in existing systems. The location-aware applications demonstrate the effective use of our proposed GPS semantic embeddings in both CNN- and RNN-based systems. In the future, we plan to increase the data scale by utilizing different types of data sources for vocabulary construction and semantic embeddings learning. If the accuracy level of a geotag is available, it is also possible to filter out noisy samples to generate more accurate semantic features for GPS coordinates.

ACKNOWLEDGMENT

This research is supported by Singapore Ministry of Education Academic Research Fund Tier 2 under MOE's official grant number MOE2018-T2-1-103.

REFERENCES

[1] K. Tang, M. Paluri, L. Fei-Fei, R. Fergus, and L. Bourdev, "Improving Image Classification with Location Context," in *IEEE International Conference on Computer Vision*, 2015, pp. 1008–1016.

[2] S. Liao, X. Li, H. T. Shen, Y. Yang, and X. Du, "Tag Features for Geo-Aware Image Classification," *IEEE Transactions on Multimedia*, vol. 17, no. 7, pp. 1058–1067, 2015.

[3] Y. Zhang and R. Zimmermann, "Efficient Summarization From Multiple Georeferenced User-Generated Videos," *IEEE Transactions on Multimedia*, vol. 18, no. 3, pp. 418–431, 2016.

[4] G. Christie, N. Fendley, J. Wilson, and R. Mukherjee, "Functional Map of the World," in *IEEE Conference on Computer Vision and Pattern Recognition*, 2018.

[5] D. Joshi and J. Luo, "Inferring Generic Activities and Events from Image Content and Bags of Geo-tags," in *International Conference on Content-based Image and Video Retrieval*, 2008, pp. 37–46.

[6] GeoNames, http://www.geonames.org/.

[7] M. Dolatshah, A. Hadian, and B. Minaei-Bidgoli, "Ball*-tree: Efficient Spatial Indexing for Constrained Nearest-Neighbor Search in Metric Spaces," *arXiv preprint arXiv:1511.00628*, 2015.

[8] X. Qian, X. Liu, C. Zheng, Y. Du, and X. Hou, "Tagging Photos Using Users' Vocabularies," *Neurocomputing*, pp. 144–153, 2013.

[9] A. Zubiaga, A. Voss, R. Procter, M. Liakata, B. Wang, and A. Tsakalidis, "Towards Real-Time, Country-Level Location Classification of Worldwide Tweets," *IEEE Transactions on Knowledge and Data Engineering*, vol. 29, no. 9, pp. 2053–2066, 2017.

[10] Y. Zheng, M. Zhao, Y. Song, H. Adam, U. Buddemeier, A. Bissacco, F. Brucher, T.-S. Chua, and H. Neven, "Tour the World: Building a Web-scale Landmark Recognition Engine," in *IEEE Conference on Computer Vision and Pattern Recognition*, 2009, pp. 1085–1092.

[11] Y. Yin, B. Seo, and R. Zimmermann, "Content vs. Context: Visual and Geographic Information Use in Video Landmark Retrieval," *ACM Transactions on Multimedia Computing, Communications, and Applications*, vol. 11, no. 3, pp. 39:1–39:21, 2015.

[12] Y. Yin, Z. Liu, and R. Zimmermann, "Geographic Information Use in Weakly-supervised Deep Learning for Landmark Recognition," in *IEEE International Conference on Multimedia and Expo*, 2017, pp. 1015–1020.

[13] M. Ye, D. Shou, W.-C. Lee, P. Yin, and K. Janowicz, "On the Semantic Annotation of Places in Location-based Social Networks," in *ACM International Conference on Knowledge Discovery and Data Mining*, 2011, pp. 520–528.

[14] J. Krumm and D. Rouhana, "Placer: Semantic Place Labels from Diary Data," in *ACM International Joint Conference on Pervasive and Ubiquitous Computing*, 2013, pp. 163–172.

[15] E. Moxley, J. Kleban, and B. Manjunath, "SpiritTagger: A Geo-Aware Tag Suggestion Tool Mined from Flickr," in *ACM International Conference on Multimedia Information Retrieval*, 2008, pp. 24–30.

[16] J. Kleban, E. Moxley, J. Xu, and B. S. Manjunath, "Global Annotation on Georeferenced Photographs," in *ACM International Conference on Image and Video Retrieval*, 2009, pp. 12:1–12:8.

[17] D. Yao, C. Zhang, J. Huang, and J. Bi, "SERM: A Recurrent Model for Next Location Prediction in Semantic Trajectories," in *ACM International Conference on Information and Knowledge Management*, 2017, pp. 2411–2414.

[18] B. Yan, K. Janowicz, G. Mai, and S. Gao, "From ITDL to Place2Vec: Reasoning About Place Type Similarity and Relatedness by Learning Embeddings From Augmented Spatial Contexts," in *ACM SIGSPATIAL International Conference on Advances in Geographic Information Systems*, 2017, pp. 35:1–35:10.

[19] Google Maps, https://maps.google.com/.

[20] American Community Survey, http://www.census.gov/acs/www/.

[21] V. Spruyt, "Loc2Vec: Learning Location Embeddings with Triplet-loss Networks," https://www.sentiance.com/2018/05/03/loc2vec-learning-location-embeddings-w-triplet-loss-networks/, 2018.

[22] X. Li, C. G. M. Snoek, M. Worring, and A. W. M. Smeulders, "Fusing Concept Detection and Geo Context for Visual Search," in *ACM International Conference on Multimedia Retrieval*, 2012, pp. 4:1–4:8.

[23] H. Mousselly-Sergieh, D. Watzinger, B. Huber, M. Döller, E. Egyed-Zsigmond, and H. Kosch, "World-wide Scale Geotagged Image Dataset for Automatic Image Annotation and Reverse Geotagging," in *ACM Multimedia Systems Conference*, 2014, pp. 47–52.

[24] S. Workman, R. Souvenir, and N. Jacobs, "Wide-area Image Geolocalization with Aerial Reference Imagery," in *ICCV*, 2015, pp. 3961–3969.

[25] T. Weyand, I. Kostrikov, and J. Philbin, "Planet-photo Geolocation with Convolutional Neural Networks," in *ECCV*, 2016, pp. 37–55.

[26] T. Salem, S. Workman, and N. Jacobs, "Learning a Dynamic Map of Visual Appearance," in *CVPR*, 2020, pp. 12 435–12 444.

[27] R. R. Shah, Y. Yu, A. Verma, S. Tang, A. D. Shaikh, and R. Zimmermann, "Leveraging Multimodal Information for Event Summarization and Concept-level Sentiment Analysis," *Knowledge-Based Systems*, vol. 108, no. C, pp. 102–109, 2016.

[28] T. Y. Lin, A. RoyChowdhury, and S. Maji, "Bilinear CNN Models for Fine-Grained Visual Recognition," in *IEEE International Conference on Computer Vision*, 2015, pp. 1449–1457.

[29] E. Park, X. Han, T. L. Berg, and A. C. Berg, "Combining Multiple Sources of Knowledge in Deep CNNs for Action Recognition," in *IEEE Winter Conference on Applications of Computer Vision*, 2016, pp. 1–8.

[30] Y. Yin, Z. Liu, Y. Zhang, S. Wang, R. R. Shah, and R. Zimmermann, "GPS2Vec: Towards Generating Worldwide GPS Embeddings," in *ACM SIGSPATIAL International Conference on Advances in Geographic Information Systems*, 2019, pp. 416—-419.

[31] W. Dongfang, P. Baojun, X. Weike, and P. Keke, "GEO Objects Spatial Density and Collision Probability in the Earth-centered Earth-fixed (ECEF) Coordinate System," *Acta Astronautica*, vol. 118, pp. 218–223, 2016.

[32] G. Wang, D. Hoiem, and D. Forsyth, "Building Text Features for Object Image Classification," in *IEEE Conference on Computer Vision and Pattern Recognition*, 2009, pp. 1367–1374.

[33] C. Keßler, K. Janowicz, and M. Bishr, "An Agenda for the Next Generation Gazetteer: Geographic Information Contribution and Retrieval," in *ACM SIGSPATIAL International Conference on Advances in Geographic Information Systems*, 2009, pp. 91–100.

[34] H. Wang, M. Terrovitis, and N. Mamoulis, "Location Recommendation in Location-based Social Networks Using User Check-in Data," in *ACM SIGSPATIAL International Conference on Advances in Geographic Information Systems*, 2013, pp. 374–383.

[35] N. Dalal and B. Triggs, "Histograms of Oriented Gradients for Human Detection," in *IEEE Computer Society Conference on Computer Vision and Pattern Recognition*, 2005, pp. 886–893.

[36] D. G. Lowe, "Distinctive Image Features from Scale-Invariant Keypoints," *International Journal of Computer Vision*, vol. 60, no. 2, pp. 91–110, 2004.

[37] K. Simonyan and A. Zisserman, "Very Deep Convolutional Networks for Large-Scale Image Recognition," *CoRR*, vol. abs/1409.1556, 2014.

[38] B. Zhou, A. Lapedriza, A. Khosla, A. Oliva, and A. Torralba, "Places: A 10 Million Image Database for Scene Recognition," *IEEE Transactions on Pattern Analysis and Machine Intelligence*, vol. 40, no. 6, pp. 1452–1464, 2018.

[39] S. Maji, A. C. Berg, and J. Malik, "Classification using Intersection Kernel Support Vector Machines is Efficient," in *IEEE Conference on Computer Vision and Pattern Recognition*, 2008, pp. 1–8.

[40] Q. Liu, S. Wu, L. Wang, and T. Tan, "Predicting the Next Location: A Recurrent Model with Spatial and Temporal Contexts," in *AAAI Conference on Artificial Intelligence*, 2016, pp. 194–200.

[41] D. Yang, D. Zhang, L. Chen, and B. Qu, "NationTelescope: Monitoring and Visualizing Large-scale Collective Behavior in LBSNs," *Journal of Network and Computer Applications*, vol. 55, pp. 170–180, 2015.

1520-9210 (c) 2021 IEEE. Personal use is permitted, but republication/redistribution requires IEEE permission. See http://www.ieee.org/publications_standards/publications/rights/index.html for more information.
Authorized licensed use limited to: DELHI TECHNICAL UNIV. Downloaded on March 27,2021 at 09:52:40 UTC from IEEE Xplore. Restrictions apply.

This article has been accepted for publication in a future issue of this journal, but has not been fully edited. Content may change prior to final publication. Citation information: DOI 10.1109/TMM.2021.3060951, IEEE Transactions on Multimedia

[42] D. Yang, D. Zhang, and B. Qu, "Participatory Cultural Mapping based on Collective Behavior in Location based Social Networks," *ACM Transactions on Intelligent Systems and Technology*, vol. 7, no. 3, pp. 30:1–30:23, 2016.
[43] X. Wu and Z. Zhou, "A Unified View of Multi-Label Performance Measures," in *International Conference on Machine Learning*, 2017, pp. 3780–3788.
[44] T.-S. Chua, J. Tang, R. Hong, H. Li, Z. Luo, and Y. Zheng, "NUS-WIDE: A Real-world Web Image Database from National University of Singapore," in *ACM International Conference on Image and Video Retrieval*, 2009, pp. 48:1–48:9.
[45] N. Duong-Trung, N. Schilling, and L. Schmidt-Thieme, "Near Real-time Geolocation Prediction in Twitter Streams via Matrix Factorization Based Regression," in *ACM International on Conference on Information and Knowledge Management*, 2016, pp. 1973–1976.
[46] W. Mathew, R. Raposo, and B. Martins, "Predicting Future Locations with Hidden Markov Models," in *ACM Conference on Ubiquitous Computing*, 2012, pp. 911–918.
[47] C. Zhang, J. Han, L. Shou, J. Lu, and T. La Porta, "Splitter: Mining Fine-grained Sequential Patterns in Semantic Trajectories," *Proceedings of the VLDB Endowment*, vol. 7, no. 9, pp. 769–780, 2014.
[48] C. Zhang, K. Zhang, Q. Yuan, L. Zhang, T. Hanratty, and J. Han, "GMove: Group-Level Mobility Modeling Using Geo-Tagged Social Media," in *ACM SIGKDD International Conference on Knowledge Discovery and Data Mining*, 2016, pp. 1305–1314.

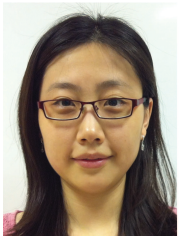

Yifang Yin received the B.E. degree from the Department of Computer Science and Technology, Northeastern University, Shenyang, China, in 2011, and received the Ph.D. degree from the National University of Singapore, Singapore, in 2016. She is currently a senior research fellow with the Grab-NUS AI Lab at the National University of Singapore. She worked as a Research Intern at the Incubation Center, Research and Technology Group, Fuji Xerox Co., Ltd., Japan, from October, 2014 to March, 2015. Her research interests include machine learning, spatiotemporal data mining, and multimodal analysis in multimedia.

Ying Zhang received the B.E. degree in computer science from Northwestern Polytechnical University, Xi'an, China, in 2009, and the Ph.D. degree in computer science from the National University of Singapore, in 2014. She was a Senior Research Fellow with NUS from 2019-2021. Before that, she was the Head of Data Security Unit and Research Scientist with the department of Cyber Security & Intelligence, Institute for Infocomm Research (I2R), A*STAR, Singapore. Her research interests include machine learning, image and video processing, multimedia.

Zhenguang Liu is currently with Zhejiang Gongshang University. He was a research fellow in National University of Singapore and Singapopre Agency for Science, Technology and Research (A* STAR) from 2015 to 2018. He respectively received his Ph.D. and B.E. degrees from Zhejiang University and Shandong University, China, in 2010 and 2015. His research interests include multimedia data analysis, deep learning, and blockchain. Various parts of his work have been published in first-tier venues including TKDE, CVPR, AAAI, ACM MM, TMM, TOMM. Dr. Liu has served as technical program committee member for conferences such as ACM MM and MMM, and a reviewer for IEEE Transactions on visualization and computer graphics, ACM Transactions on Multimedia Computing, Communications, and Applications (TOMM), Multimedia Tools and Applications, Sensors, etc.

Sheng Wang received the B.E. degree from the Department of Computer Science and Technology, Harbin Institute of Technology, Harbin, China, in 2011, and the Ph.D. degree in Computer Science from National University of Singapore in 2016. He is currently a Research Scientist in Database and Storage Lab, DAMO Academy, Alibaba Group. His research interests are mainly in large-scale data management and processing, including OLTP/OLAP/NoSQL database engines, distributed systems, cloud data security, and machine learning platforms.

Rajiv Ratn Shah currently works as an Assistant Professor in the Department of Computer Science and Engineering (joint appointment with the Department of Human-centered Design) at IIIT-Delhi. He received his Ph.D. in computer science from the National University of Singapore, Singapore. Before joining IIIT-Delhi, he worked as a Research Fellow in Living Analytics Research Center (LARC) at the Singapore Management University, Singapore. Prior to completing his Ph.D., he received his M.Tech. and M.C.A. degrees in Computer Applications from the Delhi Technological University, Delhi and Jawaharlal Nehru University, Delhi, respectively. He has also received his B.Sc. in Mathematics (Honors) from the Banaras Hindu University, Varanasi. Dr. Shah is involved in organizing and reviewing of many top-tier international conferences and journals. His research interests include multimedia content processing, natural language processing, image processing, speech processing, multimodal computing, data science, and social media computing.

1520-9210 (c) 2021 IEEE. Personal use is permitted, but republication/redistribution requires IEEE permission. See http://www.ieee.org/publications_standards/publications/rights/index.html for more information.
Authorized licensed use limited to: DELHI TECHNICAL UNIV. Downloaded on March 27,2021 at 09:52:40 UTC from IEEE Xplore. Restrictions apply.

This article has been accepted for publication in a future issue of this journal, but has not been fully edited. Content may change prior to final publication. Citation information: DOI 10.1109/TMM.2021.3060951, IEEE Transactions on Multimedia

Roger Zimmermann (M'93–SM'07) received his M.S. and Ph.D. degrees from the University of Southern California (USC) in 1994 and 1998, respectively. He is currently an Associate Professor with the Department of Computer Science at the National University of Singapore (NUS), Singapore. He is also a Deputy Director with the Smart Systems Institute (SSI), and previously co-directed the Centre of Social Media Innovations for Communities at NUS. He has coauthored a book, seven patents, and more than 250 conference publications, journal articles, and book chapters. His research interests include streaming media architectures, distributed systems, mobile and geo-referenced video management, applications of machine/deep learning, and spatial data management. He is an associate editor for IEEE MultiMedia, ACM Transactions on Multimedia Computing, Communications, and Applications (TOMM), Springer Multimedia Tools and Applications (MTAP), and IEEE Open Journal of the Communications Society (OJ-COMS). He is a distinguished member of the ACM and a senior member of the IEEE. Further information can be found at http://www.comp.nus.edu.sg/ rogerz/.

1520-9210 (c) 2021 IEEE. Personal use is permitted, but republication/redistribution requires IEEE permission. See http://www.ieee.org/publications_standards/publications/rights/index.html for more information.
Authorized licensed use limited to: DELHI TECHNICAL UNIV. Downloaded on March 27,2021 at 09:52:40 UTC from IEEE Xplore. Restrictions apply.

Materials Today: Proceedings xxx (xxxx) xxx

Contents lists available at ScienceDirect

Materials Today: Proceedings

journal homepage: www.elsevier.com/locate/matpr

Heat sink analysis in jet impingement with air foil pillars and nanoparticles

Deepak Kumar *, Mohammad Zunaid, Samsher Gautam

Dept of Mechanical Engineering, Delhi Technological University, Delhi 110042, India

ARTICLE INFO

Article history:
Received 24 December 2020
Received in revised form 9 January 2021
Accepted 19 January 2021
Available online xxxx

Keywords:
Nanoparticles
CFD
Pure water
Airfoil
Nusselt number
Jet

ABSTRACT

In the current research differentiating study has been carried out in case of impingement of jet in a heat sink. Heat sink is combined with airfoil pillars to augment the rate of heat transfer. So the effect of HDR and Nano fluid is executed for temperature rise, heat exchange coefficient, Nusselt number. Cuo Nano particles are used with 1% concentration for the investigation. Comparative analysis has been done for the case of water and Nano fluid. The analysis has been performed using CFD. The model with pillars has been validated with the available literature. From the results minimum 14% reduction in the temperature is detected for HDR with Nano fluid. Also in differentiation with water minimum 10% reduction is noticed.

© 2021 Elsevier Ltd. All rights reserved.

Selection and peer-review under responsibility of the scientific committee of the International Conference on Technological Advancements in Materials Science and Manufacturing.

1. Introduction

Shah, A. et al. [1] discussed the abstraction of blower unit with the application of impinging. Numerical study was performed for the characterization. Discussion was made for the distinct configurations of fin. The thickness of the support of the sink was varied. Distinct three values for flow rate of air were selected. Aim was focused on the excellent design of sink so that the probability for the enhancement in the heat transfer can be run. The focus was achieving the same without increasing the pressure drop significantly. The two cases were compared. In the first case material was removed from the fin near the center of the sink. In the other case material was retained. In the material cutting case lower value of fall in pressure was spotted. Chiang, K. [2] considered the various parameters of PPF used in the heat sink with the application of convection for the heat transfer improvement. The aim was to adopt the criterion of extended surfaces. Design was based on RSM. Performance was studied in terms of resistance of thermal and drop in pressure. Experimental set was used to explore the design variables. Two factors fin height and distance between the fins found to be affecting the effectiveness. Zheng, L. et al. [3] executed numerical study for the two different micro channels with lumps. The outcome of size of the lump, Re and the lump arrangements was concentrated. In the first case microchannel with circular configuration was taken and in the second case annular configuration was assessed. The first case with lump exhibited deficient capability of heat transfer. With the increase in the lump size in oriented lump, the performance increased. Unacceptable performance was characterized in staggered lump. Outer lump was found to give satisfactory results in differentiation to the inner one. The positioning did not find to affect the performance level. In terms of saving of power lump cases were found superior in comparison to the without lump case. Bahaidarah, H. [4] examined the PV system with impingent of jet in the two cases; PV system which was not cooled and cooling with impingement. The analysis was spotted in the warmer weather conditions. Six models of different characteristics were associated to determine the overall accomplishments of the system. The study was performed numerically as well as experimentally. The two exhibited sincere concurrence with each other. For the set conditions up to a certain value of h, performance increases but after this value no significant improvement was detected. The study was also concentrated for different months of a year. Maximum temperature in two different months were 342 K and 320 K for the uncooled case. Li, Y. et al. [5] used both numerical and experimental methods in case of AFPF sink.

Abbreviations: HDR, Height Diameter Ratio; NFL, Nano fluid; PDR, Pitch Diameter Ratio; PP, Pumping Power; TDP, Total drop in Pressure; h, Heat exchange coefficient; Nu, Nusselt Number.

* Corresponding author.
E-mail address: deepak209476@gmail.com (D. Kumar).

https://doi.org/10.1016/j.matpr.2021.01.582
2214-7853/© 2021 Elsevier Ltd. All rights reserved.
Selection and peer-review under responsibility of the scientific committee of the International Conference on Technological Advancements in Materials Science and Manufacturing.

Please cite this article as: D. Kumar, M. Zunaid and S. Gautam, **Heat sink analysis in jet impingement with air foil pillars and nanoparticles**, Materials Today: Proceedings, https://doi.org/10.1016/j.matpr.2021.01.582

The influence of porosity and density of pore was studied. Square cross section was taken for the channel geometry. The investigation was carried out under steady state conditions. The two sinks AF and AFPF were compared and AFPF was found better as compared to the other one. With increase in the pore density, the heat transfer increases in both the cases. The model was concurred with the experimental values in case of temperature and resistance. AFPF demonstrated better efficiency as compared to AF in terms of convection coefficient. Permeability effects were also taken into account. Izadi, A. et al. [6] conducted numerical study to examine the heat and fluid characteristics of Nano fluids in a sink with foam of metal. The equations were used for the fully developed conditions. Magnetic force influence was also studied. The consequences of different parameters which were used in non-dimensional form was observed on the fluid and thermal attributes. Augmentation in concentration of Nano particles resulted in increase in transfer of heat. CFD approach was not adopted here. Neyestani, M. et al. [7] intended the novel sink of porous nature for analysis using Nano fluids experimentally. CPU unit was adopted for the experimental investigation. The consequences of volume fractions were studied on the efficiency of CPU unit. Three configuration of sink were used. One of them was inline configuration. In this configuration thermal surge was not noticed much. The second configuration for the heat sink was staggered in which heat transportation rate was noticed to be more in comparison with inline. The third configuration was porous heat sink. In this configuration highest improvement was detected. Thirty-five percent decrement in temperature was detected using porous configuration over inline.

Chein, R., & Huang, G. [8] executed the Nano fluid consequences on the effectiveness of sink with micro channel of silicon. Water - copper was used as coolant. One phase fluid based study was undertaken. Relations based on the experimental work were discussed. Two different geometries of microchannel sink were compared in the investigation. Nano fluid consequences on the performance were noticed in the positive form. Ziaedin Miry, S. et al. [9] executed water aluminum oxide based study in a novel heat sink for the performance advancement. Elliptical section of the heat sink was proposed as a novelty in the study. Relative analysis was discussed for the cylindrical and elliptical sections. Positive pattern was seen in between concentration of Nano particles and convection coefficient. Negative pattern was detected for the resistance and rate of flow. The base temperature and the concentration relation was found in the reverse trend. Due to the density drop in pressure and Nano fluid fraction were detected in a positive trend. Fall in pressure was very insignificant for very small values of the rate of flow. Lelea, D., & Laza, I. [10] executed numerical analysis in thermal sink with micro channel with the application of swirl flow and water- aluminum oxide in different concentrations as coolant. The outcome was compared with the simple water case. K and μ were higher in case of Nano fluid but c was lower as compared to water. Multiple inlets in sink were used for the exploration of the study. The highest temperature of the surfaces was noticed better with Nano fluid for a constant value of Reynolds number. Selvakumar, P., & Suresh, S. [11] executed experimental study for 0.1 and 0.2% volumetric concentration of copper oxide – water Nano fluid in a copper heat sink. With the application of Nano fluid surge in convection coefficient was observed for different concentrations. Almost thirty percent increment was noticed for 0.2% concentration. Also surge in pumping power was detected using Nano fluid. The increase was almost fifteen percent. Ho, C. J. et al. [12] carried out experimental analysis for the decadence of heat in case of a heat sink with mini channel using water and alumina for divergent Nano particles fraction. The outcome of variables like Re, mean temperature and Nano particles was interpreted on the Nusselt number and friction. From the results it was interpreted that for Re = 483 and 968, negligible effect was thee on the friction factor in relation to entry temperature of Nano fluid. However, Re = 161, inverse shift established between the two variables. Higher temperature of the fluid decreased the Nusselt number. Izadi, A. et al. [13] exhibited analytical inspection for the application of magnetic field with anno fluid. The same was done in case of a CPU considering viscosity effects. The base of the CPU was modelled as hot surface with jets at the top and Nano fluid passed through foam. The analytical outcomes were justified with experiment. The end results of the various parameters like Re, Da, Ec, Ha and porosity were analyzed in correlation with the thermal and fluid behavior. The first step in the analysis was to convert initial PDE into nonlinear ODE and solving these ODE for the solution. Positive correlation was detected for Da and h. Wang, R. et al. [14] used grooves of trapezoidal shape arranged in a series in MCHS with water aluminum oxide as Nano fluid. The aim was to increase the efficiency with increasing PV systems. From the results two phase model was preferred over single phase model. Optimization for the geometrical variables was explored. Same was adopted for the physical parameters. The study was performed using numerical simulations for different Reynolds number. Temperature. Flow and viscosity correlations of Nano fluids were discussed. Thermal performance was noted in positive correlation with Re and fractional volume.

Selimefendigil, F., & Öztop, H. F. [15] examined a surface which was curved party using GWRFEM and COBYLA with impinging jets. Isothermal conditions were adopted for the surface udder study. Curved effects were noted to be significant at higher value of Re. Higher Nusselt number was saved for the curved shape. Also linear correlation was detected between Nusselt number and Nano fluid fraction. Vortices were found at the jet inlet. Ali, H. M., & Arshad, W. [16] executed experimental study in case of channel heat sink with different angles of channel as 22.5°, 45° and 90°. The reference for these angles was taken as $\times$ direction. The study was done for water-GNP Nano fluids at constant value of heat per unit area. Copper was taken as the material for the sink. In case of 22.5^0 resistance was low and hence highest performance was noticed. As the angle decreased, h increased. LMTD decreased with increase in rate of flow. Sun, B., Qu, Y., & Yang, D. [17] used copper water Nano fluid which was prepared experimentally. Positive correlation detected between fraction and heat dissipation performance. At a height of 0.006 m influence was maximum. Pressure drop was not significant. Circular shape was found more effective as compared to the square for the nozzle. Angle of jet was positive effect on the performance. Nakharintr, L. et al. [18] presented the characteristics using titanium oxide Nano fluids using impinging jet. Heat sink was made from aluminum. Experimental study was undertaken to note the trend of Nusselt number, resistance and pressure fall with the use of Nano fluid. Nusselt number and fractions were found in the increasing trend. Azizi, Z. et al. [19] examined the thermal sink with micro channel of cylindrical shape. At 0.3% of fraction results were noticed higher in terms of h. Maximum twenty-three percent increase in the Nusselt was initiated. Wang, R.-T., & Wang, J.-C. [20] prepared the aluminium oxide Nano fluid. Concentration influenced the efficiency.

The objective of this study is to increase the rate of heat transfer with the use of combination of technologies like impingement of jet, use of airfoil pillars and Nano fluid in a heat sink.

2. Geometrical layout

The model under examination has been shown in the Fig. 1. The model has been used with jet impingement with air foil shaped pillars. The model has been used in both the cases for water and NFL for differentiating study. Also the HDR of the model has been altered to examine the end results.

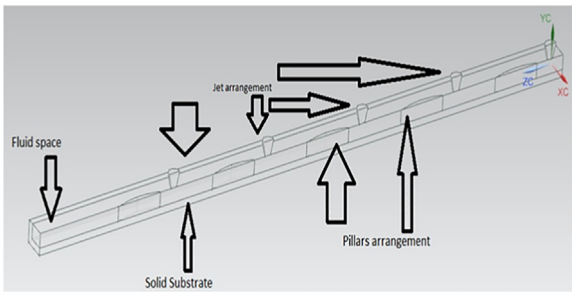

Fig. 1. Geometry.

3. Results & discussion

Computational fluid dynamics has been used as a tool for the analysis. The observations have been compared with available experimental results. The two have been found in good concurrence. With the use of pillars and Nano fluid performance improvement has been detected in the form of temperature, heat exchange coefficient.

Fig. 2 indicates the revision in the temperature of substrate with change in the HDR (1, 2, 3 and 4) for PDR = 6, 8, 10 and 12 in case of water and NFL with 1% concentration. From the Fig. 2 it is clear that at PDR = 8 for NFL temperature rise is marked as 48.19 K, analogous to HDR = 1. For the similar conditions for the water, it is marked as 75.19 K. At HDR = 2, temperature is reduced to 27.7 K in case of NFL and 45.11 in case of pure water. At HDR = 3, temperature values are found to be 21.04 K and 36.3 K for NFL and water respectively in analogous to PDR = 8. At HDR = 4, the values are noted to be 31.25 K and 17.86 K for water and NFL respectively. So at PDR = 8, increase in HDR leads to decrease in temperature rise. For PDR = 10 and HDR = 1, temperature for NFL and water is noted to be 86.4 K and 55.02 K respectively. For HDR = 2,3 and 4 and PDR = 10, temperature is marked as 54.29 K, 39.6 K, 35.48 K for water and 30.39 K, 24.31 K, 21.15 K for NFL sequentially. Similarly, for PDR = 12, HDR = 1,2,3 and 4, the values are found to be in decreasing order. Fig. 3 intimates the relation between HDR and TDP for distinct values of PDR for water and NFL. At PDR = 8 and HDR = 1, TDP is marked as17813 Pa and 4166 Pa for NFL and water sequentially. Now as HDR is increased 2,3 and 4, TDP is also increased in both the cases with values 12826 Pa, 29683 Pa and 59020 Pa in case of water sequentially. At PDR = 10 and HDR = 1,2,3 and 4, TDP = 3553 Pa, 11489 Pa, 28173 Pa and 55565 Pa respectively for water and in case of NFL higher values of TDP is noted. As HDR is increased, TDP also gets increased, which

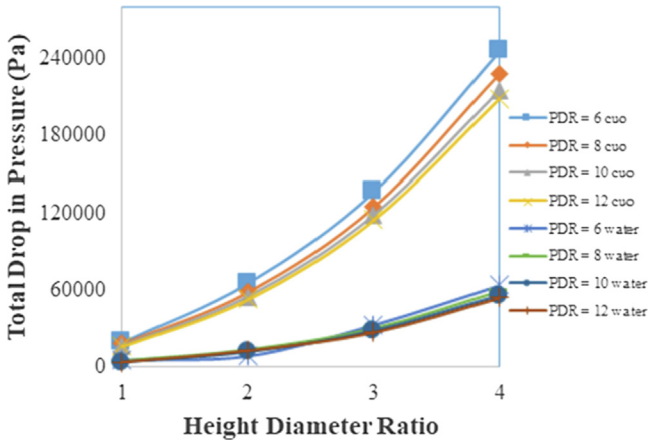

Fig. 3. TDP Vs HDR.

is not a desirable condition. So the model for HDR = 1gives optimum conditions both in case of water and NFL. The minimum values of TDP are 3508 Pa and 15844 Pa in water and NFL corresponding to HDR = 1 and PDR = 12. Fig. 4 intimates the connection between HDR and Coefficient of heat exchange (h) for distinct values of PDR in case of water and water- Cuo Nano fluid with 1% concentration. It is predicted from the Fig. 4 that with the use of NFL, h is increased in differentiation to pure water. At PDR = 8 and HDR = 1, h is marked as 13,299 for pure water and 20,751 for NFL. At HDR = 2, h is marked as 22,168 and 36,101 for water and NFL sequentially. At HDR = 3, h is noticed to be 27,548 for water and 47,528 for NFL analogous to PDR = 8. At HDR = 4, h is increased to 32,000 for pure water and 55,991 for NFL. For PDR = 10 and HDR = 4, h is found to be 28,184 and 47,281 for water and NFL. This indicates that h is detected to be more with NFL in contrast to pure water. For PDR = 12 the extreme value of h is detected to be 26,288 for water and 43,744 for NFL, which is analogous to HDR = 4. So with the augmentation in HDR, h is also augmented for a particular value of PDR. The lowest value of h is marked corresponding to PDR = 10 and HDR = 1.

In Fig. 5, connection between the HDR and Nusselt number has been executed for different values of PDR for pure water and NFL with 1% concentration. At PDR = 8 and HDR = 1, Nu = 13 for NFL and 8 for water which is lower than NFL. So the use of water – Cuo NFL with 1% concentration increased the value of Nu. At HDR = 2, Nu is marked as 11 and 3 for NFL and water sequentially. With the increase in the value of HDR, decreasing fashion is pre-

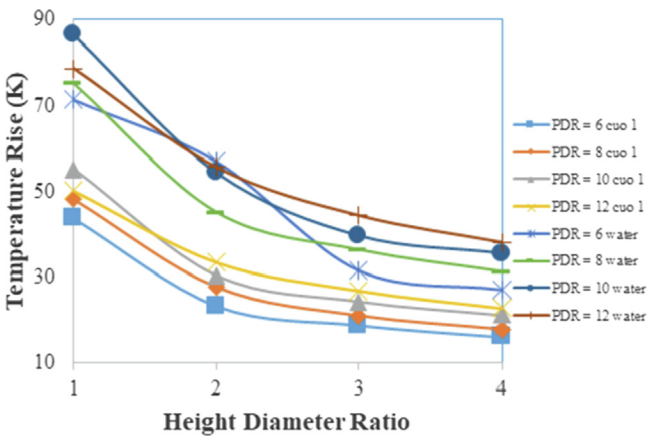

Fig. 2. Temperature rise Vs HDR.

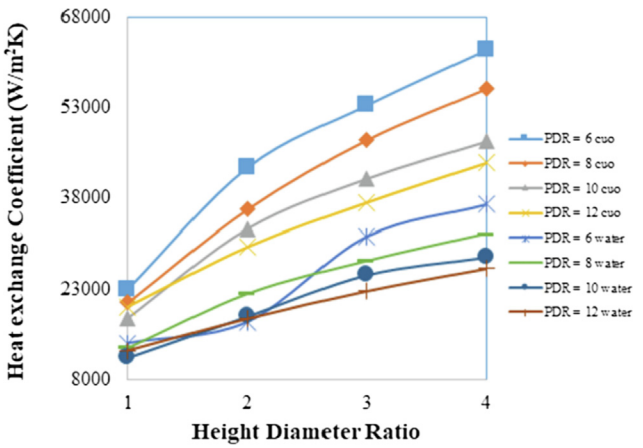

Fig. 4. h Rise Vs HDR.

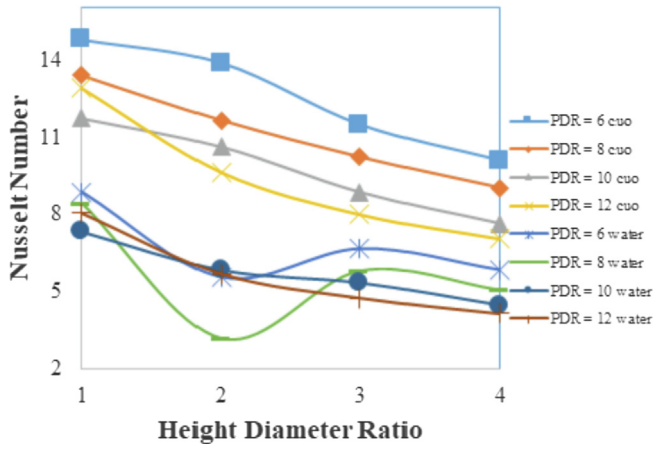

Fig. 5. Nu Rise Vs HDR.

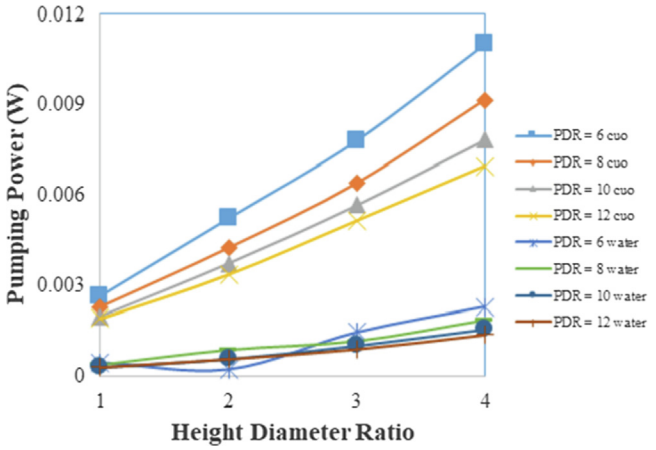

Fig. 7. PP Vs HDR.

dicted in the value of Nu both for water and NFL. The extreme value of Nu is noticed in case of NFL corresponding to HDR = 1 and PDR = 6. The lowest value of Nu is obtained corresponding to PDR = 8 and HDR = 2. Fig. 6 outlines the interconnection between HDR and thermal resistance in case of heat sink with impinging jet with airfoil pillars with and without NFL. Thermal resistance is detected to be 0.0024 and 0.0037 with and without NFL respectively for PDR = 8 and HDR = 1. For HDR = 2, resistance is noticed to be 0.0013 for NFL and 0.0022 for water at PDR = 8. Similarly, for HDR = 3 and 4, resistance is 0.001, 0.00089 for NFL and 0.0018, 0.0015 without NFL at PDR = 8. So it is concluded from the Fig. 6 that the value of resistance is more without NFL. Also with an advancement in the HDR, resistance dwindles in both the cases with and without NFL. The connection between Height diameter ratio and pumping power in case of impinging jet with airfoil pillars with and without Nano fluid is represented in the Fig. 7. For PDR = 12 and HDR = 1, pumping power is noticed to be 0.001 W and 0.0002 W with and without NFL respectively. With an advancement in HDR to 2, power requirement increased to 0.003 W and 0.0005 W in case of water and NFL respectively at PDR = 12. Similar trend is detected for HDR = 3 and 4 for PDR = 12. For PDR = 6, 8 and 10, it is noted from the figure that with an increment in the HDR, power requirement also gets increased. So the pumping power is higher with Nano fluid as compared without Nano fluid. This is due to the increase in the frictional resistance due to increased velocity.

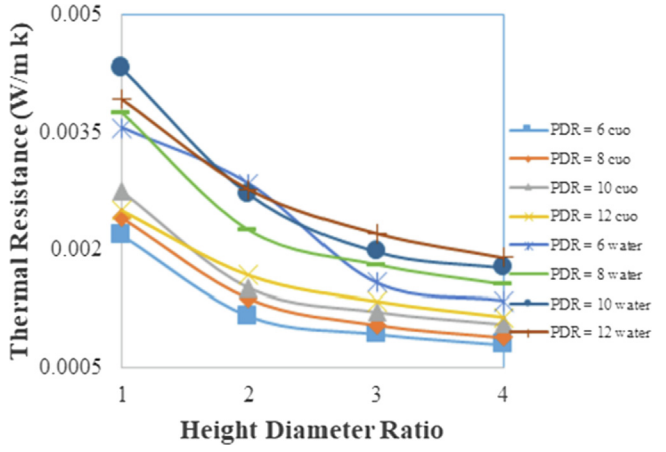

Fig. 6. Thermal resistance Vs HDR.

4. Conclusion

From the comparative study of water and Nano fluid with 1% concentration following conclusions have been made.

1. Reverse trend is observed between HDR and Temperature of the base. With the augmentation in HDR the temperature rise reduces both in case of water as well as Nano fluid. However, Nano fluid case has been found to be more effective.
2. Direct proportion has been noticed in between heat exchange coefficient and HDR for a particular value of PDR. In the case of Nano fluid higher augmentation has been found in the value of h in differentiation to pure water.
3. Indirect proportion has been accounted in between Nusselt number and HDR for a particular value of PDR. However, when differentiated with water higher value of Nusselt number has been accounted.

Declaration of Competing Interest

The authors declare that they have no known competing financial interests or personal relationships that could have appeared to influence the work reported in this paper.

Acknowledgements

The authors are indebted to Delhi Technological University for providing the support for the research.

References

[1] A. Shah, B.G. Sammakia, H. Srihari, K. Ramakrishna, A numerical study of the thermal performance of an impingement heat sink—Fin shape optimization, IEEE Trans. Compon. Packag. Technol. 27 (4) (2004) 710–717.
[2] K.-T. Chiang, Modeling and optimization of designing parameters for a parallel-plain fin heat sink with confined impinging jet using the response surface methodology, Appl. Therm. Eng. 27 (14–15) (2004) 2473–2482.
[3] L. Zheng, D. Zhang, Y. Xie, G. Xie, Thermal performance of dimpled/protruded circular and annular microchannel tube heat sink, J. Taiwan Inst. Chem. Eng. 60 (2016) 342–351.
[4] H.M.S. Bahaidarah, Experimental performance evaluation and modeling of jet impingement cooling for thermal management of photovoltaics, Sol. Energy 135 (2016) 605–617.
[5] Y. Li, L. Gong, M. Xu, Y. Joshi, Enhancing the performance of aluminum foam heat sinks through integrated pin fins, Int. J. Heat Mass Transf. 151 (2020) 119376.
[6] A. Izadi, M. Abdipour, H. Rasam, MHD forced convection of Nano fluid flow in an open-cell metal foam heatsink under LTNE conditions, J. Therm. Anal. Calorim. (2020).

[7] M. Neyestani, M. Nazari, M.M. Shahmardan, M. Sharifpur, M. Ashouri, J.P. Meyer, Thermal characteristics of CPU cooling by using a novel porous heat sink and Nano fluids, J. Therm. Anal. Calorim. (2019).
[8] R. Chein, G. Huang, Analysis of microchannel heat sink performance using nano fluids, Appl. Therm. Eng. 25 (17–18) (2005) 3104–3114.
[9] S. Ziaedin Miry, S. Lohrasbi, H. Irani, M. Ashjaee, D. Domiri Ganji, Thermal energy absorption in a heat sink with elliptical cross section and tangential impinging inlet flow of Nano fluid, Exp. Therm Fluid Sci. 89 (2017) 50–61.
[10] D. Lelea, I. Laza, The water based Al2O3 Nano fluid flow and heat transfer in tangential micro tube heat sink with multiple inlets, Int. J. Heat Mass Transf. 69 (2014) 264–275.
[11] P. Selvakumar, S. Suresh, Convective performance of CuO/water Nano fluid in an electronic heat sink, Exp. Therm. Fluid Sci. 40 (2012) 57–63.
[12] C.J. Ho, Y.-J. Hsieh, S. Rashidi, Y. Orooji, W.-M. Yan, Thermal-hydraulic analysis for alumina/water nanofluid inside a mini-channel heat sink with latent heat cooling ceiling-An experimental study, Int. Commun. Heat Mass Transfer 112 (2020) 104477.
[13] A. Izadi, M. Siavashi, H. Rasam, Q. Xiong, MHD enhanced nano fluid mediated heat transfer in porous metal for CPU cooling, Appl. Therm. Eng. 114843 (2019).
[14] R. Wang, W. Wang, J. Wang, Z. Zhu, Analysis and optimization of trapezoidal grooved microchannel heat sink using nanofluids in a micro solar cell, Entropy 20 (1) (2017) 9.
[15] F. Selimefendigil, H.F. Öztop, Jet impingement cooling and optimization study for a partly curved isothermal surface with CuO-water Nano fluid, Int. Commun. Heat Mass Transfer 89 (2017) 211–218.
[16] H.M. Ali, W. Arshad, Effect of channel angle of pin-fin heat sink on heat transfer performance using water based graphene Nano platelets Nano fluids, Int. J. Heat Mass Transf. 106 (2017) 465–472.
[17] B. Sun, Y. Qu, D. Yang, Heat transfer of single impinging jet with Cu nano fluids, Appl. Therm. Eng. 102 (2016) 701–707.
[18] L. Nakharintr, P. Naphon, S. Wiriyasart, Effect of jet-plate spacing to jet diameter ratios on Nano fluids heat transfer in a mini-channel heat sink, Int. J. Heat Mass Transf. 116 (2018) 352–361.
[19] Z. Azizi, A. Alamdari, M.R. Malayeri, Convective heat transfer of Cu–water Nano fluid in a cylindrical microchannel heat sink, Energy Convers. Manage. 101 (2015) 515–524.
[20] R.-T. Wang, J.-C. Wang, Intelligent dimensional and thermal performance analysis of Al_2O_3 Nano fluid, Energy Convers. Manage. 138 (2017) 686–697.

Further Reading

[1] A. Radwan, M. Ahmed, S. Ookawara, Performance enhancement of concentrated photovoltaic systems using a microchannel heat sink with Nano fluids, Energy Convers. Manage. 119 (2016) 289–303.
[2] L. Nakharintr, P. Naphon, Magnetic field effect on the enhancement of Nano fluids heat transfer of a confined jet impingement in mini-channel heat sink, Int. J. Heat Mass Transf. 110 (2017) 753–759.
[3] T. Ambreen, A. Saleem, C.W. Park, Numerical analysis of the heat transfer and fluid flow characteristics of a Nano fluid-cooled micro pin-fin heat sink using the Eulerian-Lagrangian approach, Powder Technol. (2019).

Research Article | Vol. 29, No. 6 / 15 March 2021 / Optics Express 8490
Optics EXPRESS

High-efficient photoacoustic generation with an ultrathin metallic multilayer broadband absorber

CHUNQI ZHENG,[1,4] HUANZHENG ZHU,[1,4] ZIQUAN XU,[1] RAVINDRA K. SINHA,[2,3] QIANG LI,[1] AND PINTU GHOSH[1,*]

[1] State Key Laboratory of Modern Optical Instrumentation, College of Optical Science and Engineering, Zhejiang University, Hangzhou 310027, China
[2] CSIR-Central Scientific Instruments Organization, Chandigarh 160030, India
[3] TIFAC-CORE in Fiber Optics and Optical Communication, Applied Physics Department, Delhi Technological University, Bawana Road, Delhi-110042, India
[4] Equal contribution
[*] ghosh@zju.edu.cn

Abstract: Metal nanomaterials have been widely used to generate photoacoustic (PA) signals because of their high optical absorption characteristics. However, the PA conversion efficiency of metal nanomaterials is limited by the single-wavelength absorption at the resonant peak. To mitigate this issue, a three-layer ultrathin film containing a thin PDMS layer sandwiched between two ultrathin chromium films is proposed. This kind of film structure can attain high optical absorbance (>80%) through the visible light range (450–850 nm). The optical absorption characteristics can be easily modulated by varying the thickness of the PDMS layer. Under the same excitation condition, the PA signal generated by this film structure is twice that of an only Cr film and three times that of an only Au film. This film structure is easily fabricated and can operate with lasers having different central wavelengths or even white light sources, leading to its applications in many fields, including photoacoustic communications and audio transducers.

© 2021 Optical Society of America under the terms of the OSA Open Access Publishing Agreement

1. Introduction

Photoacoustic (PA) conversion has been applied in many fields, such as biological functional imaging [1–5], ultrasound transducers [6], PA driving [7], and PA spectroscopy [8]. Moreover, PA generation can also be used in PA communications and audio transducers. While ultrasound signals produced by traditional sound generation methods based on the piezoelectric principle are limited by electronic components, PA conversion can generate broadband ultrasonic signals with a high frequency of several hundred megahertz when PA materials are excited by optical pulses. In the aforementioned applications, ultrasonic signals with high intensity are desired. Currently, PA conversion is achieved through the thermoelastic scheme, in which the PA signal amplitude is proportional to the volumetric thermal-expansion coefficient (β), light absorption (A), and incident laser fluence (F) [9]. Nowadays, researchers combine lossy materials with high optical absorption and elastic materials with high thermal expansion to improve the PA signal amplitude. Polydimethylsiloxane (PDMS) is usually used as a thermal expansion material for enhancing PA signal due to its high optical transmittance and high thermal expansion coefficient. Embedding light-absorbing materials in PDMS can significantly increase the thermal expansion coefficient of PA composites without influencing absorption. Common light absorbing materials include carbon black [10], reduced graphene oxide (rGO) [11], carbon nanotubes (CNT) [12], and candle soot nanoparticles [13]. Although carbon-based materials can achieve broadband absorption, their applications are limited due to the complex fabrication processes [14], easy aggregation when mixed with polymers [12], and difficulty of thickness control [15].

Another kind of PA composites is with metal nanomaterials based on localized surface plasmon resonance (LSPR) [16–18]. Owing to this characteristic, metal nanomaterials provide

#420138 https://doi.org/10.1364/OE.420138
Journal © 2021 Received 18 Jan 2021; revised 19 Feb 2021; accepted 23 Feb 2021; published 3 Mar 2021

Optics EXPRESS

distinguished advantages, such as high optical absorption in the resonance band, tunability on LSPR by controlling structural parameters [19], and high thermal conductivity for improving the efficiency of photothermal conversion [20]. Recently, researches have demonstrated that metal nanomaterials can be used in the enhancement of PA signal, such as gold nanoparticles in different shapes [1,4,5,21–23], gold-PDMS composite [15], and silver nanostructures [24]. However, metal nanostructure-based PA composites can usually only achieve single-wavelength optical absorption and only can be excited by a laser source of a particular wavelength. In PA communications for civil applications with illuminating light sources, broadband optical absorption with efficient PA generation is required. Consequently, a broadband absorptive, stable, and polymer-compatible PA material with low-cost and easy fabrications is desired to facilitate the applications of a PA conversion system.

In this work, we present a kind of lithography-free fabrication of an efficient PA conversion material based on a three-layer ultrathin film containing a thin PDMS layer sandwiched between two ultrathin chromium films. This three-layer structure can achieve high broadband absorption through the visible light range, and it can be excited by both laser with different central wavelengths and broadband white light source. The fabrication process is simple, and the structural parameters can be controlled easily to achieve large-scale uniform production.

2. Theoretical analysis of the Cr-PDMS-Cr structure

The generation of PA signal is shown in the schematic diagram in the Fig. 1. The PA conversion structure is illuminated by the light modulated at a frequency. With the high absorbance in the visible band, the structure is heated and naturally cooled down according to the modulation frequency of the illumination. The temperature of the structure is therefore periodically fluctuated at the modulation frequency. The corresponding thermal expansion for the temperature fluctuation leads to periodic displacements, and acoustic signal can be generated at the solid-fluid boundary.

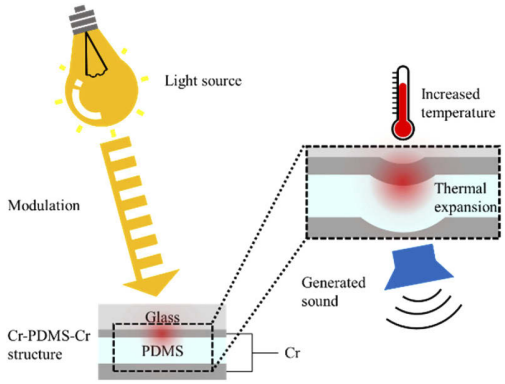

Fig. 1. A schematic illustration for optical absorption and PA generation process.

The schematic diagram of the proposed PA conversion structure is shown in Fig. 2(a), which is comprised of a thin PDMS layer sandwiched between two chromium films. This simple three-layer coating works like an asymmetric Fabry-Perot (FP) cavity [25,26]. The optical reflection and transmission spectra can be analyzed through Maxwell equations and boundary conditions at each interface [27]. Assume that the light is normally incident from the silica substrate side and the thicknesses of the bottom metallic layer, dielectric layer and the top metallic layer are d_1, d_2 and d_3, respectively. The refractive index of the silica, chromium and PDMS are denoted as n_{Silica}, n_{Cr} and n_{PDMS}, respectively. For TM polarization wave, the electric field

Optics EXPRESS

component and magnetic field component can be expressed as

$$E_y = A \cdot e^{ikz} + B \cdot e^{-ikz}, \text{and} \tag{1}$$

$$H_x = -\frac{k}{\mu_0 \mu_r \omega}(A \cdot e^{ikz} - B \cdot e^{-ikz}). \tag{2}$$

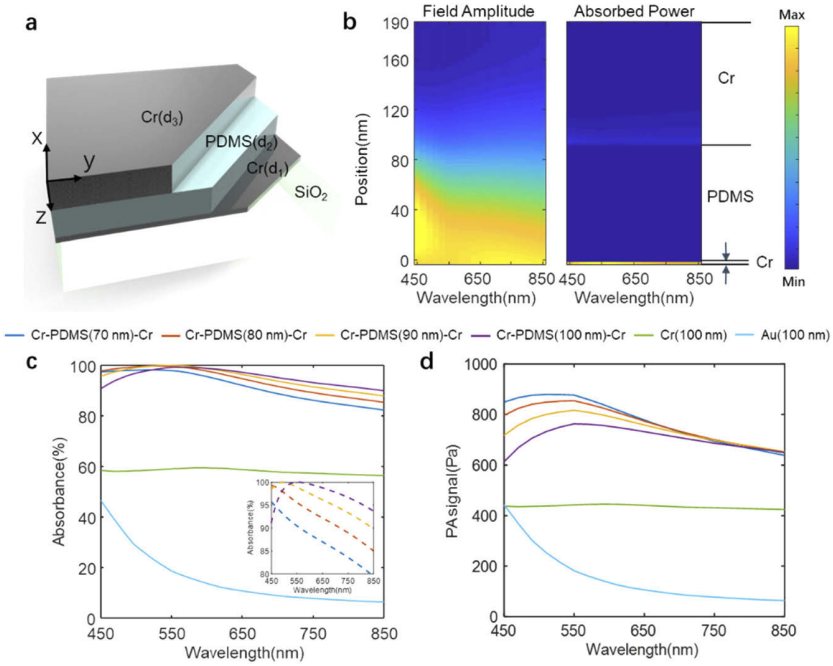

Fig. 2. Schematic configuration and optical characteristics of the Cr-PDMS-Cr three-layer thin film structure. (a) Schematic diagram of the Cr-PDMS-Cr three-layer thin film structure. (b) Simulated electric field amplitude and absorbed power along the light propagation direction as a function of wavelength. (c) Simulated absorptivity with the inset for magnified figure. (d) PA signals as a function of the incident wavelength for the Cr-PDMS-Cr three-layer thin-film structures with different PDMS thicknesses, a 100 nm Cr film, and a 100 nm Au film

According to boundary conditions, the tangential components of the electric field and magnetic field are both continuous at interfaces. Assuming $A_0 = \mathrm{R}$, $B_0 = 1$ in silica and $A_3 = 0$ in top Cr layer, the reflection coefficients can be calculated as

$$R = \frac{R_{01} \cdot (n_{Cr} + n_{Silica}) + n_{Silica} - n_{Cr}}{R_{01} \cdot (n_{Silica} - n_{Cr}) + n_{Silica} + n_{Cr}}, \text{and} \tag{3}$$

$$R_{01} = e^{2ik_1 d_1} \cdot \frac{(n_{PDMS} - n_{Cr}) \cdot \mathrm{e}^{2ik_2 d_2} + n_{Cr} - n_{PDMS}}{-\frac{(n_{Cr} - n_{PDMS})^2}{n_{Cr} + n_{PDMS}} \mathrm{e}^{2ik_2 d_2} + n_{Cr} + n_{PDMS}}, \tag{4}$$

where k_1 and k_2 are the wavenumber in the bottom Cr layer and PDMS layer, respectively. R and R_{01} are the reflection coefficient of the electric field at the silica/top Cr layer interface and top Cr layer/PDMS layer interface, respectively. Assuming that the top Cr layer is thick enough and

Optics EXPRESS

there is no transmission, the absorption A can be calculated by

$$A = 1 - r = 1 - |R|^2. \tag{5}$$

The Cr layer with a thickness of 100 nm is used as the reflection layer, which is optically opaque for visible light. On the other hand, the Cr layer with a thickness of 3 nm functions as another reflection surface and simultaneous absorption layer due to Cr′s lossy characteristics. The PDMS layer with variable thickness d (70 nm - 100 nm) is selected for its high transmittance in the visible range and high thermal expansion coefficient. The theoretical model and finite element method (FEM) are both used to analyze the optical characteristic of the Cr-PDMS-Cr structure. The permittivity of Cr is fitted by the Drude model [28], and the refractive index of PDMS is set as 1.4. Simulated electric field amplitude and absorbed power along the light propagation direction as a function of wavelength are shown in Fig. 2(b). The heat generated due to the absorption is mainly confined in the bottom thin Cr film. For comparison, optical absorption spectra corresponding to a 100 nm Cr film and a 100 nm Au film are calculated. The absorption spectra of Cr-PDMS-Cr structures with different PDMS thicknesses, a 100 nm Cr film, and a 100 nm Au film are shown in Fig. 2(c). Cr film has a relatively flat absorption from 56% to 60% within the visible light range. According to Fig. 2(c), the Cr-PDMS-Cr structure can achieve broadband strong optical absorption between 450 nm - 850 nm. With the increase of thickness of the PDMS layer, the absorption peak redshifts.

The PA properties of the Cr-PDMS-Cr structure, a Cr film as well as an Au film are also simulated via the FEM method. The excitation light is set as Gaussian-shaped with a full width at half maxima (FWHM) 2.8 ns and the power density 1000 W/m^3. The PA signals corresponding to a 100 nm Cr film, a 100 nm Au film, and the Cr-PDMS-Cr structure under different wavelength excitations are shown in Fig. 2(d). The PA signal amplitude of Cr film is proportional to the optical absorption. In a homogeneous medium, higher optical absorption can lead to higher temperature increases, therefore results in larger thermal expansion and stronger PA signal. However, for the Cr-PDMS-Cr structure, PA signal amplitude is not directly proportional to the optical absorption. At 550 nm, the optical absorption of Cr-PDMS-Cr structure with PDMS thickness of 70 nm, 80 nm, 90 nm, and 100 nm is similar, but the structure with PDMS thickness of 70 nm has the strongest PA signal amplitude followed by the structure with PDMS thickness of 80 nm, 90 nm, and 100 nm. This phenomenon can be explained by the fact that the heat is mainly generated on the bottom Cr layer. For the thinner PDMS layer, heat can be transferred quickly into PDMS and the temperature distribution is more uniform, and therefore larger acceleration and PA signal are generated. Consequently, the PA signal amplitude of the Cr-PDMS-Cr structure can be optimized by manipulating both light absorbance and the thickness of the PDMS layer.

3. Experimental result

The Cr-PDMS-Cr structure includes the 3-nm bottom Cr layer, the middle PDMS layer, and the top 100-nm Cr layer. Due to the need for optical and PA characterization, silica quartz glass with high transmittance was selected as the substrate. The first Cr layer is deposited by the magnetron sputtering. Thereafter, the PDMS is mixed with a curing agent (PDMS: curing agent = 10:1) and then diluted by n-hexane. PDMS solution is spin-coated for ultrathin PDMS layers, and the thickness varies with the dilution ratio of PDMS and n-hexane. When the ratio of n-hexane in PDMS is higher, the PDMS layer after spin coating becomes thinner. Samples with different PDMS thicknesses are shown in Fig. 3(a). The marker on the upper left corner indicates the thicknesses of the PDMS layers with the dilution ratio of 1:90,1:120,1:160, and 1:200, respectively [29]. Thereafter, PDMS solution is spin-coated with the rotation rate of 6000 r/min for 120 s on the first Cr layer. After spin coating, PDMS films are solidified under 60°C for 2 hours. In the next step, the ultrathin PDMS layer is treated by oxygen plasma to avoid

Optics EXPRESS

demoulding problem between the PDMS layer and the 100 nm top Cr layer. Finally, the top Cr layer is deposited by the magnetron sputtering.

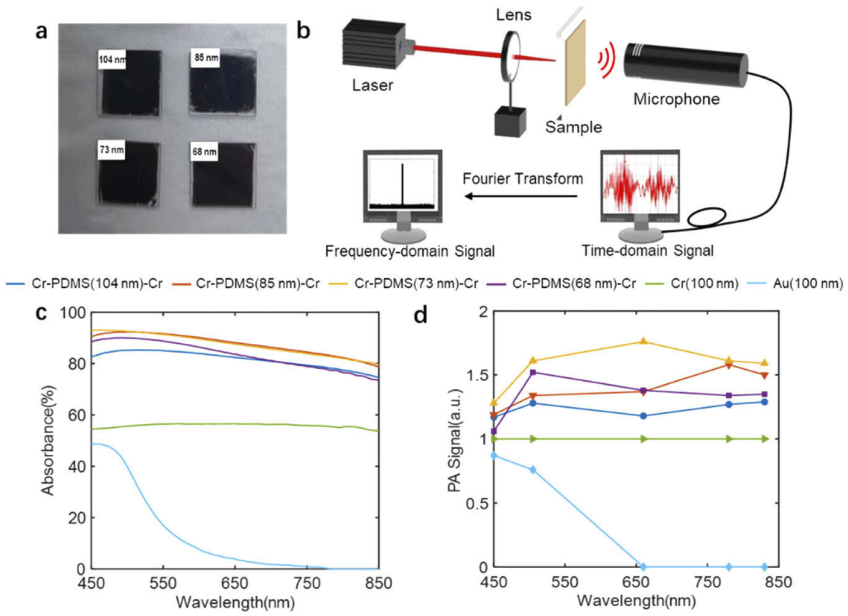

Fig. 3. (a) The optical images of the Cr-PDMS-Cr structures corresponding to different PDMS dilution ratios. The marker on the upper left corner indicates the dilution ratio of PDMS and n-hexane. (b) Experimental setup for the PA signal detection experiment. (c) Absorptivity and (d) PA signals as a function of the incident wavelength for the Cr-PDMS-Cr three-layer thin-film structures with different PDMS thicknesses, a 100 nm Cr film, and a 100 nm Au film.

For the optical characterization, an optical microscope (Nikon ECLIPSE 80i) and a spectrometer (Ocean Optics QE65 Pro) are utilized to measure the reflection and transmission spectra. According to the law of energy conservation, $A = 1 - R - T$, where R represents the reflectivity, T represents the transmittance, and A represents the absorption. Therefore, the absorption of the sample can be obtained by measuring the reflectivity and transmittance of the sample. When measuring the reflectivity, the broad spectrum light is converged on to the sample surface through an objective lens (Nikon CFILU Plan Epi ELWD, 20X). The reflected light from the sample is then collected by the same objective lens and transmitted to the spectrometer and CCD Camera (Nikon DIGITAL CAMERA HEAD DS-Fi1). While measuring the transmittance, the transmitted light from the broadband light source below the sample is collected through another objective lens and guided to the spectrometer and CCD Camera. The absorption spectra of different samples can be calculated by $A = 1 - R - T$. Optical absorption spectra for the Cr-PDMS-Cr structures with different PDMS film thicknesses, a 100 nm Cr film, and a 100 nm Au film are recorded by a microscope fitted with a spectrometer and are illustrated in Fig. 3(c). The Cr-PDMS(73 nm)-Cr structure shows the highest absorption. Cr film has a relatively flat absorption within the visible light range. On the other hand, the absorption of Au film decreases significantly above 500 nm.

The experimental setup is shown in Fig. 3(b). The PA signal needs to be excited by pulsed light and detected by a sound detector. In this work, the working current of the LDs is modulated by a pulse function arbitrary noise generator (Agilent Technologies, Pulse Function Arbitrary Generator, 81150A). The modulated current is rectangular with a pulse width of 10 μs and a

Optics EXPRESS

repetition frequency of 7250 Hz. The used laser diodes are 450 nm (Osram PLT 450B, 80 mW), 505 nm (Sharp GH05035A2G, 35 mW), 660 nm (Mitsubishi ML101U29, 130 mW), 780 nm (Sanyo 7140–211n, 80 mW), and 830 nm (Sharp GH0832BA2A, 210 mW). The laser diode is installed on a temperature-controlled mount (Thorlabs, LDM56) and controlled by a current temperature controller (Thorlabs, ITC100D). The incident light is converged through a converging lens (Daheng Optics, GCL-0101B) and focused on the sample surface. The microphone (Takstar, CM-63, 30Hz-20kHz) is placed behind the sample as near as possible without touching it. The acoustic signal is firstly recorded for 200 s by the microphone and then amplified by a preamplifier (Takstar, MA-1C). MATLAB software is used to analyze the PA signal by Fourier transforming the acoustic signal from the time domain to the frequency domain. The amplitude of PA signal can be obtained by monitoring the signal at the light repetition rate (7250 Hz). To minimize the surrounding noise, PA signal amplitude for each sample is determined by the average value of three measurements at different positions on the sample.

The PA signal amplitude is detected at the laser repetition frequency, and the detected signal amplitudes are compared for different incident light wavelengths. As LDs of different wavelengths have different response characteristics, the output powers of different LDs are different even with the same driving current. According to the above optical measurement results, the Cr film has relatively flat absorption. Therefore, the PA signal of a single-layer Cr is used as a reference to normalize the PA signals of other samples at each wavelength. The PA signals of different samples are shown in Fig. 3(d).

According to Fig. 3(d), the PA signal amplitude corresponding to the Cr-PDMS-Cr structure is higher than that of the Cr film. The PA signal amplitude of the gold film is weaker than that of the Cr film and proportional to its optical absorption. When the optical absorption is similar, the Cr-PDMS-Cr structure with a thinner thickness produces a higher PA signal. For example, at 780 nm and 830 nm, the absorption of Cr-PDMS(104 nm)-Cr and Cr-PDMS(68 nm)-Cr are similar, and absorption of Cr-PDMS(85 nm)-Cr and Cr-PDMS(73 nm)-Cr are similar. The PA signals of Cr-PDMS(68 nm)-Cr are stronger than that of Cr-PDMS(104 nm)-Cr at the corresponding wavelengths. Similarly, the PA signals of Cr-PDMS(85 nm) are stronger than that of Cr-PDMS(73 nm)-Cr at the corresponding wavelengths. This is consistent with the simulation results that the photoacoustic signal generated by the sample with a thinner PDMS layer is stronger under the condition of similar optical absorption.

As the Cr-PDMS-Cr structure can achieve broadband absorption within the visible range, it can absorb more energy when excited by a broadband light source. In order to explore its PA characteristics under broadband light excitation, a white light LED is used to excite the PA signal of different samples. The white light LED (QYSSM, 3W) is powered by a laboratory stabilized power supply unit and modulated by a pulse function arbitrary noise generator (Agilent Technologies, Pulse Function Arbitrary Generator, 81150A). To minimize the noise of electrical components, the power supply unit and the pulse function arbitrary noise generator are placed in a different room.

Figure 4(a) shows the absorption power of different samples, which is obtained by multiplying the absorptivity with the light source spectrum. According to the generated PA signals indicated in Fig. 4(b), it is observed that the Cr-PDMS-Cr structure can improve the PA signal significantly. The PA amplitude can also be controlled by varying the thickness of the PDMS layer. In this work, the sample fabricated by the PDMS layer with a thickness of 73 nm shows the highest absorption power and PA signal. Therefore, it can be concluded that the Cr-PDMS-Cr structure can achieve high absorption within the visible light range and can be used to improve PA signal intensity.

Optics EXPRESS

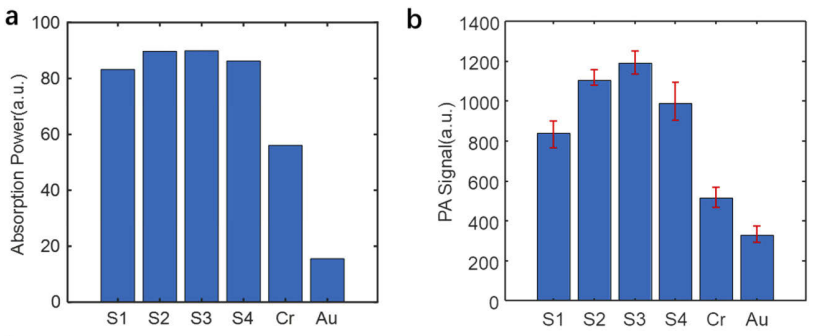

Fig. 4. (a) The absorption power and (b) PA signal of different samples. S1, S2, S3, S4, Cr, and Au represent Cr-PDMS(104 nm)-Cr, Cr-PDMS(85 nm)-Cr, Cr-PDMS(73 nm)-Cr, Cr-PDMS(68 nm)-Cr, 100 nm Cr, and 100 nm Au, respectively. PA signals are determined by the average value of three measurements and the error bar represents the maximum and minimum values.

4. Conclusion and discussion

High-frequency ultrasonic signals generated by PA conversion can be applied in many fields. In this work, we present a kind of broadband PA conversion nanostructure based on a three-layer ultrathin film containing a thin PDMS layer sandwiched between two ultrathin chromium films. The experiments show that this nanostructure can achieve high broadband absorption across the visible light range. Compared with metal films, the three-layer film structure shows a significant enhancement in the PA signal both under the excitation of laser diodes with different operation wavelengths and broadband white light. Thereby, it opens up opportunities for PA communications for civil use with a common illuminating light source at a low cost.

Fabrication of this film structure is lithography-free and realized by the magnetron sputtering and spin-coating. With simple structure and easy fabrication, it can be applied to many fields, including photoacoustic communications and audio transducers. Besides, the broadband optical absorption makes it work with lasers with different central wavelengths. It can also be excited by a modulated broadband white light source and generate a PA signal with a high amplitude.

Funding. National Key Research and Development Program of China (2017YFE0100200); National Natural Science Foundation of China (61950410608, 61775194, 61975181).

Disclosures. The authors declare no conflicts of interest.

Supplemental document. See Supplement 1 for supporting content.

References

1. N. Yan, X. Wang, L. Lin, T. Song, P. Sun, H. Tian, H. Liang, and X. Chen, "Gold Nanorods Electrostatically Binding Nucleic Acid Probe for In Vivo MicroRNA Amplified Detection and Photoacoustic Imaging-Guided Photothermal Therapy," Adv. Funct. Mater. **28**(22), 1800490 (2018).
2. N. Wu, Y. Tian, X. Zou, V. Silva, A. Chery, and X. Wang, "High-efficiency optical ultrasound generation using one-pot synthesized polydimethylsiloxane-gold nanoparticle nanocomposite," J. Opt. Soc. Am. B **29**(8), 2016–2020 (2012).
3. J. Zhong, L. Wen, S. Yang, L. Xiang, Q. Chen, and D. Xing, "Imaging-guided high-efficient photoacoustic tumor therapy with targeting gold nanorods," Nanomedicine **11**(6), 1499–1509 (2015).
4. R. Liang, J. Xie, J. Li, K. Wang, L. Liu, Y. Gao, M. Hussain, G. Shen, J. Zhu, and J. Tao, "Liposomes-coated gold nanocages with antigens and adjuvants targeted delivery to dendritic cells for enhancing antitumor immune response," Biomaterials **149**, 41–50 (2017).
5. J. S. Wi, J. Park, H. Kang, D. Jung, S. W. Lee, and T. G. Lee, "Stacked Gold Nanodisks for Bimodal Photoacoustic and Optical Coherence Imaging," ACS Nano **11**(6), 6225–6232 (2017).
6. Y. Hou, J.-S. Kim, S. Ashkenazi, S.-W. Huang, L. J. Guo, and M. O'Donnell, "Broadband all-optical ultrasound transducers," Appl. Phys. Lett. **91**(7), 073507 (2007).

Optics EXPRESS

7. Y. Yuan, C. Gu, S. Huang, L. Song, and F. Fang, "Advances on studying optical forces: optical manipulation, optical cooling and light induced dynamics," J. Phys. D: Appl. Phys. **53**(28), 283001 (2020).
8. D. V. Bageshwar, A. S. Pawar, V. V. Khanvilkar, and V. J. Kadam, "Photoacoustic spectroscopy and its applications–a tutorial review," Eurasian Journal of Analytical Chemistry **5**, 187–203 (2010).
9. T. Lee, H. W. Baac, Q. Li, and L. J. Guo, "Efficient Photoacoustic Conversion in Optical Nanomaterials and Composites," Adv. Opt. Mater. **6**(24), 1800491 (2018).
10. T. Buma, M. Spisar, and M. O'Donnell, "High-frequency ultrasound array element using thermoelastic expansion in an elastomeric film," Appl. Phys. Lett. **79**(4), 548–550 (2001).
11. S. Hwan Lee, M.-A. Park, J. J. Yoh, H. Song, E. Yun Jang, Y. Hyup Kim, S. Kang, and Y. Seop Yoon, "Reduced graphene oxide coated thin aluminum film as an optoacoustic transmitter for high pressure and high frequency ultrasound generation," Appl. Phys. Lett. **101**(24), 241909 (2012).
12. R. J. Colchester, C. A. Mosse, D. S. Bhachu, J. C. Bear, C. J. Carmalt, I. P. Parkin, B. E. Treeby, I. Papakonstantinou, and A. E. Desjardins, "Laser-generated ultrasound with optical fibres using functionalised carbon nanotube composite coatings," Appl. Phys. Lett. **104**(17), 173502 (2014).
13. W.-Y. Chang, W. Huang, J. Kim, S. Li, and X. Jiang, "Candle soot nanoparticles-polydimethylsiloxane composites for laser ultrasound transducers," Appl. Phys. Lett. **107**(16), 161903 (2015).
14. H. Won Baac, J. G. Ok, H. J. Park, T. Ling, S. L. Chen, A. J. Hart, and L. J. Guo, "Carbon nanotube composite optoacoustic transmitters for strong and high frequency ultrasound generation," Appl. Phys. Lett. **97**(23), 234104 (2010).
15. Y. Hou, J.-S. Kim, S. Ashkenazi, M. O'Donnell, and L. J. Guo, "Optical generation of high frequency ultrasound using two-dimensional gold nanostructure," Appl. Phys. Lett. **89**(9), 093901 (2006).
16. K. A. Willets and R. P. Van Duyne, "Localized surface plasmon resonance spectroscopy and sensing," Annu. Rev. Phys. Chem. **58**(1), 267–297 (2007).
17. H. Luo, Q. Li, K. Du, Z. Xu, H. Zhu, D. Liu, L. Cai, P. Ghosh, and M. Qiu, "An ultra-thin colored textile with simultaneous solar and passive heating abilities," Nano Energy **65**, 103998 (2019).
18. W. Wang, Y. Qu, K. Du, S. Bai, J. Tian, M. Pan, H. Ye, M. Qiu, and Q. Li, "Broadband optical absorption based on single-sized metal-dielectric-metal plasmonic nanostructures with high-ε'' metals," Appl. Phys. Lett. **110**(10), 101101 (2017).
19. K. L. Kelly, E. Coronado, L. L. Zhao, and G. C. Schatz, "The optical properties of metal nanoparticles: the influence of size, shape, and dielectric environment," J. Phys. Chem. B **107**(3), 668–677 (2003).
20. Y. Yan, L. Liu, Z. Cai, J. Xu, Z. Xu, D. Zhang, and X. Hu, "Plasmonic nanoparticles tuned thermal sensitive photonic polymer for biomimetic chameleon," Sci. Rep. **6**(1), 31328 (2016).
21. C. W. Wei, M. Lombardo, K. Larson-Smith, I. Pelivanov, C. Perez, J. Xia, T. Matula, D. Pozzo, and M. O'Donnell, "Nonlinear contrast enhancement in photoacoustic molecular imaging with gold nanosphere encapsulated nanoemulsions," Appl. Phys. Lett. **104**(3), 033701 (2014).
22. J. Song, X. Yang, Z. Yang, L. Lin, Y. Liu, Z. Zhou, Z. Shen, G. Yu, Y. Dai, O. Jacobson, J. Munasinghe, B. Yung, G. J. Teng, and X. Chen, "Rational Design of Branched Nanoporous Gold Nanoshells with Enhanced Physico-Optical Properties for Optical Imaging and Cancer Therapy," ACS Nano **11**(6), 6102–6113 (2017).
23. W. Wang, C. Hao, M. Sun, L. Xu, C. Xu, and H. Kuang, "Spiky Fe_3O_4@Au Supraparticles for Multimodal In Vivo Imaging," Adv. Funct. Mater. **28**, 1800310 (2018).
24. S. G. Park, S. B. Yang, M. S. Ahn, Y. J. Oh, Y. T. Kim, and K. H. Jeong, "Plasmon enhanced photoacoustic generation from volumetric electromagnetic hotspots," Nanoscale **8**(2), 757–761 (2016).
25. Z. Li, E. Palacios, S. Butun, H. Kocer, and K. Aydin, "Omnidirectional, broadband light absorption using large-area, ultrathin lossy metallic film coatings," Sci. Rep. **5**(1), 15137 (2015).
26. Z. Xu, Q. Li, K. Du, S. Long, Y. Yang, X. Cao, H. Luo, H. Zhu, P. Ghosh, W. Shen, and M. Qiu, "Spatially resolved dynamically reconfigurable multilevel control of thermal emission," Laser Photonics Rev. **14**(1), 1900162 (2020).
27. S. Shu, Z. Li, and Y. Y. Li, "Triple-layer Fabry-Perot absorber with near-perfect absorption in visible and near-infrared regime," Opt. Express **21**(21), 25307–25315 (2013).
28. C. Wu, B. Neuner III, G. Shvets, J. John, A. Milder, B. Zollars, and S. Savoy, "Large-area wide-angle spectrally selective plasmonic absorber," Phys. Rev. B **84**(7), 075102 (2011).
29. A. L. Thangawng, R. S. Ruoff, M. A. Swartz, and M. R. Glucksberg, "An ultra-thin PDMS membrane as a bio/micro-nano interface: fabrication and characterization," Biomed. Microdevices **9**(4), 587–595 (2007).

Applied Intelligence
https://doi.org/10.1007/s10489-021-02266-w

IM-ELPR: Influence maximization in social networks using label propagation based community structure

Sanjay Kumar[1,2] · Lakshay Singhla[3] · Kshitij Jindal[4] · Khyati Grover[5] · B. S. Panda[1]

Accepted: 6 February 2021
© The Author(s), under exclusive licence to Springer Science+Business Media, LLC part of Springer Nature 2021

Abstract

The popularity of social networks has grown manifolds in recent years because of various activities like fast propagation of ideas, publicity, and news. Influence maximization (IM) is one of the most highly studied problems in the field of social network analysis due to its business values. Influence maximization aims to identify influential nodes that can spread the information to the maximum number of nodes in the network through diffusion cascade. Traditional methods for IM include centrality based and greedy based measures. However, each method has some limitations. Recently, some methods of IM are introduced, which consider the presence of community structure in networks. Community structure has a significant impact on information diffusion, because of dense connections between the nodes in the community. In this paper, we propose a novel influence maximization algorithm using node seeding, label propagation, and community detection. We first use extended h-index centrality to detect the seed nodes and then use the label propagation technique to detect communities. Further, we merge smaller and related communities to a larger community with the help of a relationship matrix. Finally, top-k influential nodes from these communities are identified. These ideas lead to our proposed algorithm: Influence Maximization using Extended h-index, and Label Propagation with Relationship matrix (IM-ELPR). We adopt Independent Cascade (IC) information diffusion model to spread the information originating from chosen influential nodes. The proposed algorithm intends to identify influential nodes from different communities globally and does not depend on the specific community's antecedent structural information. Experimental results performed on several real-life data sets reveal that the proposed algorithm performs better than many other existing popular algorithms.

Keywords Complex networks · Community structure · Influence Maximization · Independent cascade model · Label propagation

1 Introduction

Many real-life networks, like online social networks, information networks, and biological networks, are complex networks [1, 2] that consist of numerous connected nodes with complicated interactions between them. An online social network (OSN) is an abstract view of our virtual social system depicting a large number of users and social acquaintances between them [3]. A social network can be modeled as graph $G = (V, E)$, where V represents a set of people or entities, and E denotes the set of edges. An edge exists between two nodes if they are socially connected like friendship, follow-followee, and colleagues. As a result of the boom of internet and electronics services, online social networks have become very popular, which connects millions of people worldwide to share ideas, information and perform many online activities [4]. These days, online social networks like Twitter, Facebook, Instagram, and Wechat play a pivotal role in shaping public perceptions and creating awareness [5]. These networks act as an excellent platform for the fast diffusion of information and viral marketing by exploiting the trust relationship between the users. Influence maximization (IM) is a hot research topic in the field of network science to measure the user's influence in spreading the information in a network [6]. It seeks to identify some seed nodes with high spreading capability such that information originating from these nodes reaches a maximum number of people in the network, and such nodes are called influential nodes [7]. Formally, the influence maximization (IM) problem is defined as "given a social

✉ Sanjay Kumar
sanjay.kumar@dtu.ac.in

Extended author information available on the last page of the article.

network represented as a graph $G(V, E)$ with $|V| = n$, $|E| = m$, and a positive number k where $k << n$, determine a set of k seed nodes, such that initially triggering them, the influence spread in the network can be maximized under a specific information dissemination model." Kempe et al. [8] proved that obtaining an optimal solution to the IM problem is an NP-hard optimization problem under the classical diffusion model. Due to mutual trust between the users, influential nodes are capable of accelerating the information spread by triggering a cascade in the diffusion process through word of mouth strategy [9, 10]. Many e-commerce companies are targeting these influential users to promote their products and to achieve optimal publicity [11].

Numerous standard node centrality based algorithms [12] based on local, semi-local, and global features of nodes are employed to solve IM problems with certain limitations and scalability issues. Degree centrality [13], betweenness centrality [14], PageRank [16], and k-shell centrality [17] are the commonly used centrality to rank the nodes based on its structural and topological position in the network. Many classical greedy based algorithms are proposed for influence maximization [8, 18, 19], which employ sub-modularity and monotony of the independent cascade (IC) model along with Monte Carlo simulations to improve the information propagation. Such algorithms are slow due to a large number of simulations and require exponential time complexity. Recently, many community structures based influence maximization algorithms are introduced with considerable improvement in the results [20, 38].

The presence of community structures in complex networks is ubiquitous [21, 22]. Finding community structure can lead to the understanding of the functional organization of the system, and community detection is one of the prominent research topics among the researchers of different fields [23, 24]. A community can be referred to as a group of nodes having more connections within themselves and fewer connections to the rest of the network. In a social network, a community can correspond to a group of people in a fan club of a particular celebrity, employees working in the same project, researchers working in a particular field, and many more. Due to a dense connection, the information can spread rapidly in the community. Hence, the underlying community structure present in social networks can be utilized to perform the influence maximization task [25].

In this paper, we introduce a novel method of IM named Influence Maximization using Extended h-index and Label Propagation with Relationship matrix (IM-ELPR) by utilizing the community structure using label propagation. The proposed algorithm is comprised of four phases, namely the seeding phase, the label propagation phase, merging communities using relationship matrix, and finally, finding k influential nodes. There is a possibility that a node acquires multiple labels signifying its presence in multiple communities during the label propagation phase. Therefore, we consider the overlapping community detection through label propagation in our algorithm. We use the popular independent cascade (IC) information diffusion model to spread the influence originating from seed nodes. Our contributions are summarised as;

1. We propose a novel algorithm to maximize the information propagation by employing seeding phase, label propagation, and community spread in the network.
2. We employ extended h-index centrality in the seeding phase, and also take care that the selected seed nodes are not adjacent to each other, rather far apart so that the entire network can be adequately covered.
3. The proposed algorithm detects the community by recognizing that a node can have multiple labels to map real-life scenarios and performs the merging of relatively smaller and related communities into a larger community.
4. The experimental results obtained on eight real-life datasets of various sizes and applications exhibit improved performance of the proposed algorithm over many contemporary IM algorithms.

The rest of the paper is organized as follows. Section 2, presents the related works of IM using various node centralities and other sophisticated methods. Section 3, describes the proposed work in detail, the time complexity of the proposed algorithm, and a toy network simulation. Section 4, presents the information diffusion model, datasets used, and performance matrices used in computing the results of the IM algorithms. Section 5, reports the experimental results generated by our algorithm and parallel analysis with some previous notable research works. Finally, Section 6 concludes the paper.

2 Related work

In complex networks, many centrality measures have been employed to estimate the significance of nodes. These centrality measures order the nodes based on their topological positions and many other critical parameters. It is assumed that nodes with higher centrality values have more spreading capability than normal nodes. Majorly, centrality based methods are classified into three categories, namely, local, semi-local, and global measures. The local measure focuses on the strength of the node and its adjacent neighbors, like degree centrality [13]. Degree centrality

is the number of direct links a node can have with the other nodes. Usually, local measures are simple and have linear time, but they ignore the topological position of other nodes and may not produce good results in a large-scale network. For example, in the degree centrality, a node with a high degree but situated at the periphery of the network may not be suitable for becoming seed nodes. Contrary, global measures consider the ranking of nodes based on the strength of a particular node like the shortest path, information flow in comparison to all other nodes in the network, and hence take care of the global structure of the nodes. Betweenness centrality, Closeness, Eigenvector, Pagerank, and k-shell centralities are popular examples of global measures. Usually, these measures produce good results but require high time. Betweenness centrality [14] of a node depends on the number of shortest paths passing through that node. In a network, it signifies the control of a node for the information flow in the network. Eigenvector centrality [15] is based upon the fact that if a node is linked to important nodes, it is considered important too. PageRank (PR) [16] is an algorithm employed by Google Search to rank web pages in search engine results. It operates by counting the number and quality of incident edges to a node to estimate its importance. The underlying assumption is that more essential nodes (web pages) are likely to receive more edges from other nodes. k-shell centrality [17] argues that a node lying the core of the network can be a better candidate for information propagation, and a larger shell value signifies that the node is more centrally located in the system.

Semi-local measures intend to maintain the balance between insignificant local measures and expensive global measures. Typically, these measures consider the nodes up to 2 or 3-hops to assess the spreading ability of a node. Local centrality [26], h-index [27] are the example of semi-local measures. Recently many semi-local measures are proposed, and they came up with promising results that produced better results [28, 29]. h-index is a popular metric formulated by J.E. Hirsch [27] to measure the impact of a researcher based on the number of citations received. The same is applied in network [30], and h-index of a node is defined as the maximum value h such that it has at least h neighbors each with degree h or more. Mathematically, h-index can also be defined in the form of a cumulative function as follows [28]:

$$h - index(v) = \max_{h}(c_h(v)),\ where\, c_h(v) \geq h, \tag{1}$$

$$c_h(v) = |\{u|u \in N_v\, and\, d_u \geq h\}|. \tag{2}$$

Where $c_h(v)$ is the function that returns the number of neighbors of node v having degree greater than or equal to h. Hence, as per (1), the value of h-index of node v is a maximal value h such that h number of its neighbors have degrees greater than or equal to h. If a node has a high degree centrality lying in the periphery of the network, it means although the node has a large number of neighbors, those neighbors may have less degrees. But in the case of nodes with a high h-index, their neighbors also have a high degree. Thus, h-index centrality considers the neighborhood of a node up to 2-hops, unlike degree centrality. Therefore, h-index is a more appropriate semi-local measure to estimate the spreading capabilities of nodes. However, many nodes can have the same h-index, so it is difficult to differentiate in the spreading capability of those nodes. To overcome this, authors in [28, 31] suggested extended h-index measures. According to Liu et. al [28], extended h-index for a node (v) is formulated as follows:

$$Extended h-index(v) = h-index(v) + \sum_{u \in N(v)} h-index(u) \tag{3}$$

where $N(v)$ is the set of neighbours of v. Extended h-index of node v is equal to the h-index of v plus sum of h-indices of all neighbours of node v. Thus, an extended h-index takes neighbors up to 3-hops from a node in consideration and can distinguish between the nodes with the same value of h-index. Authors in [29] suggested a type of semi-local algorithm Fixed Neighbor Scale (FNS) by considering neighbors of a node up to multiple levels to determine its spreading influence. They determine the spreading capability of a node by adding multi-level neighbors' weights in the form of their distances from the source node.

By exploiting the community structures in networks, the information diffusion and influence spread can be magnified in the network. This is due to the dense connection between the members of a community. In the past few years, numerous community-based influence maximization algorithms are developed with considerably improved performance. Such algorithms consider independence between communities and perform parallel execution. There are many ways to detect communities in networks. One of the most efficient ways is to uncover community structure is by using the label propagation technique. Raghav et al. [32] proposed the idea of label propagation, which proves to be an efficient method to detect communities within a social network. A vital process in the field of network science, label propagation is a semi-supervised machine learning approach that takes into consideration the topology of the network. In the case of community detection, the process starts by allocating a unique label to every node. Every single node then adopts the label, which is having the highest rate of recurrence amidst its neighbors. Zhao et al. [33]

proposed an IM algorithm named as IM-LPA based on community structure using label propagation. They practice degree centrality to find candidates for the seed nodes before performing label propagation. Salavati et al. [34] came up with the Global Local Ranking (GLR) method that uses the local critical node and gateway node of a community to rank every node in the graph using the closeness centrality measure. Berahmand et al. [35] have introduced a local ranking method named as DCL (Degree, Clustering coefficient, and Location method) that calculates the importance of node based upon the degree of a node, its clustering coefficient, and its location in the network. Rui et al. [36] proposed a Reversed Node Ranking (RNR) algorithm based on the reverse ranking of a node. The algorithm considers that a node is influential if it has a higher degree and if its neighbors are also influential. Wen et al. [37] proposed an approach for finding influential spreaders using the local information dimensionality (LID) method by considering the local structural properties around the central node(i). The method measures the information of the nodes in boxes through the Shannon entropy. The size of the box l around the central node(i) varies from one to ceil($d_i/2$), where d_i is the degree of central node. The objective of variation in the size of the box indicates that the method concentrates on the quasilocal structure about the central node and decreases the time complexity. Huang et al. [38] recommended a heuristic influence maximization technique, which combines community detection and topic awareness into influence diffusion modeling.

3 Proposed algorithm: IM-ELPR

In this section, we present the proposed algorithm named as IM-ELPR using the idea of label propagation and community detection. Information spreading through communities is the fastest way of disseminating information in the entire network because of the structural property and dense connection among the members of a community. A node in a community is more likely to circulate the information to nodes in the same community. Label Propagation is a novel procedure that finds communities in linear time complexity, which is efficient than many other community detection methods. Further, the Relationship matrix is used to refine the community detection process by infusing the modularity parameter of the algorithm. Finally, we select the top k influential nodes from the candidate seed nodes based on the number of other nodes who adopted the same label.

The proposed algorithm consists of four phases:

- Seeding Phase
- Label Propagation Phase
- Merging Communities by Relationship Matrix
- Finding k Influential Nodes

3.1 Seeding phase

In order to find influential nodes in a social network, we first select candidate seed nodes. We use the extended h-index centrality measure to determine the candidate seed nodes. From (3), extended h-index centrality for a node is calculated as the sum of h-index of itself and all of its neighboring nodes. The seeding phase should generate the best possible candidates for the seed nodes in less time. By using extended h-index centrality in the seeding phase, the neighbors up to 3-hops from the given node are taken care of. This covers the local neighborhood appropriately, thereby generating more prominent and effective seed nodes in linear time. We also discuss the reason for choosing the extended h-index over the degree and h-index centrality for the seeding phase with the help of a toy network, as shown in Fig. 1. Node 9 has the highest degree centrality of 7, but this node may not be an influential spreader because most of its neighbors are leaf nodes and are incapable of spreading the information further. Instead, nodes with a higher h-index such as nodes 1,2,3, and 4 can be better spreaders. However, since these four nodes have equal h-index values, the problem of choosing the most appropriate node from among them arises. This problem is solved by the extended h-index, which has different values for these nodes and selects node 3 as the most suitable candidate seed node. The benefit of considering extended h-index (or even h-index) is that it gets less affected by slight changes in the topology of the graph, such as the addition or deletion of some edges between the nodes, which frequently happens in the social networks. For example, the addition of a new node 16 and forming a connection with node 5 does not affect the h-index as well as the extended h-index values of the nodes 1 and 2. This is illustrated in Fig. 1.

The outline of the seeding phase algorithm is presented in Algorithm 1.

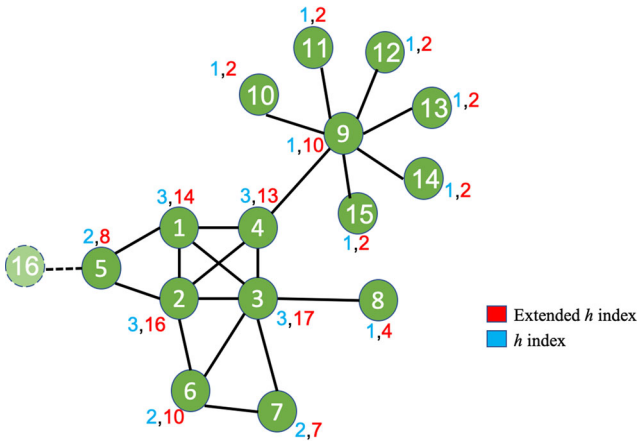

Fig. 1 Toy network for comparison of degree, h-index, and extended h-index centrality

Algorithm 1 Seeding phase.

Result: A set of seed nodes, S

1 Let V be the set of all nodes, W be the set of candidate nodes, and S be the set of seed nodes. Initialise, $W = V$ and $S = \phi$;
2 EH = calculate eh_index(W);
3 **while** $W \neq \phi$ **do**
4 Let u be the node with maximum centrality in W, i.e., $u = \max(EH(W))$;
5 Add u to S, $S = S \cup u$;
6 Remove u from W, $W = W \setminus u$;
7 **for** $v \in N(u)$ **do**
8 Remove v from W, $W = W \setminus v$;
9 **end**
10 **end**

The brief description of the seeding phase algorithm is as follows:

- Initially, we maintain two lists as discussed in line number 1. W represents the set of candidate nodes, which is initially equal to the set of all nodes, $W = V$, where V is the set of all nodes in the network. S denotes the set of seed nodes, which is initially empty, $S = \phi$.
- We calculate the extended h-index for every node and store the values in the list EH. This can be inferred from line number 2.
- Now in line number 4, we choose a node from W, which has the maximum value for extended h-index. If there is more than one node with the same maximum extended h-index value, we choose any one of them.
- As discussed in the line 5-9, we add u to S as a seed node and also remove u and its neighbors from the candidate set W. It ensures that the selected seed nodes are not adjacent to each other, rather far apart, so that the entire network can be adequately covered.
- We repeat lines 3-10 till the candidate node set gets empty, $W = \phi$ and we get the final set of seed nodes i.e. S.

3.2 Label propagation phase

In this phase, communities are formed with the help of seed nodes determined in the last phase in an asynchronous manner. Initially, every seed node is assigned a unique label, and the rest of the nodes have no label. Then in every iteration, the label of a particular node is updated to the label, which is most common among its neighbors. In case more than one label appears the maximum number of times in the neighboring nodes, both the labels are assigned to the node. Now, since each node can belong to more than one community simultaneously, we use a set of labels for each node instead of assigning one label to every node, which is done traditionally. Thus, it allows a single node to have more than one label signifying that a node may be a part of more than one community. The nodes having common labels belong to the same community. The outline of the label propagation phase algorithm is presented in Algorithm 2.

Algorithm 2 Label propagation phase.

Result: A list of label for each node, L and List of communities, C

1 Initialise a unique label for each node in seed node set S;
2 **for** $u \in S$ **do**
3 $LP(u) = random(label)$
4 **end**
5 **repeat**
6 Generate a random sequence of nodes, V;
7 **for** $u \in V$ **do**
8 Find the label set which appears maximum number of times in $N(u)$, $LP(u) = \max_{v \in N(u)} (Count(LP(v)))$;
9 **end**
10 **until** *at least 1 node is updated*;
11 C = list of communities;

The new label set acquired by each node is updated as follows:

$$LP'_u(t) = \max_{lp} \sum_{v \in N(u)} \delta(lp, LP_v(t-1)) \tag{4}$$

where $LP'_u(t)$ is the new label set for node u at time t, $LP_v(t-1)$ is the label set of node v at time $t-1$, lp denotes a particular label value, v is a neighbor of node u and $\delta(.)$ is the extended Kronecker delta function and has value $\delta(lp, LP_v) = 1$ when lp is in the set LP_v ; and $\delta(lp, LP_v) = 0$ when lp is not in the set LP_v.

The brief description of the label propagation phase algorithm 2 is as follows:

- In lines 1-4, each seed node, which has been selected from previous algorithm, is assigned a random label.
- We use the asynchronous label propagation method and generate a random sequence of nodes for each iteration of label propagation. As shown in lines 5-10, for each node, u from a randomly generated sequence of nodes, calculate the most frequent label set. That is, find the labels which occur the maximum number of times in the neighbor set of u. If more than one label has the same frequency, then select all of them and assign this label set to u.
- In line number 11, we generate a list of communities. For each community, we get to know all the nodes and their labels.

3.3 Merging communities by relationship matrix

Relationship matrix (R) is used to compute the similarity between communities and accordingly merge them [40].

We keep on merging the communities till the modularity of the network is maximized. The relationship matrix is a novel method for finding the similarity between obtained communities. It gives a quantitative measure for the relationship among all pairs of communities.

The R matrix is defined as follows:-

$$R = \begin{bmatrix} R_{11} & R_{12} & R_{13} & \cdots & R_{1n} \\ R_{21} & R_{22} & R_{23} & \cdots & R_{2n} \\ \vdots & \vdots & \vdots & \ddots & \vdots \\ R_{n1} & R_{n2} & R_{n3} & \cdots & R_{nn} \end{bmatrix}, \tag{5}$$

where $R_{ij} = \dfrac{E(c_i, c_j)}{\min(|c_i|, |c_j|)}$ subject to $i \in 1, 2, ..., |C|$ and $i \neq j$. The number of common edges between community c_i and community c_j is denoted by $E(c_i, c_j)$. $R_{ii} = m_i$, where m_i is the number of edges in community c_i. Each cell R_{ij} in the R matrix denotes the relationship between the community c_i and c_j. If there are n communities generated by label propagation, i.e. $n = |C|$, then the order of R matrix is $n \times n$. The resulting R matrix is always a sparse matrix because most of the communities are not inter-related to one another and hence, their similarity is 0.

The label propagation algorithm, which we use, forms a large number of smaller communities. Many smaller communities with large similarities can be merged to form a relatively large community for a better perspective. Having two communities c_i and c_j with many common edges can become a limitation for our use case. If both these communities contain an influential node, then their influence can be overlapped. On the contrary, if we assign only one influential node from new merged communities, then it may influence the members with no overlap. Thus, we adopt a method to merge smaller and related communities using a relationship matrix, leading to an overall less and a relevant number of communities. The Algorithm 3 depicting the merging of communities is as follows:

Algorithm 3 Merge communities using relationship matrix.

Result: Set of final community, C'

1 **repeat**
2 Calculate R matrix as per Eq. No. 5 ;
3 Choose maximum value of R_{ij} from the matrix ($i \neq j$);
4 Merge communities c_i and c_j;
5 Calculate the modularity for new communities using Eq. No. 6;
6 **until** *new modularity > previous modularity*;

We also handle the case that a node can have multiple labels to find communities using label propagation. After performing community detection, many smaller size communities arise that have overlapping features and can be a bottleneck for influence maximization purposes. In the algorithm, first, the similarity between every pair of communities is calculated to form the R matrix. We find the maximum value $R_{ij} (i \neq j)$ from the R matrix corresponding to i^{th} row and j^{th} column, and merge these two communities. The modularity for the new set of communities is calculated. The same process is repeated until the new modularity is no longer greater than the previously derived one. In this way, we merge smaller communities to form larger communities.

Modularity is the quantitative measure for detecting communities, which evaluates the structural properties of the communities [41]. The formula for modularity is given as:

$$Q = \frac{1}{2m} \sum_{u,v \in V} \delta(u, v)(A_{u,v} - \frac{d_u d_v}{2m}) \tag{6}$$

where m is total number of edges, $\delta(u, v)$ is the extended Kronecker delta function, which is equal to 1 when u and v belong to the same community and equal to 0 when they are in different communities, $A_{u,v}$ is the adjacency matrix element, d_u is the degree of node u.

3.4 Finding *k* influential nodes

After forming communities through label propagation and merging them, we get labels for each individual node. For selecting influential nodes from the initially selected seed nodes, we find a rank measure for every seed node and sort those values in descending order. Finally, we select the top k nodes as influential nodes. Let LP_v be the initial label for seed nodes. The rank measure $M(v)$ for every seed node can be calculated by the formula:

$$M(v) = \sum_{u \in V} L(u, LP_v) \tag{7}$$

where LP_v is the label of seed node v, V is set of all nodes and $L(u, LP_v)$ is a function which returns 1 when node u has acquired the label of node v, i.e., LP_v, otherwise 0. So, the rank measure $M(v)$ of seed node v is the number of nodes with the same label as that of v. In this manner, a top influential node is one whose label is adopted by the maximum nodes of the network.

Algorithm 4 Finding k influential nodes.

Result: Set of influential nodes

1 Calculate rank measure for each initially selected seed node using Eq. No. 7;
2 Select the top k influential nodes according to their rank values calculated in previous step.;

3.5 Time complexity of the proposed algorithm

We also analyze the time complexity of our proposed algorithm IM-ELPR. For this purpose we assume that our network has n nodes and m edges and $\hat{d}$ be the average degree of the nodes.

1. Seeding Phase: The extended h-index for all the nodes in the network can be calculated in $O(m)$ time. In this phase, finding the node with a maximum extended h-index to populate candidate seed nodes can be done in $O(n)$ time. Therefore, the time complexity of the seeding phase is $O(m+n) = O(m)$.
2. Label Propagation Phase: In this phase, we consider that each node can have $O(\hat{d})$ neighbors, and each of these neighbors can have minimum q labels where q is a constant. So, $O(\hat{d}q)$ time is needed to update the label of one node. For all the nodes, the time required is $O(n\hat{d}q)$ and for T iterations of label propagation, computational time is $O(Tn\hat{d}q)$.
3. Merging Communities: Let us consider that label propagation results in the formation of C communities. In each iteration of merging communities, $O(m)$ time is required to form the R matrix, which is a sparse matrix, and the size of the matrix is to be $C \times C$ leading to $O(C^2)$ time to find the maximum value in the matrix for merging. Therefore, for T' iterations where T' is a constant, total time taken is $O(T'C^2 + T'm)$.
4. Finding k influential nodes: In this phase, we calculate the rank measure for each candidate seed node based on the number of nodes that acquired its label and then finding the top k seed nodes as the influential nodes can be computed in $O(n)$ time.
5. Finally, the overall computational complexity of IM-ELPR is $O(m) + O(Tn\hat{d}q) + O(T'C^2 + T'm) + O(n) = O(T'm)$, which is linear in terms of input size.

3.6 Toy network simulation of the proposed algorithm

For a better understanding of the simulation of the proposed algorithm, we present a toy network depicting all four phases, as shown in Fig. 2. Figure 2a presents a toy network taken as an input containing 115 nodes and 613 edges where all the nodes are initially colored in red. Figure 2b displays the toy network after the seeding phase, where selected seed nodes are colored in green, and the rest nodes are colored in brown. The label propagation phase on the toy network is depicted in Fig. 2c, which generates a total of nine communities where nodes belong to the same community, are colored in the same color. Figure 2d presents the network after performing merging communities operation using R matrix, which leads to seven communities from nine communities. Finally, Fig. 2e depicts the top-10 influential nodes as selected by the proposed method where influential nodes are colored in green, and the rest nodes are colored in brown.

4 Information diffusion model, datasets, performance metrics

This section describes the information diffusion model, real-life network datasets, and performance metrics used in our study.

4.1 Information diffusion model

When a piece of information originates from seed users, predicting its overall spread in the network is essential for the influence maximization (IM). In this paper, the classical independent cascade (IC) model is used as the information diffusion [39]. In the IC model, initial seed nodes try to activate their inactive neighbors. The success of a node u in activating a neighboring node v depends on the propagation probability $p(u, v)$. Each edge $e = (u, v)$ has its own value of probability of propagation. When a set of seeds nodes is chosen, and activation probability $p(u, v)$ for each edge (u, v) is provided, a single simulation of the IC model is evolved in the following discrete steps:-

An active node (u) that gets activated at time t, tries to activate its inactive adjacent node (v), with probability of $p(u, v)$ at discrete time step $t + 1$. After every fulfilled attempt, a neighbor may get activated. In the IC model, every activated node is capable of activating its inactive neighbors only once. Once all the nodes are activated, or there are no remaining active nodes, the propagation ends. The influence spread of seed set S is referred to as the total number of nodes that got activated at the end of the spreading process. To get smooth results, we may need to run many simulations of the IC model. The resulting values are averaged over the total number of simulations of the IC model.

4.2 Datasets

The following used datasets are of different sizes and applications.

- Football [42]: The nodes represent football team and edges represent that two teams have played together.
- Email [43]: The nodes represent the users and the edges represent that email is exchanged between them.
- Jazz Musicians [44] : Network of Jazz musicians where node represents a musician and an edge denotes that two musicians have played together in an band.

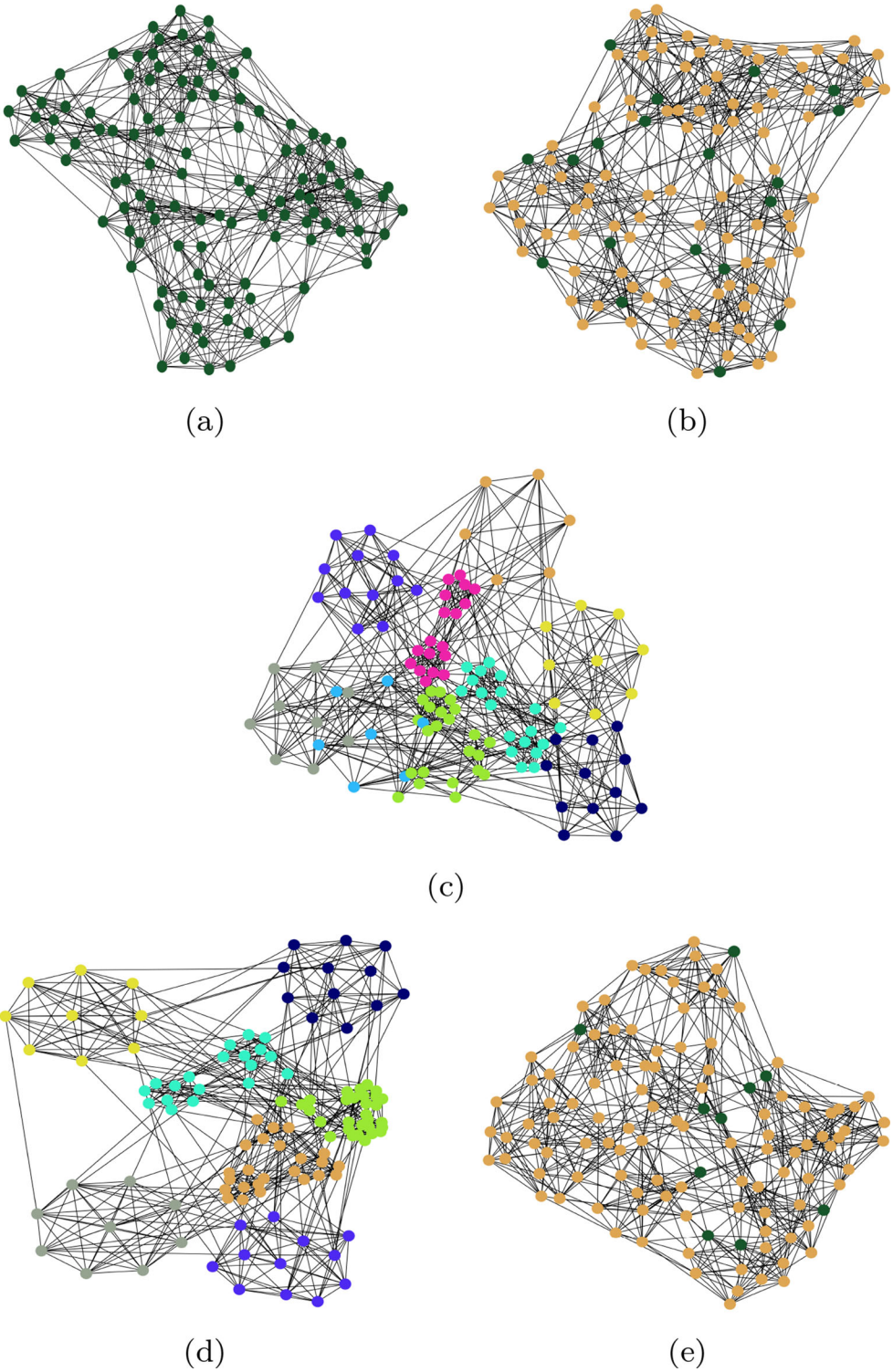

Fig. 2 Toy Network, which explains the working of our algorithm: **a** Input Toy Network **b** Seeding Phase **c** Label Propagation Phase **d** Merging communities using R matrix **e** Selected ten influential nodes colored in green

- Caenorhabditis Elegans [45]: Neural network of neurons and synapses in C. elegans, a type of worm.
- Facebook Pages [46]: This dataset represent blue verified Facebook page network of different categories. Nodes represent the pages and the edges are mutual likes among them.
- Wiki Vote [47]: The dataset contains the Wikipedia voting data from its inception till January 2008. Nodes represent Wikipedia users and the directed edges from node u to node v represent that user u voted on user v.
- Technological Routers [48]: Computer network of routers and their connectivity with one another.

- Gnutella P2P 08 [49]: This is a network of Gnutella hosts from 2002. The nodes represent Gnutella hosts, and the edges represent connections between them.

The brief statistical features of the network datasets used for conducting the experiments are summarized in Table 1 where n, m, D, d_{max}, and $\hat{d}$ represent the number of nodes, number of edges, density, the maximum degree of nodes, and average degree of the nodes respectively. Density (D) of the networks is the ratio of the number of all existing edges to the total possible number of edges in the network [50].

4.3 Performance metrics

The following performance metrics are considered in order to compute the performance of our devised algorithm along with other previously devised ones:

(i) Infected Scale ($F(t)$) The infected scale is the fraction of total nodes that become active at various time steps during the information diffusion process. The metric compares the nodes infected, relative to discrete time steps. The number of nodes getting infected continuously changes with every discrete time step, and the spread of infection peaks at a specific value of time. Infected Scale ($F(t)$) is computed using the following formula:

$$F(t) = \frac{n_a(t)}{n} \tag{8}$$

where $n_a(t)$ is the number of nodes at timestamp t and n is the total number of nodes in the system.

(ii) Final Infected Scale ($F(t_c)$) or Influence spread: The final infected scale or influence spread is the fraction of total nodes that become active at the end of the spreading process caused due to the triggering of the selected set of influential nodes. The number of initial influential nodes directly affects the final infected scale in the network. The fraction of total nodes that act as initial spreaders is called the spreader fraction. Usually, the high value of the spreader fraction leads to the high value of the final infected scale. Considering the real-life network scenarios, comprehending an optimal maximum value of the spreader fraction becomes an important task. The final infected scale ($F(t_c)$) is computed using the following formula:

$$F(t_c) = \frac{n_{\text{total active nodes}}}{n} \tag{9}$$

where n is the total number of nodes and $n_{\text{total active nodes}}$ is the number of nodes that are active after the whole process of information spreading is completed.

(iii) Kendall Tau Correlation (τ): Kendall tau correlation (τ) [51] is employed to determine the precise spreading influence of the selected nodes that act as initial spreaders. This method is to find the correlation between the rank list (L_1) generated by various algorithms with the natural ranking list (L_2) generated by the IC Model. For a pair of seed nodes, if $x_i > y_j$ in the list L_1, and $x_i > y_j$ in actual rank list L_2 then such pair is known as concordant pair otherwise it is called discordant pair. Kendall tau correlation (τ) between two ranked list L_1 and L_2 is computed using the following formula:

$$\tau(L_1, L_2) = \frac{n_{con} - n_{dis}}{\frac{1}{2}n(n-1)} \tag{10}$$

where n_{con} is the number of concordant pairs, n_{dis} is the number of discordant pairs and n is total number of nodes in both lists L_1 and L_2.

(iv) Average Shortest Path Length (L_s): The average shortest path length between selected spreaders is the average of the shortest path length between all possible pairs of selected influential nodes. It determines how efficient the information passing process in a social network is. Usually, a large value of the average shortest path length indicates that the selected influential nodes are evenly spread out across the network and are not concentrated in a small region of the network. This makes a larger value of the metric to be a desirable one as it facilitates the effective and efficient spread of information. The average shortest

Table 1 Brief statistics of datasets

Network	n	m	D	d_{max}	$\hat{d}$
Football	115	613	0.0935	12	10
Email	143	623	0.0613	42	8
Jazz Musicians	198	2742	0.1406	100	27
C. Elegans	297	2148	0.0533	134	15
Facebook Pages	620	2091	0.0109	132	6
Wiki Vote	889	2914	0.0074	102	6
Tech. Routers	2113	6632	0.0029	109	6
Gnutella P2P 08	6301	20777	0.0010	97	6

path length (L_s) is computed using the following formula:

$$L_s = \frac{1}{k \times (k-1)} \sum_{u,v \in S} l_{u,v} \tag{11}$$

where k is the number of influential nodes, S be the set of selected influential nodes, and $l_{u,v}$ is the shortest path length between influential nodes u and v, if any such path exists between them.

5 Experimental results

In this section, we present a comparative analysis of the proposed algorithm named as Influence Maximization using Extended h-index, and Label Propagation with Relationship matrix (IM-ELPR). For the performance comparison, we consider some well known classical algorithms such as Betweenness centrality [14], Greedy algorithm [8], PageRank [16], k-shell centrality [17] and some recently published influence maximization algorithms namely, IM-LPA [33], global local ranking (GLR) [34], DCL (Degree, Clustering coefficient, and location based method) [35], Reversed Node Ranking (RNR) [36], and local information dimensionality (LID) algorithm [37]. We adopt four different performance metrics, as mentioned in Section 4.3, to judge the performance of the proposed algorithm along with various algorithms stated above for the comparisons. We utilized eight different real-life datasets, as listed in Table 1, to perform the extensive analysis. The experimental results are compiled on a personal system with configuration as Intel(R) Core(TM) i7-7700T CPU @ 3.80 GHz processor and 4 Core(s), and 8GB RAM.

We present below the detailed comparisons of the experimental results obtained by the proposed method along with other methods based on each performance measure as listed in Section 4.3:

5.1 Final infected scale ($F(t_c)$) Vs. Spreader fraction

We plot the final infected scale ($F(t_c)$) or influence spread graph by taking various values of spreader fraction on the x-axis and the obtained value of the final infected scale on the y-axis. We keep spreader fraction values in the range 0.01 and 0.08 for the datasets having a total number of nodes less than 2000, and when total nodes are higher than 2000, the spreader fraction is taken in between 0.003 and 0.045. Different values of spreader fraction are used for smaller and bigger datasets because the final top k influential nodes selected may either be too small for smaller datasets or too large for larger datasets. Hence, we use relatively larger spreader fraction value for smaller datasets and relatively smaller spreader fractions for larger datasets. The $F(t_c)$ values in the resulting graphs are the average values produced by 100 independent simulations of independent cascade (IC) information diffusion model. Here, one simulation of the IC model means running the information diffusion model one time to propagate the information in the network and computing the influence spread originating from the selected seed noes. The obtained results for $F(t_c)$ are depicted in Fig. 3. The proposed algorithm, along with all the considered algorithms for comparisons, are simulated to calculate $F(t_c)$ values on all the datasets with different activation probability (p) in the IC model. This is because each dataset has a different number of nodes, density, and structural properties. Figure 3a depicts the result of the American Football dataset. We take activation probability (p) value as $p = 0.05$. This dataset is relatively small, and almost all algorithms perform similarly in the beginning. However, when the spreader fraction is more than 0.07, the proposed algorithm outperforms other algorithms. In the case of the Email dataset, we consider probability as $p = 0.30$. In this case, as the spreader fraction (number of influential nodes) increases, our approach slightly performs better as per Fig. 3b followed by the Greedy method. Figure 3c presents the result on Jazz Musicians with probability values $p = 0.1$. This network is relatively dense, and our approach performs pretty well. The second-best approach is the Greedy method. Results for C. Elegans are shown in Fig. 3d, with probability value, $p = 0.25$. For all spreader fractions, our method outperforms all other methods. Here, the second-best algorithm is LID. Figure 3e represents the results of Facebook Pages, which is a slightly larger network than previous networks. We have used probability value $p = 0.55$. This network has relatively less density, and thus the probability for activating neighboring nodes in the IC model is kept high as compared to other networks. IM-ELPR, IM-LPA, and RNR perform better than all other algorithms, but our algorithm outperforms all, including IMLPA and RNR. For the Wiki Vote network, the probability used is $p = 0.3$. As depicted in Fig. 3f, this network is also less dense. The proposed method performs better than IM-LPA, and both these methods surpass other methods. Figure 3g illustrate the result of Technological Routers, which is a medium-sized network. Probability values chosen are, $p = 0.35$. In this network, our algorithm carries out much better than others. This is because of the less density, as each node is connected to a very less number of nodes. Hence, when the probability is less, a situation may arise where a node doesn't activate any of its neighbors even when it has inactive neighbors. In the case of Gnutella P2P, we took activation probability, $p = 0.2$. For all the spreader fraction (and hence for all k), the proposed method is far better than any of the other algorithms, as depicted in Fig. 3h. From the results obtained in Fig. 3, it is observed that the

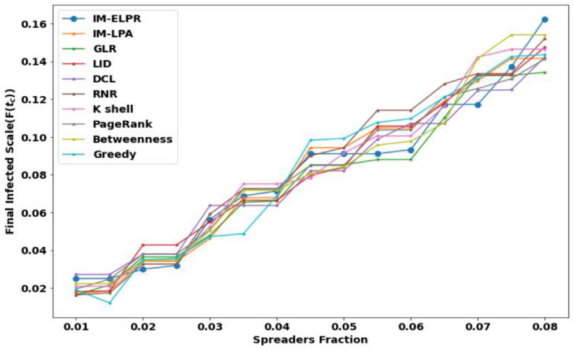

(a) Football , p=0.05

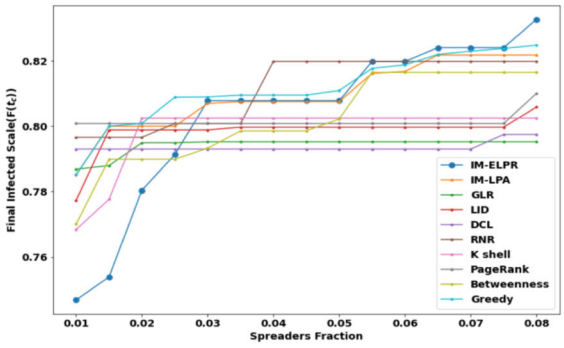

(b) Email , p=0.3

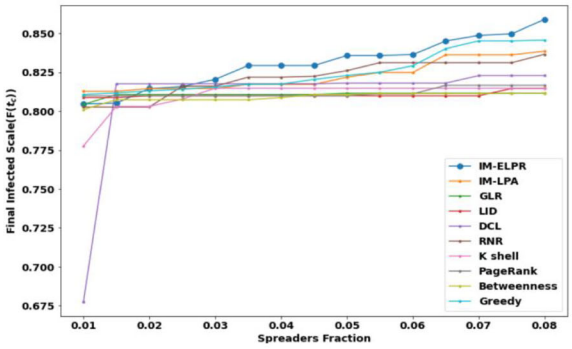

(c) Jazz , p=0.1

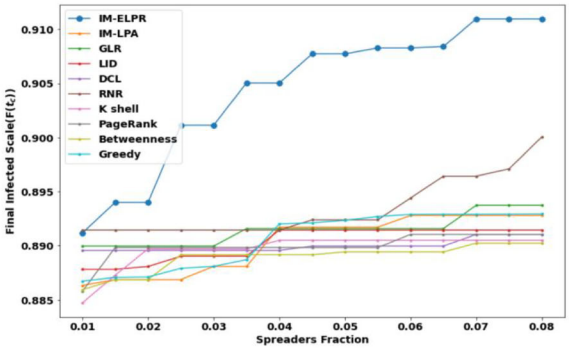

(d) C.Elegans ,p=0.25

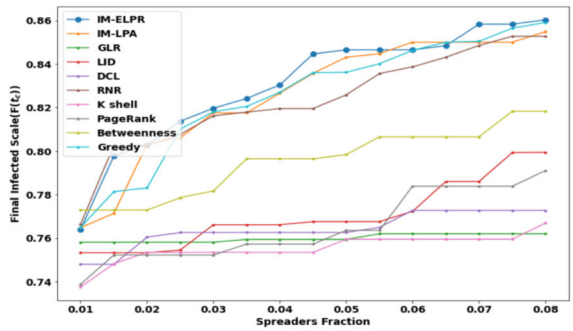

(e) Facebook Pages,p=0.55

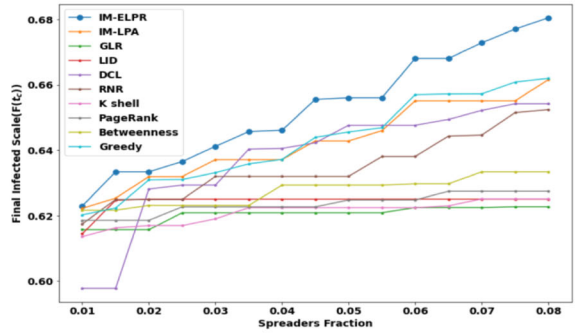

(f) Wiki-Vote, p=0.3

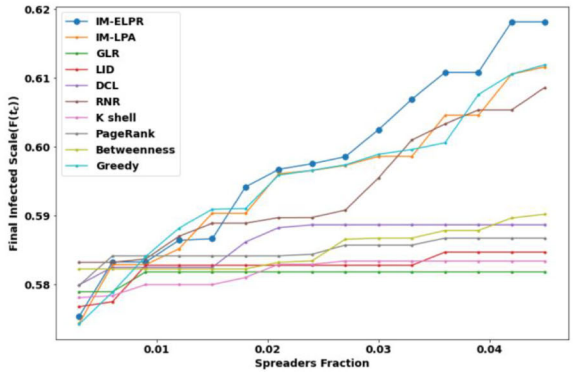

(g) Tech. Router, p=0.35

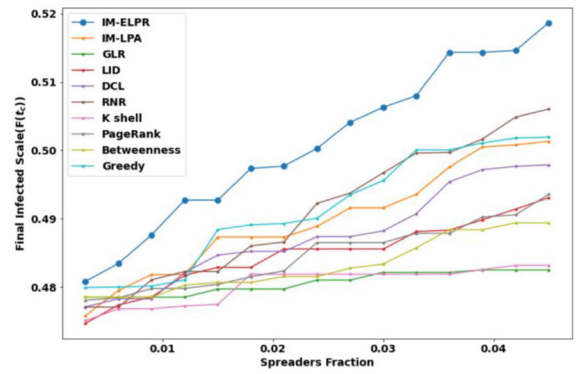

(h) Gnutella P2P 08, p=0.2

Fig. 3 **a**–**g** Final infected scale vs. spreader fraction values for different datasets- Football, Email, Jazz, C. Elegans, Facebook, Wiki Vote, Tech Router, and Gnutella P2P. The results are generated over 100 independent simulations of the IC model with given activation probability (p) value in the result of each dataset

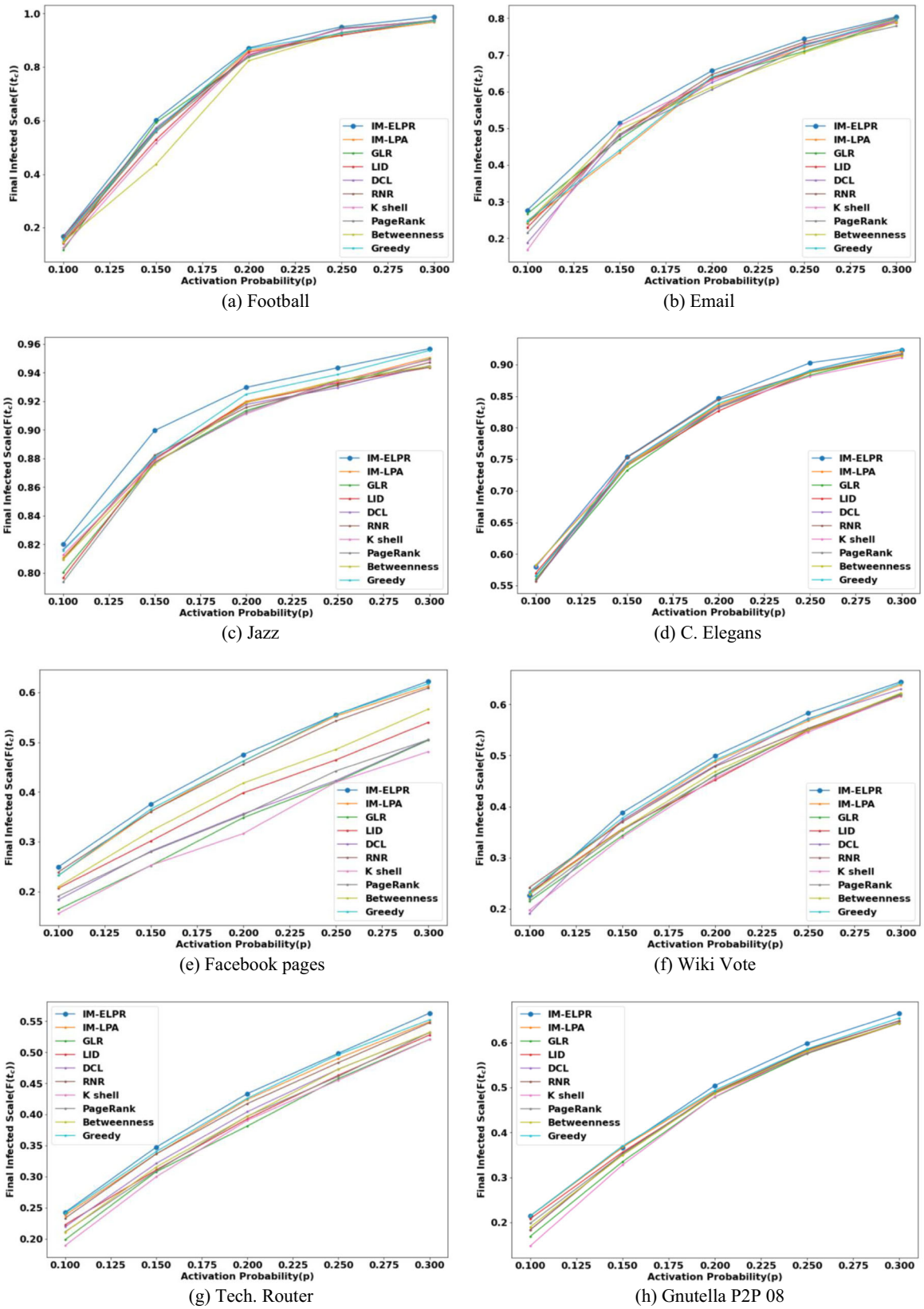

(a) Football (b) Email

(c) Jazz (d) C. Elegans

(e) Facebook pages (f) Wiki Vote

(g) Tech. Router (h) Gnutella P2P 08

Fig. 4 **a**–**g** Final infected scale vs. activation probability (p) values for different datasets- Football, Email, Jazz, C. Elegans, Facebook, Wiki Vote, Tech Router, and Gnutella P2P. The results are generated over 100 independent simulations of the IC model by taking the top 3% of nodes as the initial spreaders

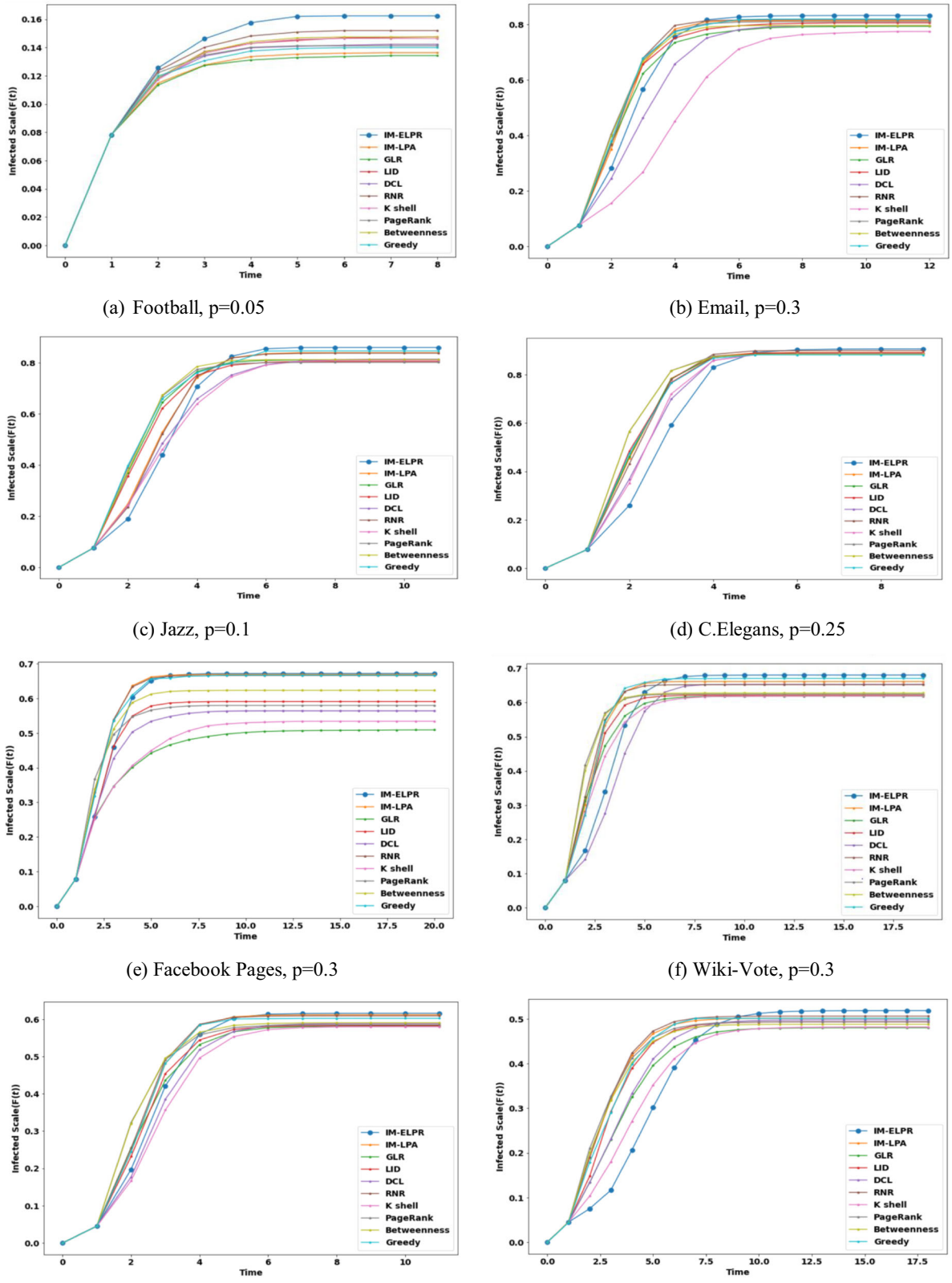

(a) Football, p=0.05

(b) Email, p=0.3

(c) Jazz, p=0.1

(d) C.Elegans, p=0.25

(e) Facebook Pages, p=0.3

(f) Wiki-Vote, p=0.3

(g) Tech Router,p=0.35

(h) Gnutella P2P 08, p=0.2

Fig. 5 **a**–**g** Infected Scale $F(t)$ vs. Time values for different datasets - Football, Email, Jazz, C. Elegans, Facebook Pages, Wiki Vote, Tech Routers, and Gnutella P2P. The results are generated over 100 independent simulations of the IC model with a given activation probability (p) value in the result of each dataset

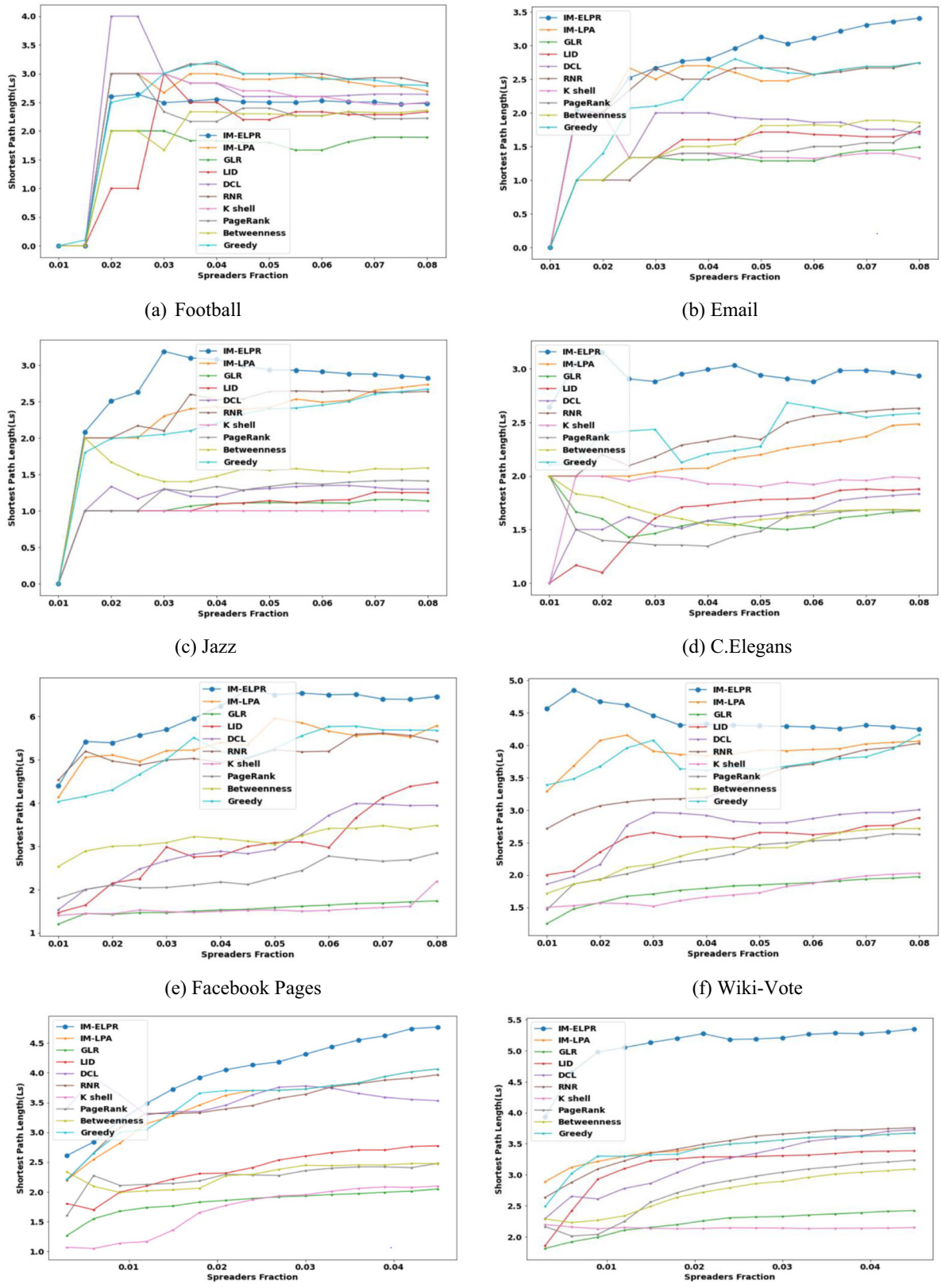

(a) Football (b) Email

(c) Jazz (d) C.Elegans

(e) Facebook Pages (f) Wiki-Vote

(g) Tech. Router (h) Gnutella P2P 08

Fig. 6 **a**–**h** Average shortest path length (L_s) Vs. Spreader Fraction values for different datasets - Football, Email, Jazz, C. Elegans, Facebook Pages, Wiki Vote, Tech Routers, and Gnutella P2P 08

proposed algorithm performs better and consistently well than other algorithms considered in the comparison. In most of the cases, the second-best algorithm is the Greedy method followed by LID, RNR, or IM-LPA, and other techniques.

5.2 Final infected scale ($F(t_c)$) Vs. Activation probability (p)

We also perform the impact on the value of final infected scale by varying activation probabilities. Figure 4 shows the plot of final infected scale ($F(t_c)$) vs. activation probability (p) on all the datasets used in this study. To perform the analysis, we keep the values of activation probability (p) in the range of 0.10, 0.15, 0.20, 0.25 and 0.30. We consider the top 3% of the nodes as the initial spreaders nodes chosen by various methods to obtain the value of final infected scale against a particular value of activation probability (p). The results are obtained over 100 independent simulations of IC model. From the results, it is evident that as the value of activation probability increases the value of final infected scale or influence spread also increases in all the algorithms of influence maximization for each dataset. The obtained results depicts that our proposed algorithm (IM-ELPR) performs uniformly well and outperforms all other algorithms on this evaluation parameter.

5.3 Infected scale ($F(t)$) Vs. Time

We employ the infected Scale ($F(t)$) metric to compare the results of various algorithms along with the proposed algorithm, which compares the fraction of active nodes at each discrete timestamp during the process of information spreading. The results for $F(t)$ vs. Time are shown in Fig 5. Here, time on x-axis denotes the time-step of the independent cascade (IC) information diffusion model. In this paper, we utilize the IC model to disseminate the information originating from selected seed nodes. At the time, t=1, only selected seed nodes are infected. At $t = 1$, initial seed nodes try to activate their neighbors with activation probability (p). Hence, the active node that gets infected at time t tries to infect its inactive neighbors at time $t = t+1$, and this process continues. We run the IC model for 100 times. The value of the infected scale ($F(t)$) on y-axis is the fraction of total nodes that are active averaged over 100 iterations of the IC model for any particular time-step. To perform the Infected scale ($F(t)$) vs. Time analysis, we consider the number of spreader fractions as 0.08, i,e, top 8% of the nodes are chosen as influential spreader nodes under each algorithm. Considering the number of nodes in each network as mentioned in Table 1, the corresponding values of influential spreader nodes come out to be 9, 11, 15, 23, 49, 71, 169, and 504 for the datasets Football, Email, Jazz, C. Elegans, Facebook Pages, Wiki Vote, Tech Routers and Gnutella P2P, respectively. For example, the Football dataset has a total of 115 nodes whose 8% comes out to be is 9. The values of the fraction of active nodes in the results are the average values produced by 100 independent simulations of the IC model.

In majority of the networks, our approach starts at a lower pace, that is in the beginning the number of active nodes in our method are less. But, as the time progresses, our method outshines other methods and the active nodes are much greater. The slow start but higher performance at later time can be explained by the use of extended h-index in the seed phase as it identifies nodes which spread influence up to nodes that are 3-hops away. Hence, the influence is spread out to a relatively more substantial part of the network. In the case of Facebook and Tech Router datasets, the performance of the proposed algorithm is similar to the Greedy, M-LPA, and RNR algorithms but leads to all other approaches. On the datasets like Football, Jazz, C. Elegans, and Wiki Vote, the Greedy method performs second-best after the proposed algorithm (IM-ELPR).

Table 2 Kendall Tau values for different datasets calculated using various algorithms such as IM-EL (IM-ELPR), IM-LPA, GLR (Global Local Ranking), LID (Local Information Dimensionality), DCL (Degree, Clustering coefficient, and Location-based method), RNR (Reversed Node Ranking), KS (k-shell), PR (PageRank), BW (Betweenness) centrality and GD (Greedy method)

Dataset	IM-EL	IM-LP	GLR	LID	DCL	RNR	KS	PR	BW	GD
FT	0.77	0.66	0.51	0.75	0.57	**0.85**	0.45	0.71	0.48	0.72
Email	**0.88**	0.54	0.49	0.82	0.54	0.81	0.47	0.65	0.50	0.67
Jazz	0.69	0.53	0.47	**0.79**	0.53	0.77	0.56	0.61	0.59	0.46
CE	0.79	0.62	0.51	**0.87**	0.58	0.79	0.53	0.74	0.56	0.62
FB	**0.83**	0.73	0.60	0.80	0.48	0.78	0.44	0.70	0.49	0.57
WV	0.71	0.65	0.51	0.69	0.60	0.63	0.42	0.66	0.45	**0.75**
TR	**0.78**	0.61	0.57	0.74	0.54	0.69	0.48	0.71	0.44	0.70
GP2P	**0.85**	0.79	0.59	**0.85**	0.47	0.78	0.57	0.67	0.53	0.75

Bold entries signify the maximum value attained by a particular method in each dataset

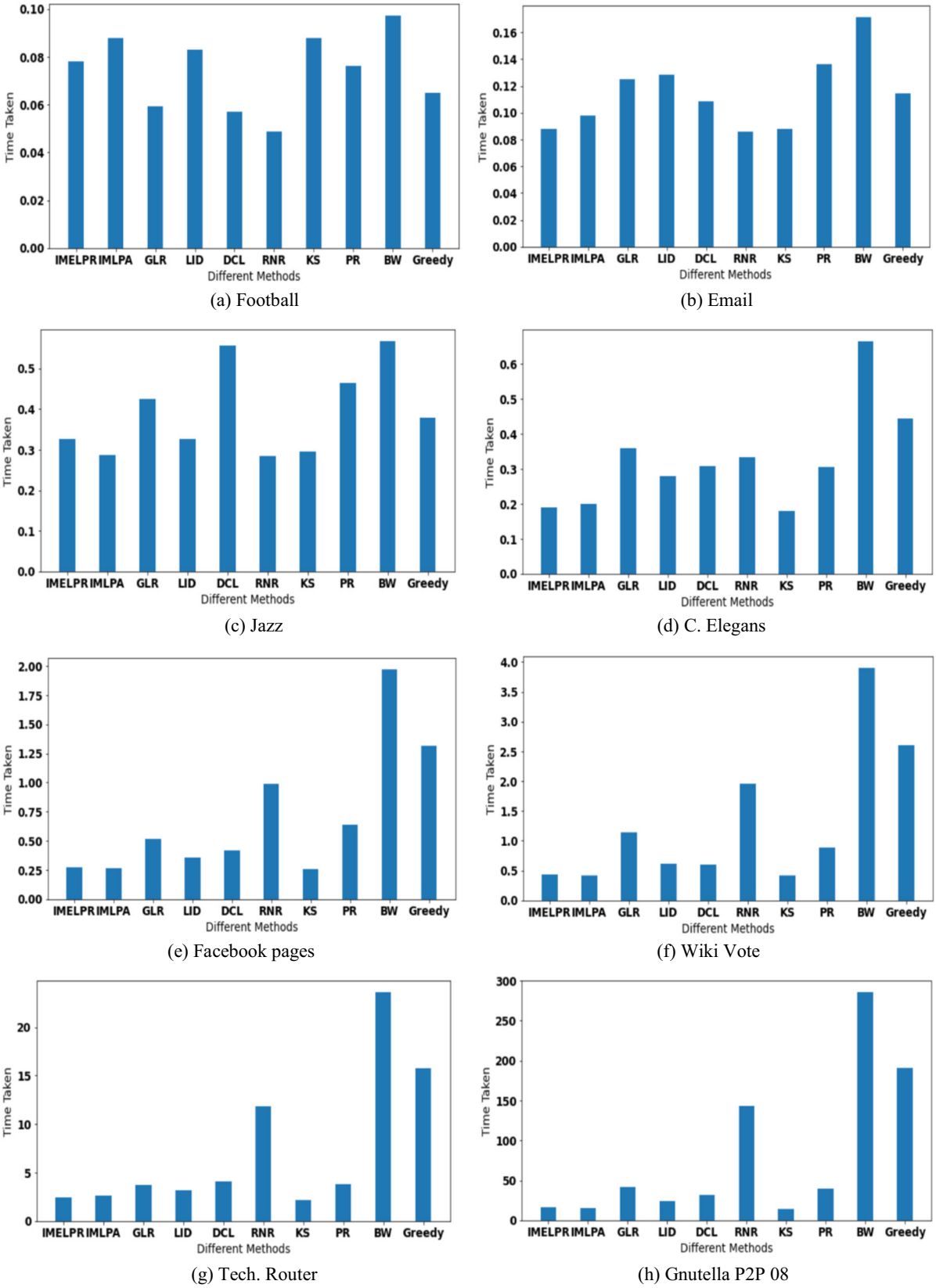

(a) Football (b) Email

(c) Jazz (d) C. Elegans

(e) Facebook pages (f) Wiki Vote

(g) Tech. Router (h) Gnutella P2P 08

Fig. 7 **a**–**h** Execution time (in second) comparison of various algorithms to rank the spreading capability of nodes for different datasets - Football, Email, Jazz, C. Elegans, Facebook Pages, Wiki Vote, Tech Routers, and Gnutella P2P 08. The result is shown for finding the top 3% of nodes based on their spreading capability

5.4 Average shortest path length (L_s) vs. spreader fraction

After locating the influential spreaders by different algorithms in this study, the average shortest path length (L_s) between selected spreaders is computed using (11). The result is plotted, taking spreader fraction on the x-axis and average shortest path length on the y-axis. The results for L_s vs. spreader fraction are shown in Fig. 6 for all datasets. In all the datasets except football, the value for L_s value attained by IM-ELPR is considerably more than all other approaches, which is the same pattern in case of the final infected scale ($F(t_c)$) Vs. Spreader fraction, as observed in Fig. 3. We can see from Fig. 6, L_s Vs. spreader fraction graph, the influential nodes are chosen by our method is more scattered in the network than the influential nodes of any other method, leading to high influence spread by the proposed method.

5.5 Kendall Tau's correlation

Kendall tau coefficient (τ) is an important metric that can be used to judge the performance of IM algorithms. It is employed to determine the correlation between the rank list generated by each algorithm with the actual rank list obtained from the IC spreading model. In order to get the results, we simulate the IC model independently 50 times. The value of activation probability (p) is considered as 0.075, 0.2, 0.1, 0.1, 0.5, 0.35, 0.35, and 0.165 for datasets Football (FT), Email, Jazz, C. Elegans (CE), Facebook Pages (FB), Wiki vote (WV), Tech. Router (TR), and Gnutella P2P 08 (GP2P), respectively. For each dataset, the activation probability (p) value used here is the same as that used in the metric $F(t_c)$. The obtained results of various algorithms on different datasets are listed in Table 2. In the majority of the datasets, the Kendall tau value produced by various methods is very close. From the results, we can observe that on the Email, Facebook pages, Tech. Routers, the Kendall tau (τ) value attained by the proposed algorithm, is maximum. However, in the case of the Football dataset, RNR performs best followed by IM-ELPR. For the Jazz and C.Elegans datasets, LID produces the best result followed by the RNR method. For the Wiki vote dataset, the greedy method produces the best result followed by IM-ELPR. For Gnutella P2P 08 dataset, IM-ELPR, and LID, both the methods produce the same results and outperform other methods.

5.6 Execution time comparison

We also assess the absolute time required to produce the ranking of nodes in terms of their spreading capability by the proposed model and other methods in comparison. In Fig. 7, we compare the actual running time required to rank the nodes based on the spreading capability using the proposed algorithm, IM-ELPR, and all other algorithms. We performed the examination on all the eight datasets as listed in Table 1. For each dataset, we compute the time taken in seconds by each algorithm to find the top 3% nodes as the chosen seed nodes. We observed that the actual time taken by IM-ELPR for the generation of the ranked list is relatively less as compared to other methods in most of the cases. In the football dataset, our algorithm takes .09 second, which is slightly more than the time taken by GLR, DCL, RNR, and Greedy method. For the Email dataset, the time requires to find the top spreaders by the proposed algorithm is 0.10 second; however, RNR, IM-LPR, RNR, and k-shell each require 0.08 second. For the Jazz dataset, the proposed method takes just 0.28 second to generate the ranking list and outperforms all other techniques. Similarly, in the case of Facebook pages, Wiki Vote, and Tech. Router datasets, our method requires 0.25 seconds, 0.5 seconds, 3 seconds respectively, and beats all other methods. To process 6301 nodes and find the top 3% nodes, i.e., 190 nodes in Gnutella P2P 08 network, the proposed algorithm takes only 21 seconds, which is significantly faster than GLR, DCL, RNR, PageRank, Betweenness, and Greedy method.

According to the results achieved in all the performance metrics namely final infected scale ($F(t_c)$), infected scale ($F(t)$), average shortest path length (L_s), Kendall tau correlation (τ), and actual execution time comparison the proposed algorithm IM-ELPR for influence maximization delivers better results than many well-known classical and recently published methodologies.

6 Conclusion

Finding influential spreaders is a prominent activity to achieve viral marketing and influence maximization in complex networks like social networks. The presence of community structure is quite common in social networks, and information propagation can take place rapidly among the members of the community. In this paper, we introduce the IM-ELPR algorithm as a solution to influence maximization problem using the idea of label propagation and community structure. We obtain the initial seed nodes using extended h-index centrality, and then label propagation is performed where each seed node is assigned a unique label. At the end of label propagation, the detection of communities is accomplished. Further, we merge the related community using a relationship matrix to increase the modularity. The relationship matrix proves to be more effective in handling larger networks as the merging of communities removes the many small communities and causes the maximum spread of information in the network

with minimal effective influential nodes chosen from the merged community. We utilise four performance metrics to judge the performance of our algorithm alongside the performance of other various popular methods of influence maximization. The experimental result obtained on eight real-life networks of different sizes and applications shows that the proposed algorithm outperforms many well-known existing algorithms. Further, the overall time complexity of the IM-ELPR algorithm is linear in terms of the network size, which suggests the effectiveness of the proposed algorithm in large-scale networks.

References

1. Boccaletti S, Latora V, Moreno Y, Chavez M, Hwang DU (2006) Complex networks: Structure and dynamics. Phys Rep 424(4-5):175–308
2. Strogatz SH (2001) Exploring complex networks. Nature 410(6825):268–76
3. Mislove A, Marcon M, Gummadi KP, Druschel P, Bhattacharjee B (2007) Measurement and analysis of online social networks. In: Proceedings of the 7th ACM SIGCOMM conference on Internet measurement, pp 29–42
4. Krasnova H, Spiekermann S, Koroleva K, Hildebrand T (2010) Online social networks: Why we disclose. J Inform Technol 25(2):109–125
5. Heidemann J, Klier M, Probst F (2012) Online social networks: a survey of a global phenomenon. Comput Networks 56(18):3866–3878
6. Li Y, Fan J, Wang Y, Tan KL (2018) Influence maximization on social graphs: a survey. IEEE Trans Knowl Data Eng 30(10):1852–72
7. Chen W, Wang C, Wang Y (2010) Scalable influence maximization for prevalent viral marketing in large-scale social networks. In: Proceedings of the 16th ACM SIGKDD international conference on Knowledge discovery and data mining, pp 1029–1038
8. Kempe D, Kleinberg J, Tardos É (2003) Maximizing the spread of influence through a social network. In: Proceedings of the ninth ACM SIGKDD international conference on Knowledge discovery and data mining, pp 137–146
9. Kumar S, Panda BS (2020) Identifying influential nodes in Social networks: Neighborhood Coreness based voting approach. Physica A: Statistical Mechanics and its Applications, pp 124215
10. Domingos P, Richardson M (2001) Mining the network value of customers. In: Proceedings of the seventh ACM SIGKDD international conference on knowledge discovery and data mining, ACM, pp 57–66
11. Goldenberg J, Libai B, Muller E (2001) Talk of the network: a complex systems look at the underlying process of word-of-mouth. Market lett 12(3):211–23
12. Lü L, Chen D, Ren XL, Zhang QM, Zhang YC, Zhou T. (2016) Vital nodes identification in complex networks. Phys Rep 650:1–63
13. Bródka P, Skibicki K, Kazienko P, Musiał K (2011) A degree centrality in multi-layered social network. In: 2011 international conference on computational aspects of social networks (CASoN), IEEE, pp 237–242
14. Freeman LC (1977) A set of measures of centrality based on betweenness, Sociometry, pp 35–41
15. Bonacich P (2007) Some unique properties of eigenvector centrality. Social Networks 29(4):555–64
16. Page L, Brin S, Motwani R, Winograd T (1999) The pagerank citation ranking: Bringing order to the web. Stanford InfoLab
17. Kitsak M, Gallos LK, Havlin S, Liljeros F, Muchnik L, Stanley HE, Makse HA (2010) Identification of influential spreaders in complex networks. Nat Phys 6(11):888–93
18. Leskovec J, Krause A, Guestrin C, Faloutsos C, VanBriesen J, Glance N (2007) Cost-effective outbreak detection in networks. In: Proceedings of the 13th ACM SIGKDD international conference on Knowledge discovery and data mining, pp 420–429
19. Liu W, Chen X, Jeon B, Chen L, Chen B. (2019) Influence maximization on signed networks under independent cascade model. Appl Intell 49(3):912–28
20. Bozorgi A, Samet S, Kwisthout J, Wareham T (2017) Community-based influence maximization in social networks under a competitive linear threshold model. Knowl Based Syst 134:149–58
21. Newman ME (2004) Detecting community structure in networks. Eur Phys J B 38(2):321–30
22. Ferrara E (2012) A large-scale community structure analysis in Facebook. EPJ Data Sci 1(1):9
23. Fortunato S (2010) Community detection in graphs. Phys Rep 486(3-5):75–174
24. Kumar S, Panda BS, Aggarwal D (2020) Community detection in complex networks using network embedding and gravitational search algorithm. Journal of Intelligent Information Systems, pp 1–22
25. Huang H, Shen H, Meng Z (2020) Community-based influence maximization in attributed networks. Appl Intell 50(2):354–64
26. Chen D, Lü L, Shang M-S, Zhang Y-C, Zhou T (2012) Identifying influential nodes in complex networks. Phys A 391:1777–1787
27. Hirsch JE (2005) An index to quantify an individual's scientific research output. Proc Natl Acad Sci 102(46):16569–72
28. Liu Q, Zhu YX, Jia Y, Deng L, Zhou B, Zhu JX, Zou P. (2018) Leveraging local h-index to identify and rank influential spreaders in networks. Physica A: Statistical Mechanics and its Applications 512:379–91
29. Rui X, Yang X, Fan J, Wang Z (2020) A neighbour scale fixed approach for influence maximization in social networks. Computing, pp 1–23
30. Lü L, Zhou T, Zhang QM, Stanley HE (2016) The H-index of a network node and its relation to degree and coreness. Nat Commun 7:10168
31. Zareie A, Sheikhahmadi A (2019) EHC: Extended H-index Centrality Measure for identification of users' spreading influence in complex networks. Physica A: Statistical Mechanics and Its Applications 514:141–55
32. Raghavan UN, Albert R, Kumara S (2007) Near linear time algorithm to detect community structures in large-scale networks. Phys Rev E 76(3):036106
33. Zhao Y, Li S, Jin F (2016) Identification of influential nodes in social networks with community structure based on label propagation. Neurocomputing 210:34–44
34. Salavati C, Abdollahpouri A, Manbari Z (2019) Ranking nodes in complex networks based on local structure and improving closeness centrality. Neurocomputing 336:36–45
35. Berahmand K, Bouyer A, Samadi N (2019) A new local and multidimensional ranking measure to detect spreaders in social networks. Computing 101(11):1711–33
36. Rui X, Meng F, Wang Z, Yuan G (2019) A reversed node ranking approach for influence maximization in social networks. Appl Intell 49(7):2684–98
37. Wen T, Deng Y (2020) Identification of influencers in complex networks by local information dimensionality. Inf Sci 512:549–62. Feb 1
38. Huang H, Shen H, Meng Z, Chang H, He H (2019) Community-based influence maximization for viral marketing. Appl Intell 49(6):2137–50

39. Goldenberg J, Libai B, Muller E (2001) Talk of the network: a complex systems look at the underlying process of word-of-mouth. Mark lett 12(3):211–23
40. Li X, Zhou S, Liu J, Lian G, Chen G, Lin CW (2019) Communities detection in social network based on local edge centrality. Physica A: Statistical Mechanics and its Applications 531:121552
41. Newman ME (2006) Modularity and community structure in networks. Proc Natl Acad Sci 103(23):8577–82
42. Girvan M, Newman ME (2002) Community structure in social and biological networks. Proc Natl Acad Sci 99(12):7821–6
43. Rossi R, Ahmed N (2015) The network data repository with interactive graph analytics and visualization. In: Twenty-Ninth AAAI Conference on Artificial Intelligence
44. Gleiser PM, Danon L (2003) Community structure in jazz. Advances in Complex Systems 6(04):565–73
45. Duch J, Arenas A (2005) Community detection in complex networks using extremal optimization. Phys Rev E 72(2):027104
46. Rozemberczki B, Davies R, Sarkar R, Sutton C (2019) Gemsec: Graph embedding with self clustering. In: Proceedings of the 2019 IEEE/ACM International Conference on Advances in Social Networks Analysis and Mining, pp 65–72
47. Leskovec J, Huttenlocher D, Kleinberg J (2010) Signed networks in social media. In: Proceedings of the SIGCHI conference on human factors in computing systems, pp 1361–1370
48. Spring N, Mahajan R, Wetherall D (2002) Measuring ISP topologies with Rocketfuel. ACM SIGCOMM Comput Commun Rev 32(4):133–45
49. Ripeanu M, Foster I, Iamnitchi A (2002) Mapping the gnutella network: Properties of large-scale peer-to-peer systems and implications for system design. arXiv:cs/0209028
50. Xu G, Zhang Y, Li L (2010) Web mining and social networking: techniques and applications. Springer Science & Business Media
51. Kendall MG (1938) A new measure of rank correlation. Biometrika 30(1/2):81–93

Publisher's note Springer Nature remains neutral with regard to jurisdictional claims in published maps and institutional affiliations.

Affiliations

Sanjay Kumar[1,2] · Lakshay Singhla[3] · Kshitij Jindal[4] · Khyati Grover[5] · B. S. Panda[1]

Lakshay Singhla
lukkysinghla@gmail.com

Kshitij Jindal
jindal.kshitij@yahoo.com

Khyati Grover
khyati.grover@yahoo.com

B. S. Panda
bspanda@maths.iitd.ac.in

1 Computer Science and Application Group, Department of Mathematics, Indian Institute of Technology Delhi, Hauz Khas, New Delhi, 110016, India

2 Department of Computer Science and Engineering, Delhi Technological University, Main Bawana Road, New Delhi, 110042, India

3 Samast Technologies Pvt Ltd, Sector 29, Gurgaon, 122001, India

4 Nuvogen Limited, Ctra. Moraira- Teulada, 444 C.C. Baraclays, Moraira, 03726, Alicante, Spain

5 Amazon India, Gurgaon, 122004, India

In Silico Drug Repositioning Of Hydroxychloroquine (HCQ) For the Treatment of Viral Diseases

Bhawna Singh[1], Asmita Das[2]

[1]*Student, Department of Biotechnology, Delhi Technological University, Main Bawana Road, Delhi.*

[2]*Assistant Professor, Department of Biotechnology, Delhi Technological University, Main Bawana Road, Delhi.*

Corresponding Author: singhbhawna031@gmail.com

Abstract: - Emerging and re-emerging viral infections are a big human concern and veterinary public health, and the development of antiviral drugs is urgently needed. The high cost of drug development limit the scalability of this antiviral approach. Drug repositioning or drug repurposing or drug profiling is the discovery of new applications for approved or failed drug. Drug repositioning is the development of new approved drug applications. The cost of bringing a medicine to the market is around one million which include clinical and preclinical trials. Repositioning of drugs help in cutting down costs as well as time involve in initial validation and authorization. Recently, there are so many drugs that have been tried and tested for COVID-19 treatment .One of these drugs is an antimalarial drug called as Hydroxychloroquine (HCQ).

Key Words: —*Hydroxychloroquine (HCQ), COVID-19, Antiviral drugs.*

I. INTRODUCTION

Antiviral activities of HCQ made them potential candidate to study against viral diseases. In this study we are going to repurposed hydroxychloroquine(HCQ) for the treatment of viral diseases[1]. The standard method of product production requires vast quantities of time and energy before a compound is labored into the free market. Despite huge investments, a lead molecule often has minimal chances of entering the open market. The research molecule's itinerary remains unpredictable in its entire lifecycle. This situation causes new pharmaceutical companies to discover new drugs on dreams. Drug repositioning is one of the feasible choices for beginners in the area of new drug science. Drug discovery is the process of identification of biologically active small molecules against different disease conditions [4]. Classical drug research starts with the identification of disease targets, the detection of compounds and optimization, ADMET studies and finally to market. Developing a Single molecule may take 10−17 years and the success rate can be as low as 0.01%. The global annual budgets of R&D became $ 130 billion with fewer new drugs. The numbers of new drugs or New Molecular Entities (NME) released in the market are decreased and there is acute pressure on the R&D circle to increase the number of candidate drugs in the late stage pipeline [5].

Considering the large amount of investment that has been put recently in drug development only 23 drugs were approved in the year 2010, which is drastically less when compared to the drugs approved (53 drugs) a decade ago. These NMEs have to go through a number of pharmacokinetic and toxicity studies for their release into market. Molecules with potential drug like activities are evaluated simultaneously for their toxicity effects in cell and animal models. After a strenuous and systematic evaluation of drug activity and other properties, several drug like molecules may have to be dropped because of undesired bio-distribution and toxicity. A new concept called “drug repositioning” is being emerged in the pharmaceutical R&D circle. Drug repositioning is the discovery of new indications for approved drugs. Drug repositioning also known as drug profiling or drug repurposing. The cost of bringing a new medicine to the market is around one million which include clinical and preclinical trials. Drug repositioning procedure is generally performed during the phase of drug development to modify or extend an active molecule's distribution line. The COVD-19 pandemic represents a significant challenge to the world from a health and financial perspective [2].The diseases has a high mortality rate and is very contagious, making it difficult to manage to manage .The complexity of COVID-19 is partially

Manuscript received March 20, 2021; revised March 21, 2021; accepted March 22, 2021. Date of publication March 23, 2021.
This paper available online at www.ijprse.com
ISSN (Online): 2582-7898

evidenced by the disparity of symptoms from extremely mild in childrens and young adults to much more severe in older age group. We propose the urgent repositioning of an old drug hydroxychloroquine (HCQ) as an ideal antiviral prophylactic against COVID-19. This drug is capable of inhibiting the replication of some intracellular microorganism which includes viruses also. HCQ has the ability to block viral infection as it increase endosomal PH and also interfaces with the glycosylation of cellular receptor of SARS-COV .It is an antiviral agents as it is also known to inhibit quinine reductase-2, which is involved in sialic acid biosynthesis .It prevents the attachment of SARS-COV-2 to the target cells by interfacing with ACE 2 receptor glycosylation.

So, the antiviral activities of HCQ made them potential candidate to study against viral diseases. Viruses are major risk for human health and economic well-being. [3] In this study we are going to repurposed hydroxychoroquine for the treatment of other viral diseases such as Ebola, Zika, influenza, chikungunya etc.

II. METHODOLOGY

Protein Selection:

X ray crystallographic structure of all the targets protein was downloaded from PDB.

Ligand Selection:

Structure of HCQ was retrieved from PubChem database (http://pubchem.ncbi.nlm.nih.gov). HCQ was downloaded in SDF format and converted into PDB format file using SMILE.

Molecular Docking:

The 3D structure of targets was used for molecular docking with hydroxychloroquine using Autodock.

III. RESULTS

The results are described in the table and figure belows.

Table.1. Showing binding free energy

PDB ID	DISEASES	DOCKING SCORE
P03120	GENITAL WARTS	-7.71
Q77DJ5	EBOLA	-5.41
OO4350	LASSA FEVER	-7.65
Q786F3	MEASLES	-8.70
QO7817	MARBURG HEMORRHEGIC FEVER	-7.71
015164	VIRAL MENINGILITIS	-5.41
P128823	VIRAL ENCEPHALITIS	-7.65
P06672	RABIES	-11.73
P08563	RUBELLA	-8.70
P0COE6	CHICKENPOX	-6.89
P07612	SMALLPOX	-7.95
P03300	POLIO	-8.38
076463	ROSEOLA	-6.89
P24941	CHICKENGUNYA	-7.95
Q03243	ROTAVIRUS	-11.73

IV. CONCLUSION

Recently, there are so many drugs that have been tried and tested for COVID-19 treatment. One of these drugs is an antimalarial drug called as hydroxychloroquine (HCQ). HCQ has antiflammatory properties and are used for immune disorder treatment such as diabetes, arthritis etc.

Reports suggest that HCQ could be a candidate for COVID treatment .This drug is capable of inhibiting the replication of some intracellular microorganism which includes viruses also. HCQ has the ability to block viral infection as it increase endosomal PH and also interfaces with the glycosylation of

Cellular receptor of SARS-COV .It is an antiviral agents as it is also known to inhibit quinine reductase-2, which is involved in sialic acid biosynthesis .It prevents the attachment of SARS-COV to the target cells by interfacing with ACE 2 receptor glycosylation.

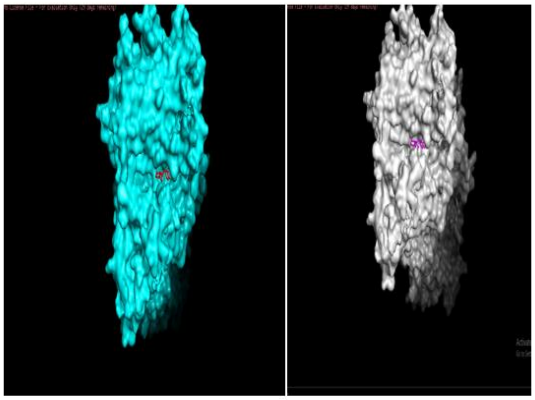

Fig.1. showing docking of Hydroxychloroquine with rabies and rubella respectively

REFERENCES

[1]. Keyaerts, L. Vijgen, P. Maes, J. Neyts and M. Ranst, "In vitro inhibition of severe acute respiratory syndrome coronavirus by chloroquine", Biochemical and Biophysical Research Communications, vol. 323, no. 1, pp. 264-268, 2004.

[2]. M. Vincent et al., "Journal search results - Cite This For Me", Virology Journal, vol. 2, no. 1, p. 69, 2005. Available: 10.1186/1743-422x-2-69.

[3]. M. Wang et al., "Remdesivir and chloroquine effectively inhibit the recently emerged novel coronavirus (2019-nCoV) in vitro", Cell Research, vol. 30, no. 3, pp. 269-271, 2020.

[4]. R. Nardi and A. Mazzone, "Italian Journal of Medicine online su Science Direct", Italian Journal of Medicine, vol. 3, no. 3, p. 125, 2009.

[5]. Sardana D, Zhu C, Zhang M, Gudivada RC, Yang L, Jegga AG (2011). Drug repositioning for orphan diseases. Brief Bioinform 6(22):484-488.

[6]. Deotarse P. P.1, Jain A. S.1, Baile. M. B, et.al. (2015). Drug repositioning: a review. Int J Pharma Res Rev22 (5):1239-1249.

[7]. Ashburn TT, Thor KB (2010). Drug repositioning: identifying and developing new uses for existing drugs. Nat Rev Drug Discov 437(7058):491-493.

[8]. Sleigh SH, Barton CL (2010). Repurposing strategies for therapeutics. Pharm Med483 (7931):570-575.

[9]. Swinney, D. C. and Anthony, J. (2011). How were new medicines discovered? Nature reviews Drug discovery, 10(7):507–519.

[10]. Teo, S. K., Stirling, D. I., and Zeldis, J. B. (2005). Thalidomide as a novel therapeutic agent: new uses for an old product. Drug discovery today, 10(2):107–114.

[11]. Y. Li and S. Jones, "Drug repositioning for personalized medicine", Genome Medicine, vol. 4, no. 3, 2012.

[12]. R. Insa, "Drug Repositioning: Bringing New Life to Shelved Assets and Existing Drugs. Edited by Michael J. Barratt and Donald E. Frail", ChemMedChem, vol. 8, no. 2, pp. 336-337, 2012.

[13]. R. Nardi and A. Mazzone, "Italian Journal of Medicine online su ScienceDirect", Italian Journal of Medicine, vol. 3, no. 3, p. 125, 2009.

[14]. Takashita E, Meijer A, Lackenby A, Gubareva L, Rebelo-de-Andrade H, Besselaar T, et al. Global update on the susceptibility of human influenza viruses to neuraminidase inhibitors, 2013-2014. Antiviral Res. (2015) 117:27–38.

[15]. Devillers J. Repurposing drugs for use against Zika virus infection. SAR QSAR Environ Res. (2018) 29:103–15.

[16]. Pushpakom S, Iorio F, Eyers PA, Escott KJ, Hopper S, Wells A, et al. Drug repurposing: progress, challenges and recommendations. Nat Rev Drug Discov. (2018).

[17]. Strittmatter SM. Overcoming drug development bottlenecks with repurposing: old drugs learn new tricks. Nat Med. (2014) 20:590–1.

[18]. Bishop NE (1998). "Examination of potential inhibitors of hepatitis A virus uncoating". Intervirology.

[19]. Hopkins AL. Network pharmacology: the next paradigm in drug discovery. Nat Chem Biol. (2008).

[20]. Reddy AS, Zhang S. Polypharmacology: drug discovery for the future. Expert Rev Clin Pharmacol. (2013).

[21]. Naveja JJ, Dueñas-González A, Medina-Franco JL. Chapter 12-drug repurposing for epigenetic targets guided by computational methods. In: Epi-Informatics, ed J. L. Medina-Franco (Boston: Academic Press).

[22]. Cichonska A, Rousu J, Aittokallio T. Identification of drug candidates and repurposing opportunities through compound-target interaction networks. Expert Opin Drug Discov. (2015) Meeting on Electrical, PC and Correspondence Designing (ECCE).

[23]. Uzman, "Molecular Cell Biology (4th edition) Harvey Lodish, Arnold Berk, S. Lawrence Zipursky, Paul Matsudaira, David Baltimore and James Darnell; Freeman & Co., New York, NY, 2000, 1084 pp., list price $102.25, ISBN 0-7167-3136-3", Biochemistry and Molecular Biology Education, vol. 29, no. 3, pp. 126-128, 2001.

Global Journal of Flexible Systems Management
https://doi.org/10.1007/s40171-021-00265-x

ORIGINAL RESEARCH

Innovation Framework for Excellence in Higher Education Institutions

Manoj Kumar Sharma[1] · **R. C. Sharma**[1]

Received: 23 January 2021 / Accepted: 1 March 2021
© Global Institute of Flexible Systems Management 2021

Abstract *Innovation is now emerging as an "Asset" in current global health scenario caused by pandemic, so higher education institute (HEI) should put high value primium on this asset, i.e. innovation, and with the passage of time, the intervention and demand of innovation in higher education cannot be undermined. In this context, it is very important that the real understanding of the process of innovation is highly desirable. Knowledge-driven economy has established its roots globally and with the passage of time, it will grow as banyan tree. The challenges before higher education institutions (HEIs) is to train the people to the highest level of efficiency, creativity and entrepreneurship. HEIs have to choose between being globally distinct and the best vs. enormous and the largest. The biggest challenge before HEIs is financially self-reliance as the government and research funding is very scarce and it will further decrease in the coming time. Innovative solutions will be in demand and the new primium currency of the future. Public objectives in teaching and learning process embedded with innovation must be supreme. In this paper, an innovative framework is emphasized for HEIs for their academic excellence. Triple helical model is no longer sufficient. HEIs have to think and add more dimensions to their innovative functioning which make them efficient and environment friendly. The objective of this study is that the HEIs should become globally distinct and competitive, by creating their own distinct products, services and related processes which proposed high value to their customers and stakeholders for their economic robustness and sustainability in flexible mode.*

Keywords Competitive · Economic strength · Flexible · Globally distinct · Higher education institutions (HEIs) · Innovation · Sustainability · Teaching and learning process

Introduction

Intrinsic motivation, autonomy and inherent diversity are the key elements of innovations. Ancient India is known for innovations—decimal system, Fibonacci numbers, binary numbers, Wootz steel, ruler, seamless metal globe and many more. Today, Pentium microprocessor chip is attributed to an Indian—Vinod Dham, and the USB port for seamless transfer of data is credited to another Indian—Ajay Bhatt. Albert Einstein rightly said, "We owe a lot to the ancient Indians, teaching us how to count. Without which most modern scientific discoveries would have been impossible". India had great teachers of all times and once considered a heaven for knowledge creation in all the areas of human endeavours. The *MAHARISHI*(महर्षि) of India not only excelled in their chosen fields but also influenced the thoughts and actions of the society through their teachings. One of the greatest teachers—Acharya Chanakya, famous wordings on education, "Education is the best friend. An educated person is respected everywhere. Education beats the beauty and the youth" is an example of diversity of all times. The very distinguished teacher of modern India—Dr. Sarvepalli Radhakrishnan's, message is very loud and

✉ Manoj Kumar Sharma
prof.mksharma@dtu.ac.in; ceo.manoj@alumni.iitd.ac.in

R. C. Sharma
rchsharma@dce.ac.in

[1] University School of Management and Entrepreneurship (USME), DTU East Delhi Campus, Delhi Technological University (Established By Govt. of NCT of Delhi), Delhi 110042, India

Published online: 26 March 2021

clear on autonomy—"The end-product of education should be a free creative man, who can battle against historical circumstances and adversities of nature, and exhibits versatility and efficacy of education". It is the intrinsic motivation that made Acharya Chanakya and Dr. Sarvepalli Radhakrishnan, and many more very distinct and innovative. The proposition is—*experiences of the past are very useful to innovate your present and future*.

Literature Review

In 2020 ranking, "*The QS World University* ranked (2020), Massachusetts Institute of Technology" as the top university in the world, while "*The Times Higher Education World University* ranked (2020) Oxford University" as number 1. The proportion of the population in higher education in India is still less than 10% of 130 crores, while Korea, Japan and the USA are having 69.8%, 61.5% and 50.4%, respectively, in the age group of 25–34 years. Demographic expert Wolfgang Lutz et al. (2014) said that education permanently improves a person's cognitive abilities, allowing better planning and self-control throughout the rest of their life. A study (Singh, 2016) on Indian higher education system revealed that we are delivering a twentieth century education to twenty-first century youth and preparing them for the unknown economy and society. There is naturally an enormous dichotomy between what is needed and what we deliver, and the result is obvious—large scale of unemployment in educated youths. New education policy has taken steps to make the education student-centric instead of teacher-centric, and it creates a hope that we shall be doing better in the time to come. The policy aims to identify and foster the unique capabilities of the students, examine and promote creativity and critical thinking, improve and enhance decision making and innovation with extensive use of technology.

Innovation in education system—mainly higher education and research, demands flexibility (Shukla et al. 2019; Evans & Bahrami, 2020) and out-of-box thinking. And when combined with the entrepreneurial philosophy, experiential learning and modern IT-enabled click, it can renovate the quality of life and prosperity of nations. Even the evaluation process should incorporate more elements, like multi-dimensional and multi-directional solutions. Greater magnitude and all-inclusive with national and global mentors and learners are the need of today as well as that of future. An optimal mix of business orientation, entrepreneurial skills and leadership skills; compassion, ethics and values; and crowd-sourcing of ideas and projects is important for gig economy. It is more pertinent to an innovative education system that higher education institutions (HEIs) should impart education and skills to create, innovate, problem solve, crisis management, design thinking, critical think, teamwork and create prototypes or templates for artificial intelligence. What comes to ones' mind when we dialogue about innovation in an HEI—a university, a science research centre, an engineering college, a medical institution, a management school, a design academy, a professional society or a scholastic foundation of national or global repute? If you say that the process of innovation is very challenging and demanding, and many times serendipitous and fortuitous, in the present era, it is very critical for the success of institutions, its students, its faculty and its reputation and global standing.

When one visits to VISION and MISSION statements of different kinds of institutions, one will always find some common words. An analysis of 291 vision statements and 338 mission statements of the universities worldwide by Cortes-Sanchez (2017) identified that the five most frequently used terms were "research", "university", "world", "knowledge" and "education", and the five least frequent terms were "enterprising", "preservation", "respect", "heritage" and "lifelong". Global, excellence, multi-skilled, learning, creative, innovation, entrepreneurial, etc., are the new additions in the Cortes-Sanchez's list. Let us have a look on mission statements of some of the universities.

- "Massachusetts Institute of Technology-To advance knowledge and educate students in science, technology, and other areas of scholarship that will best serve the nation and the world in the twenty-first century"
- "Oxford University-To deliver life-enhancing experiences to help students worldwide to develop personally and professionally and that enrich their future opportunities".

  About 30 years back, none of the university or institute in India was using mission statement (MS) and/or vision statement (VS) to exhibit its propensity. But now both mission and vision statements are used as tactical planning gadgets worldwide. Though it has been contended that these statements represent the actual purpose and future course of action for the academic institutions, the available literature on MS and VS content analyses has shown no correlation between the two. However, the use of MS and VS by the academic institutions has resulted in a necessity for self-awareness, an overall emphasis on state-of-the-art knowledge to the students, a general focus on research and innovation and an aspiration to be global. Let us examine the followings:
- "IIT Kharagpur-The Institute aligns all its activities to serve national interest and seeks-To provide broad-

based education, helping students hone their professional skills and acquire the best-in-class capabilities in their respective disciplines: To draw the best expertise in science, technology, management and law so as to equip students with the skills to visualize, synthesize and execute projects in these fields: To imbibe a spirit of entrepreneurship and innovation in its students; To undertake sponsored research and provide consultancy services in industrial, educational and socially relevant areas".

- "Delhi Technological University-To establish centres of excellence in emerging areas of science, engineering, technology, management and allied areas; To foster an ecosystem for incubation, product development, transfer of technology and entrepreneurship; To create environment of collaboration, experimentation, imagination and creativity; To develop human potential with analytical abilities, ethics and integrity; and To provide environment friendly, reasonable and sustainable solutions for local and global needs".

From the above, it is evident that mission statement of Delhi Technological University is having all the elements of innovation—ideation, execution, collaboration and value creation.

Innovative Ideation

The process (Celuch et al. 2014; Dam & Siang, 2019; Fleming, 1978; O'Reilly et al. 2019; Serdyukov & Makhluf, 2014) of forming new ideas, new images, new similes, new idioms, new horizons, new concepts, new beginning, new management, new technology or altogether a new world that makes complete sense—comprehensive, widespread, extensive, unique, exclusive and exceptional, is highly challenging. How can an HEI think, design, translate and achieve such ideation? Even ideation should embrace all the elements of innovation (Dorow et al. 2015; Scaglione et al. 2019). The HEIs need to possess some critical proficiency to have a competitive advantage during foreseeable period, which depend on half-life of change in education system. Innovative ideation process has been identified and promoted by educational leaders for the global advantage of the institution, the university or the country education. HEIs are at nascent state in the process of training or teaching others who can design and develop a valuable teaching model and curricula. As educators prepare effective human resources of tomorrow, it is critical that we understand the situational path of progress that can prompt the design of innovative annotations for the solution of complex organizational issues. Innovative ideation starts with inputs, grows with personnel and impacts the organization and keeps flowing from one end to other depending on HEI management culture. Success of one innovation takes it to others; patents and ideas are the raw materials, and design thinking is a lens that helps us to make an innovative idea to the real one.

It is now well established (Petersson & Lundberg, 2018) that ideation comprises six basic constituents: subject—the education system and its characteristics; ideation mechanism—the process of innovation; the innovators—the experts group involved in ideation; decision takers—the management group evaluating ideation; innovativeness—characteristics for evaluating idea quality; and standards—parameters for determining the worth of ideation. Evaluation of ideation along with setting standards is the most critical to reach on the top or to become number 1. Detailed R&D or deliberation on the ideation will finally depend on the rate of idea generation; the total number of ideas generated during entire duration of discourse; identification of innovative, more innovative and outstanding ideas; and then "Quantify" the "QUALITY" ideas (Reinig et al. 2007).

A large number of institutions have shown great faith in their employees and imbued in its ideation process. Adobe encourages its employees to use the company starter kit for generating new ideas which are supported by liberal seed funding. "Hackathon", an intense idea-generation process, is very popular among several MNCs, software developers and HEIs. It has been very useful in improving customer service, advertising movements, internal operations, and even for innovative process and product development (Singh & Sushil, 2004). All idea-generation techniques generally promote incremental innovations. Ideation process is composed of scale of ambition and innovation zone bounded by definite boundaries. Setting a scale of ambition involves in defining aspiration for a new business, corporates strategy and promise and propagates a thinking process from existing to large with incremental advances. Innovation in HEIs cannot be scaled to infinite. It is imperative to put precincts around ideation by defining the markets, commerce models, positive/negative situations and/or clientele to focus on. The people-oriented ideation methods, like Hackathons, Crazy 8 s, etc., can evolve a plethora of ideas that can be used for innovation. Ideation is an essential vocation but not adequate first step in ambidexterity (Katic & Agarwal, 2018; Ganuthula & Sinha, 2019). Even a creative and innovative ideation approach does not give final verdict, and finally, you have to choose the good ideas that are worth incubation.

Execution of Quality Ideation

A global model for the management and development of knowledge in HEIs is based on incubation. Equipped with potentially flexible resources (Bondzi-Simpson &

Agomor, 2021), it is capable of taking new missions in almost all the areas of global and local importance. Self-initiation by US universities during the Second World War to take on military R&D responsibilities did wonders in US victory; Resource Crunch in Brazil during 70–80s was handled successfully by the universities, initiating large-scale technology projects by establishing innovative incubators. The HEI shares innate incubators that sometimes play an entrepreneurial role in the evolution of its own development as well as in the development of innovative enterprises (Melnik et al. 2019; Sharahiley, 2020). The University of Zambia, during communication breakdown of the country, extended its internal network across the country, leading to the foundation of ZAMNET.

In the year 2019, "Blue energy" and "Life Science district" were the key technologies, which earned Stanford University the top slot among the Reuters' ranking of the World's Most Innovative Universities. Out of 728 patents, 397 were commercially successful with commercial impact score of 75.2. Innovative incubation is linked with quality ideas that HEIs can patent, publish, produce and market. Success of Stanford is facilitated by its innovative researchers and its multi-dimensional strength. Founded in 1425, KU Leuven has been assessed Europe's most innovative university in 2019. With 305 patents and commercial impact score 43.3, KU is known for new generation of solar panels that can efficiently produce hydrogen gas out of thin air, creating new record of efficiency. An array of 20×1.6 sqmtrs. panels could meet the energy needs of an average Belgian family for an entire year. Pohang University of Science & Technology has achieved a distinct position in Asia in 2019 Reuters' ranking. Founded in 1986, the university is having 349 patents with commercial impact score of 48.8 and developed artificial corneas that are 3D-printed out of tissue-derived "bioinks"; invented a method to keep therapeutic stem cells in place inside target organs using a protein secreted by mussels; and became the first university in Korea to offer short "nano-degree" masters programs. One thing is common in these top ranking HEIs and that is R&D for new technology to the benefit of world population. Also, novel thinking in R&D of academics has made these universities the most innovative in the respective region and globally also. The most distinct disclosure of incubation is that digital revolution is accelerating. Advances in automation, the digitization of information, unprecedented access to data and the globalization of knowledge are transforming every sector of economy (Sushil, 2015).

Universities and HEIs, retaining their core mission of educating the next generation, must embrace innovation to catalyse economic development by adopting all or some of the 12 technologies—mobile Internet, automation of knowledge work, the Internet of things, cloud technology, advanced robotics, autonomous and near-autonomous vehicles, next-generation genomics, energy storage, 3D printing, advanced materials, advanced oil and gas exploration and recovery and renewable energy. Innovation ecosystems and economies of the HEIs can be improved by fostering entrepreneurship, encouraging collaboration with private sector, promoting diversity and inclusion and exploring the nexus of technology and society.

The technical universities have become the focal point to fill gaps in the region's innovation. HEI experts play hybridized roles to start entrepreneurial academics, academic industrialists, business strategy in government and many more. The incubators are institutions that encourage and provide a home for these hybridized roles. The powers of knowledge, imbibed in HEIs, change the agenda for economic development policy especially at the regional level. For example, establishment of university during the decades of 70s and 80s in UP state drastically changed the patterns of higher education. Similarly, technical institutions in Tamil Nadu, Karnataka and Maharashtra widely affected the economy and the society in these States. Conversely, the exercise of power, at the multinational, national and regional levels, encourages knowledge producers. Demand in computer science and information technology, energy sciences and molecular biology has opened new vistas not only for the HEIs but also to industry. It is adopted by both to move from basic to applied research to production.

Innovations demand for triple/quadruple helix approach (Hattangadi, 2019) innovate further. Initially, a linear model of education was there in the HEIs—teachers were imparting available knowledge to the students and some research. DNA's "double helix" model was extended in education by intertwining industries into it. HEIs–industry–government interactions are the basis of triple helix model (Leydesdorff & Etzkowitz, 1998). The HEIs and other knowledge-producing institutions; industry, including high-tech start-ups and multinational corporations; and the government at various levels have joined together to innovate further. While industry and government have traditionally been epitomized as prime spheres, in the triple helix model, HEIs are posited to be a principal sphere. The extent of overlap and the dominance of the 3 will depend on situation. If State dominates, it will have major share, while in a democracy, all will share equally. The triple helix model is also diverse from separate institutional spheres. From either of the starting points, organizational spheres are "taking the role of one other" spinning-off hybrid institutions and actions—the innovation movement, embodying elements of the triple helix. HEIs are now focusing on "quadruple helix model" incorporating professional societies, alumni and research institutions as the 4th loop of system. At present, the role of these institutions

is very limited, but in future, it will expand and play a dominant role in innovating HEIs. An incremental approach is always more beneficial. Once the process of ideation is finalized, the new beginning is required to be processed. In past 3 decades, HEIs and universities, particularly in private sector, have adopted this. However, in a very well-developed system, same approach will work. To incubate, one can adopt either "outside-in" or "inside-out" model; in the former, boundaries are made permeable to all, while in the latter, core team members are involved in the process.

Chesbrough and Bogers (2014) have observed that all the smartest people do not work for a company, and that an institution does not have to conduct the research to gain from it. Apple, Google, Amazon and Intuit tap the creativity of outsiders by sharing their intellectual property to develop new products; Lego, P&G invited customers to suggest ideas for new products and services; NASA, InnoCentive and Kaggle organized contests for participants to find solutions; and IBM, Wikipedia and Facebook fostered networks or communities of interest. In HEIs, human capital is the most important. Each one of the experts can contribute in the process. However, the experience and expertise of the professors so much varied, in design as well as in concept, that its assimilation needs great thinking and efforts. HEIs and universities may establish a start-up ecosystem whose sole objective should be to gain a deep insight into the innovation proposed. Further, it may identify and exploit synergies between different opportunities for growth, new technologies and new curricula and new markets. The start-up ecosystem of HEIs may adopt the model of David Kelley/IDEO on design thinking. It provides vital clues and broad spectrum on incubation and scaling.

Innovation in Quality Ideas

Incubation of quality ideas is the pathway to reach to the goal. Though selection of quality idea itself sets the goal, achieving it successfully by marching on E^3-path (E^3 is energy efficient, environment friendly and economizing nature) is important. Madjar and Shalley (2008) examined effects of multiple goals on three different tasks and concluded that assignment of goals had a positive, significant effect on the innovation. Further research indicated that assigning goals to individual on all tasks exhibited a higher level of creative performance. Goal setting is a course of action to set intents, objectives and aspirations for HEIs, and this helps in achieving higher levels of performance. Patterson and Zibarras (2017) documented goal setting as an indispensable part of university management. Doran (1981) proposed that in an HEI, goal setting should follow SMART—specific, measurable, achievable, relevant and time bound, which will be highly beneficial for an academic administrator to achieve better results.

American Society on Higher Education (Boris et al. 2008; Brennan et al. 2010) emphasized the importance of diverse team—both demographic diversity and diversity of social roles to achieve bigger goals with higher performance. Research has identified eight common team member roles: Completer-Finisher, Implementer, Team Worker, Specialist, Monitor Evaluator, Coordinator, Plant, Shaper and Resource Investigator (Belbin, 1981, 1993, 2004; Arizet et al. 2007; Dierendonck & Groen, 2008, 2011; Smith & Yates, 2011). Effective team leaders are aware of the different roles that individual team member has adopted and uses this awareness to lead the team (Clawson & Huskin, 2006). Whatever expertise the team members may possess, they will proceed through stages, and a deep understanding of these stages is important for success. During the forming stage, it is important that the team members devise innovative process to know each other and find out the most appropriate ways and means to discuss, deliberate and work together. The storming and norming stages are the key for the successes and innovations. The team members engage themselves to resolve and find solutions to overcome the conflicts. The stages will witness setting up of formal or informal collective rules to design the framework. During the performing stage, innovation in working together with logic and openness to accomplish the goals and agreement on the detailed document for the quality idea are important. Team may go to adjourning stage, if so decided, but the innovation is a continuous process for achieving new goals for the organization. Successful team leaders always keep an eye on the whole process to keep themselves aware of the developmental stages. They choose to intervene at the time and space that makes the whole process the most effective. Integration of goals, roles and stages in HEI teams is important to have an innovative preposition to have a radiant success for the organization.

SMART will always be in the centre. Roles of team members can be compartmentalize, but it will be more appropriate to interchange the roles within a time frame to achieve higher levels of performance. All the team members must exhibit highest level of clarity in understanding each element of SMART (Aghera et al. 2018; Belbin, 1996; Bjerke & Renger, 2017; Fleming, 1978; Ogbeiwi, 2017). A goal that would simply say, "We will do our best" is fuzzy and not specific. The goal, "Department of Biotechnology is in high demand and we should increase the graduation intake by 50% in the year 2021" is specific. Specific goals are more likely to result in higher team performance. Similarly, measurable is an important element of goal setting. For example, a goal that states, "We will increase/reduce the elective papers in UG by 2 in each

semester" or "each student is required to complete a project in relevant industry in the vacations after 2nd semester" is measurable. However, a goal that states "It will be better to improve learning experiences of the students" or "writing skills of each student will be enhanced" would be difficult to measure.

Setting achievable goals are bound to motivate team. The team should always keep aside too high or not achievable goals, e.g. "We will admit only top 20% of the students who appear in the admission test 2022", could be achievable and therefore motivate the team. However, a goal that states "We will admit largest number of students in UG courses in the country in 2022" could be too high and therefore will not motivate the team because they could not see how it could be accomplished. Attainable goals are better and more likely to result in higher team performance. Relevant goals have important meaning within the context, must imbibe the mission and strategies of the university and should be consistent with aspiration of all the stakeholders within the university and to the nation at large. For example, a goal that states "We will invite 500 companies for job placement of students" is relevant. But if one say "We will increase our involvement in community based organizations and social services" may not be as relevant to the purpose of the team. Relevant goals are always better and result in higher team performance. Time is important and when one say that my goals are time-bound. Then, the HEI wishes to accomplish it by a specific time or date. By making the goal time bound, it will be possible for teams to know when they should focus their energies toward accomplishing the goal. A goal that states "In academic year 2021–2022, we will increase the number of faculty peer-reviewed publications by 10%" is time-bound. A goal that states "We need to improve the quality of our research productivity" is not time-bound. Time-bound goals (Belbin, 1996) are better and always lead to higher team performance. So, decision-making teams of the university must always opt for SMART which will result in higher performance. Setting goals alone will not achieve the optimal level of performance. The effectiveness of these goals will be enhanced when they are used in a context in which teams understand the different roles that team members play, and also the stages of the life cycle of teams. Thus, when all of the members of the team focus on the same SMART goal, the team will be more likely to accomplish that goal.

Team Roles in Higher Education-Innovations

Academic leader and team members are always building blocks of the higher education institutions. Some people have formal roles, and many others may have informal roles. Theory of Belbin (1993, 1996, 2004) is very important in team building. Idea that each of us possesses different behaviour pattern that determines the behaviour of one in relation to another in facilitating the progress of a team is well established with the passage of time. It has been identified that there are common clusters of these behaviours, and these clusters are stable enough to be separately identifiable. In a team, there are nine main roles, and all the roles are significant, though some have a higher profile than others. Everybody seems to have a preference for one or more of these "Team Roles" when behaving naturally in a group. If you have more than one 'natural role', then you can switch between them if you choose, and this is useful knowledge if you ever need to fill a different role in a team. Using Belbin model (1996), it is easier to predict whether a team would succeed or fail. Thus, the decision-making leader can make a failing group succeed by adding somebody with the right role or make a successful group fail by taking away a vital supporting role. For higher performance, it is important that team members identify, share and discuss their roles and refine things to assume more than one role.

Belbin model (1996) is significant in pinpointing of team composition, team achievement, team roles, individual roles and individual performance. Though there is a natural danger in providing "name tags" or "putting people in boxes" by using these types of approaches, it may help the team to move from the WEAKNESSES to STREGTHS. Development of individual is also important in a team, and for that, the leader has to carefully choose the tasks, goals and jobs that would give the individual the opportunity of working within a role that they can manage. They will face a developmental challenge by taking up the role, but they will not be placed in a situation where they will inevitably fail. Ideally, the individuals should be in a position within a team where they are in their preferred roles.

It has been identified that team has to adopt a strategy to complete the task, and it has to go different phases, viz. forming, storming, norming, performing and adjourning. In addition, team also move back and forward among these different stages as well. At the forming stage, it is always better for team members to leave the individual behind and accept and understand and their role as a team member. Initially, the team members may be highly attentive to information to understand how they will operate. In an HEI, the forming stage may be dominated by people with stronger personalities or with higher ranking formal roles and job titles. The team leader can facilitate effective functioning of the team by the process of de-freezing and encouraging all team members to participate and contribute. At the storming stage, the members may have different opinions and conflicts. Unanimity on team function, roles, strategies and tactics is very important for

innovation. Storming must be vibrant and effective; everyone should be free to speak their mind, leaving aside conflict and accepting the diversity of academic disciplines. The team leader can facilitate effective functioning. At the norming stage, team members find ways to resolve and finally agree to the best. Once norms are established, lot of innovative patterns of social interaction will flow in and out to make the system innovative. At this stage, team leader efficacy will be in listening the team and put forth his advises.

At the performing stage (Bjerke & Renger, 2017), the team focuses on achieving the goal. Thought process of individual member becomes very important at this stage. Active and energetic participation of all team members is highly desirable, even on those elements which percept as less important. For example, if the faculty members of the team feel that their participation is not going to add any value to them in their career progression, then it may not be viewed as important as other activities such as research and teaching. Another reason for sluggish participation in the team is when one views it as conflicting with other work roles or his ideas are not given due importance. The team leader support becomes very important, which may be provided by greater presence, reviewing team performance, encouraging and motivating team and emphasizing the importance of the goal. This generally helps the team to move further with excellent results. All the findings, suggestions, creative art and innovative process become the part of team work for the next stage—the adjourning stage. This stage is important as the several team members engage themselves in unproductive activities that are not linked to the mission. Recognition and rewards for the performance become very important at this stage. The leader can facilitate successful adjournment by praising, by thanking and by recognizing the dedication of team members. For example, in higher education settings, certificate of innovations, medals and awards, appreciation and recognition letters, etc., are considered to be very important, and the role of cash rewards is always better appreciated. There is an important relationship between team functioning levels and team performance targets. Both functioning levels and targets need to be managed synergistically in order to facilitate higher team achievements. For innovation unlimited, team leader may help the team to establish SMART goals during the early stages and maintain focus on the SMART at various stages of life cycle to avoid "mission creep".

Innovations in Teaching Learning Process

Students and professors are the key elements of an HEI. Great institutions are known by their students and faculty. Amongst all the stake holders of an HEI, faculty is always at the centre. Knowledge dissemination and creation are the main task which professors perform. Knowledge dissemination (Supermane & Tahir, 2017; Paniagua & Istance, 2018; Supermane, 2019; Acharya, 2019) must focus on sound understanding of fundamentals, their application in new areas and state-of-the-art information on the subject. Another, which is more important, is to make the student expert in the specific skill or skills, positive thinker, problem solver and ethical by nature not by design. Research and innovation are essential part of teaching learning process in HEIs. Most of the research focuses on the extension of research pursued by the faculty or its group. But, it is the pertinent time that all the professors must orient towards creating new processes, new designs and new materials which are energy efficient, environment friendly and sustainable. All the elements of innovation must be assimilated and absorbed within to implement something new. Faculty and students should have clarity that innovation is neither art or science or technology, and it is process of implementation of something new which is not only sustainable but also keeps pace with time.

A good library is indispensable, and it contributes significantly to the achievement of students and faculty of an HEI (Barathi et al. 2017). It always helps in providing high-quality research and learning environments that meet group and individual needs. An innovative library is reservoir of physical and digital knowledge of very learned academician, and it helps in developing, promoting and providing access to scholarly collections and resources across multiple sites (Yanxiang, 2016). Library should act as a classroom, laboratory and workshop by providing online lectures, virtual experiments and design and real online description of methods and processes. It can help the students and faculty by providing materials from other libraries, copyright education and advice for the development of programs and resources. With faculty participation, it can ensure explicit development of information research, learning and employability skills; research data management across the University; information related to University's research outputs; nurture culture of publishing; and facilitate and promote internationalization strategies and enrichment of library staff capabilities and skills.

Economics and enterprise development have become a very important element for an HEI in new regime (Chen et al. 2018). Financially, self-reliance is the watch word. All the HEI resources should be utilized in this direction profitably. Facilitating students in the process of enterprise development will lead to financial stability for the university and creating value addition to the enterprise owner. A rich, generous and admirable space for developing creative art and global skills in sports is equally important for the innovation. Extracurricular and sports activities help students to expand not only their networks but build HEI

image. It helps in making friends in different states and countries. Providing the best facilities for these activities, a dynamic and vibrant campus shall be visible to one and all. Moreover, it helps students and faculty to promote cultural integration and improve social skills. Participation in extracurricular and sports activities equips students with leadership skills, teamwork, time management, communications skills, interviewing skills, and office environment flexibility (Jena & Memon, 2018). Even volunteering to these activities can help you sharpen the skills and plethora of opportunities for feeling and working.

Innovations in Administration Process

Academic administrators are the backbone of any HEI. An institution will have distinct position among the local or global level if it has super infrastructure. In the present era IT-enabled classrooms, state-of-the-art laboratories, workshop and hobby centres, precision instruments for researchers and an excellent design and development centres to explore creativity, innovation and incubation have become necessity to faculty as well as to the students. All this cannot be done or achieved without the support of administration.

Parkinson's law (2003) has exposed the inefficiencies of system of governance in all organizations, and the Peter and Hull Principle (1969) has exposed the imperfections of meritocracy. No innovation is possible if "administrative work expands to fill the time available to complete it". It is very well established that the managers crave power and more people to order and, more people create more work for each other. Parkinson's law is valid for all organizations devoid of good leadership, and people are promoted to their levels of incompetence. From an innovator's standpoint, meritocracy is important and more important is to develop this culture with an efficient system to support it. However, the criteria for systematic and incremental progression must focus on collective creativity, intimate collaboration and the enormous capacity to learn and change for the better.

There are several activities related to students, faculty and team members. Each and every team member in administration has specific role. Compassion, efficiency, reliability and strict discipline are required to perform the assigned duties. Visionary administration of HEI always strives for a vigorous, young, healthy, creative, progressive, vibrant and flourishing campus. It can be achieved by replacing manual practices with ERP practices (Samiei & Habibi, 2020). For instance, computerizing the admissions process allows you to carry all the activities online which include receiving and sorting application, generating and display of merit list and subsequent notifications to the concerned persons, etc. All activities in an HEI must focus on dispensing with manual paperwork, minimize amount of time and increase the productivity. Digitalization of the whole institution is one of the most significant, positive and affirmative aspects of globally distinct and successful universities/HEIs.

Growth is a necessary element and so is the continuous improvement. Progress is associated with the awareness and implementation of latest Edu-tech to maximize student progress and optimum engagement of faculty and team. Smart data management is absolutely necessary. Analytic tools and higher education ERP helps in taking effective, timely and smart decisions. Proper data management always helps in bringing out changes and to find out what works the best. At the same time, security of data is equally important, incorporating role-based access to key data. It is important to promote e-learning aggressively, but one should also think about those who not are privileged enough to have full-time access to digital devices. Such students must be treated with compassion and should be given ample amount of time to complete their tasks. Digital equality is very important, and there must be a space for every kind of learner. An HEI will never be truly progressive until every student and faculty have equal learning, growing and exploring opportunities, so efforts should be directed to reduce the gap between the digitally privileged and the underprivileged.

Innovations in Collaboration Process

Indian philosophy always advocated for the entire whole world is a single family. Despite demographic variations, the objective of all the educational institutions is to find the truth and use the knowledge for the development of mankind. There are greater efforts on collaborative learning (Gachie, 2020; McDiarmid, 2020; Pearson et al. 2020), particularly with peer group. It has been widely recognized that students do not learn well when they are isolated "receivers" of knowledge. Peer review workshops, collaborative research assignments, group presentations, collaborative papers and discussion groups are important components of active learning. Peer collaboration develops a sense of audience and understanding the conventions of academic discourse, analysing writing and increasing the sense of mastery.

The beauty of collaborative learning is that it might be practiced in a number of ways. Collaborative exercises can be whole-class events; they might also be done in small groups. Some collaborative exercises work best with pairs, those exercises that require close attention. A student will learn to summarize the argument, predict the argument, ask questions, reflect what the writer is trying to say, label problems and make suggestions. Michigan State University and 14 others collaborated on research. The outcome of

this collaboration in the words of Barbara McFadden Allen, "Together, our universities continue to refine what is arguably the most effective means for collaboration", and in the process, our output increased tremendously both in education and research, apart from increase in our library resources, scientific equipment, number of students awarded graduation and PhD degrees, and a meaningful saving of 5.8 million dollars. Big 10 academic alliance, consisting of 10 big university of the USA, facilitates their students to study courses at any university for their graduation—online or on campus. Lauren Robel, executive vice president of this alliance, remarked, "Big Ten universities compete on the field, but until this fight is won, we are united in the critical research to battle this virus and united in the classroom".

(a). Plebeian Institution—A great institution always strives for its growth and helps in the growth of plebeian institutions of its area. The concept of university social responsibility (USR) has evolved during the past few decades. Aras and Crowther (2008, 2009) insisted that the central tenet of social responsibility is the essential requirement of civil society, and this is not limited to the present members of the society, but also to its future members and the whole environment. Alshuwaikhat and Abubakar (2008) inferred that universities should be responsible toward society and their stakeholders who provide resources such as capital, customers, employees, materials and legitimacy.

The United Nations (2015) has designed its 5-component blended sustainable development (SD) paradigm, (5Ps: People, Partnership, Peace, Planet and Prosperity), from which the goals of SD emerge. In early 2016, the implementation of SD goals of Plan 2030 has commenced, which was based on the recommendations of both the World Summit on Sustainable Development (2002), followed by the Summit on Millennium Development Objectives (2015). HEI has been subjected to a number of reforms processes; globalization for international acceptability; sustainability for long term survival; knowledge society for better understanding; innovation for value addition; and development of technologies and software for speed and time discount. Universities almost fulfil their responsibility of educating youth and developing research and innovations (Marti-Noguera 2016; Marti-Noguera et al. 2017; Razak et al. 2017). Howard and Sharma (2006) proposed "Third Mission" in which the HEIs will engage and connect with the society and the people. Universities should have shouldered its societal responsibility. It is a fact that HEI lack in the culture of SR and the commitment to ethics for development. While it is important to inculcate the values that make SR obligatory and binding to all, sustainable development agenda will help academic institutions on bringing fruitful development outcomes. The activation of the role of the USR in SD must be linked to strong implementation mechanism. HEIs/universities can easily achieve higher level of SR in a professional manner (Chatterson & Goddard, 2000; Nejati et al. 2011). It can be further facilitated if institutions own and implement their responsibility comprehensively with continuity.

Beginning with the student, his learning and skill training must be performed in the way that makes him an effective personage and a responsible citizen. For this, culture and awareness of SR can be developed by organizing large-scale campaigns, create positive attitudes for models of SR, allocate compulsory and optional courses of SR and linking them to practical field application. This should be supported by laying emphasis on the values of beneficence, placing social interests above personal interests, and observe the rights of future generations. For higher performance, it is very critical to provide incentives to the participating students of SR programs. Instead of putting influence on the students in carrying out their duties and responsibilities in education, academic research and community service, conducive environment is of vital importance to make the system self-deriving. The universities focus should be on attracting staff members, who are outstanding in the field of new disciplines (green) and enhancing moral values, work ethics, commitment, sense of belonging and sense of responsibility among faculty through meetings, workshops, etc. Conduct research and studies in the fields of USR and linking it with SD must be an essential component of academics in HEIs.

Finely, HEIs/university's commitment to its societal role necessitates the inclusion of SR in the university's vision or mission statements. University administration must extend institutional support to the SR by different ways and means, including SR within its objectives and strategic plans. All the activities, plans and programs must be green, or the methodology of implementation should be green in nature. There should be an inbuilt commitment to the development of educational curricula and extracurricular activities including sports. Continuous improvement should be ensured in the educational and skill level for the university outputs to suit the needs of the community. All kind of support be made available to specialized research studies and programs on SR and economic sustainability. Publication of SR outputs, findings and recommendations should be ensured. Minute and flexible indicators of SR on which the university depends should be specific and known to all the stakeholders. Measurement and achievements on SR should be focused on the objectives and strategic plans.

(b). Industry: The new dictum for HEI–PRI–Industries interaction (Joseph & Abraham, 2009; Mäkimattili et al. 2015) focuses on sharing knowledge, empowering one-another and bring innovation into all aspects, including management, teaching, research, manpower and profits.

Academicians in a university, researchers in public research institutions and leaders of industries, who want to drive change in their organizations, are required to design and showcase theory and best practice, and practical actions that you can take within your organization. This maxim will act as an engine of regional development, global prosperity and innovation. Today, the focus on individuals is ever more critical, as it is the front line staff that facilitates activate cooperation between business and universities.

UIIN project is designing a learning framework, educational materials and innovative training for university and business stakeholders. The University–City Action Lab project aims to strengthen the links between HEIs and the city stakeholders by having students solve city issues through a series of challenge projects in Paris, Barcelona, Porto and Ljubljana. It will do so by facilitating knowledge exchange and flow of resources, enhancing societal relevance of HEI curriculum via civic engagement, helping develop relevant skills among students, empowering universities in increasing their knowledge and practice in establishing urban partnerships and fostering adoption of city engagement models. The project will promote the engagement of universities with their immediate environment and strengthen their potential in fostering communiqué among regional population. This will help to start and continue with the joint actions towards building of smart and sustainable cities. To provide universities with resources and tools, a collection of 25 Good Practices in University–City collaboration and hands-on challenge-based learning activities have been identified to implement.

(c). R&D Centres: Public and industrial research institutions are engaged in R&D, which play important role in the innovations in industry as well as in the Governments' emerging areas of research. Energy, ocean, armaments, aeronautics and space research are the major focus of public research institutions (PRIs) and national research laboratories (NRLs). Universities and HEIs are also playing its part in the global research activities, but the focus is more on fundamental research. From a survey, it was observed that the industries are focusing on innovation and R&D increasingly as they have learned then need of these parameters to surviving the ocean of competitions. About 14% of the industries under survey have not made any investment in R&D. These establishments think that R&D is not essential for their business, and they see it too risky and expensive. Large proportion of industries who have invested money in R&D opined the solutions were beneficial to them in process development and earning more profits. Many of them attributed it the local perception which they were able to build with the stakeholders by inviting them to participate in the innovations. Most of industries were happy to share that R&D provided them creative and innovative ideas for the improvement in their business, but the element of novelty in the product/process had a very little value. Innovations in Indian industries were mainly done by the employees and the customers—the major sources of knowledge. There is a very fragile connect (Minguillo & Thelwall, 2015; Pogodaeva et al. 2015) between industries and HEI/PRI/NRLs. Recently, the large number of HEIs has taken initiative to establish incubation centres for start-ups, innovation laboratories for the industries who wish to explore new projects and the low-cost testing facilities. Most economies be it from the developed economies or from the developing economies, and the channels of linkages between industries and HEIs are formalized channels and open channels. A very few developed nations have adopted informal channels of linkages. The incidence of R&D interaction between different stakeholders is very low. In a survey of 462, only 11% claimed that they had any form of R&D collaboration with each other. However, those who have R&D interaction, the collaboration has been a success in achieving objectives. For about half a century, majority of the professors and scientists perceived that HEI/PRI/NRL/Industry interaction was very important, and the efforts of these professors substantially increased the extent of interaction for innovation.

Innovations in the R&D functioning of HEIs require a strong interaction. Students and faculty of HEIs must orient themselves to understand, analyse and provide solutions at low cost. Exchange of information and relevant information is very important for the success, as information from HEIs acts as a complement to the R&D efforts taken by the industry. It has been observed that the link between PRI/NRL and industries is much stronger in comparison with universities/HEIs. This perhaps is reflective of the nature of R&D taken up both these institutions. While research undertaken by PRIs is more commercial in nature, the universities research is considered more "basic" with lesser commercial value in it. Analysis showed that the industries that collaborated with HEIs achieved a higher level of innovation and value addition in the products.

(d). Policy Planner/Government: Functioning of HEIs is on the radar of all the governments across the world which affects its innovation and creativity. However, these liberty and authority have been provided to the researchers in the HEIs. LSE report on innovation in HEIs is adopted by several governments as a torch bearer to them. The main findings of this report propose that an HEI must cultivate an institutional culture to innovation that promote creativity, understand the benefits of the innovation, energize openness to innovation and lower resistance to transform. Incentives and rewards, new learning technologies, cross-institutional collaboration, improve student choice and quality, skills development of teaching staff are some of

the important parameters for innovation in HEIs. Above all, critical and periodic review of existing organizational boundaries and linkages is very crucial in promoting the process of innovation in an HEI. Asiedu et al. (2020) emphasized knowledge management capabilities, organizational learning and innovation performance in the context of higher education institutions (HEIs).

Policy planner of HEI must focus on the challenges resulted from globalization, dynamics of supply of and demand and resource generation for funding of higher education. These external challenges have to be addressed. On the basis of seven case studies, these challenges have been grouped in three themes.

i. Academic inputs—flexible curriculum, globally acceptable course content, student centric teaching, R&D and D&D inputs, ready-to-go to industry, capacity building for profitable enterprise and faculty centric learning
ii. Technology inputs—learning and usage of technology, methodology to enhance student performance and selection of appropriate technology.
iii. Global visibility—mini- and macro-teaching learning centres, multi-campus universities, virtual learning and skill development.

Innovations in Development Process

Development process of an HEI involves adoption, assimilation and value addition in its activities. Periodic redefining of goals, identification of new curricula and research activities, new management, products, services, and markets are important. Integration of industry, university and innovation is a powerful catalyst for job creation and economic development of all the key stakeholders. Innovation in development process of an HEI must focus on the following areas.

- Modernization of the students' preparation process in HEIs. It is necessary to train students and industry professional with state-of-the-art knowledge, innovative skills and exceptional competence that allow one to analyse and correctly measure the matter-of-fact situations and provide profitable solutions of the real problems of the business and modern enterprise.
- Creation and development of infrastructure for the successful implementation of new ideation, new projects and business plans. It should not only facilitate learning and skill development, and it should be capable of satisfying the desire and appetite of innovation and creativity within the learner and the teachers.
- Establishment and enlargement of small innovative enterprises (start-ups). New business, new strategies, cooperative market and ease of doing business should be facilitated. Government procedures, registration/patenting of idea, banking and finance, managing the market, implementation and expansion strategies should be easily available.

Further, integrated approach to the development of skills and competencies on a continuous basis be adopted by including,

a. Creation of organizational structures, platforms, laboratories, engineering workshops, contributing to the implementation of activities to build these skills and competencies;
b. Creation of innovative regional clusters. It must provide and facilitate favourable environment for developing regional innovation ecosystem.

Innovations in Value Creation Process

Knowledge has become a key resource globally, and better understanding of fundamentals either through research or through innovation can add value to the HEIs. Sánchez-Fernández et al. (2010) reviewed the relevant educational literature and observed that there is no empirically confirmed relational model of the value creation process that is commonly acceptable for either students, faculty or the HEIs. Development of intellectual capital of their citizens is very vital both for the governments and for the HEIs. The value creation and its prolongation are important for all HEIs, and it should be reflected in their policies and practices. Several models have been developed using the concepts of relationship marketing theory. Considering HEIs as service organizations, the value creation process is dependent on certain hypothesis. The students (customer) and their parents are influenced by the perceived value of an institution. This perceived value is dependent on the quality and intensity of the student–professor dialogue, the reliance on the educational institution, the university importance in public and student satisfaction. It has been confirmed that there is affirmative and distinct relationship between student perceived value, student satisfaction and student allegiance.

Both the actual value and the perceived value play an important role in the success. For an HEI/university, the difference in the perceived value and the actual value should be minimal. A student who is joining an HEI certainly has an idea about the perceived value. The actual value is what the university is actually worth without any expectations from the student. The perceived value is formed by the opinions of the market and by the benefits that a student expects to receive. The perceived value of an institution may be higher or lower depending upon the value creation process. The most important question is—how to enhance perceived and actual value? The students,

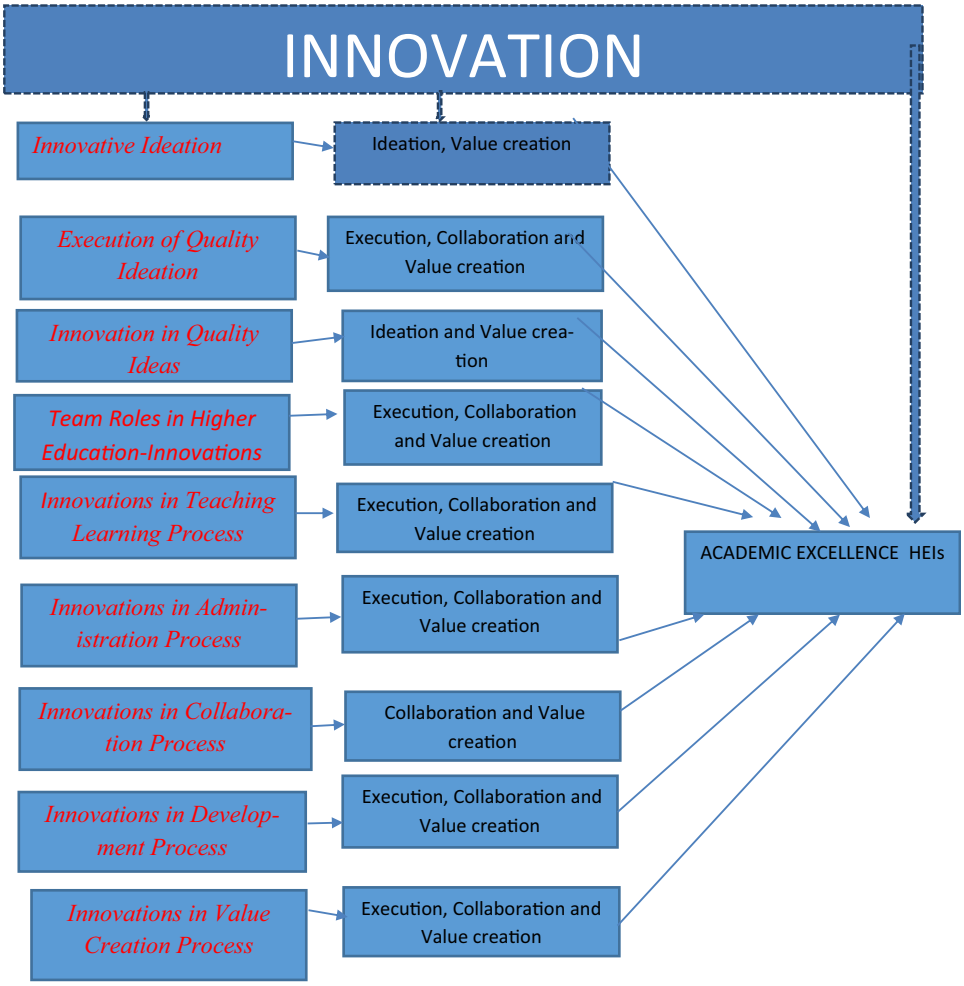

Fig. 1 Innovation framework for excellence in higher education institutions (HEIs)

the faculty and the staff are the builders of the perceived value of a HEI. Quality of teaching is the most important for a student. Infrastructure and management can add value to this. Perceived value can be enhanced publishing achievements of HEI regularly; by participating in ranking, evaluation and certification process and above all by performing social responsibilities—both towards people and to the peer/plebeian institutions. The satisfied and loyal students are the building blocks of value creation process. Improving interaction between students and professors could be useful to generate user identification with the organization, perceived value and loyalty. The universities should make meticulous effort and invest resources to reinforce links with students by organizing alumni meets, special lecture series, outreach programs, mentors meets and many more activities.

Conceptual Framework

The proposed conceptual innovation framework for excellence in HEIs based on ideation, execution, collaboration and value creation is proposed in Fig. 1.

The conceptual framework is driven by innovation let excellence of HEIs academic excellence cause by interaction of various elements, i.e. Innovative Ideation, Execution of Quality Ideation, Innovation in Quality Ideas, Team Roles in Higher Education-Innovations, Innovations in Teaching Learning Process, Innovations in Administration Process, Innovations in Collaboration Process, Innovations in Development Process and Innovations in Value Creation Process, which in turn affects organically to Execution, Collaboration and Value creation processes of HEIs leading to academic excellence in HEIs.

This conceptual framework also provides directions towards putting heavy emphasis on Execution, Collaboration and Value creation processes of HEIs.

Conclusions

Intrinsic motivation, autonomy and inherent diversity are the key elements of innovations which demands **flexibility** and out-of-box thinking in higher education and research. HEIs must exhibit it in its vision and mission statements, and process of innovation must focus on quality ideation and innovation in its execution through their vision and mission. While setting SMART goals is important, achieving it with value addition and value co-creation is still more important. Focus on teaching–learning process should not only be IT enabled or e-mediated but by live examples and hands on by design and process. Quality in patents, emphasis on green in research and enormous success in adaptation by the industry are the key elements for becoming innovative for HEIs.

Local and global collaboration both leading to value co-creation in teaching and research will be in high demand to become competitive and cost-effective through value co-creation and cooperative competition which demands very high degree of organizational flexibility (Sushil, 2017) but high degree of execution excellence (Sushil, 2009). It should not only be mere physical interaction maintaining their identities, but should also be extended to intimate organic bonding for the benefits of all stake holders in this process. Innovative HEIs may adopt multi-pronged collaborative approach. Value addition at each stage of innovation process, not only to enhance flexibility leading to *"Freedom of Choice"* of stakeholders but to enhance deep learning in value creation, must focus on GREEN—energy efficiency, environment friendly and sustainability. Finally, innovation is now becoming new assets of HEIs creating new processes leading to high value proposition offered by HEIs to students and industries, creating new models of higher education for global economies.

This paper being conceptual in nature lacks rigour of quantitative analysis, but at cognitive level, it needs more cyclic evolutions in future and quantitative validations.

This study contribute heavily on innovation by emphasizing on the fact that now *innovation* has become asset of *new normal,* having competence of embedding new processes leading to high value proposition to the HEIs system's stakeholder.

There is lack of research in the area of innovation led excellence in HEIs as only few researchers have talked about this, but this conceptual study and framework can be used as a tool to give a new concept to policy makers in the area of policy framing and management of Higher Education Institutitutions (HEIs), which is quite critical for any country to achieve excellence in this area resulting in new domains of knowledge and skills.

References

Acharya, S. (2019). Beyond learning outcomes: Impact of organizational flexibility on strategic performance measures of commercial E-learning providers. *Global Journal of Flexible Systems Management*, *20*(1), 31–41.

Aghera, A., Emery, M., Bounds, R., Bush, C., Stansfield, R. B., Gillett, B., & Santen, S. A. (2018). A randomized trial of SMART goal enhanced debriefing after simulation to promote educational actions. *Western Journal of Emergency Medicine, 19*(1), 112–120. https://doi.org/10.5811/westjem.2017.11.36524

Alshuwaikhat, H., & Abubakar, I. (2008). An integrated approach to achieving campus sustainability: assesment of the current campus environmental management practices. In: Proceedings of the 4th International Barcelona Conference on Higher Education, Vol. 7. Higher education for sustainable development. Barcelona: GUNI. http://www.guni-rmies.net.

Aras, G., & Crowther, D. (2009). Corporate sustainability reporting: a study in disingenuity? *Journal of Business Ethics, 87*(1), 279. https://doi.org/10.1007/s10551-008-9806-0

Aras, G., & Crowther, D. (2008). Governance and sustainability an investigation into the relationship between corporate governance and corporate sustainability. *Management Decision, 46*(3), 433–448. https://doi.org/10.1108/00251740810863870

Aritzeta, A., Swailes, S., & Barbara, S. (2007). Belbin's team role model: development, validity and applications for team building. *Journal of Management Studies, 44*(1), 96–118.

Asiedu, M. A., Anyigba, H., Ofori, K. S., Ampong, G. O. A., & Addae, J. A. (2020). Factors influencing innovation performance in higher education institutions. *The Learning Organization, 27*(4), 365–378. https://doi.org/10.1108/TLO-12-2018-0205

Barathi, S., Loganathan, G., & Rajan, V. R. (2017). Emerging technological innovations in library knowledge management and services. *Advances in Computational Sciences and Technology, 10*(5), 1479–1486.

Belbin, R.M. (1981, 2004). *Management teams: why they succeed or fail*. London: Butterworth Heinemann Ltd.

Belbin, R. M. (1993). *Team roles at work*. Butterworth-Heinemann Ltd.

Belbin, R. M. (1996). *Team roles and a self-perception inventory.* In J. Billsberry (Ed.), *The effective manager: perspectives and illustrations* (p. 182–189). Sage Publications, Inc; Open University Press. (Reprinted in modified form from R. M. Belbin, "Management Teams," Oxford: Butterworth Heinemann, 1981.

Bjerke, M. B., & Renger, R. (2017). Being smart about writing SMART objectives. *Evaluation and Program Planning, 61,* 125–127.

Bondzi-Simpson, P. E., & Agomor, K. S. (2021). Financing public universities in ghana through strategic agility: lessons from ghana institute of management and public administration (GIMPA). *Global Journal of Flexible Systems Management*, *22*(1), 1–15.

Brennan, J., Arthur, L., Little, B., Cochrane, A., Williams, R., Locke, W., Singh, M., David, M., Kim, T., & King, R. (2010). *Higher education and society: a research report.* CHERIs.

Boris, P., & Yifu Lin, J. (Eds.). (2008). Annual World Bank conference on development economics 2008, regional: higher education and development. The World Bank.

Celuch, K., Bourdeau, B., & Smothers, J. (2014). Thinking innovatively about teaching innovation and ideation: getting students to think differently. *Journal of Research in Innovative Teaching, 7*(1), 27–36.

Chatterton, P., & Goddard, J. (2000). The response of higher education institutions to regional needs. *European Journal of Education, 35*(4), 475–496.

Chen, J., Yin, X., & Mei, L. (2018). Holistic innovation: an emerging innovation paradigm. *Innovation Studies, 2*(1), 1–13. https://doi.org/10.1016/j.ijis.2018.02.001

Chesbrough, H., & Bogers, M. (2014). Explicating open innovation: clarifying an emerging paradigm for understanding innovation. In H. Chesbrough, W. Vanhaverbeke, & J. West (Eds.), *New Frontiers in Open Innovation*. Oxford: Oxford University Press.

Clawson, J.G.S., & Huskin, M.E. (2006). Teaching management: a field guide for professors, corporate trainers, and consultants. Cambridge: Cambridge University Press, pp 1–494. DOI: https://doi.org/10.1017/CBO9780511617850

Cortés-Sánchez, J. (2017). Mission and vision statements of universities worldwide: a content analysis. *Documentos De Investigacion, Facultad de Administracion.* https://doi.org/10.2139/ssrn.3051361

Dam, R.F., & Siang, T.Y. (2019). What is ideation—and how to prepare for ideation sessions interaction Design usability conducted by Interaction Design Foundation.

Doran, G. T. (1981). There's a SMART way to write management's goals and objectives. *Management Review., 70*(11), 35–36.

Dorow, P. F., Dávila, G., Varvakis, G., & Vallejos, R. V. (2015). Generation of ideas, ideation and idea management. *Navus, 5*(2), 51–59.

Evans, S., & Bahrami, H. (2020). Super-flexibility in practice: Insights from a crisis. *Global Journal of Flexible Systems Management*, *21*(3), 207–214.

Ganuthula, V. R. R., & Sinha, S. (2019). Flexibility in cognitive functioning: The play of paradox. *Global Journal of Flexible Systems Management*, *20*(4), 303–312.

Feldman, M.P., & Stewart, I.I. (2010). Wellsprings of modern economic growth: higher education, innovation, and local economic development.

Fleming, T. (1978). Some considerations of the goal setting and planning processes in public higher education. *The Canadian Journal of Higher Education, 8*(3), 33–45.

Gachie, W. (2020). Higher education institutions, private sector and government collaboration for innovation within the framework of the Triple Helix Model. *African Journal of Science, Technology, Innovation and Development, 12*(2), 203–215. https://doi.org/10.1080/20421338.2019.1631120

Hattangadi, V. (2019). India needs triple helix model of innovation in universities. Financial Express.

Howard, J., & Sharma, A. (2006). Universities' third mission: communities engagement. Round Table Business/Higher Education. http://www.bhert.com/publications/position-papers/B-ERTPositionPaper11.pdf

Jena, L. K., & Memon, N. Z. (2018). Does workplace flexibility usher innovation? A moderated mediation model on the enablers of innovative workplace behavior. *Global Journal of Flexible Systems Management*, *19*(1), 5–17.

Joseph, K. J., & Abraham, V. (2009). University-industry interactions and innovation in India: patterns, determinants, and effects in select industries. *Seoul Journal of Economics, 22,* 467–498.

Katic, M., & Agarwal, R. (2018). The Flexibility paradox: Achieving ambidexterity in high-variety, low-volume manufacturing. *Global Journal of Flexible Systems Management*, *19*(1), 69–86.

Leydesdorff, L., & Etzkowitz, H. (1998). Triple Helix of innovation: introduction. *Science and Public Policy, 25*(6), 358–364.

Lutz, W., Muttarak, R., & Striessnig, E. (2014). Universal education is key to enhanced climate adaptation. *Science, 346*(6213), 1061–1062. https://doi.org/10.1126/science.1257975

Madjar, N., & Shalley, C. E. (2008). Multiple tasks' and multiple goals' effect on creativity: forced incubation or just a distraction? *Journal of Management, 34*(4), 786–805. https://doi.org/10.1177/0149206308318611

Mäkimattili, M., Junell, T., & Rantala, T. (2015). Developing collaboration structures for university-industry interaction and innovations. European Journal of Innovation Management.

Martí-Noguera, J. J. (2016). Las universidades y el desarrollo humano: los retos de la educación superior experiencias iberoamericanas. *Humanismo y Trabajo Social, 16,* 41–51.

Martí-Noguera, J. J., Puerta-Lopera, I. C. Y., & Rojas-Román, P. (2017). A propósito de la Responsabilidad Social Universitaria [Eds]. *Revista Colombiana de Ciencias Sociales, 8,* 294–301. https://doi.org/10.21501/22161201.2291

McDiarmid, G. W. (2020). Innovations and collaboration to influence policy and practice: global deans speak. *ECNU Review of Education, 3*(3), 584–603.

Melnik, A. N., Ermolaev, K. A., & Kuzmin, M. S. (2019). Mechanism for adjustment of the companies innovative activity control indicators to their strategic development goals. *Global Journal of Flexible Systems Management*, *20*(3), 189–218.

Minguillo, D., & Thelwall, M. (2015). Which are the best innovation support infrastructures for universities? Evidence from R&D output and commercial activities. *Scientometrics, 102*(1), 1057–1081. https://doi.org/10.1007/s11192-014-1458-5

Nejati, M., Shafaei, A., Salamzadeh, Y., & Daraei, M. (2011). Corporate social responsibility and universities: a study of top 10 world universities' websites. *African Journal of Business Management, 5*(2), 440–447.

Ogbeiwi, O. (2017). Why written objectives need to be really SMART. *British Journal of Health Care Management, 23*(7), 324–336. https://doi.org/10.12968/bjhc.2017.23.7.324

O'Reilly, C., Andrew, J. M., & Binns, A. J. M. (2019). The three stages of disruptive innovation: idea generation, incubation, and scaling. *California Management Review, 61*(3), 49–71.

Paniagua, A., & Istance, D. (2018). Teachers as designers of learning environments: the importance of innovative pedagogies. Educational Research and Innovation, OECD Publishing, France. ERIC Number: ED582804

Parkinson, C.N. (2003). Parkinson's law, Buccaneer Books, 112 pages; Published 2003 by Buccaneer Books.

Patterson, F., & Zibarras, L. D. (2017). Selecting for creativity and innovation potential: implications for practice in healthcare education. *Advanced in Health Science Education., 22*(2), 417–428. https://doi.org/10.1007/s10459-016-9731-4

Pearson, M., Singelmann, L., Ryan Striker P.E., Vazquez, E.A., & Swartz, E.M. (2020). Benefits of long distance collaboration in higher education institutions to train students in innovation practices. ASEE's Virtual Conference, June 22–26, 2020, Paper ID #30827

Peter, L.J., & Hull, R. (1969). The Peter Principle, William Morrow & Co Inc, (Pan Books edition 1970)

Petersson, A. M., & Lundberg, J. (2018). Developing an ideation method to be used in cross-functional inter-organizational teams by means of action design research. *Research in Engineering Design, 29*(3), 433–457.

Pogodaeva, T., Zhaparova, D., & Efremova, I. (2015). Changing role of the university in innovation development. *Procedia Social and Behavioral Sciences, 214,* 359–367.

QS World University Ranking. (2020).

Razak, A., Wan, D., Da, C., & Morshidi, S. (2017). Juxtaposing economic progress with sustainability in mind: issues and way forward for Universities. In: Higher Education in the World 6: Towards a Socially Responsible University: Balancing the Global with the Local, Global University Network for Innovation (GUNI). SSRG International Journal of Economics and Management Studies (SSRG-IJEMS), 4, 1–9.

Reinig, B. A., Briggs, R. O., & Nunamaker, J. F. (2007). On the measurement of ideation quality. *Journal of Management*

Information Systems, 23(4), 143–161. https://doi.org/10.2753/MIS0742-1222230407
Samiei, E., Habibi, J. (2020). The mutual relation between Enterprise resource planning and knowledge management: A review. *Global Journal of Flexible Systems Management*, *21*(1), 53–66.
Sánchez-Fernández, R., Iniesta-Bonillo, M.A., Schlesinger-Díaz, W., & Rivera-Torres, P. (2010). Analysis of the value creation in higher institutions: a relational perspective. *Theoretical and Applied Economics,* XVII, 25–36
Scaglione, V. L. T., Meyer, V., & Mamédio, D. F. (2019). Improvisation in higher education management: Coping with complexity and organizational dynamics. *Global Journal of Flexible Systems Management, 20*(4), 291–302.
Serdyukov, P., & Makhluf, H. (2014). Growing national university research culture: goals and steps. *Journal of Research and Innovative Teaching, 7*(1), 2–13.
Sharahiley, S. M. (2020). Examining entrepreneurial intention of the Saudi Arabia's University students: Analyzing alternative integrated research model of TPB and EEM. *Global Journal of Flexible Systems Management*, *21*(1), 67–84.
Shukla, S. K., & Sushil, & Sharma, M. K., (2019). Managerial paradox toward flexibility: Emergent views using thematic analysis of literature. *Global Journal of Flexible Systems Management*, *20*(4), 349–370.
Singh, J. D. (2016). Higher education in the 21st century-issues and challenges. *International Education Journal of Chetna, 1*(2), 33–42.
Singh, N., & Sushil (2004). Flexibility in product development for success in dynamic market environment. *Global Journal of Flexible Systems Management*, *5*(1), 1–12.
Smith, G., & Yates, P. (2011). Team role theory in higher education. *Training Journal*, 54–57.
Supermane, S. (2019). Transformational leadership and innovation in teaching and learning activities: the mediation effect of knowledge management. *Information Discovery and Delivery, 47,* 242–250. https://doi.org/10.1108/IDD-05-2019-0040
Supermane, S., & Tahir, L. M. (2017). Knowledge management in enhancing the teaching and learning innovation. *International Journal of Academic Research in Business and Social Sciences, 7*(6), 721–727.
Sushil (2009). Execution Excellence. *Global Journal of Flexible Systems Management*, *10*(2), iii.
Sushil (2015). Strategic Flexibility: The Evolving Paradigm of Strategic Management. *Global Journal of Flexible Systems Management*, *16*(2), 113–114.
Sushil (2017). Small Steps for a Giant Leap: Flexible Organization. *Global Journal of Flexible Systems Management*, *18*(4), 273–274.
The Millennium Development Goals Report. (2015). https://www.un.org/millenniumgoals/2015_MDG_Report/pdf/MDG%202015%20rev%20(July%201).pdf
The Times *Higher Education* World University Rankings. (2020).
Van Dierendonck, D., & Groen, R. (2008). *Belbin revisited: the construct validity, ERIM report series–ERS-2008-017-ORG. 1–29pp*
Van Dierendonck, D., & Groen, R. (2011). Belbin revisited: a multitrait–multimethod investigation of a team role instrument. *European Journal of Work and Organizational Psychology, 20*(3), 345–366. https://doi.org/10.1080/13594321003590580
Yanxiang, L. (2016). Service innovations of university libraries in the MOOC Era. In: Proceedings of the 8th International Conference on Information Technology in Medicine and Education, pp. 744–747. https://doi.org/10.1109/ITME.2016.37.

Publisher's Note Springer Nature remains neutral with regard to jurisdictional claims in published maps and institutional affiliations.

Key Questions

1. What should be process of innovation forHigher Education Institutions (HEIs) to provide high vlaue propositions to its stake holder?
2. How innovation embedded frameworks of HEIs can help in creting robust eco-systems for them leading to excellence in academics and related activities pursued by HEIs?
3. Why Innovation this type of Frameworks for Excellence in Higher Education Institutions (HEI's) are very relevent and of importance in current 'Global Pandemic Scenario'?

Dr. Manoj Kumar Sharma is an alumnus of Delhi College of Engineering and IIT Delhi, having Bachelor and Masters Degree in Engineering with First Class & Distinction, MBA and PhD in Management (Strategic Management and Telecom area) from IIT Delhi. He has experience of 34 years in various capacities as a contributor and learner, in Academics, Industry and Government as Mentor, Teacher, Manager, Advisor and National Policy Analyst. Currently, he is Full-Time Visiting Professor in areas of Strategic Management, Innovation, Entrepreneurship and New Venture Development at University School of Management and Entrepreneurship, DTU East Delhi Campus of Delhi Technological University (Established by Govt. of NCT of Delhi), and Committee Member for framing "Startup Policy of Govt. of NCT of Delhi".

He has served as Dean, Faculty of Management, Mahamaya Technical University (State Technical University of Govt. of U.P., India) now renamed as "Dr. A.P.J. Abdul Kalam Technical University (APJAKTU), Hewas member on Board of "Centre of Excellence in Information Management" established by European Union (EU) at Management Development Institute (MDI) and on Expert panel for selection of senior faculty in area of "Strategy" for leading business school of India/Chief Examiner of Engineering for State Public Service Commission of Government. His other academic work and related experience include Honorary/Visiting/Adjunct Professorships at IIMs/IITs/National Academy for Training for Social Security and Research, Ministry of Labour & Employment, Govt. of India/Department of Personal and Training (Govt. of India) and Delhi Technological Univeristu (DTU). He has also served in Government/ As Advisory capacity (IT & E-Governance) (NOIDA, Govt. of U.P., India)/On board of directors of companies/as Member of the National Council (NCVT, an apex policy making body) of Ministry of Labour & Employment, Govt. of India/ First CEO of DTU Innovation and Incubation Foundation (Section 8 Company as per The Companies Act of India) promoted by Delhi Technological University/Officer on Special Duty (OSD) and later Director (Associate)—DTU East Delhi Campus of Delhi Technological University (Established by Govt. of NCT of Delhi)

Prof. R.C. Sharma is an alumnus of University of Delhi having PhD from the same University. He has experience of 44 years in various capacities as a Professor and Institution Builder of many Institutes. He has been on numerous committees of Govt. of India. Currently, he is First Director of DTU East Delhi Campus of Delhi Technological University (Established by Govt. of NCT of Delhi)

Proceedings of the Sixth International Conference on Inventive Computation Technologies [ICICT 2021]
IEEE Xplore Part Number: CFP21F70-ART; ISBN: 978-1-7281-8501-9

Integrated Vendor-Managed Time Efficient Application to Production of Inventory Systems

Bickey Kumar Shah
Department of CSE
Delhi Technological University
Delhi,India
Bickeyshah721@gmail.com

Vansh Kedia
Department of CSE
Delhi Technological University
Delhi,India
Vanshkedia1999@gmail.com

Rahul Kumar Jha
Department of CSE
Delhi Technological University
Delhi,India
Heavenboyrj.11@gmail.com

2021 6th International Conference on Inventive Computation Technologies (ICICT) | 978-1-7281-8501-9/21/$31.00 ©2021 IEEE | DOI: 10.1109/ICICT50816.2021.9358504

Abstract— **This paper establishes a solution for the management of the inventory products concerning time and cost for the efficient delivery of the products into the competitive market with the inventory management rules and policies where the stock deteriorates with time and recovery process is unreliable. It has focused on the demand and supply chain of the goods taking minimum time into the consideration for maximizing the profit throughout the cycle of delivering the products. It establishes a user interface software that maintains all of the records of buying and procuring the products from the stock. It emphasizes the problem related to the integrated transportation of an inventory. It has focused to manage the distribution network at minimal cost and time and optimization techniques have been performed for the maintenance work of the software and system. Both hardware and software interface has been designed. It has been designed in such a way that it becomes familiar with both users and admin in a short span of time and easy to use conveniently. Different software requirements tools and engineering has been performed to make the software efficient for both user and admin. A feasibility study and requirement analysis have been carried out to validate the software requirement with time.**

Keywords— Model, Requirement Engineering, software requirement specification, Interface, Database.

I. INTRODUCTION

In today's modern times having production and trade of millions of products involving different markets, industries, production-houses. These products are sold/purchased by people through various shops, supermarkets, stores [1]. It becomes important to maintain a record of products sold, purchased, and their details. Traditionally techniques of noting regarding product sales/purchase are managed in writing. This has certain demerits that are regularly faced by almost all the traders/industries/shops who store data traditionally. This becomes more tedious when there are multiple changes - due to Sale, Procure, Defect/Replace. To eliminate those problems in the modern system of managing the products in the markets and industries. This competitive market is facing a lot of "out of stock" issues. Around 81% of total consumers and traders involved in the product dealing are facing these issues of unavailability of products in stock [4]. The shopkeepers and traders along with the modern techniques are trying to reduce these issues. It is recorded that cost of trillions of products is being mismanaged. Many of these failures are there as a result of inefficient inventory management techniques like Manual bookkeeping, using static spreadsheets. Automated Inventory Management allows us to overcome these shortcomings and provide a better way of managing inventory. It brings inconsistency in product data, saves time by speeding up the process (sale/purchase/track), helps plan inventory according to product demand/supply as analyzed by the system. To make an efficient and usable record with some associated features, the computer-based Inventory stock management system has been developed. With this management system, incoming and outgoing records (product orders) are stored and noted in an easy to store and use data format and server [5]. It focused to create a user interface based comprehensive, easy to use inventory management program available to shops, markets, and business. This management provides centralization of the most basic and necessary warehouse functions. With the help of this traders will be able to see the complete inventory details like stock levels, product details, add/manage sales, procurements. This system will be based on a robust user interface and efficient database-server working. In this system, It is aimed to have a common storage point for Inventory's product details which is efficient to time. Any change from any side is reflected in product details in inventory [7]. Customers and owners will have their login credentials. Information regarding their details and credentials will be stored securely in a database. Record of sales/procurements will also be stored allowing to

Authorized licensed use limited to: DELHI TECHNICAL UNIV. Downloaded on March 03,2021 at 06:05:19 UTC from IEEE Xplore. Restrictions apply.

view previous sales/procurements and analyze the data. Owners can procure products, manage product changes, view sales/procurements, while customers can order products. Thus, this system will be able to meet all user demands and work to improve the handling and management of inventory with concern of time.

A. FEASIBILITY STUDY

A feasibility study is carried out to determine the degree of advantage with new product and to see the viability of Software product and its development in terms of Technical, Operational, Financial, Management aspects [8]. feasibility study is carried out with an intent to answer questions which are part of the study to gauge product development and outcome feasibility.

II. LITERATURE SURVEY

This section reviews the literature on the inventory management system. Cost and time have always been a prime focus and efficiency to be taken into the consideration. Various research work has been carried out on the management work of the Inventory system. Discrete-time control over the product management of the stock has been carried out on the system. Compensation in Delay and its mechanism has been performed that gives an accurate compensation for the unavailability of the products in the given time. Predictive Control of the model for the hybrid system predicts the model that keeps control over the predictive analysis of time and cost [12]. A multi-objective optimization system is an optimization technique that optimizes the multiple tasks and objectives together in one frame and it keeps an efficient track of the inventory products delivered and products available in the stock. Different tools and technologies are being used and developed with high computational power and work. Functional activities are taken into considerations through different learning algorithms [4]. Machine learning and deep learning is also being carried out for inventory management activities. Mathematical computations and enhancements models are practiced in order to classify the forecast feasibility of the system. Requirement engineering has been a basic part and requirement for analysis and design. The level of DFD determines the system processes and the result of the system's feasibility.

III. METHODOLOGY

A. Software Development Cycle Model

It is proposed to choose the iterative enhancement model as the software development life cycle model for the system. This model is similar to the waterfall Model (sequential, proceed irreversibly along stages), but here each stage has multiple substages with feedback, unlike the waterfall model.

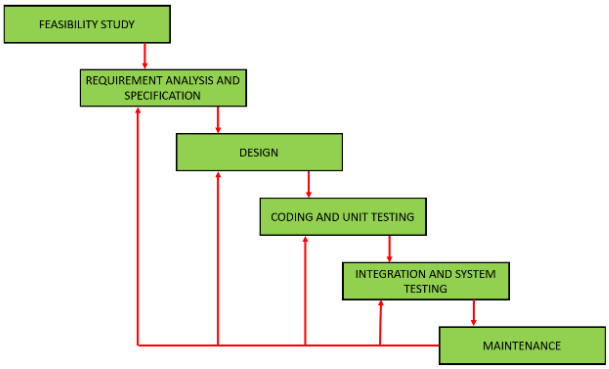

fig.1 Iterative Enhancement Model

This model is chosen as the requirements are specified beforehand and project implementation proceeds in a sequential manner from starting to end- Project planning, Requirement engineering, Design, Implementation and Integration, testing, and management. However, having feedback at each stage allows to handle errors better considering the developer experience leading to the presence of error at each stage [2].

B. Project Planning

Project planning involves the construction and designing of a plant to build software using the appropriate Development model and other techniques. It begins with requirements engineering to collect analyze and consolidate the requirements. It is then planned to move to the design and Development phase and subsequent phases.

C. Requirement Engineering

Requirement engineering is a phase of software Development Involving, Identifying, and assigning requirements which the software product is supposed to fulfill upon completion [9-11]. The first step involves the requirement elicitation which corresponds to the gathering of requirements. Brainstorming sessions and discussions are used to arrive at the elicitation. This is followed by requirement analysis, documentation, and Review [10]. Following are the prepared documents describing the system as a part of requirement engineering. These helps to determine user requirements and helps to have a robust system design to implement the project idea.

1) Use Case Approach

This involves representing the system, outside entity as an actor with each actor interacting with the system for a particular use case- an event happening to capture a functional aspect of the system while interacting with the actor.

Authorized licensed use limited to: DELHI TECHNICAL UNIV. Downloaded on March 03,2021 at 06:05:19 UTC from IEEE Xplore. Restrictions apply.

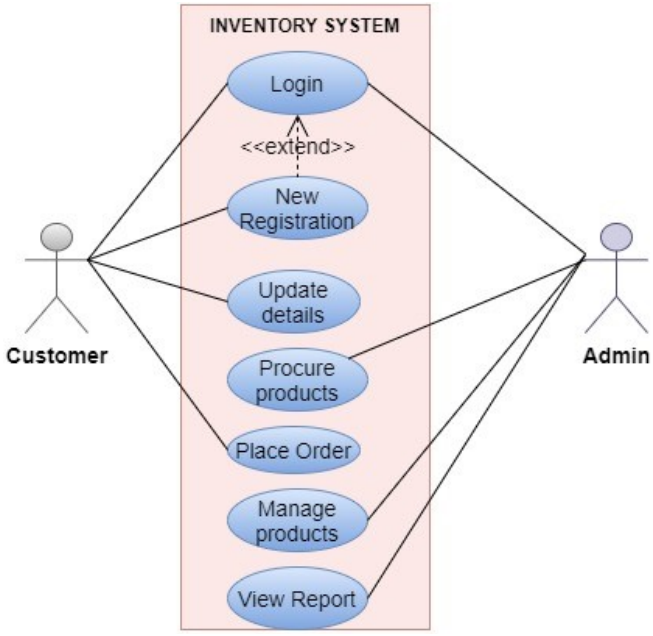

fig.2 Use Case Diagram

In the given fig.2 is the use case diagram of the system that shows how Customers and admin are related with the system. Their login issue, New registration, updating of the details, procuring products, placing orders and managing products with a function of viewing report in the system. In the system it is recognized that customer can make new registration, can login to the system, update the details and can place the order. In the same manner, admin can procure products, manage products and view the report.

2) Data Flow Diagram

Data flow Diagram is a means of representing the flow of data inside/outside the system, and flow between various actors and data store while the process in the system takes place.

- 0 Level DFD, Here system is imagined as a single unit/block where different external entities/actors the customers and admin send and receive the data from the system without describing the process involved [3].

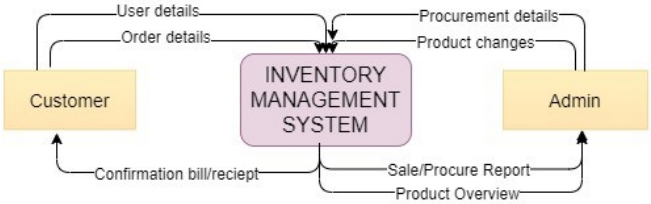

fig.3 0 Level DFD

- 1 Level DFD, here system is represented by different processes and data stored off the system, flow of the data due to process, between different actors /external entity and data stores.

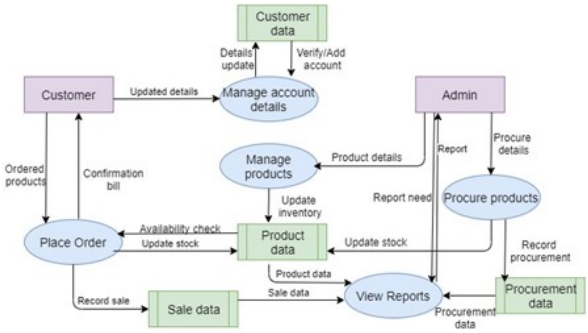

fig.4 1 Level DFD

2 level DFD, In this diagram system is decomposed with a focus on each system process. Each process has multiple sub-process and here data flow of each process is individually seen to minutely analyze the data, data flow interaction between the different components. The 2level DFD is presented in the 5 processes namely, involving customers and involving admin. The customer plays the role of managing account details and placing orders. They can also track the order in the same. The work of admin involves procuring products, managing product specifications, and, viewing the reports.

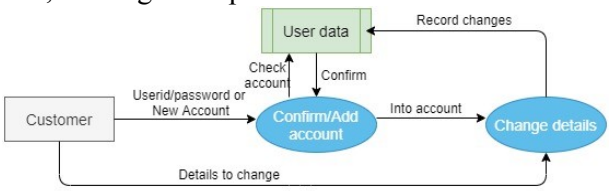

fig.5 Managing account Details

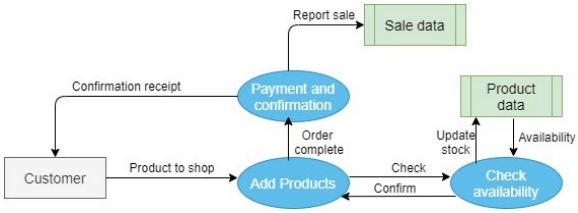

fig.6 Placing order

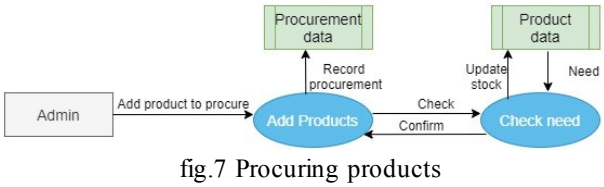

fig.7 Procuring products

Authorized licensed use limited to: DELHI TECHNICAL UNIV. Downloaded on March 03,2021 at 06:05:19 UTC from IEEE Xplore. Restrictions apply.

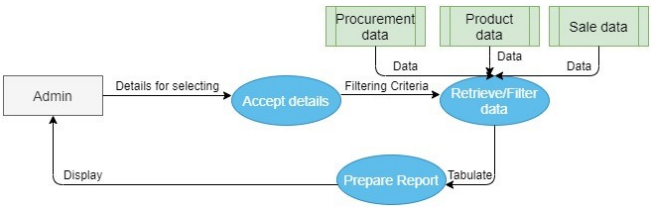

fig.8 View Report

3) ER Diagram

Following represents the different entities and attributes in the system, relation between the different entities is mentioned to overview the resultant functioning in the system.

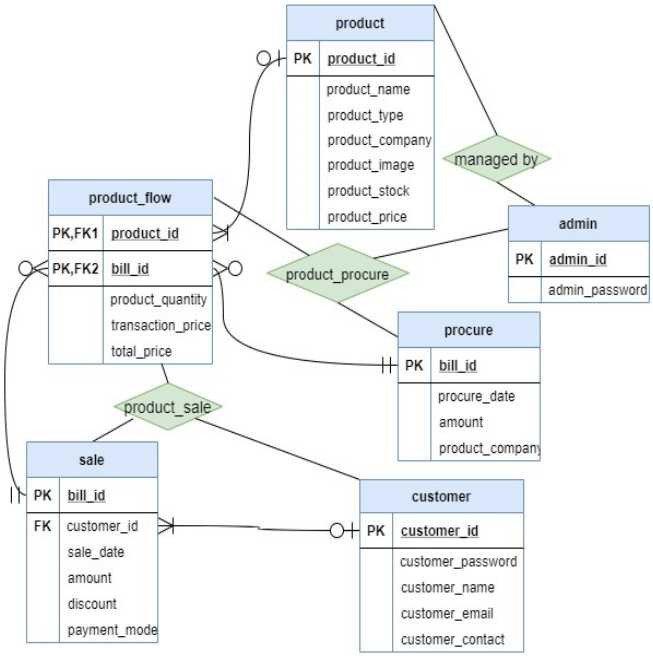

Fig.9 ER diagram

D. Design And Development

After the requirement engineering, it is focused on developing the design and code for the software. It is focused on the design and development of the database, backend development, and frontend development. Computations are made that focuses on creating a robust database that can handle a large volume of data in a short time span. Any kind of redundancies will be tried to remove wherever possible [13]. Backend processes are created to develop efficient server code that will be able to handle a large number of queries per unit of time. Similarly, Frontend processes are created to develop a user-friendly interface with the ability to navigate easily and interact with the server without any hassles. These design and development are followed by integration, testing, and maintenance. Integration involves the combining and integrating of different modules developed into a single system. This will be done once the module is designed and working without failure. Testing will focus on fixing bugs in the projects to increase efficiency, avoid failure, and make it robust enough to be used by the people. This will be done individually for each module and complete the system at an appropriate point in time [6]. Maintenance involves working on software post-launch to improve its working, fix further errors generated and adapt it to changing environment. Working on the maintenance phase will depend on time constraints, as this is the last step and possible to perform when the software is being used extensively enough to generate feedback for improvisations.

E. Tools And Technology Used

Microsoft Visual Studio Code, Microsoft SQL Server, and .NET Framework 4.5 has been used as the engineering tools for the development of the system software. The .NET framework structure has been used. It has three layers of top, middle, and bottom layers. The core potion is the bottom layer which provides the runtime environment and programs are executed. The top layers include program and user interfaces. The Microsoft SQL server is used for the database management and integration works as it supports encryption facility in its database. Further, the work of login page, backup data code, restore data code and rest works are performed by using these techniques and tools.

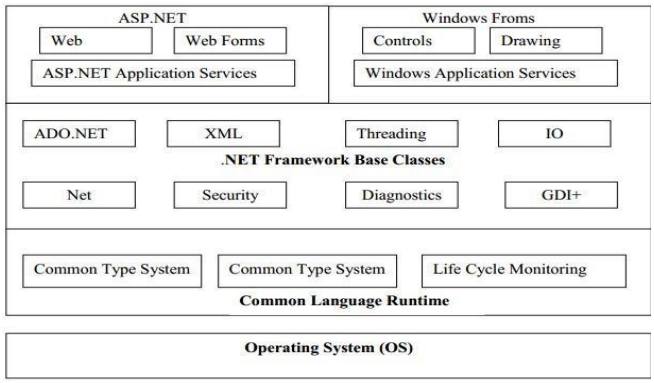

fig10 .NET framework Architecture

IV. RESULT ANALYSIS

It has been designed using software engineering specifications. This application enables people to perform different inventory and stockworks. In the final integration of code, design, and development in the hardware and software interface are considered as a technology interface.

This system has resulted in the software and hardware interface. The hardware interface is such that the user can be able to log in through their computer and mobile phones. This is designed under the convenience in all the aspects from any system supporting functions [12]. The software holds good to get operated through

Authorized licensed use limited to: DELHI TECHNICAL UNIV. Downloaded on March 03,2021 at 06:05:19 UTC from IEEE Xplore. Restrictions apply.

the hardware supporting systems. There isn't any specific memory or processing requirement and a working system with internet access and a browser can able to use it. .NET Framework is used for designing all the frontend and backend for the system. It has been designed such that one or more servers to the system can interact easily. Different sections for the inventory management modules have been created with the .NET framework in order to make the work of both sides of traders easy and comfortable.

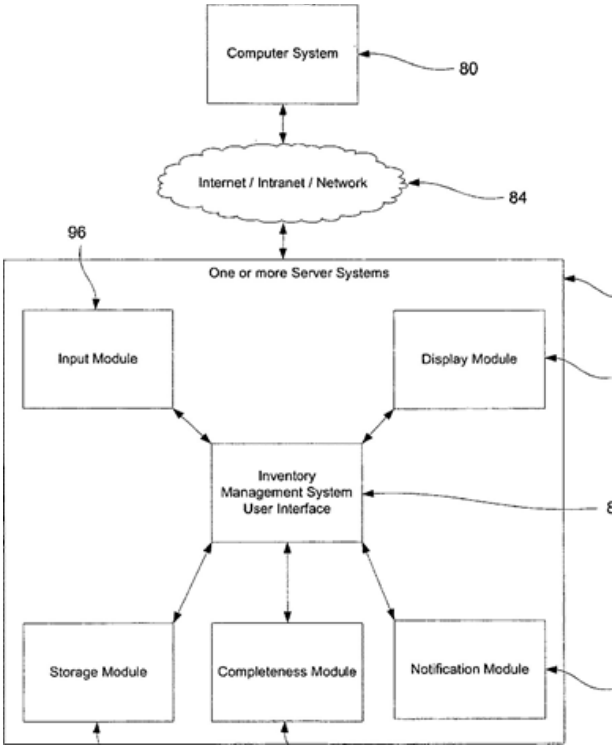

fig.11 Interface Model

The system includes the different modules that that is input modules, completeness module, a storage module, and a display module. Each module has its features and work. Each of these is deeply rooted and related. The input module gives the notification related to the attributes. The storage module stores the data which are input through the input module. The completeness module finds whether all the attributes are complete or incomplete. The display module displays the completeness and inventory items on the display device. The engineering tools and techniques used here were easy to deal with. Unit test testing was performed. This type of testing is conducted to test and analyze the software components. It is done by the programmer and not by the tester [14]. It requires detailed information and knowledge for internal design and knowledge. During unit testing, different testing such as reflection of unit data are conducted on the database and its interface.

Different functional requirements are present for both user and admin respective to carry out the works performed by them and store them in the database. User Accounts, Product Management Procuring/selling products, Report generation. It provides the facilities for the user account. Any people interested to join the software and if he/she is a new user they can sign up to the system giving some of the relevant information. The existing user can sign into the system if they want to use the service again. While signing, the system requires important information. The user can also change their existing information and can update their information. It has also product Management facilities which keep all the records of incoming and outgoing products in the warehouse. Admin holds the facility to change the product details like price, availability, and many more. Report generation facility is one of the major that gives the total summary time to time and update the system as per the requirements.

V. CONCLUSION AND FUTURE WORKS

This has been implemented successfully with a vision for medium scale industry work. It is highly accurate and sufficient enough to run a medium scale business for buying and selling of the products taking time and profits into the consideration. The best thing about this software system is that things and attributes can be inserted, updated, and deleted easily as per need. The software is very much flexible. It takes care of all the involving identities like buyer, seller, delivery person concerning time. It keeps track of all the elements involved with time. It is very time efficient. This project has made us learn various business developing strategies and financial works in a competitive market. It has also been attempted for implementing these works through machine learning and deep learning work to make things more advanced and competitive. These works can also be performed through machine learning and use it for large scale industry. This existing project can be developed and enhanced more through high mathematical computation. This is good as of now with time, but tools and technologies are being developed time and again in a more advanced and efficient manner.

ACKNOWLEDGMENT

The authors are indebted to the central library of Delhi Technological university for providing labs and materials for studying, implementing, and completing the required works.

REFERENCES

[1] P. Ignaciuk, "Discrete-time control of production-inventory systems with deteriorating stock and unreliable supplies," *IEEE Trans. Syst. Man, Cybern. Syst.*, vol. 45, no. 2, pp. 338–348, 2015, doi: 10.1109/TSMC.2014.2347012.

[2] N. N. Nandola and D. E. Rivera, "An improved

Authorized licensed use limited to: DELHI TECHNICAL UNIV. Downloaded on March 03,2021 at 06:05:19 UTC from IEEE Xplore. Restrictions apply.

formulation of hybrid model predictive control with application to production-inventory systems," *IEEE Trans. Control Syst. Technol.*, vol. 21, no. 1, pp. 121–135, 2013, doi: 10.1109/TCST.2011.2177525.

[3] L. Teng, Z. Zhang, P. Li, and D. Gong, "Integrated Inventory-Transportation Problem in Vendor-Managed Inventory System," *IEEE Access*, vol. 7, pp. 160324–160333, 2019, doi: 10.1109/ACCESS.2019.2950036.

[4] S. Lee, Y. J. Kim, T. Cheong, and S. H. Yoo, "Effects of Yield and Lead-Time Uncertainty on Retailer-Managed and Vendor-Managed Inventory Management," *IEEE Access*, vol. 7, pp. 176051–176064, 2019, doi: 10.1109/ACCESS.2019.2957595.

[5] R. M. A. Swaszek and C. G. Cassandras, "Receding Horizon Control for Station Inventory Management in a Bike-Sharing System," *IEEE Trans. Autom. Sci. Eng.*, vol. 17, no. 1, pp. 407–417, 2020, doi: 10.1109/TASE.2019.2928454.

[6] X. R. Lei and D. X. Wang, "Inventory management system of auto parts enterprises based on the Agile supply chain," *Proc. 2012 2nd Int. Conf. Instrum. Meas. Comput. Commun. Control. IMCCC 2012*, pp. 859–863, 2012, doi: 10.1109/IMCCC.2012.207.

[7] J. Huang, J. Zhao, and X. Wu, "Research on the optimization strategy of maintenance spare parts inventory management for petrochemical vehicle," *Proc. - 2011 4th Int. Conf. Inf. Manag. Innov. Manag. Ind. Eng. ICIII 2011*, vol. 1, pp. 45–48, 2011, doi: 10.1109/ICIII.2011.18.

[8] N. Nemtajela and C. Mbohwa, "Inventory management models and their effects on uncertain demand," *IEEE Int. Conf. Ind. Eng. Eng. Manag.*, vol. 2016-December, pp. 1046–1048, 2016, doi: 10.1109/IEEM.2016.7798037.

[9] Y. Fan, "Development of inventory management system," *ICIME 2010 - 2010 2nd IEEE Int. Conf. Inf. Manag. Eng.*, vol. 6, pp. 207–210, 2010, doi: 10.1109/ICIME.2010.5478077.

[10] L. P. Wang, "Study on the system optimization of inventory management of SME," *IJCAI Int. Jt. Conf. Artif. Intell.*, pp. 413–416, 2009, doi: 10.1109/JCAI.2009.49.

[11] P. Lesniewski and A. Bartoszewicz, "Optimal Model Reference Sliding Mode Control of Perishable Inventory Systems," *IEEE Trans. Autom. Sci. Eng.*, vol. 17, no. 3, pp. 1647–1656, 2020, doi: 10.1109/TASE.2020.2969493.

[12] Y. Li, F. Chu, S. Member, and C. Feng, "for Intelligent Food Logistics Systems," *IEEE Trans. Intell. Transp. Syst.*, vol. 20, no. 3, pp. 867–878, 2019.

[13] P. Hajek and M. Z. Abedin, "A Profit Function-Maximizing Inventory Backorder Prediction System Using Big Data Analytics," *IEEE Access*, vol. 8, pp. 58982–58994, 2020, doi: 10.1109/ACCESS.2020.2983118.

[14] H. Xu, P. Chen, and Y. Zhang, "Inventory Control for a Coproduction System under Demand Uncertainty," *IEEE Trans. Automat. Contr.*, vol. 64, no. 4, pp. 1627–1631, 2019, doi: 10.1109/TAC.2018.2866986.

Authorized licensed use limited to: DELHI TECHNICAL UNIV. Downloaded on March 03,2021 at 06:05:19 UTC from IEEE Xplore. Restrictions apply.

Proceedings of the Sixth International Conference on Inventive Computation Technologies [ICICT 2021]
IEEE Xplore Part Number: CFP21F70-ART; ISBN: 978-1-7281-8501-9

Internet of Things (IoT) based Assistive Devices

Malti Bansal*, Samarth Garg
Department of Electronics & Communication Engineering,
Delhi Technological University (DTU), Delhi-110042, India
*maltibansal@gmail.com

Abstract - **In the 21st century, all electronic devices have the capability to communicate and exchange data and resources through the technology known as the Internet of Things (IoT). With the number of IoT-enabled devices growing at an exponential rate, it has limitless prospects to augment the standard of living for the differently-abled as it has great potential to significantly enhance the quality of all kinds of assistive devices. In this article, a few of the many applications of IoT in assistive devices were analyzed and discussed to examine the existing prototypes that have been developed for each of them. The applications discussed here are in the fields of navigation, communication, healthcare, and education for disabled people, and the future scope of the same is also examined.**

Keywords Internet of Things (IoT),

I. INTRODUCTION

In the 21st century, all electronic devices have the capability to communicate and exchange data and resources through the internet. This vast network of technologies is termed the Internet of Things (IoT). It refers to any objects that utilize the internet to send and receive data, and in some cases, have been technologically enhanced with wireless connectivity. The number of electronic devices exceeds the population of the Earth, and continues to grow at an exponential rate. By the end of 2018, there were nearly 22 billion IoT enabled devices in use throughout the world. With the current trend, this figure is expected to rise to nearly 50 billion by 2030. A survey revealed that nearly one-third of the paralyzed people are dissatisfied with the current state of rehabilitative technology in the market. This situation can be rectified using IoT technology, which has endless prospects to augment the standard of living for disabled people. According to estimation by the World Health Organization (WHO), over a billion people are fighting some form of physical disability. Up till now, they have had to settle for a lower standard of living or rely on others. However, these limitations can be overcome by utilizing the full potential of IoT technology to improve facilities of healthcare, education, communication, navigation, etc for the differently abled.

This article is organized as follows. In Section II, IoT in navigation for the elderly and blind was discussed. Section III covers IoT based communication for deaf and dumb people. Section IV explores IoT in e-healthcare, and Section V discusses education in IoT enabled campuses. Finally, Section VI concludes this research work.

II. IOT IN NAVIGATION

One of the prominent usages of IoT applications is that it can be used to locate the position of objects in space, which can be used in various forms of navigation and guidance systems. Here, one such application of using IoT in an assistive walker to enable the elderly and visually impaired to walk on their own without having to rely on someone else for support and guidance.

The basic principle is that the walker communicates with the objects nearby to determine their exact position, and then calculates the most suitable path to walk safely, which is then communicated to the user [1]. The design involves hardware as well as software engineering. The hardware portion is composed of 3 electrical constituents such as sensor, controller, and output, while the software part includes 2 applications. The sensors determine the environment and the position of the system, and if any form of obstruction is detected, the output is immediately notified via IoT signals sent by the controller to avoid falling. The software analyses the data it receives from the sensors regarding nearby people, objects, or any other obstructions, and accordingly instructs the controller to steer the user. The device architecture is layered as follows –

a) Perception Layer – The sensors and actuators monitor the surroundings and environment

b) Network Layer – Transmits the data from the perception layer using a wireless network

c) Application Layer – Consists of the applications used to apply IoT technology to make this device work, such as Google Maps and Find Me.

All 3 layers are used in the functioning of the device. The functionality applied here can also be modified to create a device designed to prevent people from falling, or to enable their friends or family to remotely track their location to assure safety. Features can also be included to calculate distances, identify various terrains of the ground, or alert the authorities directly from the app itself.

III. IOT IN ASSISTANCE OF DEAF, DUMB AND BLIND

A. Assistance for the visually impaired

According to a WHO survey, 285 million people are visually impaired, while nearly 40 million people suffer from total blindness. This is on top of the fact that most of them belong to the low-income group [9]. NIVH's 2015-16 annual report identified 50,32,463 people as visually impaired in India. There is a stark contrast between this number for rural and urban areas with 8,17,580 males and 7,12,293 in urban areas as opposed to 18,20,936 males and 16,81,654 females in rural [12-17].

This has necessitated action in the assistive technology for blind people in the fields of navigation, reading, and asset tracking [4].

a) Navigation – A significant amount of work has already been done for outdoor navigation, leaving an urgent need for indoor navigation (crowded areas like bus and railway stations, hospitals, airports, etc).

b) Reading – A device has been developed that is capable of converting text to voice as well as

2021 6th International Conference on Inventive Computation Technologies (ICICT) | 978-1-7281-8501-9/21/$31.00 ©2021 IEEE | DOI: 10.1109/ICICT50816.2021.9358662

Authorized licensed use limited to: DELHI TECHNICAL UNIV. Downloaded on March 03,2021 at 06:11:35 UTC from IEEE Xplore. Restrictions apply.

braille. It includes a hand glove with sensors to create braille impressions on the user's fingertips.

c) Asset Tracking –The basic idea is to enable blind people to locate the position of objects in nearby space using RFID technology.

B. *Communication for deaf and dumb*

A simple, yet highly useful device for the communication of deaf people makes use of voice recognition on a mobile device to convert speech to text, transfer it to Arduino using Bluetooth connectivity, interpret it using ASCII characters, and display the content as text in the wearable device. It enables a healthy person to communicate with a disabled person without the use of sign language. The process is showcased visually in Fig. 1. [2].

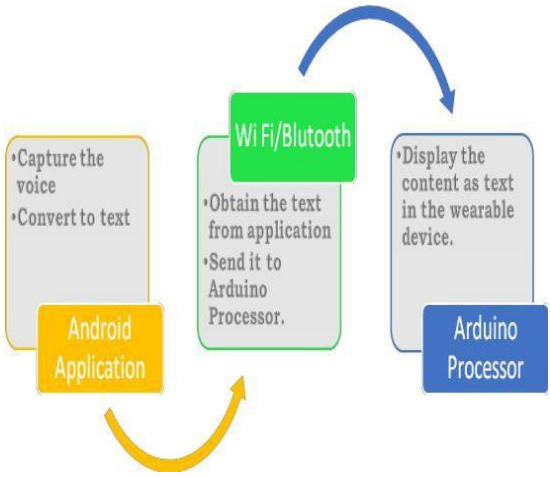

Fig. 1. Speech to text convertor

For the converse of this process, i.e. for the healthy person to understand the disabled person without knowledge of sign language, a speech to text converter has been developed to convert signs made by the users into voice. It contains 3 modules – camera, controller, speaker. The image captured by the camera is sent to the controller to be analyzed using several algorithms. Upon recognition of the sign, the corresponding digit is generated using the pre-installed dataset. In this manner, the entire text is passed in the text-to-speech module to be converted to speech and be output at the speaker. Thus, this device provides a convenient way for a two-way interaction between a healthy and disabled person.

The working of this working is depicted in the flowchart shown in Fig. 2 [5].

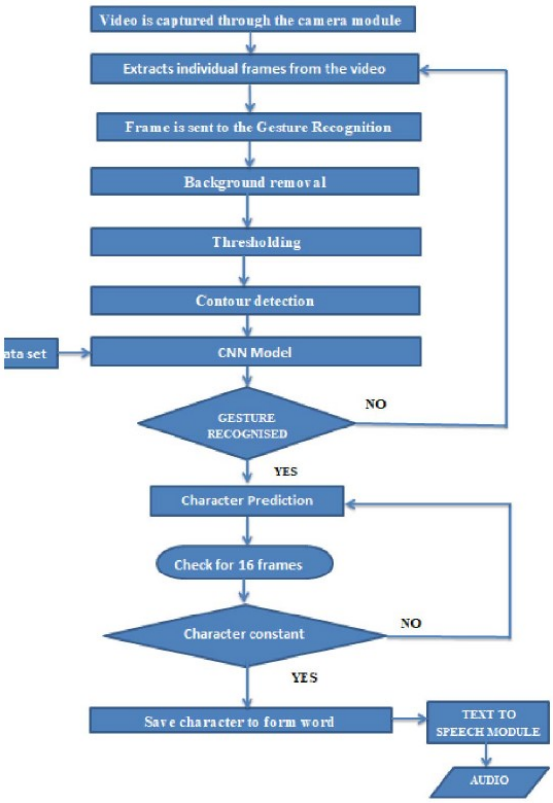

Fig. 2. Sign language to speech convertor

IV. IoT IN E-HEALTHCARE

The most useful and most important application of this emerging technology of IoT is in the field of healthcare. While the medical system in the world possesses the technology to cure a huge number of diseases known, that technology is not up to the mark in catering to the needs of physically disabled patients. In this section, discussion is made on 2 devices that make use of IoT technology to improve the healthcare system for physically disabled patients.

A. *IoT based communication device for disabled inmates*

While the disabled inmates in a hospital may be cured of their sickness, not all of them are fortunate enough to even have the ability to voice their discomfort or needs to their doctors and nurses. This device provides an effective medium of communication for the disabled inmates of a hospital. The system consists of 2 units – a transmitter and a receiver, that communicate through zig-bee protocol [8]. The transmitter unit contains images depicting various needs the user might have (considering illiterate users), and buttons that send a unique coded message describing the corresponding requirement of the user using a zig-bee transmitter in around 1.75 seconds. Such high-speed transmission is attained using an ARM controller. The transmitted signal is received as an SMS on the assistant's phone. At the receiver unit, a zig-bee receiver presents the received data to a raspberry-pi processor, which in turn sends HDMI signals to display the message on output. This whole process is completed in under 2 seconds owing to the high-speed transmission capability of the raspberry pi processor.

The workings of both units have been visually summarised in the 2 flowcharts in figures 3 and 4 **[8]**.

Authorized licensed use limited to: DELHI TECHNICAL UNIV. Downloaded on March 03,2021 at 06:11:35 UTC from IEEE Xplore. Restrictions apply.

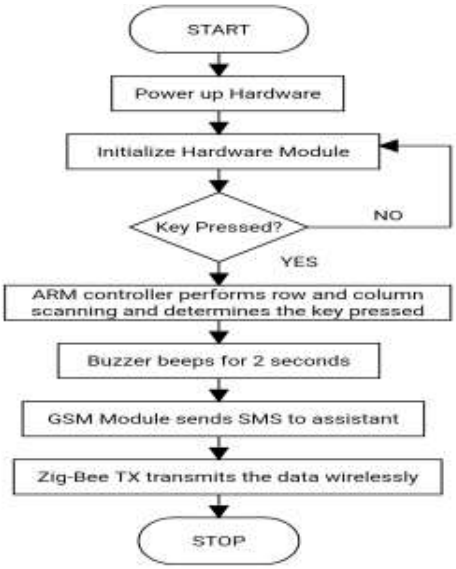

Fig. 3. Transmitter flowchart

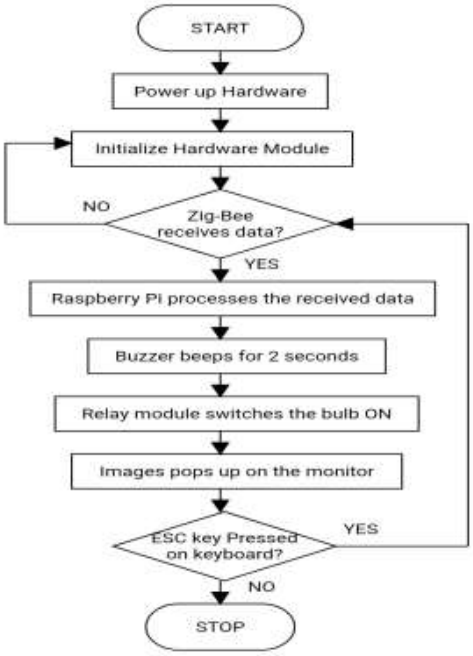

Fig. 4. Receiver flowchart

The device was tested for over 20 messages, each of which was transmitted perfectly without the loss or corruption of any data.

B. IoT enabled full-body exoskeleton

Another major development in the field of e-healthcare is the movement of paralyzed people. At this time, the most popular solution for assistance and rehabilitation of paralyzed people is exoskeletons. There are several different types of exoskeletons with varied purposes ranging from rehabilitation, assistance in transportation, and movement. The major issues with these include constraints in portability, flexibility, adaptability, and ease of wearability.

These issues can be curbed with the development of a Brain Energized Full Body Exoskeleton (BFBE) [7]. It captures brain signals using EEG sensors. When the user wishes to make a particular movement like sitting, standing, sleeping, etc, the sensors detect that intention by capturing brain signals, and a microcontroller in the Control Unit generates a signal for the corresponding body part. Through the Body-Part Actuation Module (BAM), this activation signal is passed to the required body part, and the stored potential energy in the system is used to complete said movement. The components of this BFBE can be attached and detached with ease to modify it according to the degree of paralysis of the user. It also involves a module to immediately alert the attendants in case of emergency. The prototype was tested for 6 basic movements for 10 different patients and the results were extremely promising.

V. EDUCATION IN IOT ENABLED CAMPUSES

While the disabled students in institutes of higher education get access to education, which is a fundamental right in every country in the world, their physical dysfunctions pose several barriers that stand in the way of them gaining the full experience of campus life. They are unable to access elevators, lighting, air conditioning, operate laboratory equipment, and face issues with stairs and heavy/sliding doors. Although these barriers cannot be eliminated, their impact can be softened by utilizing IoT. Of all the applications of IoT that have been discussed up till now, this is probably one of the most important.

The frontrunner in this domain at this point is the smartwatch developed for an IoT enabled campus. Coupled with a smartphone, it operates all IoT-enabled objects on campus using Web APIs [6]. These APIs can be used to access the thousands of sensors and other devices located throughout the campus, and also have the provision of operating machines like air conditioners or elevators based on concurrent values of the consumer's usage of electricity, temperature, location, etc. The basic functionality involved in this smartwatch so far permits users to check the status of quantities like illumination and temperature of a room, location of an elevator, lock and unlock a door or their lockers, etc, and these can be modified according to the user's preference. It also contains a very important "Assist Call" feature which automatically notifies the university staff when someone requires assistance over something like a closed door or a fallen wheelchair or something else the user is not able to combat themselves. Apart from visual, this prototype also has touch sensitivity to enable visually impaired students to operate it with ease.

A preliminary study conducted on 2 students with disabilities at the Tokyo University, wherein they performed a few of the basic tasks discussed above using the smartwatch as well as smartphone application was very well received. The locker control functionality was particularly appealing to both students. There are several other projects under research and development working on making education easier by developing such assistive devices.

Authorized licensed use limited to: DELHI TECHNICAL UNIV. Downloaded on March 03,2021 at 06:11:35 UTC from IEEE Xplore. Restrictions apply.

VI. CONCLUSION

At present, a significant amount of work has been done in various domains to improve the standard of living for the disabled population in the world. Outdoor navigation for the elderly and visually impaired is significantly advanced with laser cane, ultra cane, sonic guide, etc. as well as devices like an assistive walker. The visually impaired have been given the ability to read and walk of their own accord, while their capability of locating objects in physical space is still under work. Deaf and dumb people's ability is to communicate with massive leap, as with the IoT technology it can have a two-way interaction without the requirement of the healthy person knowing sign language. One of the biggest impacts IoT has had is on the healthcare industry, as patients now possess the ability to interact with their doctors and nurses remotely. The exoskeletons detecting brain waves to enable paralyzed patients to move without having to rely on anyone is arguably one of the most important inventions so far. Finally, with communication, movement, and navigation possible for the disabled, this IoT technology has been applied to ensure quality education to every disabled student. In the future, this technology can be applied to indoor navigation and asset tracking for blind people, and certain improvements can be made to assistive walkers, like detection of terrain and real-time location.

REFERENCES

[1] M. Aljahdali, R. Abokhamees, A. Bensenouci, T. Brahimi and M. Bensenouci, "IoT based assistive walker device for frail &visually impaired people," 2018 15th Learning and Technology Conference (L&T), Jeddah, 2018, pp. 171-177, doi: 10.1109/LT.2018.8368503.

[2] J. Jeyaranjani and A. Nesarani, "Internet of Things for Hearing Impaired People," 2018 Second International Conference on Intelligent Computing and Control Systems (ICICCS), Madurai, India, 2018, pp. 1943-1946, doi: 10.1109/ICCONS.2018.8663117.

[3] P. Chatterjee, R. L. Armentano and L. J. Cymberknop, "Internet of Things and Decision Support System for eHealth - Applied to Cardiometabolic Diseases," 2017 International Conference on Machine Learning and Data Science (MLDS), Noida, 2017, pp. 75-79, doi: 10.1109/MLDS.2017.22.

[4] P. Nawandar and V. V. Gohokar, "Design and development of multisensory smart assistive technology for blind persons," 2018 International Conference on Research in Intelligent and Computing in Engineering (RICE), San Salvador, 2018, pp. 1-4, doi: 10.1109/RICE.2018.8627902.

[5] L. Boppana, R. Ahamed, H. Rane and R. K. Kodali, "Assistive Sign Language Converter for Deaf and Dumb," 2019 International Conference on Internet of Things (iThings) and IEEE Green Computing and Communications (GreenCom) and IEEE Cyber, Physical and Social Computing (CPSCom) and IEEE Smart Data (SmartData), Atlanta, GA, USA, 2019, pp. 302-307, doi: 10.1109/iThings/GreenCom/CPSCom/SmartData.2019.00071.

[6] J. Kim, M. Bessho and K. Sakamura, "Towards a Smartwatch Application to Assist Students with Disabilities in an IoT-enabled Campus," 2019 IEEE 1st Global Conference on Life Sciences and Technologies (LifeTech), Osaka, Japan, 2019, pp. 243-246, doi: 10.1109/LifeTech.2019.8883995.

[7] S. Jacob et al., "An Adaptive and Flexible Brain Energized Full Body Exoskeleton With IoT Edge for Assisting the Paralyzed Patients," in IEEE Access, vol. 8, pp. 100721-100731, 2020, doi: 10.1109/ACCESS.2020.2997727.

[8] C. Tejas, V. Tejashwini and V. Murari, "Assistive Technology: An IoT based device for Physically Challenged People and Hospital Inmates," 2018 3rd IEEE International Conference on Recent Trends in Electronics, Information & Communication Technology (RTEICT), Bangalore, India, 2018, pp. 1906-1911, doi: 10.1109/RTEICT42901.2018.9012369.

[9] "Visual Impairment and Blindness," World Health Organization Factsheet Fs282, December 2014. [Online] Available Http://Www.Who.Int/Mediacentre/Factsheets/Fs282/En/

[10] M. Sarac, M. Solazzi, and A. Frisoli, ``Design requirements of generic hand exoskeletons and survey of hand exoskeletons for rehabilitation, assistive, or haptic use," *IEEE Trans. Haptics*, vol. 12, no. 4, pp. 400_413, Oct. 2019, doi: 10.1109/toh.2019.2924881.

[11] https://blog.technavio.com/blog/assistive-technology-internet-things-people-disabilities

[12] "http://nivh.gov.in/"

[13] M. Bansal and Priya, "Application Layer Protocols for Internet of Healthcare Things (IoHT)," *2020 Fourth International Conference on Inventive Systems and Control (ICISC)*, Coimbatore, India, 2020, pp. 369-376, doi: 10.1109/ICISC47916.2020.9171092.

[14] M. Bansal, Priya, "Performance Comparison of MQTT and CoAP Protocols in Different Simulation Environments". G. Ranganathan, J. Chen, A. Rocha (eds) Inventive Communication and Computational Technologies. Lecture Notes in Networks and Systems, vol. 145, pp. 549-560, Springer, Singapore, https://doi.org/10.1007/978-981-15-7345-3_47

[15] M.Bansal, Priya, "Machine Learning Perspective in VLSI Computer Aided Design at Different Abstraction Levels", 2nd Int. Conf. on Mobile Computing and Sustainable Informatics (ICMCSI 2021), Tribhuvan University, Nepal, 2021.

[16] M.Bansal, A. Goyal, A. Choudhary, "Industrial Internet of Things (IIoT): A Vivid Perspective", 5th Int. Conf. on Inventive Systems and Control (ICISC 2021), India, 2021.

[17] M. Bansal, V. Sirpal, M. K. Choudhary, "Advancing e-Government using Internet of Things", ", 2nd Int. Conf. on Mobile Computing and Sustainable Informatics (ICMCSI 2021), Tribhuvan University, Nepal, 2021.

Authorized licensed use limited to: DELHI TECHNICAL UNIV. Downloaded on March 03,2021 at 06:11:35 UTC from IEEE Xplore. Restrictions apply.

Leveraging retention sales based innovative incentive structure to turnaround automobile dealership

Fateh Bahadur Singh[1] , Brajesh Mishra[2], and Anjali Singh[3]

[1]*Research Scholar, School of Commerce & Management, Career Point University Kota, Rajasthan, India*
[2]*Research Scholar, Management Development Institute Gurgaon, India*
[3]*Business Operations Associate, ZS Associates, India*

Address of Corresponding Author:

535, Windsor Green,
Sector 50, Noida
Uttar Pradesh - 201301
India;

Email: singhfb2010@gmail.com
Phone: +91-9910015581.

A brief biographical note
Fateh Bahadur Singh

Fateh Bahadur Singh is research scholar at the School of Commerce & Management, Career Point University Kota, Rajasthan. After successfully completing B.Tech degree in Mechanical Engineering and MBA, he embarked an illustrious career of more than two decades in Indian Automobile sector. Academically, he is interested in strategic management, supply chain management, and application of business process innovation in automobile dealership network (singhfb2010@gmail.com).

Brajesh Mishra

Brajesh Mishra is a research scholar at the School of Public Policy & Governance, Management Development Institute Gurgaon. He has done Master of Engineering, MBA and Post Graduate Diploma in Public Policy & Governance. He has around 25 years of experience of Public Services in various organisations of Government of India. His research interests are focussed at public policy processes & regulatory governance, financial inclusion, and electronics sector (fpm18brajesh_m@mdi.ac.in).

Anjali Singh

Anjali Singh is working as a Business Operations Associate with the global consulting firm ZS Associates. She completed her graduation in Bachelor of Technology in year 2020 from Delhi Technological University (formerly DCE), Delhi. She has previously published her research in leading journals such as the International Journal of Advanced Science and Technology (IJAST) and her research interests lie in the areas of technology and management (anjalidtu97@gmail.com).

Leveraging retention sales based innovative incentive structure to turnaround automobile dealership

Abstract

This study aims to suggest innovative incentive structure for Indian automobile dealerships to improve their business performance. Automobile dealerships success is highly dependent on quality of people who are engaged in various operations. The sales team size is quite large where majority of employees are directly engaged in selling vehicles and other auxiliary services. The sales team has to be highly passionate and motivated to take ownership to meet the designed business plan and revenue targets assigned to them. The monthly salary package of sales team members comprises of a fixed component and a substantial variable incentive component. Hence, incentive structure has to be carefully designed to motivate each sales team member achieve assigned the assigned plan of revenues and profits. The study intends to develop practical relevant knowledge by adopting a qualitative approach based action research method and documents analysis. This research paper covers impact of changes in incentive structure on retention and net earnings per vehicle sales. The study emphasizes redesigning of incentive structure by directly linking retention per vehicle sales with incentive amount. The retention per vehicle sales closely represents the contribution of sales team members in the dealership overall profit from new vehicle sales transactions.

1. Introduction

The Indian automobile sector has emerged as a key contributor in the growth of country's economy. It not only generates direct and indirect employments but also adds around 7% to Indian GDP [1]. Automobile dealership network of any manufacturer acts an important interface between manufacturers and customers by executing sales of new vehicles and after-sales services. Most of the Indian automobile dealerships are facing continued pressure from increasing operational costs, cut-throat competition, low manpower productivity, and declining sales volume, with many even finding difficult to sustain their business operations. As per one study less than 60% of dealerships are profit making.

Subjective performance evaluations can better formulate and implement incentive systems in an automobile dealership [2]. The resulting incentive systems can be used as an effective intervention tool to remove perceived weaknesses in bonus/incentive awards, thereby reducing employee risk, increasing employee productivity, achieving greater employee satisfaction, and increasing trust between management and other employees. Such incentive systems could be applied to enhance the alignment of firm interests with its employees to reduce employees' risk.

Incentives are an important tool for manpower management in corporate or projects in which a large no of people are engaged together to deliver a task. In case of monetary incentives, when salary is attached to merit, every employee in the organization will focus on the improved quality and efficiency of work done [3]. Since various level of employees working in any organization may not share the same vision as the owner or director of the company or organization hence incentives plays a pivotal role in order to induce individuals to contribute activity [4]. In an automobile dealership, an innovative incentive structure inspires employees towards the path of achieving plans and enhances profitability as its incentive structure drives the manpower engaged and also motivates them for better results as their income is also linked with the increased earnings of the organization.

On the other side, if, an incentive structure is not designed with deeper understanding of the sales and business or work environment and competiveness of the market then employees do not get aligned with the end objective results which are revenues and profits. This leads to unfocussed efforts and manpower costs as organization keep on spending on incentives to employees which do not yield commensurate positive impact on sales revenue and profits [5].

This study aims to suggest innovative incentive structure for Indian automobile dealerships to improve their business performance (turnaround business for loss making dealerships). Further, the study intends to develop practical relevant knowledge by adopting a qualitative approach based action research method and documents analysis. Section 2 covers an overview of incentives, while the section 3 covers literatures review. The section 4 presents research methodology adopted in the study, while section 5 covers result and discussion. The section 6 contains the conclusion of the study.

2. Overview of incentives

There can be various forms of incentives which differ as per the requirement and business objectives of the organization. Depending on the type of motivation a dealership would like to pursue their employees and the resources available to be given as incentives. Incentive management in an automobile dealership includes the following three important aspects of manpower:

- Performance tracking of employees
- A plan for 'when' incentive or reward should be given/ on what basis
- 'What' should be given as a reward or incentive

Performance tracking of employees stands as the first step towards an effective incentive system at an automobile dealership or any organization for that matter. Performance tracking includes a regular, strict, and clear reporting of each employee's efforts and achievements. Typically, automobile companies and dealerships both, look forward to track the efforts of each individual employee for number of leads generated and automobiles sold either directly through customer interaction or indirectly through their initiatives for the area/ regions falling under their responsibility. The need for performance tracking must be regular, in time and strict to avoid any unfairness, bias, or confusion in measuring the efforts of employees and thus maintaining a healthy, motivating, and encouraging environment.

The second aspect which holds importance is to develop the rules of incentives planning which will define when an employee will be rewarded with an incentive. The incentive rules have to be carefully defined to keep a realistic but sufficiently high target for employees to achieve, and to ensure that it is well-aligned with the current goals of the automobile dealership. The target plan has to be also based on the potential available for achieving the designed or set business plan or sales numbers. A reward/incentive scheme that relies on unrealistic goals for employees may have a reverse effect on an employee's psychology and demotivates rather than encouraging them. Hence, a well-balanced reward scheme needs to be developed taking into consideration the potential of employees and that of the brand, territory, and time of the year.

3. Literature Review

The literature survey of academic articles, as a part of document analysis, around the research objective helped in the identification of two categories: (i) role of human resource development in automobile dealership, (ii) incentivising automobile dealership employees' performance.

3.1 Role of human resource development in automobile dealership

Tsuru [6] analyzed the economic consequences of performance-oriented reforms in HR systems in a large Japanese automobile dealership. The three major HR reform components considered are – base wages, performance ratings system, and performance connected to pay. The author also measured the productivity effects of HR reforms. The study established that a new HR system (drawing from performance-related pay scheme) may enhance the performance of the auto sales team.

Karthikeyan [7] evaluated the role of human resource development initiatives on sales team in Indian automobile dealerships facing numerous globalization based challenges. The author suggested adopting regular HR as a proactive measure to enhance employees' development processes and improve the dealership's performance. This is important due to the emergence of globalization that has allowed multinational companies to extend their products and services in developing countries like India.

A firm-specific case study presented how an automobile dealership's HR department addresses the challenges of recruiting, developing, and retaining the right talent in the organization [8]. The HR department, inter-alia, selects people with a passion for serving, positive/ right attitude, ability, and potential to perform well. The firm has adopted an employee engagement program (birthdays, festival celebrations, etc.), flexible work hours, counseling/ mentoring cells, stay interviews, etc., as a strategy to retain the firm's right talents. Through structured induction/ orientation programs and regular quality training, the firm has succeeded in reducing the incubation period to half (3 months).

3.2 Incentivising employees performance in automobile dealership

Philipps [9] in his study on matching the compensation plan to the sales role has explained about the importance of understanding the role of sales force first which they need to play and then have suggested to design a suitable compensation package which motivates to play that role. Here, it is utmost important to know the selling environment in which sales team must perform, understanding the customers, their need and the effort level required to close the sales. This includes clear understanding of business plan, competitors. After clear knowhow of selling environment, the objectives can be decided for sales team and it must be aligned with the compensation packages. Glendinning [10] studied the relationship between sales compensation with the personality and attitude of sales people in automobile industry. The study communicates that sales compensation programmes plays a vital role in developing culture of competitiveness in dealerships, an aggressive environment.

Gibbs et al. [2] have examined how subjective performance evaluations can better formulate and implement incentive systems in an automobile dealership. The study established that subjective bonuses can be used as an effective intervention tool to remove perceived weaknesses in bonus/incentive awards, thereby reducing employee risk, increasing employee productivity, achieving greater employee satisfaction, and increasing trust between

management and other employees. The authors further argued that subjectivity could be applied to enhance the alignment of firm interests with its employees to reduce employees' risk. Ho et al. [11] have examined how modification in compensation/ incentive plans can affect employees' recruitment, performance, and retention: The authors established that an inferior performance-sensitive compensation may decline individual sales productivity but may not necessarily impact overall company's performance.

Jansen et al. [12] have analyzed differences in incentive compensation practices being followed in the USA and Netherlands, wherein their impact on various financial performance measurements is also evaluated. The study revealed significant differences in practices being followed in the USA and Netherlands. The Netherland manufacturers were found less likely to extend adequate incentives to their managers. Further, in their case, the incentive compensation followed was found to be much more complicated. Merchant et al. [13] have compared performance measurement, and incentive compensation practices followed in Chinese and Western firms (USA and Netherlands) in their qualitative empirical study. The study established that Chinese firms provide better incentive compensation vis-a-vis dealers in Netherlands and USA. The Chinese firms apply subjectivity in their bonus payment plans and also consider non-financial performance measures.

A study by Zhang et al. [14] covers the linkages of pay with productivity in a firm or organization and throws lights on importance of performance-based incentives. Here, individual performance has been in focus and incentives and wages has linked with this which resulted into higher productivity in lower level jobs like front line sales team members. The results of reforms have been encouraging as it has improved individual employees' productivity substantially and has created strong motivating effect in increasing new car sales. Kaul & Singh [15] highlighted need to reduce attrition in Indian automobile industry. The article refers to industry study conducted jointly by FADA and Frost and Sullivan. The rising attrition, especially in the frontline sales force, has been one of the biggest concerns faced by Indian automobile dealerships in the recent past. There has been huge gap between required numbers and the actual skilled manpower available. There is huge pressure to optimize the costs. The study revealed that expense to revenue ratios for dealers, interest cost, and manpower costs have increased over the years hence there is a need to change the incentive structures. The incentive structure should remains attractive for front line sales team members so that their overall earnings keep growing with growth of dealership revenues and profits.

4. Research Methodology

To operationalize this study using a qualitative approach, the "action research" method is primarily applied. It is supported by document analysis on the industry reports, academic articles, and documents containing data from the automobile dealerships chosen for the case study. The business process innovation is used as a conceptual lens to suggest a solution in form of innovative incentive structure to replace the existing one. As per Coghlan [16], action research may be defined as "a participatory, democratic process concerned with developing practical knowing in the pursuit of worthwhile human purposes. It is grounded in participatory worldview." Broad characteristics of action research include: research *in* action, rather than research *about* action; a collaborative democratic process;

concurrent with action; a sequence of events and an approach to problem solving (iterative cycle of gathering data, analysis, planning action, taking action and evaluating).

For answering specific questions of this study, a case study approach is taken as it is helpful for establishment of new theory and verifying current theories along with testing specific hypotheses empirically. The automobile dealership chosen for the case study is Shiv Autowings Mahindra, located in the Pimpri Chinchwad area of Pune in Maharashtra, India. This dealership was fit for the study as it represents the Indian automobile dealerships which are facing challenges and are in need for solutions to enhance their profitability. Further, this dealership owner also allowed easy access of their business performance data.

5. Result and Discussion

In this section first the existing incentive structure followed at Shiv Autowings Mahindra dealership was analyzed. Based on this analysis and demerits identified in the existing incentive structure, an improved incentive structure was hypothesized following action research approach. Next, the merits of the new incentive structure are analyzed.

5.1 Analysis of incentive structure prior to October 2020

A snapshot of incentive structure applicable for sales consultant prior to October 2020 is presented in Table 1. As evident from Table 1, the additional incentive amount of INR 50 per vehicle is applicable from 5^{th} vehicle onwards. This was designed to push sales consultants to increase their sales numbers. Sales consultants selling less than 4 vehicles were not eligible for any incentives. For a sales consultant, the job is to convert every potential enquiry to sales and deliver the vehicle to them. The sales consultant is supposed to ensure selling of vehicles by highlighting various schemes and offers and in the process prevent the loss of business opportunity to other brands or dealerships of the same brands.

Table 1 Snapshot of incentive structure applicable for sales consultant prior to October 2020.

Existing structure	Incentive starts from 4^{th} vehicle, INR 50 approx. added on additional vehicles							
Condition	sales	on 4^{th}	on 5^{th}	on 6^{th}	on 7^{th}	on 8^{th}	on 9^{th}	10^{th} and above
Per Vehicle	Incentive	1500	1550	1650	1700	1750	1800	1800
On total vehicles	Retails#	4	5	6	7	8	9	10
Amount Earned	Total	6000	7550	9200	10900	12650	14450	16250

5.2 Shortcomings in the previous incentive structure

In automobile dealership, the revenue generation and the earning sources are many: new car sales dealer margin, pay-out incentive earnings from various banks on in-house finance cases, margins on vehicle insurance, accessories sales, extended warrantee , anti-rust and Teflon coatings etc. Here, a lot of effort is needed in marketing these auxiliary products/services along with new vehicle sales. For this, the sales consultant is required to convince

customers and maximize revenue and profits on each vehicle sales by marketing benefits of all these products and auxiliary services. Since, the incentive amount is not linked with overall net earnings and profits which include these entire services, the sales consultant are not motivated to put their best efforts by maximizing earnings in each of such possible areas.

In the incentive structure prior to action research intervention, the incentive amount for sales consultants was linked with number of vehicles sales only. The higher the number of vehicles sales means higher incentive opportunity. In this process, a majority of sales consultants put their efforts to deliver sales of more vehicles even by giving higher discounts and offers which finally erodes into dealership margin and results into loss of earnings and reduced profits on each sale. The efforts and focus of sales consultants has been found missing on selling auxiliary services as the incentive amount is not covering/linked with auxiliary services/products, which reduces the net overall earnings and profits per vehicle.

In summary, the incentive model, failed to motivate the employees to optimize the earning and profit opportunity out of each vehicle sales. In fact, in the race to selling greater number of vehicles, the sales representatives used to offer more discounts than needed. This analysis of the existing incentive structure helped to identify its demerits and propose an innovative incentive scheme which could motivate sales consultants to earn higher amounts and also deliver higher earnings and profit per vehicle to dealership.

5.3 Formulating innovative incentive structure: manpower management

5.3.1 Concept of retention

The ratio of net earnings with the net price of a vehicle with a dealership margin without tax is retention.

$$\text{Retention} = \frac{(\text{Net earnings after all offers \& } discounts)}{(\text{Net dealership billing price by OEM} + \text{Dealership Margin} - \text{taxes})}$$

The retention is the net earnings by the dealership on any new vehicle sales after all offers and discounts given to customers. Besides, dealership margin, there are many auxiliary services and areas which add to dealership per vehicle net earnings. The highest contribution comes from in-house finance pay-outs which are normally 1.0% to 2.0% on finance amount. Accessories sales are another one of the highest contributors to increase retention where margins are around 20% to 35% and per vehicle average opportunity calculates to at least INR 5,000 to INR 7,500 on an average sale of INR 20,000 worth accessories. Besides these two, there are many other opportunities to increase retention. For instance, in house insurance margins around 17%, extended warrantee, roadside assistance margins, RTO registration support income, and stockyard handling and vehicle delivery charges etc.

Many dealerships are disbursing incentives based on the number of vehicles sold by the sales consultant; hence they are just trying to deliver higher sales numbers to reach higher sales incentive slabs. Here, in this race, they start compromising on quality sales and just focus on giving higher discounts to customers to close the deal/sale quickly. In this process, dealership retention per vehicle goes down substantially but sales consultant earns their incentives.

5.3.2. Using business process innovation conceptual lens to explore new incentive structure based on 'retention'

The action research approach adopted in this study helped in exploring possible ways to address the shortcomings of the old incentive structure, through the support of experts, senior executives and owner of dealership. Finally, a revised incentive structure model for sales consultant (SC) has been developed. The revised model focused on (i) linking part of incentive with achieving sales numbers, (ii) linking incentives slabs with retention value per vehicle.

The revised structure has been designed to ensure far higher incentives to those sales consultants who deliver higher percentage of retention per vehicle along with increasing sales volume. Comparative presentation of incentive structure (prior to October 2020) and the revised incentive structure are presented in Table 2. As evident from Table 2, the revised incentive structure consists of two components - Part A (fixed) and Part B (variable). The fixed component of the incentive amount is rewarded as a fixed amount based on the number of vehicles sold. This is to ensure that the sales representatives may continue focusing on selling more number of vehicles to meet the targets set by the brand as well as ensure profitability and increases the vehicle population for after sales earning opportunities. The incentive amount given based on the number of vehicles sold comes to around 30% to 35% of the total incentive amount earned.

Table 2 Comparison of old and new incentive structure models for sales consultants

Label	Existing structure	Incentive starts from 4th vehicle, after this 50/- approx. added on additional no's							
Old	Condition		on 4	on 5	on 6th	on 7th	on 8th	on 9th	10,(+)
	Per Vehicle	Incentive	1500	1550	1650	1700	1750	1800	1800
	On total vehicles	Retails#	4	5	6	7	8	9	10
	Amount Earned	Total	6000	7550	9200	10900	12650	14450	16250
	Revised Structure	Incentive has 2 parts (no of vehicles+ retention per vehicle)							
A	Part (A): Fixed	No sale	4	5	6	7	8	9	10
	Per Vehicle	Incentive	500	550	600	650	700	750	800
	On total vehicles	Total	2000	2750	3600	4550	5600	6750	8000
	Part B- Variable Retention Slabs	Amount/ vehicle	Variable incentive based on retention slabs (<5%: 0 incentive)						
B	5%-5.9%	1000	4000	5000	6000	7000	8000	9000	10000
	6%-6.9%	1400	5600	7000	8400	9800	11200	12600	14000
	7%-7.9%	1800	7200	9000	10800	12600	14400	16200	18000
	8%-8.9%	2400	9600	12000	14400	16800	19200	21600	24000
A+B	5%-5.9%	Fix+ Total	6000	7750	9600	11550	13600	15750	18000
	6%-6.9%		7600	9750	12000	14350	16800	19350	22000
	7%-7.9%		9200	11750	14400	17150	20000	22950	26000
	8%-8.9%		11600	14750	18000	21350	24800	28350	32000

Table 3 Results of the application of revised incentive structure vis-a-vis old structure

	Performance Dec'2020					New Structure			Old structure	Differ.
Sales Consultant Name	Net Price (Ex S/R)	Profit	Retention	no of vehicles	Earning per vehicles	vehicle number	retention	Total (INR)	Incentive (INR)	(New – Old)
GK	13105607	832324	6.4%	16	52020	12800	22400	35200	27050	8150
G	3244272	162120	5.0%	4	40530	2000	4000	6000	6000	0
KL	3454463	248499	7.2%	4	62125	2000	7200	9200	6000	3200
MK	4394519	344658	7.8%	6	57443	3600	10800	14400	9200	5200
PK	2620908	201200	7.7%	3	67067	0		0	0	0
RP	937387	63166	6.7%	1	63166	0		0	0	0
SJ	5838810	413024	7.1%	8	51628	5600	14400	20000	12650	7350
SW	3348726	189209	5.7%	4	47302	2000	4000	6000	6000	0
SD	672200	42320	6.3%	1	42320	0		0	0	0
SC	2888925	178437	6.2%	2	89219	0		0	0	0
VK	5294183	393569	7.4%	6	65595	3600	10800	14400	9200	5200
Grand Total	45860908	3068526	6.7%	55	55791			105200	76100	29100

The revised incentive model intends to ensure equally high level of efforts and focus from sales consultants on variable component (Part B) of the new incentive structure. The variable component varies with the 'retention' or the net earnings achieved by the sales consultant on the sale of each vehicle. It ensures that the employees are motivated to find ways to increase the earnings on each vehicle rather than just selling a higher number of vehicles.

The incentive calculations for individual employees both using old and new incentive structures are presented in Table 3. The revised incentive structure motivated the sales team members to sale vehicles so as to achieve higher earning per vehicle by maximizing opportunities of earning from various auxiliary services and products like in-house finance, in-house insurance, accessories sales, extended warrantee sales, road side assistance package sales, etc. The net incentive amount earnings are far higher in revised structure for members who put effort in increasing retention per vehicle. This is a win-win situation for both dealership as well sales consultants. The per sales earning opportunity for a sale consultant as per old structure was INR 7,550 on sales of 5 vehicles whereas in revised structure the opportunity is as high as INR 14,750 (around double the earlier amount) in case the retention slab improves from 5% to 8%.

The important inferences drawn from the comparative incentive structure presented in Table 3 are: (i) three sales consultants (namely G, KL, and SW, despite selling the same number of passenger vehicles, took home different amounts of incentive. This was owing to the fact that KL achieved > 7% retention and hence earned INR 9,200 incentive, INR 3,200 higher than the other two; (ii) the incentive earning opportunity increased for many sales consultants (for instance GK and SJ), who earned far higher amount of incentives in new structure as compared to

the old structure. GK earned INR 8,150 additional incentive and similarly SJ earned INR 7,350 additional incentive in new structure; (iii) the dealership spent an amount of INR 29,100 more on incentives in the new incentive structure compared to old structure but for net overall increase in earnings and profits for dealership.

Since the aim of revised incentive structure is to enhance the overall profitability of the dealership, the profitability data for the period October to December 2019 is presented against the similar data for the period October to December 2020 to demonstrate the impact of implementation of new incentive structure based on business innovation process (refer to Table 4).

Table 4 Comparison of total profitability before and after the implementation of the revised incentive structure

	2019			2020			Variance (2020 Vs 2019)		
PV	Sales Volume	Total earnings (INR)	Per Vehicle Earnings (INR)	Sales Volume	Total earnings (INR)	Per Vehicle Earnings (INR)	Sales Volume	Total earnings (INR)	Per Vehicle Earnings (INR)
Oct	80	2798836	34985	40	1944816	48620	-40	-854020	13635
Nov	42	1280667	30492	57	2998116	52599	15	1717449	22106
Dec	65	2302216	35419	55	3068526	55791	-10	766310	20373
Quarter Total	187	6381719	34127	152	8011458	52707	-35	1629739	18580

On comparing the profitability data for the months of October, November and December across the years 2019 (old incentive structure was in place) and 2020 (new incentive structure), it is observed that although the volume of vehicle sales reduced by 35 numbers, the overall profitability increased by INR 1.63 million. It establishes that with increase in sales consultants' focus on retention earned per vehicle, the dealership earned more profits on the each vehicle sales. Thus, the aim of increasing the automobile dealership's profitability has been achieved using action research approach.

5.4 Advantages of the revised incentive structure

The new incentive structure ensures that the employee focuses not only on selling a higher number of vehicles but also maximize the net earnings on each vehicle sold. This has a direct effect on the profitability of the automobile dealership and ensures the employees are following the best practices in their endeavors to sell more vehicles.

In the older incentive structure, the employees were motivated with the aim of selling a higher number of vehicles while the aim of the owner was to make higher profits. These goals were misaligned and often not complementing. Particularly, in cases where more vehicles were sold on discounts but lesser profits were made.. However, after implementation of new incentive structure, each employee (even at the junior level) is motivated to strive for better earnings instead of narrowing their job to just meeting the sales number targets. It enhances a greater sense of ownership and responsibility in them. Further, it aligns the aims of every employee with that of the automobile dealership owner, thereby, giving a greater push to the dealership's profitability.

In the revised structure any sales consultant with higher retention ratio can earn higher amount of incentive even by selling lower no of cars as compare to other sales consultant who sell on higher discounts. For instance, in case one sales consultant sells 5 vehicles with 8% retention – he/she will earn INR 13,750 total incentive, whereas other sales consultant who sells 8 vehicles with 5.5% retention will earn total INR 11,550 only.

Profit sharing can motivate employees to work harder for increased profits, primarily through increased productivity [17]. The revised structure brings big opportunity for all sales consultants as opportunity to earn per month is INR 14,000 on 5 vehicles, INR 21,00 on 7 vehicles, and as high as INR 31,000 on 10 vehicles, provided he/she delivers 8% or 8% (+) average retention ratio per vehicle. In existing incentive structure, the highest opportunity level was INR 7,500 on 5 vehicles retail, INR 10,700 only on 7 vehicles, and INR 15,950 only on 10 vehicles. The revised structure is providing opportunity for sales consultants to earn double incentive amounts than the existing structure.

6. Conclusion

As established in section 5, the study succeeded in formulating an innovative incentive structure for Indian automobile dealerships to improve their business performance: turnaround business for loss making dealerships. Further, the study developed practical relevant knowledge through adoption of action research method and use of business process innovation as conceptual lens. The important advantages associated with revised incentive structure are: shift in focus from 'number of vehicles sold' to 'net earnings derived', gives a sense and responsibility and ownership to each employee, achieve quality of efforts over quantity, greater opportunity of earning for sales team members, and a win-win situation for both owner and employees. The revised innovative incentive structure has also been adopted voluntarily by two more automobile dealerships in Pune. The future studies may evaluate the suggested retention based innovative incentive structure in other automobile dealerships as well as in other industry dealerships.

References

[1] IBEF., India Brand Equity Foundation, *Automobile Industry in India, 2020,* https://www.ibef.org/industry/india-automobiles.aspx

[2] Gibbs, M. J., Merchant, K. A., Stede, W. A. V. D., & Vargus, M. E., The benefits of evaluating performance subjectively, *Performance Improvement, 44(5),* 2005, 26-32.

[3] Rehman, R., & Ali, M. A., Is pay for performance the best incentive for employees?, *Journal of Emerging Trends in Economics and Management Sciences, 4(6),* 2013, 512-514

[4] Clark, P., & Wilson, J., Incentive Systems: A Theory of Organizations, *Administrative Science Quarterly, 6(2),* 1961, 129-166. doi:10.2307/2390752

[5] Joetan, E., & Kleiner, B. H., Incentive practices in the US automobile industry. Management Research News, 2004.

[6] Tsuru, T., Transforming incentives: Analysis of personnel and employee output data in a large japanese auto sales firm, *Hitotsubashi Journal of Economics*, 2008, 109-132.

[7] Karthikeyan, A., Human Resource Development with Reference to Indian Automobile Dealerships during Globalisation, *International Journal of Engineering and Management Research*, *4(1)*, 2014, 63-65.

[8] Mathew, J., & Varkkey, B., Balancing People Care and Business Priorities at Popular Vehicles and Services Ltd., *NHRD Network Journal*, *8(1)*, 2015, 37-41.

[9] Philipps, G. (1977). Matching the Compensation Plan to the Sales Role. *Compensation Review*, *9*(4), 62-66.

[10] Glendinning, P. M., Kicking the Tires of Automotive Sales, *Compensation & Benefits Review*, *32(5)*, 2000, 47-53.

[11] Ho, J. L., Lee, L. C., & Wu, A., How changes in compensation plans affect employee performance, recruitment, and retention: An empirical study of a car dealership, *Contemporary Accounting Research*, *26(1)*, 2009, 167-199.

[12] Jansen, E. P., Merchant, K. A., & Van der Stede, W. A., National differences in incentive compensation practices: The differing roles of financial performance measurement in the United States and the Netherlands, *Accounting, Organizations and Society*, *34(1)*, 2009, 58-84.

[13] Merchant, K. A., Van der Stede, W. A., Lin, T. W., & Yu, Z., Performance measurement and incentive compensation: an empirical analysis and comparison of Chinese and Western firms' practices, *European accounting review*, *20(4)*, 2011, 639-667.

[14] Zhang, J. J., Lawrence, B., & Anderson, C. K., An agency perspective on service triads: Linking operational and financial performance, *Journal of Operations Management*, *35*, 2015, 56-66.

[15] Kaul, S., & Singh, A., Enhancing commitment and reducing attrition in Indian automobile industry, *International Journal of Education and Management Studies*, *7(4)*, 2017, 564-568.

[16] Coghlan, D., *Doing action research in your own organization*, SAGE Publications Limited, 2019.

[17] Kruse, D., Profit sharing: does it make a difference?: the productivity and stability effects of employee profit-sharing plans. Kalamazoo, MI: W.E. Upjohn Institute for Employment Research, 1993, https://doi.org/10.17848/9780585261614

frontiers in Nanotechnology

ORIGINAL RESEARCH
published: 17 February 2021
doi: 10.3389/fnano.2021.616186

Levofloxacin Detection Using L-Cysteine Capped MgS Quantum Dots *via* the Photoinduced Electron Transfer Process

S. Z. H. Hashmi[1†], *Tarun Kumar Dhiman*[1†], *Navneet Chaudhary*[1,2], *Avinash Kumar Singh*[1,3], *Rahul Kumar*[1,3], *Jai Gopal Sharma*[2], *Anil Kumar*[4*] and *Pratima R. Solanki*[1]

[1]Special Centre for Nanoscience, Jawaharlal Nehru University, New Delhi, India, [2]Department of Biotechnology, Delhi Technological University, New Delhi, India, [3]School of Physical Sciences, Jawaharlal Nehru University, New Delhi, India, [4]National Institute of Immunology, New Delhi, India

Antibiotics resistance is becoming one of the biggest problems of the 21st century. The prior detection of antibiotics resistance can help human beings in better treatment of diseases. Here, we have used L-Cysteine capped magnesium sulfide quantum dots (L-Cyst-MgS QDs) to detect Levofloxacin antibiotic. L-Cyst-MgS QDs were synthesized using the hydrothermal method. Transmission electron microscopy study showed monodispersed L-Cyst-MgS QDs of 2–4 nm in size. Energy dispersive x-ray photoemission spectroscopy study confirmed the elemental composition of the L-Cyst-MgS QDs without any impurity. UV-vis absorption study showed a peak centered around 340 nm. The photoluminescence study exhibited the maximum peak at 410 nm for 340 nm of excitation wavelength. L-Cyst-MgS QDs were studied with thirteen antibiotics, namely Thiamphenicol, Gentamicin, Erythromycin, Ofloxacin, Ampicillin, Ciprofloxacin, Tetracycline, Chloramphenicol, Florfenicol, Amoxicillin, Moxifloxacin, Norfloxacin, and Levofloxacin. Among these, Levofloxacin showed the most significant change in the peaks' intensity and was further used for the interaction study. In the interaction study, the peak corresponding to MgS showed a continuous decrease, while the peak corresponding to Levofloxacin showed an increase with the increased concentrations (0–100 μg/ml) of Levofloxacin. Linear behavior was obtained in the range of 1–90 μg/ml. FT-IR study confirmed the interaction of the Levofloxacin with L-Cyst-MgS QDs. The Time-resolved fluorescence spectroscopy showed identical lifetime for both the samples and no spectral overlap confirm the FRET free system. The underlying mechanism is explained based on the electron transfer from the conduction band of the L-Cyst-MgS QDs to the HOMO of Levofloxacin. The limit of detection was found to be 0.21 μg/ml.

Keywords: hydrothermal synthesis, levofloxacin antibiotic, MgS quantum dots, L-cysteine, photo-induced electron transfer

OPEN ACCESS

Edited by:
Kumud Malika Tripathi, Indian Institute of Petroleum and Energy (IIPE), India

Reviewed by:
Seshadri Reddy Ankireddy, Eternal University, India
Sumit Sonkar, Malaviya National Institute of Technology, Jaipur, India

***Correspondence:**
Anil Kumar
anilk@nii.ac.in

[†]*These authors have contributed equally to this work*

Specialty section:
This article was submitted to Biomedical Nanotechnology, a section of the journal Frontiers in Nanotechnology

Received: *11 October 2020*
Accepted: *08 January 2021*
Published: *17 February 2021*

Citation:
Hashmi SZH, Dhiman TK, Chaudhary N, Singh AK, Kumar R, Sharma JG, Kumar A and Solanki PR (2021) Levofloxacin Detection Using L-Cysteine Capped MgS Quantum Dots via the Photoinduced Electron Transfer Process. Front. Nanotechnol. 3:616186. doi: 10.3389/fnano.2021.616186

INTRODUCTION

The population increase in the last two centuries has considerably increased pharmaceuticals use in society because of growing health problems. The discovery of the first antibiotic in 1928 has revolutionized the pharmaceutical industry as antibiotics can cure many diseases (Martinez et al., 2008; Adzitey, 2015). There is a considerable increase in antibiotics use since then in both human and

animal hosts because of two main reasons. Firstly, because of the specific nature against bacteria and fungi (Levy, 1978; Bungau et al., 2015; Ferrone et al., 2017) and secondly, because of their capability to increase the growth rate of animals and improve their feed efficiency (Aarestrup and Wegener., 1999; Cháfer-Pericás et al., 2010; Deng et al., 2014). However, their presence in the environment is equally dangerous and alarming. If a large quantity of antibiotics is introduced in the environment, then it will give rise to bacterial resistance to antibiotics making an adverse effect on the use of antibiotics for treatment of both humans and animals (Martínez, 2008; Bungau et al., 2015; Mahmood et al., 2019). These effects necessitate the need to detect antibiotics in the environment as it is a matter of great concern in modern times. Conventionally, the methods available for detecting antibiotics are chromatography, which requires extensive equipment and preparation. The chromatography process is quite complicated since it requires accurate quantification, simultaneous detection, and high specificity based on the structural information of the analytes (Deng et al., 2014; Dai et al., 2017; Pérez et al., 2017). Other methods for antibiotic determination include electrophoresis (Dai et al., 2017; Jang et al., 2017; Ji et al., 2017), diode array (Bitas and Samanidou, 2016), or enzyme immunosorbent assay (ELISA) (Kong et al., 2017; Váradi et al., 2017), polymerase chain reaction (PCR), or immunologic reactions have been developed. While such well-established techniques are present for the detection of antibiotics, there are also some disadvantages of these techniques like costly equipment, tiring and laborious work for the preparation of samples, and a constant requirement for well-trained human resources (Chauhan et al., 2016; Yadav et al., 2020). These disadvantages give rise to the necessity of economically feasible techniques. Optical sensing of antibiotics is a solution for this significant problem since it requires fewer human resources and instruments and involves less time than other methods.

Fluorescent materials are mostly used for optical sensing applications (Sarkar et al., 2020). Among various fluorescent materials, quantum dots (QDs) have the highest fluorescence. Also, their size can be easily controlled using different capping agents and synthesis parameters. Such tunability of size allows the fluorescence emission between UV and visible range (Garimella et al., 2020; Kujur and Singh., 2020). Quantum dots as QDs only show unique optical properties, such as the dramatic enhancement of photoluminescence (PL) compared with the bulk counterpart of the same material. This happens due to the quantum confinement effect. Size is one of the significant parameters which affect the PL of a material. Several authors have shown that with the decrease in the size of the material, PL properties increases. Also, PL emission can be obtained in either the UV region or visible region. The UV region's PL spectra arise due to the direct transfer of e-from the conduction band to the valence band. The PL spectra in the visible light can be due to the material's surface defect, giving non-radiative recombination. QDs have symmetrical fluorescence emission spectra and broad absorption spectra, having only 25–40 nm of half-width. They can also emit multicolor fluorescence when excited at the same wavelength, making them ideal optical detection materials (Alivisatos et al., 2005). The capping agent also allows for making them specific toward the detection of a particular biomolecule. Magnesium sulfide (MgS) QDs have been synthesized earlier using the hydrothermal method for using as a potential replacement of electrode material in lithium-ion batteries, but this material's optical properties remain unexplored (Zhang et al., 2018). MgS is a well-known material for a potential replacement of electrode material in lithium-ion batteries, but this material's optical properties remain unexplored. Here, we have tried to explore the optical properties of MgS QDs. We have studied the absorption and emission characteristics of extremely small size of L-Cyst-MgS. This also helps us in understanding the effect of reduction in size on optical properties of MgS QDs. In this work, optical sensing of Levofloxacin was carried out by analyzing its interaction with L-Cyst-MgS QDs. In this context, a novel and fully optimized method for the synthesis of L-Cyst capped MgS QDs, and their specific nature antibiotic for the detection of Levofloxacin has been proposed. L-Cyst-MgS QDs were synthesized using the hydrothermal method and characterized using transmission electron microscopy (TEM), energy dispersive x-ray emission (EDX), UV-visible, and fluorescence spectroscopy. L-Cyst-MgS QDs were studied with thirteen antibiotics. Among these, Levofloxacin antibiotics showed the most significant change. Linear detection of Levofloxacin antibiotic was obtained in the 1–90 μg/ml range.

EXPERIMENTAL

Reagents

Magnesium nitrate [$Mg(NO_3)2.H_2O$] (98.99%) and L-cysteine (99.99%) were purchased from Sigma Aldrich, and sodium sulfide pellets [Na_2S] (99.99%) was purchased from SDL. All the antibiotics i.e., Thiamphenicol, Gentamicin, Erythromycin, Ofloxacin, Ampicillin, Ciprofloxacin, Tetracycline, Chloramphenicol, Florfenicol, Amoxicillin, Moxifloxacin, Norfloxacin, Levofloxacin, were purchased from SRL, Hi-media, and Sigma Aldrich. 10 ml of 0.1 millimolar concentration was prepared for each antibiotic.

Characterizations Techniques

The obtained L-Cyst-MgS-QDs were further characterized using high-resolution transmission electron microscopy (HR-TEM; JEOL-TEM-2100F), energy dispersive x-ray spectroscopy (EDX) (Bruker), UV-vis absorption spectroscopy (T-90+UV-vis spectrometer, P. G. Instruments), and fluorescence spectroscopy (Carry Eclipse Spectrophotometer, Agilent Technologies). The interaction of L-Cyst-MgS-QDs with thirteen antibiotics was studied using fluorescence spectroscopy. The interaction study of Levofloxacin with L-Cyst-MgS-QDs was studied at various concentrations in the range of 0–100 μg/ml. These results were further confirmed with Fourier transform infrared (FT-IR-Spectrum 2-Perkin Elmer),

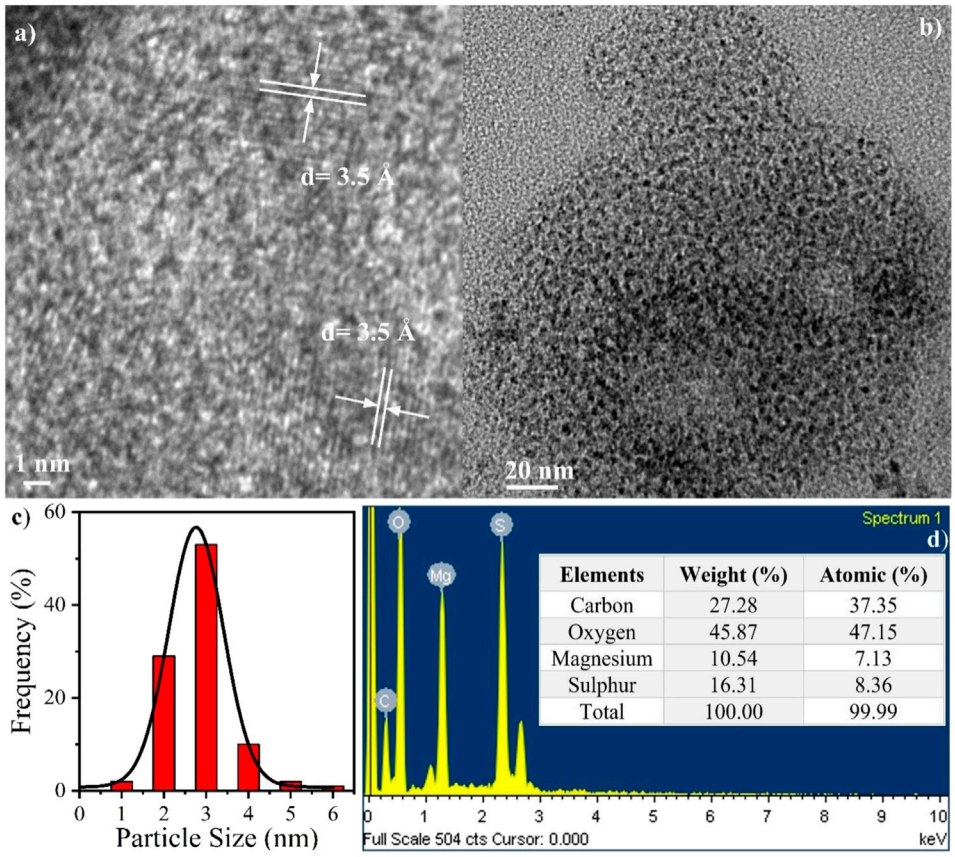

FIGURE 1 | (A) HR-TEM image, **(B)** TEM image, **(C)** size distribution bar plot fitted with Gaussian function, and **(D)** EDX results showing the constituent elements, and the inset Table shows the corresponding weight and atomic distribution.

and Fluorescence life-time decay was recorded in a commercial TCSPC setup FL-920 (Edinburgh Instruments) by exciting the samples at 375 nm using a picosecond diode laser (pulse width ~60 ps).

Synthesis of L-Cyst Capped MgS QDs

Magnesium nitrate [$Mg(NO_3)_2.H_2O$] (98.99%) powder and sodium sulfide pellets [Na_2S] (99.99) were mixed with L-Cysteine in various concentrations till the solution becomes transparent. This solution was placed in a hydrothermal teflon vessel and kept in a steel chamber for hydrothermal synthesis at 200°C for 4 h. The obtained solution was the first centrifuge for 30 min and then dialyzed overnight to remove the impurities.

RESULTS AND DISCUSSIONS

Transmission Electron Microscopy (TEM) Analysis

TEM study was carried out to observe the structure and the particle size of the synthesized QDs. **Figure 1A** shows the HR-TEM image of L-cyst-MgS-QDs. The d spacing calculated from the lattice fringes was found to be 3.5 Å. **Figure 1B** shows images of TEM of L-cyst-MgS-QDs showing uniformly distributed L-Cyst-MgS-QDs. It can be seen from the image that the L-cyst-MgS-QDs size is very small and monodispersed. The size of the QDs was calculated using a histogram and fitted with the gaussian function [**Figure 1C**] and obtained the average size ranging from 2 to 4 nm. TEM study shows that we have synthesized small size quantum dots with high surface area to volume ratio capped with L-Cysteine.

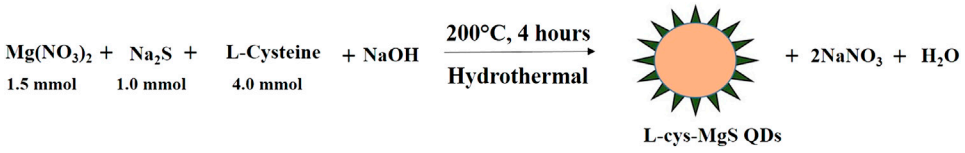

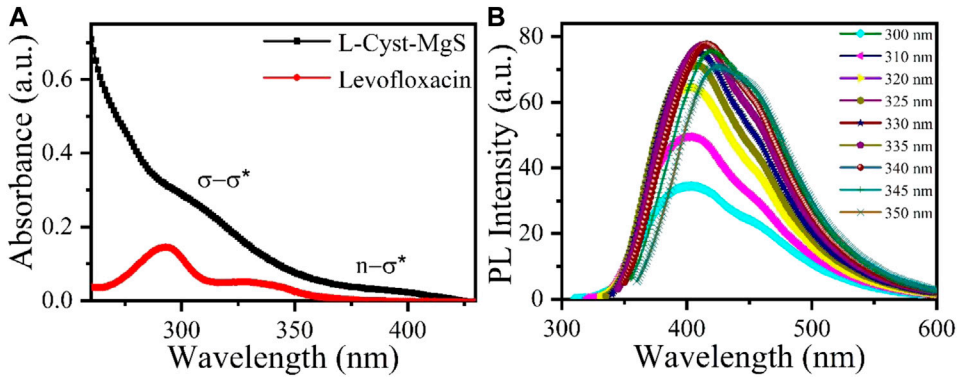

FIGURE 2 | (A) UV-Vis absorption spectra of L-Cyst-MgS-QDs and Levofloxacin and **(B)** shows the fluorescence spectra of L-Cyst-MgS-QDs for varying wavelengths.

Figure 1D shows EDX measurement to find the elemental composition. It can be seen from **Figure 1D** that the elemental composition of L-cyst-MgS-QDs consists of carbon, oxygen, magnesium, and sulfur (Sankararamakrishnan et al., 2019). Carbon and oxygen confirm the L-cysteine presence, while Mg and S confirm the presence of MgS. The inset of **Figure 1D** shows the Table for the elemental composition and their percentage by weight and atomic weight. It can be seen from the Table, the total weight and atomic of all the elements compose of L-cyst-MgS-QDs is 100 and 99.99%, respectively. This shows that the reaction was completed, and no residual precursor was left over after completing the reaction. Also, the atomic ratio of Mg and sulfur is nearly equal in the 1:1 ratio; results confirm the formation of L-cyst-MgS-QDs (Hu et al., 2010). TEM and EDX studies confirm the formation of pure and small size L-cyst-MgS-QDs without any impurity. These L-cyst-MgS-QDs were further studied using a UV-vis spectrometer and fluorescence spectrophotometer to study their optical properties.

UV-Vis Absorption Spectra and Fluorescence Study of L-Cyst-MgS-QDs

UV-VIS absorption spectrum and fluorescence emission spectra of L-Cyst-MgS QDs are shown in **Figure 2**. UV- vis absorption spectrum was recorded in the wavelength range of 270–430 nm. A small hump was obtained in L-Cyst-MgS QDs at a wavelength of 310 nm as shown in **Figure 2A**. The first peak hump around 320 nm is due to the σ - σ transition of an electron from sigma bond between Mg and S. The second hump at around 400 nm is due to the n-σ* transition due to lone pair electron of sulfur and sigma bond of Mg. The UV- vis absorption spectrum of Levofloxacin shows two peaks at 292 nm and 330 nm. Out of which broad peak at 292 nm indicate the n → π* transition while other peak at 330 nm shows the π → π* transition (Mat Amin et al., 2012). **Figure 2B** shows the fluorescence spectra obtained at different excitation wavelengths in the range of 260–360 nm. The fluorescence spectra were recorded for the varying excitation wavelengths of 300–350 nm. The highest emission was obtained at a wavelength of 410 nm for an excitation wavelength of 340 nm. These results indicate that L-Cyst-MgS QDs is an excellent candidate to study antibiotics' interaction using fluorescence spectroscopy. The quantum yield of L-Cyst-MgS QDs was calculated against the reference (quinine sulfate) that's already known. The absorbance and photoluminescence (PL) spectrum of quinine sulfate were obtained using photometry at 340 nm. The quantum yield was found to be 2%.

Response Study of L-Cyst-MgS-QDs With Levofloxacin

L-Cyst-MgS-QDs were studied with thirteen antibiotics using fluorescence spectroscopy as shown in **Figure 3A**. The thirteen antibiotics are Thiamphenicol, Gentamicin, Erythromycin, Ofloxacin, Ampicillin, Ciprofloxacin, Tetracycline, Chloramphenicol, Florfenicol, Amoxicillin, Moxifloxacin, Norfloxacin and Levofloxacin. The experiment was performed by adding 200 µL of L-Cyst-MgS-QDs into a solution of 200 µL of each antibiotic (1 mg/ml) and 2.6 ml of DI and the responses were recorded. The area was calculated for each study and a bar graph was plotted to see the specific detection of the L-Cyst-MgS-QDs toward Levofloxacin. **Figure 3A** shows the area under the curve for the response of the fluorescence signal. The area under the curve for Levofloxacin is considerably higher than that of the other antibiotics. **Figures 3B,C** show the image of all the antibiotics under visible light and UV light, respectively. The most significant change in the intensity can be observed for Levofloxacin. These results demonstrate the high selectivity of L-Cyst-MgS-QDs toward Levofloxacin. **Figure 3B** shows the response study of the L-Cyst-MgS-QDs with varying Levofloxacin concentrations in the physiological range of 0–100 µg/ml. It can be seen from **Figure 3B** that with the increase in the Levofloxacin concentration, the peak corresponding to L-Cyst-MgS-QDs (410 nm) is decreasing; however, the peak corresponding to the Levofloxacin is increasing (480 nm). The inset of **Figure 3B** shows the calibration curve obtained using the area under the curve for each concentration and plotted against the Levofloxacin concentration. Good linearity of 0.95 was obtained from the linear fit of the experimental data. Also, from this curve, it can see that the linear range was obtained from 1 to 90 µg/ml. Using this linearity plot, the limit of detection (LOD) was found to be 0.21 µg/

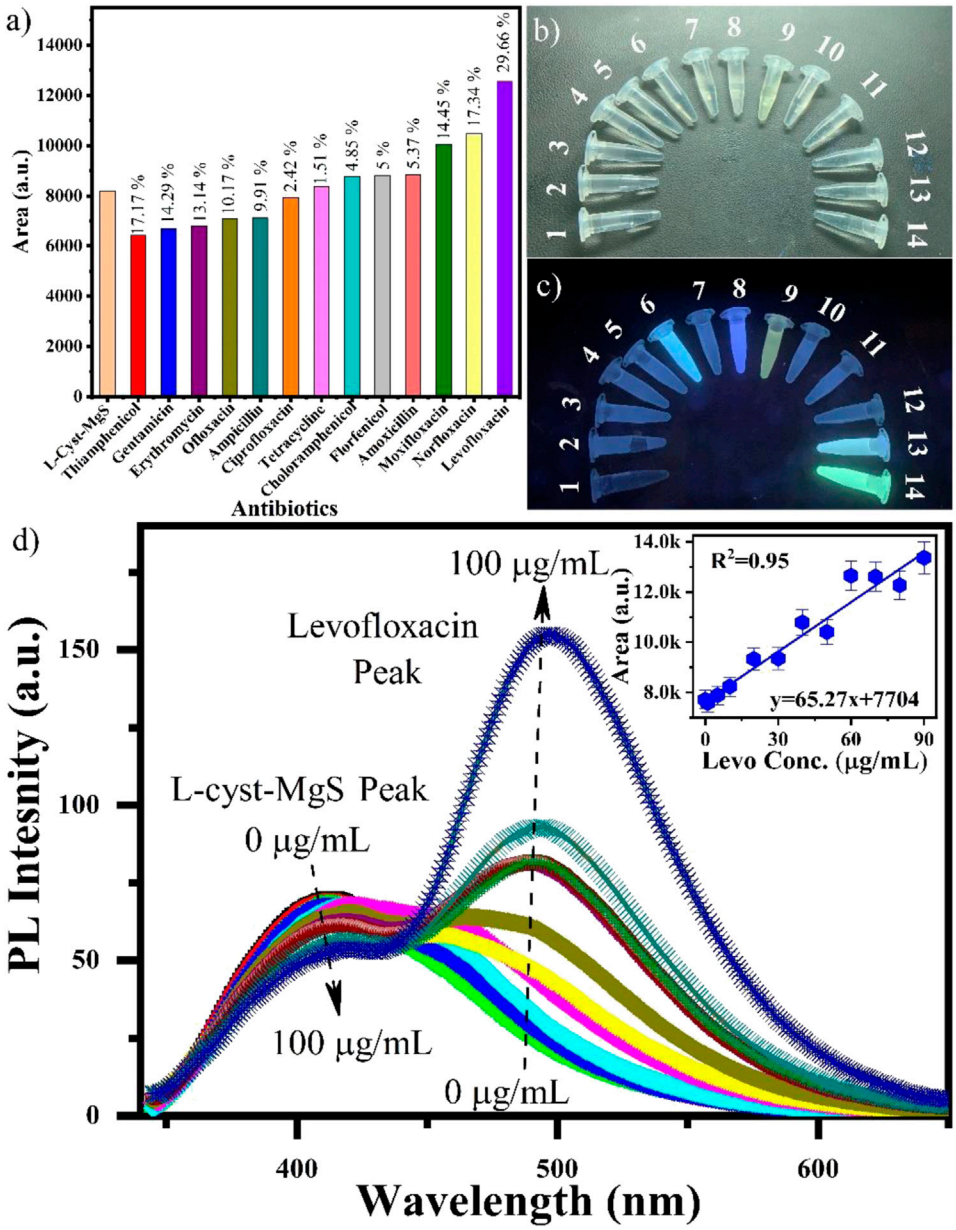

FIGURE 3 | (A) Selectivity study for L-cyst-MgS with thirteen antibiotics, photographic image of all the thirteen antibiotics 1: L-Cyst-MgS, 2: Thiamphenicol, 3: Gentamicin, 4: Erythromycin, 5: Ofloxacin, 6: Ampicillin, 7: Ciprofloxacin, 8: Tetracycline, 9: Chloramphenicol, 10: Florfenicol, 11: Amoxicillin, 12: Moxifloxacin, 13: Norfloxacin, and 14: Levofloxacin under **(B)** visible light, **(C)** UV light and **(D)** response study of L-cyst-MgS with Levofloxacin in the range of 0–100 g/ml concentrtion range. The inset shows the corresponding calibration curve.

ml. These studies suggest that L-Cyst-MgS-QDs is a suitable material for the detection of Levofloxacin.

FT-IR and TCSPC Studies of L-Cyst-MgS-QDs Interaction With Levofloxacin

Figure 4A shows the FT-IR study of L-Cyst-MgS-QDs and Levofloxacin. FTIR measurement was carried out in the wavenumber range between 400 and 4,000 cm^{-1}. **Figure 4A** represents the L-Cysteine capped MgS and having a well-resolved peak at 1,556 and 2,920 cm^{-1} are ascribed the asymmetric stretching vibration of COO- and anti-symmetric stretching of -CH_2. Considering the FTIR spectrum of pure L-Cysteine, the respective peak at 2,548 cm^{-1} corresponding to the stretching vibrations of S-H disappeared, resulting in the cleavage of the S-H bond formation of MgS bonds (Li et al., 2017). In **Figure 4B**, the symmetric stretching carboxylate (-COO-) peak of Levofloxacin was observed at 1,394 cm^{-1}, while in the case of L-Cys-MgS-Levo, this peak was shifted to 1,385 cm^{-1}, which suggests the binding of MgS with Levofloxacin (Qassim., 2015).

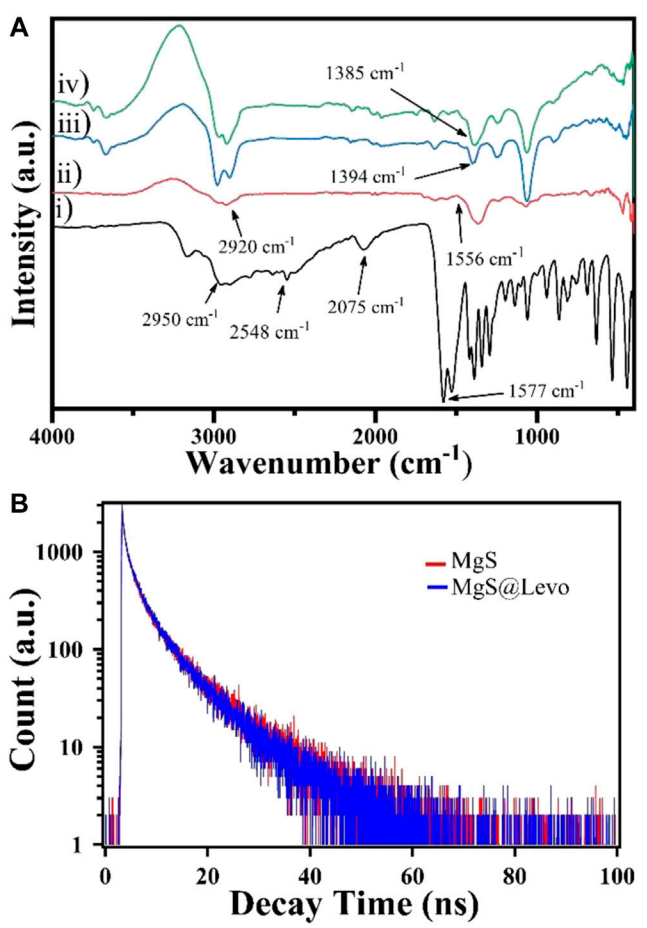

FIGURE 4 | (A) FT-IR spectra of (i) L-cysteine, (ii) L-cyst-MgS, (iii) Levofloxacin and (iv) L-cyst-MgS-levofloxacin; and **(B)** TCSPC plot for L-cyst-MgS and L-cyst-MgS-Levofloxacin.

Figure 4B shows the time-resolved fluorescence plot of L-Cyst-MgS-QDs in the presence and absence of Levofloxacin and fitted with three exponential decay function, which is given below;

$$I(t) = a_1^* \exp\left(-\frac{t}{\tau_1}\right) + a_2^* \exp\left(-\frac{t}{\tau_2}\right) + a_3^* \exp\left(-\frac{t}{\tau_3}\right)$$

The calculated lifetime was obtained nearly 8.43 ns and 7.78 ns for MgS-QDs and Levofloxacin's presence, respectively, by three exponential decay functions. There is a little difference of lifetime among these two systems that showed no spectral overlap. So, there is no fluorescence resonance energy transfer process took place (Yan et al., 2015). From the plotted and calculated life-time data, it is clear that Levofloxacin is not quenching the fluorescence of MgS and this interaction between MgS and Levofloxacin takes place through the electron transfer process.

L-Cyst-MgS Levofloxacin Interaction Mechanism

While studying the UV-absorbance curve of Levofloxacin and L-Cyst-MgS-QDs, Levofloxacin's absorption band is much closer to the UV absorbance curve of L-Cyst-MgS-QDs, allowing the transfer of electron in the L-Cyst-MgS QDs to Levofloxacin. Moreover, time-resolved fluorescence measurement also showed no significant change in the fluorescence life-time of L-Cyst-MgS-QDs-LEVO and L-Cyst-MgS QDs, as shown in **Figure 4B**. This excludes the fluorescence resonance energy transfer mechanism (Yan et al., 2015). **Figures 5A,B** shows the deconvoluted PL spectra of L-cyst-MgS and L-cyst-MgS with 100 μg/ml Levofloxacin. The spectrum was deconvoluted using the Gaussian function, and in both the spectrum, two distinct peaks were obtained. These two peaks PL 1 and PL 2 in **Figure 5A** have been explained according to the band diagram of L-Cyst-MgS explained in **Figure 5C**. The PL 1 peak in L-cyst-MgS arises due to band edge transition of excited e-from conductance band to the valence band. The PL 2 peak in L-cyst-MgS appears due to the surface defect i.e., broadband transition (Pearson., 1963; Garimella et al., 2020). In the mixture of L-Cyst-MgS QDs and Levofloxacin solution, the Levofloxacin molecules tend to come close to the surface L-Cyst-MgS QDs with the help of hydrogen bonds. This bond forms among–NH_2 group of L-Cyst with the carbonyl group of Levofloxacin and similarly carboxylic group L-Cyst with a carboxylic group Levofloxacin as shown in **Figure 5E**. On the exposure of light at a fixed wavelength of 340 nm, the photoluminescence intensity successively decreased at 410 nm (band edge) and increased at 458 nm with the increasing concentration of Levofloxacin as shown in **Figure 3D**. It is because of the absorption of light at 340 nm by L-Cyst-MgS QDs, which create the electron and hole in the valence band and conduction band, respectively. The hole of MgS QDs has more tendency to trap Levofloxacin (electron-rich) because of the vicinity between MgS and Levofloxacin molecules *via* hydrogen bonding as shown in **Figures 5F,G**. Thus electron-hole recombination does not take place between them. As a result, the emission spectra of MgS become quenched as it was coming from 410 nm (PL1) and surface defect (PL2) (**Figure 5D**). At the same time, Levofloxacin molecules were also excited at 340 nm, which generated electron and hole in the valence band (VB) and conduction band (CB), respectively. And therefore, the electron in surface defect of MgS has an alternative route of recombination of electron-hole with HOMO (hole) of Levofloxacin. Thus, emission spectra were observed with enhanced PL intensity at 458 nm (PL3) (**Figure 5D**). The shifting in the PL spectra in **Figure 3D** is due to Levofloxacin's interaction with the MgS molecule as shown in **Figure 5G**. The above results indicate that electron transfer from the MgS-QDs to Levofloxacin is responsible for the increase in Levofloxacin and a slight decrease in the intensity of L-Cyst-MgS-QDs.

CONCLUSION

L-Cyst capped MgS QDS were synthesized using the hydrothermal method. TEM study showed that L-Cyst-MgS

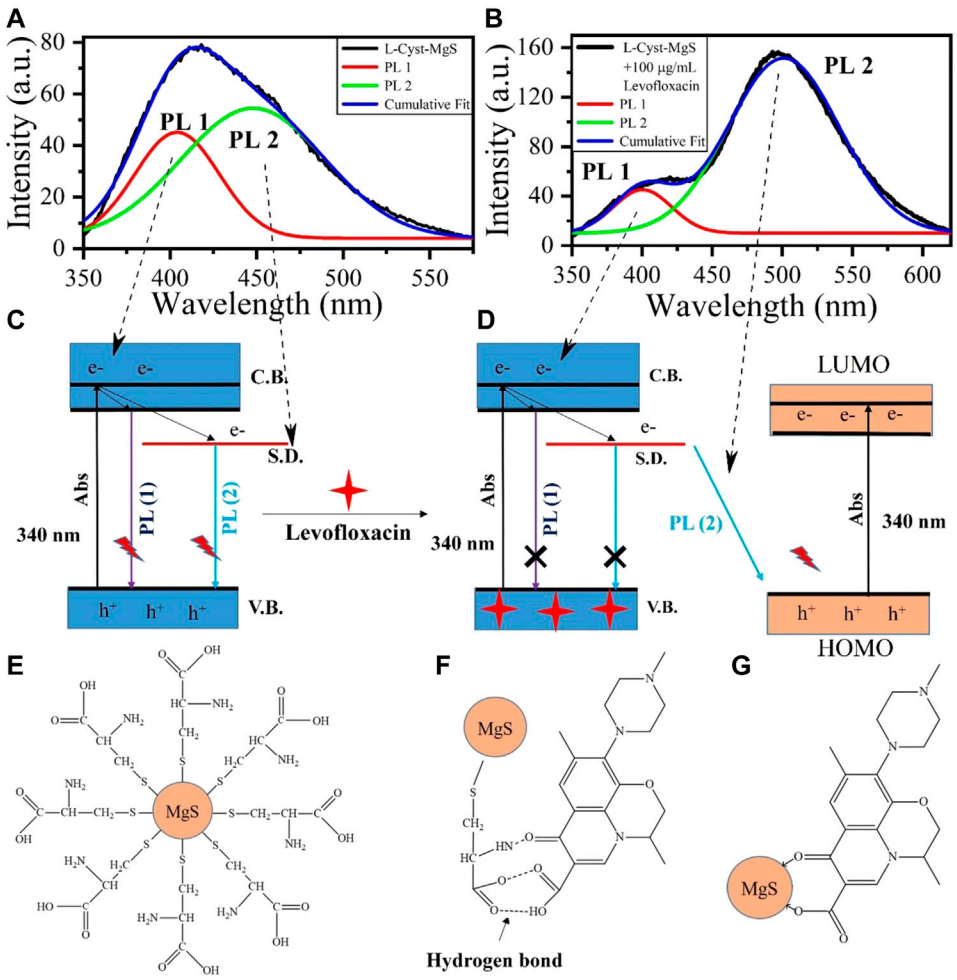

FIGURE 5 | L-Cyst-MgS interaction with Levofloxacin.

QDs have a size distribution from 2 to 4 nm and are very well dispersed. EDX study confirmed the completion of the reaction and formation of L-Cyst-MgS QDs without any impurity. UV absorbance study revealed maximum absorption in the range of 300–350 nm for L-Cyst-MgS. In the photoluminescence (PL) study, maximum emission was obtained at 410 nm for 340 nm of excitation for L-Cyst-MgS. Among Thiamphenicol, Gentamicin, Erythromycin, Ofloxacin, Ampicillin, Ciprofloxacin, Tetracycline, Chloramphenicol, Florfenicol, Amoxicillin, Moxifloxacin, Norfloxacin, Levofloxacin antibiotics, Levofloxacin showed the most significant change in PL spectra. Linear detection of Levofloxacin was obtained in the `range of 1–90 g/ml. The Time-resolved fluorescence spectroscopy showed identical lifetime for both the samples and no spectral overlap confirm the FRET free system. This was further confirmed using Fourier Transform infrared spectroscopy. The underlying mechanism can be explained based on the electron transfer from the conduction band of the L-Cyst-MgS QDs to the HOMO of Levofloxacin. The limit of detection (LOD) was found to be 0.21 µg/ml.

DATA AVAILABILITY STATEMENT

The raw data supporting the conclusions of this article will be provided after corresponding authors consent.

AUTHOR CONTRIBUTIONS

AK and PS have formulated the concept. ZH and TD have carried out the synthesis and characterization experiments. RK has helped in formulating the mechanism. JS helped in drafting the revised manuscript. AS and NC helped during measurements.

ACKNOWLEDGMENTS

The authors would like to thanks the Department of Biotechnology (DBT), India Indo-Russia project (DBT/IC-2/Indo-Russia/2017-19/02), and Department of Science and Technology (DST), India TDP/BDTP/24/2019 and ICMR,

India (34/13/2019-TF Nano/BMS), Government of India, for financial support. The authors also acknowledge the Advanced Instrument Research Facility (AIRF), JNU, New Delhi.

REFERENCES

Aarestrup, F. M., and Wegener, H. C. (1999). The effects of antibiotic usage in food animals on the development of antimicrobial resistance of importance for humans in Campylobacter and Escherichia coli. *Microb. Infect.* 1, 639–644. doi:10.1016/s1286-4579(99)80064-1

Adzitey, F. (2015). *Antibiotic classes and antibiotic susceptibility of bacterial isolates from selected poultry; a mini review*.

Alivisatos, A. P., Gu, W., and Larabell, C. (2005). Quantum dots as cellular probes. *Annu. Rev. Biomed. Eng.* 7, 55–76. doi:10.1146/annurev.bioeng.7.060804.100432

Bitas, D., and Samanidou, V. F. (2016). Effective cleanup for the determination of six quinolone residues in shrimp before HPLC with diode array detection in compliance with the European Union Decision 2002/657/EC. *J. Separ. Sci.* 39, 4805–4811. doi:10.1002/jssc.201600945

Bungau, S., Suciu, R., Bumbu, A., Cioca, G., and Tit, D. (2015). Study on hospital waste management in medical rehabilitation clinical hospital. *J. Environ. Prot. Ecol. Baile Felix.* 16, 980–987.

Cháfer-Pericás, C., Maquieira, Á., and Puchades, R. (2010). Fast screening methods to detect antibiotic residues in food samples. *Trac. Trends Anal. Chem.* 29, 1038–1049. doi:10.1016/j.trac.2010.06.004

Chauhan, R., Singh, J., Sachdev, T., Basu, T., and Malhotra, B. (2016). Recent advances in mycotoxins detection. *Biosens. Bioelectron.* 81, 532–545. doi:10.1016/j.bios.2016.03.004

Dai, T., Duan, J., Li, X., Xu, X., Shi, H., and Kang, W. (2017). Determination of sulfonamide residues in food by capillary zone electrophoresis with on-line chemiluminescence detection based on an Ag(III) complex. *Int. J. Mol. Sci.* 18, 1286. doi:10.3390/ijms18061286

Deng, F. Y., Huang, C. X., and Liu, Y. (2014). Determination of Levofloxacin in chicken tissue, manure and serum by self-ordered ring fluorescent microscopic imaging. *J. Anal. Chem.* 69, 283–289. doi:10.1134/s1061934814030046

Ferrone, V., Cotellese, R., Di Marco, L., Bacchi, S., Carlucci, M., Cichella, A., et al. (2017). Meropenem, Levofloxacin and linezolid in human plasma of critical care patients: a fast semi-automated micro-extraction by packed sorbent UHPLC-PDA method for their simultaneous determination. *J. Pharmaceut. Biomed. Anal.* 140, 266–273. doi:10.1016/j.jpba.2017.03.035

Garimella, L. B. V. S., Dhiman, T. K., Kumar, R., Singh, A. K., and Solanki, P. R. (2020). One-step synthesized ZnO np-based optical sensors for detection of aldicarb via a photoinduced electron transfer route. *ACS Omega* 5 (6), 2552–2560. doi:10.1021/acsomega.9b01987

Hu, J., Chen, Z., Chen, H., Chen, H., Song, Y., Sun, Y., et al. 2010). Single-crystal MgS nanotubes: synthesis and properties. *CrystEngComm* 12, 1286–1289. doi:10.1039/b919643a

Jang, M. G., Jang, M. D., and Park, J. (2017). Doxycycline as a new chiral selector in capillary electrophoresis. *J. Chromatogr. A* 1508, 176–181. doi:10.1016/j.chroma.2017.06.019

Ji, H., Wu, Y., Duan, Z., Yang, F., Yuan, H., and Xiao, D. (2017). Sensitive determination of sulfonamides in environmental water by capillary electrophoresis coupled with both silvering detection window and in-capillary optical fiber light-emitting diode-induced fluorescence detector. *Electrophoresis* 38, 452–459. doi:10.1002/elps.201600364

Kong, D., Xie, Z., Liu, L., Song, S., Kuang, H., and Xu, C. (2017). Development of ic-ELISA and lateral-flow immunochromatographic assay strip for the detection of vancomycin in raw milk and animal feed. *Food Agric. Immunol.* 28, 414–426. doi:10.1080/09540105.2017.1293014

Kujur, V. S., and Singh, S. (2020). Structural, magnetic, optical and photocatalytic properties of GaFeO3 nanoparticles synthesized via non-aqueous solvent-based sol–gel route. *J. Mater. Sci. Mater. Electron.* 31, 17633–17646. doi:10.1007/s10854-020-04318-2

Levy, S. B. (1978). Emergence of antibiotic-resistant bacteria in the intestinal flora of farm inhabitants. *J. Infect. Dis.* 137, 689–690. doi:10.1093/infdis/137.5.688

Li, L., Liao, L., Ding, Y., and Zeng, H. (2017). Dithizone-etched CdTe nanoparticles-based fluorescence sensor for the off-on detection of cadmium ion in aqueous media. *RSC Adv.* 7 (17), 10361–10368. doi:10.1039/c6ra24971j

Mahmood, A. R., Al-Haideri, H. H., and Hassan, F. M. (2019). *Detection of antibiotics in drinking water treatment plants in Baghdad City, Iraq*. Health: Advance Pub.

Martinez, J. L., Fajardo, A., Garmendia, L., Hernandez, A., Linares, J. F., Martínez-Solano, L., et al. (2008). A global view of antibiotic resistance. *FEMS Microbiol. Rev.* 33, 44–65. doi:10.1111/j.1574-6976.2008.00142.x

Martínez, J. L. (2008). Antibiotics and antibiotic resistance genes in natural environments. *Science* 321, 365–367. doi:10.1126/science.1159483

Mat Amin, K. A., Gilmore, K. J., Matic, J., Poon, S., Walker, M. J., Wilson, M. R., et al. (2012). Polyelectrolyte complex materials consisting of antibacterial and cell-supporting layers. *Macromol. Biosci.* 12 (3), 374–382. doi:10.1002/mabi.201100317

Pearson, R. G. (1963). Hard and soft acids and bases. *J. Am. Chem. Soc.* 85 (22), 3533–3539. doi:10.1021/ja00905a001

Pérez, R. A., Albero, B., Férriz, M., and Tadeo, J. L. (2017). Analysis of macrolide antibiotics in water by magnetic solid-phase extraction and liquid chromatography-tandem mass spectrometry. *J. Pharmaceut. Biomed. Anal.* 146, 79–85. doi:10.1016/j.jpba.2017.08.013

Qassim, A. W. (2015). Determination of Levofloxacin in pharmaceutical formulation tavanic by Visible spectrophotometry of its chelating complex with aluminum ion (iii). *Int. J. Dev. Res.* 5 (6), 4702–4706.

Sankararamakrishnan, N., Singh, R., and Srivastava, I. (2019). Performance of novel MgS doped cellulose nanofibres for Cd(II) removal from industrial effluent – mechanism and optimization. *Sci. Rep.* 9, 12639–12648. doi:10.1038/s41598-019-49076-2

Sarkar, T., Dhiman, T., Sajwan, R., Sri, S., and Solanki, P. R. (2020). Studies on carbon-quantum-dot-embedded iron oxide nanoparticles and their electrochemical response. *Nanotechnology* 31 (35), 355502. doi:10.1088/1361-6528/ab925e

Váradi, L., Luo, J. L., Hibbs, D. E., Perry, J. D., Anderson, R. J., Orenga, S., et al. (2017). Methods for the detection and identification of pathogenic bacteria: past, present, and future. *Chem. Soc. Rev.* 46, 4818–4832. doi:10.1039/c6cs00693k

Yadav, A. K., Dhiman, T. K., Lakshmi, G. B. V. S., Berlina, A. N., and Solanki, P. R. (2020). A highly sensitive label-free amperometric biosensor for norfloxacin detection based on chitosan-yttria nanocomposite. *Int. J. Biol. Macromol.* 151, 566–575. doi:10.1016/j.ijbiomac.2020.02.089

Yan, X., Li, H., Han, X., and Su, X. (2015). A ratiometric fluorescent quantum dots based biosensor for organophosphorus pesticides detection by inner-filter effect. *Biosens. Bioelectron.* 74, 277–283. doi:10.1016/j.bios.2015.06.020

Zhang, B., Xia, G., Chen, W., Gu, Q., Sun, D., and Yu, X. (2018). Controlled-size hollow magnesium sulfide nanocrystals anchored on graphene for advanced lithium storage. *ACS Nano* 12, 12741–12750. doi:10.1021/acsnano.8b07770

Conflict of Interest: The authors declare that the research was conducted in the absence of any commercial or financial relationships that could be construed as a potential conflict of interest.

Copyright © 2021 Hashmi, Dhiman, Chaudhary, Singh, Kumar, Sharma, Kumar and Solanki. This is an open-access article distributed under the terms of the Creative Commons Attribution License (CC BY). The use, distribution or reproduction in other forums is permitted, provided the original author(s) and the copyright owner(s) are credited and that the original publication in this journal is cited, in accordance with accepted academic practice. No use, distribution or reproduction is permitted which does not comply with these terms.

2021 11th International Conference on Cloud Computing, Data Science & Engineering (Confluence) | 978-1-6654-1451-7/20/$31.00 ©2021 IEEE | DOI: 10.1109/Confluence51648.2021.9377113

Machine Learning Approach Based on Hybrid Features for Detection of Phishing URLs

Awishkar Ghimire[1], Avinash Kumar Jha[2,#], Surendrabikram Thapa[1], Sushruti Mishra[1], Aryan Mani Jha[3,#]

[1]Department of Computer Science and Engineering, Delhi Technological University
[2]Department of Civil Engineering, Delhi Technological University
[3]Department of Mechanical Engineering, Delhi Technological University
[#]{avinash.jha.6696, aryanmjha}@gmail.com

ABSTRACT

Phishing attacks are one of the most widespread problems over the internet. A lot of internet users fall into the hands of attackers every day which accounts into millions of dollars of fraud around the globe every day. The availability of the internet among people who don't have the knowledge of cyber-attacks adds more to this problem. Thus, there is a need to employ intelligent algorithms to solve these serious problems. In this paper, we present different ways in which phishing URLs can be detected using machine learning algorithms. The URL based features as well as network-based features were used to feed to the machine learning classifiers. Similarly, other features that might add relevance to our problem are also discussed. The unbalanced dataset is made balanced using various oversampling and undersampling techniques and the performance for the various machine learning algorithms is evaluated for the dataset. The evaluation shows that the machine learning algorithms can show promising results in terms of precision, recall, f-score, and ROC AUC.

Keywords— Machine Learning, Phishing attacks, cybersecurity, ensemble learners

1. INTRODUCTION

Machine learning algorithms have been widely used to solve various real-world problems [1]. From accelerating businesses to providing better healthcare, the use of machine learning algorithms is well explored [2]. The priorities of researchers in making the use of artificial intelligence (AI) for making lives easier has changed our lives in different ways. The never-ending exploration of the applications of AI in smart cities has led to numerous discoveries [3]. With the technologies evolving day by day, there have been some dark sides associated with it. The fraudulent activities are happening on a very large scale which needs to be stopped. It has been estimated that the loss due to cybercrimes is projected to reach $6 trillion by 2021, which is staggeringly huge [4]. One of the fraudulent activities that happen over the internet is phishing activities. There are a lot of ways in which attackers lure the victims into clicking the malicious links which may result in the victim losing their personal data and even money in some cases. Mostly, the attackers use emails, blog posts, chat sessions, etc. for posting the phishing URLs where it is highly likely that the victims click on them. [5] The links appear to be very tempting where attackers promise free money, high paying jobs, etc. Victims often fall into such fake promises and click the URLs. Phishing is even widespread with more users using the internet who don't even have basic knowledge about phishing and cyber-attacks. In this situation, there is a need for an automated system that helps in the identification of phishing URLs by using sophisticated learning techniques. Detecting malicious URLs is one of the most important steps towards preventing fraud over the internet. Thus, to make the internet a safer place, there is a great need for systems that help in identifying phishing URLs.

2. RELATED WORKS

A lot of work has been done in using machine learning techniques for the detection of suspicious URLs. James et al. [6] have researched the detection of phishing URLs using host-based features, lexical features, and page importance features. The URLs they used were collected from phistank.com, alexa.com, dmoz.com. The novelty in their approach lies in the feature extraction and the types of features they used. In their feature extraction technique firstly host-based analysis is performed and then relevant host-based features are extracted, and subsequently page/popularity-based feature analysis and lexical feature analysis are performed extracting the relevant features. Host-based features are those features that define the who hosts the websites and where/ how it is hosted. Page/popularity based features define how popular the website is among the users of the internet. Lexical features comprise those properties that arise out of the text of the URL itself and not the contents of the website. After feature extraction, they use a machine learning classifier. The classifiers they train on are the Naive

Authorized licensed use limited to: DELHI TECHNICAL UNIV. Downloaded on March 27,2021 at 05:36:12 UTC from IEEE Xplore. Restrictions apply.

Bayes classifier, support vector machines, regression trees, and k-nearest neighbours. In their experiment, regression trees gave the highest accuracy. Similarly, Yan et al. [7] proposed an unsupervised learning algorithm that learns URL embeddings to get some features that can be used with machine learning algorithms. Kim et al. [8] also did a comprehensive research on exploring the similarity in the suspicious URLs which are due to the attacker's behavior. This enabled the authors to successfully classify the malicious and benign URLs with an accuracy of 70%. The past works give holistic information of what features can make URLs look more suspicious.

3. METHODOLOGY

The process goes through five major steps. The first and foremost step is to collect data for the study. The data collection step is followed by feature engineering where we take the features that are relevant and of our interest. After that, data preprocessing is done before feeding the data into machine learning algorithms. The performance of each classifier is evaluated as the final step. The overview of the methodology used in this paper is as shown in fig. 1.

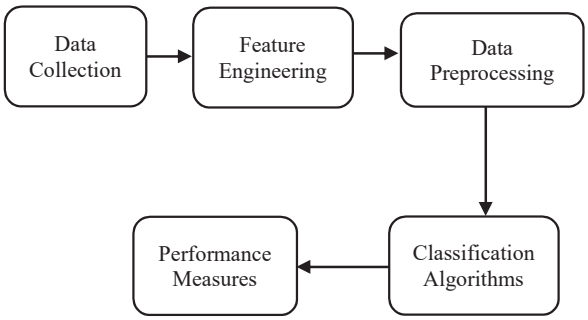

Fig. 1. Methodology of the experiment

A. Data Collection

The websites URL were collected from various sources like PhishTank etc. There are a total of 450,176 URLs out of which consists of 345,738 benign websites and 104,438 malicious websites. Statistically, 77% of the websites are benign and 23% of them are malicious. The URLs in the original form are unprocessed and need some preprocessing to extract the useful and relevant features that may serve as attributes for classifiers trained for the delineation of malicious URLs from the benign ones. The dataset used is publicly available.

B. Feature Engineering

The URLs that are related to phishing have certain anomalous features that distinguish themselves from the benign ones. Jeeva et al. used different features like domain length, number of slashes in the URLs, the number of special characters, etc. It is unanimously accepted by the researchers that certain length features and count of special tokens, digits, letters, directories, etc. play a vital role in the detection of anomalies in the URLs [9]. In our experiments, we use similar features like the length of the URLs, length of the hostname, length of the first directory, length of the path, and length of the top-level domain. Similarly, count features are also used like count of certain special characters (-, @, $, ?, /, %, . , =) and certain keywords like http, https, and www. Similarly, the count of digits, letters, and the number of directories were also taken as features that can influence the URLs trustability. On top of this, the binary features like the usage of IP (either "yes" or "no") and the use of shortening URL ("yes" or "no") have been used to make the features more robust. For the list shortening, if the shortening has been done using bit.ly, goo.gl, shorte.st, go2l.ink, x.co, ow.ly, t.co, tinyurl, tr.im, is.gd, cli.gs, yfrog.com, migre.me, ff.im, tiny.cc, doiop.com, short.ie, kl.am, wp.me, rubyurl.com, om.ly, to.ly, bit.do, t.co, lnkd.in, db.tt, qr.ae, adf.ly, bitly.com, cur.lv, tinyurl.com, url4.eu, twit.ac, su.pr, twurl.nl, snipurl.com, short.to, BudURL.com, ping.fm, post.ly, Just.as, bkite.com, snipr.com, fic.kr, loopt.us, ity.im, q.gs, is.gd, po.st, bc.vc, twitthis.com, u.to, j.mp, buzurl.com, cutt.us, u.bb, yourls.org, x.co, prettylinkpro.com, scrnch.me, filoops.info, vzturl.com, qr.net, 1url.com, tweez.me, v.gd, tr.im, and link.zip.net, the link has been labeled as shortened and the other links have been labeled as "not-shortened". In total, 21 features (5 lengths based + 14 counts based + 2 binary) were extracted and used in this research. In this experiment, the features are not just based on length but also based on counts of letters, numbers and binary values. Thus, the features are hybrid features and such features can help in building robust classifiers.

C. Data Preprocessing

The statistics of data used in this research show that more than 3/4th of the data belongs to one category and less than 1/4th of the data belongs to the other category. This situation cannot give correct performance measures in terms. The unbalanced data simply means that one class is very well represented in the dataset whereas the representation of the minority class is low. In order to tackle the unbalanced data, two major techniques are used in this research. First of all, the unbalanced data is undersampled so that both categories have nearly the same amount of data. After that, the performance measures are calculated for different classifiers. Similarly, the performance measures are also measured for original imbalanced data and oversampled data. For the undersampling of the data, the Near-miss technique is used whereas for oversampling of the data Synthetic Minority Oversampling Technique (SMOTE) is used.

Authorized licensed use limited to: DELHI TECHNICAL UNIV. Downloaded on March 27,2021 at 05:36:12 UTC from IEEE Xplore. Restrictions apply.

Near-Miss: Near-miss [10] is an undersampling method that selects examples based on the distance of majority class examples to minority class examples. Actually, there are various variants of near-miss. In this research, the technique that selects majority class examples with minimum distance to each minority class example is used. This particular near-miss method used in this research is often known as Near-miss-3. After undersampling with Near-Miss-3, the data distribution becomes a bit balanced with 104,438 malicious websites and 70,574 benign websites. Statistically, there is 60% data belonging to the malicious category and 40% belonging to the benign category.

SMOTE: Synthetic Minority Oversampling Technique, popularly known as SMOTE, is an oversampling technique that generates synthetic samples from the minority class [11]. It is a technique based on nearest neighbors judged by Euclidean distance between data points in feature space. It is a widely used technique for handling imbalanced data and data augmentation especially when there is very little data in one category like fraud detection and malicious website detection. After oversampling using SMOTE, the data distribution becomes perfectly balanced with 345,738 observations in both malicious and benign websites category.

D. Classification Algorithms

The classification is done with ten different algorithms so that the best can be used for real-time inference. In this research, five machine learning algorithms and five ensemble learning algorithms have been used. All algorithms have been used with all three kinds of data i.e. undersampled, oversampled, and unbalanced data. The first five methods discussed below are machine learning methods and the remaining five are ensemble learners.

I. K-Nearest Neighbors (KNN)

K-Nearest Neighbors is a non-parametric clustering algorithm that helps in classification problems [12]. It works on a very simple idea of storing all the available observations and predicting the class of new instances by measuring its similarity with the stored observations. It is very useful especially with datasets with lower feature dimensions. When the dimension of data increases, it has a bit of difficulty in classification. Nevertheless, it is one of the widely used algorithms in machine learning and pattern recognition.

II. Support Vector Machine (SVM)

Support Vector Machines (SVMs) are famous machine learning classifiers developed by Vapnik et al. which are used both in classification and regression problems [13]. It has the ability to distinguish between the categories by drawing a hyperplane for categorization. When the algorithm is fed with the data, it creates an optimal hyperplane that categorizes given newer examples. In this experiment, SVM with Gaussian kernel is used. SVM is a bit slower with a large number of data because it requires the order of n^2 computation while the model is trained, where n is the number of training data.

III. Decision Tree (DT)

A decision tree is a flowchart or tree-like representation which is based on the decisions and their possible consequences. It is a very basic algorithm and is capable of handling both categorical and numerical values [14]. This algorithm also works well with problems with multiple outputs. It is very simple and interpretable. Decision trees can moreover be visualized with the help of different libraries. In this experiment, the Gini index is used to measure the quality of the split. Unlike SVMs, the cost of using a decision tree is lower. It is logarithmic in the number of observations that are used for training the tree.

IV. Logistic Regression (LR)

Logistic Regression is a simple kind of algorithm that can be used to solve both regression and categorization problems. It is based on a logistic function for the prediction of the target values. The outcome of a logistic function is a probability value between 0 and 1 which gives the likelihood of a category being the correct one. In this experiment, the logistic regression has been used with C and penalty parameters as 1.0 and 'l2' respectively [15].

V. Stochastic Gradient Descent (SGD)

Stochastic Gradient Descent (SGD) is a technique to locate the ideal boundary design for a machine learning calculation. It iteratively makes little changes in accordance with a network setup of a machine-learning algorithm to diminish the mistake of the system [16]. After each training point, the configuration of the network is tuned to find the global minimum. Hingle loss and 'l2' penalty are used in this experiment.

VI. Random Forest (RF)

Random Forest is a kind of ensemble of learners that builds multiple decision trees at the time of training and the output is the modal class or the prediction of individual trees [15]. Though computationally expensive, it helps in better classification and also avoids overfitting to a larger extent.

VII. Gradient Boosting Classifier (GB)

This is another ensemble learner that is used to solve both classification and regression problems. It is a very powerful boosting algorithm that uses decision trees. With its use increasingly in Kaggle competitions for better performance, it has been widely used in classification tasks [17].

Authorized licensed use limited to: DELHI TECHNICAL UNIV. Downloaded on March 27,2021 at 05:36:12 UTC from IEEE Xplore. Restrictions apply.

VIII. Adaptive Boosting (AdaBoost) (ADB)

Adaptive boosting, popularly known by its alias AdaBoost, is one of the most widely used classification algorithms that use decision trees [18]. It gives the flexibility of combining really weak classifiers into strong classifiers. The decision stumps which are the decision trees with a single split are used as weak learners which are combined into strong classifiers using adaptive boosting schemes.

IX. Extreme Gradient Boosting (XGBoost) (XGB)

This is one of the most loved machine learning algorithms. The algorithm is often implemented using XGBoost library which is an open-source software library. XGBoost is very fast for the implementation and hence is used in a wide range of applications [19].

X. Light Gradient Boosting Machine (LGBM)

Light Gradient Boosting Machine (LGBM) is yet another tree-based algorithm that is widely used in a variety of machine learning problems. Unlike other boosting algorithms that grow trees horizontally, LGBM is a quite different one that grows trees vertically [19].

E. Performance Measures

The classifiers are used and the validation is done using a 10 fold cross-validation technique. The accuracy, precision, recall, f-score, and AUC measures are calculated after a 10 fold cross-validation scheme. The formulas for the performance measures are given as:

$$Accuracy = \frac{TP+TN}{TP+TN+FP+FN} \quad (1)$$

$$Precision = \frac{TP}{TP+FP} \quad (2)$$

$$Recall = \frac{TP}{TP+FN} \quad (3)$$

$$F1-Score = 2 \times \frac{Precision \times Recall}{Precision + Recall} \quad (4)$$

Where TP, TN, FP and FN are True Positives, True Negatives, False Positives and False Negatives respectively. AUC stands for Area Under the Curve.

4. RESULTS AND DISCUSSION

First of all, the classifiers are used with the original dataset which is an unbalanced one. Then, the dataset is balanced once using the undersampling technique and again using the oversampling technique. The performance of the machine learning algorithms, as well as ensemble learners with original data, can be found in Table I. For the original dataset, AdaBoost shows the best performance with an accuracy of 99.07%. The precision and recall for the same are 0.98 and 0.99 respectively. Similarly, the f-score and ROC AUC for the AdaBoost algorithm are 0.99 and 0.9908 respectively. Also, further analysis was done with an undersampling technique called near-miss. The results given by the dataset which was undersampled using near-miss is shown in table II. With an undersampled dataset as well, the best performing algorithm was AdaBoost with an accuracy of 98.43%. The precision, recall and f-score are all equal to 0.98. The ROC AUC for the AdaBoost in undersampled data is 0.929. However, the gradient boosting classifier has a better performance in terms of ROC AUC with a value of 0.9837. Further experiments with oversampled data using SMOTE is shown in table III. Support Vector Machines (SVM) was best-performing algorithm with an accuracy of 99.50%. Similarly, the precision, recall and f-score were all equal to 0.999. Also, ROC AUC was very high when SVM was used with oversampled dataset. The accuracy of 99.07% with original dataset is good but the phishing detection is a kind of problem where we need very high accuracy. Even a slightest decline in performance can cause a huge monetary loss. Thus, using oversampled dataset is a great choice for this problem. Despite a high time for computation due to high amount of data in oversampled dataset, the better accuracy makes it very useful to use.

TABLE I. PERFORMANCE OF ALGORITHMS FOR ORIGINAL DATA

Classifier	Accuracy	Precision	Recall	F-score	ROC AUC
K-Nearest Neighbors (KNN)	0.9125	0.88	0.87	0.87	0.8669
Support Vector Machine (SVM)	0.9836	0.99	0.97	0.98	0.9667
Decision Tree (DT)	0.9873	0.98	0.99	0.98	0.9879
Logistic Regression (LR)	0.9937	0.99	0.99	0.99	0.9899
Stochastic Gradient Descent (SGD)	0.9941	0.98	0.99	0.98	0.9881
Random Forest (RF)	0.9906	0.98	0.99	0.99	0.9906
Gradient Boosting Classifier (GB)	0.9906	0.98	0.99	0.99	0.9404
Adaptive Boosting (AdaBoost) (ADB)	0.9907	0.98	0.99	0.99	0.9908
Extreme Gradient Boosting (XGBoost) (XGB)	0.9906	0.98	0.99	0.99	0.9906
Light Gradient Boosting Machine (LGBM)	0.9906	0.98	0.99	0.99	0.9905

Authorized licensed use limited to: DELHI TECHNICAL UNIV. Downloaded on March 27,2021 at 05:36:12 UTC from IEEE Xplore. Restrictions apply.

TABLE II. PERFORMANCE OF ALGORITHMS FOR UNDERSAMPLED DATA

Classifier	Accuracy	Precision	Recall	F-score	ROC AUC
K-Nearest Neighbors (KNN)	0.7819	0.79	0.78	0.78	0.7789
Support Vector Machine (SVM)	0.9452	0.94	0.95	0.95	0.9471
Decision Tree (DT)	0.9733	0.98	0.97	0.97	0.9693
Logistic Regression (LR)	0.9828	0.98	0.98	0.98	0.9816
Stochastic Gradient Descent (SGD)	0.9782	0.97	0.97	0.97	0.9712
Random Forest (RF)	0.9786	0.98	0.98	0.98	0.9756
Gradient Boosting Classifier (GB)	0.985	0.99	0.98	0.98	0.9837
Adaptive Boosting (AdaBoost) (ADB)	0.9843	0.98	0.98	0.98	0.9824
Extreme Gradient Boosting (XGBoost) (XGB)	0.9816	0.98	0.98	0.98	0.9794
Light Gradient Boosting Machine (LGBM)	0.9813	0.98	0.98	0.98	0.9789

TABLE III. PERFORMANCE OF ALGORITHMS FOR OVERSAMPLED DATA

Classifier	Accuracy	Precision	Recall	F-score	ROC AUC
K-Nearest Neighbors (KNN)	0.9478	0.95	0.95	0.95	0.9478
Support Vector Machine (SVM)	0.9947	0.99	0.99	0.99	0.9947
Decision Tree (DT)	0.9919	0.99	0.99	0.99	0.9919
Logistic Regression (LR)	0.995	0.999	0.999	0.999	0.995
Stochastic Gradient Descent (SGD)	0.9945	0.99	0.99	0.99	0.9939
Random Forest (RF)	0.9938	0.99	0.99	0.99	0.9938
Gradient Boosting Classifier (GB)	0.9939	0.99	0.99	0.99	0.9939
Adaptive Boosting (AdaBoost) (ADB)	0.9935	0.99	0.99	0.99	0.9935
Extreme Gradient Boosting (XGBoost) (XGB)	0.9936	0.99	0.99	0.99	0.9936
Light Gradient Boosting Machine (LGBM)	0.9936	0.99	0.99	0.99	0.9936

TABLE IV. PERFORMANCE COMPARISON OF ALGORITHMS WITH BALANCED AND UNBALANCED DATA

Classifier	Original Data		Undersampled Data		Oversampled Data	
	F-score	ROC AUC	F-score	ROC AUC	F-score	ROC AUC
KNN	0.87	0.8669	0.78	0.7789	0.95	0.9478
SVM	0.98	0.9667	0.95	0.9471	0.99	0.9947
DT	0.98	0.9879	0.97	0.9693	0.99	0.9919
LR	0.99	0.9899	0.98	0.9816	0.999	0.995
SGD	0.98	0.9881	0.97	0.9712	0.99	0.9939
RF	0.99	0.9906	0.98	0.9756	0.99	0.9938
GB	0.99	0.9404	0.98	0.9837	0.99	0.9939
ADB	0.99	0.9908	0.98	0.9824	0.99	0.9935
XGB	0.99	0.9906	0.98	0.9794	0.99	0.9936
LGBM	0.99	0.9905	0.98	0.9789	0.99	0.9936

Authorized licensed use limited to: DELHI TECHNICAL UNIV. Downloaded on March 27,2021 at 05:36:12 UTC from IEEE Xplore. Restrictions apply.

Table IV draws a comparison among the machine learning model's performances with balanced and unbalanced data. In most of the cases, the performance of the models with oversampled data is seen very well. Fig. 2 graphically represents and compares the performance of algorithms with balanced and unbalanced datasets.

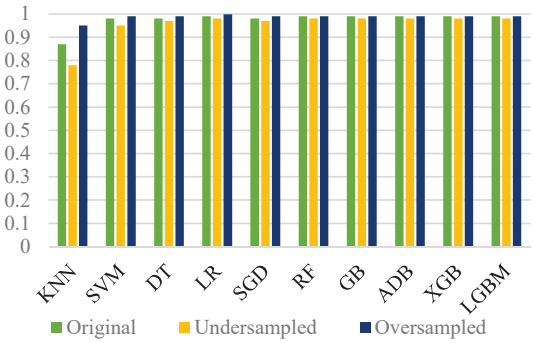

Fig. 2. F-score of the models with various data

It can thus be deciphered that with the given features and dataset, balanced data can be useful as compared to unbalanced data.

5. CONCLUSION AND FUTURE SCOPE

In this paper, we have discussed a framework for the detection of phishing URLs on the web using various features. The features are network-based and length based. The results are promising and can help us to detect the phishing URLs with great accuracy. Future works can involve the use of various other features which can be relevant to the detection of phishing URLs. More network-based features can be used in conjunction with length-based features to obtain higher accuracy. The algorithms used in the paper are used with default hyperparameters. In the future, the algorithms can be made more robust with hyperparameter optimization. This work uses machine learning algorithms only whereas deep learning algorithms can be further explored. Also, phishing has become more sophisticated with attackers using more advanced techniques for attacking. So, recent datasets that account for more sophisticated attacks should be used for carrying out the experiments.

REFERENCES

[1] A. Ghimire, S. Thapa, A. K. Jha, A. Kumar, A. Kumar, and S. Adhikari, "AI and IoT Solutions for Tackling COVID-19 Pandemic", in 2020 International Conference on Electronics, Communication and Aerospace Technology, 2020: IEEE.

[2] S. Thapa, S. Adhikari, U. Naseem, P. Singh, G. Bharathy, and M. Prasad, "Detecting Alzheimer's Disease by Exploiting Linguistic Information from Nepali Transcript," in International Conference on Neural Information Processing, 2020: Springer, pp. 176-184.

[3] C.-T. Lin et al., "IoT-based wireless polysomnography intelligent system for sleep monitoring," IEEE Access, vol. 6, pp. 405-414, 2017.

[4] A. Ghimire, S. Thapa, A. K. Jha, S. Adhikari, and A. Kumar, "Accelerating Business Growth with Big Data and Artificial Intelligence," in 2020 Fourth International Conference on I-SMAC (IoT in Social, Mobile, Analytics and Cloud)(I-SMAC), 2020: IEEE, pp. 441-448.

[5] R. Verma and A. Das, "What's in a url: Fast feature extraction and malicious url detection," in Proceedings of the 3rd ACM on International Workshop on Security and Privacy Analytics, 2017, pp. 55-63.

[6] J. James, L. Sandhya, and C. Thomas, "Detection of phishing URLs using machine learning techniques," in 2013 international conference on control communication and computing (ICCC), 2013: IEEE, pp. 304-309.

[7] X. Yan, Y. Xu, B. Cui, S. Zhang, T. Guo, and C. Li, "Learning URL Embedding for Malicious Website Detection," IEEE Transactions on Industrial Informatics, 2020.

[8] S. Kim, J. Kim, and B. B. Kang, "Malicious URL protection based on attackers' habitual behavioral analysis," Computers & Security, vol. 77, pp. 790-806, 2018.

[9] S. C. Jeeva and E. B. Rajsingh, "Intelligent phishing url detection using association rule mining," Human-centric Computing and Information Sciences, vol. 6, no. 1, pp. 1-19, 2016.

[10] I. Mani and I. Zhang, "kNN approach to unbalanced data distributions: a case study involving information extraction," in Proceedings of workshop on learning from imbalanced datasets, 2003, vol. 126.

[11] N. V. Chawla, K. W. Bowyer, L. O. Hall, and W. P. Kegelmeyer, "SMOTE: synthetic minority over-sampling technique," Journal of artificial intelligence research, vol. 16, pp. 321-357, 2002.

[12] A. Saxena et al., "A review of clustering techniques and developments," Neurocomputing, vol. 267, pp. 664-681, 2017.

[13] C. Cortes and V. Vapnik, "Support-vector networks," Machine learning, vol. 20, no. 3, pp. 273-297, 1995.

[14] S. Thapa, S. Adhikari, A. Ghimire, and A. Aditya, "Feature Selection Based Twin-Support Vector Machine for the diagnosis of Parkinson's Disease," in 2020 IEEE 8th R10 Humanitarian Technology Conference (R10-HTC), 2020.

[15] S. Thapa, P. Singh, D. K. Jain, N. Bharill, A. Gupta, and M. Prasad, "Data-Driven Approach based on Feature Selection Technique for Early Diagnosis of Alzheimer's Disease," in 2020 International Joint Conference on Neural Networks (IJCNN), 2020: IEEE, pp. 1-8.

[16] J. H. Friedman, "Stochastic gradient boosting," Computational statistics & data analysis, vol. 38, no. 4, pp. 367-378, 2002.

[17] A. Natekin and A. Knoll, "Gradient boosting machines, a tutorial," Frontiers in neurorobotics, vol. 7, p. 21, 2013.

[18] R. E. Schapire, "Explaining adaboost," in *Empirical inference*: Springer, 2013, pp. 37-52.

[19] M. Massaoudi, S. S. Refaat, I. Chihi, M. Trabelsi, F. S. Oueslati, and H. Abu-Rub, "A novel stacked generalization ensemble-based hybrid LGBM-XGB-MLP model for Short-Term Load Forecasting," Energy, vol. 214, p. 118874, 2020.

Authorized licensed use limited to: DELHI TECHNICAL UNIV. Downloaded on March 27,2021 at 05:36:12 UTC from IEEE Xplore. Restrictions apply.

e-ISSN: 2582-5208
International Research Journal of Modernization in Engineering Technology and Science
Volume:03/Issue:03/March-2021 Impact Factor- 5.354 www.irjmets.com

MAGLEV TECHNOLOGY

Dr. J.P Kesari*1, Aditya Shukla*2, Kumar Rahul*3

*1 Professor, Department of Mechanical Engineering, Delhi Technological University Bawana Road, Delhi 110042, India.

*2,3 Undergraduate Student, Department of Mechanical Engineering, Delhi Technological University Bawana Road, Delhi 110042, India.

ABSTRACT

This paper highlights about the hardware, working, principle techniques and physics of Maglev Levitation Trains. These trains are giving huge competition to the aviation sector because of its high speed and low cost consumption. Maglev trains provide high speeds, bearings, and fast transportation. The basic technique behind levitation is that like poles of magnet always repel each other and the basic technique behind propulsion is that unlike poles attract each other. There is a system that continuously changes poles of the track and thus enables the train to run smoothly. These trains are far more better than the conventional trains which consume a lot of fuel creates a lot of pollution and also had to face the frictional resistance, which makes them a lot slower than the modern maglev trains.

KEYWORDS: Maglev Technology, Magnetic Levitation, Propulsion, Bullet Trains.

I. INTRODUCTION

Maglev trains run levitated above the ground surface and thus they are free from any traction or friction offered by the ground or track. This makes them better than the conventional trains. They are also highly unaffected by the adversities of the climate and also do not pose any threat of accident as they can easily decelerate and even faster than the traditional trains. These trains also do not consume a lot of power as most amount of power consumption is only for EDS and for levitation of the train. The power consumption is also due to the air drag (friction) which these trains had to face whenever they travel at higher speeds. These trains can move with continuously high velocity than normal trains. Magnetic levitation is a very higher, efficient, and suitable technology. It also finds a good place for industrial use. These trains boost the economy of any country as they provide very fast transportation and also boost the defence sector as they could be used in weaponry. Thus it has many applications which are being used in the whole world. It returns clean energy and it "s all application gives the lack of contact and thus no friction. Maglev trains are the future of world transportation. Flying trains, flying cars are the key to future. By this paper we have tried to focus on analytical aspect of Maglev Technology and its applications in modern world

II. MAGLEV TECHNOLOGY

MAGLEV TECHNOLOGYis used to run the fastest trains in the world, i.e., BULLET TRAINS. Bullet Trains run without facing ground friction. They are levitated trains and run at a little height above the track. The mainstream tracks are not capable of running on maglev technology. Maglev technology uses powerful electromagnets to run trains, this technology uses monorail tracks.

There are various advantages of maglev levitation technology:

1. It is free of the problem of friction. As the train runs mid-air at high speed, so it only has to face air resistance.

2. Only that part of the track is electrified where the train runs, so electricity is also saved in comparison to conventional trains

3. The most significant advantage is that it is a time-saving technology and also environment friendly. The train is pushed upward by the track and the magnetism property changes as soon as the part of the train has crossed the part of the track, then next part of track gets magnetised and the train is pushed ahead again

e-ISSN: 2582-5208
International Research Journal of Modernization in Engineering Technology and Science
Volume:03/Issue:03/March-2021 Impact Factor- 5.354 www.irjmets.com

III. PRINCIPLE OF MAGNETIC LEVITATION

Levitation coils are placed on the sidewalls of the guide way. Electromagnets are attached to both the sideways of the track and the train. An electric current is set up in the coils placed in the tracks because of the swift movement of superconducting magnets that run few centimetres below the coil at a very high speed, and the coil starts behaving like a temporary electromagnet. Due to this, some forces push the superconducting magnet upwards. This system is called as ELECTROMAGNETIC SUSPENSION as they do not need any wheels or any landing gears for the support.

The undercarriage of the train has a stator which is repelled by the magnetic field produced by the guideway laid all along the track, in this way the train gets levitated.

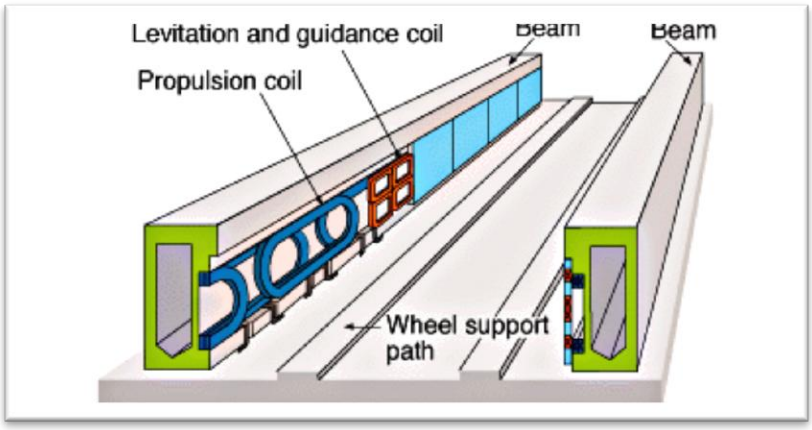

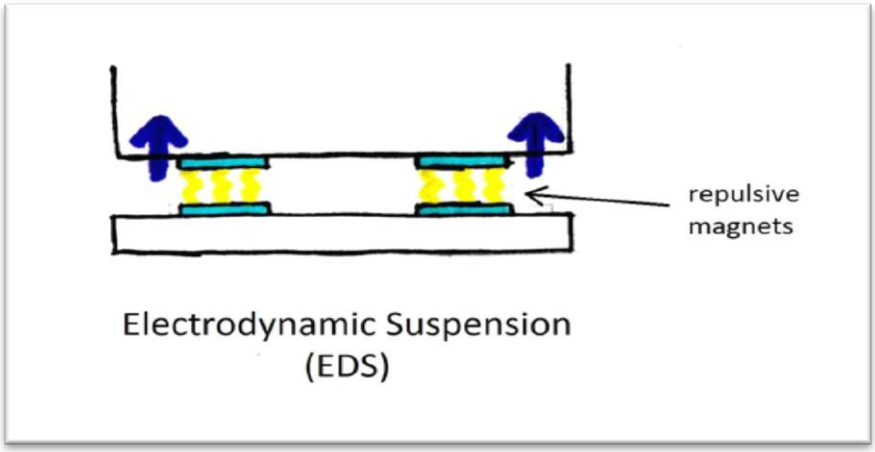

e-ISSN: 2582-5208
International Research Journal of Modernization in Engineering Technology and Science
Volume:03/Issue:03/March-2021 Impact Factor- 5.354 www.irjmets.com

IV. PRINCIPLE OF PROPULSION

By the presence of guideway laid on the track, the train firstly gets levitated in the air. Then an electric current is set up in the coils and in the guideway, which makes it an electromagnet, but the fact here is that the polarity of this electromagnet is continuously changing which changes the magnetic field in front of the train and the train is pulled ahead. By this technique of propulsion train starts floating in the air. They do not have to face any traction or friction. Magnetic field behind the train ads more thrust to the train and this technology of running trains in air has advanced the method of services and transportation.

Making life easy.

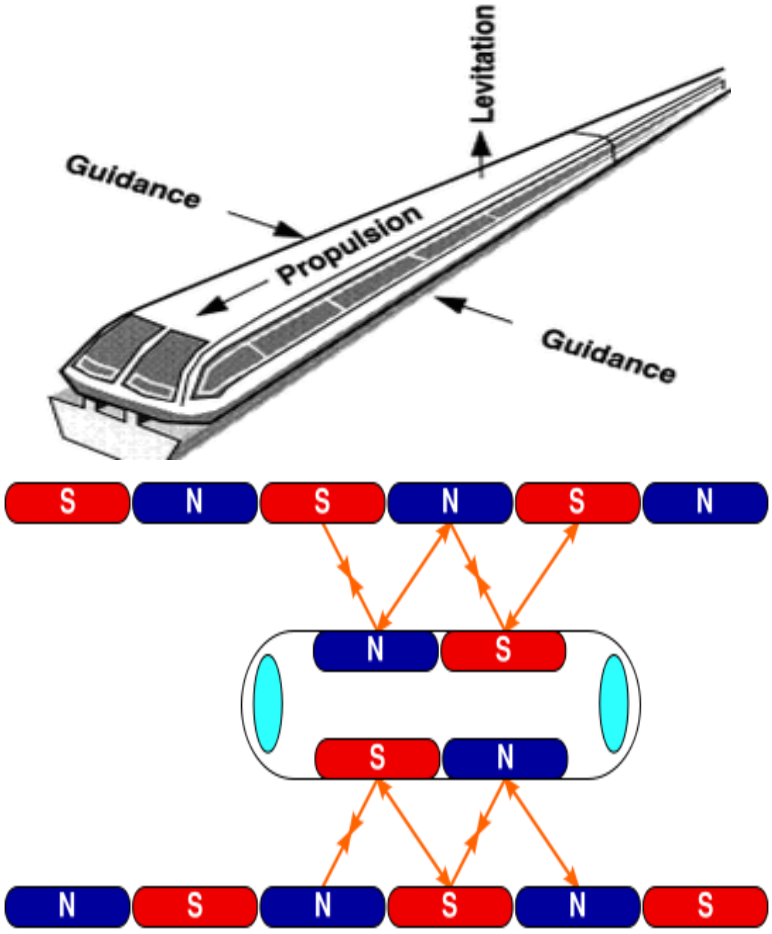

V. COMARISION BETWEEN GERMAN AND JAPANESE TECHNOLOGY

German Technology (Electromagnetic suspension)

In Germany, engineers had developed a type of maglev trains that do not need any landing gears or wheels. Well, all the maglev trains float but, they float from the starting.

These trains have supermagnets or strong ferromagnets attached to their undercarriage. The tracks have also guideway. Thus both the magnetic fields repel each other and the train gets levitated. This magnetic field keeps the train levitated even when it is not moving. There is other guidance magnet in the train and on the track that keeps the train stable even when it is moving. These trains can travel at a speed of 300mph.Earlier train uses strong electromagnets against the guidance but, nowadays supermagnets have replaced them to a large.

e-ISSN: 2582-5208
International Research Journal of Modernization in Engineering Technology and Science
Volume:03/Issue:03/March-2021 Impact Factor- 5.354 www.irjmets.com

Japanese Technology (Electrodynamic suspension)

Japanese engineers have built a different type of Maglev Trains. These trains use wheels to acquire initial speed and then they gets levitated when enough induced current is produced.

In these trains strong magnets are attached at the lower end of the train i.e. at their undercarriage and metallic sheets or induction coils are present in the track. Initially the train runs on the wheels (mostly rubber wheels are employed) and even the speed of the train reaches about 100kmnph then enough induced current is set up in the train which levitates it due to repulsion between the like poles then the sped of train increases to a considerably large amount.

Permanent magnets of supercooled magnets are employed for this purpose. Permanent magnets have not that capability of producing large magnetic field therefore supercooled magnets are nowadays in trend

VI. STABILITY AND GUIDANCE OF MAGLEV TRAINS

STABILITY:

As per Earnshaw's thesis, any pair of magnets having their poles in an opposite configuration will not exist in stable equilibrium. To attain stable equilibrium, a dynamic electromagnetic system is used. EMS systems depend on active electronic stabilization, which continually surveys the bearing range and consequently adjusts the current electromagnet. All EDS systems depend on changing magnetic fields producing electrical currents, and these can give enduring stability. Because maglev vehicles practically fly, stabilization of pitch, roll, and yaw is needed by magnetic technology. In accession to the rotation, movement in forward and backward, sway (sideways motion), or heave (up and down movements) can be unsettled with some technologies.

e-ISSN: 2582-5208
International Research Journal of Modernization in Engineering Technology and Science
Volume:03/Issue:03/March-2021 Impact Factor- 5.354 www.irjmets.com

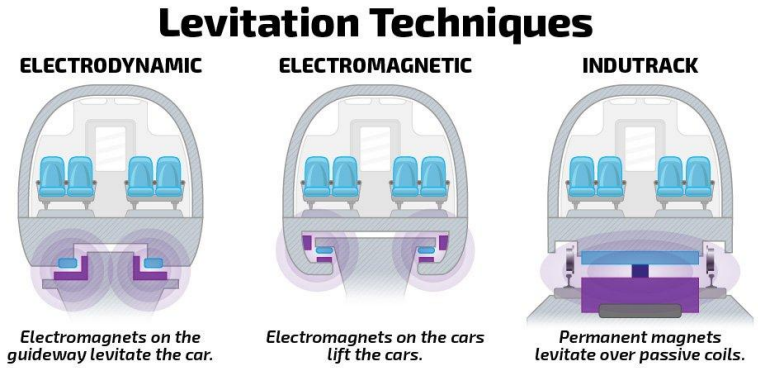

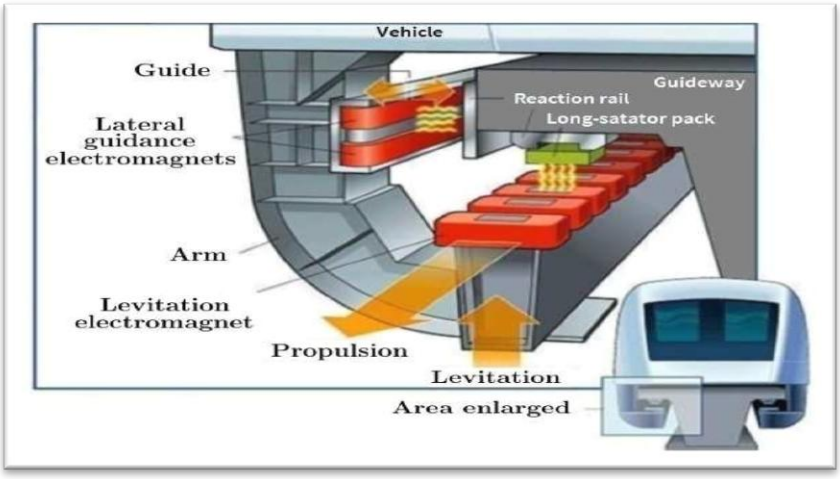

GUIDANCE

Some methods use Null Current systems (also called Null Flux systems); they use a coil that is wound to enter two contrary, alternating fields so that the mediocre flux in the loop is null. When the carrier is in the straight-ahead position, no current flows, but if it runs off-line, this generates a dynamic flux that creates a field that eventually pushes and draws it back into line.

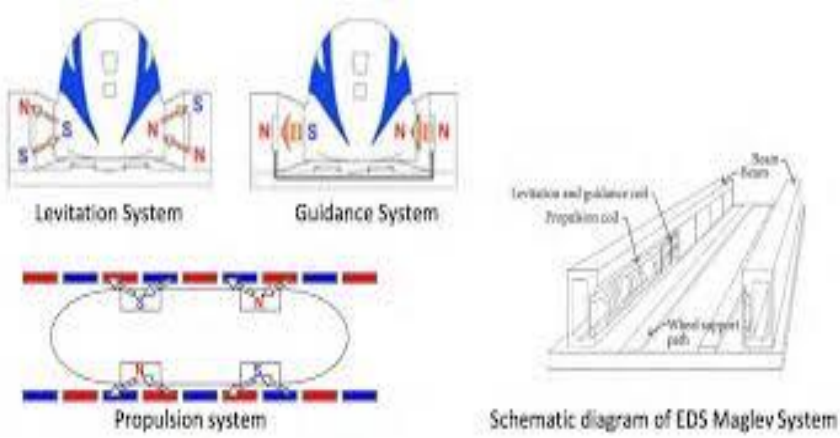

VII. TRANSFER OF ENERGY TO VEHICLE

Moreover, all Maglev trains have batteries on their carriers; an electrical power supply from the ground side is necessary for levitation, propulsion, onboard electrical appliances, battery recharging, etc. The alteration of energy along the track comprises a linear dynamo or a mechanical connection based on the movement velocity.

1) Low–Medium Speed Operation: At low rates up to 100 km/h, the Maglev train generally uses a mechanical contact such as a pantograph. As has been pointed out, this is why the SP type-LIM Maglev train is used for low–medium speed.

2) High-Speed Operation: At high velocity, the Maglev train can no longer receive power from the ground side by using a mechanical connection. Therefore, high-speed Maglev trains use their own way to fulfill the power to the vehicle from the ground. There is a linear generator in such trains which actually makes six times higher frequency electric current produced by the electromagnets present in the train; thus, it supports maglev trains at higher speeds

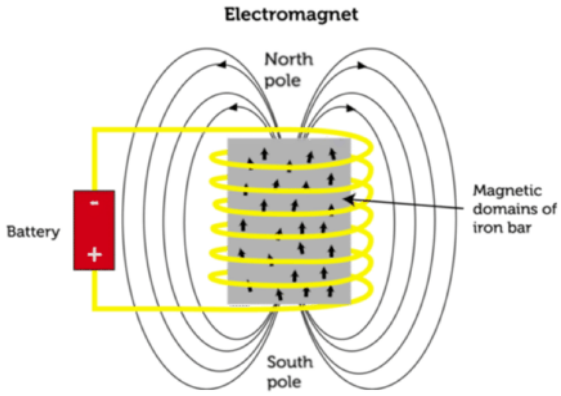

VIII. WORLDWIDE MAGLEV TRAIN PROJECTS AND ITS FUTURE ASPECT IN INDIA

The Japanese and the Germans studied and developed the Maglev Trains from the early 1960s; therefore, their technology has reached industrial levels. USA and Korea had also developed it in the 1990s, for example, the USA Inductrack and Korea's UTM, etc., and now they have brought excellence in their technologies. Some of the projects were launched in Germany. Also, an example, like the Munich project in Germany, was approved in September 2003 with public service possible from 2009.

India being a developing country, thought late about it, but maglev technology is still a challenging task to achieve for India. India has an old resolution of tracks that cannot hold or sustain such a high speed. Also, laying of new tracks is a difficult job. So establishing bullet trains is a big project of India that will require a lot of time, capital, and work.

IX. CONCLUSION

The Maglev train is considered for both metropolitan transportation and intercity transportation operations. In the low–medium velocity Maglev train, the operating cycle is shorter than the high-speed train.

Maglev trains consume very little energy compared to conventional trains. They require no large engine kind of stuff as they run using linear motors. They Move a lot faster than normal trains because they are not affected by ground friction; they would only have air resistance or drug resistance. They are incompatible with existing rail lines because they need a separate track to levitate, unlike the traditional high-speed trains. Initially, the cost is very high, but it may decrease in the near future.

ACKNOWLEDGEMENT

The authors wish to acknowledge Dr. J.P Kesari and Delhi Technological University for their complete support throughout their work.

X. REFRENCES

[1] Shwethasingh, Aradhanasingh. “Magnetic Levitation Methods and Modelling in Maglev Trains”, 2014 ISSN: 2277 128 xx.

[2] H. Yaghoubi and M. A. Rezvani, “Development of Maglev guideway loading model,” Journal of Transportation Engineering, vol. 137, no. 3, pp. 201–213, 2010. View at Publisher · View at Google Scholar · View at Scopus

[3] http://www.bmg-bayern.de/en/proj_3.php.

[4] http://www.meitetsu.jp/english/travel_info/.

[5] http://www.hsgta.com.

[6] http://www.transrapid.de/cgi-tdb/en/basics.prg.
[7] http://www.calmaglev.org/default.php?getpage=projects.
[8] http://www.maglevpa.com/project.html.
[9] https://www.researchgate.net/search

2021 11th International Conference on Cloud Computing, Data Science & Engineering (Confluence) | 978-1-6654-1451-7/20/$31.00 ©2021 IEEE | DOI: 10.1109/Confluence51648.2021.9377131

Multiclass classification for predicting Remaining Useful Life (RUL) of the turbofan engine

Piyush Soni
Mechanical Engineering Department
Delhi Technological University
Delhi, India
piyush.9868@gmail.com

Mohd Anas Khan
Mechanical Engineering Department
Delhi Technological University
Delhi, India
anas_khan0007@yahoo.com

Mohammad Zubair
Mechanical Engineering Department
Delhi Technological University
Delhi, India
zubairsaifi50@gmail.com

Prof. Suresh Kumar Garg
Mechanical Engineering Department
Delhi Technological University
Delhi, India
skgarg@dtu.ac.in

***Abstract*— For complex equipment and systems or their subsystems maintaining good health is very important. Several approaches were tried by the researchers applied by the industry professionals to predict the health of equipment, to take corrective measures. In this context, data analysis and machine learning are the latest tools that use historical data of equipment to predict the health or remaining useful life of the equipment and classify it into three categories based on predicted health namely, good, poor and average. Random forest algorithm was employed for the prediction of the health of a turbofan engine from data obtained using a simulation model C- MAPPS. The data contained attributes containing three different operating conditions along with 28 sensors to record the conditions in which the engine is running. The model gives an accuracy of 81% to predict the correct health condition of the turbofan engine.**

Keywords—classification, machine learning, RUL, turbofan engine

I. INTRODUCTION

For complex frameworks like aircraft engines, finding a suitable model that allows the infusion of health-related changes is a challenge. Data-driven prognostics face the perpetual challenge of the lack of remaining useful life data sets. Obtaining actual system fault development data is long-running and costly. The unavailability of mutual data sets that can be used by researchers to differentiate their approaches is obstructive progress in the prognostics field. In past, several competitions to prognosticate have been held but none have been conducted with a Prognostic Health Management (PHM) focus. Aircraft propulsion is a process in which thrust is generated which is achieved by the working of the turbofan which is also called fanjet. It is usually a gas turbine engine variant that converts the mechanical energy to increase air rearwards. It is a turbine engine that consists of a low-pressure fan in front of the compressor. The mass of the air is increased due to the low-pressure air which is made to evade the compressor and turbine. This system increases efficiency, decreases noise, and fuel consumption. NASA's Prognostic center of excellence established a repository with datasets to be used for benchmarking prognostics and productive maintenance-related algorithms.

The main issue we face in industries is that we cannot find out the Remaining Useful Life (RUL) of each turbofan. The dataset was wonderfully explained by Saxena et al. [1] in their research and they also talked about the importance of RUL prediction in any machinery. The objective of the current study is to help the industry in classifying their equipment for further quality testing and avoid sudden failure of any part while operation by giving away to classify the equipment or the turbofan engine into three categories based on their remaining useful life, good, poor and average so that the equipment in a good category can be used without any worries and also save the money required in the maintenance of large equipment like turbofan engine.

Listou et al. [2] probed for the result of unsupervised algorithms in RUL predictions using semi-supervised setup also using the Genetic Algorithm for tuning the setup and found it to be promising for practical prognostic health management applications. Ruihua et al. [3] proposed a fault tracking and RUL predicting framework based on Gap-DBN and SVDD where RUL is predicted using the PF algorithm and validated the framework's effectiveness using experiments. Jun et al. [4] used a method of deep long short-term memory (DLSTM) network for RUL prediction and found it to be better than other neural network models and many other algorithms. Kunyuan et al. [5] used a long-term differential method to draw out forward differential features that show actual degradation and also, the Fibonacci window is suggested for short-term feature extraction furthermore, RUL was predicted using the CatBoost algorithm. Kshitij et al. [6] presented a Multi-Agent System (MAS) architecture for collaborative prognostics, using naïve fixed-window prognostics algorithms and predicted RULs. Celestino et al. [7] used a combination of time series analysis methods (auto-regressive integrated moving average or ARIMA) to forecast the values of predictor variables and machine learning methods (Support Vector Machine or SVM) to predict RULs and compared the results found using vector auto-regressive moving average (VARMA) and found the method to be promising. Khaoula et al. [8] used discrete Bayesian Network (BN) based on decision fusion to estimate RULs in a turbofan engine and observed the model to viaduct performance of other methods. Zeqi et al. [9] show damage proliferation can be followed within the parts of aircraft engines. The sensor responses are generated and data is used to learn that gradual degradation of turbofan engines has some scope of regularity and presence of relation between an inconsistent degradation process and corresponding RUL. Relation of the degradation pattern and RUL is established employing a neural network in this paper. The improved

978-0-7381-3160-3/21/$31.00 ©2021 IEEE

Authorized licensed use limited to: DELHI TECHNICAL UNIV. Downloaded on March 27,2021 at 05:35:23 UTC from IEEE Xplore. Restrictions apply.

neural network is analyzed. Lu et al. [10] applied the Kernel-based Extreme Learning Machine i.e., a KELM algorithm with an iterative picking scheme that advances the scarceness of the KELM algorithm by two flashing components, an insertion approach to enlarge the network and an abolition approach to decrease the size of the network. Reproductions of failure analysis of a turbofan engine demonstrated that the projected algorithm performed at an accuracy similar to that of KELM with a much quicker testing speed. Yu et al. [11] used a bidirectional recurrent neural network-based approach and then improved it in the next version [12] of the similarity criterion-based curve fitting technique to estimate the RUL and concluded that the ensemble approach gives more reliable predictions. Tarek et al. [13] used Denoising Online Sequential Extreme Learning Machine (DOS-ELM) with Updated Selection Strategy (USS) and double dynamic forgetting factors (DDFF) on the same data and the model showed constancy of the network answers even beneath random results for the prediction of RUL. Lei et al. [14] wonderfully summarized machinery prognostics and also talked about the RUL prediction done based on the current dataset and talked about various situations, probable future trends, and challenges for predicting RUL for various machinery. Deng et al. [15] applied the long short-term memory (LSTM) network and the Wiener process to benchmark trade-off between uncertainty about the RUL prediction and prediction performance which improved the near-failure accuracy. Yang et al. [16] used a double convolutional neural network (CNN) for predicting RUL where emerging failure point is recognized by the first CNN model then the second CNN model is made for RUL prediction which gave higher accuracy. Lei et al. [17] reviewed the machinery prognostics talking about complete process from data procurement to estimation of RUL.

II. Objectives and Framework

The purpose of this study was to estimates the health of a turbofan engine by classifying the turbofan into three categories based on their RUL for its predictive maintenance. The data attained is from a turbofan engine simulation which closely replicates the actual engine. Artificial noise was also introduced to the data set to replicate the real-world scenarios. The data set that has been used is a multiple multivariate time series of the above-mentioned simulation model and can be considered from a fleet of engines of the same type. The data is taken from a turbofan engine simulation performed in C-MAPPS (commercial modular aero propulsion system simulation). It is used to produce health and engine parameters using a simulation of the turbofan engine. Every engine is expected to be having initial wear which is considered normal. Along with the sensor data, the data set also consists of three operational characteristics that affect engine performance considerably. One training data set has been used in this analysis. We analyzed the changes in the sensor measurements and used the Random Forest algorithm for the classification of the engine.

III. Classification of the Engine

As per the objective, the classification was done after assessing various supervised machine learning algorithms namely Logistic Regression, Decision Tree with boosting algorithms like AdaBoost, Gradient Boosting, Random Forest, and the best one was selected among them. The model that gave the best result among them was Random Forest and so the same was used for the classification of the engine's health quality into three categories based on the predicted RUL.

A. Turbofan Engine and sensors/attributes information

The C-MAPPS Simulation used in this analysis closely replicates the turbofan. A standard turbofan engine consists of a fan, a low-pressure compressor, a high-pressure compressor a combustor, a low-pressure turbine high-pressure turbine, and a nozzle. Behind the fan is a splitter that splits the incoming air from the fan into two paths- the bypass path and the second part travels in the compressor. Figure 1 shows the layout of modules and connections which was taken from the literature.

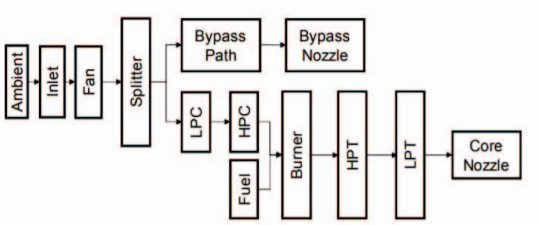

Fig. 1. Layout showing various modules and connections as modeled in the simulation [1]

TABLE I. C-MAPPS OUTPUT (SENSOR DATA)

Symbol	Description (Units)
T24	LPC outlet temperature (°R)
T2	Fan inlet temperature (°R)
T30	HPC outlet temperature (°R)
T50	LPT outlet temperature (°R)
P2	The pressure at fan inlet (psia)
P15	The total pressure in bypass-duct (psia)
P30	HPC outlet pressure (psia)
Nf	Physical fan speed (rpm)
Nc	Physical core speed (rpm)
epr	Engine pressure ratio -- P50/P2 (--)
Ps30	HPC outlet static pressure (psia)
phi	The ratio of fuel flow to Ps30 (pps/psi)
NRf	Corrected fan speed (rpm)
NRc	Corrected core speed (rpm)
BPR	Bypass Ratio (--)
farB	Burner fuel-air ratio (--)
HtBleed	Bleed Enthalpy (--)
Nf_dmd	Demanded fan speed (rpm)
PCNfR_dmd	Demanded corrected fan speed (rpm)
W31	HPT coolant bleed (lbm/s)
W32	LPT coolant bleed (lbm/s)

Authorized licensed use limited to: DELHI TECHNICAL UNIV. Downloaded on March 27,2021 at 05:35:23 UTC from IEEE Xplore. Restrictions apply.

Table I shows the explanation or the definitions of the different attributes based on the sensor data, there were 7 more attributes (Unit number, Time in cycles, Operational setting 1 (OS1), Operational setting 2 (OS2), Operational setting 3 (OS3) and two more sensor data) making the dataset to have 28 attributes among these 7, the data in the last two attributes read NULL and OS3 is constant.

B. Data Preprocessing

Preprocessing of any data is a very important and crucial part and one must do it with utmost accuracy. During this process only, we have to remove the constant or useless attributes and variables so as we are only doing the processing and training our data on useless information and dataset. In the current study, many of the attributes in the data were constant and non-reactive towards the output of remaining useful life so in this portion the cleaning of the data occurs.

1) Distribution Analysis: The data used for analysis follows, for most parts, a normal distribution. Further, data was then converted to scaled to standard normal distribution. The skewness and kurtosis were insignificant so they were ignored for further analysis. So, the assumptions were taken for all the attributes to be normally distributed.

2) General Trends in sensor data: Changes in sensor data due to an increase in the number of cycles were analyzed of the given data. Some attributes in the sensor data showed little or no fluctuations with an increasing number of cycles. These attributes are not included in prediction analysis. The attributes that showed no change with increasing no. of cycles are -T2, P2, Epr, farB, Nf_dmd, PCNfR_dmd. Other attributes/sensor output data shows variable trends in data. Analysis of trends of each sensor data with an increase in the number of cycles is depicted in figure 2. The temperatures (T24, T30, T50), as expected keep rising with the increasing number of cycles. There is an increase in static pressure values (Ps30) and a decrease in total pressure value(P30) at the HPC outlet. The ratio of fuel flow to Ps30 shows a decreasing trend as fuel flow is constant but Ps30 increases. Fan speed values (Nc, Nf, NRf, NRc) have variability in maxima values for every turbofan before failure. So, an abrupt increase or decrease in physical or core fan speed is not a cause for failure. Bypass ratio certainly increases and maxima have very little variability. Coolant bleed mass flow rate (W31 and W32)

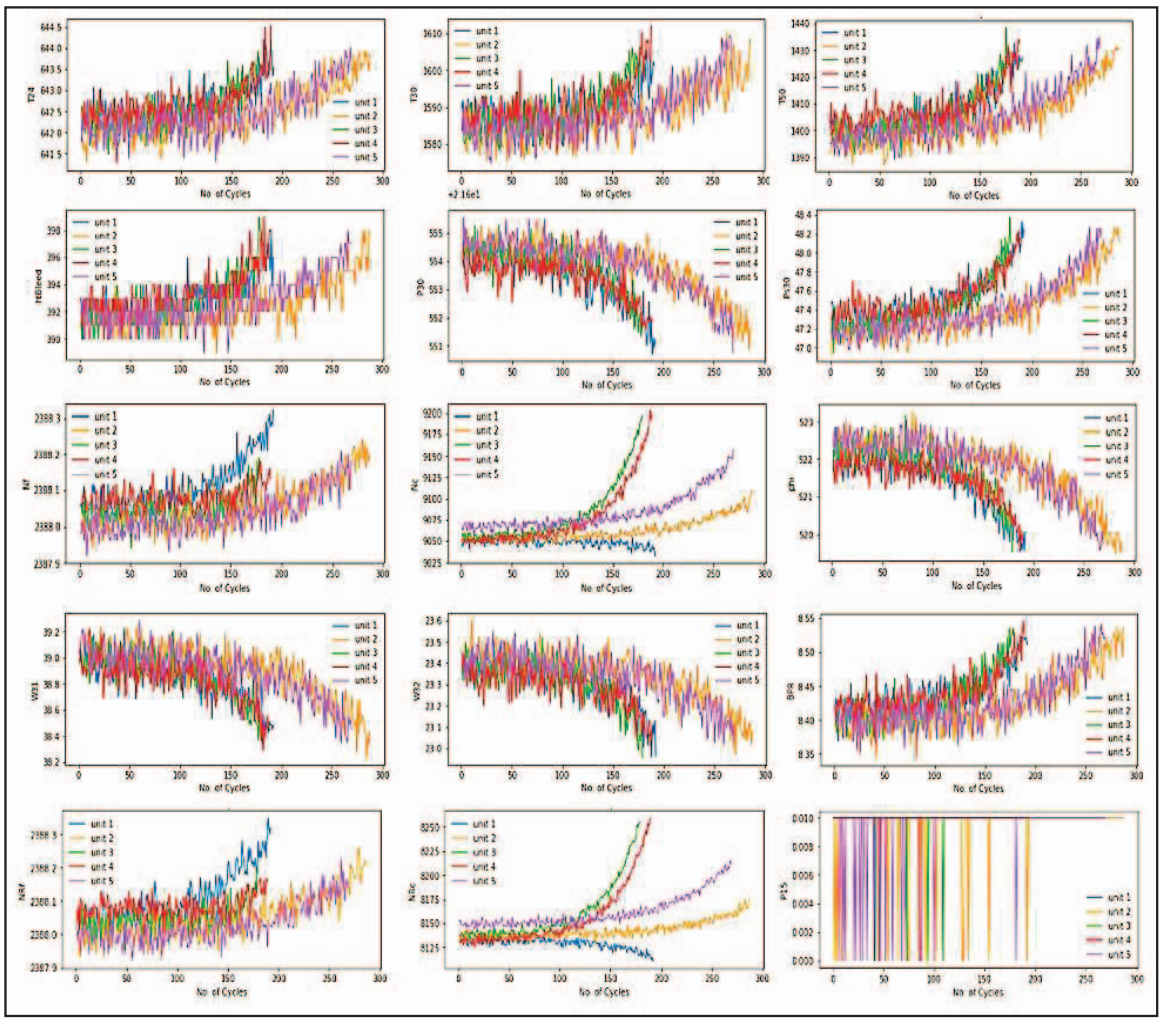

Fig. 2. Attributes vs No. Of Cycles

Authorized licensed use limited to: DELHI TECHNICAL UNIV. Downloaded on March 27,2021 at 05:35:23 UTC from IEEE Xplore. Restrictions apply.

decreases with the increasing number of cycles. Bleed enthalpy follows an increasing trend with an average peak value of 397. Hence, few deciding attributes fail the turbofan, and when the values increases/decreases from the peak values, the likelihood of failure becomes very high. These attributes with average peak values are shown in Table II. These average peak values can be assumed to be threshold values for failure.

TABLE II. PEAK VALUES BEFORE FAILURE

Attributes	Threshold Values
T24	644.0°R
T30	1605.0 °R
T50	1430 °R
P30	551 psia
Ps30	48.2 psia
BPR	8.52
phi	519.2 pps/psi
W31	38.3 lbm/s
W32	23.0 lbm/s
HtBleed	397

Although we observe an almost similar maxima/minima before failure in each turbofan for these attributes, the life/maximum number of cycles of the turbofan varies. This is due to two reasons:

- The turbofans initially have been assumed to have some wear and tear which is considered normal. As the wear and tear of each turbofan differ, so does the life.
- Operating characteristics/conditions of each turbofan keep on changing after every cycle. Although it makes a slight difference, this factor shouldn't be ignored as in actual practice as a turbofan fitted in an actual airplane goes through changes in atmospheric conditions and characteristics.

3) Remaining Useful Life (RUL): Remaining Useful Life (RUL) is an estimation of the length of time that a piece of equipment is estimated to be to function satisfying its intended purpose. It is our output of the data and this is what we have to base our classification on. The data provided is time-series data that gives us sensor information with every cycle. Calculating RUL will provide us an estimate of the remaining life of the turbofan considering the data provided by the sensors. A correlation analysis was carried out to understand the correlation of different attributes with RUL values so we can gain insight into the way the attributes are behaving and having a relationship with the output or target variable. A bar plot with sensor measurements in the y-axis and correlation in the x-axis is shown in figure 3. The bar-plot shows the extent up to which a particular attribute affects RUL values. Operating Characteristics (OS1 and OS2) have a negligible effect on RUL values. P15(Total Pressure in the bypass duct) can also be neglected from the analysis. Furthermore, in the previous section, it was clear that fan speed does not directly cause turbofan failure. But, the data from the fan speed sensor certainly cannot be neglected as it has a decent correlation value.

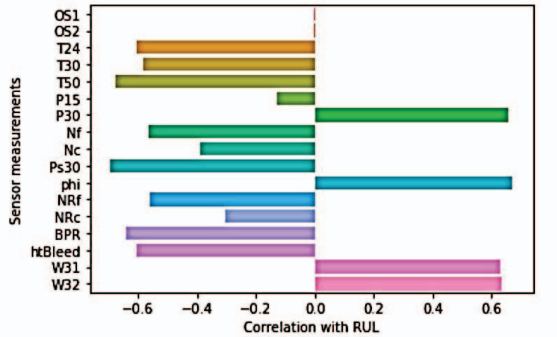

Fig. 3.- Layout showing various

C. *Algorithm*

Python has been used for building the machine learning model for the same. Libraries like pandas for data management and analysis, sklearn for building ML models along with matplotlib, and seaborn for data visualization have been used. Random forest is a supervised learning algorithm. It can be castoff both for classification and regression and is easy to use. A forest is encompassed of trees. It is said that the extra trees it has, the extra vigorous a forest is. Random forest is a combination of decision trees, grows prediction from each tree, and selects the finest solution utilizing voting. It also delivers a pretty good pointer of the feature importance. It is used in various applications such as image classification, recommendation engines, and feature selection. It can be utilized to classify loyal loan candidates, classify deceitful activity, and predict diseases. It works on the Boruta algorithm which is used to identify features in a dataset that are important. Confusion matrix, ROC curve, recall, accuracy precision, f1-score are used for performance measurement of the random forest model (or any classification model). GridSearchCV is used to find the optimal parameters for the model. There are several applications of the said algorithm like Zhu et al. [18] used random forest algorithm for predicting the loan default where they employed SMOTE method to deal with the issue of imbalanced class in the dataset and showed that random forest algorithm prevails and is better than logistic regression, decision tree, and other algorithms. Moscatelli et al. [19] say that machine learning models like random forest and gradient boosting provides extensive advantages in prejudiced power and accuracy, compared to statistical models like the logistic regression. Ji et al. [20] used a smart fault analysis approach consisting of random forests for finding faults in hydraulic valves and found that the typical accuracy ratio of the anticipated method is 98.5% for six fault types discovery. A random forest is a group of decision trees in which the apiece decision tree is unconnected. Assortment metrics we used for excruciating features in the decision tree are the Gini index, and the number of stages in each tree division hinges on the algorithm parameters [21]. Li et al. [22] used Wiener Process Model for forecasting RUL over degradation process simulation algorithm. Guo et al. [23] applied RNN based health indicator and predicted the RUL for bearings.

IV. RESULTS AND DISCUSSION

Many researchers have studied the data used and gave some of the best machine learning algorithms to predict the RUL of the turbofan engine. In the current study, several machine learning algorithms were assessed and Random Forest was selected based on overall test dataset accuracy as shown in Table III.

Authorized licensed use limited to: DELHI TECHNICAL UNIV. Downloaded on March 27,2021 at 05:35:23 UTC from IEEE Xplore. Restrictions apply.

TABLE III. OVERALL ACCURACY OF ALGORITHMS

Algorithm	Overall Accuracy
Logistic Regression	80%
Decision Tree	77%
AdaBoost	76%
Gradient Boosting	79.6%
Random Forest	81%

Among the mentioned ML models, the model made using the Random forest classifier performed best with overall test dataset accuracy of 81%. The lack of accuracy can be explained by the fact that data is presumed to be distributed normally with zero skewness and mesokurtic but it is not so in actuality. Random Forests was used in ensemble with extreme learning machine and multi-regime time series by Lin et al. [24] in their paper where the approach was found to be accurate and stable in predicting the time-series of the data given but in the current study, the random forests were individually applied just to predict the windows of the health the engine categorizes in and that too with good accuracy.

This data used in some of the literature was used with advanced algorithms for the prediction of remaining useful life but based on that there hasn't been any window segregation that can classify the given turbofan engine giving its health statement in the previous works. In the present work an effort is made to classify the health of the engine in turbofan based on the predicted RULs and for that uncorrelated attributes were removed and then many models were tried to find the said results and among those models, the best result was given by Random Forests based algorithm and so, after dropping irrelevant features, a performance window was made for the classification analysis. It is a case of multiple classifications with three options: Poor condition and requires to be sent to the facility, Average condition and requires fault analysis, and Good condition, ready to be used

The range of RUL values used for the performance window was calculated using trial & error. The graphs in figure 4 denote the performance window segregation. Recall and precision values of the model for the good condition classification has been kept as high as possible. The model gives 81% accuracy in the test dataset which is satisfactory. Overfitting and underfitting of data have been prevented so that the model can be used for any new relevant data.

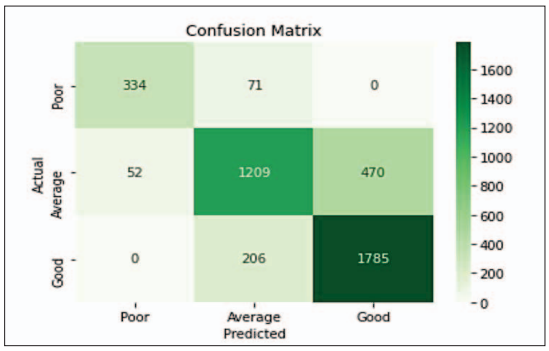

Fig. 5. Confusion Matrix

The recall is the conditional possibility that the predicted class is positive given that the actual class is positive.

Mathematically, Recall = TP / (TP + FN)

Specificity is the conditional possibility that the predicted class is negative given that the actual class is negative. Mathematically, Specificity = TN / (TN + FP)

Precision is the conditional possibility that the real value is positive given that the prediction by the model is positive. Mathematically, Precision = TP / (TP + FP)

F-Score is the harmonic average between precision and

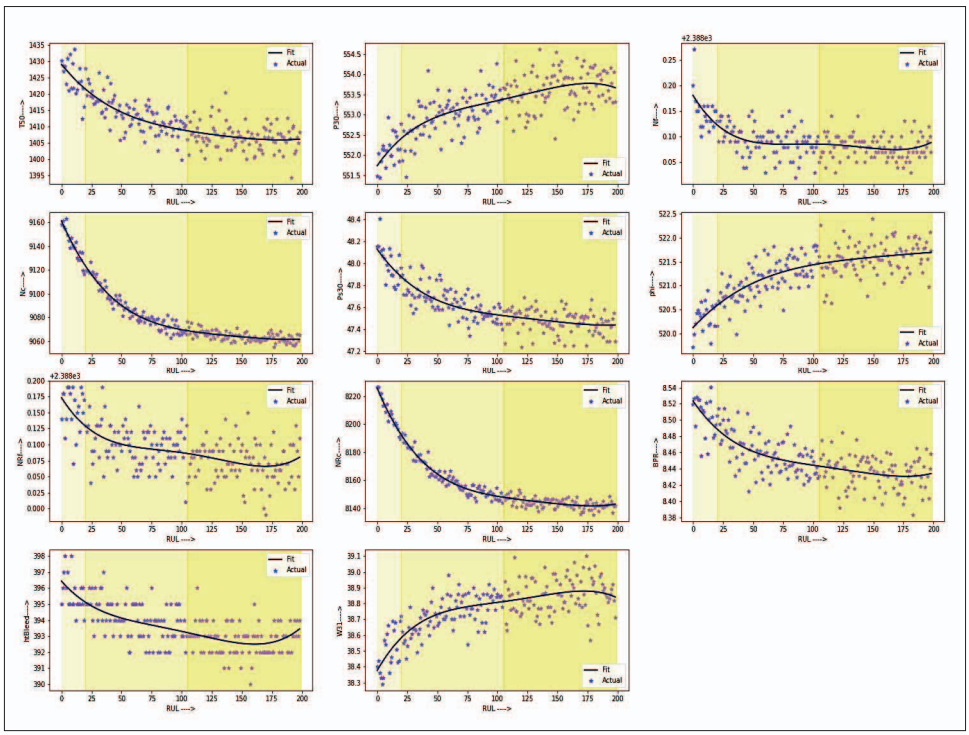

Fig. 4. Performance window classification in fitted data

Authorized licensed use limited to: DELHI TECHNICAL UNIV. Downloaded on March 27,2021 at 05:35:23 UTC from IEEE Xplore. Restrictions apply.

recall. Mathematically,

F-Score = 2*Recall*Precision / (Recall + Precision)

Where TP = True Positive, TN = True Negative, FP = False Positive, FN = False Negative

The confusion matrix of the model is depicted in figure 5 and the values of the above-mentioned parameters are depicted in Figure 6 as a classification report.

	precision	recall	f1-score	support
0	0.87	0.82	0.84	405
1	0.81	0.70	0.75	1731
2	0.79	0.90	0.84	1991
accuracy			0.81	4127

Fig. 6. Classification Report

V. Conclusion

Now and for a long time, prognostics and health supervision stimulate big attention. As a result, a variety of approaches has been industrialized. Though, there are scarce works that have fused the verdicts of prognostics methods and classified the equipment health into windows. Furthermore, the utmost of the published works is devoted to finding and predicting the specific values of RUL with utmost accuracy so there is the classification that is still missing. In the current study, the data available form C-MAPPS was successfully preprocessed and was trained and then tested on a machine learning algorithm that is supervised based on Random Forests to classify the health state of any turbofan engine in three different categories i.e., good, poor, and average through the RUL. The data had 28 attributes among which some were non-related to the output and so were removed from the analysis of the data during preprocessing based on distributions and correlation of data attributes. After preprocessing, the data was left with some attributes that would make the predictions usable. The preprocessed data was trained using various algorithms which predicted the health of the equipment and then the model was validated on all the given test data. Of all the algorithms used, Random forest gave 81% test accuracy. For example, in several 1991 turbofans, the good conditioned, 1785 were correctly classified which shows good recall. Likewise, for 2255 turbofans which were classified as 'good', 1786 were good which is attired precision.

References

[1] A. Saxena, K. Goebel, D. Simon, and N. Eklund, "Damage propagation modeling for aircraft engine run-to-failure simulation," in International Conference on Prognostics and Health Management, Denver, CO, 2008, pp. 4711414.

[2] L. Ellefsen, E. Bjørlykhaug, V. Æsøy, S. Ushakov, and H. Zhang, "Remaining useful life predictions for turbofan engine degradation using semi-supervised deep architecture," *Reliab. Eng. Syst. Saf.*, vol. 183, pp. 240–251, Nov 2018.

[3] R. Jiao, K. Peng, J. Dong, and C. Zhang, "Fault monitoring and remaining useful life prediction framework for multiple fault modes in prognostics," *Reliab. Eng. Syst. Saf.*, vol. 203, pp. 107028, Jun 2020.

[4] J. Wu, K. Hu, Y. Cheng, H. Zhu, X. Shao, and Y. Wang, "Data-driven remaining useful life prediction via multiple sensor signals and deep long short-term memory neural network," *ISA Trans*., vol. 97, Jul 2019.

[5] K. Deng, X. Zhang, Y. Cheng, Z. Zheng, F. Jiang, W. Liu, and J. Peng, "A remaining useful life prediction method with long-short term feature processing for aircraft engines," *Appl. Soft Comput.*, vol. 93, pp. 106344, May 2020.

[6] K. Bakliwal, M. H. Dhada, A. S. Palau, A. K. Parlikad, and B. K. Lad, "A Multi-Agent System architecture to implement Collaborative Learning for social industrial assets," *IFAC-PapersOnLine*, vol. 51(11), pp. 1237–1242, Aug 2018.

[7] C. Ordóñez, F. Sánchez Lasheras, J. Roca-Pardiñas, and F. J. Juez, C. de, "A hybrid ARIMA–SVM model for the study of the remaining useful life of aircraft engines," *J. Comput. Appl.*, vol. 346, pp. 184–191, Jul 2019.

[8] K. Tidriri, S. Verron, T. Tiplica, and N. Chatti, "A decision fusion based methodology for fault Prognostic and Health Management of complex systems," *Appl. Soft Comput*., vol. 83, pp. 105622, Jul 2019.

[9] Z. Zhao, B. Liang, X. Wang, and W. Lu, "Remaining useful life prediction of aircraft engine based on degradation pattern learning. Reliability Engineering & System Safety," *Reliab. Eng. Syst. Saf.*, vol. 164, Mar 2017.

[10] J. Lu, J. Huang, F. Lu, and L. Feng, "Kernel extreme learning machine with iterative picking scheme for failure diagnosis of a turbofan engine," *Aerosp. Sci. Technol*., vol. 96, pp. 105539, Nov 2019.

[11] Y. Wennian, II. Kim, and C. Mechefske, "Remaining useful life estimation using a bidirectional recurrent neural network-based autoencoder scheme," *Mech. Syst. Signal. Pr*., vol. 129, pp. 764-780, Aug 2019.

[12] Y. Wennian, II. Kim, and C. Mechefske, "An improved similarity-based prognostic algorithm for RUL estimation using an RNN autoencoder scheme," *Reliab. Eng. Syst. Saf*., vol. 199, pp. 106926, Mar 2020.

[13] B. Tarek, H. Mouss, Q. Kadri, S. Lotfi, and M. Benbouzid, "Aircraft Engines Remaining Useful Life Prediction with an Adaptive Denoising Online Sequential Extreme Learning Machine," *Eng. Appl. Artif. Intel.*, vol. 96, pp. 103396, Nov 2020.

[14] Y. Lei, N. Li, L. Guo, N. Li, T. Yan, and J. Lin, "Machinery health prognostics: A systematic review from data acquisition to RUL prediction," *Mech. Syst. Signal. Pr*., vol. 104, pp. 799-836, May 2018.

[15] Y. Deng, A. Bucchianico, and M. Pechenizkiy, "Controlling the Accuracy and Uncertainty Trade-off in RUL Prediction with a Surrogate Wiener Propagation Model," *Reliab. Eng. Syst. Saf*., vol. 196, pp. 106727, Nov 2019.

[16] B. Yang, R. Liu, and E. Zio, "Remaining Useful Life Prediction Based on A Double-Convolutional Neural Network Architecture," *IEEE T. Ind. Electron*., vol. 66, pp. 9521-9530, Jul 2019.

[17] Y. Lei, N. Li, L. Guo, N. Li, T. Yan, and J. Lin, "Machinery health prognostics: A systematic review from data acquisition to RUL prediction," *Mechanical Systems and Signal Processing,* vol. 104, pp. 799-834, 2018.

[18] L. Zhu, D. Qiu, D. Ergu, C. Ying, and K. Liu, "A study on predicting loan default based on the random forest algorithm," *Procedia Comput. Sci.,* vol. 162, pp. 503-513, Jan 2019.

[19] M. Moscatelli, F. Parlapiano, S. Narizzano, and G. Viggiano, "Corporate Default Forecasting with Machine Learning," *Expert Syst. Appl.*, vol. 161, pp. 113567, May 2020.

[20] X. Ji, Y. Ren, T. Hesheng, C. Shi, and J. Xiang, "An intelligent fault diagnosis approach based on Dempster-Shafer theory for hydraulic valves," Meas., vol. 165, pp. 108129, Jun 2020.

[21] N. Li, Y. Lei, T. Yan, N. Li, T. Han. "AWiener-Process-Model-Based Method for Remaining Useful Life Prediction Considering Unit-to-Unit Variability," *IEEE T. Ind. Electron.,* vol 66(3), pp. 2092-2101, May 2018.

[22] L. Guo, N. Li, F. Jia, Y. Lei, and J. Lin, "A recurrent neural network based health indicator for remaining useful life prediction of bearings," *Neurocomputing,* vol. 240, pp. 98-109, 2017.

[23] Breiman, L. (2001). Random forests. Machine Learning, 45(1), 5–32.

[24] L. Lin, F. Wang, and X. Xie, "Random forests-based extreme learning machine ensemble for multi-regime time series prediction," Expert *Syst. Appl.,* vol. 83, Apr 2017.

Authorized licensed use limited to: DELHI TECHNICAL UNIV. Downloaded on March 27,2021 at 05:35:23 UTC from IEEE Xplore. Restrictions apply.

Research Article

Near-surface seismic refraction tomography and MASW for site characterization in Phuentsholing, Bhutan Himalaya

Raju Sarkar[1] · Sreevalsa Kolathayar[2] · Dowchu Drukpa[3] · Kinley Choki[4] · Shrijana Rai[4] · Sangay Tenzin Tshering[4] · Kezang Yuden[4]

Received: 7 October 2020 / Accepted: 6 February 2021
© The Author(s) 2021 OPEN

Abstract
It is essential to understand the soil characteristics of the subsurface layers for any engineering construction. In difficult terrains like hilly areas, conventional methods of investigation are expensive and difficult to conduct. It calls for non-destructive testing methods to get reliable estimates of subsurface properties. In the present study, seismic refraction tomography (SRT) technique and multichannel analysis of surface waves (MASW) methods were carried out along five selected profiles in Phuentsholing region of Bhutan Himalaya. The profile length ranges from 37 to 81.5 m, and depth of imaging down to 10 m. While the SRT data imaged the P-wave velocity (V_p) structures, the MASW imaged the shear wave velocity (V_s) structures. The P-wave images provide a fair knowledge of geological layers, while the MASW images provide S-wave velocity structures (V_s). These results are useful to estimate soil parameters, like the density, Poisson's ratio, Young's modulus, shear modulus, *N*-value and the ultimate bearing capacity. The seismic images reveal the presence of sand, sandy clay, gravels and shale layers below the selected sites. Bhutan Himalayas being seismically vulnerable, the obtained results in terms of shear wave velocity were accustomed to categorize the sites as per NEHRP site classes, and a ground response analysis was performed to determine the reliable amplification factors. From the study, it is suggested that the engineering construction is feasible at all the sites except in one site, where an indication of saturated soil is observed which is vulnerable for liquefaction, and ground needs to be improved before construction at that site.

Keywords Seismic refraction tomography · MASW · Primary and shear wave velocity · Soil profile · Site class

1 Introduction

Before commencement of any engineering construction, it is important to check soil profiles and soil characteristics in order to ensure that the site is acceptable for making such construction. In Bhutan Himalaya, the terrain poses difficulties in conducting conventional soil investigations using shell and auger, open-pit, etc. These methods are noneconomic and take time to perform. The conventional methods, viz. cone penetration test (CPT), provide required parameters of the soil but are costly and invasive, particularly in hilly terrains [16]. Seismic refraction tomography technique (SRT) as well as the multichannel analysis of surface waves (MASW), on the other hand, is time efficient and cost effective. Seismic refraction tomography (SRT) provides velocity structure and the required soil parameters without disturbing the natural ground condition [2, 5, 18, 25]. Over the past years, seismic refraction methods have been used for civil engineering purposes in mountainous terrain [10, 14, 28]. They have been used to locate faults and in determining the soil parameters [4, 16]. The SRT is a geophysical method which uses inversion

✉ Sreevalsa Kolathayar, sreevalsa@nitk.edu.in | [1]Department of Civil Engineering, Delhi Technological University, Bawana Road, Delhi, India. [2]Department of Civil Engineering, National Institute of Technology, Surathkal, India. [3]Department of Geology and Mines, Ministry of Economic Affairs, Thimphu, Bhutan. [4]Department of Civil Engineering and Architecture, College of Science and Technology, Phuentsholing, Bhutan.

Published online: 01 March 2021

technique to obtain 2D velocity depth profile [17, 22, 23] that images the cross-sectional picture along the profile by using the soils' response to the energy from the external source [6, 7, 11].

The multichannel analysis of surface waves (MASW) is a method used to estimate the shear wave velocity at a shallow depth and also help to determine the elastic parameters of the soil [14, 30]. The SRT and MASW data are used for estimating seismic velocities and elastic parameters which are needed to estimate the bearing capacity of the soil mass and for the design of structures which is going to be constructed over it [15]. The damages due to seismic activity are controlled by local geology and soil parameters in addition to construction characteristics of structures. Seismic ground response at a particular location is strongly affected by in situ conditions of local geology and soil characteristics [19–21]. The soil condition has an important effect on the ground vibration. This gives the attention toward the importance of site classification in seismically vulnerable areas. Seismic site enactment due to shear wave velocity will indicate the mechanics of site amplification. The geophysical methods are seen as the most reliable for seismic site characterization [2, 26]. This paper focuses on site characterization at five locations at Phuentsholing in Bhutan Himalayas using the SRT and MASW to assess the feasibility of engineering constructions and to classify the sites as per NEHRP site classification.

2 Study area

Bhutan is a small kingdom located in the eastern Himalayas, nestling between India and China with a total area coverage of 38,394 km^2 (Fig. 1). Our study areas are located in Phuentsholing Gewog under Chukha Dzongkhag covering an area of 15.6 km^2 with an average elevation of 293 m which serves as the administrative seat of the Dzongkhag [24]. Phuentsholing, about 172 km away from Thimphu (Capital of Bhutan), is one of the commercial centers of Bhutan and is a developing border town with India. Due to the importance of trade and commerce, the town has to expand with upcoming infrastructures [8]. In this study, five sites were selected in Phuentsholing area: Kabreytar 1, Kabreytar 2, Pipaldhara 1, Pipaldhara 2 and Phuentsholing town as shown in Fig. 1. Elevation of the sites varies from 210 m (Phuentsholing town) to 392 m (Kabreytar 1), and it is mentioned in Table 1 and shown in Fig. 2.

The sites were chosen based on three factors, such as easy accessibility, terrain and vegetation cover. All the sites were accessible and near to the road available. The sites Pipaldhara 1, Pipaldhara 2 and Phuentsholing town were on plane grounds, whereas Kabreytar 1 and Kabreytar 2 were on sloping grounds with the angle of elevation with horizontal road surface of 37.38° and 21.32°, respectively. Most of the sites have vegetation cover except Phuentsholing town.

The Phuentsholing area forms a part of the Himalayan foothill belt with a youthful topography steep topography and high precipitation. The Phuentsholing formation belongs to Baxa Group of Rocks consisting of quartzite, greenish gray, variegated and carbonaceous phyllite. The formation falls over the Main Boundary Thrust. The rocks in the area are crushed and weathered. The Himalaya being youngest mountain belt is still evolving due to northward movement of the Indian Plate toward the Eurasian plate. Hence, Himalaya is seismically active with large number of earthquakes. The region has weak intact rock strength having uniaxial compressive strength (UCS) value ranging from 0.60 to 1.50 MPa. There are also infrequent interbands of quartzite and dolomite that are strong rock with (UCS) values ranging from 34 to 55 MPa [29].

3 Field operation for SRT and MASW

The equipment for SRT and MASW comprises source, detector and a seismograph. A sledgehammer of 8 kg was used to produce the seismic waves. Twelve geophones with a frequency of 4.5 Hz were used. Seismograph of DAQ LINK 3 was used to record the signals received from the geophones. An alignment was chosen along which the geophones were inserted firmly into the ground at regular intervals. The seismic cables were used to connect the geophones and the seismograph. The sledgehammer was hit on a metal plate to produce the seismic waves (P-wave). These waves travel into the ground through refraction and reflection. Only the critically refracted waves are recorded by the seismograph. The sledgehammer was hit three times on the metal plates at regular intervals of the geophones and at the mid of two geophones. Taking a stack of three, the number of stacks collected for the sites Kabreytar 1, Kabreytar 2, Pipaldhara 1, Pipaldhara 2 and Phuentsholing town was 68, 27, 28, 33, and 30, respectively. Due to limited open plain area, the geophone interval for Kabreytar 1 was kept as 2 m and for the rest of the sites, it was 2.5 m. The lengths of the profiles obtained including the offset distances were 37 m, 44.5 m, 53.5 m 81.5 m, and 43.5 m for Kabreytar 1, Kabreytar 2, Pipaldhara 1, Pipaldhara 2, and Phuentsholing town, respectively.

4 Data analysis

4.1 Analysis of primary waves

A set of refracted P-arrival data are illustrated in Fig. 3. The SRT data were analyzed using the software

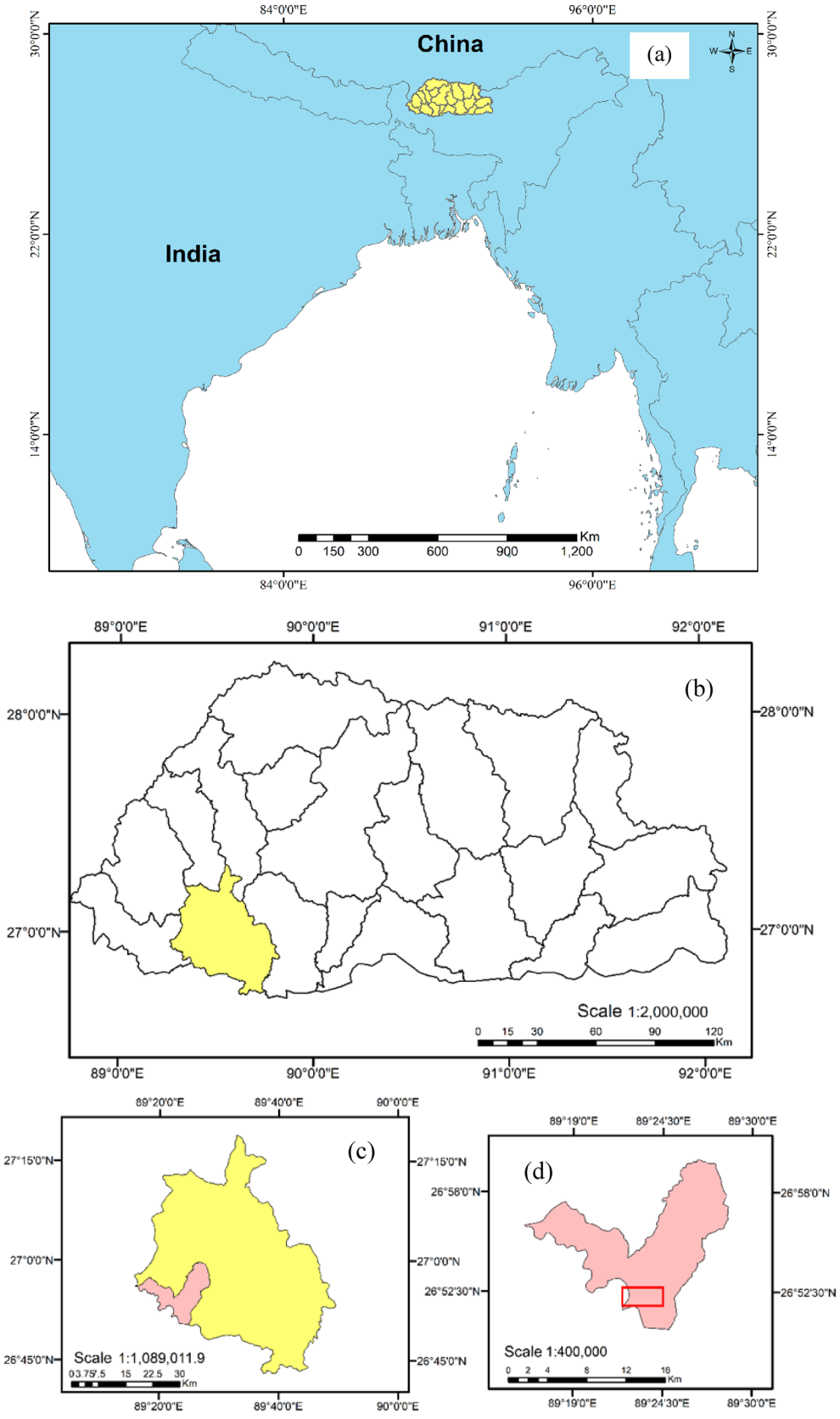

Fig. 1 Map showing **a** Bhutan on South East Asia Map, **b** Bhutan, **c** Chukha Dzongkhag, **d** Phuentsholing marking with study locations

Table 1 Study area with coordinates and elevation

Site No.	Site name	Site coordinates	Elevation (m)
1	Kabreytar 1	N 26° 52′ 07.9″, E 89° 23′ 34.60″	375–392
2	Kabreytar 2	N 26° 52′ 03.60″, E 89° 23′ 35.40″	306–316
3	Pipaldhara 1	N 26° 52′ 38.30″, E 89° 22′ 55.40″	234–236
4	Pipaldhara 2	N 26° 52′ 15.70″, E 89° 23′ 10.10″	360–362
5	Phuentsholing town	N 26° 52′ 0.50″, E 89° 22′ 40.10″	210

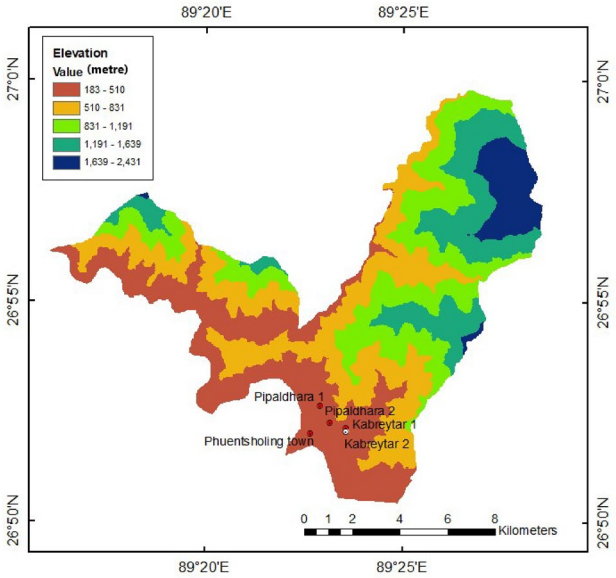

Fig. 2 Elevation map of study region

SeisImager/2D. The waveform are displayed as a graph between time and distance. The first arrival time of P-wave was picked to generate the time–distance curve. The time–distance curve provides an initial velocity model (Fig. 4). The initial model is used for inversion; iteratively, the model is reduced with minimum root mean square (RMS) error for the observed and calculated travel times. Finally, the depth velocity model is presented in 2D (Fig. 5).

4.2 Analysis of secondary waves (MASW analysis)

For the analysis of shear waves, all the waveforms generated for a site have to be opened at once using Pick win, SeisImager/SW. Similar to the primary waves, the shot points and geophone interval should be edited for all the files opened. Next, the common midpoint (CMP) cross-relation gathers have to be generated (Fig. 6). CMP shows the receiver locations the shot point locations. The yellow dots are the receiver locations, i.e., the position of the geophones and the blue dots are the locations at which the hammer was hit. The next step includes the generation of the dispersion curve using the WaveEq module. The dispersion curve is shown as a graph between phase velocity and the frequency. From the dispersion curve generated, 1D shear wave velocity profile (Fig. 7) was generated. The

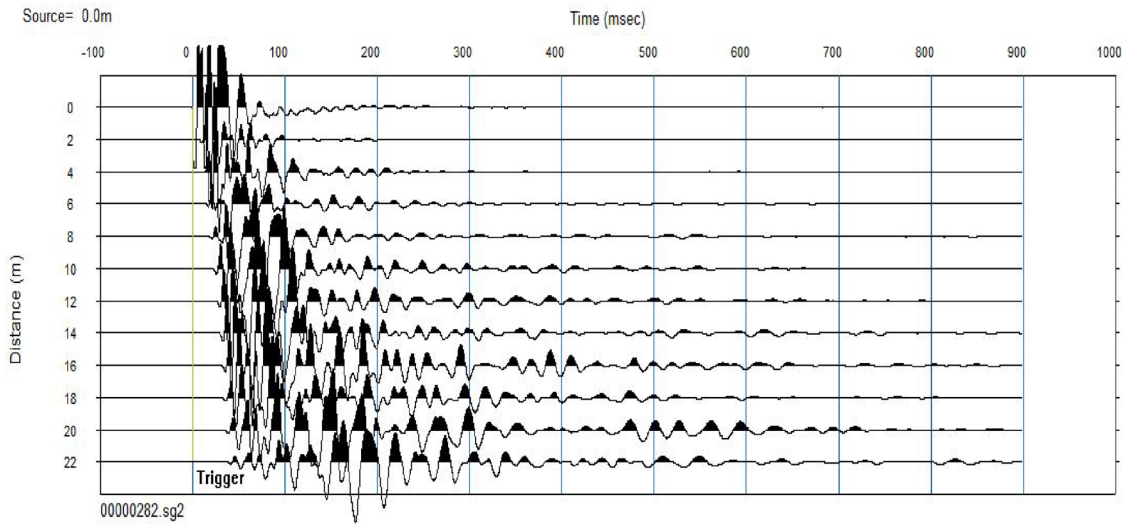

Fig. 3 Sample of raw data collected from Kabreytar 1

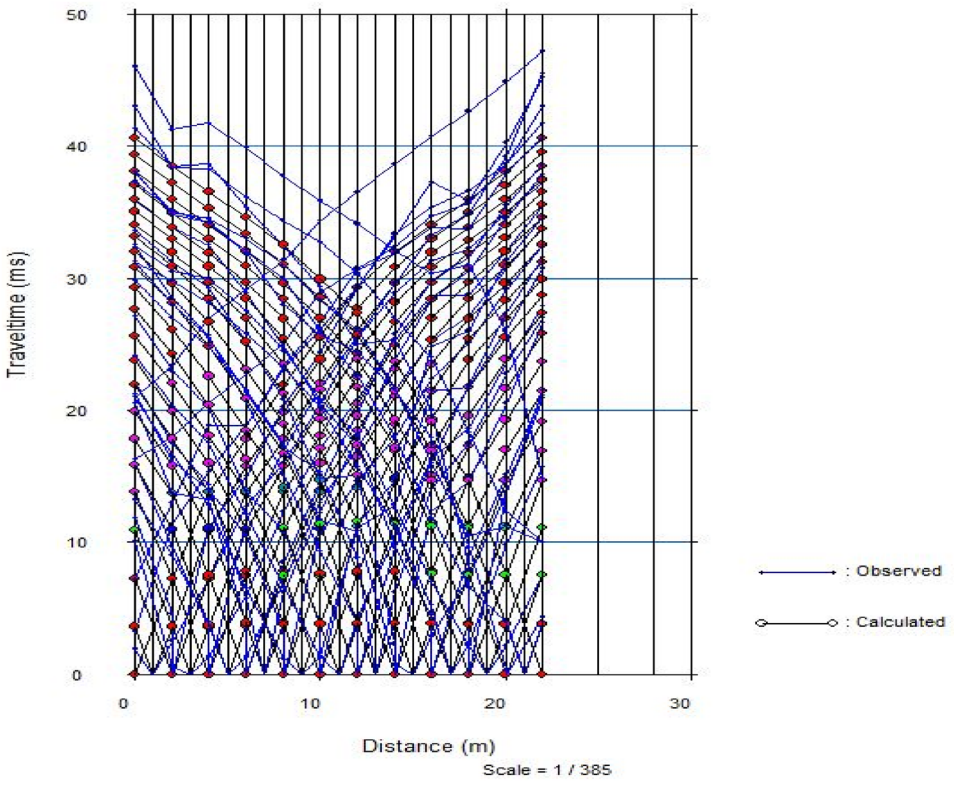

Fig. 4 Travel time graph for Kabreytar 1

1D shear wave velocity profile is shown as a plot between depth and velocity. The final step is to perform inversion analysis to get the 2D shear wave velocity, which is obtained using Geoplot (Fig. 8).

5 Results and discussion

Since no prior soil tests were done in the past and no information on the soil types was available for the sites, the velocity data were interpreted referring to Appendix B; Clause 3.2 of the IS: 1892-1979 [13]. Soil parameters such as density (ρ), Poisson's ratio (σ), Young's modulus (E), Shear modulus (μ), N-value and ultimate bearing capacity (q_{ult}) were calculated using equations as shown in Table 2. From the velocity of primary waves (V_p), the types of soil found in these sites are sand, sandy clay, gravels and shales which are presented in Table 3. Table 4 shows the soil parameters of the study areas. The density value for all the sites ranges from 13.0 to 16.5 kN/m^3 up to the depth of 5 m with minimum at location Pipaldhara 1 and maximum in the location Phuentsholing town and then increases up to 19.3 kN/m^3 at depth of 10 m for location Kabreytar 2. The value of Young's modulus and shear modulus ranges from 240–590 MPa to 85–215 MPa up to the depth of 5 m with the least at Kabreytar 1 and the highest at Phuentsholing town, respectively. The maximum value of Young's modulus and shear modulus is 733.3 MPa and 260.78 MPa at a depth of 10 m observed in Phuentsholing town location. From the same table, it is seen that the density, Young's modulus, shear modulus, N-value increase with depth which indicates that the soil becomes stiffer as the depth of soil layer increases. The stiffer soil is always hold good for construction since bearing capacity of soil increases with stiffness. The bearing capacity estimate indicates that the safe depth for the foundation has to be more than two meters. At the Kabreytar site 2, the results show existence of water in the soil at a depth of 10 m. This site needs careful treatment to avoid soil liquefaction. As proposed by NEHRP [3], the site classification should be established as per mean shear wave velocity for topmost 30 m ($V_{S,30}$) using Eq. (1).

$$V_{S,30} = \frac{30}{\sum_{i=1,N} \frac{h_i}{V_{s,i}}} \text{ (m/s)} \quad (1)$$

Here, h_i, $V_{s,i}$ are the thickness and shear wave velocity of the ith layer of N soil layer in total of existing top 30 m, respectively. In the present study, for all the five sites considered, the average shear wave velocity for top 30 m ($V_{S,30}$) lies between 180 and 360 m/s. Hence, based on

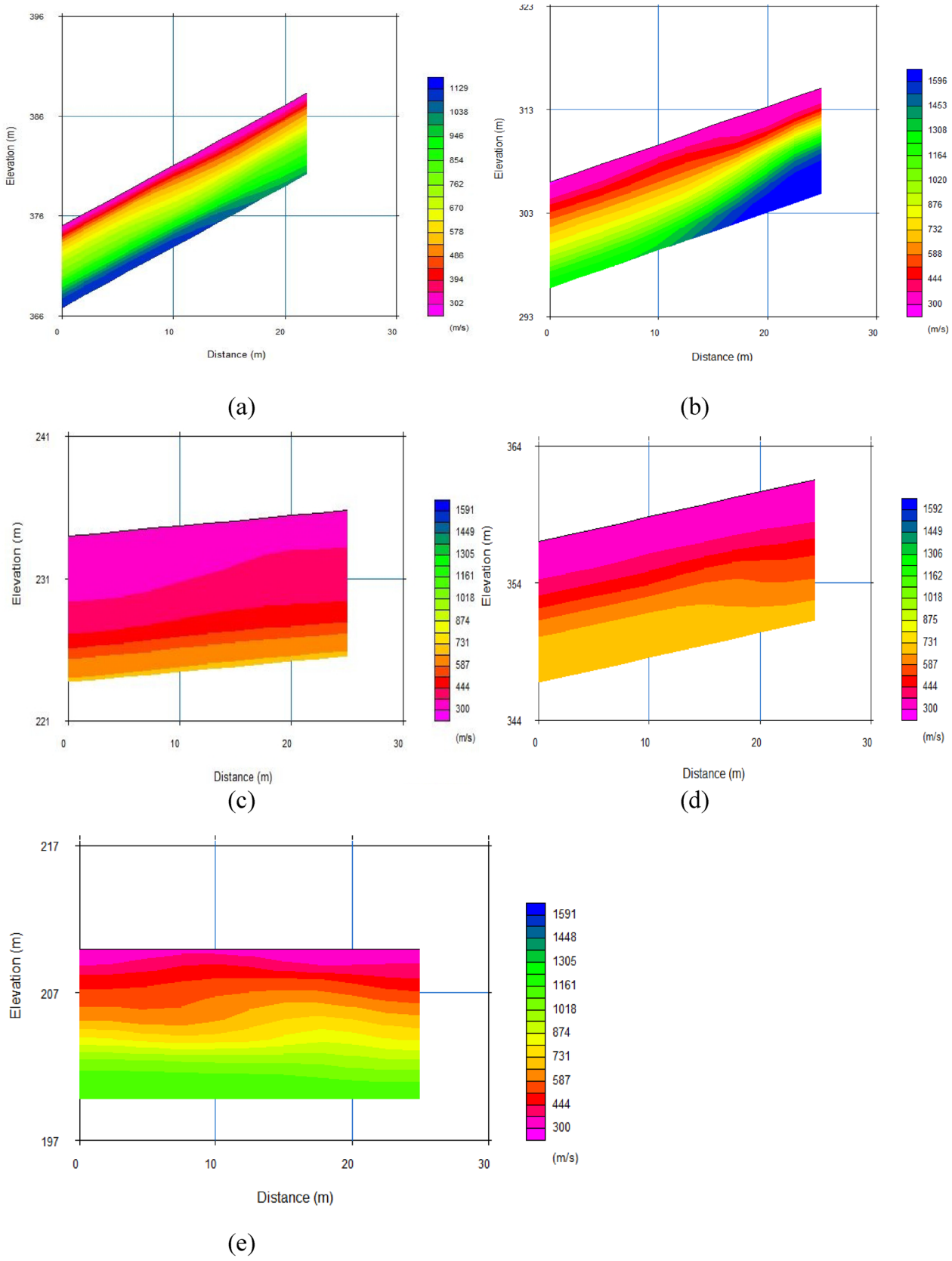

Fig. 5 Two-dimensional depth and P-wave velocity profile of **a** Kabreytar 1, **b** Kabreytar 2, **c** Pipaldhara 1, **d** Pipaldhara 2, **e** Phuentsholing town

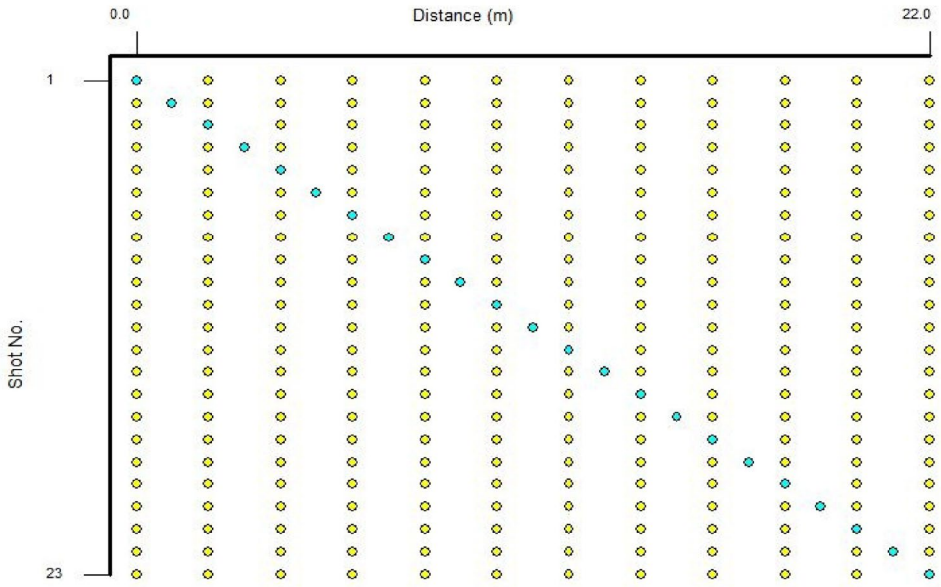

Fig. 6 CMP cross-relation gathers from Kabreytar 1

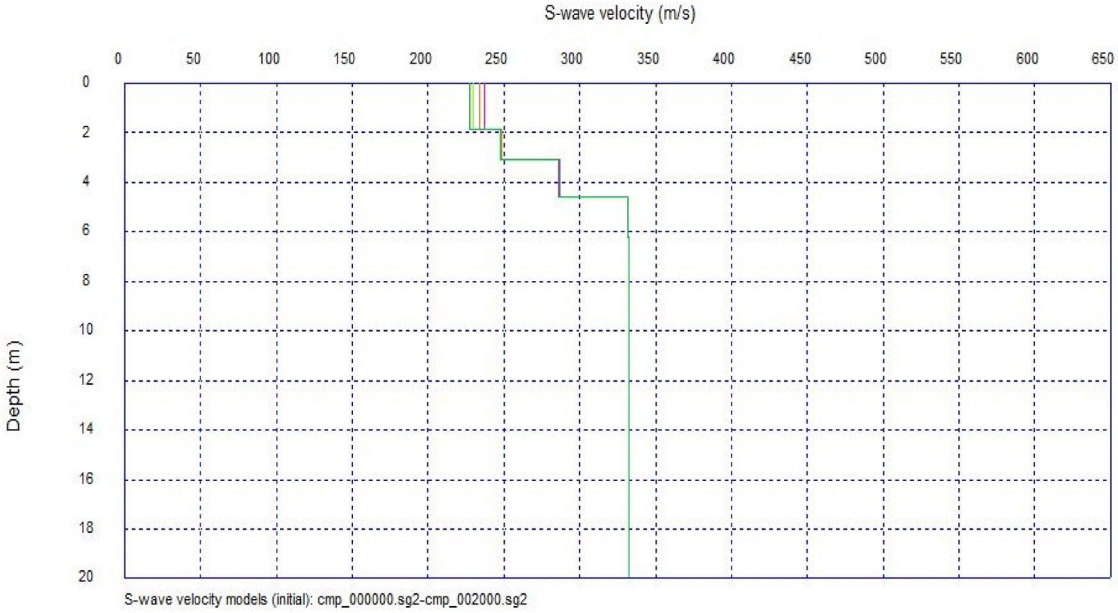

Fig. 7 One-dimensional shear wave velocity profile from Kabreytar 1

NEHRP site classification [3], all the sites can be grouped as Site Class D.

6 Ground response analysis

The results of the geophysical method indicate that all the five sites belong to site class 'D' ($180 \le V_s \le 360$) as per NEHRP soil classification. In general, sand, silt and stiff clays with SPT value of $15 \le N \le 50$ and shear strength of 50 kPa $\le S \le$ 100 kPa belong to Site Class D. The amplification factors proposed by previous researchers [22, 27] can be directly used to assess the ground surface spectral acceleration if the input motion at bedrock is known. However, equivalent ground response analysis based on the subsurface profile at the site will give a more reliable estimate of site amplification value for the surface level and the variation of acceleration with varying depth. DEEPSOIL v7 [9] was used to perform equivalent ground response analysis using the shear wave velocity profiles and soil properties estimated from the geophysical methods. Figure 9 presents the typical subsurface soil profile

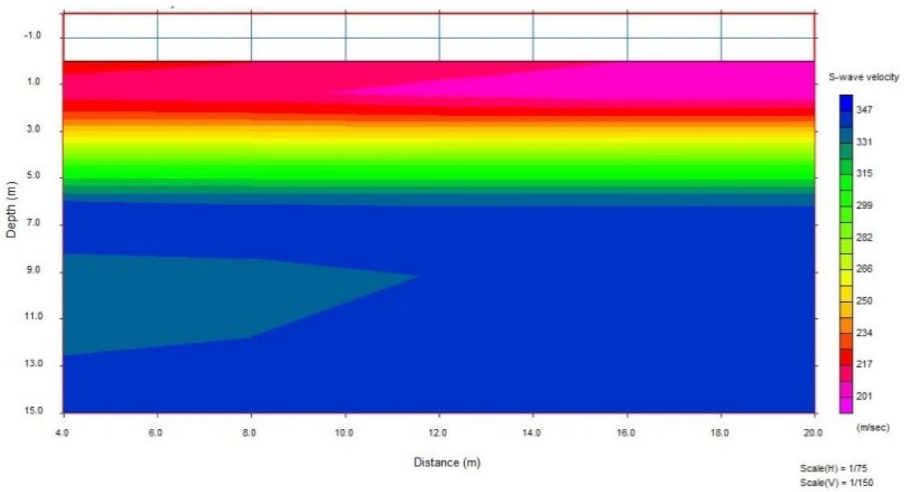

(a)

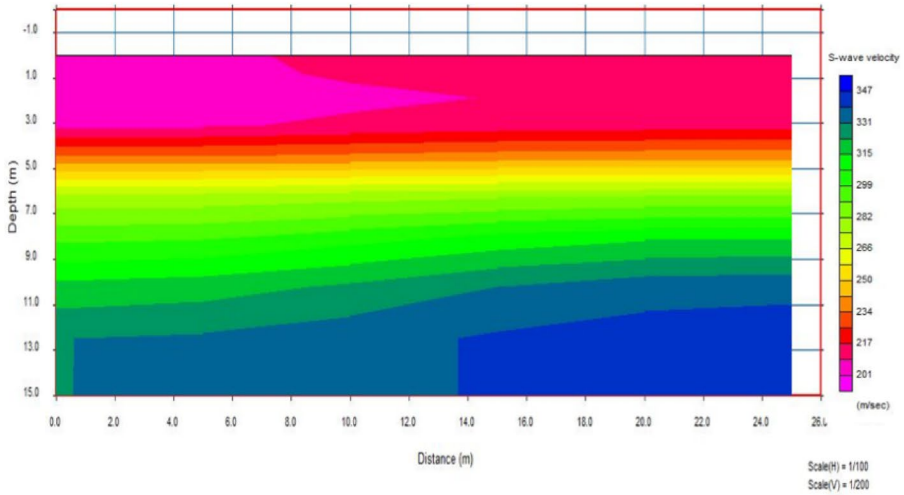

(b)

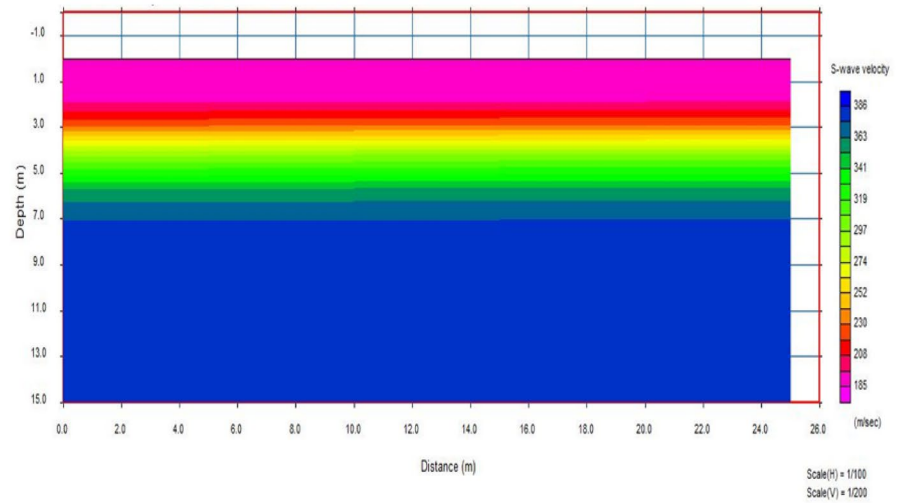

(c)

Fig. 8 Two-dimensional depth and S-wave velocity profiles, **a** Kabreytar 1, **b** Kabreytar 2, **c** Pipaldhara 1, **d** Pipaldhara 2, **e** Phuentsholing town

Fig. 8 (continued)

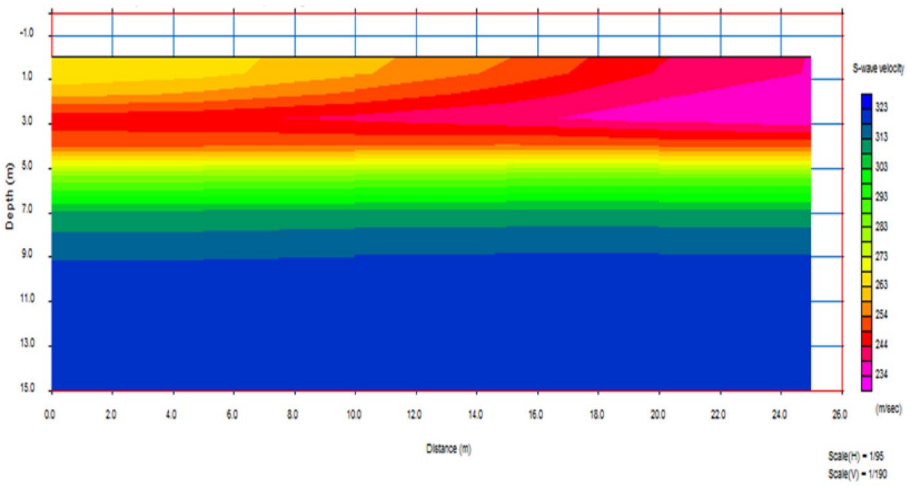

(d)

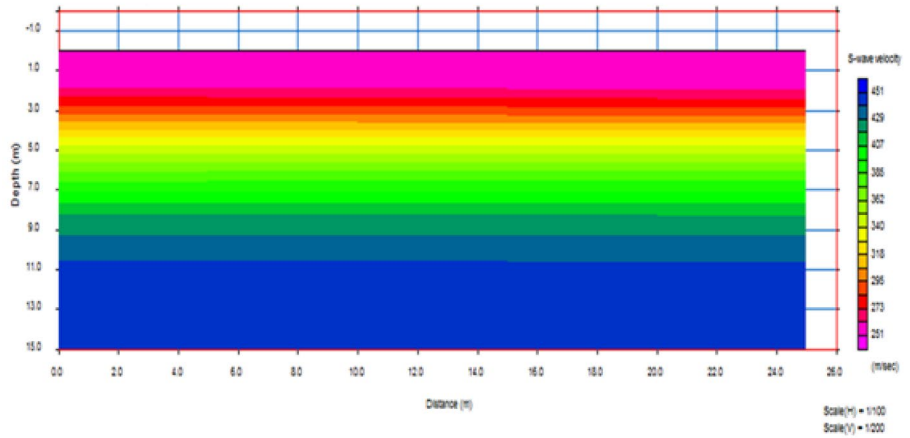

(e)

Table 2 List of equations used to determine soil parameters in the present study

Sl. No.	Soil parameters	Equations used	Reference
1	Density	$\rho = 0.31V_p^{0.25}$	Keceli [15]
2	Poisson's ratio	$\sigma = \frac{1}{2}\left(1 - \frac{1}{\left(V_p^2/V_s^2\right)-1}\right)$	Ahmed Al-Heety and Al-Saigh [1]
3	Young's modulus	$E = \left(\rho V_s^2\right)\left(\frac{3V_p^2-4V_s^2}{V_p^2-V_s^2}\right)$	Keceli [15]
4	Shear modulus	$\mu = \frac{E}{2(1+\sigma)}$	Ahmed Al-Heety and Al-Saigh [1]
5	*N*-value	$N = \left(\frac{V_s}{76.55}\right)^{2.24719}$	Khalil and Hanafy [16]
6	Ultimate bearing capacity	$q_{ult} = \frac{V_s^{2.4}}{1590}$	Imai and Yoshimura [12]

of the site Kabreytar 1. The ground response analysis was carried out for the site considering a scenario earthquake with input motion from the Chi–Chi earthquake. The acceleration time history for the input motion of Chi–Chi earthquake is shown in Fig. 10.

The analysis in DEEPSOIL considers each and every layer of the soil profile, and within a layer, the properties like $V_{s'30}$ were varied for the site. It was seen that the acceleration value gets amplified as the waves travel to the top of the surface. The plot showing the variation of peak

Table 3 Velocity ranges and soil types at the sites

Sl. No.	Site	V_p (m/s)	V_s (m/s)	Soil type (IS 1892:1979)
1	Kabreytar 1	300–1175	214–348	Up to 1 m sand and top soil
				1–5 m sandy clay
				5–8 m gravels
				8–10 m shale
2	Kabreytar 2	300–1596	260–538	Up to 2 m sand and top soil
				2–4.5 m sandy clay
				4.5–6 m gravel with shale
				6–10 m shale and water in loose soil
3	Pipaldhara 1	300–659	185–385	Up to 5 m mixture sand, top soil and sandy clay
				5–10 m sandy clay
4	Pipaldhara 2	300–733	235–323	Up to 2 m sand and top soil
				2–6 m sandy clay
				6–10 m gravels
5	Phuentsholing town	300–1305	251–409	Up to 1 m sand and top soil
				1–4 m sandy clay
				4–5 m gravels
				5–10 m shale

Table 4 Soil parameters of the study areas

Sl. No.	Site	Layer	Depth (m)	Density (kN/m^3)	Poisson's ratio	Young's modulus (kN/m^2)	Shear modulus (kN/m^2)	*N*-value	Ultimate bearing capacity (kN/m^2)
1	Kabreytar 1	1	Up to 1	14.2	0.33	184.64	69.34	11	266.16
		2	1–5	16.0	0.42	244.48	86.29	13	311.60
		3	5–8	17.4	0.44	411.41	156.48	22	570.47
		4	8–10	18.0	0.45	486.47	217.62	30	791.39
2	Kabreytar 2	1	Up to 2	15.3	0.42	204.31	71.88	10	254.75
		2	2–4.5	16.1	0.44	254.83	88.29	12	305.30
		3	4.5–6	18.1	0.47	423.01	144.00	19	477.75
		4	6–10	19.3	0.48	579.72	196.39	25	643.77
3	Pipaldhara 1	1	Up to 6	12.9	0.17	258.72	110.80	18	470.45
		2	6–10	15.5	0.22	567.24	233.03	38	1011.03
4	Pipaldhara 2	1	Up to 2	13.7	0.17	184.20	78.84	13	324.42
		2	2–6	14.6	0.29	277.32	108.47	17	440.76
		3	6–10	15.9	0.37	445.76	163.47	25	649.58
5	Phuentsholing town	1	Up to 1	15.9	0.43	286.55	100.46	14	361.26
		2	1–4	14.8	0.19	355.99	149.34	25	637.42
		3	4–5	16.5	0.38	582.72	211.63	32	847.08
		4	5–10	17.3	0.41	733.29	260.78	38	1026.74

ground acceleration (PGA) with varying depth is shown in Fig. 11a for the site Kabreytar 1. The amplification factor was estimated as 1.36 by taking the ratio of surface PGA to the PGA at the bottom layer. The ground response analysis considering the varying soil profile gives a more accurate and reliable estimate of the amplification factor. The response spectrum showing spectral acceleration corresponding to various natural periods (of the structure) at the site Kabreytar 1 for an input motion from a scenario earthquake of Chi–Chi earthquake is shown in Fig. 11b. Similar analyses were carried out for other sites as well, and the results are presented from Figs. 12, 13, 14 and 15. The surface level PGA values and estimated amplification factors for the considered sites in Bhutan Himalaya for input motion of Chi–Chi earthquake at the bottom layer are presented in Table 5. It was observed that amplification

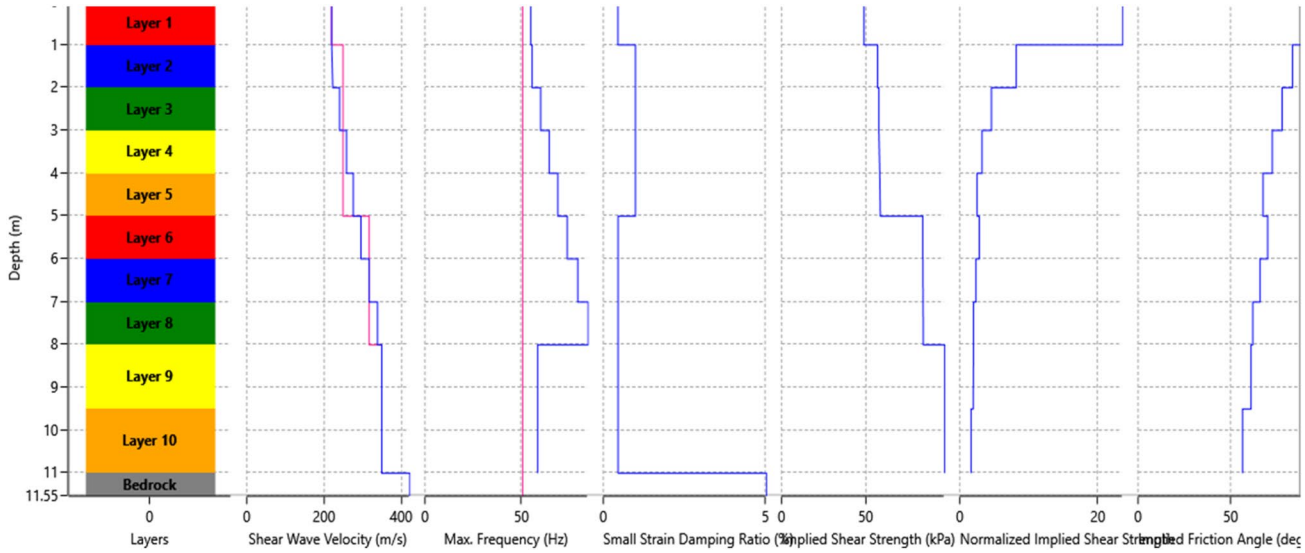

Fig. 9 Soil profile of Kabreytar 1 with respect to depth

factor is high for Kabreytar 1 and negligible for the site Phuentsholing town.

7 Conclusion

This paper presented near-surface seismic refraction tomography and MASW studies for site characterization in Phuentsholing, Bhutan Himalaya. Although various physical methods such as borehole testing, standard penetration test and drilling are available for determining soil parameters, these are not always easy to execute. Seismic refraction tomography (SRT) is an alternative. In this study, five sites were selected in Phuentsholing for the SRT and MASW studies. The major findings and conclusions are summarized below.

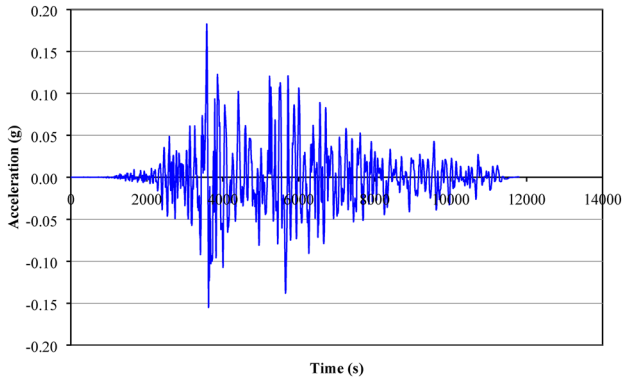

Fig. 10 Acceleration time history for the input motion of Chi–Chi earthquake at bottom layer

1. From the velocity profiles, the soil found was sand, sandy clay and shale. No hard rock strata were found down to the depth of 10 m.
2. The density value for all the sites ranges from 13.0 to 16.5 kN/m^3 up to the depth of 5 m with minimum at location Pipaldhara 1 and maximum in the location Phuentsholing town and then increases up to 19.3 kN/m^3 at depth of 10 m for location Kabreytar 2.
3. Presence of ground water in the soil at depth of 10 m at the site Kabreytar 2 may cause soil liquefaction; the ultimate bearing capacity is comparatively low with compared to other locations at a depth of 10 m.
4. The value of Young's modulus and shear modulus ranges from 240–590 MPa to 85–215 MPa up to the depth of 5 m with the least at Kabreytar 1 and the highest at Phuentsholing town, respectively.
5. The maximum value of Young's modulus and shear modulus is 733.3 MPa and 260.78 MPa at a depth of 10 m observed in Phuentsholing town location.
6. Bearing capacity estimates show feasibility for engineering construction. At the site Kabreytar 1, at the competent layer, the safe depth for construction is at 5 m.
7. At sites Pipaldhara 1 and Phuentsholing town, at second layer and fourth layer, respectively, the ultimate bearing capacity reaching up to 1000 kN/m^2.
8. The SRT requires lesser time for field work and data analysis than any other geophysical experiments.

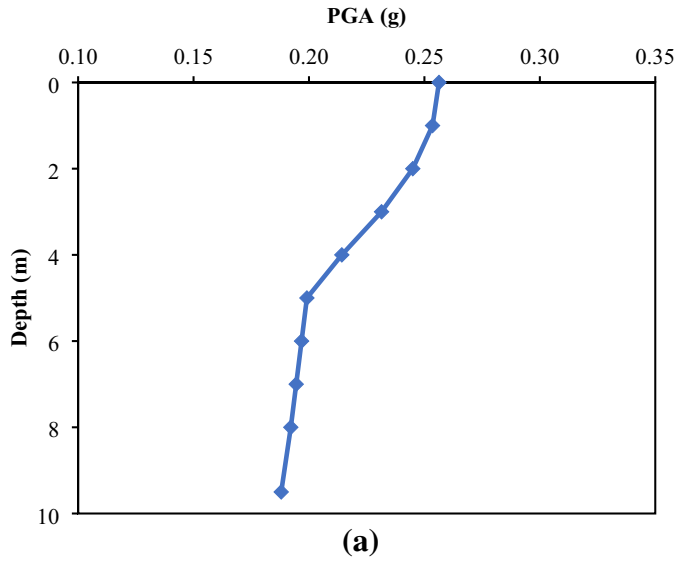

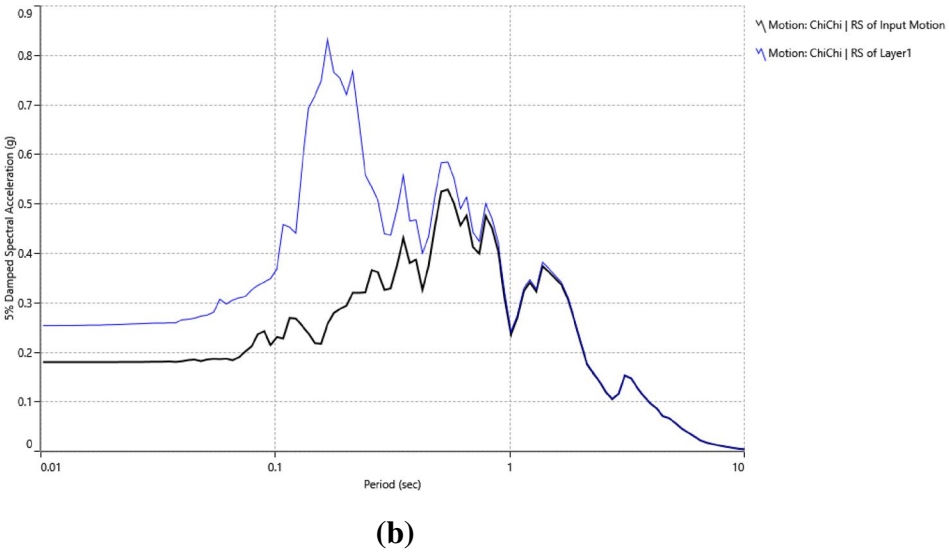

Fig. 11 **a** Variation of PGA value with varying depth for site Kabreytar 1, **b** response spectra at the bottom layer and top layer for Chi–Chi earthquake input motion at site Kabreytar 1

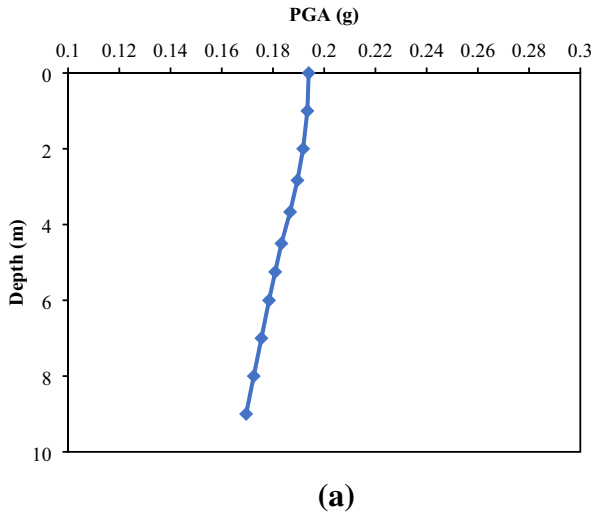

(a)

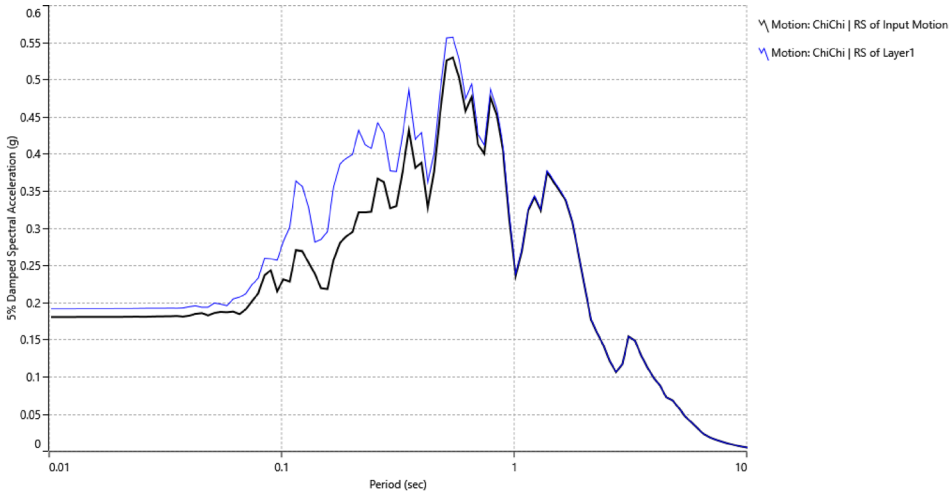

(b)

Fig. 12 **a** Variation of PGA value with varying depth for site Kabreytar 2, **b** response spectra at the bottom layer and top layer for Chi–Chi earthquake input motion at site Kabreytar 2

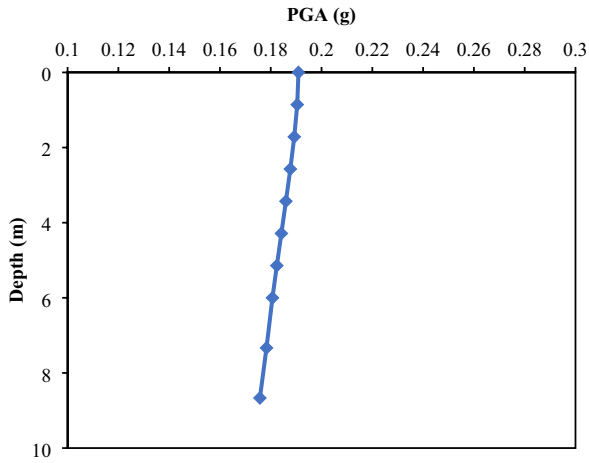

(a)

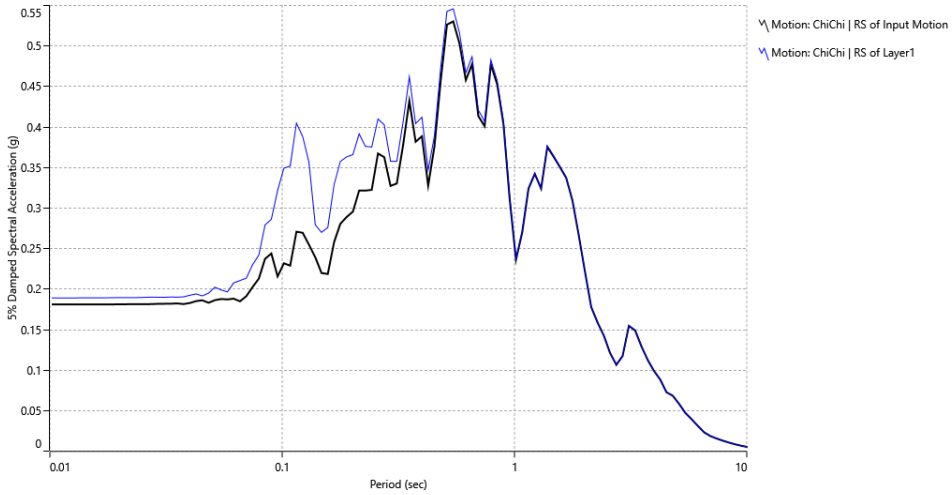

(b)

Fig. 13 **a** Variation of PGA value with varying depth for site Pipaldhara 1, **b** response spectra at the bottom layer and top layer for Chi–Chi earthquake input motion at site Pipaldhara 1

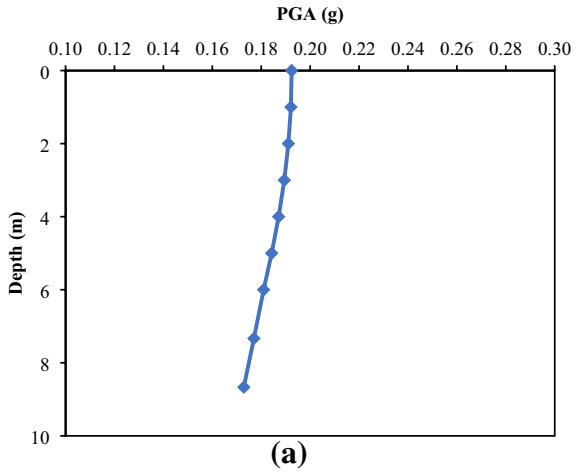

(a)

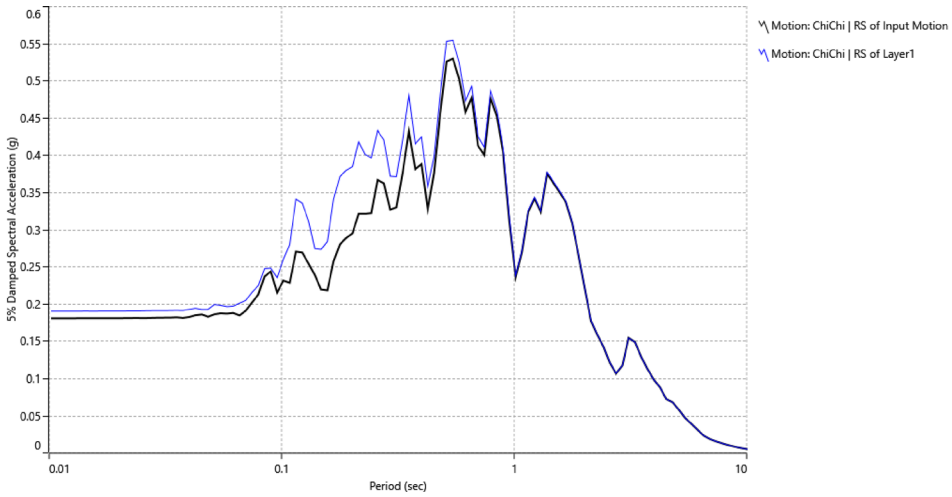

(b)

Fig. 14 **a** Variation of PGA value with varying depth for site Pipaldhara 2, **b** response spectra at the bottom layer and top layer for Chi–Chi earthquake input motion at site Pipaldhara 2

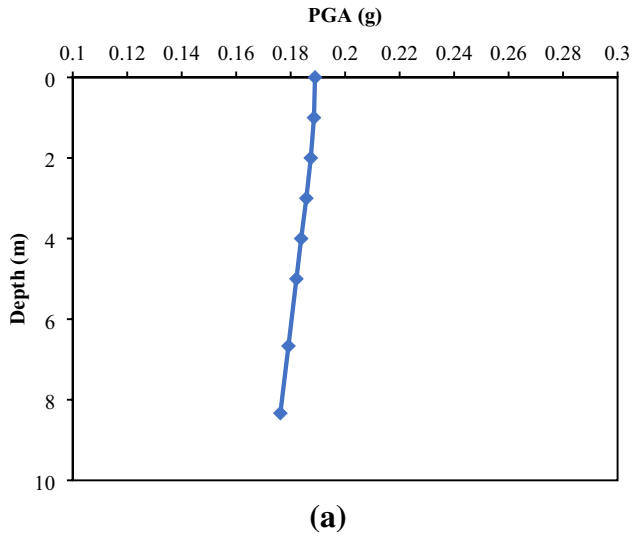

(a)

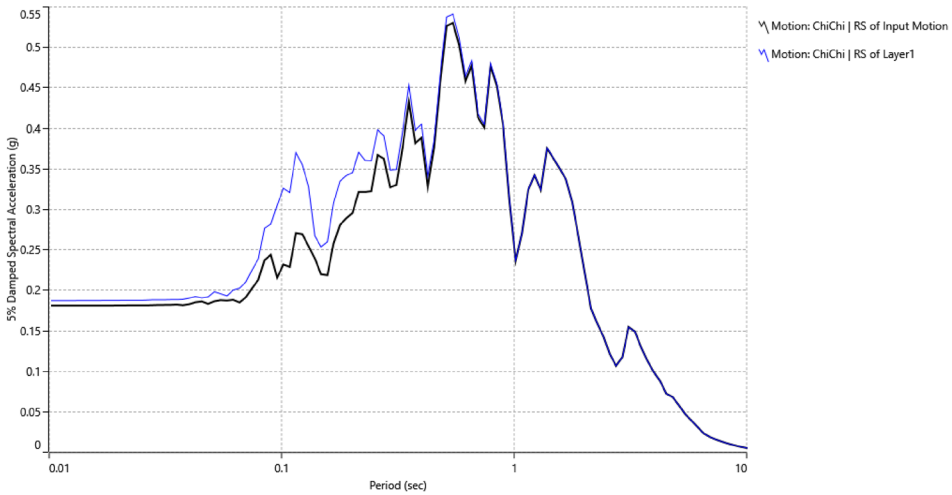

(b)

Fig. 15 **a** Variation of PGA value with varying depth for site Phuentsholing town, **b** response spectra at the bottom layer and top layer for Chi–Chi earthquake input motion at site Phuentsholing town

Table 5 Surface PGA values and amplification factors for different sites in Bhutan Himalaya considering Chi–Chi earthquake input motion

Site	Surface PGA (g)	Amplification factor
Kabreytar 1	0.256	1.36
Kabreytar 2	0.194	1.14
Pipaldhara 1	0.191	1.08
Pipaldhara 2	0.192	1.11
Phuentsholing town	0.189	1.07

9. Based on the weighted average shear wave velocity for top 30 m, the identified five sites were classified as site class D as per NEHRP site classification
10. Site-specific ground response analyses were performed for all the five sites based on shear wave velocity profiles and soil parameters at different depths. The amplification factors estimated for the sites Kabreytar 1, Kabreytar 2, Pipaldhara 1, Pipaldhara 2 and Phuentsholing town were 1.36, 1.14, 1.08, 1.11 and 1.07, respectively.

Author's contribution RS contributed to the methodology, formal analysis, investigation, visualization, validation and writing of the manuscript; SK contributed to the methodology, formal analysis, DD contributed to project administration, funding support and visualization; KC, SR, STT and KY contributed to the data acquisition and data curation and contributed to the editing of the manuscript.

Funding This research is supported by Department of Geology and Mines, Ministry of Economic Affairs, Royal Govt. of Bhutan, by providing the instruments and College of Science and Technology, Royal University of Bhutan, by providing the local logistics.

Compliance with ethical standards

Conflict of interest The authors declare that they have no known competing financial interests or personal relationships that could have appeared to influence the work reported in this paper.

Open Access This article is licensed under a Creative Commons Attribution 4.0 International License, which permits use, sharing, adaptation, distribution and reproduction in any medium or format, as long as you give appropriate credit to the original author(s) and the source, provide a link to the Creative Commons licence, and indicate if changes were made. The images or other third party material in this article are included in the article's Creative Commons licence, unless indicated otherwise in a credit line to the material. If material is not included in the article's Creative Commons licence and your intended use is not permitted by statutory regulation or exceeds the permitted use, you will need to obtain permission directly from the copyright holder. To view a copy of this licence, visit http://creativecommons.org/licenses/by/4.0/.

References

1. Ahmed Al-Heety A, Al-Saigh N (2014) Seismic refraction tomography and MASW Survey for Geotechnical Evaluation of soil for the Teaching Hospital Project at Mosul University. J Zankoy Sulaimani Part A (JZS-A) 18(1):77–86
2. Azwin I, Saad R, Nordianac M (2013) Applying the seismic refraction tomography for site characterization. APCBEE Procedia 5:227–231. https://doi.org/10.1016/j.apcbee.2013.05.039
3. Building Seismic Safety Council (BSSC) (1997) NEHRP recommended provisions for seismic regulations for new buildings, part 1—provisions, 1997th edn. Building Seismic Safety Council, Washington, DC
4. Buddensick ML, Sheng J, Crosby T (2007) Colluvial wedge imaging using traveltime and waveform tomography along the Wasatch fault near Mapleton. Geophys J Int 172:686–697. https://doi.org/10.1111/j.1365-246X.2007.03667.x
5. Cardarelli E, Cercato M, Cerreto A, Filippo GD (2009) Electrical resistivity and seismic refraction tomography to detect buried cavities. Geophys Prospect 58:1–11. https://doi.org/10.1111/j.1365-2478.2009.00854.x
6. Chiemeke CC, Osazuwa IB (2014) Assessment of the response of seismic refraction tomography and resistivity imaging to the same geologic environment: a case study of Zaria basement complex in North Central Nigeria. Int Sch Sci Res Innov 8(10):719–722
7. Fkirin MA, Badawy S, El Deery MF (2016) Seismic refraction method to study subsoil structure. J Geol Geophys 5(5):1–6
8. Gariano SL, Sarkar R, Dikshit A, Dorji K, Brunetti MT, Peruccacci S, Melillo M (2019) Automatic calculation of rainfall thresholds for landslide occurrence in Chukha Dzongkhag, Bhutan. Bull Eng Geol Environ 78:4325–4332
9. Hashash YMA, Musgrove MI, Harmon JA, Groholski DR, Phillips CA, Park D (2016) DEEPSOIL 6.1, user manual. Board of Trustees of University of Illinois at Urbana-Champaign, Urbana
10. Hayashi K, Takahashi T (2001) High resolution seismic refraction method using surface and borehole data for site characterization of rocks. Int J Rock Mech Min Sci 38:807–813
11. Hiltunen DR, Cramer BJ (2008) Application of seismic refraction tomography in karst terrane. J Geotech Geo-Environ Eng 134:938–948. https://doi.org/10.1061/(ASCE)1090-0241(2008)134:7(938)
12. Imai T, Yoshimura M (1976) The relation of mechanical properties of soils to P and S-wave velocities for soil ground in Japan. Urana Research Institute, OYO Corporation, Tokyo
13. IS Code 1892 (1979) Code of practice for subsurface investigation for foundations. Bureau of Indian Standards, Geneva
14. Kanli AI (2009) Initial velocity model construction of seismic tomography in near-surface applications. J Appl Geophys 67:52–62. https://doi.org/10.1016/j.jappgeo.2008.09.005
15. Keceli A (2012) Soil parameters which can be determined with seismic velocities. Jeofizik 16:17–29. https://doi.org/11.a02/jeofizik-1011-31
16. Khalil MH, Hanafy SM (2016) Geotechnical parameters from seismic measurements: two field examples from Egypt and Saudi Arabia. J Environ Eng Geophys 21:13–28. https://doi.org/10.2113/JEEG21.1.13
17. Leucci G, Greco F, Giorgi LD, Mauceri R (2006) Three-dimensional image of seismic refraction tomography and electrical resistivity tomography survey in the Castle of Occhiola. J Archaeol Sci 34:233–242. https://doi.org/10.1016/j.jas.2006.04.010
18. Maraio S, Bruno P, Testa G, Tedesco P, Izzo G (2014) Application of seismic refraction tomography to detect anthropogenic buried cavities in Province of Naples. GNGTS, Trieste, pp 90–94
19. Martínez-Pagán P, Navarro M, Pérez-Cuevas J, Alcalá FJ, García-Jerez A, Vidal Fr (2018) Shear-wave velocity structure from MASW and SPAC methods: the case of Adra town, SE Spain. Near Surf Geophys 16:356–371. https://doi.org/10.3997/1873-0604.2018012
20. Molina S, Navarro M, Martínez-Pagan P, Pérez-Cuevas J, Vidal F, Navarro D, Agea-Medina N (2018) Potential damage and losses in a repeat of the 1910 Adra (Southern Spain) earthquake. Nat Hazards 92:1547–1571. https://doi.org/10.1007/s11069-018-3263-6
21. Moustafa SS, Adel Mohamed ME, Abd El-Aal KA (2007) Applicability of near-surface seismic refraction technique to site characterization of South Marsa Matrouh and Sedi Abd El-Rahman. Western Desert, Egypt. J Appl Geophys 6(2):77–85
22. Raghu Kanth S, Iyengar RN (2007) Estimation of seismic spectral acceleration in peninsular India. J Earth Syst Sci 116(3):199–214
23. Rucker ML (2000) Applying the seismic refraction technique to exploration for transportation facilities. AMEC Earth & Environmental, Inc., Calgary, pp 1–18
24. Sarkar R, Dorji K (2019) Determination of the probabilities of landslide events—a case study of Bhutan. Hydrology 6:52
25. Sheehan RJ, Doll EW, Wayne AM (2005) An evaluation of methods and available software for seismic refraction tomography analysis. J Environ Eng Geophys 10:21–34
26. Sitharam TG, James N, Kolathayar S (2018) Comprehensive seismic zonation schemes for regions at different scales. Springer, Berlin
27. Stewart J, Liu A, Choi Y (2003) Amplification factors for spectral acceleration in tectonically active regions. Bull Seismol Soc Am 93(1):332–352
28. Sultan Araffa SA, Atya MA, Mohamed AM, Gabala M, Zaher MA, Soliman MM, Shaaban HM (2014) Subsurface investigation on

Quarter 27 of May 15th city, Cairo, Egypt using electrical resistivity tomography and shallow seismic refraction techniques. J Astron Geophys 3:170–183
29. Thapa et al (2015) Report on technical feasibility study for the four critical landslides within the extended township of Phuentsholing. https://www.ungm.org/UNUser/Documents/DownloadPublicDocument?docId=313634. Last accessed 14 Dec 2020
30. Uhlemann S, Hagedorn S, Dashwood B, Maurer H, Gunn D, Dijkstra D, Chambers J (2016) Landslide characterization using P and S-wave seismic refraction tomography—the importance of elastic moduli. J Appl Geophys 134:64–76

Publisher's Note Springer Nature remains neutral with regard to jurisdictional claims in published maps and institutional affiliations.

Proceedings of the Sixth International Conference on Inventive Computation Technologies [ICICT 2021]
IEEE Xplore Part Number: CFP21F70-ART; ISBN: 978-1-7281-8501-9

Organ Simulation and Healthcare Services: An Application of IoT

Malti Bansal, Tushar Chopra, Souradip Biswas
Department of Electronics and Communication Engineering,
Delhi Technological University (DTU), Delhi-110042, India
maltibansal@gmail.com

***Abstract* - With the constant evolution of wireless sensors and networks, IoT is a new revolution of the Internet, a developing research area, especially in healthcare. It is several open intelligence devices. The IoT-based extensive medical system can develop error-free medical data and alerts in critical medical emergencies. IoT has an immense impact on healthcare, education, society, and everywhere in our day to day life. IoT in medical advancements has many benefits, including cost reduction, drop-in hospital expenses, human resource costs. Many individuals live in remote areas and do not have access to medical services due to a lack of healthcare facilities in their region. IoT has made many progressions in developing various sensors and organ-on-chip platforms with integrated microelectronics in organ simulation and medical sciences. Many sensors, such as wearable ECG systems for health and fitness, sensors for health monitoring, and an antenna for power reception from deep tissues for wearable microwave thermometry, had been developed. There has been immense advancement in the healthcare sector that simulates and confirms results with maximum accuracy. In the recent pandemic, IoT has assumed a critical function in forestalling the spread of the illness utilizing remote and far-off innovation, empowering correspondence between the patients and specialists with no actual contact.**

Keywords— Internet of Things (IoT), Heath Care, Sensors, Heath Monitoring, Organ Simulation, Organ-on Chip

I. INTRODUCTION

The significant test looked at by mankind is wellbeing. Clinical problems, for example, respiratory infections, psychological well-being messes, stroke, diabetes, and a lot more are the main source of death and ailment in India. Constant sicknesses are mostly far and wide in the mediocre pieces of the nation. The coverage of public health and primary healthcare systems is generally low in these regions. Many children suffer from disorders that can be treated, but they had to suffer due to a lack of facilities. In the ongoing pandemic to prevent the spread of the disease, IoT has played a significant role as it helps the doctor monitor patients using remote health monitoring technology.[1] IoT is an assortment of numerous things, for example, RFID labels, clinical gadgets, cell phones. These are totally connected remotely through cloud and systems administration [2],[3]. Medical care is one of the most basic utilizations of IoT. It gives an occasion to a few clinical applications, for example, versatile and far-off wellbeing observing. In this article [4], there is an organ-on-chip method for controlling culture health and monitoring metabolic tumor organoids. With the introduction of present-day processing, researchers and specialists have consistently been captivated by the potential AI strategies in medication and medical services applications. The Internet of Things is a chain of articles with incomparable identifiers that can speak with one another without the help of a PC or the Internet. The correspondence is kept up through the sensors fitted into the frameworks. Numerous innovations like remote advances, microelectromechanical frameworks (MEMS), and the Internet have upheld IoT improvement. IoT applications will be more astute than the applications use as they can speak with one another and help dynamically, giving them knowledge of their own. IoT has supported the advancement of wearable ECG frameworks. There has been an increase in death due to cardiac arrest and often named "the silent killer." This is often because of the high level of stress on the body, especially the heart, during intense competition. So, identifying the people who are at greater risk and invariably monitoring them. In [6] presented the development of a Wearable ECG system for heath and sports monitoring. Logging the sensor data and accessing it remotely and accessing it could help prevent sudden cardiac arrest (SAC).

A. Challenges of IoT in healthcare

1. Processing huge volumes of information proclaimed at a high velocity needs an equivalent framework.
2. Essential, savvy, and Effective mining and assessment of the info occasions require a strong examination stage.
3. As the number of associated gadgets may rise radically, the engineering essential to be versatile applications needs to consolidate skills with different gadgets and frameworks.
4. No uniform measures for information delivered from gadgets may bring about information created and forestall far-reaching reception.
5. Security of the IoT devices.

II. LITERATURE SURVEY

Pinto, Cabral, and Gomes, [7] the authors suggested an expansion of the aged population, and the need to give living assistance to the elderly has increased. This paper intends to develop a wristband that uses the Internet of Things to help develop our healthcare and continuously monitor the patients remotely. The research work presented living assistance-based IoT solutions for older people, helping us monitor and record the patient's necessary data and provide tools to trigger alerts in emergencies. The study proposed a wrist band connecting to the cloud server for monitoring and assisting adults. It is a low power/cost solution with communication done wirelessly.

S. K. Dhar, S. S. Bhunia, and N. Mukherjee [8], the authors proposed the research introduced new solutions that help health care sensors to operate together. It is done by eliminating the interference of sensors and the consequent distortion of healthcare data. For a healthcare monitoring system to perform accurately, preserving each monitoring equipment sensor's sample rate and delay, these

2021 6th International Conference on Inventive Computation Technologies (ICICT) | 978-1-7281-8501-9/21/$31.00 ©2021 IEEE | DOI: 10.1109/ICICT50816.2021.9358677

Authorized licensed use limited to: DELHI TECHNICAL UNIV. Downloaded on March 03,2021 at 06:12:38 UTC from IEEE Xplore. Restrictions apply.

requirements are mandatory. The study implements a method, so the sampling rate is ideal and maintained, and the data collected for healthcare is excellent. Collecting the information per the necessary sampling rate and distributing the grater data by a maximum permitted size of data, the desired sampling can be achieved for multiple sensors maintained concurrently, assuring quality in the transfer of data and usage of practical Network Bandwidth.

Tugba, Kilic, et al., [9] the authors proposed about the respiratory and circulatory systems, time-varying mechanical deformations play a vital role as the lung and heart pump air and blood. To simulate the compression and expansion in the lung, He incurred a lung-on-a-chip platform where, with a vacuum pump, cyclic expansion and relaxation of the flexible membrane can be delivered. The use of smart-watches with integrated sensors and an organ-on-chip device, with the help of these a monitoring-based system with the use of IoT, can be developed. In this way, monitoring parameters become accessible from anywhere and at any time by just wearing the smart-device.

P. Dinesh Kumar et al., [10] the authors suggest the study analyses the practice of using Big Data techniques for data interpretation captured by Health Framework Sensors. These sensors are incorporating with IoT cloud-based solutions. One of the frameworks utilized to analyze the medical data obtained and employ proper alert methods to support Hadoop Framework. A report of the information collected is given to a doctor on a Real-Time basis. Various Techniques to extract crucial data from Body Sensors Network have been examined here. Doctors will be receiving patient information on a real-time basis, which would help improve healthcare standards.

Shuang Liu., [11] the author proposed the research examined the pertinence of IoT for surveillance and monitoring basis, which are practiced in day-to-day life. These include solutions like healthcare, surveillance, and many more. The author has suggested an innovative class-constrained transfer of linear discriminant analysis to inscribe the obstacles observed as the data obtained from multiple viewpoints and different sensors in IoT. The aforementioned method assists in gaining not varying characteristics from the obtained data. The research focuses on cross-view action identification by monitoring systems. It introduces a prototype that solves human action detection from images captured at various angles to obtain various invariant feature metrics. The conclusions experimentally showed that the proposed CTLDA could deliver more reliable results than previous traditional methods.

Piccini et al., [12] the author explained the method that uses Bluetooth to get bio-medical signals wirelessly, essentially Electro-oculography, Electromyography, Electroencephalography, and Electrocardiography. The design consists of two units: the first unit obtains a single-lead ECG signal and the second unit contains the cleaning the signal from the first unit, along with the DSP system. Further study is needed to combine these sensors with hardware and miniaturize it to make them wearable.

Yuanlin Song, Jinjun Jiang, Xun Wang, Dawei Yang, Chunxue Bai., [13] the authors proposed the incidence of SARIs is rising rapidly, which imposes an immense burden on prevention and treatment. There have been various cases of SARIs and cases of individuals carrying the virus and exporting it to other places, which makes prevention more difficult. At present, there are several medical teams available to support. However, it may be possible to significantly improve these medical teams' efforts by employing IoT technology. IoT is an integral part of the next generation of IT. The core of the IoT is a network that extends and expands based on the Internet. The user side can extend, thereby improving information exchange and communication among the "things." mIoT is the science of intelligent identification, location, monitoring, and AI services for SARI patients using RFID, Global Positioning Systems, different sensing devices, information exchange, and communication according to an agreed arrangement.

Nuno Vasco Lopes, Filipe Pintoz, Pedro Furtado, and Jorge Silva., the authors depicts the IoT plan for impaired individuals, which is foreseeing to distinguish the related IoT innovations and global rules for the pile of the suggested plan. Specifically, they discuss enabling IoT innovation and its achievability for individuals with handicaps. Eventually, they considered two use cases that are once in the past being conveyed for this populace.

III. OBJECTIVES OF IOT IN HEALTHCARE AND ORGAN SIMULATION

With the evolution of IoT in healthcare, there has been tremendous growth in this sector. IoT technology has been widely used to interconnect the available medical facilities and offer the latest, efficient treatment. Subsequently, this has led to improved quality of life and helped reduce the burden to a larger extent. Using this concept, many low-cost devices have been developed, and wireless technology has been encouraged. The main objective in this sector is to design a health monitoring system to analyze the patient's health on different health parameters without any difficulty. Before the arrival of IoT, there were many challenges like consulting a doctor the patient used to make visits or telecommunications. With this latest technology, doctors can monitor their patients regularly. IoT has helped patients to get faster treatments, monitoring their health regularly.

A. Objectives of IoT in healthcare

a) To improve the patient's health: This is done by updating the patient's information on a real-time cloud. This can help to prevent medical emergencies like heart attacks, strokes, etc.
b) Data Analysis: A large amount of data, medical records are difficult to store and analyze. IoT devices prove highly beneficial as they collect data, store it, and analyze it in real-time.
c) Simultaneous monitoring: IoT devices can collect all health-related data [14-18], and various parameters of someone's health like height, weight, blood pressure, etc. can be stored. These can be transferred then to

Authorized licensed use limited to: DELHI TECHNICAL UNIV. Downloaded on March 03,2021 at 06:12:38 UTC from IEEE Xplore. Restrictions apply.

physicians, the insurance company that may need them.

d) Advanced care management: IoT helps collect various health parameters like heart rate, pulse, and sleep activity. This leads to an improvement in workflow optimization and helps in monitoring patients from their homes.
e) Organ Automation: -Various tests of body organs like ECG, Liver Functioning Test, or treatments like kidney dialysis can be analyzed using IoT, and these medical reports can be stored in the cloud for future use.

B. *Objectives of IoT in Organ Simulation*

a) Organ-on-Chip helps to study in-depth knowledge of an organ and helps to simulate an organ artificially.
b) Organ-on-chip helps test drugs on human cells, and IoT could help manipulate the data and get the desired results.
c) Organ-on-chip could replace animals for the study of drugs.
d) Organ-on-chip helps us to get accurate results as it is a 3D model of the human cells. IoT could be used to improve the accuracy of these sensors.

IV. METHODOLOGY ADOPTED

This article proposes an automated system for monitoring the patient's temperature, actions, blood pressure, heart rate or perform organ simulations. If someone is suffering from any prolonged disease it can be predicted with various health parameters and additional symptoms obtained by the system.

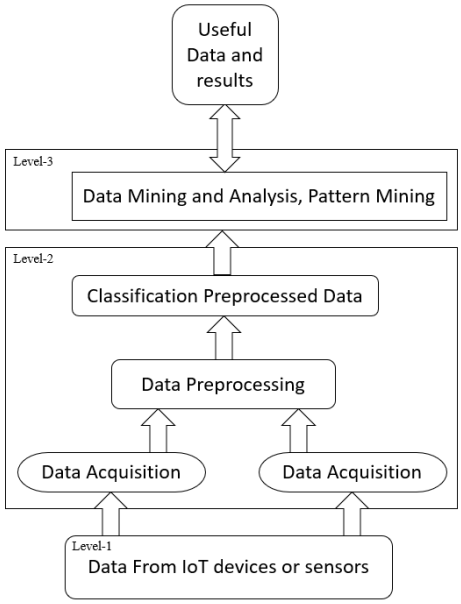

In level-1 raw data collected from IoT healthcare devices/systems are captured and saved onto the cloud. Those frameworks are furnished with sensors like galvanic skin reaction sensor, ECG sensor, EEG sensor, accelerometer, skin temperature sensor, and so on.

In level-2, data is found from the information by arranging, preparing, separating, and portraying it. Expect there exists a lot of unessential and repetitive data existing or boisterous and inconsistent information. This data is the symptoms the patient has an ailment and the patient's real-time healthcare data. It could also be inferred if the victim is suffering from some ailment. This makes the system more effective.

In level-3 or the phase in which analyzes and use the data mining methods or design algorithms to prognosticate the type and nature of the illness for which this method was created. Adopting AI, along with IoT, can improve the practice by executing it more efficiently. The illness or ailments are deduced by using the existing information base and organizing, structuring the medical results into categories like Ideal, Normal, and With Symptoms.

V. IOT HEALTHCARE STATUS AND VISION OF SOME WELLKNOWN TECHNOLOCIAL FIRMS

The health sector is expected to experience a huge transformation in the forthcoming years due to technological advances. Like IoT and artificial intelligence, many concepts would be the major factors in developing this field. Applications like cloud-based medical service for health monitoring, faster internet connectivity, wearable sensors, and embedded sensor solutions will be the major drivers in advancing this field. These factors will lead to a big transformation in the healthcare sector, leading to improved healthcare services and maximum patient outreach with minimum expenses. With IoT, there will be an increase in treatment efficiency, a reduction in health expenses, and improving the standard of health services. With the use of IoT, smart hospitals can be developed where all the patients' medical history, reports can be stored on cloud services and easily managed and accessed when required. All their information and health records can be accessed through an electronic medium, and no longer files and papers will be required to keep the data. Smart beds can be made using this technology, which can sense a patient's presence. The bed can adjust itself to the accurate position to provide proper support without any external intervention. The face to face interaction between doctors and their patients is changing. Many applications have been developed for doctors to monitor, interact with their patients remotely. Moreover, with IoT, a remote health monitoring system can be developed where doctors will monitor their patients on a real-time basis. This would be highly beneficial in saving patients' lives during medical emergencies. Especially in rural areas with less connectivity, doctors can consult their patients through video conferencing and monitor their health through this platform. These advanced technologies have already made inroads into the Western World. It will also be highly effective in organ simulation for organ-on-chip to save the animal resources and use the organ-on-chip platform for testing results getting the required output and proceeding with further research on it. All these data can be collected on a cloud platform and analyzed accordingly. Many companies have started developing medical applications, increasing research, and developing this field using the IoT concept. Microsoft has developed a cloud

Authorized licensed use limited to: DELHI TECHNICAL UNIV. Downloaded on March 03,2021 at 06:12:38 UTC from IEEE Xplore. Restrictions apply.

platform, Microsoft Azure, to promote cloud-based delivery of numerous healthcare assistance. Apple has also turned its consumer products into portable health hubs. The most up to date innovation in multi-compartment organ imitates is a strategy that joins a few organ cells to construct a human or creature on-chip. Analysts have joined different cell types in microfluidic chips to advance toward portrayals of the body, deciding for fundamental intercommunication between different organs that happen normally in vivo as these frameworks don't use microengineering approaches. Analysts have built up the model of microfabricated multi-culture frameworks in which liquid stream is controlled between the various organs. Subsequently, the microfluidic and bioMEMS stages are oftentimes adding to tissue designing severally. Further improvement in advances will build up a human model on-chip.

VI. Conclusion

Early treatment and diagnosis can save a patient's life. The primary goal of using IoT in healthcare is to improve the quality and efficiency of medical services. This paper has emphasized improving medical facilities by using the latest technologies like IoT and AI. Automatic systems that enable constant patient health monitoring and predict any disease the person has contracted were presented. This reduces face to face contact, and the doctors can monitor their patients at home on a real-time basis. IoT can be highly beneficial as it stores large amounts of data on cloud services, accessed easily. In the proposed system, the development of smart hospitals, embedded sensor solutions that are highly effective in cost reduction were deployed. A microfluidic platform contributing to the study of tissue and genetic engineering were also presented. Further studies in this field of tissue engineering can lead to the development of the human model on-chip. Health services can be further improved by applying the concept of AI in this proposed system. By applying both these latest AI and IoT, many patient health parameters' medical history can be explored using data mining.

References

[1] S.H. Almotiri, M. A. Khan, and M. A. Alghamdi. Mobile health (m-health) system in the context of iot. In 2016 IEEE 4th International Conference on Future Internet of Things and Cloud Workshops (FiCloudW), pages 39–42, Aug 2016.

[2] L. Atzori, A. Iera, and G. Morabito, "The internet of things: A survey," *Computer Networks*, vol. 54, no. 15, pp. 2787 – 2805, 2010.

[3] D. Giusto, A. Iera, G. Morabito, and L. Atzori, *The Internet of Things*, 1st ed. Springer New York, 2010.K. Elissa,

[4] J. Dornhof, J. Kieninger, J. Maurer, G. A. Urban and A. Weltin, "Next Generation Organ-on-Chip System for Directional Control of Culture Conditions and Metabolic Monitoring of Tumor Organoids," *2019 20th International Conference on Solid-State Sensors, Actuators and Microsystems & Eurosensors XXXIII (TRANSDUCERS & EUROSENSORS XXXIII)*, Berlin, Germany, 2019, pp. 1106-1108, doi: 10.1109/TRANSDUCERS.2019.8808603.

[5] Giovanni Acampora, Diane J. Cook, Parisa Rashidi and Athanasios V. Vasilakos, "A Survey on Ambient Intelligence in Healthcare", Proceedings of the IEEE , Vol. 101, No. 12, pp 2470- 2494, , December 2013.

[6] E. Valchinov, A. Antoniou, K. Rotas and N. Pallikarakis, "Wearable ECG system for health and sports monitoring," *2014 4th International Conference on Wireless Mobile Communication and Healthcare - Transforming Healthcare Through Innovations in Mobile and Wireless Technologies (MOBIHEALTH)*, Athens, 2014, pp. 63-66, doi: 10.1109/MOBIHEALTH.2014.7015910.

[7] S. Pinto, J. Cabral and T. Gomes, "We-care: An IoT-based health care system for elderly people," *2017 IEEE International Conference on Industrial Technology (ICIT)*, Toronto, ON, 2017, pp. 1378-1383, doi: 10.1109/ICIT.2017.7915565.

[8] S. K. Dhar, S. S. Bhunia and N. Mukherjee, "Interference Aware Scheduling of Sensors in IoT Enabled Health-Care Monitoring System," *2014 Fourth International Conference of Emerging Applications of Information Technology*, Kolkata, 2014, pp. 152-157, doi: 10.1109/EAIT.2014.50.

[9] Kilic, Tugba, Navaee, Fatemeh, Stradolini, Francesca, Renaud, Philippe, AND Carrara, Sandro. "Organs-on-chip monitoring: sensors and other strategies" *Microphysiological Systems* [Online], Volume 2(5 September 2018)

[10] Big data Analytics of IoT based Health Care Monitoring System by P. Dineshkumar, R. SenthilKumar, K. Sujatha, R.S.Ponmagal, V.N.Rajavarman, 2016 IEEE Uttar Pradesh Section International Conference on Electrical, Computer and Electronics Engineering

[11] Class-constrained Transfer LDA for Cross-view Action Recognition in Internet of Things by Shuang Liu, JOURNAL OF LATEX CLASS FILES, VOL. 6, NO. 1, January 2017

[12] L. Piccini et al., "Wireless DSP architecture for biosignals recording", December 2004, Volume 18 Issue 21 pages 487-490.

[13] Yuanlin Song, Jinjun Jiang, Xun Wang, Dawei Yang, Chunxue Bai," Prospect and application of Internet of Things technology for prevention of SARIs"2020 , Y. Song et al. / Clinical eHealth 3 (2020) 1–4.

[14] M. Bansal and Priya, "Application Layer Protocols for Internet of Healthcare Things (IoHT)." *2020 Fourth International Conference on Inventive Systems and Control (ICISC)*, Coimbatore, India, 2020, pp. 369-376, doi: 10.1109/ICISC47916.2020.9171092.

[15] M. Bansal, Priya, "Performance Comparison of MQTT and CoAP Protocols in Different Simulation Environments". G. Ranganathan, J. Chen, A. Rocha (eds) Inventive Communication and Computational Technologies. Lecture Notes in Networks and Systems, vol. 145, pp. 549-560, Springer, Singapore, https://doi.org/10.1007/978-981-15-7345-3_47

[16] M.Bansal, Priya, "Machine Learning Perspective in VLSI Computer Aided Design at Different Abstraction Levels", 2nd Int. Conf. on Mobile Computing and Sustainable Informatics (ICMCSI 2021), Tribhuvan University, Nepal, 2021.

[17] M.Bansal, A. Goyal, A. Choudhary, "Industrial Internet of Things (IIoT): A Vivid Perspective", 5th Int. Conf. on Inventive Systems and Control (ICISC 2021), India, 2021.

[18] M. Bansal, V. Sirpal, M. K. Choudhary, "Advancing e-Government using Internet of Things", ", 2nd Int. Conf. on Mobile Computing and Sustainable Informatics (ICMCSI 2021), Tribhuvan University, Nepal, 2021.

Authorized licensed use limited to: DELHI TECHNICAL UNIV. Downloaded on March 03,2021 at 06:12:38 UTC from IEEE Xplore. Restrictions apply.

Indian Journal of Traditional Knowledge
Vol 20(1), January 2021, pp 26-32

Phytochemicals and antioxidant activity of *Sisymbrium irio* L. seeds

T Hailu[‡], R K Gupta[$] & A Rani*[,†]

Department of Applied Chemistry, Delhi Technological University, Shahbad Daulatpur, Main Bawana Road, Delhi-110 042, India

E-mail: [‡]temesgenhailu88@gmail.com, [‡]rkg67ap@yahoo.com, [†]archnar8@yahoo.co.in

Received 26 November 2019; revised 01 May 2020

Sisymbrium irio (Family: *Cruciferae*) is used in Unani medicine. The qualitative and quantitative analysis showed the presence of different types of bioactive secondary metabolites for like phenols, flavonoids, saponins, terpenoids, except reducing sugar and cardiac glycosides. The antioxidant activity was checked by DPPH and ABTS free radical trapping methods by using standards such as ascorbic acid and trolox. The methanol extract of the Indian variety of the seeds of *Sisymbrium irio* showed a very high antioxidant activity. The major pharmacological bioactive chemical compounds identified in different solvent extracts of *Sisymbrium irio* were characterized as: 2, 4-Di-tert-butylphenol, n-Hexadecanoic acid, 3', 5'-Dimethoxyacetophenone, γ -Tocopherol, Cholesterol, 1-Nonedecene, γ -Sitosterol, Ergot-5-en-ol, (3- Beta, 24R)-3- Methylcrotononitrile, 1, 2 - Cyclopentadi-one, 1, 3 - Cyclohexanedione, 4-Isothiocyanato-1-Butene, Isosorbide, Sinapic acid methyl ester, 1, E-8, Z-10-Pentadecatriene and 7-Tetradecenal, (Z) and GC-MS fatty acid composition of the cold pressed seeds oil of plant showed the presence of major fatty acids such as: Linolenic acid (36.29%), Linoleic acid (17.99%), Oleic acid (12.58%), cis-11-Eicosanoic acid (9.2%), Erucic acid (9.19%) and Palmitic acid (6.66%). The elemental analysis of the seeds showed the presence of magnesium, calcium, strontium, titanium, chromium, manganese, copper, zinc, boron, aluminium, silicon, barium, iron, phosphorus, sodium, potassium and lead.

Keywords: Antioxidant activity, Elemental analysis, GC-MS analysis, Phytochemicals, *Sisymbrium irio* L. seeds

IPC Code: Int. Cl.[21] A61K 36/31, A61K 36/00, A61K 39/00. A01N 43/40, A61K 36/00

The medicinal plants are the foundation of effective sources of bioactive compounds used as phytomedicines & the chemical compounds obtained from these therapeutic plants played vital role in the discovery of novel drugs for the treatment of the various categories of human, and animal diseases[1]. They contain various types of secondary metabolites (phytochemicals) and these phytochemicals perform many physiological activities in humans and animals. The therapeutic plant *Sisymbrium irio* L belongs to the family *Cruciferae* and is called Khubakalan (Urdu), Asalio, Khubkalan; Khakasi, Khakshi (Persian), khubkhala (Hindi), Khubah (Arabic) and London Rocket/Rocket Mustard (Common names) and is found in various parts of the world[2]. In 1980, Vohora *et al*.[3], investigated the seeds of *Sisymbrium irio* L. Indian origin for antipyretic, analgesic and antimicrobial activity. In 1991, Khan *et al*., isolated isorhamnetin, quercetin, β-sitosterol and β-sitosterol-3 β-D-glucoside from aerial parts of the *Sisymbrium irio* L. collected from the campus of Jamia Hamdard, New Delhi, India[4]. The phytochemical and biological studies (LD_{50}, antioxidant activity) of the aerial part of Saudi Arabia species (Najed Region) of *Sisymbrium irio* L. contained flavonoids[5], β-sitosterol, stigmasterol and β-sitosterol glucoside[6]. A research study on the investigation of Baghdad-Iraq (Al-Jadrea) species of *Sisymbrium irio* L. showed the presence of nicotine in the aerial part of the plant[7]. Another study conducted on the aerial part of the *Sisymbrium irio* L. collected from the Irbid area (north of Jordan) showed the oil comprised of four fatty alcohols (2.49%), five aromatic compounds (3.53%), six aliphatic hydrocarbons (6.29%), fifteen terpenes derivative (terpenoids) (8.19%), eleven sulfur and eleven nitrogen containing compounds (36.41%), two esters and seven acids (38.80%) and three additional compounds (1.17%)[8]. Rauf and Ahmed[9] reported fatty acid distribution pattern in triacylglycerol (isolated from oil) of *S. irio*. Another research study conducted by Nengroo and Rauf stated the fatty acid composition of petroleum extract of *Sisymbrium irio* L. seed were: Palmitic acid C16: 0 (22.3%), Stearic acid C18:0 (6.1%), Oleic acid C18:1 (30.7%), Linoleic acid C18:2 (30.3%), Arachidic acid C20:0 (2.1%), Gondoic acid C20:1 (0.6%), Behenic acid C22:0 (0.5%), Erucic acid C22:1 (0.3%), Lignoceric acid C24:0 (0.3%), total unsaturated fatty acids (61.9%) and total saturated fatty acids (31.3%)[10]. The seeds of the Indian variety of *Sisymbrium irio* L. contained isorhamnetin[11] and is used

*Corresponding author

as expectorant, febrifuge, rubefacient and are used asthma, and in the preparation of poulties[12]. In 1998, Guil *et al*.[13], from Spain investigated the leaves of wild edible *Sisymbrium irio* L. (Hedge Mustard) for nutritional purposesbecause of the various amounts of nutrients (protein 3.43%, carbohydrates 1.43%, lipid 2.14%, oxalic acid/Calcium ratio 1.1) and fatty acids ω3 (46.57%) & ω6 (13.02%) together with erucic acid C22:1ω9 (2.52%). Ethanolic solvent extracts of fresh plant of *Sisymbrium irio* L. seeds collected at flowering stage from Peshawar University Campus, Pakistan reported the cytotoxic, phytotoxic and insecticidal activities[14]. Other Studies conducted on Indian variety of ethanolic extract of *Sisymbrium irio* L., seeds on *in vitro* rat mast cells has a significant broncho protective role in mast cell degranulation induced by the compound 48/80 and active anaphylaxis[15]. In 2017, Gamal *et al*., from Egypt reported the n-hexane extract of *Sisymbrium irio* L. leaves collected from Bahariya Oasis, inhibited the growth of microbial strains such as *Staphylococcus epidermidis* and *Klebsiella pneumoniae*, whereas the n-hexane extract of *Sisymbrium irio* L. seed demonstrated greater inhibitory effect against *Staphylococcus epidermidis* and *Pseudomonas aeruginosa*. The ethyl acetate fraction of the leaves of *Sisymbrium irio* L. was active against the gram-negative bacteria such as *Pseudomonas aeruginosa, Escherichia coli*, *Klebsiella pneumoniae* and the aqueous extract of *Sisymbrium irio* L was active to against all tested pathogenic microbial such as *Klebsiella pneumoniae*, *Staphylococcus aureus*, *Escherichia coli*, *Pseudomonas aeruginosa*, *Enterococcus faecium*, *Acinetobacter baumanii*, *Enterobacter cloacae* and *Candida albicans* and the purified compound showed dose dependent cytotoxic activity against Vero cell line[16]. The various polarity-based extracts of the seeds and leaves of *Sisymbrium irio* L. collected from Islamabad and Rawalpindi showed inhibition against the bacterial and fungal strains[17]. A study conducted on aerial part of *Sisymbrium irio* L. collected from Al-Jadriya area of Baghdad-Iraq declared the methanol and ethyl acetate extract of the plant owns hepatoprotective activity against CCl_4 induced hepatotoxicity in rats[18]. Research conducted on the acute-toxicity, anti-inflammatory and bronchial smooth muscles investigation of Indian variety of *Sisymbrium irio* L. (seeds) is safe up to the doses of 1000 mg/kg and caused no mortality and normal behaviour on the tested animal[19]. In view of the significance of the plant, the present investigation was conducted to carry out the chemical examination, antioxidant and elemental analysis of seeds of Indian variety of *Sisymbrium irio* L. used in Unani medicine collected from Delhi.

Experimental Methods

Assortment and Documentation of the plant material

Seeds of *Sisymbrium irio* L. were obtained from Khari Baoli, Delhi, Indian Drugs House. Botanical specimens of the plant were identified by Dr. Mokhtar Alam, Central Council for Research in Ayurvedic Sciences, Ministry of Ayush, Government of India, New Delhi and the voucher specimen/file number 6238 was deposited at the Ministry of Ayush, Government of India, New Delhi.

Preparation of extracts

The seed oil of *Sisymbrium irio* L. was extracted by cold press machine, then 100 g of the powdered seeds was extracted sequentially with the solvents of increasing polarity viz; n-Hexane, Chloroform, Ethylacetate and Methanol for 48 h on a rotary shaker. The extracts obtained after extraction were filtered using Whatman filter paper and concentrated on a rotary vacuum evaporator.

Qualitative phytochemical tests

The qualitative phytoconstituents tests of *Sisymbrium irio* L. extracts were done using standard procedures[20-22].

Estimation of the total phenolic contents

The phenolic contents were estimated following Folin-Ciocalteu index protocol[23].

Estimation of the total flavonoid contents

The flavonoid contents were calculated according to some modifications of Khalil *et al*.[24].

DPPH free radical trapping activity

DPPH free radical trapping action of the solvent extracts was carried with some modification[25].

ABTS-scavenging analyses

The positive control such as trolox used for the analyses ABTS-antioxidant activity of the extracts[26].

Gas Chromatography-Mass Spectrometry analysis

Sisymbrium irio L. seeds extracts of n-hexane, chloroform, ethyl acetate and methanol were injected in GC-MS (Shimadzu GCMS-QP2010 Plus) for obtaining the results. The samples were introduced in split mode at 300°C. The oven was heated from 40°C (1 min) to 300°C (28 min). The column flow rate was 1.21 mL/min with Helium being the carrier gas. Metal quadrupole mass filter with pre-rod with a range of m/z 1.5–1000 was used in scan mode. Electron Ionization (EI) was used as the ionization mode. The bioactive phytochemicals present in the extracts were identified by means of their retention time and comparison of their mass spectra with the National Institute of Standard and Technology (NIST) library data and literature.

Table 1 — Phytochemical investigation of *Sisymbrium irio* seeds extracts

Phytochemicals	Test	n-Hexane extract	Chloroform extract	Ethyl acetate extract	Methanol extract
Flavonoids	Alkaline test	+	+	+	++
Phenols	Ferric Chloride test	+	+	+	++
Terpenoids	Liebermann-Burchard test	-	+	+	+
Reducing sugar	Benedict's test	-	-	-	-
Saponins	Foam test	-	-	+	-
Cardiac glycosides	Salkowski test	-	-	-	-

+ = the presence of phytochemicals - = the absence of phytochemicals

Preparation of fatty acid methyl esters

In order to make fatty acids present in the seeds oil volatile, derivatization was done prior to GC-MS analysis. Derivatized fatty acid methyl esters were analyzed using a Shimadzu GC-2010.

Inductively Coupled Plasma-Mass Spectrometry (ICP-MS)

The seeds of *Sisymbrium irio* L. were milled, homogenized and digested by microwave. The elemental analysis of the sample was done by ICP-MS (Perkin Elmer Sciex Elan II DRC).

Results and Discussion

Phytochemical investigation of *Sisymbrium irio* L. seeds extracts

The qualitative phytochemical analysis showed the presence of flavonoids and phenols in all extracts, Terpenoids were found in chloroform, ethyl acetate and methanol extracts, except n-hexane extract. Saponins were only identified in the ethyl acetate extract. Reducing sugar and cardiac glycosides were not identified in any of the extracts (Table 1). The phytochemical compounds in the plant parts were recognized to be biologically active compounds and they had been accountable for diverse activity, for example, antimicrobial, antioxidant, antifungal and anticancer[27,28]. The terpenoids show antiviral, antibacterial, antimalarial, anti-inflammatory and anticancer activities[29]. The phenolic compounds are known for anti-microbial activity[30], antiviral, antimutagenic, antioxidant, antiinflammatory, anticarcinogenic activities[31-33].

Quantitative estimation of the total phenolic contents

Phenolic compounds widely distributed in plant parts are beneficial to human health due to their antioxidant activity[34,35]. Quantitative estimation of the total phenolic contents varied from n-hexane extract to methanol extract of *Sisymbrium irio* L. seeds ranging from 7.8 ± 0.278 to 55.3 ± 0.319 µg GAE/mg of dry extract (Fig. 1). Methanol extract contained the highest percentage of total phenolic components, followed by ethyl acetate, chloroform and n-hexane extracts.

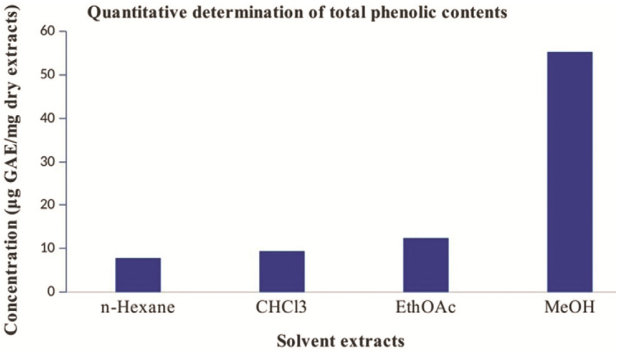

Fig. 1 — Total phenolic contents in different extracts of *Sisymbrium irio* seeds

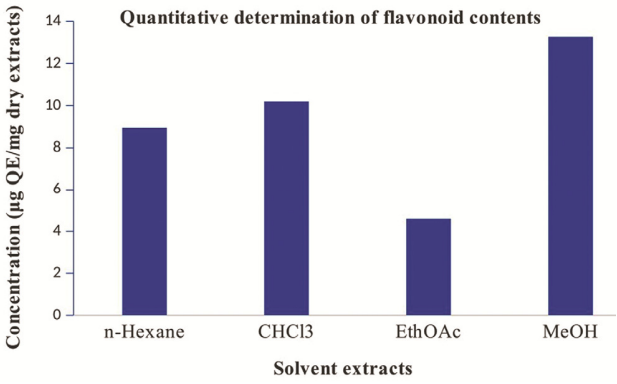

Fig. 2 — Total flavonoid content in the seeds extracts of *Sisymbrium irio*

Quantitative estimation of the total flavonoid contents

Total flavonoids content varied from 8.958 ± 0.420 to 13.266 ± 0.015 µg QE/mg of dry extract (Fig. 2). Methanol extract contained the highest number of flavonoid contents, followed by chloroform and n-hexane and ethyl acetate extracts. Unlike phenolic contents, the ethyl acetate extract contained less amount of flavonoids as compared to other extracts.

DPPH radical scavenging activity

We analysed the antioxidant activity test of extracts via DPPH (Diphenylpicrylhydrazyl) and ABTS (2, 2'-Azino-bis-(3-ethylbenzothiazoline-6-sulfonic acid) test. Diphenylpicrylhydrazyl is a steady free radical

compound & has an absorbance in its oxidized form to 515-520 nm[36,37]. Diphenylpicrylhydrazyl is moderately fast & productive technique to assess free radical. The colour changes, from purple to yellow demonstrates a decline in absorbance of DPPH radical. This is the confirmation of the interaction of the antioxidant found in sample with the free radicals[38]. DPPH free radical scavenging activities of seed extracts of Diphenylpicrylhydrazyl L extended from 22.3% to 79.94%. The methanol extract showed the highest percentage of free radical scavenging activity as shown (Fig. 3) at the concentration of 1 mg/mL.

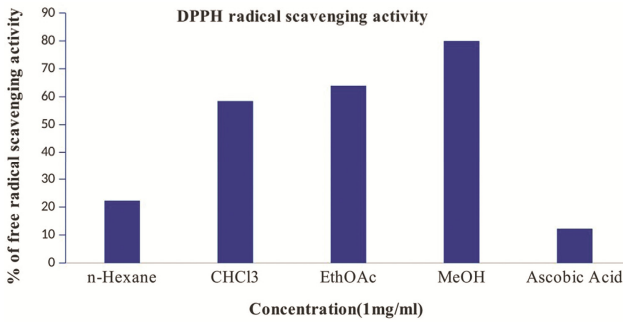

Fig. 3 — % of free radical scavenging assay of seeds extracts of *Sisymbrium irio*

ABTS radical scavenging assay

The solvent extracts of *Sisymbrium irio* L. exhibited ABTS free radical scavenging activities ranging from 43% to 94.3%. Out of all the extracts, methanol extract as shown in (Fig. 4) contain the highest percentage of free radical scavenging activity.

Gas Chromatography-Mass Spectrometry analysis of *Sisymbrium irio* L. seeds extracts

The main constituents of the seeds extracts of *Sisymbrium irio* L. identified by GC-MS as shown in (Table 2) was found to be 2, 4-Di-tert-butylphenol, 3', 5'-Dimethoxyacetophenone, n-Hexadecanoic acid, 7,10,13-Hexadecatrienal, 9, 12-Octadecadienoic acid

Table 2 — GC-MS analysis of bioactive compounds from seeds extracts of *Sisymbrium irio*

	n-Hexane extract					Chloroform extract	Ethyl acetate extract	Methanol extract
Name of compounds	R. time	Area%	Mol. formula	M.wt	Present/Absent	Present/Absent	Present/Absent	Present/Absent
2,4-Di-tert-butylphenol	24.408	0.60	$C_{14}H_{22}O$	206	+	+	-	-
3',5'-Dimethoxyacetophenone	25.668	0.55	$C_{10}H_{12}O_3$	180	+	+	+	+
n-Hexadecanoic acid	34.563	5.46	$C_{16}H_{32}O_2$	256	+	+	+	-
9,12-Octadecadienoic acid (Z, Z)-	38.060	37.57	$C_{19}H_{34}O_2$	294	+	-	-	-
9,12-Octadecadienoic acid (Z, Z)-	38.090	5.02	$C_{19}H_{26}O_2$	280	+	-	-	-
cis, cis, cis-7,10, 13-Hexadecatrienal	38.158	24.08	$C_{16}H_{26}O$	234	+	-	-	-
γ -Tocopherol	51.491	3.26	$C_{28}H_{48}0_2$	416	+	-	+	-
Cholesterol	52.383	1.91	$C_{27}H_{46}O$	386	+	+	+	-
γ-Sitosterol	54.859	9.11	$C_{29}H_{50}O$	414	+	+	+	+
1-Nonadecene	30.955	-	$C_{19}H_{38}$	266	-	-	-	-
1-Nonadecene	35.001	-	$C_{19}H_{38}$	266	-	+	-	-
(R)-(-)-14-Methyl-8-hexadecyn-1-ol	38.199	-	$C_{17}H_{32}O$	252	-	+	+	-
1-Heptacosanol	38.714	-	$C_{27}H_{56}O$	396	-	+	-	-
9,12,15-Octadecatrienoic acid, ethyl ester, (Z, Z,)	46.689	-	$C_{19}H_{32}O_2$	306	-	-	+	-
Ergost-5-en-3-ol, (3. Beta, 24R)-	53.771	-	$C_{28}H_{48}O$	400	-	+	+	-
O-Ethyl S-2-dimethylaminoethylethylphosphonothiolate	43.630	-	$C_8H_{20}NO_2PS$	225	-	-	+	+
3-Methylcrotononitrile	4.378	-	C_5H_7N	81	-	-	-	+
1,2-Cyclopentanedione	8.183	-	$C_5H_6O_2$	98	-	-	-	+
4-Isothiocyanato-1-Butene	9.683	-	C_5H_7NS	113	-	-	-	+
1,3-Cyclohexanedione, 2-methyl	13.267	-	$C_7H_{10}O_2$	126	-	-	-	+
4H-Pyran-4-one, 2,3-dihydro-3,5-dihydroxy-6-methyl	14.696	-	$C_6H_8O_4$	144	-	-	-	+
Isosorbide	19.042	-	$C_6H_{10}O_4$	146	-	-	-	+
2-Butanone, 4-(2,6,6-trimethyl-1-cyclohexen-1-yl)-	28.044	-	$C_{13}H_{22}O$	194	-	-	-	+
Sinapic acid methyl ester	36.682	-	238	$C_{12}H_{14}O_5$	-	-	-	+
1, E-8, Z-10-Pentadecatriene	37.581	-	$C_{15}H_{26}$	206	-	-	-	+
7-Tetradecenal, (Z)	37.701	-	$C_{14}H_{26}O$	210	-	-	-	+

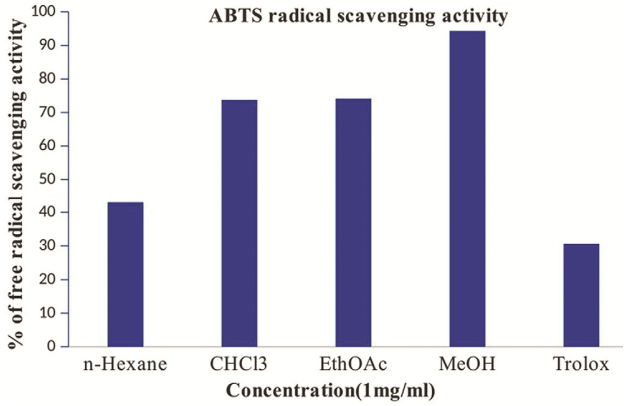

Fig. 4— % of free radical scavenging essay of seeds extracts of *Sisymbruim irio*

(Z,Z)-, γ-Tocopherol, Cholesterol, γ-Sitosterol, 1- Nonadecane, 1-Heptacosanol, 3-Methylcrotonitrile, 1,3-Cyclohexanedione, O-Ethyl S-2-dimethylaminoethylethylphosphonothiolate, 1, 2-Cyclopentadiene, Isosorbide, 4-Isothiocyanato-1-Butene, Sinapic acid ester, E-8, Z-10-Pentadecatriene, 9, 12, 15-Octadecatrienoic acid, ethyl ester, (Z, Z, Z), 7-Tetradecenal and (R)-(-)-14-methyl-8-hexadecyn-1-ol. Phytochemical examination of the different extracts namely n-hexane, chloroform, ethyl acetate and methanol identified by GC-MS revealed the presence of different types of phytochemicals and these compounds may be responsible for various pharmacological activities such as hepatoprotective, antioxidant, wound healing, and antimicrobial activities.

GC-MS fatty acid profile of *Sisymbrium irio* L. cold pressed seed oil

The major fatty acid composition of *Sisymbrium irio* L. seed oil as shown in (Table 3) was found to be: Linolenic acid (36.29%), Linoleic acid (17.99%), Oleic acid (12.58%), cis-11-eicosenoic acid (9.2%), Erucic acid (9.19%), Palmitic acid (6.66%), Stearic acid (2.2%), Arachidic acid (1.75%) and cis-11, 14 Eicosenoic acid (0.95%). Linoleic acid (omega 6) is one of the fundamental fatty acids that are not created in the human body and should be given to the body from outside as such *Sisymbrium irio* L. seed oil is a good source of linoleic acid. Likewise, linoleic acid (omega 6) as a metabolic precursor of eicosanoids which forms important lipids like prostaglandins play an important role in inflammation, immunity and blood clotting.

Metal analysis of *Sisymbrium irio* L. seeds (ICP-MS)

Elemental analysis of *Sisymbrium irio* L. seeds showed the existence of various types of minerals in different concentration (Table 4). The minerals which

Table 3 — Fatty acid composition of *Sisymbrium irio* seeds oil

Peak No.	Component Name	Area (%)
1	C14 Myristic Acid	0.05
2	C15 Pentadecanoic Acid	0.03
3	C16 Palmitic Acid	6.66
4	C16: 1 Palmitoleic Acid	0.22
5	C17 Heptadecanoic Acid	0.07
6	C18 Stearic Acid	2.2
7	C18:1 Δ9 Oleic Acid	12.58
8	C18:2 Δ9, 12 Linoleic Acid	17.99
9	C18:3 Δ9.12.15Linolenic Acid	36.29
10	C20 Arachidic Acid	1.75
11	C20: 1 Cis-11 Eicosenoic Acid	9.2
12	C20: 2 Cis-11, 14 Eicosenoic Acid	0.95
13	C20:3 Cis-11, 14, 17-Eicosatrienoic Acid	0.87
14	C22 Behenic Acid	0.63
15	C22:1 Erucic Acid	9.19
16	C22:2 Cis-13, 16-Docosadienoic Acid	0.21
17	C24 Lignoceric Acid	0.28
18	C24:1 Nervonic Acid	0.81

Table 4 — Mineral content of *Sisymbrium irio* seeds

S. No.	Analyte	Sample concentration (ppm)
1	Mg	2940.1
2	Ca	5844.7
3	Sr	18.2
4	Ti	7.7
5	Cr	2.6
6	Mn	41.8
7	Co	bdl
8	Cu	5.5
9	Ni	bdl
10	Zn	40.7
11	B	1.9
12	Al	315.4
13	Si	101.6
14	Ba	3.7
15	Fe	672.8
16	Mo	bdl
17	Ag	bdl
18	P	6393.4
19	Na	54.7
20	K	8031.9
21	Pb	2.9
22	Bi	bdl
23	Cd	bdl
24	V	bdl

bdl: below detection limit

were analyzed from *Sisymbrium irio* L. seed is very useful for the health of human beings. The elements for example calcium, phosphorus and magnesium may be helpful in the buildings of our bones; potassium and sodium support in the preservation of normal blood pressure. The metal iron is the centre of haemoglobin and a part of myoglobin. During breakdown of carbohydrates, fats and proteins the

elements copper, zinc and manganese play important roles. During the metabolic processes of bone, the elements such as zinc, manganese and copper serves as cofactors for specific enzymes[39].

Conclusions

Phytochemical analysis of the different extracts of the Indian variety of *Sisymbrium irio* L. seeds revealed the presence of phenols, flavonoids, terpenoids, saponins, and other bioactive metabolite including 2, 4-Di-tert-butylphenol, 3', 5'-Dimethyoxyacetophenone, 9, 12-Octadecadienoic acid (Z,Z)-, n-Hexanoic acid, cis, cis, cis-7, 10, 13-Hexadecatrienal, γ-Tocopherol, Cholesterol, γ-Sitosterol, 1-Heptacosanol, 1,3-Cyclohexanedione, O-ethyl-S-2-dimethylaminoethylethylphosphonothioate, 3-Methylcrotonitrile, 1,2-Cyclopentadiene, 4-Isothiocyanato-1-Butene, Isosorbide, Sinapic acid ester, 7-Tetradecenal, 9, 12, 15-Octadecatrienoic acid, ethyl ester(Z, Z, Z) and (R)-(-)-14-methyl-8-hexadecyn-1-ol. The major fatty acid profile of *Sisymbrium irio* cold pressed seed oil contained, Linolenic acid (36.29%), Linoleic acid (17.99%), Oleic acid (12.58%), cis-11-Eicosenoic acid (9.2%), Erucic acid (9.19%), Palmitic acid (6.66%), Stearic acid(2.2%), Arachidic acid (1.75%) and cis-11, 14-Eicosenoic acid (0.95%). The significant antioxidant activity of *Sisymbrium irio* L seed and its frequent use in Unani medicine prompted us to investigate this seed material of our Indian variety. There is need to validate the claims for its usage by investigating the biological activities of purified compounds and to develop a new drug candidate based on Unani system of medicines.

Acknowledgement

Temesgen Hailu wishes to show gratitude towards the Delhi Technological University, Delhi, India has Delhi, India.

Conflict of Interest

The authors express no conflict of interest

Author Contributions

T Hailu is a PhD student from the Delhi Technological University, Delhi, India has carried out all the experiments related to this manuscript. R K Gupta (co-supervisor) & A Rani (supervisor) have contributed in the manuscript writing and conceptualization of the work done.

References

1 Hailu T, Gupta R K & Rani A, *Sisymbrium irio* L.: A Herb used in Unani system of medicine for broad spectrum pharmaceutical applications, *Indian J Tradit Know,* 18 (1) (2019) 140-143.

2 Khoshoo T, Biosystematics of *Sisymbrium irio* Complex XII: Distributional pattern, Caryologia, *Int J Cytol*, *Cytosyst Cytogenet*, 19 (2) (1966) 143-150, DOI: 10.1080/00087114.1966.10796212.

3 Vohora S, Nagvi S & Kumar H, Antipyretic, analgesic and antimicrobial studies on *Sisymbrium irio* L., *Planta Med*, 38 (1980) 255.

4 Khan MSY, Javed K & Khan M, Chemical constituents of the aerial parts of *Sisymbrium irio* L., *J Indian Chem Soc*, 68 (1991) 532.

5 Al-Jaber N A, Phytochemical and biological studies of *Sisymbrium irio* L., Growing in Saudi Arabia, *J Saudi Chem Soc*, 15 (2011) 345–350.

6 Al-Massarani S M, El Gamal A A, Alam P, Al-Sheddi ES, Al-Oqail MM *et al*, Isolation, biological evaluation and validated HPTLC-quantification of the marker constituent of the edible Saudi plant *Sisymbrium irio* L., *Saudi Pharm J*, 25 (2017) 750–759.

7 Dania F, Ibrahim S & Ashour H, Investigation of the Main Alkaloid of London Rocket (*Sisymbrium irio* L) as a Wild Medicinal Plant Grown in Iraq, *Int J Pharm Sci Rev Res*, 56, (2016) 279-281.

8 Al-Qudah M A & Abu Zarga M H, Chemical composition of essential oils from aerial parts of *Sisymbrium irio* from Jordan, *E-Journal of Chemistry*, 7 (2010) 6 –10.

9 Rauf A & Ahmed S, Distribution of fatty acids in *Sisymbrium irio* seed triacyclglycerols, *J Oil Technol Assoc* India, 34 (2) (2002) 67.

10 10.Nengroo Z R & Rauf A, Fatty acid composition and antioxidant activities of five medicinal plants from Kashmir, *Ind Crops Prod,* 140 (2019) 111596.

11 Rastogi RP, Compendium of Indian Medicinal plants, CDRI and PID, 1, 373 (1960-1969).

12 Ambasta SP, Ramachandran K, Kashyap K, & Chand R, The Useful Plants of India, Publications and Information Directorate, CSIR, New Delhi, (1986).

13 Guil J, Guerrero J, Gimenez M & Tarija M, Nutritional composition of wild edible *Cruciferae* species, *J Food Biochem*, 23 (3) (1998) 283.

14 Sumaira S, Siraj D, Rehmanullah M & Zahir M, Pharmacognostic standardization and pharmacological study of *Sisymbrium irio* L., *Am J Res Commun*, 1 (7) (2013) 241-253.

15 Singh RK, Studies on ethanolic extract of *Sisymbrium irio* L, Seeds on in vitro rat mast cells, *Int J Dev Res*, 6 (7) (2016) 8336-8338.

16 Gamal M, Saad A & Mohammed H, Antimicrobial Activities and Cytotoxicity of *Sisymbrium irio* L., extract against Multi-Drug Resistant Bacteria (MDRB) and *Candida albicans*, *Int J Curr Microbiol App Sci*, 6(4) (2017) 1-13.

17 Shabnam B, Ziaur R, Khalid R & Naveed I, Biological screening of polarity-based extracts of leaves and seeds of *Sisymbrium irio* L., *Pak J Bot*, 47 (2015) 301-305.

18 Alsaffar D F, Ali K H, Alsaffar S F & Dawood A H, Hepatoprotective effects of London Rocket (*Sisymbrium irio* L) Extract against CCl_4 induced Hepatotoxicity in Albino Rats, *Int J Pharm Sci Rev Res*, 46(1) (2017) 8-12.

19 Singh R K, Acute toxicity, anti-inflammatory and bronchial smooth muscles investigation of *Sisymbrium irio* L., seeds in

experimental animal models, *Int J Res Stud Biosci*, 1, (2015) 48-53.
20 Trease G E & Evans W C, Pharmacognosy, 11th edition, BaillièreTindall, London, (1989) 45-50.
21 Harborne JB, Phytochemical Methods, Chapman and Hall Ltd, London, (1973) 49-188.
22 Sofowara A, Medicinal plants and traditional medicine in Africa, Spectrum Books Ltd, Ibadan, Nigeria, (1993) 191-289.
23 Khalil H E & Kamal M S, Phytochemical and biological studies of *Cichorium endivia* L. leaves, *J Pharm Sci Res*, 7 (8) (2015) 509-513.
24 Khalil H E, Aljeshi Y M, Saleh F A & Mohamed T S, Phytochemical Analysis and in Vitro Antioxidant Properties of *Sisymbrium irio* L Growing in Saudi Arabia, *J Chem Pharm Res*, 9 (2) (2017) 210-215.
25 Cuendet M, Hostettmann K & Potterat O, Iridoidglucosides with free radical scavenging properties from Fagraea blumei, *Helvetica Chimica Acta*, 80 (1997) 1144-1152.
26 Adedapo A A, Jimoh F O, Koduru S, Masika P J & Afolayan A J, Assessment of the medicinal potentials of the methanol extracts of the leaves and stems of Buddleja saligna. *BMC Complement Altern Med*, 9(21) (2009) 1-8.
27 Hossain M A & Nagooru M R, Biochemical profiling and total flavonoids and contents of leaves crude extract of endemic medicinal plants Corydyline terminalis L Kunth. *Pharmacogn J*, 3 (24) (2011) 25-29.
28 Suresh S N & Nagarajan N, Preliminary phytochemical and antimicrobial activity analysis of Begonia malabarica Lam., *J Basic Appl Biol*, 3(1&2) (2009) 59-61.
29 Mahato S B & Sen S, Advances in triterpenoid research, *Phytochem*, 44 (1997) 1185-236.
30 Raja R D A, Jeeva S, Prakash J W, Johnson M & Irudayaraj V, Antibacterial activity of selected ethnomedicinal plants from South India, *Asian Pac J Trop Med*, 4 (2011) 375-378.
31 Mungole A J, Await R, Chaturvedi A & Zanwar P, Preliminary Phytochemical screening of *Ipomoea obscura* (L)-A hepatoprotective medicinal plant, *Int J Pharm Tech Res*, CODEN (USA), 2 (4) (2010) 2307-2312.
32 Liu X, Zhao M, Wang J, Yang B & Jiang Y, The antioxidant activity of methanolic extract of *emblica* fruit (Phyllanthus emblica L.) from six regions in China, *J Food Compos Anal*, 21 (3) (2008) 219-228.
33 Alsabri S G, El-Basir H M, Rmeli N B, Mohamed S B, Allafi A A *et al*, Phytochemical screening, antioxidant, antimicrobial and anti-proliferative activities study of *Arbutus pavarii* plant, *J Chem Pharm Res*, 5 (1) (2013) 32-36.
34 Li B B, Smith B & Hossain M M, Extraction of phenolics from citrus peels: I. Solvent extraction method, *Sep Purif Technol*, 48 (2006) 182-188.
35 Govindarajan R, Singh D P & Rawat AKS, High-performance liquid chromatography method for the quantification of phenolics in 'Chyavanprash' a potent Ayurvedic drug, *J Pharm Biomed Anal*, 43 (2007) 527-532.
36 Jadid N, Hartanti S R, Abdulgani N, Wikanta W & Sulthoni F R, Proceeding of the International Seminar on New Paradigm and Innovation of Natural Sciences and its Application, (2015).
37 Bandonienė D, Murkovic M, Pfannhauser W, Venskutonis P & Gruzdienė D, Detection and activity evaluation of radical scavenging compounds by using DPPH free radical and on-line HPLC-DPPH methods, *Eur Food Res Technol*, 214 (2) (2002) 143-147.
38 Kedare S B & Singh R P, Genesis and development of DPPH method for antioxidant assay, *J Food Sci Technol*, 48 (4) (2011) 412-422.
39 Saltman P D & Strause L G, The role of trace minerals in osteoporosis, *J Am Coll Nutr*, 12 (4) (1993) 384-389.

Ageing Research Reviews 68 (2021) 101336

Contents lists available at ScienceDirect

Ageing Research Reviews

journal homepage: www.elsevier.com/locate/arr

Review

Post-translational modifications: Regulators of neurodegenerative proteinopathies

Rohan Gupta [1], Mehar Sahu [1], Devesh Srivastava [1], Swati Tiwari [1], Rashmi K. Ambasta, Pravir Kumar *

Molecular Neuroscience and Functional Genomics Laboratory, Department of Biotechnology, Delhi Technological University (Formerly DCE), Delhi 110042, India

ARTICLE INFO

Keywords:
Post-translational modifications
Neurodegenerative disease
Proteinopathies
Protein aggregation

ABSTRACT

One of the hallmark features in the neurodegenerative disorders (NDDs) is the accumulation of aggregated and/or non-functional protein in the cellular milieu. Post-translational modifications (PTMs) are an essential regulator of non-functional protein aggregation in the pathogenesis of NDDs. Any alteration in the post-translational mechanism and the protein quality control system, for instance, molecular chaperone, ubiquitin-proteasome system, autophagy-lysosomal degradation pathway, enhances the accumulation of misfolded protein, which

Abbreviations: PTMs, Post-translational modifications; NDDs, Neurodegenerative diseases; AD, Alzheimer's disease; PD, Parkinson's disease; ALS, Amyotrophic lateral sclerosis; HD, Huntington's disease; TDP-43, Transactivation response DNA binding protein-43; Aβ, β-amyloid; NFTs, Neurofibrils tangles; SNpc, Substantia nigra pars compacta; polyQ, Polyglutamine; LBs, Lewy bodies; htt, Huntingtin protein; SOD1, Superoxide dismutase 1; UPS, Ubiquitin-proteasome system; CMA, Chaperone mediated autophagy; HSPs, Heat shock proteins; PSEN2, Presenilin-2; IT15, Interesting transcript 15; TARDBP, TAR DNA Binding Protein; NO, Nitric oxide; CK1, Casein kinase 1; GSK-3β, Glycogen synthase kinase 3β; PKA, Protein kinase A; CDK5, Cyclin-dependent kinase 5; DYRK1A, Dual Specificity Tyrosine Phosphorylation Regulated Kinase 1A; REP, Repressor element of PARKIN; MTS, Mitochondrial targeting sequence; TM, Transmembrane; FUS, Fused in sarcoma; NLS, Nuclear localization sequence; RRMs, RNA recognition motif; NES, Nuclear export sequence; ER, Endoplasmic reticulum; UPR, Unfolded protein response; IRE1α, Inositol-requiring enzyme 1 α; PERK, Protein kinase R like endoplasmic reticulum kinase; ATF6α, Activating transcription factor 6 α; DR5, Death receptor 5; elF2α, Eukaryotic initiation factor 2 α; XBP1, X-box binding protein 1; ASK1-JNK, apoptosis signal-regulating kinase 1/ c-Jun N-terminal kinases; TRAF2, TNF receptor-associated factor 2; PAD4, Protein arginase deaminase 4; SP1, Specificity protein 1; SP2, Specificity protein 2; PARP16, poly ADP ribose polymerase 16; Umf1, ubiquitin fold modifier 1; CHOP, C/EBP homologous protein; ERAD, endoplasmic reticulum-associated degradation; APP, Amyloid precursor protein; PSEN1, Presenilin-1; BACE1, Beta-secretase 1; BiP, Binding immunoglobulin protein; PARKIN, E3 ubiquitin-protein ligase parkin; PINK1, PTEN-induced kinase 1; PDI, Protein disulfide isomerase; GADD34, Growth arrest and DNA damage-inducible protein; DJ1, Protein deglycase; ATFS1, Cyclic AMP-dependent transcription factor; PDR1, Pleiotropic drug resistance 1; CSMNs, Corticospinal motor neurons; FOXO1, Forkhead box protein O1; FTLD, frontotemporal lobar degeneration; ASK1, Signal-regulating kinase 1; PI3K, Phosphatidylinositol 3-kinase; PIP2, Phosphatidylinositol 4,5-bisphosphate; PIP3, Phosphatidylinositol (3,4,5)-trisphosphate; PH domain, Pleckstrin homology domain; PDK1, Phosphoinositide dependent kinase 1; mTORC2, Mammalian target of rapamycin complex 2; mTORC1, Mammalian target of rapamycin complex 1; IGF-1, Insulin like growth factor-1; AGEs, Advanced glycation end-product; RAGE, Receptor for advanced glycation end products; MAPK, Mitogen activated protein kinase; ERK ½, Extracellular signal regulated kinase ½; AMPK, Adenosine monophosphate activated protein kinase; CBS, cystathionine-beta-synthase; AMP, Adenosine monophosphate; ADP, Adenosine diphosphate; ATP, Adenosine triphosphate; LKB1, Liver kinase B1; TAK1, Transforming growth factor beta activated kinase 1; CaMKKβ, Calmodulin dependent protein kinase kinase-β; ACC, Acetyl CoA carboxylase; ULK1, Unc-51 like autophagy activating kinase 1; TSC 1/2, Tuberous sclerosis complex ½; SREBP, Sterol regulatory element binding protein; NAD^+, Nicotinamide adenine dinucleotide; PGC-1α, Peroxisome proliferator activated receptor gamma coactivator-1α; BCL-2, B-cell lymphoma 2; APC, Adenomatous polyposis coli; β-TrCP, β-transducin repeats containing proteins; LRP5/6, Low density lipoprotein receptor related protein 5/6; Dsh, Dishevelled; TCF/LEF, T-cell factor/lymphoid enhancer factor; DKK1, Dickkopf related protein 1; AVs, Autophagic vacuoles; PAR, UBE3A: Ubiquitin-protein ligase E3A; TRAF6, Tumor necrosis factor receptor associated factor 6; UBE2D2, Ubiquitin-conjugating enzyme E2 D2; UCH-L1, Ubiquitin carboxy-terminal hydrolase L1; USP14, Ubiquitin carboxyl-terminal hydrolase 14; BCL-xL, B-cell lymphoma-extra-large; LAMP2A, Lysosome-associated membrane protein 2A; LRRK2, Leucine-rich repeat kinase; CNS, Central nervous system; COX2, cyclooxygenase-2; iNOS, Inducible nitric oxide synthase; NF-κβ, Nuclear factor kappa-light-chain-enhancer of activated B cells; IKK, IκB kinase; Cdks, cyclin-dependent kinases; NGF, Nerve growth factor; PPIase, Peptidyl-prolyl cis/trans isomerase; Prx2, Peroxiredoxin-2; 3-NPA, 3-Nitropropionic acid; PLK2, Polo like kinase 2; VDAC1, Voltage-dependent anion-selective channel 1; DLP-1, Dynamin-like protein 1; Drp1, Dynamin-related protein 1; E-2609, Elenbacestat; ACAT, Sterol O-acyltransferase; HDAC, Histone deacetylase; ROS, Reactive oxygen species; NEDD4, Neural precursor cell expressed developmentally down-regulated protein 4; PIA2, Phytochrome-interacting ankyrin-repeat protein 2; SNX33, Sorting Nexin 33; DNMTs, DNA methyltransferases; TET-1, Ten-eleven translocation methylcytosine dioxygenase 1.

* Corresponding author.
E-mail address: pravirkumar@dtu.ac.in (P. Kumar).
[1] These authors contributed equally to this work.

https://doi.org/10.1016/j.arr.2021.101336
Received 28 October 2020; Received in revised form 10 March 2021; Accepted 22 March 2021
Available online 26 March 2021
1568-1637/© 2021 Elsevier B.V. All rights reserved.

Unfolded protein response
Cellular signaling

causes neuronal dysfunction. Post-translational modification plays many roles in protein turnover rate, accumulation of aggregate and can also help in the degradation of disease-causing toxic metabolites. PTMs such as acetylation, glycosylation, phosphorylation, ubiquitination, palmitoylation, SUMOylation, nitration, oxidation, and many others regulate protein homeostasis, which includes protein structure, functions and aggregation propensity. Different studies demonstrated the involvement of PTMs in the regulation of signaling cascades such as PI3K/Akt/GSK3β, MAPK cascade, AMPK pathway, and Wnt signaling pathway in the pathogenesis of NDDs. Further, mounting evidence suggests that targeting different PTMs with small chemical molecules, which acts as an inhibitor or activator, reverse misfolded protein accumulation and thus enhances the neuroprotection. Herein, we briefly discuss the protein aggregation and various domain structures of different proteins involved in the NDDs, indicating critical amino acid residues where PTMs occur. We also describe the implementation and involvement of various PTMs on signaling cascade and cellular processes in NDDs. Lastly, we implement our current understanding of the therapeutic importance of PTMs in neurodegeneration, along with emerging techniques targeting various PTMs.

1. Introduction

Post-translational modifications (PTMs) and protein-quality control systems, for instance, molecular chaperones, ubiquitin-proteasome system, autophagy-lysosomal degradation pathway, are crucial factors, that are responsible for the accumulation of misfolded proteins (Ren et al., 2014). Aberrant PTMs in the cellular milieu modulate dysregulated conformation, enzymatic activity, protein turnover rate, and toxic aggregates generation, which causes different proteinopathies (Stram and Payne, 2016). PTMs are considered as covalent or enzymatic modifications of protein occurring after protein synthesis. PTMs generally occur in the amino acid side chain or at protein's C-terminal or N-terminal, depending on the type of modification. PTMs are classified into different groups, such as the addition of functional groups/chemical groups (acetylation, methylation, formylation, phosphorylation, amidation, and others), the addition of the polypeptide chain (ubiquitination, SUMOylation, neddylation), the addition of complex molecules (palmitoylation, oxidation, glycation, pegylation, carbamylation, and others), and amino acids modifications (racemization, citrullination, Isoaspartate, proteolytic cleavage) (Xu et al., 2018). Different studies demonstrated the implementation of different aberrant PTMs in the pathogenesis of proteinopathies such as cancer, heart disease, neurodegenerative diseases (NDDs), diabetes, and metabolic syndromes (Varland et al., 2015). Common NDDs such as Alzheimer's disease (AD), Parkinson's disease (PD), Huntington's disease (HD) and Spinocerebellar ataxias (SCAs) are best described as progressive and slow neuronal death due to misfolded and pathogenic protein aggregates, whereas, another common NDD, Amyotrophic lateral sclerosis (ALS) also characterizes protein aggregation but is rather very fast progressing disease with median survival times ranging from 20 to 48 months. The neuronal cell death causes improper functioning of the brain cellular machinery, which results in memory impairment, synaptic dysfunction, learning disability, and cognitive defects (Biroccio et al., 2006). These NDDs can be further classified into amyloidosis, tauopathies, synucleinopathies, transactivation response DNA binding protein-43 (TDP-43) proteinopathies, depending upon the pathogenic protein accumulated.

Many studies have been conducted to explain the exact mechanism of protein aggregation and its pathogenicity in NDDs, which concluded that dysregulated PTMs are crucial for neuronal proteinopathies (Cook et al., 2014; Olzscha, 2019; Schaffert and Carter, 2020). For example, in AD and PD, decreased H3 and H4 acetylation causes transcriptional deactivation, which leads to a decrease in neurotrophic factor expression. A decrease in H3 and H4 acetylation also causes an increase in β-amyloid (Aβ) plaques, neurofibrillary tangles (NFTs), and deposition of Lewy bodies (LBs) (Cobos et al., 2019). Apart from acetylation, another modification is methylation. Studies show that hypermethylation through the addition of methyl groups causes transcription deactivation, leading to the accumulation of toxic proteins and, ultimately, neuronal cell death (Lu et al., 2013). Similarly, hyperphosphorylation of tau protein, α-synuclein, and mutant htt (mhtt) caused their misfolding and subsequent aggregation (Geschwind, 2003). Ubiquitination, SUMOylation, and neddylation are crucial for misfolded protein degradation through a polypeptide chain made up of small chemical groups. Aberrant ubiquitination, SUMOylation, and neddylation hamper the lysosomal degradation pathway and ubiquitin-proteasome degradation pathway, which causes the accumulation of toxic proteins (Chen et al., 2012b; Kumar et al., 2020; Princz and Tavernarakis, 2020). Further, studies demonstrated the role of the addition of complex molecules to the protein's side chain in the progression and pathogenesis of NDDs. For instance, glycation causes the formation of β-sheets in Aβ, α-synuclein, superoxide dismutase 1 (SOD1), TDP-43 and prion protein structure, which causes the generation of fibrillar structures and misfolded proteins (Salahuddin et al., 2014). Similarly, palmitoylation and carbamylation disrupt synaptic plasticity and neural differentiation, which causes the accumulation of toxic proteins that lead to memory impairment and cognitive defects (Cho and Park, 2016; Guru Krishna Kumar et al., 2018). Moreover, aberrant S-nitrosylation alters mitochondrial function, synaptogenesis, misfolded protein fragmentation, apoptosis, and autophagy, which leads to accumulation of excessive nitric oxide and ultimately causing neuronal cell death (Nakamura et al., 2013). Similarly, myristoylation is the addition of myristate to the N-terminal of newly synthesized glycine residue followed by caspase cleavage. However, myristoylation has been considered as both neuroprotective as well as neurotoxic. Studies demonstrated that myr-ctPAK2 prevents neuronal apoptosis, whereas, myr-htt provides an additional link between caspases and positive autophagy (Martin and Hayden, 2015). Likewise, succinylation has been involved in AD progression with site-specific succinylation of Aβ peptides and tau tangles, which promotes amyloidosis and tauopathy, respectively (Alleyn et al., 2018).

Further, mounting evidence demonstrated that irregular PTMs hampers ER functioning, which leads to the progression of NDDs. These data suggest that PTMs enzymes have beneficial therapeutic activity in neuronal dysfunction. Although, various drugs have been tested for NDDs but because of low success rate, we highlight the gaps in comprehending their pathogenic mechanism. Till the date, no effective medicine is available that can block the progression of NDDs (Agbas, 2019; Hipp et al., 2014; Soto, 2003). Herein, we summarized the influence of PTMs on peptide domain structure, plausible mechanisms for protein aggregation, implementation of PTMs on signaling cascade, impact on biological pathways, and potential treatments for NDDs that occurred due to aberrant PTMs.

2. Mechanisms of protein aggregation in NDDs

In the cytoplasm, during the translation process, a newly synthesized protein falls off as a chain of amino acids, which forms linear polypeptides that interact with each other to generate an adequately folded native protein structure. This native 3D conformation of a protein symbolizes a biologically active protein (Merlini et al., 2001). However, a protein's failure to fold into its native conformation results in the inception of inactive misfolded proteins that eventually give rise to

abnormal protein clusters (Shamsi et al., 2017). In their non-native state, misfolded proteins expose their inner hydrophobic core to the outer hydrophilic environment, which accumulates and leads to the formation of toxic aggregates (Malik and Wiedau, 2020). It has been established that intracellular and extracellular pathogenic protein aggregates are the main culprit in many NDDs that disrupt neuronal homeostasis (Ross and Poirier, 2005). These pathogenic proteins can also self-replicate and can be transmitted from one cell to another, thus promoting their neuropathogenicity (Agbas, 2019).

In healthy conditions, cells have a highly orchestrated machinery to maintain the protein quality control system, consisting of chaperones, a ubiquitin-proteasome system, and an autophagy-lysosome system. Chaperones are protein superfamilies defined as the first line of defense against protein aggregation, which helps a misfolded protein reach its native conformation, thus preventing aggregation (Ciechanover and Kwon, 2017). Various chaperones such as HSP90, HSP70, HSP60, HSP40, and small HSPs play a crucial role in maintaining protein homeostasis. However, when the chaperone system is overburdened and/or mutated, they cannot perform their normal functions, contributing to its dysfunction and protein aggregation.

Beyond a threshold, when chaperones cannot maintain protein homeostasis, cells are overburdened with non-functional proteins where the ubiquitin-proteasome system (UPS) comes into action for the breakdown of those abnormal proteins. The ubiquitin E3 ligase has

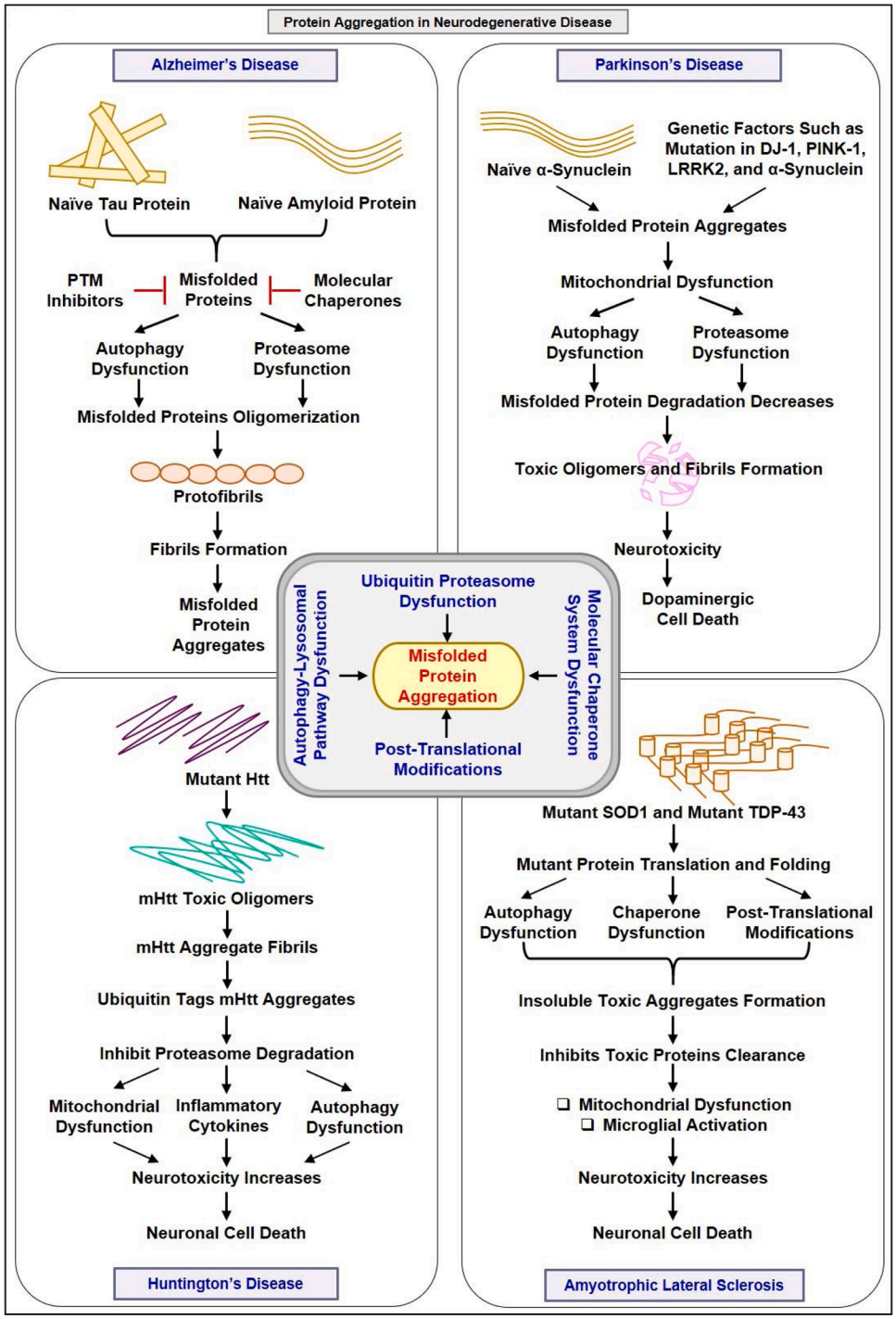

Fig. 1. NDDs are best described by the aggregation of toxic misfolded proteins, which causes neuronal cell death and leads to memory impairment and learning disability. The primary reason behind the accumulation of misfolded protein aggregates is aberrant post-translational modifications (PTMs), ubiquitin-proteasome dysfunction, molecular chaperone system impairment autophagy-lysosomal pathway dysfunction. In Alzheimer's disease (AD), PTM causes a change in the structure and orientation of naïve Tau and amyloid protein and forms misfolded proteins, which causes autophagy dysfunction and proteasome dysfunction. Upon dysfunction in the autophagy pathway and proteasome pathway, oligomerization of misfolded proteins occurs, further converting into protofibrils and fibrils. These protofibrils and fibrils then accumulated in the brain and cause neurotoxicity, which leads to neuronal cell death. Similarly, in Parkinson's disease (PD), PTM of alpha-synuclein causes misfolded protein formation, which leads to mitochondrial dysfunction followed by autophagic and proteasome impairment. This leads to the accumulation of misfolded protein aggregates and causes neurotoxicity. Similarly, in Huntington's disease (mutant htt) and amyotrophic lateral sclerosis (mutant SOD1 and mutant TDP-43), mutant protein translation and folding causes the formation of misfolded protein aggregates followed by protofibrils and fibrils. This will lead to autophagic, chaperone, and proteasome machinery dysfunction and increase neurotoxicity, which causes neuronal cell death.

played a decisive role in the UPS, where the non-functional protein is tagged with another ubiquitin. The process of tagging a protein with multiple ubiquitin moieties serves as a signal for its breakdown by the proteasome (McNaught et al., 2001). In NDDs, ubiquitinated proteins have been observed in many protein aggregates, suggesting a dysfunction in the UPS machinery. For example, an E3 ligase, HRD1, can reduce the Aβ aggregation by ubiquitination of APP protein whereas, knockdown of CHIP, another E3 ligase, showed PolyQ aggregation in ALS (Zheng et al., 2016). Further, the autophagy-lysosome system is used to degrade bulk protein aggregates, which cannot be degraded by the UPS system. In the autophagy system, abnormal protein aggregates are degraded by enzymes present in the lysosome's acidic milieu. Macroautophagy and chaperone-mediated autophagy (CMA) are the two main types of autophagic processes involved in protein degradation. In macroautophagy, aberrant proteins are engulfed by autophagosomes; this double-membraned autophagosome then fuses with the lysosomes to form autolysosomes, where abnormal proteins are deposited and then degraded by the enzymes present in it (Eskelinen and Saftig, 2009; Pan et al., 2008). CMA targets specific abnormal proteins with the KFERQ motif, which are recognized by the HSC70 chaperone, and forms a complex that interacts with lysosome membrane receptors. Abnormal proteins are then deposited in the lysosomes' lumen for degradation (Martini-Stoica et al., 2016) (Fig. 1).

Additionally, mutations in protein-coding genes can also promote abnormal protein aggregation, such as mutations in the presenilin-2 (PSEN2) gene accelerate Aβ aggregation in AD by enhancing the activity of γ-secretase. Similarly, a mutation in the SNCA gene is responsible for causing aggregation of α-synuclein in PD and mutations in the interesting transcript 15 (IT15) gene increases huntingtin aggregation in HD (Nixon, 2013). Further, mutations in the TAR DNA Binding Protein (TARDBP) gene increase TDP-43 protein aggregation in ALS (Prasad et al., 2019). In addition, mutations in protein kinase C gamma (PKCγ) lead to PKCγ aggregates in spinocerebellar ataxia type 14 (SCA14). Moreover, oxidative stress and metal ion stress can also promote protein aggregation (Weids et al., 2016). Ageing is another factor that can cause protein aggregation because, with increasing age; the protein quality control system's efficiency starts decreasing (Monaco and Fraldi, 2020; Sweeney et al., 2017).

However, many PTMs can also cause protein aggregation in NDDs, depending upon the amino acid residues modified by them. For example, phosphorylation of Aβ at S8 residue promotes Aβ aggregation and its toxicity in AD (Rezaei-Ghaleh et al., 2016). Similarly, SUMOylation refers to a covalent attachment of SUMO (small Ubiquitin-like modifiers) to the amino acid residues, and SUMOylation at K75 residue of SOD1 has been reported to stimulate the aggregation of fALS-linked SOD1 mutants in ALS (Banks and Andersen, 2019a). Some important PTMs such as acetylation, nitrosylation, glycation, nitration, palmitoylation, and carbamylation promote toxic aggregation in the NDDs. Acetylation is the covalent coupling of an acetyl group on amino acid residues, and acetylation at K145, K192 within the RRM domain of TDP-43 protein leads to pathogenic aggregation of TDP-43 proteins in ALS (Cohen et al., 2015). Glycation involves the attachment of the sugar molecules to the polypeptide chain of proteins. MGO induced glycation has been reported to promote huntingtin aggregation and toxicity in HD models (Vicente Miranda et al., 2016). Further, nitration involves the addition of the nitro group to the polypeptide chain, and research has shown that nitration at Y39 of α-synuclein facilitates its oligomer formation (Zhang et al., 2019). Palmitoylation is the covalent linkage of palmitate to cysteine residues, and palmitoylation of APP at C186 and C187 promotes Aβ aggregation in AD (Bhattacharyya et al., 2013). Additionally, nitrosylation covalently attaches nitric oxide moiety to cysteine residues, S-Nitrosylation of deubiquitinase enzyme UCHL1 at C90, C152, C220 induces α-synuclein aggregation in PD (Kumar et al., 2017). Carbamylation refers to the covalent adduction of the carbamoyl moiety to amino acid residues, and one study showed that carbamylation stimulates tau aggregation and induces amyloidogenesis (Guru KrishnaKumar et al., 2018). Glutathionylation is a covalent linkage of the glutathione moiety to cysteine groups, S-Glutathionylation of SOD1 at C111 increases the propensity of SOD1 towards aggregation (Wilcox et al., 2009). Moreover, truncation is a PTM that refers to N-terminal or C-terminal termination of a protein chain, and it has been observed that truncation of α-synuclein's C-terminal stimulates aggregation of α-syn in PD (Oueslati et al., 2010). Glycosylation is the covalent adduction of the carbohydrate moiety to proteins. In AD, it has been observed that tau glycosylation amplifies aberrant tau hyperphosphorylation (Liu et al., 2002). Additionally, ADP-ribosylation is the coupling of ADP-ribose to proteins, and in ALS, it has been observed that ADP-ribosylation induces TDP-43 aggregation (McGurk et al., 2019). Further, transglutamination results in isopeptide bond formation between the γ-carboxamide group of glutamines in one protein and ε- amino group of lysine in another protein. In SCA1, transglutamination of ataxin-1 protein promotes aggregation of ataxin-1, resulting in SCA1 neurotoxicity (D'Souza et al., 2006).

3. Domain structure of proteins in NDDs and role of PTMs

PTMs such as acetylation, phosphorylation, glycosylation, amidation, methylation, ubiquitination, and hydroxylation are prominently involved in the progression of NDDs (Table 1). In AD, the first neuropathological hallmark is the formation of senile plaques and Aβ peptide deposits (Martin et al., 2011). APP, a type 1 membrane glycoprotein, undergoes an amyloidogenic pathway where it is cleaved by β- and γ-secretase and forms soluble fragment of sAPPβ and short Aβ peptide. Alternatively, a non-amyloidogenic pathway occurs where α-secretase cleaves the Aβ sequence to prevent the formation of toxic peptides, generating sAPPα and p3 peptides (Coburger et al., 2014). APP is a multi-domain membrane protein that consists of signal peptide, cysteine-rich region, acidic domain, Kunitz proteases inhibitor (KPI)/OX2 and Aβ peptide. Multiple PTMs have been observed, like oxidation of M35 to methionine sulfoxide, which leads to the formation of Aβ protofibrils (Kummer and Heneka, 2014), whereas, cell division cycle protein 2 (cdc2) kinase generates phosphorylation at S26. In the same manner, nitration of Y10 because of nitric oxide (NO) can lead to aggregation of Aβ, whereas, glycosylation of Y10 changes the γ-secretase cleavage due to the proximity of this PTM to the transmembrane domain (Warmack et al., 2019a). Polyglutamylation of E11 can give rise to increased aggregation and formation of β-sheet *in-vitro*. Furthermore, racemization of D1 is higher in plaques, whereas, S26 shows an increased tendency to form fibrils (Warmack et al., 2019b). Similarly, the O-GlcNAcylation of APP at T576 regulates APP trafficking and processing, which increases its toxic aggregates (Chun et al., 2017). Furthermore, in AD, NFTs, which are intraneuronal aggregates of abnormally phosphorylated tau protein, is a major cause of neuronal cell death. Tau protein is subdivided into four domains, i.e., N-terminal, a proline-rich domain, microtubule-binding domain, and C-terminal. Phosphorylation is the most common PTM as it decreases the affinity for microtubule binding, which leads to neuronal cytoskeleton destabilization. Phosphorylation by casein kinase 1 (CK1) can be taken as the most significant kinase of tau. Tau phosphorylation at S262, S293 and S356 decrease tau binding to microtubules, whereas, phosphorylation at S235 and S262 has been shown to dissociate Tau microtubule (Ercan-Herbst et al., 2019; Martin et al., 2011). Glycosylation in the presence of kinases like protein kinase A (PKA), cyclin-dependent kinase 5 (CDK5), and glycogen synthase kinase 3β (GSK3β) reduces phosphorylation, which is expected to prevent NFT formation. Truncation at D13, E391, and D421 results in tau aggregation, whereas, only a single site of O-GlyNAcylation at S400 showed an inverse relationship with hyper-phosphorylation (Morris et al., 2015). However, oxidation at C322 gives no certainty, whether it takes part in tau lesion or not (Tang et al., 2018). Moreover, aberrant palmitoylation at C186 or C187 results in decreased neuronal plasticity and increased misfolded protein aggregates (Zaręba-Kozioł et al., 2018).

Table 1
A consolidated list of different PTMs and their target genes along with their respective modified amino acid residue that are involved in the different neurodegenerative disorders (shaded in grey) ((Liu et al., 2013; Manuscript and Genes, 2012; Trzeciakiewicz et al., 2017; Ferreon et al., 2018; Wang et al., 2017; de Oliveira et al., 2017b; Duncan et al., 2013; Chaibva et al., 2016; Chun et al., 2017; Sims et al., 2017; Wong et al., 2017; Diwu et al., 2013; Kumar et al., 2014; Vicente Miranda et al., 2017; Mattoo et al., 2019; Guru KrishnaKumar et al., 2018; Cohen et al., 2011; Tanikawa et al., 2018; Ishigami et al., 2015; Sheng and Christopher, 2016; Wang et al., 2019; Funk et al., 2014; Thomas et al., 2012; Sontag and Sontag, 2014, 2014; Pulido et al., 2014; Hwang et al., 2014; Kummer et al., 2011; Zhao et al., 2015; Reynolds et al., 2005; Xiang et al., 2015; Burai et al., 2015; Sims et al., 2017; Kim et al., 2011; Sims et al., 2017; Do et al., 2011; Landers et al., 2009; Jorgensen et al., 2009; Ju et al., 2013; Fei et al., 2007; Matos et al., 2016; Mueller et al., 2009; Pastori et al., 2010; Wong et al., 2017; Ralat et al., 2009; Sen et al., 2009; Qu et al., 2012; Soonpaa et al., 2009; Yang et al., 2019b; Sims et al., 2017; Wong et al., 2017; Sherva et al., 2014; Yan et al., 2013; Hong et al., 2008; Todi et al., 2010; Novoselov et al., 2013; Che et al., 2013; Koyano et al., 2013; Junqueira et al., 2019; Abeywardana and Pratt, 2015; Shinbo et al., 2006; Junqueira et al., 2019; Emerson et al., 2003; Mukhopadhyay and Dasso, 2017, 2017; Subramaniam et al., 2010; Ju et al., 2014; Almeida et al., 2015; Zhou et al., 2013; Janer et al., 2009; Mukhopadhyay and Dasso, 2017, 2017; Bhattacharyya et al., 2013; Parsons et al., 2014)).

PTM	Protein	Residue	AD	PD	ALS	HD	MDD	SCA	References
Acetylation	GFAP	K153 and K189			■				(Liu et al., 2013)
	PPP1R3B	G57	■						(Manuscript and Genes, 2012)
	Tau	K280, K281,	■						(Trzeciakiewicz et al., 2017)
	Tau	K163, K174, K190, K224, K234, K240, K254, K280, K281, K290, K311, K375, K385, K395	■						(Ferreon et al., 2018)
	TDP-43	K145			■				(Wang et al., 2017)
	α-synuclein	K6, K10		■					(R. M. de Oliveira et al., 2017)
	Ataxin-7	K257						■	(Duncan et al., 2013)
	htt	K6, K9, K15				■			(Chaibva et al., 2016)
Glycosylation	APP	T576	■						(Chun et al., 2017)
	APOE	R212							(Sims et al., 2017)
	MUC5B	V144					■		(Wong et al., 2017)
	MAPT	N.A	■						(Diwu et al., 2013)
	OGT	N.A				■			(Kumar et al., 2014)
	α-synuclein	K6, K10, K12, K21, K23, K32, K34, K43, K45		■					(Vicente Miranda et al., 2017)
Adenylation	α-synuclein	T33, T54, T75		■					(Mattoo et al., 2019)
Carbonylation	Tau	K163, K280, K281, K311	■						(Guru KrishnaKumar et al., 2018)(Cohen et al., 2011)
Citrullination	FUS, EWS, and TAF15	RG/RGG motif			■				(Tanikawa et al., 2018)
	GFAP	R270, R416	■						(Ishigami et al., 2015)
	MBP	R41, R47, R63, R96, R129	■						(L. Sheng, M. Christopher, 2016)
	NRGN	R68	■						(L. Sheng, M. Christopher, 2016)
Crotonylation	NEAT1	H3K27	■						(Wang et al., 2019)
Methylation	MAPT	K44	■						(Funk et al., 2014)
	MAPT	K163, K174, K180, K254, K267, K290	■						(Thomas et al., 2012)
	MAPT	K24, K67, K190	■						(Sontag and Sontag, 2014)

(*continued on next page*)

Table 1 (*continued*)

	PPP2CA	L309	(Sontag and Sontag, 2014)
	PINK1	K27	(Pulido, 2014)
	UBTF	K231/K254	(Hwang et al., 2014)
Nitration	amyloid β	Y10	(Kummer et al., 2011)
	amyloid β(1-40)	Y10	(Zhao et al., 2015)
	Tau	Y18, Y394	(Reynolds et al., 2005)
	α-synuclein	H50	(Xiang et al., 2015)
	α-synuclein	Y39, Y125, Y133/Y136	(Burai et al., 2015)
Phosphorylation	ABI3	S210, S213, and S216	(Sims et al., 2017)
	APOE	C147	(Kim et al., 2011)
	APOE	R212	(Sims et al., 2017)
	LRRK2	G2023	(Do et al., 2011)
	MORN2	E38	(Landers et al., 2009)
	Ataxin-1	S776, S239	(Jorgensen et al., 2009; Ju et al., 2013)
	Ataxin-3	S12, S29, S256, S236 S340, S352	(Fei et al., 2007; Matos et al., 2016; Mueller et al., 2009; Pastori et al., 2010)
	MUC5B	V144	(Wong et al., 2017)
S-Nitrosylation	IDE	C178, C789, C819, C966	(Ralat et al., 2009)
	GOSPEL	C47	(Sen et al., 2009)
	CDK5	C83, C157	(Qu et al., 2012)
	Drp1	C644	(Soonpaa et al., 2009)
Succinylation	PDHA1	K77, K244, K344	(Yun Yang et al., 2019)
	APP	K687	(Yun Yang et al., 2019)
	α-secretase	K16	(Yun Yang et al., 2019)
	Tau	K280, K311	(Yun Yang et al., 2019)
Ubiquitination	ATP5F1C	112	(Sims et al., 2017)
	FASN	R1927	(Wong et al., 2017)
	PPC2C	T2709, T2710, T2712	(Sherva et al., 2014)
	TRAF6	K63	(Yan et al., 2013)
	Ataxin-1	K589	(Hong et al., 2008)
	Ataxin-3	K117	(Todi et al., 2010)
	SOD1	N.A	(Novoselov et al., 2013)
	BAG2	N.A	(Che et al., 2013)
	PINK1	C431	(Koyano et al., 2013)
	PARKIN	K27, K48, K76	(Junqueira et al., 2019)
SUMOylation	α-synuclein	K102	(Abeywardana and Pratt, 2015)
	DJ1	K130	(Shinbo et al., 2006)
	PARKIN	N.A	(Junqueira et al., 2019)
	Amyloid-β	K11	(Emerson et al., 2003)
	Tau	K340	(Mukhopadhyay and Dasso, 2017)
	BACE1	Dileucine motif	(Mukhopadhyay and Dasso, 2017)

(*continued on next page*)

Table 1 (*continued*)

	Rhes-htt	K14, K49, K153	(Subramaniam et al., 2010)
	Ataxin-1	K16, K194, K610, K697, K746	(Ju et al., 2014)
	Ataxin-3	K166, K356	(Almeida et al., 2015; Zhou et al., 2013)
	Ataxin-7	K257	(Janer et al., 2009)
	SOD1	K75	(Mukhopadhyay and Dasso, 2017)
	EAAT2	K570	(Mukhopadhyay and Dasso, 2017)
Palmitoylation	APP	C186 and C187	(Bhattacharyya et al., 2013)
	PSD-95	C3, C5	(Parsons et al., 2014)

*AD: Alzheimer's disease; PD: Parkinson's disease; ALS: Amyotrophic lateral sclerosis: HD: Huntington's disease: MDD: Major depressive disorders; SCA: Spinocerebellar ataxia; GFAP: Glial fibrillary acidic protein; PPP1R3B: Protein phosphatase 1 regulatory subunit 3B; TDP-43: TAR DNA-binding protein 43, htt: Huntingtin; APP: Amyloid precursor protein; APOE: Apolipoprotein E; MUC5B: Mucin 5B, Oligomeric Mucus/Gel-Forming; MAPT: Microtubule-associated protein tau; OGT: O-linked N-acetylglucosamine (GlcNAc) transferase; FUS: FUS RNA binding protein; EWS: EWS-fusion-proteins; TAF15: TATA-binding protein-associated factor 15; MBP: Maltose-binding protein; NRGN: Neurogranin; NEAT1: Nuclear enriched abundant transcript 1; PPP2CA: Protein phosphatase 2 catalytic subunit alpha; UBTF: Upstream binding transcription factor; ABI3: ABI gene family member 3; ATM: ATM serine/threonine kinase; LRRK2: Leucine-rich repeat kinase 2; MORN2: MORN repeat containing 2; IDE: Insulin-degrading enzyme; GOSPEL: Glyceraldehyde-3-phosphate dehydrogenase's (GAPDH's) competitor of siah protein enhances life; CDK5: Cyclin-dependent kinase 5; Drp1: Dynamin-1- like protein(Dynamin related protein or dynamin like protein); PDHA1: Pyruvate dehydrogenase E1 component subunit alpha; ATP5F1C: ATP synthase subunit gamma, mitochondrial; FASN: Fatty acid synthase; TRAF6: Tumor necrosis factor receptor (TNFR)-associated factor 6; SOD1: Superoxide dismutase; BAG2: BAG cochaperone 2; PINK1: PTEN-induced kinase 1; PARKIN: E3 ubiquitin ligase parkin; DJ1: Protein deglycase DJ-1; BACE1: Beta-secretase 1; EAAT2: Excitatory amino acid transporter 2; PSD-95: Postsynaptic density protein 95.

The main reason behind PD is the loss of dopaminergic neuronal cells in SNpc and cytoplasmic deposition of LB and α-synuclein aggregates, comprised of three domains, viz. amphipathic domain, a central non-amyloid component and C-terminal. Various PTMs are reported to influence PD, for instance, phosphorylation at S87 by CK1 and dual-specificity tyrosine phosphorylation regulated kinase 1a (DYRK1A) can reduce the tendency of α-synuclein to form fibrils, SUMOylation at K102 is more capable of inhibiting aggregation in comparison to K96, whereas, Acetylation at K6 and K10 protects Cu(I) binding site (González et al., 2019). Ubiquitination at K10 and K23 readily fibrilize α-synuclein, and at K6, K1, and K21 inhibits the fibrillization process. Moreover, ubiquitination at K32, K34, K43, and K96 acts as a potent inhibitor as it displays no fibrillization (González et al., 2019; Zhang et al., 2019). Truncation at V74 by calpain I inhibit fibril formation and nitration at Y125, Y133, and Y136 accelerates oligomer formation, whereas, O-GlcNAcylation of T72 blocks the aggregation of both fibre and oligomer *in vitro*. Another two PD-associated proteins, PARKIN and PINK1, are dominant to mitochondrial quality control (Durcan and Fon, 2015). The domain structure of PARKIN comprises the Ubiquitin-like domain (Ub1), followed by two RING finger domains (RING0 and RING1), in between the finger domain (IBR), repressor element of PARKIN (REP) and RING3. The PINK1-dependent phosphorylation at S65 is vital for PARKIN translocation and stress-induced mitophagy. Phosphorylation by CDK5 on S131 and CK1 on S101, S127, S378 leads to a rise in PARKIN aggregation. Similarly, phosphorylation at Y143 by c-AB1 can deactivate E3-ligase activity (Chakraborty et al., 2017). The domain structure of PINK1 comprises mitochondrial targeting sequence (MTS), transmembrane (TM), and a protein kinase region. Phosphorylation at S228, S402 and S465 leads to PARKIN's recruitment, whereas, Phosphorylation at S465 results in PINK1 degradation. Ubiquitination at K137 decreases the PINK1 level inside the cell. Another causative gene of PD is DJ-1, and phosphorylation at T19 and Y67 aid as biomarkers, which are essential to PD pathogenesis (Xiangmin et al., 2012). In glycosylation, N-linked and O-linked glycosylation were prominent as compared to glypiation. In PD, a reduction in glycosyltransferase B3GACT4 and ST3GAC2 expression results in decreased GM1 ganglioside synthetic cells, which results in the downregulated activity of GM1 GD1a, GD1b, and GT1b (Moll et al., 2020) (Fig. 2).

In HD, an expansion of CAG trinucleotide repeat in the htt gene occurs where motor damage and psychiatric indications are due to neurodegeneration in the striatum and cortex (D. D. O. Martin, C. Kay, J. A. Collins, Y. T. Nguyen, 2018; Yalinca et al., 2019). The huntingtin protein domain comprises of polyQ, proline (PolyP), and four HEAT repeats. Phosphorylation of T3, S13, and S16 can control toxicity and regulate the nuclear localization of htt (Ratovitski et al., 2017), whereas phosphorylation at S1181 and S1201 by CDK5 is neuroprotective. Further, palmitoylation at C214 by HIP14 facilitates membrane attachment, and the level of palmitoylation is decreased during HD pathogenesis leading to decreased neuronal plasticity and increased misfolded protein aggregates (Yanai et al., 2006).

In ALS, the neuropathological sign is progressive paralysis, where genes such as TDP-43, fused in sarcoma (FUS) and SOD1, have been associated with its pathogenesis. The domain structure of TDP-43 consists of nuclear localization sequence (NLS), two RNA recognition motifs (RRMs), a nuclear export sequence (NES), and a glycine-rich domain. Phosphorylation at S403, S404, S409, and S410 is the hallmark feature of cytoplasmic aggregate. Further, Oxidation at C39, C173, C175, C198, and C244 could trigger TDP-43 pathology, while SUMOylation of K84 can disrupt NLS (François-Moutal et al., 2019). Domain structure of FUS consists of Q/G/S/Y rich, R/G rich, RMM, and ZnF regions. Phosphorylation at S256 regulates FUS proteolysis, whereas phosphorylation at Y526 by Src family kinase decreases FUS binding affinity to transportin-1, leading to FUS accumulation in the cytoplasm (Rhoads et al., 2018). The domain structure of SOD1 consists of an electrostatic loop and metal biding loop, and phosphorylation at T2, T58, and S59 regulates SOD1 enzyme activity, while SUMOylation of K9 results in SOD1 aggregation. SOD1 does not contain any tyrosine residue, and it can be nitrated at W32 to 6-nitrotryptophan, indicating partial loss of SOD1 enzyme activity (Banks and Andersen, 2019b). Moreover, crotonylation, citrullination, nitration, and glycation were also involved in the pathogenesis of NDDs. However, more *in vivo* and *in vitro* studies will be required to excavate the potential mechanism of these PTMs in neurodegeneration (Table 2).

Further, SCAs are a family of neurodegenerative disorders caused by the expansion of CAG repeat sequence in specific genes, resulting in the expansion of the polyQ tract of encoded proteins. SCA1 is caused by the expansion of the polyQ tract in ataxin-1 protein. Ataxin-1 comprises the expanded polyQ domain, HMG-box protein 1 (AXH) domain and NLS

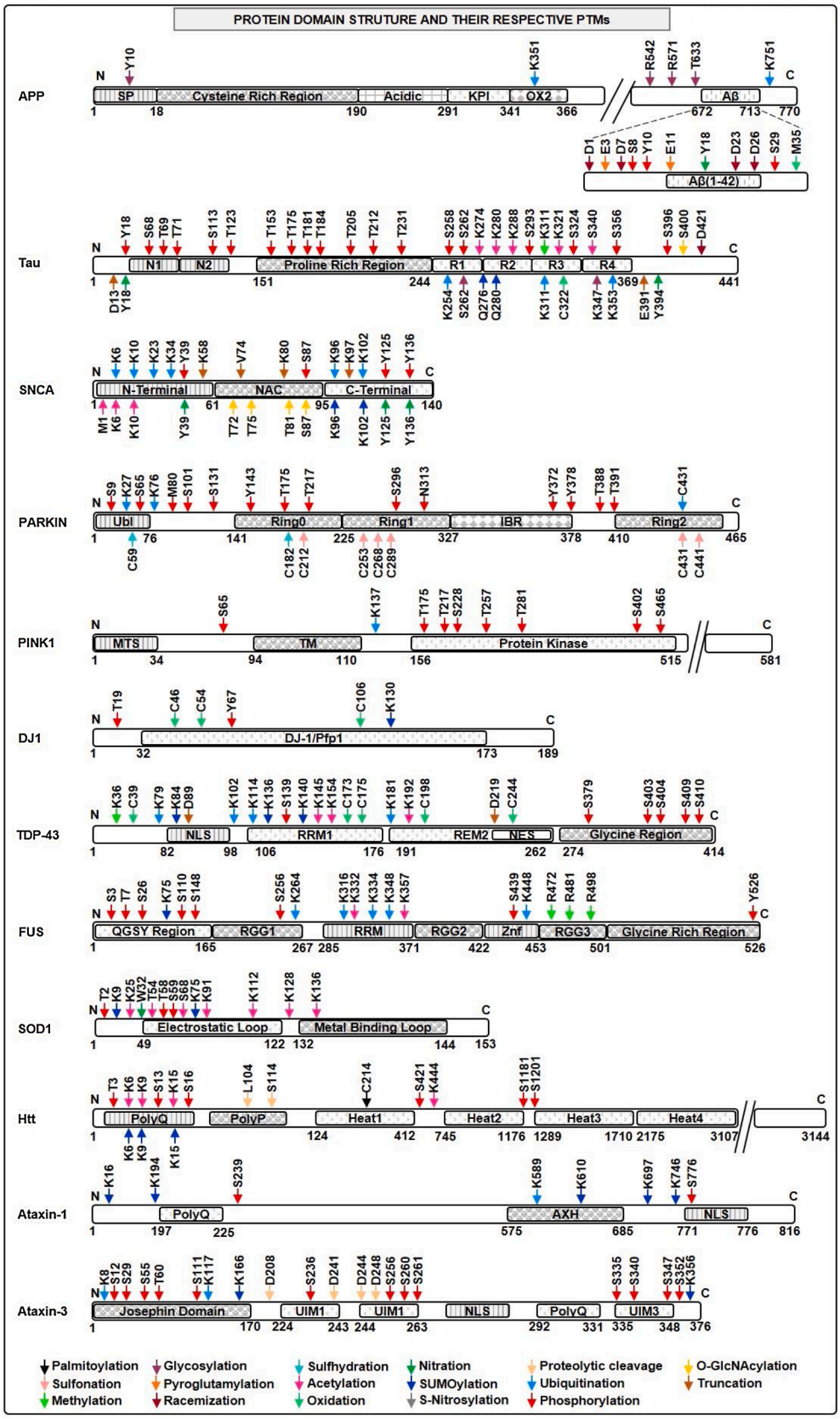

Fig. 2. Domain architectures and position of post-translational modifications in proteins of different neurodegenerative diseases. Protein domains of human (A) APP (770aa), (B) Tau (441aa) in AD; (C) α-synuclein (140aa), (D) PARKIN (465aa), (E) PINK1 (581aa), (F) DJ-1 (189aa) in PD; (G) TDP-43 (414aa), (H) FUS, (I) SOD1 in ALS; (J) Htt (3144aa) in HD; (K) Ataxin-1, (L) Ataxin-3 in SCA. Colour codes have been given for different PTMs. PTMs indicated by different coloured legends: Phosphorylation (in red), Ubiquitination (in light blue), SUMOylation (in dark blue), Sulfhydration (in turquoise blue), Oxidation (in green), Methylation (in light green), Nitration (in dark green), Sulfonation (in light pink), Acetylation (in dark pink), Racemization (in maroon), Glycosylation (in purple), Truncation (in brown), O-GlcNAcylation (in yellow), Proteolytic cleavage (in ivory), Pyroglutamylation (in orange), S-Nitrosylation (in grey), and Palmitoylation (in black).

Table 2
List of post-translational modifications associated with key proteins involved in the pathogenesis of neurodegeneration divided into *in-vivo*, *in-vitro*, and human samples.

PTM	Disease	Protein	*In vivo*	*In vitro*	Human samples	References
Acetylation	Alzheimer's Disease	Tau	–	E. coli BL21AI cells	–	(Ferreon et al., 2018)
	Parkinson's Disease	α-synuclein	*Drosophila* model of PD and substantia nigra of rats	HEK cells	–	(de Oliveira et al., 2017b)
	Huntington's Disease	htt	–	GT1-7 cells	–	(Chaibva et al., 2016)
	Amyotrophic Lateral Sclerosis	TDP-43	–	Mouse skeletal muscles	–	(Wang et al., 2017)
		GFAP	–	–	Post-mortem ALS spinal cord	(Liu et al., 2013)
	Spinocerebellar Ataxia	Ataxin-7	Mouse model	–	–	(Duncan et al., 2013)
Glycosylation	Alzheimer's Disease	APP	–	HeLa cells	–	(Chun et al., 2017)
		MAPT	Rat model of SAD	Rat model of SAD		(Diwu et al., 2013)
		Tau	–	–	Post-mortem AD and control brain tissue samples	(Liu et al., 2002)
	Parkinson's Disease	α-synuclein	Mice	*Drosophila*	–	(Vicente Miranda et al., 2017)
	Huntington's Disease	OGT	Larval eye discs of *Drosophila*	Neuroblastoma cell line Neuro2A	–	(Kumar et al., 2014)
	Parkinson's Disease	α-synuclein	–	Neurons of rat midbrain	–	(Mattoo et al., 2019)
Carbonylation	Alzheimer's Disease	Tau	–	HeLa cells	–	(Guru KrishnaKumar et al., 2018)
		Tau	–	Tau Tg mouse models	–	(Cohen et al., 2011)
Citrullination	Alzheimer's Disease	GFAP	–	–	Hippocampal extracts from post-mortem AD patients	(Ishigami et al., 2015)
	Amyotrophic Lateral Sclerosis	FUS	–	Mouse embryonic fibroblasts	–	(Tanikawa et al., 2018)
Crotonylation	Alzheimer's Disease	NEAT1	–	U251 cells	–	(Wang et al., 2019)
Methylation	Alzheimer's Disease	Tau	–	–	Post- mortem normal human brain tissue samples	(Funk et al., 2014)
		Tau	–	–	Post-mortem AD brain tissue samples	(Thomas et al., 2012)
		Amyloid β	Mice model	Mice model	Post- mortem human brain samples	(Kummer et al., 2011)
Nitration	Alzheimer's Disease	Amyloid β(1-40)	–	SH-SY5Y cells	–	(Zhao et al., 2015)
		Tau	–	BL21 (DE3) cells	–	(Reynolds et al., 2005)
	Parkinson's Disease	α-synuclein	–	H4 cells	–	(Xiang et al., 2015)
		α-synuclein	–	Semi-synthetic strategy	–	(Burai et al., 2015)
	Alzheimer's Disease	Amyloid β	–	*Drosophila* models	–	(Kumar et al., 2011)
		Tau	–	–	Post-mortem AD brain tissue samples	(Ercan-Herbst et al., 2019)
Phosphorylation	Parkinson's Disease	DJ1	–	Spectrophotometric method	Whole blood of AD, PD and controls	(Xiangmin et al., 2012)
		α-synuclein	Yeast model of PD	–	–	(Kleinknecht et al., 2016)
	Huntington's Disease	htt	HD mouse and human brain	–	Human post-mortem HD brain tissue	(Ratovitski et al., 2017)
	Spinocerebellar Ataxia	Ataxin-1	AKR mouse	–	–	(Jorgensen et al., 2009)
		Ataxin-3	Adult male Wistar rats	BL21(DE3)-SI cells	–	(Matos et al., 2016)
S-Nitrosylation	Alzheimer's Disease	IDE	–	BV-2 microglial cells	–	(Ralat et al., 2009)
		GOSPEL	–	HEK293 and HEK293FT cells	–	(Sen et al., 2009)
		CDK5	–	HEK293 T cells	–	(Qu et al., 2012)
		Drp1	HEK293 T cells	–	–	(Soonpaa et al., 2009)
Succinylation	Alzheimer's Disease	APP	–	Tg19959 mice bearing human APP	–	(Yang et al., 2019b)
		Tau	–	Tg19959 mice bearing human APP	–	(Yang et al., 2019b)
Ubiquitination	Alzheimer's Disease	TRAF6	HEK293 T cells	–	–	(Yan et al., 2013)
	Parkinson's Disease	PINK1	Mouse fetal brains taken from C57BL/6 wild-type	–	–	(Koyano et al., 2013)
	Amyotrophic Lateral Sclerosis	SOD1	EDL muscles in mice	–	–	(Novoselov et al., 2013)
	Spinocerebellar Ataxia	Ataxin-1	HEK293 cells	Ubiquitination assays	–	(Hong et al., 2008)
		Ataxin-3	–	Mammalian cells	–	(Todi et al., 2010)
SUMOylation	Alzheimer's Disease	BACE1	AD mouse model	HEK293 cells	–	(Bao et al., 2018)
	Parkinson's Disease	DJ1	H1299 cells	Mouse NIH3T3-Wt, -K130R and -L166 P cells	–	(Shinbo et al., 2006)

(*continued on next page*)

Table 2 (*continued*)

PTM	Disease	Protein	*In vivo*	*In vitro*	Human samples	References
		α-synuclein	–	SUMOylation assay	Human post-mortem PD brain tissue	(Rott et al., 2017)
	Huntington's Disease	Rhes-htt	–	Rhes knock-out mice	–	(Subramaniam et al., 2010)
		Ataxin-1	–	BOSC23 cells	–	(Ryu et al., 2010)
	Spinocerebellar Ataxia	Ataxin-3	–	SUMOylation assay	–	(Almeida et al., 2015)
		Ataxin-7	HeLa cells	SUMOylation assay	–	(Janer et al., 2009)
Palmitoylation	Alzheimer's Disease	APP	Non-Tg mouse brains	BACE1 cleavage assays using cell or mouse brain lipid rafts	–	(Bhattacharyya et al., 2013)
	Huntington's Disease	PSD-95	–	Striatal neurons from WT mice	–	(Parsons et al., 2014)
Sulfhydration	Alzheimer's Disease	AKT	–	–	Post-mortem brains from AD patients	(Sen et al., 2020)

domain. Several PTMs have been stated for ataxin-1. For instance, it has been reported that S776 phosphorylation of ataxin-1 results in stabilization of ataxin-1 and can further thwart its proteolytic degradation, thus contributing to SCA1 pathogenesis (Jorgensen et al., 2009; Orr, 2012). Likewise, one study showed that Nemo Like kinase (NLK) phosphorylates ataxin-1 at S239 and decreases NLK expression in the *Drosophila* model of SCA1, leading to a reduction in phenotypes of SCA1 (Ju et al., 2013). It has been observed that ubiquitination of ataxin-1 at K589 by UbcH6 promotes the degradation of toxic ataxin-1 proteins (Hong et al., 2008; Kang et al., 2015) K16, K194, K610, K697, K746 have been observed as significant SUMOylation sites in ataxin-1. It has been reported that SUMOylation of ataxin-1 mediated by SUMO1 increases the propensity of ataxin-1 towards aggregation, hence promoting SCA1 neurotoxicity (Ju et al., 2014). SCA2 is caused by the expansion of the polyQ tract in ataxin-2 protein. Ataxin-2 consists of polyQ domain, like sm (Lsm) domain, Lsm associated (LsmAD) domain, PABP interacting motif 2 (PAM2) domain and proline-rich domain. Phosphorylation of ataxin-2 mediated by the cyclin-dependent kinase 5-p25 (CDK5-p25) has been reported to stimulate ataxin-2 degradation, thus playing a neuroprotective role in SCA2 (Asada et al., 2014). Furthermore, SCA3 is a result of polyQ tract expansion in ataxin-3 protein. Ataxin-3 is a deubiquitinase (DUB) which is made up of a josephin domain (JD), three ubiquitin interacting motifs (UIMs), NLS domain and a polyQ stretch. Phosphorylation at S12 in ataxin-3 has been observed to protect against neurotoxicity in SCA3 models (Matos et al., 2016). Conversely, phosphorylation at S29 by GSK3β and CK2 has been reported to promote SCA3 neuropathogenesis by stimulating nuclear localization of ataxin-3 (Pastori et al., 2010). Additionally, phosphorylation at S256 by GSK3β has been reported to impede ataxin-3 aggregation (Fei et al., 2007). Furthermore, phosphorylation at S236, S340, S352 by CK2 promotes stabilization and nuclear inclusion of ataxin-3 (Mueller et al., 2009). Moreover, it has been reported that SUMOylation at K166 in ataxin-3 by SUMO-1 enhances the stability of ataxin-3 and can further lead to apoptosis in SCA3 (Zhou et al., 2013). In addition, SUMOylation at K356 has been reported to thwart the formation of ataxin-3 aggregates (Almeida et al., 2015). Furthermore, K117 ubiquitination of ataxin-3 has been reported to increase its DUB activity, which can further enhance its neuroprotective functions (Todi et al., 2010). Moreover, caspase-mediated proteolytic cleavage of ataxin-3 at D241, D244, and D248 leads to the formation of toxic ataxin-3 fragments (Liman et al., 2014; Shoesmith Berke et al., 2004). Likewise, calpain-dependent proteolytic cleavage at D208 and S256 also increases the aggregation propensity of ataxin-3 fragments (Weber et al., 2017). Further, SCA7 is a result of polyQ tract expansion in ataxin-7 protein. Ataxin-7 is made up of expanded polyQ, three NLS domains and the NES domain. SUMOylation at K257 has been observed to mitigate ataxin-7 aggregation and cytotoxicity (Janer et al., 2009). In addition, acetylation at K257 by HDAC3 has been reported to stabilize ataxin-7 contributing towards SC7 pathogenesis (Duncan et al., 2013). Likewise, it has been reported that acetylation at K257 thwarts autophagy-driven protein turnover resulting in the accumulation of toxic ataxin-7 fragments (Mookerjee et al., 2009). Furthermore, proteolytic cleavage of ataxin-7 mediated via caspase-7, at D266 and D344, promotes the generation of toxic ataxin-7 fragments (Guyenet et al., 2015).

4. Involvement of PTMs on endoplasmic stress and unfolded protein response in NDDs

In eukaryotes, the endoplasmic reticulum (ER) governs the protein translation, production and translocation from secretory pathways and extracellular space to the target locations (Fewell et al., 2001). Mutations in the secretory proteins result in conformation disorders initiating from metabolic disease to neurological and developmental disorders. Any modification/abnormality in ER functioning due to protein and calcium accumulation results in a perturbed state known as ER stress. The ER stress activates the unfolded protein response (UPR) signaling pathway, which counters the perturbed activity by upregulated expression of molecular chaperones and foldases (Lindholm et al., 2006; Schröder and Kaufman, 2005a). PTMs are considered as one of the significant factors for protein aggregation, which causes an alteration in three primary UPR sensors such as inositol-requiring enzyme 1 α (IRE1α), protein kinase R-like endoplasmic reticulum kinase (PERK), and activating transcription factor 6 α (ATF6α). Alteration in these UPR sensors leads to proteostasis dysfunction and elevated ER stress (Schröder and Kaufman, 2005b). The UPR response helps in regulating the proteostasis by modulating the misfolded protein by unfolding and refolding mechanism, but prolonged activation of UPR results in cell death (Walter and Ron, 2011). In normal conditions, PERK, IRE1α and ATF6 elevates protein folding signaling cascades to re-establish protein homeostasis and reduce ER stress, whereas, under chronic ER stress conditions, PERK and IRE1α promote cellular dysfunction and cell death (Scheper and Hoozemans, 2015). Further, ATF4 mediated regulation of PERK has been reported in the death receptor 5 (DR5) gene responsible for controlling cell fate via mitochondrial signaling (Hetz et al., 2015). Under normal conditions, PERK phosphorylation results in eukaryotic initiation factor 2 (elF2α) phosphorylation, eventually leading to ATF4 expression. IRE1α activity recruits X-box binding protein 1 (XBP1), apoptosis signal-regulating kinase 1/ c-Jun N-terminal kinases (ASK1-JNK) and TNF receptor-associated factor 2 (TRAF2) that regulates the PTM gene expression. Finally, ATF6 is released from the Golgi body and undergoes specificity protein 1 (SP1) and specificity protein 2 (SP2) mediated degradation releasing its cytosolic domain. Under perturbed state, decreased UPR signaling has been observed due to the competition between the protein accumulates to ligate to GRP78 receptor that releases the UPR protein (Wang and Kaufman, 2012; Yeganeh et al., 2015).

Moreover, ER-resident Ca^{2+} binding protein calreticulin has been observed to be subjected to various PTMs resulting in its transport to

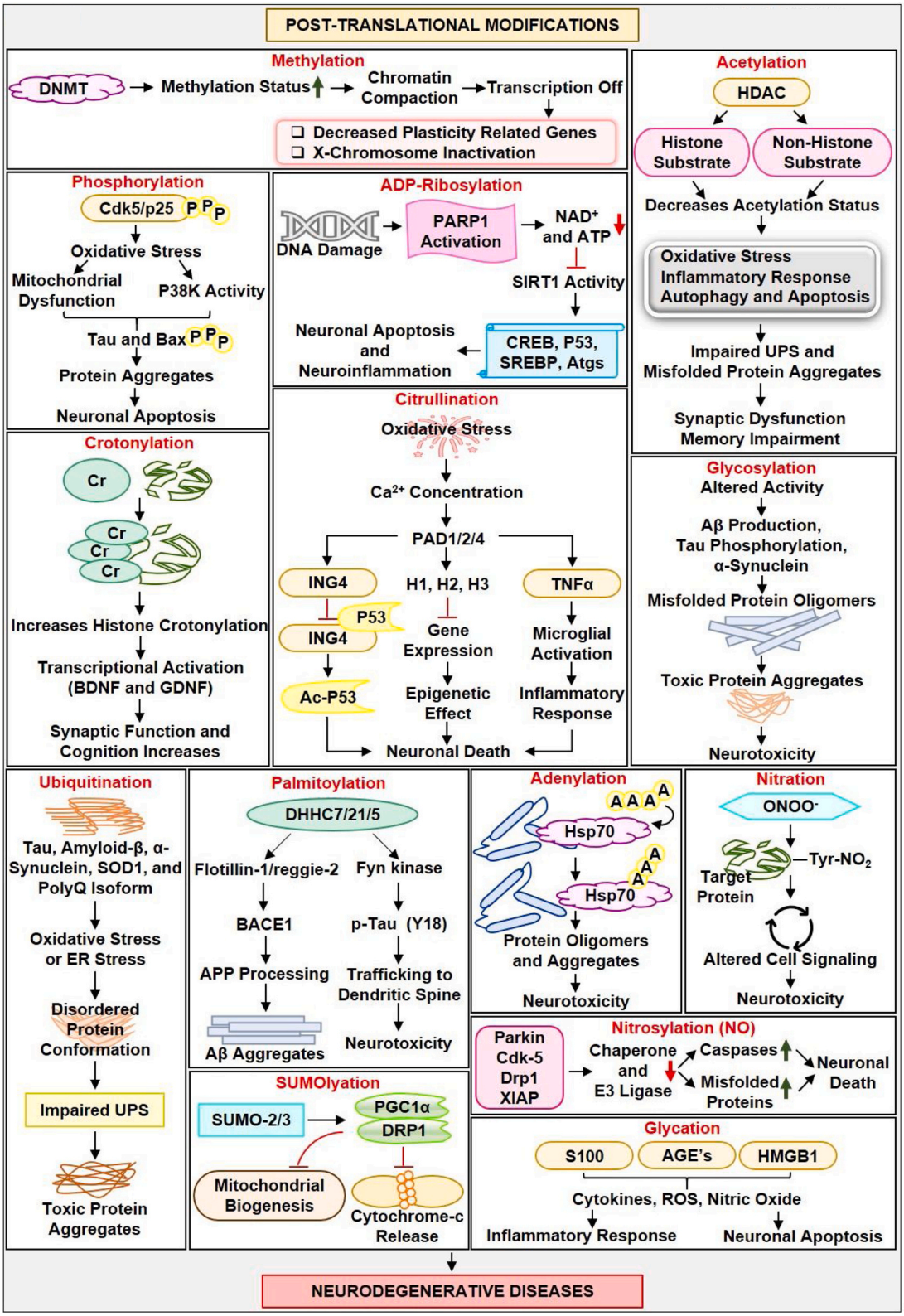

Fig. 3. Post-translational modifications of histone and non-histone substrates were involved in the pathogenesis and progression of deadly neurodegenerative diseases (NDDs) such as Alzheimer's Disease (AD), Parkinson's Disease (PD, Amyotrophic Lateral Sclerosis (ALS), and Huntington's Disease (HD). More than 50 PTMs were discovered so far in which phosphorylation, Acetylation, ubiquitination, SUMOylation, and palmitoylation were prominent were regulating different cell-signaling cascades involved in the pathogenesis of NDDs. Other PTMs such as Glycosylation, nitration, amidation, adenylation, citrullination, crotonylation, and methylation are also involved in the progression of NDDs. PTMs alter substrate protein activity, which causes an increase in stress conditions such as oxidative stress and ER stress. An increase in oxidative stress increases mitochondrial dysfunction, inflammatory response, neuronal apoptosis, autophagic cell death, and DNA damages response. This molecular phenomenon causes synaptic dysfunction, impaired neural plasticity, and memory impairment leads to neurodegeneration.

cytosol in ubiquitinated form and subjected to arginyl-tRNA generating arginylated proteins. Further, protein arginine deiminase 4 (PAD4) mediated citrullination of the protein has also been observed, and it has been reported that ER system chaperon calreticulin is citrullinated by PAD4 in the nucleus during cell stress condition (Kielbik et al., 2021; Wiersma et al., 2015). Overexpression of calreticulin triggers autophagosome formation and attenuates ER stress, probably by mitigating protein misfolding (Yang et al., 2019a). Actuation of PERK and IRE1α by poly ADP ribose polymerase 16 (PARP16), an ADP-ribosylation enzyme, in the absence of ER stress results in their modification, which leads to increased kinase activity and endonuclease activity, respectively (Jwa and Chang, 2012). PTM, such as mono-ADP-ribosylation of GRP78 or BiP at arginine residue, arises due to ER stress. Mono ADP-ribosylation of GRP78 or BiP by ARTC1 maintains the cellular activity of ER

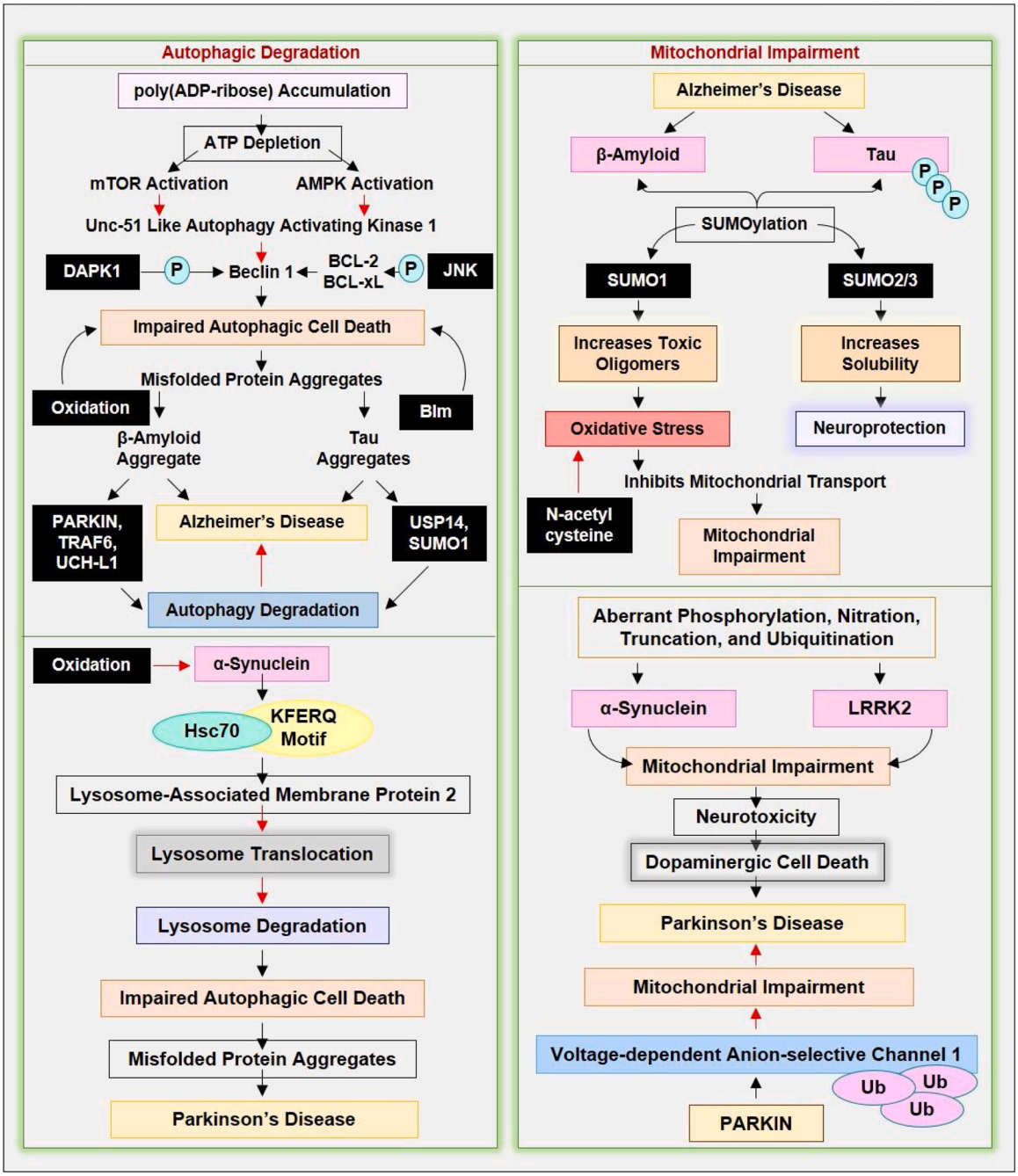

Fig. 4. Aberrant post-translational modifications (PTMs) have been linked to the progression of neurodegenerative diseases (NDDs) such as Alzheimer's disease (AD) and Parkinson's disease (PD) through defective autophagic degradation and mitochondrial impairment. In AD, activation of poly(ADP-ribose) causes AMPK and mTOR activation, which causes defective autophagic degradation of misfolded aggregates and leads to neuronal toxicity. However, PARKIN, TRAF6, and UCH-L1 mediated degradation of β–amyloid aggregates cause neuroprotection. Similarly, USP14 and SUMO1 cause clearance of toxic tau aggregates and promote neuroprotection through autophagic degradation. In PD, the association between Hsc70 and the KFERQ motif of α-synuclein inhibits lysosomal degradation, which causes impaired autophagic pathways. Furthermore, neurons require a high amount of energy supply, which will be provided by mitochondria. Mitochondrial dysfunction because of aberrant PTMs causes neurotoxicity and ultimately leads to neuronal cell death. In AD, SUMO1 causes an increase in toxic oligomers of β-amyloid and Tau, whereas, SUMO3 and SUMO3 promote neuroprotection. Similarly, in PD, aberrant PTMs in α–synuclein and LRRK2 cause mitochondrial impairment, which causes dopaminergic cell death.

Table 3
Implementation of different drug molecules and biomolecules in NDDs targeting various post-translational modifications.

Drug	PTM Enzyme	Disease	Interactors	Biological Effect	References
Nω-nitro-L-arginine methyl ester	NO (Nitration)	SNCA-A53 T PD Model	α-synuclein, α-tubulin	Blocks Axonal Mitochondrial Transport, Causes Mitochondrial Dysfunction	(Stykel et al., 2018)
catalase, 2,2,6,6-tetramethyl-1-piperidinoxyl	NO (Nitration)	ROS/NOS Induced Sprague-Dawley rat Neurotoxic model	ROS, NOS, MAPK, p53	Rescuing Neurons From ROS/H2O2 Plus NO/SNAP-Induced Insult	(Lee et al., 2016)
peroxiredoxin 6	H_2O_2 (Nitration)	Prion-related pathology	H_2O_2, $CoCl_2$	Regulating and Maintaining Cellular Homeostasis Via Its Ability to Control ROS Levels	(Asuni et al., 2015)
GKT136901	NOX-1/4 (Nitration)	AD, PD, MS	Alpha-synuclein, hydrogen peroxide, peroxynitrite	Prevented Tyrosine Nitration and Di-Tyrosine-Dependent Dimer Formation Of ASYN	(Schildknecht et al., 2013)
Ginkgolic acid	SUMOylation	Neurological Disorder	SUMO E1	Promotes Neuroprotection	(Vijayakumaran and Pountney, 2018)
Spectomycin B1	SUMOylation	Neurological Disorder	E2 enzyme, Ubc9	Promotes Autophagic Clearance	(Vijayakumaran and Pountney, 2018)
5-azacitidine	Methylation	P7 Mice Model of Neurobehavioral Defects	ERK1/2, caspase-3, Arc	Rescue cognitive functions, transcriptional activation	(Subbanna et al., 2016)
Decitabine	Methylation	HD	DNMT3A, BDNF	Promotes Neuroprotection	(Pan et al., 2016)
MS-275/Entinostat	Acetylation	AD	TNF, iNOS, IL-1β	Promotes Neuroprotection, Promotes Clearance of Neurotoxic Aggregates, Increases Histone Acetylation, Transcriptional Activation	(Gupta et al., 2020)
Vorinostat/SAHA	Acetylation		GDNF, BDNF, GRN, CBP, P/CAF, p300		
Trichostatin A	Acetylation		NRSF, BDNF, GDNF, c-fos, cAMP, CBP, Arc, Nr4a2		
Sodium Butyrate	Acetylation	AD, PD, HD, ALS	Sin3A complex, BDNF, Nrf2, Myst4		
Phenylbutyrate	Acetylation		CaMK, MEF2A, NR2B, SAP102, Drd2, BDNF, GDNF, Psma		
Valproic Acid	Acetylation		GSK3β, BACE1, APP, BCL-2, BDNF, GDNF, IDE, NEP		
Benzamil	UPS activator	HD, MS	———	Rescue acid-sensing ion channel (ASIC) dependent acid toxicity	(Al Mamun et al., 2020; Djakovic et al., 2009; Kumar et al., 2020; Myeku et al., 2011; Tundo et al., 2020)
Betulinic acid	Proteasome Activator	AD	20S βδ Subunit	Enhance GABAergic activity	
Bicuculline	UPS Activator	AD, PD	Rpt6	Stimulate calcium/calmodulin-dependent protein kinase II (CaMKII) mediated proteasomal activity	
Clioquinol	Proteasome Inhibitor	AD, HD	20S Proteasome	Inhibit 20S proteasome inhibition by clioquinol-copper complex	
Delta-9-Tetrahydrocannabinol	DUB Stimulator	PD	USP3	neuroprotective role	
Mitoxantrone	DUB Inhibitor	MS	USP11	Immunosuppressive Agent	
Doxycycline	E3 Inhibitor	AD, PD	HUWE1	Promotes Neuroprotection	
Nicotine and Resveratrol	DUB Stimulator	AD, PD	MID1, HRD1, USP10, USP16, USP14	Rescue Neurological Defects	
Sildenafil	Proteasome stimulator	AD	26 S Proteasome	Act as phosphodiesterase's 5 inhibitors and stimulate proteasome to reduce protein aggregate	
Sulforaphane	Proteasome stimulator	AD, PD, HD	26 S Proteasome	Induce Nrf2 mediated proteasomal activity and mhtt degradation	
Trehalose	E3 stimulator	HD	CHIP	Bind to expanded polyglutamine and stabilize partially unfolded polyglutamine	
Veliparib	PARP	Parp1-/- Mice After Optic Nerve Crush Injury	_____	Suppression of Parylation In the Mouse CNS, Provide Benefit for Recovery from CNS Trauma	(Grimaldi et al., 2019)
Mangiferin	Glycosylation	AD, PD	_____	Improving the Declined Memory and Cognition	(Feng et al., 2019)
Sitagliptin					
Saxagliptin	Glycosylation	APP/PS1/TAU transgenic mice	GLP-1, DPP-4, CREB, PSD95, JNK1/2	Enhance the Synapse Protein Level, increased the O-glycosylation and decreased abnormal phosphorylation of tau and neurofilaments (NFs), degraded intercellular β-amyloid (Aβ) accumulation and alleviated	(Chen et al., 2019)

(*continued on next page*)

Table 3 (*continued*)

Drug	PTM Enzyme	Disease	Interactors	Biological Effect	References
				neurodegeneration related to the GLP-1 signaling pathway	
Thiamet-G	Glycosylation	3×Tg-AD mouse model	OGA and JNPL3	Enhances autophagy in the brain through an mTOR-independent pathway	(Zhu et al., 2018)
2-hydroxypropyl-β-cyclodextrin	Glycosylation	Niemann-Pick disease, type C (NPC)	LAMP1	Prevention of Neuro-Inflammation, Prevented the Appearance of The Glycosylated LAMP1	(Cawley et al., 2020)
Neferine	Nitrosylation	AD	IL-1β, IL-6, ROS, TNF, COX-2, NF-κβ	Promotes Neuroprotection	(Yin et al., 2020)
Asarone Derivatives	Nitrosylation	AD	Aβ, NO	Promotes Neuroprotection and Have the Prophylactic and Therapeutic Potential In AD	(Lee et al., 2019)
Biglycan	Nitrosylation	AD, PD, HD	AMPK, mTOR	Protects Neuroblastoma Cells From NO-Induced Death	(Chen et al., 2020)
Protein Disulphide Isomerase	Nitrosylation	PD	____	Reduces alpha-synuclein aggregation	(Serrano et al., 2020)
Nuclear Paraspeckle Assembly Transcript 1	Affects H3k27 Acetylation (H3k27ac) And H3k27 Crotonylation (H3k27cro)	AD	P300/Cbp, Aβ, STAT3	Aβ Clearance Via Inhibiting Expression of Endocytosis-Related Genes	(Wang et al., 2019)
Etomoxir	Carnitine Palmitoyl Transferase 1	MS	IFN-β, Interleukin-17α	Promotes Neuroprotection	(Mørkholt et al., 2020)
Palmitoyl-Protein Thioesterase 1	Palmitoylation	Neurological Disease	ABHD17 s	Promotes Neuroprotection	(Koster and Yoshii, 2019)
N-(tert-Butyl) hydroxylamine	Palmitoylation	CNS disorder	AMPAR, PSD	Promotes Neuroprotection	(Xia et al., 2019)
Forskolin	Palmitoylation	HD	Adenyl cyclase	Rescue neurological defects	(Mehan et al., 2017)
Ginsenoside Rb1	Glycation	SH-SY5Y cells	PI3K/Akt	Reduces Oxidative Stress and Promotes Neuroprotection	(Nan et al., 2019)
Liraglutide	Pin1	Neurological Disease	BAX, BCL-2, CASP3, GSK3b/Akt	Rescues to Some Extent Cellular Dysfunctions	(Bianchi et al., 2019)
Tanshinone I	Glycation	SH-SY5Y cells	Nrf2/GSH Axis	Prevent Mitochondrial Dysfunction, Rescue Neurotoxicity	(de Oliveira et al., 2017a)
Curcumin	Glycation	Neurological Disease	Nrf2/TLR4/RAGE	Neuroprotective Compound Against Ethanol-Associated Neurodegenerative Diseases	(Ikram et al., 2019)
Nicotinamide	Glycation	Brain Injury	RAGE/JNK/NF-κB	Prevent Neurodegeneration	(Alam et al., 2019)
Metformin	RAGE	AD	AMPK	Prevent Inflammatory Response	(Chung et al., 2017)
Anthocyanins	Glycation	AD	SNAP-23, SNAP-25, CREB	Prevent Cognitive Impairment	(Rehman et al., 2017)
Melatonin	Glycation	AD	RAGE/NF-K B/JNK	Reverse Memory Impairment and Neuroinflammation	(Ali et al., 2015)
Donepezil	Propionylation 2-hydroxyisobutyrylation Butyrylation Succinylation crotonylation	Vascular Dementia of Rats	ACHE, Aβ1-42	Decreased the Level of Aβ1-42, Reduced the Level of Lysine Acylations	(Wang et al., 2020a)

*NO: Nitric oxide; SNCA: Synuclein alpha; ROS: Reactive oxygen species; NOS: Nitric oxide synthase; MAPK: Mitogen-activated protein kinase; CoCl2: Cobalt chloride; H_2O_2: Hydrogen peroxide; NOX-1/4: NADPH oxidase; Ubc9: SUMO-conjugating enzyme UBC9; ERK1/2: Extracellular signal-regulated kinase ½; Arc: Activity regulated cytoskeleton; DNMT3A: DNA methyltransferase 3 alpha; BDNF: Brain derived neurotrophic factor; TNF: Tumor necrosis factor; iNOS: Inducible nitric oxide synthase; IL-1β: Interleukin-1β; GDNF: Glial cell-derived neurotrophic factor; GRN: Granulin Precursor; CBP: CREB binding protein; p/CAF: P300/CBP associated factor; NRSF: Neuron restrictive silencer factor; cAMP: Cyclic adenosine monophosphate; Nr4a2: Nuclear receptor subfamily 4 group A member 2; Nrf2: Nuclear factor erythroid 2-related factor 2; Myst4: Histone acetyltransferase; CaMK: Ca2+/calmodulin-dependent protein kinase; MEF2A: Myocyte enhancer factor 2A; NR2B: N-methyl D-aspartate receptor subtype 2B; SAP102: Synapse associated protein 102; Drd2: Dopamine receptor D2; Psma: Prostate-specific membrane antigen; GSK3β: Glycogen synthase kinase 3 beta; BACE1: Beta-secretase 1; APP: Amyloid precursor protein; BCL-2: B-cell lymphoma 2; IDE: Insulin degrading enzyme; NEP: Nuclear export protein; UPS: Ubiquitin proteasome system; Rpt6: 26S proteasome regulatory subunit 8 homolog; DUB: Deubiquitinating enzymes; USP3: Ubiquitin specific peptidase 3 USP11: Ubiquitin specific peptidase 11; HUWE1: HECT, UBA And WWE domain containing E3 ubiquitin protein ligase 1; MID1: Midline 1; HRD1: ERAD-associated E3 ubiquitin-protein ligase HRD1; USP10: Ubiquitin specific peptidase 10; USP16: Ubiquitin specific peptidase 16; USP14: Ubiquitin specific peptidase 14; CHIP: E3 ubiquitin-protein ligase CHIP; PARP: Poly (ADP-ribose) polymerase; GLP-1: Glucagon-like peptide 1; DPP-4: Dipeptidyl-peptidase 4; CREB: cAMP response element-binding protein; PSD95: Postsynaptic density protein 95; JNK1/2: c-Jun N-terminal kinase; OGA: O-GlcNAcase; LAMP1: Lysosomal-associated membrane protein 1; IL-6: Interleukin-6; COX-2: Cyclooxygenase-2; NF-κβ: Nuclear factor kappa-light-chain-enhancer of activated B cells; Aβ: β-Amyloid; AMPK: 5' AMP-activated protein kinase; mTOR: Mammalian target of rapamycin; STAT3: Signal transducer and activator of transcription 3; IFNβ: Interferon beta; ABHD17 s: Alpha/beta hydrolase domain-containing protein 17 s; AMPAR: α-amino-3-hydroxy-5-methyl-4-isoxazolepropionic acid receptor; PSD: Postsynaptic density; PI3K: Phosphoinositide 3-kinases; Akt: Protein kinase B; CASP3: Caspase-3; GSH: Glutathione; TLR4: Toll-like receptor 4; RAGE: Receptor for advanced glycation end products; SNAP23: Synaptosomal-associated protein 23; SNP-25: Synaptosome associated protein 25; ACHE: Acetylcholinesterase.

chaperones. Altered BiP PTM interferes with the substrate-binding domains resulting in protein mutations and reduced protein synthesis (Laitusis et al., 1999)

In a study, patients with NDDs have been reported to experience elevated ER stress levels. In AD, the UPR markers for phosphorylated PERK (p-PERK) and phosphorylated elF2α (elF2α-P) immunoreactivity have been upregulated, resulting in toxic proteins' aggregation in the hippocampus region. Phosphorylation of elF2α mediated regulation of

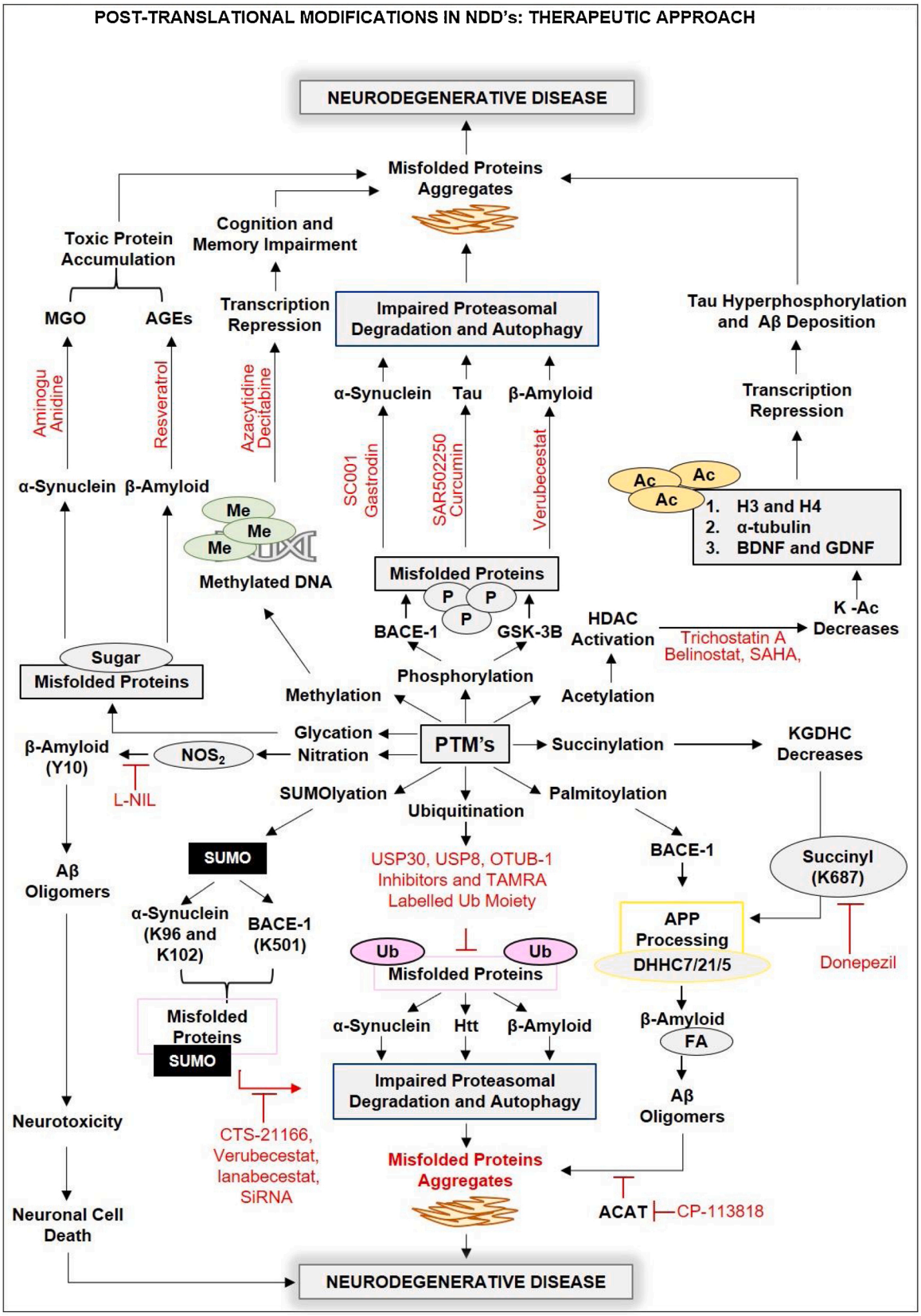

(caption on next page)

Fig. 5. Aberrant post-translational modifications (PTMs) such as methylation, phosphorylation, ubiquitination, Acetylation, nitration, SUMOylation, glycation, amidation, palmitoylation, succinylation and other has been linked with the pathogenesis and progression of neurodegenerative diseases (NDDs). Thus, different inhibitors and activators have been developed that will target various PTM enzymes. For example, USP30, USP-8, OTUB-1 inhibitors cause inhibition of the misfolded protein ubiquitination, which will increase the misfolded protein aggregates in the brain and thus increases neurotoxicity. Inhibition of misfolded protein ubiquitination causes impairment in proteasomal degradation and the autophagic pathway, which causes neuronal cell death. Similarly, SUMOylation of α-synuclein (K96 and K102) and BACE-1 (K501) lead to misfolded protein aggregation, which causes impairment in proteasomal and autophagic degradation pathway. However, CTS-21166, Verubecestat, lanabecestat, and siRNA treatment inhibit the SUMOylation of misfolded protein aggregates and lead to neuroprotection. Further, palmitoylation of BACE-1 causes APP processing, which binds with DHHC7/21/5 and causes the formation of β-amyloid and amyloid aggregates. Misfolded amyloid aggregates cause neurotoxicity and lead to AD development, which will inhibit through CP-113818, a specific ACAT inhibitor. Similarly, Donepezil inhibits the succinylation of APP at K687, and thus inhibits the progression of AD. Studies demonstrated that L-NIL inhibits NOS2 mediated β-amyloid nitration at Y10, whereas, resveratrol and Aminogu inhibit β-amyloid and α-synuclein glycation, respectively, which will decrease toxic protein accumulation and prevents neurodegeneration. Moreover, Azacytidine and Decitabine inhibit DNA methylation, whereas, Trichostatin A, Belinostat, and SAHA increase H3 and H4 acetylation, which increases transcription and causes neuroprotection. Further, phosphorylation of GSK-3β and BACE-1 causes β-amyloid, Tau, and α-synuclein misfolded aggregates, which will inhibit through verubecestat, curcumin, and gastrodin, respectively.

beta-secretase 1 (BACE1) has been reported that further increases the Aβ level, whereas, the haploinsufficiency of PERK has been reported to reduce BACE1 levels due to decreased concentration of P-elF2α, which further lowers the level of Aβ and plaque (Kaphingst et al., 2010; O'Connor et al., 2008). Similarly, presenilin-1 (PSEN1), gamma-secretase complex protein, has a crucial role in Aβ processing by APP and has been reported to increase due to glycosylation inhibitor tunicamycin, thereafter elevating the ER response in neuroblastoma (Jin et al., 2010; Selkoe, 1994). Exposure of murine podocytes with AGE-BSA was the first-ever study, which reported advanced glycation end products (AGEs) induction by ER stress. Increased expression of glucose-regulated protein 78 (GRP78) has been reported to induce apoptosis due to the formation of AGE in a time-dependent manner (Chen et al., 2008) (Piperi et al., 2012). In PD and Lewy body disorders, transport of synuclein across ER and Golgi body has been observed, where α-synuclein accumulates due to an impaired proteasomal degradation pathways, which further hampers ERAD and increase ER stress (Cooper et al., 2006). UPR stress response upregulation and α-synuclein aggregation in the dopaminergic region of SNpc has been observed along with localized reactivity of PERK (Hoozemans et al., 2007). In addition, it has been observed that aggregates of mutant PKCγ stimulate the phosphorylation of PERK, leading to induction of ER stress and cell apoptosis in SCA14 (Seki et al., 2007). S-nitrosylation of IRE1α and PERK has been associated with increased ER stress, further promoting neurodegeneration by decreasing ribonuclease activity of IRE1α and increasing activity of phosphorylated elF2α, respectively (Nakato et al., 2015). A study demonstrated that methamphetamine induces S-nitrosylation of protein disulfide isomerase (PDI) and α-synuclein aggregation, which promotes neurotoxicity (Wu et al., 2014). PDI is a crucial component to downregulate the ER stress arising due to the protein aggregates. Recently, PTMs regulating PDI have been described, where the cystine residue of PDI has been reported to undergo nitrosylation in AD and PD patients' brains (Uehara et al., 2006). Under the physiological state, S-nitrosylation regulates the protein activity; however, under pathological conditions, S-nitrosylation of PDI triggers cell death resulting in neurodegeneration. S-nitrosylation of its disulfide isomerase decreases chaperon activity, which results in the accumulation of perturbed proteins state (Andreu et al., 2012). PDI S-nitrosylation is also associated with enhanced oxidative stress resulting in protein damage. Excessive ER oxidation has been reported to result in altered S-nitrosylation of PDI encoding for neurodegenerative disorders (Nakamura et al., 2013) (Benhar et al., 2006). Further, PARKIN S-nitrosylation has been reported to elevate the ROS level, thereby promoting oxidative stress in the cell resulting in protein misfolding by reducing UPS functioning (Imai and Takahashi, 2004).

Glutathione serves an essential role in foiling excessive oxidation in ER and modulates ER proteins via S-glutathionylation by glutathione S-Transferase (GST) enzyme. Further, it maintains BiP, PDI, calnexin, and calreticulin activity to maintain ER's proper functioning. GST alteration has been reported to disturb ER activity, indicating S-glutathione's crucial role in ER stress response (Ye et al., 2017). PERK takes part in maintaining cellular homeostasis by regulating glutathione levels within the cell by activating nuclear factor erythroid 2 related factor 2 (nrf2). As earlier studies have shown that glutathione is linked with S-glutathionylation, we may conclude that PERK-dependent activation of nrf2 increases S-glutathionylation, which downregulates ER stress and promotes cell survival (Cullinan et al., 2003). Modification in the C-terminal of the CXXC motif of PDI has been reported to be a chief cause of the accumulation of polyubiquitinated proteins. Modification in the CXXC motif makes PDI susceptible to glutathionylation, an irreversible PTM on the cell surface, hampering the overall cell redox potential that exacerbates the PDI chaperone activity. This mechanism results in disproportionate masking of S-glutathionylated proteins, which have been linked to neuropathological conditions (Halloran et al., 2013).

APP palmitoylation at N-terminal cysteine residues was observed in the extracellular area, where APP serine mutants of APP did not undergo palmitoylation and remained localized in ER, which elicit the direct relation of palmitoylation in AD pathogenesis. DHHC7 and DHHC21 overexpression has been observed to be associated with APP palmitoylation. This palmitoylated APP was shown to be a better substrate for BACE1, resulting in APP cleavage in lipid rafts, making them mobile across the ER. The increased APP generates Aβ proteins that have been linked with an elevated ER stress response (Cho and Park, 2016). Disturbance in the modulation of enzyme palmitoyl acyltransferases (PATs) and thioesterases mediated palmitoylation contributes to HD pathogenesis. This aberrant palmitoylation results in erroneous mobility of htt (Young et al., 2012). Although palmitoylation of proteins has been reported to be a crucial modification, these proteins must undergo lysosomal degradation by thioesterase-1 (PPT1). The mutation in the PPT1 gene has been a reported cause for infantile neuronal ceroid lipofuscinosis (INCL). Further, a mutation in the PPT1 forces the activation of GAP43 in PPT1 deficit cells to result in palmitoylation of neuronal proteins and agglomerate formation in the ER, contributing to the stress condition. The overall outcome of this dysregulation of PPT1 is the activation of apoptotic pathways and neurodegeneration in INCL (Zhang et al., 2006).

ER lumen acetylation is regulated by multiple enzymes, including AT1, ATase1 and ATase2. ER lumen protein acetylation has been associated with the processing of Aβ precursor protein cleaving enzyme BACE1. Any modification results in amassment of juvenile proteins inside the lumen, initiating mild stress, which codes for the autophagic process. Similar results have been reported in ALS and HD, where crosstalk between ER acetylation and neuroprotection has been observed by activation of UPR, mediated autophagy that maintains the protein homeostasis (Peng et al., 2016). X-box binding protein 1 (XBP1), a key transcription factor of the UPR, is critical in maintaining ER homeostasis. Recent studies have shown that SUMOylated spliced XBP1 has been reported in ER stress conditions. The authors identified SUMO-specific protease 1 (SENP1) that enhances XBP transcriptional activity by de-SUMOylation of XBP1. The absence of SENP1 has been associated with the agglomeration of SUMOylated XBP1 and significant elevation of ER stress-induced apoptosis (Jiang et al., 2012). Another

group observed that PIAS2 mediated SUMOylation at two lysine residues of XBP1 at C-terminal were responsible for reducing its transcriptional activity (Chen and Qi, 2010).

5. Linking ageing and neurodegeneration: role of post-translational modifications

Ageing can be defined as a biological process which leads to impairment and decline in functions of tissue and organs in the body, resulting in increased susceptibility to different disease and an increased risk of death. Ageing is considered one of the significant risk factors for NDDs. Mitochondrial dysfunction, genomic instability, telomere attrition, epigenetic modification, protein quality control dysfunction and cellular senescence are major hallmarks of ageing, which are also implicated in neurodegenerative disorders, suggesting a link between ageing and neurodegeneration. Mitochondrial dysfunction is one of the major causative factors of ageing. During ageing, initially, activated reactive oxygen species (ROS) stimulates damage to mitochondria, giving rise to amplified ROS production by mitochondria, which inflicts more damage to mitochondria, resulting in a vicious cycle, leading to mitochondrial dysfunction (Grimm and Eckert, 2017). Thus, mitochondrial dysfunction is one of the trademark features of ageing, which results in an increased susceptibility to NDDs. Further, genomic instability is another major feature of ageing. DNA mutations, accumulation of damaged DNA, and DNA repair machinery error have been reported to be responsible for genomic instability, which contributes to ageing. For instance, RecQ DNA helicase is an important DNA repair enzyme, and mutations in WRN gene coding for RecQ DNA helicase result in Werner syndrome, a disease that causes accelerated ageing (Sugimoto, 2014). Likewise, a study reported that DNA double-strand breaks are accumulated in neurons during the early stage of AD and promote neurodegeneration (Shanbhag et al., 2019). Hence, genomic instability is another feature that links ageing as a risk factor for neurodegeneration.

Additionally, telomere attrition is another essential causative factor of ageing. Telomeres are non-coding repetitive DNA sequences that protect the ends of chromosomes from damage. Telomere shortening also drives the process of ageing, as an age-related decrease in telomere length has been observed. For instance, one study reported that wild-type mice that inherited short telomeres showed age-related disorders, confirming that short telomeres contribute to ageing (Armanios et al., 2009). Likewise, a study reported that telomere shortening in a mouse model of PD resulted in increased PD pathogenesis and neurodegeneration (Scheffold et al., 2016). Hence, telomere attrition is another factor that correlates ageing with an increased risk of neurodegeneration.

Moreover, epigenetic modification is also implicated in the process of ageing. Epigenetic alterations like DNA methylation and histones modifications also regulate the ageing process (Soriano-Tárraga et al., 2019). Likewise, epigenetic alternations are observed in neurodegenerative disorders. For example, altered localization and hyperphosphorylation of histone H3 was observed in AD patients' hippocampus (Ogawa et al., 2003). Moreover, dysfunction and decreased activity of protein quality control system activity comprising of chaperones, UPS, autophagy-lysosome systems is another causative factor of ageing (Arslan et al., 2006; Barbosa et al., 2019; Löw, 2011). Likewise, as we have discussed above, impairment in protein quality control systems is one of the most important causative factors for NDDs, leading to protein aggregation.

Moreover, cellular senescence, described as the cessation of the cell cycle and cell proliferation inhibition, is also observed during ageing. During ageing, DNA damage, mitochondrial dysfunction, telomere attrition can stimulate cellular senescence (Calcinotto et al., 2019). *In-vivo* studies have observed senescent cells in aged tissues (Jeyapalan and Sedivy, 2008). Chronic exposure to the senescent cell causes inflammation and tissue degeneration, thereby accelerating ageing (Saez-Atienzar and Masliah, 2020). Likewise, a study reported that clearing senescent cells in a mouse model of AD ameliorated cognitive dysfunction in the brain and prevented tau aggregation, suggesting that senescence is also involved in neurodegeneration (Bussian et al., 2018). Thus, we can see that mitochondrial dysfunction, genomic instability, telomere attrition, epigenetic modifications, protein quality control dysfunction, cellular senescence are major hallmarks of ageing and is also implicated in neurodegeneration, suggesting that ageing is indeed a significant risk factor for NDDs.

Further, various PTMs also regulate the process of ageing. For instance, it has been observed that the O-GlyNAcylation of proteins is reduced during ageing. A study reported that decreased protein O-GlycNAcylation was observed in the hippocampus of aged mouse leading to cognitive dysregulation. This study further stated that increasing neuronal O-GlcNAc transferase (OGT) in the aged mice hippocampus promoted O-GlcNAcylation and alleviated ageing-related cognitive impairments in the aged hippocampus (Wheatley et al., 2019). Further, a study observed that S129 phosphorylated and nitrated α-synuclein were found in the *substantia nigra* of aged squirrel monkeys compared to younger ones, proposing that phosphorylated and nitrated α-synuclein accumulate in the brain as a consequence of ageing (McCormack et al., 2012). It has to be noted that accumulation of phosphorylated and nitrated α-synuclein is also observed in the PD patients. Likewise, another research observed increased nitrated proteins during ageing in the rat cerebellum (Gokulrangan et al., 2007). Another study has reported that low expression levels of S-nitrosoglutathione reductase (GSNOR) are observed in humans and mice during ageing. They further reported that insufficiency of GSNOR stimulates S-nitrosylation of PARKIN, impairing its E3 ligase activity, which results in dysregulation of mitophagy (Rizza et al., 2018).

Additionally, another study observed that mitochondrial proteins' succinylation increased with age in *C. elegans* and *D. melanogaster*, leading to mitochondrial dysfunction. However, in this study, no age-dependent increase in mitochondrial protein succinylation was observed in rats, as rats possess mitochondrial SIRT3, SIRT5, which has desuccinylase activity (Hong et al., 2016). It has to be noted that even humans possess SIRT3 and SIRT5 enzymes, and their dysregulation can promote ageing. Further, one study reported that protein sialylation is neuroprotective and was depleted during ageing. They observed a decrease in sialylation with ageing, leading to neuron dysfunction and synaptic defects in a mice model's hippocampus (Klaus et al., 2020). Another study observed that palmitoylation of NMDAR proteins increased with age in mice's frontal cortex, resulting in cognitive dysfunction and memory deficits (Zamzow et al., 2019). Moreover, another research observed that s-sufhydration of proteins decreased with age in mice. This decrease in sulfhydration resulted from a deficiency in H_2S generating enzymes. In this study, even human fibroblasts of the same individual, observed at different ages, showed an age-related decline in s-sulfhydration of proteins (Zivanovic et al., 2019). Further, one study reported that age-induced oxidative stress stimulates an increase in protein carbonylation, which leads to the formation of protein aggregates in the bone marrow and spleen of an older mouse compared to younger mice. In this study, stimulating carbonyl stress in younger mice resulted in protein aggregates similar to those observed in older mice (Tanase et al., 2016). Additionally, another study reported that carbamylated proteins assembled in the skin of a human, bovine and murine, with age, suggesting that protein carbamylation is also a hallmark of ageing that can lead to age-related tissue damage (Gorisse et al., 2016). Further, the formation and accumulation of AGEs in tissues is another hallmark feature of ageing, especially skin ageing, where the accumulation of AGEs can damage elastin and collagen (Kim et al., 2017). In addition, one study reported that knockdown of deubiquitinase, ubiquitin-specific protease 7 (USP7) in the *Drosophila* resulted in the reduced lifespan of fly and attenuated the ability to combat various kinds of stresses like oxidative stress, heat stress, suggesting that USP7 is also involved in the regulation of ageing (Cui et al., 2020). Moreover,

PAD enzymes are involved in the citrullination of proteins, and a study reported that expression levels of PAD2 enzymes increased with age in mice brains, leading to an increase in protein citrullination, suggesting that protein citrullination also contributes to ageing (Shimada et al., 2010).

6. Implementations of PTMs on different signaling cascade in NDDs

PTMs are also involved in the regulation of various biological signal transduction pathways. Phosphorylation is the most commonly observed PTM in different signal transduction pathways. However, other PTMs like acetylation, SUMOylation, glycosylation, glutathionylation, palmitoylation, S-nitrosylation, and nitration can also be observed in some signaling pathways. These signal transduction pathways have been found to play a crucial role in the pathogenesis of NDDs. This section will discuss different signaling pathways implicated in NDDs and how different PTMs are implemented in these signaling pathways (Fig. 3).

6.1. PI3K/Akt/GSK3β

Phosphatidylinositol 3-kinase (PI3K)-AKT signaling pathway is a significant regulator of a plethora of cellular processes like cell proliferation, apoptosis, cell survival, autophagy, metabolism and cell growth (Heras-Sandoval et al., 2014; Song et al., 2005; Xu et al., 2020). In the PI3K-AKT pathway, binding of ligands (cytokines, growth factors, hormones) to their specific cell-surface receptors leads to receptor activation, which then recruits and activates the lipid kinase PI3K. Activated PI3K then phosphorylates membrane lipid phosphatidylinositol 4, 5-bisphosphate (PIP2), converting it into phosphatidylinositol (3,4, 5)-trisphosphate (PIP3), which acts as a second messenger, mediating remaining intracellular signaling (Rai et al., 2019). Further, PIP3 mobilizes AKT to the plasma membrane and docks with AKT via the pleckstrin homology (PH) domain of AKT (Rai et al., 2019). This binding of AKT leads to conformational changes in AKT, which allows phosphorylation of AKT at T308 by phosphoinositide-dependent kinase 1 (PDK1) and at S473 by mammalian target of rapamycin complex 2 (mTORC2), resulting in full activation of AKT (Chan et al., 2014). This fully activated AKT then further regulates desired cellular processes via phosphorylation of downstream substrates like GSK3, mammalian target of rapamycin complex 1 (mTORC1), FOXOs. It has been reported that O-GlcNAcylations of AKT at T305 and T312 can thwart interaction between PDK1 and AKT, thereby inhibiting phosphorylation of AKT at T308, resulting in the reduced biological activity of AKT (Wang et al., 2012). Conversely, AKT SUMOylation at K276, amplifies its kinase activity (Lin et al., 2016). Likewise, it has been observed that oxidation of AKT at C60 and C77 of its PH domain amplifies the affinity of AKT towards PIP3 and facilitates AKT translocation to the plasma membrane (Su et al., 2019). Another study reported that K63 ubiquitination of AKT by E3 ligase TRAF6 promotes AKT membrane translocation and amplifies its phosphorylation (Yang et al., 2009). Moreover, PI3K-AKT signaling has been implicated in various NDDs. We know that GSK3β is the major kinase responsible for tau hyperphosphorylation, and it is also a downstream substrate for AKT. AKT can downregulate GSK3β by phosphorylating GSK3β at S9. One study showed that tau hyperphosphorylation was decreased by activating the PI3K-AKT pathway, which downregulated the activity of GSK3β (Baki et al., 2004). Conversely, another study on AD has shown that sulfhydration of AKT at C77 thwarts phosphorylation of GSK3β by AKT, thereby promoting tau phosphorylation by GSK3β (Sen et al., 2020). Additionally, a study on human neuronal cells showed that acetylation of AKT at K163, K377, under an HDAC6 inhibitor's presence impairs AKT's kinase activity (Iaconelli et al., 2017). Interestingly, it has been reported that SIRT1 promoted axon development by deacetylation of AKT, which activated the AKT pathway, leading to GSK3β inhibition (Li et al., 2013). Further in AD, AGEs can also stimulate tau hyperphosphorylation by suppressing the AKT pathway, thus activating GSK3 through upregulation of receptors for advanced glycation end products (RAGE) (Li et al., 2012). Additionally, it has been observed that the S-nitrosylation of PTEN leads to its inactivation, resulting in elevation of PI3K-AKT, which can protect against Aβ neurotoxicity (Kwak et al., 2010). Furthermore, myristoylated AKT has been reported to promote neuroprotection by preventing axonal degeneration (Cheng et al., 2011). Moreover, it has been observed that AKT protects against huntingtin-induced neurotoxicity by phosphorylating ADP-ribosylation factor interacting protein-arfaptin2 at its S260 residue (Rangone et al., 2005). Likewise, another study reported that AKT activation by an insulin-like growth factor-1 (IGF-1) shows a beneficial effect against huntingtin-induced toxicity by phosphorylation of huntingtin at S421 by AKT (Rangone et al., 2005). Further, it has been reported that AKT phosphorylates ataxin-1 at S776, which stimulates binding of ataxin-1 with 14-3-3 protein, interaction of 14-3-3 protein with ataxin-1 results in accumulation and aggregate formation of ataxin-1, thus contributing towards neurodegeneration in SCA1 (Chen et al., 2003). Moreover, AKT has a role to play in PD as well, as one research showed that overexpression of PINK1prevents cell death in the SH-SY5Y cell model of PD, through enhanced phosphorylation of AKT at S743, by activated mTORC2 (Murata et al., 2011). Likewise, another study reported that overexpression of DJ1 in SH-SY5Y and PC-12 cell model of PD lead to an increase in phosphorylation of AKT at T308, which resulted in improved mitochondrial functions.

6.2. Wnt signaling pathway

Wnt signaling pathway is another important biological pathway involved in cell polarity, cell fate, cell migration, and cell proliferation (Inestrosa and Toledo, 2008; Komiya and Habas, 2008). Wnt proteins are an evolutionarily conserved glycoprotein family whose function gets activated in the ER through glycosylation at asparagine and palmitoylation at cysteine residues (Coudreuse and Korswagen, 2007; Kurayoshi et al., 2007; Takada et al., 2017). The canonical/β-catenin pathway is the most widely studied Wnt pathway in various disease conditions, where cytoplasmic protein β-catenin plays a significant role. In the canonical/β-catenin pathway, during the absence of Wnt ligands, the intracellular β-catenin protein is bound to a β-catenin destruction complex made up of proteins like Axin, adenomatous polyposis coli (APC), GSK3β, and CK1 (Palomer et al., 2019). Firstly, in this destruction complex, CK1 phosphorylates β-catenin at S45, which is followed by phosphorylation of β-catenin at S37, S33, and T41 by GSK3β (Gao et al., 2014). Further, phosphorylation of β-catenin triggers ubiquitination by E3 ligase β-transducin repeats containing proteins (β-TrCP), leading to its degradation through the UPS (Nusse and Clevers, 2017). In this way, the β-catenin destruction complex maintains a low level of β-catenin in the cytoplasm during the absence of Wnt ligands, thus promoting transcriptional inactivation of Wnt signal-related genes. However, when Wnt ligands bind to its seven-transmembrane Frizzled receptors and low-density lipoprotein receptor-related protein 5/6 (LRP 5/6) co-receptors, it activates an intracellular signal cascade, which deactivates the β-catenin destruction complex via interaction with Dishevelled (Dsh) protein, leading to stabilization and accumulation of β-catenin in the cytoplasm (Oliva et al., 2013). β-catenin then moves into the nucleus where it interacts with T-cell factor/lymphoid enhancer factor (TCF/LEF) transcription factors leading to transcription/expression of Wnt target genes (Berwick and Harvey, 2012). It has been observed that the acetylation of β-catenin at K19 and K49 improves its stability and increases its transcriptional activity (Gao et al., 2014). Interestingly, one study reported that Wnt stimulation promotes the ADP-ribosylation of axin, which increases its affinity towards LRP6 receptors, thus amplifying β-catenin signaling (Yang et al., 2016). Conversely, it has been observed that the O-GlcNAcylation of β-catenin at S23 residue impedes its transcriptional activity (Ha et al., 2014). Likewise, another study showed that glycation of Wnt antagonizes

canonical signaling by repressing β-catenin and its transcriptional activity. Additionally, it has also been reported that myristoylated nkd2 thwarts β-catenin signaling by facilitating the proteasomal degradation of the Dsh protein (Hu et al., 2010). Furthermore, NEDD4L, a neddylation enzyme, also inhibits β-catenin signaling by promoting proteasomal degradation of the Dsh protein (Ding et al., 2013). Moreover, the role of the Wnt signal pathway has been observed in NDDs. It has been reported that inhibition of the Wnt signal pathway amplifies GSK3β activity leading to tau hyperphosphorylation (Mercado-Gómez et al., 2008). Another study reported that canonical Wnt pathway activation reduced tau phosphorylation level in AD by increasing β-catenin levels, thereby inhibiting GSK3β, thus preventing cell death (Alvarez et al., 2004). In another study, it was reported that dickkopf related protein 1 (DKK1), which acts as Wnt antagonist, can inhibit canonical/β-catenin signaling, further leading to tau hyperphosphorylation in AD brain (Caricasole et al., 2004). Additionally, Wnt has been implicated in ALS as well, as one analysis done on the transgenic mice model of ALS, reported that activation of the Wnt pathway inhibits the activity of GSK3β in the pathogenesis of ALS, which can augment cell proliferation (Chen et al., 2012a).

6.3. AMPK signaling pathway

Adenosine monophosphate-activated protein kinase (AMPK) is a serine/threonine kinase regulating cellular energy metabolism (Assefa et al., 2020). AMPK, a heterotrimer protein kinase, comprises of three subunits, namely α, β and γ (Curry et al., 2018). Here, α acts as a catalytic subunit, whereas, β and γ are regulatory subunits. All these three subunits have several isoforms such as α1-α2, β1-β2, γ1-γ2-γ3, respectively (Yan et al., 2018). Further, the γ subunit is comprised of four nucleotide-binding cystathionine-beta-synthase (CBS) domains, which act as binding sites for adenosine monophosphate (AMP), adenosine diphosphate (ADP), and adenosine triphosphate (ATP) (Yan et al., 2018). During the conditions of energy scarcity, when the AMP:ATP ratio is increased, AMP is allosterically attached to the γ domain of AMPK, resulting in conformational changes in AMPK through phosphorylation of its α subunit at T172 by various kinases like liver kinase B1 (LKB1), transforming growth factor-beta activated kinase 1 (Tak1), Calmodulin dependent protein kinase kinase-β (CaMKKβ) (Peixoto et al., 2017). Phosphorylation of AMPK at T172 amplifies its activity, resulting in fully activated AMPK, which then regulates downstream substrates like acetyl CoA carboxylase (ACC), unc-51 like autophagy activating kinase 1 (ULK1), tuberous sclerosis complex 1/2 (TSC1/2), and sterol regulatory element-binding protein (SREBP) via phosphorylation (Peixoto et al., 2017). By regulating these downstream substrates, AMPK switches off all energy-consuming anabolic pathways and amplifies all energy releasing catabolic pathways (Sanz et al., 2013). It has been observed that the myristoylation of the AMPK β subunit promotes allosteric binding between AMP/AMPK and phosphorylation of the T172 site of α subunit during ATP depletion conditions (Oakhill et al., 2010). Likewise, another study has shown that SUMOylation of the AMPKβ2 subunit through SUMO2 amplifies the total activity of AMPK (Rubio et al., 2013). Besides, H_2O_2 mediated oxidation of α and β subunit's cysteine residues of AMPK increases the kinase activity of AMPK (Cardaci et al., 2012). Interestingly it has also been reported that H_2O_2 mediated S-glutathionylation at C299 and C304 of AMPK α subunit facilitates AMPK activation (Klaus et al., 2013; Zmijewski et al., 2010). Conversely, it has been observed that α and γ subunits undergo O-GlcNAcylation, and inhibition of O-GlcNAcylation suppresses AMPK activation (Bullen et al., 2014). Likewise, one study reported that ubiquitin ligase cidea suppresses AMPK activity by ubiquitin-dependent proteasomal degradation of the AMPK β subunit (Zungu et al., 2011). Moreover, the AMPK pathway has been implicated in many NDDs. Tau acetylation promotes neurofibrillary tangle formation in AD. One study reported that AMPK reduces tau acetylation by activating SIRT1. In this study, AMPK activated SIRT1 by enhancing nicotinamide adenine dinucleotide (NAD^+) concentration, followed by deacetylation of tau by SIRT1 (Wang et al., 2020b). Further, one study reported that AMPK showed neuroprotective effects in the *Drosophila* model of PD. The activation of AMPK leads to the phosphorylation of downstream target peroxisome proliferator-activated receptor-gamma coactivator-1α (PGC-1α), ameliorating dopaminergic degeneration (Ng et al., 2017). Moreover, it has also been reported that AMPK activation protected against oxidative stress induced by advanced glycosylation end products in human neural stem cells (Lin et al., 2017). Furthermore, a study on Huntington's disease reported that activation of AMPK-α1 stimulated cell death by downregulating B-cell lymphoma 2 (BCL-2). AMPK has been shown to downregulate survival gene BCL-2 by decreasing phosphorylation of the transcription factor- CREB at its S129 and S133 residues, which leads to inhibition of CREB activity (Ju et al., 2011). Additionally, another study on HD reported that S-nitrosylation of IKKβ resulted in decreased phosphorylation of AMPK, which enhanced mTORC1 activity leading to autophagy inhibition (Sarkar et al., 2011).

6.4. MAPK signaling cascade

Mitogen-activated protein kinase (MAPK) signaling pathway is a biological signal pathway regulating cell proliferation, cell survival, differentiation, immune response, apoptosis, and stress response (Soares-Silva et al., 2016; Sun et al., 2015). There are three crucial MAPK families involved in intracellular signal transduction: p38 MAPK, JNK, and extracellular signal-regulated kinase 1/2 (ERK 1/2) (Du et al., 2019). Each MAPK family is activated by a sequential cascade of three specific enzymes that work in tandem with each other, namely MAP3K, MAP2K, and MAPK (Kim and Choi, 2010). First of all, MAP3K turns on through phosphorylation when an extracellular ligand binds to cell receptors, MAP3K then phosphorylates and activates MAP2K, activated MAP2K then turns on MAPK by phosphorylation of MAPK at threonine and tyrosine residues (Albert-gasc et al., n.d.). Activated MAPK then phosphorylates various downstream substrates at serine, threonine residues to regulate different cellular processes. ERK 1/ 2 gets activated in response to growth factors and hormones, whereas p38 and JNK are mainly activated under various stress stimuli (Cowan and Storey, 2003; Du et al., 2019). MAPK families have been implicated in different NDDs. One study done on the *Drosophila* PARKIN mutant model of PD reported that loss of E3 ligase PARKIN resulted in JNK signaling activation, which contributed to dopaminergic degeneration. However, this study also observed that E3 ligase PARKIN's overexpression inhibits JNK signaling via ubiquitination (Cha et al., 2005). Further, it has been observed that the palmitoylation of JNK3 is actively involved in the modulation of axonal development and branching (Yang et al., 2012). Additionally, one study reported that ER stress-activated JNK3 phosphorylates APP at T668, which results in Aβ aggregation (Yoon et al., 2012). Another study showed that D-aspartate promotes abnormal JNK phosphorylation, which further increased SUMO1 protein level and tau phosphorylation, suggesting that JNK has a role to play in the SUMOylation process (Nuzzo et al., 2019). Likewise, it has been observed that oxidative stress can activate the JNK signaling pathway, which promotes SUMOylation of ataxin-1, leading to its aggregation (Ryu et al., 2010). Furthermore, experimental study on HD model showed that abnormal JNK1 S-nitrosylation could inhibit its autophagic activity (Nakamura et al., 2013). Moreover, a study on PD reported that overexpression of mutant α-synuclein leads to activation of p38 MAPK, which phosphorylates PARKIN at S131 residues, resulting in mitochondrial dysfunction and neuronal death (Chen et al., 2018). Further, a study on AD showed that oxidative stress-activated p38 MAPK, which results in tau hyperphosphorylation (Giraldo et al., 2014). Additionally, one study reported that deacetylase SIRT1 showed neuroprotection in the traumatic brain injury model by inhibiting the p38 MAPK pathway, suggesting that acetylation modulates p38 (Yang et al., 2017). Another study on AD reported that JNK and p38 kinases might be involved in tau hyperphosphorylation during the early stages of AD (Pei et al., 2001).

Interestingly, one study observed that p38 promotes the O-GlcNAcylation of neuronal proteins during glucose deprivation, increasing their solubility (Cheung and Hart, 2008). Moreover, a study observed that ERK activation could protect against retinal neuronal cell death induced by advanced glycation end products (Shen et al., 2010). Additionally, a study on the ALS model observed aggregation of aberrantly phosphorylated ERK 1/ 2 in motor neurons along with aggregates of TDP-43, suggesting dysfunction of the ERK pathway (Ayala et al., 2011).

7. Mechanistic role of PTMs on cellular process in NDDs

NDDs are characterized by improper functioning of a specific population of neurons, determined by clinical manifestations. The aggregation and abnormal functioning of misfolded proteins are associated with neuronal loss, which is the key feature of many neurodegenerative proteinopathies. These abnormal protein dynamics are because of the insufficiency of some cellular processes like autophagy and mitochondrial dysfunction, which ultimately lead to cell death. This section briefly discusses the implementation of different PTMs in deregulated cellular processes involved in NDDs (Fig. 4).

7.1. Autophagic pathway

Autophagic/lysosomal degradation is a significant cellular response to stress where autophagosomes containing cytosolic constituents are transported into the lysosome for degradation, which is essential for protein homeostasis and cell health. The degradation of long-lived protein aggregates is majorly carried out by autophagy, but many different PTMs are implemented to deregulate this process, leading to NDDs.

In AD, Autophagy is the primary pathway for the degradation of APP and APP cleavage products, including Aβ (Sun et al., 2016). In tau protein, autophagy dysfunction leads to tau aggregates' formation, which significantly affects Tau phosphorylation. In addition, tau hyperphosphorylation causes uncertainty in microtubule, which further halt autophagosome-lysosome fusion, leading to aggregation of immature autophagosomes (Li et al., 2017). The primary suppressor of autophagy initiation is the mTOR protein kinase, which is heavily autophosphorylated at S2481 in AD (Díaz-Troya et al., 2008). Furthermore, inhibition of BCL-2 on beclin 1 is weakened by either phosphorylation of BCL-2 by JNK-1 or by phosphorylation of beclin 1 by DAPK1, thus promoting autophagy (Ribarič and Milisav Ribarič, 2020). Experimental evidence showed a direct link between proteolytic cleavage of beclin 1 and apoptotic cell loss in the AD brain, where they indicated that the cleavage state of beclin 1 determines the functional involvement in both neurodegeneration and neuroprotection (Bieri et al., 2018). A study found that SIRT2, HDAC6 and p300 stimulate Tau phosphorylation and autophagic flux in AD, and the results also included that HDAC4 and p300 modulate Tau acetylation (Esteves et al., 2019). Another finding demonstrated that tau accumulation suppresses IST1 transcription, where the mechanism involves ANP32A-regulated mask of histone acetylation, which further represses autophagosome-lysosome fusion (Feng et al., 2020). A finding directs that SUMOylation might be involved in the autophagy-lysosome pathway in tauopathies. In progressive supranuclear palsy (PSP) brain tissues, SUMO1 colocalizes within perinuclear tau-positive inclusions in oligodendrocytes and label lysosomes oligodendrocytes containing tau inclusions, in contrast to those where tau aggregates are absent (Kontaxi et al., 2017). Moreover, the Oxidation of Aβ at M35 inhibits the autophagy pathway (Nixon, 2007).

Likewise, in PD, research efforts from several decades talk about the role of PTMs in impaired autophagy machinery during PD pathogenesis. A study showed that the Oxidation of methionine residues of α-synuclein inhibits autophagy (Kumar et al., 2020). Moreover, phosphorylation of α-synuclein at S129 controls autophagic clearance of inclusions prominently found in Lewy bodies (Kleinknecht et al., 2016). An interesting study showed that α-synuclein is acetylated at K6 and K10, but SIRT-2 deacetylates the same residues of α-synuclein, which increases transcriptional repression. Thus, α-synuclein aggregation and autophagy are modulated by the level of genetic manipulation of SIRT-2 (de Oliveira et al., 2017b). Another finding demonstrated that NLRP3 inflammasome is involved in PD progression and kaempferol (Ka), a small molecule, that can inhibit neuroinflammation through the cooperation of ubiquitination and autophagy (Han et al., 2019). It is observed that in primary cortical neurons of rats, GlcNAcylation of persistent protein due to specific inhibition of GlcNAcase activates mTOR, which further decreases autophagy and increases α-synuclein accumulation (Zulueta et al., 2020). Some evidence reports that overproduction of NO can be neurotoxic through S-nitrosylation of PARKIN, contributing to the accumulation of misfolded protein and disrupting the autophagic degradation of these misfolded proteins (Martínez-Ruiz et al., 2005; Nakamura et al., 2013). Further, several genetic variants contribute to the pathogenesis of PD, where leucine-rich repeat kinase (LRRK2) is majorly associated with neuropathological phenotypes in PD and ubiquitination at K63 signals the degradation of LRRK2 by the autophagy-lysosome pathway (Pajarillo et al., 2019). Polo-like kinase 2 (PLK2)- induced phosphorylation does not affect α-synuclein aggregation, but PLK2 directly binds to α-synuclein to regulate its clearance through the lysosome-autophagic degradation pathway, which proposes a neuroprotective role of PLK2 against PD pathology (Oueslati et al., 2013).

In HD, the degradation process is initiated when there is a mhtt, which leads to the activation of the autophagic pathway (Vidal et al., 2011). The presence of mhtt increases autophagosome formation but disturbs its motility and eventually stopping its fusion with lysosomes, which causes neuronal toxicity (Kumar et al., 2018; Lee, 2012). Several PTMs are implemented in autophagic dysfunction leading to the pathogenesis of HD. A study showed that abnormal S-nitrosylation of JNK1 and IKKβ inhibits autophagy in HD models (Sarkar et al., 2011). Another study directs that MAP1S interacts with autophagy marker LC3, which regulates the autophagy flux, but HDAC4 destabilizes the MAP1S, which suppresses the autophagic flux and promotes accumulation of mhtt aggregates due to MAP1S deacetylation (Yue et al., 2015). However, a study suggests that increased acetylation at K444 facilitates the trafficking of mhtt into autophagosomes, further improving the mutant protein's clearance by macroautophagy and reversing the toxic effects of mhtt (Jeong et al., 2009). Moreover, Deubiquitinase, Usp12, is neuroprotective in HD, which proved to improve the autophagic degradation of mhtt in rodent and patient-derived neurons (Lontay et al., 2020).

Further, p97, which is involved in removing damaged lysosomes by autophagy, has been linked to neurodegenerative disorders. It has been studied that palmitoylation of p97 at C105 promotes its participation in various cellular processes. Moreover, the accumulation of abnormal protein induces p97 phosphorylation at S612 and T613 and acetylation at K614, allowing p97 translocation, which further leads to the suppression of transcription through histone protein deacetylation, and thus the removal of misfolded protein by autophagy (Hänzelmann and Schindelin, 2017). INCL is a neurodegenerative lysosomal storage disease (LSD) initiated by the inactivation of mutation in the CLN1 gene, encoding palmitoyl-protein thioesterase-1 (PPT1). This lysosomal enzyme catalyzes the removal of palmitate residues from S-palmitoylated proteins, which is required for their degradation and clearance by lysosomal hydrolases. Moreover, Rab7, which is a small GTPase, is vital for autophagosome-lysosome fusion, and the study confirmed that C205 is the authentic S-palmitoylation site in Rab7 and C207 undergoes S-palmitoylation or, in some cases, prenylation (Sarkar et al., 2020). Studies also suggest that peroxynitrite could be a player in multiple sclerosis pathology, and peroxynitrite production induces nitration of dynamin-related protein 1 (Drp1) for mitophagy activation (Li et al., 2019). Some other studies suggest that O-GlcNAcylation regulates autophagy at multiple neurodegeneration levels, like reducing O-GlcNAcylation enhances autophagosome-lysosome fusion. Thus,

elevating autophagic flux and contrary to that O-GlcNAcylation of SNAP29, a SNARE protein inhibits autophagosome-lysosome fusion and autophagic flux. In addition to that, O-GlcNAcylation may also inhibit the autophagic pathway by decreasing the ATG protein level (Guo et al., 2014; Kumar et al., 2014; Park et al., 2015; Wani et al., 2017). The intronic C9orf72 G4C2 expansion is the most common cause of ALS and FTD, which produces non-ATG (RAN) proteins. In an experiment, the researchers designed high-affinity antibodies targeting GA and GP RAN proteins, which demonstrated that glycosylation of the Fc region of α-GA_1 is essential for cell entry. Glycosylated Fc region further interacts with TRIM21 resulting in a reduction of GA levels and co-aggregation of autophagic proteins to GA aggregates, leading to decrease neurological defects (Nguyen et al., 2020).

7.2. Mitochondrial dysfunction

Several decades of studies have realized that mitochondrial dysfunction plays an essential role in the pathomechanism of several NDDs (Johri and Beal, 2012). Mitochondrial dysfunction under any pathological conditions will increase nitroxidative stress, stimulating the PTMs of mitochondrial protein and might also cause oxidative damage to mitochondrial DNA (Lin and Beal, 2006).

In AD, Aβ translocates to the mitochondrial membrane, where it encourages intracellular calcium ion release and promotes excess accumulation of these ions to open the mPTP and damage the structure of mitochondria (Moreira et al., 2010). These opening further leads to a drop in the electrochemical gradient causing activation of apoptosis-inducing factors and caspases, which finally results in AD progression (Reddy, 2009). Many PTMs are responsive to the stressful and changing environment in which mitochondria exerts functions like phosphorylation, acetylation, ubiquitination and succinylation (Gómez-Serrano et al., 2018). Likewise, SUMOylation has been implicated in impaired mitochondrial function and high-stress conditions. Interaction of SUMO1 with Aβ and phosphorylated Tau causes an increase in oligomers' formation, whereas interaction with SUMO2/3 increases their solubility (Henley et al., 2018). However, studies suggest that N-acetylcysteine may decrease mitochondrial-related oxidative stress in AD patients. Oxidative stress at some sites may facilitate tau phosphorylation, which may be modified in AD patients. Tau protein is involved in the axonal transport of organelles like mitochondria; the hyperphosphorylated Tau might block the mitochondrial transport leading to energy deprivation and causing neurodegeneration. Moreover, abnormal communication of hyperphosphorylated tau and mitochondrial fission protein dynamin-like protein 1 (Drp-1suggests a relationship with mitochondrial dynamics alternation (García-Escudero et al., 2013). Furthermore, a study states that Drp1 S616 phosphorylation is likely to be involved in mitochondrial fragmentation and Drp1 over activation in AD (Dowding et al., 2014). It is important to note that certain proteins aid in mitochondrial transport like motor protein (kinesin 1 and dynein) and mitochondrial protein adaptors (RhoT1/T2, syntaphilin, and TRAK2). Interestingly, truncated tau expression significantly increases the association of TRAK2 with mitochondria, expressing full-length tau, and caspase-cleaved tau may affect mitochondrial transport due to an increase of TRAK2-mitochondria binding and therefore reducing the ATP production available for the transportation of mitochondria (Quintanilla et al., 2020).

Moreover, mitochondrial dysfunction has been reported with the complex I deficiency and impaired electron transfer in substantia nigra in PD. PTMs are the critical processes in regulating the stability, localization, and function of proteins (Bose and Beal, 2016). It has emerged as essential modulators of pathogenic mechanisms of α-synuclein and LRRK2. Aberrant PTMs altering phosphorylation, ubiquitination, nitration and truncation of these proteins promote PD pathogenesis, while other PTMs such as SUMOlyation may be neuroprotective (Rocha et al., 2018). One of the mechanisms describes the regulation of mitochondrial recycling by autophagy involving the E3 ubiquitin ligase PARKIN which ubiquitinates several mitochondrial proteins, such as voltage-dependent anion-selective channel 1 (VDAC1) and mitofusion that may be involved in the segregation of damaged mitochondria via inhibition of mitochondrial fusion events (Gegg et al., 2010). Furthermore, mitochondrial complex I inhibition by NO-mediated S-nitrosylation has been observed in multiple PD models (Chinta and Andersen, 2011). In addition to that, studies done on mitochondria of the PD brain indicate that oxidation of complex I subunits can result in disassembly of mitochondria and reduce its function (Keeney et al., 2006). Oxidative stress and mitochondrial dysfunction trigger glycation, affecting several mitochondrial proteins (Videira and Castro-Caldas, 2018). In PD, tyrosine nitration generates 3-nitrotyrosine whose elevated concentration results in its accumulation in the frontal cortex region, which causes mitochondrial dysfunction (Murray et al., 2003). Moreover, phosphorylation of acetyl-CoA carboxylase 1 (ACC1), recruited by phosphorylated α-synuclein, induces mitochondrial fragmentation through reduced lipoylation (Grassi et al., 2018). Experimental evidence showed that carnitine palmitoyltransferase I (CPTI) inhibitor, etomoxir, reduced mitochondrial fusion dynamics in a time-dependent manner, and dichloroacetate can partially stop this reduction caused by the parkinsonian inducing neurotoxin, 1-methyl-4-phenylpyridinium (MPP^+), thus, restoring normal mitochondrial fusion dynamics (O'Hara et al., 2019). In addition to that, quercetin could also reverse MPP^+-induced mitochondrial dysfunction and lipopolysaccharide (LPS)-induced neuroinflammation in PD (Kang et al., 2020).

Further, the altered mitochondrial structure is one of the hallmarks of HD that correlates with mitochondrial dysfunction in all HD cell types (Oliveira, 2010). It has been anticipated that mhtt mediated mitochondrial abnormalities significantly affect Medium Spiny Neurons (MSNs) due to this neuronal subtype (Pickrell et al., 2011). Altogether, PTMs play a very vital role in the regulation of htt function. A study suggests that increased acetylation of PGC-1α leads to mitochondrial dysfunction (Lee et al., 2018). Another study suggests that phosphorylation of Drp1 at S40 and S44 by GSK-3β promotes the GTPase activity of Drp1, which results in increased mitochondrial division. In addition to that, CDK5 triggers over-activation of Drp1 by phosphorylating S579 in HD mouse striatal cells, which is linked to mitochondrial dysfunction (Guo et al., 2018; Intihar et al., 2019).

Mitochondrial dysfunction has also been reported in ischemia as a response to oxidant generation due to mitochondrial succinate aggregation and superoxide radicals in the brain (Chouchani et al., 2014). In epilepsy, elevated kainic acid concentration has been observed that further hampers the mitochondrial activity by downregulating mitochondrial complex I (CI). A study demonstrated that carbonylation of R76 residue of CI results in structural changes in the complex, thereby hampering mitochondrial activity (Ryan et al., 2012). Further, NO-mediated reversible PTMs of thiols possibly result in CI inhibition, which results in eliminating the Cysteine residue or direct interactions with Fe to form dinitrosyl. This exposure results in the downregulation of thiol content signifying the role of NO in S-nitrosylation mediated CI inhibition under diseased state (Srinivas Bharath, 2017). Oxidation of Cysteine can result in S-glutathionylation, S-nitrosylation, and sulfenylation (SOH), sulfinic (SO2H) and sulfonic acid (SO3H) modifications coding for PD onset and mitochondrial dysfunction by inhibiting CI (Schilling et al., 2005; Chung et al., 2013). In age related disorders, side chains of K, R, P and T amino acid residues have been observed to be prone to protein carbonylation that induces oxidative stress and potentially hampers mitochondrial function (Marnett, 1997). Experimental evidence directed that exposure of Chlorpyrifos (CPF) on LUHMES cells increases the activation of STAT1 and phosphorylation of the same at Y701 and S727 leads to cleavage of protein kinase C delta (PKCδ), which further leads to an increase in mitochondrial dysfunction (Singh et al., 2018). Another research stated that truncated mature frataxin (79-207) is primarily found in mouse liver cytosol. In contrast, normal frataxin (78-207) is present in mitochondria, thus supporting the role of extra-mitochondrial frataxin in Friedreich's ataxia etiology and

its implication on mitochondrial dysfunction (Weng et al., 2020). Cocaine abuse can also lead to neuronal dysfunction as evidence suggests that cocaine impairs the activity of DNA methyltransferases (DNMTs), which further impacts mitochondrial DNA. (Sivalingam and Samikkannu, 2020).

8. Post translational modification enzymes as drug targets in pathogenesis of NDDs

Emerging evidence suggests the mechanistic involvement of aberrant PTMs in the pathogenesis of NDDs such as AD, PD, ALS, HD, multiple sclerosis, and frontotemporal dementia. Alteration in PTMs causes misfolded protein aggregates, which increases neurotoxicity through disrupted cell signaling cascades. These impeding cell signaling pathways hamper the biological process such as autophagy and mitophagy, inflammatory response, cell-cycle regulation, and mitochondrial function, which are the major causes of neuronal cell death. Recent studies demonstrated the implications of drug molecules and natural biomolecules targeting different PTM enzymes in the NDDs therapeutics. Drug molecules or natural biomolecules act as either inhibitors or activators of particular PTM enzymes (Table 3). For example, In AD, hyperphosphorylation of Tau at S396 residue by GSK-3 results in the formation of neural fibrils accumulate, leading to tau aggregation. SAR502250 (Griebel et al., 2019), curcumin (Sathya and Devi, 2017), 6-hydroxydopamine (Morales-García et al., 2013) have been reported to downregulate GSK3 activity, thus reducing tau aggregation. Similarly, BACE1 is an exciting target for AD therapeutics, which phosphorylates Aβ with the help of enzymes such as γ-secretase and β-secretase that cleaves APP, and thus, results in the aggregation and formation of Aβ plaques. Verubecestat, Lanabacestat, and Elenbacestat (E-2609) are considered as BACE1 inhibitors, but their phase-III trial was discontinued due to their respective inefficacy (Egan et al., 2018; Volloch and Rits, 2018). Likewise, palmitoylation of APP leads to enhanced APP cleavage by BACE1, leading to amyloidogenesis. However, inhibition of Sterol O-acyltransferase (ACAT) with CP-113818 reduces the APP palmitoylation level and can be used in AD therapeutics (Bhattacharyya et al., 2013; Hutter-Paier et al., 2004) (Fig. 5).

Moreover, TDP-43 deacetylation by histone deacetylase (HDAC) at K154 and K192 leads to hyperphosphorylation of TDP-43, which causes the formation of peptide aggregates that promote ALS pathogenesis (Sanna et al., 2020). In the SOD1-G93A mouse model, sodium butyrate and trichostatin inhibit HDAC activity promoting neuroprotection (Sanna et al., 2020). In embryonic mouse model 31B12A, scFv was observed to prompt HSP70 mediated chaperone autophagy activation resulted in TDP-43 aggregates inhibition (Tamaki et al., 2018). Similarly, in a study, it was demonstrated that α-synuclein glycation potentiated aggregation via magnesium oxide-induced oligomerization in mice and *Drosophila* (Vicente Miranda et al., 2017). Further, glycation hampers the ubiquitination of α-synuclein, thereby reducing its degradation, which could be reversed with magnesium oxide inhibitors like aminoguanidine (Thornalley, 2003). Furthermore, In AD, it has been reported that AGEs elevate oxygen radicles, thereby increases APP activity (Ko et al., 2015). However, increased reactive oxygen species (ROS) activity was suppressed by resveratrol via β-secretase downregulation (Ko et al., 2015). Furthermore, Aβ nitration at Y10 is a bit contradictory. An early study reported that Y10 nitration by peroxynitrite enhances aggregate formation, which was found in amyloid plaque core in the AD mice model (Kummer et al., 2011). However, a recent experiment showed that Y10 nitration notably curbed amyloid aggregation. The aggregates formed in the former study, when treated with L-NIL, accounted for reduced 3NTyr10-Aβ in APP/PS1 mice (Zhao et al., 2017). Similarly, in AD, SUMOylation of BACE1 at K501 residue escalated its stability, thereby altering the APP that later generates Aβ plaque (Bao et al., 2018). BACE1 inhibitors are reported to retard its activity and suppress APP cleavage. SOD-1 SUMOylation enhances protein misfolding that results in the formation of an inclusion body. MIF is observed to reduce inclusion body formation here by curbing aggregate formation (Shvil et al., 2018). Similarly, ubiquitin sequestering in inclusion bodies retards the proteasomal activity and result in the progression of NDDs.

Ubiquitination of α-synuclein at K10, K23 downregulates the protein clearance resulting in inclusion bodies in AD. Furthermore, neural precursor cell expressed developmentally down-regulated protein 4 (Nedd4) enhances the α-synuclein clearance as it is reported to interact directly with it by promoting ubiquitination at K63 (Huang et al., 2019). α-synuclein SUMOylation at K96 and K102 mediated by phytochrome-interacting ankyrin-repeat protein 2 (PIA2) suppresses the proteasomal degradation and elevates protein aggregates that promote PD, SiRNA can knock out the PIA2 UPS suppression and can enhance monoubiquitination of α-synuclein (Rott et al., 2017). Likewise, the succinylation of APP at K687 residue hampers its degradation and escalates Aβ aggregation. It was observed that the succinylated APP, along with Aβ agglomerates, was present in the hippocampus of a transgenic mouse for AD due to diminished brain glucose regulation (Wang et al., 2020a). In one experiment, inhibition of agglomerates by donepezil was observed in BCCAO rats, and donepezil escalated sorting Nexin 33 (SNX33) level in cortical neurons resulting in reduced agglomerates (Takada-Takatori et al., 2019). Moreover, one carbon methylation can perturb normal DNA; this single carbon manipulation result in AD by generating Aβ agglomerates. DNMTs, ten-eleven translocation methylcytosine dioxygenase 1 (TET-1), were associated with AD onset. The use of EGCG DNMT inhibitors has been shown to curb agglomerate growth (Wood, 2018).

9. Targeting post-translational modifications through intrabodies: a clinical approach

Apart from current PTM detection and targeting methods such as mass spectroscopy, small molecule inhibitors or activators and RNA interference, several new technologies have been developed for targeting PTM types. These techniques will enable us to target specific PTM types with high precision and specificity. Further, these techniques play an essential function in targeting PTM proteome in the context of living cells. This section discusses our current knowledge about the development and prosecution of clinical technologies to identify particular PTM.

The current development and execution of the *de novo* method such as post-translational intracellular silencing antibody or PISA technology for targeting the PTM type that plays an essential role in identifying intricacies between the native protein and PTMs. In PISA technology, for an installed PTM type, the selection for the antibody domain (ScFv or single domain) is based on a cell cytoplasm environment. PISA technology relies on ICAT yeast two-hybrid system, based on the genetic interaction between antigen domain libraries and a target antigen bait. The PTM protein bait is developed through the genetic fusion of the target protein with the PTMs modifier enzyme's catalytic domain (Meli et al., 2009; Visintin et al., 1999). The catalytic domain consists of acetylases, kinases, ligases, methylases, AGEs, and others depending on the type of PTM modifier (Fantini et al., 2017; Visintin et al., 2002). In the first step, catalytic interaction between a target protein and PTM modifier was carried out, which allows the yeast's growth on histidine-lacking plates. Subsequently, counter-screening of the mutated version of bait followed by the expression of selected colonies of in bacteria was performed (Guo et al., 2004). Further, the antibody genes were tested for *in-vitro* interactions. In this manner, the genes encoding for the selected antibody domain will be used as intrabodies against a PTM protein *in-vivo*. The advantage of the PISA system is that it is designed in such a way that the epitope selected through the intrabody is a type of PTM itself. Intrabodies-based technologies significantly impact selected protein conformation and study disbalance in protein conformation due to particular PTM type, especially in the case of NDDs. In NDDs, protein misfolding and protein disturbed conformation has a crucial role in the disease progression (Meli et al., 2014; Vielemeyer

et al., 2010). A recent experiment demonstrated the involvement of conformation-sensitive anti-Aβ oligomers (AβOs) intrabodies in the process of Aβ oligomerization, which serves as a therapeutic target (Meli et al., 2009). Similarly, applications of intrabodies have been extended to other misfolded protein-mediated NDDs such as α-synuclein, PINK, htt, TDP-43, SOD1, and others. Applications of anti-PTM antibodies will be extended to a greater extent by adding different effector functions such as imaging, degradation, and cell death. These emerging techniques include the "AND" gate PTM FRET sensor, SIT system, PROTAC technique, and Trimaway method (Cattaneo and Chirichella, 2019).

In the "AND" gate PTM FRET technique, the generated intrabodies were fused to the desired protein so that it will capture the intracellular epitope and form its picture. For example, GPF-tagged anti-acetylated intrabodies will sense histone modifications *in vivo* (Sato et al., 2013). Further, PISA intrabodies fused with FRET sensor sets of proteins will produce "AND" gates, which are being used for clinical identification of particular PTM associated with disease pathogenesis. This PTM identification method plays an essential role in tracking the role of desired PTM in the cellular pathway (Siciliano et al., 2018). However, this method is generally restricted to histone modifications to date, and further investigations will be required to extract the potential of the "AND' gate PTM FRET method. Another technique for identifying the PTM associated with disease progression is suicide intrabody technology (SIT), which exploits E3 ubiquitin ligases for targeted degradation (Melchionna and Cattaneo, 2007). Herein, the generated intrabodies were fused with the ubiquitin-proteasome pathway substrate, which causes ligand-induced degradation of the target protein. For example, the tau protein's degradation during the pathogenesis of AD is associated with the SIT method. Similarly, the SIT was recently used to reverse the synaptic plasticity defects through intrabody fused with E3 ligase, which targets postsynaptic inhibitory response protein named gephyrin (Gross et al., 2016). The significant advantage of SIT is that it will enable selective PTM protein degradation without affecting the non PTM protein. Similarly, proteolysis targeting chimera (PROTAC) is an important protein degradation technique used for PTM identification. Sometimes SIT is considered as reminiscent of PROTAC for selective protein degradation. A PROTAC is a small heterobifunctional chemical molecule consisting of two ligands attached to a linker group. The two ligands are fused with an E3 ligase and a target protein that brings both towards each other. This will decrease the distance between the E3 ligase and protein of interest, enabling selective PTM protein degradation through the ubiquitin E3 ligase (Carmony and Kim, 2012; Lu et al., 2015). Both SIT and PROTAC enable selective knockdown and degradation of PTM protein without hampering non-PTM protein conformation. Likewise, the "AND" gate PTM FRET method, both SIT and PROTAC, were associated with ubiquitination, and thus, more studies will require to understand their involvement in other PTMs. Another intrabody mediated proteasome degradation method is Trimaway, which exploits the cellular functions of Trim21. Trim21 consists of a receptor known as Fc, which promotes the proteasomal degradation of target PTM protein. In this method, the gene encoded intrabodies were injected or electroporated into the target PTM cell coupled with recombinant Fc receptor (Clift et al., 2017).

10. Conclusion

NDDs are best characterized by the loss of neuronal cells, which causes memory impairment and learning disability. The primary reason behind neuronal cell death is misfolded protein aggregates that increase toxicity in the brain. Additionally, there are four significant phenomena, such as ubiquitin-proteasomal dysfunction, autophagy-lysosomal pathway impairment, aberrant PTMs, and molecular chaperone system deregulation, which are responsible for protein aggregation. Several decades of research has demonstrated the possible involvement of different PTMs such as methylation, acetylation, ubiquitination, SUMOylation, phosphorylation, citrullination, glycation and many others in the pathogenesis of NDDs. Further, alteration in PTMs causes an increase in ER stress and UPR, which is involved in the progression of life-threatening NDDs. Diverse studies showed that different PTM enzymes affect various signaling molecules such as Akt, PI3K, Wnt, β-catenin, AMPK, MAPK, p38, GSK3β, and others, which disrupt their orientation and structure, thus hampering the signaling cascade, which contributes to neuronal cell death. Moreover, alteration in PTMs causes an alteration in the different biological processes such as autophagy and mitophagy, cell-cycle deregulation, inflammatory response, and mitochondrial dysfunction, which leads to synaptic dysfunction and cognitive disability and ultimately causes neuronal cell death. Thus, there is a growing need for useful therapeutic molecules, either drug molecules or natural biomolecules that will target PTMs enzymes, which inhibits the formation of misfolded protein aggregates or promotes the clearance of toxic aggregates. However, there is an extensive repertoire of PTMs, and as the effect of PTMs is mostly carried out *in vitro*, it is difficult to predict the same *in vivo*. Furthermore, multiple PTMs might be taking part in the same site *in vivo*. Many PTMs act on protein residues, but their contribution to aggregation, clearance, and mechanism is unknown. In this review, we have addressed the influence of PTMs involved in proteins of different NDDs, causative effects of protein aggregation, and finally, therapeutics and key residues involved.

Recently published studies have also reported the impact of PTMs on protein quality control systems and indicated the important residues in various domains of proteins that are related to NDDs (Olzscha, 2019; Schaffert and Carter, 2020). However, we highlight the implementation of PTMs on different signaling cascades and in-depth analysis of PTMs in ageing, which is consolidated for the first time and no one has reviewed so far. We have also highlighted those PTMs that are unfamiliar and open a new avenue for the neuroscientific fraternity to work on NDDs in palmitoylation, nitrosylation, sulfhydration, succinylation, glutathionylation, carbonylation, crotonylation, neddylation, and racemization. Moreover, picturesque and detailed figures provide a comprehensive application of PTMs in NDDs. Thus, we have summarized the current understanding on this topic to potentiate the development of therapies to modify PTMs involved in protein aggregation to provide therapeutic and diagnostic tools for NDDs.

Author's contribution

Conceived and designed by P.K. Materials collected and art work done by R.G., M.S., D.S., S.T. Critical evaluation and analysis of data done by R.K.A and PK. Manuscript written by R.G., M.S., D.S., S.T., R.K. A. and P.K. All authors read the manuscript and agreed to submit.

Declaration of Competing Interest

The authors report no declarations of interest.

Acknowledgments

We would like to thanks the senior management of Delhi Technological University for their constant support and guidance.

References

Abeywardana, T., Pratt, M.R., 2015. Extent of inhibition of α-synuclein aggregation in vitro by SUMOylation is conjugation site- and SUMO isoform-selective. Biochemistry 54 (4), 959–961. https://doi.org/10.1021/bi501512m.

Agbas, A., 2019. Trends of protein aggregation in neurodegenerative diseases. Neurochemical Basis of Brain Function and Dysfunction, pp. 1–26. https://doi.org/10.5772/intechopen.81224.

Al Mamun, A., Uddin, M.S., Kabir, M.T., Khanum, S., Sarwar, M.S., Mathew, B., Rauf, A., Ahmed, M., Ashraf, G.M., 2020. Exploring the promise of targeting ubiquitin-proteasome system to combat Alzheimer's disease. Neurotox. Res. 38 (1), 8–17. https://doi.org/10.1007/s12640-020-00185-1.

Alam, S., Ur Rehman, S., Ok Kim, M., 2019. Nicotinamide improves functional recovery via regulation of the RAGE/JNK/NF-κB signaling pathway after brain injury. J. Clin. Med. 8 (2) https://doi.org/10.3390/jcm8020271, 0.

Albert-gasc, H., Ros-bernal, F., Castillo-g, E., n.d. MAP / ERK signaling in developing cognitive and emotional function and its effect on pathological and neurodegenerative processes 1–30.
Ali, T., Badshah, H., Kim, T.H., Kim, M.O., 2015. Melatonin attenuates D-galactose-induced memory impairment, neuroinflammation and neurodegeneration via RAGE/NF-KB/JNK signaling pathway in aging mouse model. J. Pineal Res. 58 (1), 71–85. https://doi.org/10.1111/jpi.12194.
Alleyn, M., Breitzig, M., Lockey, R., Kolliputi, N., 2018. The dawn of succinylation: a posttranslational modification. Am. J. Physiol. - Cell Physiol. 314 (2), C228–C232. https://doi.org/10.1152/ajpcell.00148.2017.
Almeida, B., Abreu, I.A., Matos, C.A., Fraga, J.S., Fernandes, S., Macedo, M.G., Gutiérrez-Gallego, R., Pereira, P.J.B., Carvalho, A.L., Macedo-Ribeiro, S., 2015. SUMOylation of the brain-predominant Ataxin-3 isoform modulates its interaction with p97. Biochim. Biophys. Acta - Mol. Basis Dis. 1852, 1950–1959. https://doi.org/10.1016/j.bbadis.2015.06.010.
Alvarez, A.R., Godoy, J.A., Mullendorff, K., Olivares, G.H., Bronfman, M., Inestrosa, N.C., 2004. Wnt-3a overcomes β-amyloid toxicity in rat hippocampal neurons. Exp. Cell Res. 297, 186–196. https://doi.org/10.1016/j.yexcr.2004.02.028.
Andreu, C.I., Woehlbier, U., Torres, M., Hetz, C., 2012. Protein disulfide isomerases in neurodegeneration: from disease mechanisms to biomedical applications. FEBS Lett. 586, 2826–2834. https://doi.org/10.1016/j.febslet.2012.07.023.
Armanios, M., Alder, J.K., Parry, E.M., Karim, B., Strong, M.A., Greider, C.W., 2009. Short telomeres are sufficient to cause the degenerative defects associated with aging. Am. J. Hum. Genet. 85, 823–832. https://doi.org/10.1016/j.ajhg.2009.10.028.
Arslan, M.A., Csermely, P., Sőti, C., 2006. Protein homeostasis and molecular chaperones in aging. Biogerontology 7, 383–389. https://doi.org/10.1007/s10522-006-9053-7.
Asada, A., Yamazaki, R., Kino, Y., Saito, T., Kimura, T., Miyake, M., Hasegawa, M., Nukina, N., Hisanaga, Sichi, 2014. Cyclin-dependent kinase 5 phosphorylates and induces the degradation of ataxin-2. Neurosci. Lett. 563, 112–117. https://doi.org/10.1016/j.neulet.2014.01.046.
Assefa, B.T., Tafere, G.G., Wondafrash, D.Z., Gidey, M.T., 2020. The Bewildering effect of AMPK activators in Alzheimer's disease: review of the current evidence. Biomed Res. Int. 2020 https://doi.org/10.1155/2020/9895121.
Asuni, A.A., Guridi, M., Sanchez, S., Sadowski, M.J., 2015. Antioxidant peroxiredoxin 6 protein rescues toxicity due to oxidative stress and cellular hypoxia in vitro, and attenuates prion-related pathology in vivo. Neurochem. Int. 90, 152–165. https://doi.org/10.1016/j.neuint.2015.08.006.
Ayala, V., Granado-Serrano, A.B., Cacabelos, D., Naudí, A., Ilieva, E.V., Boada, J., Caraballo-Miralles, V., Lladó, J., Ferrer, I., Pamplona, R., Portero-Otin, M., 2011. Cell stress induces TDP-43 pathological changes associated with ERK1/2 dysfunction: implications in ALS. Acta Neuropathol. 122, 259–270. https://doi.org/10.1007/s00401-011-0850-y.
Baki, L., Shioi, J., Wen, P., Shao, Z., Schwarzman, A., Gama-Sosa, M., Neve, R., Robakis, N.K., 2004. PS1 activates PI3K thus inhibiting GSK-3 activity and tau overphosphorylation: effects of FAD mutations. EMBO J. 23, 2586–2596. https://doi.org/10.1038/sj.emboj.7600251.
Banks, C.J., Andersen, J.L., 2019a. Mechanisms of SOD1 regulation by post-translational modifications. Redox Biol. 26, 1012720 https://doi.org/10.1016/j.redox.2019.101270.
Banks, C.J., Andersen, J.L., 2019b. Mechanisms of SOD1 regulation by post-translational modifications - ScienceDirect. Redox Biol. 26.
Bao, J., Qin, M., Mahaman, Y.A.R., Zhang, B., Huang, F., Zeng, K., Xia, Y., Ke, D., Wang, Q., Liu, R., Wang, J.Z., Ye, K., Wang, X., 2018. BACE1 SUMOylation increases its stability and escalates the protease activity in Alzheimer's disease. Proc. Natl. Acad. Sci. U. S. A. 115 (15), 3954–3959. https://doi.org/10.1073/pnas.1800498115.
Barbosa, M.C., Grosso, R.A., Fader, C.M., 2019. Hallmarks of aging: an autophagic perspective. Front. Endocrinol. (Lausanne) 10. https://doi.org/10.3389/fendo.2018.00790.
Benhar, M., Forrester, M.T., Stamler, J.S., 2006. Nitrosative stress in the ER: a new role for S-nitrosylation in neurodegenerative diseases. ACS Chem. Biol. 1, 355–358. https://doi.org/10.1021/cb600244c.
Berwick, D.C., Harvey, K., 2012. The importance of Wnt signalling for neurodegeneration in Parkinson's disease. Biochem. Soc. Trans. 40, 1123–1128. https://doi.org/10.1042/BST20120122.
Bhattacharyya, R., Barren, C., Kovacs, D.M., 2013. Palmitoylation of amyloid precursor protein regulates amyloidogenic processing in lipid rafts. J. Neurosci. 33 (27), 11169–11183. https://doi.org/10.1523/JNEUROSCI.4704-12.2013.
Bianchi, M., D'oria, V., Braghini, M.R., Petrini, S., Manco, M., 2019. Liraglutide treatment ameliorates neurotoxicity induced by stable silencing of Pin1. Int. J. Mol. Sci. 20 (20), 5064 https://doi.org/10.3390/ijms20205064.
Bieri, G., Lucin, K.M., O'Brien, C.E., Zhang, H., Villeda, S.A., Wyss-Coray, T., 2018. Proteolytic cleavage of Beclin 1 exacerbates neurodegeneration. Mol. Neurodegener. 13 https://doi.org/10.1186/s13024-018-0302-4.
Biroccio, A., Del Boccio, P., Panella, M., Bernardini, S., Di Ilio, C., Gambi, D., Stanzione, P., Sacchetta, P., Bernardi, G., Martorana, A., Federici, G., Stefani, A., Urbani, A., 2006. Differential post-translational modifications of transthyretin in Alzheimer's disease: a study of the cerebral spinal fluid. Proteomics 6 (7), 2305–2313. https://doi.org/10.1002/pmic.200500285.
Bose, A., Beal, M.F., 2016. Mitochondrial dysfunction in Parkinson's disease. J. Neurochem. 1, 216–231. https://doi.org/10.1111/jnc.13731.
Bullen, J.W., Balsbaugh, J.L., Chanda, D., Shabanowitz, J., Hunt, D.F., Neumann, D., Hart, G.W., 2014. Cross-talk between two essential nutrient-sensitive enzymes O-GlcNAc Transferase (OGT) and Amp-Activated Protein Kinase (AMPK). J. Biol. Chem. 289, 10592–10606. https://doi.org/10.1074/jbc.M113.523068.
Burai, R., Ait-Bouziad, N., Chiki, A., Lashuel, H.A., 2015. Elucidating the role of site-specific nitration of α-synuclein in the pathogenesis of Parkinson's disease via protein semisynthesis and mutagenesis. J. Am. Chem. Soc. 137 (15), 5041–5052. https://doi.org/10.1021/ja5131726.
Bussian, T.J., Aziz, A., Meyer, C.F., Swenson, B.L., van Deursen, J.M., Baker, D.J., 2018. Clearance of senescent glial cells prevents tau-dependent pathology and cognitive decline. Nature 562, 578–582. https://doi.org/10.1038/s41586-018-0543-y.
Calcinotto, A., Kohli, J., Zagato, E., Pellegrini, L., Demaria, M., Alimonti, A., 2019. Cellular senescence: aging, cancer, and injury. Physiol. Rev. 99, 1047–1078. https://doi.org/10.1152/physrev.00020.2018.
Cardaci, S., Filomeni, G., Ciriolo, M.R., 2012. Redox implications of AMPK-mediated signal transduction beyond energetic clues. J. Cell. Sci. 125, 2115–2125. https://doi.org/10.1242/jcs.095216.
Caricasole, A., Copani, A., Caraci, F., Aronica, E., Rozemuller, A.J., Caruso, A., Storto, M., Gaviraghi, G., Terstappen, G.C., Nicoletti, F., 2004. Induction of Dickkopf-1, a negative modulator of the Wnt pathway, is associated with neuronal degeneration in Alzheimer's brain. J. Neurosci. 24, 6021–6027. https://doi.org/10.1523/JNEUROSCI.1381-04.2004.
Carmony, K.C., Kim, K.B., 2012. PROTAC-induced proteolytic targeting. Methods Mol. Biol. 832, 627–638. https://doi.org/10.1007/978-1-61779-474-2_44.
Cattaneo, A., Chirichella, M., 2019. Targeting the post-translational proteome with intrabodies. Trends Biotechnol. 37 (6), 578–591. https://doi.org/10.1016/j.tibtech.2018.11.009.
Cawley, N.X., Sojka, C., Cougnoux, A., Lyons, A.T., Nicoli, E.R., Wassif, C.A., Porter, F.D., 2020. Abnormal LAMP1 glycosylation may play a role in Niemann-Pick disease, type C pathology. PLoS One. https://doi.org/10.1371/journal.pone.0227829.
Cha, G.H., Kim, S., Park, J., Lee, E., Kim, M., Lee, S.B., Kim, J.M., Chung, J., Cho, K.S., 2005. Parkin negatively regulates JNK pathway in the dopaminergic neurons of Drosophila. Proc. Natl. Acad. Sci. U. S. A. 102, 10345–10350. https://doi.org/10.1073/pnas.0500346102.
Chaibva, M., Jawahery, S., Pilkington, A.W., Arndt, J.R., Sarver, O., Valentine, S., Matysiak, S., Legleiter, J., 2016. Acetylation within the first 17 residues of huntingtin exon 1 alters aggregation and lipid binding. Biophys. J. 111 (2), 349–362. https://doi.org/10.1016/j.bpj.2016.06.018.
Chakraborty, J., Basso, V., Ziviani, E., 2017. Post Translational Modification of Parkin, pp. 1–11. https://doi.org/10.1186/s13062-017-0176-3.
Chan, C.H., Jo, U., Kohrman, A., Rezaeian, A.H., Chou, P.C., Logothetis, C., Lin, H.K., 2014. Posttranslational regulation of Akt in human cancer. Cell Biosci. 4, 1–9. https://doi.org/10.1186/2045-3701-4-59.
Che, X., Tang, B., Wang, X., Chen, D., Yan, X., Jiang, H., Shen, L., Xu, Q., Wang, G., Guo, J., 2013. The BAG2 protein stabilises PINK1 by decreasing its ubiquitination. Biochem. Biophys. Res. Commun. 441 (2), 488–492. https://doi.org/10.1016/j.bbrc.2013.10.086.
Chen, H., Qi, L., 2010. SUMO modification regulates the transcriptional activity of XBP1. Biochem. J. 429, 95–102. https://doi.org/10.1042/BJ20100193.
Chen, H.K., Fernandez-Funez, P., Acevedo, S.F., Lam, Y.C., Kaytor, M.D., Fernandez, M. H., Aitken, A., Skoulakis, E.M.C., Orr, H.T., Botas, J., Zoghbi, H.Y., 2003. Interaction of Akt-phosphorylated ataxin-1 with 14-3-3 mediates neurodegeneration in spinocerebellar ataxia type 1. Cell 113, 457–468. https://doi.org/10.1016/S0092-8674(03)00349-0.
Chen, Y., Liu, C.P., Xu, K.F., Mao, X.D., Lu, Y.B., Fang, L., Yang, J.W., Liu, C., 2008. Effect of taurine-conjugated ursodeoxycholic acid on endoplasmic reticulum stress and apoptosis induced by advanced glycation end products in cultured mouse podocytes. Am. J. Nephrol. 28, 1014–1022. https://doi.org/10.1159/000148209.
Chen, Yanchun, Guan, Y., Zhang, Z., Liu, H., Wang, S., Yu, L., Wu, X., Wang, X., 2012a. Wnt signaling pathway is involved in the pathogenesis of amyotrophic lateral sclerosis in adult transgenic mice. Neurol. Res. 34, 390–399. https://doi.org/10.1179/1743132812Y.0000000027.
Chen, Yuzhi, Neve, R.L., Liu, H., 2012b. Neddylation dysfunction in Alzheimer's disease. J. Cell. Mol. Med. 16 (11), 2583–2591. https://doi.org/10.1111/j.1582-4934.2012.01604.x.
Chen, J., Ren, Y., Gui, C., Zhao, M., Wu, X., Mao, K., Li, W., Zou, F., 2018. Phosphorylation of Parkin at serine 131 by p38 MAPK promotes mitochondrial dysfunction and neuronal death in mutant A53T α-synuclein model of Parkinson's disease. Cell Death Dis. 9 https://doi.org/10.1038/s41419-018-0722-7.
Chen, S., Zhou, M., Sun, J., Guo, A., Fernando, R.L., Chen, Y., Peng, P., Zhao, G., Deng, Y., 2019. DPP-4 inhibitor improves learning and memory deficits and AD-like neurodegeneration by modulating the GLP-1 signaling. Neuropharmacology 157, 107668. https://doi.org/10.1016/j.neuropharm.2019.107668.
Chen, S., Guo, D., Lei, B., Bi, J., Yang, H., 2020. Biglycan protects human neuroblastoma cells from nitric oxide-induced death by inhibiting AMPK-mTOR mediated autophagy and intracellular ROS level. Biotechnol. Lett. 42 (4), 657–668. https://doi.org/10.1007/s10529-020-02818-z.
Cheng, H.C., Kim, S.R., Oo, T.F., Kareva, T., Yarygina, O., Rzhetskaya, M., Wang, C., During, M., Talloczy, Z., Tanaka, K., Komatsu, M., Kobayashi, K., Okano, H., Kholodilov, N., Burke, R.E., 2011. Akt suppresses retrograde degeneration of dopaminergic axons by inhibition of macroautophagy. J. Neurosci. 31, 2125–2135. https://doi.org/10.1523/JNEUROSCI.5519-10.2011.
Cheung, W.D., Hart, G.W., 2008. AMP-activated protein kinase and p38 MAPK activate O-GlcNAcylation of neuronal proteins during glucose deprivation. J. Biol. Chem. 283, 13009–13020. https://doi.org/10.1074/jbc.M801222200.
Chinta, S.J., Andersen, J.K., 2011. Nitrosylation and nitration of mitochondrial complex i in Parkinson's disease. Free Radic. Res. 45, 53–58. https://doi.org/10.3109/10715762.2010.509398.

Cho, E., Park, M., 2016. Palmitoylation in Alzheimer's disease and other neurodegenerative diseases. Pharmacol. Res. 111, 133–151. https://doi.org/10.1016/j.phrs.2016.06.008.

Chouchani, E.T., Pell, V.R., Gaude, E., Aksentijević, D., Sundier, S.Y., Robb, E.L., Logan, A., Nadtochiy, S.M., Ord, E.N.J., Smith, A.C., Eyassu, F., Shirley, R., Hu, C.H., Dare, A.J., James, A.M., Rogatti, S., Hartley, R.C., Eaton, S., Costa, A.S.H., Brookes, P.S., Davidson, S.M., Duchen, M.R., Saeb-Parsy, K., Shattock, M.J., Robinson, A.J., Work, L.M., Frezza, C., Krieg, T., Murphy, M.P., 2014. Ischaemic accumulation of succinate controls reperfusion injury through mitochondrial ROS. Nature 515, 431–435. https://doi.org/10.1038/nature13909.

Chun, Y.S., Kwon, O.H., Chung, S., 2017. O-GlcNAcylation of amyloid-β precursor protein at threonine 576 residue regulates trafficking and processing. Biochem. Biophys. Res. Commun. 490 (2), 486–491. https://doi.org/10.1016/j.bbrc.2017.06.067.

Chung, H.S., Wang, S.B., Venkatraman, V., Murray, C.I., Van Eyk, J.E., 2013. Cysteine oxidative posttranslational modifications: emerging regulation in the cardiovascular system. Circ. Res. 112 (2), 382–392. https://doi.org/10.1161/CIRCRESAHA.112.268680.

Chung, M.M., Nicol, C.J., Cheng, Y.C., Lin, K.H., Chen, Y.L., Pei, D., Lin, C.H., Shih, Y.N., Yen, C.H., Chen, S.J., Huang, R.N., Chiang, M.C., 2017. Metformin activation of AMPK suppresses AGE-induced inflammatory response in hNSCs. Exp. Cell Res. 352 (1), 75–83. https://doi.org/10.1016/j.yexcr.2017.01.017.

Ciechanover, A., Kwon, Y.T., 2017. Protein quality control by molecular chaperones in neurodegeneration. Front. Neurosci. 11, 185. https://doi.org/10.3389/fnins.2017.00185.

Clift, D., McEwan, W.A., Labzin, L.I., Konieczny, V., Mogessie, B., James, L.C., Schuh, M., 2017. A method for the acute and rapid degradation of endogenous proteins. Cell 171 (7). https://doi.org/10.1016/j.cell.2017.10.033, 1692-1706.e18.

Cobos, S.N., Bennett, S.A., Torrente, M.P., 2019. The impact of histone post-translational modifications in neurodegenerative diseases. Biochim. Biophys. Acta - Mol. Basis Dis. 1865 (8), 1982–1991. https://doi.org/10.1016/j.bbadis.2018.10.019.

Coburger, I., Hoefgen, S., Than, M.E., 2014. The structural biology of the amyloid precursor protein APP – a complex puzzle reveals its multi-domain architecture. Biol. Chem. 395, 485–498. https://doi.org/10.1515/hsz-2013-0280.

Cohen, T.J., Guo, J.L., Hurtado, D.E., Kwong, L.K., Mills, I.P., Trojanowski, J.Q., Lee, V.M.Y., 2011. The acetylation of tau inhibits its function and promotes pathological tau aggregation. Nat. Commun. 2, 252. https://doi.org/10.1038/ncomms1255.

Cohen, T.J., Hwang, A.W., Restrepo, C.R., Yuan, C.X., Trojanowski, J.Q., Lee, V.M.Y., 2015. An acetylation switch controls TDP-43 function and aggregation propensity. Nat. Commun. 6, 1–13. https://doi.org/10.1038/ncomms6845.

Cook, C., Stankowski, J.N., Carlomagno, Y., Stetler, C., Petrucelli, L., 2014. Acetylation: a new key to unlock tau's role in neurodegeneration. Alzheimers Res. Ther. 6, 29. https://doi.org/10.1186/alzrt259.

Cooper, A.A., Gitler, A.D., Cashikar, A., Haynes, C.M., Hill, K.J., Bhullar, B., Liu, K., Xu, K., Strathearn, K.E., Liu, F., Cao, S., Caldwell, K.A., Caldwell, G.A., Marsischky, G., Kolodner, R.D., LaBaer, J., Rochet, J.C., Bonini, N.M., Lindquist, S., 2006. α-synuclein blocks ER-Golgi traffic and Rab1 rescues neuron loss in Parkinson's models. Science (80-.) 313, 324–328. https://doi.org/10.1126/science.1129462.

Coudreuse, D., Korswagen, H.C., 2007. The making of Wnt: new insights into Wnt maturation, sorting and secretion. Development 134, 3–12. https://doi.org/10.1242/dev.02699.

Cowan, K.J., Storey, K.B., 2003. Mitogen-activated protein kinases: new signaling pathways functioning in cellular responses to environmental stress. J. Exp. Biol. 206, 1107–1115. https://doi.org/10.1242/jeb.00220.

Cui, L., Song, W., Zeng, Y., Wu, Q., Fan, Z., Huang, T., Zeng, B., Zhang, M., Ni, Q., Li, Y., Wang, T., Li, D., Mao, X., Lian, T., Yang, D., Yang, M., Fan, X., 2020. Deubiquitinase USP7 regulates Drosophila aging through ubiquitination and autophagy. Aging (Albany. NY) 12, 23082–23095. https://doi.org/10.18632/aging.104067.

Cullinan, S.B., Zhang, D., Hannink, M., Arvisais, E., Kaufman, R.J., Diehl, J.A., 2003. Nrf2 is a direct PERK substrate and effector of PERK-dependent cell survival. Mol. Cell. Biol. 23, 7198–7209. https://doi.org/10.1128/mcb.23.20.7198-7209.2003.

Curry, D.W., Stutz, B., Andrews, Z.B., Elsworth, J.D., 2018. Targeting AMPK signaling as a neuroprotective strategy in Parkinson's disease. J. Parkinsons Dis. 8, 161–181. https://doi.org/10.3233/JPD-171296.

D'Souza, D.R., Wei, J., Shao, Q., Hebert, M.D., Subramony, S.H., Vig, P.J.S., 2006. Tissue transglutaminase crosslinks ataxin-1: possible role in SCA1 pathogenesis. Neurosci. Lett. 409, 5–9. https://doi.org/10.1016/j.neulet.2006.08.003.

de Oliveira, M.R., Schuck, P.F., Bosco, S.M.D., 2017a. Tanshinone I induces mitochondrial protection through an Nrf2-Dependent mechanism in paraquat-treated human neuroblastoma SH-SY5Y cells. Mol. Neurobiol. 54 (6), 4597–4608. https://doi.org/10.1007/s12035-016-0009-x.

de Oliveira, R.M., Vicente Miranda, H., Francelle, L., Pinho, R., Szegö, É.M., Martinho, R., Munari, F., Lázaro, D.F., Moniot, S., Guerreiro, P., Fonseca, L., Marijanovic, Z., Antas, P., Gerhardt, E., Enguita, F.J., Fauvet, B., Penque, D., Pais, T. F., Tong, Q., Becker, S., Kügler, S., Lashuel, H.A., Steegborn, C., Zweckstetter, M., Outeiro, T.F., 2017b. The mechanism of sirtuin 2–mediated exacerbation of alpha-synuclein toxicity in models of Parkinson disease. PLoS Biol. 15 (3), e2000374. https://doi.org/10.1371/journal.pbio.2000374.

Díaz-Troya, S., Pérez-Pérez, M.E., Florencio, F.J., Crespo, J.L., 2008. The role of TOR in autophagy regulation from yeast to plants and mammals. Autophagy. https://doi.org/10.4161/auto.6555.

Ding, Y., Zhang, Y., Xu, C., Tao, Q.H., Chen, Y.G., 2013. HECT domain-containing E3 ubiquitin ligase NEDD4L negatively regulates Wnt signaling by targeting dishevelled for proteasomal degradation. J. Biol. Chem. 288, 8289–8298. https://doi.org/10.1074/jbc.M112.433185.

Diwu, Y., Tian, J., Shi, J., 2013. Effect of Xixin decoction on O-linked N-acetylglucosamine Glycosylation of tau proteins in rat brain with sporadic Alzheimer disease. J. Tradit. Chinese Med. 33 (3), 367–372. https://doi.org/10.1016/s0254-6272(13)60180-6.

Djakovic, S.N., Schwarz, L.A., Barylko, B., DeMartino, G.N., Patrick, G.N., 2009. Regulation of the proteasome by neuronal activity and calcium/calmodulin-dependent protein kinase II. J. Biol. Chem. 284 (39), 26655–26665. https://doi.org/10.1074/jbc.M109.021956.

Do, C.B., Tung, J.Y., Dorfman, E., Kiefer, A.K., Drabant, E.M., Francke, U., Mountain, J. L., Goldman, S.M., Tanner, C.M., Langston, J.W., Wojcicki, A., Eriksson, N., 2011. Web-based genome-wide association study identifies two novel loci and a substantial genetic component for parkinson's disease. PLoS Genet. 7 (6), e1002141 https://doi.org/10.1371/journal.pgen.1002141.

Dowding, J.M., Song, W., Bossy, K., Karakoti, A., Kumar, A., Kim, A., Bossy, B., Seal, S., Ellisman, M.H., Perkins, G., Self, W.T., Bossy-Wetzel, E., 2014. Cerium oxide nanoparticles protect against Aβ-induced mitochondrial fragmentation and neuronal cell death. Cell Death Differ. 21, 1622–1632. https://doi.org/10.1038/cdd.2014.72.

Du, W., Hu, H., Zhang, J., Bao, G., Chen, R., Quan, R., 2019. The mechanism of MAPK signal transduction pathway involved with electroacupuncture treatment for different diseases. Evid. Complement. Alternat. Med. 2019 https://doi.org/10.1155/2019/8138017.

Duncan, C.E., An, M.C., Papanikolaou, T., Rugani, C., Vitelli, C., Ellerby, L.M., 2013. Histone deacetylase-3 interacts with ataxin-7 and is altered in a spinocerebellar ataxia type 7 mouse model. Mol. Neurodegener. 8, 42. https://doi.org/10.1186/1750-1326-8-42.

Durcan, T.M., Fon, E.A., 2015. The Three 'P' S of Mitophagy: PARKIN, Modifications, pp. 989–999. https://doi.org/10.1101/gad.262758.115.GENES.

Egan, M.F., Kost, J., Tariot, P.N., Aisen, P.S., Cummings, J.L., Vellas, B., Sur, C., Mukai, Y., Voss, T., Furtek, C., Mahoney, E., Mozley, L.H., Vandenberghe, R., Mo, Y., Michelson, D., 2018. Randomized trial of verubecestat for mild-to-moderate Alzheimer's disease. N. Engl. J. Med. 378, 1691–1703. https://doi.org/10.1056/NEJMoa1706441.

Emerson, J.P., Cabelli, D.E., Donald, M., Erbayraktar, S., Grasso, G., Sfac-, A., Xie, Q., Coleman, T., Kreilgaard, M., Sager, T., Erbayraktar, Z., Gokmen, N., Yilmaz, O., Ghezzi, P., Villa, P., Fratelli, M., Casagrande, S., Leist, M., Helboe, L., Gerwein, J., Christensen, S., Geist, M.A., Ped-, L.Ø., Cerami-hand, C., Wuerth, J., Cerami, A., Erbayraktar, S., Grasso, G., Sfacteria, A., Xie, Q., Coleman, T., Kreilgaard, M., Torup, L., Sager, T., Erbayraktar, Z., Gokmen, N., Yilmaz, O., Ghezzi, P., Villa, P., Fratelli, M., Casagrande, S., Leist, M., Helboe, L., Gerwien, J., Christensen, S., Geist, M.A., Pedersen, L.Ø., Cerami-hand, C., Wuerth, J., Cerami, A., Brines, M., Li, Y., Wang, H., Wang, S., Quon, D., Liu, Y., Cordell, B., 2003. Positive and negative regulation of APP amyloidogenesis by sumoylation. Proc. Natl. Acad. Sci. U. S. A. 100, 4–10.

Ercan-Herbst, E., Ehrig, J., Schöndorf, D.C., Behrendt, A., Klaus, B., Gomez Ramos, B., Prat Oriol, N., Weber, C., Ehrnhoefer, D.E., 2019. A post-translational modification signature defines changes in soluble tau correlating with oligomerization in early stage Alzheimer's disease brain. Acta Neuropathol. Commun. 7 (1), 192. https://doi.org/10.1186/s40478-019-0823-2.

Eskelinen, E.L., Saftig, P., 2009. Autophagy: a lysosomal degradation pathway with a central role in health and disease. Biochim. Biophys. Acta - Mol. Cell Res. 1793 (4), 664–673. https://doi.org/10.1016/j.bbamcr.2008.07.014.

Esteves, A.R., Palma, A.M., Gomes, R., Santos, D., Silva, D.F., Cardoso, S.M., 2019. Acetylation as a major determinant to microtubule-dependent autophagy: relevance to Alzheimer's and Parkinson disease pathology. Biochim. Biophys. Acta - Mol. Basis Dis. 1865 (8), 2008–2023. https://doi.org/10.1016/j.bbadis.2018.11.014.

Fantini, M., Pandolfini, L., Lisi, S., Chirichella, M., Arisi, I., Terrigno, M., Goracci, M., Cremisi, F., Cattaneo, A., 2017. Assessment of antibody library diversity through next generation sequencing and technical error compensation. PLoS One 12 (5), e0177574. https://doi.org/10.1371/journal.pone.0177574.

Fei, E., Jia, N., Zhang, T., Ma, X., Wang, H., Liu, C., Zhang, W., Ding, L., Nukina, N., Wang, G., 2007. Phosphorylation of ataxin-3 by glycogen synthase kinase 3β at serine 256 regulates the aggregation of ataxin-3. Biochem. Biophys. Res. Commun. 357, 487–492. https://doi.org/10.1016/j.bbrc.2007.03.160.

Feng, S.T., Wang, Z.Z., Yuan, Y.H., Sun, H.M., Chen, N.H., Zhang, Y., 2019. Mangiferin: a multipotent natural product preventing neurodegeneration in Alzheimer's and Parkinson's disease models. Pharmacol. Res. 146, 104336 https://doi.org/10.1016/j.phrs.2019.104336.

Feng, Q., Luo, Y., Zhang, X.N., Yang, X.F., Hong, X.Y., Sun, D.S., Li, X.C., Hu, Y., Li, X.G., Zhang, J.F., Li, X., Yang, Y., Wang, Q., Liu, G.P., Wang, J.Z., 2020. MAPT/Tau accumulation represses autophagy flux by disrupting IST1-regulated ESCRT-III complex formation: a vicious cycle in Alzheimer neurodegeneration. Autophagy 16 (4), 641–658. https://doi.org/10.1080/15548627.2019.1633862.

Ferreon, J.C., Jain, A., Choi, K.J., Tsoi, P.S., Mackenzie, K.R., Jung, S.Y., Ferreon, A.C., 2018. Acetylation disfavors tau phase separation. Int. J. Mol. Sci. 19 (5), 1360. https://doi.org/10.3390/ijms19051360.

Fewell, S.W., Travers, K.J., Jonathan, S., Brodsky, J.L., 2001. The action of molecular chaperones in the early secretory pathway.

François-Moutal, L., Perez-Miller, S., Scott, D.D., Miranda, V.G., Mollasalehi, N., Khanna, M., 2019. Structural Insights Into TDP-43 and Effects of Post-translational Modifications. Front. Mol. Neurosci. 12, 301. https://doi.org/10.3389/fnmol.2019.00301.

Funk, K.E., Thomas, S.N., Schafer, K.N., Cooper, G.L., Liao, Z., Clark, D.J., Yang, A.J., Kuret, J., 2014. Lysine methylation is an endogenous post-translational modification of tau protein in human brain and a modulator of aggregation propensity. Biochem. J. 462 (1), 77–88. https://doi.org/10.1042/BJ20140372.

Gao, C., Xiao, G., Hu, J., 2014. Regulation of Wnt/β-catenin signaling by posttranslational modifications. Cell Biosci. 4, 1–20. https://doi.org/10.1186/2045-3701-4-13.
García-Escudero, V., Martín-Maestro, P., Perry, G., Avila, J., 2013. Deconstructing mitochondrial dysfunction in alzheimer disease. Oxid. Med. Cell. Longev. 2013, 162152. https://doi.org/10.1155/2013/162152.
Gegg, M.E., Cooper, J.M., Chau, K.Y., Rojo, M., Schapira, A.H.V., Taanman, J.W., 2010. Mitofusin 1 and mitofusin 2 are ubiquitinated in a PINK1/parkin-dependent manner upon induction of mitophagy. Hum. Mol. Genet. 19, 4861–4870. https://doi.org/10.1093/hmg/ddq419.
Geschwind, D.H., 2003. Tau phosphorylation, tangles, and neurodegeneration: the chicken or the egg? Neuron 40 (3), 457–460. https://doi.org/10.1016/S0896-6273(03)00681-0.
Giraldo, E., Lloret, A., Fuchsberger, T., Viña, J., 2014. Aβ and tau toxicities in Alzheimer's are linked via oxidative stress-induced p38 activation: protective role of vitamin E. Redox Biol. 2, 873–877. https://doi.org/10.1016/j.redox.2014.03.002.
Gokulrangan, G., Zaidi, A., Michaelis, M.L., Schöneich, C., 2007. Proteomic analysis of protein nitration in rat cerebellum: effect of biological aging. J. Neurochem. 100, 1494–1504. https://doi.org/10.1111/j.1471-4159.2006.04334.x.
Gómez-Serrano, M., Camafeita, E., Loureiro, M., Peral, B., 2018. Mitoproteomics: tackling mitochondrial dysfunction in human disease. Oxid. Med. Cell. Longev. 2018, 1435934. https://doi.org/10.1155/2018/1435934.
González, N., Arcos-López, T., König, A., Quintanar, L., Menacho Márquez, M., Outeiro, T.F., Fernández, C.O., 2019. Effects of alpha-synuclein post-translational modifications on metal binding. J. Neurochem. 150 (5), 507–521. https://doi.org/10.1111/jnc.14721.
Gorisse, L., Pietrement, C., Vuiblet, V., Schmelzer, C.E.H., Köhler, M., Duca, L., Debelle, L., Fornès, P., Jaisson, S., Gillery, P., 2016. Protein carbamylation is a hallmark of aging. Proc. Natl. Acad. Sci. U. S. A. 113, 1191–1196. https://doi.org/10.1073/pnas.1517096113.
Grassi, D., Howard, S., Zhou, M., Diaz-Perez, N., Urban, N.T., Guerrero-Given, D., Kamasawa, N., Volpicelli-Daley, L.A., LoGrasso, P., Lasmézas, C.I., 2018. Identification of a highly neurotoxic α-synuclein species inducing mitochondrial damage and mitophagy in Parkinson's disease. Proc. Natl. Acad. Sci. 115 (11), E2634–E2643. https://doi.org/10.1073/pnas.1713849115.
Griebel, G., Stemmelin, J., Lopez-Grancha, M., Boulay, D., Boquet, G., Slowinski, F., Pichat, P., Beeské, S., Tanaka, S., Mori, A., Fujimura, M., Eguchi, J., 2019. The selective GSK3 inhibitor, SAR502250, displays neuroprotective activity and attenuates behavioral impairments in models of neuropsychiatric symptoms of Alzheimer's disease in rodents. Sci. Rep. 9, 1–15. https://doi.org/10.1038/s41598-019-54557-5.
Grimaldi, G., Catara, G., Palazzo, L., Corteggio, A., Valente, C., Corda, D., 2019. PARPs and PAR as novel pharmacological targets for the treatment of stress granule-associated disorders. Biochem. Pharmacol. 167, 64–75. https://doi.org/10.1016/j.bcp.2019.05.019.
Grimm, A., Eckert, A., 2017. Brain aging and neurodegeneration: from a mitochondrial point of view. J. Neurochem. 143, 418–431. https://doi.org/10.1111/jnc.14037.
Gross, G.G., Straub, C., Perez-Sanchez, J., Dempsey, W.P., Junge, J.A., Roberts, R.W., Trinh, L.A., Fraser, S.E., De Koninck, Y., De Koninck, P., Sabatini, B.L., Arnold, D.B., 2016. An E3-ligase-based method for ablating inhibitory synapses. Nat. Methods 13, 673–678. https://doi.org/10.1038/nmeth.3894.
Guo, D., Hazbun, T.R., Xu, X.J., Ng, S.L., Fields, S., Kuo, M.H., 2004. A tethered catalysis, two-hybrid system to identify protein-protein interactions requiring post-translational modifications. Nat. Biotechnol. 22 (7), 888–892. https://doi.org/10.1038/nbt985.
Guo, B., Liang, Q., Li, L., Hu, Z., Wu, F., Zhang, P., Ma, Y., Zhao, B., Kovács, A.L., Zhang, Z., Feng, D., Chen, S., Zhang, H., 2014. O-GlcNAc-modification of SNAP-29 regulates autophagosome maturation. Nat. Cell Biol. 16, 1215–1226. https://doi.org/10.1038/ncb3066.
Guo, M.Y., Shang, L., Hu, Y.Y., Jiang, L.P., Wan, Y.Y., Zhou, Q.Q., Zhang, K., Liao, H.F., Yi, J.L., Han, X.J., 2018. The role of Cdk5-mediated Drp1 phosphorylation in Aβ 1-42 induced mitochondrial fission and neuronal apoptosis. J. Cell. Biochem. 119, 4815–4825. https://doi.org/10.1002/jcb.26680.
Gupta, R., Ambasta, R.K., Kumar, P., 2020. Pharmacological intervention of histone deacetylase enzymes in the neurodegenerative disorders. Life Sci. https://doi.org/10.1016/j.lfs.2020.117278.
Guru KrishnaKumar, V., Baweja, L., Ralhan, K., Gupta, S., 2018. Carbamylation promotes amyloidogenesis and induces structural changes in Tau-core hexapeptide fibrils. Biochim. Biophys. Acta - Gen. Subj. 1862 (12), 2590–2604. https://doi.org/10.1016/j.bbagen.2018.07.030.
Guyenet, S.J., Mookerjee, S.S., Lin, A., Custer, S.K., Chen, S.F., Sopher, B.L., La Spada, A. R., Ellerby, L.M., 2015. Proteolytic cleavage of ataxin-7 promotes SCA7 retinal degeneration and neurological dysfunction. Hum. Mol. Genet. 24, 3908–3917. https://doi.org/10.1093/hmg/ddv121.
Ha, J.R., Hao, L., Venkateswaran, G., Huang, Y.H., Garcia, E., Persad, S., 2014. β-Catenin is O-GlcNAc glycosylated at Serine 23: Implications for β-catenin's subcellular localization and transactivator function. Exp. Cell Res. 321, 153–166. https://doi.org/10.1016/j.yexcr.2013.11.021.
Halloran, M., Parakh, S., Atkin, J.D., 2013. The role of S-nitrosylation and S-glutathionylation of protein disulphide isomerase in protein misfolding and neurodegeneration. Int. J. Cell Biol. 2013, 90–95. https://doi.org/10.1155/2013/797914.
Han, X., Sun, S., Sun, Y., Song, Q., Zhu, J., Song, N., Chen, M., Sun, T., Xia, M., Ding, J., Lu, M., Yao, H., Hu, G., 2019. Small molecule-driven NLRP3 inflammation inhibition via interplay between ubiquitination and autophagy: implications for Parkinson disease. Autophagy 15 (11), 1860–1881. https://doi.org/10.1080/15548627.2019.1596481.
Hänzelmann, P., Schindelin, H., 2017. The interplay of cofactor interactions and post-translational modifications in the regulation of the AAA+ ATPase p97. Front. Mol. Biosci. 4, 21. https://doi.org/10.3389/fmolb.2017.00021.
Henley, J.M., Carmichael, R.E., Wilkinson, K.A., 2018. Extranuclear SUMOylation in neurons. Trends Neurosci. 41 (4), 198–210. https://doi.org/10.1016/j.tins.2018.02.004.
Heras-Sandoval, D., Pérez-Rojas, J.M., Hernández-Damián, J., Pedraza-Chaverri, J., 2014. The role of PI3K/AKT/mTOR pathway in the modulation of autophagy and the clearance of protein aggregates in neurodegeneration. Cell. Signal. 26, 2694–2701. https://doi.org/10.1016/j.cellsig.2014.08.019.
Hetz, C., Chevet, E., Oakes, S.A., 2015. Proteostasis control by the unfolded protein response. Nat. Cell Biol. 17, 829–838. https://doi.org/10.1038/ncb3184.
Hipp, M.S., Park, S.H., Hartl, U.U., 2014. Proteostasis impairment in protein-misfolding and -aggregation diseases. Trends Cell Biol. https://doi.org/10.1016/j.tcb.2014.05.003.
Hong, S., Lee, S., Cho, S.G., Kang, S., 2008. UbcH6 interacts with and ubiquitinates the SCA1 gene product ataxin-1. Biochem. Biophys. Res. Commun. 371, 256–260. https://doi.org/10.1016/j.bbrc.2008.04.066.
Hong, S.Y., Ng, L.T., Ng, L.F., Inoue, T., Tolwinski, N.S., Hagen, T., Gruber, J., 2016. The role of mitochondrial non-enzymatic protein acylation in ageing. PLoS One 11, 12–14. https://doi.org/10.1371/journal.pone.0168752.
Hoozemans, J.J.M., van Haastert, E.S., Eikelenboom, P., de Vos, R.A.I., Rozemuller, J.M., Scheper, W., 2007. Activation of the unfolded protein response in Parkinson's disease. Biochem. Biophys. Res. Commun. 354, 707–711. https://doi.org/10.1016/j.bbrc.2007.01.043.
Hu, T., Li, C., Cao, Z., Van Raay, T.J., Smith, J.G., Willert, K., Solnica-Krezel, L., Coffey, R.J., 2010. Myristoylated Naked2 antagonizes Wnt-β-catenin activity by degrading dishevelled-1 at the plasma membrane. J. Biol. Chem. 285, 13561–13568. https://doi.org/10.1074/jbc.M109.075945.
Huang, X., Chen, J., Cao, W., Yang, L., Chen, Q., He, J., Yi, Q., Huang, H., Zhang, E., Cai, Z., 2019. The many substrates and functions of NEDD4-1. Cell Death Dis. 10 https://doi.org/10.1038/s41419-019-2142-8.
Hutter-Paier, B., Huttunen, H.J., Puglielli, L., Eckman, C.B., Kim, D.Y., Hofmeister, A., Moir, R.D., Domnitz, S.B., Frosch, M.P., Windisch, M., Kovacs, D.M., 2004. The ACAT inhibitor CP-113,818 markedly reduces amyloid pathology in a mouse model of Alzheimer's disease. Neuron 44, 227–238. https://doi.org/10.1016/j.neuron.2004.08.043.
Hwang, Y.J., Han, D., Kim, K.Y., Min, S.J., Kowall, N.W., Yang, L., Lee, J., Kim, Y., Ryu, H., 2014. ESET methylates UBF at K232/254 and regulates nucleolar heterochromatin plasticity and rDNA transcription. Nucleic Acids Res. 42 (3), 1628–1643. https://doi.org/10.1093/nar/gkt1041.
Iaconelli, J., Lalonde, J., Watmuff, B., Liu, B., Mazitschek, R., Haggarty, S.J., Karmacharya, R., 2017. Lysine deacetylation by HDAC6 regulates the kinase activity of AKT in human neural progenitor cells. ACS Chem. Biol. https://doi.org/10.1021/acschembio.6b01014.
Ikram, M., Saeed, K., Khan, A., Muhammad, T., Khan, M.S., Jo, M.G., Rehman, S.U., Kim, M.O., 2019. Natural dietary supplementation of curcumin protects mice brains against ethanol-induced oxidative stress-mediated neurodegeneration and memory impairment via Nrf2/TLR4/RAGE signaling. Nutrients 11 (5), 1082. https://doi.org/10.3390/nu11051082.
Imai, Y., Takahashi, R., 2004. How do Parkin mutations result in neurodegeneration? Curr. Opin. Neurobiol. 14, 384–389. https://doi.org/10.1016/j.conb.2004.04.002.
Inestrosa, N.C., Toledo, E.M., 2008. The role of Wnt signaling in neuronal dysfunction in Alzheimer's Disease. Mol. Neurodegener. 3, 1–13. https://doi.org/10.1186/1750-1326-3-9.
Intihar, T.A., Martinez, E.A., Gomez-Pastor, R., 2019. Mitochondrial dysfunction in huntington's disease; interplay between HSF1, p53 and PGC-1α transcription factors. Front. Cell. Neurosci. 13, 1–10. https://doi.org/10.3389/fncel.2019.00103.
Ishigami, A., Masutomi, H., Handa, S., Nakamura, M., Nakaya, S., Uchida, Y., Saito, Y., Murayama, S., Jang, B., Jeon, Y.C., Choi, E.K., Kim, Y.S., Kasahara, Y., Maruyama, N., Toda, T., 2015. Mass spectrometric identification of citrullination sites and immunohistochemical detection of citrullinated glial fibrillary acidic protein in Alzheimer's disease brains. J. Neurosci. Res. 93 (11), 1664–1674. https://doi.org/10.1002/jnr.23620.
Janer, A., Werner, A., Takahashi-Fujigasaki, J., Daret, Al., Fujigasaki, H., Takada, K., Duyckaerts, C., Brice, A., Dejean, A., Sittler, A., 2009. SUMOylation attenuates the aggregation propensity and cellular toxicity of the polyglutamine expanded ataxin-7. Hum. Mol. Genet. 19, 181–195. https://doi.org/10.1093/hmg/ddp478.
Jeong, H., Then, F., Melia, T.J., Mazzulli, J.R., Cui, L., Savas, J.N., Voisine, C., Paganetti, P., Tanese, N., Hart, A.C., Yamamoto, A., Krainc, D., 2009. Acetylation targets mutant huntingtin to autophagosomes for degradation. Cell 137 (1), 60–72. https://doi.org/10.1016/j.cell.2009.03.018.
Jeyapalan, J.C., Sedivy, J.M., 2008. Cellular senescence and organismal aging. Mech. Ageing Dev. 129, 467–474. https://doi.org/10.1016/j.mad.2008.04.001.
Jiang, Z., Fan, Q., Zhang, Z., Zou, Y., Cai, R., Wang, Q., Zuo, Y., Cheng, J., 2012. SENP1 deficiency promotes ER stress-induced apoptosis by increasing XBP1 SUMOylation. Cell Cycle 11, 1118–1122. https://doi.org/10.4161/cc.11.6.19529.
Jin, H., Sanjo, N., Uchihara, T., Watabe, K., George-Hyslop, P.S., Fraser, P.E., Mizusawa, H., 2010. Presenilin-1 holoprotein is an interacting partner of sarco endoplasmic reticulum calcium-atpase and confers resistance to endoplasmic reticulum stress. J. Alzheimers Dis. 20, 261–273. https://doi.org/10.3233/JAD-2010-1360.

Johri, A., Beal, M.F., 2012. Mitochondrial dysfunction in neurodegenerative diseases. J. Pharmacol. Exp. Ther. 342 (3), 619–630. https://doi.org/10.1124/jpet.112.192138.
Jorgensen, N.D., Andresen, J.M., Lagalwar, S., Armstrong, B., Stevens, S., Byam, C.E., Duvick, L.A., Lai, S., Jafar-Nejad, P., Zoghbi, H.Y., Clark, H.B., Orr, H.T., 2009. Phosphorylation of ATXN1 at Ser776 in the cerebellum. J. Neurochem. 110, 675–686. https://doi.org/10.1111/j.1471-4159.2009.06164.x.
Ju, T.C., Chen, H.M., Lin, J.T., Chang, C.P., Chang, W.C., Kang, J.J., Sun, C.P., Tao, M.H., Tu, P.H., Chang, C., Dickson, D.W., Chern, Y., 2011. Nuclear translocation of AMPK-α1 potentiates striatal neurodegeneration in Huntington's disease. J. Cell Biol. 194, 209–227. https://doi.org/10.1083/jcb.201105010.
Ju, H., Kokubu, H., Todd, T.W., Kahle, J.J., Kim, S., Richman, R., Chirala, K., Orr, H.T., Zoghbi, H.Y., Lim, J., 2013. Polyglutamine disease toxicity is regulated by nemo-like kinase in spinocerebellar ataxia type 1. J. Neurosci. 33, 9328–9336. https://doi.org/10.1523/JNEUROSCI.3465-12.2013.
Ju, H., Kokubu, H., Lim, J., 2014. Beyond the Glutamine Expansion: Influence of Posttranslational Modifications of Ataxin-1 in the Pathogenesis of Spinocerebellar Ataxia Type 1. Mol. Neurobiol. 50, 866–874. https://doi.org/10.1007/s12035-014-8703-z.
Junqueira, S.C., Centeno, E.G.Z., Wilkinson, K.A., Cimarosti, H., 2019. Post-translational modifications of parkinson's disease-related proteins: phosphorylation, SUMOylation and ubiquitination. Biochim. Biophys. Acta - Mol. Basis Dis. https://doi.org/10.1016/j.bbadis.2018.10.025.
Jwa, M., Chang, P., 2012. PARP16 is a tail-anchored endoplasmic reticulum protein required for the PERK-and IRE1α-mediated unfolded protein response. Nat. Cell Biol. 14, 1223–1230. https://doi.org/10.1038/ncb2593.
Kang, A.R., Park, S.H., Lee, S., Choi, D.Y., Kim, K.P., Song, H.K., Hong, S., Kang, S., 2015. A key lysine residue in the AXH domain of ataxin-1 is essential for its ubiquitylation. Biochim. Biophys. Acta - Proteins Proteomics 1854, 356–364. https://doi.org/10.1016/j.bbapap.2015.01.012.
Kang, S., Piao, Y., Kang, Y.C., Lim, S., Pak, Y.K., 2020. Qi-activating quercetin alleviates mitochondrial dysfunction and neuroinflammation in vivo and in vitro. Arch. Pharm. Res. 43, 553–566. https://doi.org/10.1007/s12272-020-01238-x.
Kaphingst, K.A., Persky, S., Lachance, C., 2010. PERK mediates eIF2α phosphorylation responsible for BACE1 elevation, CREB dysfunction and neurodegeneration in a mouse model of Alzheimer's disease Latha Latha. Neurobiol. Aging 14, 384–399. https://doi.org/10.1080/10810730902873927.Testing.
Keeney, P.M., Xie, J., Capaldi, R.A., Bennett, J.P., 2006. Parkinson's disease brain mitochondrial complex I has oxidatively damaged subunits and is functionally impaired and misassembled. J. Neurosci. 26, 5256–5264. https://doi.org/10.1523/JNEUROSCI.0984-06.2006.
Kielbik, M., Szulc-Kielbik, I., Klink, M., 2021. Calreticulin-multifunctional chaperone in immunogenic cell death: potential significance as a prognostic biomarker in ovarian cancer patients. Cells 10. https://doi.org/10.3390/cells10010130.
Kim, E.K., Choi, E.J., 2010. Pathological roles of MAPK signaling pathways in human diseases. Biochim. Biophys. Acta - Mol. Basis Dis. 1802 (4), 396–405. https://doi.org/10.1016/j.bbadis.2009.12.009.
Kim, S., Swaminathan, S., Shen, L., Risacher, S.L., Nho, K., Foroud, T., Shaw, L.M., Trojanowski, J.Q., Potkin, S.G., Huentelman, M.J., Craig, D.W., Dechairo, B.M., Aisen, P.S., Petersen, R.C., Weiner, M.W., Saykin, A.J., 2011. Genome-wide association study of CSF biomarkers Aβ1-42, t-tau, and p-tau181p in the ADNI cohort. Neurology 76 (1), 69–79. https://doi.org/10.1212/WNL.0b013e318204a397.
Kim, C.-S., Park, S., Kim, J., 2017. The role of glycation in the pathogenesis of aging and its prevention through herbal products and physical exercise. J. Exerc. Nutr. Biochem. 21, 55–61. https://doi.org/10.20463/jenb.2017.0027.
Klaus, A., Zorman, S., Berthier, A., Polge, C., Ramirez, S., Michelland, S., Sève, M., Vertommen, D., Rider, M., Lentze, N., Auerbach, D., Schlattner, U., 2013. Glutathione S-Transferases interact with AMP-activated protein kinase: evidence for S-glutathionylation and activation in vitro. PLoS One 8, 1–10. https://doi.org/10.1371/journal.pone.0062497.
Klaus, C., Hansen, J.N., Ginolhac, A., Gérard, D., Gnanapragassam, V.S., Horstkorte, R., Rossdam, C., Buettner, F.F.R., Sauter, T., Sinkkonen, L., Neumann, H., Linnartz-Gerlach, B., 2020. Reduced sialylation triggers homeostatic synapse and neuronal loss in middle-aged mice. Neurobiol. Aging 88, 91–107. https://doi.org/10.1016/j.neurobiolaging.2020.01.008.
Kleinknecht, A., Popova, B., Lázaro, D.F., Pinho, R., Valerius, O., Outeiro, T.F., Braus, G. H., 2016. C-terminal tyrosine residue modifications modulate the protective phosphorylation of serine 129 of α-synuclein in a yeast model of parkinson's disease. PLoS Genet. 12 https://doi.org/10.1371/journal.pgen.1006098.
Ko, S.Y., Ko, H.A., Chu, K.H., Shieh, T.M., Chi, T.C., Chen, H.I., Chang, W.C., Chang, S.S., 2015. The possible mechanism of advanced glycation end products (AGEs) for Alzheimer's disease. PLoS One 10, 1–16. https://doi.org/10.1371/journal.pone.0143345.
Komiya, Y., Habas, R., 2008. Wnt signal transduction pathways. Organogenesis 4, 68–75. https://doi.org/10.4161/org.4.2.5851.
Kontaxi, C., Piccardo, P., Gill, A.C., 2017. Lysine-directed post-translational modifications of tau protein in Alzheimer's disease and related tauopathies. Front. Mol. Biosci. 4 (56) https://doi.org/10.3389/fmolb.2017.00056.
Koster, K.P., Yoshii, A., 2019. Depalmitoylation by palmitoyl-protein thioesterase 1 in neuronal health and degeneration. Front. Synaptic Neurosci. 11, 25. https://doi.org/10.3389/fnsyn.2019.00025.
Koyano, F., Okatsu, K., Ishigaki, S., Fujioka, Y., Kimura, M., Sobue, G., Tanaka, K., Matsuda, N., 2013. The principal PINK1 and Parkin cellular events triggered in response to dissipation of mitochondrial membrane potential occur in primary neurons. Genes Cells 18 (8), 672–681. https://doi.org/10.1111/gtc.12066.
Kumar, S., Rezaei-Ghaleh, N., Terwel, D., Thal, D.R., Richard, M., Hoch, M., Mc Donald, J.M., Wüllner, U., Glebov, K., Heneka, M.T., Walsh, D.M., Zweckstetter, M., Walter, J., 2011. Extracellular phosphorylation of the amyloid β 2-peptide promotes formation of toxic aggregates during the pathogenesis of Alzheimer's disease. EMBO J. 30, 2255–2265. https://doi.org/10.1038/emboj.2011.138.
Kumar, A., Singh, P.K., Parihar, R., Dwivedi, V., Lakhotia, S.C., Ganesh, S., 2014. Decreased O-linked GlcNAcylation protects from cytotoxicity mediated by huntingtin exon1 protein fragment. J. Biol. Chem. 289 (19), 13543–13553. https://doi.org/10.1074/jbc.M114.553321.
Kumar, R., Jangir, D.K., Verma, G., Shekhar, S., Hanpude, P., Kumar, S., Kumari, R., Singh, N., Bhavesh, N.S., Jana, N.R., Maiti, T.K., 2017. S-nitrosylation of UCHL1 induces its structural instability and promotes α-synuclein aggregation. Sci. Rep. 7, 1–16. https://doi.org/10.1038/srep44558.
Kumar, A., Dhawan, A., Kadam, A., Shinde, A., 2018. Autophagy and mitochondria: targets in neurodegenerative disorders. CNS Neurol. Disord. - Drug Targets 17, 696–705. https://doi.org/10.2174/1871527317666180816100203.
Kumar, D., Ambasta, R.K., Kumar, P., 2020. Ubiquitin biology in neurodegenerative disorders: from impairment to therapeutic strategies. Ageing Res. Rev. https://doi.org/10.1016/j.arr.2020.101078.
Kummer, M.P., Heneka, M.T., 2014. Truncated and Modified Amyloid-Beta Species, pp. 1–9.
Kummer, M.P., Hermes, M., Delekarte, A., Hammerschmidt, T., Kumar, S., Terwel, D., Walter, J., Pape, H.C., König, S., Roeber, S., Jessen, F., Klockgether, T., Korte, M., Heneka, M.T., 2011. Nitration of tyrosine 10 critically enhances amyloid β aggregation and plaque formation. Neuron 71 (5), 833–844. https://doi.org/10.1016/j.neuron.2011.07.001.
Kurayoshi, M., Yamamoto, H., Izumi, S., Kikuchi, A., 2007. Post-translational palmitoylation and glycosylation of Wnt-5a are necessary for its signalling. Biochem. J. 402, 515–523. https://doi.org/10.1042/BJ20061476.
Kwak, Y.D., Ma, T., Diao, S., Zhang, X., Chen, Y., Hsu, J., Lipton, S.A., Masliah, E., Xu, H., Liao, F.F., 2010. NO signaling and S-nitrosylation regulate PTEN inhibition in neurodegeneration. Mol. Neurodegener. 5, 49. https://doi.org/10.1186/1750-1326-5-49.
Laitusis, A.L., Brostrom, M.A., Brostrom, C.O., 1999. The dynamic role of GRP78/BiP in the coordination of mRNA translation with protein processing. J. Biol. Chem. 274, 486–493. https://doi.org/10.1074/jbc.274.1.486.
Landers, J.E., Melki, J., Meininger, V., Glass, J.D., Van Den Berg, L.H., Van Es, M.A., Sapp, P.C., Van Vught, P.W.J., McKenna-Yasek, D.M., Blauw, H.M., Cho, T.J., Polak, M., Shi, L., Wills, A.M., Broom, W.J., Ticozzi, N., Silani, V., Ozoguz, A., Rodriguez-Leyva, I., Veldink, J.H., Ivinson, A.J., Saris, C.G.J., Hosler, B.A., Barnes-Nessa, A., Couture, N., Wokke, J.H.J., Kwiatkowski, T.J., Ophoff, R.A., Cronin, S., Hardiman, O., Diekstra, F.P., Leigh, P.N., Shaw, C.E., Simpson, C.L., Hansen, V.K., Powell, J.F., Corcia, P., Salachas, F., Heath, S., Galan, P., Georges, F., Horvitz, H.R., Lathrop, M., Purcell, S., Al-Chalabi, A., Brown, R.H., 2009. Reduced expression of the Kinesin-Associated Protein 3 (KIFAP3) gene increases survival in sporadic amyotrophic lateral sclerosis. Proc. Natl. Acad. Sci. U. S. A. 106 (22), 9004–9009. https://doi.org/10.1073/pnas.0812937106.
Lee, J.-A., 2012. Neuronal autophagy: a housekeeper or a fighter in neuronal cell survival? Exp. Neurobiol. 21, 1–8. https://doi.org/10.5607/en.2012.21.1.1.
Lee, C.T., Yu, L.E., Wang, J.Y., 2016. Nitroxide antioxidant as a potential strategy to attenuate the oxidative/nitrosative stress induced by hydrogen peroxide plus nitric oxide in cultured neurons. Nitric Oxide - Biol. Chem. 54, 38–50. https://doi.org/10.1016/j.niox.2016.02.001.
Lee, M., Ban, J.J., Chung, J.Y., Im, W., Kim, M., 2018. Amelioration of huntington's disease phenotypes by beta-lapachone is associated with increases in sirt1 expression, creb phosphorylation and pgc-1α deacetylation. PLoS One 13 (5), e0195968. https://doi.org/10.1371/journal.pone.0195968.
Lee, J.E., Kim, N., Yeo, J.Y., Seo, D.G., Kim, S., Lee, J.S., Hwang, K.W., Park, S.Y., 2019. Anti-amyloidogenic effects of asarone derivatives from perilla frutescens leaves against beta-amyloid aggregation and nitric oxide production. Molecules 24 (23), 4297. https://doi.org/10.3390/molecules24234297.
Li, X.H., Lv, B.L., Xie, J.Z., Liu, J., Zhou, X.W., Wang, J.Z., 2012. AGEs induce Alzheimer-like tau pathology and memory deficit via RAGE-mediated GSK-3 activation. Neurobiol. Aging 33, 1400–1410. https://doi.org/10.1016/j.neurobiolaging.2011.02.003.
Li, X.H., Chen, C., Tu, Y., Sun, H.T., Zhao, M.L., Cheng, S.X., Qu, Y., Zhang, S., 2013. Sirt1 promotes axonogenesis by deacetylation of akt and inactivation of GSK3. Mol. Neurobiol. 48 (3), 490–499. https://doi.org/10.1007/s12035-013-8437-3.
Li, Q., Liu, Y., Sun, M., 2017. Autophagy and Alzheimer's disease. Cell. Mol. Neurobiol. 37 (3), 377–388. https://doi.org/10.1007/s10571-016-0386-8.
Li, W., Feng, J., Gao, C., Wu, M., Du, Q., Tsoi, B., Wang, Q., Yang, D., Shen, J., 2019. Nitration of Drp1 provokes mitophagy activation mediating neuronal injury in experimental autoimmune encephalomyelitis. Free Radic. Biol. Med. 143, 70–83. https://doi.org/10.1016/j.freeradbiomed.2019.07.037.
Liman, J., Deeg, S., Voigt, A., Voßfeldt, H., Dohm, C.P., Karch, A., Weishaupt, J., Schulz, J.B., Bähr, M., Kermer, P., 2014. CDK5 protects from caspase-induced Ataxin-3 cleavage and neurodegeneration. J. Neurochem. 129, 1013–1023. https://doi.org/10.1111/jnc.12684.
Lin, M.T., Beal, M.F., 2006. Mitochondrial dysfunction and oxidative stress in neurodegenerative diseases. Nature 443, 787–795. https://doi.org/10.1038/nature05292.
Lin, C.H., Liu, S.Y., Lee, E.H.Y., 2016. SUMO modification of Akt regulates global SUMOylation and substrate SUMOylation specificity through Akt phosphorylation of Ubc9 and SUMO1. Oncogene 35, 595–607. https://doi.org/10.1038/onc.2015.115.
Lin, C.H., Cheng, Y.C., Nicol, C.J., Lin, K.H., Yen, C.H., Chiang, M.C., 2017. Activation of AMPK is neuroprotective in the oxidative stress by advanced glycosylation end

products in human neural stem cells. Exp. Cell Res. 359, 367–373. https://doi.org/10.1016/j.yexcr.2017.08.019.
Lindholm, D., Wootz, H., Korhonen, L., 2006. ER stress and neurodegenerative diseases. Cell Death Differ. 13, 385–392. https://doi.org/10.1038/sj.cdd.4401778.
Liu, F., Zaidi, T., Iqbal, K., Grundke-Iqbal, I., Merkle, R.K., Gong, C.X., 2002. Role of glycosylation in hyperphosphorylation of tau in Alzheimer's disease. FEBS Lett. 512, 101–106. https://doi.org/10.1016/S0014-5793(02)02228-7.
Liu, D., Liu, C., Li, J., Azadzoi, K., Yang, Y., Fei, Z., Dou, K., Kowall, N.W., Choi, H.P., Vieira, F., Yang, J.H., 2013. Proteomic analysis reveals differentially regulated protein acetylation in human amyotrophic lateral sclerosis spinal cord. PLoS One 8 (12), e80779. https://doi.org/10.1371/journal.pone.0080779.
Lontay, B., Kiss, A., Virág, L., Tar, K., 2020. How do post-translational modifications influence the pathomechanistic landscape of Huntington's disease? A comprehensive review. Int. J. Mol. Sci. 21 (12), 4282. https://doi.org/10.3390/ijms21124282.
Löw, P., 2011. The role of ubiquitin-proteasome system in ageing. Gen. Comp. Endocrinol. 172, 39–43. https://doi.org/10.1016/j.ygcen.2011.02.005.
Lu, H., Liu, X., Deng, Y., Qing, H., 2013. DNA methylation, a hand behind neurodegenerative diseases. Front. Aging Neurosci. 5, 85. https://doi.org/10.3389/fnagi.2013.00085.
Lu, J., Qian, Y., Altieri, M., Dong, H., Wang, J., Raina, K., Hines, J., Winkler, J.D., Crew, A.P., Coleman, K., Crews, C.M., 2015. Hijacking the E3 ubiquitin ligase cereblon to efficiently target BRD4. Chem. Biol. 22 (6), 755–763. https://doi.org/10.1016/j.chembiol.2015.05.009.
Malik, R., Wiedau, M., 2020. Therapeutic approaches targeting protein aggregation in amyotrophic lateral sclerosis. Front. Mol. Neurosci. 13, 1–6. https://doi.org/10.3389/fnmol.2020.00098.
Manuscript, A., Genes, B.T.M., 2012. Alzheimer's Disease, 1, pp. 191–198.
Marnett, L.J., 1997. Free radical mechanisms of neurotoxicity. Chem. Res. Toxicol. 10, 483–484. https://doi.org/10.1021/tx970493u.
Martin, D.D.O., Hayden, M.R., 2015. Post-translational myristoylation at the cross roads of cell death, autophagy and neurodegeneration. Biochem. Soc. Trans. 43 (2), 229–234. https://doi.org/10.1042/BST20140281.
Martin, L., Latypova, X., Terro, F., 2011. Neurochemistry International Post-translational modifications of tau protein: implications for Alzheimer's disease. Neurochem. Int. 58, 458–471. https://doi.org/10.1016/j.neuint.2010.12.023.
Martínez-Ruiz, A., Villanueva, L., De Orduña, C.G., López-Ferrer, D., Ángeles Higueras, M., Tarín, C., Rodríguez-Crespo, I., Vázquez, J., Lamas, S., 2005. S-nitrosylation of Hsp90 promotes the inhibition of its ATPase and endothelial nitric oxide synthase regulatory activities. Proc. Natl. Acad. Sci. U. S. A. 102, 8525–8530. https://doi.org/10.1073/pnas.0407294102.
Martini-Stoica, H., Xu, Y., Ballabio, A., Zheng, H., 2016. The autophagy-lysosomal pathway in neurodegeneration: a TFEB perspective. Trends Neurosci. 39 (4), 221–234. https://doi.org/10.1016/j.tins.2016.02.002.
Matos, C.A., Nóbrega, C., Louros, S.R., Almeida, B., Ferreiro, E., Valero, J., De Almeida, L.P., Macedo-Ribeiro, S., Carvalho, A.L., 2016. Ataxin-3 phosphorylation decreases neuronal defects in spinocerebellar ataxia type 3 models. J. Cell Biol. 212, 465–480. https://doi.org/10.1083/jcb.201506025.
Mattoo, S., Sanyal, A., Dutta, S., Chandran, A., Koller, A., Camara, A., Watson, B., Sengupta, R., Ysselstein, D., Montenegro, P., Cannon, J., Rochet, C., 2019. Alpha-synuclein is a target of fic-mediated adenylylation/AMPylation: implications for Parkinson's disease. bioRxiv 431 (12), 2266–2282. https://doi.org/10.1101/525659.
McCormack, A.L., Mak, S.K., Di Monte, D.A., 2012. Increased a-synuclein phosphorylation and nitration in the aging primate substantia nigra. Cell Death Dis. 3, 1–9. https://doi.org/10.1038/cddis.2012.50.
McGurk, L., Rifai, O.M., Bonini, N.M., 2019. Poly(ADP-Ribosylation) in age-related neurological disease. Trends Genet. 35 (8), 601–613. https://doi.org/10.1016/j.tig.2019.05.004.
McNaught, K.S.P., Olanow, C.W., Halliwell, B., Isacson, O., Jenner, P., 2001. Failure of the ubiquitin proteasome system in Parkinson's disease. Nat. Rev. Neurosci. 2, 589–594. https://doi.org/10.1038/35086067.
Mehan, S., Parveen, S., Kalra, S., 2017. Adenyl cyclase activator forskolin protects against Huntington's disease-like neurodegenerative disorders. Neural Regen. Res. 12 (2), 290–300. https://doi.org/10.4103/1673-5374.200812.
Melchionna, T., Cattaneo, A., 2007. A protein silencing switch by ligand-induced proteasome-targeting intrabodies. J. Mol. Biol. 374 (3), 641–654. https://doi.org/10.1016/j.jmb.2007.09.053.
Meli, G., Visintin, M., Cannistraci, I., Cattaneo, A., 2009. Direct in vivo intracellular selection of conformation-sensitive antibody domains targeting Alzheimer's amyloid-β oligomers. J. Mol. Biol. 387 (3), 584–606. https://doi.org/10.1016/j.jmb.2009.01.061.
Meli, G., Lecci, A., Manca, A., Krako, N., Albertini, V., Benussi, L., Ghidoni, R., Cattaneo, A., 2014. Conformational targeting of intracellular A' 2 oligomers demonstrates their pathological oligomerization inside the endoplasmic reticulum. Nat. Commun. 5, 3867. https://doi.org/10.1038/ncomms4867.
Mercado-Gómez, O., Hernández-Fonseca, K., Villavicencio-Queijeiro, A., Massieu, L., Chimal-Monroy, J., Arias, C., 2008. Inhibition of Wnt and PI3K signaling modulates GSK-3β activity and induces morphological changes in cortical neurons: role of tau phosphorylation. Neurochem. Res. 33, 1599–1609. https://doi.org/10.1007/s11064-008-9714-9.
Merlini, G., Bellotti, V., Palladini, G., Obici, L., Casarini, S., Perfetti, V., 2001. Protein Aggregation 1, 39, pp. 1065–1075.
Mørkholt, A.S., Oklinski, M.K., Larsen, A., Bockermann, R., Issazadeh-Navikas, S., Nieland, J.G.K., Kwon, T.H., Corthals, A., Nielsen, S., Nieland, J.D.V., 2020. Pharmacological inhibition of carnitine palmitoyl transferase 1 inhibits and reverses experimental autoimmune encephalitis in rodents. PLoS One 15 (6), e0234493. https://doi.org/10.1371/journal.pone.0234493.
Moll, T., Shaw, P.J., Cooper-Knock, J., 2020. Disrupted glycosylation of lipids and proteins is a cause of neurodegeneration. Brain 143 (5), 1332–1340. https://doi.org/10.1093/brain/awz358.
Monaco, A., Fraldi, A., 2020. Protein aggregation and dysfunction of autophagy-lysosomal pathway: a vicious cycle in lysosomal storage diseases. Front. Mol. Neurosci. 13, 1–8. https://doi.org/10.3389/fnmol.2020.00037.
Mookerjee, S., Papanikolaou, T., Guyenet, S.J., Sampath, V., Lin, A., Vitelli, C., DeGiacomo, F., Sopher, B.L., Chen, S.F., La Spada, A.R., Ellerby, L.M., 2009. Posttranslational modification of ataxin-7 at lysine 257 prevents autophagy-mediated turnover of an N-terminal caspase-7 cleavage fragment. J. Neurosci. 29, 15134–15144. https://doi.org/10.1523/JNEUROSCI.4720-09.2009.
Morales-García, J.A., Susín, C., Alonso-Gil, S., Pérez, D.I., Palomo, V., Pérez, C., Conde, S., Santos, A., Gil, C., Martínez, A., Pérez-Castillo, A., 2013. Glycogen synthase kinase-3 inhibitors as potent therapeutic agents for the treatment of Parkinson disease. ACS Chem. Neurosci. 4, 350–360. https://doi.org/10.1021/cn300182g.
Moreira, P.I., Carvalho, C., Zhu, X., Smith, M.A., Perry, G., 2010. Mitochondrial dysfunction is a trigger of Alzheimer's disease pathophysiology. Biochim. Biophys. Acta - Mol. Basis Dis. 1802 (1), 2–10. https://doi.org/10.1016/j.bbadis.2009.10.006.
Morris, M., Knudsen, G.M., Maeda, S., Trinidad, J.C., Ioanoviciu, A., Burlingame, A.L., Mucke, L., 2015. Tau Post-Translational Modifications in Wild-Type and Human Amyloid Precursor Protein Transgenic Mice. https://doi.org/10.1038/nn.4067.
Mueller, T., Breuer, P., Schmitt, I., Walter, J., Evert, B.O., Wüllner, U., 2009. CK2-dependent phosphorylation determines cellular localization and stability of ataxin-3. Hum. Mol. Genet. 18, 3334–3343. https://doi.org/10.1093/hmg/ddp274.
Mukhopadhyay, D., Dasso, M., 2017. The role of SUMO in mitosis. Adv. Exp. Med. Biol. 963, 171–184. https://doi.org/10.1007/978-3-319-50044-7.
Murata, H., Sakaguchi, M., Jin, Y., Sakaguchi, Y., Futami, J.I., Yamada, H., Kataoka, K., Huh, N.H., 2011. A new cytosolic pathway from a Parkinson disease-associated kinase, BRPK/PINK1: activation of AKT via MTORC2. J. Biol. Chem. 286, 7182–7189. https://doi.org/10.1074/jbc.M110.179390.
Murray, J., Taylor, S.W., Zhang, B., Ghosh, S.S., Capaldi, R.A., 2003. Oxidative damage to mitochondrial complex I due to peroxynitrite: identification of reactive tyrosines by mass spectrometry. J. Biol. Chem. 278, 37223–37230. https://doi.org/10.1074/jbc.M305694200.
Myeku, N., Metcalfe, M.J., Huang, Q., Figueiredo-Pereira, M., 2011. Assessment of proteasome impairment and accumulation/aggregation of ubiquitinated proteins in neuronal cultures. Methods Mol. Biol. 793, 273–296. https://doi.org/10.1007/978-1-61779-328-8_18.
Nakamura, T., Tu, S., Akhtar, M.W., Sunico, C.R., Okamoto, S.I.chi, Lipton, S.A., 2013. Aberrant Protein S-nitrosylation in neurodegenerative diseases. Neuron 78 (4), 596–614. https://doi.org/10.1016/j.neuron.2013.05.005.
Nakato, R., Ohkubo, Y., Konishi, A., Shibata, M., Kaneko, Y., Iwawaki, T., Nakamura, T., Lipton, S.A., Uehara, T., 2015. Regulation of the unfolded protein response via S-nitrosylation of sensors of endoplasmic reticulum stress. Sci. Rep. 5, 1–9. https://doi.org/10.1038/srep14812.
Nan, F., Sun, G., Xie, W., Ye, T., Sun, Xiao, Zhou, P., Dong, X., Sun, J., Sun, Xiaobo, Zhang, M., 2019. Ginsenoside Rb1 mitigates oxidative stress and apoptosis induced by methylglyoxal in SH-SY5Y cells via the PI3K/Akt pathway. Mol. Cell. Probes 48, 101469. https://doi.org/10.1016/j.mcp.2019.101469.
Ng, C.H., Basil, A.H., Hang, L., Tan, R., Goh, K.L., O'Neill, S., Zhang, X., Yu, F., Lim, K.L., 2017. Genetic or pharmacological activation of the Drosophila PGC-1α ortholog spargel rescues the disease phenotypes of genetic models of Parkinson's disease. Neurobiol. Aging 55, 33–37. https://doi.org/10.1016/j.neurobiolaging.2017.03.017.
Nguyen, L., Montrasio, F., Pattamatta, A., Tusi, S.K., Bardhi, O., Meyer, K.D., Hayes, L., Nakamura, K., Banez-Coronel, M., Coyne, A., Guo, S., Laboissonniere, L.A., Gu, Y., Narayanan, S., Smith, B., Nitsch, R.M., Kankel, M.W., Rushe, M., Rothstein, J., Zu, T., Grimm, J., Ranum, L.P.W., 2020. Antibody therapy targeting RAN proteins rescues C9 ALS/FTD phenotypes in C9orf72 mouse model. Neuron 105 (645–662), e11. https://doi.org/10.1016/j.neuron.2019.11.007.
Nixon, R.A., 2007. Autophagy, amyloidogenesis and Alzheimer disease. J. Cell. Sci. 120 (Pt 23), 4081–4091. https://doi.org/10.1242/jcs.019265.
Nixon, R.A., 2013. The role of autophagy in neurodegenerative disease. Nat. Med. 19 (8), 983–997. https://doi.org/10.1038/nm.3232.
Novoselov, S.S., Mustill, W.J., Gray, A.L., Dick, J.R., Kanuga, N., Kalmar, B., Greensmith, L., Cheetham, M.E., 2013. Molecular chaperone mediated late-stage neuroprotection in the SOD1G93A mouse model of amyotrophic lateral sclerosis. PLoS One 8 (8), e73944. https://doi.org/10.1371/journal.pone.0073944.
Nusse, R., Clevers, H., 2017. Wnt/β-catenin signaling, disease, and emerging therapeutic modalities. Cell 169, 985–999. https://doi.org/10.1016/j.cell.2017.05.016.
Nuzzo, T., Feligioni, M., Cristino, L., Pagano, I., Marcelli, S., Iannuzzi, F., Imperatore, R., D'Angelo, L., Petrella, C., Carella, M., Pollegioni, L., Sacchi, S., Punzo, D., De Girolamo, P., Errico, F., Canu, N., Usiello, A., 2019. Free D-aspartate triggers NMDA receptor-dependent cell death in primary cortical neurons and perturbs JNK activation, Tau phosphorylation, and protein SUMOylation in the cerebral cortex of mice lacking D-aspartate oxidase activity. Exp. Neurol. 317, 51–65. https://doi.org/10.1016/j.expneurol.2019.02.014.
O'Connor, T., Sadleir, K.R., Maus, E., Velliquette, R.A., Zhao, J., Cole, S.L., Eimer, W.A., Hitt, B., Bembinster, L.A., Lammich, S., Lichtenthaler, S.F., Hébert, S.S., De Strooper, B., Haass, C., Bennett, D.A., Vassar, R., 2008. Phosphorylation of the translation initiation factor eIF2α increases BACE1 levels and promotes

amyloidogenesis. Neuron 60, 988–1009. https://doi.org/10.1016/j.neuron.2008.10.047.
O'Hara, D., Davis, G.M., Adlesic, N.A., Hayes, J.M., Davey, G.P., 2019. Dichloroacetate stabilizes mitochondrial fusion dynamics in models of neurodegeneration. Front. Mol. Neurosci. 12 https://doi.org/10.3389/fnmol.2019.00219.
Oakhill, J.S., Chen, Z.P., Scott, J.W., Steel, R., Castelli, L.A., Linga, N., Macaulay, S.L., Kemp, B.E., 2010. β-Subunit myristoylation is the gatekeeper for initiating metabolic stress sensing by AMP-activated protein kinase (AMPK). Proc. Natl. Acad. Sci. U. S. A. 107, 19237–19241. https://doi.org/10.1073/pnas.1009705107.
Ogawa, O., Zhu, X., Lee, H.G., Raina, A., Obrenovich, M.E., Bowser, R., Ghanbari, H.A., Castellani, R.J., Perry, G., Smith, M.A., 2003. Ectopic localization of phosphorylated histone H3 in Alzheimer's disease: a mitotic catastrophe? Acta Neuropathol. 105, 524–528. https://doi.org/10.1007/s00401-003-0684-3.
Oliva, C.A., Vargas, J.Y., Inestrosa, N.C., 2013. Wnt signaling: role in LTP, neural networks and memory. Ageing Res. Rev. 12, 786–800. https://doi.org/10.1016/j.arr.2013.03.006.
Oliveira, J.M.A., 2010. Nature and cause of mitochondrial dysfunction in Huntington's disease: focusing on huntingtin and the striatum. J. Neurochem. 114 (1), 1–12. https://doi.org/10.1111/j.1471-4159.2010.06741.x.
Olzscha, H., 2019. Posttranslational modifications and proteinopathies: how guardians of the proteome are defeated. Biol. Chem. 400 (7), 895–915. https://doi.org/10.1515/hsz-2018-0458.
Orr, H.T., 2012. SCA1-Phosphorylation, a regulator of Ataxin-1 function and pathogenesis. Prog. Neurobiol. 99, 179–185. https://doi.org/10.1016/j.pneurobio.2012.04.003.
Oueslati, A., Fournier, M., Lashuel, H.A., 2010. Role of post-translational modifications in modulating the structure, function and toxicity of α-synuclein. Implications for Parkinson's disease pathogenesis and therapies. Prog. Brain Res. 183, 115–145. https://doi.org/10.1016/S0079-6123(10)83007-9. Elsevier B.V.
Oueslati, A., Schneider, B.L., Aebischer, P., Lashuel, H.A., 2013. Polo-like kinase 2 regulates selective autophagic synuclein clearance and suppresses its toxicity in vivo. Proc. Natl. Acad. Sci. U. S. A. 110 (41) https://doi.org/10.1073/pnas.1309991110. E3945-54.
Pajarillo, E., Rizor, A., Lee, J., Aschner, M., Lee, E., 2019. The role of posttranslational modifications of α-synuclein and LRRK2 in Parkinson's disease: potential contributions of environmental factors. Biochim. Biophys. Acta - Mol. Basis Dis. 1865, 1992–2000. https://doi.org/10.1016/j.bbadis.2018.11.017.
Palomer, E., Buechler, J., Salinas, P.C., 2019. Wnt signaling deregulation in the aging and Alzheimer's brain. Front. Cell. Neurosci. 13, 1–8. https://doi.org/10.3389/fncel.2019.00227.
Pan, T., Kondo, S., Le, W., Jankovic, J., 2008. The role of autophagy-lysosome pathway in neurodegeneration associated with Parkinson's disease. Brain. 131 (Pt 8), 1969–1978. https://doi.org/10.1093/brain/awm318.
Pan, Y., Daito, T., Sasaki, Y., Chung, Y.H., Xing, X., Pondugula, S., Swamidass, S.J., Wang, T., Kim, A.H., Yano, H., 2016. Inhibition of DNA methyltransferases blocks mutant huntingtin-induced neurotoxicity. Sci. Rep. https://doi.org/10.1038/srep31022.
Park, S., Lee, Y., Pak, J.W., Kim, H., Choi, H., Kim, J.W., Roth, J., Cho, J.W., 2015. O-GlcNAc modification is essential for the regulation of autophagy in Drosophila melanogaster. Cell. Mol. Life Sci. 72, 3173–3183. https://doi.org/10.1007/s00018-015-1889-z.
Parsons, M.P., Kang, R., Buren, C., Dau, A., Southwell, A.L., Doty, C.N., Sanders, S.S., Hayden, M.R., Raymond, L.A., 2014. Bidirectional control of Postsynaptic Density-95 (PSD-95) clustering by Huntingtin. J. Biol. Chem. https://doi.org/10.1074/jbc.M113.513945.
Pastori, V., Sangalli, E., Coccetti, P., Pozzi, C., Nonnis, S., Tedeschi, G., Fusi, P., 2010. CK2 and GSK3 phosphorylation on S29 controls wild-type ATXN3 nuclear uptake. Biochim. Biophys. Acta - Mol. Basis Dis. 1802, 583–592. https://doi.org/10.1016/j.bbadis.2010.03.007.
Pei, J.J., Braak, E., Braak, H., Grundke-Iqbal, I., Iqbal, K., Winblad, B., Cowburn, R.F., 2001. Localization of active forms of C-jun kinase (JNK) and p38 kinase in Alzheimer's disease brains at different stages of neurofibrillary degeneration. J. Alzheimers Dis. 3, 41–48. https://doi.org/10.3233/JAD-2001-3107.
Peixoto, C.A., de Oliveira, W.H., da R. Araújo, S.M., Nunes, A.K.S., 2017. AMPK activation: role in the signaling pathways of neuroinflammation and neurodegeneration. Exp. Neurol. 10, 520. https://doi.org/10.1016/j.expneurol.2017.08.013.
Peng, Y., Kim, M.J., Hullinger, R., O'Riordan, K.J., Burger, C., Pehar, M., Puglielli, L., 2016. Improved proteostasis in the secretory pathway rescues Alzheimer's disease in the mouse. Brain 139, 937–952. https://doi.org/10.1093/brain/awv385.
Pickrell, A.M., Fukui, H., Wang, X., Pinto, M., Moraes, C.T., 2011. The striatum is highly susceptible to mitochondrial oxidative phosphorylation dysfunctions. J. Neurosci. 31, 9895–9904. https://doi.org/10.1523/JNEUROSCI.6223-10.2011.
Piperi, C., Adamopoulos, C., Dalagiorgou, G., Diamanti-Kandarakis, E., Papavassiliou, A. G., 2012. Crosstalk between advanced glycation and endoplasmic reticulum stress: emerging therapeutic targeting for metabolic diseases. J. Clin. Endocrinol. Metab. 97, 2231–2242. https://doi.org/10.1210/jc.2011-3408.
Prasad, A., Bharathi, V., Sivalingam, V., Girdhar, A., Patel, B.K., 2019. Molecular mechanisms of TDP-43 misfolding and pathology in amyotrophic lateral sclerosis. Front. Mol. Neurosci. 12 https://doi.org/10.3389/fnmol.2019.00025.
Princz, A., Tavernarakis, N., 2020. SUMOylation in neurodegenerative diseases. Gerontology 66, 122–130. https://doi.org/10.1159/000502142.
Pulido, R., 2014. Retraction for Berthier et al., PINK1 regulates histone H3 trimethylation and gene expression by interaction with the polycomb protein EED/WAIT1. Proc. Natl. Acad. Sci. U. S. A. 111, 16225. https://doi.org/10.1073/pnas.1419354111.
Qu, J., Nakamura, T., Holland, E.A., McKercher, S.R., Lipton, S.A., 2012. S-nitrosylation of Cdk5. Prion 6, 364–370. https://doi.org/10.4161/pri.21250.
Quintanilla, R.A., Tapia-Monsalves, C., Vergara, E.H., Pérez, M.J., Aranguiz, A., 2020. Truncated tau induces mitochondrial transport failure through the impairment of TRAK2 protein and bioenergetics decline in neuronal cells. Front. Cell. Neurosci. 14 https://doi.org/10.3389/fncel.2020.00175.
Rai, S.N., Dilnashin, H., Birla, H., Singh, S.Sen, Zahra, W., Rathore, A.S., Singh, B.K., Singh, S.P., 2019. The role of PI3K/Akt and ERK in neurodegenerative disorders. Neurotox. Res. 35, 775–795. https://doi.org/10.1007/s12640-019-0003-y.
Ralat, L.A., Ren, M., Schilling, A.B., Tang, W.J., 2009. Protective role of Cys-178 against the inactivation and oligomerization of human insulin-degrading enzyme by oxidation and nitrosylation. J. Biol. Chem. 284 (49), 34005–34018. https://doi.org/10.1074/jbc.M109.030627.
Rangone, H., Pardo, R., Colin, E., Girault, J.A., Saudou, F., Humbert, S., 2005. Phosphorylation of arfaptin 2 at Ser260 by Akt inhibits PolyQ-huntingtin-induced toxicity by rescuing proteasome impairment. J. Biol. Chem. 280, 22021–22028. https://doi.org/10.1074/jbc.M407528200.
Ratovitski, T., O'Meally, R.N., Jiang, M., Chaerkady, R., Chighladze, E., Stewart, J.C., Wang, X., Arbez, N., Roby, E., Alexandris, A., Duan, W., Vijayvargia, R., Seong, I.S., Lavery, D.J., Cole, R.N., Ross, C.A., 2017. Post-translational modifications (PTMs), identified on endogenous huntingtin, cluster within proteolytic domains between HEAT repeats. J. Proteome Res. https://doi.org/10.1021/acs.jproteome.6b00991.
Reddy, P.H., 2009. Amyloid beta, mitochondrial structural and functional dynamics in Alzheimer's disease. Exp. Neurol. 218 (2), 286–292. https://doi.org/10.1016/j.expneurol.2009.03.042.
Rehman, S.U., Shah, S.A., Ali, T., Chung Il, J., Kim, M.O., 2017. Anthocyanins reversed D-galactose-induced oxidative stress and neuroinflammation mediated cognitive impairment in adult rats. Mol. Neurobiol. 54 (1), 255–271. https://doi.org/10.1007/s12035-015-9604-5.
Ren, R.J., Dammer, E.B., Wang, G., Seyfried, N.T., Levey, A.I., 2014. Proteomics of protein post-translational modifications implicated in neurodegeneration. Transl. Neurodegener. 3, 23. https://doi.org/10.1186/2047-9158-3-23.
Reynolds, M.R., Berry, R.W., Binder, L.I., 2005. Site-specific nitration differentially influences τ assembly in vitro. Biochemistry 44 (42), 13997–14009. https://doi.org/10.1021/bi051028w.
Rezaei-Ghaleh, N., Amininasab, M., Kumar, S., Walter, J., Zweckstetter, M., 2016. Phosphorylation modifies the molecular stability of β-amyloid deposits. Nat. Commun. 7, 1–9. https://doi.org/10.1038/ncomms11359.
Rhoads, Shannon N., Monahan, Zachary T., Yee, Debra S., F.P.S, 2018. The role of post-translational modifications on prion-like aggregation and liquid-phase separation of FUS. Int. J. Mol. Sci. 19, 886.
Ribarič, S., Milisav Ribarič, I., 2020. Autophagy and cell death in alzheimer's, parkinson's and prion diseases. Programmed Cell Death. IntechOpen. https://doi.org/10.5772/intechopen.86706.
Rizza, S., Cardaci, S., Montagna, C., Giacomo, G.Di, De Zio, D., Bordi, M., Maiani, E., Campello, S., Borreca, A., Puca, A.A., Stamler, J.S., Cecconi, F., Filomeni, G., 2018. S-nitrosylation drives cell senescence and aging in mammals by controlling mitochondrial dynamics and mitophagy. Proc. Natl. Acad. Sci. U. S. A. 115, E3388–E3397. https://doi.org/10.1073/pnas.1722452115.
Rocha, E.M., De Miranda, B., Sanders, L.H., 2018. Alpha-synuclein: pathology, mitochondrial dysfunction and neuroinflammation in Parkinson's disease. Neurobiol. Dis. 109 (Pt B), 249–257. https://doi.org/10.1016/j.nbd.2017.04.004.
Ross, C.A., Poirier, M.A., 2005. What is the role of protein aggregation in neurodegeneration? Nat. Rev. Mol. Cell Biol. 6, 891–898. https://doi.org/10.1038/nrm1742.
Rott, R., Szargel, R., Shani, V., Hamza, H., Savyon, M., Elghani, F.A., Bandopadhyay, R., Engelender, S., 2017. SUMOylation and ubiquitination reciprocally regulate α-synuclein degradation and pathological aggregation. Proc. Natl. Acad. Sci. U. S. A. 114, 13176–13181. https://doi.org/10.1073/pnas.1704351114.
Rubio, T., Vernia, S., Sanz, P., 2013. Sumoylation of AMPKβ2 subunit enhances AMP-activated protein kinase activity. Mol. Biol. Cell 24, 1801–1811. https://doi.org/10.1091/mbc.E12-11-0806.
Ryan, K., Backos, D.S., Reigan, P., Patel, M., 2012. Post-translational oxidative modification and inactivation of mitochondrial complex I in epileptogenesis. J. Neurosci. 32, 11250–11258. https://doi.org/10.1523/JNEUROSCI.0907-12.2012.
Ryu, J., Cho, S., Park, B.C., Lee, D.H., 2010. Oxidative stress-enhanced SUMOylation and aggregation of ataxin-1: implication of JNK pathway. Biochem. Biophys. Res. Commun. 393, 280–285. https://doi.org/10.1016/j.bbrc.2010.01.122.
Saez-Atienzar, S., Masliah, E., 2020. Cellular senescence and Alzheimer disease: the egg and the chicken scenario. Nat. Rev. Neurosci. 21, 433–444. https://doi.org/10.1038/s41583-020-0325-z.
Salahuddin, P., Rabbani, G., Khan, R.H., 2014. The role of advanced glycation end products in various types of neurodegenerative disease: a therapeutic approach. Cell. Mol. Biol. Lett. 19 (3), 407–437. https://doi.org/10.2478/s11658-014-0205-5.
Sanna, S., Esposito, S., Masala, A., Sini, P., Nieddu, G., Galioto, M., Fais, M., Iaccarino, C., Cestra, G., Crosio, C., 2020. HDAC1 inhibition ameliorates TDP-43-induced cell death in vitro and in vivo. Cell Death Dis. 11 https://doi.org/10.1038/s41419-020-2580-3.
Sanz, P., Rubio, T., Garcia-Gimeno, M.A., 2013. AMPKbeta subunits: more than just a scaffold in the formation of AMPK complex. FEBS J. 280, 3723–3733. https://doi.org/10.1111/febs.12364.
Sarkar, S., Korolchuk, V.I., Renna, M., Imarisio, S., Fleming, A., Williams, A., Garcia-Arencibia, M., Rose, C., Luo, S., Underwood, B.R., Kroemer, G., O'Kane, C.J., Rubinsztein, D.C., 2011. Complex inhibitory effects of nitric oxide on autophagy. Mol. Cell 43, 19–32. https://doi.org/10.1016/j.molcel.2011.04.029.

Sarkar, C., Sadhukhan, T., Bagh, M.B., Appu, A.P., Chandra, G., Mondal, A., Saha, A., Mukherjee, A.B., 2020. Cln1-mutations suppress Rab7-RILP interaction and impair autophagy contributing to neuropathology in a mouse model of infantile neuronal ceroid lipofuscinosis. J. Inherit. Metab. Dis. 43, 1082–1101. https://doi.org/10.1002/jimd.12242.

Sathya, S., Devi, K.P., 2017. The use of polyphenols for the treatment of alzheimer's disease. Role Mediterr. Diet Brain Neurodegener. Dis. 239–252. https://doi.org/10.1016/B978-0-12-811959-4.00015-8.

Sato, Y., Mukai, M., Ueda, J., Muraki, M., Stasevich, T.J., Horikoshi, N., Kujirai, T., Kita, H., Kimura, T., Hira, S., Okada, Y., Hayashi-Takanaka, Y., Obuse, C., Kurumizaka, H., Kawahara, A., Yamagata, K., Nozaki, N., Kimura, H., 2013. Genetically encoded system to track histone modification in vivo. Sci. Rep. 3, 2436. https://doi.org/10.1038/srep02436.

Schaffert, L.N., Carter, W.G., 2020. Do post-translational modifications influence protein aggregation in neurodegenerative diseases: a systematic review. Brain Sci. 10 https://doi.org/10.3390/brainsci10040232.

Scheffold, A., Holtman, I.R., Dieni, S., Brouwer, N., Katz, S.F., Jebaraj, B.M.C., Kahle, P. J., Hengerer, B., Lechel, A., Stilgenbauer, S., Boddeke, E.W.G.M., Eggen, B.J.L., Rudolph, K.L., Biber, K., 2016. Telomere shortening leads to an acceleration of synucleinopathy and impaired microglia response in a genetic mouse model. Acta Neuropathol. Commun. 4, 1–17. https://doi.org/10.1186/s40478-016-0364-x.

Scheper, W., Hoozemans, J.J.M., 2015. The unfolded protein response in neurodegenerative diseases: a neuropathological perspective. Acta Neuropathol. 130 (3), 315–331. https://doi.org/10.1007/s00401-015-1462-8.

Schildknecht, S., Weber, A., Gerding, H., Pape, R., Robotta, M., Drescher, M., Marquardt, A., Daiber, A., Ferger, B., Leist, M., 2013. The NOX1/4 inhibitor GKT136901 as selective and direct scavenger of peroxynitrite. Curr. Med. Chem. 21 (3), 365–376. https://doi.org/10.2174/0929867311320999017 9.

Schilling, B., Srinivas Bharath, M.M., Row, R.H., Murray, J., Cusack, M.P., Capaldi, R.A., Freed, C.R., Prasad, K.N., Andersen, J.K., Gibson, B.W., 2005. Rapid purification and mass spectrometric characterization of mitochondrial NADH dehydrogenase (Complex I) from rodent brain and a dopaminergic neuronal cell line. Mol. Cell Proteomics 4, 84–96. https://doi.org/10.1074/mcp.M400143-MCP200.

Schröder, M., Kaufman, R.J., 2005a. ER stress and the unfolded protein response. Mutat. Res. - Fundam. Mol. Mech. Mutagen. 569, 29–63. https://doi.org/10.1016/j.mrfmmm.2004.06.056.

Schröder, M., Kaufman, R.J., 2005b. The mammalian unfolded protein response. Annu. Rev. Biochem. 74, 739–789. https://doi.org/10.1146/annurev.biochem.73.011303.074134.

Seki, T., Takahashi, H., Adachi, N., Abe, N., Shimahara, T., Saito, N., Sakai, N., 2007. Aggregate formation of mutant protein kinase C gamma found in spinocerebellar ataxia type 14 impairs ubiquitin-proteasome system and induces endoplasmic reticulum stress. Eur. J. Neurosci. 26, 3126–3140. https://doi.org/10.1111/j.1460-9568.2007.05933.x.

Selkoe, D., 1994. Cell Biology of Amyloid, pp. 373–403.

Sen, N., Hara, M.R., Ahmad, A.S., Cascio, M.B., Kamiya, A., Ehmsen, J.T., Aggrawal, N., Hester, L., Doré, S., Snyder, S.H., Sawa, A., 2009. GOSPEL: a neuroprotective protein that binds to GAPDH upon S-nitrosylation. Neuron. https://doi.org/10.1016/j.neuron.2009.05.024.

Sen, T., Saha, P., Jiang, T., Sen, N., 2020. Sulfhydration of AKT triggers Tau-phosphorylation by activating glycogen synthase kinase 3β in Alzheimer's disease. Proc. Natl. Acad. Sci. U. S. A. 117, 4418–4427. https://doi.org/10.1073/pnas.1916895117.

Serrano, A., Qiao, X., Matos, J.O., Farley, L., Cilenti, L., Chen, B., Tatulian, S.A., Teter, K., 2020. Reversal of Alpha-Synuclein Fibrillization by Protein Disulfide Isomerase. Front. Cell Dev. Biol. 8, 726. https://doi.org/10.3389/fcell.2020.00726.

Shamsi, T.N., Athar, T., Parveen, R., Fatima, S., 2017. A review on protein misfolding, aggregation and strategies to prevent related ailments. Int. J. Biol. Macromol. 105, 993–1000. https://doi.org/10.1016/j.ijbiomac.2017.07.116.

Shanbhag, N.M., Evans, M.D., Mao, W., Nana, A.L., Seeley, W.W., Adame, A., Rissman, R. A., Masliah, E., Mucke, L., 2019. Early neuronal accumulation of DNA double strand breaks in Alzheimer's disease. Acta Neuropathol. Commun. 7, 1–18. https://doi.org/10.1186/s40478-019-0723-5.

Shen, J., Wu, Y., Xu, J.Y., Zhang, J., Sinclair, S.H., Yanoff, M., Xu, G., Li, W., Xu, G.T., 2010. ERK- and Akt-dependent neuroprotection by erythropoietin (EPO) against glyoxal-AGEs via modulation of Bcl-xL, Bax, and BAD. Investig. Ophthalmol. Vis. Sci. 51, 35–46. https://doi.org/10.1167/iovs.09-3544.

Sheng, L., Christopher, M., 2016. 乳鼠心肌提取 HHS public access. A.M. Physiol. Behav. 176, 100–106. https://doi.org/10.1016/j.gde.2016.03.011.

Sherva, R., Tripodis, Y., Bennett, D.A., Chibnik, L.B., Crane, P.K., De Jager, P.L., Farrer, L. A., Saykin, A.J., Shulman, J.M., Naj, A., Green, R.C., 2014. Genome-wide association study of the rate of cognitive decline in Alzheimer's disease. Alzheimer's Dement. 10 (1), 45–52. https://doi.org/10.1016/j.jalz.2013.01.008.

Shimada, N., Handa, S., Uchida, Y., Fukuda, M., Maruyama, N., Asaga, H., Choi, E.K., Lee, J., Ishigami, A., 2010. Developmental and age-related changes of peptidylarginine deiminase 2 in the mouse brain. J. Neurosci. Res. 88, 798–806. https://doi.org/10.1002/jnr.22255.

Shinbo, Y., Niki, T., Taira, T., Ooe, H., Takahashi-Niki, K., Maita, C., Seino, C., Iguchi-Ariga, S.M.M., Ariga, H., 2006. Proper SUMO-1 conjugation is essential to DJ-1 to exert its full activities. Cell Death Differ. 13 (1), 96–108. https://doi.org/10.1038/sj.cdd.4401704.

Shoesmith Berke, S.J., Flores Schmied, F.A., Brunt, E.R., Ellerby, L.M., Paulson, H.L., 2004. Caspase-mediated proteolysis of the polyglutamine disease protein ataxin-3. J. Neurochem. 89, 908–918. https://doi.org/10.1111/j.1471-4159.2004.02369.x.

Shvil, N., Banerjee, V., Zoltsman, G., Shani, T., Kahn, J., Abu-Hamad, S., Papo, N., Engel, S., Bernhagen, J., Israelson, A., 2018. MIF inhibits the formation and toxicity of misfolded SOD1 amyloid aggregates: implications for familial ALS article. Cell Death Dis. 9 https://doi.org/10.1038/s41419-017-0130-4.

Siciliano, V., Diandreth, B., Monel, B., Beal, J., Huh, J., Clayton, K.L., Wroblewska, L., McKeon, A., Walker, B.D., Weiss, R., 2018. Engineering modular intracellular protein sensor-Actuator devices. Nat. Commun. 9 (1), 1881. https://doi.org/10.1038/s41467-018-03984-5.

Sims, R., Van Der Lee, S.J., Naj, A.C., Bellenguez, C., Badarinarayan, N., Jakobsdottir, J., et al., 2017. Rare coding variants in PLCG2, ABI3, and TREM2 implicate microglial-mediated innate immunity in Alzheimer's disease. Nat. Genet. 49 (9), 1373–1384. https://doi.org/10.1038/ng.3916.

Singh, N., Lawana, V., Luo, J., Phong, P., Abdalla, A., Palanisamy, B., Rokad, D., Sarkar, S., Jin, H., Anantharam, V., Kanthasamy, A.G., Kanthasamy, A., 2018. Organophosphate pesticide chlorpyrifos impairs STAT1 signaling to induce dopaminergic neurotoxicity: implications for mitochondria mediated oxidative stress signaling events. Neurobiol. Dis. 117, 82–113. https://doi.org/10.1016/j.nbd.2018.05.019.

Sivalingam, K., Samikkannu, T., 2020. Neuroprotective effect of piracetam against cocaine-induced neuro epigenetic modification of dna methylation in astrocytes. Brain Sci. 10, 1–15. https://doi.org/10.3390/brainsci10090611.

Soares-Silva, M., Diniz, F.F., Gomes, G.N., Bahia, D., 2016. The mitogen-activated protein kinase (MAPK) pathway: role in immune evasion by trypanosomatids. Front. Microbiol. 7, 1–9. https://doi.org/10.3389/fmicb.2016.00183.

Song, G., Ouyang, G., Bao, S., 2005. The activation of Akt/PKB signaling pathway and cell survival. J. Cell. Mol. Med. 9, 59–71. https://doi.org/10.1111/j.1582-4934.2005.tb00337.x.

Sontag, J.M., Sontag, E., 2014. Protein phosphatase 2A dysfunction in Alzheimer's disease. Front. Mol. Neurosci. 7, 16. https://doi.org/10.3389/fnmol.2014.00016.

Soonpaa, M.H., Field, L.J., Spalding, K., Bhardwaj, R.D., Buchholz, B., Druid, H., Vries, H..De, Nydal, R., Lovseth, K., Levin, I., Kromer, B., Spalding, K.L., Buchholz, B. A., Druid, H., Libby, W.F., Berger, R., Mead, J.F., Alexander, G.V., Ross, J.F., Harkness, D.D., Rubart, M., Field, L.J., Parmacek, M.S., Solaro, R.J., Olivetti, G., Melissari, M., Capasso, J.M., Anversa, P., Sarkisov, D.S., Arefyeva, A.M., Panova, N. W., Gvasava, I.G., Oberpriller, J.O., Oberpriller, J.C., Mauro, A., Myerson, D., Saffitz, J.E., Murry, C.E., Hanawalt, P.C., Spalding, K., Toro, M., Cassidy, R., Stahlberg, M., Bergman, T., Kurdyla, D., Stiftelse, W., Frontiers, H., Program, S., 2009. S-Nitrosylation Of Drp1 Mediates B -Amyloid – Related Mitochondrial Fission and Neuronal Injury, pp. 102–106.

Soriano-Tárraga, C., Jiménez-Conde, J., Roquer, J., 2019. Epigenetics and aging. Handb. Nutr. Diet, Epigenetics 2, 1413–1433. https://doi.org/10.1007/978-3-319-55530-0_123.

Soto, C., 2003. Unfolding the role of protein misfolding in neurodegenerative diseases. Nat. Rev. Neurosci. 4 (1), 49–60. https://doi.org/10.1038/nrn1007.

Srinivas Bharath, M.M., 2017. Post-translational oxidative modifications of mitochondrial complex i (NADH: ubiquinone oxidoreductase): implications for pathogenesis and therapeutics in human diseases. J. Alzheimers Dis. 60, S69–S86. https://doi.org/10.3233/JAD-170117.

Stram, A.R., Payne, R.M., 2016. Post-translational modifications in mitochondria: protein signaling in the powerhouse. Cell. Mol. Life Sci. 73 (21), 4063–4073. https://doi.org/10.1007/s00018-016-2280-4.

Stykel, M.G., Humphries, K., Kirby, M.P., Czaniecki, C., Wang, T., Ryan, T., Bamm, V., Ryan, S.D., 2018. Nitration of microtubules blocks axonal mitochondrial transport in a human pluripotent stem cell model of Parkinson's disease. FASEB J. 32 (10), 5350–5364. https://doi.org/10.1096/fj.201700759RR.

Su, Z., Burchfield, J.G., Yang, P., Humphrey, S.J., Yang, G., Francis, D., Yasmin, S., Shin, S.Y., Norris, D.M., Kearney, A.L., Astore, M.A., Scavuzzo, J., Fisher-Wellman, K.H., Wang, Q.P., Parker, B.L., Neely, G.G., Vafaee, F., Chiu, J., Yeo, R., Hogg, P.J., Fazakerley, D.J., Nguyen, L.K., Kuyucak, S., James, D.E., 2019. Global redox proteome and phosphoproteome analysis reveals redox switch in Akt. Nat. Commun. 10, 1–18. https://doi.org/10.1038/s41467-019-13114-4.

Subbanna, S., Nagre, N.N., Shivakumar, M., Basavarajappa, B.S., 2016. A single day of 5-azacytidine exposure during development induces neurodegeneration in neonatal mice and neurobehavioral deficits in adult mice. Physiol. Behav. 167, 16–27. https://doi.org/10.1016/j.physbeh.2016.08.036.

Subramaniam, S., Mealer, R.G., Sixt, K.M., Barrow, R.K., Usiello, A., Snyder, S.H., 2010. Rhes, a physiologic regulator of sumoylation, enhances cross-sumoylation between the basic sumoylation enzymes E1 and Ubc9. J. Biol. Chem. https://doi.org/10.1074/jbc.C110.127191.

Sugimoto, M., 2014. A cascade leading to premature aging phenotypes including abnormal tumor profiles in Werner syndrome (Review). Int. J. Mol. Med. 33, 247–253. https://doi.org/10.3892/ijmm.2013.1592.

Sun, Y., Liu, W.-Z., Liu, T., Feng, X., Yang, N., Zhou, H.-F., 2015. Signaling pathway of MAPK/ERK in cell proliferation, differentiation, migration, senescence and apoptosis. J. Recept. Signal Transduct. Res. 35, 600–604. https://doi.org/10.3109/10799893.2015.1030412.

Sun, M., Asghar, S.Z., Zhang, H., 2016. The polarity protein Par3 regulates APP trafficking and processing through the endocytic adaptor protein Numb. Neurobiol. Dis. 93, 1–11. https://doi.org/10.1016/j.nbd.2016.03.022.

Sweeney, P., Park, H., Baumann, M., Dunlop, J., Frydman, J., Kopito, R., McCampbell, A., Leblanc, G., Venkateswaran, A., Nurmi, A., Hodgson, R., 2017. Protein misfolding in neurodegenerative diseases: implications and strategies. Transl. Neurodegener. 6, 1–13. https://doi.org/10.1186/s40035-017-0077-5.

Takada, S., Fujimori, S., Shinozuka, T., Takada, R., Mii, Y., 2017. JB special review-wnt signaling: biological functions and its implications in diseases differences in the secretion and transport of Wnt proteins. J. Biochem. 161, 1–7. https://doi.org/10.1093/jb/mvw071.

Takada-Takatori, Y., Nakagawa, S., Kimata, R., Nao, Y., Mizukawa, Y., Urushidani, T., Izumi, Y., Akaike, A., Tsuchida, K., Kume, T., 2019. Donepezil modulates amyloid precursor protein endocytosis and reduction by up-regulation of SNX33 expression in primary cortical neurons. Sci. Rep. 9, 1–11. https://doi.org/10.1038/s41598-019-47462-4.

Tamaki, Y., Shodai, A., Morimura, T., Hikiami, R., Minamiyama, S., Ayaki, T., Tooyama, I., Furukawa, Y., Takahashi, R., Urushitani, M., 2018. Elimination of TDP-43 inclusions linked to amyotrophic lateral sclerosis by a misfolding-specific intrabody with dual proteolytic signals. Sci. Rep. 8, 1–16. https://doi.org/10.1038/s41598-018-24463-3.

Tanase, M., Urbanska, A.M., Zolla, V., Clement, C.C., Huang, L., Morozova, K., Follo, C., Goldberg, M., Roda, B., Reschiglian, P., Santambrogio, L., 2016. Role of carbonyl modifications on aging-associated protein aggregation. Sci. Rep. 6, 1–14. https://doi.org/10.1038/srep19311.

Tang, H., Wu, Y., Wang, D., Razak, Y.A., Wei, N., Almansob, Y.A.M., He, W., Liu, D., 2018. Uncorrected Author Proof Tau Abnormalities and the Potential Uncorrected Author Proof. https://doi.org/10.3233/JAD-180868.

Tanikawa, C., Ueda, K., Suzuki, A., Iida, A., Nakamura, R., Atsuta, N., Tohnai, G., Sobue, G., Saichi, N., Momozawa, Y., Kamatani, Y., Kubo, M., Yamamoto, K., Nakamura, Y., Matsuda, K., 2018. Citrullination of RGG motifs in FET proteins by PAD4 regulates protein aggregation and ALS susceptibility. Cell Rep. 22 (6), 1473–1483. https://doi.org/10.1016/j.celrep.2018.01.031.

Thomas, S.N., Funk, K.E., Wan, Y., Liao, Z., Davies, P., Kuret, J., Yang, A.J., 2012. Dual modification of Alzheimer's disease PHF-tau protein by lysine methylation and ubiquitylation: a mass spectrometry approach. Acta Neuropathol. 123 (1), 105–117. https://doi.org/10.1007/s00401-011-0893-0.

Thornalley, P.J., 2003. Use of aminoguanidine (Pimagedine) to prevent the formation of advanced glycation endproducts. Arch. Biochem. Biophys. 419, 31–40. https://doi.org/10.1016/j.abb.2003.08.013.

Todi, S.V., Scaglione, K.M., Blount, J.R., Basrur, V., Conlon, K.P., Pastore, A., Elenitoba-Johnson, K., Paulson, H.L., 2010. Activity and cellular functions of the deubiquitinating enzyme and polyglutamine disease protein ataxin-3 are regulated by ubiquitination at lysine 117. J. Biol. Chem. 285, 39303–39313. https://doi.org/10.1074/jbc.M110.181610.

Trzeciakiewicz, H., Tseng, J.H., Wander, C.M., Madden, V., Tripathy, A., Yuan, C.X., Cohen, T.J., 2017. A dual pathogenic mechanism links tau acetylation to sporadic tauopathy. Sci. Rep. 7, 44102. https://doi.org/10.1038/srep44102.

Tundo, G.R., Sbardella, D., Santoro, A.M., Coletta, A., Oddone, F., Grasso, G., Milardi, D., Lacal, P.M., Marini, S., Purrello, R., Graziani, G., Coletta, M., 2020. The proteasome as a druggable target with multiple therapeutic potentialities: cutting and non-cutting edges. Pharmacol. Ther. 213, 107579. https://doi.org/10.1016/j.pharmthera.2020.107579.

Uehara, T., Nakamura, T., Yao, D., Shi, Z.Q., Gu, Z., Ma, Y., Masliah, E., Nomura, Y., Lipton, S.A., 2006. S-Nitrosylated protein-disulphide isomerase links protein misfolding to neurodegeneration. Nature 441, 513–517. https://doi.org/10.1038/nature04782.

Varland, S., Osberg, C., Arnesen, T., 2015. N-terminal modifications of cellular proteins: the enzymes involved, their substrate specificities and biological effects. Proteomics 15 (14), 2385–2401. https://doi.org/10.1002/pmic.201400619.

Vicente Miranda, H., Gomes, M.A., Branco-Santos, J., Breda, C., Lázaro, D.F., Lopes, L.V., Herrera, F., Giorgini, F., Outeiro, T.F., 2016. Glycation potentiates neurodegeneration in models of Huntington's disease. Sci. Rep. 6, 1–12. https://doi.org/10.1038/srep36798.

Vicente Miranda, H., Szego, É.M., Oliveira, L.M.A., Breda, C., Darendelioglu, E., De Oliveira, R.M., Ferreira, D.G., Gomes, M.A., Rott, R., Oliveira, M., Munari, F., Enguita, F.J., Simões, T., Rodrigues, E.F., Heinrich, M., Martins, I.C., Zamolo, I., Riess, O., Cordeiro, C., Ponces-Freire, A., Lashuel, H.A., Santos, N.C., Lopes, L.V., Xiang, W., Jovin, T.M., Penque, D., Engelender, S., Zweckstetter, M., Klucken, J., Giorgini, F., Quintas, A., Outeiro, T.F., 2017. Glycation potentiates α-synuclein-associated neurodegeneration in synucleinopathies. Brain 140 (5), 1399–1419. https://doi.org/10.1093/brain/awx056.

Vidal, R., Caballero, B., Couve, A., Hetz, C., 2011. Converging pathways in the occurrence of endoplasmic reticulum (ER) stress in Huntingtons disease. Curr. Mol. Med. 11 (1), 1–12. https://doi.org/10.2174/156652411794474419.

Videira, P.A.Q., Castro-Caldas, M., 2018. Linking glycation and glycosylation with inflammation and mitochondrial dysfunction in Parkinson's disease. Front. Neurosci. 12, 381. https://doi.org/10.3389/fnins.2018.00381.

Vielemeyer, O., Nizak, C., Jimenez, A.J., Echard, A., Goud, B., Camonis, J., Rain, J.C., Perez, F., 2010. Characterization of single chain antibody targets through yeast two hybrid. BMC Biotechnol. 10, 59. https://doi.org/10.1186/1472-6750-10-59.

Vijayakumaran, S., Pountney, D.L., 2018. SUMOylation, aging and autophagy in neurodegeneration. Neurotoxicology 66, 53–57. https://doi.org/10.1016/j.neuro.2018.02.015.

Visintin, M., Tse, E., Axelson, H., Rabbitts, T.H., Cattaneo, A., 1999. Selection of antibodies for intracellular function using a two-hybrid in vivo system. Proc. Natl. Acad. Sci. U. S. A. 96 (21) https://doi.org/10.1073/pnas.96.21.11723, 11723-8.

Visintin, M., Settanni, G., Maritan, A., Graziosi, S., Marks, J.D., Cattaneo, A., 2002. The intracellular antibody capture technology (IACT): Towards a consensus sequence for intracellular antibodies. J. Mol. Biol. 317 (1), 73–83. https://doi.org/10.1006/jmbi.2002.5392.

Volloch, V., Rits, S., 2018. Results of beta secretase-inhibitor clinical trials support amyloid precursor protein-independent generation of beta amyloid in sporadic Alzheimer's disease. Med. Sci. 6, 45. https://doi.org/10.3390/medsci6020045.

Walter, P., Ron, D., 2011. The unfolded protein response: from stress pathway to homeostatic regulation. Science (80-.) 334 (6059), 1081–1086. https://doi.org/10.1126/science.1209038.

Wang, S., Kaufman, R.J., 2012. The impact of the unfolded protein response on human disease. J. Cell Biol. 197 (7), 857–867. https://doi.org/10.1083/jcb.201110131.

Wang, S., Huang, X., Sun, D., Xin, X., Pan, Q., Peng, S., Liang, Z., Luo, C., Yang, Y., Jiang, H., Huang, M., Chai, W., Ding, J., Geng, M., 2012. Extensive crosstalk between O-GlcNAcylation and phosphorylation regulates Akt signaling. PLoS One 7, e37427. https://doi.org/10.1371/journal.pone.0037427.

Wang, P., Wander, C.M., Yuan, C.X., Bereman, M.S., Cohen, T.J., 2017. Acetylation-induced TDP-43 pathology is suppressed by an HSF1-dependent chaperone program. Nat. Commun. 8 (1), 82. https://doi.org/10.1038/s41467-017-00088-4.

Wang, Z., Zhao, Y., Xu, N., Zhang, S., Wang, S., Mao, Y., Zhu, Y., Li, B., Jiang, Y., Tan, Y., Xie, W., Yang, B.B., Zhang, Y., 2019. NEAT1 regulates neuroglial cell mediating Aβ clearance via the epigenetic regulation of endocytosis-related genes expression. Cell. Mol. Life Sci. https://doi.org/10.1007/s00018-019-03074-9.

Wang, H., Lu, J., Gao, W.C., Ma, X., Li, N., Ding, Z., Wu, C., Zhu, M., Qiao, G., Xiao, C., Zhang, C., Chen, C., Weng, Z., Yang, W., Zheng, C.B., 2020a. Donepezil down-regulates propionylation, 2-hydroxyisobutyrylation, butyrylation, succinylation, and crotonylation in the brain of bilateral common carotid artery occlusion-induced vascular dementia rats. Clin. Exp. Pharmacol. Physiol. 47 (10), 1731–1739. https://doi.org/10.1111/1440-1681.13352.

Wang, L., Shi, F.X., Li, N., Cao, Y., Lei, Y., Wang, J.Z., Tian, Q., Zhou, X.W., 2020b. AMPK ameliorates tau acetylation and memory impairment through Sirt1. Mol. Neurobiol. 57 (12), 5011–5025. https://doi.org/10.1007/s12035-020-02079-x.

Wani, W.Y., Chatham, J.C., Darley-Usmar, V., McMahon, L.L., Zhang, J., 2017. O-GlcNAcylation and neurodegeneration. Brain Res. Bull. 133, 80–87. https://doi.org/10.1016/j.brainresbull.2016.08.002.

Warmack, R.A., Boyer, D.R., Zee, C., Richards, L.S., Sawaya, M.R., Cascio, D., Gonen, T., Eisenberg, D.S., Clarke, S.G., 2019a. reveals a distinct proto fi lament interface. Nat. Commun. 1–12. https://doi.org/10.1038/s41467-019-11183-z.

Warmack, R.A., Boyer, D.R., Zee, C.T., et al., 2019b. Structure of amyloid-β (20-34) with Alzheimer's-associated isomerization at Asp23 reveals a distinct protofilament interface. Nat. Commun. 10, 3357 https://doi.org/10.1038/s41467-019-11183-z.

Weber, J.J., Golla, M., Guaitoli, G., Wanichawan, P., Hayer, S.N., Hauser, S., Krahl, A.C., Nagel, M., Samer, S., Aronica, E., Carlson, C.R., Schöls, L., Riess, O., Gloeckner, C.J., Nguyen, H.P., Hübener-Schmid, J., 2017. A combinatorial approach to identify calpain cleavage sites in the Machado-Joseph disease protein ataxin-3. Brain 140, 1280–1299. https://doi.org/10.1093/brain/awx039.

Weids, A.J., Ibstedt, S., Tamás, M.J., Grant, C.M., 2016. Distinct stress conditions result in aggregation of proteins with similar properties. Sci. Rep. 6, 1–12. https://doi.org/10.1038/srep24554.

Weng, L., Laboureur, L., Wang, Q., Guo, L., Xu, P., Gottlieb, L., Lynch, D.R., Mesaros, C., Blair, I.A., 2020. Extra-mitochondrial mouse frataxin and its implications for mouse models of Friedreich's ataxia. Sci. Rep. 10 https://doi.org/10.1038/s41598-020-72884-w.

Wheatley, E.G., Albarran, E., White, C.W., Bieri, G., Sanchez-Diaz, C., Pratt, K., Snethlage, C.E., Ding, J.B., Villeda, S.A., 2019. Neuronal O-GlcNAcylation improves cognitive function in the aged mouse brain. Curr. Biol. 29 (3359–3369), e4. https://doi.org/10.1016/j.cub.2019.08.003.

Wiersma, V.R., Michalak, M., Abdullah, T.M., Bremer, E., Eggleton, P., 2015. Mechanisms of translocation of ER chaperones to the cell surface and immunomodulatory roles in cancer and autoimmunity. Front. Oncol. 5, 1–14. https://doi.org/10.3389/fonc.2015.00007.

Wilcox, K.C., Zhou, L., Jordon, J.K., Huang, Y., Yu, Y., Redler, R.L., Chen, X., Caplow, M., Dokholyan, N.V., 2009. Modifications of superoxide dismutase (SOD1) in human erythrocytes: a possible role in amyotrophic lateral sclerosis. J. Biol. Chem. 284, 13940–13947. https://doi.org/10.1074/jbc.M809687200.

Wong, M.L., Arcos-Burgos, M., Liu, S., Vélez, J.I., Yu, C., Baune, B.T., Jawahar, M.C., Arolt, V., Dannlowski, U., Chuah, A., Huttley, G.A., Fogarty, R., Lewis, M.D., Bornstein, S.R., Licinio, J., 2017. The PHF21B gene is associated with major depression and modulates the stress response. Mol. Psychiatry 22 (7), 1015–1025. https://doi.org/10.1038/mp.2016.174.

Wood, I.C., 2018. The contribution and therapeutic potential of epigenetic modifications in Alzheimer's disease. Front. Neurosci. 12, 1–11. https://doi.org/10.3389/fnins.2018.00649.

Wu, X.F., Wang, A.F., Chen, L., Huang, E.P., Xie, W.B., Liu, C., Huang, W.Y., Chen, C.X., Qiu, P.M., Wang, H.J., 2014. S-nitrosylating protein disulphide isomerase mediates α-synuclein aggregation caused by methamphetamine exposure in PC12 cells. Toxicol. Lett. 230, 19–27. https://doi.org/10.1016/j.toxlet.2014.07.026.

Xia, Z.X., Shen, Z.C., Zhang, S.Q., Wang, J., Nie, T.L., Deng, Q., Chen, J.G., Wang, F., Wu, P.F., 2019. De-palmitoylation by N-(tert-Butyl) hydroxylamine inhibits AMPAR-mediated synaptic transmission via affecting receptor distribution in postsynaptic densities. CNS Neurosci. Ther. 25 (2), 187–199. https://doi.org/10.1111/cns.12996.

Xiang, W., Menges, S., Schlachetzki, J.C.M., Meixner, H., Hoffmann, A.C., Schlötzer-Schrehardt, U., Becker, C.M., Winkler, J., Klucken, J., 2015. Posttranslational modification and mutation of histidine 50 trigger alpha synuclein aggregation and toxicity. Mol. Neurodegener. https://doi.org/10.1186/s13024-015-0004-0.

Xiangmin, Lin, Cook, Travis J., Zabetian, Cyrus P., Leverenz, James B., Peskind, Elaine R., Hu, Shu-Ching, Cain, Kevin C., Pan, Catherine, Edgar, John Scott, Goodlett, David R., Racette, Brad A., Checkoway, Harvey, Montine, Thomas J., M.S.& J.Z, 2012. DJ-1 Isoforms in Whole Blood as Potential Biomarkers of Parkinson Disease _ Scientific Reports.

Xu, H., Wang, Y., Lin, S., Deng, W., Peng, D., Cui, Q., Xue, Y., 2018. PTMD: a database of human disease-associated post-translational modifications. Genomics Proteomics Bioinf. 16 (4), 244–251. https://doi.org/10.1016/j.gpb.2018.06.004.

Xu, F., Na, L., Li, Y., Chen, L., 2020. Roles of the PI3K/AKT/mTOR signalling pathways in neurodegenerative diseases and tumours. Cell Biosci. 10, 1–12. https://doi.org/10.1186/s13578-020-00416-0.

Yalinca, H., Gehin, C.J.C., Oleinikovas, V., Lashuel, H.A., Gervasio, F.L., Pastore, A., 2019. The role of post-translational modifications on the energy landscape of huntingtin N-terminus. Front. Mol. Biosci. 6 https://doi.org/10.3389/fmolb.2019.00095.

Yan, R., Farrelly, S., McCarthy, J.V., 2013. Presenilins are novel substrates for TRAF6-mediated ubiquitination. Cell. Signal. 25 (9), 1769–1779. https://doi.org/10.1016/j.cellsig.2013.05.015.

Yan, Y., Zhou, X.E., Xu, H.E., Melcher, K., 2018. Structure and physiological regulation of AMPK. Int. J. Mol. Sci. 19 https://doi.org/10.3390/ijms19113534.

Yanai, A., Huang, K., Kang, R., Singaraja, R.R., Arstikaitis, P., Gan, L., Orban, P.C., Mullard, A., Cowan, C.M., Raymond, L.A., Drisdel, R.C., Green, W.N., Ravikumar, B., Rubinsztein, D.C., El-Husseini, A., Hayden, M.R., 2006. Palmitoylation of huntingtin by HIP14is essential for its trafficking and function. Nat. Neurosci. 9, 824–831. https://doi.org/10.1038/nn1702.

Yang, W.-L., Wang, J., Chan, C.-H., Lee, S.-W., Campos, A.D., Lamothe, B., Hur, L., Grabiner, B.C., Lin, X., Darnay, B.G., Lin, H.-K., 2009. The E3 ligase TRAF6 regulates Akt ubiquitination and activation. Science 325, 1134–1138. https://doi.org/10.1126/science.1175065.

Yang, G., Liu, Y., Yang, K., Liu, R., Zhu, S., Coquinco, A., Wen, W., Kojic, L., Jia, W., Cynader, M., 2012. Isoform-specific palmitoylation of JNK regulates axonal development. Cell Death Differ. 19, 553–561. https://doi.org/10.1038/cdd.2011.124.

Yang, E., Tacchelly-Benites, O., Wang, Z., Randall, M.P., Tian, A., Benchabane, H., Freemantle, S., Pikielny, C., Tolwinski, N.S., Lee, E., Ahmed, Y., 2016. Wnt pathway activation by ADP-ribosylation. Nat. Commun. 7 https://doi.org/10.1038/ncomms11430.

Yang, H., Gu, Z.T., Li, L., Maegele, M., Zhou, B.Y., Li, F., Zhao, M., Zhao, K.Sen, 2017. SIRT1 plays a neuroprotective role in traumatic brain injury in rats via inhibiting the p38 MAPK pathway. Acta Pharmacol. Sin. 38, 168–181. https://doi.org/10.1038/aps.2016.130.

Yang, Yunzhi, Ma, F., Liu, Zhengshuai, Su, Q., Liu, Y., Liu, Zhixue, Li, Y., 2019a. The ER-localized Ca2-binding protein calreticulin couples ER stress to autophagy by associating with microtubule-associated protein 1A/1B light chain 3. J. Biol. Chem. 294, 772–782. https://doi.org/10.1074/jbc.RA118.005166.

Yang, Yun, Tapias, V., Acosta, D., Xu, H., Chen, H., Bhawal, R., Anderson, E., Ivanova, E., Lin, H., Sagdullaev, B.T., Klein, W.L., Viola, K.L., Gandy, S., Haroutunian, V., Beal, M.F., Eliezer, D., Zhang, S., Gibson, G.E., 2019b. Succinylation links metabolic reductions to amyloid and tau pathology. bioRxiv. https://doi.org/10.1101/764837. PPR92598.

Ye, Z.W., Zhang, J., Ancrum, T., Manevich, Y., Townsend, D.M., Tew, K.D., 2017. Glutathione S-transferase P-mediated protein S-glutathionylation of resident endoplasmic reticulum proteins influences sensitivity to drug-induced unfolded protein response. Antioxidants Redox Signal. 26, 247–261. https://doi.org/10.1089/ars.2015.6486.

Yeganeh, B., Jäger, R., Gorman, A.M., Samali, A., Ghavami, S., 2015. Induction of autophagy: role of endoplasmic reticulum stress and unfolded protein response. Autophagy Cancer Other Pathol. Inflammation Immunity Infect. Aging 7, 91–101. https://doi.org/10.1016/B978-0-12-801043-3.00005-4.

Yin, S., Ran, Q., Yang, J., Zhao, Y., Li, C., 2020. Nootropic effect of neferine on aluminium chloride–induced Alzheimer's disease in experimental models. J. Biochem. Mol. Toxicol. 34 (2), e22429. https://doi.org/10.1002/jbt.22429.

Yoon, S.O., Park, D.J., Ryu, J.C., Ozer, H.G., Tep, C., Shin, Y.J., Lim, T.H., Pastorino, L., Kunwar, A.J., Walton, J.C., Nagahara, A.H., Lu, K.P., Nelson, R.J., Tuszynski, M.H., Huang, K., 2012. JNK3 perpetuates metabolic stress induced by aβ peptides. Neuron 75, 824–837. https://doi.org/10.1016/j.neuron.2012.06.024.

Young, F.B., Butland, S.L., Sanders, S.S., Sutton, L.M., Hayden, M.R., 2012. Putting proteins in their place: palmitoylation in Huntington disease and other neuropsychiatric diseases. Prog. Neurobiol. 97, 220–238. https://doi.org/10.1016/j.pneurobio.2011.11.002.

Yue, F., Li, W., Zou, J., Chen, Q., Xu, G., Huang, H., Xu, Z., Zhang, S., Gallinari, P., Wang, F., McKeeha, W.L., Liu, L., 2015. Blocking the association of HDAC4 with MAP1S accelerates autophagy clearance of mutant Huntingtin. Aging (Albany. NY) 7, 839–853. https://doi.org/10.18632/aging.100818.

Zamzow, D.R., Elias, V., Acosta, V.A., Escobedo, E., Magnusson, K.R., 2019. Higher levels of protein palmitoylation in the frontal cortex across aging were associated with reference memory and executive function declines. eNeuro 6. https://doi.org/10.1523/ENEURO.0310-18.2019.

Zaręba-Kozioł, M., Figiel, I., Bartkowiak-Kaczmarek, A., Włodarczyk, J., 2018. Insights into protein S-palmitoylation in synaptic plasticity and neurological disorders: potential and limitations of methods for detection and analysis. Front. Mol. Neurosci. 11, 175. https://doi.org/10.3389/fnmol.2018.00175.

Zhang, Z., Lee, Y.C., Kim, S.J., Choi, M.S., Tsai, P.C., Xu, Y., Xiao, Y.J., Zhang, P., Heffer, A., Mukherjee, A.B., 2006. Palmitoyl-protein thioesterase-1 deficiency mediates the activation of the unfolded protein response and neuronal apoptosis in INCL. Hum. Mol. Genet. 15, 337–346. https://doi.org/10.1093/hmg/ddi451.

Zhang, J., Li, X., Li, J.Da, 2019. The roles of post-translational modifications on α-Synuclein in the pathogenesis of Parkinson's diseases. Front. Neurosci. 13 https://doi.org/10.3389/fnins.2019.00381.

Zhao, J., Wang, P., Li, H., Gao, Z., 2015. Nitration of Y10 in Aβ1-40: is it a compensatory reaction against oxidative/nitrative stress and Aβ aggregation? Chem. Res. Toxicol. 28 (3), 401–407. https://doi.org/10.1021/tx500353s.

Zhao, J., Wu, J., Yang, Z., Li, H., Gao, Z., 2017. Nitration of tyrosine residue Y10 of Aβ1-42 significantly inhibits its aggregation and cytotoxicity. Chem. Res. Toxicol. 30 (4), 1085–1092. https://doi.org/10.1021/acs.chemrestox.6b00447.

Zheng, Q., Huang, T., Zhang, L., Zhou, Y., Luo, H., Xu, H., Wang, X., 2016. Dysregulation of ubiquitin-proteasome system in neurodegenerative diseases. Front. Aging Neurosci. 8, 1–10. https://doi.org/10.3389/fnagi.2016.00303.

Zhou, Y.F., Liao, S.S., Luo, Y.Y., Tang, J.G., Wang, J.L., Lei, L.F., Chi, J.W., Du, J., Jiang, H., Xia, K., Tang, B.S., Shen, L., 2013. SUMO-1 modification on K166 of PolyQ-expanded ataxin-3 strengthens its stability and increases its cytotoxicity. PLoS One 8, 1–9. https://doi.org/10.1371/journal.pone.0054214.

Zhu, Y., Shan, X., Safarpour, F., Erro Go, N., Li, N., Shan, A., Huang, M.C., Deen, M., Holicek, V., Ashmus, R., Madden, Z., Gorski, S., Silverman, M.A., Vocadlo, D.J., 2018. Pharmacological inhibition of O-GlcNAcase enhances autophagy in brain through an mTOR-independent pathway. ACS Chem. Neurosci. 9 (6), 1366–1379. https://doi.org/10.1021/acschemneuro.8b00015.

Zivanovic, J., Kouroussis, E., Kohl, J.B., Adhikari, B., Bursac, B., Schott-Roux, S., Petrovic, D., Miljkovic, J.L., Thomas-Lopez, D., Jung, Y., Miler, M., Mitchell, S., Milosevic, V., Gomes, J.E., Benhar, M., Gonzales-Zorn, B., Ivanovic-Burmazovic, I., Torregrossa, R., Mitchell, J.R., Whiteman, M., Schwarz, G., Snyder, S.H., Paul, B.D., Carroll, K.S., Filipovic, M.R., 2019. Selective persulfide detection reveals evolutionarily conserved antiaging effects of S-sulfhydration. Cell Metab. 30 (1152–1170), e13. https://doi.org/10.1016/j.cmet.2019.10.007.

Zmijewski, J.W., Banerjee, S., Bae, H., Friggeri, A., Lazarowski, E.R., Abraham, E., 2010. Exposure to hydrogen peroxide induces oxidation and activation of AMP-activated protein kinase. J. Biol. Chem. 285, 33154–33164. https://doi.org/10.1074/jbc.M110.143685.

Zulueta, A., Mingione, A., Signorelli, P., Caretti, A., Ghidoni, R., Trinchera, M., 2020. Simple and Complex Sugars in Parkinson's Disease: a Bittersweet Taste. Mol. Neurobiol. 57, 2934–2943. https://doi.org/10.1007/s12035-020-01931-4.

Zungu, M., Schisler, J.C., Essop, M.F., McCudden, C., Patterson, C., Willis, M.S., 2011. Regulation of AMPK by the ubiquitin proteasome system. Am. J. Pathol. 178, 4–11. https://doi.org/10.1016/j.ajpath.2010.11.030.

Applied Intelligence
https://doi.org/10.1007/s10489-021-02201-z

Random area-perimeter method for generation of unimodal and multimodal cancelable biometric templates

Rajesh Asthana [1] · Gurjit Singh Walia [2] · Anjana Gupta [1]

Accepted: 6 January 2021
© The Author(s), under exclusive licence to Springer Science+Business Media, LLC part of Springer Nature 2021

Abstract
In recent times, biometric based authentication systems have seen a tremendous growth in various applications. However, if databases in multiple applications are created using the same biometric characteristic and algorithm, then any compromise of the stored template in one biometric system may jeopardise the security of the other biometric systems as well. More importantly, such a compromise may also lead to a permanent loss of the biometric characteristic. Therefore, the cancelability or revocability of biometrics has become quite an essential requirement. In this paper, a novel scheme, the Random Area & Perimeter Method (RAPM)) is presented in which a biometric characteristic of an individual is transformed into random values which are stored as cancelable biometric templates. The proposed scheme computes area and perimeter of the Bezier curve which are obtained through interpolation of feature points of original biometrics and a random point chosen by the user. The area and perimeter thus computed exhibit pseudo-random properties. This technique outperforms many existing techniques. Moreover, a dimensionality reduction to the tune of more than 95% has been obtained without compromising the matching performance. The average values obtained for EER, DI and RI are 0.0045, 6.28 and 99.64 respectively. These values are better than those obtained from the available state of the art approaches. The proposed scheme has also been analysed for various privacy issues like non-invertibility, revocability, and unlinkability.

Keywords Multimodal · Revocability · Cancelable biometrics

1 Introduction

In the modern era of technological advancement, many real life applications viz., computer login, e-commerce, access control, etc. make use of automatic personal authentication systems in order to protect our lives, physical properties, and vital digital informations. Earlier, two types of approaches: token-based and knowledge-based, were adopted for authentication. The token-based approach primarily uses physical items such as physical keys, smart cards, passports, etc., whereas the knowledge-based approach is dependent on personal knowledge like PIN, passwords etc.. There are limitations to both these approaches as it is quite possible that "tokens" and "knowledge" could be forgotten, duplicated, stolen, or lost. All these can effectively be countered by the physiological or behavioural characteristics of an individual which are known as Biometrics [1]. Physiological traits, like face, fingerprints, iris etc., and behavioural characteristics like voice, gait, keystroke dynamics etc., are unique to an individual. Moreover, these biometrics do not vary much over time means they have attribute of permanence. Due to these peculiar features, biometrics are reliably used for personal identification [2]. Now biometric systems are widely been used in smart devices like mobile phones, tablets etc.. Biometric systems are now being applied in several domains like banking, forensics, surveillance, and law enforcement.

Despite the fact that biometric systems are being used in numerous applications, there are various security and privacy concerns which are illustrated as under:

(a). Biometrics are authentic but not secret: Despite the fact that most of the biometrics possess quite a personalized attributes, some of them can potentially be misused without the user's consent. In contrast, tokens and

✉ Rajesh Asthana
asthana.rajesh30@gmail.com

[1] Department of Applied Mathematics, Delhi Technological University, Delhi, India

[2] Scientific Analysis Group, DRDO, Delhi, India

Published online: 04 March 2021

knowledge get compromised when user willingly shares them.

(b). Biometrics cannot be cancelled or revoked: Knowledge-based authentication entities can be reset if they get compromised. Similarly, token-based items can be replaced if they are stolen. Biometric characteristics of an individual are of permanent nature and therefore they are non-replaceable or non-revocable if they get compromised.

(c). Biometrics may be compromised forever: Biometrics provide usability advantages as passwords/identities are no longer needed to be remembered and their management becomes easier. However, compromise of a biometric in one application may lead to a compromise of all other applications where the same biometric have been used.

(d). Individuals can be tracked by Cross-matching of Biometrics: In case, a particular biometric is used repeatedly in a number of applications and locations, there is possibility of tracking of individual when the concerned agencies collude and share the enrolled or registered biometric templates.

Scientific communities are putting a lot of research efforts to resolve these security and privacy issues so that biometric systems could be protected against the possible attacks. The measures adopted should be able to enhance the security of biometric systems in terms of its resilience against possible attacks. A robust authentication system which has the capability to overcome the limitations posed by the conventional approaches for authentication, viz., token-based and knowledge-based, is the need of the hour. One such prominent measure is use of Cancelable biometric templates which is obtained through revocable and non-invertible transformation of original biometric features [3].

2 Motivation of the work and contribution

In any biometric based authentication system, the cross-matching and revocability of biometrics are two major issues. If a hacker gets access to the original biometric template of the user, then he might misuse it and thus there will be no trust associated with the biometrics. In this scenario, the following aspects/limitations are needed to be dealt with:

- Non-invertibility: Most of the non-invertible transformation approaches tend to be vulnerable to partial or complete inversion. Achieving complete non-invertibility is particularly challenging because increased non-invertibility results in reduced template distinctiveness, which degrades the performance. As a result, there must be a fine trade-off between non-invertibility and performance of a cancelable biometric system.
- Revocability: The system should have revocability feature in the sense that once a stored template gets compromised, a new template corresponding to same biometric feature could be generated.
- Un-linkability: The biometric templates stored in multiple applications must be unlinkable. The knowledge of one biometric template registered in one application should not reveal anything about the templates stored in other applications.

To meet these objectives, we have proposed a method where instead of storing the original biometric, their transformed values using a one-way function are stored. The transformation can be applied either in the original domain or in the feature domain.

The proposed scheme generates Cancelable templates from various modalities. Apart from the uni-modal biometrics, multi-modal biometrics derived from various combination of these biometrics have also been studied. A summary of the proposed method is given below:

- Uni-modal and multi-modal biometric systems involving biometrics like palmprint, face, palmvein, thermal face, and fingervein, have been studied. A novel scheme for generation of cancelable templates for these uni-modal and multi-modal biometrics is proposed.
- Features have been extracted from these biometric traits by using Log-Gabor filters. For generation of cancelable templates from these features, random key set as chosen by the user, are used. Feature points whose abscissa and ordinate are obtained from the extracted feature vectors and random keys are represented in the Cartesian plane.
- Bezier curves are interpolated using four control points. Out of these three control points are obtained from extracted feature vector whereas one control point is taken from the random key. Area and perimeter of these Bezier curves are computed and the random values thus obtained are used for the generation of protected templates.
- Scheme is evaluated using various performance evaluation metrics like EER, DI, RI, ROC curve, and CMC curve on the benchmark data sets. The proposed scheme gives better security and privacy and performance in comparison to state of the art approaches.

In this paper, we have devised a new method of generation of cancelable biometric templates having the desired property of revocability since a compromised biometric can be re-enrolled using another random key chosen by the user. It preserves privacy also as it is computationally difficult to recover the original biometric from a transformed one. Further, it also prevents cross-matching between databases since each

application will use a different parameter setting in the form of different random grids as conceived in the proposed method. The generated templates exhibit pseudo-random properties. This technique outperforms many existing techniques. Moreover, a dimensionality reduction to the tune of more than 95% has been obtained without compromising the matching performance. The average values obtained for Equal Error Rate (EER), Decidability Index (DI), and Recognition Index (RI) are better than those obtained from other available state of the art approaches.

The remaining paper is organised in the following manner: In Section 3, the related work in the field of Cancelable Biometrics is elaborated. In Section 4, a novel non-invertible transform based approach, namely, Random Area-Perimeter Method (RAPM) is introduced for Generation of Cancelable Biometric Templates. Generation of Bezier curves from the randomized features have been elaborated. In addition, the core design of the biometric template transformation has been described. Various Datasets and Performance Evaluation Metrics have been discussedin Section 5. Representation of the Original and Transformed Templates in the Cartesian plane have been shown in Section 6. Performance evaluation of the method have also been discussed in this section. Finally, concluding remarks and future directions in the related field have been discussed in Section 7.

3 Related work: Cancelable biometrics

A lot of research is being done in the field of Biometrics and Cryptology to address the vulnerabilities which are there in the biometric based systems. One of the most challenging areas is related to biometric template protection for which several techniques have been developed. Cancelable biometrics is one such concept in which the original biometric features/templates are not stored, rather their transformation is done by one-way function and then they are stored [4]. Such one-way transformation ensures privacy as recovering the original biometric from the transformed one is computationally difficult. In some schemes the transformation is carried out in the original (raw data) domain while in others it is done in the feature domain [5]. The most important feature of cancelable biometrics is 'revocability'. This feature ensures re-enrolment of the biometric template by another one-way function when an already enrolled biometric template gets compromised [6]. The one-way function should be chosen in such a manner that the statistical characteristics of the resultant features should remain intact so that the matching accuracy does not degrade after transformation [7–9]. The transformation techniques are broadly categorised into Non-Invertible Transforms and Biometric Salting. One way function based on non-invertible transforms use user-key and biometric as input parameters [10]. In Biometric salting, the templates are distorted by salting them with an auxiliary data. Then, some additional operations are performed on the blended data to achieve the condition of non-invertibility [11].

Davida et al. [12] started the work on Cancelable biometrics when they proposed a majority decoding scheme for iris biometrics. Ratha et al. [13] made significant contributions in concretizing the concept of Cancelable biometrics. Juels [14, 15] modified the error-correcting codes of the scheme proposed by Davida et al. and reduced the code size. Clancy et al. [16] developed a technique in which polynomial based secret-sharing scheme based was used on a locking set created by the minutiae points of the fingerprint. Ratha et al. developed non-invertible transformations based cancelable fingerprint template schemes [17]. A transformation method on fingerprint minutiae using a user defined key, was proposed by Ang et al. [18], whereas a hash-based transformation method was developed by Tulyakov et al. [19]. A new authentication approach called Bio-Hashing was proposed by Teoh et al., wherein a biometric code is generated by combining biometric feature vectors with the tokenized random vectors specific to a user [20]. Biometric cryptosystems is another important concept where in cryptology is blended with biometrics to provide security [21]. Soutar et al. proposed the concept of bioscrypt in which fingerprint image is used to generate a biometric code [22]. Sadhya et al. generated secure, cancelable iris features through locally sensitive hashing [23]. Live fingerprints were determined by exploiting the quality of fingerprint features by Sharma et al. [24]. Minutiae informations from fingerprint were modified using a key set by Ali et al. to produce cancelable biometric [25]. Cancelable biometric were generated from fingerprint by Trivedi et al. by using binary key provided by the user [26]. Wu et al. applied the method of signal subspace collapsing on ECG biometric to generate revocable biometric templates [27]. Kumar et al. introduced the concept of Random Permutation Principal Component Analysis (RP-PCA) to generate cancelable biometric using face, iris, and ear modalities [28]. Dwivedi and Dey combined Mean-Closure Weighting (MCW) with Dempster-Shafer (DS) theory to develop a hybrid cancelable multi-biometric system [29]. The concept of cross-diffusion of graphs have been used by Walia et al. [30] to develop a cancelable biometric system. Random distance method for transformation of biometric features was given by Kaur and Khanna [31]. Key images were used by Walia et al. to generate cancelable templates [32]. Gomez-Barrero et al. [33] generated cancelable templates by using bloom filters on face-iris and face-finger vein. El-Samie et al. [34] applied bio-convolving encryption on face image to generate cancelable templates. Zuo et al. [35] proposed Gray salting method which works with conventional iris recognition systems, either at the unwrapped image level or at the binary iris code level. A random-projection (RP)-based method was given by Wang et al. [36] to transform biometric data using a random matrix with each entry an independent and

identically distributed Gaussian random variable. The 2D BioHashing method presented by Teoh et al. [37], is a novel two factor authenticator based on iterated inner products between tokenised pseudo-random number and the user specific fingerprint feature, which generated from the integrated wavelet and Fourier–Mellin transform. Maiorana et al. [38] proposed bio-convolving method which is a protected on-line signature-based biometric authentication system, where the considered biometrics are secured by means of non-invertible transformations, able to generate templates from which retrieving the original information is computationally as hard as random guessing it. Lu Leng & Jiashu Zhang [39] presented a 2D BioPhasor method in which in order to reduce the computational complexity and storage cost, cancelable palmprint coding frameworks are extended from one dimension to two dimensions. Lu Leng et al. [40] also proposed a novel cancelable palmprint template, called "PalmPhasor", which is a set of binary code fusing the user-specific tokenised pseudo-random number (PRN) and multi-orientation texture features of PalmCodes. Random Permutation Maxout (RPM) transform method was proposed by S Cho & A B Teoh [41] wherein a real-valued face feature vector (template) is transformed into a discrete index code as a means of protected form of face template. H Kaur & P Khanna [42] presented a template protection approach which generates revocable binary features from phase and magnitude patterns of Log-Gabor filters. They also proposed random slope methods for generation of cancelable features [43]. A random distance based approach was presented by the same authors for protection of biometric templates [44]. Kapil et al. [45] proposed a multimodal biometric system, which adaptively combines the scores from individual classifiers. In this, three modalities viz. face, finger, and iris have been used to extract individual classifier scores where the concurrent modalities were boosted and discordant modalities were suppressed. A secure multimodal cancelable biometric system was proposed by Walia et al. [46] in which key images based generic feature extraction technique reduces feature dimension and achieves revocability. The non-invertibility and unlinkability were ensured through cross-diffusion of complementary information from different modalities. Shengmin Xu et al. [47] proposed a cryptographic primitive 'ElGamal type cryptosystem' which derive a variety of attribute-based encryption (ABE) schemes. They presented a generic construction of revocable attribute-based encryption and dual-policy attribute-based encryption with formal definitions and security proofs. Yin et al. [48] presented a novel concept of revocability in terms of decryption rights delegation. In this method he used binary-tree structure to implement the revocation of decryption rights, so that the update of re-encryption key is reduced to O(logN) (instead of O(N)), where N is the maximum number of delegatee. A partial Hadamard transform to securely protect binary biometric representations in the design of cancelable biometrics was proposed by Wang et al. [49]. In this method, non-invertible transform is applied to the DFT of the binary biometric representations, the resultant templates are complex vectors, from which the original binary vectors cannot be restored. This method also preserves the stochastic distance between binary vectors after the transformation.

As described above, various approaches have been adopted for protection of biometric templates. However, there is a great scope for improvement in terms of dimensionality reduction, storage requirement and performance of the cancelable template generation technique. Thus, a robust, non-invertible and revocable biometric template generation mechanism should be accorded top priority for the maximum usage of biometric based systems. In this paper a new technique for the template protection is proposed which satisfies all the four essential requirements as mentioned in the previous section.

4 Proposed cancelable biometric system (RAPM)

An architecture of the proposed cancelable biometric system is shown in Fig. 1.

As shown in the above diagram, in the proposed scheme two modalities e.g., face and palmvein, are taken. From these biometrics, features are extracted using Log-Gabor filters. The extracted features for the first modality are divided in to two sets e.g., $\{x_1,x_2,\ldots,x_{n-1}, x_n\}$and $\{y_1,y_2,\ldots,y_{n-1},y_n\}$. The corresponding values from both these sets are used to form features points. Similarly, the extracted features for the second modality are divided in to two sets e.g., $\{w_1,w_2,\ldots, w_{n-1},w_n\}$ & $\{z_1,z_2,\ldots, z_{n-1},z_n\}$ and feature points are formed. User selects a random key which is also divided into two sets e.g., $\{u_1,u_2, \ldots,u_{n-1},u_n\}$ and $\{v_1,v_2,\ldots,v_{n-1}, v_n\}$. The corresponding values from both these sets are used to form random points. The feature points and the random points are used to interpolate cubic Bezier curves. The perimeters **P** of these curves are computed. Also, the area **A** enclosed by these curves and x-axis are computed. The areas and perimeters are used to derive the transformed templates $\mathbf{T_f}$ after certain steps as described in Section 3.2. These templates are stored in the database at the time of registration of the user. For authentication, user presents his modalities to the system. The above procedure is followed again to get the transformed value T_f. This value is compared with the template already stored in the database and accordingly decision is taken whether the subject is genuine or imposter.

4.1 Multi-modal feature extraction

For extraction of features from several biometric traits, Log-Gabor filters have been used. The Log-Gabor filters are used

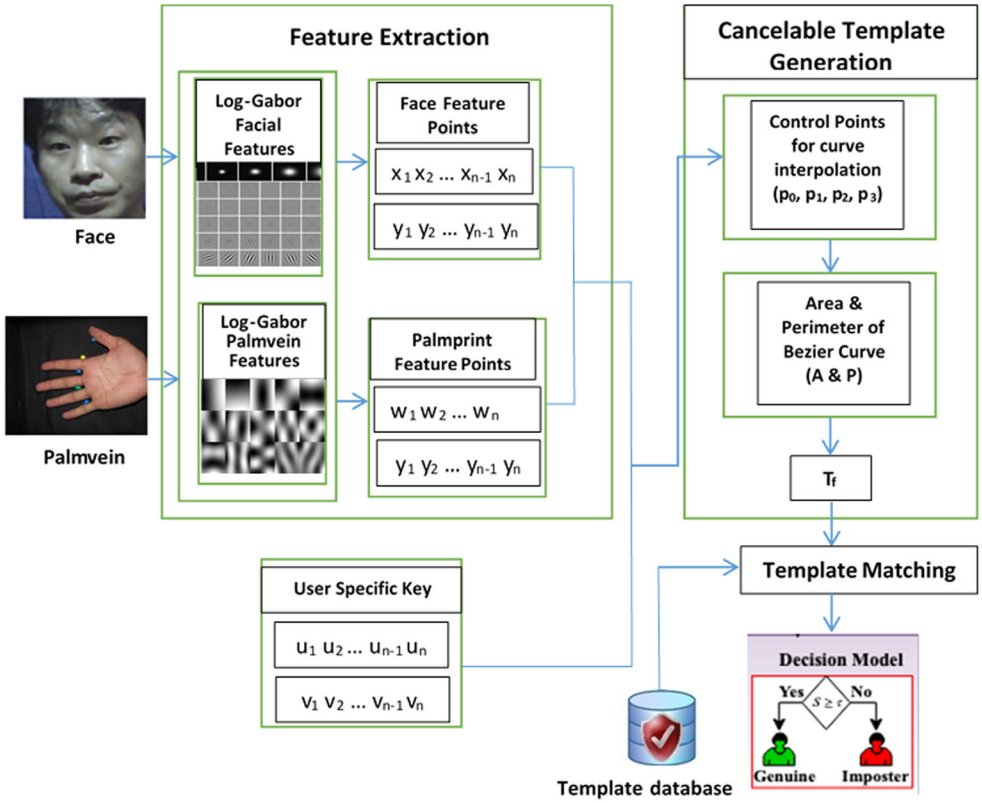

Fig. 1 Architecture of the proposed recognition system based on multi-modal biometric

for texture analysis. The Log-Gabor filter describes a signal in terms of the local frequency responses. The Log-Gabor filter is quite useful in image processing as it captures the statistics of natural images [50].

In pattern recognition, features are extracted which are fed into the classification algorithms for classification of objects into separate classes. Features extracted through Log-Gabor filters are quite useful in many applications because it can locally represent frequency information [51].

A 2-D Gabor filter has been modulated in the form of a complex sinusoidal wave using Gaussian kernel function $G_{\mu,\theta}(x,y)$, as given in Eq. (1).

$$G_{\mu,\theta}(x,y) = exp\left[-\frac{1}{2}\left\{\frac{x_{\theta_n}^2}{\sigma_x^2}+\frac{y_{\theta_n}^2}{\sigma_y^2}\right\}\right]\exp(2\pi\mu x_{\theta_n}) \tag{1}$$

where,

$$\begin{bmatrix} x_{\theta_n} \\ y_{\theta_n} \end{bmatrix} = \begin{bmatrix} \sin\theta_n & \cos\theta_n \\ -\cos\theta_n & \sin\theta_n \end{bmatrix}\begin{bmatrix} x \\ y \end{bmatrix} \tag{2}$$

Here, μ is sinusoidal frequency, whereas standard deviation along x and y direction of Gaussian envelop are represented by σ_x, σ_y while the orientation θ_n is as defined in eq. (3):

$$\theta_n = \frac{\pi}{m}(n-1) \tag{3}$$

For $n = 1, 2.. . m$, where m represents the orientation count. In our experimentation validation, 40 Gabor filters have been used to convolve input grey facial image in five scales and eight orientations to form a feature vector.

4.2 Proposed method for cancelable template generation

In the proposed scheme, the random values of the area and perimeter of the Cubic Bezier Curves are used to generate random biometric templates which have the features of revocability. The Cubic Bezier Curves are obtained through interpolation of data points obtained from the extracted features. A key set, which is chosen randomly by the user, is also taken into account while forming the data points. This also ensures the formation of random curves whose area and perimeter are obviously random. The biometric templates thus generated can be revoked and a new template can be generated, just by changing the key set. Apart from being random, the

generated cancelable biometric templates are also non-invertible. Therefore, even if the stored cancelable biometric templates get compromised, the original biometric data remain safe in the sense that they cannot be derived from the compromised templates.

The feature vector f_x of n-dimension, generated from a particular biometric trait using Log-Gabor filters is added with another feature vector f_y of the same dimension obtained from a randomly chosen image by the user. The resultant feature vector is divided into two equal parts such that the i^{th} value in the first half forms *abscissa* and the corresponding i^{th} value in the second half forms *ordinate* of a point in Cartesian coordinate system. Thus, an extracted feature obtained from a biometric template is represented as feature points in a 2-dimensional plane. Similarly, a random key chosen by the user is also represented as random points in a 2-dimensional plane. A Cubic Bezier Curve is plotted using four control points out of which three points are taken from feature points whereas one point is taken from the random points. In the proposed approach, area and perimeter of such random curves have been considered. Moreover, the area of the region bounded by such curves and x-axis, as illustrated in Fig. 1, has been taken into account. The area and perimeter thus computed are random values. Through this approach, each biometric template is transformed into random values which are stored as cancelable biometric template.

4.2.1 Interpolation of cubic Bezier curve

A Cubic Bezier Curve is interpolated using four control points and thus it is built in space as four points lie in a space [52].

Suppose the four control points as mentioned above are $\mathbf{p_0}(x_1,y_1)$, $\mathbf{p_1}(x_2,y_2)$, $\mathbf{p_2}(x_3,y_3)$, and $\mathbf{p_3}(u_1,v_1)$. Let $z \in R$, then by using points p_0 and p_1 the point p_0^1 may be derived as shown in in Eq. (4):

$$p_0^1(z) = (1-z)p_0 + zp_1 \tag{4}$$

Similarly, points p_1^1 and p_2^1 can be derived as shown in Eq. (5) and (6) given below:

$$p_1^1(z) = (1-z)p_1 + zp_2 \tag{5}$$

$$p_2^1(z) = (1-z)p_2 + zp_3 \tag{6}$$

Using these first order derived points the second order points p_0^2, p_1^2 and the third order derivative p_0^3 can be computed as per Eq. (7), (8) and (9) given below:

$$p_0^2(z) = (1-z)p_0^1(z) + zp_1^1(z) \tag{7}$$

$$p_1^2(z) = (1-z)p_1^1(z) + zp_2^1(z) \tag{8}$$

$$p_0^3(z) = (1-z)p_0^2(z) + zp_1^2(z) \tag{9}$$

By using first three equations i.e. Eq (4), (5) and (6) into the next two equations i.e. (7) and (8) we get:

$$p_0^2(z) = (1-z)^2 p_0 + 2(1-z)zp_1 + z^2 p_2 \tag{10}$$

$$p_1^2(z) = (1-z)^2 p_1 + 2(1-z)zp_2 + z^2 p_3 \tag{11}$$

By solving eqs. (9), (10) and (11), we get

$$\begin{aligned} p_0^3(z) = {} & (1-z)^3 p_0 + 2(1-z)^2 zp_1 + (1-z)z^2 p_2 + (1-z)^2 zp_1 \\ & +2(1-z)z^2 p_2 + z^3 p_3 \Rightarrow p_0^3(z) = (1-z)^3 p_0 + 3(1-z)^2 zp_1 \\ & +3(1-z)z^2 p_2 + z^3 p_3 \end{aligned} \tag{12}$$

The point p_0^3 is a point on the curve at parameter value z. For $z = ½$, the geometric construction is as shown in the Fig. 2.

In this manner, a cubic Bezier curve is formed using the feature points, obtained from the extracted feature and a random key, chosen by the user.

4.2.2 Template transformation with random area perimeter method

Suitable sensors have been used for biometric traits like face, thermal face, palm print, palmvein and fingervein. These biometric images are cropped and resized into 128×128 pixels. Then Log Gabor filter feature extraction technique is applied on these images to get an n-

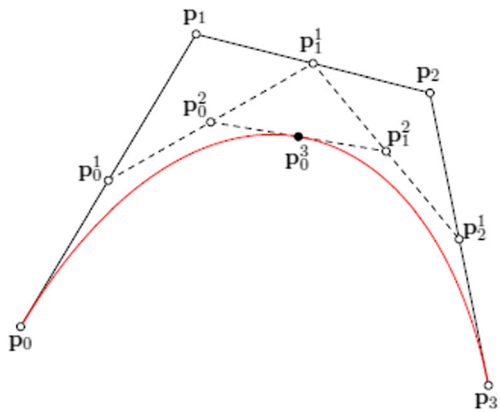

Fig. 2 Interpolation of cubic Bezier curve using four control points

dimensional feature vector χ. These extracted features have values which are in low dynamic range; so they are multiplied by 100 to get reasonably higher values. The entropy of the biometric template is increased by salting the feature vector χ with an n-dimensional random vector β. So, we get

$$\Psi = \chi + \beta$$

The vector Ψ is divided into two equal parts $\Omega = \Psi$ **(1: n/2)** and $\Phi = \Psi$ **(n/2 + 1: n)**. A feature point $\mathbf{F_i}$ is defined as ($x_i = \Omega(i)$, $y_i = \Phi(i)$) for i = 1…n/2. A random key $\mathbf{K}$ of size n is chosen by the user. The key $\mathbf{K}$ is also divided into two equal parts K_1 and K_2. A random point R_i is defined as ($x_i = \mathbf{K_1}(i)$, $y_i = \mathbf{K_2}$ (i)) for i = 1…n/2. Three feature points (say $\mathbf{p_0}$, $\mathbf{p_1}$ and $\mathbf{p_2}$) and one random point (say $\mathbf{p_3}$) are taken as four control points which are used to interpolate a cubic Bezier curve. So, there will be n/6 random cubic Bezier curve corresponding to each set of four control points. The area A_j (where j = 1,…,n/6) of the region bounded by the j^{th} curve, x-axis and lines which are parallel to y-axis and passing through end points ($\mathbf{p_0}$ and $\mathbf{p_3}$) is computed. Also, the perimeter P_j (where j = 1,…,n/6) is computed for each of these curves. Thus, we get two arrays of area **A** and perimeter **P**. The size of both these arrays are quite large so in order to reduce the size, the arrays are downsized by 2 to get arrays of size n/12.This downsizing is done by dropping every alternate element of each array. In addition, pairwise mean of the elements of these arrays are taken to form new arrays of size n/24. Now, calculate the mean of each array and add them to all the elements of the array. This will increase the Uniqueness in the vectors. Apply another transformation formula, S = Area/(Perimeter)^2. Calculate the mean m of the resultant vector **S** and then add m^2 to the vector **S** to form $\mathbf{T_f}$, which is the final transformed template. This vector $\mathbf{T_f}$ of dimension n/24 is the cancelable template for the original biometric.

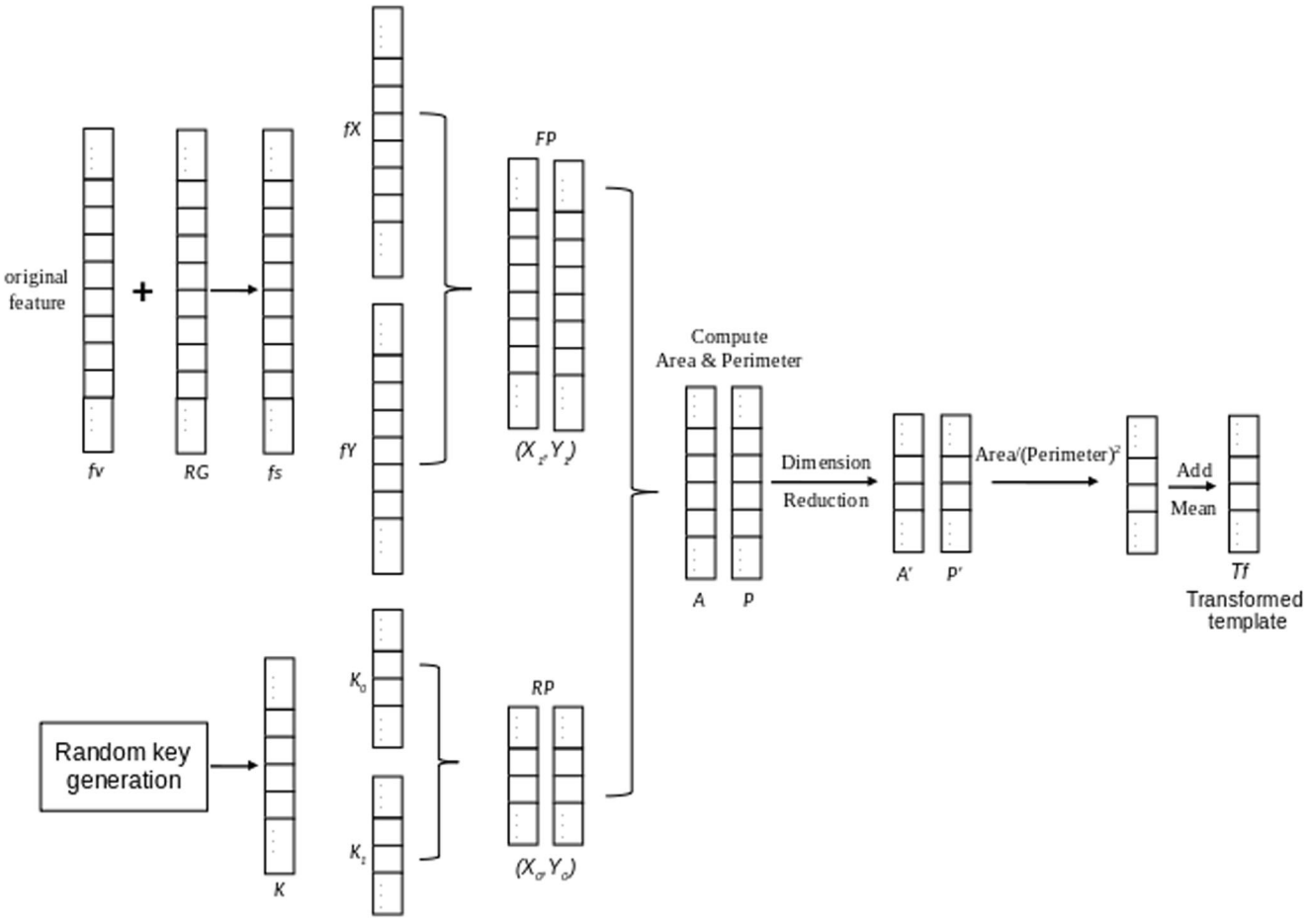

Fig. 3 Cancelable template generation process

This method ensures a dimensionality reduction of more than 95%. If required, a new cancelable biometric can be obtained using a different key. This complete process is illustrated in Fig. 3.

A pseudocode of the proposed method is given below:

1. **Function** TemplateGeneration (χ, β, K)
2. **for** (i = 1 to n)
   $\Psi = \chi \oplus \beta$ ← Salting by random grid RG
   end
3. $\Omega = \Psi$ (1 : n/2) and $\Phi = \Psi$ (n/2 + 1 : n)
4. **for** (j = 1 to n/2)
   $x_j = \Omega$ (j), $y_j = \Phi$ (j) ← Feature point FP_j
   end
5. $K_0 = K$ (1 : n/2) and $K_1 = K$ (n/2 + 1 : n)
6. **for** (j = 1 to n/2)
   $x_j = K_0(j)$, $y_j = K_1(j)$ ← Random point RP_j
   end
7. **for** (j = 1 to n/6)
   Constructing Bezier curve C_j using FP_j, FP_{j+1}, FP_{j+2} and RP_j
   Computing the area A_j bounded by C_j
   Computing the Perimeter P_j of C_j
   end
8. $\mathbf{A} = \{A_1, A_2, \ldots, A_{n/6}\}$
9. $\mathbf{P} = \{P_1, P_2, \ldots, P_{n/6}\}$
10. Dropping the alternate elements $\mathbf{A1} = \{A'_1, A'_2, \ldots, A'_{n/12}\}$
11. Dropping the alternate elements $\mathbf{P1} = \{P'_1, P'_2, \ldots, P'_{n/12}\}$
12. Taking pairwise mean $\mathbf{A2} = \{A''_1, A''_2, \ldots, A''_{n/24}\}$
13. Taking pairwise mean $\mathbf{P2} = \{P''_1, P''_2, \ldots, P''_{n/24}\}$
14. Taking mean of **A2** M_A = Mean (**A2**)
15. Taking mean of **P2** M_P = Mean (**P2**)
16. Adding **A2** with M_A $\mathbf{A3} = \{A''_1 + M_A, A''_2 + M_A, \ldots, A''_{n/24} + M_A\}$
17. Adding **P2** with M_P $\mathbf{P3} = \{P''_1 + M_P, P''_2 + M_P, \ldots, P''_{n/24} + M_P\}$
18. **for** (j = 1 to n/24)
    $S_j = {}^{A3_j}/_{P3_j^2}$
    end
19. $\mathbf{S} = \{S_1, S_2, \ldots, S_{n/24}\}$
20. Taking mean of **S** m = Mean (**S**)
21. Adding **S** with m^2 $\mathbf{T_f} = \{S_1 + m^2, S_2 + m^2, \ldots, S_{n/24} + m^2\}$
22. Return ($\mathbf{T_f}$)

5 Experimental validation

The experimental validation of the proposed scheme has been carried out on databases of various modalities like face, thermal face, palm print, palm vein and finger vein. All these modalities have been taken into consideration since these modalities are the one which are extensively been used in various real life applications. The performance metrics which have been used for the evaluation of the performance of the proposed scheme include Equal Error Rate (EER), Recognition Index (RI), Decidability Index (DI), Receiver Operating Characteristics (ROC) Curve, and Cumulative Matching Characteristics (CMC) Curve. The proposed scheme has been implemented using MATLAB on a PC having 8GB RAM and Intel i5 processor.

5.1 Database for experimentation

For the experimental validation of the proposed scheme, the biometrics that we have considered are palmprint, face, palmvein, thermal face and fingervein. The face biometric has been taken from CASIA Face Image Database Version 5.0 (or CASIA-FaceV5) which contains 2500 color facial images of 500 subjects. The images show considerable intra-class variations in terms of pose, eye-glasses, illumination,, expression, imaging distance, etc.. Apart from this, 290 face images of 10 subjects have been taken from the IRIS database. The thermal face biometric has been collected from CASIA-NIR-VIS 2.0 database consisting of images of 197 subjects. Besides these, 290 thermal face images of 10 subjects have been taken from the IRIS LWIR database. For the palmprint biometric we have taken 4000 palmprint images from CASIA Palmprint Image Database. For each subject, images have been collected from both left and right palms. We have also taken 1200 images corresponding to 200 subjects from CASIA Multi-Spectral Palmprint Image Database. For palmvein, 1200 images have been taken from CASIA-MS-V1(940). Fingervein biometric data consisting of 3816 images of 636 subjects has been taken from SDUMLA_HMT database. The format of images of vein is .bmp. Of each person, images of both two hands were taken. Data of three fingers (index, middle and ring fingers) were collected for each hand.

The databases of various modalities as shown in Table 1 have been considered for the study [53–56].

Table 1 Databases for various modalities

Modality	Database	No of Subjects	No of Samples
Face	CASIA Face V5	500	5
	IRIS	29	10
Thermal Face	CASIA NIR	197	10
	IRIS(LWIR)	29	10
Palmvein	CASIA MS V1(940)	200	6
Palmprint	CASIA	500	8
	CASIA MS V1(WHT)	200	6
Fingervein	SDUMLA-HMT	636	6

These modalities have also been used for constructing the following four chimeric multi-modal datasets namely D1, D2, D3, and D4, on which the experimentation was performed. D1 contains 1200 face images from CASIA-Face V5 database and 1200 palmvein images from CASIA-MS V1(940) database. D2 consists of 1200 palmvein images from CASIA-MS V1(940) database and 1200 fingervein images from SDUMLA-HMT database. D3 includes 1200 palmvein images from CASIA-MS V1(940) database and 1200 palmprint images from CASIA-MS V1(WHT) database. The chimeric data set D4 contains 290 face images from IRIS database and 290 thermal face images from IRIS(LWIR) database. These chimeric multi-modal datasets are shown in the Table 2.

5.2 Performance evaluation metrics

The proposed scheme has been quanitatively analysed by using following performance evaluation metrics:

(i) Equal Error Rate (EER): When the False Acceptance Rate (FAR) is equal to the False Rejection Rate (FRR) then that common value is known as Equal Error Rate (ERR). A lower value of ERR ensures a higher accuracy of the biometric system [57].

(ii) Decidability Index (DI): This index shows the quantum of separation of a genuine distribution from the imposter ones [58]. A higher value of DI shows a better separability which in turn results a lower FAR and FRR. DI is calculated as

$$DI = \frac{|\mu_g - \mu_i|}{\sqrt{\left(\sigma_g^2 + \sigma_i^2\right)^2}}$$

where (μ_g, σ_g) are mean and standard deviation of genuine and (μ_i, σ_i) are means and standard deviations of imposter.

(iii) Recognition Index (RI): The identification rate of a system at rank-1 is known as its Recognition Index. This index is well supported by Cumulative Matching Characteristics (CMC) curves [59].

(iv) Receiver Operating Characteristics (ROC) Curve: A curve between a True Match Rate (TMR) and False Match Rate(FMR) is called Receiver Operating Characteristic (ROC) Curve. This curve is used to compare biometric samples against each other [60].

(v) Cumulative Matching Characteristics (CMC) Curve: A CMC curve is a curve between True Positive Identification Rate (TPIR) against the rank of correct detection or recognition precision. The rank of recognition is shown horizontally while the precision percent is shown in a vertical line is [61].

6 Experimental results and analysis

A qualitative as well as quantitative analysis has been done for the proposed method for generation of cancelable biometric templates.

6.1 Qualitative analysis

In the Qualitative analysis, the consistency, non-invertibility, revocability and unlinkability features of the proposed scheme have been studied.

6.1.1 Consistency

A transformation function is considered consistent if the transformed features are able to preserve the intra-class and inter-class variations. The extracted features of the original biometric templates as well as the transformed templates have been converted into 2-dimensional points and have been displayed in the Cartesian plane as shown in Figs. 4 and 5. Two biometric samples I1 & I2 (Fig. 4a & b) of the same subject have been taken from CASIA face database and their original features have been plotted in Fig. 4c. The transformed features for both the samples have been obtained using the same transformation parameters RG and K in order to cater the worst-case scenario. Feature points and random points are shown in Fig. 4d. A plot between location and intensity for the transformed features of the images I1 and I2, in the worst-case scenario, is shown in Fig. 4e. In another experiment, the biometric samples I1 & I2 (Fig. 5a & b) of the two different users have been taken and their transformed features have been obtained using the same transformation parameters RG and K in the worst case

Table 2 Chimeric Datasets for various modalities

Chimeric Dataset	Multi-Modalities	Databases	Images
D1	Face & Palmvein	CASIA-Face V5 & CASIA-MS V1(940)	1200
D2	Palmvein & Fingervein	CASIA-MS V1(940) & SDUMLA-HMT	1200
D3	Palmvein & Palmprint	CASIA-MS V1(940) & CASIA-MS-V1(WHT)	1200
D4	Face & Thermal Face	IRIS & IRIS(LWIR)	290

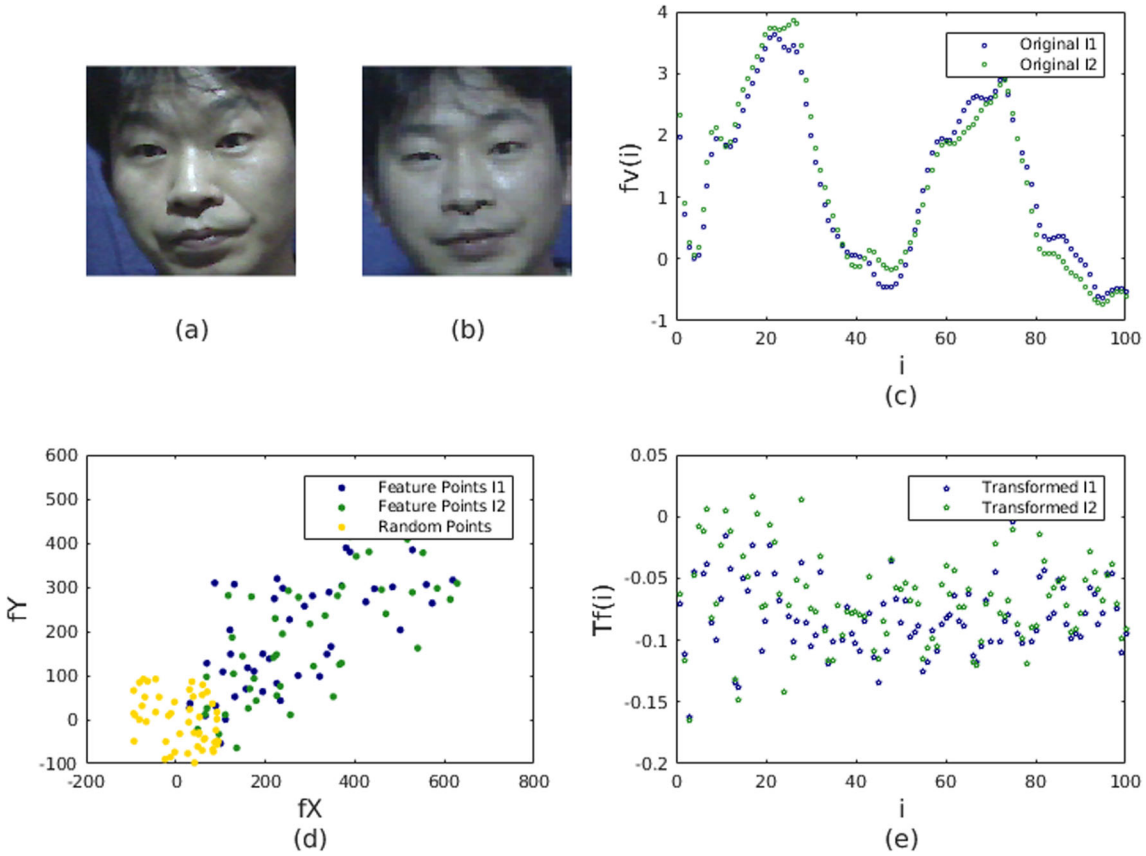

Fig. 4 **a**-**b** sample images I1 and I2, **c** original features, **d** feature points and random points, and **e** transformed features

scenario. Figure 5c represents the original biometric features whereas Fig. 5d represents Cartesian representation of the random points and feature points. A plot between location and intensity for the transformed features of the images I1 and I2 in the worst-case scenario, is shown in Fig. 5e. In both cases, we have considered the first 100 features obtained at m = 1 orientation and $n = 1$ scale. Then these features have been converted into Cartesian points.

It is observed that both intra-class and inter-class variations are preserved for the transformation function in both the cases i.e., when samples are taken for the same subject or for two different subjects. Therefore, the proposed method is consistent with respect to different biometric samples and modalities.

6.1.2 Non-Invertibility

An essential requirement for any cancelable biometric template is that it should be non-invertible i.e., the original biometric template should not be recoverable even if the key and the cancelable template get compromised. The proposed method is non-invertible as it is impossible to trace back the Bezier curve from the values of area and perimeter. Even if the curve is obtained, it is impossible to find actual source of interpolation of the Bezier curve i.e., the actual feature points as there are infinite points over the curve. This becomes even more difficult as more than 95% of the information is discarded while generating the cancelable biometric template.

6.1.3 Revocability

The very concept of cancelable biometric system is that in case of loss of the stored templates, it should be able to generate a new template which is to be stored i.e., already stored biometric templates is discarded and in place a new template is stored [62]. In the proposed scheme a random key which is chosen by the user plays a crucial role in generating cancelable template. Using this random key, random point is generated which is used in interpolating a Bezier curve whose area and perimeter is computed. Thus, by just changing the key a new curve is interpolated and we get new values of area and perimeter. This way a new template is generated and stored. Therefore, the revocability analysis shows that the stolen template can be easily replaced by a new template by using a different set of keys in the proposed system.

6.1.4 Unlinkability

The concept of unlinakbility means that the various templates corresponding to a particular biometric of an individual stored

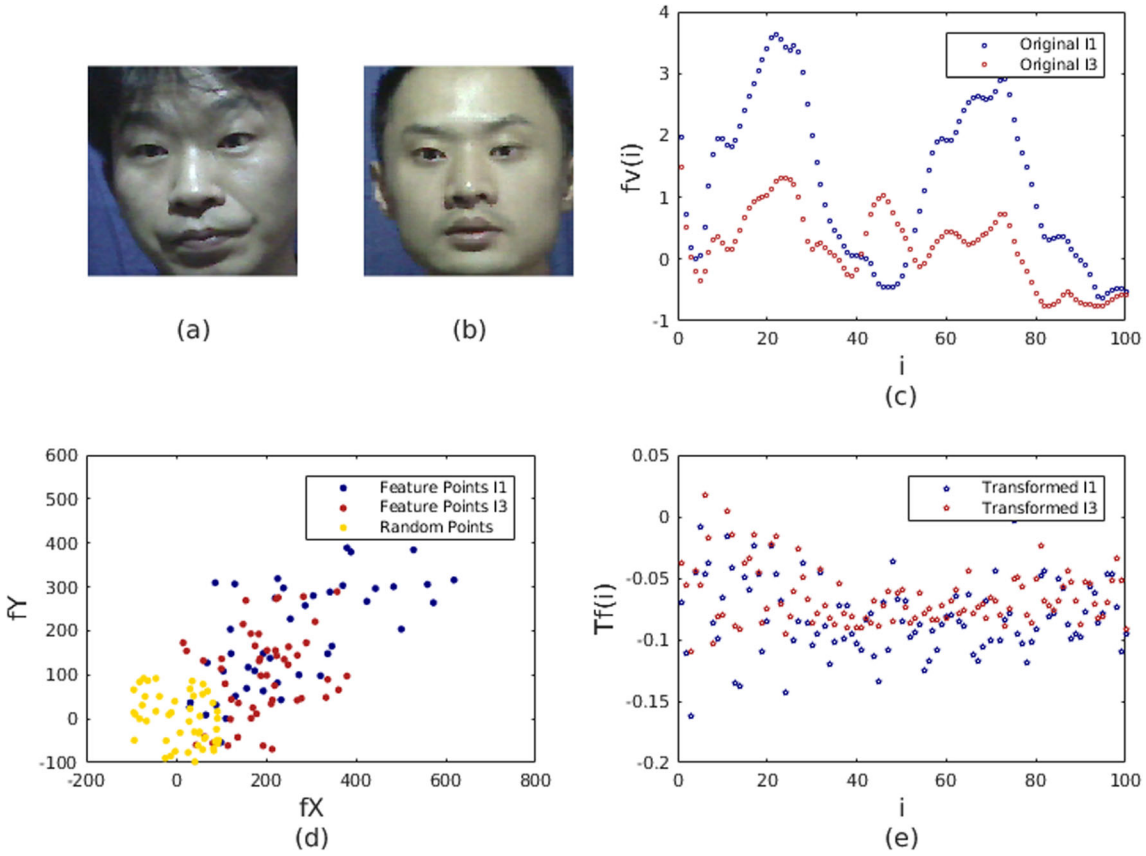

Fig. 5 **a**-**b** sample images I1 and I2, **c** original features, **d** feature points and random points, and **e** transformed features

in the databases of various applications must be unlinkable. In the proposed scheme, the user has to choose a random key which is used to generate a random Bezier curve whose area and perimeter are computed for generation of cancelable template. Thus, different user keys lead to generation of different random cancelable templates for a particular biometric. Various test modules have been used to test the randomness of the generated values stored as cancellble template. It is observed that the generated values exhibit a good randomness behaviour which ensures the unlinkability of the cancelable templates. The feature of unlinkability ensures the security of the identity of the individual when it is enrolled in multiple applications.

Qualitative analysis of the proposed scheme shows that the system ensures the privacy of each user by means of consistency, non-invertibility, revocability and unlinkability of the cancelable templates.

6.2 Quantitative analysis

An important criterion for a robust cancelable biometric is that it should preserve the discriminative characteristics in the transformed domain also. Therefore, the authentication performance of the cancelable biometric must be atleast as good as that of the original biometric. The experimentations have been carried out using eleven state of the art feature transformation techniques viz., Gray Salting [35], Random Projection with vector translation (RPV) [36], 2D BioHash [36, 37], BioConvolving [38], 2D BioPhasor [39, 40], Random Permutation Maxout (RPM) transform [41], XOR based salting [42], Random Slope Version 1 [43], Random Slope Version 2 [43] and Random Distance Method [44]. BioHashing technique has also been applied in two forms BH and BH-50 technique. In BH all the features in the transformed domain have been taken for experimentation, whereas in BH-50 technique only 50% of the features have been considered. The advantage of all these techniques and the proposed RAPM technique is that they can be used for different type of biometrics. All these transformation techniques have been applied on the same biometric template so that their matching performance can be compared on the same scale.

Support Vector Machine (SVM) has been applied for measuring the classification and matching performance. Total 5 images per user are transformed using the above method. The training the model has been done using 4 images while testing has been using the fifth image. The prediction scores are generated in the score variable.

Same random points have been used for interpolating Bezier curves for different biometric samples for evaluating the discriminating property of the RAPM. The performance in

Table 3 Comparative Performance in terms of EER

Modalities	Face		Thermal Face	Palmprint		Palmvein	Fingervein
Databases→ Techniques ↓	CASIA- V5	IRIS	IRIS(LWIR)	CASIA	CASIA-MS	CASIA-MS(940)	SDUMLA-HMT
Original Templates	2.17	2.06	0.72	0.50	1.00	0.98	1.10
Gray Salting	4.71	1.27	2.42	0.65	1.02	2.19	1.04
RPV	2.92	1.16	0.38	0.53	0.60	0.81	0.71
BH	3.03	3.56	1.39	0.56	0.60	1.25	1.40
BH-50	4.52	3.62	2.05	0.65	0.70	1.50	1.70
BioConvolving	7.84	2.50	7.20	2.88	5.95	5.50	2.20
BioPhasor	3.50	10.34	4.41	1.36	1.30	2.00	2.27
RPM	9.28	6.75	13.49	4.00	2.91	4.50	1.73
XOR	2.78	1.33	0.41	0.55	0.60	1.03	0.66
Random Slope-V1	2.40	0.99	0.22	0.42	0.48	0.68	0.71
Random Slope-V2	3.08	1.19	0.36	0.52	0.64	1.11	0.78
Random Distance	2.60	2.68	0.09	0.53	0.60	0.99	1.19
Proposed Method (RAPM)	1.21	0.22	0.08	0.11	0.02	0.67	0.77

terms of EER, DI and RI for both the original and transformed biometric templates in the worst case scenario have been compared with the state of the art techniques as shown in Tables 3, 4 and 5 respectively.

As it is evident from the Table 3, the matching performance in terms of EER for the proposed RAPM method in the worst-case scenario is quite better as compared to various state of the art techniques for all the biometric modalities. The DI values in Table 4 suggest that the cancelable biometric templates generated through RAPM retain the discriminating characteristics to correctly identify between the genuine and impostor. Table 5 suggests that the recognizing capability of the proposed RAPM technique is far better than the BioHashing, BioPhasor and Random distance techniques.

Multimodal biometric templates have been obtained from different combination of biometric modalities as described in the Section 4.1. The matching performances of RAPM technique in terms of EER and RI in the worst-

Table 4 Comparative Performance in terms of DI

Modalities	Face		Thermal Face	Palmprint		Palmvein	Fingervein
Databases→ Techniques ↓	CASIA- V5	IRIS	IRIS(LWIR)	CASIA	CASIA-MS	CASIA-MS(940)	SDUMLA-HMT
Original Templates	4.188	4.542	4.946	9.876	5.970	6.635	7.657
Gray Salting	3.596	5.112	4.310	7.896	7.914	4.850	3.921
RPV	4.412	5.309	5.454	7.151	8.120	5.979	4.314
BH	3.442	4.464	6.545	9.851	5.820	5.979	7.314
BH-50	3.074	4.320	5.783	9.621	5.658	5.841	7.101
BioConvolving	2.562	3.980	2.727	3.624	2.628	2.903	3.721
BioPhasor	3.351	2.672	3.857	7.692	5.040	5.117	6.050
RPM	2.577	2.954	2.636	5.351	4.065	3.383	3.747
XOR	4.401	4.432	5.217	7.214	8.118	5.352	4.921
Random Slope-V1	4.456	5.282	5.612	7.523	8.259	6.210	5.498
Random Slope-V2	4.408	5.126	5.388	7.338	8.110	5.280	4.788
Random Distance	3.860	4.244	4.629	9.736	6.684	5.985	7.474
Proposed Method (RAPM)	5.402	4.932	4.461	5.964	13.120	4.768	5.321

Table 5 Comparative Performance in terms of RI

Modalities	Face		Thermal Face	Palmprint		Palmvein	Fingervein
Databases→ Techniques ↓	CASIA- V5	IRIS	IRIS(LWIR)	CASIA	CASIA-MS	CASIA-MS(940)	SDUMLA-HMT
Original Templates	92.10	97.85	99.65	99.42	98.60	98.90	98.39
BH	83.89	92.41	97.25	99.34	98.40	98.25	97.48
BioPhasor	79.20	68.96	87.24	98.88	97.10	96.50	95.47
BH-50	73.88	91.37	95.51	98.68	98.20	98.25	96.30
Random Distance	85.88	94.48	99.35	99.33	98.59	98.60	98.30
Proposed Method (RAPM)	99.22	99.70	99.82	99.87	99.65	99.68	99.22

Table 6 Comparative Performance in terms of EER for multimodal biometrics

Modalities	Face+Palmvein	Palmvein+Fingervein	Palmvein+Palmprint	Face+Thermal Face
Databases→ Parameters ↓	CASIA-V5+ CASIA-MS(940)	CASIA-MS(940)+ SDUMLA-HMT	CASIA-MS(940)+ CASIA-MS(WHT)	IRIS+IRIS(LWIR)
Random Distance	0.60	0.60	0.39	0.34
Proposed Method (RAPM)	0.09	0.06	0.01	0.06

case scenario on some multimodal templates have been shown in Tables 6 and 7.

Thus, it is observed that the cancelable biometrics obtained through RAPM for both uni-modal as well as multi-modal biometrics, give better result than the original biometrics, in the worst-case as well as in the best-case scenario.

In almost all the results, there is significant reduction in the value of EER, and increase in the values of DI and RI. This shows that the proposed RAPM technique is very effective for generation of cancelable biometric templates for both uni-modal and multi-modal cases.

The ROC curves for various uni-modal biometrics in the worst-case scenario have been shown in Fig. 6. In the first row, the ROC curves for the databases CASIA-Face V5, IRIS, IRIS (LWIR) and CASIA Palmprint have been shown respectively from left to right. In the second row the ROC curves for the databases CASIA MS V1(WHT), CASIA MS V1(940) and SDUMLA-HMT have been shown respectively from left to right.

Similarly, the CMC curves in the worst-case scenario for various uni-modal biometrics have been shown in Fig. 7. In the first row, the CMC curves for the databases CASIA-Face V5, IRIS, IRIS (LWIR) and CASIA Palmprint have been shown respectively from left to right. In the second row the CMC curves for the databases CASIA MS V1(WHT), CASIA MS V1(940) and

Table 7 Comparative Performance in terms of RI for multimodal biometrics

Modalities	Face+Palmvein	Palmvein+Fingervein	Palmvein+Palmprint	Face+Thermal Face
Databases→ Parameters ↓	CASIA-V5+ CASIA-MS(940)	CASIA-MS(940)+ SDUMLA-HMT	CASIA-MS(940)+ CASIA-MS(WHT)	IRIS+IRIS(LWIR)
Random Distance	99.10	99.40	99.20	99.65
Proposed Method (RAPM)	99.55	99.80	99.76	99.89

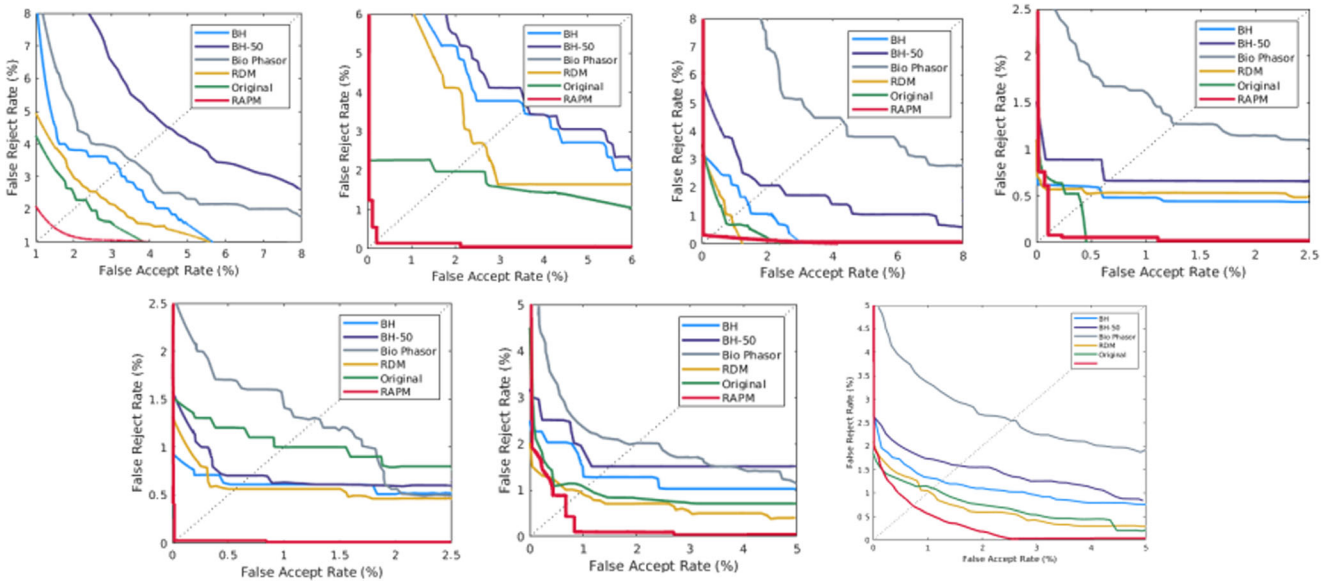

Fig. 6 ROC curves for various uni-modal biometrics in the worst-case scenario

SDUMLA-HMT have been shown respectively from left to right.

The Roc curves in Fig. 6 and CMC curves in Fig. 7 show that the proposed cancelable template generation method performs better in comparison to other state of the art techniques for uni-modal cases.

The ROC curves and CMC curves in the worst-case scenario for various multi-modal biometrics have been shown in Fig. 8.

The Roc curves in Fig. 8a and CMC curves in Fig. 8b show that the proposed cancelable template generation method performs better in comparison to other state-of-the-art techniques for multi-modal cases.

7 Conclusion

The method presented in this paper is found to be very effective in generation of cancelable biometric templates for various biometric traits like face, palmprint, fingervein, thermal face and palmvein. These templates have been experimentally verified and compared with the transformed templates generated through various other state of the art transformation techniques. The performances of the generated cancelable biometrics measured in terms of various evaluation metrics like EER, DI, RI, ROC and CMC confirm the reliability and robustness of the proposed approach. The proposed scheme is also validated on four chimeric multi-modal datasets generated from

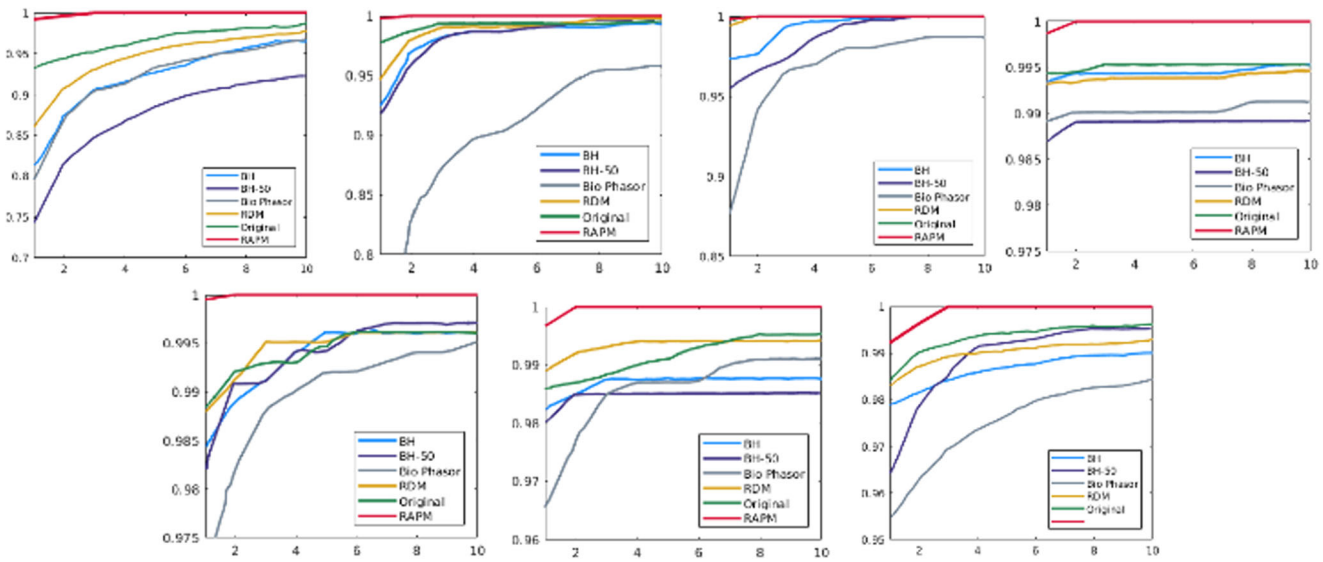

Fig. 7 CMC curves for various uni-modal biometrics in the worst-case scenario

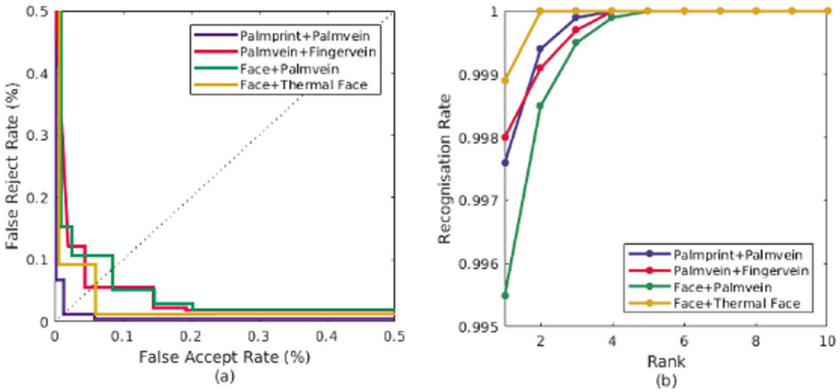

Fig. 8 **a** ROC curves **b** CMC curves, in the worst-case scenario for various multimodal biometrics

benchmark databases of face, palmvein, fingervein, palmprint and thermal face. Exhaustive result analysis shows that the proposed scheme also performs well for multi-modal case and surpasses many state of the art fusion methods. The qualitative analysis shows that the proposed scheme exhibit high level of consistency, non-invertibility, revocability and unlinkability resulting in high reliability and accuracy of the system. Moreover, a dimensionality reduction of more than 95% has been achieved for uni-modal biometrics in both the worst-case and the best-case scenarios. The average values obtained for EER, DI and RI are 0.0045, 6.28 and 99.64 respectively which are better than those obtained for the available state of the art approaches. Better performance results have been obtained for both uni-modal as well as multi-modal biometric templates and in both the worst-case as well as the best-case scenarios.

This study further entails the possibility of analysis on other databases and application of other performance evaluation metrics. Performance of most of the biometric systems is dependent on image quality. Poor image quality results in low-quality features and hence low recognition rates. In future, the issue of image quality may be incorporated as a reliability factor into the proposed cancelable biometric system. It will help in enhancing the adaptability of the system so that it may address various other challenges like poor quality input images, improper sensor interaction, etc. This will lead the way to make a highly reliable and robust cancelable biometric system.

References

1. Ratha NK (2010) Privacy protection in high security biometrics applications. In: Kumar A, Zhang D (eds) Ethics and policy of biometrics, ser. Lecture notes in computer science. Springer, Berlin Heidelberg. vol. 6005, pp 62–69
2. Hirata S, Takahashi K (2009) Cancelable biometrics with perfect secrecy for correlation-based matching. In: Tistarelli M, Nixon M (eds) Advances in biometrics, ser. Lecture notes in computer science. Springer, Berlin Heidelbergvol. 5558, pp 868–878
3. Bolle RM, Connel JH, Ratha NK (2002) Biometrics perils and patches. Pattern Recogn 35(12):2727–2738
4. Sutcu Y, Li Q, Memon (2007) Protecting biometric templates with sketch: theory and practice. IEEE Transact Inform Forens Secur 2(3):503–512
5. Hmmerle-Uhl J, Pschernig E, Uhl A (2009) Cancelable iris biometrics using block re-mapping and image warping. In: Samarati P, Yung M, Martinelli F, Ardagna C (eds) Information security, ser. Lecture notes in computer science. Springer, Berlin Heidelbergvol. 5735, pp 135–142
6. Takahashi K, Hirata S (2011) Cancelable biometrics with provable security and its application to fingerprint verification. IEICE Trans Fundam Electron Commun Comput Sci 94-A(1):233–244
7. Johnson W, Lindenstrauss J (1984) Extensions of lipschitz maps into a hilbert space. Contemporary Mathematics 26:189–206
8. Nandakumar K, Jain AK (2015) Biometric template protection: bridging the performance gap between theory and practice. IEEE Signal Process Mag 32(5):88–100
9. Patel VM, Ratha NK, Chellappa R (2015) Cancelable biometrics: a review. IEEE Signal Process Mag 32(5):54–65
10. Goh A, Ngo DL (2003) Computation of Cyrptographic keys from face biometrics. In: Proc IFIP: Int'l federation for information processing, pp 1–13
11. Ratha NK, Connell J, Bolle R, Chikkerur S (2006) Cancelable biometrics: a case study in fingerprints. In: Proc. Int'l Conf. Pattern recognition
12. Davida GI, Frankel Y, Matt BJ (1998) On enabling secure applications through off-line biometric identification. In: IEEE symposium on security and privacy, pp 148–157
13. Ratha NK, Connell J, Bolle RM (2001) Enhancing security and privacy in biometrics-based authentication systems. IBM Syst J 40(3):614–634
14. Juels A, Sudan M (2006) A fuzzy vault scheme. Des Codes Crypt 38(2):237–257
15. Juels A, Wattenberg MA (1999) Fuzzy commitment scheme. In: ACM conference on computer and communications security, pp 28–36
16. Clancy TC, Kiyavashand N, Lin DJ (2003) Secure smartcard-based fingerprint authentication. In: ACM SIGMM 2993 multimedia, biometrics methods and applications workshop, pp 45–52
17. Ratha NK, Chikkerur S, Connell JH, Bolle RM (2007) Generating cancelable fingerprint templates. IEEE Trans Pattern Anal MachIntell 29(4):561–572

18. Ang R, Rei SN, McAven L (2005) Cancelable key-based fingerprint templates. Information security and privacy: 10th Australasian conference, ACISP, Brisbane, pp 242–252
19. Tulyakov S, Farooq F, Govindaraju V (2005) Symmetric hash functions for fingerprint minutiae. In: Proc. Int. workshop pattern Recog. For crime prevention, security and surveillance, pp 30–38
20. Teoh ABJ, Ngo DCL, Goh A (2004) Biohashing: two factor authentication featuring fingerprint data and tokenised random number. Pattern Recogn 37(11):2245–2255
21. Rathgeb C, Uhl A (2011) A survey on biometric cryptosystems and cancelable biometrics EURASIP J. Inf. Sec, A survey on biometric cryptosystems and cancelable biometrics
22. Soutar C, Roberge D, Stoianov AR, Gilroy BVK, Kumar V (1999) Biometrics encryption. In: Nichols RK (ed) ICSA guide to cryptography. McGraw-Hill, New York, pp 649–675
23. Sadhya D, Raman B (2019) Generation of cancelable iris templates via randomized bit sampling. IEEE Transact Inform Forens Secur 14(11):2972–2986
24. Sharma RP, Dey S (2019) Fingerprint liveness detection using local quality features. Vis Comput 35(10):1393–1410
25. Ali SS, Ganapathi II, Prakash S, Consul P, Mahyo S (2020) Securing biometric user template using modified minutiae attributes. Pattern Recogn Lett 129:263–270
26. Trivedi AK, Thounaojam DM, Pal S (2020) Non-invertible cancellable fingerprint template for fingerprint biometric. Comput Secur 90:101690
27. Wu SC, Chen PT, Swindlehurst AL, Hung PL (2019) Cancelable biometric recognition with ECGs: subspace-based approaches. IEEE Transact Inform Forens Secur 14(5):1323–1336
28. Kumar N, Singh S, Kumar A (2018) Random permutation principal component analysis for cancellable biometric recognition. Appl Intell 48(9):2824–2836
29. Dwivedi R, Dey S (2019) A novel hybrid score level and decision level fusion scheme for cancellable multi-biometric verification. Appl Intell 49(3):1016–1035
30. Walia GS, Rishi S, Asthana RK, Kumar A, Gupta A (2019) Secure multimodal biometric system based on diffused graphs and optimal score fusion. IET Biometrics 8(4):231–242
31. Kaur H, Khanna P (2018) Random distance method for generating unimodal and multimodal cancellable biometric features. IEEE Transact Inform Forens Secur 14(3):709–719
32. Walia G S, Jain G, Bansal N, Singh K (2019) Adaptive weighted graph approach to generate multimodal cancelable biometric templates. IEEE transactions on information forensics and security 1{1doi:https://doi.org/10.1109/TIFS.2019.2954779
33. Gomez-Barrero M, Rathgeb C, Li G, Ramachandra R, Galbally J, Busch C (2018) Multi-biometric template protection based on bloom filters. Inform Fusion 42:37–50
34. Abdellatef E, Ismail NA, Elrahman SESA, Ismail KN, Rihan M, El-Samie FEA (2019) Cancelable multi-biometric recognition system based on deep learning. The visual computer, pp 1–13
35. Zuo J, Ratha NK, Connell JH (2008) Cancelable iris biometric. 19th International Conference on Pattern Recognition (ICPR). IEEE, Tampa, pp 1–4. https://doi.org/10.1109/ICPR.2008.4761886
36. Wang Y, Plataniotis KN (2010) An analysis of random projection for changeable and privacy-preserving biometric verification. IEEE, Trans Syst Man Cybern Part B (Cybernetics) 40:1280–1293. https://doi.org/10.1109/TSMCB.2009.2037131
37. Teoh A, Ngo D, Ling C, Goh A (2004) Biohashing: two factor authentication featuring fingerprint data and tokenised random number. Pattern Recognit 37:2245–2255. https://doi.org/10.1016/j.patcog.2004.04.011
38. Maiorana E, Campisi P, Neri A (2011) Bioconvolving: cancelable templates for a multi-biometrics signature recognition system. IEEE, International systems conference (SysCon), Montreal, Canada, pp 495–500. https://doi.org/10.1109/SYSCON.2011.5929064
39. Leng L, Zhang J (2013) PalmHash code vs. PalmPhasor code. Neurocomputing 108:1–12. Elsevier. https://doi.org/10.1016/j.neucom.2012.08.028
40. Leng L et al (2009) Two dimensional palmPhasor enhanced by multi-orientation score level fusion. Communications in computer and information science book series (CCIS), Springer, Berlin, Heidelberg, p 186. https://doi.org/10.1007/978-3-642-22339-6_15
41. Cho S, Teoh AB (2017) Face template protection via random permutation maxout transform. Proceedings of the International Conference on Biometrics Engineering and Application (ICBEA). Hongkong, ACM International Conference Proceeding Series, Part F128052, pp 21–27. https://doi.org/10.1145/3077829.3077833
42. Kaur H, Khanna P (2017) Cancelable features using log-gabor filters for biometric authentication, Multimed. Tools Appl, New York 76:4673–4694. https://doi.org/10.1007/s11042-016-3652-3
43. Kaur H, Khanna P (2019) Random slope method for generation of cancelable biometric features. Pattern Recognition Letters 126:31–40. Elsevier. https://doi.org/10.1016/j.patrec.2018.02.016
44. Kaur H, Khanna P (2019) Random distance method for generating unimodal and multimodal cancelable biometric features. IEEE Transactions on Information Forensics and Security 14(3)709–719. https://doi.org/10.1109/TIFS.2018.2855669
45. Sharma K, Walia GS, Gupta K (2020) Quality based adaptive score fusion approach for multimodal biometric system. Appl Intell, Springer 50:1086–1099. https://doi.org/10.1007/s10489-019-01579-1
46. Walia G S, Jain G, Bansal N, Singh K (2019) Adaptive weighted graph approach to generate multimodal cancelable biometric templates. IEEE, Transactions on information forensics and security 15:1945–1958. https://doi.org/10.1109/TIFS.2019.2954779
47. Xu S, Yinghui Z, Yingjiu Li, Ximeng Liu, Guomin Y (2019) Generic construction of elGamal-type attribute-based encryption schemes with revocability and dual-policy. Proceedings of the 15th EAI International Conference, SecureComm 2019, Orlando, FL, USA, Springer Link, vol 10, pp 184–204, https://doi.org/10.1007/2F978-3-030-37231-6_10
48. Yin W, Wen Q, Liang K, Zhang Z, Chen L, Yan H, Zhang H (2018) Delegation of decryption rights with revocability from learning with errors.IEEE, Access 6:61163–61175. https://doi.org/10.1109/ACCESS.2018.2875069
49. Wang S, Deng G, Hu J (2017) A partial hadamard transform approach to the design of cancelable fingerprint templates containing binary biometric representations. Pattern Recognit 61:447–458. https://doi.org/10.1016/j.patcog.2016.08.017
50. Redondo R, Sroubek F, Fischer S, Crist´obal G (2009) Multifocus image fusion using the log-Gabor transform and a multisize windows technique. Information Fusion 10(2):163–171. Elsevier. https://doi.org/10.1016/j.inffus.2008.08.006
51. Wang W, Li J, Huang F, Feng H (2008) Design and implementation of log-gabor filter in fingerprint image enhancement. Pattern Recogn Lett 29:301–308. https://doi.org/10.1016/j.patrec.2007.10.004
52. Farin G (1999) Curves and surfaces for computer aided geometric design. A practical guide, Academic Press, 2 edition. https://doi.org/10.1016/C2009-0-22351-8
53. Tan T, Zhaofeng H, Sun Z (2010) Efficient and robust segmentation of noisy iris images for non-cooperative iris recognition. Image Vis Comput 28(2):223–230

54. Tan T, Ma L (2004) Iris recognition: recent Progress and remaining challenges. Proc SPIE 5404:183–194
55. Sun Z, Tan T (2009) Ordinal measures for iris recognition. IEEE Trans Pattern Anal Mach Intell 31(12):2211–2226
56. Yin Y, Liu L, Sun X (2011) SDUMLA-HMT: a multimodal biometric database. CCBR 2011, LNCS 7098. Springer-Verlag, Berlin Heidelberg, pp 260–268
57. Campbell JP, Campbell WM, McCree AV, Weinstein CJ, Lewandowski CM (2009) Cognitive radio technology. In: IEEE transactions on pattern analysis and machine intelligence, 2nd edn, pp 305–324 Cognitive Services for the User
58. Lobrano C, Tronci R, Giacinto G, Roli F (2010) A score decidability index for dynamic score combination IEEE Xplore, International Conference on Pattern Recognition
59. Weinberg H, Cooper R (2012) The recognition index: a pattern recognition technique for noisy signals. In: Index de reconnaissance: Une technique de reconnaissance de pattern pour les signaux bruyants
60. Hosmer DW, Stanley L (2000) Applied logistic regression, 2nd edn. Wiley, New York ISBN 0-471-35632-8
61. Chia C, Sherkat N, Nolle L (2010) Towards a best linear combination for multimodal biometric fusion. In: Pattern recognition (ICPR), 20th international conference, pp 1176–1179
62. Gupta K, Walia GS, Sharma K (2019) Quality based adaptive score fusion approach for multimodal biometric system. Appl Intell 50: 1086–1099. https://doi.org/10.1007/s10489-019-01579-1

Publisher's note Springer Nature remains neutral with regard to jurisdictional claims in published maps and institutional affiliations.

Rajesh Asthana is a Senior Scientist in Defence Research and Development Organization, New Delhi. He did his Master's degree in Mathematics from DDU University, Gorakhpur. His current research interests include machine learning, pattern recognition, and information security. He is an expert in mathematical and statistical analysis of crypto algorithms. He has published more than 15 research papers in international/national journals and conferences. He is a life member of CRSI. He is reviewer of various journals and IEEE transactions.

Gurjit Singh Walia received his Ph.D. degree in the field of computer vision from Delhi Technological University (Formerly Delhi College of Engineering), New Delhi, and the M.E. degree in electronics from Punjab Engineering College, Chandigarh. He is working as a Senior Scientist with Defence Research and Development Organization, New Delhi. His current research interests include machine learning, pattern recognition, and information security. He has published over 40 research papers in international journals and conferences. He is Fellow of IETE, Fellow of Institute of Engineering, Senior Member of IEEE, Member of CSI and CRSI. He is reviewer of various IEEE transactions, Elsevier and Springer journals.

Anjana Gupta is a Professor in Department of Applied Mathematics, Delhi Technological University, New Delhi. She received her Ph.D. degree in the field of vector optimization from Delhi University, Delhi. She is a domain expert in Optimization Techniques, Fuzzy Logics, Multicriteria Group Decision Making Problems. She has published more than 50 research papers in international journals, proceedings and conferences. She is a life time member of the Indian Science Congress Association. She has authored a book on Discrete Mathematics, Kataria Publication.

Review of Text Summarization in Indian Regional Languages

Surendrabikram Thapa, Surabhi Adhikari, and Sushruti Mishra

Abstract Propelled by the advancements in the field of natural language processing, generating summaries of long texts using various NLP tools and techniques has always been a subject of great interest for scientists all over the world. Data is ubiquitous, and a large amount of data is processed every second in the digital space. For these reasons also, there is need of machine learning algorithms that can automatically shorten longer texts or documents and provide the accurate and meaningful summaries. These summaries find their applications in a wide variety of fields like medicine, market review, business analytics, etc. In other languages like English, an ample amount of study and research can be observed. However, in context of the Indian regional languages, the research in text summarization is very limited and is still in the infancy state. This paper tries to explain the research and works that have been performed in the field of text and document summarization in Indian regional languages.

Keywords Text summarization · Extractive summarization · Abstractive summarization · Indian regional languages

1 Introduction

Natural language processing (NLP) in particular deals with programming the computers to parse, process and perform analysis of huge amount of human language data that surrounds us. Today, the world is so centralized on computers, and for that

S. Thapa (✉) · S. Adhikari · S. Mishra
Department of Computer Science and Engineering, Delhi Technological University, New Delhi, India
e-mail: surenthapa5803@gmail.com

S. Adhikari
e-mail: suravi.prasiddi@gmail.com

S. Mishra
e-mail: mishrasushruti99@gmail.com

© The Author(s), under exclusive license to Springer Nature Singapore Pte Ltd. 2021

A. Abraham et al. (eds.), *Proceedings of 3rd International Conference on Computing Informatics and Networks*, Lecture Notes in Networks and Systems 167,
https://doi.org/10.1007/978-981-15-9712-1_3

reason, natural language processing is widely used these days [1]. Text summarization is a sub-domain of NLP which deals with extracting or collecting the important information from the given text or document and gives concise information regarding the text or document in the form of brief summary. Automated summarizers reduce reading time, and, in many cases, these summarizers can provide unbiased summaries than that of human beings. Text summarization has a lot of applications like customer review summary, online news article summary, a summary of the minutes of the meeting, automated research abstract, etc. Automatic text summarizers in languages such as English were in existence from 1950, but the advancement in summarization has seen a rapid pace in the last two decades. Indian regional languages have however seen good development in recent 10 years. In India, there is no one single language that is used across India as an official language. There are more than 22 official languages in India, and each of them is used for official purposes. So, our concern should not be getting too focused on a single language, but the summarization techniques in every language should also be explored. There cannot be a single system that can generalize the summarization process of all Indian regional languages. This is because all languages have their own linguistic features, and hence, each language should be dealt with independently. But works and study in the field of such text summarization in Indian regional languages are very less and are still in infancy state.

Based on the techniques used, text summarization techniques can be broadly divided into two major categories, namely extractive summarization and abstractive summarization. Extractive method of text summarization selects phrases and sentences from the source documents or text and includes such information extracted in the newly generated summary. The summary is based on key features in the text. For finding the phrases and sentences required, extractive methods make use of statistical features like sentence position, proper noun, numerical data, topic frequency, topic token frequency, normalized sentence length, cluster frequency, etc. Mostly, extractive summarization techniques make use of three tasks viz. tokenization of the text, calculating the word scores mainly TF/IDF scores, calculation of scores of the sentences based on such word scores and selection of summary comprising highest scores. In this way, the extractive summarization method, in short, extracts the most relevant information from the text document and includes them in summary. Since the phrases or sentences of generated summaries are directly extracted from the given document or text, the summaries are sometimes not meaningful and complete. However, this method is preferred because of its easy implementation. The abstractive text summarization technique, on the other hand, generates a meaningful summary, and the summary is more human-like. This method generates entirely new phrases and sentences to provide a summary of the source text. The system generates new phrases by rephrasing instead of simply extracting phrases or even using the words that are not present in the source text or document. Since the abstracted summary may contain phrases or sentences that are not in the source document or text, this is a more challenging approach. For a good abstractive summary, the built model should be given the independent ability to understand the given document, and the model will output its understanding in its own words [2]. Mostly deep learning models are

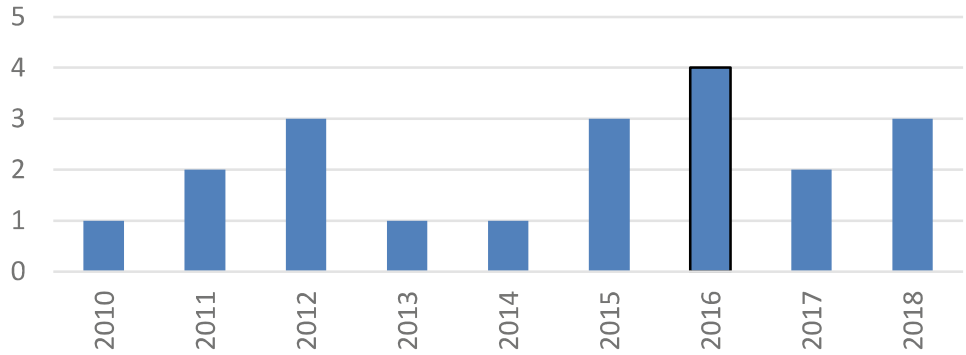

Fig. 1 Distribution of the number of papers discussed and year of publishing

used to generate an abstractive summary. It is much harder than extractive techniques, but the human-like summary outweighs its drawbacks in implementation.

In Indian regional languages, the extractive methods are very widely used. Research in abstractive methods, on the other hand, is very nominal and needs to be explored more extensively. In this paper, we present the summarization techniques that are used in various Indian regional languages in great detail. The paper describes the methods, different works carried out in various Indian regional languages and comparative analysis of different methodologies used in text summarization of Indian languages in the past 10 years, and the distribution of number of papers and year of publishing is as shown in Fig 1.

2 Related Works

With more than 122 languages and 22 designated official languages, India has a huge diversity in languages [2]. The need for text summarization in regional languages is much needed as they are used extensively in official works. A lot of effort has been made by a lot of researchers to effectively summarize the texts written in Indian regional languages. In this paper, we majorly discuss the text summarization techniques used in seven major languages used in India viz. Hindi, Bengali, Telugu, Marathi, Tamil, Urdu and Punjabi. The techniques that were used in the past 10 years for the text summarization in Indian regional languages have been discussed in this paper. Figure 2 shows the distribution of the number of papers that we have studied and the languages.

Generally, the approach followed by each of the summarizing technique can be represented by flow chart diagram as shown in Fig 3. The summarization usually starts with input of text which is followed by preprocessing steps done to it. After preprocessing of the text, there is iterative calculation based on the model of the summarizer (mostly calculations are based on word vector, word–sentence relationship and graph model). The process is followed by final step of summary generation after doing the analysis of processes done before.

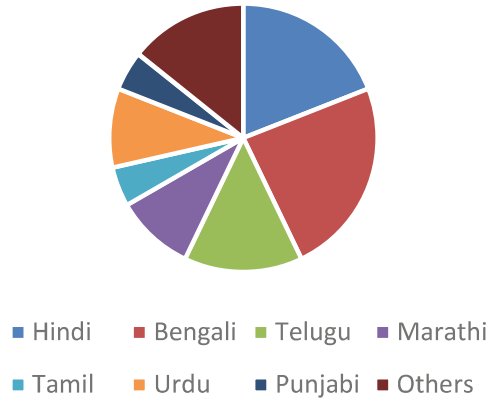

Fig. 2 Distribution of the language and the number of papers discussed

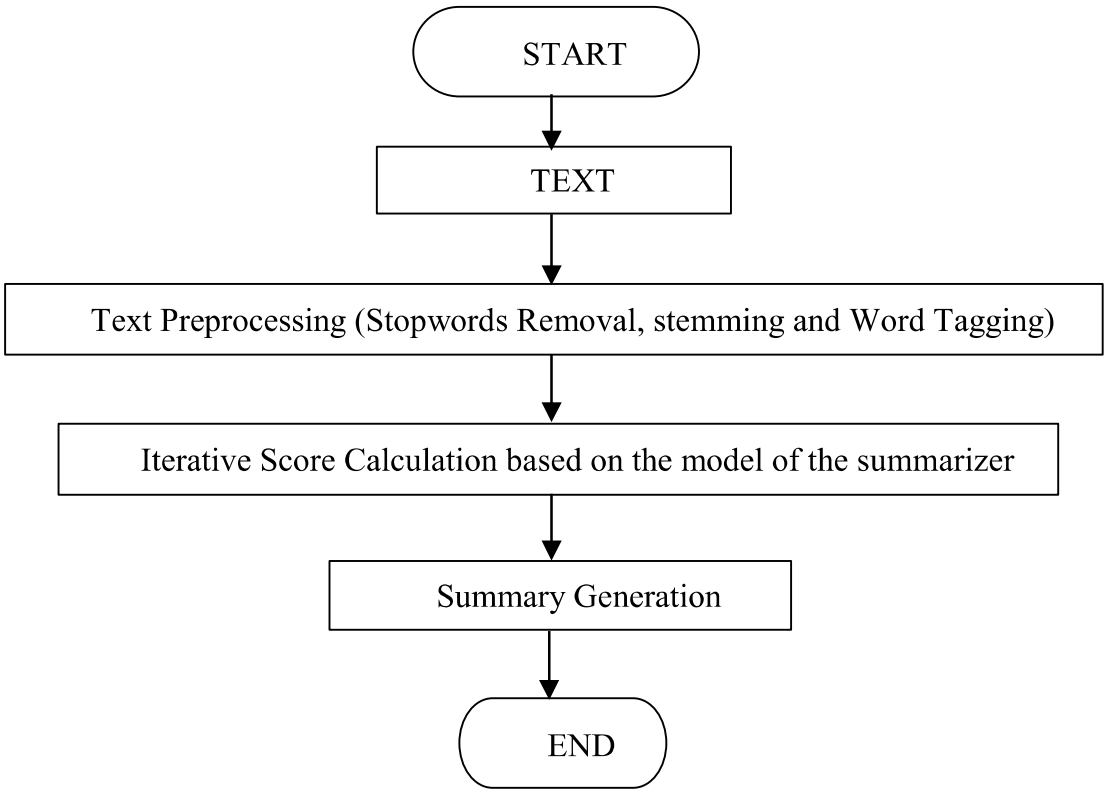

Fig. 3 Flow chart for working of text summarizer in Indian regional languages

2.1 Hindi

Thaokar et al. [3] discussed on how we can carry out summarization of given text or documents in Hindi language using the sentence extraction method. The technique used six statistical features along with two linguistic features. It used Hindi WordNet for tagging of the appropriate part of speech of the word to check subject–object–verb of the given sentences. The result was optimized using a genetic algorithm. Gupta et al. [4] proposed the rule-based technique for the summary generation of the

Hindi text documents based upon the linguistic rules. Five features for each sentence were discovered, and the proposed methodology was then subject to testing on thirty different documents that belonged to various domains. Input size was decreased to 60–70% with an accuracy of 96% when testing was done on given thirty given documents for generation of the summary of provided Hindi text. Kumar et al. [5] proposed the system based on an extractive approach that selected the important and meaningful sentences from the text based on some thematic approach. The system relies on the scoring based on the occurrence of root words, and the sentences with the highest scores were then included in the generated summary. Subramaniam et al. [6] in 2015 have proposed an abstractive method for the generation of summaries.

2.2 *Bengali*

The extractive method that is used in conjunction with the approach proposed by Abujar et al. [7] and a set of Bengali text analysis rules derived from the heuristics was able to give summaries nearly equivalent to human-generated. In the approach proposed by the authors [7], the importance of sentences and phrases was identified based on word scoring, sentence scoring and graph scoring to find the appropriate texts that need to be included in the summary.

Sarkar [8] discussed an effective extractive summarizer that gives a summary using sentence length feature along with TF/IDF weights (TF: term frequency and IDF: inverse document frequency). The evaluation results in the paper showed that the methodology proposed had better performance in terms of different performance measures than given three systems compared to the paper.

Akter et al. [9] proposed a method that extracts important sentences or phrases from the text document. Word score in the system was calculated by TF/IDF. After calculation of word scores, sentence scores were calculated. The scores of words that constituted the sentence were added, and value for position of sentence was also given while calculating sentence scores. Finally, the K-means clustering algorithm was used for the generation of required summary. Das et al. [10] proposed another topic-based opinion summarizer for Bengali language. Features were extracted in forms like syntactic and lexico-syntactic features. Aggregation of such topic-sentiment was then done using a clustering algorithm (K-means).

2.3 *Telugu*

Telugu is a Dravidian language and is mostly spoken by the people residing in Indian states of Telangana, Andhra Pradesh and Union Territory of Puducherry. Reddy et al. [11] proposed an extractive summarization technique that summarizes the articles in the Telugu language by using key features such as sentence's order of appearance in the given document, sentence similarity with title, word-frequency and centrality

of the sentence. The sentences were then ranked by calculating scores for each sentence by taking all given features into consideration. Naidu et al. [12] have also suggested a summarization technique that summarizes text with automatic keyword extraction from the dataset used in Telugu e-newspapers. In their described technique, the researchers have used human evaluation to train the system for seeking the key phrases or keywords that have maximum probability of inclusion in summary. They were able to get great accuracy when tested with different datasets with this method. Similarly, Kallimani et al. [13] have proposed the abstractive method for summary generation of text documents in the Telugu language.

2.4 Marathi

Giri et al. [14] discussed the extractive summarization in the Marathi language by extracting relevant sentences using the application of statistical features as well as features that depended on Marathi language. Similarly, the works of Sarwadnya et al. [15] discussed the text or document summarization technique that used a graph-based model that also used the extractive approach of text summarization in the Marathi language.

2.5 Tamil

The Tamil language is another Dravidian language that is spoken predominantly in Singapore, Sri Lanka, Tamil Nadu and Puducherry. Among the very few works done in Tamil language, Priyadharshan et al. [16] have proposed the method which can automatically summarize Tamil online sports news articles using natural language processing and a generic stochastic ANN. The feature matrix was created with various linguistic features to enhance accuracy.

2.6 Urdu

Burney et al. [17] in 2012 had designed and developed an add-in for MS word which summarized text in Urdu language. The approach that used a statistical method of sentence weight algorithm was able to summarize the Urdu text to the accuracy of over 80% when one human verifier was used. Humayoun et al. [18] have discussed the effect of preprocessing setting in the accuracy of summarization of text in the Urdu language which is one of the great works done in the field of NLP in the Urdu language.

2.7 Punjabi

Punjabi is another widely spoken language in India. Gupta et al. [19] have described the automatic summarizer for Punjabi text for summarizing the news articles in the Punjabi language. In their proposed method, the score of the sentences was calculated by making use of a feature-weight equation, and the sentences with highest rankings were then arranged to get a summary of the news articles.

2.8 Other Regional Languages

NLP and the works in summarization of text are still in the premature stage in other regional languages. In the Kannada language, Geetha et al. [20] have discussed extractive text summarization using latent semantic analysis. Similarly, Kabeer et al. [21] proposed the text summarizer for Malayalam text documents in 2014. The paper implemented a statistical technique for calculating the sentence scores and made use of a semantic graph-based method for summary generation. Also, Krishnaprasad et al. [22] have described a similar extractive approach for summarization of text in the Malayalam language. The works in other languages such as Assamese, Nepali, Santali and Dogri are very limited. Works in semantic analysis have been done, but the work in text summarization has not yet been explored.

3 Discussion

From the above works, we have seen that researchers who are doing their research in text summarization of Indian regional languages extensively use extractive text summarization techniques. We have also seen that an ample amount of work has been done in the Hindi language than any other Indian regional language. Figure 4 gives the picture of distribution of the number of papers that we have studied and the methods used in those papers. Despite some inaccuracy extractive models pose, researchers have found their way to make summaries of long text more accurate by various methods. The extractive summarization process that involves the conventional process of primarily ranking sentences with scores and including the sentences with highest scores can be improved with various techniques such as improvement in preprocessing and sentence scoring methods.

Krishnaprasad et al. [22] have suggested that our summarizers can generate even great quality summaries if we can improve the sentence scoring stage. Sarkar [8] has also suggested that the system performance may be further improved by improving stemming process including more number of effective features. Similarly, the relevancy of sentences should also be measured to get better summary. Akter et al. [9] in their work suggested that the relevancy of sentences can be measured by using

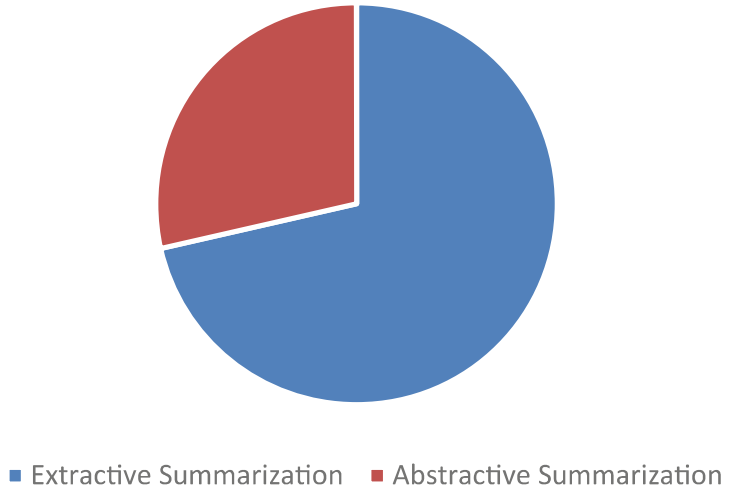

Fig. 4 Distribution of number of papers with summarization techniques used

syntactic and similarity in the future to get good accuracy. Apart from this, a lot of time and work must be done in the addition of more features to get more accurate summaries. Reddy et al. [11] who proposed their works in Telugu text summarization also suggested that with addition of more features like cue phases, the existence of some punctuation marks, day-month names, numeric, literals, etc., to the existing methodologies can boost up the quality of summary generated by the system.

The efforts have been made by authors to attain maximum accuracy with the extractive text summarization process. Sometimes, the sentences that are extremely important and are extremely important for inculcating in final generated summary are long sentences. This makes generated summaries lengthier, and we might also be missing some other relevant information that might be present in other shorter sentences when our model includes such long sentences by keeping such shorter sentences aside. Kabeer et al. [21] in their paper discuss the need for abstractive summarization processes to deal with such problems. Sunitha et al. [23] in their paper have presented experimental works that have been performed by using the abstractive summarization techniques in Indian regional language. They have also put an emphasis on promoting method of abstractive summarization in Indian regional language. With rapid advancement in deep learning and advanced researches in neural networks and various deep models, abstractive summarization can serve as a very great technique for summarizing text documents. Also, generative models can prove to be a great summarizer for text documents. Liu et al. [24] have proposed a generative adversarial network for an abstractive summary generation. Their work was concentrated on the English language but the same can also be done in Indian regional languages also. Similarly, the use of transfer learning can also facilitate the task of summarization using abstractive methods. Also, various scoring methods which provide a better method for evaluating the quality of the summary can be explored.

4 Conclusion and Future Works

The enormous amount of data that surrounds us needs summarization, and we are mostly surrounded by text that is in our regional languages. So, text summarization in regional languages should be of great priority of research. The study of above discussed paper also roughly presents that we should shift more towards abstractive summarization so that the machines can generate human-like summaries. The irrelevant information in extracted summary sometimes might lead us to confusion and that can be solved slowly with techniques that will be available with the advent of newer technologies. Also, very less works have been done in regional languages other than the abovementioned. The work should be taken with high priority especially by the native speakers of those languages. The paper has clearly explained that we lack in the field of abstractive summary and future works should be towards making summarizers for an abstractive summary generation. Similarly, further works should be done in addressing the complex morphological variations in Indian regional languages.

References

1. Collobert R, Weston J, Bottou L, Karlen M, Kavukcuoglu K, Kuksa P (2011) Natural language processing (almost) from scratch. J Mach Learn Res 12:2493–2537
2. Anthes G (2010) Automated translation of Indian languages. Commun ACM 53:24–26
3. Thaokar C, Malik L (2013) Test model for summarizing hindi text using extraction method. In: 2013 IEEE conference on information and communication technologies. IEEE, pp 1138–1143
4. Gupta M, Garg NK Text summarization of Hindi documents using rule based approach. In: 2016 international conference on micro-electronics and telecommunication engineering (ICMETE). IEEE, pp 366–370
5. Kumar KV, Yadav D (2015) An improvised extractive approach to hindi text summarization. In: Information systems design and intelligent applications, pp 291–300
6. Subramaniam M, Dalal V (2015) Test model for rich semantic graph representation for Hindi text using abstractive method. Int Res J Eng Technol 2
7. Abujar S, Hasan M, Shahin M, Hossain SA (2017) A heuristic approach of text summarization for Bengali documentation. In: 2017 8th international conference on computing, communication and networking technologies (ICCCNT). IEEE, pp 1–8
8. Sarkar K (2012) An approach to summarizing Bengali news documents. In: proceedings of the international conference on advances in computing, communications and informatics, pp 857–862
9. Akter S, Asa AS, Uddin MP, Hossain MD, Roy SK, Afjal MI (2017) An extractive text summarization technique for Bengali document (s) using K-means clustering algorithm. In: 2017 IEEE international conference on imaging, vision and pattern recognition (icIVPR). IEEE, pp 1–6
10. Das A, Bandyopadhyay S (2010) Opinion summarization in Bengali: a theme network model. In: 2010 IEEE second international conference on social computing. IEEE, pp 675–682
11. Reddy PV, Vardhan BV, Govardhan A (2011) Corpus based extractive document summarization for Indic script. In: 2011 international conference on Asian language processing. IEEE, pp 154–157
12. Naidu R, Bharti SK, Babu KS, Mohapatra RK (2018) Text summarization with automatic keyword extraction in telugu e-newspapers. Smart computing and informatics. Springer, pp 555–564

13. Kallimani JS, Srinivasa K (2011) Information extraction by an abstractive text summarization for an Indian regional language. In: 2011 7th international conference on natural language processing and knowledge engineering. IEEE, pp 319–322
14. Giri VV, Math M, Kulkarni U (2016) A survey of automatic text summarization system for different regional language in India. Bonfring Int J Softw Eng Soft Comput 6:52–57
15. Sarwadnya VV, Sonawane SS (2018) Marathi extractive text summarizer using graph based model. In: 2018 fourth international conference on computing communication control and automation (ICCUBEA). IEEE, pp 1–6
16. Priyadharshan T, Sumathipala S (2018) Text summarization for Tamil online sports news using NLP. In: 2018 3rd international conference on information technology research (ICITR). IEEE, pp 1–5
17. Burney A, Sami B, Mahmood N, Abbas Z, Rizwan K (2012) Urdu text summarizer using sentence weight algorithm for word processors. Int J Comput Appl 46:38–43
18. Humayoun M, Yu H (2016) Analyzing pre-processing settings for Urdu single-document extractive summarization. In: Proceedings of the tenth international conference on language resources and evaluation (LREC'16), pp 3686–3693
19. Gupta V, Lehal GS (2012) Automatic Punjabi text extractive summarization system. In: Proceedings of COLING 2012: demonstration papers, pp 191–198
20. Geetha JK, Deepamala N (2015) Kannada text summarization using latent semantic analysis. In: 2015 international conference on advances in computing, communications and informatics (ICACCI). IEEE, pp 1508–1512
21. Kabeer R, Idicula SM (2014) Text summarization for Malayalam documents—an experience. In: 2014 international conference on data science and engineering (ICDSE). IEEE, pp 145–150
22. Krishnaprasad P, Sooryanarayanan A, Ramanujan A Malayalam text summarization: an extractive approach. In: 2016 international conference on next generation intelligent systems (ICNGIS). IEEE, pp 1–4
23. Sunitha C, Jaya A, Ganesh A (2016) A study on abstractive summarization techniques in Indian languages. Proc Comput Sci 87:25–31
24. Liu L, Lu Y, Yang M, Qu Q, Zhu J, Li H (2018) Generative adversarial network for abstractive text summarization. In: Thirty-second AAAI conference on artificial intelligence

Evolving Systems
https://doi.org/10.1007/s12530-021-09367-4

ORIGINAL PAPER

Robust copy-move forgery detection using modified superpixel based FCM clustering with emperor penguin optimization and block feature matching

Ritu Agarwal[1] · **Om Prakash Verma**[1]

Received: 5 August 2019 / Accepted: 9 January 2021
© The Author(s), under exclusive licence to Springer-Verlag GmbH, DE part of Springer Nature 2021

Abstract
Digital images face widespread tampering through a copy-move attack, wherein objects are added or removed from an image to create the copy-move forged image. This paper proposes a robust Copy Move Forgery Detection (CMFD) scheme by integrating both block-based and keypoint-based CMFD techniques. The input image is first segmented into non-overlapping blocks using a modified FCM clustering algorithm based on superpixels. The neighboring and similar superpixels influences are encompassed into FCM, and Emperor Penguin Optimization (EPO) is used to optimize the influential degree, which increases the segmentation performance. Gabor filter is applied to extract the features from each block. The Block features are then matched with each other to show the suspected forgery regions. The experimental results illustrate that the proposed technique attains better performance in terms of precision, recall, F1-score, and E-measure. It accomplishes excellent forgery detection outcomes compared with other existing CMFD processes, even under different perplexing circumstances.

Keywords Copy-move forgery detection · Superpixel · Emperor penguin optimization · RANSAC · Forgery region extraction

1 Introduction

With the expanding accessibility of upcoming image processing and editing software, one can easily forge a digital image. Image forgery detection is a popular research area to ensure image integrity. Image forgery detection techniques will always be in demand for the protection of copyrights, justice concerns, elections and many more such areas. Existing CMFD approaches are generally classified as active and passive (blind) methods. The input images' prior statistics are required to develop active approaches like watermarking or illicit image copy recognition. But, prior information about an image is not always accessible, hence the need for passive approaches. These are based on the fact that the modification operations introduce new offshoots to the image due to the change in a digital image's basic properties. The inconsistencies resulting from them can further be used for tampering detection. Due to the feasibility and the extensive applications of passive methods, they become a prominent research area (Qureshi and Deriche 2015).

A typical digital image forgery is a copy-move or region duplication which copies the particular portion from an image and pastes it in another part of the same image (Yang et al. 2017). The tracing of a tampered image using a human's naked eye is a challenging task. Thus, image authentication and verification processes turn out to be a challenging chore. The characteristics of an image are grasped in the digital art of image tampering. Instead of directly pasting, a copied portion can undergo different transformations such as blurring, resampling, filtering, scaling, rotation, and cropping (Alkawaz et al. 2018).

In recent days, passive CMFD stands out amongst the most critical and advanced digital image forensic techniques because of the wide accessibility of image processing tools. This paper emphasizes on passive CMFD approaches. Different passive approaches have been established to identify the forged images and analyze a digital image's genuineness.

✉ Ritu Agarwal
ritu.jeea@gmail.com

Om Prakash Verma
opverma.dce@gmail.com

[1] Delhi Technological University, Shahbad Daulatpur, Bawana Road, Delhi 110042, India

Published online: 04 March 2021

Most of the existing CMFD methods can be classified as block-based approaches and keypoint-based approaches.

In the block-based CMFD approaches, the tampered images are segmented into various intersecting blocks, and subsequently, the matching blocks are determined. The existing block-based methods differ from each other by the procedures used to depict the blocks. The different descriptors utilized to obtain features in block-based CMFD approaches are quantized Discrete Cosine Transform (DCT) (Fridrich et al. 2003), Principal Component Analysis (PCA) (Popescu and Farid 2004), Fourier-Mellin Transform (FMT) (Bayram et al. 2009). All these strategies depend on an enormous amount of blocks; also, the extricated features from these blocks create a mass vector, which increases the complexity of the process. These methods do not consider the geometrical changes of copied regions, namely scaling and rotation. The unstable capturing of image information by the extracted feature depiction leads to a low recall rate for the block-based approach. The more significant part of the current CMFD is developed mostly for grey images wherein the critical data correlation among various shading channels is ignored. They are inefficient for photometric changes, for example, brightening course, force, hues, and features.

An alternative approach for CMFD detection depends on the image key points. The tampered images' key features are extricated, and matching is done with the full image to detect the copied region and withstand certain image conversions. These approaches reduce the computational complication presented in feature matching and post-processing by estimating few feature vectors. The most commonly used feature points for CMFD are Scale Invariant Feature Transform SIFT (Amerini et al. 2011) and Speeded up Robust Features SURF (Shivakumar and Baboo 2011. The keypoint-based approaches specify the suspected keypoint sets. These approaches not able to determine the image contour precisely. The keypoint based methods give poor results when the images are multi cloned, and adequate keypoints are not available. Recent fusion approaches combine both block-based approaches and keypoint-based approaches. The block-basis approach and the SIFT technique are combined with Zernike moments (Zheng et al. 2016). The fusion technique can section the image adaptively to form identical locales and uses the morphological process.

In this paper, a robust CMFD detection method using a superpixel based modified FCM clustering is proposed with EPO and feature matching method. The proposed method combines the conventional block-basis CMFD approaches and keypoint-basis CMFD approaches. The technique uses an image-block approach called the superpixel based modified FCM clustering with EPO segmentation to fragment the host images into non-overlapping and uneven blocks similar to the block-based CMFD approaches. The FCM approach has been utilized as a clustering and classification approach in different intelligent, expert and automation systems including data mining, image processing, and bioinformatics (Di Martino et al. 2019; Askari 2020; Li et al. 2020). The advantages of FCM approach on these application motivates us to develop a new superpixel based FCM clustering scheme for segmenting the host images in the proposed forgery detection system. The features extracted from each image block (IB) are not same as the keypoint-based CMFD method, because, in this key-point based method, the features are extracted from the host images rather than IB. Consequently, the matching Block features are identified and the false matches are removed with the help of the RANSAC algorithm (Fischler and Bolles 1981; Hossein-Nejad and Nasri 2017; Wang et al. 2018). The matched feature points are labeled, which can roughly denote the suspected forgery regions (SFR). The FRE algorithm (Pun et al. 2015) is used to identify the forgery regions precisely. In this algorithm, the smaller superpixels are substituted with the feature points and are called Feature Blocks (FB), then the adjacent blocks that consume the same local color features as FB are merged. In the end, a morphological process is performed to get the detected forgery regions. The main contributions of the proposed work are as follows:

The noise-free images are segmented using the conventional FCM process. However, FCM has its limitations while segmenting the images when the image is either degraded by noise or intensity inhomogeneity and imaging artifacts and therefore provides non-robust outcomes. It is because of the non-robust Euclidean distance usage and the exploiting relevant spatial data in the picture. To overcome this problem, the neighboring and similar superpixel are included in the proposed superpixel based FCM clustering method of segmentation to measure a robust distance. Hence, the segmentation process is carried out by considering pixel intensities and position of nearby pixel. The size of superpixels may lead to irregularities in clustering performance. When the superpixel size is large, the relative distance offsets the color proximity which generates compacted superpixels. These superpixels do not adequately penetrate the boundaries of images. The opposite is true for smaller superpixels. Thus the optimized values of the influence degree of similar and neighboring superpixels provide better segmentation outputs and offer a right balance between spatial proximity and color similarity, whereas inappropriate values degrade the results. Hence, the main problem addressed here is parameter optimization to enhance segmentation performance. Also, to improve the precision and recall rate and provide robust detection results under certain geometrical transformation and noise addition, the Influential degree of spatial superpixels is optimized using EPO.

This article is structured as follows. The literature review for this CMFD process and recent optimization algorithms are provided in Sect. 2. The overview of the EPO algorithm

is provided in Sect. 3. Section 4 defines the proposed methodology for CMFD. In Sect. 5, the experimental results and estimation are deliberated. Finally, the work is concluded in Sect. 6, which also includes future studies.

2 Related work

Nowadays, the CMFD methods are used in various solicitations such as surveillance networks, criminalization, medicinal imaging, and news media. An accurate duplication typically is not just copying and pasting; instead, a few extra transformations/processing are done. Changes like diminishing the visual tracking of tampering, introducing Gaussian noise to the cloned image make the CMFD significantly more challenging to accomplish visually and by forensic strategies. Numerous methodologies have been proposed to take care of these types of cloning techniques.

In a CMFD technique based on SIFT (Yang et al. 2018), the key points are initially determined using a modified SIFT dependant descriptor. Second, a new keypoint dissemination approach has been utilized to distribute the key points uniformly throughout the image. The forgery regions are then identified by matching the key-points. This technique has been used to determine the duplication of the textureless regions, where the key points are not present. Dixit et al. (Dixit et al. 2017) developed a scientific method for blur-invariant CMFD in digital images. They utilized stationary wavelet transform (SWT) for decomposing an image into its frequency subbands, and these features are extracted using singular value decomposition (SVD). The idea of the auto-threshold fitting is presented to optimize manual exertion. This method withstands blur variations through the use of Colour-based segmentation. Further, an 8-connected neighborhood check would decrease many false positives created when an image comprises wide-ranging of a similar texture. But these methods determined the copied portion based on key points only. Thus, such methods' performance is not very good when the copied portion contains more smooth regions.

In another approach, the forged image is identified by extracting features from different scales and using the adaptive matching technique (Bi et al. 2018). The properties of both the block approach and keypoint approaches are combined to attain superior detection consequences. The input images are initially segmented into non-overlapping uneven patches on various scales. At that point, feature points are extricated from the entire patches by SIFT to create multiple-scale features. An adaptable patch matching process is then utilized to identify the matches that could specify the suspected areas on every scale. Even though this method's performance is good enough in CMFD application, it can be further improved using certain optimization algorithms in the segmentation process of CMFD.

In recent days, several optimization algorithms have been proposed to obtain optimal possible solutions for real-time applications. Dhiman and Kumar proposed a Spotted Hyena Optimizer (SHO) which functioned based on the behavior of spotted hyenas (Dhiman and Kumar 2017). The basic process of SHO is prey search, encircling, and prey attack. This SHO is utilized to solve a number of engineering problems such as optical buffer design and airfoil design (Dhiman and Kaur 2018) and can be extended to solve multiple objective optimization problems. These multiple objective optimization algorithms employed a fixed size archive to store the non-dominated solution. Also, a roulette wheel mechanism is utilized for the selection of an optimal solution from the archive. Sooty Tern Optimization Algorithm (STOA) is an alternative optimization algorithm proposed in (Dhiman and Kaur 2019). This algorithm gets its inspiration from the movement and attacking the behaviour of sea bird *sooty tern.* Dhiman and Kumar also proposed an EPO algorithm that mimics the huddling behavior of the emperor (Dhiman and Kumar 2018).

In this work, the EPO algorithm is chosen to optimize the modified FCM clustering algorithm's influence degree parameters due to its fine-tuning convergence behavior between the exploration and exploitation stages. The performance of the EPO algorithm in terms of convergence, accuracy, and stability has been proved in most of the recent applications (Cao et al. 2019; Jia et al. 2019). Also, it can give optimal results for both constrained and unconstrained optimization problems.

3 Overview of EPO algorithm

Emperor penguins (Aptenodytes forsteri) huddling actions are mimicked by EPO (Dhiman and Kumar 2018). EPO's critical processes are the generation of huddle boundary, computation of huddle temperature, calculation of distance, and effective mover determination. In general, emperor penguins are located on a polygon plane during huddling. The emperor penguins contain a minimum of two randomly selected neighbors in the huddle. The wind flow calculation everywhere in the huddle is required to estimate the huddling limit in a polygon vicinity. Anyhow, an emperor penguin movement is slower than the wind flow. The notion of complex variables describes arbitrarily created huddle limit of the emperor penguin. Let ν define the airstream velocity, and ψ be the gradient of ν.

$$\psi = \nabla \nu \tag{1}$$

The complex potential is generated by combining vector $\mathbf{\Omega}$ with ν

$$f = \nu + i\boldsymbol{\Omega} \tag{2}$$

where i represents the imaginary part and the polygon plane logical operation is denoted as f.

The huddle is created by the emperor penguins to preserve power and maximize the temperature of the huddle. The exploration and exploitation method of emperor penguins for distinct positions depends on the temperature profile. The huddle's temperature profile T'_p is calculated as:

$$T'_p = \left(t - \frac{I_{\max}}{c - I_{\max}}\right) t = \begin{cases} 0 \text{ if } r > 1 \\ 1 \text{ if } r \leq 1 \end{cases} \tag{3}$$

where the present cycle is denoted as c, an extreme iteration count is represented as I_{max}, r represents the radius, and t represents the time required for determining the best optimum result in the space of search.

After the production of the huddle boundary, the separation of the emperor penguin and the best optimum result is calculated. If the fitness value is very similar to the optimum value, then the solution is called the current best optimal solution. The remaining emperor penguins locations are refreshed based on the present best optimum result and is statistically described as:

$$\boldsymbol{d_{ep}} = Abs\big(Q(\boldsymbol{R})\boldsymbol{B}(c) - \boldsymbol{S}\boldsymbol{B_{ep}}(c)\big) \tag{4}$$

where $\boldsymbol{d_{ep}}$ describes the emperor penguin's distance from the best fittest search agent, which has a smaller fitness cost, c represents the present iteration. The collisions between emperor penguins are avoided by using vectors $\boldsymbol{R}$ and $\boldsymbol{S}$. $\boldsymbol{B}$ denotes the best optimum solution, $\boldsymbol{B_{ep}}$ indicates the emperor penguin's location vector. The common force of emperor penguin enables the movement towards the best optimum search agent, and it is represented as function Q. The vectors $\boldsymbol{R}$ and $\boldsymbol{S}$ are calculated using Eqs. 5, 6, and 7.

$$\boldsymbol{R} = \left(m(T'_p + B_{\text{grid}}(\text{Accuracy})\text{Rand}()\right) - T'_p \tag{5}$$

$$B_{\text{grid}}(\text{Accuracy}) = Abs\big(\boldsymbol{B} - \boldsymbol{B_{ep}}\big) \tag{6}$$

$$\boldsymbol{S} = \text{Rand}() \tag{7}$$

where m is the motion limit, which keeps a gap in-between the searching agents to avoid the collisions.. The limit m is assigned with the value of 2. T'_p represents the temperature profile throughout the huddle, $B_{\text{grid}}(\text{Accuracy})$ determines the accuracy of the polygon grid using the comparison of penguin's differences, and Rand() represents a random function, and its value is in the range of 0 to 1. The following equation is used to calculate the function Q:

$$Q(\boldsymbol{R}) = \left(\sqrt{p \cdot e^{-c/q} - e^{-c}}\right)^2 \tag{8}$$

where controlling variables q and p are used to improve exploitation and exploration, and their values are in the range of 2 to 3 and 1.5 to 2, respectively. The Emperor penguins' positions are updated based on the best optimum result or mover. The primary purpose of this mover is to change the location of further search agents in a provided exploration space and to force the search agents to leave its current location. The next location of an emperor penguin is updated using the following expression:

$$\boldsymbol{B_{ep}}(c+1) = \boldsymbol{B}(c) - \boldsymbol{R}\,\boldsymbol{d_{ep}} \tag{9}$$

where $\boldsymbol{B_{ep}}(c+1)$ denotes the next updated location of emperor penguin. If the mover has been repositioned, then the huddling process of emperor penguins is recalculated during the iteration process.

4 Image forgery detection using modified superpixel based FCM clustering with EPO and feature matching

The proposed structure for robust CMFD using modified superpixel based FCM clustering with feature-point matching and EPO segmentation is shown in Fig. 1. This proposed forgery detection is carried out in four steps. EPO-based modified FCM superpixel clustering is proposed, which creates uneven and non-overlapped image blocks (IB) by segmenting the input tampered image. Then, the block features are extracted using Gabor filter, and then block feature matching is performed by comparing the features of one block with another. Here, the matched feature points denote the SFR. The block features extracted using Gabor filters are robust to geometrical changes (e.g., rotation, scaling, and translation) as these transformations are the primary parameters of the Gabor filter. False matches or outliers are eliminated by the RANSAC algorithm, and finally, the forgery regions presented in the input tampered image are determined with the help of the FRE algorithm based on the extricated features.

4.1 Modified Superpixel based FCM clustering with EPO

The CMFD scheme of this paper proposes a modified superpixel based FCM clustering segmentation with the EPO algorithm, which divides the input tampered image into blocks similar to the conventional block-basis duplication detection algorithms. The traditional block-based forgery detection algorithm generally segments the tampered

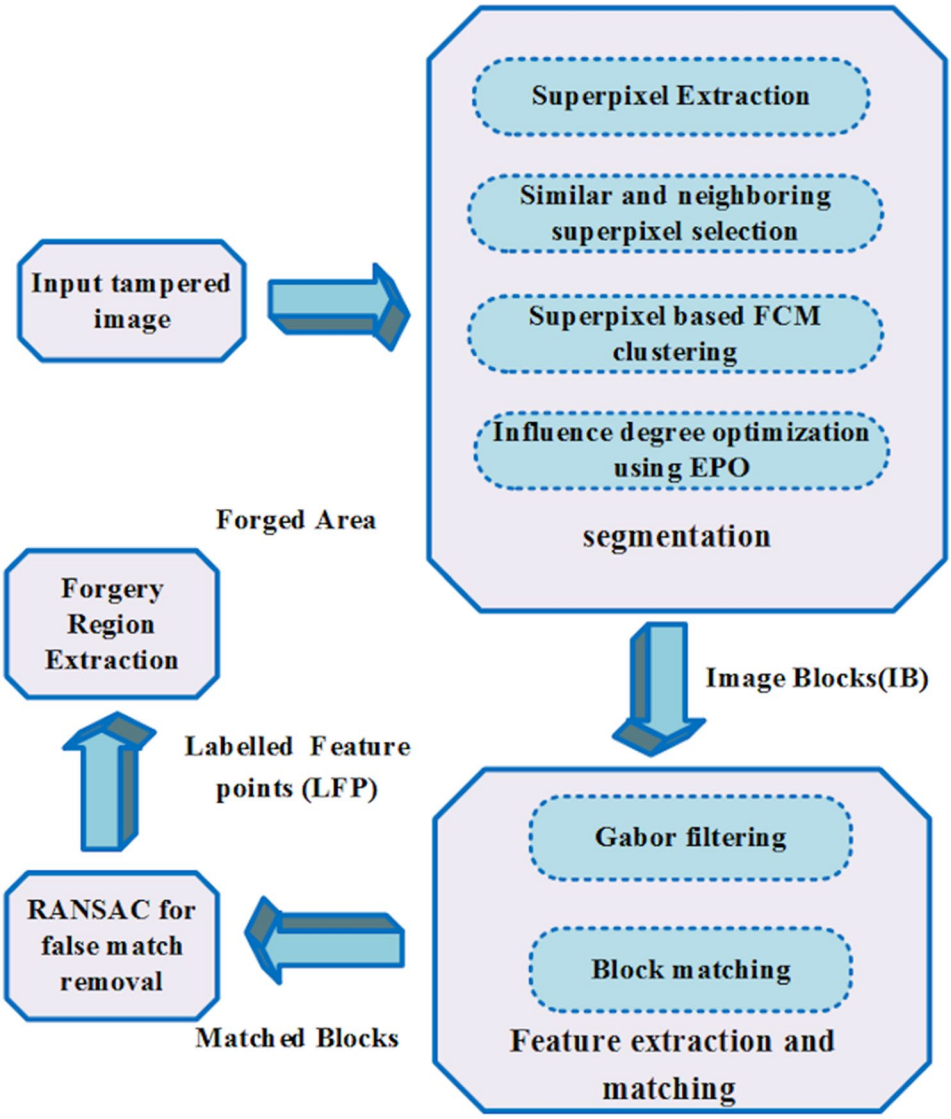

Fig. 1 The framework of the proposed CMFD method

images into intersecting blocks, wherein the size of the blocks is described and set beforehand. After that, these blocks are matched to determine the forgery regions. The forgery detected areas using this process are consisting of fixed blocks at all times, and it cannot represent the exact forgery region properly. Thus, these methods tend to lower the recall rate. To tackle these issues, a novel segmentation procedure is proposed, which segments the tampered image into uneven and non-overlapping IB. Finally, these non-overlapping and uneven blocks are matched to determine the forgery regions.

In the proposed segmentation process, the superpixels are initially extricated using the Turbo pixel algorithm. Then, the superpixels based FCM clustering is realized wherein the neighboring and similar superpixels influences are encompassed into FCM to obtain robust results once the image is degraded with noise. Also, the segmentation performance is improved by optimizing the influential degree.

4.1.1 Superpixel extraction

Superpixels roughly segment the image into a number of sections with equal size and shapes. Every superpixel illustrates a similar visual appearance, which is used to fasten the successive processes. Thus, the superpixel method and its parameters should be carefully selected for the specific applications. Here, superpixels from an image are extricated using Turbo Pixels (Levinshtein et al. 2009). Here K number of initial seeds are located on image with the distance of $\sqrt{M/K}$, where M represents the total number of pixels in the image. Then, the superpixels are extracted using a geometric-flow-based algorithm. The detail description for this

algorithm is provided in (Levinshtein et al. 2009). It preserves the region boundaries because every superpixel is approximately uniform in texture and gray. The texture, gray and spatial information are encoded into superpixels by describing every superpixel j using a 7-D wavelet feature vector $\boldsymbol{W}_j = (w_1, w_2, w_3, w_4, w_5, w_6, w_{7)}$. The mean of every pixel's wavelet values in superpixel j around three layers are denoted as $\boldsymbol{W}_j$. The mean position of every pixel presented in *j-th* superpixel is denoted as. S_{p_j}.

4.1.2 Neighboring and similar superpixel selection

The similar superpixels are generally selected by searching a specific number of most comparable superpixels. The similarity between the selected superpixel and the adjacent superpixel is measured and is used to achieve the searching process. Generally, the similarities of any adjacent superpixels are defined based on the clustering distances, color difference, and so on. However, the histogram of any superpixels provides richer information with strong discriminable characteristics. The histogram difference can measure the superpixel similarities efficiently due to its lower sensitivity to motion and noise. When compared to the original image, the superpixels consist of fewer number of pixels. One can easily compute the superpixel histogram due to the presence of fewer different colors. Thus, a histogram difference kernel (Liu et al. 2013) is utilized here to measure similarity. Generally, each superpixels contain a number of pixels and are used to calculate the super pixel-level histogram H_j. These histograms are then normalized to one as given below:

$$\sum_{i=1}^{N} H_{j(i)} = 1 \tag{10}$$

The superpixel similarities between every superpixel pairs are expressed as

$$\text{Similarity}(j,k) = s_c(j,k)s_d(j,k) \tag{11}$$

where s_c represents color similarity which is calculated using the histogram intersection kernel and s_d represents spatial similarities. The expression for s_c and s_d are given below:

$$s_c(j,k) = \sum_{i=1}^{N} \min\left(H_j(i), H_k(i)\right) \tag{12}$$

$$s_d(j,k) = 1 - \frac{c_j - c_k}{d} \tag{13}$$

where, d represents the diagonal length and $c_j and c_k$, represents superpixel's spatial centers. The feature and relative distance difference of selected superpixel from the adjacent and similar superpixels are used to modify the objective function of traditional FCM (Tian et al. 2015).

4.1.3 Modified superpixel-based FCM and influence degree optimization using EPO

FCM is a data clustering technique in which a membership grade specifies the degree to cluster the data points. In the superpixel-based FCM method, limited groups of superpixels are partitioned into C number of fuzzy clusters based on provided standards. The mathematical expression for the objective function of the superpixel-based FCM clustering to partition a superpixel data $\left\{\boldsymbol{W}_j\right\}_{j=1}^{N}$ into C clusters can be expressed as

$$F(l,v) = \sum_{i=1}^{C}\sum_{j=1}^{N} m_{ij}^{l} D_{ij}^2 \tag{14}$$

where m_{ij} represents membership value and its value in the range of [0,1]; C represents predefined cluster's count, and N denotes the number of pixels in the image and $\boldsymbol{v} = \left\{v_{1,} v_{2,} \ldots v_{C,}\right\}$ represents the cluster centers; Euclidean distance between the *i-th* center and the *j-th* superpixel is denoted as D_{ij}. $l \in [1, \infty]$ is the fuzziness constant. The fuzzy partitioning of the recognized superpixel samples are obtained by minimizing the objective function iteratively:

$$m_{ij} = \frac{1}{\sum_{k=1}^{C}\left(\frac{D_{ij}}{D_{kj}}\right)^{\frac{2}{l-1}}}, v = \frac{\sum_{j=1}^{N} m_{ij}^{l}\boldsymbol{W}_j}{\sum_{j=1}^{N} m_{ij}^{l}} \tag{15}$$

The nearest and similar superpixels are introduced into the similarity metric D_{ij}^2 to modify the superpixel based FCM. Here, a half-done structure, depending on membership and the spatial model is established using an influential degree. This clustering process, depends on the likeness of similar and adjacent superpixels.

$$\hat{D}_{ij}^2 = D_{ij}^2\left(1 - \beta_1 \frac{\sum_{k=1}^{S_n^j} m_{ik} r_{jk}^2}{\sum_{k=1}^{S_n^j} r_{jk}^2}\right)\left(1 - \beta_2 \frac{\sum_{k=1}^{S_n^j} m_{ik} R_{jk}}{\sum_{k=1}^{S_n^j} R_{jk}}\right) \tag{16}$$

where S_n^j represents the number of adjacent and similar superpixels of superpixel j. β_1 and β_2 are the influential degree of r_{jk} and R_{jk} respectively. r_{jk} is the relative distance between superpixel j and k. R_{jk} represents the spatial feature difference that is obtained between the superpixels j and k and represented as:

$$r_{jk}^2 = S_{pj} - S_{pk}^2, R_{jk} = \boldsymbol{W}_j - \boldsymbol{W}_k \tag{17}$$

The objective function of modified superpixel-based FCM clustering is defined as:

$$F(l,v) = \sum_{i=1}^{C}\sum_{j=1}^{N} m_{ij}^{l}\widehat{D_{ij}^{2}} \tag{18}$$

The cyclic objective function optimization procedure is the same as Eq. (6), wherein the D_{ij}^2 is substituted with $\hat{D}_{ij}^2$. The performance of this segmentation is affected by the influence degree parameters (β_1, β_2) due to the direct proportionality of these parameter with the objective function. Here, an EPO algorithm is used to optimize the influence degrees. The fitness value is calculated for each search agent using the objective function provided in Eq. (9). A polygon shape grid boundary is considered to position the random values of (β_1, β_2). Here, the effective mover of EPO is $\boldsymbol{B_{ep}} = (\boldsymbol{B_{ep1}}, \boldsymbol{B_{ep2}})$ related with the influential degree (β_1, β_2) which simplifies the explanation. The EPO algorithm initially determines the boundary of the parameters positioned on the polygon grid. Once the huddling limit is generated, the difference between the current influence degree parameters and the best optimum solution is computed. When the solution's fitness is equal to the optimal result then it is known as the present best optimum solution. The positions of all other parameters are updated based on the current best optimum solution. The algorithm for the proposed Modified Superpixel based FCM Clustering with EPO is provided below:

Step 1: Initialize parameters: number of cluster center C, membership matrixm_{ij}, the cluster center v, stop iteration threshold $T = 0.1\%$,(β_1, β_2), the population size of EPO and other parameters of EPO.

Step 2: Extract superpixels using Turbo pixel algorithm.

Step 3: Determine the number of similar and neighboring superpixel using a histogram difference kernel.

Step 4: Cluster the similar and neighboring superpixels using modified superpixel based FCM clustering with EPO.

i. Determine the objective function using Eq. (18)
ii. Evaluate the huddling boundaries of the influence degrees using Eqs. (1) and (2)
iii. Compute the temperature profile using Eq. (3)
iv. Find the difference between the current influence degree parameter and best optimum solution using Eqs. (4, 5, 6, 7, 8)
v. Update the parameters (β_1, β_2) when its solution is better than the previous optimal solution using Eq. (9)
vi. Return optimal values of (β_1, β_2)

Step 5: Update cluster centers and membership values of all superpixels.

Step 6: Check the stopping criteria $\left|F^{i}(l,v)\right| - \left|F^{i+1}(l,v)\right| / F(l,v) \leq T$ to terminate the iteration. Otherwise, go to step 4.

Here, the forged image can be accurately segmented into non-overlapping and uneven IB using the proposed segmentation algorithm even the image is corrupted by noise, as mentioned earlier. The proposed CMFD method's evaluation outcome can be increased compared to existing methods that divide the input image into equal-sized blocks. In addition, the computational complexity of the proposed method can be reduced compared to the duplication detection approaches, which divide the input image into intersecting blocks.

4.2 Block feature extraction and matching using Gabor filter

This section discusses the procedure for block feature extraction from IB. In the conventional block-based CMFD algorithm, the sizes of the extracted block features are similar to one another. The pixels presented in all image blocks are simply considered as block feature in some existing algorithms. These extracted features replicate the contents of the image blocks but fail to give location information. Also, different image transformations can degrade the block features. Hence, the features from every image block should be extracted and are called block features, and these features are robust to different changes like rotation, scaling, and additive noise.

The duplicated region of the tampered image is detected by extracting the Gabor features of an image. The various rotation angles, scaling factors, and frequencies of Gabor filter represent the images Gabor feature. The Gabor filter is used for filtering the image blocks to generate the vectors of block features. Then, these vectors are matched with each other to obtain the matching score. The image blocks' relationships are represented by this matching score.

4.2.1 Block feature extraction using rotation invariant Gabor filter

The impulse response of the linear Gabor filter (Yohannan and Manuel 2016) is described by the multiplication of harmonic function and Gaussian function. Generally, the Gabor filters aim to improve the edges and to smoothen the basins. Spatio-spectral information can be correctly provided by Gabor filtering even the images undergone some contrast and brightness changes. The rotation-invariant Gabor depiction suggested in (Han and Ma 2007) is used in this work. This Gabor depiction necessitates some summations on the impulse response of traditional Gabor filter. Here, $\chi(s,t)$ is used to represent a single block after segmenting the tampered image. The rotation invariant concept is utilized to

create feature vectors for every single image block. The expression for 2-dimensional Gabor function is given as:

$$g(s,t) = \frac{1}{2\pi\sigma_s\sigma_t} e^{\left[-\frac{1}{2}\left(\frac{s^2}{\sigma_s}+\frac{t^2}{\sigma_t}\right)+2\pi i\omega s\right]} \tag{19}$$

Here σ_s and σ_t represents the Gabor filter spatial range and frequency bandwidth, and $(\omega, 0)$ denotes the center frequency of the filter. Consider $g(s,t)$ as the primary function of the Gabor filter family. This primary function $g(s,t)$ is rotated and scaled to generate Gabor functions set $g_{xy}(s,t)$:

$$g_{xy}(s,t) = A^{-2x} g\left(s', t'\right) \tag{20}$$

$$s' = A^{-m}\left(s\cos\varphi_y - t\sin\varphi_y\right); t' = A^{-m}\left(t\cos\varphi_y - t\sin\varphi_y\right) \tag{21}$$

where $A > 1, \varphi_y = \frac{y\pi}{K}, x = 0, 1, \ldots L-1, y = 0, 1, \ldots K-1$, variable L represents the complete scale count, and variable K represents the total number of orientations. The image $\chi(s,t)$ is filtered using Gabor filter to obtain $GF_{x,y}(s,t)$ as:

$$GF_{x,y}(s,t) = \sum_{s_1}\sum_{t_1} \chi\left(s_1,t_1\right) g_{x,y}\left(s-s_1, t-t_1\right) \tag{22}$$

In order to obtain the family of rotation invariant Gabor filter, the entire K filters in (16) are summed with various orientations at every scale.

$$g_x(s,t) = \sum_{y=0}^{K-1} g_{x,y}(s,t), x = 0, 1, \ldots L-1 \tag{23}$$

Thus, the transformed image $\chi(s,t)$ is defined as:

$$GF_x(s,t) = \sum\sum \chi\left(s_1,t_1\right) g_x\left(s-s_1, t-t_1\right), x = 0, 1, \ldots L-1 \tag{24}$$

The feature vector is calculated using the mean μ_x of the transformed coefficients $GF_x(s,t)$ and this mean value is given as:

$$\mu_x = \frac{1}{N}\sum_s\sum_t \left|GF_x(s,t)\right| \tag{25}$$

The feature vector is then constructed as follows:

$$\boldsymbol{B}_f^1 = \left[\mu_0, \mu_1, \ldots \mu_{L-1}\right] \tag{26}$$

The rotation-invariant Gabor filter is utilized for calculating the robust feature vector of every block of the image. Once a feature vector is computed, it is stored in a feature matrix B_F. This feature matrix now represents the whole image. The further processing of the forgery detection method utilizes this feature matrix.

4.2.2 Block feature matching

Once the block features are acquired, it is necessary to position the matched blocks using the block features. Here, the block feature Matching Algorithm developed in (Pun et al. 2015) is applied for positioning the matched blocks. The steps of the block feature matching process are given below:

Step 1: consider the block features, $\boldsymbol{B_f} = \left\{B_f^1, B_f^2, \ldots B_f^M\right.$ where M denotes the number of image blocks.

Step 2: Compute the image blocks correlation coefficients R_C which represents the number of matched feature points of two IB.

If the image contains M number of blocks after the EPO based superpixel segmentation, then $M(M-1)/2$ correlation coefficients can be generated. When the Euclidean distance between the two feature points is larger than the known feature point matching threshold T_p, then these feature points are considered to be matched points. The feature points f_i and f_j are said to be matched points only when they satisfy the condition given in Eq. (27):

$$D\left(f_i,f_j\right)T_p \le D\left(f_i,f_a\right) \tag{27}$$

where $D\left(f_i,f_j\right)$ and $D\left(f_i,f_a\right)$ represents the Euclidian distance between the feature points, f_a represents the a-th feature points.

Step 3: Compute the block matching threshold T_{bf} based on the correlation coefficient dissemination.

Initially, the various correlation coefficient components are arranged in ascending order for calculating T_{bf}. Subsequently, the first-order derivative and second-order derivatives are estimated. When the second-order derivative of the correlation coefficient is greater than the average value of the respective first-order derivative, that coefficient is chosen as the minimum correlation coefficient denoted as T_{bf}.

Step 4: Position the matched blocks M_b based on the block matching threshold T_{bf}.

A match point represents the coordinates of the block. Many points are found to be matched because of the smaller block sizes. The forged region may contain a large number of matched points when the image regions are more similar to each other. Few false matches may be present after the completion of feature point extrication and feature matching, which affects the quality of image matching. The false matches need to be filtered out to guarantee subsequent work quality. RANSAC is utilized here for removing the false matches.

4.3 Random sample consensus (RANSAC) algorithm

The aim of the RANSAC algorithm is to extricate different feature point pairs from matching pairs in random order. In

the RANSAC algorithm (Fischler and Bolles 1981; Hossein-Nejad and Nasri 2017; Wang et al. 2018), a set of matched points are randomly selected, and then the perspective transformation matrix H is estimated. The residual matching points are then transformed and then compared to their respective matches in terms of distance, and a threshold value is determined. The distance is represented as inliers if it is less than the threshold value, otherwise, it is categorized as outliers. The matched feature points obtained after removing the false match in the matched blocks are labeled to acquire the Labelled Feature Points (LFP), and it specifies the SFR. The LFP is represented as

$$\boldsymbol{LFP} = \left\{ \left(L^1_{FP}, \overline{L^1_{FP}}\right), \left(L^2_{FP}, \overline{L^2_{FP}}\right), \ldots \left(L^n_{FP}, \overline{L^n_{FP}}\right) \right\} \tag{28}$$

where $\left(L^i_{FP}, \overline{L^i_{FP}}\right)$ represents the *i-th* matched feature point pair.

4.4 Forgery Region Extraction Algorithm

The extricated LFP are representing the coordinates of the forgery region. Thus, the forgery region needs to be positioned using FRE algorithm. The superpixels based FCM with EPO optimization algorithm segments the host image very well. SFR is obtained by replacing the smaller superpixels with the LFP. The representation of SFR after replacing small superpixel is given as

$$\boldsymbol{SFR} = \left\{ \left(S^1_{LFP}, \overline{S}^1_{LFP}\right), \left(S^2_{LFP}, \overline{S}^2_{LFP}\right) \ldots \left(S^n_{LFP}, \overline{S}^n_{LFP}\right) \right\} \tag{29}$$

The local color feature of the neighborhood superpixel of SFR is measured to increase the precision and recall rate. If the local color features are the same as the SFR, then the neighboring blocks are fused with the SFR to generate the merged regions (MR). The adjacent blocks for each suspected forgery region $SFR^i = \left(S^i_{LFP}, \overline{S}^i_{LFP}\right)$ are described as:

$$SFR^i_{\text{neighbour}} = \left(S^{i-\varphi}_{LFP}, \overline{S}^{i-\varphi}_{LFP}\right) \tag{30}$$

where $\varphi = \{45^o, 90^o, 135^o, 180^o, 225^o, 270^o, 315^o, 360^o,\}$.

The SFR and adjacent block's local color features are computed by:

$$S^i_{LFP} = \frac{R\left(S^i_{LFP}\right) + G\left(S^i_{LFP}\right) + B\left(S^i_{LFP}\right)}{3}; \ \overline{S}^i_{LFP} = \frac{R\left(\overline{S}^i_{LFP}\right) + G\left(\overline{S}^i_{LFP}\right) + B\left(\overline{S}^i_{LFP}\right)}{3} \tag{31}$$

$$S^{i-\varphi}_{LFP} = \frac{R\left(S^{i-\varphi}_{LFP}\right) + G\left(S^{i-\varphi}_{LFP}\right) + B\left(S^{i-\varphi}_{LFP}\right)}{3}; \ \overline{S}^i_{LFP} = \frac{R\left(\overline{S}^{i-\varphi}_{LFP}\right) + G\left(\overline{S}^{i-\varphi}_{LFP}\right) + B\left(\overline{S}^{i-\varphi}_{LFP}\right)}{3} \tag{32}$$

The local color feature satisfies the condition expressed in (33) only if the adjacent block local color feature is the same as the respective SFR suspected regions, and then the adjacent block is merged with the suspected region.

$$\left.\begin{aligned} \left|S^i_{LFP} - S^{i-\varphi}_{LFP}\right| &\le T_{\text{similarity}} \\ \left|\overline{S}^i_{LFP} - \overline{S}^i_{LFP}\right| &\le T_{\text{similarity}} \end{aligned}\right\} \tag{33}$$

$T_{\text{similarity}}$ denotes the threshold used for measuring the local color feature similarity. For the experiments, $T_{\text{similarity}} = 15$. Finally, the duplicated regions are determined using a close morphological process.

As mentioned earlier, the proposed forgery detection method can provide robust results because modified FCM based superpixel clustering with EPO split the input tampered image into non-overlapping blocks by considering the influence of similar and neighboring superpixels. This superpixel based algorithm reduces computational complexity. Also, block features are accurately extracted using Gabor filter when the contrast and brightness of images are varied. Furthermore, the block feature matching approach uses two thresholds for identifying the matched blocks. When the duplicated portions are the same as that of the image background then they are considered as mismatching features and are avoided using these thresholds. Then the RANSAC algorithm is applied to remove the false matches. Finally, the FRE algorithm is applied to locate the duplicated regions.

5 Experimental results

In this section, several experiments are performed to evaluate the performance of the proposed work. This section is divided into three subsections. The dataset utilized for the analysis of the proposed method is described in subsection 5.1. Section 5.2 describes the evaluation metrics utilized to determine the performance of the proposed method. And Sect. 5.3 illustrates the experimental outputs of the proposed forgery detection approach and the comparison with other forgery detection methods under plain copy-move and the detection result under different attacks.

5.1 Dataset Description

In this work, the MICC-F600 dataset (Amerini et al. 2013) is utilized, consisting of plain copy-move images and images with specific geometrical changes. Six hundred images are presented in this dataset, among which 448 images are original, and 152 images are tampered ones. Different tampering processes create these 152 images namely rotation, multiple cloning, and scaling. The MICC-F600 dataset consists of forged images, and the size and shapes of the tampered area in these images are not the same. Hence, this dataset is more challenging. The spatial separation of tampered portions isn't visible and the prediction of shapes of duplicated regions can be a challenging task.

5.2 Evaluation Metrics

The pixel level and image level analysis are used to validate the performance of the proposed approach. The image-level analysis is used to check the capability of the CMFD method to correctly identify the tampered image. The pixel-level analysis is used to check the capability to precisely pinpoint the tampered portions. Three performance metrics are chosen to estimate the effectiveness of the proposed methodology at the pixel and image level. They are precision, recall, and F1 score. Precision is defined as the ratio of exactly determined copied pixels to the total number of determined copied pixels. The formula used to calculate the precision is given as:

$$\text{Precision} = \frac{TP}{TP + FP} \tag{34}$$

The recall represents the number of exactly determined copied pixels to the total number of copied pixels obtained in the duplicated image's ground-truth. The recall is computed by,

$$\text{Recall} = \frac{TP}{TP + FN} \tag{35}$$

where TP represents the true positives count, and FP describes the false positives count. FN represents the count of erroneously chosen pixels as uncopied. Along with precision and recall, another estimation measure, the F1 score, is also used, which unites recall and precision to give a single value

$$F_1 = 2\frac{\text{precision} \times \text{recall}}{\text{precision} + \text{recall}} \tag{36}$$

Furthermore, another measurement called Enhanced Alignment Measure (E-measure) (Fan et al. 2018) is added wherein the local pixel values, and image-level mean values are combined to encapsulate both the local pixel matching and image-level information together. The E-measure can be defined as

$$E - \text{measure} = \frac{1}{h * w} \sum_{a=1}^{h} \sum_{b=1}^{w} \emptyset(a, b) \tag{37}$$

where w and h represent the image's width and height respectively and $\emptyset$ represents the enhanced alignment matrix.

5.3 Evaluation of the proposed work

The proposed segmentation approach splits the tampered image into non-overlapping uneven blocks, as defined in Sect. 4.1. The detection result performance is increased using the proposed modified FCM based superpixel clustering with the EPO algorithm compared to other forgery detection algorithms that divide the tampered images into blocks with uniform size. The parameter settings for the proposed modified FCM based superpixel clustering with the EPO algorithm are summarized in Table 1.

The forgery detection outputs for four tampered images under plain copy-move are shown in Fig. 2. The tampered host images I_1, I_2, I_3, I_4 are depicted in the first column; the second column illustrates the superpixel segmentation results of I_1, I_2, I_3, I_4; the third column displays the detection output of I_1, I_2, I_3, I_4.

The outputs of the proposed approach are related to some existing approaches to validate the performances. The selected existing methods for comparison are block-based method, Zernike (Ryu et al. 2013), keypoint-based methods SURF (Shivakumar, B.L., Baboo 2011), Hybrid feature method (Yang et al. 2017) and hybrid method of block and keypoint basis methods, Adaptive over-segmentation method (Pun et al. 2015), Binary Discriminative Feature

Table 1 Parameter initialization

Algorithms	Parameter	Value
Modified superpixel based FCM clustering	Number of initial seeds K	300
	Influence parameters ($\beta_1, \beta_{2)}$	[0,1]
	Iteration threshold T	0.1%
EPO	Population size	80
	Number of iteration $I_{\max}$	100
	Rand	[0,1]
	Motion limit m	2
	Controlling parameter q	[2,3]
	Controlling parameter p	[1.5,2]

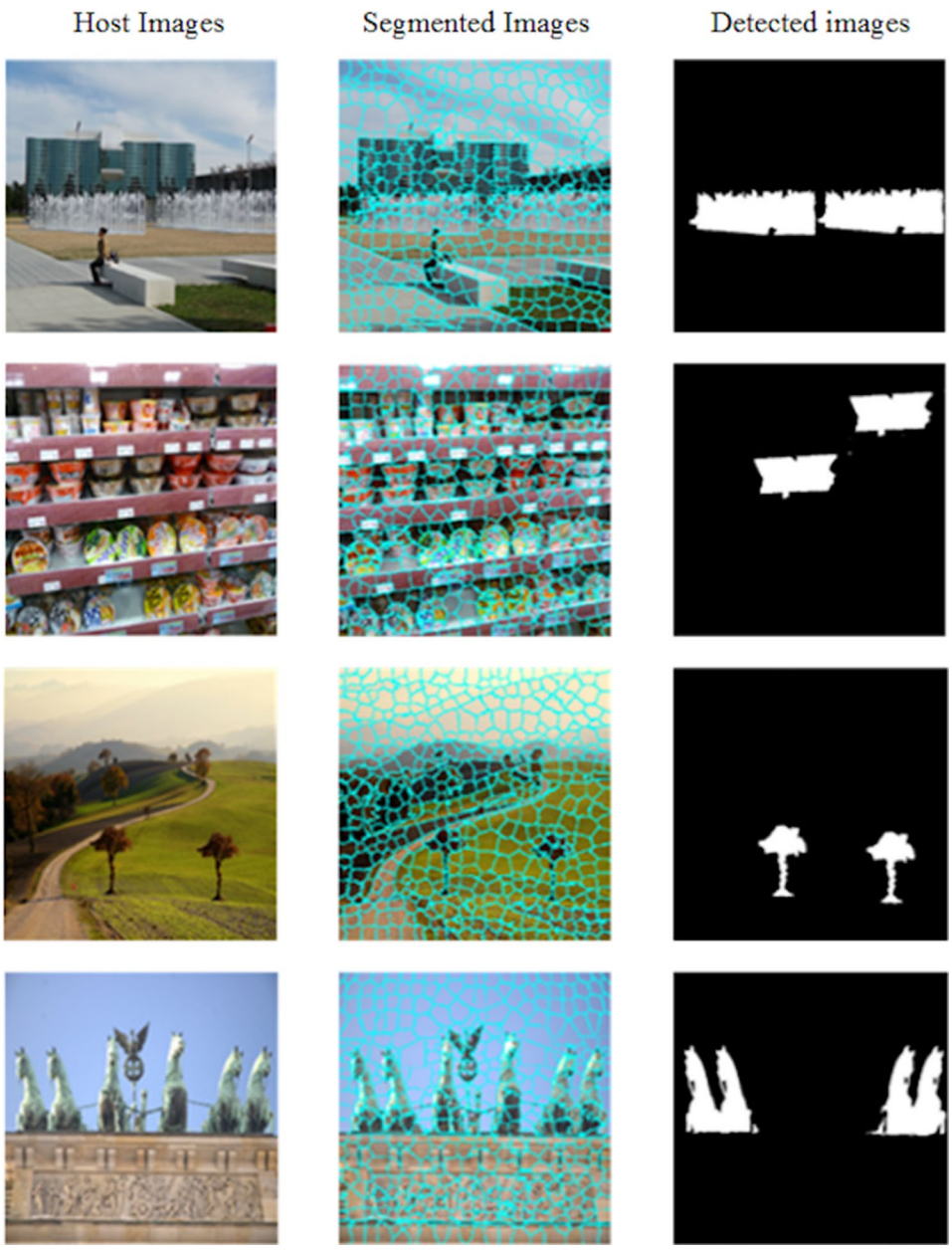

Fig. 2 Results of Forgery detection approach under plain copy-move

Table 2 Detection results at image level under plain copy-move

Methods	Precision (%)	Recall (%)	F_1 (%)
Zernike	88.46	95.83	91.99
SURF	77.27	70.83	73.90
Hybrid feature method (HF)	78.33	97.92	87.04
Adaptive over-segmentation method (AOS)	96.00	97.92	97.96
BDF method	97.50	87.50	92.23
Proposed	96.96	99.21	97.34

Table 3 Detection results under plain copy-move at the pixel level

Methods	Precision (%)	Recall (%)	F_1 (%)
Zernike	99.41	68.76	81.29
SURF	84.50	44.83	58.58
Hybrid feature method (HF)	90.27	78.61	58.58
Adaptive over-segmentation method (AOS)	97.22	83.73	89.97
BDF method	90.55	86.74	88.35
Proposed	99.53	89.66	92.78

Table 4 Comparison of E-measure values

Methods	E-measure (%)
Zernike	87.32
SURF	67.58
Hybrid feature method	73.81
Adaptive over-segmentation method	92.36
BDF method	90.29
Proposed	95.06

(BDF) method (Raju and Nair 2018). Tables 2 and 3 show the comparison results under plain copy-move at pixel and image-level, respectively.

Table 3 illustrates that the precision of the block-basis approach like Zernike is high compared to the keypoint-basis approaches like SURF, hybrid features, and BDF scheme at the pixel level, but its recall rate is very low. Because certain images in the dataset consist of few analogous structural portions, and they can produce false matched points that destruct the overall performance. And our proposed algorithm can achieve a precision of 96.96% and a recall of 99.21% at image level and precision of 99.53% and a recall of 89.66% at the pixel level. Along with precision and recall, the F1 score of the proposed scheme is 97.34 at the image level and 92.78% at the pixel level which are better than other block-based approach and key-point based approaches and also a fusion method like Adaptive over-segmentation.

Moreover, the hybrid method of BDF shows somewhat better performance than our method in terms of precision at the image level. But the recall rate of the method is very low when compared to our approach. Hence, the overall performance of such a method is decreased.

Table 4 compares the E-measure values of the proposed algorithm with the existing approaches. This measure consists of a solid term to consider the image level information and local pixel matching information. Generally, a higher E-measure value indicates better performance. The E-measure of the proposed method is 95.06% (see Table 3), which is higher than the existing methods. The outcomes of this evaluation metrics indicate that this proposed method attains high accuracy in the CMFD process after introducing the EPO algorithm.

Figure 3 shows the comparison chart for F-1 score, recall, precision, and E-measure under plain copy-move. It also shows that the precision, recall rate, F1 score, and E-measure of the proposed CMFD-EPO method is much better than that of traditional algorithms because of fewer false matches. Thus the proposed modified FCM superpixel based clustering with the EPO algorithm can give very accurate detection performance with higher recall and maintain good precision at the pixel level. It illustrates that the proposed approach can trace the forged area more accurately.

The proposed method is verified under geometrical changes like rotation, scaling, multi-cloned, and noise addition along with plain copy-move forgery. Here, the tampered images are produced utilizing all 38 images in the dataset, and the duplicated portions are attacked by various attacks. The forged images in the MICC-F600 data set are created by rotation of copied portions of 38 non-tampered images by 30^0. Also, the duplicated portions in all 38 images are scaled by 120% and rotated by 30^0. Furthermore, a translation process is used to duplicate the forged potions two or three times, which forms multi-cloned images. To check the performance of the proposed method under a noise attack, the duplicated image is corrupted by adding Gaussian noise with the standard deviation of 0.05 after normalization. The CMFD result when the image is undergone different transformation is illustrated in Fig. 4.

The input image I_1 after tampering using rotation attack, rotation and scaling attack, noise attack and multi-cloned is presented in Fig. 4a–d respectively. The extracted superpixels of the corresponding are shown in Fig. 4e. Figure 4f illustrates the forgery detection result of Fig. 4a–d. From this result, one can understand that the proposed approach based on modified FCM superpixel clustering with EPO algorithm can achieve robust forgery detection result under different attacks.

6 Conclusion

It is very difficult to identify copy-move forgeries when the copied portions undergo certain geometrical changes and are corrupted by noise. In such circumstances, block-basis approaches are generally insufficient and the key-point-basis approaches give better performances. Even though keypoint-basis approaches are robust to geometric changes and reduced cost, they may not be used for managing smooth areas because there are insufficient

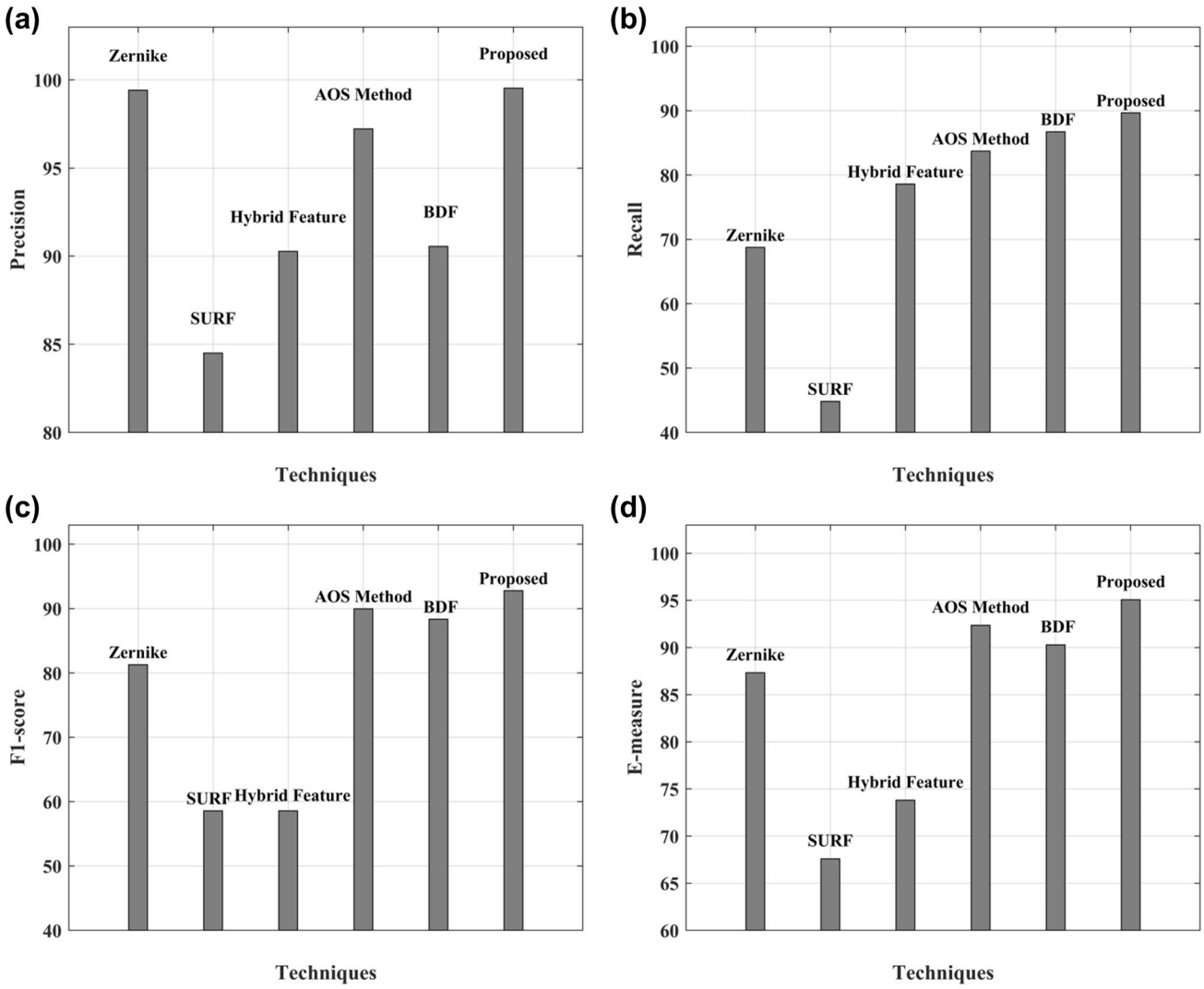

Fig. 3 Comparison chart **a** precision **b** recall **c** F1-score **d** E-measure

keypoints. Thus, a combined algorithm of block basis and keypoint basis approach has been proposed in this paper to identify the forgeries. The proposed superpixel based FCM clustering segmentation method gave robust forgery detection results due to the influence of similar and neighboring superpixels incorporation and optimization using EPO and reduced the computational expenses. The use of Gabor filters to extricate the block features improved the accuracy of the proposed approach and provided robust result against changing contrast and brightness of images. The recall rate of the proposed work has been further increased by measuring the local color features of the SFR. The experimental results demonstrate how the proposed technique could successfully recognize the duplicated portion of an image when the copied portions experience different geometrical conversions or when the image is corrupted by noise. In future, the proposed work may be extended by introducing an optimized deep fully resolution convolutional neural network (CNN) for the extraction of features from the forged images and to identify the forged regions with greater accuracy.

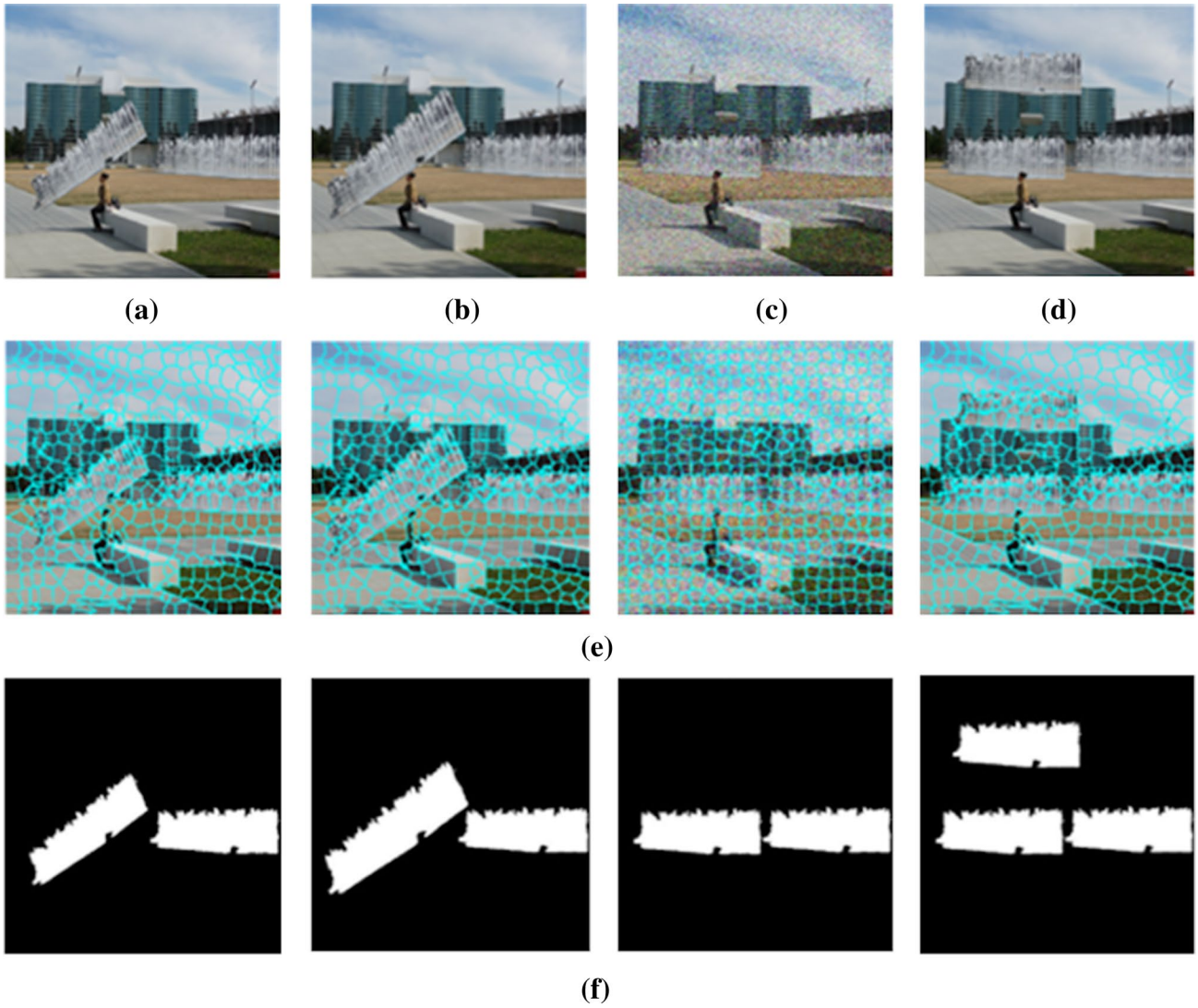

Fig. 4 Forgery detection result of proposed approach for different attacks **a** rotation attack **b** Scaling and rotation **c** noise addition **d** multicloned **e** superpixel extraction **f** detection results

References

Alkawaz MH, Sulong G, Saba T, Rehman A (2018) Detection of copy-move image forgery based on discrete cosine transform. Neural Comput Appl. https://doi.org/10.1007/s00521-016-2663-3

Amerini I, Ballan L, Caldelli R et al (2011) A SIFT-based forensic method for copy-move attack detection and transformation recovery. IEEE Trans Inf Forensics Secur 6:1099–1110. https://doi.org/10.1109/TIFS.2011.2129512

Amerini I, Ballan L, Caldelli R et al (2013) Copy-move forgery detection and localization by means of robust clustering with J-Linkage. Signal Process Image Commun. https://doi.org/10.1016/j.image.2013.03.006

Askari S (2020) Fuzzy C-means clustering algorithm for data with unequal cluster sizes and contaminated with noise and outliers: review and development. Expert Syst Appl. https://doi.org/10.1016/j.eswa.2020.113856

Bayram S, Sencar HT, Memon N (2009) An efficient and robust method for detecting copy-move forgery. In: ICASSP, IEEE International Conference on Acoustics, Speech and Signal Processing-Proceedings.

Bi XL, Pun CM, Yuan XC (2018) Multi-scale feature extraction and adaptive matching for copy-move forgery detection. Multimed Tools Appl. https://doi.org/10.1007/s11042-016-4276-3

Cao Y, Wu Y, Fu L et al (2019) Multi-objective optimization of a PEMFC based CCHP system by meta-heuristics. Energy Rep. https://doi.org/10.1016/j.egyr.2019.10.029

Dhiman G, Kaur A (2018) Optimizing the design of airfoil and optical buffer problems using spotted hyena optimizer. Designs. https://doi.org/10.3390/designs2030028

Dhiman G, Kaur A (2019) STOA: A bio-inspired based optimization algorithm for industrial engineering problems. Eng Appl Artif Intell. https://doi.org/10.1016/j.engappai.2019.03.021

Dhiman G, Kumar V (2017) Spotted hyena optimizer: a novel bio-inspired based metaheuristic technique for engineering

applications. Adv Eng Softw. https://doi.org/10.1016/j.advengsoft.2017.05.014
Dhiman G, Kumar V (2018) Emperor penguin optimizer: a bio-inspired algorithm for engineering problems. Knowl-Based Syst. https://doi.org/10.1016/j.knosys.2018.06.001
Di Martino F, Senatore S, Sessa S (2019) A lightweight clustering–based approach to discover different emotional shades from social message streams. Int J Intell Syst. https://doi.org/10.1002/int.22105
Dixit R, Naskar R, Mishra S (2017) Blur-invariant copy-move forgery detection technique with improved detection accuracy utilising SWT-SVD. IET Image Process. https://doi.org/10.1049/iet-ipr.2016.0537
Fan DP, Gong C, Cao Y, Ren B, Cheng MM, Borji A (2018) Enhanced-alignment measure for binary foreground map evaluation. In: Proceedings of the 27th International Joint Conference on Artificial Intelligence, pp 698–704
Fischler MA, Bolles RC (1981) Random sample consensus: a paradigm for model fitting with applications to image analysis and automated cartography. Commun ACM. https://doi.org/10.1145/358669.358692
Fridrich J, Soukal D, Lukáš J (2003) Detection of copy-move forgery in digital images. Int J 3:4
Han J, Ma KK (2007) Rotation-invariant and scale-invariant Gabor features for texture image retrieval. Image Vis Comput. https://doi.org/10.1016/j.imavis.2006.12.015
Hossein-Nejad Z, Nasri M (2017) An adaptive image registration method based on SIFT features and RANSAC transform. Comput Electr Eng. https://doi.org/10.1016/j.compeleceng.2016.11.034
Jia H, Sun K, Song W et al (2019) Multi-strategy emperor penguin optimizer for RGB histogram-based color satellite image segmentation using masi entropy. IEEE Access. https://doi.org/10.1109/ACCESS.2019.2942064
Levinshtein A, Stere A, Kutulakos KN, et al (2009) TurboPixels: Fast superpixels using geometric flows. In: IEEE Transactions on Pattern Analysis and Machine Intelligence.
Li M, Hu S, Xia J et al (2020) Dissolved oxygen model predictive control for activated sludge process model based on the Fuzzy C-means cluster algorithm. Int J Control Autom Syst. https://doi.org/10.1007/s12555-019-0438-1
Liu Z, Meur L, Luo S (2013) Superpixel-based saliency detection. In: International Workshop on Image Analysis for Multimedia Interactive Services.
Popescu AC, Farid H (2004) Exposing Digital Forgeries by Detecting Duplicated Image Regions. Tech Report, TR2004–515, Dep Comput Sci Dartmouth Coll Hanover, New Hampsh,pp 1–11
Pun CM, Yuan XC, Bi XL (2015) Image forgery detection using adaptive oversegmentation and feature point matching. IEEE Trans Inf Forensics Secur. https://doi.org/10.1109/TIFS.2015.2423261
Qureshi MA, Deriche M (2015) A bibliography of pixel-based blind image forgery detection techniques. Signal Process Image Commun. https://doi.org/10.1016/j.image.2015.08.008
Raju PM, Nair MS (2018) Copy-move forgery detection using binary discriminant features. J King Saud Univ Comput Inf Sci. https://doi.org/10.1016/j.jksuci.2018.11.004
Ryu SJ, Kirchner M, Lee MJ, Lee HK (2013) Rotation invariant localization of duplicated image regions based on zernike moments. IEEE Trans Inf Forensics Secur. https://doi.org/10.1109/TIFS.2013.2272377
Shivakumar BL, Baboo S (2011) Detection of Region Duplication Forgery in Digital Images Using SURF. Int J Comput Sci Issues 8:199–205
Tian X, Jiao L, Yi L et al (2015) The image segmentation based on optimized spatial feature of superpixel. J Vis Commun Image Represent. https://doi.org/10.1016/j.jvcir.2014.11.005
Wang XY, Liu YN, Xu H et al (2018) Robust copy–move forgery detection using quaternion exponent moments. Pattern Anal Appl. https://doi.org/10.1007/s10044-016-0588-1
Yang F, Li J, Lu W, Weng J (2017) Copy-move forgery detection based on hybrid features. Eng Appl Artif Intell 59:73–83. https://doi.org/10.1016/j.engappai.2016.12.022
Yang B, Sun X, Guo H et al (2018) A copy-move forgery detection method based on CMFD-SIFT. Multimed Tools Appl. https://doi.org/10.1007/s11042-016-4289-y
Yohannan RP, Manuel M (2016) Detection of copy-move forgery based on Gabor filter. In: Proceedings of 2nd IEEE International Conference on Engineering and Technology, ICETECH 2016.
Zheng J, Liu Y, Ren J et al (2016) Fusion of block and keypoints based approaches for effective copy-move image forgery detection. Multidimens Syst Signal Process 27:989–1005. https://doi.org/10.1007/s11045-016-0416-1

Publisher's Note Springer Nature remains neutral with regard to jurisdictional claims in published maps and institutional affiliations.

Proceedings of the Sixth International Conference on Inventive Computation Technologies [ICICT 2021]
IEEE Xplore Part Number: CFP21F70-ART; ISBN: 978-1-7281-8501-9

Security and privacy Aspects for Internet of Things (IoT)

Malti Bansal, Marshal Nanda, Md. Nazir Husain
Department of Electronics & Communication Engineering,
Delhi Technological University (DTU), Delhi-110042, India
maltibansal@gmail.com

2021 6th International Conference on Inventive Computation Technologies (ICICT) | 978-1-7281-8501-9/21/$31.00 ©2021 IEEE | DOI: 10.1109/ICICT50816.2021.9358665

Abstract - In today's world, technologies are closely connected to our day-to-day life with a large number of variations. And operations like accessing files, downloading, cloud computing, recognizing pictures, and video cassettes are handled using remote devices at home and offices. All these internets connected devices are usually known as the Internet of Things (IoT), and it is used in numerous applications ranging from health care to a smart city environment. Data from these devices are generally shared through the internet, so there are several challenges in deploying any IoT-based devices at any place, and the most crucial challenges are security and privacy.

***Keywords - History, IoT, problems, Security, Privacy issues*, security risk and issues, GDPR.**

1. History of IoT

The knowledge of linked gadgets was first introduced in 1832, when the principle of electromagnetic was introduced by Michael Faraday. This principle states that two devices/machines can be linked together through the exchange of electrical signals. The main history of IoT began with the creation of the web (extremely basic part) in the late 1960s, from that point it grew quickly throughout the subsequent years.

Introducing sensor devices and understanding to essential needs were considered about all through the 1980s and 1990s, yet parted from some initial tasks, candy machine is introduced which was web-based but the progress was restrained just because the innovation wasn't prepared at that time. They were too huge and cumbersome and there was no chance to get for stuff to impart sufficiently. IoT term was introduced in 1999 by Kevin Ashton, which has claimed a few definitions that hold pretty much similar undertones. Ashton's played an important role in the history of the Internet of Things and technical advancement.

In the 1980s - the first linked gadget was introduced by students and professors from Carnegie Melon University and that was Coca-Cola vending machine. These developers combined small switches into the machine and applied an initial type of the web that works to check whether the refrigeration gadget was keeping the drinks sufficiently cold and if these were accessible or not. These creations encouraged more examinations in the ground and the advancement of machines in the whole world.

In 1990, John Romkey uses a new protocol that was TCP/IP and designed a web-based toaster for the very first time, and next year, researchers in the University of Cambridge understood this concept and design a web camera model which when connected to screen it shows the measure of coffee accessible in their nearby coffee pot. They modified the webcam to take photos of the coffee pot three times each second, and at the same point, it sends the pictures to nearby PCs.

In the year 1999, Kevin Ashton introduced the countenance "The Internet of Things." He was a visionary technician; Ashton was giving an introduction for Procter and there he introduces the term IoT as an innovative idea that related to any gadgets with the assistance of RFID labels for elegant restraint the executives. He explicitly introduces the term "internet" in the title of his introduction, because the internet is newly introduced and successfully implemented so it draws the most people's interest.

In the year 2000 - At the beginning of the 20th century, the term "internet of things" came into existence and broadly used by the peoples and media, with outlets like computing, mining, and so on. Interest for the IoT and its innovation was continuously expanding which leads to the first International Conference on the topic of "The Internet of Things"that was held in Switzerland in 2008, where associates from the 23 different countries talked about Radio-frequency identification, smart devices, and sensor organizations.

In the year 2010 - The IoT still expanding more in the year 2009 were almost 90 crores is invested IoT devices and in 2010 it increases to 125 crores.

Authorized licensed use limited to: DELHI TECHNICAL UNIV. Downloaded on March 03,2021 at 06:13:45 UTC from IEEE Xplore. Restrictions apply.

In the 2010 IPv6 protocol was introduced which plays a vital role in the expansion of IoT. From that year ahead, these gadgets have increased wide and used in our regular activities. Worldwide most topmost tech companies like Cisco, Apple, Google, Samsung, and Microsoft are advancing in their activities on the creation of IoT based sensors and gadgets like interconnected devices via Bluetooth or hotspot and specs, and automatic cars and smart home devices. IoT has exposed in almost every industry such as production, medical services, transport, oil and energy, cultivation, trade, and so on. Now big companies like HP and IBM are also building their base in the field of IoT. In developing countries like India IoT devices and their business will be developing exponentially. Initially, some companies may face difficulties, but over time they will make a profit.

Table 1: Connected devices till now

year	2003	2010	2015	2020
World population	6.3 billion	6.8billion	7.2billion	7.6billion
Connected devices	500 million	12.5billion	25billion	50 billion
Devices per person	0.08	1.84	3.47	6.58

2. Internet of Things (IoT)

Internet of Things (IoT)addresses the millions and billions of physical devices around the world that are currently linked to the web, that allows all gathering and sharing of information. Because of quick headways in portable correspondence, Wireless Sensor Networks (WSNs), and Radio Frequency Identification (RFID) development in IoT can work together with each other in anyplace, and in any structure. There are numerous possible application areas because of these brilliant things and smart items. The major IoT target is simply the development of intelligent conditions and cognizant/self-ruling gadgets: smart transport, keen things, shrewd urban areas, smart living, smart cities, etc. Interfacing up all these different types of articles and adding the latest tech sensors to comprises a degree of hi-tech understanding to devices that would be generally moronic, allowing them to communicate continuous data without including anindividual person and medium. IoT is to sustain the quality of our universal surroundings brighter and more receptive, combining the progressive and physical worlds.

Despite the efforts of various governments to reinforce the IoT security guidelines, insurance systems for interconnectivity, information security, and protection issues are not solved yet. Cybercriminals utilize an ever-increasing number of modern strategies so as to discover weaknesses in associated gadgets, subsequently accessing private data. Thus, customers and associations are progressively worried about IoT security and consider it to be the main hindrance to inescapable IoT appropriation.

Fig.1: IoT

2.1 Security remains the leading barrier for IoT

Top barriers for speculation in the IoT
Security concerns - 45%
Integration difficulty – 34%
Unclear ROI – 30%
Lack of expertise to implement – 28%
Interoperability concerns - 28%
Data portability and ownership - 25%
Vendor sustainability concerns - 24%
Transition risk - 24%
Legal & compliance barriers - 23%
Network constraints - 21%
Vendor lock-in concerns - 18%

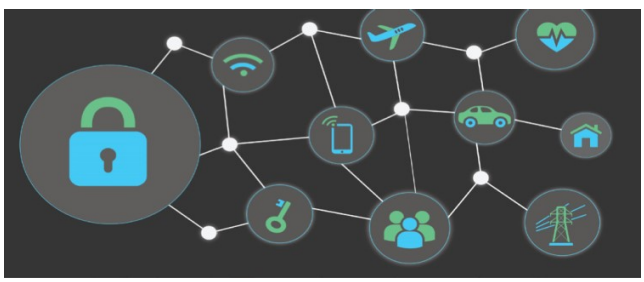

Fig.2: Security Issues

Authorized licensed use limited to: DELHI TECHNICAL UNIV. Downloaded on March 03,2021 at 06:13:45 UTC from IEEE Xplore. Restrictions apply.

2.2 Security issues in auto coupled and self-governing vehicles: The linked and self-reliant vehicle areas are difficult to implement as this involves various sensors, infrastructure, and communication protocols. With the advancement of software and communicating protocols, it makes linked and a self-reliant vehicles more prone to attacks. If security fails in automatic devices then it can prove to be severe and it is necessary to take effective safety measures and strong cyber security solutions.

1. Attacks on Smart Remote - Since Passcodes are based on infrared radiations and Bluetooth technologies so they can be easily hacked by Keys Hackers.
2. Attacks on Cloud-Based Networks - Cloud storage is a place where the data are stored online in an account and then those data can be accessed anywhere with an internet connection. Hackers can use those data to manipulate us if there is not enough security in that account or company. Automatic cars have huge data saved on these cloud servers, if there is any loophole in security then it can prove dangerous to us.
3. Malware Attacks - Some of the difficulties faced during software security are lack of skills to develop advanced security systems, errors in testing all cases while developing the software, and pressure to meet the deadlines.
4. Sensors fitted autonomous- vehicles have a variety of sensors equipped with them that help them detecting vehicles around them, in navigating roads, when to stop for people, animals crossing the pedestrian and generates an alarm, or give any signal if any danger is encountered. Those who have no idea about the roads, about route map, hackers can hack their GPS data and manipulate them accordingly to do the heinous crime. They can control their cars in their own ways and do whatever they want or make the drivers do the same.
5. Network Attack: - Every transmitting and receiving point of data in the network is prone to attack by hackers. For gaining access to the network hackers make use of the malware and APTs threats on the endpoints and the network is subjugated through the Wi-Fi and sometimes even networks of the Local Area Networks (LANs).

2.3 Security issues in health: The utilization of sensors is necessary for developing clinical and medical care advancements. IoT can possibly be coordinated into various medical care administrations and applications. Common medical care information makes patients more secure while likewise putting them in danger.

Medicinal organizations have significant budgetary data. Almost everyone's data is available in some form which can be easily practiced by hackers, and they may threaten them. In current years it is has been seen that many assaults are being notable in their scale and superficial. The first attack discovered by Trend Micro was the MEDJACK attack, affected on blood gas analyzers, mechanized device, magnetic imaging systems, and x-beam machinery. Hackers mostly target infrastructure protocols as well as internet-connected devices. It is also a major concern that there are several flaws found in their system which is easily attacked by hackers that causes a lot of damage.

2.4 Security issues on industries: The advancement of IoT and selection of Manufacturing Internet ventures have allowed experts for security purposes to reduce the chance to assess the new dangers and weaknesses that are being brought into associations anywhere. IoT and network safety meet with various existing security disciplines like information Technology security that prevent information system to the hackers that provide Physical Security to protect buildings, offices, facilities and the like; and Operational Technology (OT) security to protect operating systems for plant computerization and environmental monitoring systems.

2.4.1 Problems: The primary glaring issue is an absence of principles with regards to IoT security highlights. Various merchants and IoT designers are chipping away at expected arrangements, there is definitely not a standard arrangement can be applied to all gadgets and frameworks. The issue is a great extent because of the restricted handling force and capacities of the gadgets; 'conventional' PCs will utilize normalized working frameworks and programming and can be made sure about utilizing attempted and tried techniques, however sensors and other IoT gadgets are not administered by a typical arrangement of programming instruments and applications. This makes sending strong safety efforts more troublesome.

Authorized licensed use limited to: DELHI TECHNICAL UNIV. Downloaded on March 03,2021 at 06:13:45 UTC from IEEE Xplore. Restrictions apply.

2.5 Security issues in logistics: The logistic security issue is expansive in scope influencing both little and huge organizations just as purchasers who at last bear the expense. As per industry specialists, an appropriately conveyed security plan must address and ensure the organization against four basic dangers: robbery, psychological oppression, theft, and physical calamity.

It may seem to bid serious proficiency and occupational opportunity in logistics. There are so many different requests, circumstances, which unavoidably make a huge attack surface. One of the assaults is to control of installed information, either by vindictive replacement of labels or by the change of label data.

Security issues in households, and workplaces: There is a huge choice of gadgets and appliances for the home which have enough information about house members and our lifestyle. While these gadgets and devices offer monetary and practical advancement but expands security hazards as well. The key dangers that these appliances conveys classification and security gadgets/devices like printers, camera, home router, electronic gates are hackable by the hackers and it can be easily misused.

2.6 Cyber threats: As indicated by one industry study, the worldwide IoT security market is anticipated to reach or surpass $35.2 billion (USD) by 2023, a spike of 33.7% dependent on the compound yearly development rate (CAGR). In 2019, SonicWall Capture Labs danger specialists found a moderate 5% expansion in IoT malware, with a complete volume arriving at 34.3 million assaults. Normal IoT security shortcoming incorporates frail or hard-coded passwords, shaky organizations and interfaces, and the absence of secure update instruments and mechanisms.

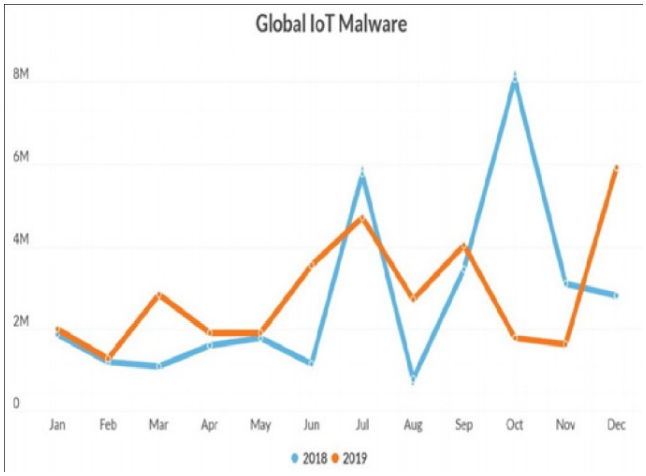

3. Some other types of IoT security threats

1. **Botnets** -hackers can use botnets to hack IoT based devices that are interconnected and internet-connected such as laptops, desktops, and smartphones.
2. **Denial of service** - To disrupt a company or to use that company for their own cause, Denial of Service can be used.
3. **Man-in-the-Middle (**MITM)-Attackers or hackers can seize communications between numerousIoTbased devices, leading to life-threatening device malfunction.
4. **Identity and data theft**- Hackers can attack gadgets like a fitness tracker, Bluetooth earphones, and other essential devices present at house and administrations, to extract confidential and delicate data about the people.
5. **Social engineering**–hackers can gain Personal discernable information that can be illicitly accessed to gain private information like home address, bank details, or any other confidential data.
6. **Ransomware**- Hackers can grant for ransom in form of anything if they disable people's gadgets.

Authorized licensed use limited to: DELHI TECHNICAL UNIV. Downloaded on March 03,2021 at 06:13:45 UTC from IEEE Xplore. Restrictions apply.

3.1 Privacy in the IoT: IoT development is growing rapidly and providing consumer privacy becomes more and more difficult. It is one of the major concerns in IoT. Through IoT, it is possible to access a huge amount of information, not only by customers but to residents of general, assemblies, and groups or society. This can make anyone possible to track anyone without knowing them. As more and more devices are associated through the internet with different devices it increases the data collection which substituent results in less control over data. control of data and control of the different devices that are connected are in danger of hackers. While this can give extraordinary chances to improved administrations, it must be assessed against our craving for protection. Fundamentally, shoppers trust the managements they draw in with to regard their security. The crucial factor in the mounting of any association, and is a vital factor in the reception of the latest innovation. People will not utilize innovation if they don't believe in the protection, safety, security, safety, and welfare and this is especially obvious in complex frameworks, for example, the IoT. Sensors, including those connected to cell phones, gather a variety of information about the daily life of residents. This information will be accumulated, investigated, ready, intertwined, and extracted to extricate helpful data for empowering canny and universal administrations.

4. IoT Privacy Issues

4.1 Access of data

As the devices are connected through the internet there are a lot of data that can be accessible to anyone without our concern, which may be used against us in any form.

4.2 Eavesdropping

In this assault, while the data is communicated between the two hubs over the organization, the intruder tunes in to the data. Here, the data remain the same as before but its protection is undermined. This data can be utilized by the intruders against the clients.

4.3 Undesirable Public Profile

Without knowing the terms and conditions of various apps and software people simply accept them. The FTC report found that fraud companies could use our private information that users are ready to do tasks. For example, any fraud insurance agency may take these data from you without your concern and associated vehicle while tracking your insurance rate.

4.4 Stalking or tracking

Every single move can be traced by UID through IoT devices. Hackers can also determine the current location which proves dangerous to the people.

4.5 Data stealing

Having your gadget stolen is a major problem in itself. If the thief is utilizing your gadget's information to follow up for your sake and mimics your character, at that point you have a much more serious issue within reach. Different gadgets, and conceivably a portion of your own or business contacts, that trust your character, are in danger of succumbing to "your" taken personality. Data fraud can thusly be considered perhaps the greatest danger in the IoT.

5. General Data Protection Regulation (GDPR)

A legitimate system that sets the rules for the various and management of each individual data from people living in European countries is known as GDPR or general data protection regulation. It regulates where the fraud sites are based and which European guest is accessing this site so that guest can be identified regardless of wheatear his/her intentions are doing of fraud or not. The GDPR command that guests regarding various data exposed and their sites were banned.

This regulation takes two years to come into full existence and continuous change in order to improve them.

Authorized licensed use limited to: DELHI TECHNICAL UNIV. Downloaded on March 03,2021 at 06:13:45 UTC from IEEE Xplore. Restrictions apply.

In the study, numerous buyers internationally need the kinds of information about the security rights that EU residents will appreciate when GDPR comes into power. When requested to refer to the most significant rights with respect to outsider utilization of their own data, most of the buyers (57%) most every now and again refer to one side to deletion of their data (otherwise called "the option to be overlooked"), trailed by the rights to protest the utilization of their own information, and to be educated in an way how the information is being utilized.

References

[1] Sandra Khvoynitskaya - blog -The history of the internet of things.

[2] https://consoltech.com/blog/security-threats-healthcare-systems/

[3] Shaun Bligh-Wall – "Industry 4.0: Security imperatives for IoT — converging networks, increasing risks"

[4] Cliff Holste – "supply chain digest"

[5] https://www.businessinsider.com/iot-security-privacy?IR=T

[6] R. H. Weber, "Internet of things – new security and privacy challenges," Computer Law & Security Review, vol. 26, pp. 23-30, 2010

[7] J. F. Wan, H. H. Yan, H. Suo, and F. Li, "Advances in cyber-physical systems research," KSII Transactions on Internet and Information Systems, 2011, 5(11): 1891-1908.[10] C. Ding, L. J. Yang, and M. Wu, "Security architecture and key technologies for IoT/CPS", ZTE Technology Journal, vol. 17, no. 1, Feb. 2011.

[8] Z. H. Hu, "The research of several key question of internet of things," in Proc. of 2011 Int. Conf. on Intelligence Science and Information Engineering, pp. 362-365.

[9] J. F. Wan, H. Suo, H. H. Yan, and J. Q. Liu, "A general test platform for cyber-physical systems: unmanned vehicle with wireless sensor network navigation," in Proc. of 2011 Int. Conf. on Advances in Engineering, Nanjing, China, December, 2011.

[10] J. H. Shi, J. F. Wan, H. H. Yan, and H. Suo, "A survey of cyber-physical systems," in Proc. of the Int. Conf. on Wireless Communications and Signal Processing, Nanjing, China, November, 2011.

[11] M. Bansal and Priya, "Application Layer Protocols for Internet of Healthcare Things (IoHT)." *2020 Fourth International Conference on Inventive Systems and Control (ICISC)*. Coimbatore, India, 2020, pp. 369-376, doi: 10.1109/ICISC47916.2020.9171092.

[12] M. Bansal, Priya, "Performance Comparison of MQTT and CoAP Protocols in Different Simulation Environments". G. Ranganathan, J. Chen, A. Rocha (eds) Inventive Communication and Computational Technologies. Lecture Notes in Networks and Systems, vol. 145, pp. 549-560, Springer, Singapore, https://doi.org/10.1007/978-981-15-7345-3_47

[13] M.Bansal, Priya, "Machine Learning Perspective in VLSI Computer Aided Design at Different Abstraction Levels", 2nd Int. Conf. on Mobile Computing and Sustainable Informatics (ICMCSI 2021), Tribhuvan University, Nepal, 2021.

[14] M.Bansal, A. Goyal, A. Choudhary, "Industrial Internet of Things (IIoT): A Vivid Perspective", 5th Int. Conf. on Inventive Systems and Control (ICISC 2021), India, 2021.

[15] M. Bansal, V. Sirpal, M. K. Choudhary, "Advancing e-Government using Internet of Things", ", 2nd Int. Conf. on Mobile Computing and Sustainable Informatics (ICMCSI 2021), Tribhuvan University, Nepal, 2021.

Authorized licensed use limited to: DELHI TECHNICAL UNIV. Downloaded on March 03,2021 at 06:13:45 UTC from IEEE Xplore. Restrictions apply.

Proceedings of the Sixth International Conference on Inventive Computation Technologies [ICICT 2021]
IEEE Xplore Part Number: CFP21F70-ART; ISBN: 978-1-7281-8501-9

Security in Mobile ADHOC Networks: Survey

Sharat S Kariyannavar
Department of Computer Engineering
Delhi Technological University
Delhi, India
sharat238@gmail.com

Shreyas Thakur
Department of Computer Engineering
Delhi Technological University
Delhi, India
shreyasthakur622@gmail.com

Aastha Maheshwari
Department of Computer Engineering
Delhi Technological University
Delhi, India
aasthamaheswari_phdco2k18@dtu.ac.in

2021 6th International Conference on Inventive Computation Technologies (ICICT) | 978-1-7281-8501-9/21/$31.00 ©2021 IEEE | DOI: 10.1109/ICICT50816.2021.9358611

***Abstract*—Mobile Adhoc Networks (MANETs) are dynamic, flexible, and mobile. While they enjoy several advantages over traditional wireless networks due to these characteristics, their lack of infrastructure leaves them susceptible to a plethora of security threats. To better understand these threats, the traits of MANETs are elucidated and their vulnerable features are brought to light. Subsequently, the paper classifies and differentiates security attacks into various categories on several bases. Here, Data Traffic attacks, which directly affect the information being transmitted over the network, and Control Traffic attacks, which affect the flow of traffic in a network, are the primary focus. Examples of each of these attacks are explained with their functioning. Research work regarding the same have been studied and most effective countermeasures are mentioned. This paper aims to concisely summarize existing excellent research to defog uncertainties regarding the practical implementation of MANETs.**

Keywords—Mobile ADHOC Networks, Routing protocols, Attacks in MANET, Blackhole, Gray Hole, Jellyfish, Worm Hole, Rushing, Sybil attacks, mitigation techniques

I. Introduction

A Mobile Ad-hoc Network (MANET) is a network comprising of nodes that are mobile and are lacking a central node for any message passing. These nodes are also able to intercommunicate without any prior infrastructure needing to be set up. As a result of this feature, communication in this network is done dynamically via temporary paths established between the nodes. If the nodes are in range, communication occurs directly in a single hop, else communication occurs via other nodes that are in range. This is called multiple hopping [1].

Due to communication being wireless and dynamic in MANETs, they enjoy the advantages of flexibility and mobility, but also suffer drawbacks of security and resource consumption [2]. To handle the issues of routing and resource constraints, several routing protocols have been suggested. These are broadly classified into Reactive and Proactive routing protocols. Protocols, such as the Ad-hoc On-Demand Distance Vector protocol (AODV), perform routing only when the need for communication arises. These are called Reactive routing protocols. On the other hand, protocols like the Optimized Link State Routing protocol (OSLR), which performs regular information exchange of node topology to find routes are called Proactive routing protocols.

Due to the lack of central administration in these networks, all the aforementioned routing protocols are dependent on node cooperation. This makes these networks extremely susceptible to hostile or malicious nodes which can invade these networks and cause damage [1].

The widespread use of MANETs is the most significant reason to consider security as the most crucial feature in our discussion. MANETs can be used ubiquitously, some of its applications are[2] diagrammatically represented in fig. 1.

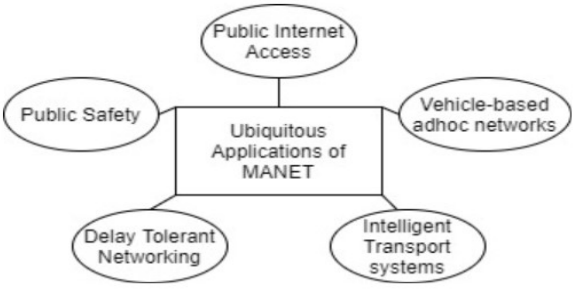

Fig. 1. Applications of MANETs

It is self-explanatory that the compromise of MANETs in these applications can have devastating effects.

As a result, while MANETs offer a plethora of features for communication, it is heavily reliant on security to be considered for practical implementations. The multitude of attacks that can occur need to be studied to provide countermeasures. To tackle security problems, several countermeasures have been devised over the years. These include ARAN [3], SEAD [4], SSL [5], 802.11 WEP [6]. These proposals, however, have been found to be lacking when it comes to dealing with the multitude of attacks a MANET is exposed to. Intrusion Detection Systems (IDS) have also been employed to bolster MANET's defenses. These are introduced to passively supervise the behavior of the nodes in the network in order to identify and discern the presence of any malicious node that might have invaded the MANET [1].

This paper will describe the features of MANETs in detail in section 2. Subsequently, section 3 will differentiate between the different types of MANETs. While there are several types of attacks on MANETs, this paper will only concern itself with two pervasive classes - Data Control Attacks and Control Traffic Attacks. Sections 4 and 5 will describe them, respectively. The paper will conclude with a discussion on the surveyed countermeasures and possible future works and summarize our findings in sections 6 and 7, respectively.

II. Characteristics of MANETs

The development and innovation of infrastructure-less networks have seen a significant rise. Mobile ADHOC Networks (MANET) has become increasingly popular. Any kind of wireless device equipped with a radio transmitter and receiver can be established as a node of the MANET.

Authorized licensed use limited to: DELHI TECHNICAL UNIV. Downloaded on March 03,2021 at 06:01:34 UTC from IEEE Xplore. Restrictions apply.

The focal characteristics of MANETs are as follows[7]:

A. Autonomous and infrastructure-less

Nodes in a MANET do not exist in a pre-defined infrastructure. Each node behaves as an individual router while generating its data. Nodes operate in distributed peer-to-peer mode, implying network management distribution is over different nodes. This makes it prone to fault detection.

B. Decentralized and Distributed

Since none of the nodes are completely reliable, the network control is not in the hands of any single node but allocated equally to several nodes. The MANET will function on cooperation between all the nodes. But, the implementation of a protocol requiring an administrator or centralized authority becomes arduous.

C. Dynamic Network Topology

As there exists no infrastructure or central control to the network nodes have the freedom to move in any direction. Due to this, the network's topology will undergo changes frequently and erratically. The network predominantly comprises of bidirectional links.

D. Limited battery power and Low Bandwidth

The nodes in MANETs do not consist of machines built primarily for the means of mass communication. These nodes lack CPU capability, have low power storage, and smaller memory size. Compared to fixed infrastructure, these nodes have a shorter transmission range and lower capacity.

E. Unsafe Communication

Owing to the fact that MANETs have a shared medium and are unstable rerouting instability and high packet loss rate are a familiar phenomenon that leads to throughput drops in the multi-hop networks. Moreover, in comparison to fixed cable nets, MANETs are more prone to physical security threats. The small dimensions of these nodes increase the ease of theft which leads to unauthorized users gaining access

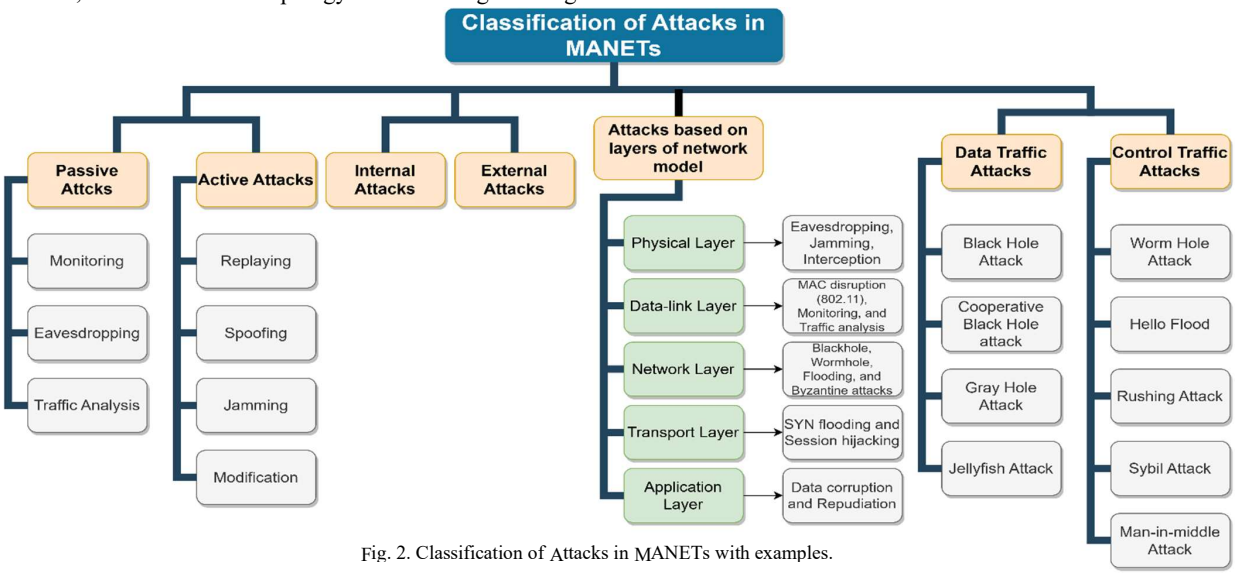

Fig. 2. Classification of Attacks in MANETs with examples.

III. Classification of MANET attacks

Mobile ADHOC Networks can be attacked through several means and for various purposes. The domain of attackers or techniques used is some of the criteria for the classification of MANETs. As depicted above in fig. 2, the following are the most common classifications of attacks in Mobile ADHOC Networks:

- **Passive versus Active attacks:**

  This is an important classification for MANET attacks. A passive attack procures data flowing in the MANET but does not interrupt the communication itself. Meanwhile, active attacks not only obtain data but also involves data interruption, modification, or fabrication, and hence disrupting the MANET itself.

- **Internal versus External attacks:**

  This classification is as the name suggests; internal attacks are those attacks done by nodes already present in the network, whereas external attack is accomplished by nodes existing outside the network. It is important to realize that internal attacks are more malicious as these nodes are privy to private data, and disclose this information.

- **Attacks based on layers of the network model:**

  Different layers of the network model warrant a different approach for attacks. The five layers of the internet being – Physical Layer, Data-link Layer, Network Layer, Transport Layer, and Application Layer. An example of each type of attack is offered in fig. 2.

In this paper, we consider another way of classifying MANET attacks. The two widespread categories are Control Traffic Attacks and Data Traffic Attacks[8]. This assortment is based on their attack goals and common features. When an attacker wantonly tampers routing messages to gain access to the route being used by the MANET, they are carrying out a Control traffic attack. Whereas in Data traffic attacks, it involves data packets being dropped by the nodes it was passing through or delayed by the node. The fig. 2 above shows examples of Data traffic attacks and Control traffic attacks. This paper will only be looking at some of these attacks

Authorized licensed use limited to: DELHI TECHNICAL UNIV. Downloaded on March 03,2021 at 06:01:34 UTC from IEEE Xplore. Restrictions apply.

IV. Data Traffic Attacks

Data Traffic attacks affect the flow of message packets in the network. They have two major means of attacking [4]:

- Dropping of packets: This can be either selective or indiscriminate. Leads to critical loss of data in the network.
- Delaying the transmission of packets: The forwarding of message packets from one node to another is slowed down to hamper network efficiency.

All of these attacks target the Ad-hoc On-demand Distance Vector (AODV) protocol [9]. We will first delve deeper into the vulnerabilities of AODV for a better understanding of future discussions.

Vulnerabilities of AODV Protocol

As mentioned earlier, the AODV protocol is reactive in nature. It provides and maintains transmission routes only when required. While this protocol provides a dynamic network, it also conveniently reduces memory consumption and processing loads. Due to its reactive nature, however, it is not capable of handling security threats [10]. As per the AODV protocol, the crucial information contained in the reply header packets is the hop count and the destination sequence. A higher destination sequence indicates a path that is more recent or "fresh". Attackers are aware of this characteristic and exploit it in different manners under different attacks. Consequently, the network employing AODV will become vulnerable [11].

The AODV consists of two phases [10]:

i. Route Discovery: For data transmission between nodes, the sender first polls its routing table to the receiver for a route. In case a route is available, data is sent through it. Otherwise, the route discovery phase takes place by broadcasting an RREQ to its adjacent nodes, who then check their tables for the requested route. If a route is available, the requested node replies with an RREP, and forward an RREQ to its neighbors if not. This process occurs until a path has been discovered.

ii. Route Maintenance: If the route breaks during transmission, all associated nodes are alerted with an RRER message. After the source node receives the RRER, route discovery restarts.

Now, we will see some examples of Data Traffic Attacks.

A. Black Hole Attack

The black hole attack is one of the more prominent attacks in infrastructure-less systems. The reason for this being its very simple yet effective nature. This attack causes damage by packet drops and information loss in the network, hence it is also called a "packet drop attack".

Going into more detail, the black hole attack is an example of Denial of Service (DOS) attacks. Here, a malicious node baits network traffic by using a higher destination sequence. After the traffic has been successfully directed towards the malicious node, the node simply drops all packets it has received.

To combat this attack, the mechanism of the malicious node baiting to traffic needs to be made clear. During route discovery, the malicious node can attract the traffic either proactively or reactively [12]. Proactively, the attacker continuously sends RREP messages to each node in the network with a low minimum hop count followed by a high destination sequence. Reactively, the attacker replies with the false information in the RREP only when it receives an RREQ. Fig. 3 illustrates an example case of black hole attacks.

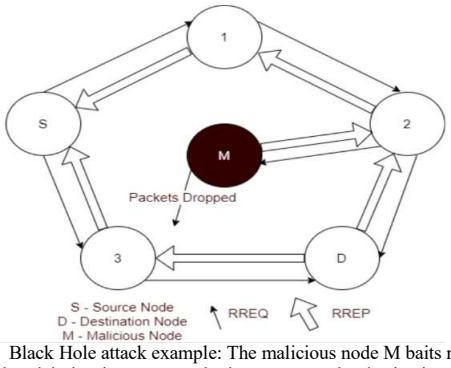

Fig. 3. Black Hole attack example: The malicious node M baits network traffic by claiming it possesses the best route to the destination node D and then drops the packets.

Proposed methods for black hole attack mitigation:

i. Collection of multiple RREP messages. This can result in the discovery of redundant paths to the destination. Consequently, the packets can then be buffered to locate a safe route [4].

ii. AODV based secure routing. A validity value is attached to RREP messages which are stockpiled in the routing table of every participating node in the currently active route. Whenever a node receives an RREQ, the RREP will be generated using the validity bit and sent back. If the validity bit matches the one present in the requester's routing table, the route is safe [10].

iii. Detecting the black hole attack based on DSR, in short, the DBA-DSR scheme. As per this scheme, before the actual AODV protocol is executed, scouting RREQ packets are transmitted across the network. This can allow the network to detect attacker nodes and consequently avoid them [13].

B. Gray Hole Attack

A more specific case of the black hole attack is the gray hole attack. Once again, the attacking node pretends to be harmless in the network and attracts data traffic using false claims, only to drop the diverted traffic. The factor that differentiates the two is that the Gray Hole drops only selective data packets with a certain fixed probability distribution, and on the other hand the black hole attack is indiscriminate [14][15].

The reason for discussion for the gray hole attack is that gray hole attacks have varied executions [14][15]:

- They can selectively drop packets only from (or to) a specific node. This is also called the Sequence Number Gray hole attack.
- They can show normal behavior during route discovery to avoid detection, and then cause damage during transmission. This is also called the Smart Gray hole attack.
- They can also have a hybrid execution of the above two variations to make detection even more difficult.

Authorized licensed use limited to: DELHI TECHNICAL UNIV. Downloaded on March 03,2021 at 06:01:34 UTC from IEEE Xplore. Restrictions apply.

Consequently, Gray hole attacks are more difficult to detect, handle, and mitigate. Fig. 4 and Fig. 5 show Sequence Number and Smart Gray Hole attacks respectively.

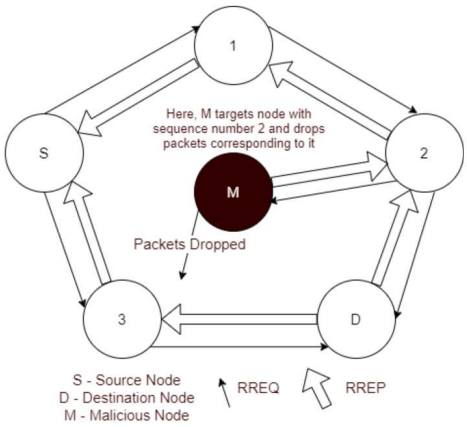

Fig. 4. An example of a Sequence Number gray hole attack

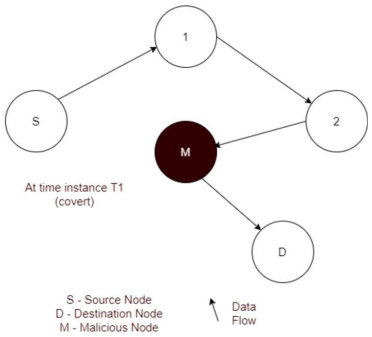

Fig. 5(a). An example of a Smart Gray hole attack

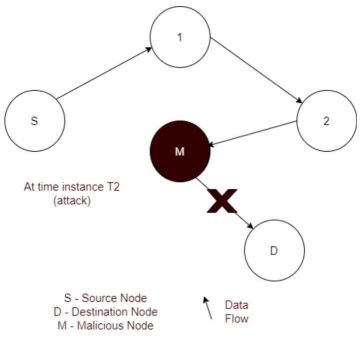

Fig. 5(b). An example of a Smart Gray hole attack

Although there have not been immensely successful measures against Gray hole attacks, some of the proposed methods for Gray hole mitigation are:

i. Implementation of an Association Based- Data Routing Information (AB-DRI) table [12]. An example of the AB-DRI table is shown in table 1.

Table 1. An example of an AB-DRI table

Node Address	Starting From	Through	Status	Value of Threshold	Level of Trust
4	1	0	K	0.4-0.6	Medium
M	0	0	UN	0.0-0.3	Very Low
D	1	1	C	0.7-1.0	High
3	0	1	W	Inhibition mode	Low

As per this table, a degree of "trust" is associated with each node to help detect malicious nodes.

ii. Implementation of Mitigation Gray hole Attack Mechanism (MGAM) via Gray hole intrusion detection systems (G-IDS). G-IDS nodes listen in on the transmission of packets in neighboring nodes and alert the network regarding packet drop if the packet count drops below a threshold value [14].

C. *Jellyfish Attack*

Jellyfish (JF) attack is another example of a Denial of Service (DOS) attack. This passive attack slows down effective packet transmission, resulting in higher end-to-end delays and reduced network efficiency [16][17].

Targets for JF attacks are closed-loop flows. Some common implementations are delayed file transfers, lagging video streams, and TCP (Transfer Control Protocol) desynchronization [16].

The mechanism of delay cause forms the basis of classification for three types of JF attacks:

- JellyFish Reorder Attack: The attack creates a buffer that reorders a select number of packets and then retransmits it to the rest of the network. This causes confusion and congestion [16]. Fig. 6 illustrates a JF Recorder attack.

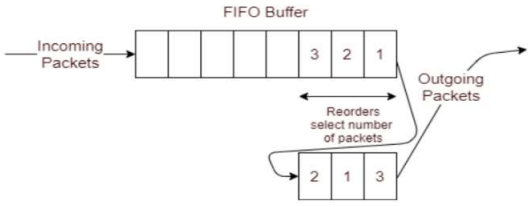

Fig. 6. An example of a JF Reorder attack

- JellyFish Periodic Dropping Attack: The JF discards a few packets regularly to send the source of the packets into a timeout. To deal with this, the TCP network enters

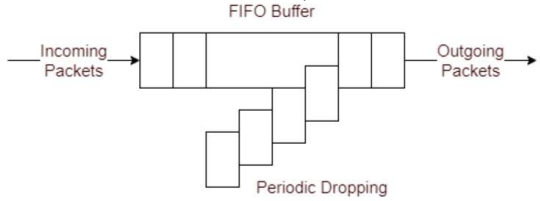

a congested state where packet transmission is highly inefficient. Once the network stabilizes, the JF discards packets to restart a similar situation [17]. Fig. 7 illustrates this attack.

Authorized licensed use limited to: DELHI TECHNICAL UNIV. Downloaded on March 03,2021 at 06:01:34 UTC from IEEE Xplore. Restrictions apply.

- JellyFish Delay Variance Attack: The affected node retransmits data after some random delays. This causes more traffic in the network and more packet collisions [16][17]. This attack is schematically represented in Fig. 8.

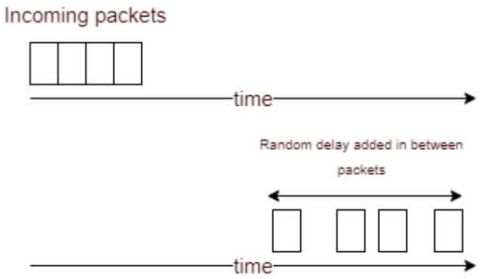

Fig. 8. An example of JF Delay Variance Attack

JF attacks are also very deceptive because they comply with all protocol rules. Consequently, the detection and mitigation of these attacks are very expensive and difficult. Some proposed methods are:

i. Credit based systems. Usage of tokens to incentivize successful transmissions [4].
ii. By considering the time taken for transmission and reception of a packet, an allotted threshold time and network load [16]. If a delay is detected, the network load is checked. Exceeding the predefined load threshold would imply mere congestion, else it is a JF attack.
iii. Accurate Prevention and Detection of Jellyfish Attack (APD-JFA) [17]. This employs a hierarchical system of trust in the network and transmission is carried out via trusted nodes only. Support Vector machines are utilized to learn packet forwarding behavior. Fig. 9 is a flow diagram for the APD-JFA.

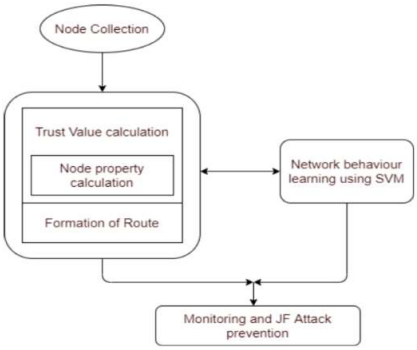

Fig. 9. Mechanism of APD-JFA

V. Control Traffic Attack

The fundamental feature of a MANET leaves it inherently impuissant to attacks. Each routing protocol conceived for MANETs has its unique rules and procedure. Dynamic MANET on-demand(DYMO) and Ad-Hoc On-Demand Distance Vector routing protocol (AODV) are the two most commonly used protocols[8]. When establishing a viable routing table AODV counts on the cooperation of each node. For fast multi-hop networks, DYMO is used. But both these protocols rely on trust, that nodes joining the network are not malicious. On the contrary, accessing the network through a node is the first step in carrying out an attack. As MANETs have no restrictions on nodes connecting to the network, malicious nodes are able to easily join the network and orchestrate the attack. These attacks range from overturning valid routes to eavesdropping on the network.

In this section, the attacks discussed will be – Worm Hole Attack, Rushing attack, Sybil attack.

A. Worm Hole Attack

When a malicious node only eavesdrops on the data being sent across the network it is said to be carrying out a passive attack. Whereas active attacks may drop, imitate, or modify the data. The severity of such attacks increases if nodes of the network are complicit in the act. An example of such a cooperative attack is the Wormhole attack.

In a Worm Hole attack, multiple malignant nodes generate a private channel called a tunnel between them [18]. These hostile nodes create a shortcut path for connection in the topology. Now, the hostile nodes on receives a routing request will provide the network with a shorter route with lesser hops. The packet then reaches the destination with lesser hops. Here the attackers can not only obtain the data being transmitted but can also disable network performance.

As shown in fig. 10, the number of hops between the destination and the source is generally five. But on the creation of the tunnel between nodes 1 and 2, the number of hops reduces to three. This reduction in the number of hops encourages the network to choose the new path leaving the data passing through vulnerable.

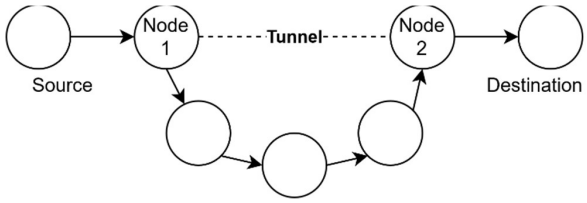

Fig. 10. Working of a Worm Hole attack

It is very easy to establish a tunnel required to carry out a Wormhole attack. The two nodes need to be connected via a Wormhole link, which is a high-speed off-channel link. This connection is usually set up by using a wired technology or a wireless transmission [18].

The Proposed Worm Hole mitigation methods are:

i. Ref [19] has classified detection algorithms into 4 categories – Nearest route based, range-based, geographical location-based, and position-based. These algorithms commonly use route length for determining neighboring nodes.
   - In the Nearest route-based algorithm, the distance between the sensor nodes is used. Here, a threshold is established, and if the distance between neighboring nodes exceeds this threshold the connection is not established.
   - In the Range-based algorithm, a message is first sent through all the nodes to recognize every node's neighbors. Then the K-means algorithm is applied to cluster similar nodes and detect attacking nodes.

Authorized licensed use limited to: DELHI TECHNICAL UNIV. Downloaded on March 03,2021 at 06:01:34 UTC from IEEE Xplore. Restrictions apply.

- The proposed Geographical location-based uses the *Dijkstra* Algorithm to determine the shortest path for sending packets. The path is established using geographical distances between nodes.
- In the Position-based algorithm, the Secure DV-Hop Localization [20] scheme developed upon the DV-Hop model is utilized. Here, the nodes covey their spatial information to the network to calculate the mean distance between two sections or the mean step-length. Nodes will detect the distance to other nodes by acquiring the mean value of the distance. This estimation is then used to calculate its position.

ii. The model presented in Ref [21] carries out the detection of Wormholes by having every connected node in the network measure the trustworthiness and accuracy of its neighboring nodes. Meanwhile, for Wormhole evasion, the Dynamic Source Routing (DSR) is used. Before launching a new route, the DSR cache is scanned to determine an already working route. If no route is present, to determine the shortest route *Dijkstra* algorithm is used. Here the cost of each connection is replaced by the node's trust level, hence the algorithm establishes the route with the maximum trust.

iii. Ref [22] proposes a technique based on the scrutiny of the misbehaving nodes. The model focuses on the detection of misbehaving nodes and preventing these nodes from being part of a transmission route. Here, the DSR protocol is modified with this new functionality. On detecting a malignant node, the routes that contain said node is dropped and the node is not added to the table of DSR to prevent the node from being used again.

B. *Rushing Attack*

Before transmitting data, each sender first determines a valid route to the target. A Route Request (RREQ) message is relayed by the sender which receives Router Replies (RREP) that supply route information[7]. If an attacker is present in the system and receives this RREQ, then this node will use a neighbor with a faster transmission speed to send the confirmation to the destination. On receiving this, the destination node will discard any other routes that come later. On finding this valid route, the receiver will use it for further communication, hence giving access to the attacker. attack.

This is only possible in those networks that use protocols that utilize duplicate suppression mechanism. This mechanism limits the reply chatter and route request in the network. Exploiting this mechanism, the attacker node sends the packet after accessing the data sent, hence delaying the message.

Below, fig. 11 depicts a Rushing attack. The attacker node can establish a quicker route to the destination. Therefore, the legitimate RREQs will not reach the destination node before that of the attackers.

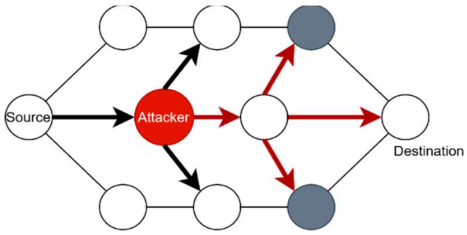

Fig. 11. Working of a Rushing attack

Some proposed Rushing attack mitigation techniques are:

i. Ref [23] suggests discovering a secure neighbor and a secure route. Any on-demand protocol carries out secure neighbor detection, but in this process, the attacker still manages to get the request which is then forwarded to the destination. Whereas, in the secure route discovery technique, a route is selected at random. Here the destination node compiles all the incoming requests and chooses a random one before forwarding it. In case of a large number of requests, a timeout is set based on the geographical locations of the sender and receiver. A threshold of time is also suggested by the authors. Here, a threshold is set within which the requests that arrive earlier than this are not accepted.

ii. The technique proposed in Ref [24] suggests using three special packets to prevent rushing attacks –

- Route Check (RCHE) packet –The round trip time (RTT) for the currently selected route is evaluated using this packet.
- Route Verify (RVER) packet – These check if the previously calculated RTT is valid and does not fluctuate.
- Route Failure (RFAI) packet – This packet is used when one of the nodes in the route fails.

The technique also utilizes the "neighbor map mechanism", where the source node has a neighbor map that maps the nodes in the network. In this table, each row is a distinct node.

iii. Ref [25] proposes a modification to DSR – Secured Dynamic Source Routing (SDSR). The property of discarding the requests after receiving the first one is changed. Every node doesn't forward the first request it receives and instead waits for a predetermined amount of time which is proportionate to the distance between the source and the current node. Then the node forwards a randomly selected request. Ref [26] proposes that only event nodes carry out this action. On receiving the request, the nodes check for chain number. If it is equal to the event node's number the algorithm is applied. If not then the request is forwarded and consequent requests are discarded. This reduces the time to execute SDSR by half.

C. *Sybil Attack*

Shirley Ardell Mason was an American art teacher who was reputed to have dissociative identity disorder. Similarly, the Sybil attacks in MANETs manifest themselves by faking multiple identities, meaning one single node pretends to be multiple nodes in the

Authorized licensed use limited to: DELHI TECHNICAL UNIV. Downloaded on March 03,2021 at 06:01:34 UTC from IEEE Xplore. Restrictions apply.

network[7]. This way this single node can hamper and monitor multiple nodes simultaneously.

Fig. 12 demonstrates the Sybil attack. The Sybil nodes create a network of their own and try to attack a node of the network. The nearest honest node is targeted. Without any prevention mechanisms or security, the Sybil node will replace the honest node, and gain access to the network. Multiple Adhoc network protocols are vulnerable to Sybil attack. Spammers use it to gain access to multiple accounts concurrently.

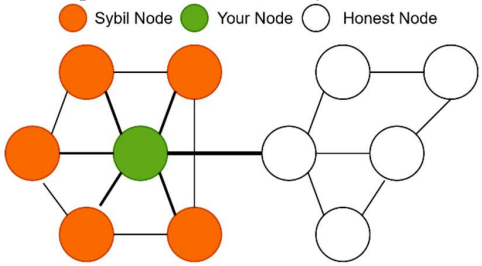

Fig. 12. Working of a Sybil attack

Few detection techniques proposed are [7]:

- Trusted Certification – This method relies on a centralized authority that can provide the guarantee that only one identity will be assigned to any node. This procedure is costly as it needs to be done manually and offers no method to assure uniqueness.
- Resource Testing – Here the network checks the number of physical entities held by each node. This value is corroborated using the value that an individual node would have. The entities checked include – computing power, storage ability, and network bandwidth.
- Random key distribution – To communicate with each other, randomly a key set is assigned to a node permitting it to compute and share common keys with its neighbors. This common key assures safe and secure communication between nodes. The fake Sybil node is found by carrying out a Validation test, where the network confirms whether the key is a valid one that belongs to an identity. The random key will most likely not have a valuable intersection with the set of compromised keys. Because of this, the fake Sybil node will not pass the validation test.

VI. Discussion

The following table 2 summarizes the countermeasures detailed in the paper and adds our remarks on the same. The table details the working principle of the countermeasures developed.

Table 2. Summary of Countermeasures proposed in the papers surveyed.

Name of Attack	Countermeasure	Working Principle	Remarks
Data Traffic Attacks			
Black Hole Attack	Collection of multiple RREP messages [4] Discovery of redundant paths to the destination.		As a result, the packets can then be buffered to locate a safe route. Computationally intensive.
	AODV based secure routing [16]	A validity value is attached to RREP messages which are stockpiled in the routing table of every participating node in the currently active route.	If the validity bit in the sender's routing table matches the one present in the requester's routing table, the route is safe. Relatively simple to implement, may cause delays in highly congested systems.
	Detecting the black hole attack based on DSR (DBA-DSR scheme) [19]	Before the actual AODV protocol is executed, scouting RREQ packets are transmitted across the network.	This can allow the network to detect attacker nodes and consequently avoid them. If the route discovered is in use for a long period of time, the initial procedure is worth the delay, else not for several short-lived routes.
Gray Hole Attack	Implementation of an Association Based- Data Routing Information (AB-DRI) table [12]	A table with columns node address, whether a route starts from it (0/1), whether a route passes through it (0/1), node status, and an associated threshold value is referred. Based on the column values, a "degree of trust" is associated with each node.	Both methods of trust and vigilance are not flexible enough to account for the more flexible temporal nature of hybrid Gray hole attacks. More research is needed on this subject.
	Implementation of Mitigation Gray hole Attack Mechanism (MGAM) via Gray hole intrusion detection systems (G-IDS) [20]	G-IDS nodes listen in on the transmission of packets in neighbouring nodes and alert the network regarding packet drop if the packet count drops below a threshold value.	
Jellyfish Attack	Credit based systems [4]	Usage of tokens to incentivize successful transmissions.	Requires a threshold system for throughput to understand when a transmission is successful.
	Allotted threshold time and network load [22]	Time taken for transmission and reception of message packet is considered. If a delay is detected, the network load is checked. Exceeding the predefined load threshold would imply mere congestion, else it is a JF attack.	Can detect an attack only after the fact. Improvement can be made to implement this with dummy messages prior to actual route discovery and transmission.

Authorized licensed use limited to: DELHI TECHNICAL UNIV. Downloaded on March 03,2021 at 06:01:34 UTC from IEEE Xplore. Restrictions apply.

	Accurate Prevention and Detection of Jellyfish Attack (APD-JFA) [17]	Employs a hierarchical system of trust in the network and transmission is carried out via trusted nodes only. Support Vector Machines are utilized to learn packet forwarding behavior.	While strict and effective, also limits the full capability of the network. The trade-off between "trust" and "network efficiency" must be balanced.
Control Traffic Attacks			
Worm Hole Attack	Ref[19] proposes 4 detection algorithms - Nearest Route based, Range-based, Geographical Location-based, and Position-based. These algorithms are mostly based on the route length.		The geographical location can be an important factor in determining the validity of nodes. The paper uses this well to detect unsavory nodes.
	Modification to Dynamic Source Routing(DSR) [21]	Dijkstra Algorithm is used when there is no pre-existing route. The cost of each connection is replaced by trust level.	The trustworthiness and accuracy of each neighboring node are measured.
	The model proposed by Ref [22] focuses on the detection of misbehaving nodes and preventing these nodes from being part of a transmission route. DSR has been modified accordingly.		On detecting a malignant node, the routes that containing the node are dropped and the node is removed from the DSR table to prevent it from being used.
Rushing Attack	Secure Route discovery technique[23]	Here the destination node compiles all the incoming requests and chooses a random one before forwarding it.	A threshold time is set within which the requests that arrive earlier than this are not accepted.
	3 Special Packets used [24]	Packets track Round Trip Time (RTT), the fluctuation in RTT, and failure of route.	The technique also utilizes the "neighbor map mechanism", where the source node has a neighbor map that maps the nodes in the network.
	Secured Dynamic Source Routing (SDSR) [25]	Every node doesn't forward the first request it receives and instead waits for a predetermined amount of time which is proportionate to the distance between the source and the current node. Then the node forwards a randomly selected request.	Only specific nodes known as event nodes carry out this action.
Sybil Attack [7]	Trusted Certification	The centralized authority provides the guarantee that only one identity will be assigned to any node.	This procedure is costly as it needs to be done manually and offers no method to assure uniqueness.
	Resource Testing	The network checks the number of physical entities held by each node. This value is corroborated using the value that an individual node would have.	The node could easily transmit false data about its capabilities to the network.
	Random Key Distribution	The fake Sybil node is found by carrying out a Validation test. In this test, the network confirms whether the key assigned is a valid one that belongs to an identity.	The fake Sybil node will not pass the validation test because the random key will most likely not have a valuable intersection with the set of compromised keys.

VII. Future Works and Conclusion

The fundamental characteristics of a MANET leave it inherently vulnerable to attacks. Each routing protocol conceived for MANETs has its unique rules which can be exploited by various types of attacks. This paper has discussed two broad classifications of such attacks – Data Traffic attacks and Control Traffic attacks.

The instances of Data Traffic attacks studied were the Black Hole attacks, Gray Hole attacks, and Jellyfish attacks. These attacks are observed to be associated with the complete or partial dropping of packets, or the hampering of network throughput. The common trend in the countermeasures suggested were improvised versions of the AODV protocol utilizing a trust-based or token-based system.

Control Traffic attacks involve unauthorized access to the network to either observe or manipulate the data being communicated. The Worm Hole attack utilizes a shorter route between the sender and destination to achieve its goal, whereas in the Rushing attack the sender node is misinformed about a viable path. A Sybil attack involves legitimate nodes being replaced by Sybil nodes. These situations arise due to faults in the on-demand protocols being used in the networks. As seen, several new criteria have been proposed to these protocols to combat said attacks.

Our goal with this survey is to aid fellow researchers in laying down a solid groundwork as a starting point for new and improved research on this matter. As seen, countermeasures to attacks like the Gray Hole attack and Sybil attacks leave much to be desired. This paper hopes it has given researchers a head start on the matter. Models based on Machine Learning can be used to enhance the environment of MANETs[27]. It is also possible to use block chain trust verification as used in fly wireless networks[28]. This helps to avoid vulnerabilities in the communication route and supplementing the network's capabilities. Researchers can use this paper to understand the existing models and strive to improve and innovate with their ideas.

References

[1] B. Kannhavong, H. Nakayama, Y. Nemoto, N. Kato, and A. Jamalipour, "A survey of routing attacks in mobile ad hoc networks," *IEEE Wirel. Commun.*, vol. 14, no. 5, pp. 85–91, 2007, doi: 10.1109/MWC.2007.4396947.

[2] V. Shanmuganathan and M. E. T.Anand, "A Survey on Gray Hole Attack in MANET," *Int. J. Comput. Networks Wirel. Commun.*, vol. 2, no. 6, pp. 647–650, 2012.

[3] F. Fu, J. Liu, and J. M. Xiao, "Secure routing protocol

Authorized licensed use limited to: DELHI TECHNICAL UNIV. Downloaded on March 03,2021 at 06:01:34 UTC from IEEE Xplore. Restrictions apply.

for Ad hoc networks," *Dianzi Keji Daxue Xuebao/Journal Univ. Electron. Sci. Technol. China*, vol. 38, no. 3, pp. 389–392, 2009, doi: 10.3969/j.issn.1001-0548.2009.03.017.

[4] Y. C. Hu, D. B. Johnson, and A. Perrig, "SEAD: Secure efficient distance vector routing for mobile wireless ad hoc networks," *Proc. - 4th IEEE Work. Mob. Comput. Syst. Appl. WMCSA 2002*, pp. 3–13, 2002, doi: 10.1109/MCSA.2002.1017480.

[5] M. S. C. Kaufman and R. Perlman, in *Network Security Private Communication in a Public World*, 2002.

[6] "A STUDY OF DIFFERENT TYPES OF ATTACKS IN MOBILE AD HOC NETWORKS Hoang Lan Nguyen , Uyen Trang Nguyen Department of Computer Science and Engineering," pp. 2–7, 2012.

[7] S. K. Chowdhury and M. Sen, "Attacks and mitigation techniques on mobile ad hoc network -A survey," *Proc. - Int. Conf. Trends Electron. Informatics, ICEI 2017*, vol. 2018-Janua, no. July 2018, pp. 11–18, 2018, doi: 10.1109/ICOEI.2017.8300907.

[8] A. Bhattacharyya, A. Banerjee, D. Bose, H. N. Saha, and D. Bhattacharjee, "Different types of attacks in Mobile ADHOC Network: prevention and mitigation techniques," *Dep. Comput. Sci. Eng. Inst. Eng. Manag. Saltlake*, vol. 1, no. 1, 2011.

[9] C. Panos, C. Ntantogian, S. Malliaros, and C. Xenakis, "Analyzing, quantifying, and detecting the blackhole attack in infrastructure-less networks," *Comput. Networks*, vol. 113, pp. 94–110, 2017, doi: 10.1016/j.comnet.2016.12.006.

[10] S. R. Deshmukh, P. N. Chatur, and N. B. Bhople, "AODV-Based secure routing against blackhole attack in MANET," *2016 IEEE Int. Conf. Recent Trends Electron. Inf. Commun. Technol. RTEICT 2016 - Proc.*, pp. 1960–1964, 2017, doi: 10.1109/RTEICT.2016.7808179.

[11] S. Gurung and S. Chauhan, *A survey of black-hole attack mitigation techniques in MANET: merits, drawbacks, and suitability*, vol. 26, no. 3. Springer US, 2020.

[12] M. Jeevamaheswari, R. Anandha Jothi, and V. Palanisamy, "AODV Routing Protocol to Defence Against Packet Dropping Gray Hole Attack In MANET," vol. 4, 2018.

[13] I. Woungang, S. K. Dhurandher, M. S. Obaidat, and R. D. Peddi, "A DSR-based routing protocol for mitigating blackhole attacks on mobile ad hoc networks," *Secur. Commun. Networks*, vol. 9, no. 5, pp. 420–428, 2016, doi: 10.1002/sec.766.

[14] S. Gurung and S. Chauhan, "A novel approach for mitigating gray hole attack in MANET," *Wirel. Networks*, vol. 24, no. 2, pp. 565–579, 2018, doi: 10.1007/s11276-016-1353-5.

[15] J. Sen, M. Girish Chandra, S. G. Harihara, H. Reddy, and P. Balamuralidhar, "A mechanism for detection of gray hole attack in mobile ad hoc networks," *2007 6th Int. Conf. Information, Commun. Signal Process. ICICS*, pp. 0–4, 2007, doi: 10.1109/ICICS.2007.4449664.

[16] B. Patel Pooja, M. Patel Manish, and B. Patel Megha, "Jellyfish attack detection and prevention in MANET," *Proc. 2017 3rd IEEE Int. Conf. Sensing, Signal Process. Secur. ICSSS 2017*, pp. 54–60, 2017, doi: 10.1109/SSPS.2017.8071564.

[17] S. Doss *et al.*, "APD-JFAD: Accurate prevention and detection of jelly fish attack in MANET," *IEEE Access*, vol. 6, no. c, pp. 56954–56965, 2018, doi: 10.1109/ACCESS.2018.2868544.

[18] P. K. Sharma and V. Sharma, "Survey on security issues in MANET: Wormhole detection and prevention," in *2016 International Conference on Computing, Communication and Automation (ICCCA)*, Apr. 2016, pp. 637–640, doi: 10.1109/CCAA.2016.7813799.

[19] G. Farjamnia, Y. Gasimov, and C. Kazimov, "Review of the Techniques Against the Wormhole Attacks on Wireless Sensor Networks," *Wirel. Pers. Commun.*, vol. 105, no. 4, pp. 1561–1584, 2019, doi: 10.1007/s11277-019-06160-0.

[20] H. Chen, W. Lou, Z. Wang, J. Wu, Z. Wang, and A. Xi, "Securing DV-Hop localization against wormhole attacks in wireless sensor networks," *Pervasive Mob. Comput.*, vol. 16, no. PA, pp. 22–35, 2015, doi: 10.1016/j.pmcj.2014.01.007.

[21] S. Jain and S. Jain, "Detection and Prevention of Wormhole Attack in Mobile Adhoc Networks," *Int. J. Comput. Theory Eng.*, vol. 2, no. 1, pp. 78–86, 2009, doi: 10.7763/ijcte.2010.v2.120.

[22] Y. Singh, A. Khatkar, P. Rani, Deepika, and D. D. Barak, "Wormhole attack avoidance technique in mobile Adhoc networks," *Int. Conf. Adv. Comput. Commun. Technol. ACCT*, pp. 283–287, 2013, doi: 10.1109/ACCT.2013.68.

[23] S. K. Upadhayay, V. Mainanwal, and M. S. Kinra, "Detection & Prevention of Rushing Attack in Wireless Ad-hoc Network : A Survey," vol. 2, no. 7, pp. 3230–3233, 2015.

[24] H. Kim, R. De Oliveira, B. Bhargava, and J. Song, "A novel robust routing scheme against rushing attacks in wireless ad hoc networks," *Wirel. Pers. Commun.*, vol. 70, no. 4, pp. 1339–1351, 2013, doi: 10.1007/s11277-012-0751-y.

[25] L. Tamilselvan and V. Sankaranarayanan, "Solution to prevent rushing attack in wireless mobile ad hoc networks," *ISAHUC' 06 - Proc. 2006 Int. Symp. Ad Hoc Ubiquitous Comput.*, pp. 42–47, 2006, doi: 10.1109/ISAHUC.2006.4290645.

[26] A. S. Al Shahrani, "Rushing attack in mobile ad hoc networks," *Proc. - 3rd IEEE Int. Conf. Intell. Netw. Collab. Syst. INCoS 2011*, pp. 752–758, 2011, doi: 10.1109/INCoS.2011.145.

[27] D. Baraneetharan, "Role of Machine Learning Algorithms Intrusion Detection in WSNs: A Survey," *J. Inf. Technol. Digit. World*, vol. 02, pp. 161–173, 2020, doi: 10.36548/jitdw.2020.3.004.

[28] B. Natarajan, "QOS AND DEFENSE ENHANCEMENT USING BLOCK CHAIN FOR FLY WIRELESS NETWORKS," *J. Trends Comput. Sci. Smart Technol.*, vol. 01, pp. 1–13, 2019, doi: 10.36548/jtcsst.2019.1.001.

Authorized licensed use limited to: DELHI TECHNICAL UNIV. Downloaded on March 03,2021 at 06:01:34 UTC from IEEE Xplore. Restrictions apply.

Nature Environment and Pollution Technology
An International Quarterly Scientific Journal

p-ISSN: 0972-6268
(Print copies up to 2016)
e-ISSN: 2395-3454

Vol. 20 | No. 1 | pp.93-103 | 2021

Original Research Paper

https://doi.org/10.46488/NEPT.2021.v20i01.010

Open Access Journal

SEM-EDAX analysis of the Soil Samples of River Yamuna in Delhi Region

Vivek Chopra* and Jai Gopal Sharma†**
*Department of Botany, Hindu College, University of Delhi, Delhi-110007 India
**Department of Biotechnology, Delhi Technological University, Delhi-110042, India
†Corresponding author: Jai Gopal Sharma; sharmajaigopal@gmail.com

Nat. Env. & Poll. Tech.
Website: www.neptjournal.com

Received: 24-03-2020
Revised: 27-04-2020
Accepted: 27-05-2020

Key Words:
SEM-EDAX
River Yamuna
Soil analysis
Niobium
Aluminium

ABSTRACT

A total of 18 samples were collected from two different sites at different depths of Yamuna river bed in Delhi. Nine samples were collected at Site A (Palla Village) from three different locations at different depths of the river bed. A similar set of 9 samples were collected from Site B (Okhla barrage). All samples were analysed for atomic and weight percentage of elements using SEM-EDAX. The major elements found in the study were Si, O, Al and Nb. Si and O are found in a maximum amount in all the samples with a varying range of atomic percentage 25.3-89.27 and 55.09-95.78 respectively. The recorded atomic percentage of Nb was 0.32 while Al was 16.7-25.51. Site A, Palla is least affected by pollution while at Site B the presence of Al revealed contamination from pollutants. The weight percentage of the elements has also been calculated. SEM images of soil samples revealed the platy flakes, irregular and spongy structure of soil particles.

INTRODUCTION

The River Yamuna is the longest and second largest tributary of river Ganga. Originating from the Yamunotri glaciers at a height of 6,387 M on the uppermost region of the lower Himalayas in Uttarakhand. Its 48 km stretch which passes from Delhi is a major source of drinking and potable water for the 70% population of Delhi (CPCB 2006). It shows the importance of river Yamuna as a major source of water and an indispensable part of the ecosystem. Many studies explain about the water quality of the river but hardly any are available about soil elemental composition. The present study reveals the atomic and weight percentage of different elements as well as some physical properties of soil samples collected from different depths of the river bed. The important elements observed in the following study are Silica (Si), Oxygen (O), Aluminium (Al) and Niobium (Nb). The aim of the study is to reveal the concentration of the elements at different depths of the river bed using SEM-EDAX techniques to enhance our knowledge about the physicochemical nature of the alluvial deposits in the river bed.

MATERIALS AND METHODS

A total of 18 samples were collected from two different sites (Fig. 1) of river Yamuna in March 2019. Site A (28°85'61.7"N; 77°20'80.2"E) was located at Palla village which is the point where River Yamuna enters in Delhi. Site

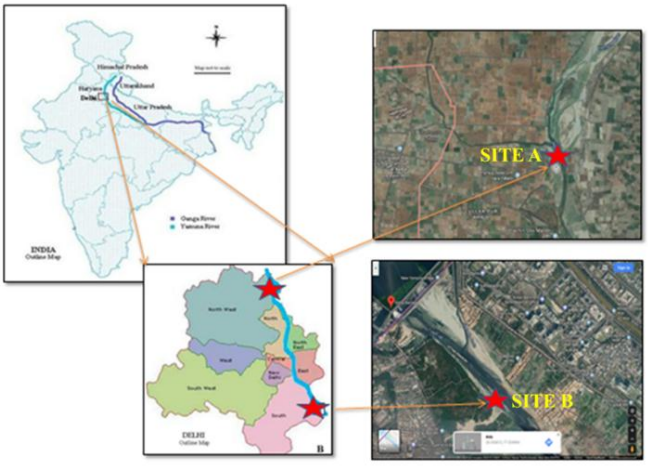

Fig. 1: Location of Site A (Palla village) and Site B (Okhla barrage) in Delhi.

A is comparatively free from pollutants and other anthropogenic activities beside agriculture in the vicinity. Multiple samples were collected to yield a better and authentic interpretation of results. Nine samples were collected from 3 different locations of Site A.

At location 1, the samples were taken from the surface (0-2 cm) and at the depth of 30-32 cm and 78-80 cm of the river bed. From location 2 and location 3, samples were taken from the surface (0-2 cm), 30-32 cm and 74-76 cm and 0-2 cm, 26-28 cm and 59-61 cm respectively. The

same set of sampling was done at Site B, i.e. Okhla barrage (28°32'10.5"N, 77°19'29.6"E) with 9 samples in total from three different locations at the surface (0-2 cm) and at various depths of 30-32 cm and 96-98 cm from location 4 and from location 5 and 6 at the surface (0-2 cm), 30-32 cm and 62-64 cm and 0-2 cm, 30-32 cm and 62-64 cm respectively. Site B is one of the most polluted stretches of river Yamuna where it receives a heavy load of industrial effluents and household sewage discharge from many major drains. Geographical locations were taken by Garmin GPSMAP 76 CSX global positioning system. Five-10 mg subsamples were homogenized, sun-dried and sieved out to remove excess unwanted debris, later the samples were dried in an oven at 60ºC for three days to remove moisture completely (Das & Mondal 2011, Tan 2005). Dried samples were mounted and microstructure was analysed using Scanning Electron Microscope model Zeiss EVO 18 research. The elemental composition was determined by an Energy Dispersive X-ray Spectroscopy (EDAX) attached to SEM.

RESULTS AND DISCUSSION

In all the 18 samples, EDAX analysis was performed to study the elements present in the soil. Si, O, Nb, and Al

Table 1: Elements Atomic % of three locations at Site A (Palla Village).

Elements	Depths at Location 1			Depths at Location 2			Depths at Location 3		
	0-2 cm	30-32 cm	78-80 cm	0-2 cm	30-32 cm	74-76 cm	0-2 cm	26-28 cm	59-61 cm
	Atomic %								
Oxygen (O)	57.78	0	55.09	0	58.92	95.35	0	0	91.84
Silicon (Si)	36.78	83.85	38.69	89.27	35.49	0	79.82	81.94	0
Niobium (Nb)	0.32	0	0	0	0	0	0	0	0
Aluminium (Al)	0	0	0	0	0	0	0	0	0

Table 2: Elements Weight % of three locations at Site A (Palla Village).

Elements	Depths at Location 1			Depths at Location 2			Depths at Location 3		
	0-2 cm	30-32 cm	78-80 cm	0-2 cm	30-32 cm	74-76 cm	0-2 cm	26-28 cm	59-61 cm
	Weight %								
Oxygen (O)	30.86	27.6	0	0	31.01	62.51	0	0	47.76
Silicon (Si)	34.48	34.03	42.54	54.26	32.79	0	36.06	39.28	0
Niobium (Nb)	0.98	0	0	0	0	0	0	0	0
Aluminium (Al)	0	0	0	0	0	0	0	0	0

Table 3: Elements Atomic % of three locations at Site B (Okhla barrage).

Elements	Depths at Location 4			Depths at Location 5			Depths at Location 6		
	0-2 cm	30-32 cm	76-98 cm	0-2 cm	30-32 cm	67-69 cm	0-2 cm	26-28 cm	62-64 cm
	Atomic %								
Oxygen (O)	86.66	92.36	0	62.31	0	92.2	95.78	94.43	56.2
Silicon (Si)	0	0	81.67	31.75	60.17	0	0	0	25.3
Niobium (Nb)	0	0	0	0	0	0	0	0	0
Aluminium (Al)	0	0	0	0	25.51	0	0	0	16.7

Table 4: Elements Weight % of three locations at Site B (Okhla barrage).

Elements	Depths at Location 4			Depths at Location 5			Depths at Location 6		
	0-2 cm	30-32 cm	76-98 cm	0-2 cm	30-32 cm	67-69 cm	0-2 cm	26-28 cm	62-64 cm
	Weight %								
Oxygen (O)	34.54	49.54	0	32.6	0	48.98	64.86	57.94	37.24
Silicon (Si)	0	0	38.85	29.16	32.5	0	0	0	29.43
Niobium (Nb)	0	0	0	0	0	0	0	0	0
Aluminium (Al)	0	0	0	0	13.24	0	0	0	18.67

were the main elements found in the analysis. Si and O were present in major quantities in almost all the samples while Nb was recorded in very less amount in the sample taken from the surface (0-2 cm) of location 1 of Site A (Palla). Al was recorded from location 5 and 6 of Site B at the depth of 30-32 cm and 62-64 cm. Elemental weight percentage and atomic percentage distribution in all the soil samples and the various depths on which samples were taken have been elucidated in Tables 1-4, while SEM images showing soil particles and EDAX spectrum representing all observed elements are shown in Figs. 2-7 and Figs. 8-25 respectively [Gold (Au) was also shown in graphs because soil samples

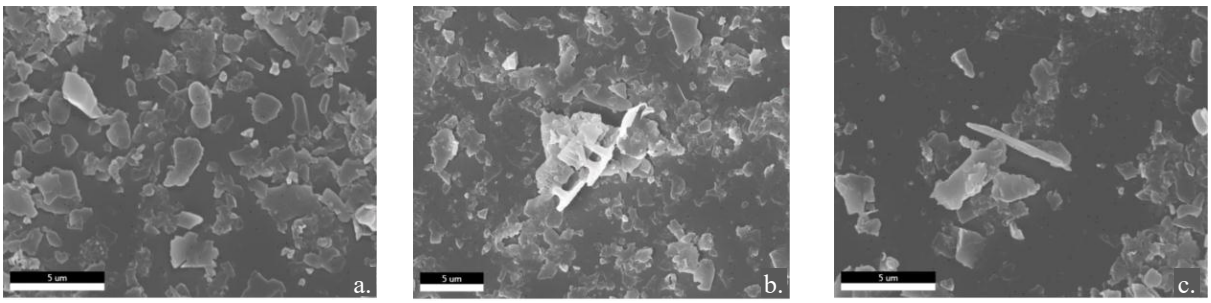

Fig. 2: a,b,c. SEM images showing soil particles of different depths 0-2 cm(a), 30-32 cm(b), 78-80 cm(c) at Location 1 at Site A (Palla Village).

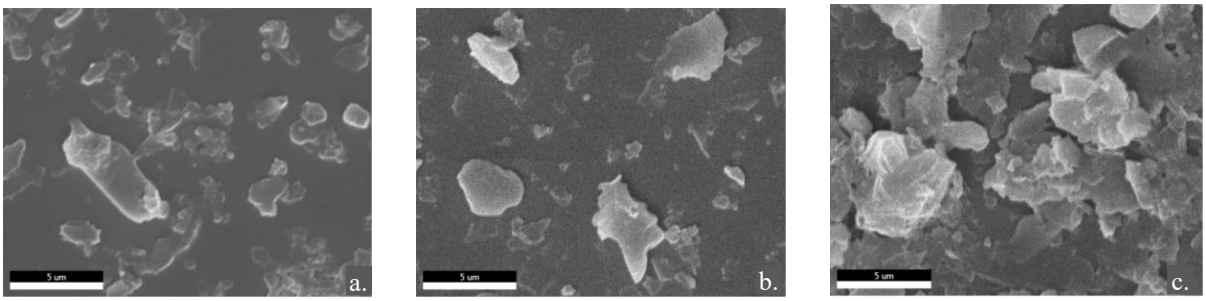

Fig. 3: a,b,c. SEM images showing soil particles of different depths 0-2 cm (a), 30-32 cm (b), 74-76 cm (c) of Location 2 at Site A (Palla Village).

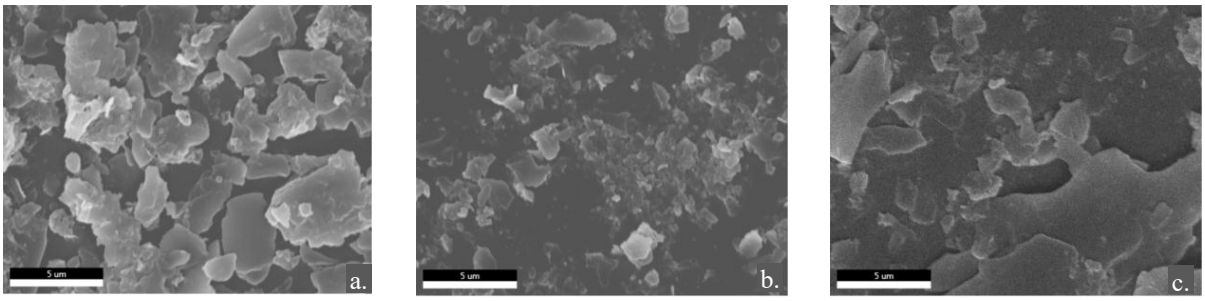

Fig. 4: a,b,c. SEM images showing soil particles of different depths 0-2 cm (a), 26-28 cm (b), 59-61 cm(c) of Location 3 at Site A (Palla Village).

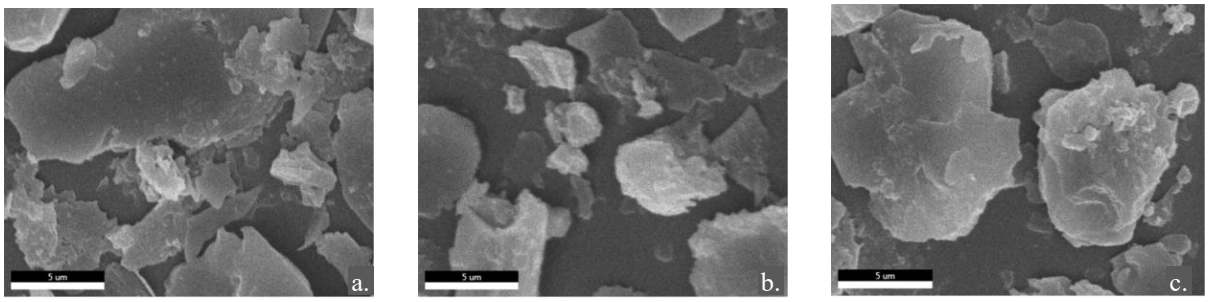

Fig. 5: a,b,c. SEM images showing soil particles of different depths 0-2 cm (a), 30-32 cm (b) and 76-98 cm (c) at Location 1 at Site B (Okhla barrage).

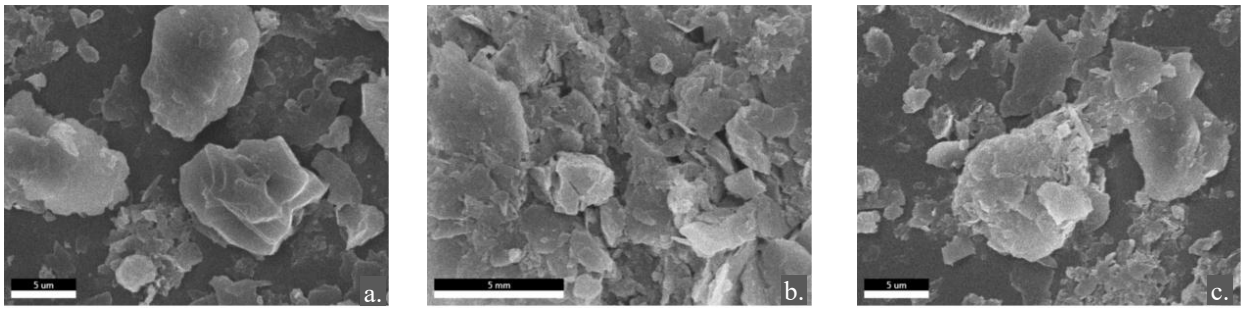

Fig. 6: a,b,c. SEM images showing soil particles of different depths 0-2 cm (a), 30-32 cm (b) and 67-69 cm (c) at Location 2 at Site B (Okhla barrage).

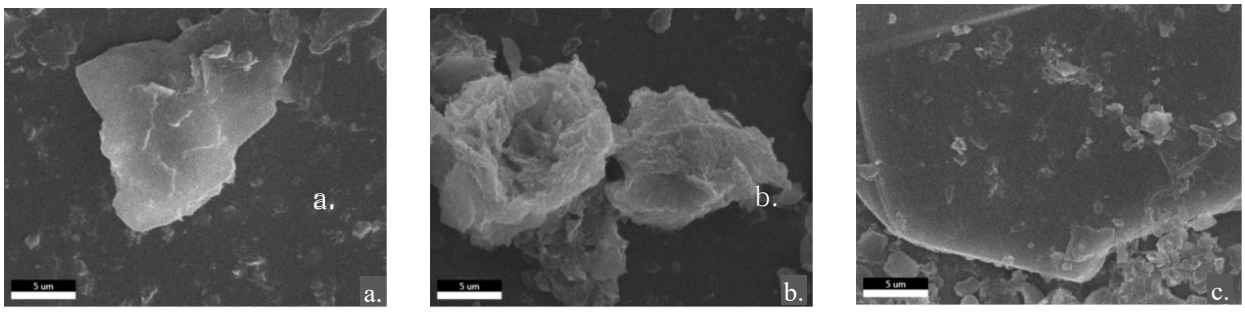

Fig. 7: a,b,c, SEM images showing soil particles of different depths 0-2 cm (a), 26-28 cm (b) and 62-64 cm (c) at Location 3 at Site B (Okhla barrage).

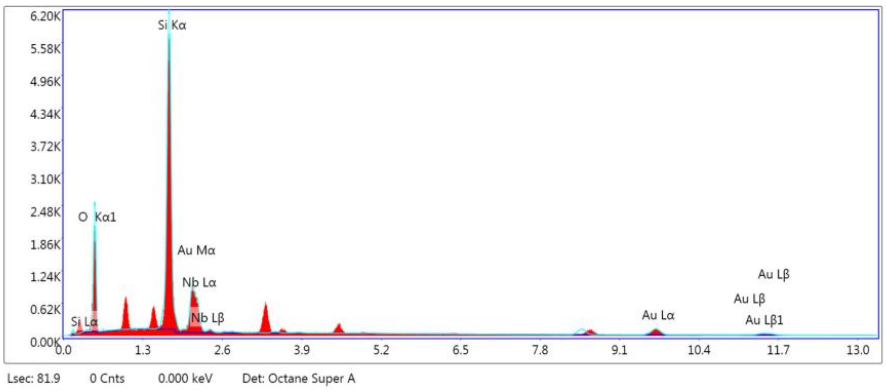

Fig. 8: EDAX spectrum of Location 1 (Depth 0-2 cm) at Site A (Palla Village).

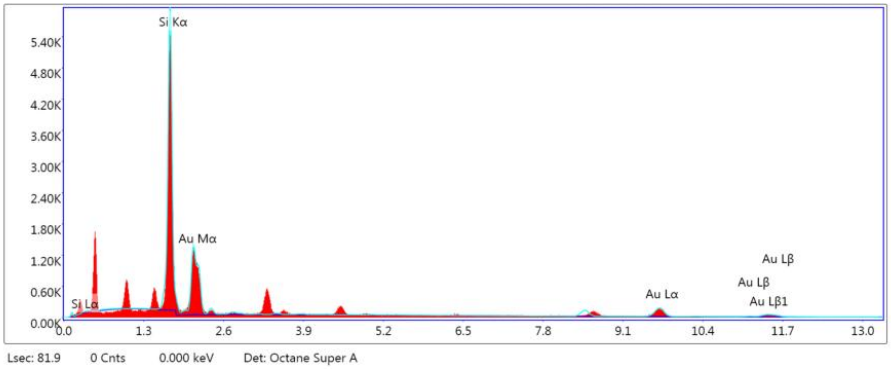

Fig. 9: EDAX spectrum of Location 1 (Depth 30-32 cm) at Site A (Palla Village).

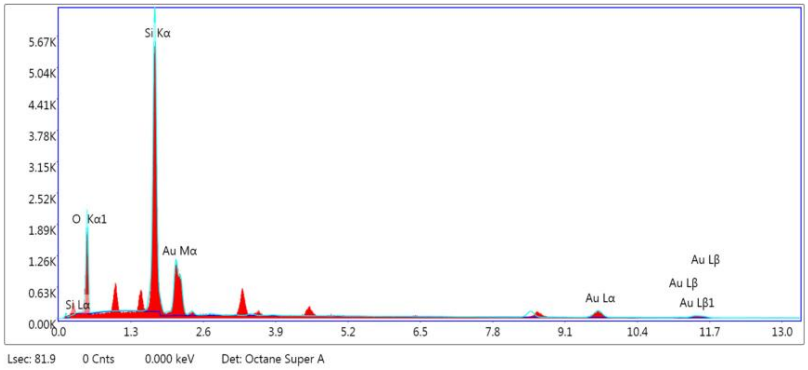

Fig. 10: EDAX spectrum of Location 1 (Depth 80-82 cm) at Site A (Palla Village).

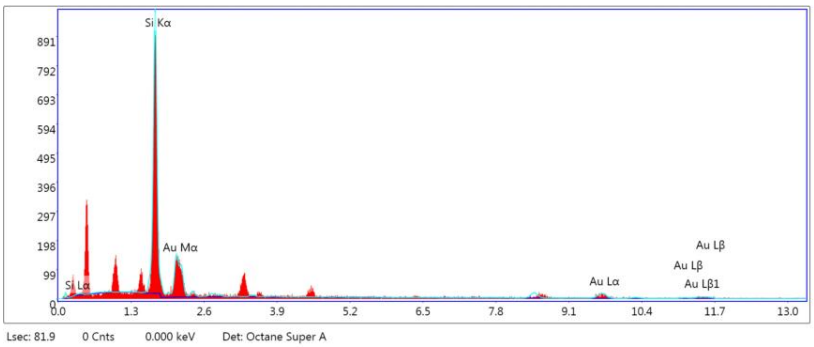

Fig. 11: EDAX spectrum of Location 2 (Depth 0-2 cm) at Site A (Palla Village).

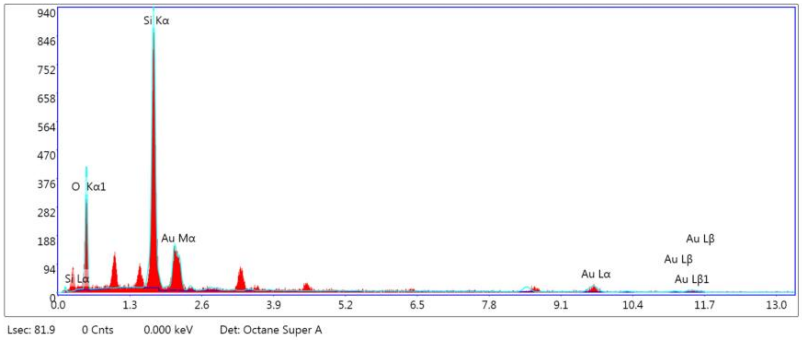

Fig. 12: EDAX spectrum of Location 2 (Depth 30-32 cm) at Site A (Palla Village).

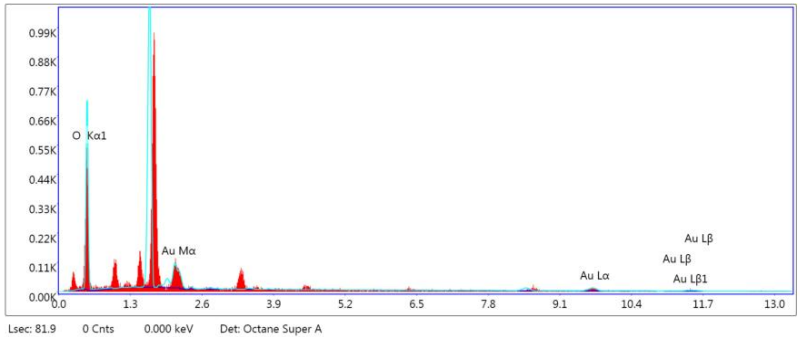

Fig. 13: EDAX spectrum of Location 2 (Depth 74-76 cm) at Site A (Palla Village).

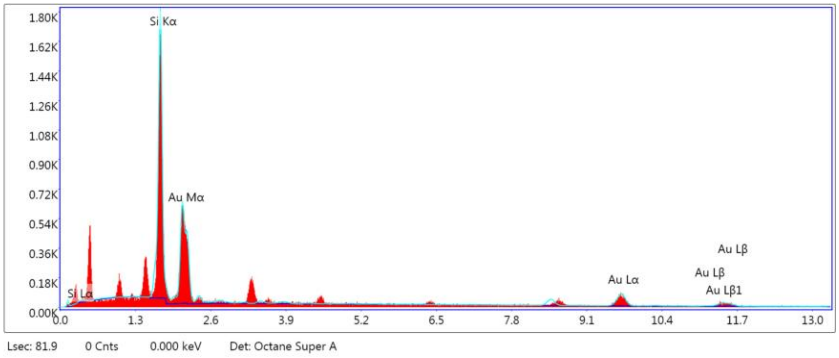

Fig. 14: EDAX spectrum of Location 3 (Depth 0-2 cm) at Site A (Palla Village).

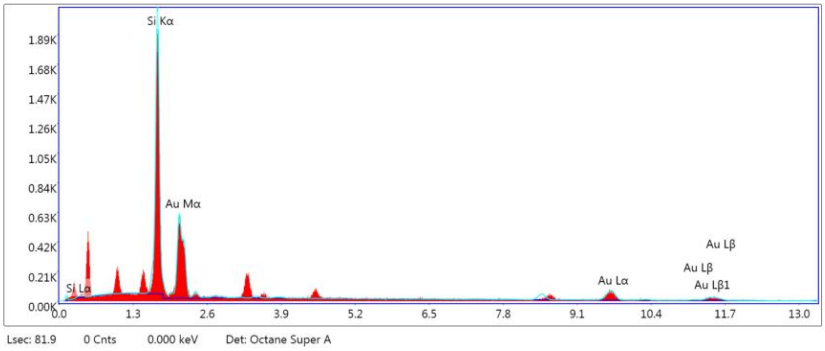

Fig. 15: EDAX spectrum of Location 3 (Depth 26-28 cm) at Site A (Palla Village).

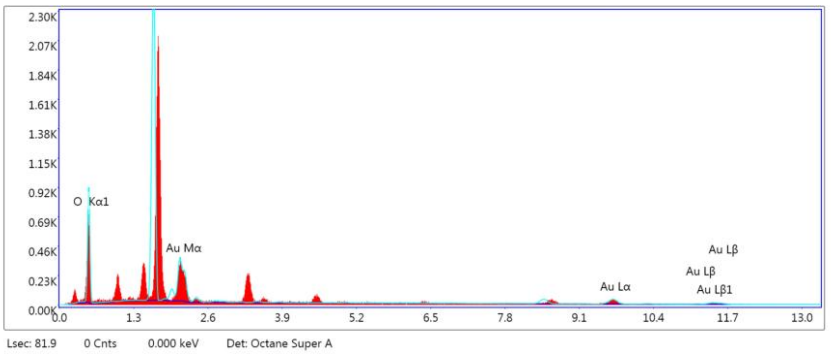

Fig. 16: EDAX spectrum of Location 3 (Depth 59-61 cm) at Site A (Palla Village).

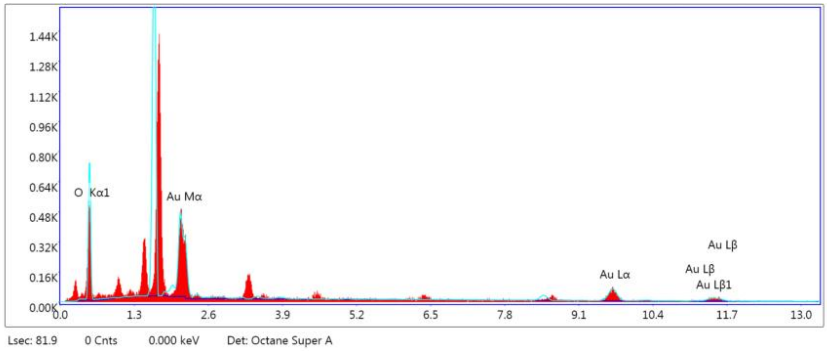

Fig. 17: EDAX spectrum of Location 1 (Depth 0-2 cm) at Site B (Okhla barrage).

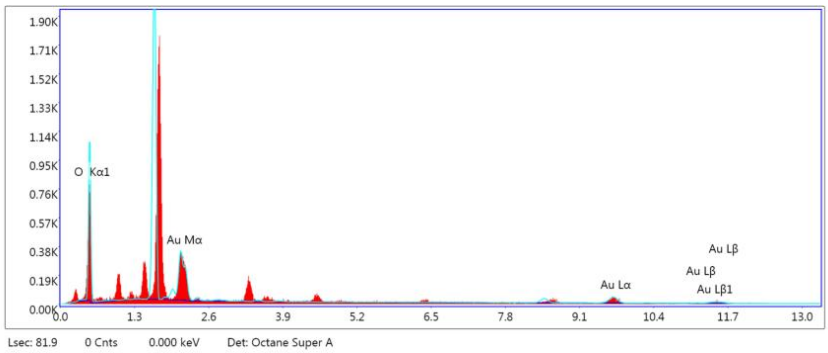

Fig. 18: EDAX spectrum of Location 1 (Depth 30-32 cm) at Site B (Okhla barrage).

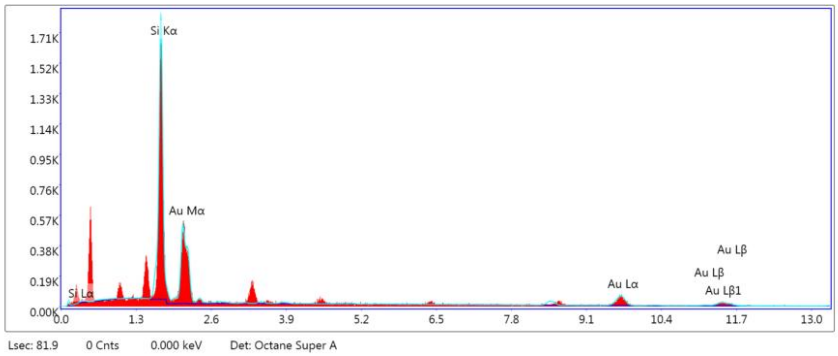

Fig. 19: EDAX spectrum of Location 1 (Depth 76-98 cm) at Site B (Okhla barrage).

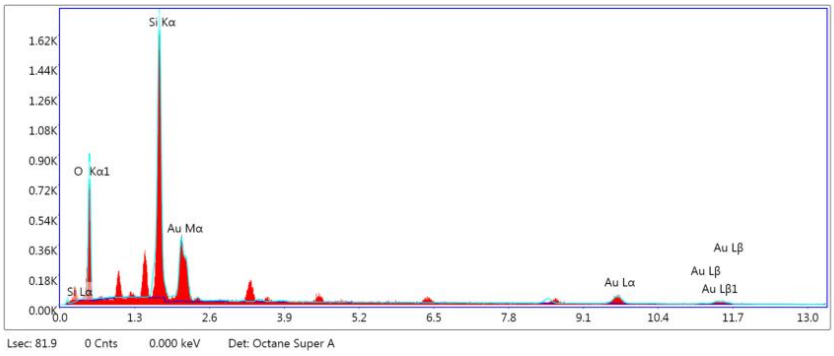

Fig. 20: EDAX spectrum of Location 2 (Depth 0-2 cm) at Site B (Okhla barrage).

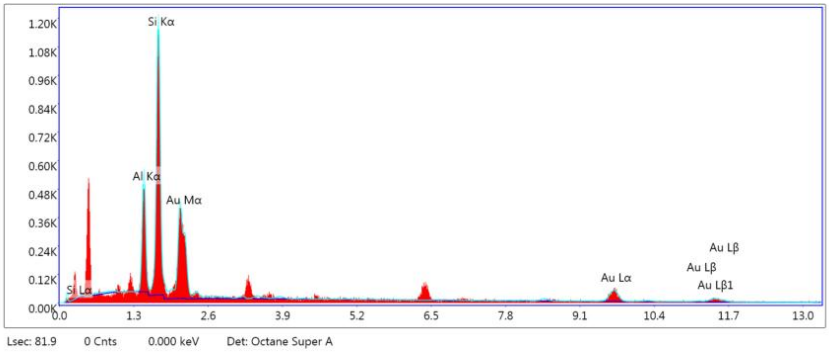

Fig. 21: EDAX spectrum of Location 2 (Depth 30-32 cm) at Site B (Okhla barrage).

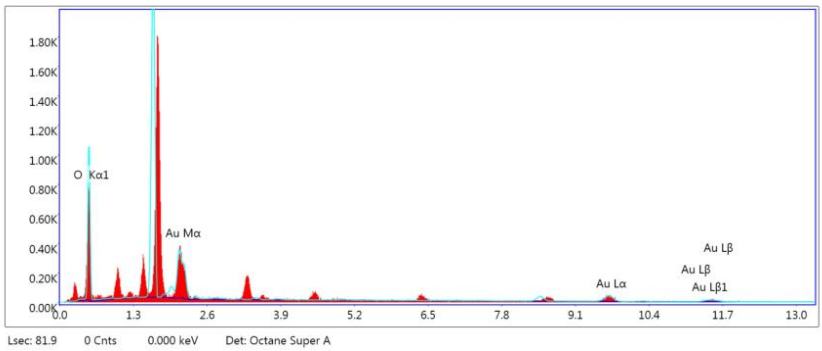

Fig. 22: EDAX spectrum of Location 2 (Depth 67-69 cm) at Site B (Okhla barrage).

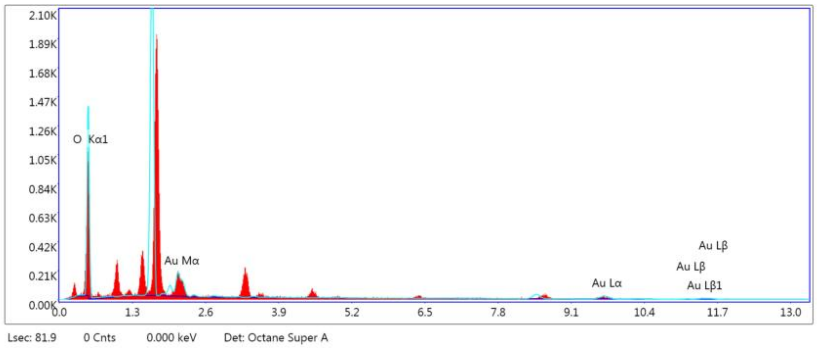

Fig. 23: EDAX spectrum of Location 3 (Depth 0-2 cm) at Site B (Okhla barrage).

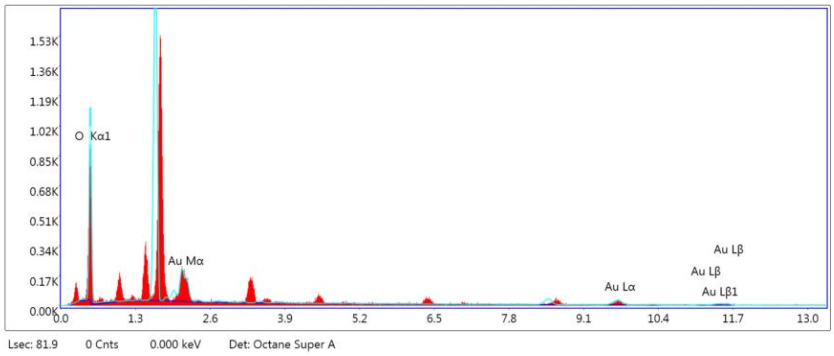

Fig. 24: EDAX spectrum of Location 3 (Depth 26-28 cm) at Site B (Okhla barrage).

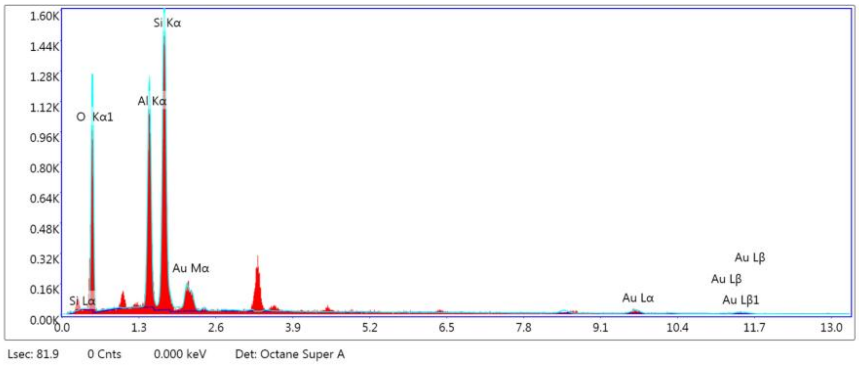

Fig. 25: EDAX spectrum of Location 3 (Depth 62-64 cm) at Site B (Okhla barrage).

were plated with gold to observe diatoms, therefore, Au value has been discarded in the present study].

Isotopic composition of silicon in river sediments and its relation to climate was explained by Bayon et al. (2018). Distribution and retention of silicon in river beds and its effects on biogeochemical nature and aquatic food webs in coastal environments were discussed by Humborg et al. (2000), while the distribution of biogenic silica in sediments of the Yellow River was discussed by Yang et al. (2016). Mil-Homens et al. (2013) has talked about the occurrence of silicon as aluminosilicates in the sediments of Minho River, Spain. In the present study, the spatial distribution pattern of Si in different soil samples does not show any specific trend. Silicon affects the uptake and accumulation of different plant nutrients and most of the silicon is locked up in intractable silicate minerals and only a much smaller fraction is available for plants (Struyf et al. 2010). Silicon forms solid-phase phytoliths after absorbed in plants and with the deterioration of dead plant material these are recycled to the soil solution which may again be taken up by plants (Carey & Fulweiler 2012). Hydrogen bound Si-organic complexes are often found in plant tissues (Carlisle et al. 1977) which permeates the walls of vessels and epidermis and reduces fungal infections and water transpiration by strengthening the plant tissues (Kaufmian et al. 1969). It also associates with cell wall components like lignins, polysaccharides, and proteins (Perry & Lu 1992). Silicon affects the uptake, distribution and functionality of several mineral nutrients like nitrogen (N), phosphorus (P), potassium (K), magnesium (Mg) and calcium (Ca) (Wallace 1989, Miyake 1993, Brackhage et al. 2013, Neu et al. 2016, Sattar et al. 2016, Kostic et al. 2017) and strongly influence the uptake of boron (B), iron (Fe), zinc (Zn) and manganese (Mn) (Nable et al. 1990, Bityutskii et al. 2014). Soil concentrations of oxygen in solution are comparatively lesser than in the soil atmosphere which is used by aerobic microorganisms as a terminal electron acceptor for the period of degradation of organic compounds and xenobiotics and percentage volume basis of oxygen varies in the atmosphere, well-aerated soil surface and fine clay or saturated soil (Pepper & Gerba 2019). Yamada et al. (2012) explained Dissolved Oxygen concentration in sediments of downstream of rivers in Lake Biwa in Japan. Similar studies on Dissolved Oxygen and Nutrient Fluxes across the Sediment-Water Interface of the Neckar River in Germany was performed by Haag et al. (2006). Concept of sediment oxygen demand (SOD) and the importance of oxygen was discussed by Belo (2008) in Pasing River.

Rock-forming minerals such as sphene, cassiterite rutile and biotite contain trace levels of Niobium and it shows a strong correlation with Ti, Ta, Th, U, Zr, Rb, Ga, Fe, V, Y and with some heavy Rare Earth Elements like Dy, Ho, Er, Tm and Yb while has a good negative correlation with CaO and forms some relatively rare, but economically significant minerals (Forges Geochemical Atlas of Europe). Production of steel, nuclear fuel and welding practice are some main human activities which lead Niobium in the environment (Reimann & De Caritat 1998). It also has some industrial significance like manufacture cutting tools, pipelines and super magnets. It is considered non-essential and very less is known about its toxicity but its existence is not denied in living organisms and stream sediment. Astrom et al. (2008) did extensive studies on 807 streams spread over 26 countries in Europe for necessary statistics on the abundance, movement and transportation of Niobium in sediments of boreal stream water. Borghesi et al. (2015) studied the geochemical classification of surface sediments from wetlands around the Po river delta in Italy and suggested that organic matter in these wetlands can influence Niobium sediments. Periodic variations occurring in water quality in streams and rivers were demonstrated by Henriksen et al. (1984). In water bodies, Al can be added by industrial sources which are lethal for aquatic fauna (Hunter et al. 1980). The acidification caused by Al in water streams has generally been a reason for declining numbers of benthic and planktonic invertebrates (Okland & Okland 1986, Haines 1981). The biological significance of Al toxicity on freshwater invertebrates was revealed by Herrmann (1987) and on fish by Driscoll et al. (1982). Horst et al. (1982) found aluminium traces in the mucilage layer on the root tips and the cell wall pectins while only a small extent is translocated to shoots. Physiological and biochemical implications of AI studies have been reported on humans as well as animals (Siegel 1985, Trapp 1986).

The shape, size and chemical constituents of soil reserves are vastly variable (Takahashi et al. 2001). SEM images revealed the irregular, elliptical, platy and spongy structures of soil particles in almost all the samples. Similar results and such inhomogeneous nature of the soil was reported by Sharma et al. (2016) in Hasdeo river basin in Chhattisgarh and by Thambavani & Kavitha (2014) in Suruli river, Karnataka in India. Soils were sandy as all the samples were taken from the river bed which is mainly constituted of alluvial deposits. Sajitha et al. (2017) also used SEM EDAX to analyze Mineralogical and Morphological Characterization of Coastal Soil Samples of Kanyakumari District. The colour of the soil was light greyish at the Site A while it was darker and blackish at Site B because of the accumulation of sewage pollutants from nearby drains.

Studies revealed that the type and concentration of elements vary at different depths of the river bed and there

is no unique pattern of occurrence of elements along the gradients of the river bed. It can be explained by the fact that the river ecosystem is a very dynamic one and the alluvial deposition can be easily disturbed by the flow of water or floods. Though the percentage of Si and O was significantly distributed in all the sites, the occurrence of Al at Site B proves the heavy load of pollution in the area and the potential source of the Al contamination might be from industrial effluents. The occurrence of Nb at Site A could be because of depositions from weathered rocks as Nb is an important part of many forms of rocks.

CONCLUSION

The extent of pollution faced by the Yamuna is a severe threat to its identity as a river. The study reveals that Site A lacks any type of heavy pollutant while the occurrence of Al at Site B confirms the presence of pollutants. The concentration of elements keeps varying from the surface to the bottom of the river bed and they do not follow any particular pattern of concentration. The present study helps us to understand the elemental composition and morphology of soil grains in the river bed. This further enhances our knowledge about the complex nature of elements distribution along the depths of the river bed which can be used for conservation studies and protection of such a fragile wetland ecosystem of our rivers.

ACKNOWLEDGEMENTS

We would like to thank Dr Neel Ratan, Mr Jogender Singh, Mr Virender Kumar and Mr Lalit Yadav for their kind help in the collection of soil samples. A kind thanks are also due to Mr. Madan Mohan Sharma for his assistance during SEM-EDAX analysis at SAIF, AIIMS, Delhi.

REFERENCES

Astrom, M., Peltola P., Virtasalo, J., Kotilainen, A. and Salminen, R. 2008. Niobium in boreal stream waters and brackish-water sediments. Geochemistry Exploration Environment Analysis, 8: 139-148. 10.1144/1467-7873/07-155.

Bayon, G., Delvigne, C., Ponzevera, E., Borges, A. V., Darchambeau, F., De Deckker, P. and André, L. 2018. The silicon isotopic composition of fine-grained river sediments and its relation to climate and lithology. Geochimica et Cosmochimica Acta, 229: 147-161. 10.1016/j.gca.2018.03.015.

Belo, Lawrence 2008. Measurement of the Sediment Oxygen Demand in Selected Stations of the Pasig River Using a Bench-scale Benthic Respirometer. 10.13140/2.1.3159.1369.

Bityutskii, N., Pavlovic, J., Yakkonen, K., Maksimović, V. and Nikolic, M. 2014. Contrasting effect of silicon on iron, zinc and manganese status and accumulation of metal-mobilizing compounds in micronutrient-deficient cucumber. Plant Physiology and Biochemistry, 74: 205-211.

Borghesi, F., Migani, F. and Dinelli, E. 2015. Geochemical characterization of surface sediments from the northern Adriatic wetlands around the Po river delta. Part I: Bulk composition and relation to local background. Journal of Geochemical Exploration, 156. 10.1016/j.gexplo.2015.05.003.

Brackhage, C., Schaller, J., Bäucker, E. and Dudel, E.G. 2013. Silicon availability affects the stoichiometry and content of calcium and micro nutrients in the leaves of common reed. Silicon, 5(3): 199-204.

Carey, J.C. and Fulweiler, R.W. 2012. The terrestrial silica pump. PLoS One, 7(12): e52932.

Carlisle, E.M., McKeague, J.A., Siever, R. Van and Soest, P.J. 1977. Silicon. In: Geochemistry and the Environment, Elsevier, Washington, DC, USA, Volume 2.

CPCB, 2006. Assessment and development of the river basin series, water quality status of Yamuna River 1999-2005. Eds Sengupta, B. Central Pollution Control Board, Delhi, India

Das, B. and Mondal, N. K. 2011. Calcareous soil as a new adsorbent to remove lead from aqueous solution: equilibrium, kinetic and thermodynamic study. Universal Journal of Environmental Health and Biology, 1(4): 515-530.

Driscoll, C.T., Baker, J.P., Bisogni, J.J.Jr. and Schofield, C.L. 1982. Effects of aluminum speciation on fish in dilute acidified waters. Nature, 284: 161-164.

Forges Geochemical Atlas of Europe. Website address:weppi.gtk.fi>publ>foregsatlas>text>Nb

Haag, I., Schmid, G. and Westrich, B. 2006. Dissolved oxygen and nutrient fluxes across the sediment-water interface of the Neckar river, Germany: in situ measurements and simulations. Water, Air & Soil Pollution, Focus, 6(5-6): 413-422.

Haines, T. 1981. Acidic precipitation and its consequences for aquatic ecosystems: A review. Trans. Am. Fish. Soc., 110: 669-707.

Henriksen, A., Skogheim, O.K. and Rosseland, B.O. 1984. Episodic changes in pH and aluminium-speciation kill fish in a Norwegian salmon river. Vatten, 40: 255-260.

Herrmann, J. 1987. Aluminium impact on freshwater invertebrates at low pH: A review. In: Speciation of Metals in Water, Sediment and Soil Systems, 157-175. Springer, Berlin, Heidelberg.

Horst, W.J., Wagner, A. and Marschner, H. 1982. Mucilage protects root meristems from aluminium injury. Zeitschrift für Pflanzenphysiologie, 105(5): 435-444.

Humborg, C., Conley, D.J., Rahm, L., Wulff, F., Cociasu, A. and Ittekkot, V. 2000. Silicon retention in river basins: Far-reaching effects on biogeochemistry and aquatic food webs in coastal marine environments. AMBIO: A Journal of the Human Environment, 29(1): 45-50.

Hunter, J.B., Ross, S.L. and Tarmahill, J. 1980. Aluminium pollution and fish toxicity. Water Pollut. Contr., 79: 413-420.

Kaufmian, P.B., Bigelow, W.C., Petering, L.B. and Drogosz, F.B. 1969. Silica in developing epidermal cells of Avena internodes. Science, 166: 1015-1017.

Kostic, L., Nikolic, N., Bosnic, D., Samardzic, J. and Nikolic, M. 2017. Silicon increases phosphorus (P) uptake by wheat under low P acid soil conditions. Plant Soil, 419: 447-455.

Miyake, Y. 1993. Silica in soil and plants. Sci. Rep. Fac. Agric., 81: 61-79.

Mil-Homens, M., Costa, A.M., Fonseca, S., Trancoso, M.A., Lopes, C., Serrano, R. and Sousa, R. 2013. Characterization of heavy-metal contamination in surface sediments of the Minho River Estuary by way of factor analysis. Archives of Environmental Contamination and Toxicology, 64(4): 617-631.

Nable, R.O., Lance, R.C.M. and Cartweight, B. 1990. Uptake of boron and silicon by barley genotypes with differing susceptibilities to boron toxicity. Ann. Bot. Rev., 66: 83-90.

Neu, S., Schaller, J. and Dudel, G.D. 2016. Silicon availability modifies nutrient use efficiency and content, C:N:P stoichiometry, and productivity of winter wheat (*Triticum aestivum* L.). Sci. Rep., 7: 1-8.

Okland, J. and Okland, K.A. 1986. The effects of acid deposition on benthic animals in lakes and streams. Experientia, 42: 471- 486.

Pepper, I.L. and Gerba, C.P. 2019. Environmental and Pollution Science. Elsevier.

Perry, C.C. and Lu, Y. 1992. Preparation of silica from silicon complexes: Role of cellulose in polymerisation and aggregation control. J. Chem. Soc. Faraday Trans., 88: 2915-2921.

Reimann, C. and De Caritat, P. 1998. Chemical elements in the environment: Factsheets for the geochemist and environmental scientist. Springer Science & Business Media. 398 pp. Berlin, Heidelberg, New York, London, Paris, Tokyo, Hong Kong, Springer-Verlag.

Sajitha, S.S., Metilda, P. and Jenin, G.A. 2017. Morphological and mineralogical characterization of coastal soil samples of Kanyakumari District by FT-IR, XRD, SEM/EDAX. International Journal of Scientific Research and Management (IJSRM), 5(10): 7163-7171. 10.18535/ijsrm/v5i10.01.

Sattar, A., Cheema, M.A., Ali, H., Sher, A., Ijaz, M., Hussain, M., Hassan, W. and Abbas, T. 2016. Silicon mediates the changes in water relations, photosynthetic pigments, enzymatic antioxidants activity and nutrient uptake in maize seedling under salt stress. Grassl. Sci., 62: 262-269.

Sharma, R., Patel, K.S., Lata, L. and Milosh, H. 2016. Characterization of urban soil with SEM-EDX. American Journal of Analytical Chemistry, 7(10): 724-735. 10.4236/ajac.2016.710065.

Siegel, N. 1985. Aluminum interaction with biomolecules: The molecular basis for aluminium toxicity. Am. J. Kidney Dis., 6: 353-357.

Struyf, E., Smis, A., Van Damme, S., Garnier, J., Govers, G., Van Wesemael, B., Conley, D.J., Batelaan, O., Frot, E., Clymans, W. and Vandevenne, F. 2010. Historical land use change has lowered terrestrial silica mobilization. Nat. Commun., 1: 129.

Takahashi, T., Dahlgren, R.A., Theng, B.K.G., Whitton, J.S. and Soma, M. 2001. Potassium-selective, halloysite-rich soils formed in volcanic materials from Northern California. Soil Science Society of America Journal, 65: 516. http://dx.doi.org/10.2136/sssaj2001.652516x.

Tan, K.H. 2005. Soil Sampling, Preparation and Analysis. 2nd Edition, CRC Press, Boca Raton.

Thambavani, S. and Kavitha, B. 2014. Mineralogical characterization of river bed soil from Tamilnadu by FT-IR, XRD and SEM/EDAX. International Journal of Advanced Research, 2: 656-659.

Trapp, G.A. 1986. Interactions of aluminum with co-factors, enzymes, and other proteins. Kidney Int., 29, Suppl.,18: S12-S16.

Wallace, A. 1989. Relationships among nitrogen, silicon, and heavy metal uptake. Soil Sci., 147: 457-460.

Yamada, Y., Mito, Y., Igeta, A. and Wada, E. 2012. Dissolved oxygen concentration in river sediment of the Lake Biwa tributaries, Japan. Limnology, 13: 149-154. https://doi.org/10.1007/s10201-011-0348-2.

Yang, X.H., Yang, H.W., Li, W.J. and Li, P. 2016. Distribution of biogenic silica in sediments of the Yellow River (Upper and Middle Reaches). Chemical Engineering Transactions, 55: 361-366.

Sensorless Speed Control of PMSM Motor for Wide Speed Range

Pratyush Kumar Dwivedi
Department of Electrical Engineering
Delhi Technological University
Delhi-110042, India
pratyush.knit@gmail.com

Aakash Kumar Seth
Department of Electrical Engineering
Delhi Technological University
Delhi-110042, India
akrseth@gmail.com

Mukhtiar Singh
Department of Electrical Engineering
Delhi Technological University
Delhi-110042, India
mukhtiarsingh@dce.ac.in

***Abstract*--This paper compares the sensorless vector control techniques of Permanent Magnet Synchronous Motors (PMSM). Sliding mode observer (SMO) and Model reference adaptive system (MRAS) are compared. SMO are known for their robust nature. The SMO is traditionally used for sensorless control. Although the SMO performs well in high-speed range but struggles at low speed and could not provide wide speed operation. MRAS provide wide speed operation and has better rotor angle estimation in dynamic condition. Both the techniques have been simulated under MATLAB environment with different dynamics condition. It is shown that the dynamic performance of MRAS is better than the SMO.**

Keywords— PMSM, Vector, SMO, MRAS, Sensorless

I. INTRODUCTION

Permanent Magnet Synchronous Motors (PMSM) are popular due its ratio high power/mass and higher Efficiency. According to [10], PMSM are popularly used in the EVs even though they are costly. They are more economical than induction motor because they have high efficiency and the battery packs are more costly than PMSMs.

Vector control of motor is more popular method due to increased efficiency and output power quality. Sensors are required for the vector control. This decreases the reliability of the motor and ability of motor to operate under harsh environment [1-2]. Hence, more focus is on the sensor less techniques to increase the reliability of the powertrain.

The Sliding Mode Observer (SMO) is a popular sensorless techniques due to its robust nature against the parameter variation. SMO are based on back emf estimation of the PMSM [3].

Chattering is a major disadvantage of sliding mode observer. Literature [4-5] uses different switching function, in order to resolve chattering problem. Various different techniques are used to reduce the chattering effect. In [4], proposes sliding mode observer for PMSM with washing machine application. Instead of signum function, saturation function is proposed in order to reduce the chattering effect. Although the presence of low pass filter demerits the dynamic performance of system. Various phase compensation techniques are described in literature [6]. Lookup tables are used to calculate the phase compensation in [6] which uses a significant amount of memory space due to which extra memory is required. Variable phase compensation is also used which compensates according to the rotor velocity and filter cut-off frequency.

Although chattering can be reduced but at the starting and low speed, back emf resolution is low. The SMO fails to estimate the rotor angle under low speed operation which limits the wide speed operation of SMO. A starting method is required in the SMO which increases the complexity of the system and decreases the reliability of system.

The MRAS is popular because of simple implementation and wide speed operation [7, 8]. As shown in Fig. 1, the motor model is taken same as the reference model which took into the account parameter deviation of the system with time. The state variable such as current or power are taken as output from the reference model and adjustable model and error e(t) is obtained. By using adaptive mechanism, the speed ω_r is estimated and fed to adaptive Traditionally PI controller is used in adaption mechanism because of easy implementation but better result also obtained with artificial neural network (ANN) [9].

The MRAS provides better dynamic performance than SMO because of absence of low pass filter. MRAS has wide speed operation and performs fairly at low speed. As no starting techniques are required, hence the reliability of system is more.

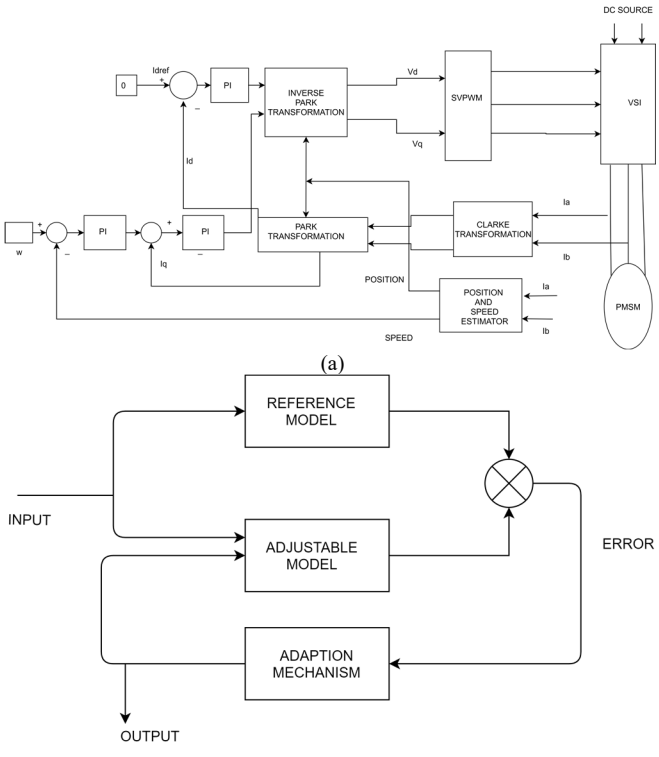

Fig. 1. (a) Sensorless control and (b) Model reference adaptive system (MRAS).

978-1-7281-8774-7/21/$31.00 ©2021IEEE

2021 1st International Conference on Power Electronics and Energy (ICPEE) | 978-1-7281-8774-7/21/$31.00 ©2021 IEEE | DOI: 10.1109/ICPEE50452.2021.9358766

Authorized licensed use limited to: DELHI TECHNICAL UNIV. Downloaded on March 03,2021 at 06:04:00 UTC from IEEE Xplore. Restrictions apply.

II. Mathematical Model Of PMSM

The mathematical model of PMSM alpha-beta frame is given by following equations:

$$L_S\left(\frac{d\hat{\imath}_\alpha}{dt}\right) = -R_S i_\alpha - e_\alpha + u_\alpha \quad (1)$$

$$L_S\left(\frac{d\hat{\imath}_\beta}{dt}\right) = -R_S i_\beta - e_\beta + u_\beta \quad (2)$$

Where $L_S, R_S, i_\alpha, i_\beta, e_\alpha, e_\beta, u_\alpha, u_\beta$ are the phase currents, stator inductance, stator resistance, back emf and phase voltages respectively.

The back emf equations are given by

$$e_\alpha = -\varphi_f\, \omega_r \sin\theta \quad (3)$$

$$e_\beta = \varphi_f\, \omega_r \cos\theta \quad (4)$$

Where, φ_f , θ and ω_r is the electrical rotor angle, flux linkage and electrical angular velocity of the motor. It shows that the back emf of motor is dependent on the rotor position and speed, but it cannot be measured directly. Hence, an observer is required to extract the rotor position.

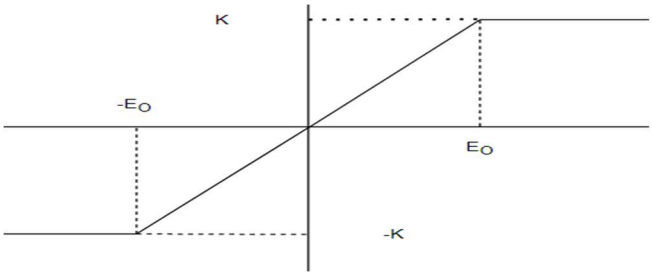

(a)

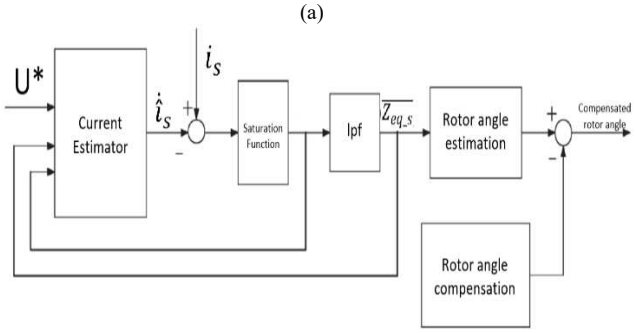

(b)

Fig 2. (a) Saturation function (b) Sliding Mode Observer.

III. Sliding Mode Observer (SMO)

A. SMO with signum function.

The SMO is given by following equations,

$$L_S\left(\frac{d\hat{\imath}_\alpha}{dt}\right) = -R_S i_\alpha + u_\alpha - k * sgn(\overline{\imath_\alpha}) \quad (4)$$

$$L_S\left(\frac{d\hat{\imath}_\beta}{dt}\right) = -R_S i_\beta + u_\beta - k * sgn(\overline{\imath_\beta}) \quad (5)$$

$$\overline{\imath_\alpha} = \hat{\imath}_\alpha - i_\alpha$$

$$\overline{\imath_\beta} = \hat{\imath}_\beta - i_\beta$$

Where k is the observer gain, sgn is the signum function. saturation function is used instead of signum function so as to reduce chattering.

By eq. (1), the SMO equation is shown as follows

$$L_S\left(\frac{d\hat{\imath}_\alpha}{dt}\right) = -R_S \hat{\imath}_\alpha + u_\alpha - k(l\overline{Z_{eq_\alpha}} + \overline{Z_\alpha}) \quad (6)$$

$$L_S\left(\frac{d\hat{\imath}_\beta}{dt}\right) = -R_S \hat{\imath}_\beta + u_\beta - k(l\overline{Z_{eq_\beta}} + \overline{Z_\beta}) \quad (7)$$

$$l = \begin{cases} -0.5 & n < 375\ rpm \\ 1 & n > 750\ rpm \end{cases}$$

k and l are the switching gain and feedback gain . The value of switching gain must be just above the maximum amplitude of back emf.

$$\bar{Z} = -K * sign(\hat{\imath}_s - i_s)$$

The equivalent $\overline{Z_{eq}}$ is given by,

$$\overline{Z_{eq}} = \frac{1}{1+p\tau}\bar{Z}$$

$$p = \frac{d}{dt}$$

B. SMO with saturation function.

If the value of $\hat{\imath}_s - i_s$ is less than E_0, the value of control signal

$$\bar{Z} = -K_s\,(\hat{\imath}_s - i_s), \text{ where } K_s = \frac{K}{E_0}$$

$$\text{Else } \bar{Z} = K$$

Then the equation for sliding mode observer are written as,

$$L_S\left(\frac{d\hat{\imath}_\alpha}{dt}\right) = -R_S \hat{\imath}_\alpha + u_\alpha - (1+l)\overline{Z_{eq_\alpha}} \quad (8)$$

$$L_S\left(\frac{d\hat{\imath}_\beta}{dt}\right) = -R_S \hat{\imath}_\beta + u_\beta - (1+l)\overline{Z_{eq_\beta}} \quad (9)$$

Verifying the stability of the modified SMO, the Lyapunov function is

$$V = \frac{1}{2}S(X)^T S(X) \quad (10)$$

Where, $S(X) = [\overline{\imath_\alpha}\ \overline{\imath_\beta}]$

$$\overline{\imath_\alpha} = \hat{\imath}_\alpha - i_\alpha$$

$$\overline{\imath_\beta} = \hat{\imath}_\beta - i_\beta$$

The stability condition is defined as following:

$$\dot{V} = S(X)^T \dot{S}(X) \leq 0$$

By subtracting (1) and (2) by (6) and (7) respectively, we have

$$L_S[\dot{S_\alpha}(X)] = -R_S S_\alpha(X) + e_\alpha - (1+l)k\overline{Z_{eq_\alpha}} \quad (11)$$

$$L_S[\dot{S_\beta}(X)] = -R_S S_\beta(X) + e_\beta - (1+l)k\overline{Z_{eq_\beta}} \quad (12)$$

Therefore, we have

Authorized licensed use limited to: DELHI TECHNICAL UNIV. Downloaded on March 03,2021 at 06:04:00 UTC from IEEE Xplore. Restrictions apply.

$$\dot{V} = [\bar{\imath}_\alpha \quad \bar{\imath}_\beta]\begin{bmatrix} -\frac{R_S\bar{\imath}_\alpha}{L_S} + \frac{e_\alpha}{L_S} - \frac{k}{L_S}(1+l)\overline{Z_{eq_\alpha}} \\ -\frac{R_S}{L_S}\bar{\imath}_\beta + \frac{e_\beta}{L_S} - \frac{k}{L_S}(1+l)\overline{Z_{eq_\beta}} \end{bmatrix} \quad (13)$$

$$\dot{V} = \left[-\left(\frac{R_S}{L_S}\bar{\imath}_\alpha^{\,2} + \frac{R_S}{L_S}\bar{\imath}_\beta^{\,2}\right)\right] + \left[\frac{1}{L_S}\left(e_\alpha - k(1+l)\overline{Z_{eq_\alpha}}\right)\bar{\imath}_\alpha + \frac{1}{L_S}\left(e_\beta - k(1+l)\overline{Z_{eq_\beta}}\right)\bar{\imath}_\beta\right] \quad (14)$$

The first term in the equation is less than zero hence, the second term in the above equation must be less than zero. Therefore the observer gain must be

$$k > \max\left(\left|\frac{e_\alpha}{\overline{Z_\alpha}}\right|, \left|\frac{e_\beta}{\overline{Z_\beta}}\right|\right) \quad (15)$$

If k is large enough then the SMO is asymptotically stable and converges to its sliding surface

Then, $S(X) = \dot{S}(X) = 0$

From the above equation we have

$$e_\alpha = (1+l)\overline{Z_\alpha} \quad (16)$$

$$e_\beta = (1+l)\overline{Z_\beta} \quad (17)$$

IV. Model Reference Adaptive System (MRAS)

MRAS is used to estimate the real time rotor velocity which in turn is used to estimate the rotor angle. Two models are used, one is the reference model which is the motor itself and other is the adjustable model which has all the input of the reference model as well has rotor electrical velocity as input. The output current from both the model is compared and fed to the adaptive mechanism. The adaptive mechanism may be the simple PI control, ANN control and SMC. The adaptive mechanism estimates the rotor velocity. The estimated rotor velocity is fed to the adjustable model.

Mathematical Modelling

The state space model of PMSM in dq coordinates is given by:

$$\dot{x} = \mathrm{Ax} + \mathrm{Bu} \quad (18)$$

$$y = Cx \quad (19)$$

Where, $A = \begin{bmatrix} \frac{-R_S}{L_S} & \omega_{el} \\ -\omega_{el} & \frac{-R_S}{L_S} \end{bmatrix}$, $Bu = \begin{bmatrix} \frac{v_d}{L_S} \\ \frac{(v_q - \varphi_r\omega_{el})}{L_S} \end{bmatrix}$,

$$C = \begin{bmatrix} 1 & 0 \\ 0 & 1 \end{bmatrix}, x = [\, i_d \; i_q]^T$$

Where v_d, v_q, i_d , i_q are the rotor voltage and current in dq frame. ω_{el} is the rotor velocity.R_S, L_S are the stator resistance and inductance, respectively.

The adjustable model is given by the following equations,

$$\dot{\hat{x}} = \hat{A}\hat{x} + \hat{B}u \quad (20)$$

$$y = C\hat{x} \quad (21)$$

Where,

$$\hat{A} = \begin{bmatrix} \frac{-R_S}{L_S} & \widehat{\omega_{el}} \\ -\widehat{\omega_{el}} & \frac{-R_S}{L_S} \end{bmatrix}, \hat{B}u = \begin{bmatrix} \frac{v_d}{L_S} \\ \frac{(v_q - \varphi_r\omega_{el})}{L_S} \end{bmatrix},$$

$$\hat{x} = [\, \widehat{\imath_d} \; \widehat{\imath_q}]^T$$

The generalized error can be measured $\epsilon = \hat{x} - x$. By analyzing the generalized error, the transfer function of the adaptive mechanism is given by (23),

The rotor angle is estimated by integral action as in (22).

$$\widehat{\theta_{el}} = \int \widehat{\omega_{el}}\, dt \quad (22)$$

$$\widehat{\omega_{el}} = \left(K_p + \frac{K_i}{s}\right)\left[(\widehat{\imath_q} - i_q)\left(i_d + \frac{\varphi_r}{L_S}\right) - (\widehat{\imath_d} - i_d)i_q\right] + \widehat{\omega_{el}}(0) \quad (23)$$

V. Simulation Results

Table I
Specification of PMSM.

Rated power	9.4 kw
Stator Resistance (R_S)	0.203 Ω
Pole pairs (p)	4
Inductance (L_d=L_q)	2.10 mH
Inertia (J)	0.0048 kg.m^2
Permanent Magnet flux	0.123 Wb
Rated torque	20 Nm

The PMSM with SMO and MRAS is modelled in MATLAB Simulink. The motor with following specification as shown in table I is modelled in Simulink. The system is simulated under two dynamic conditions: 1) Speed reference is changed 400 rpm to 750 rpm at 1 sec with constant torque load of 20 Nm, and 2) The torque load is changed from 20 Nm to 10 Nm with rated speed of 750 rpm.

A. SMO

Rotor velocity has certain noise due to inherent nature of sliding mode observer. The rotor velocity response with SMO is shown Fig. 3 (a). The developed electromagnetic torque is shown Fig. 3 (b). The estimated rotor angle and the actual rotor angle are compared in Fig. 3 (c). The rotor angle between the actual rotor angle and estimated SMO rotor angle is compared and error b/w them is displayed in Fig. 3 (d) and it is observed that there is significant deviation of 0.6 radians in estimated rotor angle deviation when the motor is in transient state. Hence, there is danger of motor going out of synchronous.

The rotor angle between the actual rotor angle and estimated SMO rotor angle is compared and error b/w them is displayed Fig. 4 (c) and 4 (d) , it is observed that there is no significant deviation in estimated rotor angle when the motor is in transient state.

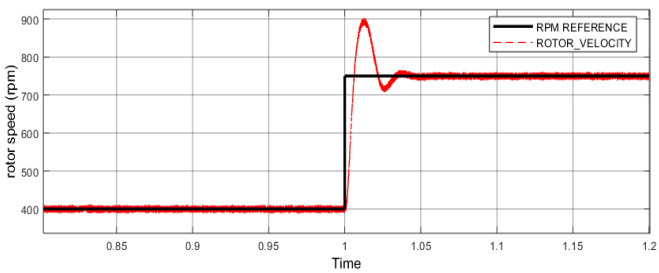

(a)

Authorized licensed use limited to: DELHI TECHNICAL UNIV. Downloaded on March 03,2021 at 06:04:00 UTC from IEEE Xplore. Restrictions apply.

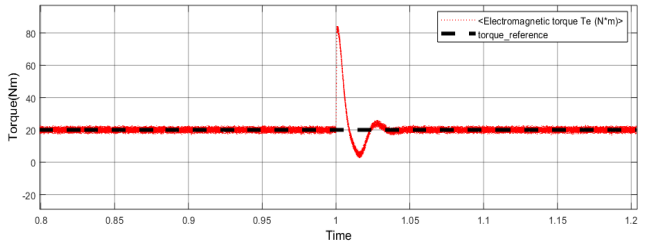

(b)

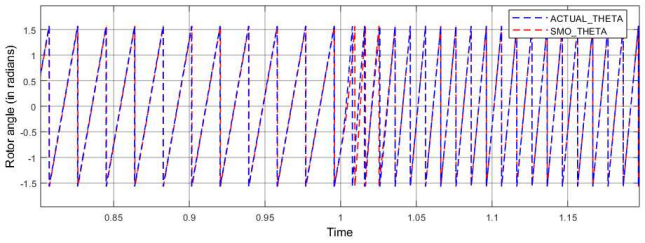

(c)

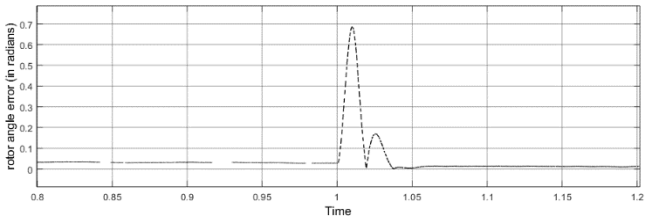

(d)

Fig 3. Speed reference is changed 400 rpm to 750 rpm at 1 sec with constant torque load of 20 Nm with SMO (a) Rotor velocity, (b) Electromagnetic torque, (c) Rotor angle and (d) Rotor angle error.

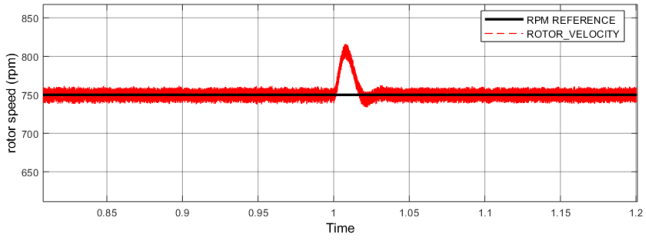

(a)

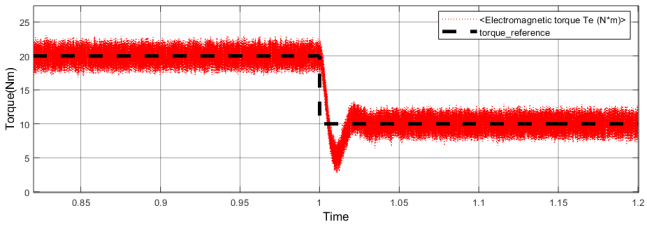

(b)

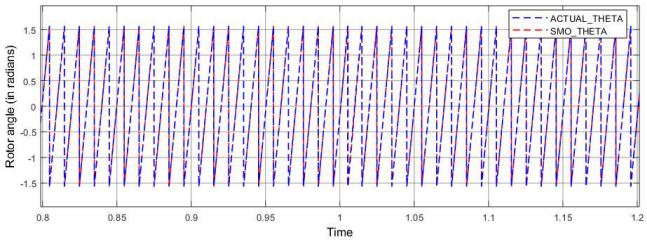

(c)

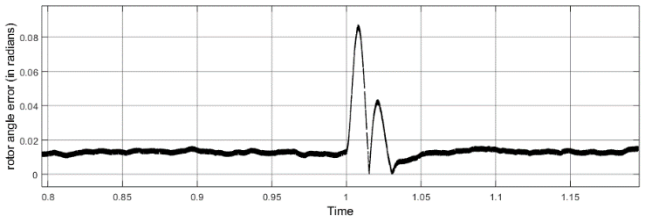

(d)

Fig 4.The torque load is changed from 20 Nm to 10 Nm with rated speed of 750 rpm with SMO (a) Rotor velocity, (b) Electromagnetic torque, (c) Estimated rotor angle and (d) Estimated rotor angle error.

B. Model Reference Adaptive System (MRAS)

The MRAS is used to develop the sensorless vector control of PMSM is tested under different test conditions. SMC controller is used as adaptive control law. These test cased are satisfactorily test the performance of motor under the various loading conditions. Simulation should mirror the performance of the drive in real world conditions. The speed reference is changed from 0 to 400 rpm at 0 s and from 400 rpm to 750 rpm with rated load torque of 20 Nm.

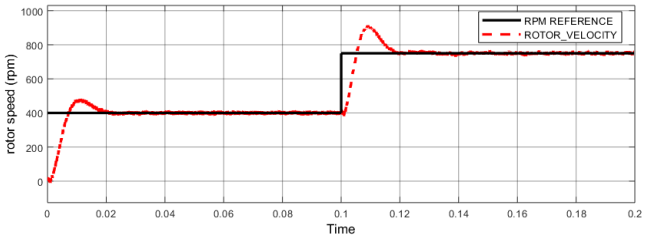

(a)

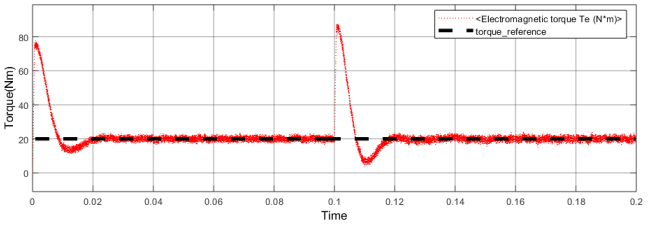

(b)

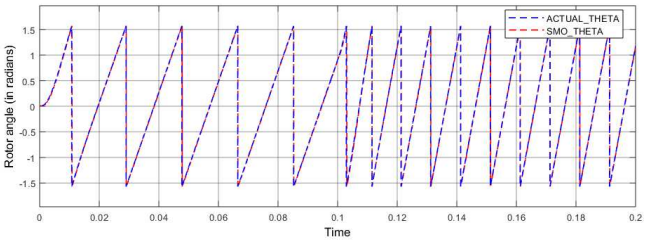

(c)

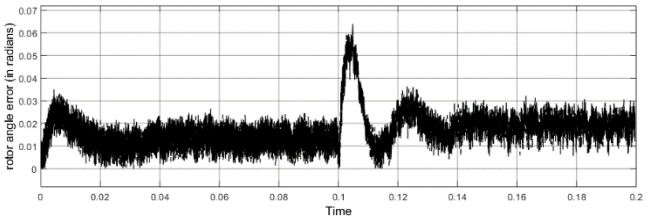

(d)

Fig 5. Speed reference is changed 400 rpm to 750 rpm at 1 sec with constant torque load of 20 Nm with MRAS (a) Estimated rotor velocity, (b) Electromagnetic torque, (c) Estimated rotor angle and (d) Estimated rotor angle error.

The Fig. 5 (a) shows the rotor velocity response when the speed reference is changed from 400 to 750 rpm at 0.1s with rated load torque of 20 Nm. The rotor velocity response is as good as response obtained in SMO as in Fig. 2 (a). Fig. 5 (c) and 5 (d) shows the comparison of estimated rotor angle and actual rotor angle and rotor angle error.

As shown in Fig. 5 (d), the maximum rotor angle error deviation which is 0.04 rad is significantly less than SMO (Fig. 3(d)). From the above, it can be inferred that dynamic performance of model reference adaptive system is better than SMO.

The rotor angle between the actual rotor angle and estimated MRAS rotor angle is compared and error between them is displayed Fig. 6 (c) and 6 (d), it is observed that there is no significant deviation in estimated rotor angle from true rotor angle deviation when the motor is in transient state. It is shown that the estimated rotor angle is as good as the new SMO developed.

Authorized licensed use limited to: DELHI TECHNICAL UNIV. Downloaded on March 03,2021 at 06:04:00 UTC from IEEE Xplore. Restrictions apply.

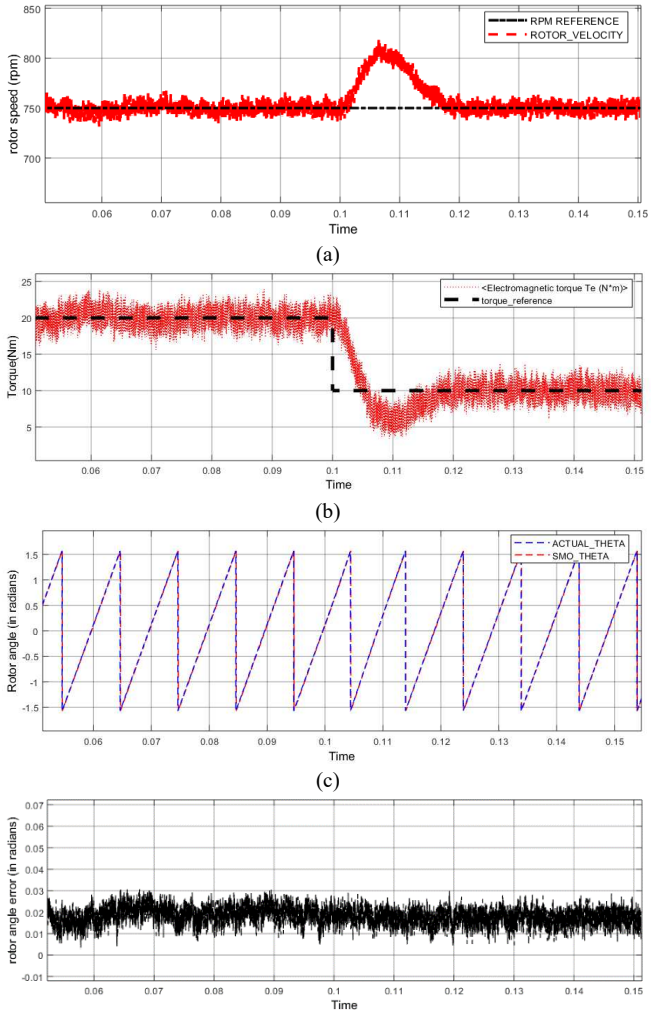

Fig 6. The torque load is changed from 20 Nm to 10 Nm with rated speed of 750 rpm with MRAS (a) Estimated rotor velocity, (b) Electromagnetic torque (c) Estimated rotor angle and (d) Estimated rotor angle error.

VI. Conclusion

SMO performs fairly in high speed range, but performance degrades in low speed range. Also, SMO requires a starting techniques as the back emf is zero at the start up, whereas MRAS does not suffer from this problem and provide wide speed operation. It is demonstrated that MRAS provide better dynamic performance than SMO for sensorless control. As the MRAS does not suffer from the chattering problem the steady state rotor angle estimation is better than SMO.

References

[1] Gopinath, Gulur & Shyama, Prasad. (2019). Sensorless control of PMSM using an adaptively tuned SCKF. The Journal of Engineering. 2019. 10.1049/joe.2018.8081.

[2] S. Bolognani, L. Tubiana and M. Zigliotto, "Extended Kalman filter tuning in sensorless PMSM drives," in IEEE Transactions on Industry Applications, vol. 39, no. 6, pp. 1741-1747, Nov.-Dec. 2003, doi: 10.1109/TIA.2003.818991.

[3] Dianguo Xu, Gaolin Wang, and Guo-Qiang Zhang, "Position Sensorless Control Techniques for Permanent Magnet Synchronous Machine Drives" Springer Nature, 2019.

[4] S. Chi, Z. Zhang and L. Xu, "Sliding-Mode Sensorless Control of Direct-Drive PM Synchronous Motors for Washing Machine Applications," in IEEE Transactions on Industry Applications, vol. 45, no. 2, pp. 582-590, March-april 2009, doi: 10.1109/TIA.2009.2013545.

[5] C. Gong, Y. Hu, J. Gao, Y. Wang and L. Yan, "An Improved Delay-Suppressed Sliding-Mode Observer for Sensorless Vector-Controlled PMSM," in IEEE Transactions on Industrial Electronics, vol. 67, no. 7, pp. 5913-5923, July 2020, doi: 10.1109/TIE.2019.2952824.

[6] L. Jiaxi, Y. Guijie and Y. Pengfei, "Rotor Position Estimation for PMSM Based on Sliding Mode Observer," 2007 International Conference on Mechatronics and Automation, Harbin, 2007, pp. 3684-3689, doi: 10.1109/ICMA.2007.4304159.

[7] O. C. Kivanc and S. B. Ozturk, "Sensorless PMSM Drive Based on Stator Feedforward Voltage Estimation Improved With MRAS Multiparameter Estimation," in IEEE/ASME Transactions on Mechatronics, vol. 23, no. 3, pp. 1326-1337, June 2018, doi: 10.1109/TMECH.2018.2817246.

[8] A. Mishra, V. Mahajan, P. Agarwal and S. P. Srivastava, "MRAS based estimation of speed in sensorless PMSM drive," 2012 IEEE Fifth Power India Conference, Murthal, 2012, pp. 1-5, doi: 10.1109/PowerI.2012.6479492.

[9] Wang Zhifu, Teng Qizhi and Zhang Chengning, "Speed identification about PMSM with MRAS," 2009 IEEE 6th International Power Electronics and Motion Control Conference, Wuhan, 2009, pp. 1880-1884, doi: 10.1109/IPEMC.2009.5157702.

[10] https://auto.economictimes.indiatimes.com/news/auto-components/high-efficiency-gains-to-spur-use-of-pm-motor-in-future-ev-designs-report/72317517.

Authorized licensed use limited to: DELHI TECHNICAL UNIV. Downloaded on March 03,2021 at 06:04:00 UTC from IEEE Xplore. Restrictions apply.

Research Square

Preprints are preliminary reports that have not undergone peer review.
They should not be considered conclusive, used to inform clinical practice,
or referenced by the media as validated information.

Smart Traffic Management and Control system Based on IoT

Dominic Abuga (abugah.dominic@gmail.com)
VLSI & Embedded Systems, Delhi Technological University
Nallanthighal Raghava
VLSI & Embedded Systems, Delhi Technological University

Short Report

Keywords: NTSA, Traffic jams, Internet of Things, greenhouse gases

DOI: https://doi.org/10.21203/rs.3.rs-314224/v1

License: This work is licensed under a Creative Commons Attribution 4.0 International License.
Read Full License

Abstract

Over the last two decades, there has been an exponential increase in population in many cities globally, posing a challenge in managing and controlling traffic. According to the National Transport and Safety Authority of Kenya, in the year 2020, 134,000 crashes led to 3600 fatalities. During peak hours of traffic, Kenya's average city resident wastes two litres of fuel in traffic daily. Traffic jams result in wastage of time with an average motorist using almost an hour daily. They cause fuel wastage and environmental pollution as a result of the emission of greenhouse gases that cause global warming. Pollution has a devastating effect on human beings, animals, and plants around us. IoT technology is best suited for tackling the problem of traffic management and control in the city. This paper will focus on the design and development of IoT based real-time monitoring framework for the city that also incorporates the use of remote sensing technology. The proposed system has an advantage over other existing methods because it is easy to design, develop and implement; it will reduce the amount of time spent in traffic, will lower the consumption of fuel and the number of fatalities and accidents on the roads.

I. Introduction

The major problem cities face having an effective real-time traffic monitoring system. IoT technology can monitor and learn the patterns of traffic in specific areas such as cities. RFID and RSU can be used to collect information about traffic density from various lanes on the highways, and this data which is in real-time, is stored in a central database. RSU is a dedicated short-range communication unit (DSRU) that is strategically placed on the sides of highways. DSRC serves as a gateway between the communication infrastructure and OBU (on-board Unit). The RSU contains of a microcontroller with an IP smart camera affixed to it. The IP camera takes the photo images of the vehicles in real-time, then through the process of image processing, it takes the information on the running time of the traffic lights and eventually computes the vehicles speed. The information about the speed at which a vehicle should move at in order to pass the traffic lights without any further delay is provided by a mobile interface developed using HTML5.

Ii. Experimental

According to [1], a system based on real-time intelligent vehicle monitoring using IoT is implemented. The system also provides for real-time tracking of vehicles using IoT, RFID, and cloud computing. This system is accountable for the provision of real-time information about the traffic timings. This helps in calculating the distance covered by using Global Positioning System technology and hence the speed of the vehicle can be calculated. This system is essential because it minimizes road fatalities and accidents by notifying all the drivers when they have exceeded certain speed limits.

According to [2], Traffic status queries in real-time for intelligent traffic systems were modelled using PEPA, IoT, and TOPSIS. By using performance evaluation process algorithm methods, a real-time query

status in the intelligent traffic system can be processed, and performance analysis can also be done. The status of traffic in real-time is obtained and can be used to optimize the process.

According to [3], the authors have focused on an Intelligent Traffic Management System (ITMS) and the graph theory. The model proposed here has many nodes that are used in collecting information from all the city roads. The ITMS helps motorists reach their destinations safely by using the shortest optimal routes with less traffic.

According to [4], they have proposed a smart traffic lights management and control mechanism based on distributed multi-agent Q learning. The system will use both non-motorized and motorized to optimize the traffic lights control within a city. The system also provides solutions for pedestrians' queue length and the waiting time at highway intersections.

According to [5], an urban intelligent traffic management mechanism using both IoT and cloud-computing has been used to solve the problem traffic congestion problems that have limited cities' development. The system manages the traffic situation in the cities intelligently by use of ISR (intelligent service request) and RSS (response scheduling strategy.

According to [6], they have proposed a model of tackling the issue of traffic jams and making roads free from vehicle obstruction. This makes roads clear to pave the way for emergency vehicles such as police vehicles, ambulances, and fire brigades. The model proposed includes the management of traffic signals using RFID tag and reader, Raspberry Pi, and Node MCU. When there is an incoming emergency vehicle, the traffic light signal changes instantaneously by accurately communicating with the vehicle's sensors.

According to [7], an intelligent traffic management system based on IoT is implemented with the RSU, central database, mobile interface, and environmental sensors. The system is crucial in providing information on all the traffic light signals that are far ahead and the minimum speed at which the vehicles should accelerate in order to pass the traffic lights faster with minimal or no further delay. The proposed system helps in reducing fuel consumption, prevent accidents, and saves on time.

According to [8], a system on intelligent parking system based on IoT that uses image processing algorithms has been proposed. The system is accountable for all the information that concerns image processing of all images that are captured by the roadside unit and then sent to the central server. The proposed system helps in reducing vehicle theft, ensures efficiency in parking, and decongest the city roads.

According to [9], an intelligent vehicle monitoring system based on IoT framework, machine learning, correlation methods, and emergency detection is proposed. The proposed system provides a review on selection filters that are based on fast based correlation feature algorithm and correlation measurements which are widely used in increasing industrial facilities by intelligent networks based on IoT.

According to [10], a secure traffic management and control system for all emergency vehicles using internet of things technology is proposed. The system entirely uses hacking traffic signals. IoT helps

maintain the steadiness of the traffic signals using intelligent transport systems for all the incoming emergency vehicles, it also aids at least all the emergency vehicles to reach their preferred destination without any delay. The system also helps reduce traffic jams.

Iii. Methodology

Road Side Unit has been commonly used to make communication much easier between transportation infrastructure, vehicles, and other physical devices. The data is transferred to the RSU by complying with the industry standards. Besides the roadside unit, the vehicles are also equipped with other sensors used to measure the vehicle's external surroundings. The system basically involves collecting data from the vehicles and the road side unit and then provides information to all end users by the use of a mobile interface.

The roadside unit is deployed on all major roads of the city. The RSU comprises a microcontroller that has an IP smart camera affixed to it. This IP camera takes real-time image photos of the traffic lights and their respective timers. Thereafter, the RSU performs a quick scan in accordance with a specified algorithm in the embedded microcontroller and then sends the generated traffic data to a centralized database. Radio frequency identification unit will be deployed to each vehicle and equally, the RFID tags will also be installed at every traffic signal. Active RFID tags will be used because they can communicate wirelessly. The RFID tags are used to precisely identify the vehicles. The readers automatically detect the active RFID tags that are placed in the vehicles, then the traffic data collected is sent to the database.

The following happens at the central database server; the scanned images from the roadside unit are first received. The traffic lights timings are extracted, and a processing time of between five to ten seconds is added to the extracted time before being updated and stored sequentially in a central database server.HTML5 is used to develop a mobile interface that all end-users will use in accessing all the real-time information about the city's traffic lights status. The mobile interface has the capacity to show all the locations where the RSU has been deployed in every traffic signal. The information is shown in a pattern of dots. An end-user who wants to recognize the traffic light situation on a particular road has to click a specific dot. The dot will pop-up and provide the required information to the end-user. When a vehicle using HTML5 Interface needs to access information on a distinct traffic signal, a timestamp affixed to every vehicle helps the vehicle find the actual distance between the traffic signal and the vehicle by use of the Global Positioning System technology.

Since the proposed system can provide the required real-time information regarding the traffic light signal, the PEPA algorithm helps track real-time traffic information, and the exact distance will be computed using the Global Positioning System technology. Once the distance and time has been obtained, the speed can be calculated using this formula $speed = \frac{distance}{time}$, this provides the speed at which the vehicle can accelerate to cross a highway junction without any delay. The speed also helps to determine the time-based optimal shortest path or distance-based optimal shortest path, and the end-users have the freedom to choose any shortest path. This means the proposed system provides these three crucial

information; the speed required to accelerate to cross the highway junction, information regarding the traffic light signals, and alerts to end-users when to slow down on a highway.

The proposed system also aids in finding the traffic density of the vehicles on roads and highways; this is done by retrieving all the information from the installed radio frequency identification units. The highway or road with higher vehicle density will be marked colour red; this will depend entirely on the traffic data from the central server that the RFID unit has collected. The active RFID tags that the RFID readers have captured will specify the roads with more traffic density. The images captured by the smart camera and regularly updated to the central system will also indicate the traffic density of a particular road or highway. This collected information from both the RFID and camera is stored as a dataset. Machine learning algorithms can be used to detect and predict any road's traffic density by using the collected dataset anytime an end-user requires the information.

These are the components required for the proposed system

- Central database server
- Sensors and active RFID tags
- GPS technology
- Roads Side Unit

Iv. Discussion

Many city residents have to endure traffic jams, which results in numerous hours spent on the road during peak hours. Traffic jams also cause unnecessary consumption of fuel that leads to wastage. Accidents that occur in the traffic signals are majorly caused by human negligence and motorists' urgency to ignore the traffic signals. The RSU module is used to collect information on the existing road conditions and the weather conditions in the area where it is deployed. The RSU also captures the information showing the traffic density patterns across major roads and stores the information in the central database server. By using the PEPA algorithm, the system can be modelled to expedite the processing of the real-time status of any traffic query in an intelligent transport system (ITS). All end-users using HTML5 mobile interface can access the required information about the road conditions and the weather pattern on a particular day. In the proposed system HTML5 mobile interface has the sole purpose of displaying real-time information showing the traffic lights signals' status to all road users.

V. Conclusion

The Smart traffic management and control system based on IoT enables many end-users to access real-time information on the roads' traffic density status. The system has a roadside unit with a microcontroller with an IP smart camera affixed to it. The proposed system uses the current technology that is cost-effective, consistent, and reliable. The system is also scalable and can be modified in the near future by any existing technology. Implementing this system will cause rapid changes in the management

and control of traffic by reducing traffic jams on the roads. The system will reduce road fatalities and accidents, and finally, the system will help motorists in efficient use of fuel due to reduction in traffic jams.

Declarations

DATA AVAILABILITY

Data sharing not applicable to this article as no datasets were generated or analyzed during the current study.

CONFLICTS OF INTEREST

The authors declare that they have no conflict of interest.

AUTHORS' CONTRIBUTION

Dominic was involved in writing of the manuscript, which included the introduction, literature review, discussion, conclusion, and acknowledgment.

Nallanthighal Raghava was involved in conceptualizing the methodology, review, editing, and final approval of the manuscript.

ACKNOWLEDGMENT

We will like to acknowledge Delhi Technological University for the access they gave us to the IEEE repository to acquire related papers for this proposed system.

References

[1] Sarika B. Kale, Gajanan P. Dhok "Design of Intelligent Ambulance and Traffic Control", International Journal of Innovative Technology and Exploring Engineering (IJITEE) ISSN: 22783075, Volume-2, Issue-5, April 2013.

[2] B. Jan, H. Farman, M. Khan, M. Talha, and I. U. Din, "Designing a smart transportation system: an internet of things and big data approach," *IEEE Wireless Communications*, vol. 26, no. 4, pp. 73–79, 2019.

[3] Laisheng Xiao, Zhengxia Wang*, Internet of Things: a New Application for Intelligent Traffic Monitoring System* JOURNAL OF NETWORKS, VOL. 6, NO. 6, JUNE 2011.

[4] L. Foschini, T. Taleb, A. Corradi, and D. Bottazzi, "M2M based metropolitan platform for IMS-enabled road traffic management in IoT," *IEEECommunicationsMagazine*,vol.49, no. 11, pp. 50–57, 2011.

[5] ShaoHuaGang, ChengJin, WangHui, etc. "The system and middleware design face to IOT," in Computer engineering, vol. 4, 2010,pp: 84-86.
[6] Intelligent Traffic Light System to Prioritized Emergency Purpose Vehicles based on Wireless Sensor Network", by Amnesh Goel, Sukanya Ray, Nidhi Chandra International Journal of Computer Applications, 2012.

[7] L. Da Xu, W. He, and S. Li, "Internet of Things in Industries: A Survey," IEEE Trans. Ind. Informatics, vol. 10, no. 4, pp. 2233–2243, Nov. 2014.
[8] Ni, W. Wu, K. Li," A message efficient intersection control algorithm for intelligent transportation in smart cities," Future Generation Computer Systems, 2016.

[9] Laisheng Xiao, Zhengxia Wang*, Internet of Things: a New Application for Intelligent Traffic Monitoring System* JOURNAL OF NETWORKS, VOL. 6, NO. 6, JUNE 2011.
[10] B. Jin, D. Zou and Y. Gan, "Research and design of traffic detection based on GPS", IEEE conf. on advanced computer control (ICACC), (2010) March.

[11]The system architecture https://github.com/apoorvt95/SMTS

Software Reliability Prediction Using Various Ensemble Methods

Rohit Prasad, Abhishek Kumar, Perdun Kumar Mandal

Department of Computer Science and Engineering
Delhi Technological University
New Delhi, India

Abstract**—***Softwares covers an important aspect of human life today. A normal human being is surrounded by considerable amounts of softwares in his day-to-day life requiring it for all of his basic needs and activities pertaining to their survival. Moreover, our country has also been digitized by the Honourable Prime Minister of India through his Digital India Initiative famously known as "Digital India".Thus the demand for effective software systems has also increased. Most of the industries in various disciplines depend on computer software for their basic functioning. Thus the software companies need to deliver reliable and quality software on time. Reliability is treated as the key factor for the quality of a software system. A number of researches has been performed on software quality management reliability estimation. The objective of this paper is to use the ensemble methods and different machine learning techniques for software reliability prediction and evaluating them on the basis of selected performance criteria. In this paper Software Reliability modelling based on test data is done to estimate whether the current reliability level is up to mark of requirement for product. Software Reliability Modelling also helps to predict the reliability of different modules in the software.*

In this paper we used different ensemble methods on different machine learning techniques and studied performance using bagging, Adaboosting and Stacking. Using Ensembling a module in a software can be classified as having faults or not on the basis of certain attributes of software module and prediction of next failure in a software using the mean time between failure.

Keywords**—***Softwares, Digital India, Review and synopsis, Software Reliability Prediction, Ensemble methods, Machine Learning, Ada-boosting, Stacking, Bagging, faults, failure.*

1. INTRODUCTION

A software is something or we can say a product which is penetrating vigorously into our daily lives. Most of the day-to-day systems and activities are now driven by a lot of softwares. It has become a crucial part of critical and non-critical applications of many aspects of society, some of them of which probably are telecommunications, web teaching, home appliances, auditing, shopping, personal entertainment, airplanes, automobiles and so on. In particular, science and technology demand high-quality software for making improvements and breakthroughs and for delivering useful outputs. Most of the systems are now driven by software. Using software and its services has become a basic need for nearly 51% of the urban population of the country and will reach upto 66% of the total global population by 2023 as predicted by Cisco annual report(2018-2023)[1]. Also the size and complexity of software systems have grown drastically during the past few decades, and the trend will undeniably continue in the future. Previous researches show that size of the software for various systems and applications has been growing exponentially for the past 40 years[2]. Because of this accelerating dependency, software failures can lead to serious, even fatal, consequences in safety-critical systems as well as in normal business. Previ-

ous software failures have diminished several high- visibility programs and have led to deprivation of businesses.

So evaluation, assurance and prediction of the quality of the software becomes an issue of critical concern. A software firm or a company must check the quality and performance of their software products before its final launch and delivery to end customers otherwise they may face several consequences or losses like the product may not survive in the market for long. In short, the software product should be reliable. Thus software quality assurance becomes an important feature to consider. Out of all software quality attributes such as reliability, availability, safety, security, and performance, software reliability is generally considered as the most important factor[3]–[6]. A software should be reliable for qualifying as a high quality software[7]. It quantifies software faults and failures, which can lead to serious consequences in safety-critical systems as well as in normal business[2].Therefore predicting software reliability is increasingly demanded in large, medium as well as small sized projects in order to achieve highly reliable and functional software systems.

Reliability of a software specifies the probability of failure free operation of the software for a given time duration in a given environment for a predefined number of input cases, assuming that the hardware and the input are free of errors. Software Reliability is a dynamic system characteristic which can be characterized as a function of the number of software or system failures(presence of faults) that are encountered and reported during the functioning of the software within the given time period. A failure is an execution event where the software behaves unexpectedly. Failure is something that has to be executed, i.e., it is self dynamic in nature. Thus, more is the failure rate, less will be the reliability of the software. Not all software faults have equal probability of manifestation/execution. Removing software faults from those software faults which are rarely used makes little improvement in reliability. Failure of a software depends on two factors: Number of faults being evaluated in software, and, the operational profile of execution of software.

In this research paper, we have evaluated the functioning of different machine learning techniques and algorithms for Software Reliability Prediction on three ensemble methods and successfully noted the effectiveness and accuracy and error in each of the ensemble methods and tried to find out the best fit model for reliability prediction with greater accuracy and least error rate. The remaining part of this paper is arranged as follows: Section II describes the ensemble techniques used such as bagging, boosting, stacking, etc. Section III describes the Machine Learning Techniques used and applied on the software prediction models like the ANN, KNN, Linear Regression, Decision Trees, etc. The list of tables and figures and dataset, results and the Conclusion isdescribed in the sections IV, V and VI respectively.

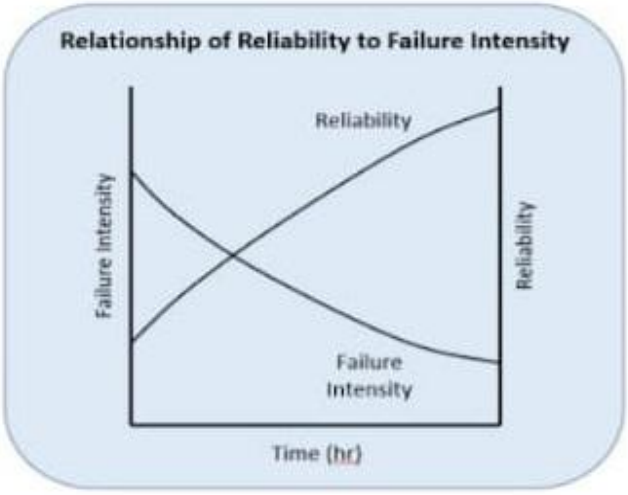

Figure 1. Reliability and Failure Intensity

1.1 Software Reliability Growth Model :-

Software Reliability Model is classified into two models, the static and the dynamic model. In static models, the modelling and analysis of the logic of the program is done on the same code. In dynamic models, the debugging process is carried out temporarily and synchronously during the testing phase. A model describing the error detection in Software

Reliability is known as Software Reliability Growth Model[8].

The Software Reliability Growth Model's Characteristics are as follows:-

- SRGM can be viewed as a product of a cumulative density function and a positive constant.

$$H(t) = a\left[1 - exp\left(-\int_0^1 f(x)dx\right)\right] = aG(t)$$

Here H(t) is a mean value function.

G(t) is Cumulative Density Function.

- The fault detection rate must be finite; G(t) must meet the condition that the corresponding failure rate function is finite.

$$h(t) = d(t)[a - H(t)] = ag(t)$$

where g(t)=dG(t)/dt is the probability density function(pdf) associated with G(t).

$$d(t) = ag(t)\frac{ag(t)}{a-aG(t)} = \frac{g(t)}{1-G(t)} = r(t) \text{.....(1)}$$

Where r(t) is the failure rate function associated with G(t). h(t) is intensity function. Since the fault detection rate must be finite, G(t) must meet the condition that the corresponding failure rate function is finite.

- We need to represent appropriately the right tail of g(t) behaviour to achieve a good reliability prediction. The right tail of SRGM associated with g(t) should be heavy. All these Characteristics should be satisfied for the Software Reliability Model[9].

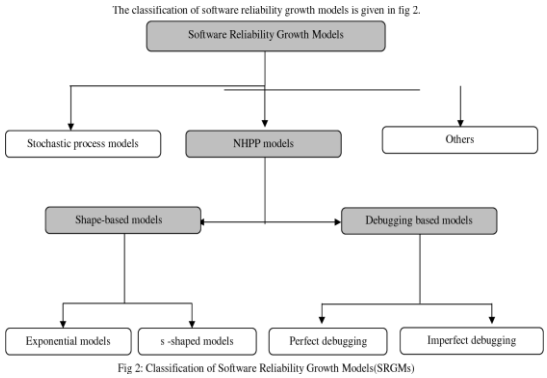

Figure 2: Classification of Software Reliability Growth Model[10]

1.2 Non-Homogeneous Poisson Process :-

Non-Homogeneous Poisson Process(NHPP) models are also termed as fault counting models and can be either finite failure or infinite failure models, depending on how they are specified. These models are useful for both the calendar time data as well as the execution time data[11].

Some Features of NHPP model:-

- A process which follows Poisson distribution with a time-dependent failure rate is called NHPP.
- Based on NHPP assumptions.
- Widely used by practitioners because they can be applied to hardware systems as well.
- Poisson distribution is suitable for modelling rare and random events such as failure of telephone calls.
- If NHPP can be assumed both for hardware and software systems, it becomes easier to find system reliability.

Basic Assumptions of NHPP models:-

- A software system is subject to failure at random times caused by software faults.
- There are no failures at time t=0.

- The probability that a failure will occur in a small interval 'h' is (t)h + 0(h), where (t) is instantaneous failure intensity.
- The probability that more than 1 failure will occur in a small interval 'h' is 0(h).This means that there is little chance of more than 1 failure occurring at small intervals of time.
- The expected number of failures during any time 't' to 't+t' is proportional to expected number of undetected faults at time 't'.
- The mean value function is also assumed to be bounded non-decreasing function of time in case of finite failure model such that:

$$\lim_{t\to\infty} u(t) = N < \infty$$

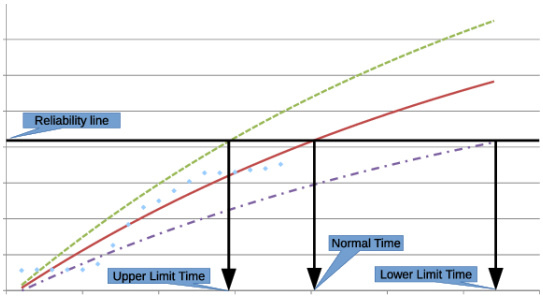

Figure 3: Time ranges based on NHPP model.

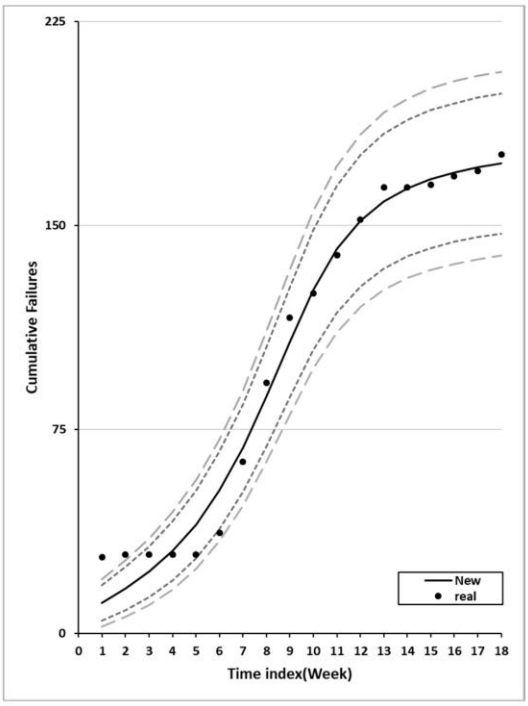

Figure 4: Time vs failure graph for NHPP model.

2. ENSEMBLE TECHNIQUE USED

2.1 Bootstrap Aggregating (Bagging)

It is a method to train a lot of decision trees on a data set to reduce the variance, increase stability and improve accuracy which in turn removes challenges of over-fitting.

Bootstrap aggregating, often abbreviated as bagging, involves having each model in the ensemble vote with equal weight. To promote model variance, bagging trains each model in the ensemble using a randomly drawn subset of the training set. As an example, the random forest algorithm combines random decision trees with bagging to achieve very high classification accuracy.

Example: We are given a training Data set T whose size is m, by using bagging it generates n new Training sets in which each has a size of mi by sampling from the trained data set D and replacement if m=mi then for large m Di have 63.2% of unique examples of D, the rest are duplicates. This type of sample is known as bootstrap sample.
Bagging can also degrade the performance of some stable algorithms such as k-nearest neighbours.

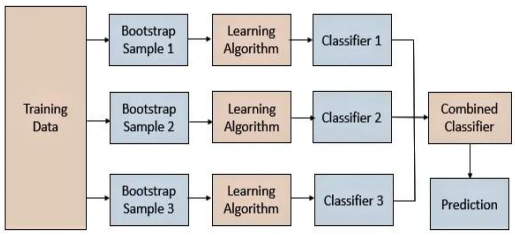

Figure 5. Bagging Model

2.2 Boosting

Boosting involves incrementally building an ensemble by training each new model instance to emphasize the training instances that previous models' mis-classified. In some cases, boosting has been shown to yield better accuracy than bagging, but it also tends to be more likely to overfit the

training data. By far, the most common implementation of boosting is Adaboost, although some newer algorithms are reported to achieve better results. In this work Adaboost algorithm is used to improve the accuracy of the weak classifiers. A boosting algorithm create an ensemble of classifiers, each one gives a weighted vote.

Boosting algorithm improves prediction power by training weak models, in which each weak model compensates for the weakness of its previous weak model. It is a generic model rather than a specific model.

Ada-boost was the first successful boosting algorithm developed for binary classification.

Algorithm:

i. Initialise the dataset and assign equal weight to each of the data points.

ii. Provide this as input to the model and identify the wrongly classified data points.

iii. Increase the weight of the wrongly classified data points.

iv. if(got required results)

    1. Goto step 5

v. else

    1. Goto step 2

vi. End

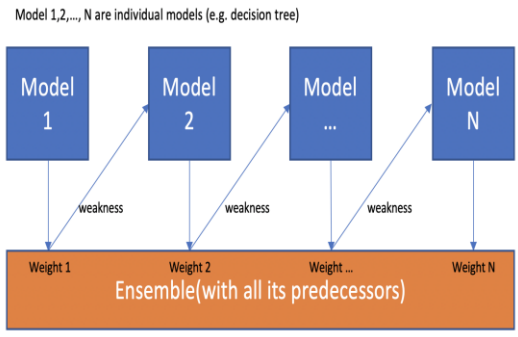

Figure 6. Boosting Model

2.3 Stacking

Stacking (sometimes called stacked generalization) involves training a learning algorithm to combine the predictions of several other learning algorithms. First, all the other algorithms are trained using the available data, then a combiner algorithm is trained to make a final prediction using all the predictions of the other algorithms as additional inputs. If an arbitrary combiner algorithm is used, then stacking can theoretically represent any of the ensemble techniques described in this article, although, in practice, a logistic regression model is often used as the combiner. The stacking model is represented as shown in Fig. 7 and Fig. 8.

Stacking is used to explore different models for a single problem. It is called Stacking because the final model is stacked on top of different models. This improves the overall performances as the final model is better than all other individual models.

How Stacking works:

i. The training data is divided into k-folds.

ii. In the k-1 part the base model is fitted and for the k-th part we make predictions.

iii. This is done for each part in training data.

iv. Base model is shaped into the whole train set and we calculate the test set performance.

v. Step 2,3,4 is repeated for every other model.

vi. The prediction of the initial set serve as a feature for 2nd level model.

vii. The prediction on the test set is made by using a 2nd level model.

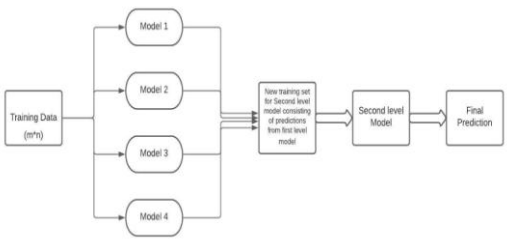

Figure 7. Stacking Model

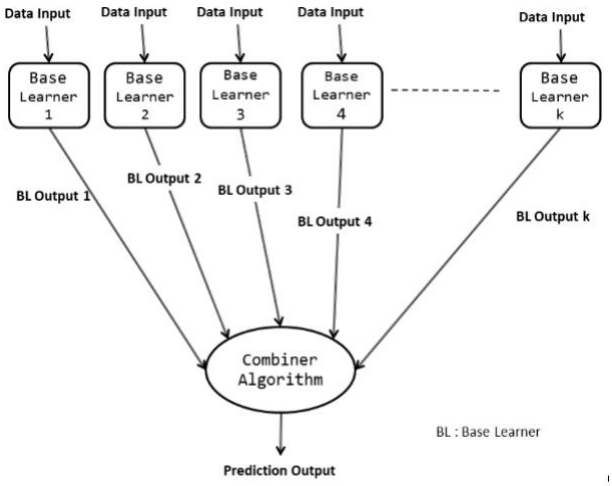

Figure 8. Stacking Model

2.4 Bayesian Parameter Averaging

- It is an estimate or new predicted observation which we get by averaging results of different models which we have used and in which each is weighted by its model probability.
- Conventionally after analysis we select the best model according to different parameters and then we learn about the parameters of the finalised model.
- But in this approach the uncertainty about the model-selection process is ignored. We can alternatively first learn the parameters of all models and then estimates can be combined by posterior probabilities of associate models.
- The above discussed approach is known as the Bayseian model averaging or the BMA.

Advantages of BMA:

- BMA reduces overconfidence as it does not ignore the uncertainties of the models.
- In case of logarithmic loss function or squared error loss the BMA predictions are most optimal.
- BMA is comparatively robust to model failure.

3. MACHINE LEARNING TECHNIQUES USED

3.1 Linear Regression

The linear model assumes the relation between features and target vector as approximately linear. Mathematically, it can be represented by equation:

$$y=mx + c + E$$

Here, y : target, x : data for a single feature, m and c are coefficients identified by fitting the model and E: error. The aim is to match the values of m and c to establish better relation between variable x and variable y.

Working:

We take a tuple from data set and enter the input to equation and predict the expected values. Now calculate the loss using a loss function. Also keep updating m(variance) and c(bias) to minimize the error. The loss function used is mean squared error.

Mathematically:

$$\sum_{i=1}^{n}\left(actual_{output} - predicted_{output}\right)^2$$

Equation of bias and variance are:

$$b_0 = \bar{y} - b_1\bar{x}$$

$$b_1 = \frac{\sum_{i=1}^{n}(x_i - \bar{x})\,(y_i - \bar{y})}{\sum_{i=1}^{n}(x_i - \bar{x})^2}$$

We update the values of m and c as:

$$m = m - \alpha\frac{d}{dm}(Error)$$

$$c = c - \alpha\frac{d}{dc}(Error)$$

When the model gets trained for minimum error, we fix bias and variance.

3.2 Logistic Regression

Logistic Regression produces results in a binary format which is used to predict the outcome of a categorical dependent variable. So the outcome should be discrete/categorical. The value of Y in logistic Regression is between 0 and 1, the linear line is clipped at 0 and 1.

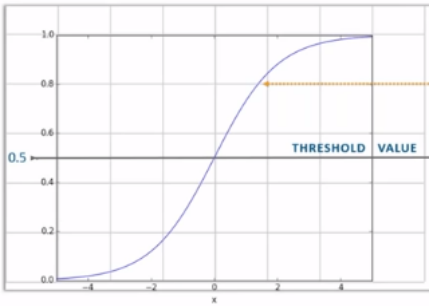

Figure 9: Logistic Regression Curve

Here the threshold value indicates the probability of winning or losing.

Logistic Regression Equation:

$$Y = b_0 + b_1x_1 + b_2x_2 + b_3x_3 + \ldots\ldots + b_nx_n$$

To limit the value of Y to 0 and 1, we divide the above equation by (1-y) and take logarithmic of the equation:

$$log\left(\frac{y}{1-y}\right) = b_0 + b_1x_1 + b_2x_2 + b_3x_3 + \ldots\ldots + b_nx_n$$

Above one is the final Logistic Regression Equation.

3.3 Support Vector Machine

This model is generally used for performing classification tasks using a multidimensional space. In this, the example is represented as points in space that we map so that the points of different categories are as wide as possible.

3.4 Ridge Regression

It is one of the types of special linear regression models. Ridge regression contracts coefficients and reduces model complexity and multi-collinearity. In Ridge regression function is altered by adding a penalty value.

$$\sum_{i=1}^{M}(y_i - \bar{y})^2 = \sum_{i=1}^{M}\left(y_i - \sum_{j=0}^{p} w_j * x_{ij}\right)^2 + \lambda\sum_{j=0}^{p} w_j^2$$

Lower the value of, the model will resemble the Linear Regression Model.

3.5 Lasso Regression

It is a special type of linear regression model. It reduces over-fitting and also helps us in feature selection. The cost function for lasso regression is:

$$\sum_{i=1}^{M}(y_i - \bar{y})^2 = \sum_{i=1}^{M}\left(y_i - \sum_{j=0}^{p} w_j * x_{ij}\right)^2 + \lambda\sum_{j=0}^{p}|w_j|$$

For some t > 0, $\sum_{j=0}^{p}|w_j| < t$

3.6 Elastic Net Regression

It is combination of both Lasso and Ridge regression model into one model with two penalty factors , one is proportional to L1 norm and other is proportional to L2 norm.

3.7 ANN

From speech recognition to marketing and from healthcare to face recognition neural networks are widely used. Deep Learning uses Artificial Neural Networks which mimic the behaviour of the human brain to solve complex data driven problems. A neural Network works when some input data is given to it. The data is processed using layers of Preceptors to produce the output we require. Some real-world applica-

tions of ANN: self-driving cars are being perfected with the help of Neural Network. MuseNet, a Deep Neural Network that can generate 4-minute musical compositions with 10 different instruments.

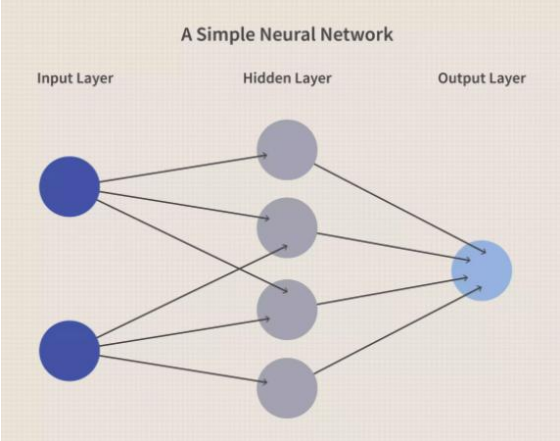

Figure 10:Simple Neural Network

3.8 KNN

K Nearest Neighbour is a simple algorithm that stores all the available cases and classifies the new data or case based on similarity measure.

Industrial application of KNN algorithm

1. Recommender system: In amazon when we search for a product in result it also shows relevant products.
2. Concept Search: Like an ocr and image search.

Example of KNN algorithm:

For predicting the T-shirt size for data H:161cm, W:61kg find out the Euclidean Distance from each Points, here value of k is 5 so find 5 nearest neighbours of the point, 4 points have size=M and 1 have size=L so the t-shirt size predicted is **M**.

Table 1. KNN example

S.NO	HEIGHT(CM)	WEIGHT(CM)	T Shirt Size	Euclidean Distance	Minimum Euclidean Distance
1.	158	58	M	4.242	
2.	158	59	M	3.605	
3	158	63	M	3.605	
4.	160	59	M	2.236	4
5.	160	60	M	1.414	1
6.	163	60	M	2.236	3
7.	163	61	M	2	2
8.	160	64	L	3.162	5
9.	163	64	L	3.605	
10.	165	61	L	4	
11.	165	62	L	4.123	
12.	165	65	L	5.656	
13.	168	62	L	7.071	
14.	168	63	L	7.280	
15.	168	66	L	8.602	
16.	170	63	L	9.219	
17.	170	64	L	9.486	
18.	170	68	L	11.401	

3.9 Naive Bayes Classifier

It is a classification technique based on Bayes theorem. Assumes that the presence of a particular feature in a class is unrelated to the presence of any other feature. Some of the industrial use of Naive Bayes Classifier are :-

1.)News Categorization

2.) Spam Filtering

3.) Object and face recognition

4) Medical Diagnosis

5) Weather Prediction.

These are the steps involved in naive Bayes:

Step 1: Handling Data

Step 2: Summarizing Data

Step 3: Making a predictions

Step 4: Making all predictions

Step 5: Evaluate Accuracy

Step 6: Tying all together

3.10 Random Forest

Random forest developed by Leo Breiman[12] is a group of un-pruned classification or regression trees made from the random selection of samples of the training data. Random features are selected in the induction process. Prediction is made by aggregating (majority vote for classification or averaging for regression) the predictions of the ensemble.

It is a model which is used by operating Many Decision Trees during the training phase. For choosing the final decision the decision of majority decision Trees are chosen.

Why Random Forest is used:

i. No overfitting: because we use multiple trees it reduces the risk of overfitting upto a great extent.
ii. It runs very accurately on large databases.
iii. Random Forest can be used to Estimate missing data.

Applications of Random Forest:

i. Remote sensing

ii. Object detection

iii. Kinect: it is a gaming console that tracks the body movement and recreates it in a game.

Each tree is grown as described in[12]:

i. By Sampling N randomly, If the number of cases in the training set is N but with replacement, from the original data. This sample will be used as the training set for growing the tree.
ii. For M number of input variables, the variable m is selected such that m << M is specified at each node, m variables are selected at random out of the M and the best split on these m is used for splitting the node. During the forest growing, the value of m is held constant.
iii. Each tree is grown to the largest possible extent. No pruning is used.

Random forest generally exhibits a significant performance improvement as compared to single tree classifiers such as C4.5. The generalization error rate that it yields compares favourably to Ada-boost, however it is more robust to noise.

3.11 Decision Tree

Decision Tree is a decision support tool that uses a tree-like graph or model of decisions and their possible consequences, including chance event outcomes, resource costs, and utility. It is one way to display an algorithm that only contains conditional control statements. It is the graphical representation of all the possible solutions to a decision. The Decisions are based on some conditions. Decisions made can be easily explained.

Example of decision tree:-

Day	Weather	Temperature	Humidity	Wind	Play?
1	Sunny	Hot	High	Weak	No
2	Cloudy	Hot	High	Weak	Yes
3	Sunny	Mild	Normal	Strong	Yes
4	Cloudy	Mild	High	Strong	Yes
5	Rainy	Mild	High	Strong	No
6	Rainy	Cool	Normal	Strong	No
7	Rainy	Mild	High	Weak	Yes
8	Sunny	Hot	High	Strong	No
9	Cloudy	Hot	Normal	Weak	Yes
10	Rainy	Mild	High	Strong	No

Figure 11. Decision Tree example

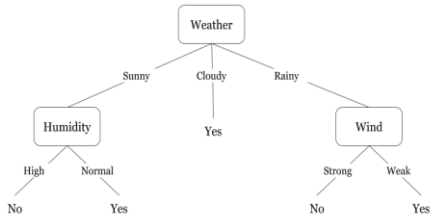

Figure 12: Decision tree

4. DATASETS USED

This section describes about the two dataset that is used in this proposed work. In this section, it is described about the two-benchmark datasets that have been used in this proposed work. Many standardized published works have been done on these datasets and statistical error measures are available.

For prediction of time of failure, dataset used: Musa, J.D: Software reliability data, IEEE Computer Society Repository(1979), Raj and Kiran: Software reliability data (2008), Iyer and Lee Software reliability dataset (1996).Failure data during system testing phase of various projects collected at Bell Telephone Laboratories, Cyber security and Information Systems Information Analysis Centre(CSIAC) by John D. Musa are considered.

For classification, the software reliability classification dataset used : Source : NASA, then the NASA Metrics Data Program, http://mdp.ivv.nasa.gov. Mike Chapman, Galaxy Global Corporation.

1. loc : McCabe's line count of code
2. v(g) : McCabe's "cyclomatic complexity"
3. ev(g) : McCabe's "essential complexity"
4. iv(g) : McCabe's "design complexity"
5. n : Halstead total operators + operands
6. v : Halstead "volume"
7. I : Halstead "program length"
8. d : Halstead "difficulty"
9. i : Halstead "intelligence"
10. e : Halstead "effort"
11. b : Halstead value
12. t : Halstead's time estimator
13. IOCode : Halstead's line count
14. IOComment : Halstead's count of lines of comments
15. IOBlank : Halstead's count of blank lines
16. IOCodeAndComment : IO lines
17. uniq_Op : unique operators
18. uniq_Opnd : unique opearnds
19. total_Op : total operators
20. total_Opnd : total operands
21. branchCount : of the flow graph
22. prediction : {false,true}module has one or more reported defects or not

5.RESULTS

In this work of Software Reliability Prediction we used a different Machine Learning Prediction Algorithm. While working on the actual data both Ridge regression and Bayesian Ridge regression perform better together on both the datasets. The performance was found to be better compared to the existing algorithms on the Normalized Root Mean Square Error values(NRMSE). After interpolating some points some models like K-nearest neighbours(KNN), Artificial Neural Network(ANN) perform better. As a whole we observed, logarithmic scaling was an important factor in the improvement of the model performance because of uneven distribution of data values and the time series datasets having peaks at certain points. As we observed that when the lag length was between 7 and 11 Ridge, Bayesian Ridge, Radial Basis Function Network regressors gave the best result. Random Forest, Artificial Neural Network(ANN) regressors give their best while increasing the lag length but on the actual dataset.

So for Prediction of time of failure we use a Dataset from IEEE computer Society Repository namely Musa, J.D: Software Reliability Data.

Different accuracies and confusion matrix obtained on the testing dataset, by several machine learning algorithms like ANN, KNN, Decision Tree algorithm for bagging method are shown in TABLE 2.

Table 2. Bagging Accuracy(in %) for different machine learning algorithms along with the confusion matrix.

Model	Accuracy	Confusion Matrix
Random Forest	95.87	255 71 16 1767
ANN	89.81	149 177 38 1745
KNN	88.48	135 191 52 1731
Decision Tree	96.68	280 46 24 1759
SVM	88.90	97 229 5 1778
Logistic Regression	86.25	74 252 38 1745
Naïve Bayes	82.50	122 204 165 1618

Stacking is used to explore different models for a single problem. It is called Stacking because the final model is stacked on top of different models. This improves the overall performance as the final model is better than all other individual models. The stacking accuracy for different machine learning algorithms under the stacking ensemble method are shown in TABLE 3.

Table 3. Stacking Accuracy(in %) for different machine learning algorithms for three values of k.

Model	K = 7	K = 9	K = 11
Random Forest	85.15	86.57	85.15
KNN	84.67	86.09	85.78
Decision Tree	84.36	83.57	84.04
SVM	84.83	85.15	83.72
Logistic Regression	84.04	85.93	85.3

Naïve Bayes	84.2	83.57	84.044

Reliability prediction for ada-boost ensemble method was performed using Logistic regression, Naive Bayes, and KNN machine learning algorithms for different values of k and the results obtained is shown in TABLE 4.

Table 4. Individual and Boosted Ada-Boost Accuracy(in %) for different machine learning algorithms.

Model	Logistic Regression	Naïve Bayes	KNN
K = 9	**Ind:** 86.30 **Boosted:** 86.15	**Ind:** 82.74 **Boosted:** 82.36	**Ind:** 89.76 **Boosted:** 91.84
K = 11	**Ind:** 86.58 **Boosted:** 86.30	**Ind:** 82.84 **Boosted:** 82.46	**Ind:** 89.33 **Boosted:** 92.65
K = 13	**Ind:** 86.44 **Boosted:** 86.15	**Ind:** 82.65 **Boosted:** 82.55	**Ind:** 89.38 **Boosted:** 92.70
K = 15	**Ind:** 86.44 **Boosted:** 86.20	**Ind:** 83.03 **Boosted:** 82.46	**Ind:** 88.90 **Boosted:** 91.75

There is no software that is purely perfect or error-free. It is not possible for a software to have 100% accuracy. There always are some errors that resides. So we have also calculated the mean square errors tested for bagging prediction and stacking prediction under various machine learning models which is shown below in TABLE 5.

Table 5. Mean Square Errors(in %) of different algorithms for bagging prediction and stacking prediction.

Model	Bagging Prediction Result	Stacking Prediction Result
Ridge	0.000015	0.001428
Lasso	0.000015	0.001440
Decision Tree	0.000005	0.000480
Random Forest	0.000005	0.001038
SVM	0.016254	1.660045
Linear Regression	0.000014	0.001445
Bayesian Ridge	0.000014	0.001430
Lasso Lars	0.000014	0.001437
Logistic Regression	0.015817	1.773583

6. CONCLUSION

Various machine learning Prediction & Classification algorithms have been used in ensemble learning for software reliability prediction. As we know that in the bagging approach of the classification the output is classified in different class and then the final output with maximum vote is chosen using voting method.

Boosting algorithm improves prediction power by training weak models, in which each weak model compensates for

the weakness of its previous weak model. It is a generic model rather than a specific model. For Binary classification Ada-boost was proven to be the very first successful boosting algorithm.

It is a method to train a lot of decision trees on a data set to reduce the variance, increase stability and improve accuracy which in turn removes challenges of overfitting. This method is useful when a single Model is giving very high variance so to reduce the variance we run the same dataset on multiple models and take the vote count of output. The different model used in this technique were Naive-Bayes, KNN, Logistic Regression, ANN, Random forest.

We are getting very less error rate in prediction problem for prediction. In boosting model, weak machine learning model have been taken and then by Ada-Boost algorithm the accuracy of the model has been improved. In stacking we are combining different base learner algorithm and then predicting the dataset and finally we are using a combiner algorithm to predict the output. All the output value is stored in xlsx file and tableau software is used to visualize the data or the output that we got from the Ensemble method for software reliability prediction. In bagging method of classification, we can see that for k=7 the decision tree gives a highest performance among all other machine learning model. In boosting method, for different value of k the output of KNN model is improved and the accuracy value is increased by maximum 1%. For stacking for different value of k, i.e. 7, 9 or 11 KNN model gives highest accuracy among all.

On linearly interpolated data K-Nearest Neighbours(KNN) and Support Vector Machines(SVM) regressors were performing better which was observed to be the best performance among all the cases in certain lag lengths.

REFERENCES

[1] "Cisco Annual Internet Report - Cisco Annual Internet Report (2018–2023) White Paper - Cisco." https://www.cisco.com/c/en/us/solutions/collateral/executive-perspectives/annual-internet-report/white-paper-c11-741490.html (accessed Nov. 30, 2020).

[2] M. R. Lyu, "Software reliability engineering: A roadmap," *FoSE 2007 Futur. Softw. Eng.*, pp. 153–170, 2007, doi: 10.1109/FOSE.2007.24.

[3] "Software Reliability Characteristics | Download Scientific Diagram." https://www.researchgate.net/figure/Software-Reliability-Characteristics_fig2_228872404/actions#reference (accessed Nov. 29, 2020).

[4] "Quality Assurance » Software Quality Attributes." http://www.qasigma.com/2008/12/software-quality-attributes.html (accessed Nov. 29, 2020).

[5] A. Amin, L. Grunske, and A. Colman, "An approach to software reliability prediction based on time series modeling," *J. Syst. Softw.*, vol. 86, no. 7, pp. 1923–1932, 2013, doi: 10.1016/j.jss.2013.03.045.

[6] M. Palviainen, A. Evesti, and E. Ovaska, "The reliability estimation, prediction and measuring of component-based software," *J. Syst. Softw.*, vol. 84, no. 6, 2011, doi: 10.1016/j.jss.2011.01.048.

[7] "What Makes Software High-Quality? - Shlomi Fish's Homesite." https://www.shlomifish.org/philosophy/computers/high-quality-software/ (accessed Nov. 30, 2020).

[8] L. Shanmugam, "A Comparison of Parameter Best Estimation Method for Software Reliability Models," *Int. J. Softw. Eng. Appl.*, vol. 3, no. 5, pp. 91–102, 2012, doi: 10.5121/ijsea.2012.3508.

[9] R. Jiang, "Required characteristics for software reliability growth models," in *2009 WRI World Congress on Software Engineering, WCSE 2009*, 2009, vol. 4, doi: 10.1109/WCSE.2009.157.

[10] B. John, "A Brief Review of Software Reliability Prediction Models," *Int. J. Res. Appl. Sci. Eng. Technol.*, vol. V, no. IV, pp. 990–997, 2017, doi: 10.22214/ijraset.2017.4180.

[11] R. Lai and M. Garg, "A detailed study of NHPP software reliability models," *J. Softw.*, vol. 7, no. 6, pp. 1296–1306, 2012, doi: 10.4304/jsw.7.6.1296-1306.

[12] J. Ali, R. Khan, N. Ahmad, and I. Maqsood, "Random Forests and Decision Trees," Int. J. Comput. Sci. Issues, vol. 9, no. 5, pp. 272–278, 2012.

Arabian Journal of Geosciences (2021) 14:595
https://doi.org/10.1007/s12517-021-06723-1

ORIGINAL PAPER

Spectral library creation and analysis of urban built-up surfaces and materials using field spectrometry

Dwijendra Pandey[1] · Kailash Chandra Tiwari[2]

Received: 26 March 2020 / Accepted: 16 February 2021
© Saudi Society for Geosciences 2021

Abstract
Hyperspectral remote sensing is useful for the study of urban environment due to its ability to examine the comprehensive spectral characteristics of urban built-up surfaces and materials. This study deals with the creation of a spectral library and statistical analysis of spectral signatures of urban built-up surfaces and materials. Field measurement has been carried out using a spectroradiometer over the wavelength range of 350 to 2500 nm. Further, this study investigates the unique spectral characteristics and complexity of heterogeneous urban environments using mean spectral signatures of major built-up surfaces and materials. The study area belongs to the Udaipur, Rajasthan, India, which is an amalgamation of urban built-up and non-built-up surfaces. The results of the analysis suggest that various built-up surfaces and materials can be identified by investigating different absorption features in different spectral regions of a particular urban built-up class.

Keywords Hyperspectral remote sensing · Spectral library · Built-up surfaces · Engineered surfaces

Introduction

Urban environments characterize only a small percentage of the total land area, but these environments have turned into increasingly populated as larger number of individuals move from rural to urban areas and towns (Lu and Weng 2007; Weng 2012; Weng et al. 2018). A report of United Nations in year 2002 mentioned that urbanization has increased in all over the world, growing from 30% in year 1950 to 47% in 2000, and approximately 60% of the population is likely to reside in the cities by year 2030. Urbanization brings social and economic benefits (e.g., improved quality of life and economic prosperity); it also originates a number of environmental effects, such as degradation in the water quality (Praskievicz and Chang 2009), urban heat island effect, and loss of biodiversity (Xu 2010). Urban environments basically consist of various built-up surfaces, i.e., roads, roofs and pavements, sports infrastructure, and railway tracks as well as non-built-up surfaces, i.e., vegetation, soil, and water. Due to aforementioned major environmental effects, the understanding of urban environment and their spatio-temporal analysis become necessary for urban planning, environmental management, risk assessment, and disaster management. The dynamic behaviors of urban environments demand technologies that are fast and repeatable and offer large areal coverage at a reasonable price, making remote sensing as one of the most feasible technologies (Xu 2010; Weng et al. 2008; Kerekes et al. 2013; Giannandrea et al. 2013; Hecker et al. 2019; Herold and Roberts 2005; Lachérade et al. 2005; Priem et al. 2016; Singh and Sirohi 1995).

Modern advancement in the technology has witnessed the extensive applications of hyperspectral remote sensing (HSRS) in the field of image processing for identification of different urban built-up surfaces and materials on the basis of their unique characteristics (Roberts and Herold 2004; Kerekes et al. 2013; Giannandrea et al. 2013). HSRS technology is very useful for the study of urban environment due to its ability to demonstrate high potential in investigating the spectral properties or characteristics of urban surfaces and materials (Herold et al. 2003, 2004). The spectral properties of a different surfaces and materials are responsible for the identification of various

Responsible Editor: Biswajeet Pradhan

✉ Dwijendra Pandey
dwijpandey068@gmail.com

Kailash Chandra Tiwari
kcchtphd@gmail.com

[1] Department of Electronics and Communication Engineering, Delhi Technological University, Delhi 110042, India

[2] Department of Civil Engineering, Delhi Technological University, Delhi 110042, India

Published online: 23 March 2021

classes and sub-classes using HSRS (Heiden et al. 2007; Roessner et al. 2001; Andreou et al. 2011).

Urban environment may be considered one of the most demanding areas to carry out remote sensing analysis (Ben-Dor et al. 2001; Mueller et al. 2006; Milton et al. 2009). It is due to high heterogeneity of urban built-up surfaces and materials (Herold and Roberts 2010). Further, difficulty is attributed to the fact that urban area is characterized by typical land cover surface along with existence of various types of materials (Herold et al. 2003; Abebe 2013). Therefore, in remote sensing, it is primary requirement to study the spectral behavior of different built-up surfaces and materials. In view to this, most of the studies of urban built-up surfaces and materials have been created a spectral library of these features followed by analysis on the basis of their unique spectral characteristics (Wan et al. 1994; Heiden et al. 2001, 2007; Herold et al. 2004; Ben-Dor et al. 2001; Nasarudin and Shafri 2011; Kotthaus et al. 2014; Baldridge et al. 2009; Baldridge et al. 2009; Kokaly et al. 2017; Sobrino et al. 2013; Ilehag et al. 2019). The details about existing libraries are listed in Table 1. These libraries include pure spectral signatures of the various built-up surfaces called as end members. Such libraries also include wide range of materials over different wavelengths in different spectral regions along with other information in the form of metadata and documentation regarding the quality of the spectral signature and surface characteristics (Herold and Roberts 2010). The spectral samples of different surface and materials can be derived from the HSRS observations together with laboratory or field spectral measurement (Swayze et al. 1992; Van Der Meer 2004). Further, in Indian continent, no such spectral library has been explored for urban built-up surfaces and the study of urban surfaces and materials using HSRS is also yet to be explored intensively.

Therefore, this study concerns with the examination of spectral characteristics of various urban built-up surfaces using field spectrometry. Further, to carry out the spectral analysis, all the urban built-up surfaces (Level-1) are categorized into different levels, in which roofs, roads and pavements, railway tracks, and sports infrastructure are considered Level-2 surfaces. Next, these sub-surfaces are further divided into different types of sub-classes and materials in third and fourth level. The objective of this study is to develop a spectral library of built-up surfaces and materials in Indian continent and carry out a critical analysis of all the spectral signatures of aforementioned surfaces and materials in different spectral regions of the spectra.

Urban built-up or engineered surfaces

An urban built-up or engineered surface may be defined as a stationary surface bearing the following characteristics:

- A man-made surface created artificially
- Limited thickness/depth as compared to other dimensions
- Single/mixed composition
- Stationary over a large span of time

On the basis of aforementioned characteristics, these surfaces have been categorized into different levels (Level-1, 2, 3, and 4), which are tabulated in Table 2.

Study area

The area under examination belongs to the Udaipur, Rajasthan, India, which is a mixture of built-up and non-built-up surfaces. This study basically carries out with the built-up surfaces. Therefore, built-up surfaces are further categorized into

Table 1 Existing spectral libraries of urban built-up surfaces and materials

Spectral library	Study area	Spectral range (nm)	No. of samples	Data acquisition platform
Wan et al. 1994	Various locations, USA	2500–14,500	74	Laboratory and in situ
Heiden et al. 2001, 2007	Dresden and Potsdam, Germany	400–2500	32	Airborne and in situ
Herold et al. 2004	Santa Barbara, CA, USA	350–2400	26	In situ
Ben-Dor et al. 2001	Tel-Aviv, Israel	400–1100	55	Airborne and in situ
Nasarudin and Shafri 2011	Serdang, Malaysia	350–2500	15	In situ
Kotthaus et al. 2014	London, UK	350–15,400	74	Laboratory and in situ
Baldridge et al. 2009	Various locations, USA	400–15,400	3420	Laboratory
Kokaly et al. 2017	Various locations, USA	200–200,000	2468	Airborne, laboratory and in situ
Sobrino et al. 2013	Madrid, Spain	350–2500	27	Airborne and in situ
Ilehag et al. 2019	Karlsruhe, Germany	8000–14,000 350–2500	181	In situ

Table 2 Categorization of various engineered surfaces in different levels

Level-1	Level-2	Level-3	Level-4
Urban built-up/ engineered surfaces	Roof/building	Concrete	
		Asbestos	
		CGI sheet	New Irony
		Cement	
		Wood	
		DPC brick	
		Sandstone	
	Roads and pavements	Bitumen road	New Old Repaired
		Bitumen parking lot	
		Asbestos pavement	
		Concrete road	
		Concrete pavement	
		Concrete bridge	
		Charcoal	
		Brick pavement	
	Railway track	Sleeper	
		Track iron	
		Ballast boulder	
		RCC	
		Concrete log	
	Sports infrastructure	Basketball court	Concrete Blue fabric Red fabric Bitumen
		Volleyball court	Fabric Cement
		Tennis court	Fabric
		Cricket pitch	Cement

different levels up to material level, which will be discussed in the upcoming section. Spectral signatures of these surfaces and materials may be utilized for identification of significant spectral wavelengths and regions for extraction of various classes.

Dataset and methodology

Ground spectral data in the study region is collected using Spectral Evolution Spectroradiometer. This instrument is having proven effectiveness in the applications in different areas, which require measurement of reflectance, radiance, and irradiance. It has 2151 spectral channels over the spectral range of 350 to 2500 nm. The whole spectral range is divided into various regions, which are visible, near infrared (NIR), and short wave infrared (SWIR), respectively. Further, the data collection has been carried out using gun as well as contact probe, depending on the lightning condition. The field data has been collected between 10 am and 3 pm in cloud-free atmospheric condition. The spectral signature has been collected in a set of four for each sample of built-up surfaces. Before recording the spectral signature of target, white reference is recorded. Figure 1a represents the satellite imagery of Udaipur with some points representing the field sample locations of built-up surfaces, which have been utilized for the analysis of spectral signatures. There are various fields of metadata which have been included in the spectral library of built-up surfaces and materials. These fields are Fore Optics (Contact Probe/Gun), Scan ID of Spectra, Latitude, Longitude and Altitude, Material Composition, Name of class and sub-class, Observation, Temperature, Relative Humidity, Radiometric Calibration, and GPS Time.

The spectral analysis of different built-up surfaces has been carried out visually along with using continuum-removed spectra, which is utilized for identification of significant regions and wavelengths for a particular surface or material using various statistical parameters. Continuum analysis has been carried out using IDL DISPEC 18.03 tool (Van Der Meer 2004).

The basic software utilized in this study includes Environment for Visualizing Images (ENVI) 5.3 and ArcGIS 10.4. ENVI 5.3 accepts all the spectral data in ASCII format and converts it in the form of spectral library, which can be represented in any of the graphical format for analysis. Further, ArcGIS 10.4 is utilized for mapping of all the point coordinates associated with field data into satellite imagery of study region, as shown in Fig. 1a. Figure 1b represents some of the photographs of ground data collection campaign of different built-up surfaces and materials.

As mentioned in the study area, the spectral signatures of built-up surfaces have been captured in the wavelength range of 350 to 2500 nm with 1-nm spectral sampling. These wavelengths are divided into different spectral regions for the analysis of various spectral signatures of built-up surfaces, as shown in Table 3.

This research has been carried out into following steps:

i. Obtaining in situ spectral signatures of different urban built-up surfaces and materials
ii. Categorization of urban built-up surfaces (Level-1) into sub-surfaces (Level-2) and then further these sub-surfaces into materials (Level-3 and 4)
iii. Creation of spectral library of aforesaid surfaces and materials in Level-1, 2, 3, and 4
iv. Division of full spectral range, i.e., 350–2500 nm into different spectral regions, which are visible, VNIR, FNIR, ESWIR, and FSWIR
v. Visual analysis of spectral signatures of built-up surfaces (Level-1, 2, 3, and 4)
vi. Generation of continuum-removed spectra of all the built-up surfaces and materials
vii. Critical analysis of spectral signatures of built-up surfaces and materials using various statistical parameters

viii. Finding out the significant wavelengths of absorption in different regions of built-up surfaces and materials

Results

Spectral library creation

Roof/building

The mean spectral signatures of different types of roof surfaces and materials along with the observations are tabulated in Table 4.

Table 3 Division of full spectral range into different wavelength regions

Region	Wavelength range
Visible	350–700 nm
Very near infrared (VNIR)	700–1000 nm
Far near infrared (FNIR)	1000–1500 nm
Early short wave infrared (ESWIR)	1500–2000 nm
Far short wave infrared (FSWIR)	2000–2500 nm

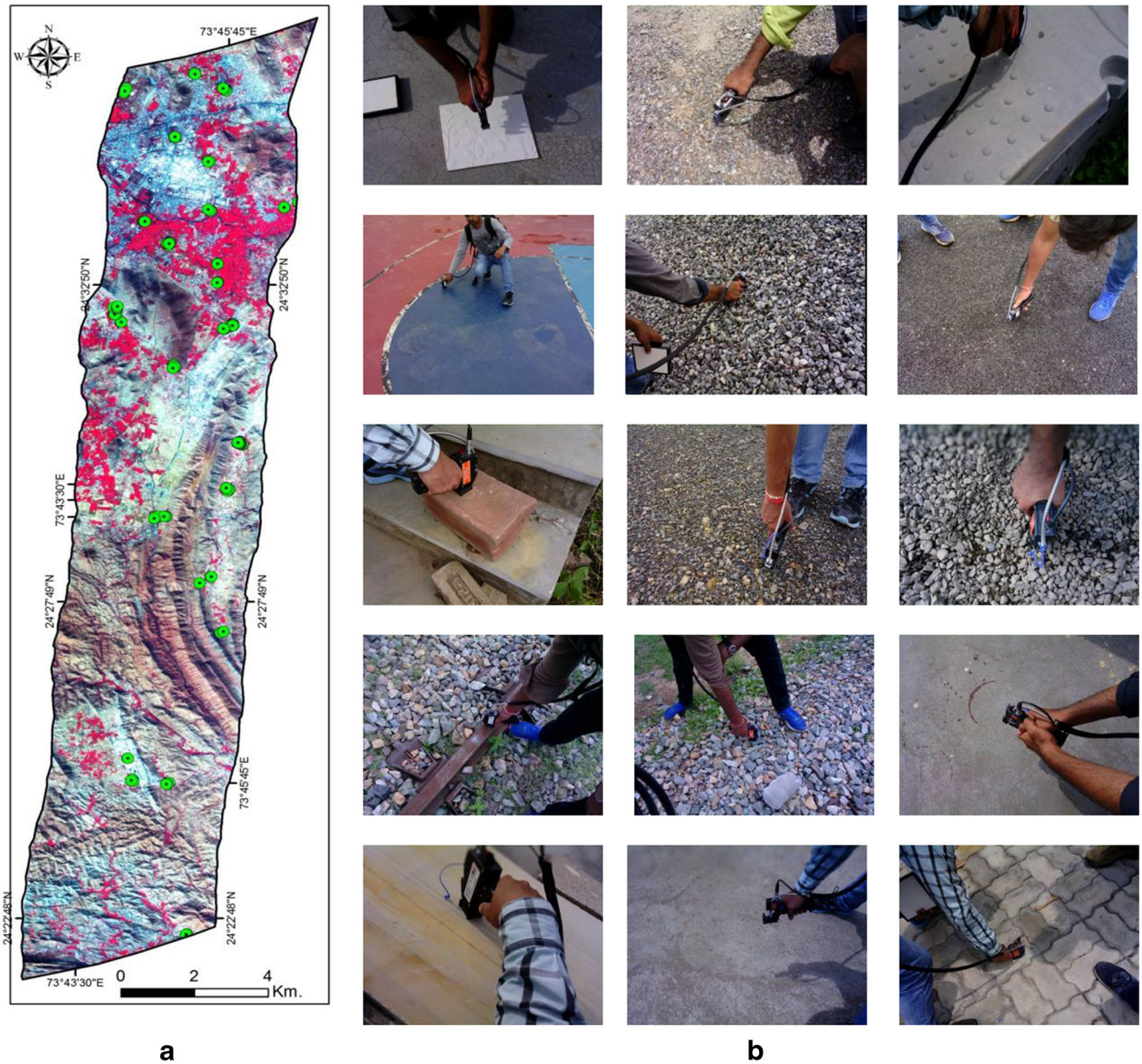

Fig. 1 **a** The green points on the imagery of Udaipur, Rajasthan, India, represent the actual locations of ground spectral data collection. **b** Some of the photographs of field data collection campaign

Table 4 Spectral library creation and analysis of roof surfaces.

Spectral Signature	Observation
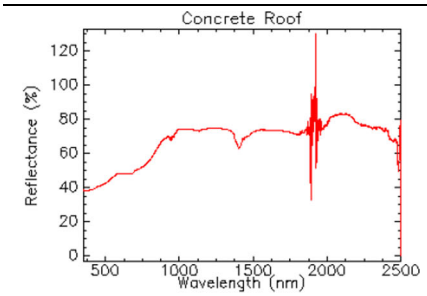	The reflectance is almost constant in all the regions except in visible. Some small absorption features due to metallic component and hydrocarbons are observed in visible, VNIR, and FSWIR regions, respectively.
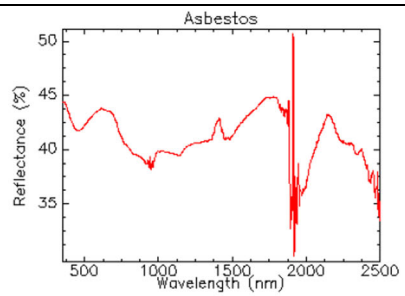	In visible and FSWIR, the response is almost concave with some major peaks. The reflectance decreases from visible to VNIR, while having sinusoidal behavior in FNIR. The response is almost constant in ESWIR. Further, iron oxide and hydrocarbon absorption features dominate in VNIR, FNIR, and FSWIR regions, respectively.
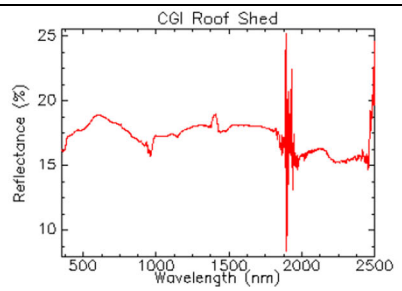	In fresh CGI sheet, response is almost constant in all the regions, which has some absorption features near 1020, 1250 and 2250 nm.
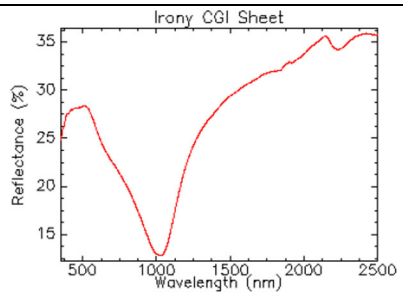	In irony CGI sheet, the reflectance decreases from visible to VNIR while it increases from VNIR to FSWIR with a major absorption near 1050 nm. A minor absorption also appears near 2250 nm.
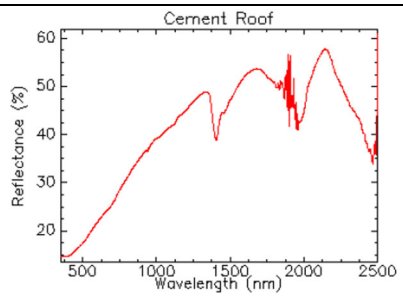	The spectral response of cemented roof surface increases from visible to FNIR while having sinusoidal behavior in ESWIR and FSWIR regions. It has a major peak in FSWIR with some minor absorptions in FNIR.

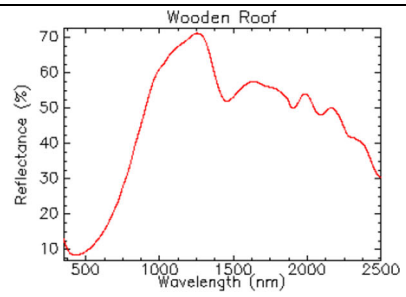	There is a sudden increase in reflectance from visible to VNIR and FNIR while behaves as a decreasing sinusoid in all the other regions with different peaks and absorptions.
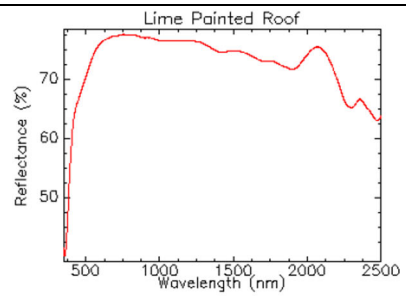	The reflectance is high and almost constant in all the regions with different peaks and absorptions in FSWIR. Some minor absorptions also appear in VNIR and FNIR regions.
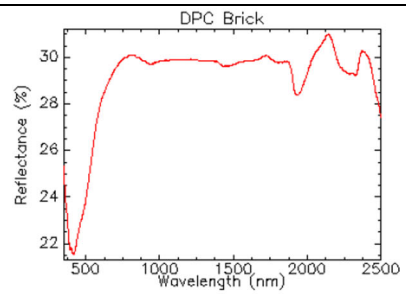	Spectral signature of DPC brick is almost constant in all the regions with a peak and major absorption in FSWIR. Further, some minor absorptions are observed in visible, FNIR and ESWIR regions.
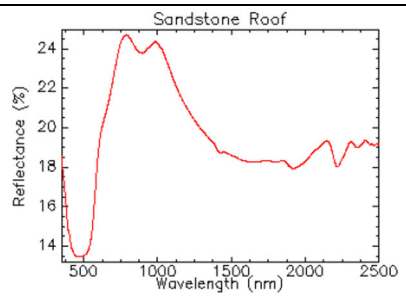	The response of sandstone roof increases from visible to VNIR while decreases from VNIR to ESWIR and almost constant in FSWIR regions. Some absorption features are observed near 890, 2250 and 2390 nm.

Roads and pavements

The mean spectral characteristics of various types of roads and pavements are shown in Table 5. The observations drawn from the analysis of signatures are also tabulated in Table 5.

Railway track

The mean spectral responses of various types of surfaces and materials associated with railway track are given in Table 6. Several observations have been derived from the analysis of spectral signatures, which are also shown in Table 6.

Sports infrastructure

The spectral characteristics and observations of different types of surfaces and materials used in the construction of sports infrastructure are shown in Table 7.

Discussion

For quantification of absorption features in spectra, the overall concave shape of a spectrum should be removed. This normalization procedure is referred as continuum removal or convex-hull transform; continuum equation is given as:

Table 5 Spectral library creation and analysis of roads and pavements.

Spectral Signature	Observation
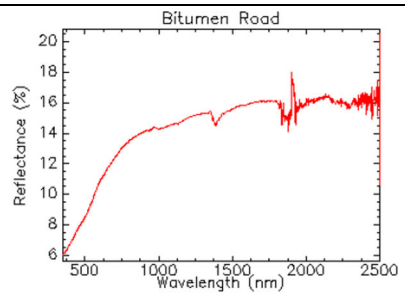	The spectral response of bitumen roads linearly increases in visible region while almost constant in all the other regions with minor absorptions near 1190 and 2350 nm.
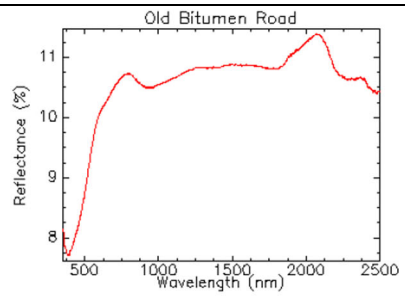	The spectra of old bitumen road is almost flat in all the regions with major peak in FSWIR region. Iron oxide absorption appears in VNIR.
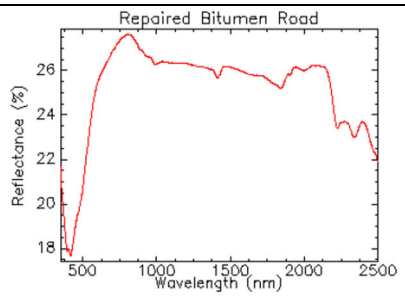	The response of repaired bitumen road is almost flat in all the regions with some hydrocarbon absorptions near 2250 and 2400 nm. A minor absorption due to metallic component is observed in VNIR.
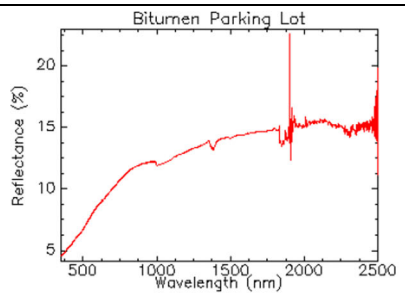	Bitumen Parking lots are having same response as road but more flatter with two absorption bands near 1050 and 2260 nm.
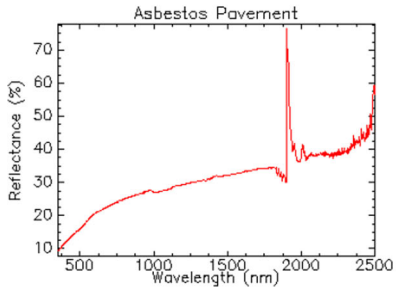	The spectra of asphalt pavement linearly increases in all the regions with lesser slop. Some small absorptions are observed in VNIR and FNIR regions.

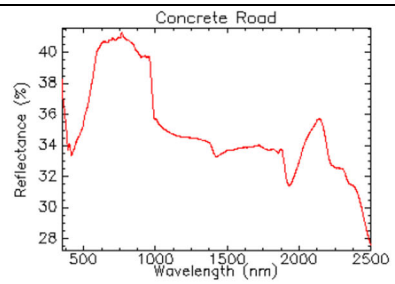	The spectral signature of concrete road appears to have some minor absorptions in VNIR and FSWIR regions.
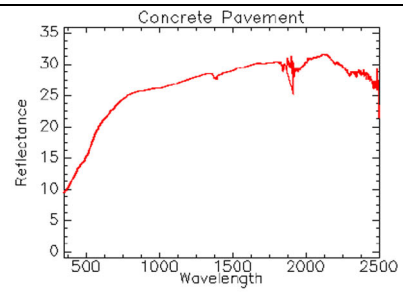	Signature of concrete pavement is almost flat in all the regions except in visible while more concavity with hydrocarbon absorptions is observed near 2290 nm in FSWIR.
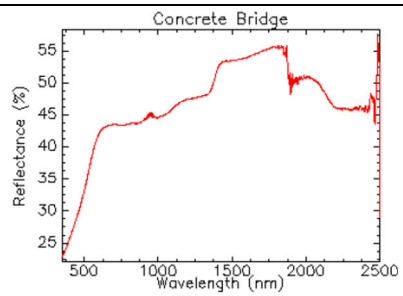	The spectral signature of concrete bridge linearly increases in all the regions except FSWIR, while it becomes almost flat in FSWIR region. Some iron oxide and hydrocarbon features highlight in FNIR and FSWIR regions, respectively.
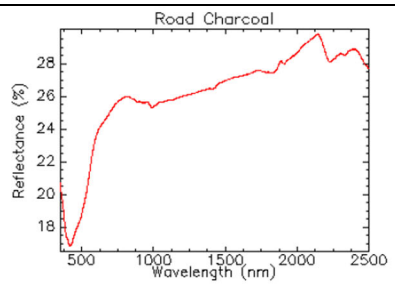	Spectra of road charcoal is almost flat in all the regions with clay absorption near 2350 nm. The iron component appears to dominate in FNIR region near 1020 nm.
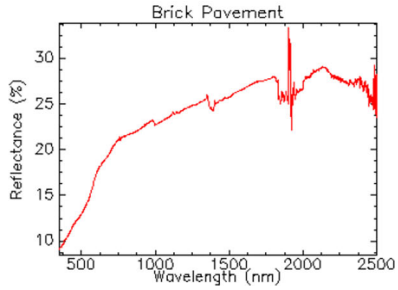	The response of brick pavement gradually increases in all the regions with two minor absorptions near 1050 and 2250 nm.

Table 6 Spectral library creation and analysis of railway track

Spectral Signature	Observation
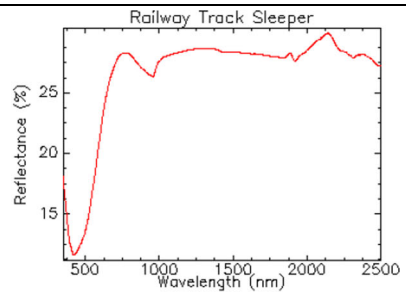	The response of railway track sleeper is almost constant in all the regions with some iron oxide and hydrocarbon absorptions in VNIR and FSWIR, and a peak in FSWIR region.
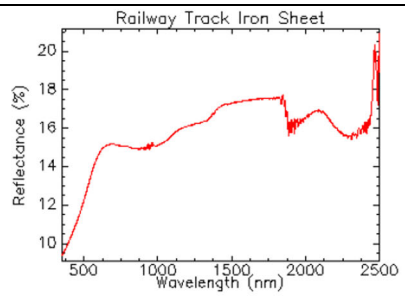	Here, the iron properties seem to be disappear, as slight absorption is observed in VNIR Also, the hydrocarbon absorption dominates in FSWIR
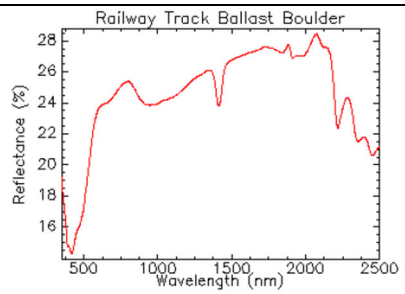	Spectra of ballast boulder is almost flat and having different absorptions in FNIR, ESWIR and FSWIR regions. These absorptions may be due to iron oxide and different hydrocarbons.
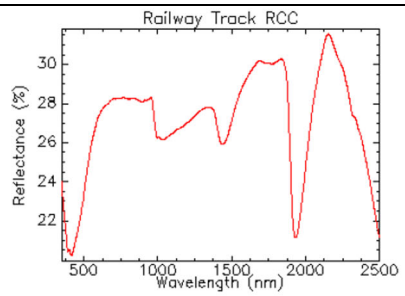	Here, the more absorption features appear in FNIR and ESWIR regions. The hydrocarbon absorptions in FSWIR are disappeared.
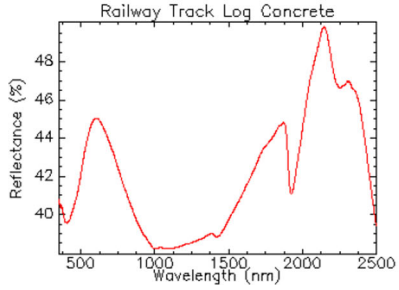	In concrete log, absorption features are observed due to iron oxide and hydrocarbons near 1000 and 2240 nm, respectively.

Table 7 Spectral library creation and analysis of sports infrastructure.

Spectral Signature	Observation
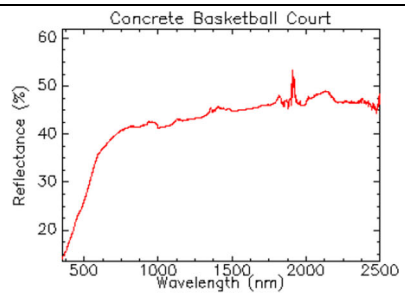	The signature of concrete surface is almost constant in all the regions except in visible. Further, two minor absorptions due to iron oxide are observed in VNIR with a slight concavity in FSWIR.
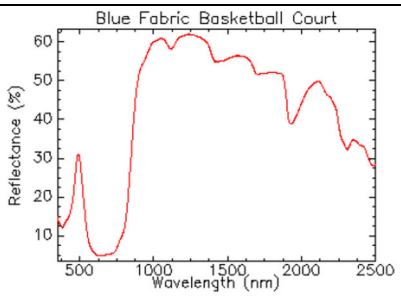	The signature of blue fabric behaves as decreasing sinusoid in FNIR, ESWIR and FSWIR regions with a blue peak in visible region.
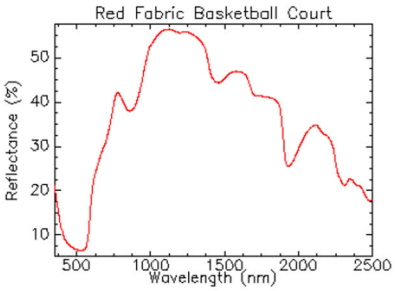	Here, the signature is almost similar to blue fabric but a red peak is observed near 670 nm.
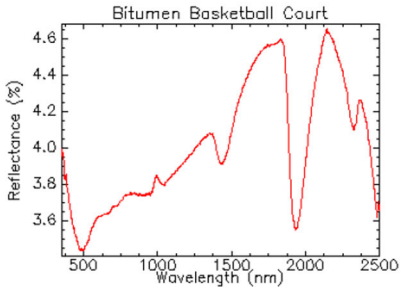	The reflectance of bitumen court appears to have very less reflectance in all the regions with a major peak and concavity in FSWIR. Minor iron oxide and hydrocarbon absorption features appear near 1030 and 2380 nm, respectively.

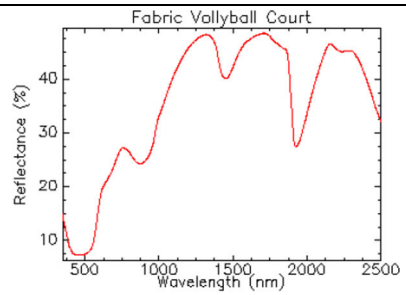

The signature of fabric increases linearly in all the regions with different iron oxide and hydrocarbon absorptions in visible, VNIR and FSWIR regions. Further, due to color of fabric, the red band is dominating at 665 nm.

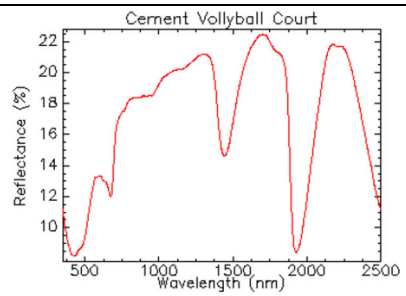

The spectral characteristics of cemented volleyball court is almost flat in all the regions with different iron oxide absorptions in visible and VNIR regions.

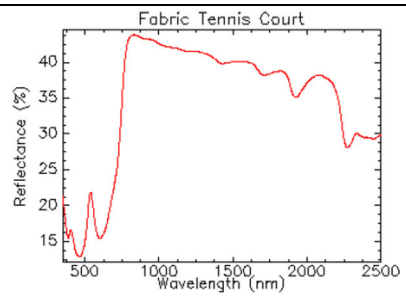

The signature of tennis court fabric is having a red peak with different hydrocarbon absorptions near 1750 and 2420 nm, while it is almost flat in VNIR, FNIR and ESWIR regions.

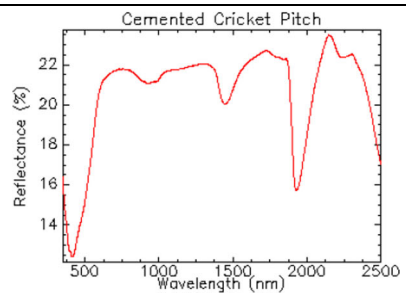

In spectral response of cemented cricket pitch, a major peak appears in the FSWIR region with different iron oxide and hydrocarbon absorptions near 890 and 2240 nm, respectively.

$$S_{CR}(\lambda) = \frac{S(\lambda)}{C(\lambda)} \quad (1)$$

where *SCR (λ)* is continuum-removed spectra while *S (λ)* is original spectra and *C (λ)* is continuum curve.

Figure 2 explains the sample spectra of a particular class along with its continuum-removed curve along with a processing tool box. The resulting spectrum, i.e., *SCR (λ)*, is equal to 1.0 where the continuum and the spectra match, and less than 1.0 where absorption features occur. The resulting spectrum has been analyzed for determining the changes in absorption features in different regions of spectra. The continuum-removed spectra were further analyzed to calculate the parameters that depict the absorption feature, such as central wavelength position, area of the absorption *A*, absorption asymmetry, and feature depth. The relative depth, *D*, is defined as the difference between the continuum line and minimum value in the continuum-removed spectra,

$$D = 1 - \min(S_{CR}(\lambda)) \quad (2)$$

The area of absorption feature is defined as the summation of individual areas between continuum line and the channels in the continuum-removed feature; it is given as,

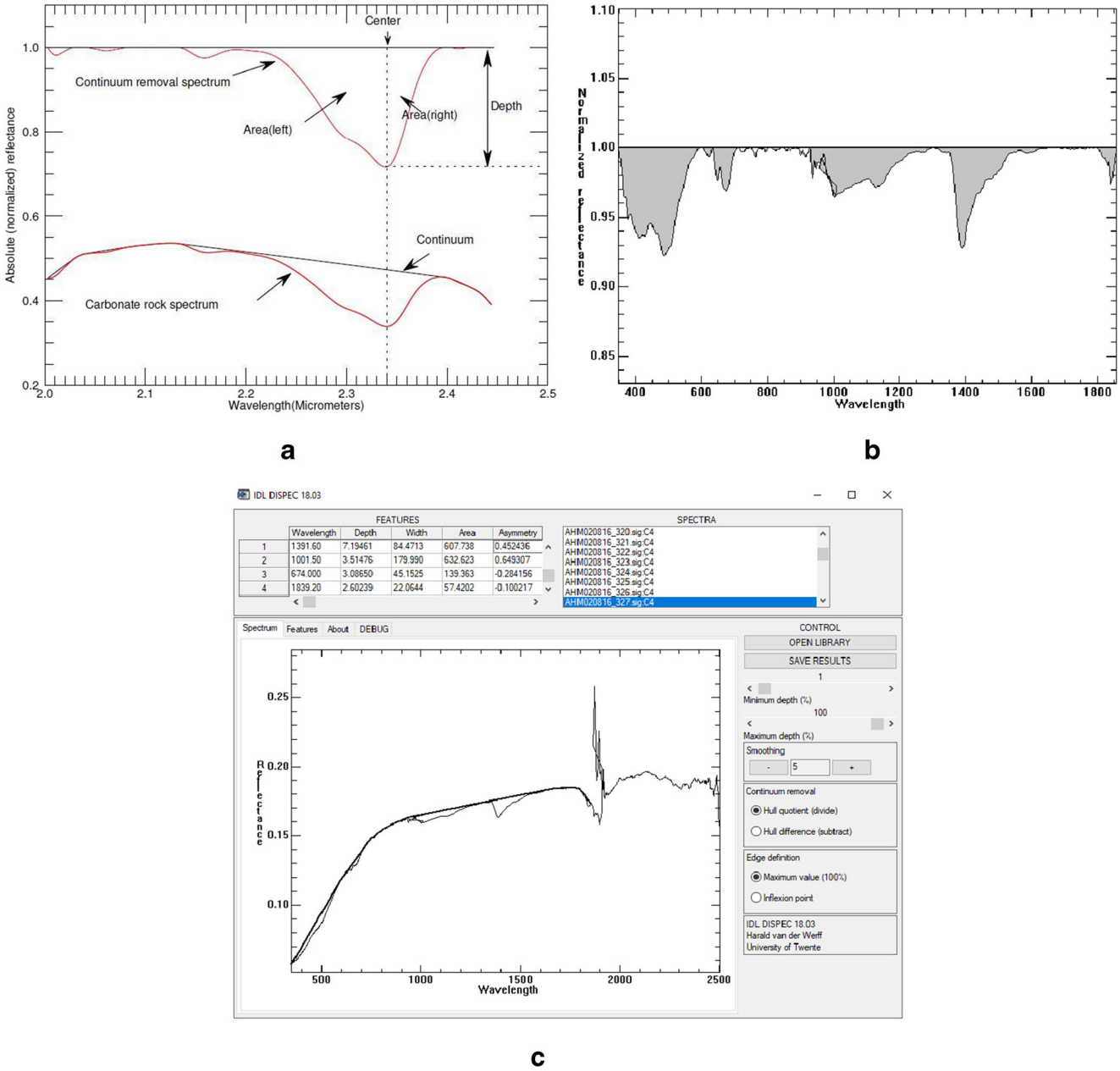

Fig. 2 **a** Sample spectral signature of a rock with continuum removal curve. **b** Normalized reflectance of a sample. **c** Spectral analysis in IDL DISPEC 18.03 tool

$$A = \sum_{i=1}^{n} (1 - S_{CR}(i)) \tag{3}$$

where i is the number of channels from the starting point to end point. The asymmetry factor AF of the absorption feature is given as,

$$AF = \frac{Area_{left}}{Area_{right}} \tag{4}$$

On the basis of spectrum generated by continuum removal analysis and different aforesaid parameters, various significant wavelengths in different regions are obtained, which can prove to be effective for extraction of a particular built-up class or material from remote sensing imagery. The whole continuum analysis has been carried out using IDL DISPEC 18.03 tool developed by University of Twente, Netherlands (Van Der Meer 2004). The significant absorption parameters and central wavelengths of spectral signature of different built-up surfaces and materials are shown in Table 8. In this study, these central wavelengths are termed as significant wavelengths. Table 9 describes the various significant wavelengths and regions for different sub-categories of urban built-up surfaces. These significant wavelengths cab be utilized for

Table 8 Significant absorption parameters and wavelengths of different built-up surfaces and materials

Built-up surfaces	Material	Center wavelength (nm)	Absorption parameters		
			Depth	Area	Asymmetry factor
Roof/building	Concrete	576	0.3589	27.8990	0.3426
		733	0.4318	38.3658	0.9486
		2120	0.3687	28.9285	1.1042
		2172	0.4565	40.2638	0.7327
	Asbestos	480	0.2342	20.1669	0.9239
		933	0.2589	21.2892	1.2068
		1119	0.3187	25.5869	0.7139
		1357	0.3713	31.3185	1.8132
		2245	0.2982	28.1563	1.1253
		2290	0.2678	23.7865	1.6747
	New CGI sheet	985	0.2489	21.0563	2.5136
		1235	0.3256	26.1860	0.6142
		2230	0.2769	24.8906	0.1632
	Irony CGI sheet	1029	0.1582	16.4378	1.1241
		2250	0.2864	23.5620	0.9285
	Cement	1572	0.4065	35.3217	0.6837
		2120	0.3874	33.1226	3.0921
		2245	0.3689	29.8856	0.5986
	Wood	1632	0.3654	28.3547	1.7143
		1955	0.2986	28.1538	1.1726
		2110	0.2740	23.0542	1.2631
		2230	0.3152	24.6495	1.5204
	Lime painted	834	0.3354	27.1549	1.2683
		2080	0.2786	24.3209	0.3225
		2340	0.2579	22.5438	2.7532
	DPC brick	980	0.3245	25.9942	1.3129
		2040	0.2465	21.4376	0.2931
		2235	0.2842	25.6203	2.4364
	Sandstone	910	0.2669	24.0962	0.8962
		2240	0.2474	22.1903	0.9626
		2320	0.3128	24.9860	0.7219
Roads and pavements	Bitumen	490	0.4589	35.6032	0.3749
		560	0.4123	32.8937	0.7302
		832	0.3936	29.6039	0.2253
		2115	0.3924	27.1586	1.4542
	Old Bitumen	618	0.4563	31.4679	0.7468
		890	0.3165	27.1834	0.5196
		2142	0.3454	30.3545	2.3184
		2260	0.3786	25.1673	2.0472
	Repaired bitumen	672	0.4235	31.0589	1.2153
		840	0.3589	29.2130	0.5327
		932	0.3182	31.3902	0.3269
		2258	0.2865	24.5439	2.4326
		2320	0.2674	27.0498	0.9845
	Bitumen parking lot	1046	0.2915	25.6548	0.6389
		2065	0.3134	32.5639	1.2545
		2115	0.3060	27.0940	2.2341
	Asbestos pavement	570	0.3471	28.3871	0.7218
		685	0.4005	35.6232	0.9342
		2352	0.3512	26.7129	0.7894
	Concrete road	590	0.3265	29.5603	1.3876
		2245	0.2969	24.1689	2.6548
		2310	0.3050	26.8560	0.9030
	Concrete pavement	2210	0.3267	30.6811	1.4276
		2250	0.2849	26.6232	1.2135
	Concrete bridge	745	0.3173	28.3019	0.9684
		890	0.3035	23.6833	0.7782
		932	0.3785	24.5627	0.6598
		1366	0.2914	27.1131	0.4973
		2032	0.4189	34.5139	0.3259
		2195	0.3485	27.8523	0.9438
	Road charcoal	1012	0.2876	25.3910	0.5489
		1265	0.3348	23.6504	0.6578

Table 8 (continued)

Built-up surfaces	Material	Center wavelength (nm)	Absorption parameters		
			Depth	Area	Asymmetry factor
	Brick pavement	2045	0.3187	26.3219	0.5764
		2256	0.2965	31.5921	1.2867
		1032	0.3090	26.6125	0.5364
		1380	0.3365	29.1927	0.6485
		2172	0.3498	24.3195	0.4358
		2355	0.3649	21.3295	2.1043
Railway track	Sleeper	1024	0.2819	23.4675	2.1546
		2210	0.3117	28.5198	0.5467
		2235	0.3276	29.0341	0.8965
	Track iron	932	0.3456	25.9315	0.9327
		2118	0.4678	37.3776	0.7689
		2350	0.3129	26.1732	1.6785
	Ballast boulder	985	0.2854	29.1654	0.4528
		1352	0.3817	31.4187	0.5674
		2250	0.2654	22.3549	2.3583
		2325	0.2918	27.0183	2.1739
	RCC	1013	0.2478	20.6798	0.6549
		2235	0.3587	29.1169	1.5127
		2352	0.3159	26.9932	2.1589
	Concrete log	2240	0.2878	23.8232	2.8631
		2375	0.3295	28.1428	1.7647
Sports infrastructure	Basketball court:				
	Concrete	1052	0.2967	24.1832	0.6538
		1132	0.2789	28.4259	1.3672
		2140	0.3456	29.3274	1.3281
		2235	0.3080	26.5798	1.6782
	Blue fabric	670	0.2134	19.3459	0.9658
		1085	0.2767	24.9512	0.8359
		1133	0.3585	30.2649	0.7527
		1365	0.2786	21.6341	1.1324
		1750	0.2675	25.5875	0.8376
		2275	0.3298	30.7023	1.2673
		2340	0.3050	24.9456	2.1273
	Red fabric	550	0.2334	20.2192	1.2468
		1052	0.2754	23.4236	1.1835
		1136	0.4030	35.7529	0.8694
		1754	0.3125	27.8031	1.3259
		1815	0.3876	29.2643	0.9854
		2245	0.3126	22.8249	1.5284
		2320	0.3656	28.6324	2.2543
	Bitumen	490	0.2345	19.7248	2.3459
		985	0.2786	23.1952	1.7538
		2210	0.2643	24.9562	0.8954
		2355	0.3564	29.0913	1.2143
	Volleyball court:				
	Fabric	972	0.2605	22.7620	0.3427
		2080	0.3320	27.3546	0.9236
		2135	0.3420	25.9126	0.7395
		2260	0.4007	31.1852	0.9638
	Cement	692	0.2730	22.3482	0.7659
		832	0.3023	26.5127	1.3946
		2245	0.3546	30.2454	0.8638
	Tennis court:				
	Fabric	425	0.2693	25.1165	0.6392
		635	0.2809	23.8327	0.2955
		1750	0.2846	21.8205	0.9243
		2355	0.3107	27.5720	1.2967
	Cricket ground:				
	Cement pitch	885	0.2871	27.2293	1.7649
		962	0.3628	30.3629	0.6548
		2162	0.3912	32.4105	0.9352
		2332	0.2915	23.0058	1.4283

Table 9 Significant wavelengths and regions for different built-up surfaces and materials (Level-1, 2, 3 and 4)

Roof/building surfaces										
	Concrete	Asbestos	New CGI sheet	Irony CGI sheet	Cement	Wood	Lime pained	DPC brick	Sandstone roof	
Significant regions and wavelengths (nm)	VIS (576, 733), FSWIR (2120,2172)	VIS (480), VNIR (933), FNIR (1119, 1375), FSWIR (2245, 2290)	VNIR (985), FNIR (1235), FSWIR (2230)	FNIR (1029), FSWIR (2250)	ESWIR (1572), FSWIR (2120, 2245)	ESWIR (1632, 1955), FSWIR (2110, 2230)	VNIR (834), FSWIR (2080, 2340)	VNIR (980), FSWIR (2040, 2235)	VNIR (910), FSWIR (2240, 2320)	
Road and pavement surfaces										
	Bitumen	Old bitumen	Repaired bitumen	Bitumen parking lot	Asbestos pavement	Concrete road	Concrete pavement	Concrete bridge	Road charcoal	Brick pavement
Significant regions and wavelengths (nm)	VIS (490, 560), VNIR (832), FSWIR (2115)	VIS (618), VNIR (890), FSWIR (2142, 2260)	VIS (672), VNIR (840, 932), FSWIR (2258, 2320)	FNIR (1046), FSWIR (2065, 2115)	VIS (570, 685), FSWIR (2352)	VIS (590), FSWIR (2245, 2310)	FSWIR (2210, 2250)	VNIR (745, 890, 932), FNIR (1366), FSWIR (2032, 2195)	FNIR (1012, 1265), FSWIR (2045, 2256)	FNIR (1032,138-0), FSWIR (2172, 2355)
Railway track										
	Sleeper	Track iron				Ballast boulder		RCC	Concrete log	
Significant regions and wavelengths (nm)	FNIR (1024), FSWIR (2210, 2235)	VNIR (932), FSWIR (2118, 2350)				VNIR (985), FNIR (1352), FSWIR (2250, 2325)		FNIR (1013), FSWIR (2235, 2352)	FSWIR (2240, 2375)	
Sports infrastructure										
	Concrete basketball court	Blue fabric basketball court	Red fabric basketball court	Bitumen basketball court	Fabric volleyball court	Cement volleyball court	Fabric tennis court	Cemented cricket pitch		
Significant regions and wavelengths (nm)	FNIR (1052, 1132), FSWIR (2140, 2235)	VIS (670), FNIR (1085, 1133, 1365), ESWIR (1750), FSWIR (2275, 2340)	VIS (550), FNIR (1052, 1136), ESWIR (1754, 1815), FSWIR (2245, 2320)	VIS (490), VNIR (985), FSWIR (2210, 2355)	VNIR (972), FSWIR (2080, 2135, 2260)	VIS (692), VNIR (832), FSWIR (2245)	VIS (425, 635), ESWIR (1750), FSWIR (2355)	VNIR (885, 962), FSWIR (2162, 2332)		

detection and identification of a particular surface and material in hyperspectral imagery. Further, the aforesaid spectral library can be used for extraction and unmixing of different engineered surfaces and materials in hyperspectral imagery. The significant wavelengths and absorption features of the most the surfaces and materials have been validated with the existing literature on spectral library creation and analysis (Wan et al. 1994; Heiden et al. 2001, 2007; Herold et al. 2004; Ben-Dor et al. 2001; Nasarudin and Shafri 2011; Kotthaus et al. 2014; Baldridge et al. 2009; Baldridge et al. 2009; Kokaly et al. 2017; Sobrino et al. 2013; Ilehag et al. 2019).

Conclusions

A comprehensive collection of spectral signatures of various urban built-up surfaces and materials have been obtained in the field using spectral evolution spectroradiometer over the range of 350 to 2500 nm. Further, these built-up or engineered surfaces (Level-1) have been divided into roofs/buildings, roads and pavements, railway track, and sports infrastructure in second level while different subclasses and materials related to these surfaces into third and fourth level. The aforesaid signatures were captured in the urban environment of Udaipur, Rajasthan, India. Further, a spectral library of built-up surfaces and materials is created with a critical analysis of spectral signatures of these surfaces and materials in different spectral regions, which are visible, VNIR, FNIR, ESWIR, and FSWIR, respectively. The results of the analysis suggested that various engineered surfaces and materials can be differentiated on the basis of different significant absorption features at different wavelengths. These features may be due to iron oxide, silicates, organic components, hydrocarbons, and clay etc. These significant wavelengths in different spectral regions can be effective for extraction of different built-up surfaces and materials in hyperspectral imagery. These wavelengths can also be useful for determining the age, condition, and deterioration status of various engineered surfaces.

Acknowledgements The authors are thankful to the Department of Science and Technology (DST), Ministry of Science and Technology, India; Defense Research and Development Organization (DRDO), Ministry of Defense, India; and Space Application Centre (SAC), Indian Space Research Organisation (ISRO), India, for providing instruments, data, and financial support for the project.

Declarations

Conflict of interest The authors declare that they have no competing interests.

References

Abebe GA (2013) Quantifying urban growth pattern in developing countries using remote sensing and spatial metrics: a case study in Kampala. University of Twente Faculty of Geo-Information and Earth Observation (ITC), Kampala

Andreou C, Karathanassi V, Kolokoussis P (2011) Investigation of hyperspectral remote sensing for mapping asphalt road conditions. Int J Remote Sens 32(21):6315–6333

Baldridge AM, Hook SJ, Grove CI, Rivera G (2009) The ASTER spectral library version 2.0. Remote Sens Environ 113:711–715

Ben-Dor E, Levin N, Saaroni H (2001) A spectral based recognition of the urban environment using the visible and near-infrared spectral region (0.4-1.1 μm): a case study over Tel-Aviv, Israel. Int J Remote Sens 22(11):2193–2218

Giannandrea A, Raqueno N, Messinger DW, Faulring J, Kerekes JP, van Aardt J, Canham K, Hagstrom S, Ontiveros E, Gerace A, Kaufman J (2013) The SHARE 2012 data campaign. In Algorithms and technologies for multispectral, hyperspectral, and ultraspectral imagery, International Society for Optics and Photonics: 19(8743):87430F

Hecker C, van Ruitenbeek FJ, Bakker WH, Fagbohun BJ, Riley D, van der Werff HM, van der Meer FD (2019) Mapping the wavelength position of mineral features in hyperspectral thermal infrared data. Int J Appl Earth Obs Geoinf 79:133–140

Heiden U, Roessner S, Segl K, Kaufmann H (2001) Analysis of spectral signatures of urban surfaces for their identification using hyperspectral HyMap data. In Proceedings of the IEEE/ISPRS joint workshop on remote sensing and data fusion over urban areas (Cat. No. 01EX482), Rome, Italy: 173–177

Heiden U, Segl K, Roessner S, Kaufmann H (2007) Determination of robust spectral features for identification of urban surface materials in hyperspectral remote sensing data. Remote Sens Environ 111(4): 537–552

Herold M, Gardner ME, Roberts DA (2003) Spectral resolution requirements for mapping urban areas. IEEE Trans Geosci Remote Sens 41(9):1907–1919

Herold M, Roberts DA, Gardner ME, Dennison PE (2004) Spectrometry for urban area remote sensing— development and analysis of a spectral library from 350 to 2400 nm. Remote Sens Environ 91(3–4):304–319

Herold M, Roberts DA (2010) The spectral dimension in urban remote sensing. In remote sensing of urban and suburban areas Springer Dordrecht:47–65

Herold M, Roberts D (2005) Spectral characteristics of asphalt road aging and deterioration: implications for remote-sensing applications. Appl Opt 44(20):4327–4334

Ilehag R, Schenk A, Huang Y, Hinz S (2019) KLUM: an urban VNIR and SWIR spectral library consisting of building materials. Remote Sens 11(18):2149

Kerekes JP, Ludgate K, Giannandrea A, Raqueno NG, Goldberg DS (2013). SHARE 2012: subpixel detection and unmixing experiments. In Algorithms and technologies for multispectral, hyperspectral, and ultraspectral imagery, International Society for Optics and Photonics XIX (8743): 87430H

Kokaly RF, Clark RN, Swayze GA, Livo KE, Hoefen TM, Pearson NC, Wise RA, Benzel WM, Lowers HA, Driscoll RL (2017) USGS spectral library version 7: U.S. Geological Survey data series 1035. U.S. Geological Survey: Reston, VA, USA

Kotthaus S, Smith TE, Wooster MJ, Grimmond CSB (2014) Derivation of an urban materials spectral library through emittance and reflectance spectroscopy. ISPRS J Photogramm Remote Sens 94:194–212

Lachérade S, Miesch C, Briottet X, Le Men H (2005) Spectral variability and bidirectional reflectance behaviour of urban materials at a 20 cm spatial resolution in the visible and near infrared wavelengths. A

case study over Toulouse (France). Int J Remote Sens 26(17):3859–3866

Lu D, Weng Q (2007) A survey of image classification methods and techniques for improving classification performance. Int J Remote Sens 28(5):823–870

Milton EJ, Schaepman ME, Anderson K, Kneubühler M, Fox N (2009) Progress in field spectroscopy. Remote Sens Environ 113:S92–S109

Mueller M, Segl K, Heiden U, Kaufmann H (2006) Potential of high-resolution satellite data in the context of vulnerability of buildings. Nat Hazards 38(1–2):247–258

Nasarudin NEM, Shafri HZM (2011) Development and utilization of urban spectral library for remote sensing of urban environment. J Urban Environ Eng 5:44–56

Praskievicz S, Chang H (2009) A review of hydrological modelling of basin-scale climate change and urban development impacts. Prog Phys Geogr 33(5):650–671

Priem F, Okujeni A, van der Linden S, Canters F (2016) Use of multi-spectral satellite imagery and hyperspectral endmember libraries for urban land cover mapping at the metropolitan scale. In Remote sensing technologies and applications in urban environments, International Society for Optics and Photonics10008: 100080K

Roberts DA, Herold M (2004) Imaging spectrometry of urban materials. Infrared spectroscopy in geochemistry, exploration and remote sensing. Mineral Association of Canada. Short Course Series 33:155–181

Roessner S, Segl K, Heiden U, Kaufmann H (2001) Automated differentiation of urban surfaces based on airborne hyperspectral imagery. IEEE Trans Geosci Remote Sens 39(7):1525–1532

Singh RP, Sirohi A (1995) Spectral reflectance properties of different types of built-up surfaces. J Aerosp Eng 8(1):25–31

Sobrino JA, Oltra-Carrió R, Sòria G, Jiménez-Muñoz JC, Franch B, Hidalgo V, Mattar C, Julien Y, Cuenca J, Romaguera M, Gómez JA (2013) Evaluation of the surface urban heat island effect in the city of Madrid by thermal remote sensing. Int J Remote Sens 34(9-10):3177–3192

Swayze G, Clark RN, Kruse F, Sutley S, Gallagher A (1992) Ground-truthing AVIRIS mineral mapping at Cuprite, Nevada

Van Der Meer F (2004) Analysis of spectral absorption features in hyperspectral imagery. Int J Appl Earth Obs Geoinf 5(1):55–68

Wan Z, Ng D, Dozier J (1994) Spectral emissivity measurements of land-surface materials and related radiative transfer simulations. Adv Space Res 14(3):91–94

Weng Q, Hu X, Lu D (2008) Extracting impervious surfaces from medium spatial resolution multispectral and hyperspectral imagery: a comparison. Int J Remote Sens 29(11):3209–3232

Weng Q, Quattrochi D, Gamba PE (2018) Urban remote sensing. CRC press

Weng Q (2012) Remote sensing of impervious surfaces in the urban areas: requirements, methods, and trends. Remote Sens Environ 117:34–49

Xu H (2010) Analysis of impervious surface and its impact on urban heat environment using the normalized difference impervious surface index (NDISI). Photogramm Eng Remote Sens 76(5):557–565

AIP Conference Proceedings

Study of a prey–predator model with preventing crop pest using natural enemies and control

Cite as: AIP Conference Proceedings **2336**, 020002 (2021); https://doi.org/10.1063/5.0045745
Published Online: 26 March 2021

Sudhakar Yadav, and Vivek Kumar

View Online Export Citation

ARTICLES YOU MAY BE INTERESTED IN

A delayed version of prey predator system with modified Holling-Tanner response
AIP Conference Proceedings **2336**, 020005 (2021); https://doi.org/10.1063/5.0046306

Preface: International Conference on Computational Sciences-Modelling, Computing and Soft Computing (CSMCS-2020)
AIP Conference Proceedings **2336**, 010001 (2021); https://doi.org/10.1063/12.0003727

Enhanced absorption in thin film silicon solar cell using plasmonic nanoparticles: An FDTD study
AIP Conference Proceedings **2336**, 020003 (2021); https://doi.org/10.1063/5.0045725

Challenge us.
What are your needs for periodic signal detection?
Watch

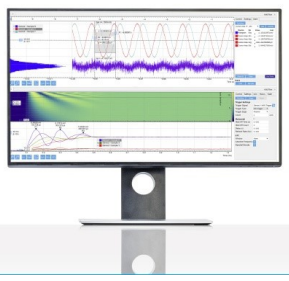

Zurich Instruments

AIP Publishing

© 2021 Author(s).

Study of a Prey–Predator Model with Preventing Crop Pest Using Natural Enemies and Control

Sudhakar Yadav[1,a)] and Vivek Kumar[1,b)]

[1]*Department of Applied Mathematics,*
Delhi Technological University,
Shahbad Daulatpur, Main Bawana Road, Delhi-110042, India.

[a)]*Electronic mail: sudhakarbhu10@gmail.com*
[b)]*Corresponding author: vivekkumar.ag@gmail.com*

Abstract. In this article, we propose a mathematical model of an ecological model that is presented of prey, pest, and natural enemy of pest. Different equilibrium points are obtained, their existence and stability of the steady states are investigated. Further, a mathematical model is obtained in the presence of the control variable for designing optimal pest control problems and to study the effect on crop pest. An optimal control technique is one that minimizes the loss due to crop damage and causes minimum harm to the environment. Several chemicals, biological, physical control, and mechanisms are used. We apply Pontryagin's maximum principle to find the existence, characterization, and necessary conditions of the optimal control. Numerical simulations are further verified to support analytical results and to illustrate a different system that can be observed in the model.

INTRODUCTION

In the last 50 years, the world population has risen at an unprecedented pace. New agricultural technology has increased the production of major crops yet, besides causing deterioration of the climate. However, there is a lack of effective data on food loss or damage caused by such biotic agents, mainly in developing nations. The small available information demonstrates that an estimated 18-20% of yearly food crops globally may be damaged by pests. Moreover, losses are comparatively higher in the emerging tropics of Asia and Africa, at which population is also projected to grow rapidly over the next 50 years. There is a significant need to accurately measure the level of waste production at various levels from farming to consumer use. It is vital to the advancement of secure, productive, and sustainable methods of pest control and food safety for the long term. More recently, the topic of the management of agricultural insects has received more and more research interest. Unscientific and unjustified application of insecticides has led to catastrophic results. It has been noticed that 10-30% of yield reductions are attributed to pests. The changing agro–climatic factors have contributed significantly to the infestation of several predatory insects in different areas of the world. Approximately 30–35% of the annual agricultural productivity loss in India is attributed to pests, as reported by the Indian Agricultural Research Council. In recent days, nematodes have become a serious risk to crops and lead to the loss of 60 million tons of grains annually worldwide. This has contributed to a detrimental effect on agricultural biosecurity, which is critical to food security. The output of agricultural crops is affected by the occurrence of pests. Numerous methods exist to avoid or reduce these crop losses. The various types of crop waste as well as the various pest control techniques evolved over the last century have been summarized below. An outline of grain declines is provided for wheat, maize, rice, soybeans, potatoes, and cotton for the period 2001-03 on both a local and worldwide basis, despite the current crop protection methods. The cumulative pest loss ranged from around 50% in wheat to 80% in cotton yield. It is expected that yield reduction for wheat, cotton, and soybean is about 26–29%, and 31%, 37 %, and 40%, respectively, for rice, maize, and potatoes. Lastly, weeds generated the highest possible liability (34%). Cultivation security in cash crops was much more beneficial than in food crops. While the use of pesticides has helped farmers to increase crop yield, it has also increased susceptibility to the pest's harmful effects. The definition of integrated pest/crops aims to find the optimal standard for the use of pest control methods and to decrease the quantity or frequency of pesticides to an environmentally safe degree. At the global level [17], about one-third of the total grain production has been lost due to insects, viruses, and weeds. Arthropods are killing about 18-20% percent of annual crops, worth more than US$470 billion worldwide. Big problems (13–16%) exist in the areas due to disease, and the declines in underdeveloped nations are higher. Globally around 27 to 32% of all agricultural food produce in the world are wasted [18]. But these losses did not include the agricultural crop losses in the field. For example Table 1 shows the loss of crops attributable to insect plagues in India. The data shown in Table 1 taken from first row references.

International Conference on Computational Sciences-Modelling, Computing and Soft Computing (CSMCS 2020)
AIP Conf. Proc. 2336, 020002-1–020002-13; https://doi.org/10.1063/5.0045745
Published by AIP Publishing. 978-0-7354-4080-7/$30.00

TABLE 1. Reports of crop damage caused by pests (%) in India

Crop	[2]	[20]	[7]	[6]	[29]	[19]	[11]	[15]
Oilseeds	5	5	35	25	25	25	15	20
Cotton	18	18	50	22	50	50	30	30
Pulses	5	5	30	7	15	15	15	15
Rice	10	10	25	18.6	25	25	25	25
Wheat	3	-	5-10	11.4	5	5	5	5
Maize	5	-	25	-	25	25	20	18
Sorghum and millets	3.5	-	35	10	30	30	10	8
Groundnut	5	-	15	-	15	15	15	15
Sugarcane	10	-	20	15	20	20	20	20

Agricultural crop damages caused by pests in India were also reported from periodically [2, 10] and, after the green revolution, the increase in crop losses was higher than that reported at the global stages [2, 10]. The crop wastage rose significantly from 7.2% percent in the 1960s to 23.3% in the early 2000s, but after that, the losses fell to 17.5% [11]. In the pre-green revolution period, it was reported that losses incurred by pest species ranged from 3.5 % in sorghum and millets to 16% in cotton. Vegetable crop damage was estimated to be very massive in India, which was around 30–40 % [16]. In addition to harvest and post-harvest losses, which were reported to be 10–30 % of production, pre–harvest yield reduction of about 40% was unavoidable [14]. As calculated by [11], yield losses declined from 23.3% in the 1990s to 17.5% in 2010 and 15.7% recently [15]. [12] reported a real loss of 39% caused by pests in potatoes globally and without crop security about 71% can be lost to pests. Actual overall losses have been reported to range from 24% in Europe to over 50% in Africa. The yield losses in Indian vegetables due to huge insects are given in Table 2 [13, 16].

TABLE 2. Loss of yields in Indian vegetable crops caused by large pest species

Crop	Pest	Yield loss (%)
Chilli Thrips	Chilli Thrips	12–90
	Mites (Polyphagotarsonemus latus)	34
Tomato	Fruit borer (H. armigera)	24–73
Okra	Fruit borer (H. armigera)	22
	Leafhopper (A. biguttula biguttula)	54–66
	Whitefly (B. tabaci)	54
	Shoot and fruit borer (E. vittella)	23–54
Cabbage	Diamondback moth (P. xylostella)	17–99
	Cabbage caterpillar (P. brassicae)	69
	Cabbage leaf webber	28–51
	Cabbage borer (H. undalis)	30–58
Cabbage	Aphid	3–6
	Tobacco caterpillar	4–8
	Potato tuber moth	6–9
	Mite (P. latus)	4–27
Cucurbits	Fruit fly (B. cucurbitae)	20–100
Brinjal	Fruit and shoot borer	11–93

Because of the animals, pests, diseases, and weeds at least one–third to half of the world crop output is destroyed. Reducing the loss of food would lead to a major increase in the supply of food for use. A precise estimation of these damages is the first important step in reducing these losses. However, it is acknowledged that damage is rising due to different biotic and abiotic stresses in the face of the growing strength of agriculture and the environment on farmland. Thus, there is an urgent need to establish effective pest control techniques and agricultural pests enemy that is at the same time productive, healthy, and persistent. Using pest–resistant cultivars provides so many benefits and can form the center in which to build sustainable farming production. Pest control has appeared recently being one of the most important problems impacting ecologically sustainable due to the growing people communities and increasing food crisis. Hence, there is detailed research of effective pest control strategies. Prey–predation mechanism of prey disease and stage-structured model behaviour are studied by [36, 37, 38]. [35] built up a prey-predator model of the Lokta–volta model kind with irrational impact for integrated pest control. [39] researched a model that consists of

predator species, susceptible prey, and infected prey and two pushes for integrated control of the pest. The optimal management technique was explored by [40] using a balanced mix of controls (infection, chemical, and predation pest control aspects) to avoid the pest population. The [42, 43] suggested a state-dependent dynamic impulsive mechanism by releasing natural enemies and sprinkling pesticides. [44] has mentioned a pest–natural enemy model focused on the application of impulsive pest-specific pesticides. Relevant studies were performed using various kinds of prey–predator models and stage–structured populations. The goal of the present research is to increase crop production and to reduce the pest population. For this, at the higher trophic level of the pest species, we find an appropriate predator(the natural enemy of pest). The study seeks to determine how natural enemy use and balance pesticide can manage the pests. Also, the aim is to illustrate how the monitoring of pest control is greatly influenced by the deletion of the natural enemy due to predation by its predators or the use of dangerous chemical substances.

THE MODEL

Many species like spiders, birds, frogs, etc. are recognized as the natural enemy as they feed on agricultural pests. Biological monitoring is the beneficial of predators operation for controlling pests and their serious harm. Through the number of insects and mites, the natural enemies could be used as a biological control for pest management. The use of natural enemies is also useful for the biological management of the land area and wildland weeds. High levels of residues from pesticides can interfere with the reproduction of natural enemies and they are trying to identify and destroy pests. Therefore, the elimination of pests and the protection of the natural enemy from an agriculture sector and ecological viewpoint is very important. By using pesticides, apply them selectively and handle only highly infested areas instead of whole plants. Use more common insecticides in the kinds of invertebrates they destroy, like Bacillus thuringiensis, which only destroys caterpillars that consume treated foliage. Here, we find the prey–predator model [41] since it is renowned for displaying excitable activity and expanding this model by introducing another equation of the prey-treated crop species. In this model, The mathematical model is set up to protect crops from pests through the effective use of natural enemies along with the balanced application of pesticides. To examine the effect of the natural enemy on control of the pest species, we first find a framework of prey–predator in three dimensions. The following is a purely ecological model:

$$\frac{dP_1}{dt} = r_1 P_1 (1 - \frac{P_1}{K_1}) - \alpha_1 P_1 P_2, \tag{1}$$

$$\frac{dP_2}{dt} = r_2 P_2 (1 - \frac{P_2}{K_2}) - \frac{m P_3 P_2^2}{\alpha_2^2 + P_2^2} + \alpha_3 P_1 P_2, \tag{2}$$

$$\frac{dP_3}{dt} = \frac{\gamma P_3 P_2^2}{\alpha_2^2 + P_2^2} - \mu P_3, \tag{3}$$

with initial data $P_1(0) > 0$, $P_2(0) > 0$ and $P_3(0) > 0$. Context of parameters is shown in the Table 3.

TABLE 3. Parameters used in the model

Parameter	Description
$P_1(t)$	Density of crops (prey) at time t
$P_2(t)$	Density of pest at time t
$P_3(t)$	Density of natural enemies of pest at time t
r_1	Intrinsic growth rate of prey
K_1	The carrying capacity of prey
r_2	Intrinsic growth rate of pest
K_2	The carrying capacity of pest
m	Holling type-III functional response with consumption rate
α_1	Predation rate coefficient
α_2	Half saturation constant
α_3	Reproduction rate of pest per prey eaten
γ	Predator conversion rate
μ	The natural mortality rate of the predator

The predation loss term $\frac{mP_3P_2^2}{\alpha_2^2+P_2^2}$ has a moving property in the pest equation. We also assumed that the natural enemy is removed from the ecosystem due to predation by its predator apart from natural death. In population ecology, the natural enemies of pest population has different functional responses. We assume that the overall functional response is Holling type III. The carrying capacity K_1 is the number of prey population that can fill a unit area in the absence of pest,$K2$is the population density of pest capable of filling a unit area in the nonexistence of predators and m indicates that the natural enemy may eat the available pest per unit time by converting γ of that quantity into a predator. Also, μ means that through natural death, the predator population dies per unit time. Finally, δ is the rate of natural enemy removal.

BOUNDEDNESS OF THE SYSTEM

Theorem 1. *The solutions of the system ((1), (2), (3)) in the region* $\mathbb{R}^2_+$ *are bounded.*

Proof. We establish the function

$$w(P_1,\, P_2,\, P_3) = P_1 + P_2 + P_3.$$

The derivative of the $w(P_1,\, P_2,\, P_3)$ with respect to time t is

$$\begin{aligned}
\frac{dw}{dt} =& \frac{dP_1}{dt} + \frac{dP_2}{dt} + \frac{dP_3}{dt} \\
=& r_1P_1(1-\frac{P_1}{K_1}) - \alpha_1P_1P_2 + r_2P_2(1-\frac{P_2}{K_2}) - \frac{mP_3P_2^2}{\alpha_2^2+P_2^2} + \alpha_3P_1P_2 + \frac{\gamma P_3P_2^2}{\alpha_2^2+P_2^2} - \mu P_3 \\
\frac{dw}{dt} \leq& r_1P_1(1-\frac{P_1}{K_1}) + r_2P_2(1-\frac{P_2}{K_2}) - \mu P_3 \\
\frac{dw}{dt} + \tau w \leq& r_1P_1(1-\frac{P_1}{K_1}) + r_2P_2(1-\frac{P_2}{K_2}) - \mu P_3 + \tau(P_1+P_2+P_3) \\
\frac{dw}{dt} + \tau w \leq& r_1P_1(1-\frac{P_1}{K_1}) + r_2P_2(1-\frac{P_2}{K_2}) - \mu P_3 + \tau(P_1+P_2+P_3) \\
=& (r_1+\tau)P_1 + (r_2+\tau)P_2 - \frac{r_1}{K_1}P_1^2 - \frac{r_2}{K_2}P_2^2 - (\mu-\tau)P_3 \\
\frac{dw}{dt} + \tau w \leq& \frac{K_1(r_1+\tau)^2}{4r_1} + \frac{K_2(r_2+\tau)^2}{4r_2} = L,
\end{aligned}$$

here $0 < \tau < \mu$ and $L = \frac{K_1(r_1+\tau)^2}{4r_1} + \frac{K_2(r_2+\tau)^2}{4r_2}$. Using application of Gronwalls inequality [22], we obtain

$$0 < w(t) \leq e^{-\tau t}(w(0) - \frac{L}{\tau}) + \frac{L}{\tau},$$

when $t \to \infty$, yields $0 < w(t) < \frac{L}{\tau}$. □

LOCAL STABILITY ANALYSIS

Equilibria of the system

The model (1), (2) and (3) has the following equilibrium points
(i) The trivial equilibrium $E_0(P_1 = 0,\, P_2 = 0,\, P_3 = 0)$, which always exists.
(ii) $E_1(P_1 = 0,\, P_2 = K_2,\, P_3 = 0)$.
(iii) $E_2\,(P_1 = K_1,\, P_2 = 0,\, P_3 = 0)$.
(iv) $E_3\left(P_1 = 0,\, P_2 = -\frac{\sqrt{\mu}\alpha_2}{\sqrt{\gamma-\mu}},\, P_3 = \frac{\gamma r_2\alpha_2^2\left(\sqrt{\gamma-\mu}K_2+\sqrt{\mu}\alpha_2\right)}{m(\gamma-\mu)^{3/2}K_2}\right)$.

(v) $E_4\left(P_1=0,\, P_2=\frac{\sqrt{\mu}\alpha_2}{\sqrt{\gamma-\mu}},\, P_3=\frac{\gamma r_2\alpha_2^2\left(\sqrt{\gamma-\mu}K_2-\sqrt{\mu}\alpha_2\right)}{m(\gamma-\mu)^{3/2}K_2}\right)$.

(vi) $E_5\left(P_1=\frac{K_1r_2(r_1-K_2\alpha_1)}{r_1r_2+K_1K_2\alpha_1\alpha_3},\, P_2=\frac{K_2r_1(r_2+K_1\alpha_3)}{r_1r_2+K_1K_2\alpha_1\alpha_3},\, P_3=0\right)$.

(vii) $E_6\left(P_1=K_1\left(1+\frac{\sqrt{\mu}\alpha_1\alpha_2}{\sqrt{\gamma-\mu}r_1}\right),P_2=-\frac{\sqrt{\mu}\alpha_2}{\sqrt{\gamma-\mu}},\, P_3=\frac{\gamma\alpha_2^2\left(\sqrt{\mu}r_1r_2\alpha_2+K_2\left(\sqrt{\mu}K_1\alpha_1\alpha_2\alpha_3+\sqrt{\gamma-\mu}r_1(r_2+K_1\alpha_3)\right)\right)}{m(\gamma-\mu)^{3/2}K_2r_1}\right)$.

(viii) $E_7\left(P_1=K_1\left(1-\frac{\sqrt{\mu}\alpha_1\alpha_2}{\sqrt{\gamma-\mu}r_1}\right),P_2=\frac{\sqrt{\mu}\alpha_2}{\sqrt{\gamma-\mu}},\, P_3=\frac{\gamma\alpha_2^2\left(-\sqrt{\mu}r_1r_2\alpha_2+K_2\left(-\sqrt{\mu}K_1\alpha_1\alpha_2\alpha_3+\sqrt{\gamma-\mu}r_1(r_2+K_1\alpha_3)\right)\right)}{m(\gamma-\mu)^{3/2}K_2r_1}\right)$.

Local Stability

The equilibrium stability of smooth differential equations is evaluated by the sign of a real part of eigenvalues of the Jacobian matrix. The Jacobian matrix is the matrix of the partial derivatives of the right–hand side with respect to state variables where all derivatives are assessed at the equilibrium points and its eigenvalues decide stability. An equilibrium is asymptotically stable if all eigenvalues have negative real parts; it is unstable if there is at least one positive real part in eigenvalues of the Jacobian matrix. Moreover, the Routh–Hurwitz stability criterion uses the characteristic polynomial of a Jacobian matrix to provide stability information. Now, to examine the local stability of equilibrium points, the Jacobian matrix $J(P_1,\, P_2,\, P_3)$ of the prey–pest–natural enemy of system ((1), (2), (3)) at any equilibrium point $(P_1,\, P_2,\, P_3)$ is evaluated as

$$J(P_1,\, P_2,\, P_3)=\begin{pmatrix} -\frac{P_1r_1}{K_1}+\left(1-\frac{P_1}{K_1}\right)r_1-P_2\alpha_1 & -P_1\alpha_1 & 0 \\ P_2\alpha_3 & -\frac{P_2r_2}{K_2}+\left(1-\frac{P_2}{K_2}\right)r_2+\frac{2mP_2^2P_3}{(P_2^2+\alpha_2^2)^2}-\frac{mP_3}{P_2^2+\alpha_2^2}+P_1\alpha_3 & -\frac{mP_2}{P_2^2+\alpha_2^2} \\ 0 & -\frac{2\gamma P_2^3P_3}{(P_2^2+\alpha_2^2)^2}+\frac{2\gamma P_2P_3}{P_2^2+\alpha_2^2} & -\mu+\frac{\gamma P_2^2}{P_2^2+\alpha_2^2} \end{pmatrix}.$$

(i)The Jacobian matrix at equilibrium point $E_0(P_1=0,\, P_2=0,\, P_3=0)$ is

$$\begin{pmatrix} r_1 & 0 & 0 \\ 0 & r_2 & 0 \\ 0 & 0 & -\mu \end{pmatrix}$$

and the eigen values at the E_0 is r_1, r_2 and $-\mu$. Therefore the equilibrium point is saddle.

(ii) The Jacobian matrix for the equilibrium point $E_1(P_1=0,\, P_2=K_2,\, P_3=0)$ is

$$\begin{pmatrix} r_1-K_2\alpha_1 & 0 & 0 \\ K_2\alpha_3 & -r_2 & -\frac{mK_2}{K_2^2+\alpha_2^2} \\ 0 & 0 & -\mu+\frac{\gamma K_2^2}{K_2^2+\alpha_2^2} \end{pmatrix}.$$

The eigenvalues of $J(E_1)$ are $-r_2$, $r_1-K_2\alpha_1$ and $\frac{\gamma K_2^2-\mu K_2^2-\mu\alpha_2^2}{K_2^2+\alpha_2^2}$. Therefore the equilibrium point $E_1(P_1=0,\, P_2=K_2,\, P_3=0)$, is locally asymptotically stable if $r_1-K_2\alpha_1<0$ and $\frac{\gamma K_2^2-\mu K_2^2-\mu\alpha_2^2}{K_2^2+\alpha_2^2}<0$.

(iii) The Jacobian matrix for the equilibrium point $E_2(P_1=K_1,\, P_2=0,\, P_3=0)$ is

$$\begin{pmatrix} -r_1 & -K_1\alpha_1 & 0 \\ 0 & r_2+K_1\alpha_3 & 0 \\ 0 & 0 & -\mu. \end{pmatrix}.$$

The eigenvalues of $J(E_2)$ are $-\mu$, $-r_1$ and $r_2+K_1\alpha_3$. Since two eigenvalues are negative and other is always positive, therefore the system around the (E_2) point is saddle point.

(iii) The Jacobian matrix for the equilibrium point $E(P_1=0,\, P_2\neq 0,\, P_3\neq 0)$ is

$$\begin{pmatrix} r_1-P_2\alpha_1 & 0 & 0 \\ P_2\alpha_3 & -\frac{P_2r_2}{K_2}+\frac{2mP_2^2P_3}{(P_2^2+\alpha_2^2)^2}-\frac{mP_3}{P_2^2+\alpha_2^2}+\frac{mP_3P_2}{P_2^2+\alpha_2^2} & -\frac{mP_2}{P_2^2+\alpha_2^2} \\ 0 & -\frac{2\gamma P_2^3P_3}{(P_2^2+\alpha_2^2)^2}+\frac{2\gamma P_2P_3}{P_2^2+\alpha_2^2} & 0 \end{pmatrix}.$$

The characteristic polynomial of jacobian matrix is

$$x^3 + a_1x^2 + a_2x + a_3 = 0,$$

where, $a_1 = \left(-r_1 + \frac{P_2r_2}{K_2} + P_2\alpha_1 - \frac{2mP_2^2P_3}{(P_2^2+\alpha_2^2)^2} + \frac{mP_3}{P_2^2+\alpha_2^2} - \frac{mP_2P_3}{P_2^2+\alpha_2^2}\right)$,

$a_2 = \left(-\frac{P_2r_1r_2}{K_2} + \frac{P_2^2r_2\alpha_1}{K_2} + \frac{2mP_2^2P_3r_1}{(P_2^2+\alpha_2^2)^2} - \frac{2mP_2^3P_3\alpha_1}{(P_2^2+\alpha_2^2)^2} - \frac{mP_3r_1}{P_2^2+\alpha_2^2} + \frac{mP_2P_3r_1}{P_2^2+\alpha_2^2} + \frac{mP_2P_3\alpha_1}{P_2^2+\alpha_2^2} - \frac{mP_2^2P_3\alpha_1}{P_2^2+\alpha_2^2}\right)$, $a_3 = 0$.

For the local asymptotically stable of the system, the following Routh-Hurwitz criterion must be satisfied: (1) $a_1 > 0$, $a_2 > 0$, $a_3 > 0$, (2) $a_1a_2 - a_3 > 0$.

(iv) The Jacobian matrix for the equilibrium point $E(P_1 \neq 0,\ P_2 = 0,\ P_3 \neq 0)$ is

$$J = \begin{pmatrix} -\frac{P_1r_1}{K_1} & -P_1\alpha_1 & 0 \\ 0 & r_2 - \frac{mP_3}{\alpha_2^2} + P_1\alpha_3 & 0 \\ 0 & 0 & 0 \end{pmatrix}.$$

The eigenvalues of $J(E)$ are 0, $-\frac{P_1r_1}{K_1}$ and $r_2 - \frac{mP_3}{\alpha_2^2} + P_1\alpha_3$. In this case, system is not local asymptotically stable.

(v) The Jacobian matrix for the equilibrium point $E(P_1 \neq 0,\ P_2 \neq 0,\ P_3 = 0)$ is

$$\begin{pmatrix} -\frac{P_1r_1}{K_1} & -P_1\alpha_1 & 0 \\ P_2\alpha_3 & -\frac{P_2r_2}{K_2} + \frac{mP_3P_2}{P_2^2+\alpha_2^2} & -\frac{mP_2}{P_2^2+\alpha_2^2} \\ 0 & 0 & -\mu + \frac{\gamma P_2^2}{P_2^2+\alpha_2^2} \end{pmatrix}.$$

The characteristic polynomial of jacobian matrix is

$$x^3 + a_1x^2 + a_2x + a_3 = 0,$$

where $a_1 = \left(\mu + \frac{P_1r_1}{K_1} + \frac{P_2r_2}{K_2} - \frac{\gamma P_2^2}{P_2^2+\alpha_2^2} - \frac{mP_2P_3}{P_2^2+\alpha_2^2}\right)$

$a_2 = \left(\frac{\mu P_1r_1}{K_1} + \frac{\mu P_2r_2}{K_2} + \frac{P_1P_2r_1r_2}{K_1K_2} + \frac{m\gamma P_2^3P_3}{(P_2^2+\alpha_2^2)^2} - \frac{m\mu P_2P_3}{P_2^2+\alpha_2^2} - \frac{\gamma P_1P_2^2r_1}{K_1(P_2^2+\alpha_2^2)} - \frac{mP_1P_2P_3r_1}{K_1(P_2^2+\alpha_2^2)} - \frac{\gamma P_2^3r_2}{K_2(P_2^2+\alpha_2^2)} + P_1P_2\alpha_1\alpha_3\right)$

$a_3 = \frac{\mu P_1P_2r_1r_2}{K_1K_2} + \frac{m\gamma P_1P_2^3P_3r_1}{K_1(P_2^2+\alpha_2^2)^2} - \frac{m\mu P_1P_2P_3r_1}{K_1(P_2^2+\alpha_2^2)} - \frac{\gamma P_1P_2^3r_1r_2}{K_1K_2(P_2^2+\alpha_2^2)} + \mu P_1P_2\alpha_1\alpha_3 - \frac{\gamma P_1P_2^3\alpha_1\alpha_3}{P_2^2+\alpha_2^2}$.

For the local asymptotically stable of the system, the following Routh–Hurwitz criterion must be satisfied:
(1) $a_1 > 0$, $a_2 > 0$, $a_3 > 0$,
(2)$a_1a_2 - a_3 > 0$.

(vi) The Jacobian matrix for the equilibrium point $E(P_1 \neq 0,\ P_2 \neq 0,\ P_3 \neq 0)$ is

$$\begin{pmatrix} -\frac{P_1r_1}{K_1} & -P_1\alpha_1 & 0 \\ P_2\alpha_3 & -\frac{P_2r_2}{K_2} + \left(1 - \frac{P_2}{K_2}\right)r_2 + \frac{2mP_2^2P_3}{(P_2^2+\alpha_2^2)^2} - \frac{mP_3}{P_2^2+\alpha_2^2} + P_1\alpha_3 & -\frac{mP_2}{P_2^2+\alpha_2^2} \\ 0 & -\frac{2\gamma P_2^3P_3}{(P_2^2+\alpha_2^2)^2} + \frac{2\gamma P_2P_3}{P_2^2+\alpha_2^2} & 0 \end{pmatrix}.$$

The characteristic equation of system around the equilibrium is

$$x^3 + a_1x^2 + a_2x + a_3 = 0,$$

where $a_1 = \left(\frac{P_1r_1}{K_1} + \left(-1 + \frac{2P_2}{K_2}\right)r_2 - \frac{2mP_2^2P_3}{(P_2^2+\alpha_2^2)^2} + \frac{mP_3}{P_2^2+\alpha_2^2} - P_1\alpha_3\right)$

$a_2 = \left(P_1\left(-1 + \frac{2P_2}{K_2}\right)r_1\frac{r_2}{K_1} - \frac{2m\gamma P_2^4P_3}{(P_2^2+\alpha_2^2)^3} + \frac{2m\gamma P_2^2P_3}{(P_2^2+\alpha_2^2)^2} - \frac{2mP_1P_2^2P_3r_1}{K_1(P_2^2+\alpha_2^2)^2} + \frac{mP_1P_3r_1}{K_1(P_2^2+\alpha_2^2)} - \frac{P_1^2r_1\alpha_3}{K_1} + P_1P_2\alpha_1\alpha_3\right)$

$a_3 = \frac{2m\gamma P_1P_2^4P_3r_1}{K_1(P_2^2+\alpha_2^2)^3} + \frac{2m\gamma P_1P_2^2P_3r_1}{K_1(P_2^2+\alpha_2^2)^2}$.

For the local asymptotically stable of the system, the following Routh–Hurwitz criterion must be satisfied:
(i) $a_1 > 0$, $a_2 > 0$, $a_3 > 0$,
(ii)$a_1a_2 - a_3 > 0$.

THE MODEL IN THE PRESENCE OF CONTROL

Lately, pest-control has become a remarkable issue in ecological field as it can reduce the losses of both food and economy. Recent studies and research has shown that pest population can be decreased by using natural enemy of pest and chemicals like pesticides. It is noticed that spraying of pesticides had reduced the growth of pest population initially but the pest population may revival rapidly after a period of little time or larger than pre treatments level in later stages. Recently, [40] considered the mixture of controls based on prey infection, predation and chemical pesticide application and implemented an optimal plan for monitoring. It is importance that our model can also be modified by using balance pesticides as a control variable when pesticides kill pests. Thus, our new model is

$$\frac{dP_1}{dt} = r_1 P_1(1 - \frac{P_1}{K_1}) - \alpha_1 P_1 P_2, \tag{4}$$

$$\frac{dP_2}{dt} = r_2 P_2(1 - \frac{P_2}{K_2}) - \frac{mP_3 P_2^2}{\alpha_2^2 + P_2^2} + \alpha_3 P_1 P_2 - ubP_2, \tag{5}$$

$$\frac{dP_3}{dt} = \frac{\gamma P_3 P_2^2}{\alpha_2^2 + P_2^2} - \mu P_3. \tag{6}$$

with initial data $P_1(0) > 0$, $P_2(0) > 0$ and $P_3(0) > 0$. Here, natural enemies of pest P_3 have been used as a biological control strategy for removing harmful organism species. Biological organism control helps to find the natural enemies of a pest and implementing such natural predators into the specific community where the pest has accumulated. The natural enemies must be before release to establish that they do not have a detrimental effect on the climate or the economy. Furthermore, many entomopathogens are widely viable in a dosage form that can be treated like a pesticide. Term $\frac{mP_3P_2^2}{\alpha_2^2+P_2^2}$ is negative impact on harmful pests in agriculture. We presume that functional response of type III happens between pest species and their natural enemies, as survival first increases with increasing density of pests, and then decreases. When pest density is controlled by biological control and pesticides, crop density increases. Therefore, P_1 and P_3 are not taken in minimize the objective functional. In addition, pesticide regulation u should concentrate on time and should be used as needed. While our main goal throughout this section is to minimize the number of pests by using pesticide. The aim is to minimize the pest density of P_1. To attain the objective, through this way we construct the functional objective of our optimal control problem as regards:

$$J(u) = \min_u \int_0^{T_f} (A_1 P_2(t) + A_2 u(t)^2) dt, \tag{7}$$

where $A_1 > 0$ and $A_2 > 0$ are weights. A_1 is corresponding to the pest density and A_2 is the parameter of the square of control. The harmful side outcome of the pesticide are remove by the square of the control [21, 32, 33]. The objective functional is subject to ((4), (5) (6)). The term A_2u^2 is the cost of control on rate of application of pesticide strategy. We want to find a optimal control such that

$$J(u^*) = min\{J(u)|u \in U\}, \tag{8}$$

where U is control set defined by below:

$$U = \{u(t)|u(t) \text{ are lebesgue measurable with } 0 \leq t \leq 1,\ t \in [0,T].\} \tag{9}$$

Based on its relative significance, the weight of state variables is typically allocated while many of the control are allocated according to their expense impacts. With the help of Pontryagins maximum principle [25], we obtain the requisite criteria to evaluate the value of the control such that the J is optimized. If this feasible control occurs then this is recognized as optimal control [26, 27]. By establishing the Hamiltonian H and then introducing the maximum Pontryagin principle, We establish the necessary criteria for the existence of optimal control. Adjoint functions also have a common theme in multivariate calculus as Lagrange multipliers, which add constraints to the function of multiple variables to be optimized. Thus, we consider finding suitable requirements that the adjoint function should fulfill. Then, by separating the diagram from control to functional objective. For minimization, the control variables are strongly convex in the Hamiltonian equation. Let the Hamiltonian H is

$$H(t,P(t),\lambda(t),u(t)) = f(t,P(t),u(t)) + \lambda(t)g(t,P(t),u(t)),$$

where $f(t,P(t),u(t))$ is integrand of the functional $J(u)$ and $g(t,P(t),u(t))$ is right hand side of the equation (4), (5) and (6). If $P_1^*(t)$, $P_2^*(t)$, $P_3^*(t)$ and $u^*(t)$ is an optimal solution, then there is a non–trivial vector function $\lambda(t)$ satisfying the following equations:

$$\begin{cases} \frac{dP}{dt} = \frac{\partial H(t,P^*(t),\lambda(t),u^*(t))}{\partial \lambda}, \\ 0 = \frac{\partial H(t,P^*(t),\lambda(t),u^*(t))}{\partial u}, \\ \lambda'(t) = -\frac{\partial H(t,P^*(t),\lambda(t),u^*(t))}{\partial P}. \end{cases}$$

If the control is bounded, i.e. $a \leq u(t) \leq b$, then optimal control $u^*(t)$ [27] is given by

$$\begin{cases} u^* = a, & \text{if } \frac{\partial H}{\partial u} < 0, \\ a \leq u^* \leq b, & \text{if } \frac{\partial H}{\partial u} = 0, \\ u^* = b, & \text{if } \frac{\partial H}{\partial u} > 0. \end{cases}$$

Thus, to find the optimal value of J, we make the Hamiltonian as:
$H = A_1P_2 + A_2u^2 + \lambda_1(r_1P_1(1-\frac{P_1}{K_1}) - \alpha_1P_1P_2) + \lambda_2(r_2P_2(1-\frac{P_2}{K_2}) - \frac{mP_3P_2^2}{\alpha_2^2+P_2^2} + \alpha_3P_1P_2 - ubP_2) + \lambda_3(\frac{\gamma P_3P_2^2}{\alpha_2^2+P_2^2} - \mu P_3)$
with $\lambda = [\lambda_1,\ \lambda_2,\ \lambda_3]^T$, the adjoint vector associated to the state P_1, P_2 and P_3 associated to the prey-predator model. Pontryagin's maximum principle calculate the exact evolution of the adjoint functions. The optimality scheme of equations can be computed by taking partial derivatives of the Hamiltonian corresponding to the state variable. The optimality technique consists of the state and adjoint systems along with the characterization of the control variables.

Theorem .2. *Given the objective functional* $J(u) = \min_u \int_0^{T_f} (A_1P_2(t) + A_2u(t)^2)dt$, *with initial data* $P_1(0) = P_{10} > 0$, $P_2(0) = P_{20} > 0$, $P_3(0) = P_{30} > 0$, $t \in [0,T_f]$ *and* $u(t)$ *is measurable with* $0 \leq u(t) \leq 1$, *then there is an optimal control* $u^*(t)$ *which minimizes the objective functional* $J(u^*)$ *such that*

$$J(u^*) = min\{J(u)|0 \leq u(t) \leq 1\}$$

.

Proof. To investigate the existence of optimal control, we must first show the following result using the boundedness of the system over a finite given period. The following condition should be fulfilled:
(i) The set of state variables and controls is non–empty.
(ii) The control set U is closed and convex.
(iii) Objective functional (integrand) is convex in U.
(iv) The state system R.H.S is bounded by a linear function in the variables of state and control where coefficients depend on the state and time.
(v) The integrand bounded below by $c_1(|u|^2)^{\frac{\beta}{2}} - c_2$ for $c_1 > 0$, $c_2 > 0$ and $\beta > 1$. We use the results from [27, 28] to check the above conditions. The state and control variables are non–negative values, and in the minimization problem, the convexity of the necessary condition of the objective functional in $u(t)$ is met. The control set is convex and closed by definition and the admissible Lebesgue measurable control variables set $u(t)$ is also convex and closed, integrand $f(t,p,u) = A_1P_2 + A_2u^2$ is clearly convex in u.

For the forth condition, The system is linear in the control and can be expressed as

$$\overrightarrow{g}(t,\overrightarrow{P},u) = \overrightarrow{\alpha}(t,\overrightarrow{P}) + \overrightarrow{\beta}(t,\overrightarrow{P})u,$$

where $\overrightarrow{g}(t,\overrightarrow{P},u)$ is R.H.S of the state equation, $\overrightarrow{P} = (P_1,P_2,P_3)$, $\overrightarrow{\alpha}$ and $\overrightarrow{\beta}$ is a vector valued function of $\overrightarrow{P}$. Using solution of bounded, we see that

$$\left|\left[\ \overrightarrow{g}(t,\overrightarrow{P},u)\ \right]\right| \leq \left|\begin{bmatrix} r_1 & 0 & 0 \\ \alpha_3 P_2 & r_2 & 0 \\ 0 & 0 & \gamma \end{bmatrix}\right|\left|\begin{bmatrix} P_1 \\ P_2 \\ P_3 \end{bmatrix}\right| + \left|\begin{bmatrix} 0 \\ -b_2 u P_2 \\ 0 \end{bmatrix}\right|$$
$$\leq \left|\begin{bmatrix} r_1 & 0 & 0 \\ \alpha_3 K_2 & r_2 & 0 \\ 0 & 0 & \gamma \end{bmatrix}\right|\left|\begin{bmatrix} P_1 \\ P_2 \\ P_3 \end{bmatrix}\right| + \left|\begin{bmatrix} 0 \\ b_2 u K_2 \\ 0 \end{bmatrix}\right|$$
$$\leq C_1|\overrightarrow{P}| + C_2|u|,$$

where C_1 is dependent on system coefficients and C_2 is maximum norm value.
For the last condition (5),

$$A_1P_2 + A_2u^2 \geq A_2(|u|^2)^{\frac{\beta}{2}} \geq c_1(|u|^2)^{\frac{\beta}{2}} - c_2,$$

where c_1 and $c_2 > 0$, Hence, there exists constants c_1, c_2 and $\beta > 1$ such that $A_1P_2 + A_2u^2 \geq c_1(|u|^2)^{\frac{\beta}{2}} - c_2$.
The optimal system satisfies all the above conditions and it has been bounded closed, which determines the compactness for the existence of the optimal control. □

Theorem .3. *If $u^*(t)$ be an optimal control which minimize $J(u)$. Let $P_1^*(t)$, $P_2^*(t)$ and $P_3^*(t)$ are optimal state solutions for the control system* (4)*,* (5) *and* (6)*, then there exist adjoint variables $\lambda_1(t)$, $\lambda_2(t)$ and $\lambda_3(t)$ such that:*

$$\frac{d\lambda_1}{dt} = -(\frac{\partial H}{\partial P_1}) = -\frac{(K_1 - 2P_1)r_1\lambda_1}{K_1} + P_2(\alpha_1\lambda_1 - \alpha_3\lambda_2),$$
$$\frac{d\lambda_2}{dt} = -(\frac{\partial H}{\partial P_2}) = -A_1 + bu\lambda_2 - r_2\lambda_2 + \frac{2P_2r_2\lambda_2}{K_2} - \frac{2mP_2^2P_3\lambda_2}{(P_2^2+\alpha_2^2)^2} + \frac{mP_3\lambda_2}{P_2^2+\alpha_2^2} + P_1(\alpha_1\lambda_1 - \alpha_3\lambda_2) + \frac{2\gamma P_2^3P_3\lambda_3}{(P_2^2+\alpha_2^2)^2} - \frac{2\gamma P_2P_3\lambda_3}{P_2^2+\alpha_2^2},$$
$$\frac{d\lambda_3}{dt} = -(\frac{\partial H}{\partial P_3}) = \frac{mP_2\lambda_2 + (-\gamma+\mu)P_2^2\lambda_3 + \mu\alpha_2^2\lambda_3}{P_2^2+\alpha_2^2}, \tag{10}$$

with the transversality conditions are

$$\lambda_i(T_f) = 0 \text{ for } i = 1,\ 2,\ 3. \tag{11}$$

Further, the optimal control variable u^* that minimize $J(u)$ is given by

$$u^*(t) = min\ \{max\ \{0,\ \frac{\lambda_2 bP_2^*}{2A_2}\},\ 1\}. \tag{12}$$

Proof. The transversality and adjoint conditions are given result by [27, 45], using the Hamiltonian function H:

$$H(t,\ \overrightarrow{P},\ \overrightarrow{u}) = f(t,\ \overrightarrow{P},\ \overrightarrow{u}) + \sum_{i=1}^{3}\lambda_i g_i(t,\ \overrightarrow{P},\ \overrightarrow{u}),$$

where $f(t,\ \overrightarrow{P},\ \overrightarrow{u})$ is integrand of the functional and $g_i(t,\ \overrightarrow{P},\ \overrightarrow{u})$ are state equations.

$H = A_1P_2 + A_2u^2 + \lambda_1(r_1P_1(1-\frac{P_1}{K_1}) - \alpha_1P_1P_2) + \lambda_2(r_2P_2(1-\frac{P_2}{K_2}) - \frac{mP_3P_2^2}{\alpha_2^2+P_2^2} + \alpha_3P_1P_2 - ubP_2) + \lambda_3(\frac{\gamma P_3P_2^2}{\alpha_2^2+P_2^2} - \mu P_3)$

with $\lambda = [\lambda_1,\ \lambda_2,\ \lambda_3]^T$, the adjoint vector associated to the state P_1, P_2 and P_3. The Pontryagin's maximum principle [1] provides adjoint system which can be followed as:

$$\frac{d\lambda_1}{dt} = -(\frac{\partial H}{\partial P_1}) = -\frac{(K_1 - 2P_1)r_1\lambda_1}{K_1} + P_2(\alpha_1\lambda_1 - \alpha_3\lambda_2),$$
$$\frac{d\lambda_2}{dt} = -(\frac{\partial H}{\partial P_2}) = -A_1 + bu\lambda_2 - r_2\lambda_2 + \frac{2P_2r_2\lambda_2}{K_2} - \frac{2mP_2^2P_3\lambda_2}{(P_2^2+\alpha_2^2)^2} + \frac{mP_3\lambda_2}{P_2^2+\alpha_2^2} + P_1(\alpha_1\lambda_1 - \alpha_3\lambda_2) + \frac{2\gamma P_2^3P_3\lambda_3}{(P_2^2+\alpha_2^2)^2} - \frac{2\gamma P_2P_3\lambda_3}{P_2^2+\alpha_2^2},$$
$$\frac{d\lambda_3}{dt} = -(\frac{\partial H}{\partial P_3}) = \frac{mP_2\lambda_2 + (-\gamma+\mu)P_2^2\lambda_3 + \mu\alpha_2^2\lambda_3}{P_2^2+\alpha_2^2}.$$

The transversality conditions are

$$\lambda_i(T_f) = 0 \text{ for } i = 1,\ 2,\ 3.$$

The optimality condition provides

$$\begin{aligned}\frac{\partial H}{\partial u} = 2A_2u - \lambda_2 bP_2 = 0 \text{ at } u = u^*(t)\\ \Rightarrow 2A_2u^* - \lambda_2 bP_2 = 0 = 0\\ \Rightarrow u^*(t) = \frac{.\lambda_2 bP_2^*}{2A_2}.\end{aligned}$$

□

NUMERICAL SIMULATION

For the simulation objective, we take a simulated set of parameters for minimize pest population and maximize the crop population and we take the initial population for the prey, pest and natural enemies as 2, 1.2, and 0.8 respectively. Fig. 1 explore the dynamics of the system (1), (2) and (3) by using numerical simulations and computations. Next, we obtain the solution of optimal control problem numerically using fourth order Runge-Kutta procedure [27, 31, 32, 33, 34]. Fig. 2 shows the solution curves of the state variables crop(prey), pest and natural enemy population in the presence of control and natural enemies versus in the absence of control and natural enemies. Observation shows that the application of optimal control variables and natural enemy reduce a quite larger number of pest population compared to in the absence of the control and natural enemy. Crop population increases from 2 $gram\ cm^{-3}$ to more than 5.5 $gram\ cm^{-3}$ approximately at $t = 2$ $months$. Again from the Fig. 2, it is easy to observe that pest population increases rapidly in the absence of control and natural enemies and almost constant in the presence of control and natural enemies. Fig. 2(c) and Fig. 2(d) represent the variation of natural enemy and control variables with respect to time respectively. In Fig. 4, there are some changes in parameters like weight $A_1 = 1$ to 100, $A_2 = 1$ to 50, $r_1 = 0.9\ month^{-1}$ to $0.5\ month^{-1}$, $r_2 = 0.258\ month^{-1}$ to $0.35\ month^{-1}$, $\alpha_2 = 0.25; gram\ cm^{-3}$ to $0.2; gram\ cm^{-3}$, $b = 1$ to 2, $t = 2$ $months$ to 0.5 $months$. Fig. 4(a) shows the crop production increase from 2 $gram\ cm^{-3}$ to 2.25 $gram\ cm^{-3}$ at $t = 0.5$ months, Fig. 4(b) represent the pest population variation in the presence and absence of natural enemy and pesticide.

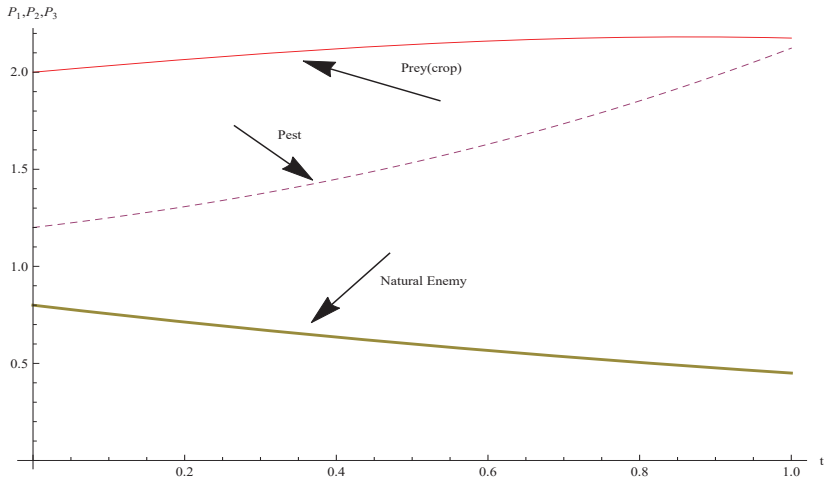

FIGURE 1. This figure illustrates the dynamics of the system between prey, pest and natural enemy of pest with respect to the time, where values of parameters are $r_1 = 0.5\ month^{-1}, K_1 = 20\ gram\ cm^{-3}, m = 0.7\ month^{-1}$, $\alpha_1 = 0.23\ gram^{-1}\ cm^3\ month^{-1}, r_2 = .35\ month^{-1}, K_2 = 15\ gram\ cm^{-3}, \alpha_2 = 0.3\ gram\ cm^{-3}, \alpha_3 = .25\ gram^{-1}\ cm^3\ month^{-1}$, $\gamma = .026\ month^{-1}$, $\mu = 0.6\ month^{-1}$, $P_{10} = 2\ gram\ cm^{-3}$, $P_{20} = 1.2\ gram\ cm^{-3}$, $P_{30} = 0.9\ gram\ cm^{-3}$ and $t = 2$ $months$.

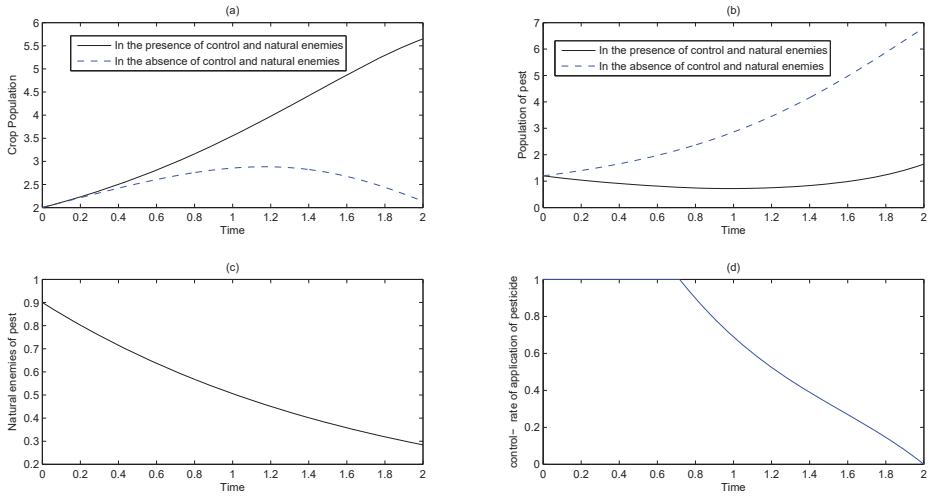

FIGURE 2. This graph depicts the results of the comparison between the curves of prey(crops), pest and predator individuals in the presence of control and natural enemies versus in the absence of control and natural enemies, natural enemies population and control variable with respect to the time, where values of parameters are $A_1 = 1\ month^{-1}$, $A_2 = 1$, $r_1 = 0.9$, $K_1 = 20\ gram\ cm^{-3}$, $\alpha_1 = 0.23\ gram^{-1}\ cm^3\ month^{-1}$, $r_2 = 0.258\ month^{-1}$, $K_2 = 15\ gram\ cm^{-3}$, $m = 0.7\ month^{-1}$, $\alpha_2 = 0.25\ gram\ cm^{-3}$, $\alpha_3 = 0.258\ gram^{-1}\ cm^3\ month^{-1}$, $b = 1$, $\gamma = 0.0256\ month^{-1}$, $\mu = 0.6\ month^{-1}$, $P_{10} = 2\ gram\ cm^{-3}$, $P_{20} = 1.2\ gram\ cm^{-3}$, $P_{30} = 0.9\ gram\ cm^{-3}$ and $t = 2\ months$.

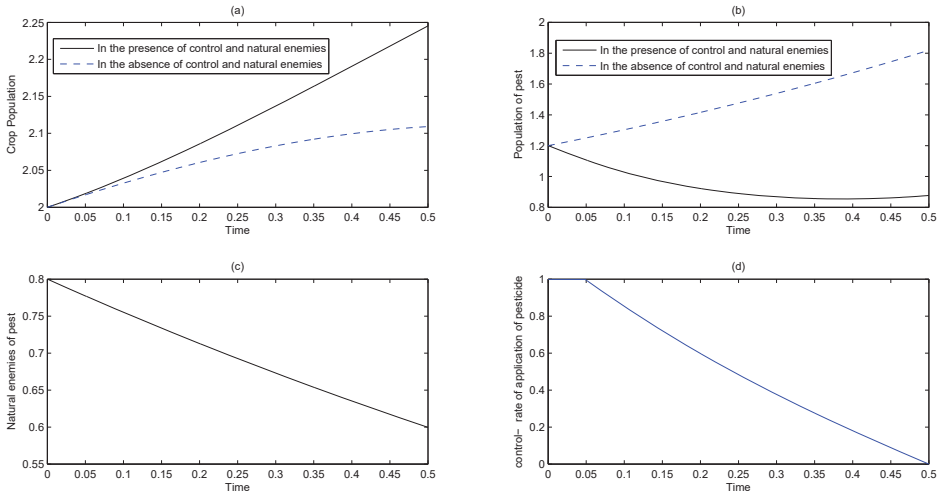

FIGURE 3. This figure depicts the results of the comparison between the curves of prey(crops), pest and predator population in the presence of control and natural enemies versus in the absence of control and natural enemies, natural enemies population and control variable with respect to the time, where values of parameters are $A_1 = 100$, $A_2 = 50$, $r_1 = 0.5\ month^{-1}$, $K_1 = 20\ gram\ cm^{-3}$, $\alpha_1 = 0.23\ gram^{-1}\ cm^3\ month^{-1}$, $r_2 = 0.35\ month^{-1}$, $K_2 = 15\ gram\ cm^{-3}$, $m = 0.7\ month^{-1}$, $\alpha_2 = 0.2\ gram\ cm^{-3}$, $\alpha_3 = 0.25\ gram^{-1}\ cm^3\ month^{-1}$, $b = 2$, $\gamma = 0.026\ month^{-1}$, $\mu = 0.6\ month^{-1}$, $P_{10} = 2\ gram\ cm^{-3}$, $P_{20} = 1.2\ gram\ cm^{-3}$, $P_{30} = 0.8\ gram\ cm^{-3}$ and $t = 0.5\ months$.

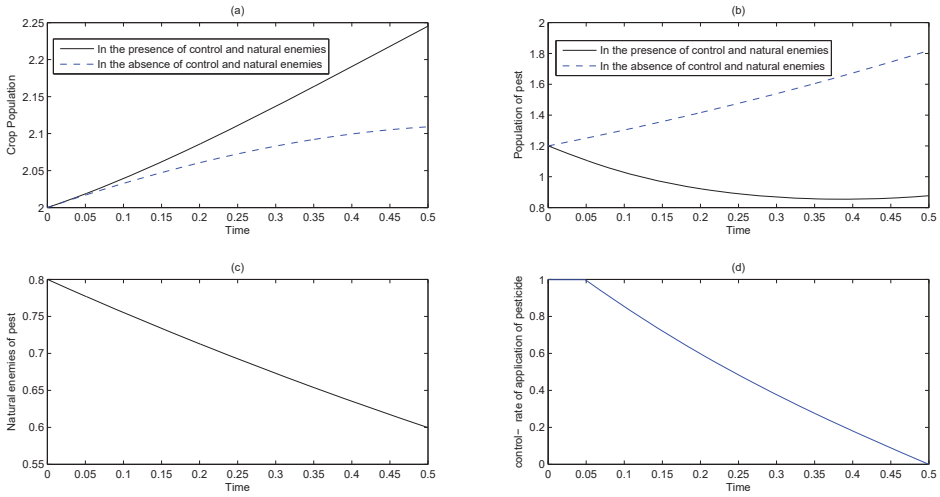

FIGURE 4. This figure depicts the results of the comparison between the curves of prey(crops), pest and predator.

CONCLUSION

In this study, we proposed a three-dimensional model of prey(crop), pest(a predator of prey), and natural enemy of pest(a predator of pest) and a systematic approach has been applied to control the pest population using a combination of pesticide and a natural enemy of pest. The studies have shown the system is bound. The existence and stability criteria of the equilibrium point have been established. Further, by applying the Pontryagins maximum principle, we proved the existence and determined the necessary conditions of the optimal control. We have also numerically analyzed the significantly affect of the natural enemy on the pest population and crop production in the model. In the presence of the natural enemy and control variables, the pest population has been decreased and crop(prey) production has been increased in the prey–pest–natural enemy of pest model. Thus, our results showed that the natural enemy has a significant role in regulating the pest population.

ACKNOWLEDGEMENT

Authors are thankful to the reviewers for the very useful and valuable suggestions.

REFERENCES

1. L. S. Pontryagin, V. G. Boltyanskii, R. V. Gamkrelidze and E. F. Mishchenko, The Mathematical Theory of Optimal Processes (Gordon and Breach Science Publishers, 1986).
2. Pradhan S Assessment of losses caused by insect pests of crops and estimation of insect population. In: Pant NC (ed) Entomology in India. Entomological Society of India, New Delhi, pp17–58, 1964.
3. Krishnamurthy Rao BH, Murthy KSRK (eds), Proceedings of national seminar on crop losses due to insect pests. Jan 7–9, Hyderabad, Indian JEnt I–II(Spl issue), 1983.
4. Atwal AS, Future of pesticides in plant protection. Proc Indian Natn Sci Acad 52:77–90, 1986.
5. Jayaraj S, Biopesticides and integrated pest management for sustainable crop production, 1993.
6. Lal OP, Recent advances in Indian entomology. APC, New Delhi, 1996.
7. Dhaliwal GS, Arora R (1996) An estimate of yield losses due to insect pests in Indian agriculture, Indian JEcol, 23:70–73, 1996.
8. Dhaliwal GS, Arora R, Estimation of losses due to insect pests in field crops In: Sarath Babu B, Varaprasad KS, Anitha K, Prasada Rao RDVJ, Chakrabarty SK, Chandukar PS (eds) Resources management in plant protection, Vol 1. Plant Protection Association of India, Hyderabad,pp 11–23, 2002.

9. Dhaliwal GS, Arora R, Dhawan AK, Crop losses due to insect pests and determination of economic threshold levels. In: Singh A, Trivedi TP, Sardana HR, Sharma OP, Sabir N (eds) Recent advances in integrated pest management. National Centre for Integrated Pest Management, New Delhi, pp12–20, 2003.
10. Dhaliwal GS, Arora R, Dhawan AK, Crop losses due to insect pests in Indian agriculture: An update. Indian JEcol, 31:1–7, 2003.
11. Dhaliwal GS, Jindal V, Dhawan AK, Insect pest problems and crop losses: Changing trends. Indian JEcol, 74:1–7, 2010.
12. Oerke EC, Dehne HW, Safeguarding production losses in major crops and the role of crop protection. Crop Prot, 23:275–285, 2010.
13. Culliney T Crop losses to arthropods. In: Pimentel D, Peshin R, Integrated pest management reviews, vol 3. Chapman & Hall, London, pp 201–225, 2014.
14. Swaminathan MS, Plant protection for global food security. In: Proceedings of 10th international congress on plant protection Brighton, British Crop Protection Council, Oxford, Nov 20–25, vol 1.1, 1983.
15. Dhaliwal GS, Jindal V, Mohindru B, Crop losses due to insect pests: Global and Indian scenario. Indian J Ecol 77:165–168, 2015.
16. Rai AB, Halder J, Kodandaram MH, Emerging insect pest problems in vegetable crops and their management in India: An appraisal. Pest Mgmt Hort Ecosyst, 20:113–122, 2014.
17. Oerke EC, Crop losses to pests. J Agric Sci 144:31–43, 2006.
18. Schuster M, Torero M, Towards a sustainable food system: reducing food loss and waste. In: 2016 Global food policy report, International Food Policy Research Institute. Available via `http://ebrary.ifpri.org/cdm/ref/collection/p15738coll2/id/130211`. Accessed 28 June, 2016.
19. Puri SN, Ramamurthy VV, Insects and integrated pest management in the context of climate change-an overview. In: Ramamurthy VV, Gupta GP and Puri SN (eds) Proceedings of national symposium on IPM strategies to combat emerging pests in the current scenario of climate change, Pasighat, Jan 28–30, p 1–7, 2009.
20. Pradhan S, Agricultural entomology and pest control. Indian Council of Agricultural Research, New Delhi, 1983.
21. Joshi, H.R.: Optimal control of an HIV immunology model. Optim. Control Appl. Methods 23, 199–213, 2002.
22. G. Birkhoff and G.C. Rota, Ordinary Differential Equations, Blaisdell,Walthem, MA 1982.
23. Kar, T.K., Batabyal, A.: Stability analysis and optimal control of an SIR epidemic model with vaccination. Biosystems 104, 127–135, 2011.
24. Kar, T.K., Jana, S.: Application of three controls optimally in a vector-borne diseasea mathematical study. Commun. Nonlinear Sci. Numer. Simul. 18(10), 2868–2884, 2013.
25. Pontryagin, L.S., Boltyanskii, V.G., Gamkrelidze, R.V., Mishchenko, E.F.: The Mathematical Theory of Optimal Processes. Wiley, New York 1962.
26. Clark, C.W.: Mathematical Bioeconomics: The Optimal Management of Renewable Resources. Wiley, New York 1990.
27. Lenhart, S., Workman, J.T.: Optimal Control Applied to Biological Models. Mathematical and Computational Biology Series. Chapman & Hall/CRC, London, 2007.
28. W.H.Fleming and R.W.Rishel ,Deterministic and Stochastic Optimal Control(Springer-Verlag, New York, 1975.
29. Dhaliwal GS, Dhawan AK, Singh R, Biodiversity and ecological agriculture: Issues and perspectives. Indian JEcol 34:100–109, 2007.
30. Y. Hsieh, S. Sheu., "The effect of density-dependent treatment and behaviour change on the dynamics of HIV trans–mission". Journal of Mathematical Biology, 43: 69–80, 2001.
31. Jung, E., Lenhart, S., Feng, Z.: Optimal control of treatments in a two-strain tuberculosis model. Discrete Contin. Dyn. Syst., Ser. B 2–4, 473–482, 2002.
32. Kar, T.K., Ghosh, B.: Sustainability and optimal control of an exploited prey–predator system through provision of alternative food to predator. Biosystems 109, 220–232, 2012.
33. Kar, T.K., Jana, S.: A theoretical study on mathematical modelling of an infectious disease with application of optimal control. Biosystems 111, 37–50, 2013.
34. Birkoff, G., Rota, G.C.: Ordinary Differential Equations. Ginn, Boston, 1982.
35. Liu B, Chen L, Zhang Y, The dynamics of a prey-dependent consumption model concerning impulsive control strategy, Appl Math Comput, 169(1):305–320, 2005.
36. Kant, S., Kumar V.: Dynamics of a prey-predator system with infection in prey, Electronic Journal of Differential Equations 209, 1–27, 2017.
37. Kant, S., Kumar V.: Dynamical behavior of a stage structured prey-predator model, International Journal of Nonlinear Analysis and Applications 7 (1), 231–241, 2016.
38. Mehra, M., Malik, R.K., Solutions of differential–difference equations arising from mathematical models of granulocytopoiesis, differential equations and dynamical systems 22 (1), 33–49, 2014.
39. Shi R, Jiang X, Chen L, A predator–prey model with disease in the prey and two impulses for integrated pest management, Appl Math Model, 3(5):2248–2256, 2009.
40. Jana S, Kar T, A mathematical study of a prey–predator model in relevance to pest control, Nonlinear Dyn, 74:667–683, 2014.
41. JE, Brindley J, Ocean plankton populations as excitable media, Bull Math Biol, 56(5):981–998, 1994.
42. Tang S, Cheke RA, State-dependent impulsive models of integrated pest management (IPM) strategies and their dynamic consequences, J Math Biol, 50(3):257–292, 2005.
43. Tang S, Xiao Y, Chen L, Cheke RA, Integrated pest management models and their dynamical behavior, Bull Math Biol, 67(1):115–135, 2005.
44. Lu Z, Chi X, Chen L, Impulsive control strategies in biological control of pesticide. Theor Popul Biol, 64(1):39–47, 2003.
45. L. S. Pontryagin, V. G. Boltyanskii, R. V. Gamkrelidze and E. F. Mishchenko, The Mathematical Theory of Optimal Processes (Gordon and Breach Science Publishers, 1986.

2021 11th International Conference on Cloud Computing, Data Science & Engineering (Confluence) | 978-1-6654-1451-7/20/$31.00 ©2021 IEEE | DOI: 10.1109/Confluence51648.2021.9377068

Support Vector based Oversampling Technique for Handling Class Imbalance in Software Defect Prediction

Ruchika Malhotra
Department of Computer Science
Delhi Technological University
New Delhi, India
ruchikamalhotra@dtu.ac.in

Vaibhav Agrawal
Dept. of Computer Science
Delhi Technological University
New Delhi, India
vaibhavagrawal_2k17se122@dtu.ac.in

Vedansh Pal
Dept. of Computer Science
Delhi Technological University
New Delhi, India
vedanshpal_2k17se125@dtu.ac.in

Tushar Agarwal
Department of Computer Science
Delhi Technological University
New Delhi, India
tusharagarwal_2k17se121@dtu.ac.in

***Abstract*—The importance of software defect prediction has risen significantly over the past decade and is an inseparable part of software quality. Owing to the drawbacks of traditional techniques used for software quality assurance, machine learning algorithms are used to detect the defect in software modules. By the means of this study, we present a support vector based oversampling technique as a part of the software defect procedure and compare it with two other oversampling techniques namely Synthetic minority oversampling technique and Adaptive Synthetic oversampling technique. For the purpose of this study, we chose 5 datasets from the PROMISE and AEEEM repositories. After extracting a subset of attributes from the original dataset through Linear discriminant Analysis, we utilize the improved oversampled dataset to train a support vector machine classifier and a Naïve Bayesian classifier. The proposed Support Vector based oversampling technique along with Linear Discriminant Analysis performs better than the other techniques for the performance evaluation metric of F-measure score and the area under receiver operating characteristic curve and the consistency of result is maintained.**

Keywords— Defect Prediction, Support Vector, Naive Bayes, imbalanced data, oversampling, SMOTE, SVMSMOTE, ADASYN.

I. Introduction

Software defect prediction has become a vital part of the software development cycle in recent years [1]. The aim of SDP revolves around detecting modules in which faults are more likely to appear before the testing phase [2]. As documented by previous studies, support vector classifiers and Naive Bayes classifiers remain two of the most effective ML classifiers used for classification problems [2].

However, when met with imbalance data, these classifiers tend to show bias towards the minority class. Considering the nature of various defect datasets available to the public domain, one can observe a class imbalance with major under representation of the fault-prone classes [3].

Keeping in mind the requirement of accurate prediction to keep away from disastrous consequences, it is only fitting to ensure that the faulty classes are not predicted as non-faulty ones.

Another issue that reduces the effectiveness of a machine learning model is the excess presence of attributes in the data sets which negatively affects the ability of the classifier often resulting in over fitting [4].

By the means of this study, through our paper we propose an algorithm that would be able to handle the issue of imbalanced datasets and dimensionality reduction for SDP using SVM and Naive Bayes classifiers.

To subjugate class imbalance, we try to explore over the possibility of utilizing Synthetic Minority Oversampling Technique (SMOTE) which utilizes K nearest neighbours to create synthetic samples) [5] and ADASYN which is an extension of SMOTE Technique and will compare them with our proposed algorithm of using an SVM algorithm based variant of SMOTE [6] along with Linear Discriminant Analysis for two commonly used classifiers, Naive Bayes and Support Vector Classifier.

The rest of paper is organized as follows: Section II presents related work and section III presents details of list of abbreviations used in the work. Section IV presents details of experimental design and section V describes the research methodology followed. In section VI, list of performance measures used to validate the results are present and section VII. The nest section presents the results of the work followed by the conclusion of the work.

II. Related Work

Malhotra [7] assessed the performance capability of machine learning techniques for software defect prediction and based on the results concluded that the techniques have the ability for predicting software defects.

In order to rebalance the imbalance of data, one either oversamples (creating more samples) the minority class samples of undersamples (Ignoring samples) the majority class instances [6], [8]. Kubat [9], presented a single sided undersampling algorithm to eliminate the noisy majority class instances.

C. X. Ling and C. Li, [10] tried to combine undersampling and oversampling, however, this did process didn't perform well on their chose evaluation matrix of 'lift index'. Chawla et al. [5] put together the technique of Synthetic Minority Oversampling Technique [SMOTE] which utilized the concept of 'phantomtransduction' to create new instances.

Authorized licensed use limited to: DELHI TECHNICAL UNIV. Downloaded on March 27,2021 at 05:34:16 UTC from IEEE Xplore. Restrictions apply.

Akbani, Kwek and Japkowic [6] conducted a study on imbalanced datasets' performance with a SVC classifier, and had given possible explanations towards why the performance of an SVC classifier dropped for skewed datasets.

H. M. Nguyen, E. W. Cooper, K. Kamei [11] proposed a variant of SMOTE, the Borderline SMOTE exploring and comparing its performance with other oversampling techniques. Wang and Yao [12] conducted a study on imbalanced datasets for SDP through data resampling. Galar [13] did a comparison study for the various kinds of sampling methodologies through ensemble machine learning models for SDP.

A. Kalsoom et al. [2] conducted a similar study on imbalance data trying out various machine learning classifiers along with oversampling and undersampling techniques.

J. Li, P. He, J. Zhu and M. R. Lyu [14] used Convolutional Neural Network to generate useful features from the original handcrafted features. They then combined the learned elements with the handcrafted features for accurate defect prediction. They evaluated the algorithm based on F-measure and concluded that their approach improved the state-of-the-art method [13].

Singh and Chugh [15] compared 5 Machine Learning algorithms - Particle Swarm Optimization, Naive Bayes, Decision Tree, Linear Classifier and Artificial Neural Network - on the data sets for Software Defect Prediction [16]. Linear Classifiers outperformed the other algorithms in terms of defect prediction accuracy. Neural Networks, however, had the lowest error rate [14].

Singh, Malhotra and Kaur [17], [18] built a Support Vector Machine (SVM) model to find the relationship between object-oriented metrics and based on the results proposed that SVM method may also be used in constructing software quality models.

Kumar and Elavarasan [19] used different feature engineering techniques for reducing the attributes of high dimensional data. Various statistical measures such as information theory, mutual information, information gain, gain ratio, symmetric uncertainty, correlation and chi-square statistics were used for feature selection. Techniques such as Principal Component Analysis, Principal Feature Analysis, Fisher Criterion and Linear Discriminant Analysis were studied as a part of feature extraction [19].

Bowes, Hall and Petrić [20] compared the performance of Random Forest, Naïve Bayes, RPart and SVM classifiers for opensource and commercial datasets using sensitivity as the performance metric.

Malhotra and Khanna [21] used various sampling techniques for handling imbalanced datasets and showed that using sampling techniques over MetaCost learners gives better results when evaluated on the basis of AUC, balance and GMean.

III. Abbreviations Used

This section talks about all the abbreviations that have been used in this paper.

SDP	Software Defect Prediction
SVC	Support Vector Classifier
SVM	Support Vector Machine
SMOTE	Synthetic Minority Oversampling Technique
ADASYN	Adaptive Synthetic
ROC	Receiver Operating Characteristic
LDA	Linear Discriminant Analysis
AUC	Area Under Curve
ML	Machine Learning

IV. Experimental Design and Setup

For the purpose of this study, we have selected 5 publicly available data sets from the PROMISE, AEEEM and NASA repositories. The five selected databases were:

1. KC1
2. MW1
3. Synapse 1.2
4. Mylyn
5. PC4

More details about the class distribution for the aforementioned data sets is given below in table I.

TABLE I. Characteristics of Data

Dataset	No. of Instances	Faulty	Non- Faulty
KC1	2109	326	1783
MW1	403	31	372
Synapse 1.2	256	86	170
Mylyn	1862	245	1617
PC4	1458	1280	178

V. Proposed Methodology

Initially datasets mentioned in section IV were collected. They were then checked for outliers, missing and inconsistent values and were cleaned.

In our proposed methodology, we intend to employ a variant of SMOTE which utilizes SVM as the underlying algorithm rather than K Nearest Neighbour algorithm with the aim to create minority samples only across the boundary cases where the chances of misclassification are higher. Once the dataset's imbalance is dealt with via our proposed methodology, we use it to train a Naive Bayesian and Support Vector Machine learners.

Step by step methodology is outlined in Fig. 1. A detailed description of all the steps is given in the following sections.

A. Support Vector Machine

Support Vector Machine is a kernel-based machine learning technique which can be utilized in both regression and classification problems [2]. SVM's are based on statistical learning suppositions and try to form decision

Authorized licensed use limited to: DELHI TECHNICAL UNIV. Downloaded on March 27,2021 at 05:34:16 UTC from IEEE Xplore. Restrictions apply.

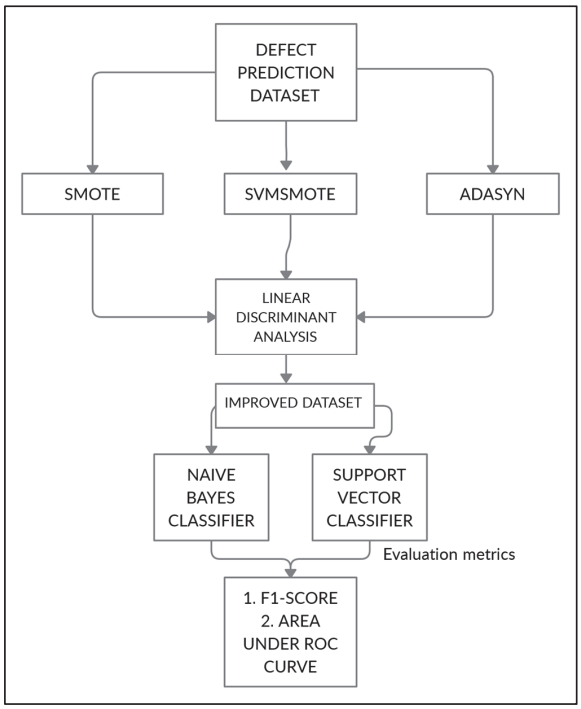

Fig. 1. Proposed Methodology

boundaries that would provide optimal separation between the different classes.

To differentiate between class boundaries, a support vector machine creates hyperplanes in higher dimensional space. For a given dataset, the total amount of features determines the feature vector for it [22]. The guiding principle remains to maximize the gap between the different classes of data in the feature space [23]. All the vectors lying on either side of the hyperplane are labelled as -1 and +1 respectively and the predictions are based on the label.

For an imbalance dataset, the majority class' density overpowers that of the minority class even around the hyperplane resulting in minority class instances being placed far from the hyperplane. Thus, in order to handle misclassifications, the hyperplane is shifted towards the minority class resulting in higher probability of false negatives. Akbani, Kwek and Japkowicz [6] had mentioned 2 other possible reasons behind the performance drop-in support vector classifiers for imbalance data.

Initially, SVM classifiers were utilized for binary classification. Whilst dealing with multi-classification problems, Cortis and Vapnik [23] had recommended comparing one class with the other classes taken together. This would generate P classifiers, where P stands for number of classes. For such cases, P hyperplanes are created by solving P Quadratic Programming optimization problems [23].

B. Naive Bayes Classifier

Naive Bayes classifier uses the Bayes Theorem to determine and predict the class of a particular instance [24]. It calculates the likelihood based on the assumption that every feature in the feature space has class conditional independence [25].

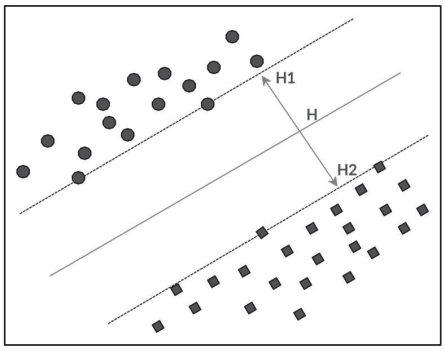

Fig. 2. The maximum margin hyperplane

As per the Bayes Theorem, for target class y and attribute A, the posterior probability P $(y|A)$ is given as

$$P(y|A) = \frac{P(A|y).P(y)}{P(A)} \qquad (1)$$

Considering there are k independent attributes (implies 2k! assumptions) in total:

$$P(y|A) = \frac{P(y)\prod_1^k P(A_i|y)}{P(A)} \qquad (2)$$

Despite the assumption made the Naive Bayes classifier, it performs well in a lot of real-life situations. H Zhang [26] provided a possible explanation for the high performance of naive bayes classifier despite the strong dependencies, crediting it to the cancellation of these dependencies internally itself, thus rendering no effect on the performance of the classifier.

C. Imbalanced Data

Data sets with imbalanced class distributions are pretty common in software defect datasets. A data set is said to be imbalance if the density of a particular class (called as the majority class) is very high as compared to the other classes (called as the minority classes) [27]. Classifiers perform badly on imbalance datasets as they have the propensity to follow the principle of Occam's razor where the simplest hypothesis remains to not classify any the instances as the minority class. Let us suppose that in a binary classification problem, 97 instances belong to class 1 and 3 instances belong to class 2. In a bid to achieve an accuracy of 97 percent, the machine learning model would predict all instances as the 1st class, however when seen in context of SDP, the three misclassified instances can potentially cost hours of manpower, and renders the process of SDP redundant.

Discussing about the specific effect of data imbalance on SVM classifiers, Akbani, Kwek and Japkowicz [6] had mentioned 3 possible reasons for the drop in performance

- Positive points lie further from the ideal boundary

Authorized licensed use limited to: DELHI TECHNICAL UNIV. Downloaded on March 27,2021 at 05:34:16 UTC from IEEE Xplore. Restrictions apply.

- Weakness of soft margins [28]
- Imbalanced support vector ratio

This drop in performance can be compensated by either inducing a bias in the classifier by imposing a penalty for every majority class classification or by conducting data oversampling and / or under sampling.

D. SMOTE

When classification is done for the imbalance data the result is biased for the majority class. This class imbalance data can be balanced using the under sampling and oversampling techniques. These techniques produce balanced data which improves the learning of the classifiers. SMOTE is an oversampling technique which deals with class imbalance problems. Smote is a technique which oversamples the minority class to create the synthetic examples of minority class [29]. SMOTE uses k nearest neighbour algorithm across the entire minority class. This technique works by taking the samples and its k nearest neighbour. Depending on the oversampling required the value of k neighbours is chosen. For example, if there are 5 nearest neighbours and the amount of oversampling required is 200 percent, then only two neighbours out of five is selected.

This technique of generating new instances of minority class works as follows:

- Distance between the sample and its neighbours is calculated.
- The distance obtained is multiplied by a number which is obtained by randomly generating numbers between 0 and 1.
- The number obtained after above step is then added with a sample which is considered. This will generate the random point between the two selected feature vectors or samples.

By applying this the boundary between both the classes will become clearer and will make the learning of classifiers easy. Thus, by applying this technique the problem of class imbalance is handled.

E. SVMSMOTE

SVMSMOTE is an oversampling technique which increases the minority class to deal with class imbalance of data [30]. This technique mainly focuses on the borderline area between the two classes rather the whole minority class, as the border-line area has much higher probability of being misclassified. SVMSMOTE uses the SVMs algorithm rather than k nearest neighbors as in SMOTE. In this approach, the original training set is first trained using Support vector classifier. Once trained, the obtained support vectors are approximated towards the border line area [31].

New instances are created on the line segment joining each minority support vectors and nearest neighbors of it using the two techniques i.e., interpolation and other is extrapolation. These two techniques are applied depending upon the density of the majority class around it.

F. ADASYN

In oversampling, the minority class is copied multiple times till the minority class' size becomes similar to that of the majority class. However, this leads to over-fit of minority data due to the same entries appearing many times. To avoid this problem, ADASYN can be used. ADASYN algorithm improves class imbalance by synthetically generating fresh examples from the minority class following linear interposing between prevailing minority class instances [32]. It is an augmentation of SMOTE, generating extra instances at the boundary instead of generating them in the inside of the minority class [32]. This also leads to an issue since great amount of data gets generated along the borders with high majority class examples and it might be possible that this data generated is similar to the one already presents in the majority class, causing many false positives [33].

G. Linear Discriminant Analysis

Dimensionality reduction aims to reduce the dimensions by removing redundant attributes. There are 2 major approaches for Dimensionality Reduction

- Supervised
- Unsupervised

Unsupervised approach does not need labelling classes of the data whereas in supervised approach class labels are taken into consideration.

In this paper of ours, we have used supervised dimensionality reduction technique- Linear Discriminant Analysis (LDA). LDA seeks to maximize the separation distance between the classes and minimize the interspace between the mean and sample of each class [34].

For Software Defect Prediction, Datasets contain two classes- faulty and non-faulty. These classes in turn contain many features or attributes. Using a single attribute for classification could lead to overlapping and thus, it is required to avoid overlapping. We specify the target variable, once done information related to it can be extracted out to check the effectiveness of the attributes on target Variable thus reducing out the data such that only important features stay.

LDA proceeds by calculating the separability between the classes (between class variance, σ_b followed by the calculation of distance between the mean and sample of each class (within class variance, σ_W. Lastly the lower dimensional space is made where in the between class variance is maximized and within class variance is minimized. The lower dimensional space L is calculated through:

$$L = arg_L max \frac{|L^T \sigma_b L|}{|L^T \sigma_W L|} \quad (3)$$

VI. Performance Measures and Validation Technique

A. F Measure

Sometimes, Accuracy can lead to misinterpretation of results. Hence F Measure score is taken into consideration. F-Measure score is the weighted harmonic mean of Precision and Recall [35]. Precision is the ratio of actual positive instances to that to predicted positive instances i.e.

$$Precision = \frac{TruePositive}{TruePositive+FalseNegative} \quad (4)$$

Recall is the ratio of correctly predicted positive instances to total positive instances [36].

Authorized licensed use limited to: DELHI TECHNICAL UNIV. Downloaded on March 27,2021 at 05:34:16 UTC from IEEE Xplore. Restrictions apply.

$$Recall = \frac{TruePositive}{TruePositive+FalsePositive} \quad (5)$$

$$F1 - Score = \frac{2*Recall*Precision}{Recall+Precision} \quad (6)$$

B. Area Under Receiver Operating Characteristic Curve

Receiver Operating Curve (ROC) is the graphical plot of sensitivity on y-coordinate versus its specificity on x-coordinate [37]. It is an effective technique for evaluating the performance of predicted model. It evaluates the performance of models by plotting the ROC curve and evaluating area under the curve.

VII. Experimental Results

For the ease of the reader, we have displayed the values of the performance evaluation criteria in the form of tables. In each of the table, the columns represent the algorithm used and the rows represent the data set which was utilized for the training and testing of the algorithms. The cell value represents the performance measure value for the corresponding algorithm and data set.

Table II and Table III represent the F Measure Score and the AUC score respectively for support vector classifier. Table IV and Table V represents the F Measure Score and the AUC score respectively for the Naive Bayes classifier.

From Table II, III, IV and V, one can notice that our SVMSMOTE algorithm outperforms every other algorithm for the area under the ROC curve and F Measure Score evaluation criteria for all the 5 data sets and both the classifiers.

It should also be recognized that for only one particular dataset for the performance measure of F Measure score, does our algorithm is matched by SMOTE oversampling technique, whereas for the rest of the datasets, our proposed algorithm produces better results.

Table VI shows the results of the Friedman Statistics Test for all the combinations of machine learning classifiers and the performance measures. With the null hypothesis being that all the algorithm performances are equal. The significance level for the test was kept at 0.05.

For all the results mentioned in tables II, III, IV and V ,the P-value came out to be less than the significance level value, hence making it safe for us to reject the null hypothesis and thus allowing us to safely assume that at least one of the algorithms has a different effect than the others, thus further strengthening the case for our proposed algorithm.

VIII. Conclusion

Class imbalance is a persistent issue with software defect data sets [11]. If not properly dealt with, this imbalance, it Will result in erratic predictions, which in turn would increase the cost of the project. Through this study, we have proposed an algorithm to deal with imbalanced data sets for SDP, where in SVMSMOTE uses support vector machine algorithms to push the learned boundary closer to the ideal boundary as compared to interpolation as done in SMOTE. This aids in refinement and enhancements in the predictions made by the classifiers. The results of this study show that our proposed algorithm of adopting SVMSMOTE with LDA outperforms the remaining algorithms for the chosen

TABLE II. F MEASURE SCORES FOR VARIOUS OVERSAMPLING TECHNIQUES USING SUPPORT VECTOR CLASSIFIER

Dataset	Algorithm			
	LDA	LDA+SMOTE	LDA+SVMSMOTE	LDA+ ADASYN
KC1	0.62	0.74	**0.80**	0.68
MW1	0.67	0.93	**0.95**	0.42
Synapse	0.71	0.71	**0.72**	0.69
PC4	0.69	0.90	**0.92**	0.59
Mylyn	0.50	0.73	**0.74**	0.66

TABLE III. AUC SCORES FOR VARIOUS OVERSAMPLING TECHNIQUES USING SUPPORT VECTOR CLASSIFIER

Dataset	Algorithm			
	LDA	LDA+SMOTE	LDA+SVMSMOTE	LDA+ ADASYN
KC1	0.60	0.74	**0.80**	0.70
MW1	0.62	0.92	**0.93**	0.55
Synapse	0.70	0.71	**0.76**	0.57
PC4	0.64	0.90	**0.91**	0.64
Mylyn	0.52	0.73	**0.74**	0.67

TABLE IV. F MEASURE SCORES FOR VARIOUS OVERSAMPLING TECHNIQUES USING NAIVE BAYES CLASSIFIER

Dataset	Algorithm			
	LDA	LDA+SMOTE	LDA+SVMSMOTE	LDA+ ADASYN
KC1	0.66	0.74	**0.83**	0.61
MW1	0.68	0.93	**0.94**	0.64
Synapse	0.67	0.73	**0.75**	0.69
PC4	0.73	0.90	**0.91**	0.56
Mylyn	0.59	**0.70**	**0.70**	0.46

TABLE V. AUC SCORES FOR VARIOUS OVERSAMPLING TECHNIQUES USING NAIVE BAYES CLASSIFIER

Dataset	Algorithm			
	LDA	LDA+SMOTE	LDA+SVMSMOTE	LDA+ ADASYN
KC1	0.64	0.74	**0.83**	0.64
MW1	0.67	0.92	**0.94**	0.64
Synapse	0.67	0.73	**0.75**	0.69
PC4	0.68	0.89	**0.91**	0.61
Mylyn	0.57	0.70	**0.72**	0.54

TABLE VI. The results of Friedman Statistics test for the various combinations of classifiers and performance measures

Classifier + Performance Metric	χ_R^2	$p - value$
Support Vector+ F Measure	12.78	0.00514
Support Vector+ Area Under Curve	9.18	0.02699
Naïve Bayes + F Measure	13.5	0.00367
Naïve Bayes + Area Under Curve	13.74	0.00328

α=0.05, Degree of Freedom=3

Authorized licensed use limited to: DELHI TECHNICAL UNIV. Downloaded on March 27,2021 at 05:34:16 UTC from IEEE Xplore. Restrictions apply.

performance evaluation measures. Thus, the SVMSMOTE algorithm achieves superior SVM and Naïve Bayes performance taking into consideration F Measure Score and AUC for the Regional Operational characteristic curve for the imbalanced datasets, as shown in Tables II through VI. We come to the conclusion that SVMSMOTE algorithm together with Linear Discriminant Analysis can help in improving the quality of prediction made by Support Vector classifiers and Naive Bayes classifiers.

REFERENCES

[1] R. Malhotra and K. Khan, "A Study on Software Defect Prediction using Feature Extraction Techniques," 2020 8th International Conference on Reliability, Infocom Technologies and Optimization (Trends and Future Directions) (ICRITO), Noida, India, 2020, pp. 1139-1144, doi: 10.1109/ICRITO48877.2020.9197999.

[2] A. Kalsoom, M. Maqsood, M.A.Ghazanfar et al.A dimensionality reduction-based efficient software fault prediction using Fisher linear discriminant analysis (FLDA).J Supercomput74,4568–4602 (2018). https://doi.org/10.1007/s11227-018-2326-5.

[3] A.R. Gray, S.G. MacDonell, "Software Metrics Data Analysis—Exploring the Relative Performance of Some Commonly Used Modeling Techniques". Empirical Software Engineering 4, 297–316 (1999). https://doi.org/10.1023/A:1009849100780.

[4] Kotsiantis, S.., "Feature selection for machine learning classification problems: A recent overview". Artificial Intelligence Review - AIR. 42. 10.1007/s10462-011-9230-1. (2011)

[5] Chawla, V. Nitesh, K. Bowyer, L. Hall and W. P. Kegelmeyer. "SMOTE: Synthetic Minority Over-sampling Technique", J. Artif. Intell. Res.16 (2002): 321-357.

[6] Akbani, Rehan & Kwek, Stephen & Japkowicz, Nathalie. (2004). Applying Support Vector Machines to Imbalanced Data Sets. Lecture Notes Artif. Intell.. 3201. 39-50. 10.1007/978-3-540-30115-8_7.

[7] R. Malhotra, "A systematic review of machine learning techniques for software fault prediction", Applied Soft Computing. 27. 504-518. 10.1016/j.asoc.2014.11.023. (2015)

[8] M. Awad & R. Khanna, "Support Vector Machines for Classification". In: Efficient Learning Machines. Apress, Berkeley, CA. (2015) https://doi.org/10.1007/978-1-4302-5990-9_3

[9] Kubat, M.., "Addressing the Curse of Imbalanced Training Sets: One-Sided Selection", Fourteenth International Conference on Machine Learning. (2000)

[10] C. X. Ling and C. Li, "Data Mining for Direct Marketing: Problems and Solutions," Proceedings of International Conference on Knowledge Discovery from Data (KDD 98), New York City, 27-31 August 1998, pp. 73-79.

[11] H. M. Nguyen, E. W. Cooper, K. Kamei, "Borderline over-sampling for imbalanced data classification," International Journal of Knowledge Engineering and Soft Data Paradigms, 3(1), pp.4-21, 2009.

[12] S. Wang and X. Yao, "Using Class Imbalance Learning for Software Defect Prediction," in IEEE Transactions on Reliability, vol. 62, no. 2, pp. 434-443, June 2013, doi: 10.1109/TR.2013.2259203.

[13] M. Galar, A. Fernandez, E. Barrenechea, H. Bustince and F. Herrera, "A Review on Ensembles for the Class Imbalance Problem: Bagging-, Boosting-, and Hybrid-Based Approaches," in *IEEE Transactions on Systems, Man, and Cybernetics, Part C (Applications and Reviews)*, vol. 42, no. 4, pp. 463-484, July 2012, doi: 10.1109/TSMCC.2011.2161285.

[14] J. Li, P. He, J. Zhu and M. R. Lyu, "Software Defect Prediction via Convolutional Neural Network," 2017 IEEE International Conference on Software Quality, Reliability and Security (QRS), Prague, 2017, pp. 318-328, doi: 10.1109/QRS.2017.42.

[15] P. Singh & A. Chug," Software defect prediction analysis using machine learning algorithms",2017,775-781. 10.1109/CONFLUENCE.2017.7943255.

[16] X. Yang, K. Tang and X. Yao, "A Learning-to-Rank Approach to Software Defect Prediction," in IEEE Transactions on Reliability, vol. 64, no. 1, pp. 234-246, March 2015, doi: 10.1109/TR.2014.2370891.

[17] Y. Singh, A. Kaur & R. Malhotra, "Application of support vector machine to predict fault prone classes", ACM SIGSOFT Software Engineering Notes. (2009). 34. 1-6. 10.1145/1457516.1457529.

[18] Y. Singh, A. Kaur& R. Malhotra,. Empirical validation of object-oriented metrics for predicting fault proneness models.Software Qual J18,3 (2010). https://doi.org/10.1007/s11219-009-9079-6

[19] V. A. Kumar, N. Elavarasan, " A Survey on Dimensionality Reduction Technique," in International Journal of Emerging Trends Technology in Computer Science, Volume 3, Issue 6, November-December 2014.

[20] D. Bowes, T. Hall, & J. Petri´c"Software defect prediction: do different classifiers find the same defects". Software Qual J 26, 525–552 (2018). https://doi.org/10.1007/s11219-016-9353-3

[21] R. Malhotra and M. Khanna, "An empirical evaluation for software change prediction using imbalanced data", Automated Software Engineering, August 2016

[22] S. Ghosh, A. Dasgupta & A. Swetapadma, "A Study on Support Vector Machine based Linear and Non-Linear Pattern Classification". (2019). 24-28. 10.1109/ISS1.2019.8908018.

[23] C. Cortes, V. Vapnik, Support-vector networks. Mach Learn 20, 273–297 (1995). https://doi.org/10.1007/BF00994018

[24] R.O. Duda and P.E. Hart,*Pattern Classification and Scene Analysis.*New York:John Wiley 1973

[25] T. Dong, W. Shang & H. Zhu. Naive Bayesian Classifier Based on the Improved Feature Weighting Algorithm. (2011). 10.1007/978-3-642-21402-8_23.

[26] H. Zhang. "The Optimality of Naive Bayes." Proceedings of the Seventeenth International Florida Artificial Intelligence Research Society Conference, FLAIRS 2004. 2. (2004)

[27] C. Beyan, R. Fisher, "Classifying imbalanced data sets using similarity based hierarchical decomposition", Pattern Recognition, Volume 48, Issue 5, 2015, Pages 1653-1672, ISSN 0031-3203, https://doi.org/10.1016/j.patcog.2014.10.032.

[28] S. Zou, Y. Huang, Y. Wang, C. Zhou, "A Novel Method for Prediction of Protein Domain Using Distance-Based Maximal Entropy", Journal of Bionic Engineering, Volume 5, Issue 3, 2008, Pages 215-223, ISSN 1672-6529, https://doi.org/10.1016/S1672-6529(08)60027-X.

[29] El-Alfy, M. El-Sayed & S. Al-Azani, "Empirical study on imbalanced learning of Arabic sentiment polarity with neural word embedding". Journal of Intelligent & Fuzzy Systems. 38. 1-12, (2020). 10.3233/JIFS-179703.

[30] B. Krawczyk. Learning from imbalanced data: Open challenges and future directions. Progress in Artificial Intelligence. 5. 10.1007/s13748-016-0094-0.[1](2016)

[31] K. Savetratanakaree & K. Sookhanaphibarn & S. Intakosum & R. Thawonmas, "Borderline over-sampling in feature space for learning algorithms in imbalanced data environments". 43. 363-373. (2016)

[32] D. Siedhoff, ADASYN (improves class balance, extension of SMOTE)(https://www.mathworks.com/matlabcentral/fileexchange/50541-adasyn-improves-class-balance-extension-of-smote), MATLAB Central File Exchange. Retrieved November 9, 2020.

[33] V. López, A. Fernandez, S. Garcia, V. Palade and F. Herrera, "An Insight into Classification with Imbalanced Data: Empirical Results and Current Trends on Using Data Intrinsic Characteristics." Information Sciences 250 (2013) 113-141 doi: 10.1016/j.ins.2013.07.007

[34] J. Wu, J. Xin and N. Zheng, "SVM learning from imbalanced microanuerysm candidate datasets used feature selection by gini index," 2015 IEEE International Conference on Information and Automation, Lijiang, 2015, pp. 1637-1641, doi: 10.1109/ICInfA.2015.7279548.

[35] E. Zhang, Y. Zhang F-Measure. In: LIU L., ÖZSU M.T. (eds) Encyclopedia of Database Systems. Springer, Boston, MA. (2009) https://doi.org/10.1007/978-0-387-39940-9483

[36] C. Goutte & E. Gaussier, "A Probabilistic Interpretation of Precision, Recall and F-Score, with Implication for Evaluation", Lecture Notes in Computer Science. 3408. 345-359. (2005). 10.1007/978-3-540-31865-1_25.

[37] L.B. Lusted. "Signal Detectability and Medical Decision-Making." Science 171, no. 3977 (1971): 1217-219. Accessed November 9, 2020. http://www.jstor.org/stable/1731167.

Authorized licensed use limited to: DELHI TECHNICAL UNIV. Downloaded on March 27,2021 at 05:34:16 UTC from IEEE Xplore. Restrictions apply.

Silicon
https://doi.org/10.1007/s12633-021-01040-4

ORIGINAL PAPER

TCAD Temperature Analysis of Gate Stack Gate All Around (GS-GAA) FinFET for Improved RF and Wireless Performance

Bhavya Kumar[1] · Rishu Chaujar[1]

Received: 2 February 2021 / Accepted: 1 March 2021
© Springer Nature B.V. 2021

Abstract
In this article, we investigated the impact of temperature variation on DC, analog, RF, and wireless performance of Gate Stack Gate All Around (GS-GAA) FinFET using SILVACO Atlas 3D simulator. The GAA structure introduction enhances the switching ratio (I_{on}/I_{off}) by ~152.37% and reduces the subthreshold swing (SS) by ~6.5%. At gate voltage (V_{gs}) ~ 0.725 V, the GS-GAA FinFET device exhibits the ZTC (Zero-Temperature-Coefficient) bias point, i.e., the effect of temperature on drain current gets nullified. DC parameters such as leakage current (I_{off}), on current (I_{on}), SS, and threshold voltage (V_{th}) deteriorate with the rise in temperature. The enhancement in temperature degrades the RF and analog performance of the device by suppressing the parameters like transconductance (g_m), device efficiency (TGF), cut-off frequency (f_T), gain frequency product (GFP), gain-bandwidth product (GBP), etc. The device's wireless performance is analyzed using linearity and harmonic distortion parameters such as gm_3, gm_2, 1-dB compression point, IIP3, VIP3, VIP2, IMD3, HD3, and HD2, and it shows significant improvement as the temperature increases from 300 K to 500 K.

Keywords Analog/RF performance · Gate Stack (GS) · Gate All Around (GAA) FinFET · High-temperature · Quantum effects · Wireless performance

1 Introduction

In recent years, CMOS technology is being aggressively scaled-down and is reaching its fundamental limits. MOSFET's continuous scaling results in increased I_{off} current and short channel effects (SCEs), which deteriorates the device performance [1–3]. FinFET, a "3D" field-effect transistor, emerged as one of the encouraging devices in comparison to other multi-gate devices due to its (1) reduced SCEs owing to increased electrostatic control over the channel by the multiples gates of the device, (2) favourable switching ratio, and (3) increased drive current per unit cross-sectional area [4]. Gate All Around (GAA) structure has been explored further to enhance the performance of the FinFET [5]. As per the International Technology Roadmap for Semiconductors (ITRS) guideline, the GAA structure is also known as the "ultimate structure" [6]. GAA FinFET exhibits increased electrostatic control over the channel, as the channel is covered from all four sides by the gate. Consequently, GAA FinFET shows improved SCEs and can be further scaled-down compared to Tri-Gate (TG) FinFET. Another concern in the continued scaling of CMOS technology is the increment in the gate direct tunneling current with the decreasing gate oxide thickness, resulting in the enhanced off-state leakage current [7, 8]. The most technological solution is the use of high-κ dielectric materials, like ZrO_2 (κ = 25) and HfO_2 (κ = 25) [9, 10].

However, there are certain drawbacks in the head-on deposition of high-κ dielectrics on Si substrate. It includes maintaining the interface's quality between Si substrate and high-κ dielectric, threshold voltage instability, mobility degradation accompanied by below-par subthreshold swings [11, 12]. The implementation of the Gate Stack (GS) configuration resolves the problem. GS architecture inserts a thin SiO_2 layer between the high-κ dielectrics and Si substrate while maintaining the effective oxide thickness constant [13]. Thus, considering all considerations, we propose a Gate Stack Gate All Around (GS-GAA) FinFET.

✉ Rishu Chaujar
chaujar.rishu@dtu.ac.in

Bhavya Kumar
bhavyakumar_phd2k18@dtu.ac.in

[1] Microelectronics Research Lab, Department of Applied Physics, Delhi Technological University, Delhi, India

Published online: 09 March 2021

Recently, the demand for portable and high battery backup electronic devices has substantially increased. Thus, to maintain the increased demand, there is a need to increase the transistor density in the IC [14]. The heat dissipated in the IC increases considerably with the increase in the transistor density, thereby increasing the operating temperature [15, 16]. When the device dimension reaches below 20 nm, the high temperature can significantly affect the device operation or even damage it. The high-temperature reliability of a device ensures its long durability and stability [17]. Therefore, it is vital to examine the temperature variation impact on the device's RF, analog, and wireless performance for better reliability.

The temperature effect on the digital and analog performance of SOI FinFETs has been investigated extensively [18, 19]. In another simulation study, Das et al. reported that at low temperatures, gate-source overlapped FinFET provides enhanced drain current characteristics [20]. Saha et al. reported the temperature effect on RF/analog and linearity figure of merits (FOMs) in Fe-FinFET [21]. However, to the best of authors' knowledge, no report has been published on the temperature impact on RF, analog, and wireless performance of GS-GAA FinFET. In this article, simulations have been carried out to analyze the temperature impact on various important electrostatic, analog, RF, linearity, and harmonic distortion parameters of GS-GAA FinFET by varying the temperature from 300 K to 500 K in steps of 50 K. We have also shown a comparison between GAA FinFET and Tri-Gate FinFET and highlighted the superior performance of GAA FinFET in terms of enhanced transconductance, increased drain current, improved switching ratio, and reduced subthreshold swing. Starting with the introduction, section 2 narrates the device structure. Section 3 deals with the simulation methodology used and calibration between the simulation data and experimental data. Section 4 analyzes the impact of temperature variation on device performance with concluding remarks in section 5, authenticating the paper's originality.

2 Device Structure

Figure 1(a) displays the proposed 3D structure of GS-GAA FinFET. In contrast, Fig. 1(b) and (c) portrays the vertical and horizontal cross-sectional view cut along the proposed device's silicon fin, respectively. Table 1 exhibits all the device parameters used for simulation. Silicon material is used in the fin structure with width (W_{Fin}) and height (H_{Fin}) of the fin fixed at 5 nm and 10 nm, respectively, thereby following the width quantization property, which says that W_{Fin} must be a multiple of H_{Fin} [22, 23]. A combination of SiO_2 ($\kappa = 3.9$) [10] and HfO_2 ($\kappa = 25$) is used to stacking gate oxide. All the regions are uniformly doped with n-type doping species. The source and drain regions are heavily doped compared to the channel region to reduce the parasitic capacitance [24]. TiN metal gate is considered due to its thermal stability, high purity, low resistivity, and compatibility with CMOS processing [25, 26].

3 Simulation Framework and Calibration

The SILVACO Atlas 3D simulator has simulated the proposed device GS-GAA FinFET. Poisson's and continuity equations expressed by Eqs. (1), (2), and (3) provide the general framework for device simulation [27].

1. Poisson's Equation

$$\mathrm{div}(\varepsilon \nabla \psi) = -\rho \tag{1}$$

where ρ, ψ, and ε represent the space charge density, electrostatic potential, and permittivity. Poisson's equation provides a relation between local space charge density and electrostatic potential.

2. Continuity Equation

For electrons,

$$\frac{\partial n}{\partial t} = \frac{1}{q}\mathrm{div}\left(\overrightarrow{J_n}\right) + G_n - R_n \tag{2}$$

For holes,

$$\frac{\partial p}{\partial t} = -\frac{1}{q}\mathrm{div}\left(\overrightarrow{J_p}\right) + G_p - R_p \tag{3}$$

where n and p represent the electron and hole concentration, R_p and R_n are the recombination rates for holes and electrons, G_n and G_p represent the generation rates for electrons and holes. The magnitude of an electron charge is denoted by q, whereas J_n and J_p represent the electron and hole current densities. The way electron and hole densities evolve because of transport, recombination, and generation is described by continuity and transport equations.

But to obtain more realistic and accurate results, secondary equations and physical models are needed. Thus, to correlate the low-field carrier mobility with temperature and impurity concentration, Arora analytical model is used as the temperature has been varied from 300 K - 500 K [28]. SRH recombination model is used to include the recombination and generation effects with a fixed carrier lifetime of 1×10^{-7} s, and to consider the specific properties of highly doped materials, Fermi-Dirac statistics are implemented. Klaassen band to band tunneling model is invoked to consider the tunneling of electrons (both direct and indirect transitions) between valence and conduction band. Crowell-Sze impact ionization model is also enabled [27]. Furthermore, quantum confinement effects play an important role and may not be overlooked in the enormously scaled devices. Thus, Bohm Quantum Potential (BQP) model with alpha = 0.3 and gamma = 1.4 (default parameter values for Si) is employed in the device simulation to consider the quantum confinement effects in the channel region [27, 29]. The physical models and equations

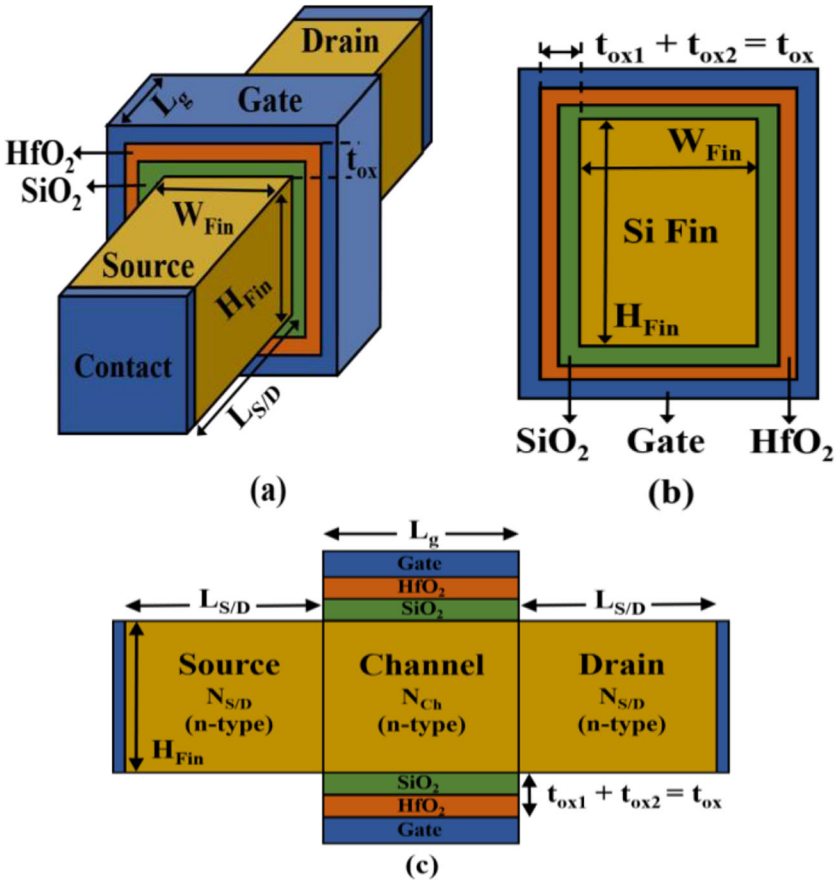

Fig. 1 (**a**) Systematic 3-D structure of the proposed GS-GAA FinFET (**b**) Vertical (**c**) Horizontal cross-sectional view cut along the silicon fin of the proposed GS-GAA FinFET

invoked during the device simulation are shown in Table 2. In SRH recombination, T_L denotes the lattice temperature in Kelvin. The difference between the trap energy level and intrinsic Fermi level is E_{TRAP}, τ_p and τ_n represent the hole electron lifetimes, and k is the Boltzmann's constant. In Fermi-Dirac statistics, ε and E_F represent energy and Fermi level, respectively. In Crowell-Sze impact ionization, λ is the carrier mean free path for optical phonon generation. In Klaassen band to band tunneling, BB.GAMMA, BB.B, BB.A is user-definable parameters, D is a statistical factor, and E represents the magnitude of the electric field. In BQP, n represents electron (or hole) density, α and γ are adjustable parameters, ħ is Planck's constant, and M^{-1} denotes inverse effective mass tensor.

Table 1 Different Device Parameters Used for Simulation

Device Parameters	GS-GAA FinFET
Gate Length (L_g)	7 nm
Length of Source/Drain Regions ($L_{S/D}$)	10 nm
Width of Fin (W_{Fin})	5 nm
Oxide Thickness (t_{ox})	1 nm
Height of Fin (H_{Fin})	10 nm
Channel Doping (N_{Ch})	1×10^{16} cm^{-3}
Source/Drain Doping ($N_{S/D}$)	5×10^{18} cm^{-3}
Work Function (ϕ_m)	4.65 eV (TiN)
Drain-Source Voltage (V_{ds})	0.5 V
Gate-Source Voltage (V_{gs})	1.0 V

The physical models discussed above have been validated with the published results of Hyunjin Lee et al. [30]. Figure 2(a) reflects the simulated and experimental $I_d - V_{ds}$ characteristics of a 5 nm All-Around-Gate (AAG) FinFET at $V_{gs} = 0.2$ V and $V_{gs} = 0.4$ V. The $I_d - V_{gs}$ characteristics for the same device at $V_{ds} = 1.0$ V is shown in Fig. 2(b). Also, as the focus of the results is on temperature dependence, Fig. 2(c) displays the experimental and simulated $I_d - V_{gs}$ characteristics at two different temperatures [31]. It is visible that the results are well-calibrated. Thus, validating the choice of simulation models used in the device simulation. Furthermore, Fig. 3 displays the fabrication feasibility of the proposed GS-GAA FinFET through a fabrication process flow chart.

4 Results and Discussion

4.1 Performance Comparison between FinFET and GAA FinFET

The device dimension of both FinFET and GAA FinFET is the same, as discussed in section 2. Instead of a gate oxide

Table 2 Physical models and equations included in the device simulation

Models	Equations
Shockley-Read-Hall recombination	$R_{SRH} = \frac{pn-n_{ie}^2}{\tau_p\left[n+n_{ie}\exp\left(\frac{E_{Trap}}{kT_L}\right)\right]} + \tau_n\left[p + n_{ie}\exp\left(\frac{-E_{Trap}}{kT_L}\right)\right]$
Fermi-Dirac statistics	$f(\varepsilon) = \frac{1}{1+\exp\left(\frac{\varepsilon - E_F}{kT_L}\right)}$
Crowell-Sze impact ionization	$\alpha_{n,p} = \frac{1}{\lambda}\exp[C_0(r) + C_1(r)x + C_2(r)x^2]$
Klaassen band to band tunneling	$G_{BBT} = D\ \ BB.A\ \ E^{BB.GAMMA}\ \exp\left(-\frac{BB.B}{E}\right)$
Bohm Quantum Potential	$Q = \frac{\hbar^2}{2}\gamma\frac{\nabla\left[M^{-1}\nabla(n^\alpha)\right]}{n^\alpha}$

stack, only a single layer of SiO_2 is used as the gate oxide for this comparison. Figure 4(a) reflects the performance comparison between FinFET and GAA FinFET in terms of g_m and I_d, and the GAA FinFET structure shows significant improvement in g_m and I_d. This significant increment in I_d and g_m for the GAA FinFET device is because of the reduced SCEs and enhanced control over the channel by the gate. Furthermore, leakage current reduces by ~59.25% in GAA FinFET due to the improved gate coupling capacitances and reduced tunneling current. Figure 4(b) outlines the plot of switching ratio and subthreshold swing (SS) for further performance comparison between FinFET and GAA FinFET. In GAA FinFET, the switching ratio increases immensely by ~152.37% due to the increased drain current and reduced leakage current, and consequently, superior switching speed is obtained for GAA FinFET configuration. The SS reduces by ~6.5% in GAA FinFET due to the increased gate controllability over the channel. On account of these advantages over FinFET, the impact of temperature variation on device scalability, analog, RF, and wireless performance has been presented for the proposed device.

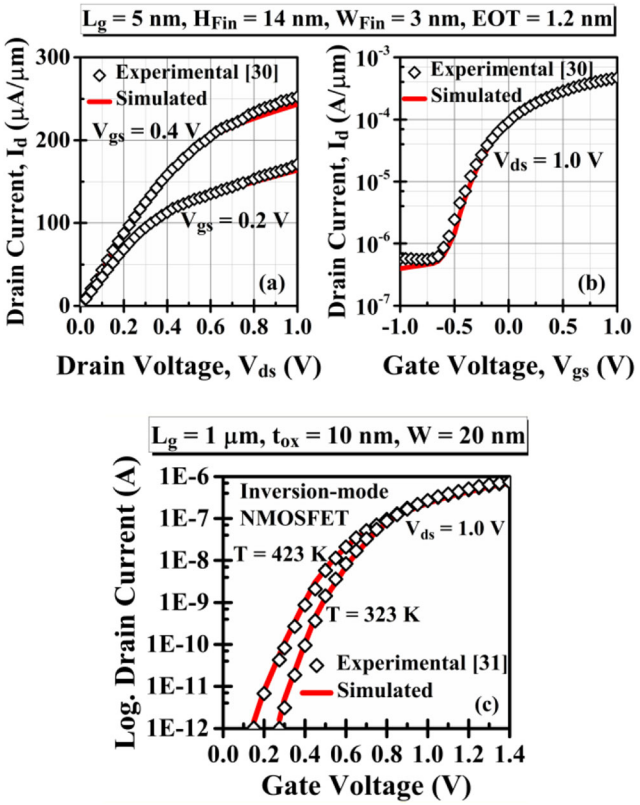

Fig. 2 Calibrated (**a**) I_d-V_{ds} (**b**) I_d-V_{gs} characteristics of 5 nm All-Around-Gate FinFET [30] (**c**) transfer characteristics at two different temperatures [31]

4.2 Temperature Impact on DC Performance in GS-GAA FinFET

Figure 5(a) and (b) display the device's transfer characteristics in linear and log scales for different temperatures. The opposite effect of temperature on drain current (I_d) is observed at high and low gate-source voltages (V_{gs}). At low gate voltage, the energy band gap decreases as the temperature increases, enhancing the device's leakage current. At high V_{gs}, with the temperature rise, the decrease in mobility due to scattering of

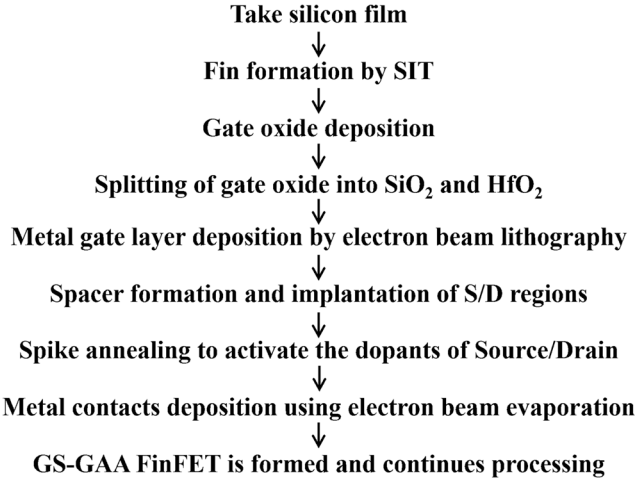

Fig. 3 Fabrication process flow chart of proposed GS-GAA FinFET

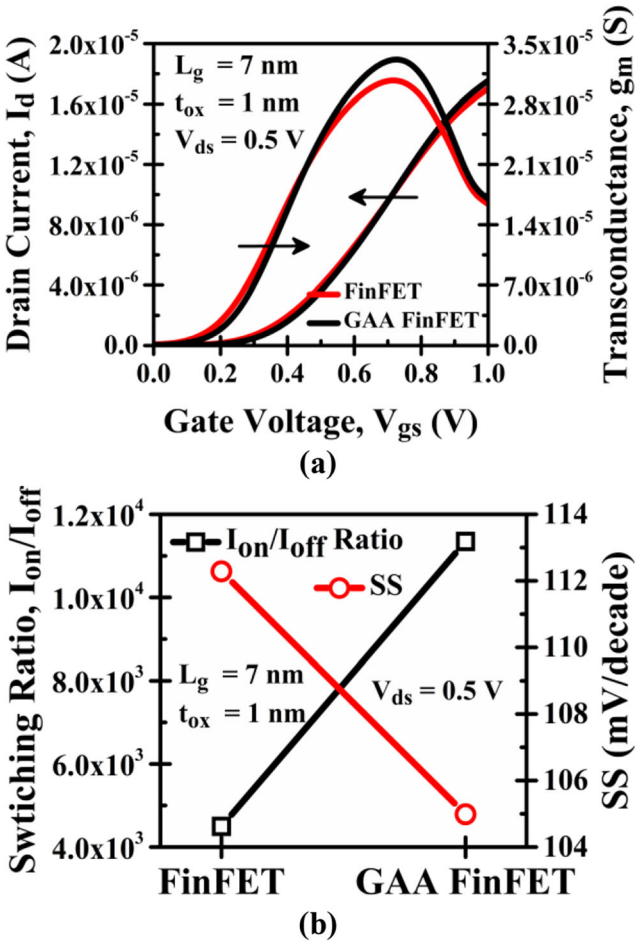

Fig. 4 (**a**) I_d and g_m (**b**) I_{on}/I_{off} ratio and SS comparison between FinFET and GAA FinFET

the carrier dominates over the energy bandgap decrease, resulting in a degradation of on-current (I_{on}) of the device [21]. Thus, an increase in the temperature results in the degradation of both I_{on} and I_{off}, as shown in Fig. 6(a). However, at $V_{gs} \sim 0.725$ V, the impact of temperature variation on I_d gets nullified. Consequently, the ZTC (Zero-Temperature-Coefficient) bias point of the GS-GAA FinFET is at $V_{gs} \sim 0.725$ V [32, 33]. The variation of subthreshold swing (SS) with temperature is portrayed in Fig. 6(b). The subthreshold swing as a function of temperature (Kelvin) is given as SS = (60*T)/300 [34]. Thus, with the rise in temperature, SS increases, resulting in device performance degradation. In Fig. 6(b), the threshold voltage (V_{th}) is plotted against the temperature. The increase in drain current in the subthreshold region with the temperature leads to a decrease in V_{th}. Thus, raising the temperature deteriorates the performance of GS-GAA FinFET in terms of I_{on}, I_{off}, switching ratio, SS, and threshold voltage.

Furthermore, Fig. 7(a) reflects the change in surface potential with temperature along the channel. Surface potential (ϕ_f) is directly related to temperature by the Eq. (4) [17]:

$$\phi_f = \frac{kT}{q} \ln\left(\frac{n}{n_i}\right) \tag{4}$$

where n_i signifies the intrinsic carrier concentration, q denotes the elementary charge, T and k represent temperature, Boltzmann's constant, respectively. The n_i is also dependent on the temperature as $n_i \propto \exp.(-E_g/2kT)$. The increase in temperature increases the intrinsic carrier concentration, resulting in a decreased $\ln(n/n_i)$ term in Eq. (4). Thus, the overall surface potential decreases slightly with the rise in T. The electric field change with temperature along the channel is depicted in Fig. 7(b), and it increases as the temperature is raised from 300 K to 500 K. Also, the electric field at the drain end is significantly lower than the source end, indicating the corner effect's reduction. Figure 8(a) and (b) depicts the corresponding contour profile of the surface potential and electric field with the temperature, respectively.

4.3 Temperature Impact on Analog/RF Performance in GS-GAA FinFET

Figure 9(a) outlines the plot of peak transconductance (g_m) at $V_{gs} = 0.75$ V for temperatures ranging from 300 K to 500 K. Transconductance ($g_m = \partial I_d/\partial V_{gs}$) is a parameter that computes the change in drain current to the shift in V_{gs} at constant V_{ds}. Thus, the transconductance plot shows the same temperature trend as the I_d-V_{gs} plot. At low gate voltage, it increases with an increase in temperature, and at high gate voltage, the opposite behaviour of transconductance is observed. Moreover, it decreases with an increase in temperature owing to the reduction in mobility. The transconductance generation factor (TGF = g_m/I_d) is the proportion of gain generated per unit power loss. A higher value of TGF at low gate voltage indicates a reliable and effective ultra-low-power (ULP) circuit [35]. In the subthreshold region, a higher value of TGF is obtained for all the temperatures considered, as shown in Fig. 9(b), which demonstrates the suitability of GS-GAA FinFET for ULP applications. At low gate voltage, with the increase in T, the increase in I_d is very significant than the rise in g_m, resulting in a decrease in TGF. However, the temperature impact on TGF decreases with an increase in V_{gs} and eventually becomes negligible at high gate voltage.

Figure 9(c) represents the variation of output conductance (g_d) as a function of V_{ds} and T. Output conductance ($g_d = \partial I_d/\partial V_{ds}$) determines the driving ability of a device. It follows the same temperature trend as followed by drain current. At low drain voltage, g_d increases with an increase in temperature and decreases at high V_{ds}. Figure 9(d) reflects the effect of temperature on the early voltage (V_{EA}) as a function of V_{gs}. For the device's enhanced analog performance, early voltage ($V_{EA} = I_d/g_d$) must be as high as possible. In the subthreshold region, the temperature impact on the V_{EA} is almost

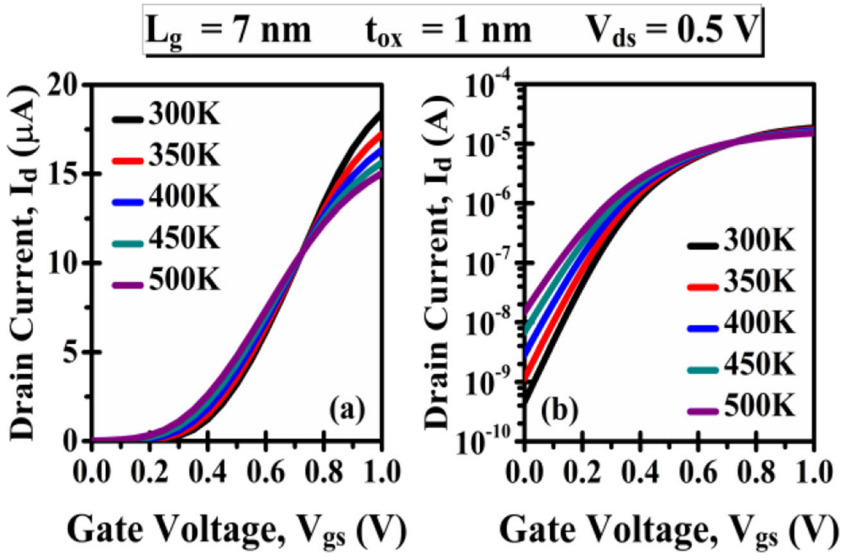

Fig. 5 Impact of temperature variation on transfer characteristics in (**a**) linear scale and (**b**) log scale

negligible. However, early voltage increases with the temperature at a high gate voltage.

Figure 10(a) portrays the temperature impact on total gate capacitance (C_{gg}), and it increases with a rise in T. As the temperature changes from 300 K to 500 K, the carrier concentration in the channel increases due to a reduction in the energy band gap, which increases the charge in the gate region and consequently increases the gate capacitance. The frequency at which current gain becomes unity (0 dB) is the cut-off frequency (f_T) [36]. Figure 10(b) shows the variation of cut-off frequency with T at V_{gs} = 0.65 V. The reduction in peak value of f_T is observed as the temperature is raised from 300 K to 500 K. As expressed in Eq. (5), the main reason for this behaviour is the dependence of f_T on g_m and C_{gg} [37]. The f_T decreases because of an increment in gate capacitance and a reduction in transconductance with temperature. Also, at low gate voltage, f_T increases as temperature rises and falls off at high gate voltage.

$$f_T \approx g_m/2\pi\left(C_{gs}+C_{gd}\right) \tag{5}$$

The gain-bandwidth product (GBP) and gain frequency product (GFP) are essential parameters used in high-frequency applications. Figure 11(a) and (b) depict GBP and GFP variation for temperatures ranging from 300 K to 500 K at V_{gs} = 0.65 V. As specified in Eq. (6) and Eq. (7), the peak value of both GBP and GFP decreases with the rise in temperature due to the increment in gate-drain capacitance (C_{gd}) and reduction in transconductance and cut-off frequency [38, 39].

$$\mathrm{GBP} = g_m/\left(20\pi \times C_{gd}\right) \tag{6}$$

$$\mathrm{GFP} = \left(g_m/g_d\right) \times f_T \tag{7}$$

$$\mathrm{TFP} = \left(g_m/I_d\right) \times f_T \tag{8}$$

$$\mathrm{GTFP} = \left(g_m/g_d\right) \times \left(g_m/I_d\right) \times f_T \tag{9}$$

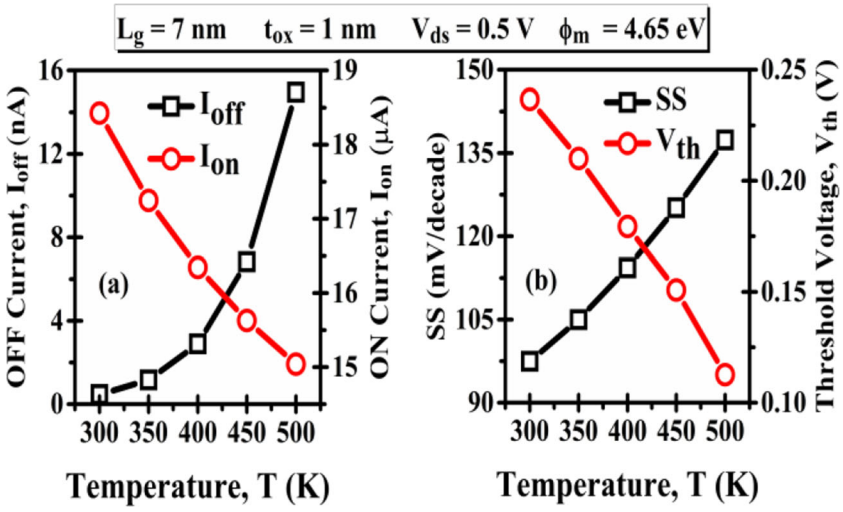

Fig. 6 (**a**) I_{off} current and I_{on} current and (**b**) subthreshold swing and threshold voltage at different temperatures

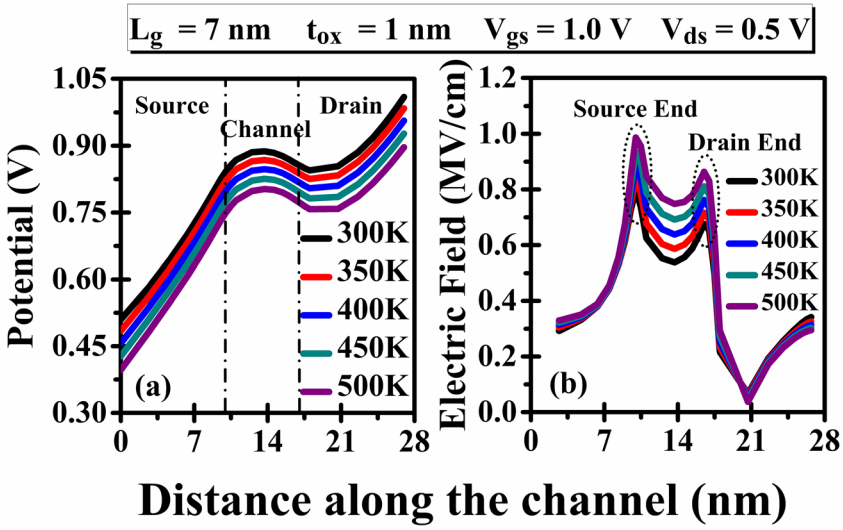

Fig. 7 Impact of temperature variation on (**a**) surface potential and (**b**) electric field

Transconductance frequency product (TFP) is mainly utilized in high-speed designs as it exhibits an agreement between bandwidth and power [40]. In Fig. 11(c), the change in TFP with the temperature is outlined. Transconductance frequency product decreases for higher temperature due to reduced g_m and f_T with a temperature rise, as defined in Eq. (8). Also, TFP shifts towards the low gate bias as temperature changes from 300 K to 500 K due to higher mobility degradation. The gain transconductance frequency product (GTFP) evaluates the complete device performance. As indicated in Eq. (9), GTFP exhibits an agreement between cut-off frequency, TGF, and intrinsic gain. Figure 11(d) displays the temperature impact on GTFP, and as expected, the peak value of GTFP reduces as the temperature is increased from 300 K to 500 K.

4.4 Temperature Impact on Wireless Performance in GS-GAA FinFET

In wireless communication systems, transistors with low distortion parameters are desirable. Linearity is an essential parameter that ensures the least intermodulation and harmonic distortion at the output [41]. The higher-order coefficients of transconductance, i.e., gm_2 and gm_3, provide an estimate about the non-linearity of a transistor. Eq. (10) evaluates these parameters and should be low for better linearity [42].

$$g_{mn} = \left(1/n!\left(\partial^n I_{DS}/\partial V_{GS}^n\right)\right) \quad \text{where, } n = 2, 3 \tag{10}$$

Figure 12(a) and (b) portrays the impact of temperature variation on gm_2, and gm_3 as a function of V_{gs}, respectively. The peak value of gm_2 and gm_3 decreases with the rise in temperature due to the deterioration of short channel characteristics, indicating the device's improved linearity performance. The primary reason for the negative value of gm_2 is the reduction in transconductance at a high gate voltage. The extrapolated gate voltage at which fundamental tone amplitude and second-order harmonic amplitude are equal is VIP2. Similarly, VIP3 is the extrapolated gate voltage at which fundamental tone amplitude is equal to the third-order harmonic amplitude. The high peak value of VIP2 and VIP3, as expressed in Eq. (11) and Eq. (12), respectively, indicates better linearity characteristics of the device [41]. Figure 12(c) and (d) display a plot of VIP2 and VIP3 as a function of V_{gs} for all the temperatures considered, respectively. The peak value of both VIP2 and VIP3 rises with the temperature rise. The reason for this increase is the reduction in gm_2 and gm_3 with the increased temperature.

$$\text{VIP2} = 4 \times (g_m/g_{m2}) \tag{11}$$

$$\text{VIP3} = \sqrt{24 \times (g_m/g_{m3})} \tag{12}$$

The third-order input intercept point (IIP3) is that extrapolated input power at which first and third-order harmonics powers are equal. IMD3, third-order intermodulation distortion, symbolizes the extrapolated intermodulation distortion power at which the first and third-order intermodulation power is equal. Eqs. (13) and (14) evaluates IIP3 and IMD3, respectively [42].

$$\text{IIP3} = (2/3) \times (g_m/(g_{m3}R_s)) \tag{13}$$

$$\text{IMD3} = \left((9/2) \times (\text{VIP3})^2 \times g_{m3}\right)^2 \times R_s \tag{14}$$

where R_s is taken as 50 Ω for analog and RF applications [42].

A high value of IIP3 and a low value of IMD3 are desirable for improved linear characteristics. Figures 13 and 14(a) outlines the impact of temperature variation on IIP3 and IMD3 as a function of V_{gs}, respectively. The value of IIP3 increases with the temperature rise, indicating the improvement in linearity. In the IMD3-V_{gs} plot, for $V_{gs} < 0.5$ V, IMD3 increases

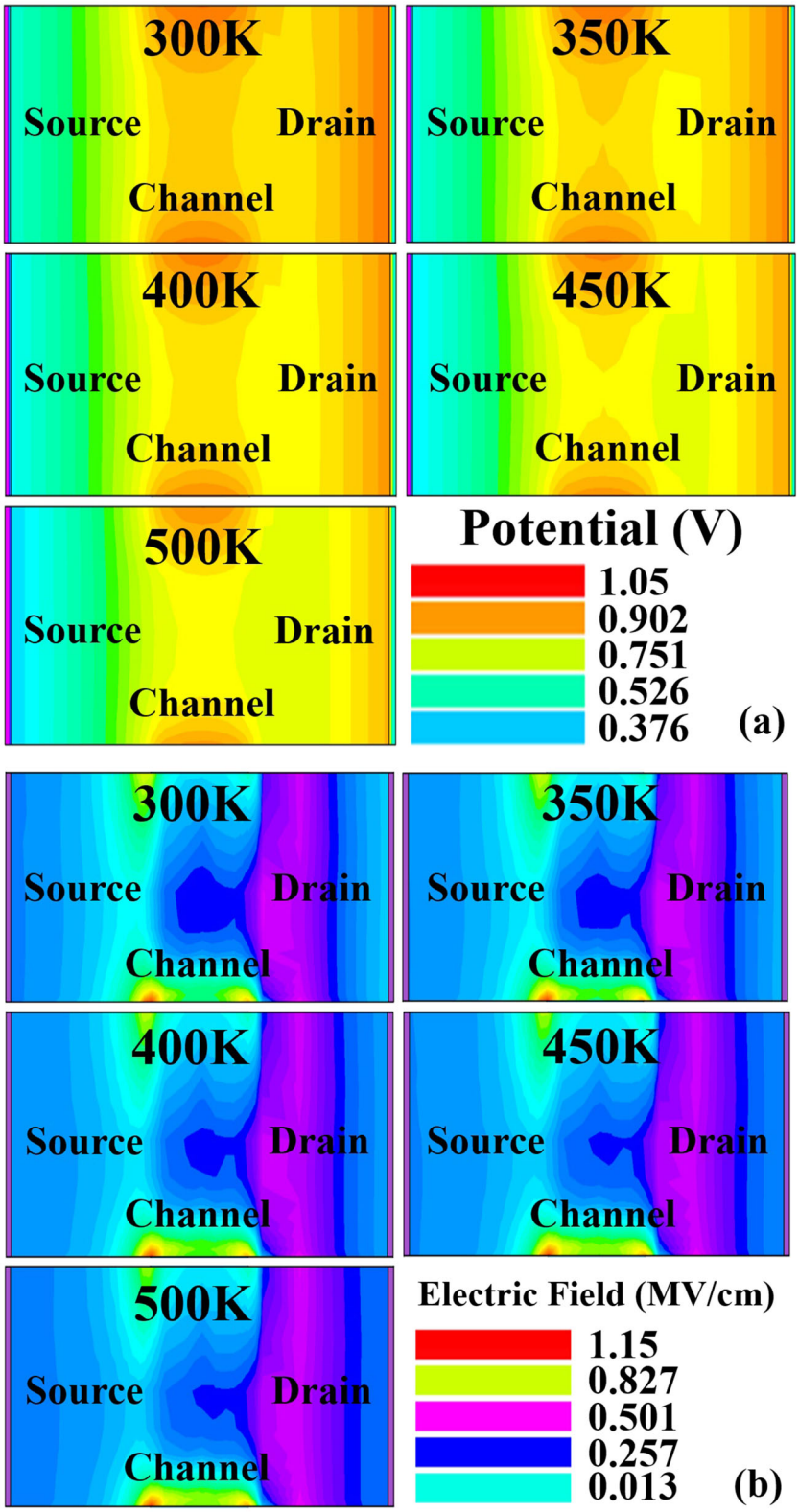

Fig. 8 Contour profile of (**a**) surface potential, and (**b**) electric field at different temperatures

with the temperature, and for $V_{gs} > 0.5$ V, IMD3 decreases with the temperature. Furthermore, at low gate voltage, IIP3 is higher than the IMD3, which implies a reduction in hot carrier effect and improved device performance. 1-dB compression point, as expressed in Eq. (15), is the level of input power at which shifting of output power from linearity by 1 dB occurs. Figure 14(b) reflects the 1-dB compression point variation as a function of V_{gs} and T. The rise in 1-dB

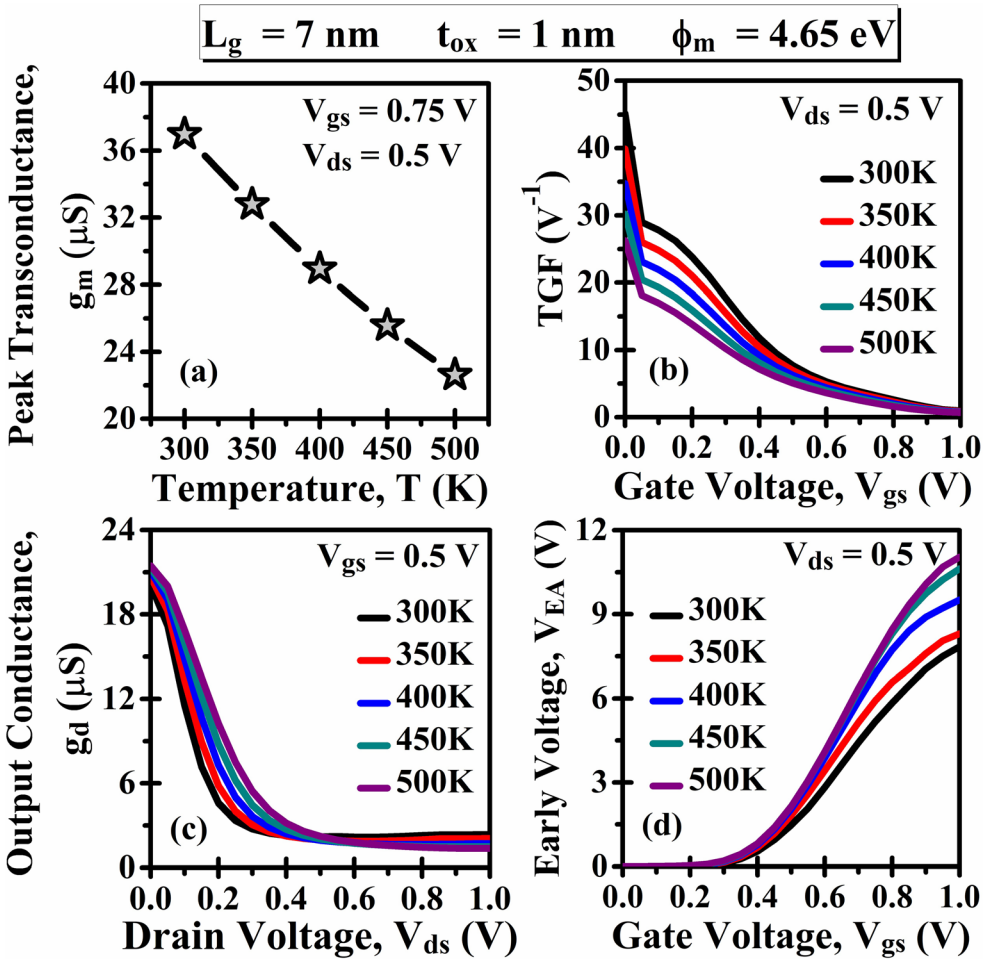

Fig. 9 Impact of temperature variation on (**a**) transconductance (g_m) (**b**) device efficiency (TGF) (**c**) output conductance (g_d) and (**d**) early voltage (V_{EA})

compression point values with temperature indicates superior linearity performance.

$$1\text{−dB compression point} = 0.22 \times \sqrt{(g_m/g_{m3})} \tag{15}$$

$$HD2 = 0.5\, V_a \frac{\left(\frac{dg_m}{dV_{gs}}\right)}{2g_m} \tag{16}$$

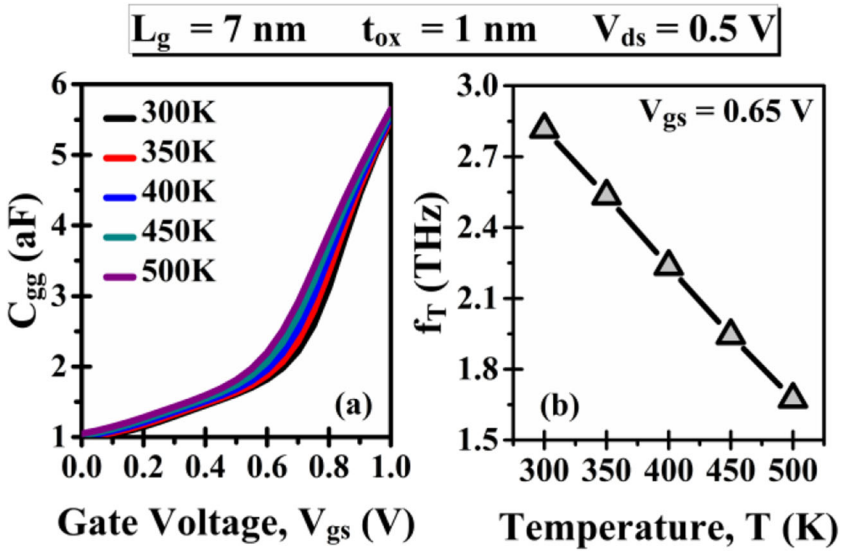

Fig. 10 Impact of temperature variation on (**a**) total gate capacitance (C_{gg}) and (**b**) cut-off frequency (f_T)

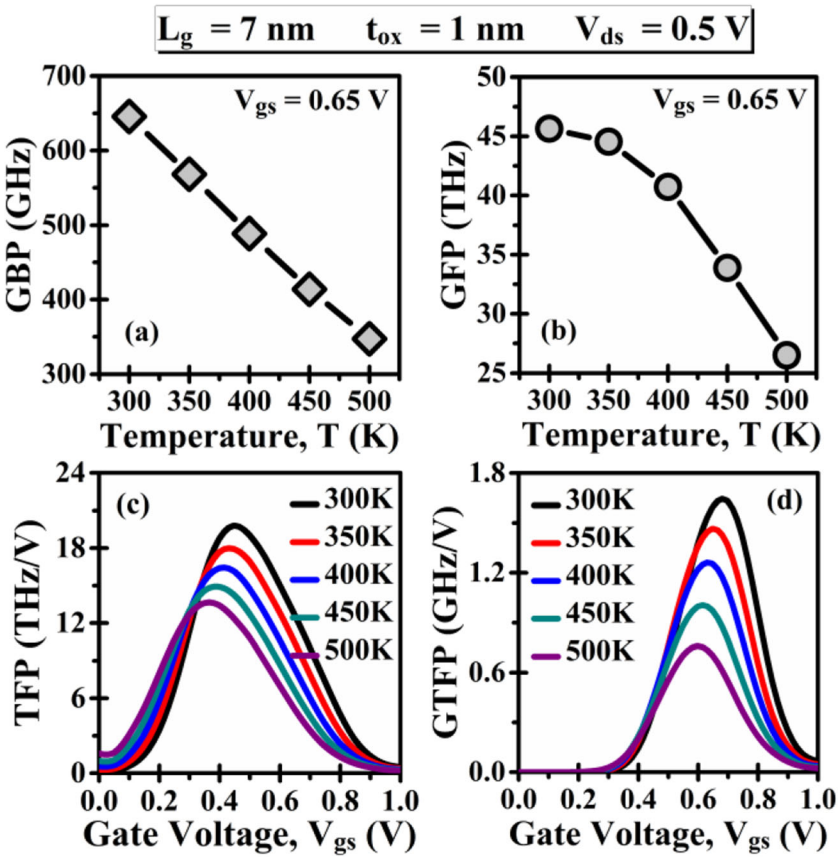

Fig. 11 Impact of temperature variation on (**a**) GBP (**b**) GFP (**c**) TFP and (**d**) GTFP

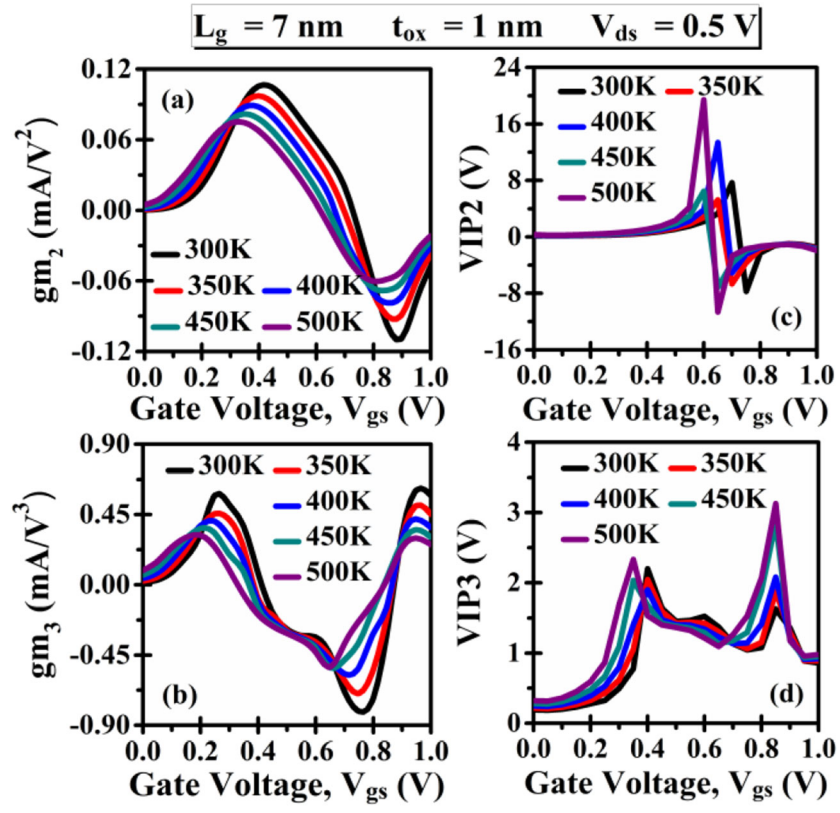

Fig. 12 Impact of temperature variation on (**a**) g_{m2} (**b**) g_{m3} (**c**) VIP2 and (**d**) VIP3

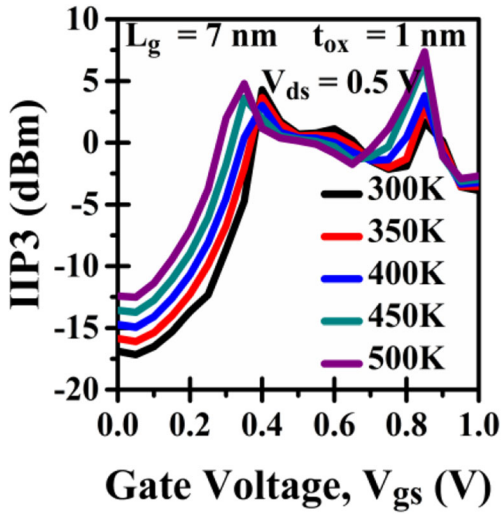

Fig. 13 Impact of temperature variation on IIP3

$$HD3 = 0.25\, V_a^2 \frac{\left(\frac{d^2 g_m}{dV_{gs}^2}\right)}{6 g_m} \tag{17}$$

To evaluate the temperature impact on distortion characteristics, HD2 and HD3 are estimated using the approximate analytical expression given by Eqs. (16) and (17), respectively [43]. The AC signal (V_a) amplitude is taken to be 50 mV [43, 44]. The values of HD2 and HD3 should be as low as possible for lesser distortion in device operation. Figure 14(c) and (d) outlines the temperature impact on HD2 and HD3. The value of HD2 and HD3 decreases with the rise in temperature because, at higher T, due to higher intrinsic carrier density, g_m increases more rapidly than the dg_m/dV_{gs} and d^2g_m/dV^2_{gs}, respectively.

5 Conclusion

It is observed that in GAA FinFET, I_{off} reduces by 59.25%, SS by 6.5%, and I_{on}/I_{off} increases by 152.37% in comparison to TG FinFET. Thus, GAA FinFET can be further scaled-down and is suitable for low-power applications. The ZTC bias point of the GS-GAA FinFET is obtained at $V_{gs} \sim 0.725$ V. The impact of temperature variation on DC, analog, RF, and wireless performance is reported for GS-GAA FinFET. Results revealed that as the temperature rises from 300 K to 500 K, the DC parameters degrade with I_{on} reduced by 18.38%, and SS increased by 40.93%. Analog and RF parameters also deteriorate with the temperature rise with g_m, TGF, f_T, GBP, GFP, TFP, and GTFP reduced by 38.82%, 41.90%,

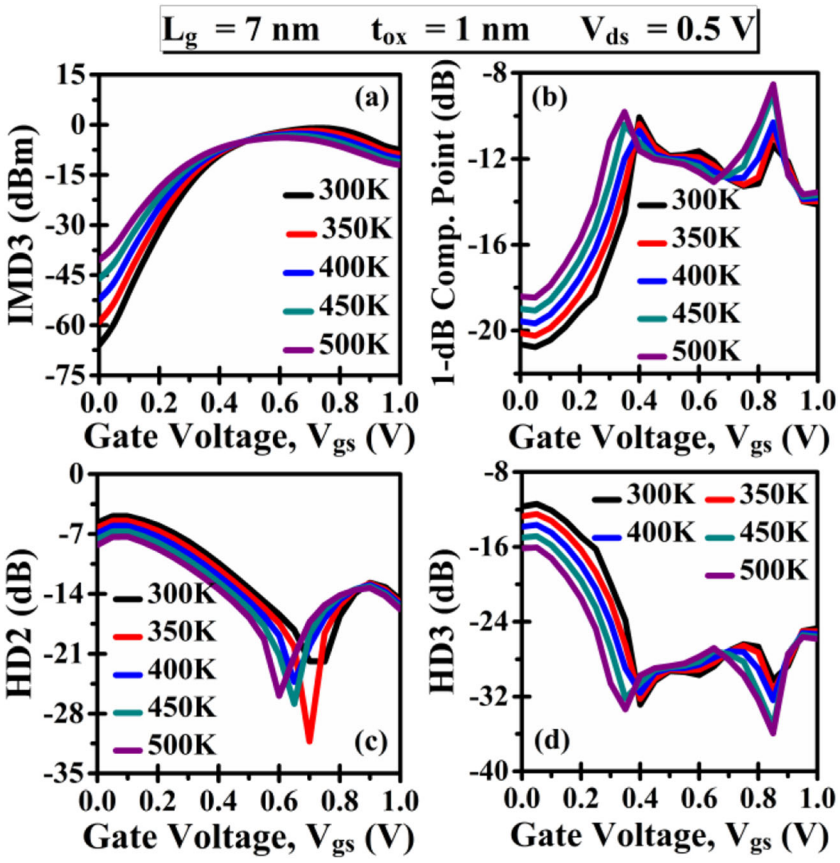

Fig. 14 Impact of temperature variation on (**a**) IMD3 (**b**) 1-dB compression point (**c**) HD2 and (**d**) HD3

40.58%, 46.24%, 41.94%, 31.31%, 53.37%, respectively. On the other hand, with a rise in temperature from 300 K to 500 K, harmonic distortion parameters such as HD3 and HD2 are reduced by 18% approx, and linearity parameters like 1-dB compression point, IIP3, VIP3, VIP2 are significantly improved. Thus, the rise in temperature suppresses the analog, RF performance and enhances the wireless performance of the GS-GAA FinFET.

Acknowledgements The authors acknowledge the Microelectronics Research Laboratory, Delhi Technological University, for assisting this research work.

Availability of Data & Material The authors mentioned above have all the relevant data associated with this research work and will be dedicated to sharing that they will be asked to do so in the future.

Authors' Contribution All authors contributed to the study conception and design.

Declarations The authors have seen all the Ethical Standards and will supposed to follow them in the future.

Consent to Participate & for Publication Since the concerned research paper is based on the 'non-life science journal.' So, 'Not Applicable' here.

However, the authors have gone through all journal policies and consent the authorities for further processing.

Conflict of Interests The authors declare that they have no known conflict of interests or personal relationships that could have influenced the work reported in this paper.

References

1. Kumar A, Gupta N, Chaujar R (2016) TCAD RF performance investigation of transparent gate recessed channel MOSFET. Microelectron J 49:36–42. https://doi.org/10.1016/j.mejo.2015.12.007
2. Jeon DY, Park SJ, Mouis M, Barraud S, Kim GT, Ghibaudo G (2013) Low-temperature electrical characterization of junctionless transistors. Solid State Electron 80:135–141. https://doi.org/10.1016/j.sse.2012.10.018
3. Doria RT, Pavanello MA, Lee CW, Ferain I, Dehdashti-Akhavan N, Yan R, Razavi P, Yu R, Kranti A, Colinge JP (2010) Analog operation and harmonic distortion temperature dependence of nMOS Junctionless transistors. ECS Trans 31(1):13–20. https://doi.org/10.1149/1.3474137
4. Hisamoto D, Lee WC, Kedzierski J, Takeuchi H, Asano K, Kuo C, Anderson E, King TJ, Bokor J, Hu C (2000) FinFET—A self-aligned double-gate MOSFET scalable to 20 nm. IEEE Trans. Electron Devices 47(12):2320–2325. https://doi.org/10.1109/16.887014
5. Huang YC, Chiang MH, Wang SJ, Fossum JG (2017) GAAFET versus pragmatic FinFET at the 5nm Si-based CMOS technology node. IEEE J Electron Devices Soc 5(3):164–169. https://doi.org/10.1109/JEDS.2017.2689738
6. The International Technology Roadmap for Semiconductors 2.0 (2015) Itrpv, 2015 [Online]. Available: http://www.itrs2.net/
7. Lo SH, Buchanan DA, Taur Y, Wang W (1997) Quantum-mechanical modeling of electron tunneling current from the inversion layer of ultra-thin-oxide nMOSFET's. IEEE Electron Device Lett 18(5):209–211. https://doi.org/10.1109/55.568766
8. Ribes G, Mitard J, Denais M, Bruyere S, Monsieur F, Parthasarathy C, Vincent E, Ghibaudo G (2005) Review on high-k dielectrics reliability issues. IEEE Trans Device Mater Reliab 5(1):5–19. https://doi.org/10.1109/TDMR.2005.845236
9. Gupta N, Kumar A (2020) Assessment of High-k Gate Stack on Sub-10 nm SOI-FinFET for High-Performance Analog and RF Applications Perspective. ECS J Solid State Sci Technol 9(12):123009. https://doi.org/10.1149/2162-8777/abcf14
10. Robertson J (2004) High dielectric constant oxides. Eur Phys J Appl Phys 28:265–291. https://doi.org/10.1051/epjap:2004206
11. Onishi K, Kang CS, Choi R, Cho HJ, Gopalan S, Nieh RE, Krishnan SA, Lee JC (2003) Improvement of surface carrier mobility of HfO2 MOSFETs by high-temperature forming gas annealing. IEEE Trans Electron Devices 50(2):384–390. https://doi.org/10.1109/TED.2002.807447
12. Kerber A, Cartier E, Pantisano L, Degraeve R, Kauerauf T, Kim Y, Hou A, Groeseneken G, Maes HE, Schwalke U (2003) Origin of the threshold voltage instability in SiO2/HfO2 dual layer gate dielectrics. IEEE Electron Device Lett 24(2):87–89. https://doi.org/10.1109/LED.2003.808844
13. Gupta N, Chaujar R (2016) Optimization of high-k and gate metal work function for improved analog and intermodulation performance of gate stack (GS)-GEWE-SiNW MOSFET. Superlattice Microst 97:630–641. https://doi.org/10.1016/j.spmi.2016.07.021
14. Mohapatra SK, Pradhan KP, Singh D, Sahu PK (2015) The role of geometry parameters and fin aspect ratio of sub-20nm SOI-FinFET: an analysis towards analog and RF circuit design. IEEE Trans Nanotechnol 14(3):546–554. https://doi.org/10.1109/TNANO.2015.2415555
15. Madan J, Chaujar R (2018) Temperature associated reliability issues of heterogeneous gate dielectric-gate all around-tunnel FET. IEEE Trans Nanotechnol 17(1):41–48. https://doi.org/10.1109/TNANO.2017.2650209
16. Dutta A, Koley K, Saha SK, Sarkar CK (2016) Impact of temperature on linearity and harmonic distortion characteristics of underlapped FinFET. Microelectron Reliab 61:99–105. https://doi.org/10.1016/j.microrel.2016.01.017
17. Kumar A, Gupta N, Chaujar R (2020) Reliability of Sub-20 nm black phosphorus trench (BP-T) MOSFET in high-temperature harsh environment. Silicon:1–7. https://doi.org/10.1007/s12633-020-00531-0
18. Akarvardar K, Mercha A, Simoen E, Subramanian V, Claeys C, Gentil P, Cristoloveana S (2007) High-temperature performance of state-of-the-art triple-gate transistors. Microelectron Reliab 47(12):2065–2069. https://doi.org/10.1016/j.microrel.2006.10.002
19. Groeseneken G, Colinge JP, Maes HE, Alderman JC, Holt S (1990) Temperature dependence of threshold voltage in thin-film SOI MOSFET's. IEEE Electron Device Lett 11(8):329–331. https://doi.org/10.1109/55.57923
20. Das RR, Maity S, Muchahary D, Bhunia CT (2017) Temperature dependent study of fin-FET drain current through optimization of controlling gate parameters and dielectric material. Superlattice Microst 103:262–269. https://doi.org/10.1016/j.spmi.2017.01.041
21. Saha R, Goswami R, Bhowmick B, Baishya S (2020) Dependence of RF/analog and linearity figure of merits on temperature in ferroelectric FinFET: a simulation study. IEEE Trans Ultrason Ferroelectr Freq Control 3010(c):1–6. https://doi.org/10.1109/TUFFC.2020.2999518
22. Bhattacharya D, Jha NK (2014) FinFETs: from devices to architectures. Adv Electron 2014:21–55. https://doi.org/10.1155/2014/365689

23. Kumar B, Kumar A, Chaujar R (2020) The Effect of Gate Stack and High-K Spacer on Device Performance of a Junctionless GAA FinFET. In IEEE VLSI Device, Circuit and System Conference (VLSI-DCS), pp 159–163. https://doi.org/10.1109/VLSIDCS47293.2020.9179855
24. Biswas K, Sarkar CK (2018) Optimizing Fin aspect ratio of junctionless bulk FinFET for application in Analog/RF circuit, in 2018 IEEE Electron Devices Kolkata Conference (EDKCON), pp 591–595. https://doi.org/10.1109/EDKCON.2018.8770515
25. Liu Y, Kijima S, Sugimata E, Masahara M, Endo K, Matasukawa T, Ishii K, Sakamoto K, Sekigawa T, Yamauchi H, Takanashi Y, Suzuki E (2006) Investigation of the TiN gate electrode with tunable work function and its application for FinFET fabrication. IEEE Trans Nanotechnol 5(6):723–728. https://doi.org/10.1109/TNANO.2006.885035
26. Vitale SA, Kedzierski J, Healey P, Wyatt PW, Keast CL (2011) Work-function-tuned TiN metal gate FDSOI transistors for subthreshold operation. IEEE Trans Electron Devices 58(2):419–426. https://doi.org/10.1109/TED.2010.2092779
27. ATLAS (2016) User's manual. SILVACO International, Santa Clara
28. Arora ND, Hauser JR, Roulston DJ (1982) Electron and hole Mobilities in silicon as a function of concentration and temperature. IEEE Trans Electron Devices 29(2):292–295. https://doi.org/10.1109/T-ED.1982.20698
29. Gupta N, Kumar A, Chaujar R (2015) Impact of device parameter variation on RF performance of gate electrode workfunction engineered (GEWE)-silicon nanowire (SiNW) MOSFET. J Comput Electron 14(3):798–810. https://doi.org/10.1007/s10825-015-0715-z
30. Lee H, Yu LE, Ryu SW, Han JW, Jeon K, Jang DY, Kim KH, Lee J, Kim JH, Jeon SC, Oh JS, Park YC, Bae WH, Lee HM, Yang JM, Yoo JJ, Kim SI, Choi YK (2006) Sub-5nm all-around gate FinFET for ultimate scaling. Digest Tech Papers-Sympos VLSI Technol 25(9):58–59. https://doi.org/10.1109/VLSIT.2006.1705215
31. Lee CW, Borne A, Ferain I, Afzalian A, Yan R, Akhavan ND, Razavi P, Colinge JP (2010) High-temperature performance of silicon junctionless MOSFETs. IEEE Trans Electron Devices 57(3):620–625. https://doi.org/10.1109/TED.2009.2039093
32. Osman AA, Osman MA, Dogan NS, Imam MA (1995) Zero-temperature-coefficient biasing point of partially depleted SOI MOSFET's. IEEE Trans Electron Devices 42(9):1709–1711. https://doi.org/10.1109/16.405293
33. Barman KR, Baishya S (2020) Study of temperature effect on analog/RF and linearity performance of dual material gate (DMG) vertical super-thin body (VSTB) FET. Silicon. https://doi.org/10.1007/s12633-020-00561-8
34. Saha R, Bhowmick B, Baishya S (2018) Temperature effect on RF/analog and linearity parameters in DMG FinFET. Appl Phys A Mater Sci Process 124(9):1–10. https://doi.org/10.1007/s00339-018-2068-5
35. Sahu PK, Mohapatra SK, Pradhan KP (2014) Impact of downscaling on analog/RF performance of sub-100nm GS-DG MOSFET. Inf MIDEM 44(2):119–125
36. Madan J, Chaujar R (2016) Gate drain-overlapped-asymmetric gate dielectric-GAA-TFET: a solution for suppressed ambipolarity and enhanced ON state behaviour. Appl Phys A Mater Sci Process 122(11):973. https://doi.org/10.1007/s00339-016-0510-0
37. Malik P, Gupta RS, Chaujar R, Gupta M (2012) AC analysis of nanoscale GME-TRC MOSFET for microwave and RF applications. Microelectron Reliab 52(1):151–158. https://doi.org/10.1016/j.microrel.2011.07.070
38. Pradhan KP, Mohapatra SK, Sahu PK, Behera DK (2014) Impact of high-k gate dielectric on analog and RF performance of nanoscale DG-MOSFET. Microelectron J 45(2):144–151. https://doi.org/10.1016/j.mejo.2013.11.016
39. Kumar B, Chaujar R (2021) Analog and RF performance evaluation of Junctionless accumulation mode (JAM) gate stack gate all around (GS-GAA) FinFET. Silicon. https://doi.org/10.1007/s12633-020-00910-7
40. Kumar A, Tripathi MM, Chaujar R (2017) Investigation of parasitic capacitances of In2O5Sn gate electrode recessed channel MOSFET for ULSI switching applications. Microsyst Technol 23(12):5867–5874. https://doi.org/10.1007/s00542-017-3348-2
41. Kumar SP, Agrawal A, Chaujar R, Gupta RS, Gupta M (2011) Device linearity and intermodulation distortion comparison of dual material gate and conventional AlGaN/GaN high electron mobility transistor. Microelectron Reliab 51(3):587–596. https://doi.org/10.1016/j.microrel.2010.09.033
42. Ghosh P, Haldar S, Gupta RS, Gupta MG (2012) An investigation of linearity performance and intermodulation distortion of GME CGT MOSFET for RFIC design. IEEE Trans Electron Devices 59(12):3263–3268. https://doi.org/10.1109/TED.2012.2219537
43. Kumar A, Gupta N, Tripathi SK, Tripathi MM, Chaujar R (2020) Performance evaluation of linearity and intermodulation distortion of nanoscale GaN-SOI FinFET for RFIC design. AEU - Int J Electron Commun 115:153052. https://doi.org/10.1016/j.aeue.2019.153052
44. Gupta N, Chaujar R (2016) Investigation of temperature variations on analog/RF and linearity performance of stacked gate GEWE-SiNW MOSFET for improved device reliability. Microelectron Reliab 64:235–241. https://doi.org/10.1016/j.microrel.2016.07.095

Publisher's Note Springer Nature remains neutral with regard to jurisdictional claims in published maps and institutional affiliations.

International Research Journal of Engineering and Technology (IRJET) e-ISSN: 2395-0056
Volume: 08 Issue: 03 | Mar 2021 www.irjet.net p-ISSN: 2395-0072

TWO-STAGE CUSTOMER SEGMENTATION USING K-MEANS CLUSTERING AND ARTIFICIAL NEURAL NETWORK

Harshit Muhal[1], Harsh Jain[2]

[1]*Student, Dept. of Computer Engineering, Delhi Technological University, Delhi, India*
[2]*Student, Dept. of Computer Engineering, Delhi Technological University, Delhi, India*

Abstract - *Customer segmentation is a very important technique used by companies to target their product features and prices and better serve their customers providing them the best of both worlds. In this project, we use the K-means algorithm to perform customer segmentation on data and try to analyze the results with regards to how many clusters give us the best results and use clustering. Then we train a neural network on the data obtained from clustering to classify new samples so as to present the problem in a supervised way instead of finding clusters using K-means in an unsupervised fashion. Using Neural networks we have not only segmented data into various clusters to perform customer segmentation but we also managed to capture the complex relationships that exist between the data attributes and the different clusters the observation points belong to without sacrificing the generalization used for the formation of initial clusters. We received an accuracy of 90.62% on training and 92.5% on the testing data.*

Key Words: Customer segmentation, clustering, Neural Networks, K-Means, Two-stage approach.

1. INTRODUCTION

In today's highly competitive world, companies need a way to efficiently make and manage products, in regard to their pricing, features, as well as other add-ons. Machine learning is one of the latest fields in innovation and engineering with applications in a vast variety of topics, subjects, and ways. Since machine learning is based around data, it is perfect for a data-centric world such as ours. By using this technology, we can efficiently perform customer segmentation, which is the task of dividing customers into classes that will group customers with similar purchasing behavior, feature demands, or other factors such as geographical variance, add-on, and extra services demanded, etc. This makes companies make better products as they can model their product around the classes of customers they want to cater to and thus balance both the features and price of the products giving the customers the best of both worlds.

Past work done in the field of customer segmentation includes the use of the Apriori algorithm [1], which is one of the fastest and earliest tools for association mining for segmentation. The use of Customer Value and Customer Behavior is made in customer segmentation using data mining techniques of simple CRM method for mobile VIP customer segmentation in [2]. In [3] Customer segmentation is done using an integrated approach with the Apriori algorithm as well as CRM method with associated mining, bringing the benefits of both these methods to solve this problem. In [4] The customer segmentation was done based on the e-commerce data . In [5], two approaches using LRFM (Length, Recency, Frequency, Monetary) model and extended model called LRFM -Average Item (AI) model were used for customer segmentation, in this, they found that adding simple parameter and averages did not produce better segmentation and did not show a significant difference in results indicating that complex parameters are required to get better results for customer segmentation.[6] showed an analysis of silent customers were performed and as silent customers are part of customers that a company can very easy to lose. Thus, it is necessary to analyze the features of such customers and make appropriate market decisions. To improve the enterprise's revenue in the telecom industry, that paper proposed a K-means++ method for customer segmentation based on silent customers. In [7], a segmentation algorithm based on density-based spatial clustering of applications with noise(DBSCAN) along with the K-means method was designed to satisfy the requirement of the Yunnan Electricity Market. In [8] K-means clustering technique and SPSS Tool were used to develop a real-time and online system to predict seasonal sales on annual cycles, which incorporated an important complex parameter of temporal spikes in sales of certain items. [9] chronicles the use of unsupervised machine learning to solve the problem of customer segmentation using the data for credit card based purchases for users in Africa. In [10]

Customer segmentation using a multi-layer perceptron (MLP) neural network which classifies customers into different sets according to attributes.

1.1 Advantage Over Other Methods

These methods use either a single complex technique or merge a few simpler ones to solve the task of customer segmentation and thus are mostly able to generalize well and some approaches are also able to capture a few complex parameters such as the inclusion of silent customers, but still lack the ability to deal extensively with the complex relationships which are required to be processed for better segmentation. These complex relationships give rise to some invisible parameters which are not directly obtained from the customers but form an important part of the segmentation task. The first stage of our approach helps in generalizing the classes with the initial formation of clusters. The second stage with the neural network helps capture the intricacies of these relationships between customers by selecting which attributes to use and combining them to form newer complex attributes that are present in the hidden layers of the network.

1.2 Contribution Of This Work

This paper introduces the idea of using a two-stage approach for customer segmentation, unlike any which has been proposed earlier. This method uses both unsupervised and supervised learning methods to achieve a meaningful segmentation and continuously update the model with new data without having to do the whole process again thus reducing the resources required for the task. This method also discusses the need to view and process complex relationships between the customers as part of the segmentation process which has not been discussed in earlier works.

2. THE DATA

The data used for this project has some basic information like Customer ID, annual income, spending score, gender, and age of the customer. The Spending Score is a variable that is calculated based on customer behavior and purchasing information. In the dataset, it is already calculated and available to us. The data is available at LINK.

3. METHODOLOGY

1. **Data Collection:** This step involves the collection of customer data which includes attributes like Age, Gender, income, and spendings.
2. **Data Preprocessing:** It involves Preprocessing of data by removing features that bring redundancy to the data and keeping only necessary features.
3. **Training:** Use the K-means algorithm to cluster the customers into different segments.
4. **Testing:** clusters will be used for extracting the associative buying pattern of the segmented customer to benefit the organization.
5. **Labeling:** Each observation in the dataset is labeled with the cluster it belongs to. This data will act as a base for training the neural networks.
6. **Model Architecture:** Feed-forward neural network is made for the prediction of the cluster to which a given observation belongs.
7. **Training Neural Network:** Training the neural network by using appropriate optimizers like Adam and loss functions like categorical cross-entropy.
8. **Predictions:** Neural Network is used to predict the cluster to which the given observation belongs to.

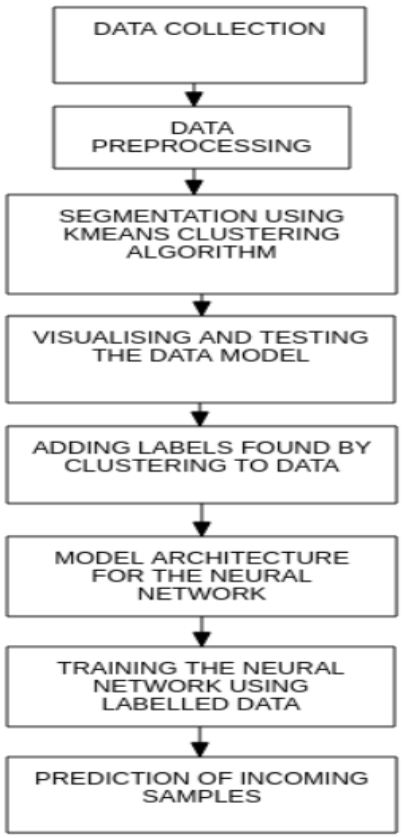

Fig -1: Methodology

4. K-Means Technique

K-Means is an algorithm that works iteratively and attempts to isolate the dataset into K distinct non-overlapping subgroups. The K-means algorithm assigns each observation in data to the cluster such that the squared distance of that point from the centroid of the cluster is minimum. Kmeans algorithm tries to attain a configuration in which clusters are far from each other but points in each cluster are similar.

K-Means algorithm follows the principle of expectation and maximization which consists of the following procedure:

1. Initialize all cluster centers randomly.
2. Repeat the steps given below until convergence.
3. E-Step: Points are assigned to the cluster center with a minimum distance from the point.
4. M-Step: New Cluster center will be updated to the mean.

The Expectation step is responsible for updating the expectation of which cluster each point belongs to. To do it the distance of the points is calculated from each cluster. The Maximization step is responsible for maximizing a cost function that represents the location of the centroid of the clusters. In K-Means maximization is done by taking a mean of the data in each cluster.

If we have (x1, x2,....., xn) as input, where each observation in the input is a p-dimensional vector with real values. K-Means will divide the input into k clusters (k<=n).

4.1 K-means Algorithm

1. **Begin** with input as X=(x1,x2,...xn)
2. **Initial Centroids** are taken as C1, C2,...Ck.
3. **Assign points** to the cluster which has a minimum distance from the point.
4. **Determine:** Update all Centroids -C1, C2,..Ck
5. **Repeat:** Until the significant change is not seen in centroids.
6. **Output:** Final Centroids - C1, C2,...Ck
7. **End**

5. DEEP NEURAL NETWORKS

Deep Neural Networks are used in modern computing in a variety of applications such as computer vision and NLP. This is due to their merit of being able to identify complex relationships by breaking them into smaller parts. We have used this deep neural network to classify new customers into the clusters by training on the labeled data we obtained by running k means on the unlabeled source data.

5.1 FULLY CONNECTED DENSE LAYER

A fully connected dense layer is a layer of neurons, each of which is connected to all the neurons of the previous layer, this helps us as we can weigh in all the possible combinations pertaining to the relationships.

5.2 DROPOUT LAYER

Dropout helps us reduce overfitting in our model so that even though the relationships are complex, they can still be generalized over a large audience. This layer sets weights of few edges passing through it to 0 during the forward training process. Since this happens randomly and variably, this reduces the chances of us missing out on better relationships.

5.3 BATCH NORMALIZATION

Batch normalization helps us to reduce training time as it normalizes the data using the mean. This helps with reducing computation resources required as everything is scaled using the mean and thus elementary operations are faster to perform(numbers are smaller). This adds the batch mean and standard deviation as parameters for our model.

5.4 PROPOSED NEURAL NETWORK :

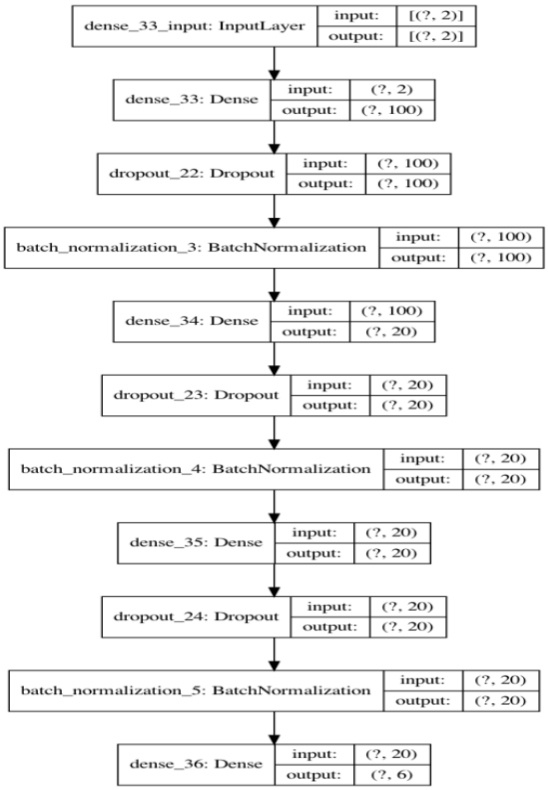

Fig -2: Model Architecture

In our experiment, we used a sequential deep neural network of fully connected dense layers. There are 4 fully

connected dense layers in the model with 100, 20, 6, 6 numbers of neurons in each layer respectively. Each dense layer is followed by one Dropout layer and one Batch Normalisation Layer. All dropout layers have a frequency of rate 0.5 while the Batch Normalization layer doesn't have any parameters.

6. EXPERIMENTATION:

Clusters were obtained for different numbers of cluster centers as 4,5,6,7.

For training neural network RMSprop and adam optimizers were experimented and the best results were provided by adam optimizer. For our dataset optimal no of epochs was around 200 and no of dense layers were 4. Training is done in 2 parts. Different learning rates with values 0.005, 0.008,0.01 were experimented with. The model was trained with a learning rate of 0.001 for 200 epochs then the model is trained further trained but with a different learning rate that is 0.0001. The best model was saved by creating checkpoints by monitoring the accuracy.

For both stages training various parts of the model was done using google colab (collaboratory). Python 3.7.6 is used to write code for the project. Different Libraries like Numpy, Pandas, random, matplotlib, Keras, scikit-learn, and seaborn were used.

Chart -1: Training

7. Accuracy:

Accuracy = No of Correct predictions/ Sample Size

The model was able to get 90.625% accuracy on training data and 92.5% on the testing data.

8. RESULTS AND ANALYSIS:

8.1 Clustering With Different Values Of Cluster Centers

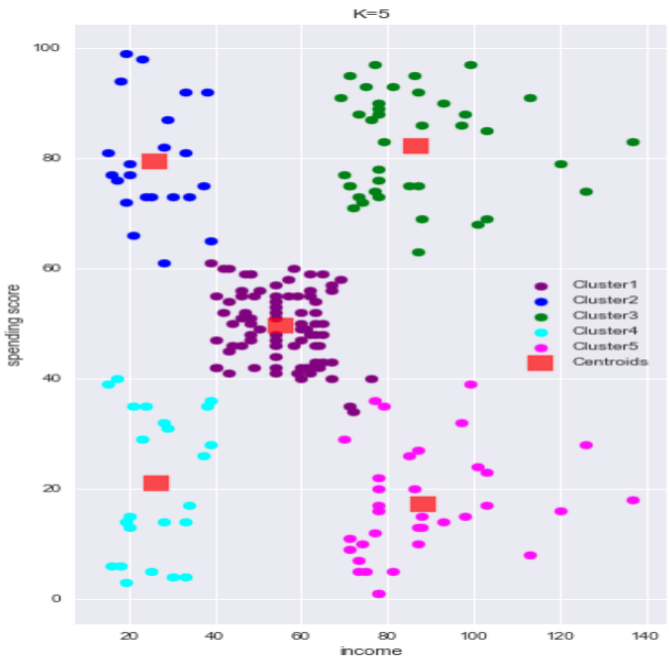

Chart - 2.1: Clustering with k=5

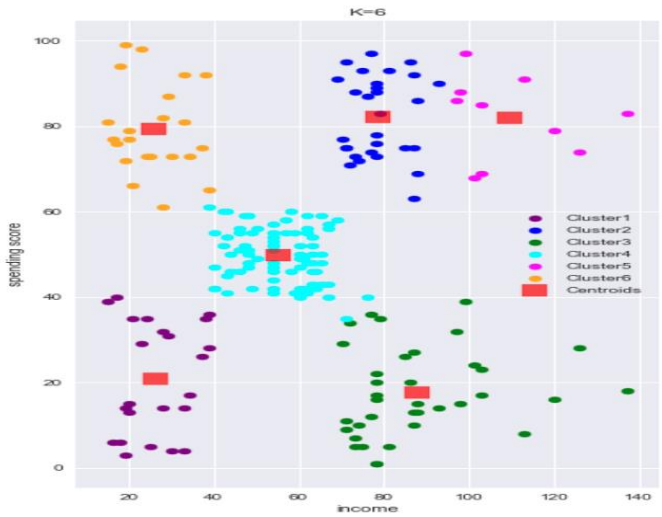

Chart - 2.2: Clustering with k=6

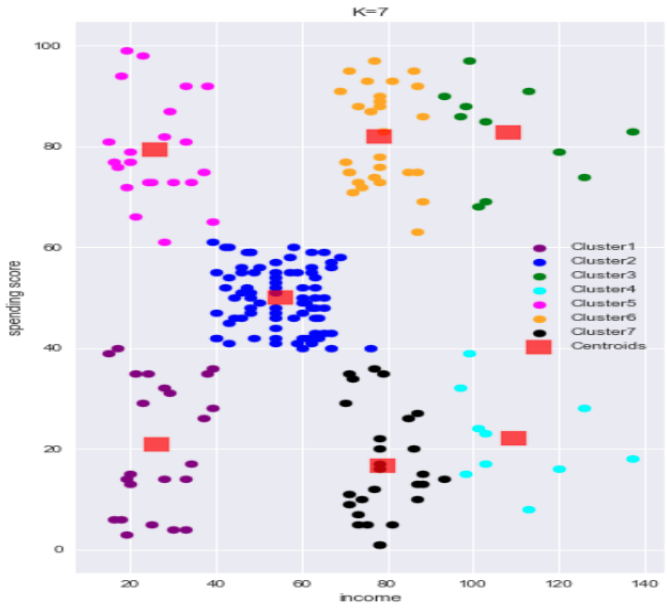

Chart - 2.3: Clustering with k=7

For the first clustering with k=5 as shown in chart 2.1, we see that we get some meaningful clusters but cluster 3 seems to try to integrate varied data into a single cluster and is thus constricted with this value.

For clustering with k=6 in chart 2.2, we see cluster 3 is broken into two clusters which have a better representation of the target audience and a meaningful split in the clusters.

For clustering with k=7 shown in chart 2.3, we see that the clusters are now being forced to split meaningful clusters into even more groups that incorporate noisy data into these clusters.

We see that for the value of k=6 we get the best results for our data with meaningful clusters whereas other values either miss clusters or try to integrate noise into the clusters. This value of k can be decided based on the data.

8.2 Cluster Analysis

Here are our findings from the clusters obtained :

Cluster 1 has medium income and low expenditure annually

Cluster 2 has low income and low annual spend

Cluster 3 has both income and annual spend high.

Cluster 4 has low income but has high annual spending.

Cluster 5 has both income and annual expenditure as a medium.

Cluster 6 has even higher income and high annual spending.

8.3 Key Strategies For These Clusters

Both clusters 3 and 6 have higher income and high expenditure, this might lead to strategizing the most feature-full and top quality products and services for them.

Cluster 4 has a low income and high expenditure, this reveals that they show some aspect of branding impact so they can be targeted with a discount or promotional offers on higher-end brand valued products.

Clusters 1 and 2 have lower expenditure so the focus for them would be basic level features or products which bring the best features for the price.

Cluster 5 has some flexibility as to what strategies can be applied to them, this brings some flexibility to the strategies that can be applied to them with a mixture of promotional offers for higher-end products to improve the best-valued products and services by a small margin to accommodate for the increased demand for features.

The reaction of clusters 1,2 and 5 will provide important information as to how the market will be progressing in terms of feature importance at a basic stage and feature qualities, i.e the quality of features at the upper level of expenditure.

9. CONCLUSION:

In this paper, various solutions to customer segmentation proposed by various authors have been explored. Using the K-Means technique we were able to cluster the data into meaningful clusters and provided key strategies based on associative customer behavior as observed from the obtained clusters. A Feed-Forward neural network was trained to present the customer segmentation as a supervised problem.

10. FUTURE SCOPE:

Algorithms like DBSCAN, CRM and LRFM, Fuzzy clustering, and Hierarchical clustering may be tried for the primary stage of clustering. These may prove to be advantageous in different scenarios based on different datasets. For the second stage, to capture relationships between data attributes and clusters more complex layers can be added in the neural network like convolutional layers. Different values of the learning rate, batch size, and other hyperparameters can also be experimented with.

ACKNOWLEDGEMENT

We would like to thank **Sanjay Patidar**, Assistant professor in the Department of Computer Engineering,

Delhi Technological University (Formerly Delhi College of Engineering), Delhi, India for his continuous support and encouragement throughout the process and for guiding us while writing the research paper. We offer him our sincere appreciation for his excellent supervision.

REFERENCES

[1] S. S. Güllüoğlu, "Segmenting customers with data mining techniques," in International Conference on Digital Information, Networking, and Wireless Communications, Moscow, Russia, Feb. 2015, pp. 154-159.

[2] Z. Yihua, "Vip customer segmentation based on data mining in mobile-communications industry", Computer Science and Education (ICCSE) 2010 5th International Conference on, pp. 156-159, 2010.

[3] Balmeet Kaur, Pankaj Kumar Sharma, "Implementation of Customer Segmentation using Integrated Approach", IJITEE, ISSN: 2278-3075, Volume-8 Issue-6S, April 2019.

[4] Juni Nurma Sari1,2, Lukito Edi Nugroho ,Ridi Ferdiana ,P. Insap Santosa, "Review on Customer Segmentation Technique on Ecommerce",American Scientific Publishers, Vol. 4, 400–407, 2011.

[5] Pradnya Paramita Pramono, Isti Surjandari, Enrico Laoh , "Estimating Customer Segmentation based on Customer Lifetime Value Using Two-Stage Clustering Method", 2019 16th International Conference on Service Systems and Service Management (ICSSSM).

[6] Yuhang Qiu , Pingping Chen , Zhijian Lin , Yongcheng Yang , Lanning Zeng , Yaqi Fan, "Clustering Analysis for Silent Telecom Customers Based on K-means++",2020 IEEE 4th Information Technology, Networking, Electronic and Automation Control Conference (ITNEC), pp. 123-127.

[7] Xuejin Wang *et al*, "Electricity Market Customer Segmentation Based on DBSCAN and K-Means", 2020 Asia Energy and Electrical Engineering Symposium, pp. 869-874.

[8] Kishana R. Kashwan, Member, IACSIT, and C. M. Velu,"Customer Segmentation Using Clustering and Data Mining Techniques", IJCTE Journal, Vol. 5, No. 6, December 2013.

[9] Eric Umuhoza, Dominique , Jane Awuah , and Beatrice Birir, "Using Unsupervised Machine Learning Techniques for Behavioral-based Credit Card Users Segmentation in Africa", Vol.111(3) September 2020.

[10] Şukru Ozan and Leonardo O. Iheme, "Artificial Neural Networks in Customer Segmentation", 2019 27th Signal Processing and Communications Applications Conference (SIU).